Lecture Notes in Civil Engineering

Mahendrakumar Madhavan
James S. Davidson
N. Elumalai Shanmugam *Editors*

# Proceedings of the Indian Structural Steel Conference 2020 (Vol. 1)

ISSC 2020

Springer

# Lecture Notes in Civil Engineering

Volume 318

**Lecture Notes in Civil Engineering** (LNCE) publishes the latest developments in Civil Engineering—quickly, informally and in top quality. Though original research reported in proceedings and post-proceedings represents the core of LNCE, edited volumes of exceptionally high quality and interest may also be considered for publication. Volumes published in LNCE embrace all aspects and subfields of, as well as new challenges in, Civil Engineering. Topics in the series include:

- Construction and Structural Mechanics
- Building Materials
- Concrete, Steel and Timber Structures
- Geotechnical Engineering
- Earthquake Engineering
- Coastal Engineering
- Ocean and Offshore Engineering; Ships and Floating Structures
- Hydraulics, Hydrology and Water Resources Engineering
- Environmental Engineering and Sustainability
- Structural Health and Monitoring
- Surveying and Geographical Information Systems
- Indoor Environments
- Transportation and Traffic
- Risk Analysis
- Safety and Security

To submit a proposal or request further information, please contact the appropriate Springer Editor:

– Pierpaolo Riva at pierpaolo.riva@springer.com (Europe and Americas);
– Swati Meherishi at swati.meherishi@springer.com (Asia—except China, Australia, and New Zealand);
– Wayne Hu at wayne.hu@springer.com (China).

**All books in the series now indexed by Scopus and EI Compendex database!**

Mahendrakumar Madhavan · James S. Davidson · N. Elumalai Shanmugam
Editors

# Proceedings of the Indian Structural Steel Conference 2020 (Vol. 1)

ISSC 2020

Springer

*Editors*
Mahendrakumar Madhavan
Structural Steel Research Group
Department of Civil Engineering
Indian Institute of Technology Hyderabad
Sangareddy, India

James S. Davidson
Department of Civil and Environmental Engineering
Auburn University
Auburn, AL, USA

N. Elumalai Shanmugam
Former Professor
National University of Singapore
Queenstown, Singapore

Former Professor
National University of Malaysia
Selangor, Malaysia

Chennai, India

ISSN 2366-2557 ISSN 2366-2565 (electronic)
Lecture Notes in Civil Engineering
ISBN 978-981-19-9389-3 ISBN 978-981-19-9390-9 (eBook)
https://doi.org/10.1007/978-981-19-9390-9



This Springer imprint is published by the registered company Springer Nature Singapore Pte Ltd.
The registered company address is: 152 Beach Road, #21-01/04 Gateway East, Singapore 189721, Singapore

# Foreword I

Civil infrastructure is universally an area requiring continued attention of the engineers and architects, be it because of creation of additions, or, the quest for improved quality. The volume of additional infrastructure needed is huge in many countries including India. Fulfilment of this demand has to be backed by an adequate supply of building materials, of which the two that are most commonly in use are either concrete or steel. Structurally, both these have their merits, whether used separately, or as steel-concrete composites. Steel offers the merits of high strength-to-weight ratio, thus reduced deadweights, superior seismic performance and economy in applications requiring longer spans or greater heights, flexibility in planning, rapid construction, easy repairability and so on. Another reason for considering use of steel as an alternative to concrete wherever possible is the ongoing difficulty in finding adequate quantities of constituents of concrete such as aggregates, river sand and water. In this respect, the substantially increased production of steel in India over the last few decades augers well for the growth of civil infrastructure in the country.

Steel is almost always the major construction material in landmark structures. There is a long list of such examples in both India and abroad. Just to cite a few, the Golden Gate Bridge in San Francisco, the Disney Concert Hall in Los Angeles, the Beijing Olympic Stadium, the Millennium Bridge in London, the Rabindra Setu and the Vidyasagar Setu in Kolkata, India, the upcoming railway arch bridge across the river Chenab in J&K, India, the tower of unity in Gujarat, India and so on. Today, innovative solutions like steel-concrete composites for flooring systems, columns, beams and shear walls are preferred by structural engineers. However, the quest for the economy has been pushing researchers to explore possibilities to obtain more reliable and optimized solutions. Extensive research is actively carried out around the globe on light gauge steel which is observed as a promising building material. In addition, the reduction of the deadweight of composite slab by using lightweight concrete has been intensively studied by the researchers at IIT Hyderabad. The strengthening of existing steel structures using reinforcements like CFRP and GFRPs is another challenging area of research that is carried out around the globe.

The Structural Steel Research Group, Department of Civil Engineering of IIT Hyderabad has organized this, the First Conference focused on structural steel and

its applications. This conference envisages boosting the ideology of paradigm shift from conventional wet-based construction to dry-based construction which may offer advantages in meeting rapidly the big demands for additional housing units.

Prof. Prem Krishna
Formerly with Indian Institute of Technology Roorkee
Roorkee, India

# Foreword II

Steel structures are the landmarks of modern societies. Examples include the Golden Gate Bridge in San Francisco, the Disney Concert Hall in Los Angeles, the Beijing Olympic Stadium, the Millennium Bridge or the Orbit in London, Calatrava's train stations and thousands more. Steel structures can provide a high strength-to-weight ratio, ultimate flexibility, airy spaces, rapid construction, long spans, superior seismic performance and much more providing economical as well as optimal solutions compared to concrete structures.

Unfortunately, the use of structural steel in India is very less either due to lack of knowledge in structural steel design or outdated codal provisions. Therefore, on the one hand it is necessary to invest more into R&D sector to understand the science behind the behaviour of structural steel in infrastructure applications and update the existing codal provisions. It would encourage and acknowledge the work of young researchers who are investing their lives for a noble cause of providing an affordable, sustainable and respectable shelter for every citizen of our nation through light gauge steel framing systems (LGSFs) and fulfilling the government of India's mission "Housing for all". On the other hand, it is necessary to promote special steels like cold-formed steel for mass housing projects in both rural and urban India which can be done by the establishment of a centre of excellence. It would be a wise decision to invest in emerging areas of research like structural steel which can boost up the national economy tremendously. In addition, it is essential to make the new generation of structural engineers feel comfortable in the design of steel structures by creating chair professorships at leading institutes for both knowledge creation and knowledge dissemination.

Today, innovative solutions like steel-concrete composites for flooring systems, columns, beams and shear walls are preferred by structural engineers. However, the quench for the economy has been pushing researchers to carry out a large number of experiments to obtain more reliable and optimized solutions. Extensive research is actively carried out around the globe on light gauge steel which is observed as a promising building material. In addition, the reduction of the deadweight of composite slab by using lightweight concrete has been intensively studied by the researchers at IITH.

The Structural Steel Research Group, Department of Civil Engineering of IIT Hyderabad has organized the First Conference focused on structural steel and its applications. This conference envisages to encourage the use of structural steel in infrastructure projects in India and explore the unexplored areas of research in special steels like cold-formed steel in India.

Prof. B. S. Murty
Director
Indian Institute of Technology Hyderabad
Sangareddy, India

# Foreword III

Currently, India is second in terms of production of crude steel surpassing Japan and USA. The production and consumption figures for FY 20 are 103.044 MT and 94.140 MT, respectively. The capacity augmentation by Indian steel producers is planned in the same way.

However, at present, India is among a handful of countries which suffer from massive deficit in construction. The per capita consumption of steel being 75 kgs in 2019 (19 kgs only in rural sector) compared to world average of 230 kgs, 636 kgs in China and a wobbling 1039 kgs in S. Korea the potential in India looks positive. The projection of steel consumption in the FY 2031 is predicted to be 196 MT of which 73.9 MT is in building construction only. Application of steel may be explored into areas like Infrastructure, rural and urban building et al. The institutes may work in areas of "application" with thrust in developing modular concepts, standard designs, use the results of research in the application field. Use of hot rolled has been pursued for a long time. Advent of cold-formed steel is welcomed as its usage also has a potential. The research in this area and the formulation of proper code and guidebook will ease the designing part culminating to more usage of the same.

The research in the application side needs to be improved in terms of Indian perspective and context. Proper funding from stakeholders and the government needs to be channelized to the research Institutes for developing "India specific" applications with steel and help to make the country be ATMA NIRBHAR.

This conference delves with various topics aiming towards the consumption side, i.e. application of steel. Being the head of this Institute that is into the area of increasing the consumption of steel, I look forward to getting newer ideas from Indian and foreign brains so that the outcome from this conference can be converted to tangible gains for the well-being of the country.

We are proud enough to find that an esteemed Institute like Indian Institute of Technology, Hyderabad, has selected a topic which is the need of the hour and has gathered experts globally.

I wish the conference a great success. Jai Hind.

Pradip Kumar Mishra
Director General
Institute for Steel Development and Growth
Kolkata, India

# Foreword IV

Steel construction is a key consideration in the design of buildings and infrastructures. Significant advances in research and development have increased the knowledge of the structural performance of steel structures. To know about the innovation and advances, we need a forum for researchers, practitioners and engineers to share and discuss their research, practical experience and innovations related to steel structures with their peers in an open, international conference forum.

International conference, ISSC 2020 (Indian structural steel Conference), organized by the Structural Steel Research Group, Department of Civil Engineering of IIT Hyderabad is the First Conference focused on structural steel and its applications are scheduled to be conducted via Air meet on 6–8 January 2022 in online mode, with the association of ASCE India Section and Springer Publications.

The aim of the conference is to provide a common platform to share and discuss novel ideas, technologies and research findings to promote interdisciplinary research and to ignite young brains. The conference provides a forum for discussion and dissemination by researchers and designers of recent advances in the analysis, behaviour, design and construction of steel structures. Research papers were contributed from all around the world, with the research ideas in the area of cold-formed steel, structural steel, steel-FRP composites, steel-concrete composites. Dedicated funding from the government and private sectors towards the development of techniques for steel-intensive infrastructure will expedite sustainable construction practices in India.

The efforts of Prof. Madhavan and his entire team at IIT, Hyderabad, to proliferate emerging construction systems including steel-intensive structural systems are laudable.

Wishing the conference grand success.

Dr. Shailesh Kr. Agrawal
Executive Director, Building Materials and Technology
Promotion Council
Ministry of Housing and Urban Affairs
Government of India
New Delhi, India

# Indian Structural Steel Conference

This international conference organized by the Structural Steel Research Group, Department of Civil Engineering of IIT Hyderabad is the First Conference focused on structural steel and its applications. This conference was planned to be held from 25 to 27 March 2020 in Hyderabad but due to COVID-19, it got postponed and held online from 06 to 08 January 2022. This ISSC 2020 conference is being organized with an association of ASCE India Section and Springer.

It will be of interest to steel and aluminium structure designers and manufacturers, trade associations, design engineers, steel fabricators, architects, owners and developers of steel and aluminium structures, researchers, academics and postgraduate students.

## Aim and Scope of the ISSC

Steel structures are a fairly vast field covering different constructional engineering branches and various materials used in combination of steel to provide a composite system. The applications of structural steel encompass various industries including construction, automotive, aerospace and marine. However, the development of novel structural materials and technologies, together with the computational tools and design specifications, is necessary for continuous advancement in the use of structural steel in numerous areas. In addition, the role of the construction engineer is also to maintain the existing structures for the desired load and purpose, and therefore, there is also a need for new retrofitting techniques using sustainable materials.

Hence, this ISSC 2020 conference aims at providing a forum where researchers, designers and construction engineers, structural steel manufacturing engineers and consultants having explicit backgrounds but encountering similar challenges, joining together in a friendly environment, to discuss and disseminate the most recent advances in the analysis, behaviour, design and construction of structural steel.

# Message from the Conference Organizing Secretary

The Structural Steel Research Group at the Indian Institute of Technology, Hyderabad, is glad to announce the inauguration of the first Indian Structural Steel Conference (ISSC) to be held at IIT Hyderabad.

As our nation celebrates the 75th Year of its Independence, many challenges lie ahead in terms of basic infrastructure and the difficulties faced by the millions of fellow citizens without proper housing for a safe livelihood. This conference aims to shed light on some of these challenges and is focused on sustainability to promote steel-intensive sustainable construction practices for a sustainable India. A galaxy of eminent keynote speakers from across the globe will present their latest research work which will create awareness among researchers, industry leaders and policymakers.

I am grateful to the IIT Hyderabad Former Director Prof. U. B. Desai and Current Director Prof. B. S. Murty for their continuous encouragement to conduct this conference. I thank all the keynote speakers for the acceptance to deliver a technical session in this conference.

Special thanks to Mr. T. V. Narendran, MD and Global CEO of Tata Steel and President of CII and Mr. P. K. Mishra, Director General, INSDAG (INSTITUTE FOR STEEL DEVELOPMENT AND GROWTH), Ministry of Steel Government of India for accepting to be the chief guest for this conference.

This conference attracted 193 papers from 12 countries. A total of 380 authors from 120 institutions (notably IISc, 11 IITs and 12 NITs) have contributed to this conference.

I would like to express my great gratitude to the reviewers for their excellent work. The editorial team also wish to appreciate the staff at the Indian Institute of Technology Hyderabad who helped to throughout to conduct the conference. Special

thanks are owed to my student's team for their effort on this conference. I wish to express my sincere gratitude to all the presenting authors and participants whose contributions have made this conference possible.

Thank you.

Prof. Mahendrakumar Madhavan
Structural Steel Research Group
Department of Civil Engineering
Indian Institute of Technology Hyderabad
Sangareddy, India

# Contents

# About the Editors

**Prof. Mahendrakumar Madhavan** is Professor in the Department of Civil Engineering, Indian Institute of Technology (IIT) Hyderabad, India. He has obtained Ph.D. and MBA (Finance) from the University of Alabama at Birmingham and his master's degree from the National University of Singapore. He is a Registered Professional Engineer (PE) in the State of Alabama USA. Prior to IIT Hyderabad, he worked as a Structural Engineer at Alabama Power Company, Birmingham, USA. He is an international expert in structural steel, cold-formed steel and steel-concrete composite construction and has published more than 50 peer-reviewed internationally reputed journals and holds membership in the "American Society of Civil Engineers (ASCE) Structural Engineering Institute (SEI) Technical Administrative Committee on Metals" and in "ASCE SEI Cold-Formed Steel Members Committee". He has significantly contributed to the revision of IS 801: Indian Design Code for Cold-formed Steel Members based on the original research work carried out at IIT Hyderabad to fulfil the Government of India's goal of "Housing for All" through sustainable construction. He is an editorial board member of the Journal of Structures and is an Associate Editor for the *ASCE Journal of Structural Engineering* and serves as a reviewer for more than ten international journals. He is a Fellow of the Institution of Civil Engineers (ICE), London, and is also the first Indian to be elected as a Fellow of ASCE's Structural Engineering Institute (SEI).

**Prof. James S. Davidson** is currently the Gottlieb Professor of Structural Engineering in the Department of Civil and Environmental Engineering, Auburn University, USA. He is an expert in mechanics of materials, advanced stress analysis, finite element methods, and stability of structures. He has mentored more than 50 research students including MS and Ph.D., has served as associate editor, review director, and editorial board member on five technical journals and has served as a reviewer for more than 25 different technical journals.

**Prof. N. Elumalai Shanmugam** has taught for more than 20 years at the National University of Singapore. Prior to this he taught in College of Engineering, Guindy, Delhi University, University of Wales (Cardiff) and Polytechnic of Wales. After

50 years of teaching at graduate and undergraduate levels, he retired recently from National University of Malaysia where he taught for nine years. His research interest includes steel-plated structures, steel-concrete composite construction, long-span structures and connections, cold-formed steel structures, etc. He has published more than 200 research papers in international refereed journals conference proceedings and contributed chapters in *Civil Engineering Handbook*, *Structural Engineering Handbook* and *Bridge Manual*. He is a member of the editorial board of a number of international journals.

# Coupled Dynamic Analysis of Deepwater Semi-submersible with Spread Mooring System


**S. Chandrasekaran and Syed Azeem Uddin**

**Abstract** Exploration and production in deepwaters are dominated by compliant offshore structural systems due to the advantages that arise from their geometry and construction practices. Semi-submersibles are a class of floating offshore structures, which are widely preferred for deep and ultra-deepwater applications due to their better stability characteristics and lesser sensitivity to the harsh ocean environment. A semi-submersible is positioned-restrained using the spread mooring system with either a steel catenary geometry or taut-mooring. The present study highlights dynamic response analysis of a semi-submersible with the spread mooring system, and its fatigue life under cyclic environmental loads is estimated. Lateral loads that arise from waves, wind, and current cause dynamic tension variations in the moorings, influencing their fatigue life significantly, and it is observed that fatigue life of catenary mooring lines is higher than that of taut mooring lines. Lateral loads under different directions are considered to exhibit the influence of wave directionality on the semi-submersible response. The nonlinear coupled dynamic analysis between the semi-submersible and spread mooring system is carried out using commercially available tool ANSYS AQWA, and fatigue life of the mooring system is evaluated based on the S–N curve approach.

**Keywords** Coupled analysis · S–N curve · Fatigue · Time domain · Semi-submersible and spread mooring

S. Chandrasekaran (✉) · S. A. Uddin
Department of Ocean Engineering, Indian Institute of Technology Madras, Chennai, India
e-mail: drsekaran@iitm.ac.in



M. Madhavan et al. (eds.), *Proceedings of the Indian Structural Steel Conference 2020 (Vol. 1)*, Lecture Notes in Civil Engineering 318,
https://doi.org/10.1007/978-981-19-9390-9_1

## 1 Introduction

Rapidly depleting oil reserves and proliferate market demand for oil and gas production has shifted from deepwaters to ultra-deepwaters using floating offshore platforms (also known as floaters) like semi-submersibles, Drillships, FPSOs, etc., which are unique based on their geometric form, i.e. they are form dominated designed. However, as we move towards ultra-deepwaters the choice of platform varies depending upon the applications. The development and design of semi-submersible hulls can be traced back to the early 1960s when there was a rapid need to increase the stability of deepwater floating platforms. Bruce Collipp is known as the father of semi-submersible, who first coined the term semi-submersible in 1960. His early design and development of this structure were inspired by the stability, obtained by partially submerging the floating structure to avoid capsizing in rough sea conditions. The configuration of semi-submersible platforms has evolved since the 1960s owing to their good stability even in deepwaters since they have a small water-plane area which makes them less sensitive even under harsh environmental loadings. Due to the few advantages, semi-submersible platforms have best opted as the floating production platform until today.

In the recent past, many scholars studied various models of semi-submersible, design of the mooring system, etc., for reducing the response of the platform. Webster [1] conducted a parametric study on the damping induced by moorings and reveals that for high pretension in mooring lines, damping induced by the mooring lines is inversely proportional to the drag coefficient. Yilmaz and Incecik [2] developed a time-domain model for predicting the dynamic response of moored semi-submersible with thrusters and mooring lines for evaluating platform response and mooring forces. Based on the results obtained, they concluded that for extreme weather conditions maximum surge or sway response occurs based on their mean values. Senra et al. [3] suggested that there is great need of fully integrated design methodology, considering the coupling between structural behaviour of the vessel with mooring lines and risers. Chen et al. [4] studied coupled motion responses of semi-submersible with taut mooring system and found that more the number of mooring lines better will be the performance, mooring arrangement angle has a significant effect on the platform motion and response of dynamic tension of mooring line. Zhai et al. [5] numerically simulated the dynamic behaviour of deepwater semi-submersible and found that heave period as 22 s, while wave period was 8–16 s. By avoiding the maximum response in heave degrees-of-freedom, the peak coefficient has a significant effect on the response of the platform. Ng et al. [6] conducted experimental studies on semi-submersible model for various bi-directional wave crossing angles, to estimate the optimum wave crossing angle at which the response of the semi-submersible is maximum. They found that response of the model is affected by the wave crossing angles and the optimum wave crossing angles 40° and 55° are found to produce maximum heave, surge and pitch responses at low-frequency range.

Zhu and Ou [7], studied the motion performance of semi-submersible with mooring under combined wind and wave loads by numerically and experimentally. He found maximum surge motion of the platform is about 2% of water depth, which is one of the important criteria for drilling operation to run smoothly; otherwise, the riser connected for drilling operation will be subjected to dynamic loads and may even fail due to large surge response of the platform. Qiao and Ou [8] conducted model tests of a semi-submersible and validated with numerical results of semi-submersible with different mooring systems under various water depths and concluded that dynamic forces on mooring lines increases with increase in length of the mooring lines, and low-frequency (LF) motion dominates the surge, sway motion whereas, wave frequency (WF) motion dominates heave motion while pitch motion is due to both LF and WF motions. Wu et al. [9] have conducted analytical studies on the fatigue life of mooring lines and found various factors such as mooring pattern, length of mooring lines, pretension, mass concentration components, damping coefficients, and water depth, etc., are affecting the fatigue damage of mooring lines. They have also found critical locations where fatigue damage can occur such as at fairlead point for catenary mooring and top of the lower chain for taut mooring.

Yang et al. [10] investigated for mooring damping effects due to superimposition of low-frequency motion with wave frequency and concluded that response amplitude operators (RAO's) and pretension of mooring plays a dominant role in damping of the mooring system. Du et al. [11] conducted a dynamic analysis of semi-submersible and estimated the fatigue damage of the mooring lines and concluded that platforms in deepwaters have less stiffness, high damping ratio for which the WF components increases and LF components decreases with increase in water depth due to higher damping. Hence, there is a decrease in LF fatigue damage with an increase in wave periods. Xu et al. [12], conducted model tests and numerical simulations for dynamics of semi-submersible, mooring damping and found that taut mooring with buoy causes stable semi-submersible motion with great mooring damping. The present study is conducted for estimating the motion responses of the semi-submersible under spread catenary (case 1) & taut mooring (case 2) system and evaluating the fatigue life of the spread mooring system.

## 2 Description of Semi-submersible Platform

The platform geometry selected for present work is based on the configuration of the Hai Yang Shi You–981 which is a sixth generation deepwater semi-submersible platform which was deployed in the disputed waters of the South China Sea and Vietnam. The semi-submersible platform consists of the deck (superstructure) with drilling derrick, accommodation and production facilities, a helipad, accessories, four-column members, and two horizontal pontoons members connected with horizontal cylindrical members (braces). The numerical model of the semi-submersible is shown in Fig. 1, and detailed description is shown in Table 1.

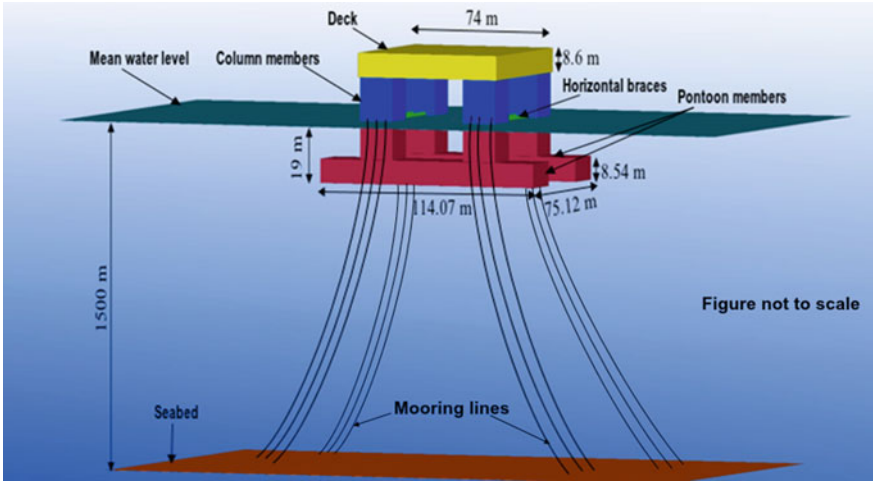


**Fig. 1** Numerical model of semi-submersible

**Table 1** Detailed description of semi-submersible

| Description | Value | Units |
|---|---|---|
| Deck | 74.42 × 74.42 × 8.6 | m |
| Columns (4 in no's) | 17.385 × 17.385 × 21.46 | m |
| Pontoons (2 in no's) | 114.07 × 20.12 × 8.54 | m |
| Displacement | 48,206,800 | kg |
| Water depth | 1500 | m |
| Draft | − 19 | m |
| The diameter of the brace | 1.8 | m |
| Centre of gravity below water level | − 5.8 | m |
| The radius of gyration for roll ($R_x$) | 32.4 | m |
| The radius of gyration for pitch ($R_y$) | 32.1 | m |
| The radius of gyration for yaw ($R_z$) | 34.4 | m |

## *2.1 Spread Mooring System*

During the drilling operation, the platform should not displace too much from its home position; otherwise, connected riser will be damaged. The platform is position-restrained with either of the dynamic positioning system and spread mooring system to avoid large displacements. In present work, a twelve-point symmetric mooring system is used which is made up of studless chain, and the layout of mooring system

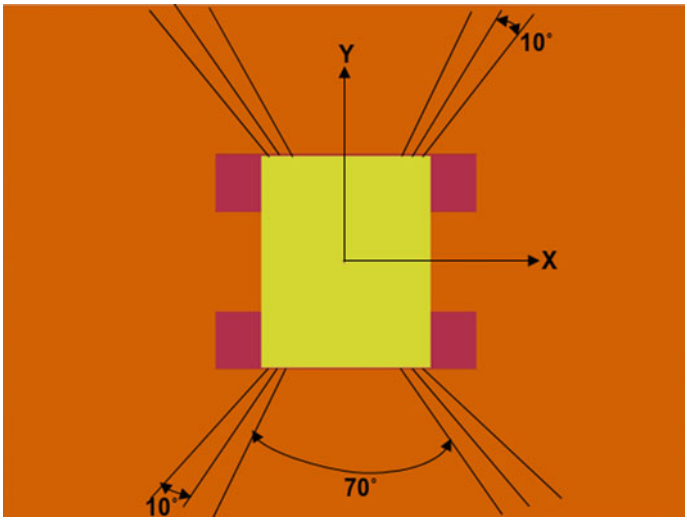


**Fig. 2** Layout of the spread mooring system

**Table 2** Configuration of the spread mooring system

| Mooring type | Length of mooring system (m) | | | Pretension (kN) |
|---|---|---|---|---|
| | Upper chain | Middle wire | Bottom chain | |
| Catenary mooring | 500 | 2000 | 1500 | 3500 |
| Taut mooring | 900 | 1000 | 200 | 2850 |

is shown in Fig. 2. The angle between each cable of the bundle is 10°, and the angle between each bundle is 70°.

Each mooring line is a combination of upper section as chain, middle section as wire, and the lower section as chain, and the configuration and properties of spread mooring system used are shown in Tables 2 and 3.

## *2.2 Environmental Conditions*

The environmental conditions to which the semi-submersible is subjected to the present work is considered for 1 year and 100 year return period for the South China Sea. The wave, wind, and current loadings are considered in present work and are along the 0° (following sea condition), 45° (quarter sea condition), and 90° (beam sea condition). Because, a minimum of the bow, beam, quarter, down-line, and between-line environmental conditions should be analysed [13]. The wind spectrum used for the present study is the API spectrum, and the JONSWAP spectrum is used for irregular waves. The current loading (i.e. varying nonlinearly with respect to water

**Table 3** Properties of mooring lines

| Description | Upper chain (studless K-4 chain) | Middle wire (spiral strand) | Bottom chain (studless K-4 chain) |
|---|---|---|---|
| Mass per unit length (kg/m) | 163.86 | 36.41 | 163.86 |
| Equivalent cross-section ($m^2$) | 0.014 | 0.014 | 0.014 |
| Stiffness (kN) | 676,810 | 833,910 | 676,810 |
| Equivalent diameter (m) | 0.095 | 0.095 | 0.095 |
| Longitudinal drag coefficient | 0.025 | 0.025 | 0.025 |

**Table 4** Environmental loads

| Description | The return period of the event | | Units |
|---|---|---|---|
| | 1 year | 100 year | |
| Wind speed, $V_{\text{wind}}$ | 23.15 | 55 | m/s |
| Wave height, $H_{\text{s}}$ | 6 | 13.3 | m |
| Peak period, $T_{\text{p}}$ | 11.2 | 15.5 | s |
| Current speed, $V_{\text{current}}$ | 0.93 | 1.97 | m/s |

depth) is applied to the platform and is user-defined up to a depth of 150 m (i.e. 10% of water depth) below the mean water level. Environmental conditions for which the semi-submersible are subjected are shown in Table 4.

## *2.3 Governing Equations*

### 2.3.1 Wind Force Calculation

Ansys AQWA calculates the effect of fluctuation of wind about the mean speed on the dynamic load on the structure, and these dynamic loads generate low-frequency motions on floating offshore structures. In the present study, API wind spectrum is used, and Ansys AQWA calculates the wind fluctuation effect about the mean speed on dynamic loads acting on the semi-submersible, and these loads causes low-frequency (LF) motions on the semi-submersible. The API wind spectrum [14] used is represented by the expression given below:

$$S\left(\tilde{f}\right) = \frac{\tilde{f}}{\left(1 + 1.5\tilde{f}\right)^{5/3}} \tag{1}$$

$$\tilde{f} = \frac{f}{f_p} \tag{2}$$

$$f_p = 0.025\left(\frac{\overline{V}_Z}{Z}\right) \tag{3}$$

While $f$ and $f_p$ are frequencies in Hz, and $\overline{V}_Z$ is the mean speed for the one-hour duration at height (Z).

### 2.3.2 Wave Force Calculation

The wave loads acting on the semi-submersible are calculated by boundary element method (BEM) based on the diffraction theory using commercially available tool Ansys AQWA. For irregular waves with slow-drift, waves can be represented in the form of wave spectra, and the present study JONSWAP spectrum is used.

### 2.3.3 Coupled Dynamic Analysis of Semi-submersible and Spread Mooring System

In a coupled analysis approach, a time-domain analysis is employed to represent coupled semi-submersible and mooring response at every instant of time. The semi-submersible is considered as a rigid element with six degrees-of-freedom, i.e. three translational (surge, sway, and heave) and three rotational (roll, pitch, and yaw) in the finite element model of the semi-submersible. The dynamic equilibrium equation for rigid element, i.e. semi-submersible, is written as [15]:

$$F_I(x, \ddot{x}, t) + F_D(\dot{x}, t) + F_S(x, t) = P_{\text{External}}(x, \dot{x}, t) + F_{\text{Radiation}}(\dot{x}, t) \tag{4}$$

$$F_I(x, \ddot{x}, t) = M(x)\ddot{x} \tag{5}$$

where

$F_I(x, \ddot{x}, t)$ is inertia force vector; '$M$' is mass matrix of semi-submersible which includes structural mass and added mass, i.e. $M = m + m_{\text{a}}$

$$F_D(\dot{x}, t) = C(\dot{x}) \tag{6}$$

$$F_S(x, t) = K(x) \tag{7}$$

$F_D(\dot{x}, t)$ is damping force vector; '$C$' is damping matrix; '$K$' is the stiffness matrix.

$P_{\text{External}}(x, \dot{x}, t)$ is external force vector, due to wind, wave, and current loads including buoyancy, and $F_{\text{Radiation}}(\dot{x}, t)$ is radiation force vector.

$x, \dot{x}, \ddot{x}$ = Nodal displacement, velocity, and acceleration vector.

The dynamic variations in tension of mooring lines caused by the wave frequency motions are calculated, and mooring cables are modelled as a dynamic system [16].

$$(M + M_{\text{a}})\ddot{x} + C\dot{x} + Kx = F_{\text{Static}} + F_{WF} + T_M \tag{8}$$

'$M$' being the structural mass matrix, '$M_{\text{a}}$' is added mass matrix, '$x$' is a displacement vector, '$\dot{x}$' is velocity vector, '$\ddot{x}$' is acceleration vector, '$C$' is the damping matrix, '$K$' is stiffness matrix, '$F_{\text{static}}$' is the static load, '$F_{WF}$' is first-order wave loads, and '$T_M$' is tension in the mooring system.

## 3 Numerical Simulation and Analysis

To carry out coupled dynamic analysis of the semi-submersible with spread mooring system commercially available tool Ansys AQWA is employed, and the simulations have been carried out for 10,000s with a time step of 0.1 s.

### *3.1 Comparison of Response Amplitude Operators*

Before carrying out further analysis, response amplitude operators (RAOs) of the semi-submersible is checked. The response amplitude operators of the present study and that obtained by Zhai et al. [5] are found to be closely matching and can be seen from Figs. 3, 4, and 5. But, there is little shift in the plots is observed, and this might be due to the reason that we have considered slow-drift with an irregular wave in the analysis, and Zhai et al. [5] has not given details whether they have considered slow-drift with irregular wave for analysis or not.

Surge response amplitude operator (RAO) of the present study is having a less initial amplitude of 1.1 m as shown in Fig. 3, which is advantageous for response analysis because RAO helps in determining the response spectrum. Heave response amplitude operator (RAO) curve in closely matching except, but there is a shift in the frequencies has been observed, and this can be due to the effect of slow-drift with an irregular wave.

The magnitude of heave RAO is quite high for Zhai et al. [5] compared to the present study, which indicates the better heave response of the platform considered for the present study. Response amplitude operator of pitch response for the present study shows less amplitude, as seen in Fig. 5 and possesses better response. From Figs. 4, 5, and 6, it is evident that RAO plots are closely matching, but there is a slight shift in the RAO plots has been observed, and this can be due to the effect of slow-drift with irregular waves. The present study considered the slow-drift with an

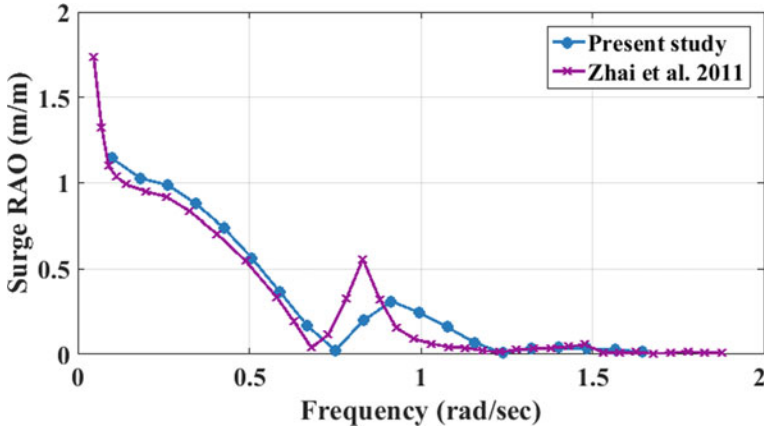


**Fig. 3** Surge RAO

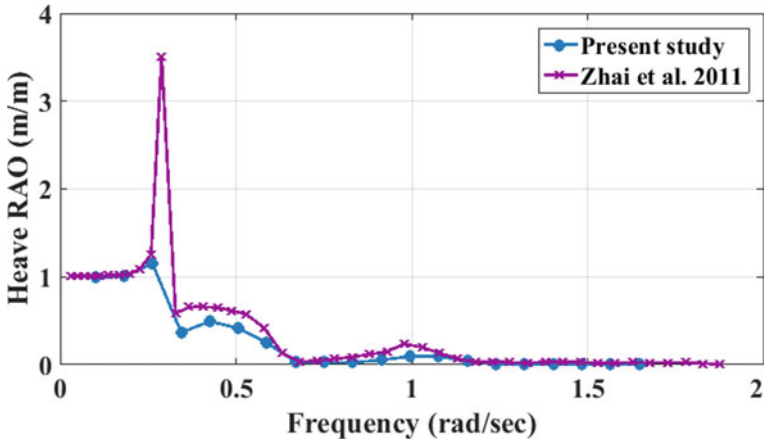


**Fig. 4** Heave RAO

irregular wave to assess the importance of wave-frequency effects on the drift of the vessel.

## *3.2 Natural Periods and Damping Ratios*

Free decay tests were conducted in commercially available numerical solver Ansys AQWA. Semi-submersible is found to be active in all six degree of freedom, i.e. it has motion even in stiff degrees-of-freedom, i.e. vertical plane motion (roll, pitch, and heave). Unlike in triceratops, which is flexible in the horizontal plane of motion,

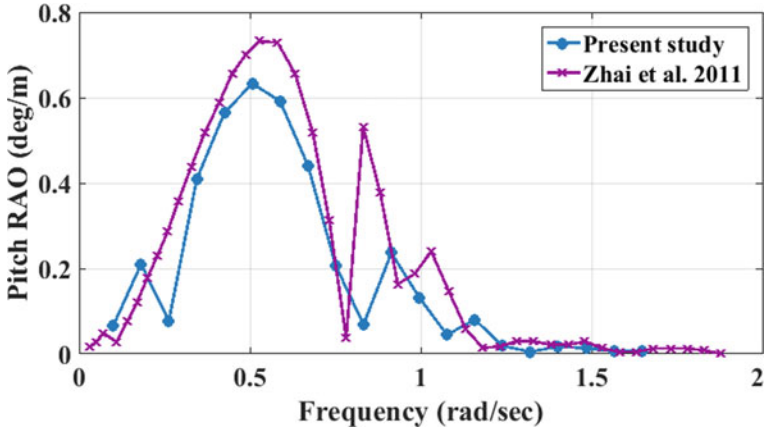


**Fig. 5** Pitch RAO

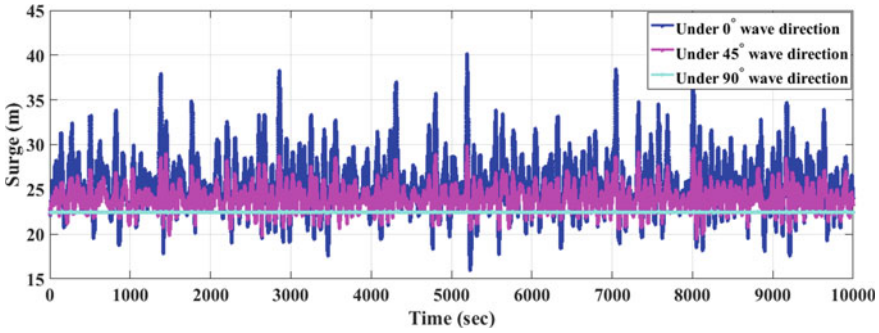


**Fig. 6** Surge response time history using catenary mooring for the 1 year return period

i.e., surge, sway, and yaw and stiff in the vertical plane of motion, i.e. heave, roll, and pitch [17]. Natural damping ratios for catenary mooring are larger than that of taut mooring in almost all degrees of freedom, and this can be due to large length of catenary mooring lines (Table 5).

## *3.3 Motion Responses of the Semi-submersible*

### 3.3.1 Time History Response of Semi-submersible

The semi-submersible motion time history plots with catenary and taut mooring under 1 year return period for 0°, 45°, and 90° wave directions are shown below. Motion responses under surge, heave, and pitch d-o-f and during 1 year return period

**Table 5** Natural periods and damping ratios

| D-o-f | Catenary mooring | | Taut mooring | |
|---|---|---|---|---|
| | Natural periods (sec) | Damping ratio (%) | Natural periods (sec) | Damping ratio (%) |
| Surge | 85.82 | 0.2–13.9 | 84.62 | 0.8–6.2 |
| Sway | 117.55 | 0.6–12.1 | 118.73 | 0.05–6.9 |
| Heave | 20.8 | 2.1–3.4 | 20.94 | 1.3–2.07 |
| Roll | 23.82 | 3–4.4 | 24 | 2.9–10.9 |
| Pitch | 24.56 | 0.008–5.28 | 24.74 | 1.6–6.6 |
| Yaw | 39.82 | 3.1–4.8 | 54 | 1.3–3.6 |

are only shown, while other responses being insignificant and during 100 years return period are omitted for brevity.

The motion of semi-submersible is shown in the form of time history response plots, which is considered from the position of the centre of gravity of semi-submersible in global coordinates, i.e. $x = 22.4$ m for the surge d-o-f and $z = -5.8$ m for heave d-o-f. From Figs. 6 and 7, it is clear that the surge response with catenary and taut is significant for 0°, 45° wave directions.

From Figs. 8 and 9, it can be seen that the heave response under catenary and taut moorings are almost the same, irrespective of wave directions. Also, one can conclude that the heave response of the semi-submersible under taut mooring is more than that under catenary mooring. Figures 10 and 11 show that the pitch response of the semi-submersible is almost the same under the catenary and taut mooring system (Table 6).

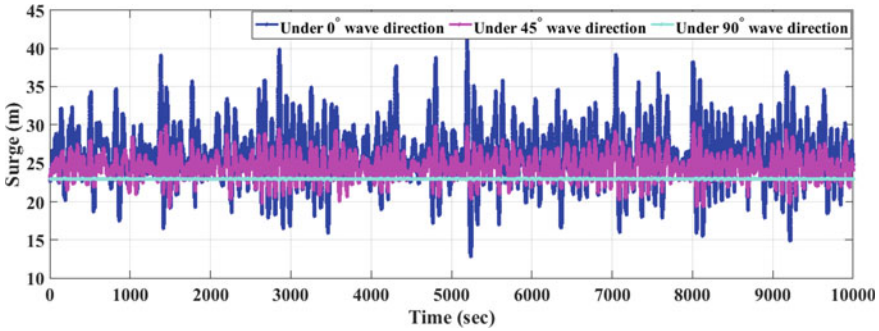


**Fig. 7** Surge response time history using taut mooring for the 1 year return period

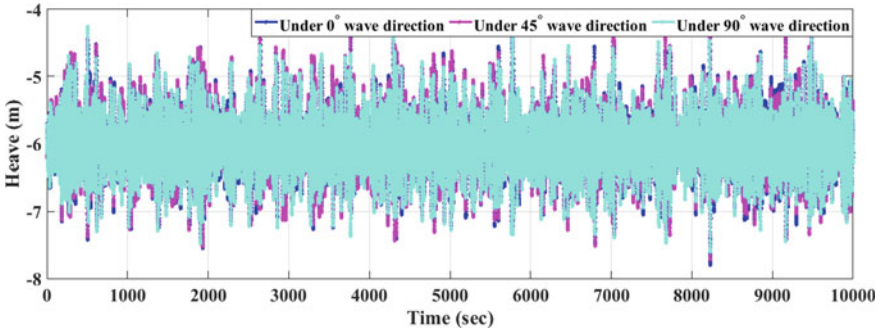


**Fig. 8** Heave response time history using catenary mooring for the 1 year return period

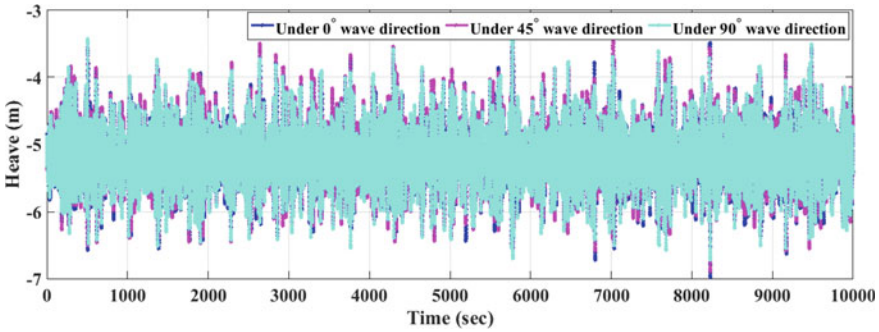


**Fig. 9** Heave response time history using taut mooring for the 1 year return period

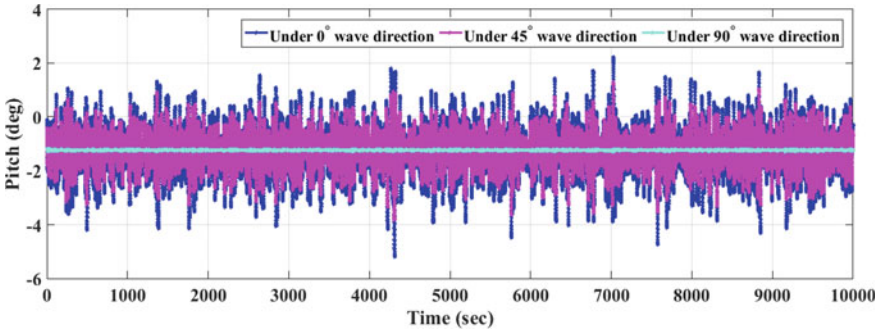


**Fig. 10** Pitch response time history using catenary mooring for the 1 year return period

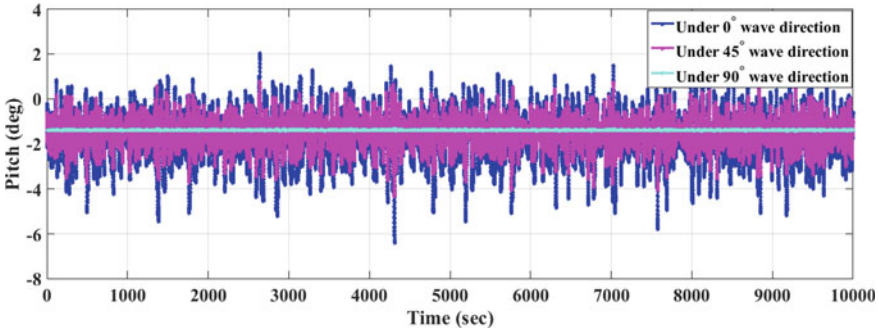


**Fig. 11** Pitch response time history using taut mooring for the 1 year return period

**Table 6** Semi-submersible response statistics for the 1 year return period

| D-o-f | Statistics | Spread catenary mooring | | | Spread taut mooring | | |
|---|---|---|---|---|---|---|---|
| | | 0° | 45° | 90° | 0° | 45° | 90° |
| Surge (m) | Minimum | 15.97 | 19.45 | 22.37 | 12.88 | 19.33 | 22.86 |
| | Maximum | 40.15 | 29.83 | 22.51 | 41.13 | 30.22 | 23.11 |
| | Mean | 25.6 | 23.9 | 22.44 | 26.11 | 24.48 | 23 |
| | Standard deviation | 3.28 | 1.51 | 0.02 | 3.98 | 1.73 | 0.03 |
| Heave (m) | Minimum | − 7.79 | − 7.71 | − 7.6 | − 6.98 | − 6.88 | − 6.72 |
| | Maximum | − 4.12 | − 4.23 | − 4.25 | − 3.48 | − 3.45 | − 3.4 |
| | Mean | − 6 | − 6 | − 6.01 | − 5.18 | − 5.17 | − 5.18 |
| | Standard deviation | 0.44 | 0.46 | 0.43 | 0.42 | 0.44 | 0.43 |
| Pitch (deg) | Minimum | − 5.17 | − 3.81 | − 1.3 | − 6.41 | − 4.31 | − 1.43 |
| | Maximum | 2.21 | 1.27 | − 1.17 | 2.04 | 0.76 | − 1.34 |
| | Mean | − 1.32 | − 1.26 | − 1.24 | − 1.71 | − 1.53 | − 1.39 |
| | Standard deviation | 0.86 | 0.63 | 0.01 | 1.01 | 0.66 | 0.01 |

## *3.4 Mooring Line Tension*

In deep waters mooring lines will become more flexible and dynamic effects on mooring lines will be strong under the dynamic motion of the platform due to environmental loads. Hydrodynamic loads acting on the mooring lines are due to the combined effect of inertial loads, incident wave forces, and drag forces, and the total load is evaluated using the Morison formula. From mooring tension statistics, it is evident that the mooring tensions in environmental loading for catenary mooring > taut mooring for directions 0° > 45° > 90°. The tension in mooring lines which are significant, i.e. most loaded mooring lines, based on the mooring tension statistics is only shown, and others are omitted for brevity (Fig. 12).

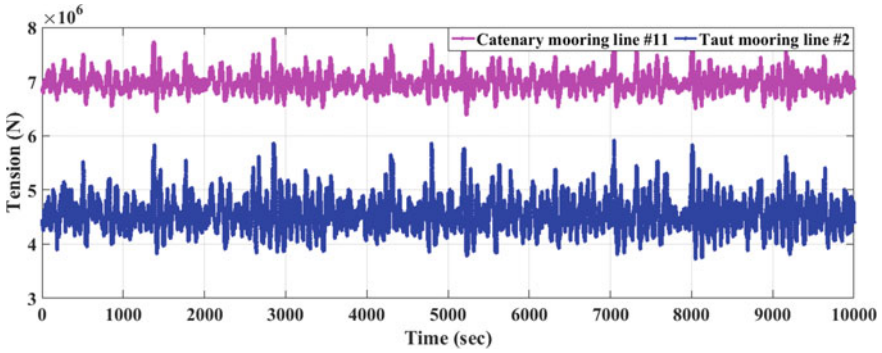


**Fig. 12** Tension in the catenary mooring line—11 and taut mooring line—2 for 0° wave direction

# 4 Fatigue Analysis

## *4.1 Palmgren-Miners Rule-Based Fatigue Analysis*

The nonlinear dynamic variation in mooring line tensions will cause the fatigue damage of mooring lines, which will be estimated by Palmgren-Miners rule based on the S–N curve approach [18]. According to the Palmgren-Miners rule, the annual cumulative fatigue damage of the mooring line can be predicted by using the formula:

$$D = \sum_{i=1}^{m} \frac{n_i}{N_i} \tag{9}$$

where $n_i$ is the number of cycles per year for tension range interval, and $N_i$ is the number of cycles to failure under constant tension range '$i$' as per the S–N curve. The stress in the mooring lines we have got is non-zero mean stress, which is modified as effective stress using Goodman criteria [19], and rain flow counting method is used to analyse the time history of the mooring stress. Parameters for S–N curve are chosen according to the standard code [20], and fatigue life is then calculated from estimated damage and then extrapolated for 10,000 s to find the fatigue life of the spread mooring system.

Fatigue life for a mooring line from the group of mooring lines, which are extremely loaded and least loaded are only discussed, because of a profuseness of data. The most loaded catenary mooring lines for 1 year return period under 0° wave loading are found to be mooring line #11 for which corresponding fatigue life 2.12 years. Similarly, under 45° wave loading for mooring line #3 having fatigue life 11.56 years and for 90° wave direction mooring line #6 is the most loaded having fatigue life of 18.5 years as shown in Fig. 13. The most loaded taut mooring line #2 have 1.28 years fatigue life for 0° wave direction. For 45° wave heading mooring

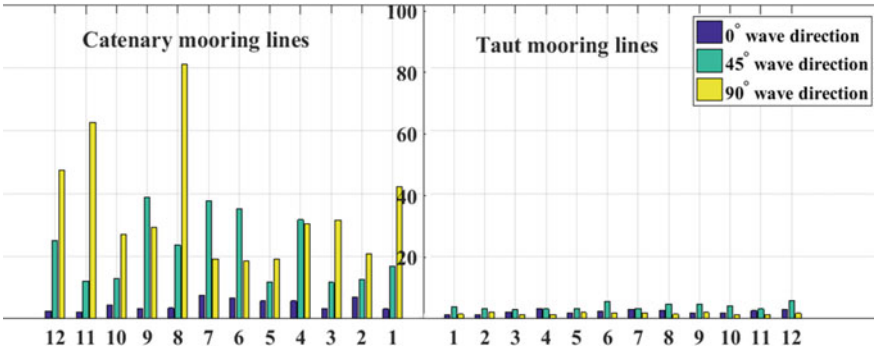


**Fig. 13** Fatigue life of catenary and taut mooring lines under 1 year return period

line #3 is found to be most loaded and have 3 years of fatigue life, and mooring lines #4 and #10 are observed to be the most loaded having fatigue life of 1.36 years.

The fatigue life for spread catenary and taut moorings under various wave directions for one year return period is only shown. While fatigue life of the mooring lines under 100 years return period is omitted for brevity. Hence, based on the results obtained as shown in Fig. 13, one can conclude that fatigue life for spread catenary mooring is more than that of taut mooring.

## 5 Conclusion

Coupled dynamic response analysis of semi-submersible with spread mooring system has been carried out, and observations are made based on the results obtained. The natural periods of semi-submersible with taut mooring is greater than that of catenary mooring, and this can be due to less horizontal force component in taut mooring. The damping ratios of catenary mooring are greater than taut mooring, and this might be due to more length of catenary mooring. The semi-submersible response in surge d-o-f using catenary mooring under 0°, 45° environmental loading is better than that of taut mooring, while the response in the pitch d-o-f is nearly same for both taut and catenary mooring for 45° loading. While heave response is almost the same for both mooring system, under 0° and 45° loading. Based on the mooring tension statistics shown in Table 7, the standard deviation of tension in taut mooring lines is less than that of catenary mooring lines irrespective of the direction of environmental loading. Hence, the fatigue life of the spread catenary mooring is found to be more than that of taut mooring and possesses various advantages over taut mooring lines.

In general, global responses of the semi-submersible are affected by mooring configuration, water depth, and pretension in mooring lines due to the coupling effects. For future work, one can consider the effect of vortex-induced vibration on

**Table 7** Mooring tension statistics for 1 year return period

| Mooring lines | Mooring tension statistics | Spread catenary mooring | | | Spread taut mooring | | |
|---|---|---|---|---|---|---|---|
| | | 0° | 45° | 90° | 0° | 45° | 90° |
| # 2 (MN) | Minimum | 6.08 | 6.15 | 6.31 | 3.72 | 3.84 | 3.7 |
| | Maximum | 7.15 | 7.03 | 7.04 | 5.9 | 5.37 | 5.12 |
| | Mean | 6.69 | 6.68 | 6.71 | 4.56 | 4.5 | 4.4 |
| | Standard deviation | 0.12 | 0.11 | 0.1 | 0.31 | 0.2 | 0.19 |
| # 3 (MN) | Minimum | 6.44 | 6.62 | 6.58 | 3.02 | 3.23 | 3.34 |
| | Maximum | 7.71 | 7.43 | 7.23 | 4.95 | 4.88 | 4.91 |
| | Mean | 6.95 | 6.94 | 6.89 | 4.06 | 4.09 | 4.15 |
| | Standard deviation | 0.16 | 0.11 | 0.08 | 0.25 | 0.2 | 0.22 |
| # 4 (MN) | Minimum | 6 | 6.51 | 6.58 | 3.25 | 3.23 | 3.23 |
| | Maximum | 7.24 | 7.12 | 7.24 | 4.89 | 4.87 | 5.02 |
| | Mean | 6.68 | 6.8 | 6.89 | 4.16 | 4.14 | 4.17 |
| | Standard deviation | 0.15 | 0.08 | 0.08 | 0.21 | 0.2 | 0.23 |
| # 6 (MN) | Minimum | 6.09 | 6.5 | 6.55 | 3.09 | 3.67 | 3.63 |
| | Maximum | 7.15 | 7.15 | 7.29 | 4.98 | 4.92 | 5.2 |
| | Mean | 6.69 | 6.82 | 6.9 | 4.13 | 4.28 | 4.4 |
| | Standard deviation | 0.12 | 0.08 | 0.1 | 0.24 | 0.17 | 0.21 |
| # 11 (MN) | Minimum | 6.38 | 6.64 | 6.6 | 3.12 | 3.22 | 3.28 |
| | Maximum | 7.86 | 7.43 | 7.19 | 4.93 | 4.87 | 4.97 |
| | Mean | 6.98 | 6.95 | 6.88 | 4.11 | 4.11 | 4.16 |
| | Standard deviation | 0.18 | 0.11 | 0.07 | 0.23 | 0.2 | 0.22 |

the moorings and effect of corrosion, for evaluating the fatigue life of the spread mooring system.

## References

1. Webster WC (1995) Mooring induced damping. Ocean Eng 22(6):571–591
2. Yilmaz O, Incecik A (1996) Extreme motion response analysis of moored semi-submersibles. Ocean Eng 23(6):497–517
3. Senra SF, Correa FN, Jacob BP, Mourelle M, Masetti I (2002) Towards the integration of analysis and design of mooring systems and risers: part I—studies on a semisubmersible platform. In: ASME 21st international conference on offshore mechanics and arctic engineering, vol 1, Oslo, Norway, 23–28 June 2002, pp 41–48
4. Chen P, Chai S, Ma J (2011) Performance evaluations of taut-wire mooring systems for the deepwater semi-submersible platform. In: ASME 2011 30th international conference on ocean, offshore and arctic engineering, pp 207–215

5. Zhai GJ, Tang DY, Xiong HF (2011) Numerical simulation of the dynamic behaviour of deep-water semi-submersible platform under wind and waves. In: Advanced materials research, vol 243. Trans Tech Publications, pp 4733–4740
6. Ng CY, Kurian VJ, Liew MS (2011) Experimental investigation for the responses of the semi-submersible platform subjected to bidirectional waves. In: 2011 national postgraduate conference, IEEE, pp 1–5
7. Zhu H, Ou J (2011) The dynamic performance of a semi-submersible platform subject to wind and waves. J Ocean Univ China 10(2):127–134
8. Qiao D, Ou J (2013) Global responses analysis of a semi-submersible platform with different mooring models in the South China Sea. Ships Offshore Struct 8(5):441–456
9. Wu Y, Wang T, Eide Ø, Haverty K (2015) Governing factors and locations of fatigue damage on mooring lines of floating structures. Ocean Eng 96:109–124
10. Yang Y, Chen JX, Huang S (2016) Mooring line damping due to low-frequency superimposed with wave-frequency random line top-end motion. Ocean Eng 112:243–252
11. Du J, Wang S, Chang A, Li H (2016) An investigation on low-frequency fatigue damage of mooring lines applied in a semi-submersible platform. J Ocean Univ China 15(3):438–446
12. Xu S, Ji C, Soares CG (2018) Experimental study on taut and hybrid moorings damping and their relation with system dynamics. Journal of Ocean Engineering 154:322–340
13. API RP 2SK (2008) Design and analysis of station keeping systems for floating structures, 3rd edn. American Petroleum Institute
14. Aqwa Theory Manual (2016) Century Dynamics Limited
15. Ormberg H, Lie H, Stansberg CT (2005) Coupled analysis of offshore floating systems. WIT Trans State-of-the-art Sci Eng 18:389–429
16. Barltrop NDP (1998) Floating structures: a guide for design and analysis, vol 2. Oilfield Publications Limited, The Centre for Marine and Petroleum Technology
17. Chandrasekaran S, Nassery J (2015) Springing and ringing response of offshore triceratops. In: ASME 2015 34th international conference on ocean, offshore and arctic engineering. American Society of Mechanical Engineers, pp 1–6
18. Xue X, Chen NZ, Wu Y, Xiong Y, Guo Y (2018) Mooring system fatigue analysis for a semi-submersible. Ocean Eng 156:550–563
19. OrcaFlex Theory Manual (2014) Orcina Ltd.
20. DNV-RP-C203 (2005) Fatigue design of offshore steel structures

# Effect of Power Pack Unit on Modular Trailer Spine Beam Deflection


**Manish Arya, Pratik Chakraborty, and Munish Dhawan**

**Abstract** For Modularization projects in Oil and Gas industry, Transportation of Structures (i.e. Modules or Pipe Racks) through modular trailers is usually considered as an important activity. Two types of modular trailers, Self-Propelled Modular Trailer (SPMT) and Propelled Modular Trailers (PMT) are used for this purpose. As a part of structural analysis, Trailer deflections and stability are also checked. Excessive deflection of trailer can have adverse impact on transportation operation including effect on structural integrity and/or trailer stability. Power Pack Units (PPU) are considered as essential component of the trailers which provide motion and suspension power to SPMT and PMT. Typically those units are cantilevered from one end or both ends of trailer. Generally consideration of power pack weight in analysis results in lesser deflection of trailer, as effect of those load counteracts to the sagging deflection profile of the trailer. So in general, it is considered that exclusion of the power pack loads will yield conservative result. This chapter discusses how the weight of PPU can generate high trailer deflection and describes viable solution for reduction of such deflection and thus obtaining a favorable trailer profile necessary for safe modular transportation per given project parameters.

**Keywords** Deflection · Modularization · Power pack · Trailer spine beam

M. Arya (✉) · P. Chakraborty · M. Dhawan
Civil Structural and Architectural Department, Fluor Daniel (I) Pvt Ltd., Gurugram, India
e-mail: manish.arya@fluor.com

P. Chakraborty
e-mail: pratik.chakraborty@fluor.com

M. Dhawan
e-mail: munish.dhawan@fluor.com



M. Madhavan et al. (eds.), *Proceedings of the Indian Structural Steel Conference 2020 (Vol. 1)*, Lecture Notes in Civil Engineering 318,
https://doi.org/10.1007/978-981-19-9390-9_2

# 1 Introduction

SPMTs or PMTs are often used to transport heavy and large objects such as heavy process structures, pipe racks etc. It is important to create optimum and required stability to ensure quality, safety, and reliability in these kinds of transportations. Generally the responsibility of stability during transportation of structures rests with logistics service provider as they analyze all the technical measurement required to achieve the stability. However, structural analysis also must be made before handing the structure to Logistics Service Provider to ensure no failure of structural members and serviceability of structure and SPMT/PMT during transportation.

The stability and effective distribution of imposed load from structure are achieved through hydraulic grouping of combination of trailers and hydraulic suspension of axles. In normal operation, generally two methodologies named three points loading and four points loading are adapted to create stability. In these methods, loads are distributed among different trailer group based on their positions with respect to Center of Gravity (COG) of structure.

The trailers are connected through hydraulic circuits to form into trailer groups, which support the structure. The axles/tires in each trailer groups are assumed to have equal pressure within that trailer group and the total structure weight is distributed as per the individual trailer group COG position in relation to the structure COG.

To analyze the trailer behavior, SPMT trailers are modeled as spine beams in structural analysis software (STAAD Pro). Structure/modules are placed on top of SPMT (spine beams) and the loads/reactions from SPMTs are transferred at the bottom of structure. Under heavy loading of the structures, the spine beams assume a sagging profile. On the other hand, when power pack loads are applied in analysis at the ends of spine beams, those loads create hogging effect on the spine beams and thus reduce the sagging deflection at central span.

For light weighted structure it has been found that sagging deflection of spine beam due to structure load alone is getting converted to hogging profile after application of PPU weight. On some case the magnitude of hogging deflection has been found to be higher than the allowable limit, thus proving analysis with PPU weight consideration as more onerous case. It was found that weights of lighter structures are sometimes insufficient to counteract the moment generated by the application of PPU loads at the cantilever ends of spine beam.

Two possible alternative methods for reducing the trailer deflection are Ballasting and Trailer wheel disengagement. For Ballasting, heavy surcharge load is placed on central span of trailer, which helps in counteracting the end hogging moments. For trailer wheel disengagement method, different set of wheel axles are made off-contact to ground.

Similarly, it was found that the PPU loading is also having impact on the strength parameters (Unity ratios) of pipe rack members. This chapter discusses the trailer wheel disengagement method along with two sample case studies to demonstrate the effect of PPU loading on spine beam deflection and pipe rack members. The effect of trailer wheel disengagement method on above parameters has also been studied.

## 2 Analysis of Trailer and Deflected Profile—Effect of PPU Load

Sample comparative study is performed for 2 different pipe rack structures. One pipe rack is a continuous braced structure and other is a discontinuous braced pipe bridge. Spine beam deflected shapes for both structures are presented to illustrate the effect of PPU weight on trailer spine beam deflection. For large length of transportation route, two PPUs are used many times. So, as more stringent case, weights of 2-PPUs are considered here. Structure and trailer spine beams are modeled and analyzed to get deflected shape of trailer spine beam.

### *2.1 Example 1: Continuous Braced Structure (Pipe Rack)*

Length of rack = 60 m; Width of rack = 8 m; Height of structure = 10.455 m.

COG in longitudinal direction = 30.011 m.

COG in transverse direction = 4.585 m.

Weight of structure (including steel, pipe, cable trays) = 248 metric ton (Figs. 1, 2, and 3).

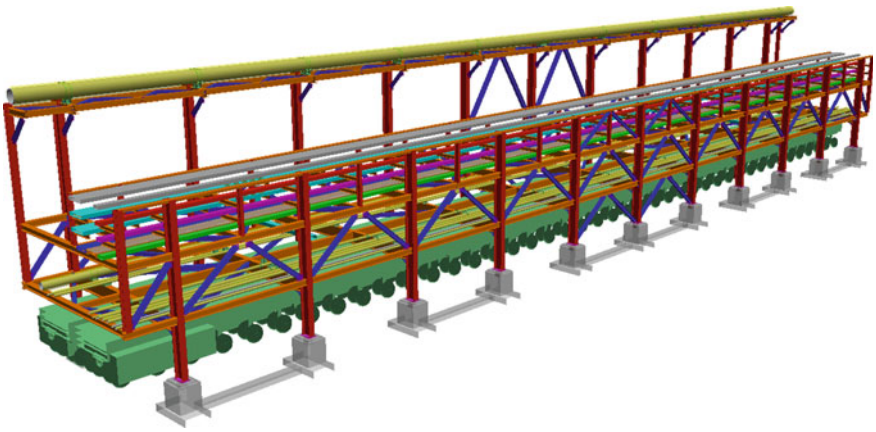

**Fig. 1** 3D view of example-1 pipe rack

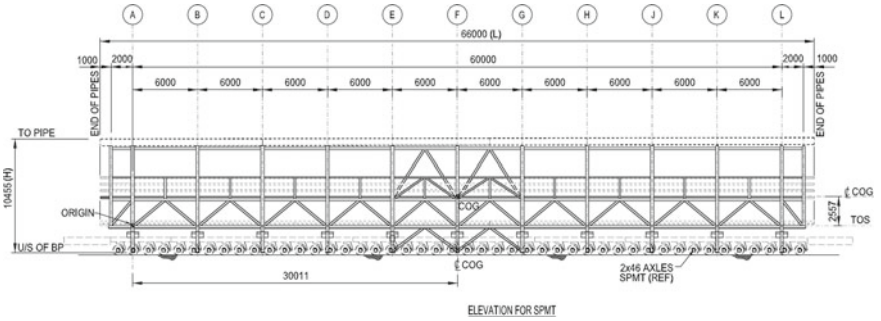


**Fig. 2** Longitudinal section of example-1 pipe rack

**Fig. 3** Transverse section of example-1 pipe rack

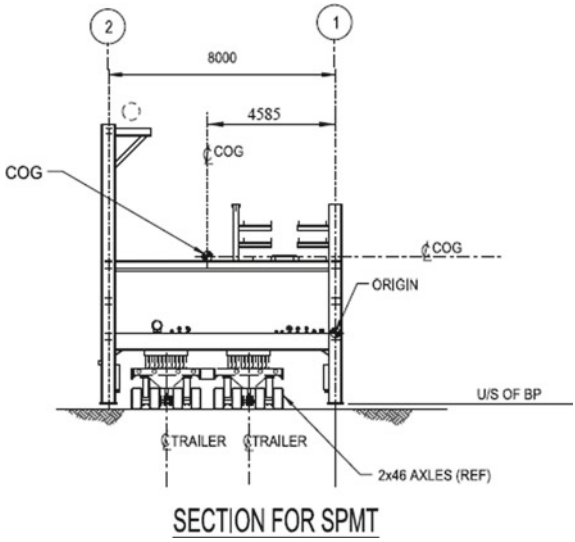


## *2.2 Example 2: Discontinuous Braced Structure (Pipe Bridge)*

Length of rack = 60 m; Width of Rack = 8 m; Height of structure = 12.217 m.

COG in longitudinal direction = 29.794 m.

COG in transverse direction = 3.825 m.

Weight of structure (including steel, pipe, cable trays) = 317 metric ton (Figs. 4, 5, and 6).

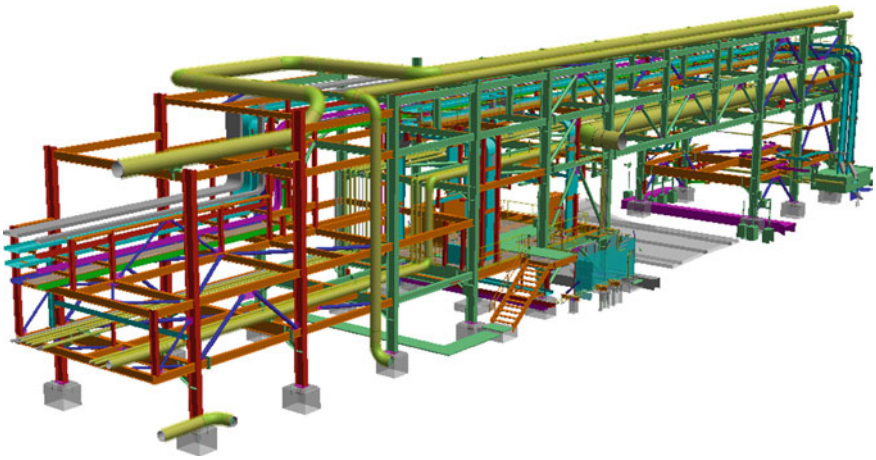

**Fig. 4** 3D view of example-2 pipe bridge

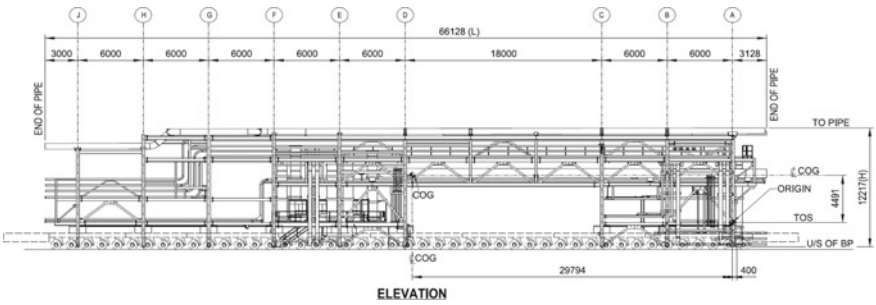


**Fig. 5** Longitudinal section of example-2 pipe bridge

## 3 Modular Trailer and PPU Details

KAMAG K25H SPMT;

Numbers of axles = 46; Longitudinal grouping of axles;

Center to center distance between 2 trailers = 3.3 m in transverse direction;

Spacing of axles = 1.5 m in longitudinal direction;

2 PPU weight = 20 metric ton (Fig. 7).

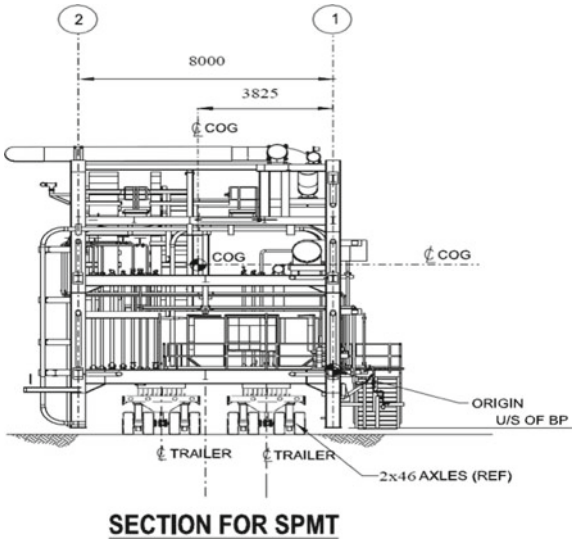


**Fig. 6** Transverse section of example-2 pipe bridge

**Fig. 7** Picture of modular trailer with double PPU

## 4 Analysis Approach

To analyze pipe rack and pipe bridge, two type of analysis are performed.

First Analysis—In this analysis, both Pipe Rack (Example-1) and Pipe Bridge (Example-2) are analyzed to calculate the SPMT spine beam deflection with all wheel engaged, without PPU and with PPU condition.

**Table 1** Two distinct trailer axles-disengagement profiles

| Example 1 (pipe rack) | Example 2 (pipe bridge) |
|---|---|
| Case (i): 11 + 6D + 3 + 6D + 3 + 6D + 11 | Case (i): 21 + 4D + 21 |
| Case (ii): 9 + 6D + 6 + 4D + 4 + 6D + 11 | Case (ii): 11 + 4D + 6 + 4D + 6 + 4D + 11 |

Where "*n*D" denotes "*n*" number of wheel disengaged

Before development of software analysis model, the wheel reactions for each trailer groups are determined by using equation of static equilibrium. When all axles are engaged (i.e. in contact with the ground), the reaction gets generated at each tire. These reactions are kept uniform within particular trailer group (through hydraulic circuit) but differ between each group. Accordingly, the calculated tire reactions for each group have been manually applied as upward uniformly distributed force i.e. UDL (owing to the closely spaced tires). Pseudo supports are modeled in software to make a valid model and it has been ensured that those supports do not attract any reaction.

PPUs get connected to the end of spine beam as cantilever elements. For double PPU case, an adapter is used to connect the PPUs together and then the adapter is attached to the trailer along with the PPUs. To simulate that, a concentrated load equal to the PPU and the adapter weight is applied at the end of spine beam along with a concentrated moment to cater for the cantilever nature of the PPUs. Second Analysis—To control the SPMT spine beam deflection for "with PPU" condition, few wheel axles are disengaged. Weight of disengaged axles, which are not in contact with ground, counteract the moment generated due to PPU weights and at the same time the disengaged axles result into local omission of reaction values. Both of these effects help in increasing the sagging behavior and reducing hogging profile.

To simulate the axle disengagement in software model, reactions have been recalculated considering lesser number of axles for applicable trailer groups and then the upward UDL loads have been omitted at the location of the disengaged axles.

Multiple iterations of disengagement of axles are performed to obtain most favorable deflection profile. Pipe Rack and Pipe Bridge are analyzed with 2 distinct trailer axles-disengagement profiles given in Table 1.

## *4.1 Result of First Analysis*

Sagging deflected profile occurred in spine beam when PPU weight is not applied. This sagging profile changes to hogging profile when PPU weights are applied at the cantilever end of spine beam (Figs. 8, 9, 10, and 11). Significant change in trailer spine beam local deflection and member unity ratios due to PPU weight are noticed (refer Figs. 9 and 11 for deflection and Fig. 18 for Member URs).

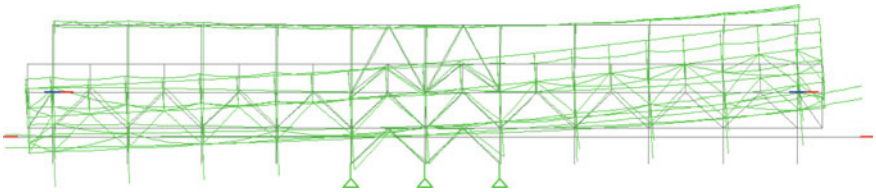

**Fig. 8** Example 1 (pipe rack) deflected shape—without PPU weight (local deflection 13.49 mm)

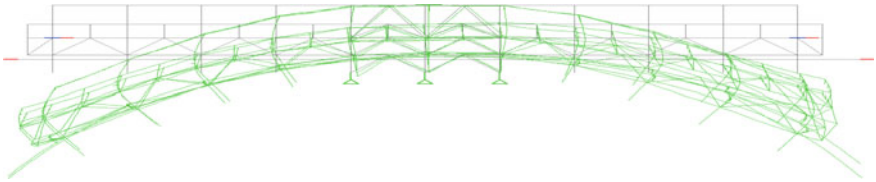

**Fig. 9** Example 1 (pipe rack) deflected shape—with PPU weight (local deflection 175.40 mm)

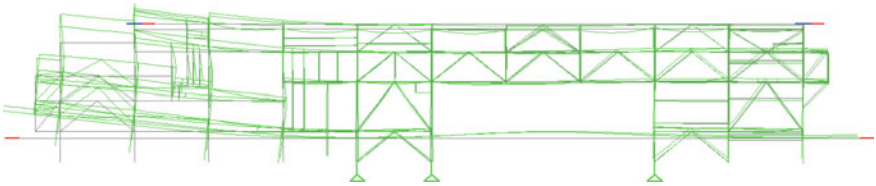

**Fig. 10** Example 2 (pipe bridge) deflected shape—without PPU weight (local deflection 60.55 mm)

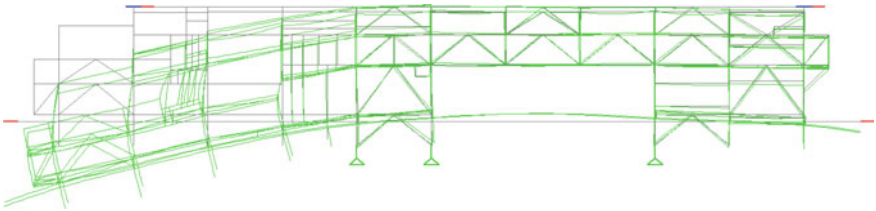

**Fig. 11** Example 2 (pipe bridge) deflected shape—with PPU weight (local deflection 252.58 mm)

Generally allowable SPMT spine beam deflection is 100 mm. Hence per above analysis it is clear that we cannot ignore PPU weight while doing the analysis. To bring trailer spine beam deflection under allowable limit, multiple axles of trailer are disengaged and second analysis is performed and results are as below.

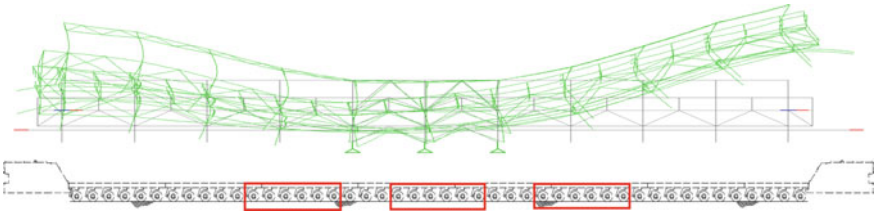

**Fig. 12** Case (i) 11 + 6D + 3 + 6D + 3 + 6D + 11 for example 1 (pipe rack) (local deflection 93.87 mm)

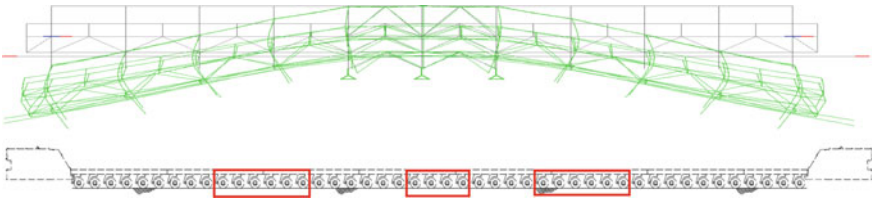

**Fig. 13** Case (ii) 9 + 6D + 6 + 4D + 4 + 6D + 11 for example 1 (pipe rack) (local deflection 30.78 mm)

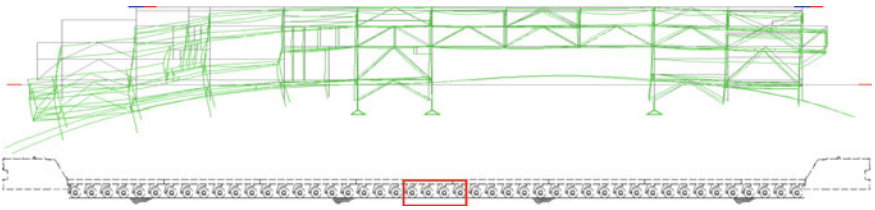

**Fig. 14** Case (i) 21 + 4D + 21 for example 2 (pipe bridge) (local deflection 202.67 mm)

## *4.2 Result of Second Analysis*

Analysis based on 2 distinct trailer axles-disengagement profiles is carried out and outcomes are presented here. Figures 12 and 13 show the deflection diagram of example-1 structure (pipe rack) for both cases. Figures 14 and 15 show the deflection diagram of example-2 structure (Pipe Bridge) for both cases. Figures 18 and 19 show the variation in Member URs.

Below Figs. 16 and 17 show the comparison of trailer's deflection and Figs. 18 and 19 show the variation in member URs with/without PPU weight and with both disengagement profiles.

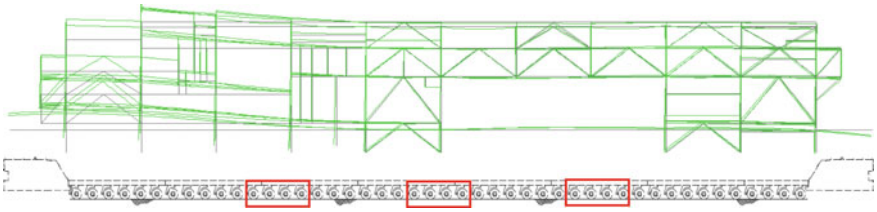

**Fig. 15** Case (ii) 11 + 4D + 6 + 4D + 6 + 4D + 11 for example 2 (pipe bridge) (local deflection 31.09 mm)

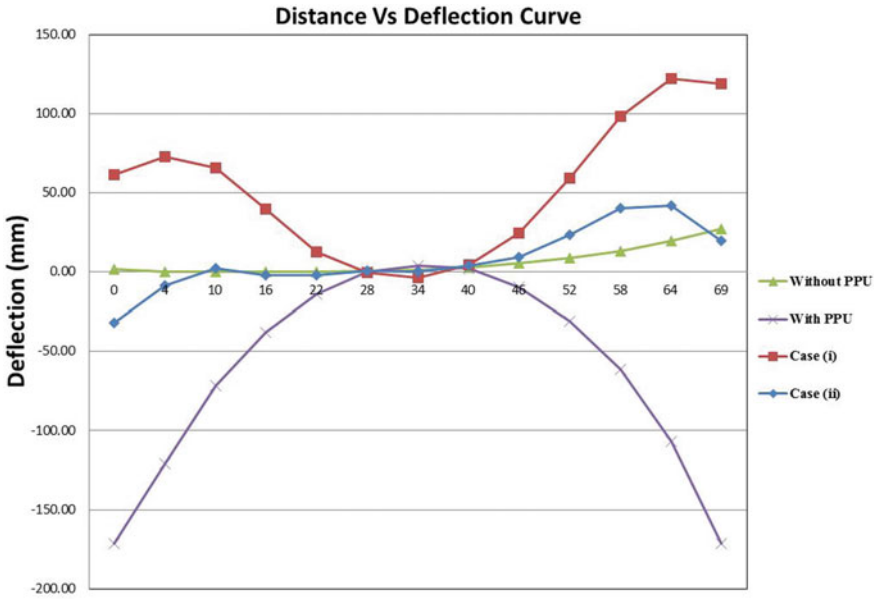


**Fig. 16** Trailer spine beam versus deflection curve for axles-disengagement profiles (example 1)

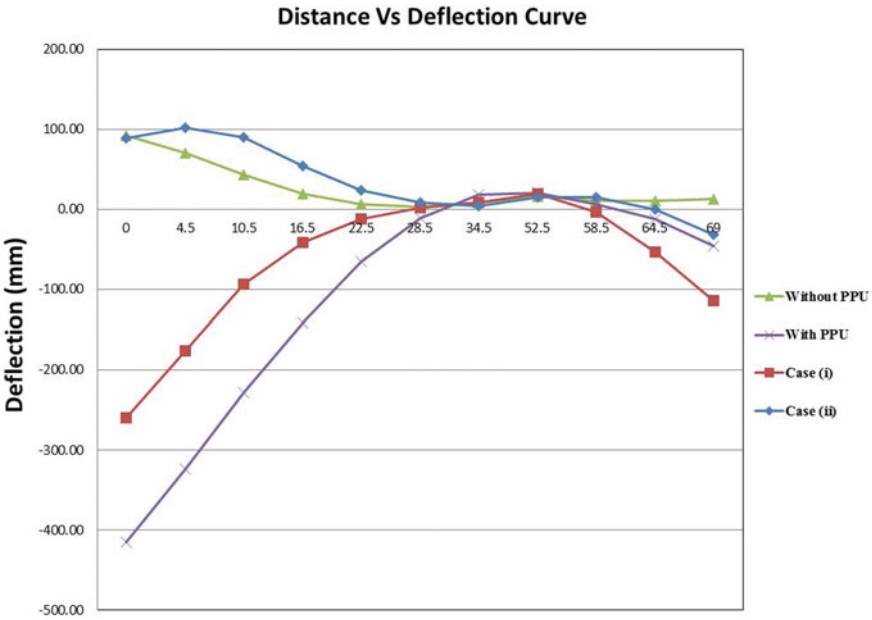


**Fig. 17** Trailer spine beam versus deflection curve for axles-disengagement profiles (example 2)

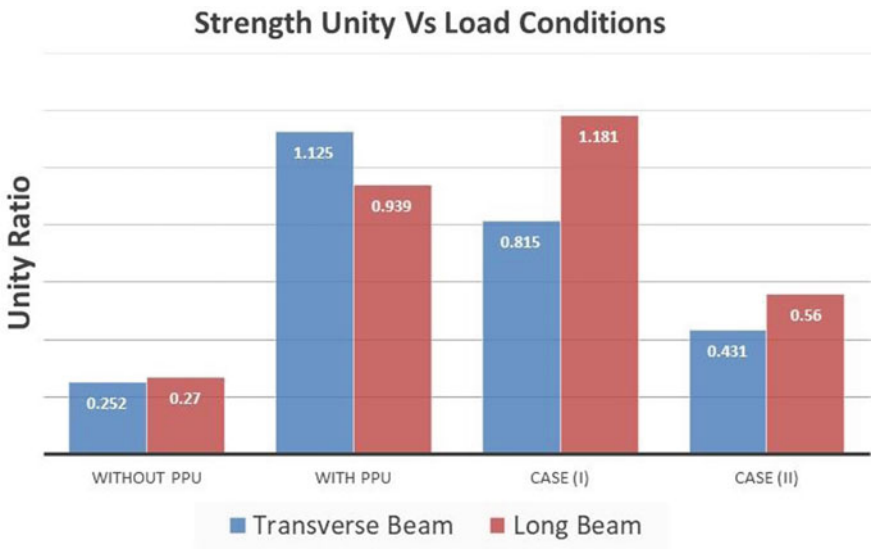


**Fig. 18** Variation in member UR (example 1)

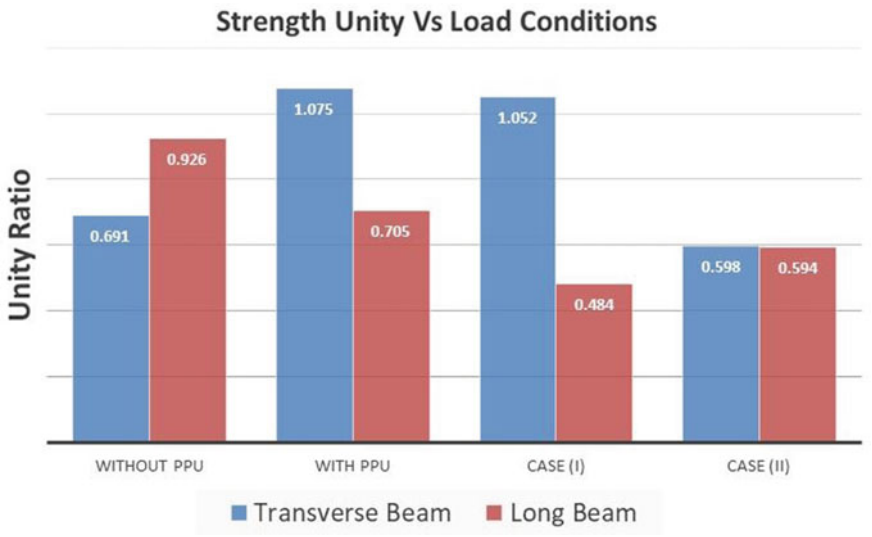


**Fig. 19** Variation in member UR (example 2)

## 5 Conclusion

Figures 16 and 17 curves are based on results of analysis without PPU and with PPU. Results in these figures clearly show that SPMT trailer's deflection with PPU is much higher than without PPU consideration. Deflection of trailer's spine beam varies with different axles-disengagement consideration. Typically each set of disengaged axles yields local sagging effect. Iterative analysis is required to reach at the most optimum trailer profile. In addition to trailer deflection, other aspects like Stability, Member and Connection unity ratios (Strength checks) shall also be looked at with the considered trailer profile. However, it is found that nature of variation in Member URs is generally consistent with that of deflection, i.e. the most favorable trailer profile from serviceability consideration also generally yields toward favorable effect for strength checks.

From the aforesaid case studies, we can safely conclude that PPU weight should not be ignored in land transport analysis. To cater trailer deflection exceedance, method of axles-disengagement can be used in analysis. Disengaged axle profile shall be determined in a way which results into reduction of spine beam deflection.

Having said this, the engineer needs to judiciously apply the recommendations herein to suit particular project requirements, with application of his/her engineering judgment based on project specific consideration. Also, close coordination between Structural Engineer and Logistics Service Provider is required for determination of trailer profile. The final trailer profile shall be mutually agreed upon between both the parties.

# Analysis of Guyed Mast Using Gust Factor and Patch Load Method


**Srinivas Tanuku and K. Rama Mohana Rao**

**Abstract** Guyed masts have unique structural behaviour among other civil engineering structures due to their height, slenderness, light weight and overall flexibility of mast. Wind is predominant on these structures, are very sensitive to dynamic excitation from gusty wind due to flexibility associated with both mast-slender and guy cables. As per IS 875 (Part 3)-2015, dynamic wind loading shall be considered for such flexible structure using gust factor (G) method which is based on spectral characteristics of wind velocities, first natural frequency and damping ratio of structure, assuming that dynamic response at every point is a simple multiple of its static response of steady winds. Gust factor method is valid for structures with one or two dominant vibration modes, and it is not appropriate for guyed mast where 15–20 vibration modes contribute significantly to the response of structure to turbulent wind. In lieu of dynamic analysis Sparling et al. (J Int Assoc Shell Spatial Struct 37(2):89–106, 1996, [6]) proposed patch load method of analysis that utilizes a series of static load pattern to replicate effects of wind gusts and systematically accounts for the characteristics of mast and wind using empirical scaling factors. In this paper, study of gust factor method and patch load method for 100 m high guyed mast is undertaken through load calculation using gust factor and patch load method with geometrically non-linear analysis using STAAD Pro Advanced Analysis software along with comparison statement presented. From the analysis, gust factor method heavily underestimate leg forces in upper spans and bracing forces in middle of each spans and concluded that patch load method gives better approximation compared to gust factor method for analysis of guyed mast.

S. Tanuku (✉) · K. Rama Mohana Rao (✉)
Department of Civil Engineering, Jawaharlal Nehru Technological University, Hyderabad, Telangana, India
e-mail: Srinit@ramboll.com

K. Rama Mohana Rao
e-mail: rkunapareddy@yahoo.com



M. Madhavan et al. (eds.), *Proceedings of the Indian Structural Steel Conference 2020 (Vol. 1)*, Lecture Notes in Civil Engineering 318,
https://doi.org/10.1007/978-981-19-9390-9_3

## 1 Introduction

Guyed mast consists of tall structure laterally supported with pre-tensioned cables providing horizontal supports of greatest possible stiffness at several elevations spaced at equal angle around mast. The stability of guyed mast is influenced by the cross-section area of guy cables, second moment of area of mast cross-section and Guy cable initial tension which has both beneficial and determinantal effect on overall stability.

Wind is predominant load on analysis of guyed mast and due to turbulent nature of wind velocities, the wind loads acting on structure are also highly fluctuating. The back-ground response made up largely low-frequency contribution below the lowest natural frequency vibration is the largest contributor for along wind loading. The resonant contribution becomes more significant, when the lowest natural frequency is less than 1 Hz, will eventually dominate as structure becomes taller in relation to their width. When structure experience resonant dynamic response, Inertia force proportional to mass of structure, Damping and stiffness force proportional to deflection play counteracting structural forces to balance wind forces.

Maximum along wind response of flexible structures is obtained from product of mean static displacement and non-dimensional constant, the gust factor $G$, which involve spatial correlation and energy spectrum of gusty wind and as well dynamic characteristics of structures such as first natural frequency, damping ratio for the first vibration mode. Gust factor method ($G$) assumes that dynamic response at every point is a simple multiple of its static response of steady winds and shape of fundamental mode of vibration is a linear function of height. While this assumption is valid for one or two dominant vibration modes, it may not be appropriate for guyed mast where 15–20 vibration modes contribute significantly to the response of structure to turbulent wind.

The significance of non-uniform gust loading on continuous structure like guyed masts has been recognized for some time. As early as 1960, Cohen advocated the use of multiple load patterns to quantify gust effects. In addition to full wind loading on all spans, Cohen (1960) recommended the use of load patterns in which 25% of the wind load was removed from one span at a time while full wind load was applied to remaining spans.

The International Association for Shell and Spatial Structures (IASS) adopted a similar approach in their recommendation for the design and analysis of guyed mast [3]. In the IASS Procedure, the dynamic wind load (Defined as the difference between the gust and mean wind loads) is applied to mast using different load patterns: Load acting on all spans simultaneously, load acting on each span individually and load acting on all but one span for each span in turn. The total response envelope for each point along the mast is then obtained by determining the extreme positive and negative values of dynamic response from the patterned load cases and combining them with the response due to the mean wind load.

Gerstoft (1984) proposed a patch load method based partly on the dynamic analysis approach suggested by Allsop (1983). Gerstoft's method deals specifically with

bending moments in the mast and does not address shear or deflections. The approximate back ground response is generated by utilizing two series of patch loads: one series consists of load patches applied to each span individually and is used to produce bending moment at guy support levels, while the second series consists of load patches extending from mid span to mid span of adjacent spans and is used to produce mid span moments. To model the lack of correlation between wind gusts, Gerstoft obtained the resultant back-ground response by combining the load path results as the root-sum-of-squares.

Davenport and Sparling (1992) introduced analysis procedure is an extension of Gerstoft's method. A simple, yet accurate method is provided to quantify the effects of resonant response. In addition, the scope of method is expanded to include shear forces in the mast as well as deflections. The dynamic response of guyed mast is clearly influenced by large number of factors including the structural properties, geometry and drag characteristics of the mast and guys as well as the velocity profile and turbulence characteristics of the wind. Results from a full dynamic analysis typically indicate a response (e.g. Displacement or force) that fluctuates about a mean value.

Davenport and Sparling (1992) divided the fluctuating part in to,

- Back-ground response
- Resonant response.

The back-ground response is slowly varying and occurs at a frequency below the fundamental frequency. Back-ground response will be influenced by the relative magnitude of the mast and support stiffness and by the distribution as well as magnitude of load. Allsop (1983) demonstrated that the shape of a given influence line was determined in part by the relative stiffness of the guys and mast. The back-ground component of dynamic response can be completely defined based on three factors,

- Result from the static patch load analysis
- A scaling factor based on stiffness parameter
- A scaling factor based on the length scale parameters.

The resonant response varies rapidly and includes contribution from a large number of vibration modes, each with distinct modal properties. The relative importance of the various vibration modes will vary from mast to mast and depend on type and location of the response being considered. For the broadest range of application, therefore, it is preferable that parameters used to represent resonant response be independent of modal properties so that they apply equally well to all modes. Allsop (1983) related the resonant response of guyed mast to a dimensionless parameter termed the inertial resistance factor, Q. This factor can be derived from the resonant response equations. Q is useful in that it reflects many of the variable associated with resonant response, including the mass, stiffness, drag characteristics and size of the mast, as well as the strength of the windstorm.

Sparling et al. [6] proposed simplified dynamic analysis by replacing gust factor technique with a method that utilizes a series of static load pattern to replicate the effects of wind gusts and systematically account for characteristics of mast and wind

through use of empirical scaling factors. The resulting response eliminate location of zero response that are unavailable in conventional static methods, there by provide better approximation of full dynamic results.

Current paper deals with application of patch load method for parametric study for comparing to gust factor method. Detailed specifications, calculations are presented in subsequent sections.

## 2 Mast Specifications

A guyed mast of 100 m height with equilateral triangular cross-section is considered in current study to support telecom antenna equipment (3 × GSM + 3 × 1.2 m ø MW) for wind speed of 160 kmph of 3 s duration. Guy wires are connected at three levels spaced at 120° in three radial directions at 75 m radius from centre of mast. Mast is divided in to 17 sections consists of 6 m height except top section of 4.0 m with uniform face width of 1.0 m throughout mast height. Each section contains single lacing bracing pattern closed with horizontal member at every section. All legs are consisting of circular hollow section by considering their higher stiffness for small steel area, lesser wind resistance and bracings are of angular profiles for easy fabrication and installation with bolted connection on gusset plate (Fig. 1; Tables 1 and 2).

## 3 Load Calculations

Wind is predominant loads on these slender structures, the basic wind speed of 44 m/s, of peak gust velocity averaged over a short time interval of about 3 s with a mean probable structure deign life of 100 years situated in open terrain (Terrain category 1) is considered for analysis. The basic wind speed ($V_b$) shall be modified to include the effects of importance of structure, terrain roughness and height, local topographical features and cyclonic effects (if any) to obtain design wind speed ($V_z$) at any height is given by

$$V_z = V_b k_1 k_2 k_3 k_4 \tag{1}$$

### *3.1 Design Hourly Wind Pressure*

The design hourly mean wind speed at height $z$, for terrain category 1 can be obtained as below.

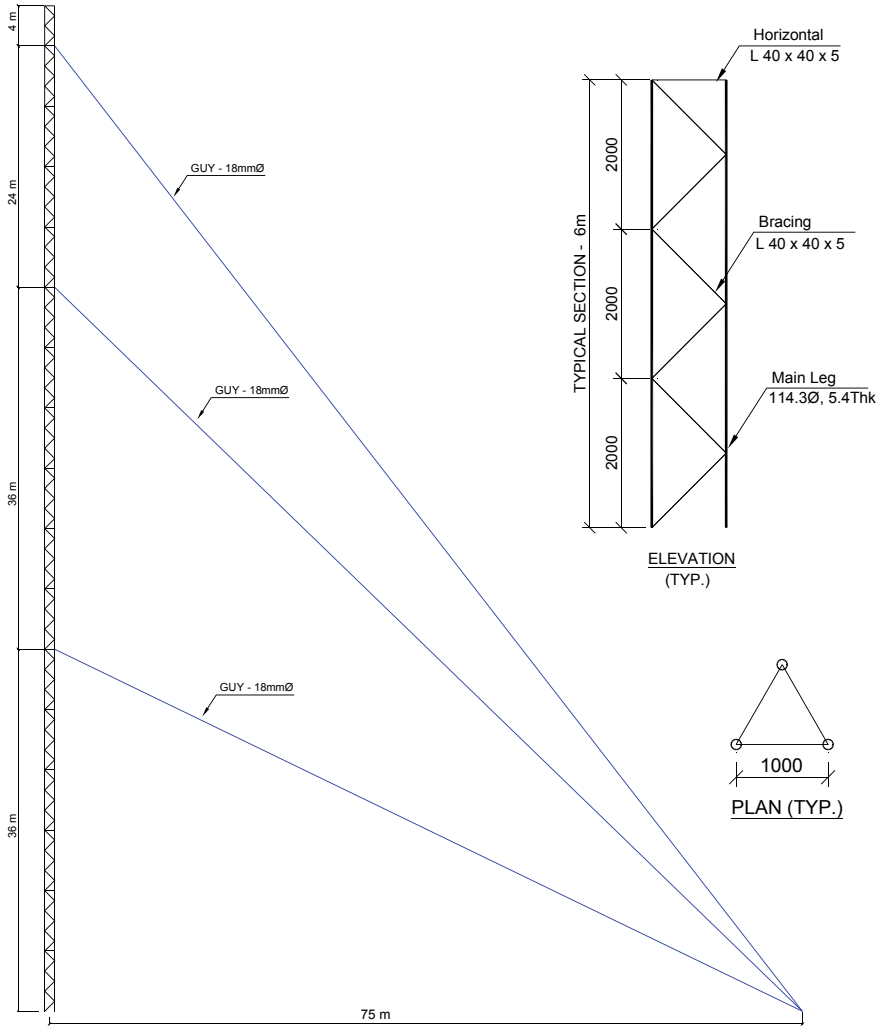


**Fig. 1** 100 m guyed mast configuration

$$\overline{V}_{z,d} = \overline{V}_b k_1 \overline{k}_{2,i} k_3 k_4 \tag{2}$$

where $\overline{k}_{2,i}$ is hourly mean wind speed factor for terrain category 1 is as follow:

$$\overline{k}_{2,i} = 0.1423\left[In\left(\frac{z}{z_{0,i}}\right)\right]\left(z_{0,i}\right)^{0.0706} \tag{3}$$

$k_1$ Risk coefficient, 1.07 for 100 years return period

**Table 1** Material properties

| Description | | Legs | Bracings | Horizontal |
|---|---|---|---|---|
| Grade | | S 355 | E 250 | E 250 |
| Standard | | IS 1161 | IS 2062 | IS 2062 |
| Yield stress | MPa | 355 | 250 | 250 |
| Ultimate tensile strength | MPa | 490 | 410 | 410 |
| Cross-sectional area | $mm^2$ | 1268 | 378 | 378 |
| $R_{min}$ | mm | 29.8 | 7.7 | 7.7 |
| $R_{med}$ | mm | 29.8 | 12 | 12 |
| Unit weight per metre | kg/m | 9.96 | 3.0 | 3.0 |

**Table 2** Guy wire details

| Description | | Guy 1 | Guy 2 | Guy 3 |
|---|---|---|---|---|
| Height from base | m | 36 | 72 | 96 |
| Radius | m | 75 | 75 | 75 |
| Chord angle | Deg | 25.79 | 44.02 | 52.19 |
| Chord length | m | 82.74 | 103.61 | 121.52 |
| Nominal diameter | m | 0.018 | 0.018 | 0.018 |
| Area | $m^2$ | 1.9E−04 | 1.9E−04 | 1.9E−04 |
| Weight per metre | kg/m | 1.22 | 1.22 | 1.22 |
| Modulus of elasticity | KPa | 1.65E+08 | 1.65E+08 | 1.65E+08 |
| Breaking strength | kN | 232 | 232 | 232 |
| Initial tension | kN | 23.2 | 23.2 | 23.2 |

$k_3, k_4$ 1.00 assuming flat terrain and non-coastal zone respectively.

The design hourly wind pressure at any height ($z$) is given by (Fig. 2)

$$\overline{p}_d = K_d K_a K_c \left(0.6\, \overline{V}_{z,d}^2\right) \tag{4}$$

## *3.2 Wind Resistance*

Wind resistance is defined as the resistance to the flow of wind offered by the assembled components of tower and by any elements which it supports shall be derived from the force coefficient given in IS 875 (Part 3). The term wind resistance to encompass the combination of area, shielding effects and drag characteristics. For calculation of wind resistance, 100 m guyed mast has been divided in to series of sections to enable

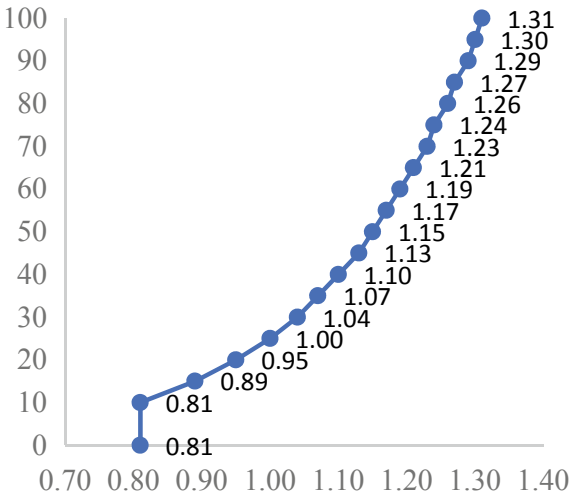


**Fig. 2** Mean hourly design wind pressure (kN/m$^2$)

**Table 3** Wind resistance

| | | |
|---|---|---|
| Mast, 6 m section | m$^2$ | 2.95 |
| Linear accessories | m$^2$/m | 0.17 |
| 3 × GSM antenna | m$^2$ | 2.80 |
| 3 × 1.2 m ø MW antenna | m$^2$ | 4.28 |

the wind loading to be adequately represented in analysis. Wind resistance of mast is constant throughout height due to constant cross-section. In addition, wind resistance of linear accessories (non-structural components that extend over several panels such as feeders, ladders) are calculated by assuming single frame and wind resistance of discrete accessories (Non-structural components that is concentrated within a few panels such as dishes, platform) are calculated by assuming individual member and their aspect ratio. Wind resistance of mast, linear and discrete accessories of mast are summarized as below (Table 3).

## *3.3 Wind Loads—Gust Factor*

The design peak wind load on structure at any height is given by,

$$F_z = C_{f,z}\, A_z \overline{\rho}_d\, G \tag{5}$$

Gust factor ($G$) is the ratio of the expected peak value of response variable to the mean values, and is dependent on both the overall height and level under consideration. Gust factor accounts for the resonant and non-resonant effects of random wind

**Table 4** Basic wind parameter

| | | |
|---|---|---|
| Aero dynamic roughness height | $Z_0$ | 0.002 |
| Peak factor for upwind velocity fluctuation | $g_v$ | 3.0 |
| Effective turbulence length scale | $L_h$ | 151 |
| Structure first mode frequency | $f_a$ | 0.55 |
| Peak factor for resonance | gR | 3.98 |
| Damping coefficient | $\beta$ | 0.02 |
| Basic wind speed | $V_b$ | 44 |

pressure. It does not include allowance for a cross-wind loading effects, vortex shedding, instability due to galloping. Gust factor is estimated using following formula as per clause 10.2 of IS 875 (Part 3)-2015 as per notation in the code.

$$G = 1 + r\sqrt{\left[g_{v^2} B_s (1 + \Phi)^2 + \frac{H_s g_{R^2} \mathrm{SE}}{\beta}\right]} \tag{6}$$

Gust factor is reducing with increase in height. Using Eq. 6 and wind parameters as per Table 4 wind parameters, an average value of 2.06 is observed for 100 m high guyed mast.

Wind forces on tower body and linear accessories are distributed in all sectional points at an elevation equally, with a fact that force coefficient has accounted for both wind ward and leeward tower faces including shielding effect and symmetrical location of linear accessories with respect to centre of mast. And wind forces on discrete accessories are distributed to the respective member connecting joints as concentrated vector loads. In Triangular mast, the maximum leg loads occur in the single leg on axis of the tower in the wind direction with wind normal to one face. For bracing members, the maximum forces occur for wind parallel to face in the plane of bracing in wind direction. Therefore, three wind directions, i.e. 0°, 90°, 180° with respect to mast are considered for analysis (Fig. 3).

## 4 Patch Load Method

Patch load method analysis is undertaken in two stages, with the mean wind load effects considered separately from the fluctuating load effects. The design dynamic response $\hat{r}$ may be expressed as,

$$\hat{\mathbf{r}} = \overline{\mathbf{r}} \pm \hat{\mathbf{r}}_{\mathrm{PL}} \tag{7}$$

In which the peak fluctuating response is represented by the effective patch load response, $\hat{r}_{\mathrm{PL}}$. As with simplified procedure, the fluctuating response can be added to or subtracted from the mean response. Minimum criteria—height of cantilever,

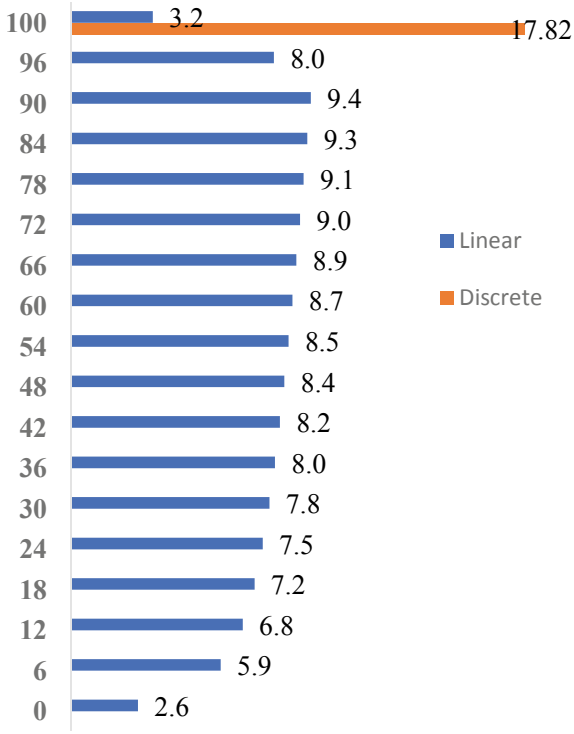


**Fig. 3** Wind load (kN) at each section by gust factor

tower stiffness and mast drag characteristics shall meet to apply patch load method in lieu of full dynamic analysis of guyed mast.

## *4.1 Mean Response*

The mean component of the wind load is applied to the tower by taking in to account the large displacement effects in the tower, i.e. the non-linear properties of the guys and the second-order ($P$-$\Delta$) effects associated with axial forces acting on the mast. This displaced position of the system under mean wind load is referred to as the mean equilibrium position. Mean wind speed profile shall be based on design hourly mean wind speed for mast site.

The mean wind load $\overline{F}(z)$ acts simultaneously at all points along the mast as well as on each of the cables and is given by expression

$$\overline{F}(z) = \frac{1}{2}\rho_a C_D(z)\ A(z)\ \overline{v}(z)^2 \tag{8}$$

To simplify calculations, the mean wind load applied to each cable is assumed to be uniform along its length with a magnitude based on the mean wind speed at mid height of cable. The mean equilibrium position of the mast is determined by using iterative Newton–Raphson solution technique. The static solution allows for non-linear guy stiffness characteristics, displacements of the guys due to the mean wind load, the effects of eccentric guy attachment to mast and $P$-$\Delta$ effects arising from vertical forces acting on the mast.

## 4.2 Peak Fluctuating Response

Calculation of the fluctuating response requires that a series of static analyses be performed for each wind direction. Results from the individual analyses are combined in the prescribed manner and scaled to the approximate magnitude using scaling factors.

The Magnitude for individual patch load may be calculated as below

$$\overline{F}(z) = 2\, i_o q_0 \tag{9}$$

$i_o$ is a Turbulence intensity, is often related to root-mean-square value of wind speed fluctuations and is depending on site condition, $q_0$ is mean hourly design wind pressure at a given height. For each load patch, the reference elevation used to calculate $q_0$ should be taken at mid height of that patch (Fig. 4).

The patch loads should be applied to structure in its equilibrium position under the action of mean wind loading. This may necessitates calculating the response for each

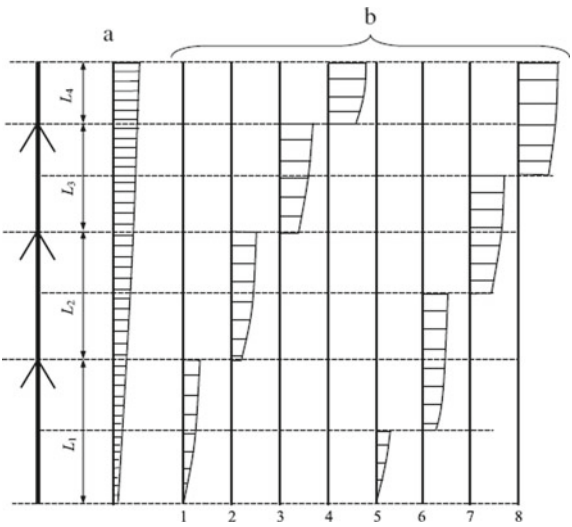


**Fig. 4** Patch load cases for guyed mast with three guy levels

patch load as the difference between the response due to the patch load combined with mean wind load and the response due to mean wind load acting alone.

To simulate the lack of correlation in the fluctuating wind loads, the responses due to individual load patches are combined as the root-sum-of-squares as follows:

$$\overline{r}_{\mathrm{PL}} = \sqrt{\sum_{i=1}^{n} r_{\mathrm{PL}i}^2} \tag{10}$$

where $\overline{r}_{\mathrm{PL}}$ is the resultant patch load response, $r_{\mathrm{PL}i}$ is the response due to the $i$th patch load, and $n$ is the total number of load patches that are required. By allowing for the lack of correlation in the gust load, at least in an approximate fashion, the root-sum-of-squares method of combining patch load results generates response pattern that similar to the back-ground component from the full dynamic analysis.

The design fluctuating response $\hat{\boldsymbol{r}}_{\mathbf{PL}}$ is then determined by the expression

$$\hat{r}_{\mathrm{PL}} = \overline{r}_{\mathrm{PL}}\ \lambda_B\ \lambda_R\ \lambda_{\mathrm{TL}}\ g \tag{11}$$

where

$\lambda_B$ Back-ground scaling factor,
$\lambda_R$ Resonant magnification factor,
$\lambda_{\mathrm{TL}}$ Turbulent length scale factor,
$g$ Statistical peak factor equal to 4.0.

Using conservative values for scaling factors ($\lambda_B = 0.75$, $\lambda_R = 1.20$, $\lambda_{\mathrm{TL}} = 1.05$), the design fluctuating response $\hat{\boldsymbol{r}}_{\mathbf{PL}}$ can be simplified in to

$$\hat{r}_{\mathrm{PL}} = 3.78\ \overline{r}_{\mathrm{PL}} \tag{12}$$

## *4.3 Criteria for Use Patch Load Method*

(a) The height of cantilever must be less than one-half the distance between the top two guy levels.

$$\begin{aligned}\text{Height of Cantilever} &= 6\text{ m} < 1/2 \times 36\text{ m},\\ &= 6\text{ m} < 18\text{ m, Ok}\end{aligned}$$

(b) Stiffness parameter ($\beta_s$). The ratio of bending stiffness of mast to the lateral stiffness of guys must be less than 1.0

**Table 5** Elastic stiffness of guy wire

| | | Guy details | | |
|---|---|---|---|---|
| | | G1 | G2 | G3 |
| $A_{Gi}$ | $m^2$ | 1.9E−04 | | |
| $E_G$ | kPa | 1.65E+08 | | |
| $\theta_{Gi}$ | Deg. | 25.79 | 44.02 | 52.19 |
| $L_{Gi}$ | m | 82.74 | 103.61 | 121.52 |
| $H_{Gi}$ | m | 36 | 72 | 96 |
| $K_{Gi}$ | | 469 | 238.9 | 148.1 |

**Table 6** Calculation of stiffness parameter ($\beta_s$)

| | | | |
|---|---|---|---|
| Elastic modulus of mast | $E_m$ | kPa | 2.00E+08 |
| Average moment inertia of mast | $I_m$ | $m^4$ | 9.24E-04 |
| Average span length between guy levels | $L_s$ | m | 32 |
| Number of guy levels | $n$ | Qty | 3 |
| Stiffness parameter | $\beta$ | | **0.254** |

$$\beta_s = \frac{4\left(\frac{E_m I_m}{L_s^2}\right)}{\frac{1}{n}\sum_{i=1}^{n} K_{Gi}\ H_{Gi}} \tag{13}$$

Elastic Stiffness of Guy at any level given as (Tables 5 and 6),

$$K_{Gi} = \frac{0.5\ N_i A_{Gi}\ E_{Gi} \cos^2 \theta_{Gi}}{L_{Gi}} \tag{14}$$

(c) Inertial resistance parameter ($Q$) which measures inertial forces relative to the damping forces must be less than 1.0 (Table 7)

$$Q = \frac{1}{30}\left(\frac{H\overline{V}_H}{D_o}\right)^{\frac{1}{3}}\left(\frac{m_0}{HR}\right)^{\frac{1}{2}} \tag{15}$$

From the above, current mast specification are comply with minimum criteria, hence patch load method can be applicable.

## *4.4 Mean and Patch Wind Load*

See Tables 8 and 9.

**Table 7** Mast inertia resistance parameter (Q)

| | | | |
|---|---|---|---|
| Height of mast | H | m | 100 |
| Hourly mean wind speed at top | $\overline{V}_H$ | m/s | 46.7 |
| Average mast face width | $D_o$ | m | 1.0 |
| Average unit mass of mast including ancillaries | $m_0$ | kg/m | 117.3 |
| Average wind resistance of the mast | $R$ | $m^2/m$ | 0.49 |

**Table 8** Design wind pressure ($kN/m^2$) for each patch load

| Patch | Range (m) | $p_a$ ($kg/m^3$) | $z$ (m) | $K_{2,i}$ | $\overline{v}(z)$ | $i_o$ | $\overline{v}_{\text{ref}}$ | Wind pressure ($kN/m^2$) |
|---|---|---|---|---|---|---|---|---|
| 1 | 0–36 | 1.22 | 15 | 0.82 | 41.2 | 0.14 | 39.3 | 2.78 |
| 2 | 36–72 | 1.22 | 45 | 0.92 | 46.2 | 0.12 | 39.3 | 2.56 |
| 3 | 72–96 | 1.22 | 75 | 0.97 | 48.6 | 0.11 | 39.3 | 2.42 |
| 4 | 96–100 | 1.22 | 95 | 0.99 | 49.7 | 0.10 | 39.3 | 2.35 |
| 5 | 0–18 | 1.22 | 7.5 | 0.76 | 38.0 | 0.16 | 39.3 | 2.85 |
| 6 | 18–54 | 1.22 | 30 | 0.88 | 44.4 | 0.13 | 39.3 | 2.66 |
| 7 | 54–84 | 1.22 | 60 | 0.95 | 47.6 | 0.11 | 39.3 | 2.49 |
| 8 | 84–100 | 1.22 | 88 | 0.98 | 49.3 | 0.10 | 39.3 | 2.37 |

**Table 9** Wind Load (kN) at section wise for each patch load

| # | Section Ht | Cum. Ht | Only mean (kN) | Mean load + respective patch load (kN) | | | | | | | |
|---|---|---|---|---|---|---|---|---|---|---|---|
| | | | | P1 | P2 | P3 | P4 | P5 | P6 | P7 | P8 |
| P1 | 4.0 | 100.0 | 3.36 | 3.36 | 3.36 | 3.36 | 4.03 | 3.36 | 3.36 | 3.36 | 4.03 |
| P2 | 6.0 | 96.0 | 4.95 | 4.95 | 4.95 | 5.95 | 4.95 | 4.95 | 4.95 | 4.95 | 5.95 |
| P3 | 6.0 | 90.0 | 4.89 | 4.89 | 4.89 | 5.89 | 4.89 | 4.89 | 4.89 | 4.89 | 5.89 |
| P4 | 6.0 | 84.0 | 4.82 | 4.82 | 4.82 | 5.82 | 4.82 | 4.82 | 4.82 | 5.83 | 4.82 |
| P5 | 6.0 | 78.0 | 4.75 | 4.75 | 4.75 | 5.75 | 4.75 | 4.75 | 4.75 | 5.76 | 4.75 |
| P6 | 6.0 | 72.0 | 4.68 | 4.68 | 5.69 | 4.68 | 4.68 | 4.68 | 4.68 | 5.68 | 4.68 |
| P7 | 6.0 | 66.0 | 4.59 | 4.59 | 5.61 | 4.59 | 4.59 | 4.59 | 4.59 | 5.60 | 4.59 |
| P8 | 6.0 | 60.0 | 4.51 | 4.51 | 5.52 | 4.51 | 4.51 | 4.51 | 4.51 | 5.52 | 4.51 |
| P9 | 6.0 | 54.0 | 4.41 | 4.41 | 5.42 | 4.41 | 4.41 | 4.41 | 5.42 | 4.41 | 4.41 |
| P10 | 6.0 | 48.0 | 4.30 | 4.30 | 5.31 | 4.30 | 4.30 | 4.30 | 5.31 | 4.30 | 4.30 |
| P11 | 6.0 | 42.0 | 4.18 | 4.18 | 5.19 | 4.18 | 4.18 | 4.18 | 5.19 | 4.18 | 4.18 |
| P12 | 6.0 | 36.0 | 4.04 | 5.02 | 4.04 | 4.04 | 4.04 | 4.04 | 5.05 | 4.04 | 4.04 |
| P13 | 6.0 | 30.0 | 3.87 | 4.86 | 3.87 | 3.87 | 3.87 | 3.87 | 4.89 | 3.87 | 3.87 |
| P14 | 6.0 | 24.0 | 3.67 | 4.65 | 3.67 | 3.67 | 3.67 | 3.67 | 4.68 | 3.67 | 3.67 |
| P15 | 6.0 | 18.0 | 3.41 | 4.39 | 3.41 | 3.41 | 3.41 | 4.35 | 3.41 | 3.41 | 3.41 |
| P16 | 6.0 | 12.0 | 3.03 | 4.01 | 3.03 | 3.03 | 3.03 | 3.97 | 3.03 | 3.03 | 3.03 |
| P17 | 6.0 | 6.0 | 2.29 | 3.27 | 2.29 | 2.29 | 2.29 | 3.23 | 2.29 | 2.29 | 2.29 |

## 5 Analysis and Results

A guyed tower is analysed by approximating it as an equivalent continuous beam-column on non-linear elastic support. The initial condition of a structure for analysis taken as that under the un-factored dead load with the guys, at their initial tensions. The analysis is based on second-order theory to take in to account the effects caused by changes in geometry of the shaft and guys due to loading. This ensures that all important influences of the mast's deformation (the variation in guy stiffness depending on their axial stress and applied load, the influence of axial forces on the bending moments) on the distribution of internal forces are taken in to account. STAAD Pro Advanced Analysis software has been used for geometrical non-linear analysis of guyed mast through applying loads as indicated in Sect. 3.3 (Fig. 5).

### *5.1 Member Forces*

See Fig. 6.

### *5.2 Displacements*

See Fig. 7.

## 6 Summary and Conclusion

From the detailed analysis, following conclusions are drawn using patch load method compared to gust factor method.

- No Difference observed in leg forces at cantilever portion in both methods.
- 50% forces in Top Span and 15–16% increase in middle and bottom span leg forces observed, and 3% forces are increased in bottom most section in patch load method.
- 40% forces are increased in bracings which are located at mid location of each span in patch load method.
- 3%, 13% and 33% increase of guy forces are observed in bottom, middle and Top guy wires, respectively.
- Displacements are reduced in patch load method due to loading pattern and 20% reduction observed in top span while 5–8% observed in remaining spans.

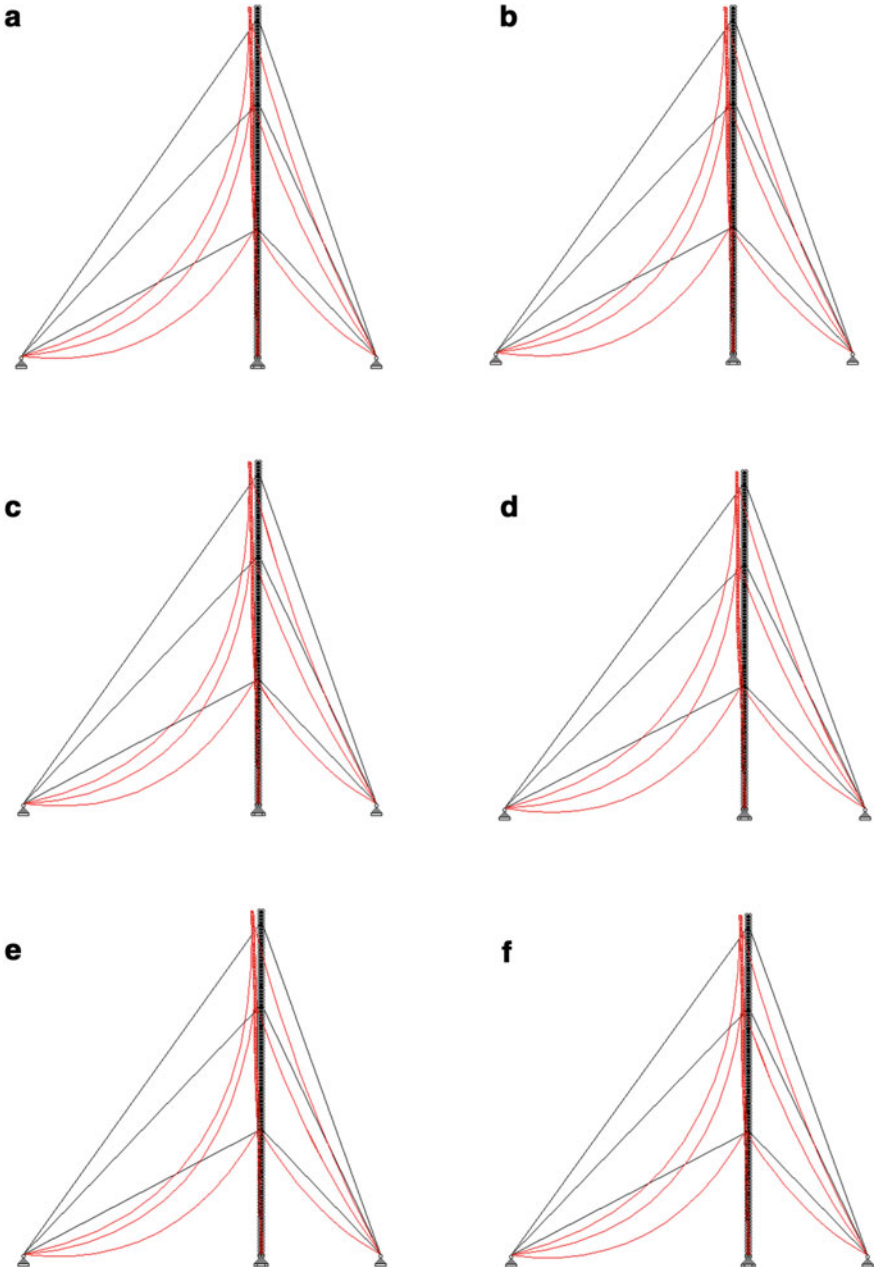


**Fig. 5** Deflected profile of guy mast under various load cases. **a** Mean wind. **b** Mean wind + patch 1. **c** Mean wind + patch 2. **d** Mean wind + patch 3. **e** Mean wind + patch 4. **f** Mean wind + patch 5. **g** Mean wind + patch 6. **h** Mean wind + patch 7. **i** Mean wind + patch 8. **j** Gust factor

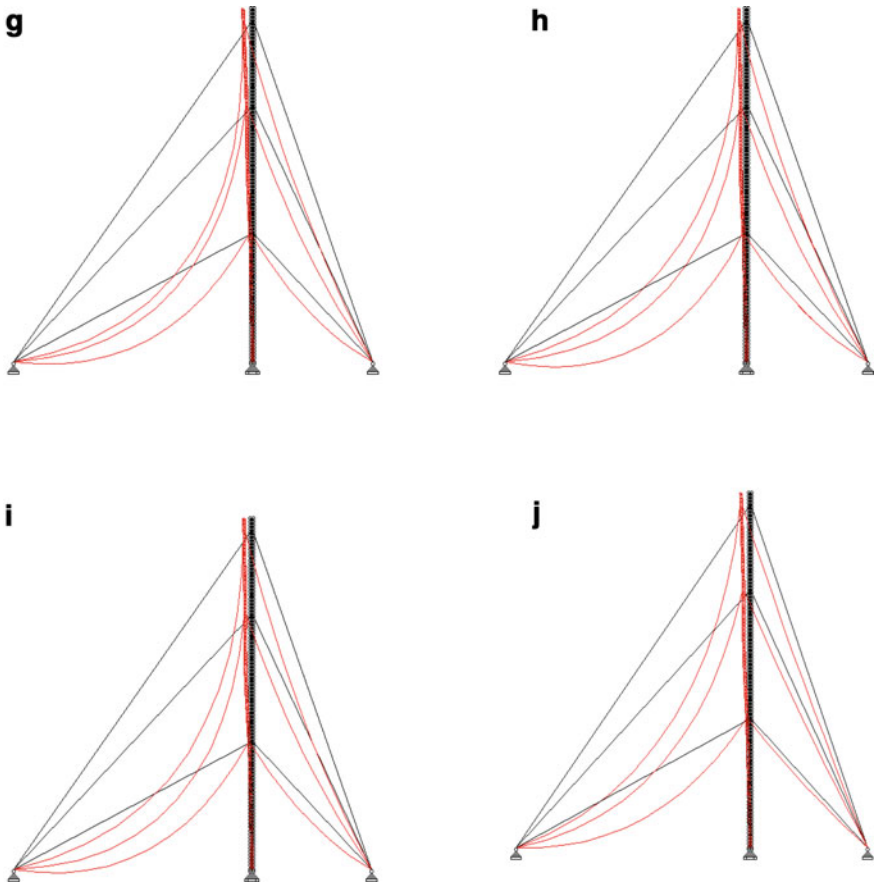


**Fig. 5** (continued)

## 7 Conclusion

From the detailed analysis it is noticed that, gust factor method under estimated leg forces (15% leg up to middle span and 50% in Top Span). Similarly, 40–70% bracing forces are underestimated in middle of each span. Also, Guy Tension in Top Guy location is heavily underestimated. Hence, more emphasize shall be given at top span for main leg force (Huge Variation), bracing forces in middle of each span as well Top Guy Wire while using gust factor method compared to path load method. It is also realized that these variations of forces may vary based on stiffness parameters and Mast Inertia resistance perimeter. Therefore, patch load method gives better approximation of analysis results in lieu of full dynamic analysis compared to gust factor method for guyed mast.

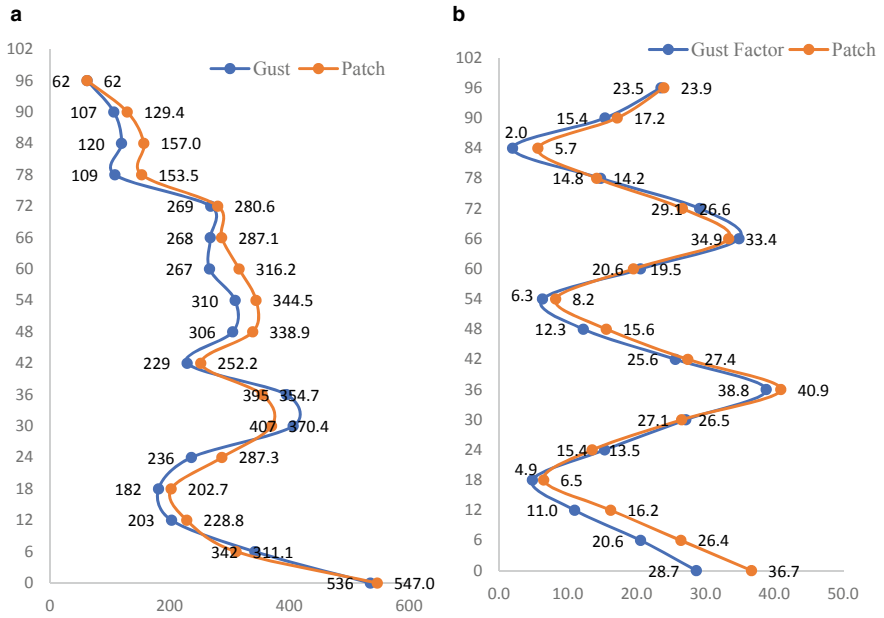


**Fig. 6** **a** Leg force comparison. **b** Bracing force comparison

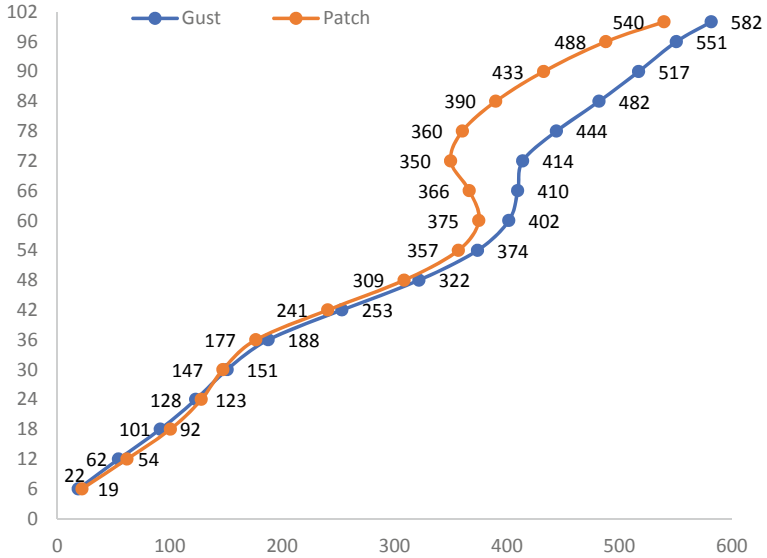


**Fig. 7** Maximum displacements (mm) @ service loads, design wind speed

## References

1. Ben Kahla N (1994) Dynamic analysis of guyed towers. Engg Strut 16(4)
2. Davenport AG, Sparling BF (1992) Dynamic gust response factors for Guyed Towers. J Wind Eng Ind Aerodyn 44:2237–2248
3. IASS (1981) Recommendations for guyed masts, International Association for Shell and Spatial Structures, Madrid, Spain
4. Gerstoft P, Davenport AG (1986) A simplified method for dynamic analysis of guyed mast. J Wind Eng Ind Aerodyn 23:487–499
5. Issa RRA, Avent RR (1991) Microcomputer analysis of guyed towers as lattice. J Struct Eng 117(4)
6. Sparling BF, Smith BW, Davenport AG (1996) Simplified dynamic analysis methods for guyed masts in turbulent winds. J Int Assoc Shell Spatial Struct 37(2):89–106
7. Wahb YMF, Madugula MKS (1996) Effect of guy initial tension on design of guyed antenna tower. Can J Civil Eng 23:457–463
8. Simiu E, Scanlan RH (1996) Wind effects on structures, fundamentals and application to design, 3rd edn. Wiley
9. Madugula M (ed) (2002) Dynamic response of lattice towers and guyed mast. ASCE, Virginia
10. Ziemian RD (ed) Guide to stability design criteria for metal structures, 6th edn. Wiley
11. British Standard, BS 8100-4:1995, Lattice towers and masts—part 4: code of practice for loading of guyed mast
12. European Standard, EN 1993-3-1, Eurocode 3—design of steel structures—part 3-1: towers, masts and chimneys—towers and masts
13. Indian Standard, IS 875 (Part 3): 2015, Design loads (other than earthquake) for buildings and structures—code of practice
14. Indian Standard, IS 2266:2002, Steel wire ropes for general engineering purposes—specifications (fourth revision)
15. Indian Standard, IS 6594:2001, Technical supply conditions for steel wire ropes and standards (second revision)

# Non-linear Analysis of Cylindrical Pressure Hull with Functionally Graded Materials


**Shilpa SajiKumar and Krupa Mary Varghese**

**Abstract** The pressure hull is one of the main structures of underwater vehicle, mainly designed to withstand the compressive forces associated with hydrostatic pressure. The ring-stiffened cylindrical hulls have better structural performances and are widely used in underwater vehicles and submarines. Functionally Graded Material (FGM) may be characterized by the variation in structure and composition gradually over volume, resulting in corresponding changes in the material properties. FGM found its applications in marine, submarine industry and defence especially for pressure hull and bullet proof underwater vehicle. In this study, non-linear static and dynamic analysis on cylindrical pressure hull with FGM has been done using ANSYS Mechanical APDL. The study included modelling and analysis of cylindrical pressure hull with different materials such as Steel, Titanium, Steel-Aluminium FGM and Titanium-Aluminium FGM with fixed and pinned boundary conditions. Deflection, von-Mises stress and von-Mises strain of different models were compared.

**Keywords** Submarine · Pressure hull · Functionally graded material · Non-linear analysis

S. SajiKumar (✉) · K. M. Varghese
Department of Civil Engineering, Saintgits College of Engineering, Kottayam, Kerala, India
e-mail: shilpasajikumar2016@gmail.com

K. M. Varghese
e-mail: krupa.mary@saintgits.org



M. Madhavan et al. (eds.), *Proceedings of the Indian Structural Steel Conference 2020 (Vol. 1)*, Lecture Notes in Civil Engineering 318,
https://doi.org/10.1007/978-981-19-9390-9_4

**Fig. 1** Pressure hull

# 1 Introduction

## *1.1 Pressure Hull*

Pressure hull is the inner hull of submarine designed to use at great depths. The hull structure, which is a very important part of the submarine become more and more important since its strength is the main concern. When submerged, the water pressure on the submarine hull increases and hull surrounding them must be able to withstand high water pressure at the desired depth, usually around 300 m. A thin walled cylindrical shell is used for the submarine as shown in Fig. 1. Ring stiffeners in circumferential and longitudinal directions considerably increase the resistance of the shell. Non-linearity arises when the load displacement graph is non-linear. The cause of non-linearity may be material or geometric. Material non-linearity may be due to the non-linear stress strain relation and geometric non-linearity due to non-linear strain displacement relation. The critical load could not be determined with sufficient accuracy if pre-buckling non-linearity is neglected. Normally the loss of stability occurs at the limit point, rather than at the bifurcation point. In such cases the critical load must be determined through the solution of non-linear system of equations. Geometric non-linearity may be due to the follower force effect of hydrostatic force.

## *1.2 Functionally Graded Materials*

The functionally graded material (FGM) is a two-component composite material characterized by a compositional gradient from one component to the other. In this study mainly two types of Functionally Graded Materials are used such as Titanium-Aluminium FGM and Steel-Aluminium FGM. Steel-Aluminium FGM, in which the hull plates are composed of outer layer fully of Steel and the quantity of Aluminium is increased throughout the thickness. Continuous and layered type FGM are shown in Fig. 2.

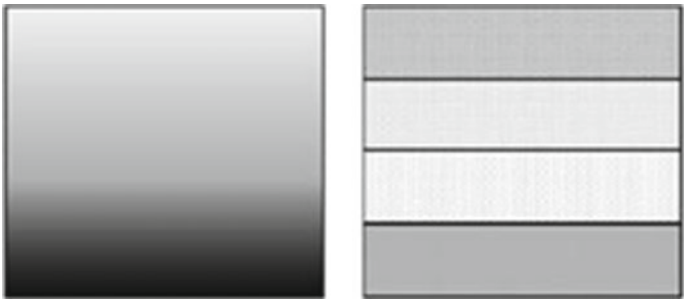

**Fig. 2** Continuous and layered type FGM

## 2 Literature Review

Pandey [1], conducted a study on buckling pressure of moderately thick walled filament-wound carbon–epoxy stiffened composite pressure hull subjected to external hydrostatic pressure through finite element analysis and compare the result with un-stiffened filament-wound carbon or epoxy composite pressure hull. It was observed that the critical buckling pressure of stiffened filament-wound composite cylinder is much higher than to that of carbon or epoxy composite cylinder without stiffener.

Ankit et al. [2], studied about the functionally graded materials (FGMs), types of FGM, manufacturing techniques of FGM different areas of applications of FGM, analytical and experimental solution techniques for FGMs and different stress measuring techniques. Study of stress analysis will continue with changes in the parameters like, effect of stress analysis of FGM plate with isotropic and orthotropic material, change in loading conditions, effects of changes in radius of circular cut-out.

Francoa et al. [3], a parametric study is conducted to find the optimum thickness of pressure hull. Linear buckling analysis was used to predict the feasibility of CFRP submarine pressure hull at deep waters. The design of these pressure vessels is made with reduced thickness walls and ring stiffeners joined to the walls. From the study conducted regarding the weight reduction, it is estimated that replacing steel by CFRP results saves up to 60% in the structural weight.

Bohra et al. [4], presents a complete review of applications of FGM, various processing methods of FGM, developments, different mathematical idealizations of functionally graded materials, modelling techniques, temperature profiles and various solution methods and techniques which are adopted for the vibration analysis of FGM plates. Efforts have been made to focus the discussion on the various research studies conducted until recently for the vibration analysis of FGM plates.

Aileni et al. [5], buckling analysis of ring stiffened circular cylinders subjected to external uniform pressure has been studied by varying radius to thickness ratio, cylinder thickness, ring spacing and stiffener thickness. During the analysis the optimal thickness, loading and boundary conditions are kept constant and the cross-section of the stiffener was varied (Z, square, rectangle, C, I and T sections). It is

observed that the buckling pressure decreases as the spacing between ring stiffeners increases for a given radius to shell thickness ratio. The Z section and square section stiffened cylinders have higher buckling pressures and Z section stiffened cylinder has more deformation at buckling initiation.

Asif and Varghese [6], conducted a study to find the best material for the pressure hull according to the Tsai-Wu failure criteria with the optimized values for input and output parameters using response surface optimization technique. Three different composites such as CFRP, BFRP, GFRP were used to analyse the failure criteria to provide the optimum strength. The failure index of the orthotropic composite material should be less than one as per the Tsai-Wu Criteria. The properties of CFRP depend on the layouts of the carbon fibre and the proportion of the carbon fibres relative to the polymer. CFRP have higher tensile strength with lower density comparing with the others. The CFRP fibre shows better results as compared with the GFRP and BFRP fibre in case of failure index.

## 3 Methodology

- The load, dimensions and various influential factors for the analysis of pressure hull is calculated.
- In accordance with the purpose of hull most appropriate FGM is selected and its properties are calculated.
- Non-linear static and dynamic analysis was done on pressure hull with different materials using ANSYS APDL.
- The deflection, von-Mises stress and von-Mises strain of all hull models were studied and comparisons were made.

## 4 Modelling of Pressure Hull

For modelling of thin cylindrical stiffened shell eight nodded quadrilateral shell element, SHELL 181 and BEAM188 are used. Pressure hull is modelled using following parameters.

The dimensions of the hull considered in this study are:

- Total Length of Hull = 66 m
- Internal Diameter of the hull = 6 m
- Design depth = 350 m

Materials used are:

- Steel
- Steel FGM: Steel-Aluminium
- Titanium
- Titanium FGM: Titanium-Aluminium

The Steel used for hull is HY 100 grade Steel which has a yield strength of 690 MPa and Grade 19 Titanium plates are used for Titanium models which has yield strength of 1170 MPa.

After several trial and errors of modelling of pressure hulls, an optimum thickness was chosen. A quarter portion of the cylindrical hull is taken and symmetric boundary conditions are provided at the continuous ends and fixed at one end is considered to represent the whole cylinder and corresponding stiffening elements. Inverted T section is used as stiffener and a hydrostatic pressure of 3.5 MPa is applied on the external shell of the hull. Figure 3 shows quarter portion of hull modelled in Ansys APDL. Loading and support conditions are shown in Fig. 4. Figure 5 represent extruded view of pressure hull.

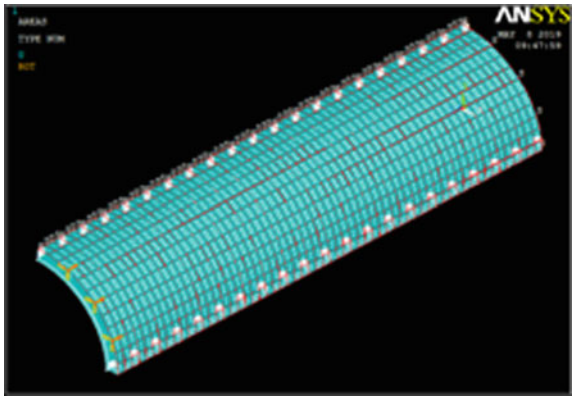


**Fig. 3** Quarter portion of hull model

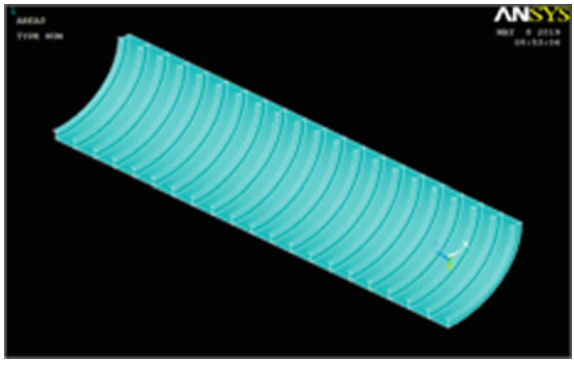


**Fig. 4** Loading and support conditions

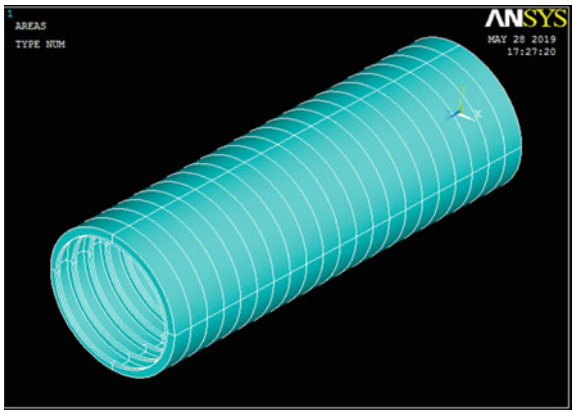


**Fig. 5** Extruded view of pressure hull

## 5 Results and Discussion

### *5.1 Non-linear Static Analysis Results*

Non-linear static analysis on Steel, Steel FGM, Titanium and Titanium FGM hull with fixed support has been done and the results are given in Tables 1 and 2. von-Mises stress and von-Mises strain in Steel, Steel FGM, Titanium, Titanium FGM hull models with fixed supports are shown in Figs. 6, 7, 8, 9, 10, 11, 12 and 13.

Non-linear static analysis on Steel, Steel FGM, Titanium and Titanium FGM hull with pinned support has been done and the results are given in Tables 3 and 4.

Steel hull model shows lower values of deflection, von-Mises stress and von-Mises strain compared to that of Steel-Aluminium FGM and similarly Titanium model shows lower values of deflection, von-Mises stress and von-Mises strain compared to that of Titanium-Aluminium FGM. Steel, Titanium and its FGM models with fixed support shows minimum values of deflection, von-Mises stress and strain compared to that of pinned models. In general, deflection, stress and strain values of FGM models are higher than that of Steel and Titanium Models. Stress and strain in each model are within the yielding limit of corresponding material.

**Table 1** von-Mises stress and strain of steel and steel-aluminium FGM with fixed support

| Material | Deflection | von-Mises stress (MPa) | von-Mises strain |
|---|---|---|---|
| Steel | 4.86 | 469.17 | 0.0023 |
| Steel-aluminium FGM | 7.077 | 558.9 | 0.0028 |

**Table 2** von-Mises stress and strain of titanium and titanium-aluminium FGM with fixed support

| Material | Deflection | von-Mises stress (MPa) | von-Mises strain |
|---|---|---|---|
| Titanium | 13.06 | 635 | 0.0053 |
| Titanium-aluminium FGM | 16.09 | 761.6 | 0.0069 |

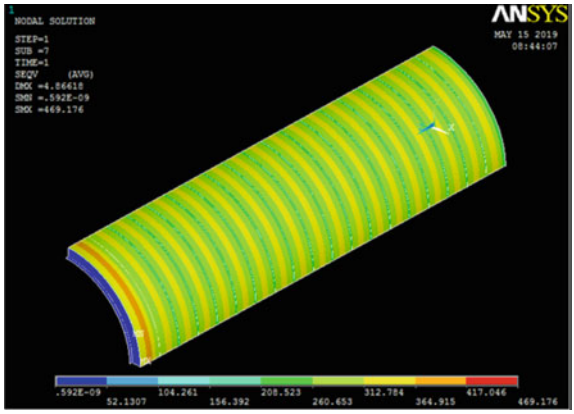


**Fig. 6** von-Mises stress of steel hull

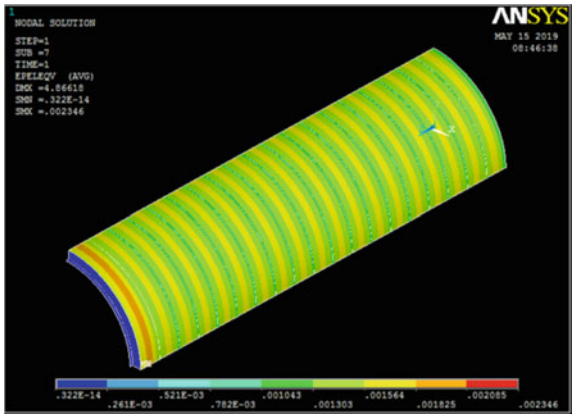


**Fig. 7** von-Mises strain of steel hull

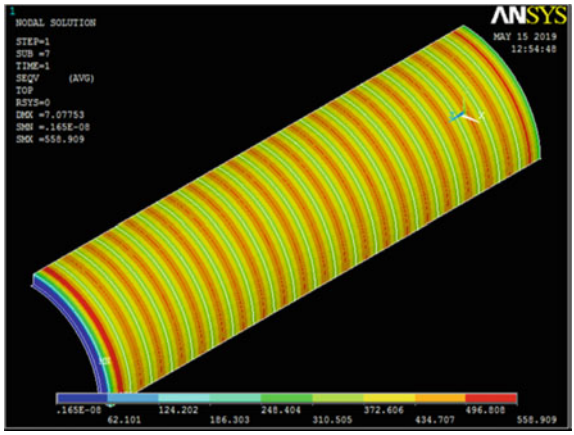


**Fig. 8** von-Mises stress of steel FGM hull

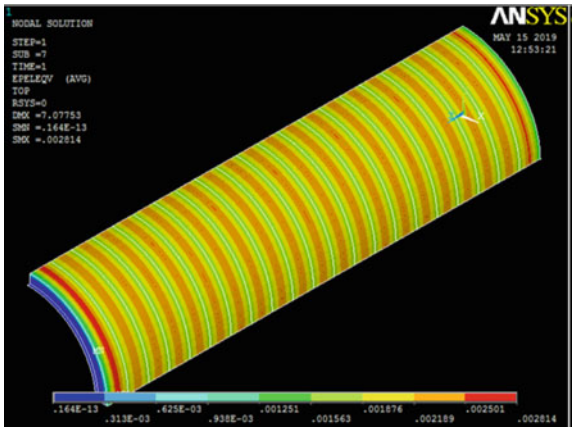


**Fig. 9** von-Mises strain of steel FGM hull

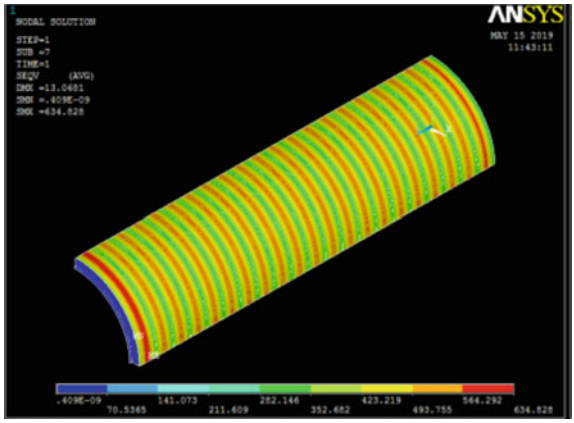


**Fig. 10** von-Mises stress of titanium hull

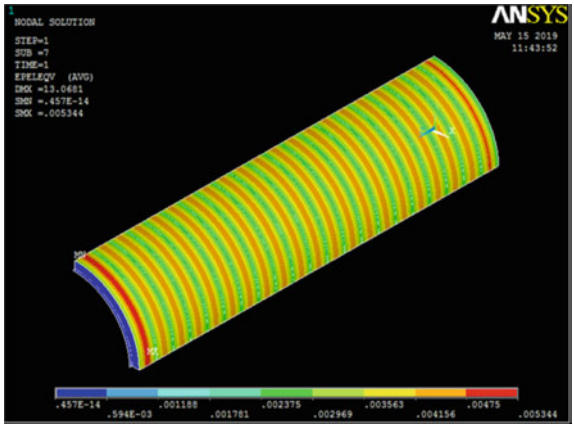


**Fig. 11** von-Mises strain of titanium hull

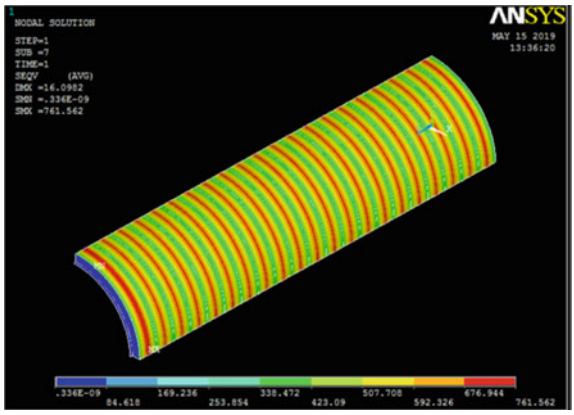


**Fig. 12** von-Mises stress of titanium FGM hull

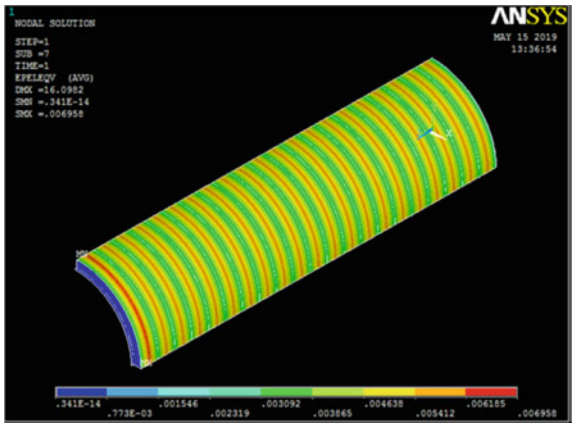


**Fig. 13** von-Mises strain of Titanium FGM hull

**Table 3** von-Mises stress and strain of steel and steel-aluminium FGM with pinned support

| Material | Deflection | von-Mises stress (MPa) | von-Mises strain |
|---|---|---|---|
| Steel | 12.89 | 504.26 | 0.0025 |
| Steel-aluminium FGM | 19.45 | 615.18 | 0.00307 |

**Table 4** von-Mises stress and strain of titanium and titanium-aluminium FGM with pinned support

| Material | Deflection | von-Mises stress (MPa) | von-Mises strain |
|---|---|---|---|
| Titanium | 39.01 | 815.26 | 0.0067 |
| Titanium-aluminium FGM | 51.92 | 828.15 | 0.0087 |

## 5.2 Non-linear Dynamic Analysis Results

Non-linear dynamic analysis was performed on quarter portion of cylindrical hull using Steel, Steel-Aluminium FGM, Titanium and Titanium-Aluminium FGM with fixed boundary condition. The dynamic analysis has been carried out on pressure hull models, by varying the hydrostatic loading on the hull at different time corresponding to the different depth of submergence. Graphical comparison of stress and strain values of Steel, Steel FGM, Titanium and Titanium FGM at different depth such as at 87.5, 175, 262.5 and 350 are shown in Figs. 14 and 15, respectively.

For each models von-Mises stress and strain at different depth are studied for dynamic analysis. As the depth increases von-Mises stress and strain of all models are increased but all these values are within the yielding limit of corresponding

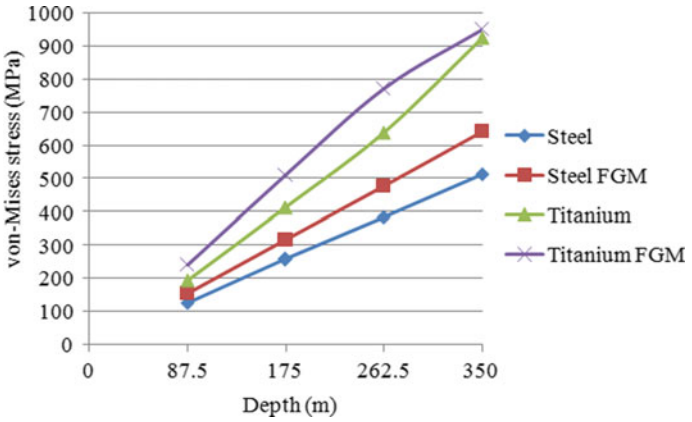


**Fig. 14** Graphical comparison of stress values at different depth

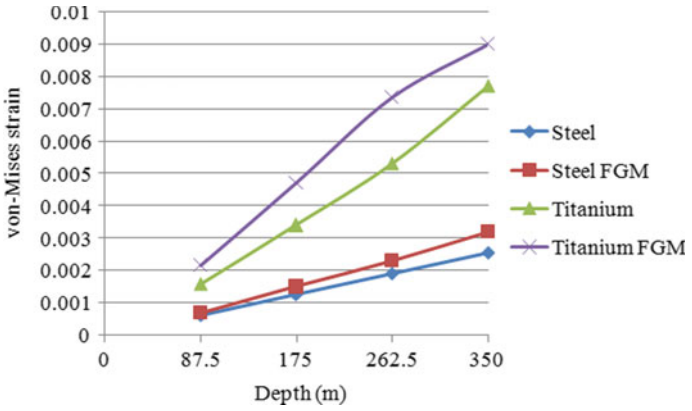


**Fig. 15** Graphical comparison of strain values at different depth

materials of hull. Therefore the hull is safe at the design depth. Stress and strain values of FGM models are higher than that of Steel and Titanium Models.

## 6 Conclusion

Non-linear static and dynamic analysis was done on pressure hull with Steel, Titanium, Steel-Aluminium FGM and Titanium-Aluminium FGM with fixed boundary conditions. The following were concluded from this study.

Steel FGM models were found to give better results as compared to Titanium FGM models. FGM hull models show larger values of deflection, stress and strain compared to that of Steel and Titanium hull models. The stress and strain values of outer layers of FGM models are larger than that of inner layers but, the stresses and strain are found to be slightly increased closer to the inner layers of the hull, this is because the variation of material from FGM to the pure form of metal. Deflection, von-Mises stress and von-Mises strain of all hull models from dynamic analysis are found to be increased with increase in depth of submersion. Titanium models have higher yield strength therefore it helps in reducing thickness of hull and overall weight of hull.

## References

1. Pandey (2014) Buckling behaviour of circular ring stiffened filament wound composite pressure hull through finite element analysis. Appl Mech Mat 656
2. Ankit B, Makwana G, Panchal K (2014) A review of stress analysis of functionally graded material plate with cut-out. Int J Eng Res Technol 3(3):2020–2025
3. Francoa J, Corza A, Penab A (2014) Optimization of pressure hulls of composite materials. In: European conference on composite materials
4. Bohra P, Bhandari M, Bohra S, Sharma P (2017) Vibrational analysis of FGM plates a critical review of various solution methods and modelling techniques. Int Res J Eng Technol 4(10):1800–1822
5. Aileni K, Prasanna P, Jain PC (2017) Buckling analysis of ring stiffened circular cylinders using ANSYS. Int J Res Appl Sci Technol 5
6. Asif A, Varghese J (2018) Optimization of submarine ring stiffened composite pressure hull using numerical methods. Int J Innov Sci Eng Technol 5(4):194–199

# Turbo Generator Foundation Inside TG Building—An Unconventional Approach


**Mainak Mallik, D. S. Anjaneya Murthy, and Eswarappa Sudeep**

**Abstract** In any power plant, Turbo Generator is the most dynamic as well as the most expensive equipment and placed inside the Turbo Generator building. TG substructure being a dynamic structure conventionally, the foundation system of Turbo Generator and TG building is kept separately. This leads to not only tedious design calculation of TG deck supporting structure and TG building supporting structure but also the extensive requirement of time for carrying out the construction work. Also, the supporting structure for the TG deck is generally made up of concrete columns, which adds more to the construction time. In one of the power plant projects having capacity 600 MW, the analysis and design of the TG substructure were carried out using a structural steel column framework for supporting the TG deck slab of Turbo Generator. The springs which act as a dampener were placed in between the TG deck slab and the steel columns. For the analysis and design, the TG substructure is integrated with TG building. Due to this the structural analysis and design become simple, more space is available compared to the concrete structure, construction time is less compared to the concrete structure and also sustainable when compared to the concrete structure. In this paper, a complete detail design approach has been presented. The 3-D model and analysis were done using STAAD software. The comparison between the supporting system of Turbo Generator with steel column and concrete column has also been presented to find the most desirable system.

**Keywords** Power plant · TG foundation · Steel column · STAAD · Sustainability

M. Mallik (✉)
National Institute of Technology, Itanagar, Arunachal Pradesh, India
e-mail: mainak@nitap.ac.in

D. S. Anjaneya Murthy
Compendious Engineering Solutions Private Limited, Bangalore, India

E. Sudeep
WSP Consultants, Bangalore, Karnataka, India



M. Madhavan et al. (eds.), *Proceedings of the Indian Structural Steel Conference 2020 (Vol. 1)*, Lecture Notes in Civil Engineering 318,
https://doi.org/10.1007/978-981-19-9390-9_5

## 1 Introduction

Any heavy machinery, whether it is reciprocating, rotating, or impacting type needs a support system that will resist the dynamic forces resulting from vibrations. When it is beyond the operational limit, such vibrations are not only detrimental to the machine itself but also impair the foundation system and any operating personnel associated with them.

In any power plant, Turbo Generator (TG) is the most dynamic as well as the most expensive equipment and placed inside the Turbo Generator building. Generally, Tabletop-type foundation (Fig. 1) is adopted where TG is placed on a concrete deck slab at an elevated level so that ducts, piping and ancillary items may be located below the equipment. As the TG substructure is a dynamic structure-conventionally, the foundation system of Turbo Generator and TG building are kept separately. This type of practice leads to not only tedious design calculation of supporting structure of TG Deck as well as TG building but also an extensive requirement of time for carrying out the construction work. To overcome this problem Tabletop-type foundation with isolators (Fig. 2) (springs and dampers) located at the top of supporting columns are provided. But the supporting structure for the TG deck is generally made up of concrete columns that adds more to the construction time. In one of the power plant projects in India having capacity 600 MW—to get over all these shortcomings, the Tabletop-type foundation with isolators placed on steel columns has been adopted. Also, the foundation system of the TG and the TG building are integrated with the common concrete base raft. The unbalance force developed due to the rotating mass has normally been calculated based on the Grade of balance of the machine [1] .

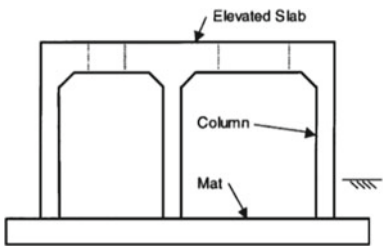


**Fig. 1** Tabletop-type foundation [2]

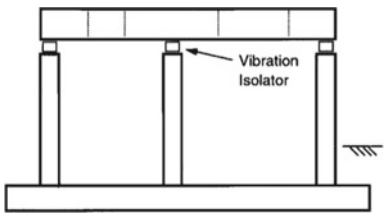


**Fig. 2** Tabletop-type foundation (with isolator) [2]

The 3-D model and analysis were done using STAAD-pro software [3]. The comparison between the supporting system of Turbo Generator with steel column and concrete column has also been presented to find the most desirable system.

## 2 Review of Literature

Ming et al. [4], analyzed a 1000 MW turbine-foundation-soil system subjected to force generated due to rotor unbalances and earthquakes. With three-dimensional viscous-spring boundary elements, the influence of soil-structure interaction (SSI) on the response of the system has been calculated. It has been observed that under rotor unbalance excitation the effect of SSI strongly influences the displacements and internal forces of the system.

Using the software SAP2000 Jayarajan and Kouzer [5], modeled the foundation of a Turbo Generator foundation and demonstrated the analysis procedure. According to them, for the dynamic analysis of the Turbo Generator foundation, careful attention is needed while detailing for modeling will be done. Various issues on mathematical modeling of structure, machine and soil for dynamic analysis of foundation have also been highlighted.

Fleischer and Trombik [6] have proposed simplified design principles for a large machine foundation with specific requirements for Turbo Generators. Due to first Eigen frequencies are in strong dependence on the bedding condition and usually lied within the critical earthquake frequency range soil-structure interaction (SSI) also played a major role.

Nawrotzki et al. [7] presented a systematic overview of the static and dynamic analysis of turbine foundations made of reinforced concrete. Salient features for designing like the load cases to be applied, the required ultimate limit and service-ability limit state checks, the assessment of the static and dynamic foundation stiffness and special provisions in seismic areas have also been discussed.

Adhikari [8], with the citation of critical aspects in the design of the Turbo Generator foundation and also concerning IS 2974 (P-3)-1992 [9], and other international standards explained the design of a Turbo Generator foundation of a thermal power plant.

Abdullah and Abdul Hamid [10] compared the yield drift limit for two earthquakes—Imperial Valley earthquake and San Fernando earthquake using RAUMOKO program applied on a rigid supporting frame. It has been observed that the SDOF model, as considered, yield draft exceeds the limit for the second earthquake and prone to collapse.

Most of the papers on the Turbo Generator foundation are limited to dynamic analysis. However, any literature regarding TG supported on spring which in turn supported on steel columns/concrete columns is not available.

# 3 Design Methodology

## *3.1 Design Concept*

TG Building houses Turbo Generator bay of 35 m width and Boiler Feed Pump/ Deaerator bay of 12 m width. In TG bay, the crane is running along the longitudinal direction. BFP bay has a separate crane running within the TG unit. TG building structure is a moment-resisting frame in the transverse direction with fixity along major axis and pinned along minor axis. The structure is braced in the longitudinal direction. TG bay has the mezzanine floor at EL 10.00 m and the Operating floor at EL17.0 m. BFP bay mounts LP Heaters in the mezzanine floor at EL 10.0 m and HP Heaters in the Operating floor at EL 17.0 m and Air Washer/Deaerator at EL 36.5 m floor. Elevators have been provided in the Maintenance bay along with the machine room. The height of the TG bay is around 38 m and, BFP bay is around 48 m from ground level.

In the framing system, TG building is supported by the Main Columns along A, B and C Row along with Auxiliary Columns within the TG bay to support the TG bay floors. Main Beams in the BFP bay have a moment connection with main columns, and all main/secondary beams in the TG bay has a shear connection with the main and Auxiliary Columns. TG deck is supported with steel columns with spring.

The introduction of a base isolation system leads to a dynamic system with stable, identifiable properties. Elimination of other conservative factors, viz., limitation of amplitude and frequency depends on the consistency of the isolator. The stiffness and damping of the system with the equipment and inertia block have been provided by the isolation system. Actually, the isolation system allows the machine foundation mass to "float" to lessen the impact of transmission of vibrations. There are three basic isolator concepts generally adopted for dynamic machinery application—rubber pad-type materials, steel springs often coupled with viscous dampers and air mounts.

The general arrangement of TG deck supporting steel column for supporting deck slab of 600 MW Turbo Generator as per the requirement of the vendor has been shown in Fig. 3.

Steel springs (Fig. 4) as a base isolation system are used. TG deck is supported on spring-mounted structural steel columns and the columns are tied at different levels. With the introduction of the base isolation system, the dynamic effect of TG has been nullified. And as a result of that—structural arrangement supporting the TG and the TG main Building has been modeled together, subsequently analyzed and designed. As the whole system is completely made of structural steel, all the tie beams and other floor beams are transferring moments and shears as well. The structural steel columns are directly connected to the raft foundations through base plates and anchor bolts.

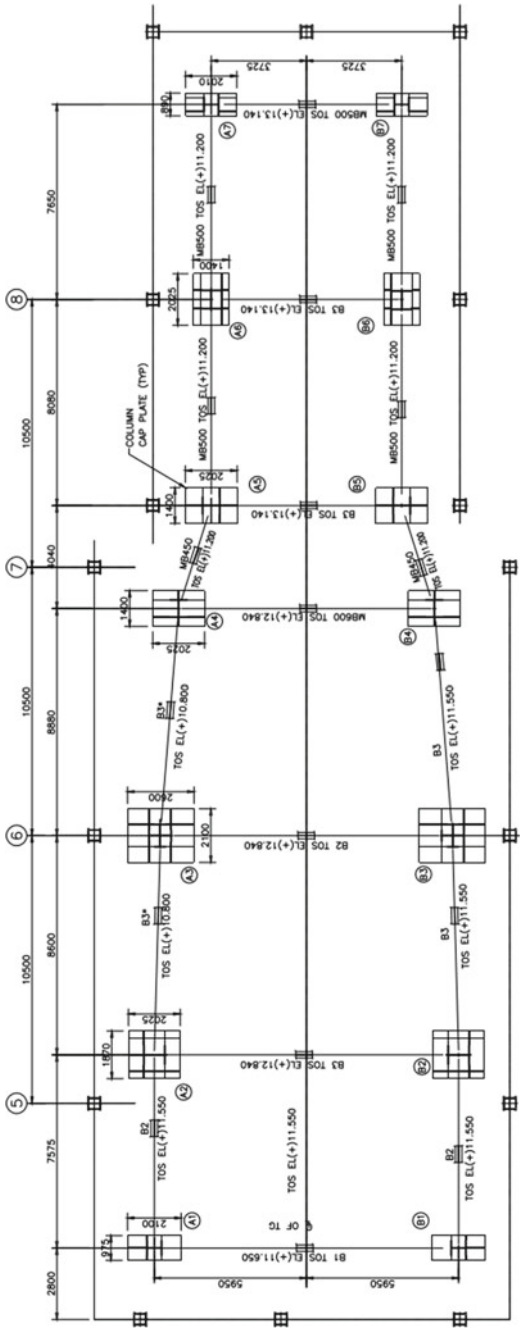


**Fig. 3** Layout of supporting column of deck slab (plan at the top of cap plate)

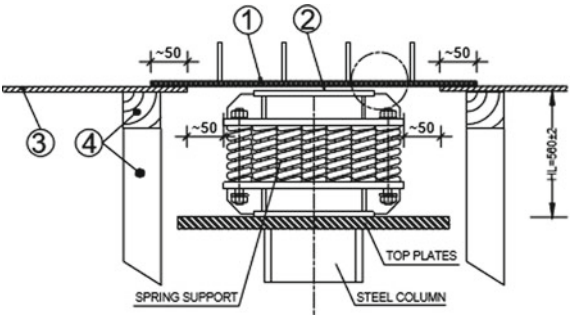


**Fig. 4** Typical arrangement and detail of spring support (1-steel cover plates with anchors, 2-airgap equal to compression of falsework, 3-soffit shuttering, 4-falsework)

## *3.2 Machine Data*

Machine data based on which spring has been designed shown in Table 1:

Turbine building (TG Bay) framing consists of structural steel with moment connected framing in the transverse direction and bracing in the longitudinal direction. There is fourteen number of steel columns placed symmetrically with respect to the centerline of TG.

The arrangement of spring combination based on the properties of spring (Table 2) is shown in Fig. 5.

The load data transferred to the top of the steel column through spring isolation as furnished by the vendor has been shown in Table 3.

**Table 1** Machine data

| Item | Static weight (including rotating weight) (kN) | Rotating weight (kN) | Remarks |
|---|---|---|---|
| Turbine | 7130 | 1536 | Operating frequency 50 Hz |
| Generator | 5908 | 866 | Operating frequency 50 Hz |
| Excitor | 473 | 43 | Operating frequency 50 Hz |

**Table 2** Properties of spring

| Spring marked as | Vertical stiffness (kN/mm) | Horizontal stiffness (kN/mm) | Remarks |
|---|---|---|---|
| 1 | 37.80 | 7.56 | Spring with viscous damper |
| 2 | 47.25 | 9.45 | |
| 3 | 40.50 | 8.10 | |
| 4 | 33.75 | 6.75 | |
| 5 | 24.30 | 4.86 | |

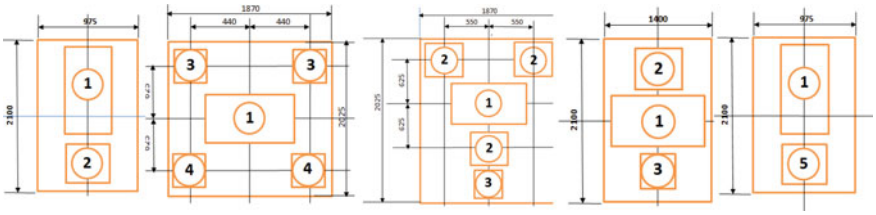

**Fig. 5** Combined arrangement of spring on the top structural column

**Table 3** Load on top of the column from TG deck

| Column marked as | Vertical load (kN) | Horizontal load (kN) | Remarks |
|---|---|---|---|
| A1, B1 | 2722 | 94 | Horizontal load has been calculated based on seismic zone-III, soil type 1 and response reduction factor 1 |
| A2, B2 | 5962 | 195 | |
| A3, B3 | 7042 | 220 | |
| A4, B4 | 3802 | 145 | |
| A5, B5 | 4018 | 130 | |
| A6, B6 | 4018 | 130 | |
| A7, B7 | 1988 | 71 | |

## *3.3 Modeling*

Based on the above consideration, a combined 3D-model (Fig. 6) of TG building and TG deck supporting structure has been developed using STAAD-PRO software (Figs. 7, 8, 9 and 10).

To compare with the conventional practice models have also been prepared where the TG deck supporting columns are made of concrete (Fig. 11) and supporting TG building structure (Fig. 12) is made of steel, and the foundation system for both the structure is a common base raft.

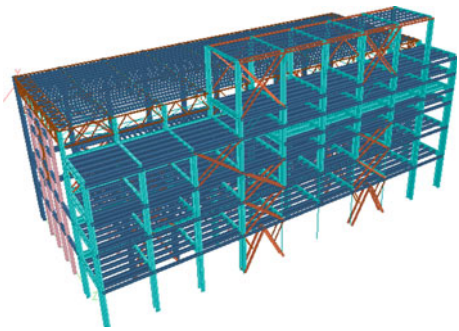

**Fig. 6** Combined 3D model of the building and TG deck supporting structure

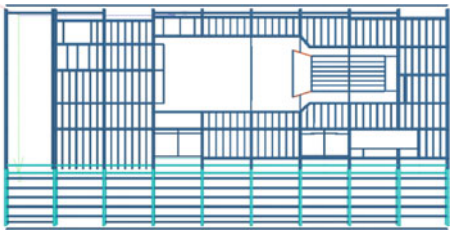

**Fig. 7** Arrangement of floor beam at + 8.5 m level

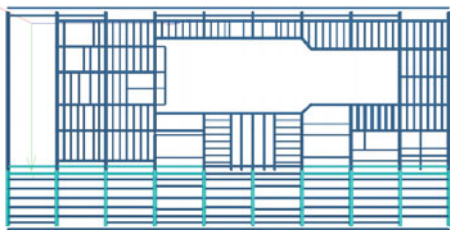

**Fig. 8** Arrangement of floor beam at + 17.0 m level

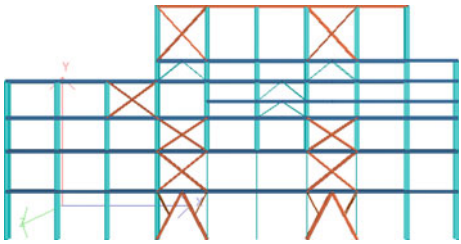

**Fig. 9** Arrangement of bracing along longitudinal direction (outer row)

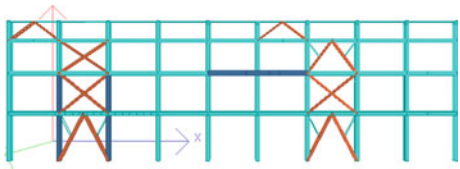

**Fig. 10** Arrangement of bracing along longitudinal direction (inner row)

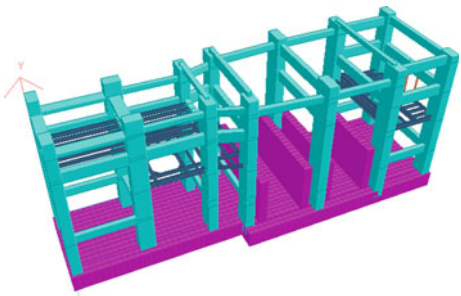

**Fig. 11** 3D model of TG deck support with concrete column

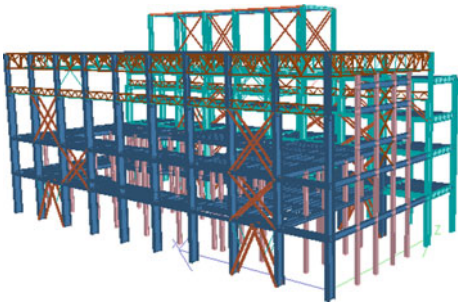

**Fig. 12** 3D model of TG building only

## *3.4 Load Data and Load Combination*

Following loads are considered for the analysis:

(a) Load 1-Dead load—weight of slabs, gratings, platforms, projection of the slabs from the center line of column, empty weight of major equipment like LP heater, HP heater, Deaerator, wt of inter-connecting platforms between Boiler and PHB at different levels, loads due to the staircase, wall loads and cladding loads.
(b) Load 2-Equipment load—as the empty weight of the equipment are considered in dead load case the flooded weight is taken, major equipment load at 8.5 level, major equipment at mezzanine floor, oil room load, main oil tank, oil coolers, oil purifiers, air dryer, liquid detector racks, pw pumps and analyzer units, pw plate type coolers, plate heat exchanger units.
(c) Load 3-Live load—the following intensity of live load has been considered at different floor level:

  (i) At mezzanine floor level = 5 kN/m$^2$
  (ii) At operating floor level = 15 kN/m$^2$

(d) Load 4-Dead load of crane crab near row (A)
(e) Load 5-Dead load of crane crab near row (B)
(f) Load 6-Lifted load of crane crab near row (A)
(g) Load 7-Lifted load of crane crab near row (B)
(h) Load 8-Wind along +ve X-direction-pressure
(i) Load 9-Wind along −ve X-direction-pressure
(j) Load 10-Wind along +ve X-direction-suction
(k) Load 11-Wind along −ve X-direction-suction
(l) Load 12-Wind along +ve Z-direction-pressure
(m) Load 13-Wind along −ve Z-direction-pressure
(n) Load 14-Wind along +ve Z-direction-suction
(o) Load 15-Wind along −ve Z-direction-suction
(p) Load 16-Seismic Load along +ve X-direction
(q) Load 17-Seismic Load along +ve Z-direction
(r) Load 18-Temperature Load

Based on the above loads—major load combinations are as follows:

(a) D.L + EQ.L + L.L
(b) D.L + EQ.L + L.L + T.L
(c) D.L + EQ.L + L.L + T.L + W.L
(d) D.L + EQ.L + L.L + T.L + S.L

With the above combinations, the effect of crane crab is also added as a separate load case. Total load cases considered are about 185.

## *3.5 Summary of Result*

Based on the analysis carried out for different load combinations, the summary of sections required for TG deck supporting columns and beams required for different models are as follows: (Tables 4 and 5).

**Table 4** Summary of TG deck supporting steel columns (Model I)

| Column marked as | Size (DXB) (mm × mm) | | Thickness (t) (mm) |
|---|---|---|---|
| A1, B1 | 600 | 1100 | 50 |
| A2, B2 | 800 | 1100 | 50 |
| A3, B3 | 1200 | 1400 | 50 |
| A4, B4 | 900 | 700 | 40 |
| A5, B5 | 1200 | 1200 | 40 |
| A6, B6 | 700 | 1100 | 40 |
| A7, B7 | 900 | 700 | 36 |

**Table 5** Summary of TG deck supporting concrete columns (Model II)

| Column marked as | Size (DXB) (mm × mm) | | Reinforcement | |
|---|---|---|---|---|
| | | | Longitudinal | Link |
| A1, B1 | 1900 | 1100 | 30–28ϕt | 5-set 8ϕT @150c/c |
| A2, B2 | 2300 | 1200 | 40–28ϕt | 5-set 8ϕT @150c/c |
| A3, B3 | 2450 | 1150 | 40–28ϕt | 5-set 8ϕT @150c/c |
| A4, B4 | 2000 | 1100 | 32–28ϕt | 5-set 8ϕT @150c/c |
| A5, B5 | 2100 | 1100 | 36–28ϕt | 5-set 8ϕT @150c/c |
| A6, B6 | 1200 | 1800 | 32–28ϕt | 5-set 8ϕT @150c/c |
| A7, B7 | 1900 | 1100 | 30–28ϕt | 5-set 8ϕT @150c/c |

## 3.6 Design and Detailing of the Columns

### 3.6.1 Building Materials

In this project, Grade of concrete used is M35 of IS 456 [11], reinforcing steel conforms to Grade Fe-415 of IS 1786 [12], and structural steel conforms to E 250 (Fe410W) A of IS 2062 [13].

### 3.6.2 Steel Columns

As per the requirement of the client, the design of steel structures has been done by the working stress method, in accordance with the provisions of IS: 800-1984 [14] and other relevant IS codes as applicable to specific structures.

The schedule of columns with base plate detail is shown in Fig. 13.

### 3.6.3 RC Columns

Typical RC details of the TG deck supporting column have been shown in Fig. 14.

## 3.7 Comparison

See Table 6.

## 3.8 Check Against Serviceability

Under different load combinations value of the deflection at the topmost node has been calculated from the STAAD output for different types of frame foundation and represented in Table 7. All the values are within the permissible limit.

## 3.9 Conclusion

Based on the study, the unconventional approach results are showing more realistic in terms of sustainability, ease of construction, construction time, availability of more space, ease of analyzing the whole structure.

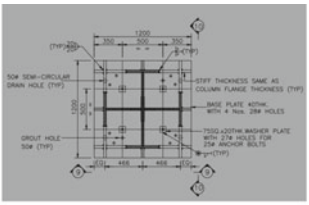


SCHEDULE OF COLUMNS

| FRAME ALONG GRID | ELEVATION | 1 WEB PL (A) | 2 FLG PL (B) | SHAPE | REMARK |
|---|---|---|---|---|---|
| (A1) & (B1) | EL(−)4.600 TO EL(+)12.840 | 720x36 | 400x40 | 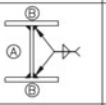 | 16THK. WELD FOR WEB PLATE GREATER THAN 28mm |
| (A2) & (B2) | EL(−)4.600 TO EL(+)12.840 | 728x25 | 600x36 | 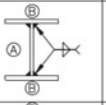 | 16THK. WELD FOR WEB PLATE GREATER THAN 28mm |
| (A3) & (B3) | EL(−)4.600 TO EL(+)12.840 | 900x36 | 500x36 | 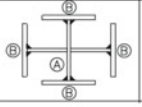 | 16THK. WELD FOR WEB PLATE GREATER THAN 28mm |
| (A4) & (B4) | EL(−)4.600 TO EL(+)12.840 | 650x25 | 500x25 | 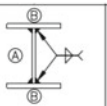 | 16THK. WELD FOR WEB PLATE GREATER THAN 28mm |
| (A5) & (B5) | EL(−)4.600 TO EL(+)0.460 | 900x32 | 400x32 | 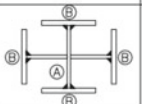 | 16THK. WELD FOR WEB PLATE GREATER THAN 28mm |
| (A5) & (B5) | EL(−)0.460 TO EL(+)13.140 | 900x32 | 400x32 | 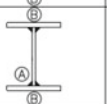 | 16THK. WELD FOR WEB PLATE GREATER THAN 28mm |
| (A6) & (B6) | EL(−)4.600 TO EL(+)13.140 | 828x36 | 500x36 | 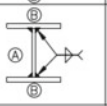 | 16THK. WELD FOR WEB PLATE GREATER THAN 28mm |
| (A7) & (B7) | EL(−)4.600 TO EL(+)13.140 | 650x25 | 500x25 | 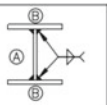 | 16THK. WELD FOR WEB PLATE GREATER THAN 28mm |

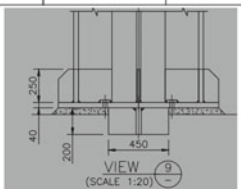


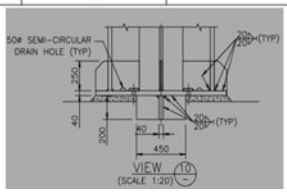


**Fig. 13** Typical detail of base plate of steel column supporting deck slab and column schedules

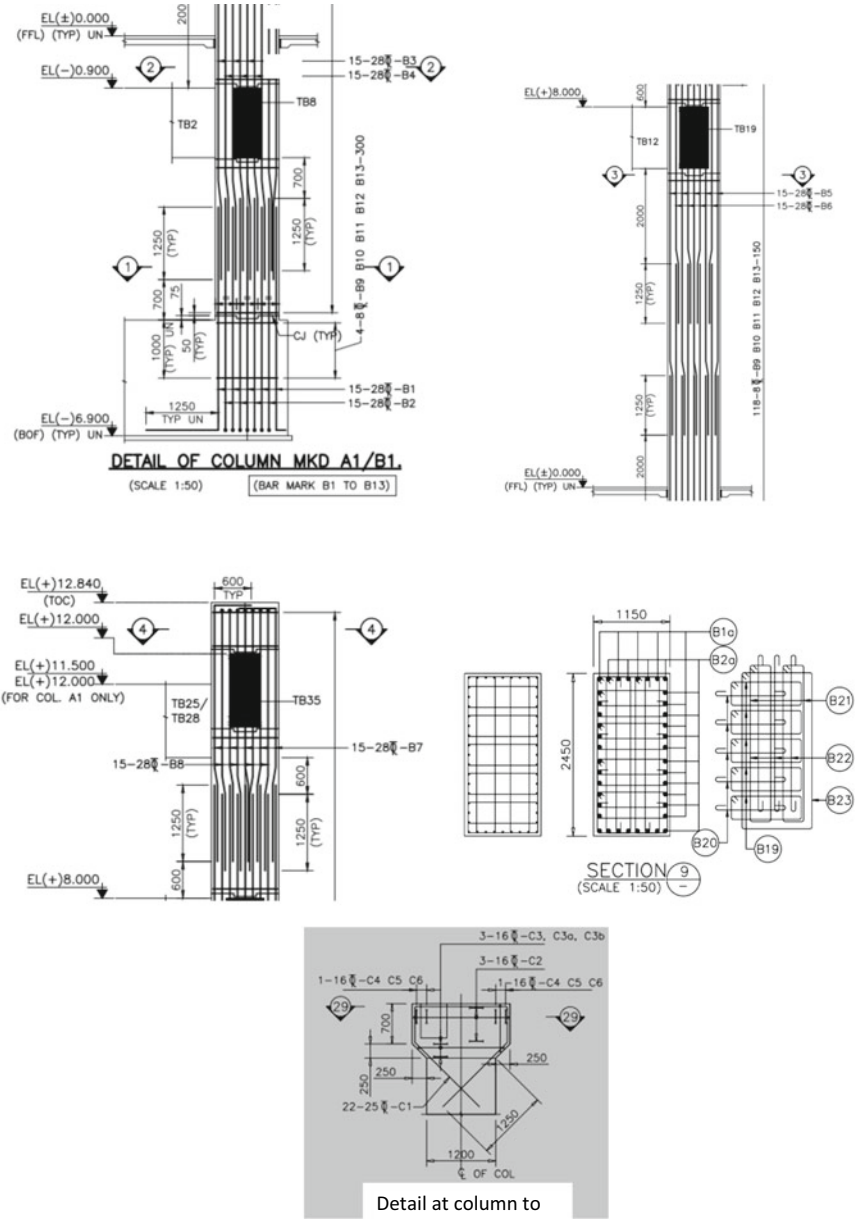


**Fig. 14** Typical detail of RC column supporting deck slab

**Table 6** An overview of the two approaches

| Serial no. | Conventional approach RCC type structure | Unconventional approach Structural steel type structure |
|---|---|---|
| 1 | Concrete is less sustainable material when compared to structural steel | Structural steel is more sustainable material when compared to RCC |
| 2 | Minimum RCC column size is around 1100 mm × 1800 mm (Rectangular column type) | The maximum size of the structural steel column size is approximately 1000 mm × 500 mm (star column type). More space is available when compared to RCC columns |
| 3 | Construction time requires more when compared to structural steel | Construction time requires less when compared to RCC |
| 4 | Turbo generator supporting structure is isolated with the main building structure | Turbo generator supporting structure is combined with the main building and analyzed as a single structure |
| 5 | The RCC section size is more when compared to the structural steel structure. In turn, the self-weight of the supporting structure will increase when compared to structural steel. As a result, loading on the foundation will also increase, including the seismic force of the structure | The structural section size is less when compared to RCC structure. In turn, the self-weight of the supporting structure will decrease when compared to the RCC structure. Due to this, loading on the foundation will also decrease, including the seismic force of the structure |

**Table 7** Check against serviceability

| Type of foundation | Actual horizontal deflection | Allowable deflection (mm) | Remarks |
|---|---|---|---|
| RCC TG foundation | 39.54MM ($x$-dir.) | $(18.59 \times 1000)/250 = 74.36$ | SAFE |
| RCC TG foundation | 4.73MM ($z$-dir.) | $(18.59 \times 1000)/250 = 74.36$ | SAFE |
| STEEL TG foundation | 32.43MM ($x$-dir.) | $(18.59 \times 1000)/250 = 74.36$ | SAFE |
| STEEL TG foundation | 9.6MM ($z$-dir.) | $(18.59 \times 1000)/250 = 74.36$ | SAFE |

# References

1. ISO 1940-1 (1993) Mechanical vibration-balance quality requirements of rigid rotors-part 1: determination of permissible residual unbalance
2. ACI 351.3R-04 Foundations for Dynamic Equipment, Reported by ACI committee 351
3. 3D Structural Analysis and Design Software, STAAD. Pro. Bentley.com
4. Ming F, Tao W et al. (2012) Dynamic behavior of turbine foundation considering full interaction among facility, structure, and soil, 15 WCEE
5. Jayarajan P, Kouzer KM (2014) Dynamic analysis of turbo-generator machine foundations. J Civil Eng Environ Technol I:30–35
6. St. Fleischer P, Trombik PG (2008) Turbo generator machine foundations subjected to earthquake loadings. In: The 14th world conference on earthquake engineering
7. Nawrotzki P, Huffmann G, Uzunoglu T (2008) Static and dynamic analysis of concrete turbine foundations. Struct Eng Int 265–270
8. Adhikari S (2008) Turbo generator foundation

9. IS 2974 (Part 3): 1992, Indian Standard Design and Construction of Machine Foundations—Part 3: foundations for rotary type machines (medium and high frequency), Bureau of Indian Standards, New Delhi
10. Abdullah S, Abdul Hamid NH (2012) Modelling of turbine-generator and foundation as single degree of freedom using Ruaumoko programme. Int J Eng Adv Technol (IJEAT) 2
11. IS 456:2000—Plain and reinforced concrete, Bureau of Indian Standards, New Delhi
12. IS 1786: High strength deformed steel bars and wires for concrete reinforcement—specification, Bureau of Indian Standards, New Delhi
13. IS 2062:2011-Hot rolled medium and high tensile structural steel—specification, Bureau of Indian Standards, New Delhi
14. IS 800:1984-General construction in steel-code of practice, Bureau of Indian Standards, New Delhi

# Fragility Analysis of Steel Building Frame Considering Different Nonlinear Material Modeling


**Vikash Sundriyal and Shashi Narayan**

**Abstract** Nonlinear time-history analysis is used to assess a structure's ability to resist future earthquakes. The nonlinear behavior of the buildings is greatly affected by material nonlinearity considered during the analysis. This paper examines the nonlinear time-history analysis of steel frame by taking four different nonlinear steel material models into account, namely steel with elastic-perfectly plastic behavior which fails at yield strength, Menegotto and Pinto model with isotropic hardening, Menegotto and Pinto model with kinematic hardening and Ibarra–Medina–Krawinkler (IMK) model. Menegotto and Pinto's model is used to simulate cyclic response. This is uniaxial material model and is used to describe the steel response in fiber-discrete cross-sections and under normal stress. IMK model is a deterioration model which takes degradation of material properties like strength and stiffness into account. In order to study the effect of material nonlinearity on the behavior of six-story building frame during an earthquake, the fragility analysis on these models is conducted by multiple stripe analysis.

**Keywords** Nonlinear time-history analysis · Menegotto and Pinto model · Kinematic hardening · Isotropic hardening · Ibarra–Medina–Krawinkler model · Distributed plasticity · Fragility analysis

## 1 Introduction

The major aim of a structural engineer is to design a structure and protect it from collapse. This collapse means the inability of any structure to withstand its own gravity load after severe conditions like earthquake. The structures are designed

V. Sundriyal (✉)
Quantum University, Roorkee, India
e-mail: vikashsundriyal@gmail.com

S. Narayan
NIT Uttarakhand, Srinagar, India
e-mail: shashi@nituk.ac.in



M. Madhavan et al. (eds.), *Proceedings of the Indian Structural Steel Conference 2020 (Vol. 1)*, Lecture Notes in Civil Engineering 318,
https://doi.org/10.1007/978-981-19-9390-9_6

considering the elastic nature of the material. During extreme events like earthquakes, Tornado or Cyclones, the deformation in the structures is such that the materials are tested beyond the elastic limits. The materials' behavior (stress–strain curves) of any ductile material used in the design have two zones, namely elastic and plastic. The yield point is the point up to which the material could be safely assumed elastic, and after this point, the plastic nature of the material is activated. The behavior of the structures during the earthquake can be evaluated analytically using nonlinear analysis.

Different nonlinear analyses' techniques used are Pushover Analysis and nonlinear time-history analysis. These are used to determine the performance of structure subjected to past earthquakes and design the buildings to withstand future earthquakes. The nonlinear behavior of the buildings is greatly affected by material nonlinearity considered during the analysis. The material nonlinearity is modeled by backbone curve based on envelop of hysteresis of the material. There are different backbone curves defined for the steel. In this paper, four different backbone curves, namely steel with elastic-perfectly plastic behavior, Menegotto and Pinto model with isotropic hardening, Menegotto and Pinto model with kinematic hardening and Ibarra–Medina–Krawinkler (IMK) models, are considered for comparison. Steel with elastic-perfectly plastic behavior fails at yield strength and the stress–strain curve is parallel to the strain axis after the yield point [1]. Hereon, the model is referred to as *Steel01*. Menegotto and Pinto's model is used to simulate cyclic response. This is uniaxial material model and is used to describe the steel response in fiber-discrete cross-sections and under normal stress [2]. The Menegotto and Pinto model to referred to as Steel02. The *Steel02* with isotropic hardening is termed as *Steel02*, whereas *Steel02* with kinematic hardening is termed as *Steel4*. IMK model is a deterioration model which takes degradation of material properties like strength and stiffness into account [3]. IMK model hereon is referred to as *IMK*.

The material nonlinearity is assumed to occur at any place in the element section instead of lumped plasticity as in case of most of the works (for example, Ibarra et al. [3]). The specific points of nonlinearity in the element are calculated with the help of weighted integration. A six-story steel moment-resisting frame designed by Tsai and Popov [4] is considered as an example illustration. The effect of material nonlinearity is evaluated using fragility analysis. The fragility analysis is carried out as per multiple stripe methods [5]. In order to obtain the fragility curve, 19 different earthquakes are considered in the study. Peak ground acceleration is taken as intensity measure and roof drift is taken as damage measures while developing the fragility curves.

## 2 Methodology

The damage to the structure during an earthquake depends upon the dynamic properties of the structure and characteristics of the seismic waves. There are uncertainties in the characteristics of strong ground motion, such as the spectral shape, duration

and frequency contents. These uncertainties lead to a probabilistic assessment of the risk of the collapse of structures. The effects of material nonlinearity on the behavior of building frame during an earthquake can influence the numerically approximated response of the structure in the nonlinear range.

The effect of the material nonlinearity on the behavior of building frame during an earthquake is evaluated using fragility curves. The fragility curve is defined as "*the conditional failure probability of a structure, element or component, given the seismic load intensity (IM)* $\alpha$". In other words, a fragility function postulates the probability of failure of a structure as a function of a measure of intensity of the earthquake termed as intensity measure (IM). In this regard, the failure may not be indicated by the collapse of the structure, rather it is described by measure of failures known as damage measures (DMs). Different failure levels are expressed by damage states ($D_s$) given by threshold values of the DM. The fragility curve is defined by a log-normal cumulative distribution function given by the following equation:

$$P_f(\alpha) = P_f(\mathrm{DM} > D_s|\mathrm{IM} = \alpha) = \Phi\left(\frac{\ln \alpha/\theta}{\beta}\right), \tag{1}$$

where $P_f(\mathrm{DM} > D_s|\mathrm{IM} = \alpha)$ is the probability that a ground motion with the intensity measure as $\mathrm{IM} = \alpha$ will cause a damage of the structure greater than or equal to the damage measure; $\Phi$ is the normal cumulative distribution function (CDF); $\theta$ is the intensity measure with 50% probability of collapse and $\beta$ is the dispersion of the intensity measure in terms of the standard deviation. In the above equation, because the intensity measure (PGA) is a random variable that can never be negative, it is better to use a log-normal distribution rather than a normal distribution to explain it [6, 7]. The log-normal distribution has been considered consequently.

The building frame is subjected to different earthquakes with varying intensity measures. The response of the building frame is evaluated for each ground motion and intensity levels. The response is recorded and compared with damage measure at different damage states. If the response exceeds the damage measure, the building is treated to be collapsed. The probability of collapse is determined using Eq. 1. The values of $\theta$ and $\beta$ are evaluated using the multiple stripe methods.

## *2.1 Multiple Stripe Analysis (MSA)*

In this method, the structures are analyzed at discrete intensity measure (IM) levels with different earthquakes at each IM level. It is a dynamic analysis in which the response values of a structure are obtained in form of stripes by subjecting it to a group of earthquake after scaling them to multiple levels. First, unscaled earthquake data are normalized with respect to the intensity measures. A scalar is used so that we can accost more ground motions ($a_\lambda = \lambda a_1$) by scaling its amplitudes. Then with the help of a scalar $\lambda$, a scaled accelerogram is produced by multiplying the $\lambda$ to the unscaled acceleration time history. The response of structure for some ground

motions may be beyond the damage state (collapse). There may be an instance at a lower value of $\mathrm{IM}_i$, that the response is not beyond the damage state. The probability of observing $z_i$ collapses out of $N$ earthquake considered at the intensity measure, $\mathrm{IM}_i$, is given by binomial distribution as:

$$P(z_i) = \binom{N}{Z_i} P_i^{z_i} (1 - P_i)^{N - z_i}, \tag{2}$$

where $P_i$ is the probability of collapse at $\mathrm{IM}_i$ and $\binom{N}{Z_i} = \frac{N!}{Z_i!(N-Z_i)!}$. $P_i$ is given by Eq. 1. For multiple stripes, the probability of collapse for the set of earthquakes at different levels of an earthquake is given by the product of Eq. 2 for different intensity measures $\mathrm{IM}_i$ and termed as the likelihood and given as:

$$\text{Likelihood} = \prod_{i=1}^{m} \binom{N}{Z_i} P_i^{z_i} (1 - P_i)^{N - z_i}, \tag{3}$$

where $m$ is the number of levels of intensity measures considered in the analysis. The estimates of parameters $\theta$ and $\beta$ are obtained by maximizing the likelihood function. Once the estimates are determined, fragility function can be uniquely defined by Eq. 1.

## 3 Numerical Results and Discussion

The six-story, three-bay office building frame as shown in Fig. 1 is used to conduct the nonlinear time-history analysis using different nonlinearity models on OpenSees. The beams' and columns' sections used are shown in the figure besides the corresponding beams and columns. The roof-level beams are subjected to uniform dead and live loads of 87.74 kN/m and 17.55 kN/m, respectively, while the dead load and live load on the floor beams are 94.2 kN/m and 70.12 kN/m, respectively. The building frame is assumed to be built in location where site soil class is C. The building frame is modeled using the centerline line method and $p - \delta$ effects are modeled using the leaning column design. The gravity columns are imaginary and are portrayed as a leaning column. Pin-jointed and axially stiff beams link the leaning columns and the MRF. The leaning column is designed to withstand the structure's gravity load, whereas the MRF is designed to withstand the lateral stresses caused by the earthquake. On both sides of the MRF, the leaning column is represented so that the center of gravity is located in the geometrical center of the model (centroid) and there is no eccentricity between the center of gravity and the center of stiffness. The hinge property is modeled as distributed plasticity. The time period for the modeled building for the first three modes is 2.02 s, 0.71 s and 0.39 s, respectively.

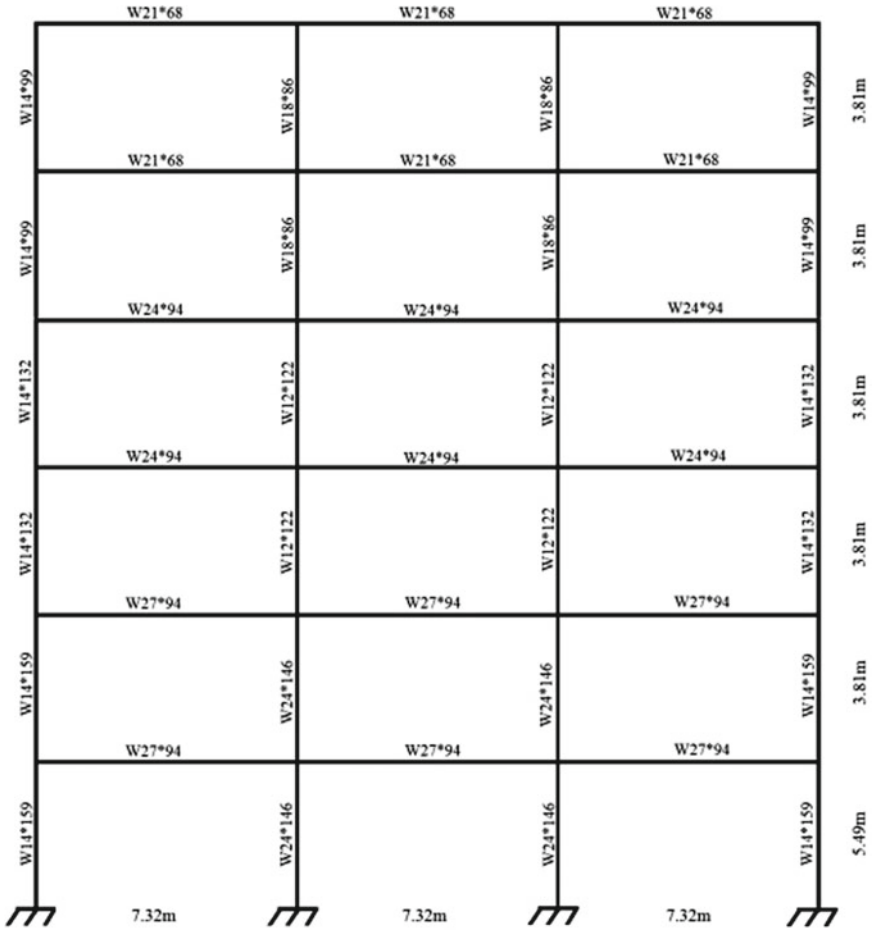


**Fig. 1** Building frame considered in the study

## *3.1 Earthquakes Considered*

Nineteen different earthquakes are considered for the study for the fragility analysis. The 19 different earthquakes are considered, and their characteristics are given in Table 1.

## *3.2 Intensity Measure and Damage Measure*

The fragility analysis requires unified quantification of the earthquake as well as damage. The earthquake is quantified by intensity measures (IMs). Intensity measure

**Table 1** Earthquake considered and their characteristics

| S. no. | Earthquakes | Date | Recording station | PGA(g) |
|---|---|---|---|---|
| 1 | Borrego_1942 | 10/21/1942 | El Centro Array #9, 0 | 0.0659 |
| 2 | Cape_Mendocino_1992 | 04/25/1992 | Petrolia, 0 | 0.591 |
| 3 | Denali_Alaska_2002 | 11/03/2002 | TAPS Pump Station #10, 47 | 0.333 |
| 4 | Duzce_Turkey_1999 | 11/12/1999 | Bolu, 0 | 0.739 |
| 5 | Helena_Montana_01_1935 | 10/31/1935 | Helena Fed Bldg, 0 | 0.0477 |
| 6 | Humbolt_Bay_1937 | 02/07/1937 | Ferndale City Hall, 225 | 0.0363 |
| 7 | Imperial_Valley_01_1938 | 06/06/1938 | El Centro Array #9, 0 | 0.0149 |
| 8 | Imperial_Valley_03_1951 | 09/12/1938 | Ferndale City Hall, 45 | 0.15 |
| 9 | Imperial_Valley_04_1953 | 06/14/1953 | El Centro Array #9, 0 | 0.0067 |
| 10 | Imperial_Valley_05_1955 | 12/17/1955 | El Centro Array #9, 0 | 0.0508 |
| 11 | Irpinia_Italy_01_1980 | 11/23/1980 | Bagnoli Irpinio, 0 | 0.13 |
| 12 | Kocaeli_Turkey_1999 | 08/17/1999 | Arcelik, 0 | 0.21 |
| 13 | Landers_1992 | 06/28/1992 | Barstow, 0 | 0.13 |
| 14 | Montenegro_Yugoslavia_1979 | 11/12/1999 | Bolu, 0 | 0.739 |
| 15 | Northern_Calif_02_1952 | 09/22/1952 | Ferndale City Hall, 44 | 0.0542 |
| 16 | Northwest_Calif_01_1938 | 01/24/1951 | El Centro Array #9, 0 | 0.0307 |
| 17 | Northwest_Calif_03_1951 | 02/07/1937 | Ferndale City Hall, 225 | 0.0363 |
| 18 | Parkfield_1966 | 06/28/1966 | Cholame—Shandon Array #5, 85 | 0.444 |
| 19 | Tabas_Iran_1978 | 09/16/1978 | Tabas, L | 0.854 |

is an indicator of the intensity of ground motion. One of the essential features for good IM is that the earthquake time history should easily be scaled to different levels of intensity measures. There are several ground motion intensity measures (IMs) that have been used in assessing the seismic performance of a structure which satisfies the above parameters. The peak ground acceleration, spectral acceleration at the fundamental period, arias intensity, effective peak acceleration, earthquake power index, peak ground velocity, spectral velocity, effective peak velocity, peak ground displacement, peak spectral displacement are few examples of IMs.

The collapse of the structure is quantified by the damage measure (DM). The DMs are chosen such that it relates to structural and non-structural damages. The different damage indexes are roof displacement, roof drifts, story drift, story ductility, residual roof displacement, residual roof drift, residual story drift, plastic rotation and the square root of the sum of squares of maximum plastic rotations. These parameters are evaluated by the nonlinear time-history analysis of the structure. The damage to structural and non-structural elements is a quantification of the damage parameters. This quantification of the damage at different discrete levels is termed as damage states. These damage states may be associated with the immediate occupancy (IO), life safety (LS), collapse prevention (CP) and collapse of the structure.

**Table 2** Damage measure for different damage states

| Immediate occupancy (%) | Life safety (%) | Collapse prevention (%) |
|---|---|---|
| 0.4 | 1 | 4 |

In the present work, peak ground acceleration (PGA) is taken as intensity measures as it is convenient to scale the ground motions using the PGA. Each of the ground earthquake record is normalized corresponding to their PGA level. After this, each normalized earthquake is multiplied by 30 different scalar quantities starting from 0.05 to 1.5 g. These 30 levels are the intensity measures.

Top story displacement is taken as the indicator of the damages of structural and non-structural elements. For damage measure, three conditions are specified corresponding to the percentage displacement of the top story with respect to the height of the building which are considered. These damage states can be termed as immediate occupancy, life safety and collapse prevention. The DM for different damage states is given in Table 2. The first damage state relates to the story drift allowance according to Indian standards [8]. The intermediate occupancy level is calculated using FEMA 356 (FEMA), and the collapse prevention is calculated using 10 times the Indian permitted limit.

## *3.3 Fragility Curves*

The building frames are subjected to the earthquakes as given in Table 1. The earthquake is scaled to different intensity measures as mentioned in above. The response parameters in terms of the roof displacement are recorded. Fragility analysis as described in methodology is performed for the building frames. In the process of determining the risk probability, the likelihood function given by Eq. 3 is minimized to determine $\theta$ and $\beta$.

The fragility curve for different material models is shown in Figs. 2, 3, 4 and 5 corresponding to different damage states. From Fig. 2, for intensity measure less than 0.36 probability of collapse of the building frame is nearly 40%, that means that there are 40% chances of failure for the building frame subjected to an earthquake in zone-V. The chances of collapse of 50% steel MRFs for Steel01 are between 0.4 and 1 intensity measure. Figure 2 shows comparison of probability of collapse with respect to IM for material model chosen as Steel01 for 0.4, 1 and 4% damage state; for 0.4% damage state, the intensity measure is 0.8 for 90% probability of collapse; for 1%, it is 1 and for 4%, it is 1.5. Damage state of 0.4% is the plot for immediate occupancy, 1% for life safety and 4% for collapse prevention. It is seen that 0.4% envelopes the 1 and 4% curve, which is expected as the building which has failed for 0.4% drift fails for higher. The same is true for other material models as depicted from Figs. 3, 4 and 5.

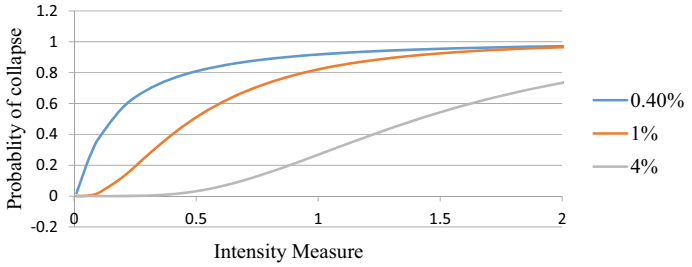


**Fig. 2** Comparison of the damage state of 0.4, 1 and 4% for Steel01

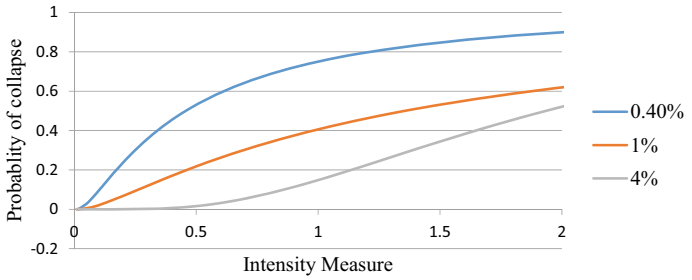


**Fig. 3** Comparison of the damage state of 0.4, 1 and 4% for Steel02

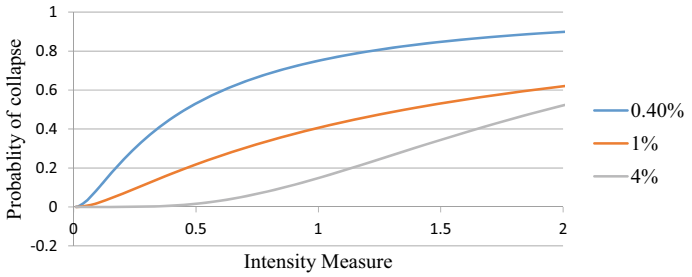


**Fig. 4** Comparison of the damage state of 0.4, 1 and 4% for Steel4

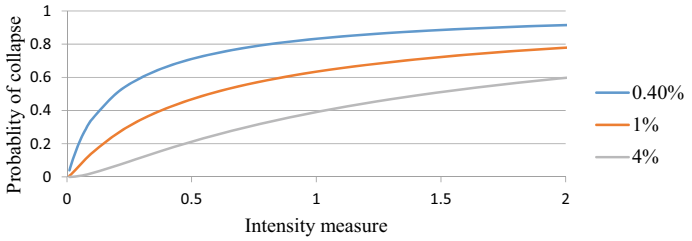


**Fig. 5** Comparison of the damage state of 0.4, 1 and 4% for IMK Model

Figures 3 and 4 show comparison of probability of collapse with respect to IM for material model chosen as Steel02 and steel04, respectively, for 0.4%, 1% and 4% damage state; the collapse of one-third steel MRFs for Steel02 occurs before 0.5 intensity measure, the collapse of 40% steel MRFs for Steel02 is between 0.5 and 1.1 intensity measure, while the probability that 26.67% frames will collapse is after 1.1 intensity measures. On comparing the plots of Steel02 and Steel4, for 0.4% damage state, the intensity measure is 0.5 for 50% probability of collapse; for 1%, it is 1.4 and for 4% damage state, the intensity measure is 1.5.

Figure 5 shows the fragility function for IMK material model, the collapse of 30% steel MRFs for IMK before 0.5 intensity measure, the collapse of 33.33% steel MRFs for IMK is between 0.5 and 1 intensity measure while the probability that 36.67% frames will collapse is after 1.1 intensity measures. On comparing the plots of IMK for 0.4, 1 and 4% damage state, 0.4% is the plot for immediate occupancy, 1% for life safety and 4% for collapse prevention. For 0.4% damage state, the intensity measure is 0.2 for 50% probability of collapse; for 1%, it is 0.6 for 50% probability of collapse; and for 4%, it is 1.5.

Figures 5, 6 and 7 show the comparison of different steel models used for immediate occupancy (0.4%), life safety (1%) and collapse prevention (4%), respectively. One may note that the fragility curve for Steel02 and Steel04 is same. So, both the models have been clubbed as one model for the comparisons. For damage state of immediate occupancy (0.4%), the intensity measure is 0.2 for 50% probability of collapse for Steel01, Steel02 and Steel4, while for IMK it is 0.7. And for the same damage state, the intensity measure is 0.7 for 80% probability of collapse for Steel01, 0.9 for Steel02 and Steel4, while for IMK it is 1.2. For damage state of life safety (1%), the intensity measure is 0.4 for 50% probability of collapse for Steel01, Steel02 and Steel4, while for IMK it is 1.3. And for the same damage state, the intensity measure is 1 for 80% probability of collapse for Steel01, 1.5 for Steel02 and Steel4 and IMK. For damage state of 4%, the intensity measure is 1.4 for 50% probability of collapse for Steel01, Steel02 and Steel4, while for IMK it is 1.5. And for the same damage state, the intensity measure is 1.5 for 80% probability of collapse for Steel01, 0.9 for Steel02 and Steel4, while for IMK it is 1.5.

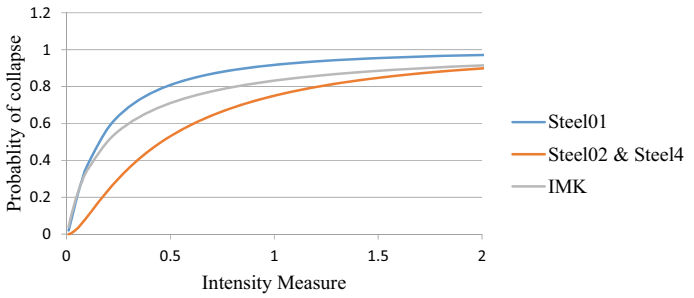


**Fig. 6** Damage state of 0.4% for different models

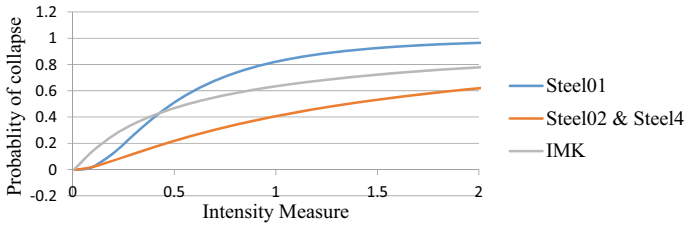


**Fig. 7** Damage state of 1% for different models

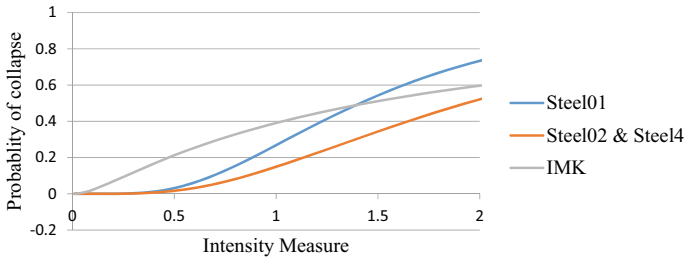


**Fig. 8** Damage state of 4% for different models

It is also observed from Figs. 6, 7 and 8 that the Steel01 overestimates the damage probability among all the material models. The initial probability of collapse (probability of collapse at lower intensity levels) is lower for the Steel01 material models. For damage state, immediate occupancy the difference between the models is not distinct. But as the damage state is increased to higher state, the difference between the material models is visible. One may note that the IMK material model is based on the experimental data. So, it is recommended to use IMK material model rather than that of the other two models.

## 4 Conclusion

The probability of seismic collapse (in terms of damage states) of building frames subjected to an earthquake considering different materials models is evaluated. The building frame has been modeled on OpenSEES. An ensemble of 19 earthquake sequences is selected for the probabilistic seismic collapse analysis. For developing the fragility curves, the multiple stripe method is used. PGA is considered as IM and roof displacement is considered as the damage measure. Three damage states have been considered, namely, immediate occupancy, life safety and collapse prevention.

Fragility curves are developed using nonlinear time-history analysis. The results of the numerical study lead to the following conclusions:

- The choice of material nonlinearity in modeling the steel effect the response of the structure.
- Elastic-perfectly plastic material model overestimates the engineering demand parameters. The modeling method is useful for analytical modeling.
- Menegotto and Pinto's underestimates the engineering demand parameters with respect to IMK model.
- IMK model is based on the experimental work, so IMK model is suggested for use in numerical modeling of constructional steel material.
- Distributed plasticity and lumped plasticity results in same values of demand parameter.

## References

1. Baker J, Baker L, Heyman J (1980) Plastic design of frames 1 fundamentals, vol 1. CUP Archive
2. Filippou FC, Bertero VV, Popov EP (1983) Effects of bond deterioration on hysteretic behavior of reinforced concrete joints
3. Ibarra LF, Medina RA, Krawinkler H (2005) Hysteretic models that incorporate strength and stiffness deterioration. Earthq Eng Struct Dynam 34(12):1489–1511
4. Tsai KC, Popov EP (1988) Steel beam-column joints in seismic moment resisting frames, vol 2. University of California, Berkeley
5. Baker JW (2015) Efficient analytical fragility function fitting using dynamic structural analysis. Earthq Spectra 31(1):579–599
6. Haldar A, Mahadevan SS (2000) Probability, reliability and statistical methods in engineering design
7. Park SW, Park HS, Oh BK, Choi SW (2018) Fragility assessment model of building structures using characteristics of artificial aftershock motions. Comput Aided Civil Infrastruct Eng 33(8):691–708
8. IS1893 BIS (2016) Indian Standard criteria for earthquake resistant design of structures (part 1): general provisions and buildings (sixth revision). Bureau of Indian Standards, New Delhi

# Behavior of the Liquid Storage Tank Under Coupled Effect of Bidirectional Excitations and Angle of Incidence of Earthquake


**Sourabh Vern, Vijay R. Sharma, Mahendra K. Shrimali, Shiv D. Bharti, and Tushar K. Datta**

**Abstract** The liquid storage tanks (LSTs) are the paramount structures in oil, nuclear and various chemical industries. The structural properties and sloshing of stored fluid can significantly alter the nature of the seismic response. Several failure incidences of LSTs are available in history because of earthquakes. Despite exhaustive research on this topic, the behavior of the rectangular steel LSTs under the near-field earthquake and long period far-field earthquakes demands more attention for a more stable design. The finite element (FE) analysis of LST is done on the ABAQUS platform. The behavior of the LSTs is studied by varying the angle of incidence of the earthquakes and the ratio between the different components of the earthquake. The resultant response due to bidirectional interaction and angle of incidence shows an increase in sloshing height; von Mises stress and top board displacement.

**Keywords** Bidirectional excitation · FSI · Angle of incidence · FEM · Coupled acoustic-structural approach · LSTs

## 1 Introduction

The liquid storage tanks are regarded as one of the most important civil and industrial structures. They can be divided into various groups such as underground, elevated and simply fixed to the ground, or depending on the construction material they can be further classified as steel or concrete tank. The ground supported liquid storage tanks (LSTs) are widely used for storing chemical, nuclear material, and water. The exposure of the ground supported steel rectangular LSTs to the seismic hazards is a

S. Vern (✉) · M. K. Shrimali · S. D. Bharti · T. K. Datta
National Centre for Disaster Mitigation and Management, MNIT Jaipur, Jaipur, India
e-mail: sourabh.vern@gmail.com

V. R. Sharma
Applied Mechanics Department, Government Engineering College Palanpur, Palanpur, India



M. Madhavan et al. (eds.), *Proceedings of the Indian Structural Steel Conference 2020 (Vol. 1)*, Lecture Notes in Civil Engineering 318,
https://doi.org/10.1007/978-981-19-9390-9_7

matter of concern, as failure in the LSTs can result in a disaster of huge magnitude. The most common failures seen in the failed structures were elephant foot buckling, damage of the roof and uplifting of the LST base. Some of these failures were reported in the Alaska earthquake, Alaska, (1964), Tabas earthquake, Iran (1978), Sierra Madre earthquake, California (1991), Hokkaido earthquake, Japan (2003), Sumatra Earthquake, Indonesia (2004), Yushu earthquake, China (2010) and Central Mexico earthquake, Mexica (2017). The continuous research on the seismic response of the ground supported LSTs has shown the current design philosophy of LSTs has some shortcomings.

The analysis of an LST can be divided into two different sections, i.e. impulsive and convective parts. The impulsive response contributes to the major part of the shear forces, overturning moments, stress in tank walls whereas, convective response provides the sloshing response which is responsible for the roof damage in the LSTs. For a complete behavioral analysis of the LSTs under the excitations, both impulsive and convective responses need to be studied. This combined response of impulsive and convective gives pressure on the tank wall and the base shear force of the LSTs. Thus, to determine the safety in the steel LSTs, an updated approach is required.

The past approaches for the LSTs models can be grouped under the 2D or 3D models, and numerical or analytical. Housner [1, 2] presented results in the closed-form of mathematical expressions for both elevated and ground supported tank. Some other analytical expressions were given by various researchers (Gupta and Hutchinson 1988; Fischer and Seeber 1988). Several numerical method and techniques were developed to study the dynamic behavior of LSTs which were verified by the experimental analysis by many notable researchers [3–8].

Many studies were made on the dynamic response of LSTs under the earthquake motion using FEM. The FEM approach taken by researchers provides the exhaustive analysis of fluid–structure interaction (FSI) by different FEM elements [9–19].

In the most recent past, Kianoush and Ghaemmaghami [20] studied the three-dimensional FSI and SSI which was numerically simulated using FEM for a partially filled concrete rectangular tank for different ground motion records. The response quantities were base shear, base moments and sloshing height. Mandal and Maity [21] discussed the effect of change of horizontal harmonic excitation frequencies and amplitudes. The author reported that altering the magnitude of the harmonic excitations developed the nonlinear responses. However, the linear and nonlinear hydrodynamic pressures were not significantly affected. Bakalis et al. [22] designed the three-dimensional surrogate model, which can be used to investigate the multidirectional support system for both the fixed and pinned tanks. The results of the study were validated by the existing experimental results. Zhang and Wan [23] investigated the effect of Young's modulus of the tank wall on the sloshing phenomenon. The study was carried out by the application of a fully lagrangian FSI solver. The solution to the impact of the sloshing wave on the tank wall with smaller Youngs modulus took more time than that for rigid wall tank. Rawat et al. [24] investigated the coupled acoustic-structural (CAS) and Euler–Lagrange approach (CEL) of FE approaches to simulate the sloshing effect in a steel cylindrical liquid storage tank. Although both the methods yielded identical results, it was concluded that the CAS

approach was more numerically efficient. Jin and Lin [25] studied the viscous effect of the fluid sloshing due to the external excitations. The sloshing motion was captured by a 3D numerical model NEWTANK which employs spatially averaged Navier–Stokes equations and large eddy simulation approach. Moslemi et al. [26] studied the nonlinear sloshing in rectangular storage tank. The effect of the different parameters was taken in the consideration such as tank aspect ratio, bidirectional loading and earthquake frequency.

With help of FEM suites like ABAQUS and ANSYS, the analysis of LSTs under seismic excitation becomes more accurate and realistic. For understanding the FSI in the LSTs various FEM elements are present. Among the available FE elements, acoustic elements are selected because of their low cost.

Despite the various studies available in the research community on the LSTs, the studies for the rectangular steel tanks are still very less, and its behavior under the bidirectional interaction is even less. The present research focuses on the FEM approach of the square steel tanks under the bidirectional interaction of different types of earthquakes (far-field and near-field). The coupled effect of the structural geometry with the angle of the incidence of the earthquake is also examined to determine the critical angle of incidence of the earthquake. The different response quantities under study include base shears, overturning moments, sloshing height and top board displacement in the tank.

## 2 Theory

The response of the liquid storage tanks subjected to the earthquake ground motion develops a nonlinear and complex FSI. Due to the sudden application of the ground motion, a very high magnitude of the inertial forces is generated in the tank walls. Due to the hydrodynamic pressure on the tank walls the resistive inertial forces get amplified. The flexibility of the tank walls further pushes the fluid media which develops an overall imbalance in the liquid media. Due this imbalance the tank material is further pushed into the nonlinear domain. To simulate the nonlinearity, behavior of the FSI ABAQUS uses an implicit operator. For solving the nonlinearity in the solution, Newton's method is used as its convergence rate is faster than any other method. For a solution iteration an $i$ approximate solution is approached, $u_i^M$ and $C_{i+1}^M$ is defined as the difference of the solution and is the exact solution for the discrete equilibrium equation,

$$F^N(u_i^M + c_{i+1}^M) = 0 \tag{1}$$

Form the expansion by the Taylor series with respect to the solution approximation $u_i^M$, the following equation is achieved.

$$F^N(u_i^M) + \frac{\partial F^N}{\partial u^P}(u_i^M)c_{i+1}^P + \frac{\partial^2 F^N}{\partial u^P \partial u^Q}(u_i^m)c_{i+1}^P c_{i+1}^Q + \cdots = 0 \tag{2}$$

If the solution of each step $u_i^M$ is in close approximation, then the magnitude of each $C_{i+1}^M$ will be small. By neglecting the initial two terms of the equation gives a linear system of equations as,

$$K_i^{NP} c_{i+1}^P = -F_i^N \tag{3}$$

$$K_i^{NP} = \frac{\partial F^N}{\partial u^P}(u_i^M) \tag{4}$$

$$P = \frac{\pi^2 E I_y}{L^2} \tag{5}$$

If Eq. (3) is the Jacobian matrix and $F_i^N = F^N(u_i^M)$, then the equation of next iteration is given by

$$u_{i+1}^M = u_i^M + c_{i+1}^M \tag{6}$$

The convergence of solution is measured by ABAQUS by ensuring that all values of $F_i^N$ and $c_{i+1}^N$ are small. After checking the conditions, ABAQUS provides the peak values of force residual and displacement.

## *2.1 Details of Finite Element Modeling*

The present FE analysis is performed for a typical rectangular liquid storage tank. The LST is fixed at the base. To understand the complex FSI due to the seismic ground motion coupled acoustic structure, FE formulation technique is adopted. The fluid is modeled by acoustic continuum three-dimensional eight-nodded brick element (AC3D8R). The tank is modeled by a regular four-nodded quadrilateral shell element with reduced integration (S4R). For accurate results a mesh convergence study is carried out; the minimum mesh size of 0.125 m is selected.

The use of the acoustic element in FSI is advantageous because it has only one degree of freedom, which reduces the computational time. The suitable boundary conditions are applied between the inner tank surface and a fluid outer surface. The boundary condition facilitates the transfer of energy and momentum in the fluid media from tank walls. The top fluid surface requires a different surface condition to incorporate the sloshing effect. The boundary impedance condition is applied at the top of the free surface of the fluid. This boundary condition at the free surface is defined as:

$$\dot{u}_{\text{out}} = \frac{1}{k_1}\dot{p} + \frac{1}{c_1}p \tag{7}$$

Here, $\dot{u}_{\text{out}}$ is known as acoustic particle velocity, which is in normal outward direction of the acoustic medium surface; $p$ is acoustic pressure; $\dot{p}$ is the time rate of change of the acoustic pressure. The value of coefficient $1/k_1$ and $1/c_1$ are calculated with respective fluid properties [27]. A dynamic implicit procedure with automatic time incrementation technique is selected as per the problem requirement. For simulating the seismic motion in the tank, an acceleration time history is applied as an acceleration boundary condition in the base of the tank. A couple of dynamic procedure steps are created to model the nonlinear dynamic behavior in tank. The interaction between the tank wall motion and liquid motion is a tie constraint, in which the master surface is tank wall, and water surface is slave surface.

The earthquake motions consist of two major groups, far-field and near-field excitations. Furthermore, to extend the understanding, near-field (NF) earthquakes are extended into primarily three groups, and those are NF-fling step, NF-low directivity, and NF-high directivity. The criteria for the NF earthquakes are the Joyer Boore distance ($R_{jb} < 15$ km). In the present study, the behavior of the LST under the bidirectional excitation for the array of near-field and far-field earthquakes is studied. The response of near-field is quite different than the far-field response, near-field earthquakes have large amplitude of the acceleration and the frequency range of the near-field earthquakes is limited. The fling step earthquake has the strike-slip rapture fault direction parallel to the strike and a significant monotonic step in displacement time history. The directivity of the near-fault earthquake arises when the rapture direction is toward the structures.

## 3 Numerical Study

For the numerical study, a steel rectangular liquid storage tank is considered. The tank is subjected to bidirectional earthquake excitation at the base. The tank is a plan square geometry with length of 6 m and height being equal to 4.8 m. The thickness of the tank wall is taken as 0.0152 m. The tank is considered as partially filled up to a height of 3.6 m with $h/L$ ratio of 0.75 where $h$ is fluid height and $L$ is the tank length. The various material properties taken in the analysis are given in Table 1.

For the proper assessment of the stresses in the tank wall and other responses of interests, three different types of the near-field earthquakes are taken, whereas, for the far-field response, a single time history is taken up for the analysis. Table

**Table 1** Material properties

| Steel | Water |
|---|---|
| Modulus of elasticity, $E_s =$ 200 GPa | Density, $\rho_w = 983.204$ kg/m$^3$ |
| Density $\rho_s = 7900$ kg/m$^3$ | Bulk modulus, $K = 2250$ MPa |
| Poisson's ratio, $\upsilon = 0.33$ | |

**Table 2** Properties of various earthquakes

| Earthquake | Recording station | Magnitude |
|---|---|---|
| Kern County (1952) | Taft Lincoln School | 7.3 |
| Imperial Valley (1940) | El-Centro | 6.6 |
| Kocaeli (1999) | Sakarya | 7.5 |
| Parkfield (2004) | Chalome 1E station | 6.0 |

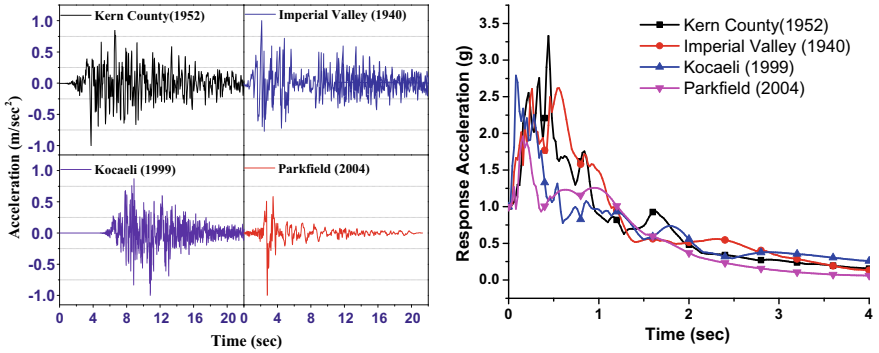


**Fig. 1** **a** Earthquake time history plot. **b** Response spectra plot

2 illustrates various earthquakes taken in present study along with their recording stations (Fig. 1).

## *3.1 Validation of the FEM*

To validate the current FEM results, an FE analysis is done in which, the tank and water are modeled by a two-node linear beam in a plane (B21) and a four-node bilinear plane strain quadrilateral (A2CD4) finite element programmed in ABAQUS, respectively. Figure 2 displays the obtained sloshing height time history. The results are determined at the right-side node of the fluid media. The sloshing height in Fig. 2 lucidly shows that the responses from the current FE method are in excellent agreement with the existing FE solution [17] for an extended period of analysis time.

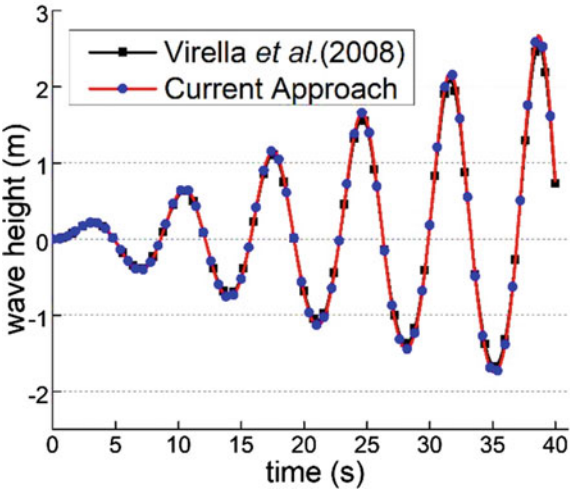


**Fig. 2** Validation of FE approach

## *3.2 Comparison Between Unidirectional and Bidirectional Responses*

To illustrate the importance of the bidirectional interaction in the earthquake analysis, the LST is examined for the unidirectional effect, and then the contrast is made between the bidirectional excitation. Figure 3a, b gives the percentage change in the von Mises stress, base shear, base moment and sloshing height. These values are taken as the absolute maximum value of the response. For calculating the maximum, von Mises stress comparison between uni and bidirectional response is extracted at the base of the tank. There is a change in the value for the von Mises stress. There is a notable increase of 12% when bidirection excitation is studied. The effect of the nature of the earthquake can be seen, maximum increase can be observed in the case of the Kocaeli earthquake. This difference is minimum for the shear force. It can be seen from the figures that Kern county earthquake shows more difference for the von Mises stress whereas, shear stress, base moment and sloshing height display lowest change in the present group of the earthquake.

The base shear and overturning moment show a change of 4–8%, which is very low, whereas sloshing height shows a notable change of 50–70%.The increase in sloshing height points to the need for the importance of the bidirectional interaction. The sloshing height change is maximum for the Kocaeli earthquake with 70% increase with respect to the unidirection excitation. Thus, these results lucidly indicate that the effect of the near-field earthquake is more devesting then the far-field earthquakes.

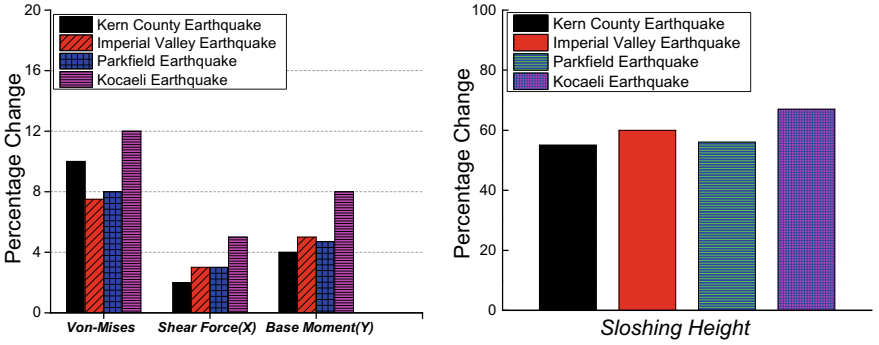


**Fig. 3** Percentage change in **a** von Mises stress, shear force (X) and base moment (Y) **b** Sloshing height

## *3.3 Effect of Incidence Angle on Responses of LST*

The impact of the angle of incidence of earthquake on the various outputs is shown in Fig. 4. The six variations of angle of the incidence earthquake are studied for the steel LST under bidirectional excitation of the earthquake with a PGA level of 0.4 g and 0.27 g in X and Y directions, respectively. It can be seen from the figure that von Mises stress varies mildly at an angle of 30° to 45°. The maximum value of the von Mises stress can be seen for the Imperial valley earthquake which is a near-field earthquake. The sloshing height also varies with angle of the incidence. The peak sloshing height is achieved at an angle of 0°.

The variation of the maximum shear force and overturning moment remained unchanged toward the angle of the incidence. The maximum value of the base shear and the overturning moment is observed for the Kocaeli earthquake, thus while examining responses in LSTs, it is important to also study the nature of the earthquakes.

The absolute top board displacement variation in *X*-direction is as shown in Fig. 4. It can be seen from the figure that angle of earthquake has a significant impact. The top board displacement attains a maximum magnitude at 60° angles. Here again, the maximum top board displacement is observed for the near-field earthquakes, whereas minimum is for the far-field earthquakes. The above results indicate that bidirectional interaction effect along with impact of the angle of the incidence should be considered to identify the most critical cases for the analysis of steel LSTs under the seismic excitations.

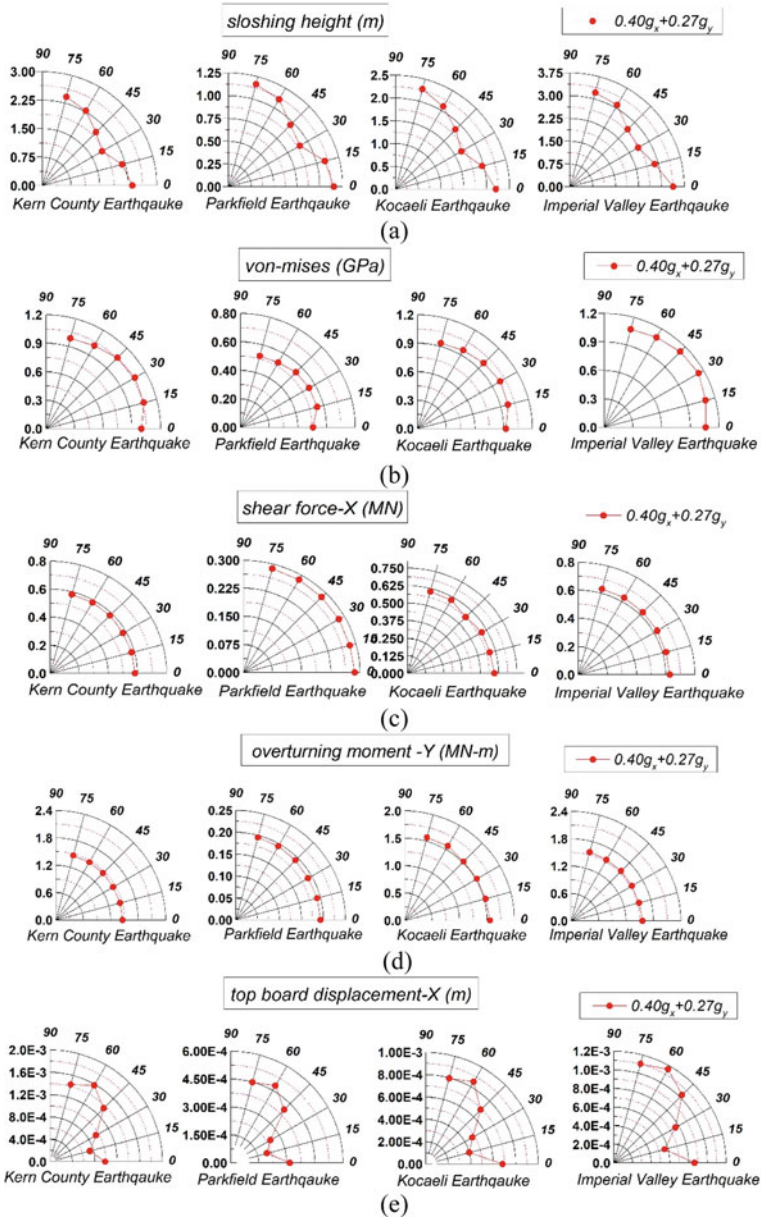


**Fig. 4** Change in responses with angle of incidence. **a** Sloshing, **b** von Mises stress, **c** Shear force (X), **d** Base moment (Y) and **e** Top board displacement (X)

## 4 Conclusions

The dynamic analysis of steel LSTs under the far and near-field earthquake is investigated. The different parameters include overturning moment, base shear, sloshing height, top board displacement and von Mises stress in tank. For the numerical case study, a steel square tank of dimension 6 m × 6 m × 4.8 m is taken. The FE study is carried out on ABAQUS software. For reliable results, the current acoustic approach is verified with previously available results. The results lead to the following conclusions.

1. The bidirectional interaction indicates an overall increase in the response quantities, the significant increase of 45–70% is seen for the case sloshing height.
2. The maximum increase in the responses is observed for the near-field earthquakes, particularly for the fling step earthquakes.
3. The base shear, the overturning moment remains unchanged for the different angle of incidence, whereas the von Mises stress values showed an increase for the 45° angle configuration.
4. The effect of the angle of incidence is observed to be significant for the sloshing height, top board displacement, the sloshing height gets reduced at the angle of 45° whereas, top board displacement attains a minimum value at initial angle configuration, after that it goes on increasing with a decrease at the 60° angle.

The results of the study indicate that for a more critical assessment of LSTs behavior under earthquake motion requires an exhaustive analysis in the form of reliability analysis.

## References

1. Housner GW (1957) Dynamic pressures on accelerated fluid containers. Bull Seismol Soc Am 47(1):15–35
2. Housner GW (1963) The dynamic behavior of water tanks. Bull Seismol Soc Am 53(2):381–387
3. Akyildiz H, Erdem Ünal N (2006) Sloshing in a three-dimensional rectangular tank: Numerical simulation and experimental validation. Ocean Eng 33(16):2135–2149
4. Faltinsen OM, Rognebakke OF, Lukovsky IA, Timokha AN (2000) Multidimensional modal analysis of nonlinear sloshing in a rectangular tank with finite water depth. J Fluid Mech 407:201–234
5. Frandsen JB (2004) Sloshing motions in excited tanks. J Comput Phys 196(1):53–87
6. Gavrilyuk IP, Lukovsky IA, Timokha AN (2005) Linear and nonlinear sloshing in a circular conical tank. Fluid Dyn Res 37(6):399–429
7. Liu D, Lin P (2008) A numerical study of three-dimensional liquid sloshing in tanks. J Comput Phys 227(8):3921–3939
8. Shrimali MK, Jangid RS (2002) Seismic response of liquid storage tanks isolated by sliding bearings. Eng Struct 24(7):909–921
9. Chen JZ, Kianoush MR (2005) Seismic response of concrete rectangular tanks for liquid containing structures. Can J Civ Eng 32(4):739–752
10. Haroun MA, Housner GW (1981) Earthquake response of deformable liquid storage tanks. J Appl Mech 48:411–418

11. Liu WK (1981) Finite element procedures for fluid-structure interactions and application to liquid storage tanks. Nucl Eng Des 65(2):221–238
12. Livaoglu R (2008) Investigation of seismic behavior of fluid-rectangular tank-soil/foundation systems in frequency domain. Soil Dyn Earthq Eng 28(2):132–146
13. Mitra S, Sinhamahapatra KP (2007) Slosh dynamics of liquid-filled containers with submerged components using pressure-based finite element method. J Sound Vib 304(1–2):361–381
14. Mitra S, Sinhamahapatra KP (2008) 2D simulation of fluid-structure interaction using finite element method. Finite Elem Anal Des 45(1):52–59
15. Ozdemir Z, Souli M, Fahjan YM (2010) Application of nonlinear fluid—structure interaction methods to seismic analysis of anchored and unanchored tanks. Eng Struct 32(2):409–423
16. Virella JC, Godoy LA, Su LE, Suárez LE (2006) Dynamic buckling of anchored steel tanks subjected to horizontal earthquake excitation. J Constr Steel Res 62(6):521–531
17. Virella JC, Prato CA, Godoy LA (2008) Linear and nonlinear 2D finite element analysis of sloshing modes and pressures in rectangular tanks subject to horizontal harmonic motions. J Sound Vib 312(3):442–460
18. Wall WA, Genkinger S, Ramm E (2007) A strong coupling partitioned approach for fluid-structure interaction with free surfaces. Comput Fluids 36(1):169–183
19. Wei W, Junfeng L, Tianshu W (2008) Modal analysis of liquid sloshing with different contact line boundary conditions using FEM. J Sound Vib 317(3–5):739–759
20. Kianoush MR, Ghaemmaghami AR (2011) The effect of earthquake frequency content on the seismic behavior of concrete rectangular liquid tanks using the finite element method incorporating soil-structure interaction. Eng Struct 33(7):2186–2200
21. Mandal KK, Maity D (2016) Nonlinear finite element analysis of water in rectangular tank. Ocean Eng 121:595–601
22. Bakalis K, Fragiadakis M, Vamvatsikos D (2017) Surrogate modeling for the seismic performance assessment of liquid storage tanks. J Struct Eng 143(4):04016199
23. Zhang Y, Wan D (2017) MPS-FEM coupled method for sloshing flows in an elastic tank. Ocean Eng 152(October):416–427
24. Rawat A, Mittal V, Tanusree C, Matsagar V (2019) Earthquake induced sloshing and hydrodynamic in rigid liquid storage tanks analyed by coupled acoustic-structural and Euler-Lagrange methods. Thin-Walled Struct 333–346
25. Jin X, Lin P (2019) Viscous effects on liquid sloshing under external excitations. Ocean Eng 0029(8018):695–707
26. Moslemi M, Farzin A, Kianoush MR (2019) Nonlinear sloshing response of liquid-filled rectangular concrete tanks under seismic excitation. Eng Struct 188(August):564–577
27. Dassault Systèmes Simulia (2012) Analysis user's manual volume 2: analysis. Abaqus 6.12, Vol. II

# Stress Analysis of Plates Subjected to Uniform and Non-uniform Uniaxial Tensile Loads


**Danish Fayaz, S. N. Patel, and Rajesh Kumar**

**Abstract** This paper deals with the study of the stress characteristics of isotropic and orthotropic plates under a uniform and non-uniform uniaxial tensile load. Numerical analysis of stress characteristics of both the plates has been performed, and a comparative study has been made. The obtained results are compared with the available results for validation. The stress results for two types of boundary conditions are presented for both the plates. The effect of the uniform and parabolic in-plane tensile pressure on the stress distribution has been studied. It is observed that the loading profile has significant effect of stress distribution of the plates. The effect of the orientation of the fibers has also been studied.

**Keywords** Composite laminates · Orthotropic materials · Stress characteristics · Analytical solution

## 1 Introduction

Plates are widely used as a principal structural component in aerospace, mechanical, civil engineering, and marine applications, as well as in industrial design such as ships, aircraft, plants, bridges, and machines. The use of orthotropic composite laminates plays a significant role in lightweight structures due to its higher strength–weight ratio compared to other isotropic materials [2]. The composite laminates made of boron/epoxy or graphite/epoxy orthotropic materials generally used in the aerospace sector for the manufacturing of aircraft wings, aircraft nose, or flaps that

D. Fayaz · S. N. Patel (✉) · R. Kumar
Department of Civil Engineering, BITS PILANI, Pilani, India
e-mail: shuvendu@pilani.bits-pilani.ac.in

D. Fayaz
e-mail: p20180402@pilani.bits-pilani.ac.in

R. Kumar
e-mail: rajesh.kr@pilani.bits-pilani.ac.in



M. Madhavan et al. (eds.), *Proceedings of the Indian Structural Steel Conference 2020 (Vol. 1)*, Lecture Notes in Civil Engineering 318,
https://doi.org/10.1007/978-981-19-9390-9_8

must be light in weight should have enough strength against the imposed loads and also high wear and temperature resistance. The composites in manufacturing of body or pressure/fuel tanks in rockets and missiles subjected to high loads should have high temperature and wear resistance. In general, the plates or shells are subjected to various uniform and non-uniform in-plane loads depending upon their usage in different sectors. The in-plane loads are generated from the neighboring components with which the plate is connected. To design the plates efficiently, it is necessary to understand the effect of these loads on the stress behavior of the plate. The in-plane loads can be compressive or tensile and can be static or dynamic. However, in the present study, the effect of static, in-plane tensile loads is considered.

Different researchers have dealt with the different theoretical approaches for the calculation of different parameters in plates. Kassapoglou and Bauer [4] presented an exact solution of the governing equations with the use of the Fourier series approach to determine the stresses in a composite plate under concentrated load on one edge and a uniform load on the opposite edge. Results were obtained for three different panel layups $(\pm 45)_4$, $(0/90)_4$, and the quasi-isotropic $[(\pm 45)/(0/90)]_s$. Kumar Panda and Ramachandra [6] presented a study of buckling and post-buckling behavior of simply supported composite plates subjected to non-uniform in-plane loading. A simplified energy-based approach was used to evaluate the prebuckling stress within the plate. The buckling loads are calculated for three different aspect ratios and three different types of non-uniform in-plane loadings using Galerkin's method. Displacement potential approach of orthotropic materials for plane stress conditions has been employed by Deb Nath [2] to calculate the lateral displacement and normal lateral stresses when the section was subjected to a combined loading at its lateral edge. The effect of fiber orientation and material isotropy was also studied. The analytical solution of the same problem has been presented at different sections of the panel with a fiber orientation of 90°. Li et al. [7] investigated the problems on bending of free orthotropic rectangular thin plates on elastic foundations by an analytical finite integral transform method with supported, clamped, and free boundary conditions. A new trigonometric higher-order shear deformation theory for isotropic and laminated composite and sandwich plates was discussed by Mantari et al. [8]. The theory accounts for adequate distribution of the transverse shear strains through the plate thickness and tangential stress-free boundary conditions on the plate boundary surface. Khechai et al. [5] studied the stress concentration factors (SCF) in cross-and-angle-ply laminated composite plates as well as in isotropic plates with single circular holes subjected to uniaxial loading. Yazdani Sarvestani and Naghashpour [13] determined the interlaminar stresses close to the free edges of general cross-ply composite laminates based on higher-order equivalent single-layer theory. Buckling analysis of laminated composite stiffened plates subjected to partial in-plane edge loads was carried out by Patel and Sheikh [10]. The finite element method was applied, and eight-noded isoparametric degenerated shell element with C° continuity and first-order shear deformation was considered. Effect of different parameters like the orientation of fibers, number of layers, and loading types was considered in the investigation. Nath [9] solved two elastic plate problems analytically using the

displacement potential approach for the case of the plane strain and plane stress conditions. Two different boundary conditions have been implemented. In the first case, one edge was kept fixed with the other edges stiffened. A uniform tensile in-plane load of 50 MPa was applied to the end opposite to the fixed one. In the second case, all the edges were stiffened, and the same tensile in-plane load was applied. Hussein and Alasadi [3] investigated experimentally and numerically combined effects of thermal and mechanical loadings on the distribution of stress–strain for E-glass fiber/polyester composite plates. The results presented showed that the maximum absolute of total strain in longitudinal direction occurred at 50 N tension load and fiber angle 60º, while the minimum absolute values of it occurred at 15 N tension loads and fiber angle 0º. Cheuk and Tong [1] studied the effect of cracks in strap adherend when a composite laminate adherend with 8 plies at 0-degree fiber orientation subjected to in-plane loads. At different crack lengths (0, 2, 4, 8, and 10 mm), failure loads and failure modes were predicted by maximum stress criteria. The analytical solution has also been formulated for lap shear joint with embedded crack. It was found that in the presence of embedded cracks, there was a significant reduction in failure loads. There was a good agreement between axial forces acting on the section predicted by finite element analysis (FEA) and the formulated analytical solution.

A systematic study is conducted on a steel plate and a composite laminated plate subjected to uniform and parabolic tensile loading. Efforts are made in three aspects: theoretical model development, computer simulation using finite element method, and analytical evaluation using unidirectional plies for the composite plate. Theoretically, two models are proposed to describe the normal stress distribution of the steel plate and a laminated plate. The finite element method is extensively used in the stress analysis of the unidirectional laminates in this study using ABAQUS and ANSYS software. The responses of an orthotropic composite plate under the effect tensile load are performed using analytical solutions, ABAQUS and ANSYS. The load is kept constant, the boundary conditions are changed, and the stresses are analyzed at different sections of the plates.

## 2 Theory

In this section, the analytical solution for the case of plane stress problem for isotropic as well as the orthotropic plate has been presented. The case of uniform as well as parabolic in-plane tensile pressure has also been taken into account in this section.

### *2.1 Analytical Solution for Isotropic Plate*

With reference to a rectangular coordinate system ($x$, $y$), as shown in Figs. 1 and 2, the governing differential equation of equilibrium for the isotropic plate ($a \times b$) for the present problem is given by Timoshenko and Goodier [12]:

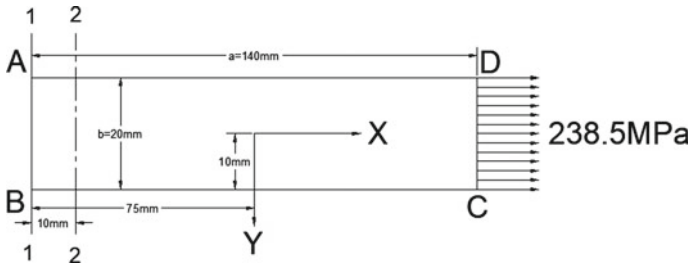


**Fig. 1** Model of both isotropic steel and orthotropic composite plate subjected to uniform in-plane tensile pressure

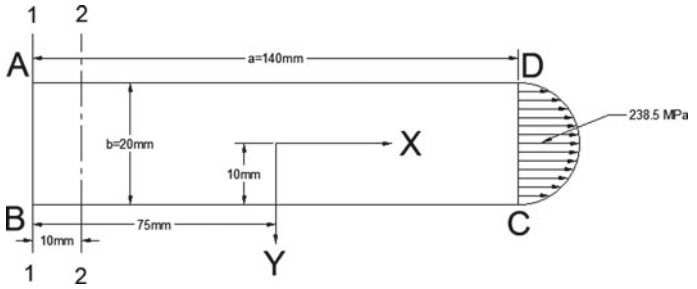


**Fig. 2** Model of both isotropic steel and orthotropic composite plate subjected to parabolic in-plane tensile pressure

$$\frac{\partial^4 \phi}{\partial x^4} + \frac{2\partial^4 \phi}{\partial x^2 \partial y^2} + \frac{\partial^4 \phi}{\partial y^4} = 0 \tag{1}$$

where $\phi$ is the stress function in a series form given by:

$$\phi = \sum_{n=1}^{\infty} f_n(x) * \cos \frac{2n\pi}{b} y + C_0 y^2 \tag{2}$$

On differentiating Eq. (2) and then substituting in Eq. (1), we get

$$\left[ \frac{\partial^4 f_n}{\partial x^4} - 2 * \left( \frac{2n\pi}{b} \right)^2 \frac{\partial^2 f_n}{\partial x^2} + \left( \frac{2n\pi}{b} \right)^4 f_n \right] \cos \frac{2n\pi}{b} y = 0 \tag{3}$$

The solution of the Eq. (3) is given by

$$f_n(x) = \sum_{n=1}^{\infty} \left( A_n * \cosh \frac{2n\pi}{b} x + B_n * x * \sinh \frac{2n\pi}{b} x \right) \tag{4}$$

where $A_n$ and $B_n$ are the arbitrary constants. Substituting Eq. (4) in Eq. (2), we will get

$$\phi = \sum_{n=1}^{\infty}\left(A_n * \cosh\frac{2n\pi}{b}x + B_n * x * \sinh\frac{2n\pi}{b}x\right) * \cos\frac{2n\pi}{b}y + C_0 y^2 \quad (5)$$

where

$$C_0 = \frac{1}{b}\int_0^{b/2} P(y)\mathrm{d}y$$

And

$$P(y) = N_t = 238.5 \text{ MPa} \quad \text{(For Uniform Loading)}$$

$$P(y) = \frac{4}{b^2}\left(\frac{b^2}{4} - y^2\right)N_t \quad \text{(For Parabolic Loading)}$$

The stress at any point in two dimensional object can be represented by three dependent variables, namely $\sigma_{xx}$, $\sigma_{yy}$, and $\tau_{xy}$, where $\sigma_{xx}$ is the normal stress acting on face x along $x$-axis, $\sigma_{yy}$ is the normal stress acting on face y along $y$-axis, and $\tau_{xy}$ is the shearing stress which acts on face $x$ along $y$-direction.

$$\sigma_{xx} = -\left(\frac{2n\pi}{b}\right)^2 * \left(A_n * \cosh\frac{2n\pi}{b}x + B_n * x * \sinh\frac{2n\pi}{b}x\right) * \cos\frac{2n\pi}{b}y + 2C_0 \quad (6)$$

$$\sigma_{yy} = \left(\frac{2n\pi}{b}\right)^2 * \left(A_n * \cosh\frac{2n\pi}{b}x + B_n * \left(x * \sinh\frac{2n\pi}{b}x + \frac{b}{n\pi} * \cosh\frac{2n\pi}{b}x\right)\right) * \cos\frac{2n\pi}{b}y + 2C_0 \quad (7)$$

$$\tau_{xy} = \left(-\frac{2n\pi}{b}\right)^2 * \left(A_n * \sinh\frac{2n\pi}{b}x + B_n * \left(x * \cosh\frac{2n\pi}{b}x + \frac{b}{2n\pi} * \sinh\frac{2n\pi}{b}x\right)\right) * \sin\frac{2n\pi}{b}y \quad (8)$$

The boundary conditions for Fig. 1 are:

$\sigma_{xx}\left(\pm\frac{a}{2}, y\right) = P(y)$; $\sigma_{yy}\left(x, \pm\frac{b}{2}\right) = 0$; $\tau_{xy}\left(\pm\frac{a}{2}, y\right) = 0$; and $\tau_{xy}\left(x, \pm\frac{b}{2}\right) = 0$where $P(y)$ corresponds the values for uniform and parabolic loading case. Applying the above boundary conditions in Eqs. (6), (7), and (8), we get

$$A_n = -B_n\left(\frac{a}{2}\coth\frac{n\pi a}{b} + \frac{b}{2n\pi}\right)$$

$$B_n = \frac{b}{n\pi} \frac{I \sinh \frac{n\pi a}{b}}{\left(\frac{2n\pi}{b} a + \sinh \frac{2n\pi}{b} a\right)}$$

where $I = [P(y) - 2C_0]/\cos\left(\frac{2n\pi}{b} y\right) C_0$.

After the values of $A_n$ and $B_n$ are known, these values can be directly substituted in Eqs. (6), (7), and (8) to calculate $\sigma_{xx}$, $\sigma_{yy}$, and $\tau_{xy}$.

## 2.2 Analytical Solution for Orthotropic Composite Plate

The governing differential equation for a composite plate given by Reddy [11] is as follows:

$$a_{11} \frac{\partial^4 \phi}{\partial x^4} + 2a_{12} \frac{2\partial^4 \phi}{\partial x^2 \partial y^2} + a_{66} \frac{\partial^4 \phi}{\partial x^2 \partial y^2} + a_{22} \frac{\partial^4 \phi}{\partial y^4} = 0 \tag{9}$$

where $\phi$ is the stress function in the series form given by:

$$\phi = \sum_{n=1}^{\infty} f_n(x) * \cos \frac{2n\pi}{b} y \tag{10}$$

and $a_{11}$, $a_{12}$, $a_{66}$, and $a_{22}$ the material coefficients.

On differentiating Eq. (10) and then substituting in Eq. (9), we get

$$\left[ a_{22} \frac{\partial^4 f_n(x)}{\partial x^4} - \left(\frac{2n\pi}{b}\right)^2 (2a_{12} + a_{66}) \frac{\partial^2 f_n(x)}{\partial x^2} + \left(\frac{2n\pi}{b}\right)^4 f_n(x) \right] \cos \frac{2n\pi}{b} = 0 \tag{11}$$

The roots of Eq. (11) come out as

$$f_n(x) = C_1 * \cosh \alpha_n x + C_2 * \cosh \beta_n x$$

where

$$\alpha_n = \frac{n\pi}{a} \quad \text{and} \quad \beta_n = \frac{n\pi}{b}$$

The assumed solution is

$$\phi = \sum_{n=1}^{\infty} f_n(x) * \cos \frac{2n\pi}{b} y + C_0 y^2 \tag{12}$$

On substituting the roots in the assumed solution given by Eq. (11), we get

$$\phi = \sum_{n=1}^{\infty}(C_1 * \cosh \alpha_n x + C_2 * \cosh \beta_n x) * \cos \frac{2n\pi}{b} y + C_0 y^2$$

After differentiating the above equation twice w.r.t $x$ and $y$, we get

$$\sigma_{xx} = -\left(\frac{2n\pi}{b}\right)^2 * \sum_{n=1}^{\infty}(C_1 \cosh \alpha_n x + C_2 \cosh \beta_n x) * \cos \frac{2n\pi}{b} y + 2C_0 \quad (13)$$

$$\sigma_{yy} = \sum_{n=1}^{\infty}\left(\alpha_n^2 C_1 \cosh \alpha_n x + \beta_n^2 C_2 \cosh \beta_n x\right) * \cos \frac{2n\pi}{b} y \quad (14)$$

$$\tau_{xy} = \left(\frac{2n\pi}{b} y\right) * \sum_{n=1}^{\infty}(\alpha_n C_1 \sinh \alpha_n x + \beta_n C_2 \sinh \beta_n x) * \sin \frac{2n\pi}{b} y \quad (15)$$

The boundary conditions in Fig. 2 are:
$\sigma_{xx}\left(\pm\frac{a}{2}, y\right) = P(y)$; $\sigma_{yy}\left(x, \pm\frac{b}{2}\right) = 0$; $\tau_{xy}\left(\pm\frac{a}{2}, y\right) = 0$; and $\tau_{xy}\left(x, \pm\frac{b}{2}\right) = 0$
where $P(y)$ corresponds the values for uniform and parabolic loading cases. Applying the above boundary conditions, we get

$$C_1 = \frac{-\beta_n}{\alpha_n} C_2 \frac{\sinh \beta_n \frac{a}{2}}{\sinh \alpha_n \frac{a}{2}}$$

$$C_2 = \left(\frac{b}{2n\pi}\right)^2 * \frac{I \alpha_n \sinh \alpha_n \frac{a}{2}}{\left(\beta_n \sinh \beta_n \frac{a}{2} - \alpha_n \cosh \beta_n \frac{a}{2} \sinh \alpha_n \frac{a}{2}\right)}$$

where

$$I = \frac{4}{b} \int_0^{b/2} P(y) \cos \frac{2n\pi}{b} y \mathrm{d}y$$

Once the values of the $C_1$ and $C_2$ are known, these values can be directly substituted in Eqs. (13), (14), and (15) to obtain the expression for the different parameters of interest, namely the three stress components.

## 3 Results and Discussion

This section starts with the problem description, in which the finite analytical model of the problem has been presented, followed by the convergence and validation study and the discussion on the results.

### 3.1 Problem Description

The rectangular plate ($a \times b$) is considered for the analysis in the present investigation with the longer side of the plate as $a = 140$ mm along the $x$-axis and the shorter side of the plate as $b = 20$ mm along the $y$-axis as shown in Fig. 1. Two plates are considered for the investigation, isotropic plate (case-I) and orthotropic plate (case-II). In case-I, the plate used is made of steel of overall thickness 1.72 mm with the mechanical properties given in Table 1. For case-II, the plate is made of T300/934 carbon epoxy plain-woven prepreg. The composite plate consists of 8 plies with woven bidirectional fibers in each ply with $(0)_{4s}$ configuration. Here, (0) indicates a single ply of woven fabric with warp fibers oriented at 0° to the laminate longitudinal axis and the interlaced weft fibers oriented at 90°. The thickness of each ply is 0.215 mm. The overall in case-II is kept 1.72 mm. The mechanical properties of composite plate are given in Table 1.

Two types of loading profiles are considered: one is uniform in-plane tensile pressure as shown in Fig. 1, and the other is parabolic in-plane tensile pressure shown in Fig. 2. In both cases, two types of boundary conditions are considered and are mentioned below.

**B.C.-1**: Edge AB is made fixed, i.e., $u = 0$, $v = 0$, $w = 0$, and $\theta_x = 0$, $\theta_y = 0$, $\theta_z = 0$.

**B.C.-2**: Center node of edge AB is made fixed, i.e., $u = 0$, $v = 0$, $w = 0$, and $\theta_x = 0$, $\theta_y = 0$, $\theta_z = 0$, and all the other nodes along the same edge are set with the conditions as $u = 0$, $w = 0$, and $\theta_z = 0$.

FEM analysis is employed to study the stress distribution in plates at different sections using ABAQUS/Standard and ANSYS. The results have been validated analytically. Solutions of both the problems are presented for the case of plane stress condition. S4R and SHELL181-type mesh elements have been used in ABAQUS/Standard and ANSYS, respectively, to carry out the analysis. The analytical solution

**Table 1** Mechanical properties of isotropic plate and composite plate

| Mechanical property | Isotropic plate | Composite plate (T300/934 carbon epoxy plain-woven prepreg) |
|---|---|---|
| Longitudinal modulus ($E_1 = E_2$) | 200,000 MPa | 57,226 MPa |
| Transverse modulus ($E_3$) | – | 4800 MPa |
| In-plane shear modulus ($G_{12}$) | – | 4481 MPa |
| Out-of-plane shear modulus ($G_{13} = G_{23}$) | – | 4400 MPa |
| In-plane Poisson ratio ($\mu_{12}$) | 0.3 | 0.05 |
| Out-of-plane Poisson ratio ($\mu_{13} = \mu_{23}$) | – | 0.2 |

is performed with B.C.-2 only, and the finite element solution is performed with ABAQUS/Standard and ANSYS software for both B.C.-1 and B.C.-2.

## 3.2 Convergence and Validation Study

For the convergence and validation study, an isotropic steel plate ($2a \times 2b$) with two different loading conditions is taken into consideration. In case-1, parabolic in-plane tensile load is taken as shown in Fig. 3, and in case-2, parabolic in-plane compressive load is taken. The problem is solved using FEM software ABAQUS/Standard, and the results are compared with the available results. The dimensions of the plate are taken as 1 m × 1 m along the length and width, and the thickness is kept 0.01 m. For case-1, a parabolic in-plane tensile edge load of maximum intensity 1 N/m (which is equivalent to $1/0.01 = 100$ N/m$^2$ pressure, i.e., $S = 100$ N/m$^2$) at the center of the parabola is applied on edges AB and CD. The equation of the applied load is given by

$$p_{xx} = S\left(1 - \frac{y^2}{b^2}\right)$$

where

$p_{xx}$ parabolic pressure,
$S$ maximum intensity of the parabolic pressure at center.

For case-2, a compressive in-plane load with the same magnitude in case-1 is applied. The boundary conditions taken in the analysis for both the cases are: $w = 0$ and $\theta_x = 0, \theta_y = 0, \theta_z = 0$ applied to the whole plate, and the in-plane displacements $u$ and $v$ are kept free. The dimensionless normal stresses for case-1 are calculated considering different mesh sizes for the whole plate. The values of the stresses are plotted at two different sections in Fig. 4 for different mesh sizes. It is observed from Fig. 4 that the results with 40 × 40 mesh size are converged for both the sections. So, for the comparison of the present results, 40 × 40 mesh size is considered. The dimensionless normal stress with respect to $y/2b$ along the lines $x/a = 0$ and along the line $x/a = 1$ is plotted in Figs. 5 and 6. It is observed that the FEM results are

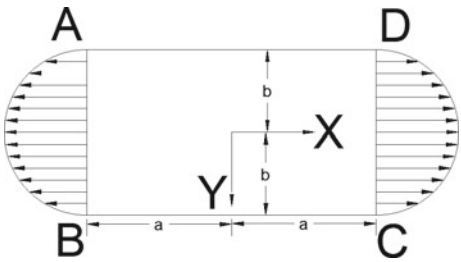


**Fig. 3** Geometry of the plate with tensile in-plane parabolic load

matching well with the available results taken from the equations of Timoshenko and Goodier [12, p. 169].

The results drawn from the present analysis in case-2 for plate shown in Fig. 7 are also compared with the available results of Kumar Panda and Ramachandra [6] and Timoshenko and Goodier [12]. Kumar Panda and Ramachandra [6] have normalized the stress results as $\frac{N_{xx}}{N_{cr}}$, which is same as $\frac{\sigma_{xx}}{S}$ as $\left(1-\frac{y^2}{b^2}\right)$. It is observed that at $x/a = 0.5$, the present results from FEM are matching well with the available results which

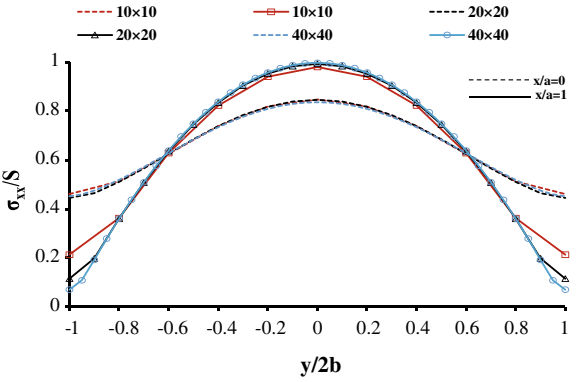


**Fig. 4** Dimensionless normal stress distribution by FEM software

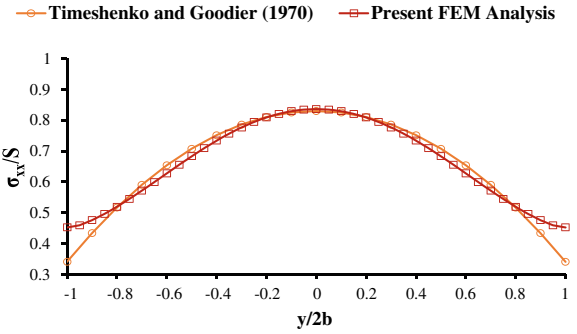


**Fig. 5** Dimensionless normal stress distribution at $x/a = 0$

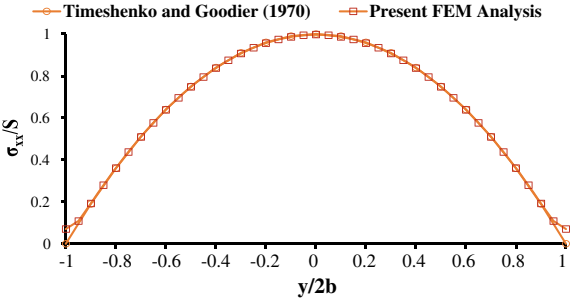


**Fig. 6** Dimensionless normal stress distribution at $x/a = 1$

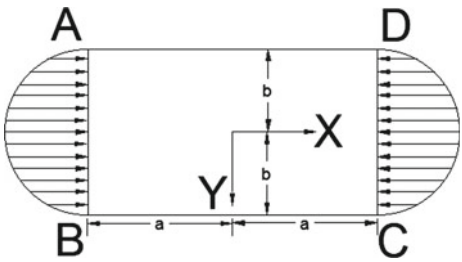


**Fig. 7** Geometry of the plate with compressive in-plane parabolic load

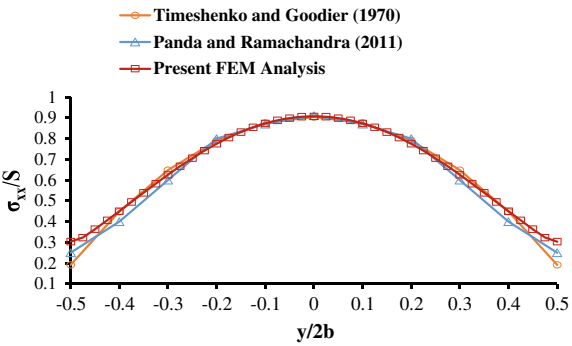


**Fig. 8** Dimensionless normal stress distribution at $x/a = 0.5$

are shown in Fig. 8. However, a deviation is found in the plots while considering Eq. (6) of our analytical solution.

## *3.3 Stress Analysis of the Plate Under Consideration*

After the convergence and validation study, the results based on the effect of the loading profile, the effect of the boundary conditions, and effect of the position on the normal and shear stress distribution are discussed in the following sections. The mesh size for the present problem is taken as 140 × 20. The stresses results are converged at the same mesh size.

### 3.3.1 Effect of the Loading Profile on the Stress Distribution

Since the two loading profiles are chosen, namely uniform in-plane tensile pressure and parabolic in-plane tensile pressure, the effect of the loading profiles at the edge CD is discussed and presented graphically. In this case, the B.C-1 is considered, and the results are obtained from ABAQUS/Standard. The stress ($\sigma_{xx}$) results along CD edge at different points along $y$-axis for uniform load and parabolic load are presented in Figs. 9 and 10 for isotropic and composite plates, respectively. The stress ($\sigma_{xx}$)

results at section 2-2, edge CD, and edge AB for parabolic loading are presented in Figs. 11 and 12 for isotropic and composite plates, respectively.

In Figs. 9 and 10, it is observed that in the case of uniform loading, the normal stresses ($\sigma_{xx}$) at the end where the load is applied are uniform ($\sigma_{xx} = 238.5$ MPa). While in the case of parabolic loading, the stresses along the edge CD are parabolic. It is also observed from Figs. 11 and 12 that the stresses try to become linear (constant) from the rightmost end of the plate where the load is applied toward section 2-2 in accordance with St. Venant's Principle.

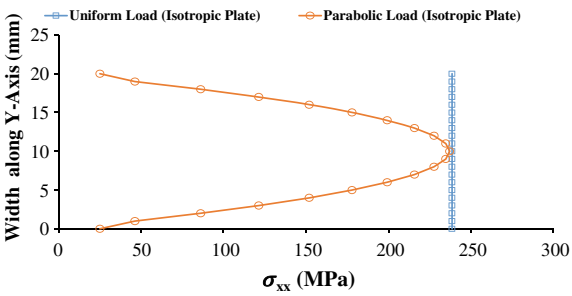


**Fig. 9** Stress at edge CD for isotropic plate

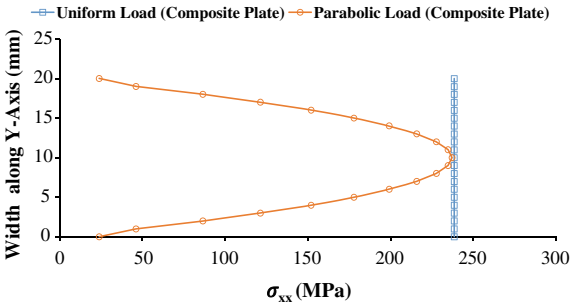


**Fig. 10** Stress at edge CD for composite plate

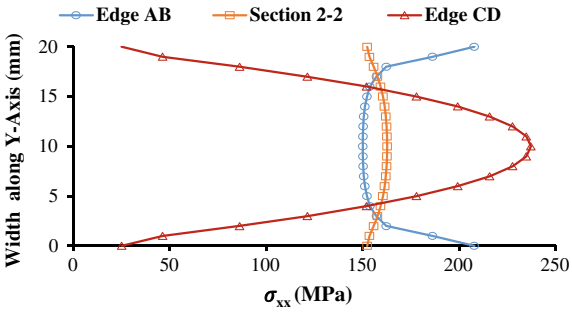


**Fig. 11** Stress in isotropic plate with parabolic load

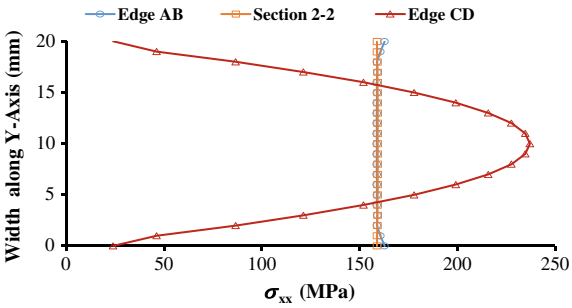


**Fig. 12** Stress in composite plate with parabolic load

### 3.3.2 Effect of the Boundary Conditions on the Stresses

The stresses have been calculated analytically and then validated by finite element analysis using ABAQUS/Standard and ANSYS at different sections of the plate, but our primary emphasis is on the calculation of stresses at the edge AB, i.e., at section 1-1. The results of our present study (stress distribution along the width of the plate) are presented below. The presentation of the results is graphically drawn. In each case below, the results are obtained on the supported edge AB, i.e., along section 1-1 only.

In Fig. 13, it is evident that for the case of isotropic steel plate with B.C-1 and applied uniform pressure, the value of normal stress ($\sigma_{xx}$) at the middle of edge AB (section 1-1), ABAQUS/Standard and ANSYS gives almost the equal values of 224.7 MPa. At the ends of the same edge AB, the normal stresses ($\sigma_{xx}$) considerably vary as $\sigma_{xx} = 311.13$ MPa (ABAQUS/Standard) and $\sigma_{xx} = 358.73$ MPa (ANSYS). This variation of stress is due to the restriction of the movement at edges along $y$-axis. Figure 14 represents the normal stresses ($\sigma_{xx}$) calculated from the analytical solution which are found to be uniform ($\sigma_{xx} = 238.5$ MPa) throughout the whole plate and exactly matches the same plate configuration with the B.C-2, calculated from ABAQUS/Standard and ANSYS.

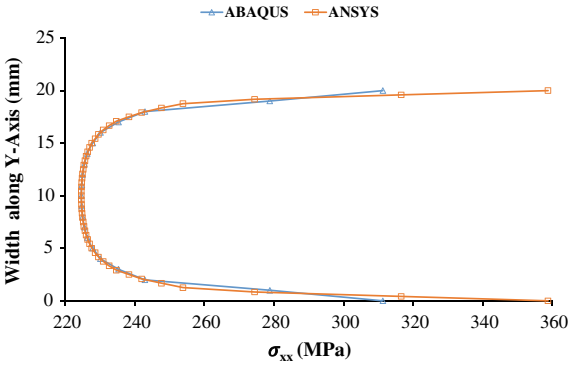


**Fig. 13** Stress in isotropic plate with B.C-1 at edge AB and a uniform tensile load on edge CD

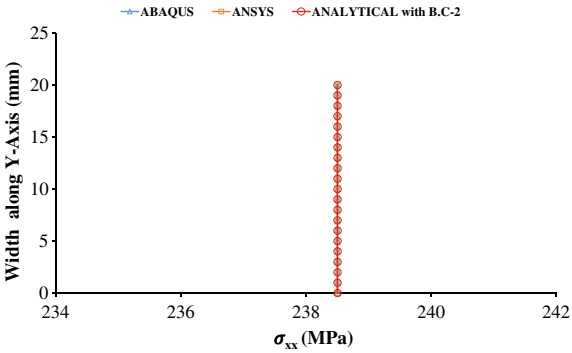


**Fig. 14** Stress in isotropic plate with B.C-2 at edge AB and a uniform tensile load on edge CD

Figures 15 and 16 represent the respective stress distribution along the edge AB of the composite plate with parabolic load for B.C-1 and B.C-2. For a composite plate with B.C-1 and uniform applied pressure as referred in Fig. 17, the maximum normal stress along the width of the plate is obtained at the ends of the edge AB as $\sigma_{xx}$ = 243.856 MPa (ABAQUS/Standard) and $\sigma_{xx}$ = 242.92 MPa (ANSYS). However, in this case, the analytical results match the same plate configuration with B.C-2 as shown in Fig. 18. The same fashion with different values of $\sigma_{xx}$ is obtained for the composite plate with B.C-1 and B.C-2 with parabolic loading as shown in Figs. 19 and 20, respectively. The shear stresses ($\tau_{xy}$) with respect to the width for B.C-1 for both the plates with uniform as well as parabolic loading, as shown in Figs. 21 and 22, have also been analyzed. It is found that the shear stress increases while shifting from the center toward the ends of both the plates. Shear stresses are found out to be higher in case of isotropic plate than the composite plate.

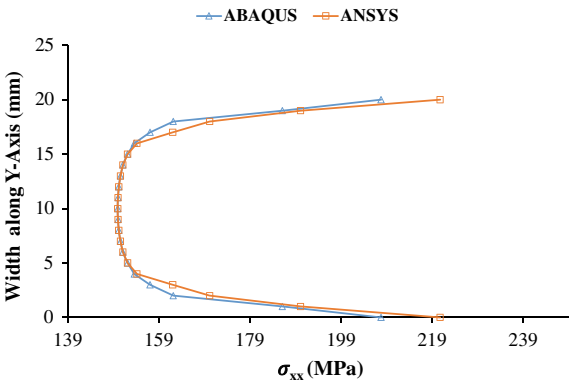


**Fig. 15** Stress in isotropic plate with B.C-1 at edge AB and a parabolic tensile load on edge CD

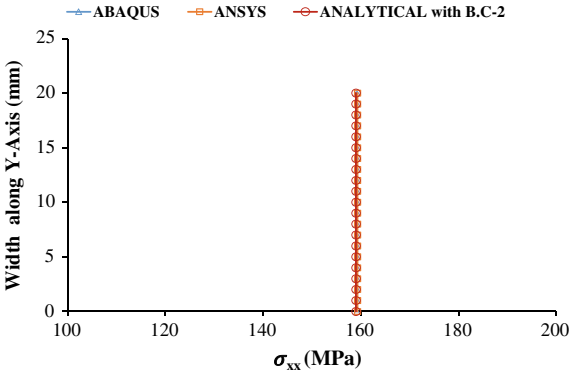


**Fig. 16** Stress in isotropic plate with B.C-2 at edge AB and a parabolic tensile load on edge CD

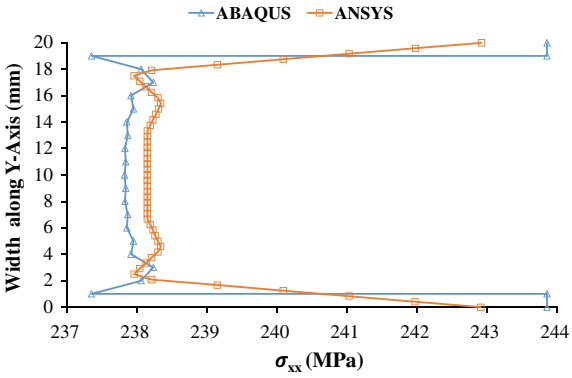


**Fig. 17** Stress in composite plate with B.C-1 at edge AB and uniform tensile load on edge CD

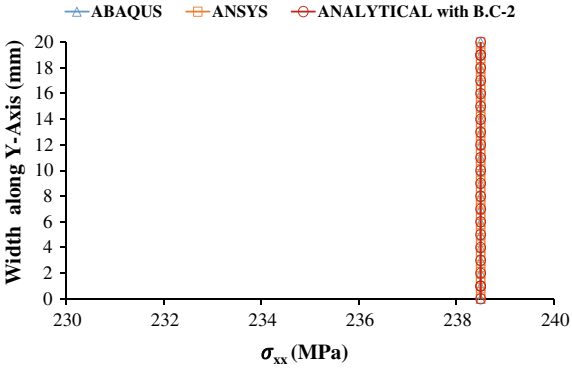


**Fig. 18** Stress in composite plate with B.C-2 at edge AB and uniform tensile load on edge CD

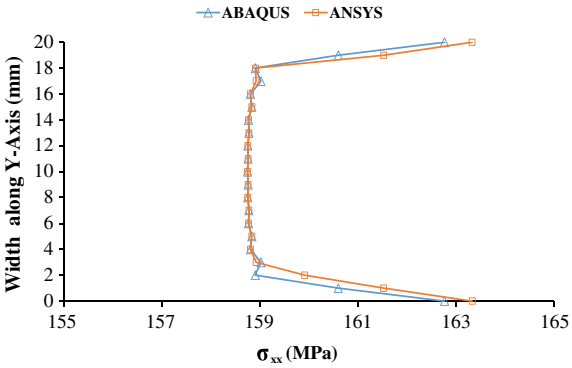


**Fig. 19** Stress in composite plate with B.C-1 at edge AB and parabolic tensile load on edge CD

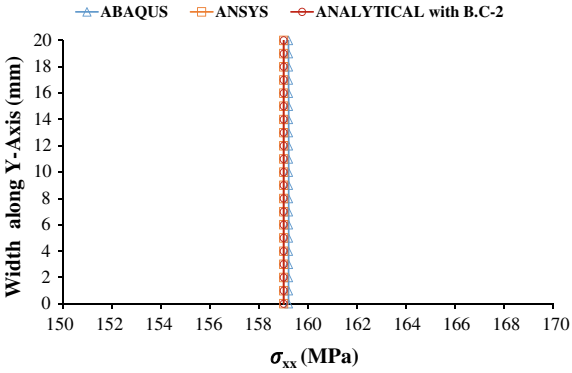


**Fig. 20** Stress in composite plate with B.C-2 at edge AB and parabolic tensile load on edge CD

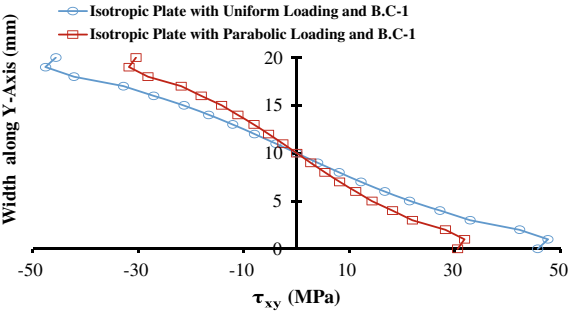


**Fig. 21** Shear stress along *y*-axis in isotropic plate

### 3.3.3 Effect of Position on Stress Distribution

The stresses are also presented at different sections of the plate. The variation in stresses at three positions, viz., at edge AB, section 2-2, and edge CD with B.C-1 is presented in Figs. 23, 24, 25, and 26.

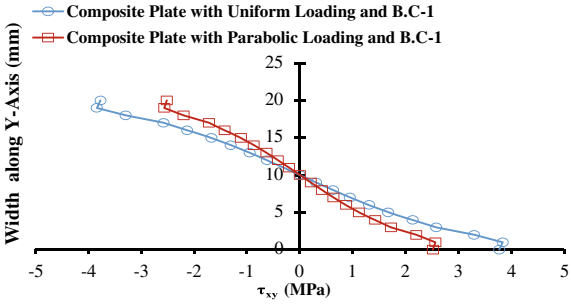


**Fig. 22** Shear stress along *y*-axis in composite plate

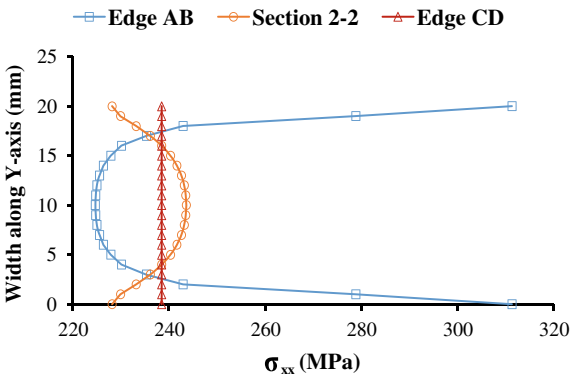


**Fig. 23** Stress variation for the isotropic plate with uniform load

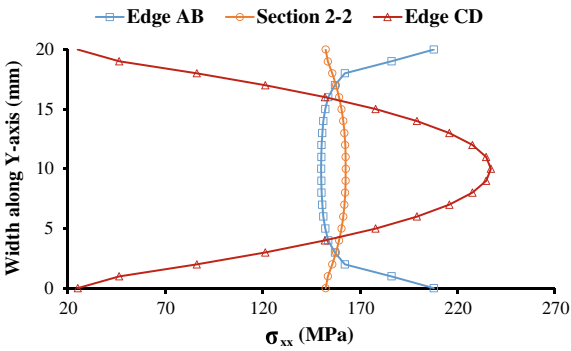


**Fig. 24** Stress variation for isotropic plate with parabolic load

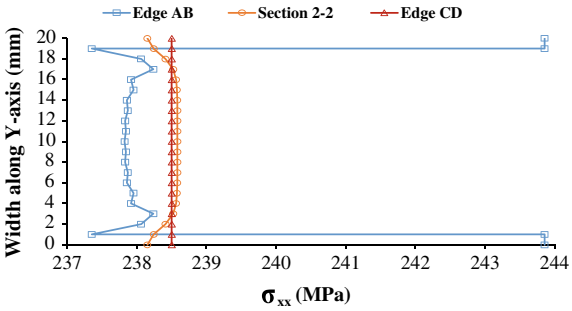


**Fig. 25** Stress variation for the composite plate with uniform load

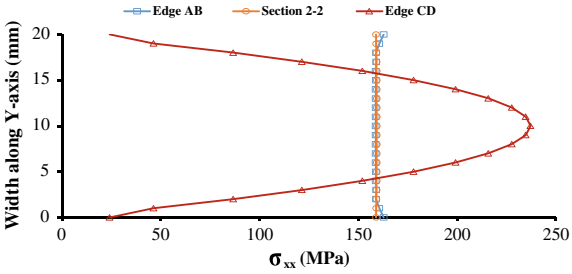


**Fig. 26** Stress variation for the composite plate with parabolic load

## 4 Conclusions

Based on the results obtained from analytical and numerical (FEA) efforts, the following conclusions have been reached:

1. The proposed analytical models can be used to provide predictions for unidirectional laminated composite plates and an isotropic plate subjected to tensile load. These predictions include the normal stress and shear stress calculations at the different sections of the plate.
2. Stresses in the direction of the *x*-axis ($\sigma_{xx}$) by analytical solution come out to be 238.5 MPa in both the plates while applying B.C-2 and uniform tensile pressure. While in the case of parabolic loading, the stresses in the direction of the *x*-axis ($\sigma_{xx}$) by analytical solution come out to be 159 MPa. If the edge AB is kept fixed, the stresses increase near the same edge in both the plates when ANSYS and ABAQUS analyzed the structural component.
3. It has been found out that the shear stress increases along *y*-axis while shifting from the center toward the ends of both the plates while applying B.C-1.

## References


1. Cheuk PT, Tong L (2002) Failure of adhesive bonded composite lap shear joints with embedded precrack. Composit Sci Technol 62(7–8):1079–1095
2. Deb Nath SK (2013) Effects of fiber orientation and material isotropy on the analytical elastic solution of a stiffened orthotropic panel subjected to a combined loading. Adv Mater Sci Eng
3. Hussein E, Alasadi S (2018) Experimental and theoretical stress analysis investigation for composite plate under thermal load. Kufa J Eng 9(1):205–221
4. Kassapoglou C, Bauer G (2010) Composite plates under concentrated load on one edge and uniform load on the opposite edge. Mech Adv Mater Struct 17(3):196–203
5. Khechai A, Tati A, Guettala A (2014) Finite element analysis of stress concentrations and failure criteria in composite plates with circular holes. Front Mech Eng 9(3):281–294
6. Kumar Panda S, Ramachandra LS (2011) Buckling and postbuckling behavior of cross-ply composite plate subjected to nonuniform in-plane loads. J Eng Mech 137(9):589–597
7. Li R, Tian B, Zhong Y (2013) Analytical bending solutions of free orthotropic rectangular thin plates under arbitrary loading. Meccanica 48(10):2497–2510
8. Mantari JL, Oktem AS, Guedes Soares C (2012) A new trigonometric shear deformation theory for isotropic, laminated composite and sandwich plates. Int J Solids Struct 49(1):43–53
9. Nath SKD (2017) Analytical solution of mixed boundary value problems using the displacement potential approach for the case of plane stress and plane strain conditions. Int J Appl Mech Eng 22(2):269–291
10. Patel SN, Sheikh AH (2016) Buckling response of laminated composite stiffened plates subjected to partial in-plane edge loading. Int J Computat Methods Eng Sci Mech 17(5–6):322–338
11. Reddy JN (2003) Mechanics of laminated composite plates and shells: theory and analysis, p 840
12. Timoshenko S, Goodier JN (1970) Theory of elasticity—Timoshenko.Pdf. McGRAW-HILL Education, Newyork
13. Yazdani Sarvestani H, Naghashpour A (2014) Analysis of free edge stresses in composite laminates using higher order theories. Ind J Mater Sci 2014:1–15

# Ductile Fracture Initiation in Braces of Concentrically Braced Frames


**Tamilselvan Nambirajan, Viresh Singh, and P. C. Ashwin Kumar**

**Abstract** Braces in concentrically braced frame system dissipate majority of the seismic energy imparted to the structure through inelastic cyclic axial deformations. During the inelastic cyclic deformations, the braces might initiate fracture prematurely if the selection of the brace geometry is not decided properly. Hence, the main objective of the study is to couple the continuum-level study with micro-mechanical fracture model to decipher the localized mechanism behind the origin of brace fracture initiation phenomenon. Monotonic and cyclic notched bar test results available in the literature have been used to calibrate the numerical model for capturing the inelastic cyclic material response. The calibrated numerical model has then been used to model the braces across a wide range of brace geometries, using which the stress and strain histories for cyclic loading have been evaluated. The evaluated stress and strain histories with the help of micro-mechanical fracture model have been used to capture the ductile fracture initiation of braces. From the obtained results, it has been observed that the slenderness ratio and width to thickness ratio have a strong influence over the initiation of ductile fracture in braces.

**Keywords** Passive devices · Ductile fracture initiation · Slenderness ratio · Stress triaxiality · Equivalent plastic strain · Low cycle fatigue

T. Nambirajan (✉) · P. C. A. Kumar
Indian Institute of Technology, Roorkee, India
e-mail: ntamilselvan@eq.iitr.ac.in

P. C. A. Kumar
e-mail: ashwin.pc@eq.iitr.ac.in

V. Singh
Indian Institute of Technology, Tirupati, India
e-mail: ce17b026@iittp.ac.in



M. Madhavan et al. (eds.), *Proceedings of the Indian Structural Steel Conference 2020 (Vol. 1)*, Lecture Notes in Civil Engineering 318,
https://doi.org/10.1007/978-981-19-9390-9_9

## 1 Introduction

Steel braces are designed as a sacrificial element in a concentrically braced frame (CBF) to dissipate the seismic energy imparted to the structure during earthquakes. Premature fracture in braces has been found to be detrimental to the global performance of the structure during a seismic event [2]. Hence, it is imperative that the inelastic cyclic performance of braces including the fracture phenomenon needs to be studied thoroughly. Till now, many studies [5, 6, 8, 15] have been conducted to capture the inelastic behavior and predict the fracture initiation point of steel braces subjected to reversed cyclic displacements. These studies observed that the high strains and rotations generated at the corners of compressive side, located at the middle of the brace, caused fracture after one to four cycles of local buckling. These high inelastic strains generated in the middle region are due to concentration of tensile elongation in the post-buckling stage. Accurate modeling of braces and capturing the micro-mechanical changes are thus necessary to capture these stress concentration and local buckling effects. Few recent studies have used both micro-mechanics-based method and accurate numerical modeling to predict fracture initiation [5, 6]. Among these studies, the cyclic void growth model (CVGM-extended model of void growth model) by Kanvinde et al. [7] has been found to be most accurate. The parameters like stress triaxiality and equivalent plastic strain incorporated in this model enable to capture complex interactions of stress–strain histories. Thus, the main objective of this study is to correlate the fracture initiation point with the collapse assessment study of steel braces. The corresponding validation of the fracture model and the effects of slenderness ratio and width to thickness ratio of braces on the fracture initiation are evaluated in this study.

## 2 Objective and Scope of Study

The objective of this study is mainly focused on developing numerical model of hollow square steel (HSS) braces and to accurately capture stress–strain histories at maximum stress concentrated point and to apply the principles of CVGM to predict the fracture initiation point. The validation of the process, including the method and the numerical model, is sought through the results obtained from a previous study [5]. The validated numerical model is then utilized to find the influence of slenderness ratio and width to thickness ratio on prediction of fracture initiation point. Six specimens with three HSS braces of same slenderness ratio but varying width to thickness ratio and other three with same width to thickness ratio with varying slenderness ratio have been modeled for this study. The selected HSS brace specimens are as given in Table 1.

**Table 1** Brace details considered in this study

| $B$ (mm) | $t$ (mm) | SR | $B/t$ |
|---|---|---|---|
| SET 1 | | | |
| 203.2 | 9.5 | 37 | 10.8 |
| 203.2 | 15.9 | 39 | 19.9 |
| 177.8 | 3.2 | 42 | 57 |
| SET 2 | | | |
| 355.6 | 22.2 | 22 | 14.2 |
| 76.2 | 4.8 | 102 | |
| 50.8 | 3.2 | 153 | |

## 3 Element Model Description

Steel braces are modeled using S4R (four node quadrilateral shell element) elements in ABAQUS v6.14 (2014). The reduced integration element possesses six degree of freedom per node and three translational and three rotational degrees. Distribution of stress nonlinearity has been estimated by adopting seven integration points along the element thickness. Local buckling and brace fracture (through micro-mechanics-based method) have also been captured using this element. The middle of the brace where plastic hinge is expected is densely meshed, and at location away from the center, the mesh sizes have been gradually increased (Fig. 1a). For the regions in the gusset plate where yielding is expected, fine mesh has been provided (Fig. 1b) to explicitly include the response due to out of plane buckling effect of brace under cyclic loading. Interface nodes have been used to connect the gusset plate with HSS specimens. Since the final failure response desired in this study is the fracture of the brace at the middle, weld detailing between gusset plate and brace has not been considered in the numerical model. The brace numerical model has been provided with fixed (rigid)-end boundary conditions at the ends of the gusset plates. Since the cyclic performance of steel braces highly depends on the dimensions of gusset plate and connections detailing [12], their effects have been accounted in the model to determine the effect of slenderness ratio on prediction of fracture initiation point of HSS braces. The gusset plate for all study specimens have been designed using the balanced design procedure developed by Roeder et al. [12]. The balanced design procedure provides the required brace ductility level through incorporation of inelastic deformation of gusset plate and also takes cares of the yielding hierarchy of braces and gusset plates.

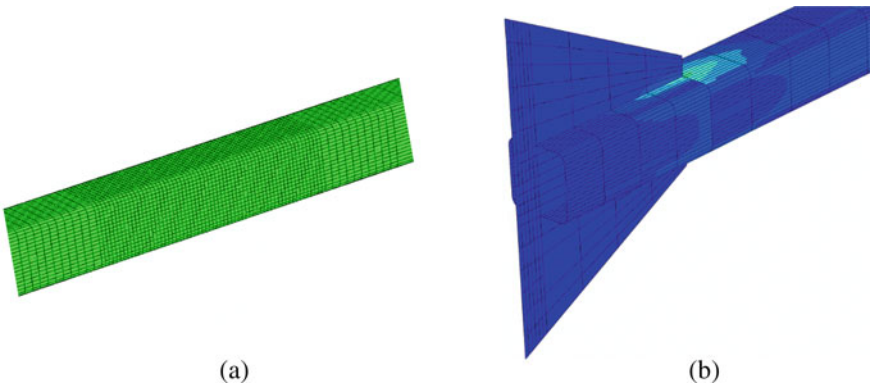


**Fig. 1** Mesh pattern of **a** Brace mid-length and **b** Gusset plate

### *3.1 Material Properties*

The assumption of von-Mises yield criterion has been used to determine the material yielding using the finite element model of steel braces used in this study. This assumptions have been found to be satisfied by most of the metals [4]. The yield surface growth is captured by isotropic hardening model; however, this fails to include (1) the effect of cold working anisotropic behavior and (2) effect of local stress generation due to internal dislocation of atoms along one direction during cyclic loading. Therefore, for exact consideration of (1) all shifts and volume change of yield surface in three-dimensional stress space, (2) to evaluate the functional influence of stress at yield stage on inelastic loading protocol, and (3) the influence of cyclic behavior of metals on loading history, the HSS brace model has been supported with combined hardening material model (both isotropic and kinematic hardening). The definition of the yield surface for a combined hardening material model is given using Eq 1.,

$$f(\sigma_{ij}, k) = \left[\frac{3}{2}(S_{ij} - \alpha_{ij}^{d})(S_{ij} - \alpha_{ij}^{d})\right]^{1/2} - \sigma_{y_0} - k = 0 \tag{1}$$

where $\sigma_{ij}$ represents the stress tensor; $S_{ij}$ represents the back stress tensor that possesses a deviatoric part $\alpha_{ij}^{d}$; and $\sigma_{y0}$ represents the initial yield stress with $k$ as the hardening parameter defining the yield surface size.

The purely kinematic hardening yielding surface function can be obtained by putting $k = 0$ in Eq. (1). On the other hand, by making the deviatoric part as zero, we can get the yielding surface function for pure isotropic hardening. Different inelastic or plastic hardening models [3, 16] can be used to subtract the yield surface shift from the respective stresses. Among them, the Ziegler's kinematic hardening rule [16] has been found to possess the capacity of shifting the yield surface in three-dimensional stress space for the model used in this study. Correspondingly, the nonlinear kinematic hardening component can be divided into two terms: (1) linear

kinematic term conforming with the Ziegler hardening law and (2) to introduce nonlinearity, back stress term is used that can be expressed by the function given in Eq. (2).

$$\alpha_k = C_k \frac{1}{\sigma_0}(\sigma - \alpha)\varepsilon^p - \gamma_k \alpha_k \varepsilon^p \tag{2}$$

where $\sigma^0$ represents the initial yield stress; $\varepsilon^p$ represents the equivalent plastic strain rate; and $C_k$ and $\gamma_k$ represent the initial kinematic hardening modulus and its rate of variation corresponding to the incremental variation of inelastic deformation. The back stress developed is represented by $\alpha$, which is expressed by the function given in Eq. (3),

$$\alpha = \sum_{k=1}^{N} \alpha_k \tag{3}$$

where the term $N$ represents the quantity of back stress used. The effect of hardening and softening of the material has been taken into account by the isotropic hardening component expressed as a function of equivalent plastic strain $\varepsilon^p$ given by Eq. (4),

$$\sigma^0 = \sigma^0(\varepsilon_p) = \overline{\sigma}_0 + Q_\infty(1 - e^{-b\varepsilon_p}) \tag{4}$$

where $\vec{\sigma}_0$ represents the yield stress corresponding to zero plastic strain; $Q_\infty$ represents maximum growth in yield surface size; and $b$ represents the growing rate of yield surface size with plastic strain increment. The present study utilizes the values of yield stress and combined hardening parameters obtained from a previous study [5]. In this previous study, the standard tension coupon test has been used to provide the yield stress value $\sigma_y$. The isotropic and kinematic hardening parameters have been evaluated by using circumferentially large notched cyclic test and small smooth notched monotonic test. The parameters obtained have been compared and refined slightly with the numerical model of coupon notched test. The parameters used for small-scale elements have been then applied to numerical models of large-scale braces, which are then verified with the experimental results. These hardening parameters thus obtained may vary slightly with the dimensions and shape of the brace section used and do not represent a unique value for a particular grade of material. However, in this study, a constant single value of these parameters has been assumed (Table 2), which have been taken directly from [5].

### *3.2 Simulating Global Buckling Behavior*

ANSI/AISC 341-16 [1] provisions corresponding to slenderness ratio and width to thickness ratio have been considered in the selection of brace sizes to be used in this

**Table 2** Calibrated hardening parameters [5]

| Element | $\sigma_y$ (Pa) | $C$ (MPa) | $\gamma$ | $Q_\infty$ (MPa) | $b$ |
|---|---|---|---|---|---|
| Brace corner | 503 | 5861 | 160 | 100 | 5.25 |
| Brace wall | 469 | 2069 | 25 | 69 | 6 |
| Gusset plate | 345 | 3448 | 38 | 118 | 5 |

study. Fracture initiation of braces mainly depends on the strain development at the stage of local and global buckling of braces. Both the stages have to be accurately captured by the numerical model for significant prediction of fracture initiation point. With regard to capturing the initial imperfection and out of straightness effect of brace, an elastic analysis has been carried out to capture the mode shapes. Scaled eigenvector of the first mode (global buckling of brace) has been used to perturb the brace while being loaded axially. To simulate the brace buckling, the initial perturbation magnitude has been provided as 0.001 $L$, where $L$ is the brace length. For capturing of local buckling, no extra perturbation has been provided.

### *3.3 Loading Protocol*

The study of Fell [5] on the loading protocol revealed that the ground motions of far-field earthquakes are highly critical for assessing the performance of steel braces in comparison with the ground motions representing near field earthquakes. Thus in this study, the standard cyclic loading protocol provided by the guidelines of ATC-24 (1992) provisions has been followed. Loading protocol provided by ATC-24 (1992) has been obtained from the investigation of nonlinear dynamic analyses of many ductile moment frame systems. For accurate capturing of braced frame response, the selected loading protocol has been modified according to the suggestions provided by Krawlinker et al. [9, 10]. The modified loading protocol is as given in Fig. 2.

The initial elastic steps in the loading protocol are followed by four cycles representing the onset of brace buckling initiation under compressive loading cycle. As a whole, nine steps of loading cycle have been provided with the maximum deformation of braces corresponding to five percent story drift [14]. The story drift has been related to the axial deformation of steel braces by Eq. (5) as,

$$\Delta_a = \left(\cos^2 45^\circ\right) L_B \theta \tag{5}$$

where $\Delta_a$ represents the brace axial deformation, $L_B$ is brace effective length, and $\theta$ is the brace inter-story drift angle. Equation (5) is only valid for chevron type of brace configuration with an inclination of brace to the horizontal as 45°. The effect of (1) influence of flexural deformation of beams and columns and (2) panel zone deformation on the cyclic behavior of steel braces has not been accounted in this study.

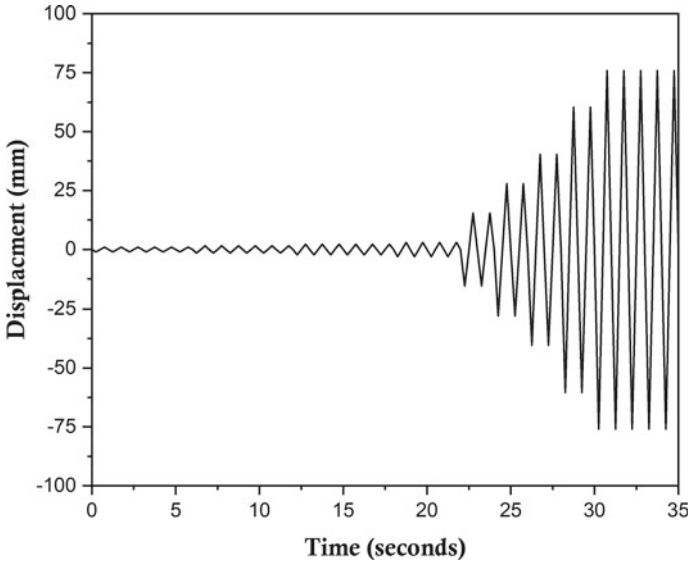


**Fig. 2** Modified standard loading protocol used in this study

### *3.4 Selection of Brace Section*

The upper limiting value of slenderness ratio (SR) for steel brace used in SCBFs according to the ANSI/AISC 341-16 [1] provision is 200. Hence, three SRs 22, 102, and 153 have been chosen for this study. To determine the effect of slenderness ratio (SR), three SRs of 22, 102, and 153 with fixed *B/t* ratio of 14.2 have been selected for this study. To evaluate the effect of width to thickness ratio on fracture initiation of braces, three *B/t* ratios 10, 19.9, and 57 for fixed SR near to 40 have been selected in this study. The limiting value of width to thickness ratio provided by ANSI/AISC 341-16 [1] is as given in Eq. 6,

$$\left(\frac{B}{t}\right)_{\max} = 0.65\sqrt{\left(\frac{E}{F_y}\right)} \tag{6}$$

The section width is considered as ($B$-3$t$) in the calculation of width to thickness ratio. The upper limit of *B/t* for steel with Young's modulus of 200 GPa and fy (yield stress of steel brace wall) of 486 MPa is found to be 13.2. The *B/t* ratio for some sections has been intentionally selected beyond the limit to evaluate the effect of local buckling and different SR on fracture initiation of braces. The *B/t* ratios (within limit) 10, (on border of upper limit) 14.2, and (far beyond the upper limit) 57 with same SR nearly to 40 have been selected to evaluate the effect of limiting width to thickness ratio on fracture initiation of braces. The selected brace section with its properties is given in Table 1. All sections have a constant length of 2946 mm. This

constant length system assumption in this study fits well with the practical design cases, where the fixed brace length exists due to constant floor height of the building.

## 4 Cyclic Void Growth Model

Traditional fracture model have very limited accuracy on fracture initiation prediction of steel subjected to cyclic loading. These model works on the assumption that the crack already exists in the material. Moreover, extensive inelastic yielding that occurs under cyclic loading brings extra inaccuracy to the traditional fracture models. Low cycle fatigue of steel braces under reversed axial displacements makes the steel braces more vulnerable to earthquakes. To reduce the vulnerability, the fracture initiation of steel braces has to be evaluated accurately under cyclic type of loading. Rice and Tracey [13] using the micro-mechanism of void growth and coalescence provided an empirical relation to predict fracture initiation of steel under monotonic loading. Kanvinde et al. [7] extended the void growth model (VGM) for the application of VGM under cyclic loading and termed it as cyclic void growth model (CVGM).

When the monotonic degradation capacity is less than the demand cyclic growth, fracture in steel braces is initiated, and the above phenomenon is given as

$$\exp\left(-\lambda_{\mathrm{CVGM}}\varepsilon_p\right)\eta_{\mathrm{monotonic}} \leq \sum_{\text{Tensile - cycles}} \int_{\varepsilon_1}^{\varepsilon_2} \exp(|1.5T|)\mathrm{d}\varepsilon_t - \sum_{\text{compressive - cycles}} \int_{\varepsilon_1}^{\varepsilon_2} \exp(|1.5T|)\mathrm{d}\varepsilon_c \quad (7)$$

The CVGM depends on two factors: (1) stress triaxiality ($T$) and (2) equivalent plastic strain ($\varepsilon_p$). The tensile cycles are represented by positive $T$, and compressive cycles are represented by negative $T$. The intersection of critical void growth index (VGI) (degradation of monotonic capacity) and cyclic VGI (demand cyclic growth) decides the fracture initiation point as shown in Fig. 3.

## 5 Analysis Results

The influence of slenderness ratio and width to thickness ratio (within, near, and beyond the upper limit) on prediction of fracture initiation is evaluated from the post processed results of validated numerical model and discussed in the following sections.

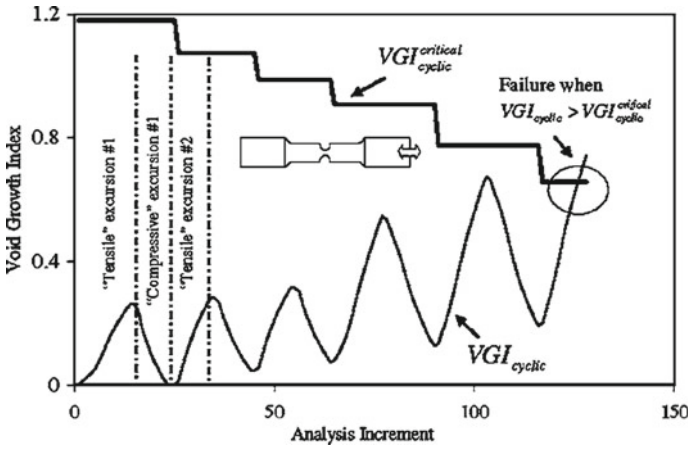


**Fig. 3** Graphical representation of prediction of fracture initiation in steels

## *5.1 Validation of Numerical Model*

The numerical model developed in this study is first validated with the results of experiment conducted by Fell [5]. Geometry, loading protocol, and material properties have been kept exactly same as the experiment conducted.

The validated hysteresis response of steel brace is shown in Fig. 4a. Even though there is a slight variation in the hysteresis, the critical stages, i.e., the onset of global and local buckling, matched accurately. The last loading cycles of numerical model continue even after the fracture of brace because no ductile damage model has been fed into the numerical model. Local buckling of steel brace with high width to thickness and low SR is shown in Fig. 4b. The stress and strain histories obtained from the maximum stressed point in the numerical model have been processed with CVGM substituting the constants $\lambda_{\text{CVGM}} = 0.17$ and $\eta_{\text{monotonic}} = 5.98$ taken from Fell [5] in Eq. (7) to predict the fracture initiation point. The obtained fracture initiation point has then been compared with the results of Fell [5]. It is found that the numerical model predicts the fracture initiation one loading step before the results of Fell [5] as shown in Fig. 5a. This prior prediction of fracture initiation is mainly due to the effect of mesh sensitivity and localized behaviour in the plastic hinge region developed in the middle of the brace section. Figure 5b shows the monotonic degradation capacity, cyclic demand growth obtained from the numerical model used, and the fracture initiation point with the respect to loading time step.

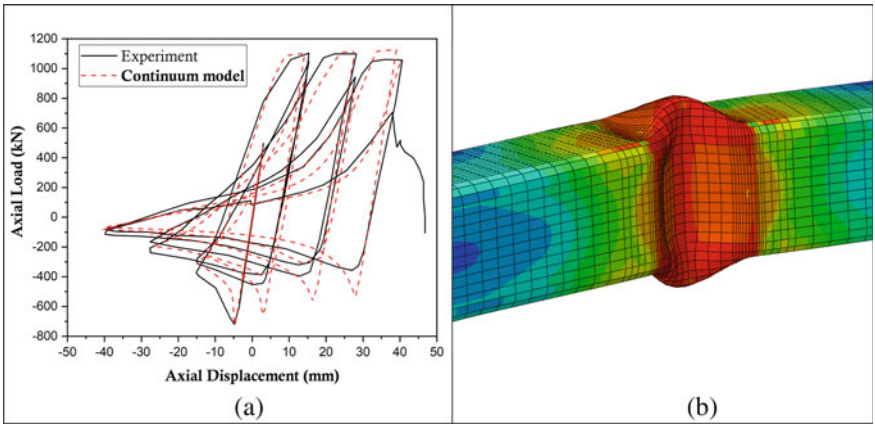


**Fig. 4** **a** Comparison of hysteresis response. **b** Local buckling at half-length plastic hinge region

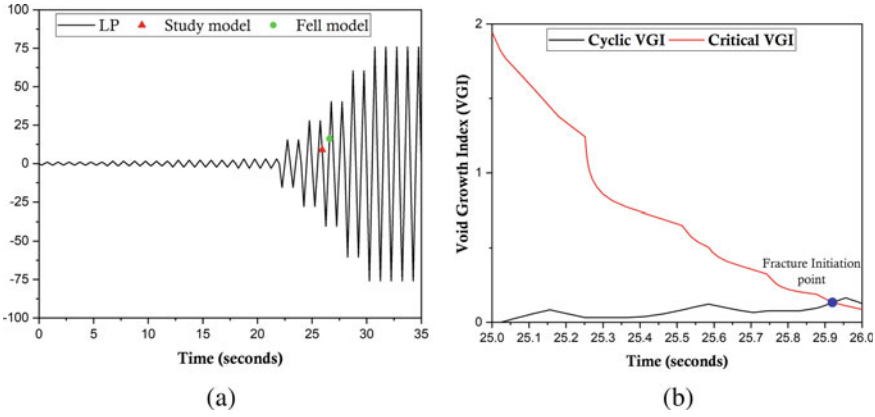


**Fig. 5** **a** Comparison of fracture initiation prediction. **b** Graphical representation of intersection of critical VGI and cyclic VGI obtained from continuum model

## 5.2 *Influence of Width to Thickness Ratio on Fracture Initiation Prediction*

Set 1 given in Table 1 consists of sections with varying width to thickness ratio selected in an order of being within the upper limit, near to the upper limit, and far beyond the upper limit and having almost equal SR. The fracture predicted in all the three sections is as given in Fig. 6a. It can be observed that the upper limit provided by ANSI/AISC 341-16 [1] delays the fracture initiation in steel braces. *B/t* of 19.9 and 10 fractured nearly at same drift cycle. The fracture initiation for *B/t* of 57 is observed in the tensile loading cycle at a drift of 2%, and for other two *B/t* ratio of

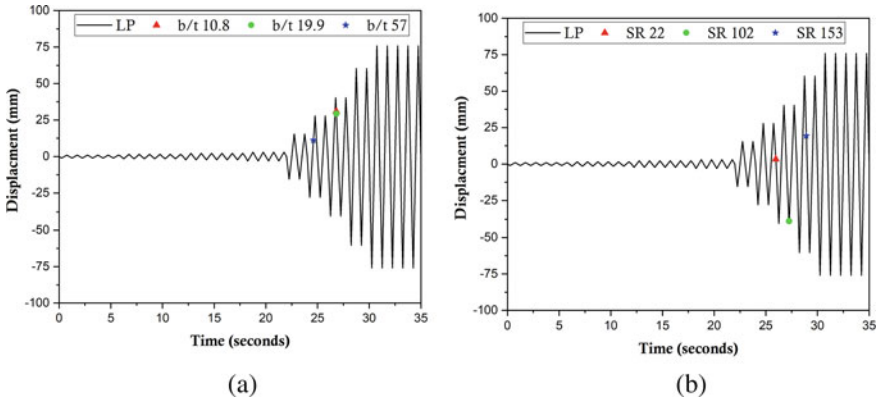


**Fig. 6** Variation in fracture initiation for **a** different width to thickness ratio **b** different slenderness ratio

10 and 19.9, it is observed in the tensile unloading cycle at a drift of 3%. The early fracture of brace with larger B/t ratio is in line with past research results.

### *5.3 Influence of Slenderness Ratio on Fracture Initiation Prediction*

Set 2 given in Table 1 consists of section with varying slenderness ratio of 22, 102, and 153 with constant *B/t* of 14.2. The influence of slenderness ratio on prediction of fracture initiation is shown in Fig. 6b. It is observed that increase in SR delays the fracture initiation in steel braces. Also low SR with high *B/t* ratio resulted in early fracture initiation in steel braces which matches previous experimental result trends. High SR range initiates fracture at a drift of 4%, whereas the low slenderness initiates fracture at 2%, respectively.

## 6 Conclusions

The numerical model validated with the experiment conducted by Fell [5] has been used to validate the CVGM model, and it has then been used to evaluate the influence of SR and *B/t* ratio on prediction of fracture initiation in steel braces. The following conclusions can be drawn from this study:

1. The sensitivity of mesh size, localized effects, and ombined hardening parameters play a major role in accurately predicting the fracture initiation in brace.

2. Numerical model accurately captures the instances of local and global buckling in the braces and in combination with CVGM method predicts the instances of fracture initiation with great accuracy.
3. Early fracture of braces with low slenderness ratio and high *B/t* ratio and delayed fracture in cases of higher slenderness ratio have been captured accurately by the micro-mechanics-based method employed in this study.

## References

1. ANSI/AISC 341-16 (2016) Seismic provisions for structural steel buildings. American Institute of Steel Construction, Chicago, IL, p 60601
2. Bruneau M, Uang CM, Whittaker A (2011) Ductile design of steel structures, vol 389. McGraw-Hill, New York
3. Chaboche JL (1986) Time-independent constitutive theories for cyclic plasticity. Int J Plast 2(2):149–188
4. Chen WF (1994) Constitutive equations for engineering materials. Vol. 2 plasticity and modeling. Elsevier
5. Fell BV (2008) Large-scale testing and simulation of earthquake-induced ultra-low cycle fatigue in bracing members subjected to cyclic inelastic buckling. University of California, Davis
6. Haddad M (2015) Concentric tubular steel braces subjected to seismic loading: finite element modeling. J Constr Steel Res 104:155–166
7. Kanvinde AM, Deierlein GG (2007) Cyclic void growth model to assess ductile fracture initiation in structural steels due to ultra low cycle fatigue. J Eng Mech 133(6):701–712
8. Kumar PA, Sahoo DR (2018) Fracture ductility of hollow circular and square steel braces under cyclic loading. Thin-Walled Struct 130:347–361
9. Krawinkler H (1992) Guidelines for cyclic seismic testing of components of steel structures, vol. 24. Applied Technology Council
10. Krawinkler H, Gupta A, Medina R, Luco N (2000) Loading histories for seismic performance testing of SMRF components and assemblies. SAC Joint Venture, Report no. SAC/BD-00/10. Richmond, CA
11. Manual AU (2014) Abaqus theory guide. Version 6.14. Dassault Systemes Simulia Corp, USA
12. Roeder CW, Lumpkin EJ, Lehman DE (2011) A balanced design procedure for special concentrically braced frame connections. J Constr Steel Res 67(11):1760–1772
13. Rice JR, Tracey DM (1969) On the ductile enlargement of voids in triaxial stress fields∗. J Mech Phys Solids 17(3):201–217
14. Sabelli R, Roeder CW, Hajjar JF (2013) Seismic design of steel special concentrically braced frame systems. NEHRP, Gaithersburg, USA, Seismic Design Technical Brief, 8
15. Shaback B, Brown T (2003) Behaviour of square hollow structural steel braces with end connections under reversed cyclic axial loading. Can J Civ Eng 30(4):745–753
16. Ziegler H (1959) A modification of Prager's hardening rule. Q Appl Math 17(1):55–65

# Damping Characteristic Identification of a Three-Storey Aluminium Frame Using Vibration Response Data


**T. S. Akhila and K. P. Saji**

**Abstract** Monitoring large structural systems for assessing the potential degradation of structural properties by identifying the dynamic characteristics is needed for assuring safety of the system. Measurements made at a single point in the structure can be used to detect, locate and quantify damage. In this work, a method for determining the damping characteristics of a structure from the measured modal characteristics is presented. This method uses the dynamic properties obtained from the vibration response of the structure. A three-storied aluminium base frame and 8 damage-induced frames were experimentally studied by horizontal shake table. Damage was induced on the base frame by reducing the cross section of the column. The experimental observations on frequency, displacement and acceleration were used to obtain the dynamic characteristics of the structure. By comparing both theoretical and experimental results of the storey-level deflection, damping ratio of the structure is identified.

**Keywords** Dynamic · Natural frequency · Shake table · Vibration response · Harmonic · Excitation

T. S. Akhila (✉) · K. P. Saji
Department of Civil Engineering, Government College of Engineering Kannur, Kannur, Kerala, India
e-mail: akhilats95@gmail.com

K. P. Saji
e-mail: kpsaji@gcek.ac.in



M. Madhavan et al. (eds.), *Proceedings of the Indian Structural Steel Conference 2020 (Vol. 1)*, Lecture Notes in Civil Engineering 318,
https://doi.org/10.1007/978-981-19-9390-9_10

## 1 Introduction

India witnessed several devastating earthquakes over the past century. Earthquake occurred in urban area causes the most severe damages to human lives and structures. Also, human ambition results in construction of taller infrastructures. Structural Health Monitoring (SHM) is an important methodology that evaluates the health of civil infrastructure system by assessing its level of deterioration and remaining service life. The effective monitoring of systems has highlighted its importance by the appearance of wide spread failures in structures.

This monitoring should be able to identify structural problems at an early stage and guarantee the public safety. The monitoring systems have the potential to verify the effectiveness of repair procedures and to reduce operational maintenance costs by identifying problems at an early stage. For important civil structures such as nuclear power plants, dams, bridges, high-rise buildings and power utilities, SHM is found to be highly essential.

Any structural damage occurred in a structure can be identified from the reduction in stiffness and increase in damping of the structure. A new mathematical expression is proposed by Bajri and Høgsberg [1] which reconstructs the damping matrix from the complex valued eigenvectors and eigenvalues of a non-classically damped structure with an assumed mass distribution. This expression solved the limitation that the representation of the viscous damping matrix from modal parameter is only applicable to structures with light damping [1]. Arora [2] proposed a new structural damping identification method using normal frequency response function (NFRF). It is a direct method. In this method, normal FRFs are estimated from the complex FRFs, which are obtained experimentally of the structure. NFRF s is used to identify general structural damping. This method is applicable to simpler structures [1].

The Rayleigh damping model, when used in combination with assumptions commonly used in engineering practice, typically leads to overestimations of mean peak floor accelerations, peak floor velocities and inter-storey drift ratio demands with respect to those computed using the damping model inferred from the recorded data [3]. A study conducted by Macro et al. [4] on the philosophy and performance of different approaches for the determination of linear viscous damping shows that inverse receptance matrix method is the best-performing method. This study includes a closed-form solution, identification methods based on inverting the matrix of receptances, energy expressions developed from single-frequency excitation and responses as well as first-order perturbation methods. The closed-form solution restricts the damping matrix to real solutions. The inverse receptance matrix method places no such restriction on the systems mass, damping and stiffness matrices [4]. Damping matrix updating method proposed by Modak et al. [5] insulates the process of damping matrix updating from that of mass and stiffness matrix updating. Hence, damping matrix identification can be performed satisfactorily in case of incomplete data [5]. Study of time-domain structural damping identification shows that there will be significant changes in the damping mechanism with time, due to changing environmental conditions in the service life of the structure. Hence, among time invariant

Rayleigh damping, time-variant Rayleigh damping and modal damping, the time-variant modal damping is utilized for the long-term structural health monitoring [6].

Damage in a structure leads to the reduction in stiffness of the structure and increase in the damping characteristics of the same. In most of the methods used for damage assessment, damping ratio is taken as an assumed value depending on the material. In this study, a method for identifying the damping ratio of an aluminium frame from the vibration response data obtained from shake table test is presented.

## 2 Damping Ratio Identification Method

For a damped structural system subjected to forced vibration, the equation for displacement of each floor is given by,

$$X_i(t) = M^{-1/2} P r_i(t), \;\; i = 1, 2, 3 \tag{1}$$

where $r_i(t) = \frac{f_i}{\omega_{di}} e^{\xi \omega_i t} \sin \omega_{di} t$

$$f_i = P^T M^{-1/2} f(t)$$

where $f(t) =$ force vector. Force corresponding to 2 mm displacement in the base is calculated using MATLAB code.

$P$ is the matrix obtained by assembling the eigenvectors of three modes.

$\omega_d =$ damped natural frequency, $\xi =$ damping ratio.

The value obtained from the equation is in time domain, and the experimental results are in frequency domain. Hence to compare the analytical result with the experimental value either the time domain needs to converted into frequency domain (using Fourier transform) or frequency domain is to be converted into time domain (using inverse Fourier transform). The damping value, for which the difference between experimental and analytical results is a minimum, is taken as the damping ratio of the frame.

## 3 Experimental Programme and Results

### *3.1 Horizontal Shake Table Apparatus*

The shake table is an equipment to simulate the vibratory support motions, with known frequency and amplitude of vibrations. The experimental setup is as shown in Fig. 1

**Fig. 1** Experimental setup

## *3.2 Specifications*

| | | |
|---|---|---|
| 1. | Motion | Horizontal |
| 2. | Load capacity | 30 kg |
| 3. | Operating Frequency | 0–25 Hz |
| 4. | Frequency control | ± 5% |
| 5. | Amplitude | 0–10 mm |
| 6. | Resolution | 1 mm |
| 7. | Table size | 400 × 400 mm |
| 8. | Rotating table diameter | 390 mm |

### 3.2.1 Three Storied Aluminium Base Frame

The aim of this experimental programme is to study the structural characteristics of the aluminium frame with and without damage and also to identify the damping characteristics and damage occurred in the structure. The frame is three-storied aluminium frame. With density 2.7 g/cm$^3$ and Young's modulus 69 GPa, the dimensions are shown in Fig. 2.

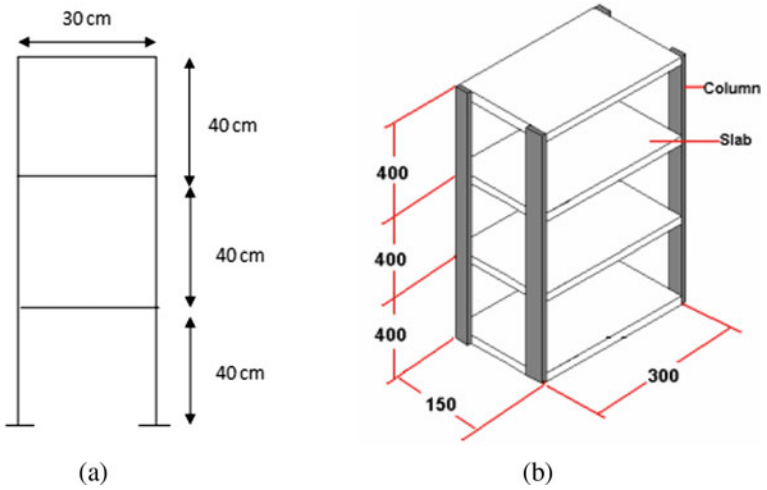


**Fig. 2** Dimensions of the aluminium frame. **a** Elevation, **b** 3D view

From the data given, the mass and stiffness matrix of the base frame are obtained as shown below.

$$[M] = \begin{bmatrix} 1.789 & 0 & 0 \\ 0 & 1.789 & 0 \\ 0 & 0 & 1.62 \end{bmatrix} \text{kg}, \quad [K] = \begin{bmatrix} 5820 & -2910 & 0 \\ -2910 & 5820 & -2910 \\ 0 & -2910 & 2910 \end{bmatrix} \text{N/m} \quad (2)$$

### 3.2.2 Damage-Induced Model

After studying the characteristics of the base frame, experiment was conducted on the frame with induced damage. The damage is induced in one column in the position as shown in Fig. 3. The details of considered damage patterns are listed in Table 1. The damage ID for each specimen is built with a general form of $D_x$ T $F_1$ $F_2$ $F_3$. $D_x$ represents number of damaged specimen, $T$ represents thickness of the damage-induced column, and F indicates the width of damage-induced column in each floor ($F_1$—first floor, $F_2$—second floor, $F_3$—third floor).

The study was carried out by conducting shake table test on the frame before and after inducing damage. Firstly, the base frame is subjected to external excitation using shake table. Frequency was increased from zero with an increment of 0.5 Hz with time interval of 1 min. The response of the frame is recorded as displacement frequency data for the first, second and third natural frequencies. The test is repeated by replacing one column with the damaged one. The results are given in Table 2.

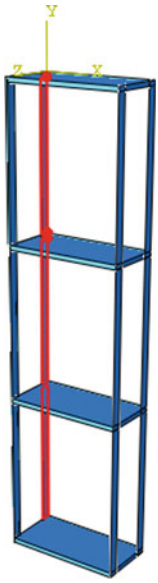


**Fig. 3** Damage-induced model

Damping Ratio Identification

Here, the time-domain analytical result is converted into frequency domain by taking Fourier transform of Eq. (1) using MATLAB code. The result shows that the first natural frequency is 2.343 Hz, and maximum displacement is 75.85 mm. From the experiment, the maximum displacement is obtained as 75.6 mm at frequency of 2.46 Hz. The results are comparable. This procedure is repeated for different values of damping ratio from zero to two. The damping ratio corresponding to the value for which the difference between experimental and analytical results is minimum is taken as the damping ratio of the frame. For the given frame, the Fourier transform result for damping ratio 0.0015 is as shown in Fig. 4. The maximum displacement is obtained as 76 mm for frequency 2.46 Hz. Hence, the damping ratio is taken as 0.0015.

Similarly for each frame, the procedure is repeated using the natural frequency value obtained from the experiments. The damping ratio of all damage condition is identified by trial and error method. The obtained results are given in Table 3.

**Table 1** Details of damage pattern

| Damage ID | Location | Width (mm) | Thickness (mm) |
|---|---|---|---|
| $D_1T1.5F_112.5F_225F_325$ | Floor 1 | 12.5 | 1.5 |
| | Floor 2 | 25 | 1.5 |
| | Floor 3 | 25 | 1.5 |
| $D_2T1.5F_125F_225F_312.5$ | Floor 1 | 25 | 1.5 |
| | Floor 2 | 25 | 1.5 |
| | Floor 3 | 12.5 | 1.5 |
| $D_3T1.5F_125F_212.5F_325$ | Floor 1 | 25 | 1.5 |
| | Floor 2 | 12.5 | 1.5 |
| | Floor 3 | 25 | 1.5 |
| $D_4T1.5F_112.5F_212.5F_325$ | Floor 1 | 12.5 | 1.5 |
| | Floor 2 | 12.5 | 1.5 |
| | Floor 3 | 25 | 1.5 |
| $D_5T1.5F_125F_212.5F_312.5$ | Floor 1 | 25 | 1.5 |
| | Floor 2 | 12.5 | 1.5 |
| | Floor 3 | 12.5 | 1.5 |
| $D_6T3F_112.5F_225F_325$ | Floor 1 | 12.5 | 3 |
| | Floor 2 | 25 | 3 |
| | Floor 3 | 25 | 3 |
| $D_7T3F_125F_225F_312.5$ | Floor 1 | 25 | 3 |
| | Floor 2 | 25 | 3 |
| | Floor 3 | 12.5 | 3 |
| $D_8T3F_125F_212.5F_325$ | Floor 1 | 25 | 3 |
| | Floor2 | 12.5 | 3 |
| | Floor 3 | 25 | 3 |

**Table 2** Experimental observations

| Mode | 1 | | | 2 | | | 3 | | |
|---|---|---|---|---|---|---|---|---|---|
| Floor | 1 | 2 | 3 | 1 | 2 | 3 | 1 | 2 | 3 |
| $UDT3F_125F_225F_325$ | | | | | | | | | |
| Frequency (Hz) | 2.46 | | | 5.9 | | | 7.33 | | |
| Mode shape (mm) | 34.51 | 54.81 | 75.60 | − 3.99 | − 0.755 | 3.64 | − 31.75 | 2.06 | − 26.65 |
| $D_1T1.5F_112.5F_225F_325$ | | | | | | | | | |
| Frequency (Hz) | 2.017 | | | 5.24 | | | 6.45 | | |
| Mode shape (mm) | 117.75 | 177.11 | 125.08 | − 3.44 | − 0.456 | 3.89 | − 22.36 | 15.7 | − 31.29 |

(continued)

**Table 2** (continued)

| Mode | 1 | | | 2 | | | 3 | | |
|---|---|---|---|---|---|---|---|---|---|
| $D_2T1.5F_125F_225F_312.5$ | | | | | | | | | |
| Frequency (Hz) | 2.165 | | | 4.9 | | | 6.398 | | |
| Mode shape (mm) | 99.99 | 85.76 | 141.82 | − 2.77 | 0 | 2.65 | − 30.36 | 14.47 | − 26.95 |
| $D_3T1.5F_125F_212.5F_325$ | | | | | | | | | |
| Frequency (Hz) | 2.017 | | | 4.84 | | | 6.58 | | |
| Mode shape (mm) | 108.12 | 138.31 | 99.63 | − 2.36 | − 3.86 | 4.13 | − 30.54 | 2.04 | − 35.43 |
| $D_4T1.5F_112.5F_212.5F_325$ | | | | | | | | | |
| Frequency (Hz) | 2.017 | | | 4.53 | | | 6.29 | | |
| Mode shape(mm) | 70.88 | 114.01 | 94.46 | − 4.25 | − 0.145 | 3.83 | − 29.56 | 2.12 | − 36.94 |
| D5T1.5F125F212.5F312.5 | | | | | | | | | |
| Frequency (Hz) | 2.067 | | | 4.85 | | | 6.13 | | |
| Mode shape (mm) | 84.811 | 92.48 | 157.29 | − 2.84 | 0 | 3.22 | − 30.58 | 4.12 | − 36.97 |
| $D_6T3F_112.5F_225F_325$ | | | | | | | | | |
| Frequency (Hz) | 2.313 | | | 5.61 | | | 6.92 | | |
| Mode shape (mm) | 95.73 | 146.28 | 119.69 | − 1.98 | 0 | 2.10 | − 26.57 | 12.15 | − 25.32 |
| $D_7T3F_125F_225F_312.5$ | | | | | | | | | |
| Frequency (Hz) | 2.51 | | | 5.78 | | | 7.23 | | |
| Mode shape (mm) | 39.58 | 94.50 | 111.04 | − 3.27 | − 0.25 | 3.59 | − 26.89 | 15.82 | 32.58 |
| $D_8T3F_125F_212.5F_325$ | | | | | | | | | |
| Frequency (Hz) | 2.214 | | | 5.61 | | | 7.31 | | |
| Mode shape (mm) | 97.99 | 36.9 | 140.44 | − 3.25 | − 0.64 | 3.67 | − 30.81 | 2.18 | − 25.97 |

## 4 Conclusion

In the present study, damping ratio identification of a three-storied aluminium frame was done. Eight conditions of damage were induced on the base frame by replacing the columns of the frame with reduced cross section. The damping ratio of each

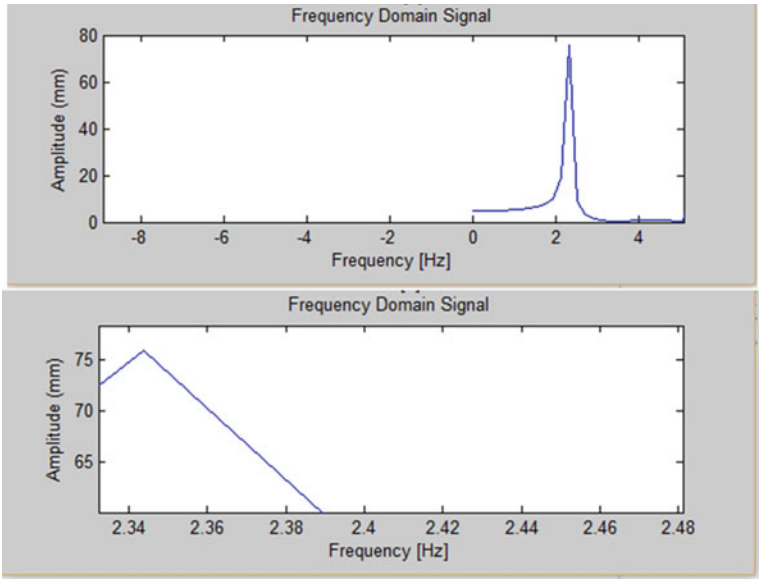


**Fig. 4** Fourier transform—amplitude frequency data

**Table 3** Calculated damping ratio of damaged frame

| Frame | Damping ratio |
|---|---|
| UDT3$F_1$25$F_2$25$F_3$25 | 0.0015 |
| $D_1$T1.5$F_1$12.5$F_2$25$F_3$25 | 0.0025 |
| $D_2$T1.5$F_1$25$F_2$25$F_3$12.5 | 0.0027 |
| $D_3$T1.5$F_1$25$F_2$12.5$F_3$25 | 0.0017 |
| $D_4$T1.5$F_1$12.5$F_2$12.5$F_3$25 | 0.0025 |
| $D_5$T1.5$F_1$25$F_2$12.5$F_3$12.5 | 0.0025 |
| $D_6$T3$F_1$12.5$F_2$25$F_3$25 | 0.0015 |
| $D_7$T3$F_1$25$F_2$25$F_3$12.5 | 0.0017 |
| $D_8$T3$F_1$25$F_2$12.5$F_3$25 | 0.0015 |

frame is calculated with sufficient accuracy. Identification of dynamic characteristics is possible when the frequency–displacement data of the undamaged and damaged structures is available.

Any structural change occurred in a structure results in change in dynamic characteristics such as natural frequency, stiffness and damping. Increase in damping indicates the occurrence of damage. When the thickness of 1 of 4 columns in a floor changes from 3 to 1.5 mm, the damping ratio reduced about 10%. When thickness and cross section of 1 of the 4 column of a floor are reduced, the reduction in stiffness of the floor is about 25%.

## References

1. Bajri A, Høgsberg J (2018) Identification of damping and complex modes in structural vibrations. J Sound Vibr (431):367–389
2. Arora V (2014) Structural damping identification method using normal FRFS. Int J Solids Struct 51:133–143
3. Cruz C, Miranda E (2017) Evaluation of the Rayleigh damping model for building. Eng Struct 138:324–336
4. Prandina M, Mottershead JE, Bonisoli E (2009) An assessment of damping identification method. J Sound Vibr 323:662–676
5. Modak SV, Pradhan S (2012) A method for damping matrix identification using frequency response data. Mech Syst Signal Process 33:69–82
6. Li XY, Law SS (2009) Identification of structural damping in time domain. J Sound Vibr 328:71–84

# Preliminary Stage OpenSEES Simulation of the Collapse of Plasco Tower in Fire


**Ramakanth Domada, Tejeswar Yarlagadda, Liming Jiang, and Asif Usmani**

**Abstract** The Plasco tower, built in 1962, was the tallest building with 17 storeys in Iran at the time of its construction and was considered as an iconic high-rise dominating the Tehran skyline. In January 2017, a fire started on the 10th floor which eventually led to its collapse and caused many deaths and injuries. The building was used as a residential and commercial building, with a major shopping centre on its ground floor, a restaurant on its upper floor, and several clothing workshops. It was a steel structure with built-up sections fabricated using standard European channels and angles without any fire protection. The tower had four strong core columns to transfer the load from primary beams to the foundation and relatively closely spaced interconnected columns along the periphery. This exterior framing is designed to be sufficiently strong to resist all lateral loads on the tower, thereby allowing the interior of the tower to be simply framed for gravity loads. For modelling, OpenSEES fibre-based sections and displacement-based beam-column elements are used. The thermal properties and elevated temperature mechanical properties are as recommended in the Eurocodes. As documented, the fire started at the 10th floor and then involved stories 11–14 as a result of a horizontally and vertically spreading fire. The thermo-mechanical analyses are performed assuming no variation of temperature across the thin sections. Based on the best available information, the floor in plan is believed to be structurally divided into nine individual blocks by two centrally running primary truss beams in both directions. This leads to an understanding that each block is structurally isolated except at the peripheral beams and central core columns, however, if the reinforced concrete floor slab is composite with steel beams of the floor system, this will not be the case. This paper presents the structural response of the tower over a single floor as a preliminary analysis.

**Keywords** Plasco tower · Steel building · OpenSEES for fire · Thermo-mechanical analysis · Fire-induced collapse

R. Domada (✉) · T. Yarlagadda · L. Jiang · A. Usmani
The Hong Kong Polytechnic University, Hung Hom, Hong Kong
e-mail: ramakanth.domada@connect.polyu.hk



M. Madhavan et al. (eds.), *Proceedings of the Indian Structural Steel Conference 2020 (Vol. 1)*, Lecture Notes in Civil Engineering 318,
https://doi.org/10.1007/978-981-19-9390-9_11

## 1 Introduction

The Plasco tower was a 16-storey high-rise steel structure dominating the Tehran skyline after its construction during 1960s. Until its collapse, it was the tallest building in Tehran, the capital city of Iran. On 19th January 2017, a fire accident occurred on the 10th floor which eventually resulted in the collapse of the building after four hours. The accident resulted in loss of many lives and billions of dollars in economic losses. It was reported that the fire was caused by a short circuit in the electric system. For decades, it remained famous for being the tallest high-rise structure in Iran and dominated Tehran's skyline. Because of that, the fire and its consequence drew lot of attention.

The Plasco building was designed as braced steel frame where many light columns are placed peripherally and sturdier columns at the core of the tube. The light exterior columns are intended to resist the lateral loads, whereas the central strong columns to safely transfer the gravity load of each floor to the foundation. The Plasco building was never designed to withstand fire. There was no sprinkler system, no fire alarm system and no fire protection on the steel frame whatsoever. Unlike the WTC towers, only limited structural drawings are available and most of the information obtained was by post-collapse inspection. Therefore, there hasn't been much research which focused on what exactly caused the collapse.

The overall aim of this paper is to carry out preliminary structural analysis of Plasco tower under fire during initial stage of fire using the Open System for Earthquake Engineering Simulation (OpenSEES) which is a software framework for simulating the seismic response of structural and geotechnical systems. The fire module in OpenSEES has been developed by Jiang et al. [2–4] and his students over past 10 years at the University of Edinburgh, UK and this work is being carried forward by his current students at PolyU.

Accidents offer structural engineers an opportunity to learn and improve. The Broadgate Phase 8 fire which occurred in 1999 is a modern steel fast track building which incorporated steel deck/concrete floor construction [6]. There was no collapse, but the examination of damage provided an opportunity to consider the validity of design codes which had been developed from small-scale fire test data. This eventually led BRE and erstwhile British Steel to carry out six full-scale fire tests on an eight-storey steel frame composite structure at the BRE Large Building Test Facility at Cardington (Bedfordshire, UK). The collapse of the WTC Buildings in 2001 following a terrorist attack also offered valuable lessons about adequate preparedness with fire safety and structural stability in fire. Initial attempts to analyze the WTC collapse indicated that, although there had been considerable progress, there were too many counterintuitive and subtle phenomena in the thermo-mechanical response of large frame structures to fires which were not well-understood, even by experts in the profession. Therefore, multiple explanations for WTC collapse surfaced. Kotsovinos

and Usmani [5], Usmani et al. [9] and his research team at the University of Edinburgh found that the WTC towers had an unusual vulnerability to large fires. The team was able to produce a credible scenario of collapse, which did not depend upon any gross assumptions about the fire or failure of connections or even structural damage. A clean stability failure mechanism was evident from a simple computational analysis. Not only this, the analysis was entirely consistent with the fundamental principles developed previously during the simulation of Cardington tests led by Usmani et al. [7].

Greater understanding and knowledge of structural frame performance in fire can only be gained by rigorous analysis, just as it is customary to determine the response of structures to earthquake or wind loading.

## 2 Plasco Tower Description

The Plasco tower, which was located at a densely populated area, was initially intended to be a light commercial centre but eventually transformed into a major clothing distribution centre at the time of its collapse. The building had never been designed according to fire safety regulations; and the change of usage of the building had significantly increased the fire load. It had no sprinkler system, alarm and not even an emergency evacuation plan. The electrical wiring was outdated. The recommendations of Tehran Fire Safety Department (TFSD) were completely ignored.

The building had two separate structural blocks—the main tower which is 17-storeyed standing besides a five-storeyed building. The five storey building has 105 m long in along the North–South direction and has approximately 3200 $m^2$ floor area. The 17-storey building was 30 × 30 m in plan with two floors below the ground level with height of the ground floor as 6.3 m and other floors being 3.8 m tall.

The light columns were put along the periphery to resist lateral loads like wind and seismic, and the central bulky columns to safely transfer the gravity loads to the foundation. The peripheral columns had been connected via radial foundation. The four central core columns had been raised up to ground level using strong pedestals. The perimeter columns on the south side had not been continued to the foundation level, in order to give free access to give adjoining five-storey part of the structure.

As the structural drawings and other information, had been lost during the fire accident, many field trips were needed to establish the dimensions of all structural members.

All the structural members were welded built-up sections, meaning that they had been made by adding some light steel profiles such as U- and L-shaped profiles. The flooring system contained a concrete slab with a thickness of 120 mm, which was rigidly connected to a series of ceiling trusses placed over both perpendicular directions. The details about the structure have been discussed in detail by Behnam [1].

## 2.1 Fire Description

It was reported by TFSD that the fire started on the 10th storey of the building at northwest corner. Then the fire had travelled to the 11th floor and eventually involved 11–14 storeys.

In this work, the behaviour of the structure during the initial stages of fire spread has been considered. From the visual evidence, it has been observed that fire which started at 7:50 am in a single block had spread to many other blocks in the same floor by 8:10 am. The more information about the fire accident and post-inspection is available in Tehran municipality report and Plasco national report.

Four fire loads for the analysis are considered which involve one, three and four blocks and the entire floor as shown in Fig. 1.

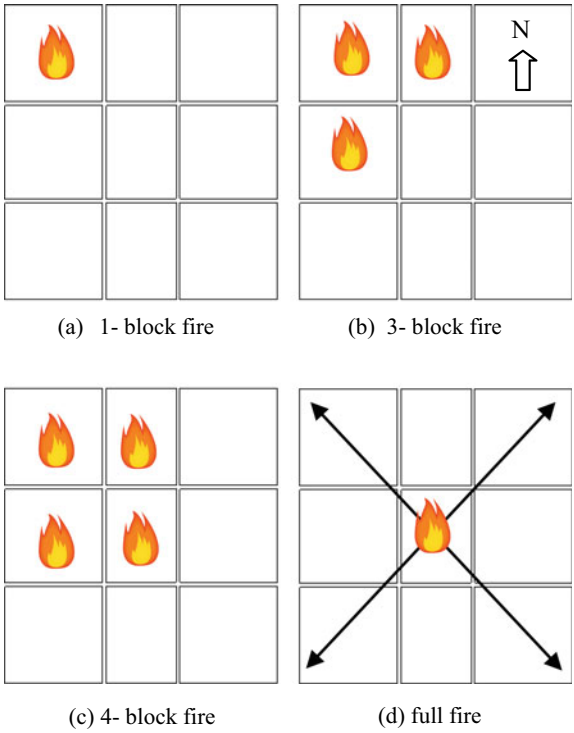


**Fig. 1** Considered fire load scenarios with block-wise extents (secondary beams are hidden in these representative pictures)

## 3 Model Description

The GiD preprocessor has been used to model the Plasco tower. To reduce the size of the problem, only the top 10 floors of the 17 floors have been considered in the FE model.

The Plasco tower floor plan can be seen as nine individual blocks separated by two primary beams running in both the directions. The only structural continuity among the blocks was due to the ceiling trusses spanning in both NS and EW directions.

Trusses had been provided along the EW directions and Vierendeel beams along the NS direction. The plan looks almost square except that the distance in the NS direction is slightly longer than the EW directions (Fig. 2).

The fibre section approach has been followed in the modelling of sections. Each fibre section object is composed of fibres with thermal properties, with each fibre containing a uniaxial thermal material, an area and a location ($y$, $z$). The *fibreSec-Thermal* object class enables the user to apply thermal load at 2, 5 or 9 points across the depth of the section. Since the thickness of member sections used in the Plasco tower were very thin, it has been assumed that there is no temperature variation across the depth of sections; in other words, the temperature gradient is taken as zero.

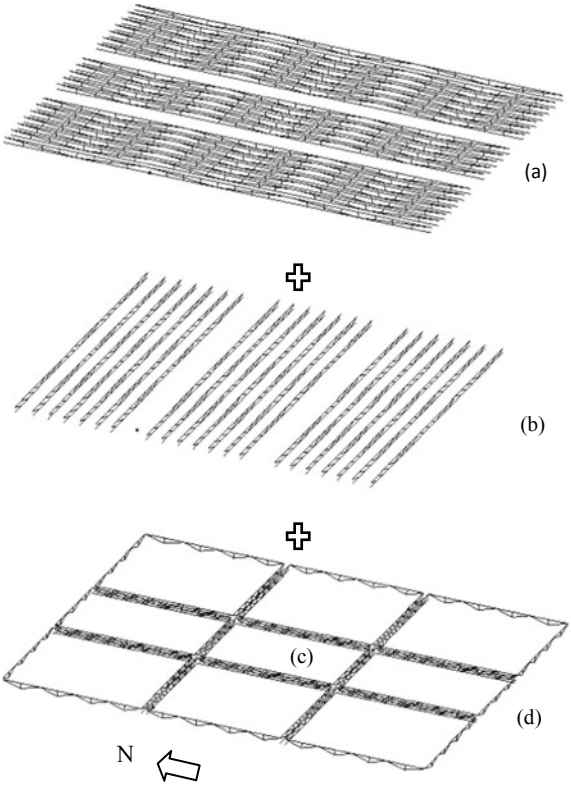


**Fig. 2** Plasco tower floor assembly is made of **a** and **b** Secondary truss beams running in both directions, **c** Primary beams, **d** Edge beams

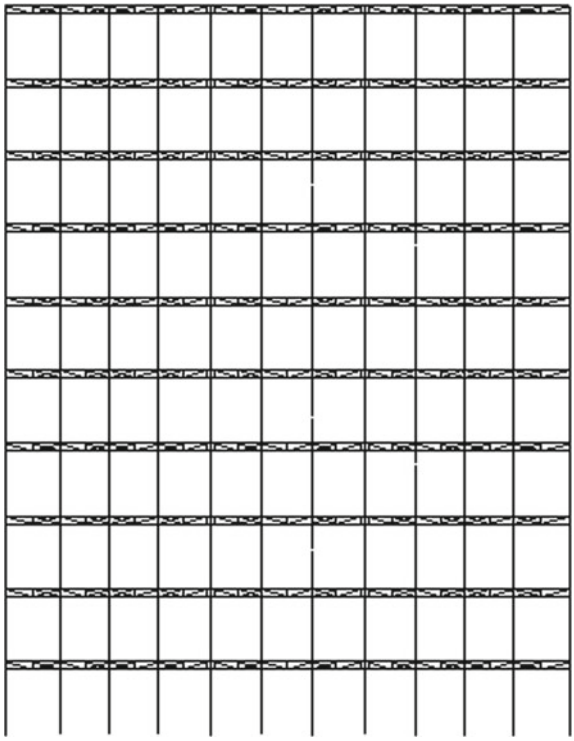

**Fig. 3** Finite element model of Plasco tower visualized in OpenSEES GiD preprocessor

A UDL of 20 kN/m representing dead load, live load and super imposed dead load has been applied on all top cords of ceiling trusses. The element type of *dispBeamColumnThermal* has been used in this analysis which is a modification of existing *dispBeamColumn* element to accommodate thermal properties (Fig. 3).

## 4 Analysis Parameters

The following settings have been used in OpenSEES analysis. The dead load has been applied in 10 load increments whereas temperature load in 200 steps, i.e. 4 °C in each load increment.

| Dead load and thermo-mechanical | |
|---|---|
| `system` | `UmfPack` |
| `numbered` | `Plain` |
| `constraints` | `Plain` |
| `integrator` | `LoadControl` |

(continued)

(continued)

| Dead load and thermo-mechanical | |
|---|---|
| `test` | `NormDispIncr` |
| `algorithm` | `Newton` |
| `analysis` | `Static` |

Element sizes varying from 100 to 300 mm are used for meshing the truss members and 750 mm for columns. The fully meshed OpenSEES model has 199,410 elements with 172,270 nodes.

### *4.1 Computational Information*

The analyses have been performed on a Windows machine with processor Intel® Xeon® W-2155 @3.30 GHz (base speed) equipped with 64 GB RAM.

| | |
|---|---|
| Analysis time | 2.5 h |
| RAM usage | 30 GB |
| Clock speed | 3.30 GHz (81% of maximum overclock speed of 4.1 GHz) |
| OpenSEES.exe output | 7.8 GB |
| GiD postprocessor | 22.6 GB of cached RAM |
| Post-processing time | 0.67 h |

## 5 Results

Observations have been made at the following locations in the floor and locations as shown in Fig. 4.

Ce1, Ce2 represent locations on the less stiff perimeter columns and C1, C2 are for stiffer columns which support primary beams. Beam mid-point deflections under fire have been observed at the locations A, B, C and D. Points A and B are on beams with equal length but they support different secondary trusses. C and D are on interior beams.

As the fire accident happened on the 10th floor, the fire load has been applied to the 11th floor. The analyses have been carried out to simulate the behaviour of the structure under fire during the first 20 min. The fire which broke out in the north-west corner block of the 10th floor had spread to blocks within 20 min before spreading to the 11th floor. The extent of fire during this period is not known, hence three different fire load scenarios have been created to represent the initial stage fire as shown in Fig. 1. A fourth scenario with fire load on the entire floor which is used to represent the worst case.

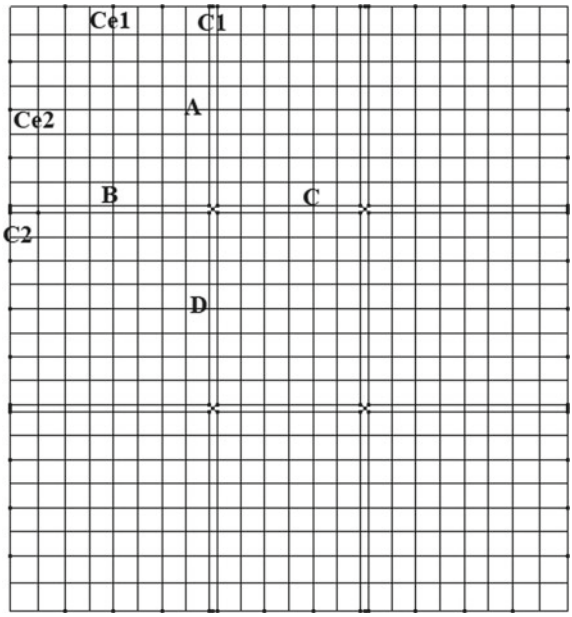


**Fig. 4** Points of observation in OpenSEES model (plan)

Figure 5 shows the floor deformations under the fire load scenarios b and c (see Fig. 1).

In the EW direction, the lengths of primary beams longer in comparison with the NS direction, hence the deflections in beams along the EW direction are higher.

In the blocks under fire, the in-plane deformation near the edge is not uniform because of presence of alternate perimeter columns. Because of that, the grid of secondary beams in the top view appeared like waves passing in both the directions.

Figure 6 depicts the interaction of expanding floor with stiff columns and less stiff perimeter columns.

The results in Fig. 7 show push-out deformations of columns C1, Ce1, C2 and Ce2 on 11th under the four considered fire scenarios.

The results in Fig. 8 show the beam deflections in primary beams at locations A, B, C, D under the four considered fire scenarios.

The plot in Fig. 9 highlights results of the analysis carried out assuming three floor fire on north side of the structure. The two graphs show (a) the in-floor deformations in case of three floor fire (b) column outwards deformations.

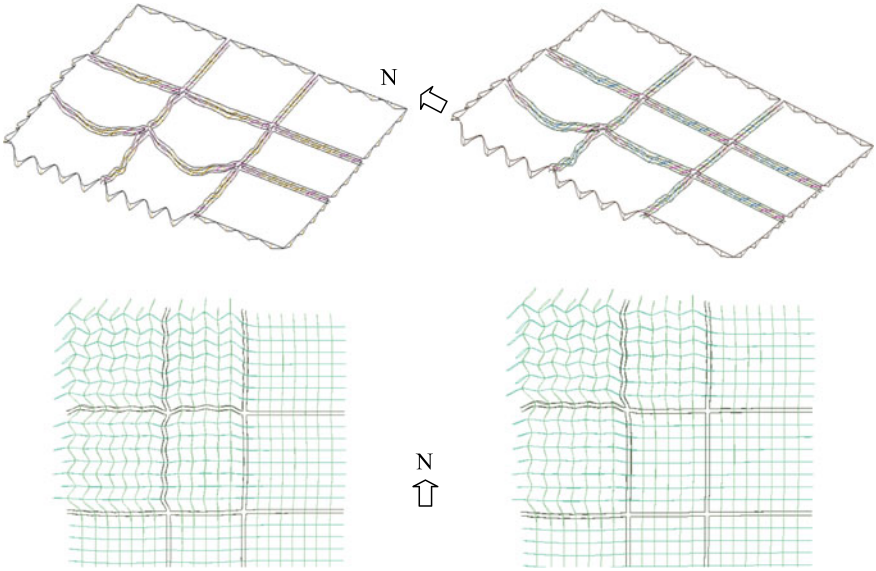


**Fig. 5** Floor deflections under the 3-block and 4-block fire scenarios in perspective (secondary beams hides) and in the plan view

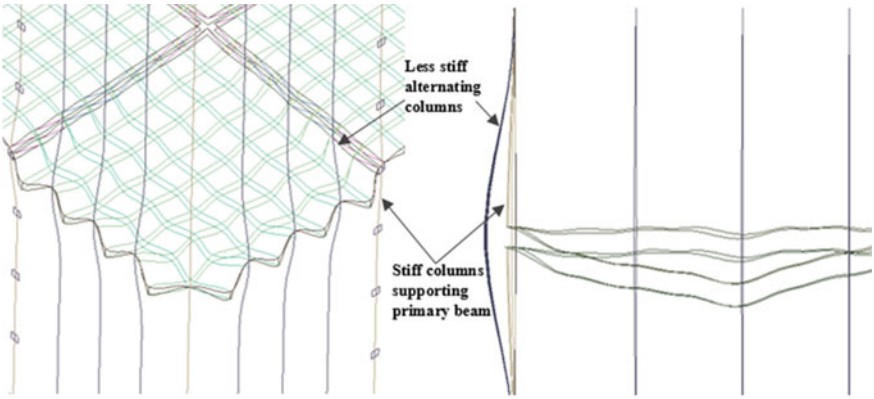


**Fig. 6** Visualization of columns getting pushed by the expanding floor

The development of compressive forces in the top chord members of primary beam trusses at locations A and B during the 1-block fire and 4-block fire scenarios are shown in Fig. 10. As location 'B' is on the beam whose supporting column is relatively stiffer, higher compressive forces are observed in the beam because of the higher lateral restraint. The extent of fire is also a factor influencing the forces, because lateral displacement restraints are higher in the 1-block fire than the 4-block fire.

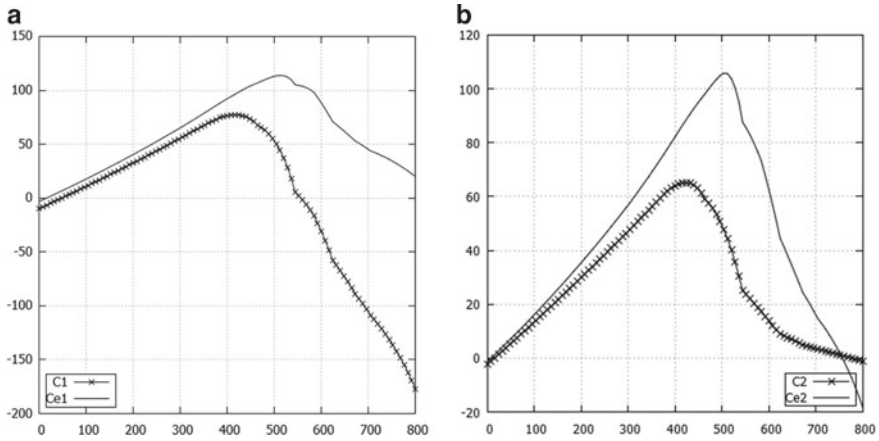


**Fig. 7** Temperature versus horizontal displacement plot for column **a** C1, Ce1 and **b** C2, Ce2

## 6 Conclusions

(a) The fire zone involving 3 or 4 blocks of the plan is enough to cause a similar magnitude of floor deflections as caused by the full floor fire.
(b) The behaviour of the structure is very sensitive to fire load in the core region.
(c) The ceiling trusses are slightly longer along the NS than the EW direction, hence the horizontal displacement of perimeter columns because of thermal expansion of floor is higher in NS direction.
(d) When three blocks are under fire, the relative lateral column deflections are highest along the EW direction. See Fig. 10a. After 700 °C, the difference between C2 and Ce2 plots is greater in comparison with C1 and Ce1.
(e) The secondary truss and Vierendeel beams in both directions are restrained by perimeter columns support in an alternating fashion, i.e. every second secondary beam is restrained. This causes uneven lateral deflection of edge beams. The edge beams which are supporting walls on east and west faces cannot be seen a stable support system.

## 7 Further Research

(a) Fire effects on the columns will be considered
(b) Diaphragm action of the slab will be included
(c) Analyses for later stage of the fire will be done
(d) Realistic fire scenario will be taken.

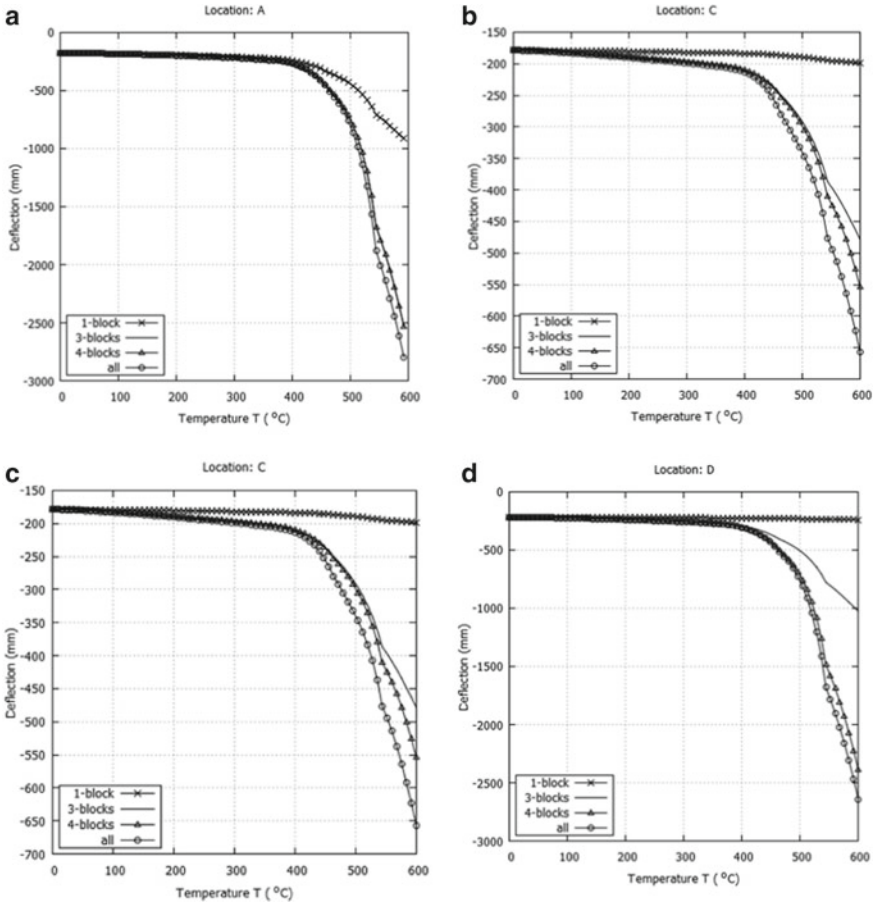


**Fig. 8** Comparison of mid-point displacements in beams A, B, C and D under the four fire zone extents

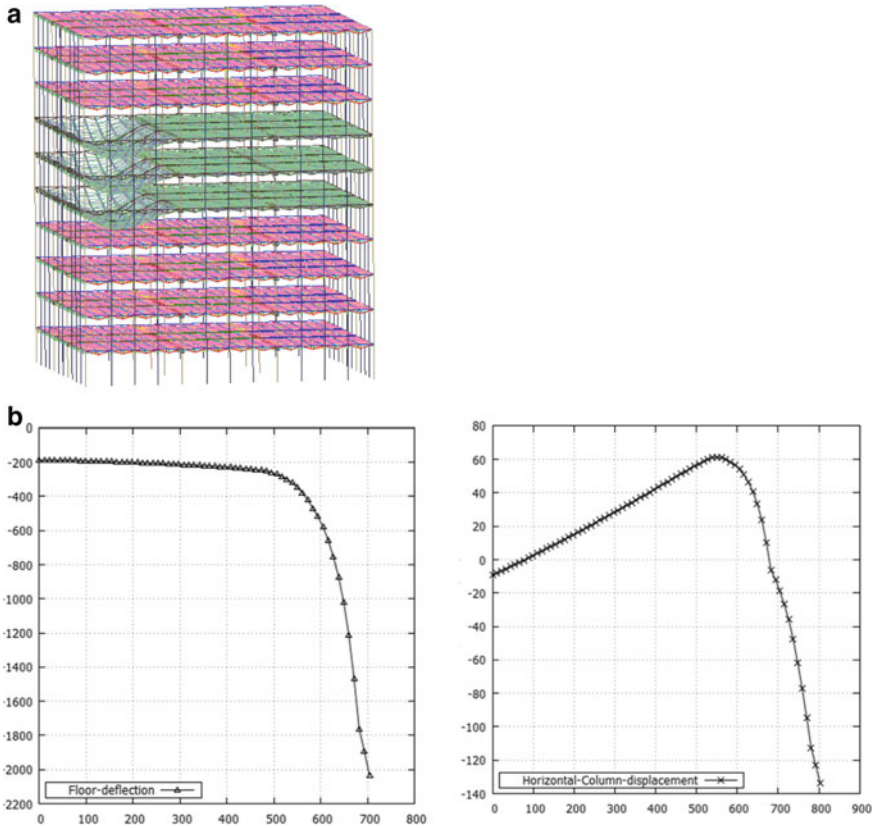


**Fig. 9** **a** Horizontal displacements in and **b** Difference in deflection between Ce2 and C2 columns under critical 4-block fire loading

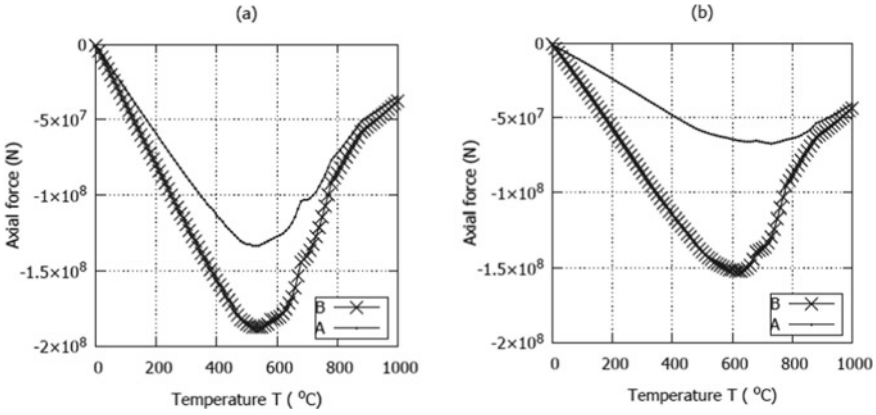


**Fig. 10** Comparison of top chord axial forces at the mid-sections of primary beam at locations A and B during **a** 1-block fire and **b** 4-block fire

**Acknowledgements** The authors gratefully acknowledge the support from the Department of Building Services and Engineering, FCE, The Hong Kong Polytechnic University for providing Ph.D.

The authors are grateful towards Chinese National Engineering Research Centre for Steel (CNERC)-Hong Kong Branch for providing the grant to carry out further research into this project.

## References

1. Behnam B (2019) Fire structural response of the Plasco building: a preliminary investigation report. Int J Civ Eng 17(5):563–580
2. Jiang J et al (2013) OpenSEES software architecture for the analysis of structures in fire. J Comput Civ Eng 29(1):04014030
3. Jiang J, Usmani A, Li GQ (2014) Modelling of steel-concrete composite structures in fire using OpenSEES. Adv Struct Eng 17(2):249–264
4. Jiang J, Li GQ, Usmani A (2015) Effect of bracing systems on fire-induced progressive collapse of steel structures using OpenSEES. Fire Technol 51(5):1249–1273
5. Kotsovinos P, Usmani A (2013) The World Trade Centre 9/11 disaster and progressive collapse of tall buildings. Fire Technol 49(3):741–765
6. Newman G (1991) Structural fire engineering investigation of Broadgate phases 8 fire. Steel Construction Industry Forum, Ascot
7. Usmani A, Rotter JM, Lamont S, Sanad AM, Gillie M (2001) Fundamental principles of structural behaviour under thermal effects. Fire Saf J 36(8):721–744
8. Usmani A, Zhang J, Jiang J, Jiang Y, May I (2012) Using OpenSEES for structures in fire. J Struct Fire Eng 3(1):57–70
9. Usmani A, Chung YC, Torero JL (2003) How did the WTC towers collapse: a new theory. Fire Saf J 38:501–533

# Extension of Variational Principles for Non-conservative Greenhill's Shafts


**Heera M. Titus and S. Arul Jayachandran**

**Abstract** This paper lays out a procedure to quantify the buckling loads of Greenhill shafts using variational iteration method. Lack of approximate methods for Greenhill shafts is attributed to the non-self-adjointness property of its governing differential equation. For a Greenhill shaft, a series solution is assumed for the displacement in terms of polynomials, and a correction functional is applied, which requires a Lagrange multiplier function. An exact general Lagrange multiplier is difficult to identify for a fourth-order differential equation as it requires solution procedures for quartic polynomials. Hence, simplified approximate formulae for Lagrange multiplier are chosen from the literature, and the effectiveness is demonstrated for a pinned–pinned shaft, subjected to a conservative axial load, and a non-conservative axial torque.

**Keywords** Buckling of shafts · Axial torsion · Greenhill's problem · Variational iteration method · Non-conservative loads · Nicolai's variant

## 1 Introduction

Systems subjected to non-conservative loads can become dynamically unstable (flutter) or statically unstable (divergence). But, systems subjected to conservative loads could only buckle by divergence. Thus, to identify the buckling loads, irrespective of the nature of loads, a dynamic instability analysis is always necessary. Flutter leads to a self-sustaining oscillation, whereas divergence leads to a blowing-up motion. Flutter is the region, which separates the stable region from divergence instability region. Most of the systems, with a finite value of flutter load, finally fail by divergence only. Flutter happens in structural systems, usually when follower forces

H. M. Titus (✉) · S. Arul Jayachandran
Department of Civil Engineering, Indian Institute of Technology Madras, Chennai 600036, India
e-mail: ce17d203@smail.iitm.ac.in

S. Arul Jayachandran
e-mail: aruls@iitm.ac.in



M. Madhavan et al. (eds.), *Proceedings of the Indian Structural Steel Conference 2020 (Vol. 1)*, Lecture Notes in Civil Engineering 318,
https://doi.org/10.1007/978-981-19-9390-9_13

are present. These forces do not admit a potential and are therefore non-conservative, i.e. a non-zero work is done in a closed path.

Exact analysis methods [1, 2] are tedious when applied for continuous mass systems. The search for an approximate tool for non-conservative stability paved way for application of variational calculus (Leipholz), in dynamic stability. In conservative systems, variational calculus yields good results, because the governing differential equation of the system is self-adjoint, and hence, a well-behaved functional could be found; minimization of which will yield accurate results. The non-self-adjointness of the differential operators in the governing equation makes variational calculus less effective [3]. It could be seen that incomplete variational methods available in the literature are only applicable to systems, which are non-self-adjoint with respect to boundary conditions. (e.g. systems subjected to tangential loads). Even then, the error associated with these solution techniques is of the order of 1–5%. Variational iteration method (VIM) is found to be very effective for use in the analysis of systems subjected to tangential loads (Beck's problem, Pfluger's rod and Leipholz rod). Variational iteration method combines the Lagrange multiplier method with a correction functional and formulates an equation which needs to be solved iteratively. Application of restricted variations on this iterative equation yields excellent results for systems subjected to tangential loads [4].

For systems subjected to an axial moment, the governing differential equation itself is non-self-adjoint. Hence, variational principles lack accuracy for systems subjected to non-conservative torsion. The classic problem of a rod subjected to an axial moment was first studied by Greenhill, and he found out that for such systems, critical value of the axial moment is zero. Nicolai considered a variant of the same problem, where he replaced the axial moment with a tangential moment, and suggested critical buckling values for different boundary conditions. He found the critical values for moment for five different boundary conditions. All these researches were based on exact analysis of the differential equation and boundary conditions.

This paper attempts to demonstrate the effectiveness of VIM on Greenhill's buckling problem. The governing differential equations and boundary conditions are taken from the literature. It could be seen that the VIM gives excellent results for Greenhill's buckling problem and is suggested for use in developing interaction curves for systems subjected to moment and axial load.

## 2 Greenhill's Buckling Problem

Buckling is not caused only by compression; a shaft may also become unstable under the action of a torque. Greenhill [5] analysed stability of an elastic shaft of circular cross section, length $L$ and mass per unit length $\mu$ under the action of a compressive force, $P$, and an axial torque, $M$. Table 1 shows the five variants of the Greenhill's buckling problem. In the absence of the axial torque ($M = 0$), the Greenhill problem reduces to the famous Euler's buckling under compression of 1757. The critical load at the onset of static instability can be found by the equilibrium method, which seeks

values of axial force, for which there are nontrivial equilibrium configurations. This yields the Euler formula for critical buckling force [6].

$$P_{\text{cr}} = k\frac{\pi^2 \text{EI}}{L^2}, \tag{1}$$

where

Ziegler studied the five cases with $P = 0$, using Lyapunov's stability theory, and found the values for critical moment of Greenhill's shaft (Table 2).

$$M_{\text{cr}} = k\frac{\pi \text{EI}}{L}, \tag{2}$$

where

This paper deals with the Case III (clamped-free) of Fig. 1 to demonstrate the effectiveness of variational iteration method (VIM). All other boundary conditions are outside the scope of this paper. Small vibrations of the Greenhill's shaft near its non-deformed rectilinear configuration are described by the following partial differential equation [2]:

$$I_0 w^{\text{IV}} + I_1 w''' + I_2 w'' + \mu \ddot{w} = 0, \quad 0 \le x \le L, \quad w = \begin{Bmatrix} u \\ v \end{Bmatrix} \tag{3}$$

where $I_0 = \begin{pmatrix} \text{EI} & 0 \\ 0 & \text{EI} \end{pmatrix}$ $I_1 = \begin{pmatrix} 0 & M \\ -M & 0 \end{pmatrix}$ $I_2 = \begin{pmatrix} P & 0 \\ 0 & P \end{pmatrix}$

The non-conservative clamped-free Case (III) is characterized by the following conditions:

$$\begin{aligned} &w(0,t) = w'(0,t) = 0 \\ &I_0 w''(L,t) + I_1 w'(L,t) = 0 \\ &I_0 w'''(L,t) + I_1 w''(L,t) + I_2 w'(L,t) = 0 \end{aligned} \tag{4}$$

**Table 1** Values of $k$ in Eq. (1)

| BC | I | II | III | IV | V |
|---|---|---|---|---|---|
| $k$ | 4 | 1 | 0.25 | 2.046 | 1 |

**Table 2** Values of $k$ in Eq. (2)

| BC | I | II | III | IV | V |
|---|---|---|---|---|---|
| $k$ | 2.861 | 2 | 0 | 0 | 2 |

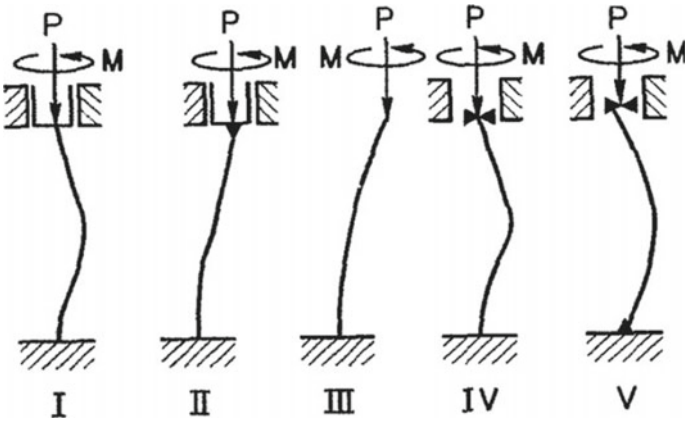


**Fig. 1** Five variants of Greenhill's problem. *Source* Kirillov [6]

corresponding to the constrained deflection and slope at the clamped end ($z = 0$) and vanishing axial force and axial torque at the free end ($z = L$). Separating time from displacement,

$$\begin{aligned} &w(x,t) = y(x)e^{i\omega t} \\ &y(0) = y'(0) = 0 \\ &I_0 y''(L) + I_1 y'(L) = 0 \\ &I_0 y'''(L) + I_1 y''(L) + I_2 y'(L) = 0 \end{aligned} \tag{5}$$

## 3 Variational Iteration Method (VIM)

Variational iteration method (VIM) has been put forward by He [7, 8] and is capable of generating fast and convergent numerical solutions for a wide class of differential equations. The fundamental aspects of VIM are available in the literature. To illustrate its basic idea of the technique, we consider following general nonlinear system:

$$L[u(t)] + N[u(t)] = g(t) \tag{6}$$

where $L$ is a linear operator, $N$ is a nonlinear operator, and $g(t)$ is a given continuous function. The basic character of the method is to construct a correction function of the form:

$$u_{n+1}(t) = u_n(t) + \int_0^t \lambda(\xi)[Lu_n(\xi) + Nu_n(\xi) - g(\xi)].\mathrm{d}\xi \tag{7}$$

where λ is a general Lagrange multiplier which can be identified optimally via variational theory and $u_n$ is the $n$th approximate solution. Assuming a trial function for $u_n(t)$, it has been shown that the above equation converges very rapidly, depending on the accuracy of Lagrange multiplier function. Glabisz et al. [4] demonstrated the effectiveness of VIM in the analysis of the stability of prismatic and non-prismatic Euler–Bernoulli beams under static non-conservative loads. So far, VIM is not used in the analysis of Greenhill's problem. This paper lays the foundation for use of VIM, in buckling of shafts.

## 4 Effectiveness of Vim in Greenhill's Buckling Problem

As mentioned before, the two governing differential equations for shaft buckling could be combined by introducing a complex deflection, $r = u + iv$. Then,

$$\mathrm{EI}\frac{\partial^4 r}{\partial X^4} + iM\frac{\partial^3 r}{\partial X^3} + P\frac{\partial^2 r}{\partial X^2} - \mu\Omega^2 r = 0, \qquad 0 \le X \le L \tag{8}$$

Substituting $x = X/L$,

$$\frac{\partial^4 r}{\partial x^4} + im\frac{\partial^3 r}{\partial x^3} + p\frac{\partial^2 r}{\partial x^2} - \omega^2 r = 0, \qquad 0 \le x \le 1 \tag{9}$$

where $m = \frac{ML}{\mathrm{EI}}$ $p = \frac{PL^2}{\mathrm{EI}}$ $\omega^2 = \frac{\mu\Omega^2}{\mathrm{EI}}$

Taking into account Eq. (7), the correct function for Eq. (9) assumes the form:

$$r_{n+1}(x) = r_n(x) + \int_0^x \lambda(\xi)\left(r_n^{\mathrm{IV}}(\xi) - imr_n'''(\xi) + pr_n''(\xi) - \omega^2 r_n(\xi)\right)\mathrm{d}\xi \tag{10}$$

After integrating by parts and performing the variation operation with respect to $r_n$ on both sides of Eq. (10), one gets the following stationary conditions:

$$[\lambda(\xi)]_0^x = 0 \tag{11}$$

$$\left[-\lambda'(\xi) - im\lambda(\xi)\right]_0^x = 0 \tag{12}$$

$$\left[\lambda''(\xi) + im\lambda'(\xi) + p\lambda(\xi)\right]_0^x = 0 \tag{13}$$

$$\left[-\lambda'''(\xi) - im\lambda''(\xi) - p\lambda'(\xi)\right]_0^x = 0 \tag{14}$$

$$\lambda^{IV}(\xi) + im\lambda'''(\xi) + p\lambda''(\xi) - \omega^2\lambda(\xi) = 0 \tag{15}$$

$\lambda = \lambda(\xi, x)$ is the Lagrangian multiplier function.

The solution of Eq. (16) cannot be found using exact methods. Using the exact formula $\lambda = \lambda(\xi, x)$ will give the actual solution for $u(x)$, after the first iteration. Approximate formulae for $\lambda(\xi, x)$ will need more number of iterations to converge [7].

Hence, assuming $m = 0$, the general Lagrange multiplier is found as:

$$\lambda(\xi) = \frac{\sqrt{2}}{\sqrt{p^2 + 4\omega^2}} \left\{ -\frac{\sinh\left(\frac{P_1}{\sqrt{2}(\xi - x)}\right)}{P_1} + \frac{\sinh\left(\frac{P_2}{\sqrt{2}(\xi - x)}\right)}{P_2} \right\}, \tag{16}$$

where $P_1 = \sqrt{-p - \sqrt{p^2 + 4\omega^2}}$ $P_2 = \sqrt{-p + \sqrt{p^2 + 4\omega^2}}$

If $p$ is assumed as zero, then:

$$\lambda(\xi) = \frac{(\xi - x)^3}{6} \tag{17}$$

Assuming $r(x) = a + bx + cx^2 + dx^3$, where $a$, $b$, $c$ and $d$ are constant complex coefficients,

If Eq. (16) is used as the Lagrangian multiplier, then Eq. (11) becomes:

$$r_1(x) = r_0(x) + \int_0^x \frac{\sqrt{2}}{\sqrt{p^2 + 4\omega^2}} \left\{ -\frac{\sinh\left(\frac{P_1}{\sqrt{2}(\xi - x)}\right)}{P_1} + \frac{\sinh\left(\frac{P_2}{\sqrt{2}(\xi - x)}\right)}{P_2} \right\} \left(r^{\mathrm{IV}}(\xi) - imr'''(\xi) + pr''(\xi) - \omega^2 r(\xi)\right) \mathrm{d}\xi \tag{18}$$

If Eq. (17) is used as the Lagrangian multiplier, then Eq. (11) becomes:

$$r_1(x) = r_0(x) + \int_0^x \frac{(\xi - x)^3}{6} \left(r^{\mathrm{IV}}(\xi) - imr'''(\xi) + pr''(\xi) - \omega^2 r(\xi)\right) \mathrm{d}\xi \tag{19}$$

After a set of iterations, substituting $r(x)$ in the boundary conditions:

$$r(0) = 0 \quad r'(0) = 0 \quad r''(1) - imr'(1) = 0 \quad r'''(1) - imr''(1) + pr'(1) = 0 \tag{20}$$

The set of values of ($m$, $p$), at which the shaft buckles, could be identified by setting the determinant of the homogenous system of equations to zero. If $m$ is set to zero, then the value at which the shaft buckles is $p = \pi^2/4 = 2.467$. This is the classic case of Euler buckling. This convergence is shown in Table 3. If $p$ is set to zero, then $m$ has no real root. This gives the Nicolai's result ($m = 0$). For a particular value of EI, this formulation could be used to generate a $p$-$m$ interaction curve, which could be used for design purposes.

**Table 3** Convergence of non-dimensionalized value for Euler's buckling load

| $i$ | $p = PL^2/\text{EI}$ |
|---|---|
| 0 | 13.44 |
| 1 | 2.3119 |
| 2 | 2.4795 |
| 3 | 2.4669 |
| 4 | 2.4674 |
| 5 | 2.4674 |
| 6 | 2.4674 |

## 5 Summary and Conclusions

The following conclusions emerge:

- The effectiveness of VIM for instability of shafts subjected to axial load and axial moment is discussed.
- It could be seen that depending on the accuracy of the Lagrangian multiplier function, the formulation could become exact and can give accurate values, even from a single iteration.
- A confirmation for Nicolai's paradox is given in a space of parameters.

## References

1. Ziegler H (1956) On the concept of elastic stability. Adv Appl Mech 4:351–403
2. Bolotin VV (1963) Nonconservative problems of the theory of elastic stability. Pergamon Press, Oxford
3. Anderson GL (1972) A comparison of approximate methods for solving non-conservative problems of elastic stability. J Sound Vib 22(2):159–168
4. Glabisz W, Jarczewska K, Zielichowski-Haber W (2013) Variational iterational method in stability analysis of beams under nonconservative forces. Arch Civ Mech Eng 13(1)
5. Greenhill AG (1883) On the strength of shafting when exposed both to torsion and to end thrust. Proc Inst Mech Eng 34:182–225
6. Kirillov ON (2019) Classical results and modern approaches to nonconservative stability. CISM International Centre for Mechanical Sciences-586
7. He JH (1999) Variational iteration method—a kind of non-linear analytical technique: some examples. Int J Non-Linear Mech 34:699–708
8. He J-H (2007) Variational iteration method—some recent results and interpretations. J Comput Appl Math 207

# Evaluation of Response Spectrum for Models of Structures Against Blast Loading


**Krishna Kumar Maurya, Anupam Rawat, Govinda Jha, and A. Nitesh**

**Abstract** The destruction as loss of life and prosperity occurs due to several types of blast explosives. Explosive upon explosion produces a huge amount of pressure and gases, which moves in all directions from the source point, cause damage to structures and the structure may collapse. Models of a few structures have been designed and analyzed to resist the physical and chemical explosives. The effect of the blast on structures also depends on the ductility ratio of structures. Study contains three types of structures, viz. reinforced—concrete frame structure, masonry structure, and reinforced—concrete frame structure with masonry infill, respectively. The structural properties of models are such as the height, width, size of the column, size of the beam of structural models are 3.2 m, 4.5 m, 500 mm × 500 mm, and 400 mm × 400 mm respectively. The thickness of masonry wall, grade of concrete, and grade of steel of structural models are 250 mm, M30, and Fe-415 HYSD steel, respectively. Analysis of the response spectrum has been done for structural models. The force–time—history is considered as a linear—equivalent triangle and a dynamic analysis has been performed. Calculation of blast load parameters has been done using IS: 4991-1968. The response spectrum of structures has been found from analysis with respect to the variation of structural stiffness for blast load of 20 kg explosive placed at a distance of 5 and 25 m. The study of response spectrum characteristics for models subjected to blast loads have been made with the variation of damping 0 and 5%.

**Keywords** Blast load · Response spectrum · Standoff distance · Charge weight · Structural models · SAP 2000 software

K. K. Maurya · A. Rawat · G. Jha (✉)
Department of Civil Engineering, MNNIT Allahabad, Prayagraj, Uttar Pradesh 211004, India
e-mail: govindajha19@gmail.com

K. K. Maurya
e-mail: kkmaurya@mnnit.ac.in

A. Rawat
e-mail: anupam@mnnit.ac.in

A. Nitesh
Department of Civil Engineering, Structural Dynamics, N. I. T. Silchar, Assam 788010, India



M. Madhavan et al. (eds.), *Proceedings of the Indian Structural Steel Conference 2020 (Vol. 1)*, Lecture Notes in Civil Engineering 318,
https://doi.org/10.1007/978-981-19-9390-9_14

## 1 Introduction

The terror attacks and accidents ground breakdown of structures since these are exposed to the atmosphere for all kinds of threats. Therefore, there is a necessity to protect the structures against the blast phenomenon [5]. The advancement of technology and the availability of high levels of chemical explosives the destructive ability of blast loads on structures. Which one may be explosive materials, viz., Tri Nitro Toluene (TNT), Ammonium Nitrate, Liquid Petroleum Gas (LPG) cylinders, moving vehicles, static vehicles, etc. [6]. Out of these explosives, TNT explosives are used as standard explosives. In the present scenario, there may be a possibility of war among countries; hence, the structures are not safe against blast loading. Therefore, structures are more vulnerable to blast loading. The blast causes the loss of property and human life. It is not necessary to design all kinds of buildings to sustain blast loads. The structures of national importance that may be taken into consideration for blast resistant design are, viz. hospitals, schools, huge structures, chemical factories, research centers, city malls, lifeline structures, etc.

The blast produces shock waves and pressure which moves in all directions and causes the damage of structures. The blast wave carries a large amount of dust and different types of gases, which creates social panic. If the quantity of the explosive is less, then we can minimize the damage and reduce the social panic between the public. Generally, the blast is categorized into two types, internal and external, respectively [8]. These are known as a confined and unconfined explosion. The internal blast occurs inside the building and produces high pressure and gases that cause damage to the structure. If blast occurs inside the building, we cannot protect structures, and for these type of cases, the analysis and the design are not possible. Furthermore, the external blast is categorized as the surface blast and the air blast. The air blast occurs when the blast is at a distance and above the structure. The blast is considered as surface blast when blast occurs near to the ground [1].

Blast may occur on the ground also, which comes under external explosion. The main parameters which govern the safety of the building are the standoff distance and ductility ratio. Standoff distance is the distance between the face of the building and the center of the explosive [3]. If the standoff distance is more, then the structure is safe against the blast. Therefore, for the high-performance level of the structure the standoff distance is minimum. The ductility ratio is the ratio of actual deformation to the yield deformation of the structure. The ductility of structure can be increased by using low grades of mild steel, glazing, and other materials [7]. If the structure is ductile, then damage of structure is minimum and performance level of structure is high [2]. The study has been done for the evaluation of response spectrum curves for

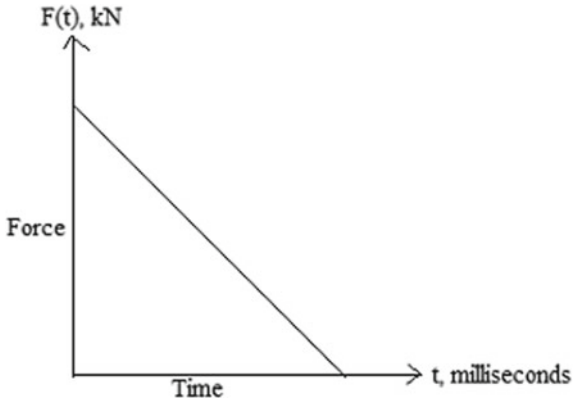


**Fig. 1** Force time—history curve

models of structures against blast loading. Analysis of structural models against blast loading will be helpful for evaluation of real life structures in respect to blast loading. Hence, the research paper will result new research directions for the sustainable buildings.

## 2 Blast Wave Behavior and Time History Function

The generation of exponential blast waves due to an explosion moves in all directions and causes damage to structures. Figure 2 shows the exponential blast wave profile formed due to an explosion. The vertical axis contains pressure, $P(t)$ (MPa) and on the horizontal axis time, $t$ (milliseconds), respectively. The blast waves have two phases such as the negative phase and positive phase. These are known as positive specific impulse and negative specific impulse. The $P_{os}$ and $P_o$ are described as overpressure and atmospheric pressure. The positive phase pressure is more than the negative phase pressure; therefore, positive pressure is considered in the analysis of structures [10]. According to IS: 4991-1968 [4], the time–history function of the blast is assumed as an equivalent triangle which acts as time history function. Figure 1 shows that the equivalent force (kN) versus time (milliseconds), which is termed as time—history function. In Fig. 2, $t_d^+$ and $t_d^-$ indicated that positive phase duration and negative phase duration, respectively.

## 3 Blast Load Calculation

Table 1 shows the calculated blast parameters from IS: 4991-1968 [4] for 20 kg explosive placed at 5 m actual distance ($R$). In Table 1, $t$, $Z$, $P_{ro}$, $A$, $F$, and UDL represent the duration of equivalent triangular phase, scaled distance, reflected overpressure,

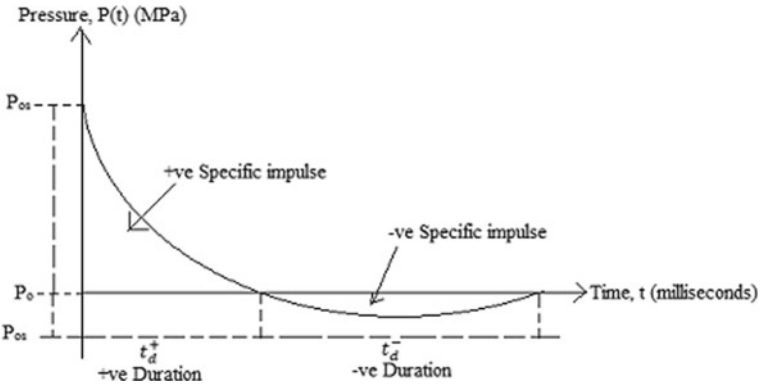


**Fig. 2** Exponential blast wave behavior curve

**Table 1** Calculated blast parameters

| Explosive (kg) | $R$ (m) | $Z$ (m) | $t$ (ms) | $P_{ro}$ (kN/m$^2$) | UDL (kN/m) | $A$ (m$^2$) | $F$ (kN) |
|---|---|---|---|---|---|---|---|
| 20 | 5 | 18.4 | 7.5 | 2076 | 9342 | 3.6 | 7473.6 |
| | 25 | 92.10 | 34.03 | 43.36 | 195.12 | 3.6 | 156.10 |

tributary area of joint, blast force, and uniformly distributed load, respectively. The blast force is calculated by multiplying the tributary area and the reflected overpressure. For static analysis, the blast force is applied to each joint [1]. In the case of areal structures, the blast pressure is applied to the whole area. The blast force versus duration of the equivalent triangle acts as time—history function. Force time—history has been used for dynamic analysis [9]. The dynamic analysis has been performed on the structural models.

## 4 Methodology and Modeling

The method of analysis of structures, viz. Reinforced Concrete Frame (m1), Masonry Wall (m2), and Reinforced Concrete Frame with Masonry Wall (m3) is totally based on the numerical method. The time—history function is assumed linear. The time—history function is applied to the structural models in each direction such as translation as well as rotation in SAP 2000 software. The dynamic analysis of structures has been performed. The analysis of response spectrum curves of structures, viz. m1, m2, and m3, is done for 20 kg explosive placed at 5 m distance. Structures are modeled in SAP 2000 software. The structures contain four joints, joint 1, joint 2, joint 3, and joint 4, respectively. The joint 1 and joint 3 are fixed and joint 2 and joint 4 are at the floor level. The common structural properties of models are as follows: The height and width of structural models are 3.2 m and 4.5 m, respectively. The size of

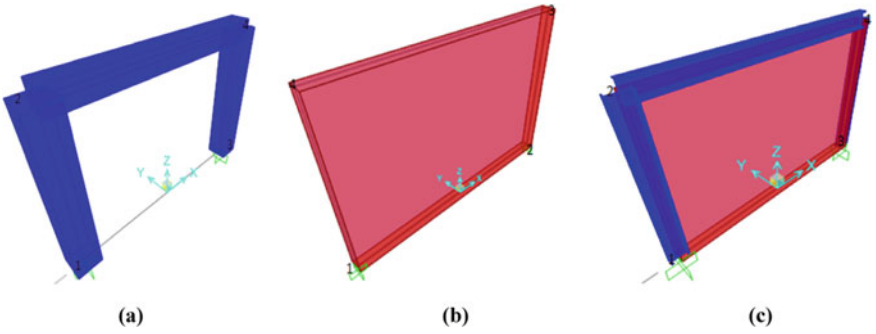


**Fig. 3** **a** Reinforced concrete frame model (m1), **b** masonry wall model (m2), **c** reinforced concrete frame with masonry wall (m3)

the column and the size of the beam of structural models are 500 mm × 500 mm and 400 mm × 400 mm, respectively. The thickness of the masonry wall, grade of concrete, and grade of steel of structural models are 250 mm, M30, and Fe 415 HYSD steel, respectively. Figure 1 shows the correlation of acceleration responses of model 1, model 2, and model 3 with 0 and 5% damping for the explosive placed at 5 m distance. Figure 3 shows that (a) reinforced concrete frame model (m1), (b) masonry wall model (m2), and (c) reinforced concrete frame with masonry wall (m3), respectively.

## 5 Analysis of Response Spectrum Curves

Analysis of response spectrum of structures, viz. m1, m2, and m3 has been done for 20 kg explosive placed at 5 m distance using SAP 2000 software of joint 4 in *Y*-direction [9]. In the response spectrum curves, the red color shows the zero damping and green color shows 5% damping, respectively. Figure 4a–c shows response spectrum curve of displacement (m) versus time (s), velocity (m/s) versus time (s), and acceleration ($m/s^2$) versus time, respectively for model m1. Similarly, Fig. 5a–c for model m2 and Fig. 6a–c for model m3 at a distance of 5 m. Similarly, Fig. 7a–c, Fig. 8a–c, and Fig. 9a–c show response spectrum curves of models m1, m2, and m3 at a distance of 25 m, respectively. The analyzed values of the response spectrum are given in Table 2.

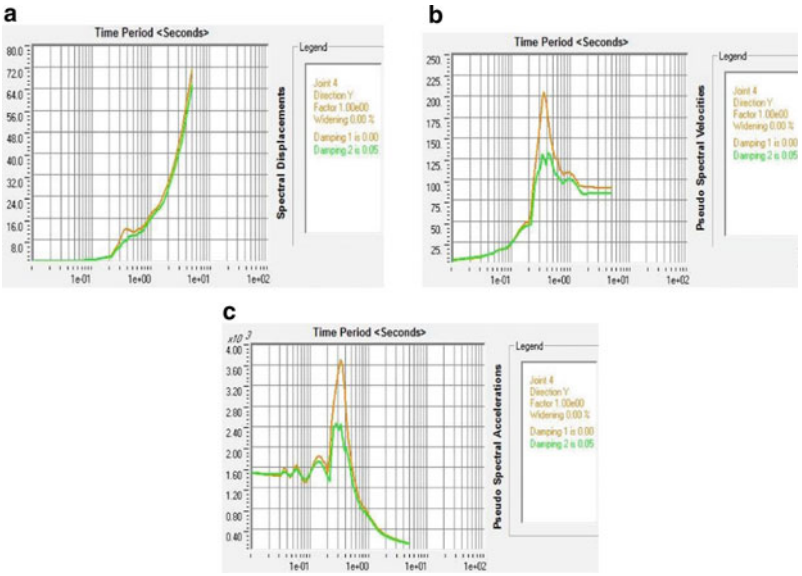


**Fig. 4** **a** Spectral displacement versus time, **b** pseudo spectral velocity versus time, **c** pseudo spectral acceleration versus time

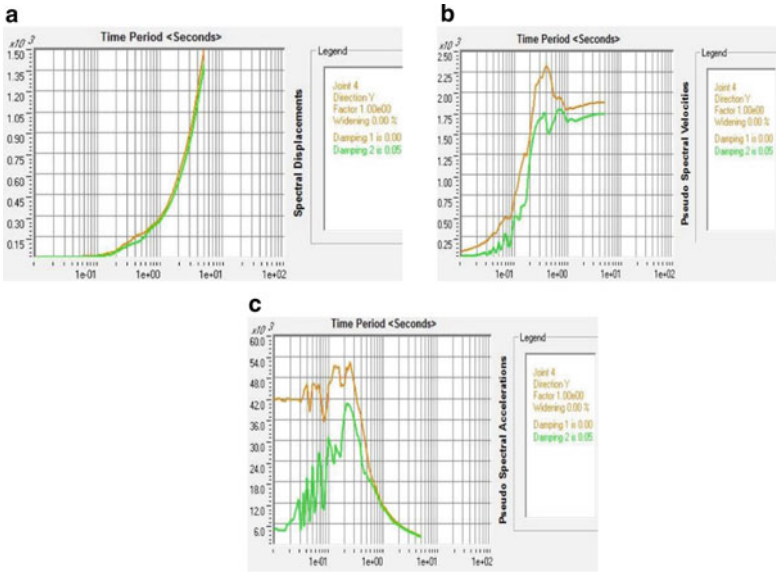


**Fig. 5** **a** Spectral displacement versus time, **b** pseudo spectral velocity versus time, **c** pseudo spectral acceleration versus time

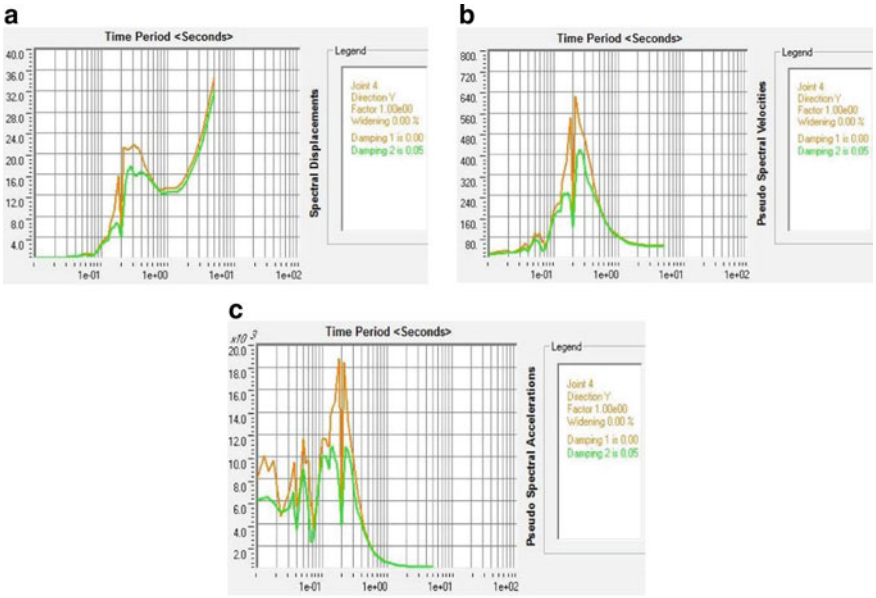


**Fig. 6** **a** Spectral displacement versus time, **b** pseudo spectral velocity versus time, **c** pseudo spectral acceleration versus time

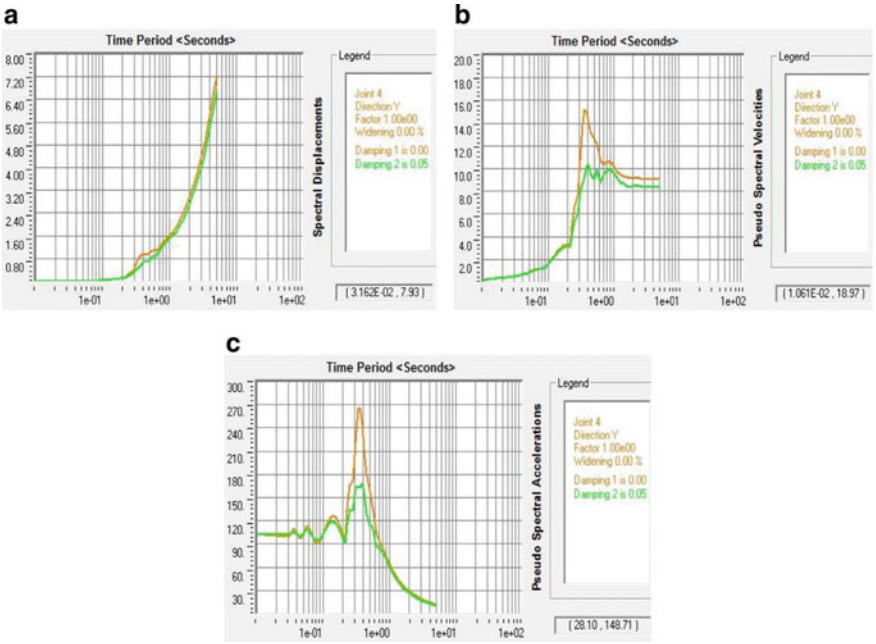


**Fig. 7** **a** Spectral displacement versus time, **b** pseudo spectral velocity versus time, **c** pseudo spectral acceleration versus time

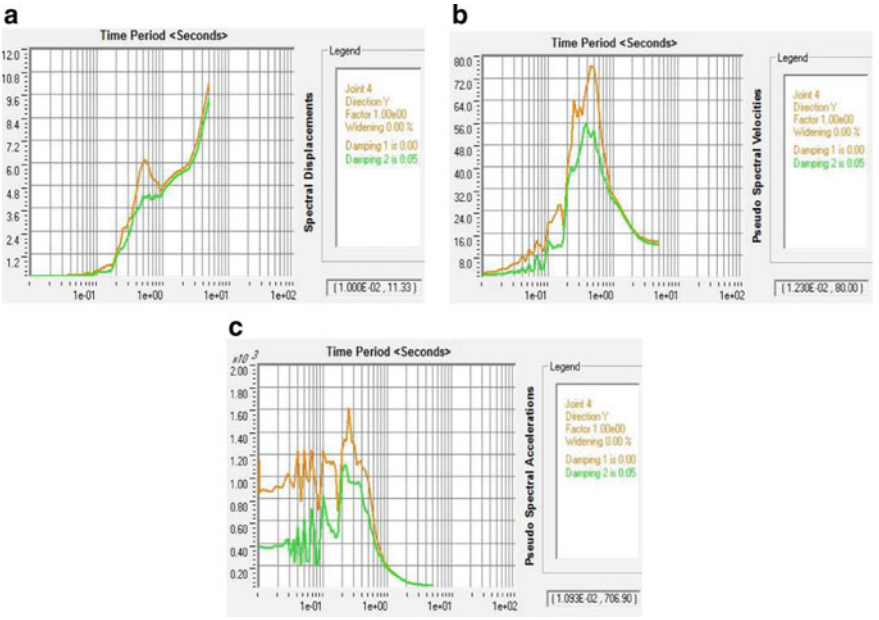


**Fig. 8** **a** Spectral displacement versus time, **b** pseudo spectral velocity versus time, **c** pseudo spectral acceleration versus time

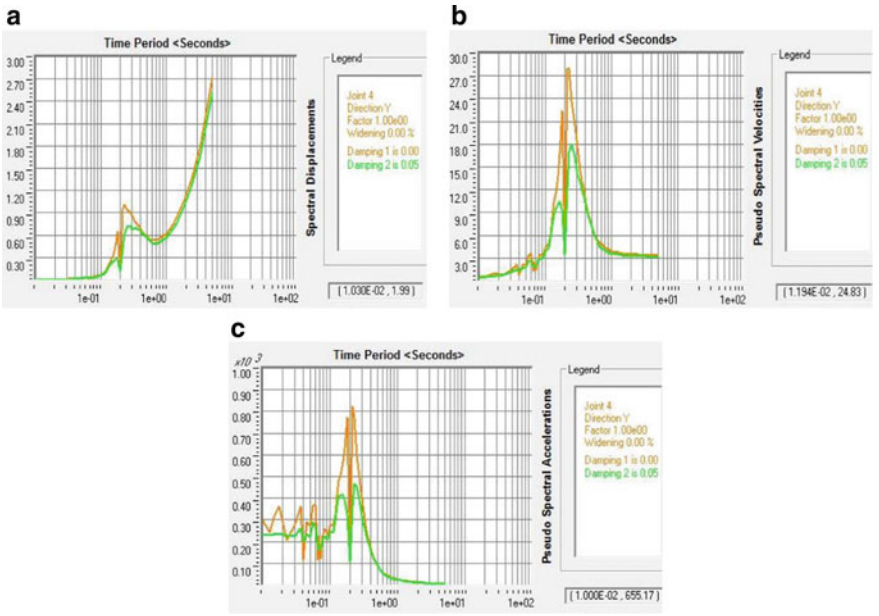


**Fig. 9** **a** Spectral displacement versus time, **b** pseudo spectral velocity versus time, **c** pseudo spectral acceleration versus time

**Table 2** Values of response spectrum with 20 kg explosive

| Distance (m) | Description | m1 | | m2 | | m3 | |
|---|---|---|---|---|---|---|---|
| | Damping responses | 0 | 0.05 | 0 | 0.05 | 0 | 0.05 |
| 5 | Displacement (m) | 7.1E+01 | 6.6E+01 | 1.5E+03 | 1.4E+03 | 3.4E+01 | 3.2E+01 |
| | Velocity (m/s) | 2.0E+02 | 1.3E+02 | 2.3E+03 | 1.8E+03 | 6.3E+02 | 4.2E+02 |
| | Acceleration ($m/s^2$) | 3.7E+03 | 2.5E+03 | 5.2E+04 | 4.1E+04 | 1.9E+04 | 1.1E+04 |
| 25 | Displacement (m) | 7.2E+00 | 6.7E+00 | 1.0E+01 | 9.4E+00 | 2.7E+00 | 2.5E+00 |
| | Velocity (m/s) | 1.5E+01 | 1.0E+01 | 7.6E+01 | 5.6E+01 | 2.8E+01 | 1.8E+01 |
| | Acceleration ($m/s^2$) | 2.7E+02 | 1.7E+02 | 1.6E+03 | 1.1E+03 | 8.2E+02 | 4.7E+02 |

## 6 Correlation of Models

The absolute maximum values of the response spectrum are given in Table 2. Corresponding absolute maximum response spectrum values, correlation of structures, viz. m1, m2, and m3 have been done (ChBV et al. 2014). Figures 10, 11, 12, 13, 14, and 15 show the correlated curves of displacement, velocity, and acceleration, respectively. The red color is showing 0% damping, correlated curve, and blue color 5% damping correlation curve of models, respectively. Table 3 shows the correlation of the results of models of 20 kg explosive placed at 5 and 25 m distance. The correlation has done for 0 and 5% damping. The displacement of response spectrum due to blast action of m3, minimize with respect to m1 and m2 with 51.5% and 97.7% in case of 0% damping and in case of 5% damping, 51.4% and 97.7% when explosive placed at 5 m distance, respectively. Similarly, the correlation has done for velocity and acceleration. The velocity with 0% damping of m3 with respect to m1 increased by 205.5% and with respect to m2 decreased by 72.9%, respectively. However, the overall velocity of m3 minimizes. According to the results, the overall displacement, velocity, and acceleration minimize after combining models m1 and m2. Similarly, it has been done for explosive placed at 25 m.

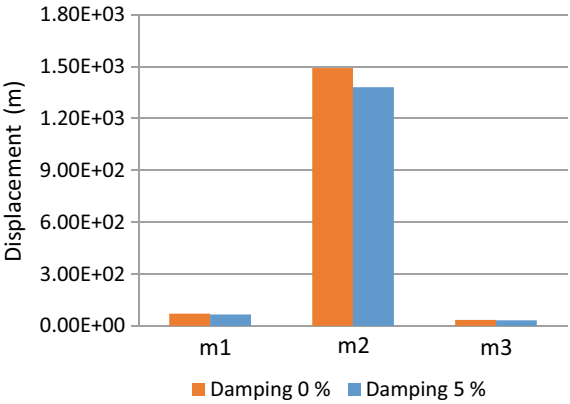


**Fig. 10** Spectral displacement (m) versus m1, m2, and m3 with 5 m distance of 20 kg explosive

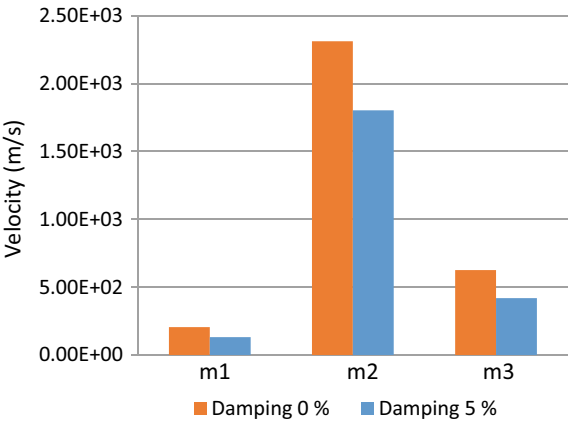


**Fig. 11** Pseudo spectral velocity (m/s) versus m1, m2, and m3 with 5 m distance of 20 kg explosive

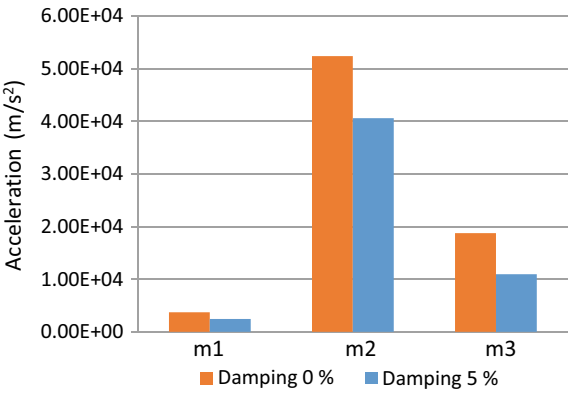


**Fig. 12** Pseudo spectral acceleration (m/s$^2$) versus m1, m2, and m3 with 5 m distance of 20 kg explosive

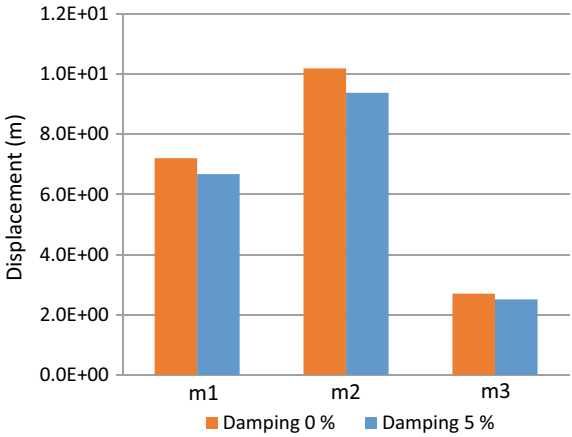


**Fig. 13** Spectral displacement (m) versus m1, m2, and m3 with 25 m distance of 20 kg explosive

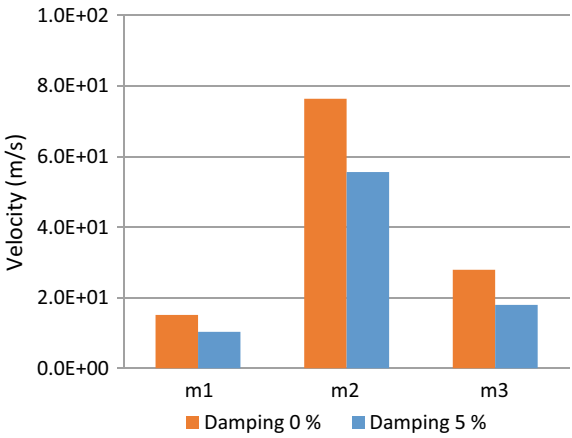


**Fig. 14** Pseudo spectral velocity (m/s) versus m1, m2, and m3 with 25 m distance of 20 kg explosive

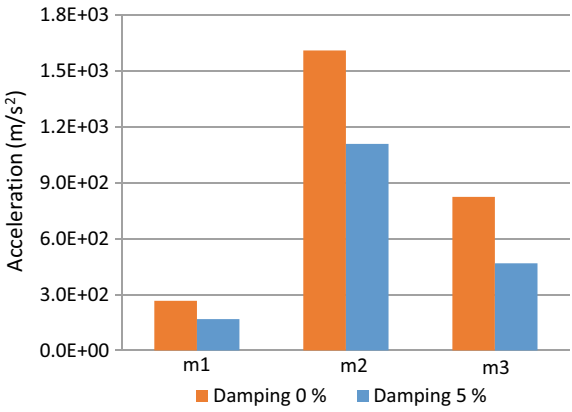


**Fig. 15** Pseudo Sp. Acceleration ($m/s^2$) versus m1, m2, and m3 with 25 m distance of 20 kg explosive

**Table 3** Result correlation of models with 20 kg explosive

| Distance (m) | Description | % Increase/decrease of model 3 w.r.t. model 1 | | % Increase/decrease of model 3 w.r.t. model 2 | |
|---|---|---|---|---|---|
| | Damping responses | 0 | 0.05 | 0 | 0.05 |
| 5 | Displacement (m) | −5.1E+01 | −5.1E+01 | −9.8E+01 | −9.8E+01 |
| | Velocity (m/s) | 2.1E+02 | 2.2E+02 | −7.3E+01 | −7.7E+01 |
| | Acceleration (m/s$^2$) | 4.1E+02 | 3.4E+02 | −6.4E+01 | −7.3E+01 |
| 25 | Displacement (m) | −6.3E+01 | −6.2E+01 | −7.4E+01 | −7.3E+01 |
| | Velocity (m/s) | 8.4E+01 | 7.4E+01 | −6.3E+01 | −6.8E+01 |
| | Acceleration (m/s$^2$) | 2.1E+02 | 1.8E+02 | −4.9E+01 | −5.8E+01 |

## 7 Conclusion

Analysis of the response spectrum has been done for 20 kg explosive placed at 5 m distance of models m1, m2, and m3, respectively. The following conclusions are found:

1. If 20 kg explosive placed at 5 m distance produces a huge amount of pressure, which causes damage to the structures and structure may collapse but in the case of 25 m structure may safe up to a certain level.
2. The performance level of the structures is good, for maximum standoff distance.
3. The displacement response of m3 with respect to the m1 and m2 minimized by 51.50% and 97.70%, respectively, in case of without damping. Similarly, it has done for 5% damping case also.
4. Blast analysis needs to carry out for the important structures by keeping in view the terrorist activities in the present scenario.

The study shall contribute to the minimization of damage of important structures due to blast loading with lesser economic it will input. Therefore, save the economy and provide protection against blast loads of the structures.

## References

1. Bhatt AC, Mevada SV, Patel SB (2016) Comparative study of response of structures subjected to blast and earthquake loading. IJERA 6(5):62–66
2. Goel MD, Matsagar VA (2014) Blast—resistant design of structures. ASCE Pract Periodical Struct Des Constr 19(2):1–9
3. Hinman E (2011) Blast safety of the building envelope. National Institute of Building Sciences, pp 1–14
4. IS:4991-1968 (n.d.) Criteria for blast resistant design of structures for explosion above ground. Bureau of Indian Standards, New Delhi, pp 1–43
5. Jamakhandi U, Vanakudre SB (2015) Design and analysis of blast load on structures. Int Res J Eng Technol 2(7):745–747
6. Janssen M (2009) Blast—resistant building design. Thesis, pp 1–142

7. Jayashree SM, Bharatwaj RR, Helen SM (2013) Dynamic response of a space framed structure subjected to blast load. Int J Civ Struct Eng 4(1):98–105
8. Jomy P, Arun KA (2010) Architectural and structural design blast resistant buildings. Thesis, pp 1–43
9. Kashif Q, Varma MB (2014) Effect of blast on G + 4 RCC frame structure. Int J Emerg Technol Adv Eng 4(11):145–149
10. Mendis P, Gupta A, Ramsay J, Ngo T (2007) Blast loading and blast effects on structures—an overview. Electron J Struct Eng 7:76–91

# Shake Table Study of Dynamic Characteristics of a Typical Pallet Racking System


**N. Raviswaran, N. N. Unnikrishnan, V. Nagendiran, S. Pradeep Shankar, C. Bharathi Priya, and K. Sathish Kumar**

**Abstract** Industrial pallet racking system was the commonly used structure for storing palletized goods. They were built up from thin-walled cold-formed steel profiles. The upright (column of the rack) has perforations which ensure the typical functionality, adaptability and flexibility needed for accommodating the variability of dimensions of the stored goods. Connections were custom made, where in the beams were generally hooked on to the upright. These connections were significantly semi-rigid in behaviour. The complexity associated with the nonlinear moment-rotation behaviour of the joints in the design of cold-formed steel structure was to be accounted for a realistic capacity estimation. These racks when installed in seismic prone zones must be qualified for different levels of safety such as collapse prevention and immediate occupancy. To assess these performance levels, static and shake table tests were performed on full-scale racking system simulating earthquake conditions. An attempt has been made to quantify the dynamic behaviour of the structure based on the experimental results of both static and dynamic shake table tests. Based on the test results, it was seen that the requirements with respect to performance levels specified by FEMA 460 were met by the structures. With respect to the behaviour of the pallet under severe dynamic excitation, it was observed that the wooden pallets

N. Raviswaran · N. N. Unnikrishnan · V. Nagendiran · S. Pradeep Shankar (✉)
Godrej Storage Solutions, Godrej & Boyce Mfg Co. Ltd, Chennai, India
e-mail: spradeep@godrej.com

N. Raviswaran
e-mail: ravish@godrej.com

N. N. Unnikrishnan
e-mail: unni@godrej.com

V. Nagendiran
e-mail: nag@godrej.com

C. Bharathi Priya · K. Sathish Kumar
CSIR-Structural Engineering Research Centre, Taramani, Chennai, India
e-mail: bharathipriya@serc.res.in

K. Sathish Kumar
e-mail: ksk@serc.res.in



M. Madhavan et al. (eds.), *Proceedings of the Indian Structural Steel Conference 2020 (Vol. 1)*, Lecture Notes in Civil Engineering 318,
https://doi.org/10.1007/978-981-19-9390-9_15

did not have relative body motion and were vibrating integrally with the structure. Therefore, in a full-scale test, the relative performance of pallet/rack system could be quantified for the first time.

**Keywords** Storage rack · Static load–displacement · Shake table test · Pallet rack system · Dynamic characterization · Performance levels · Seismic behaviour

## 1 Introduction

The effects of earthquake on industrial steel storage systems which were widely used for storing goods were a matter of concern. Nowadays, storage racks were more frequently used in distribution centres and supermarkets. Hence, their safety under seismic condition was evaluated. The uprights were open thin-walled members, with omega section stiffened by lips. The uprights usually contain perforations at regular spacing to allow for the beam and the bracing connections. Beams which usually have closed cross sections were provided by endplates which were hooked on to the upright. This hooked beam-column connection was generally semi-rigid, and the performance of this connection depends on the effectiveness of the beam end connector. The connection to the floor was built up by means of base plate which was bolted to the upright and anchored to the floor. The frame diagonal bracings were usually of open cross-section profiles which were bolted to the upright.

The prediction of the behaviour of these structures was complex because the structural components were thin-walled perforated profiles. These profiles were prone to global, local and distortional buckling. Therefore, the most appropriate method of assessing the behaviour of the perforated sections seems to be an experimental approach. Seisrack project, a joint project undertaken by academic as well as industrial collaboration, investigated various issues by conducting component testing and full-scale (push over) testing. The full-scale testing consisted of monitoring racking system in operating warehouses. This project resulted in the development of design guidelines and recommendations for seismic design of racking systems based on static push over tests.

This paper examines the behaviour under dynamic shake table environment with respect to applicability of the above recommendations.

## 2 Literature Review

The first published in-site dynamic investigation of storage racks was performed in the mid-1970s [5, 6]. The first published shake table studies on storage racks in the USA was performed in the late seventies in the shake table at University of California, Berkeley [2]. This study provided the background information for the seismic design provisions for storage racks in the USA. Seismic behaviour of steel storage pallet racking system was studied by Structural Engineering Department of Politecnio, Milano [1].

Within Seisrack project [8], various investigations were done by means of component testing, full-scale (push over) testing and in-site testing of racking systems in operating warehouses. In this Seisrack project, the assessment of the global behaviour of full-scale racks was carried out on the shake table. An experimental study to understand the seismic behaviour of the cold-formed steel pallet racks under El Centro earthquake acceleration was performed, and an attempt was made to evaluate the realistic dynamic characteristics [7].

## 3 Experimental Investigation

The experimental investigation described herein consists of series of shake table tests conducted on a full-scale, single bay rack with 4 levels. Two specimens, one with spine bracing system as shown in Fig. 1 and the other without spine bracing system as shown in Fig. 2, were tested. The objective of this experimental study was to evaluate the stiffness, natural frequency, damping and to observe the modes of failure of the structure using the spectrum of IS 1893:2016 [4].

The specifications of the specimen used for this study were as follows. Overall height, width and depth of the rack were 6.3 m, 2.7 m and 1 m, respectively. The profile of the upright, beam and frame bracing was shown in Figs. 3, 4 and 5, respectively. The section details of the same were listed in Table 1, and the material properties were listed in Table 2. The connection between the beam columns was a typical semi-rigid connection as with the stiffness value arrived from the joint stiffness test. Beams were hooked on to the upright using lip connector. Plan and Back bracings were standard flats as shown in Fig. 1. Uprights were identified as Legs 1, 2, 3 and 4 as shown in Figs. 1 and 2 for both braced and unbraced racks.

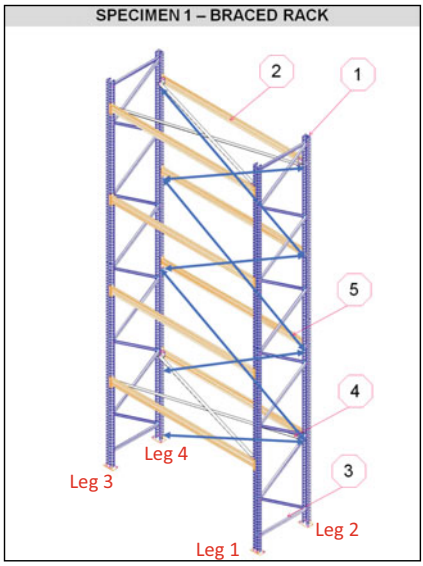


**Fig. 1** Specimen 1—braced rack

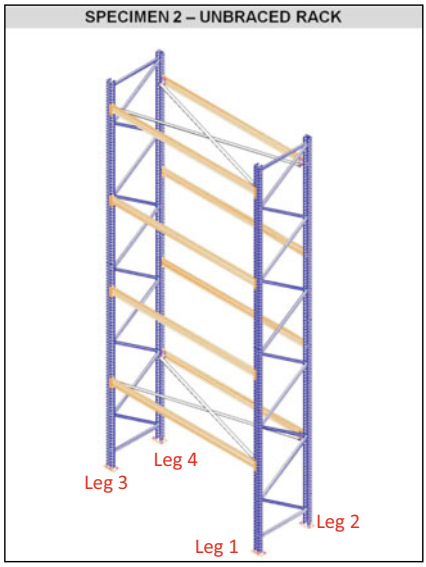


**Fig. 2** Specimen 2—unbraced rack

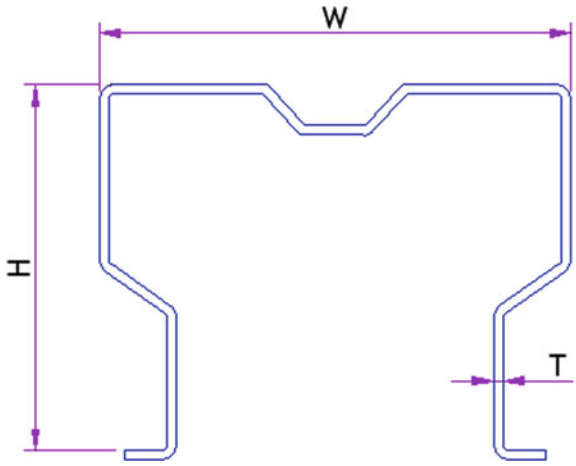


**Fig. 3** Upright section

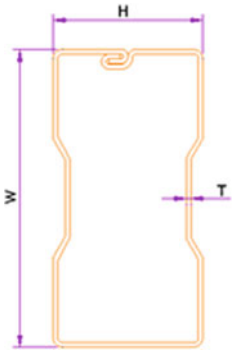


**Fig. 4** Beam section

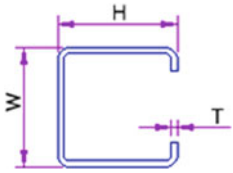


**Fig. 5** Bracing section

**Table 1** Details of cross sections

| S. No | Profile | Web 'W' (mm) | Flange 'H' (mm) |
|---|---|---|---|
| 1 | Upright | 90 | 70 |
| 2 | Beam | 110 | 50 |
| 3 | Bracing | 30 | 30 |
| 4 | Plan bracing | 50 | – |
| 5 | Back bracing | 60 | – |

**Table 2** Material properties

| S. No | Property | Value |
|---|---|---|
| 1 | Modulus of elasticity, E | 210,000 MPa |
| 2 | Poisson's ratio, U | 0.3 |
| 3 | Min. yield strength (upright) | 355 MPa |
| 4 | Min. yield strength (beam, bracing) | 255 MPa |
| 5 | Min. yield strength (back, plan bracing) | 210 MPa |

# 4 Test Setup, Instrumentation and Testing Procedure

## *4.1 Test Setup*

The test was conducted on the shake table with a platform of 4 m × 4 m normal payload capacity of 50 tonnes at 0.5 g. The specification of the shake table was given in Table 3: horizontal (H) and vertical (V).

Reinforced concrete (RCC) slabs of height 200 mm were cast with holes to match the holes on the shake table. The RCC slab was fixed on the shake table using 4 numbers of M24-diameter high-strength studs. The specimen was installed on the RCC slab by fixing the upright to the base plate and anchoring the base plate on the RCC slab using M12-diameter anchor bolts. A load of 2000 kg at each level was placed on the structure using two wooden pallets (1000 kg each), such that the total load on the structure was 8000 kg. The pallets were placed with a clearance of 100 mm with respect to the frame.

A steel frame supporting structure was provided as a safety fixture around the specimen, so that the added mass and the test specimen can be supported on it in case of failure, if any, during tests. The steel supporting frame was appropriately designed to avoid any interaction with the test structure. The overall assembly of the tested rack was shown in Fig. 6.

**Table 3** Shake table specification

| S. No | Specification | Value |
|---|---|---|
| 1 | Frequency | 0.1–50 Hz |
| 2 | Actuators | 4 × 250 kN (H) and 4 × 250 kN (V) |
| 3 | Displacement | ± 150 mm (H) and ± 100 mm (V) |
| 4 | Velocity | 0.8 m/s (H) and 0.4 m/s (V) |
| 5 | Waveforms | Sine, sine sweep, random and artificial |

**Fig. 6** Overall assembly of the testing specimen on shake table

## *4.2 Instrumentation*

Three sets of instrumentation were used to evaluate the seismic response of the test specimen. Displacement, acceleration and strains were measured at salient locations identified based on the performance requirement of the structure. The details of the instrumentation were given in Table 4.

Non-contact-type displacement transducers (NCDTs) were fixed on a reference frame kept outside the shake table; hence, the measured displacements were absolute displacement inclusive of table displacement. Horizontal displacement of each structure was measured at levels 2, 3 and 4 on all four uprights. Strain gauges were pasted on the tension and compression flanges of the upright as well as the beam near the

**Table 4** Instrumentation details

| S. No | Parameter to be measured | Instrument | Make | Range |
|---|---|---|---|---|
| 1 | Displacement | NCDT | Micro epsilon | 200 mm |
| 2 | Acceleration | Accelerometer | Bruel & Kjaer | $\pm$ 140 $ms^{-2}$ |
| 3 | Strain | Strain gauge | TML | 2 mm |

joints. This could measure the strain response at levels 1 and 4. For measuring acceleration response of the structure, triaxial accelerometers were fixed on the beams of levels 1, 3 and 4. For measuring the acceleration of the pallets placed on the beams, triaxial accelerometers were fixed on one pallet each on levels 3 and 4. All the measured accelerations are absolute acceleration responses. For instrumentation details for specimen 1 and specimen 2, refer Figs. 7 and 8, respectively.

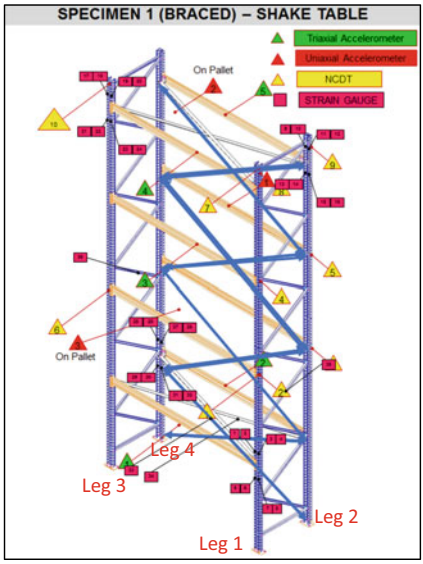


**Fig. 7** Specimen 1—instrumentation

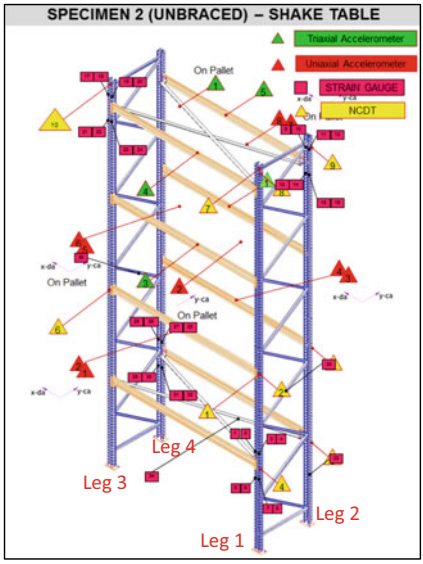


**Fig. 8** Specimen 2—instrumentation

### *4.3 Testing Procedure*

Seismic testing of full-scale pallet racking system was carried out by applying three non-correlated acceleration-time histories at the base of the pallet racking structural system in three orthogonal directions. PGA applied in the vertical direction ($Z$) was two-third of that applied at horizontal directions ($X$ and $Y$). IS 1893:2016, based on Housner's average spectrum for medium-type soil, was applied. This has a peak plateau region between 0.1 and 0.5 s (2–10 Hz). The spectrum-compatible time history for the medium soil type defined in IS 1893:2016, Part 1, was generated and applied. The time periods and corresponding acceleration coefficient are marked in Fig. 9 for specimen 1 and specimen 2.

The test specimen without pallet mass was rigidly fixed on the shake table along with the instrumentation. The specimen was subjected to free vibration using pulse excitation of both 1 and 3 mm in $X$ and $Y$ directions independently using shake table. Response acceleration was recorded separately in each direction for both the specimens. Natural frequency of the rack structure was estimated from this free vibration test. After this, the specimen was loaded with 2000 kg of mass at each floor level, and free vibration tests were repeated. Subsequently, the specimen was subjected to seismic ground motion progressively increasing triaxial earthquake input of ground acceleration equivalent to 0.01, 0.025, 0.05, 0.075, 0.1, 0.16, 0.2, 0.24, 0.3 and 0.36 g (Fig. 10). The response values of NCDTs, accelerometers and strain gauges were recorded for every acceleration cycle of 60 s each. After every test, the structure was inspected for any component-level damage.

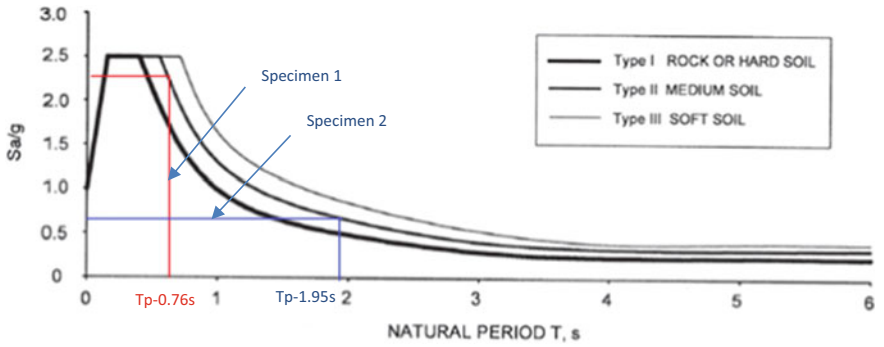


**Fig. 9** IS spectrum as per IS 1893:2016 [4]

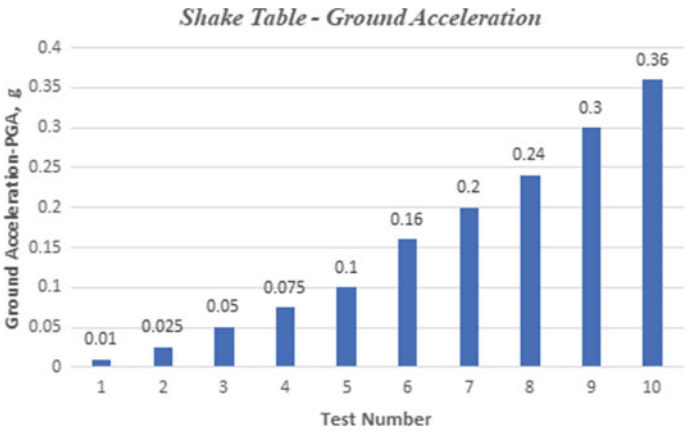


**Fig. 10** Ground acceleration details

## 5 Results and Discussions

### *5.1 Free Vibration Test*

Response acceleration measured at the last loading level of the loaded specimen was used to calculate natural frequency and damping using Fast Fourier Transform (FFT) and half power bandwidth method, respectively. A typical time history response of a free vibration test is shown in Fig. 11. Free vibration tests were carried out on the structure, with and without added pallet mass.

The predominant frequencies and its corresponding damping values of both the specimens are listed in Table 5.

It was observed that the frequency of the braced system (specimen 1) remained same for both the pulse excitations, though there was an increase in damping. For

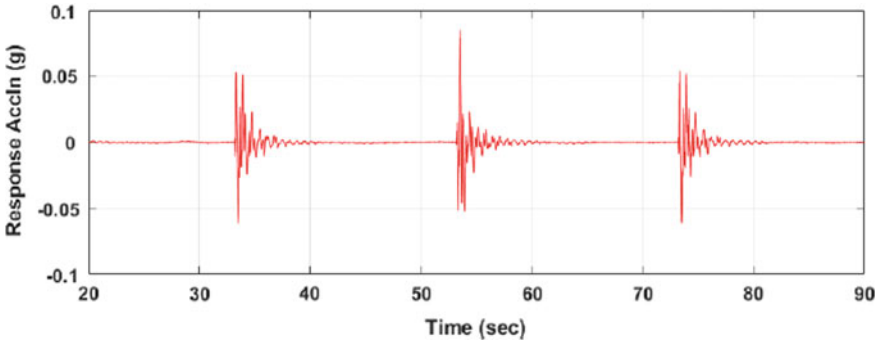


**Fig. 11** Typical time history response for free vibration (pulse excitation)

**Table 5** Predominant frequencies and damping

| | Specimen 1 | | Specimen 2 | |
|---|---|---|---|---|
| | 1 mm pulse | 3 mm pulse | 1 mm pulse | 3 mm pulse |
| Frequency (Hz) | 1.318 | 1.318 | 1.929 | 0.5127 |
| Damping | 0.021 | 0.068 | 0.021 | 0.07 |

unbraced system (specimen 2), the frequency dropped drastically with increase in pulse associated with increase in damping. It should be noted that the damping values of both braced and unbraced system are same. However, a change is noticed for the frequency of the two systems.

## *5.2 Shake Table Test*

In shake table test, the displacement–time history, acceleration-time history and dynamic strains were recorded for every acceleration cycle. The recorded displacement was the total displacement (structure displacement + table input). Suitable corrections were made on the recorded responses to arrive at absolute displacement response of the structure. This is presented in Figs. 12 and 13 for specimens 1 and 2, respectively. From the figure, it is seen that for 0.36 g acceleration, the maximum displacement of level 4 with respect to the base was 1.84 times that of specimen 2 as shown in Figs. 12 and 13, respectively. The maximum inter-storey drift between levels 3 and 4 of the specimen 1 was 2 times that of inter-storey drift between levels 1 and 2 of specimen 2 in the down aisle direction. The acceleration response of braced system being stiffer falls in the plateau of the spectral acceleration curve. Hence, it experiences very high lateral loads. Unbraced system having higher time period experiences lesser lateral loads.

For each shake table test, the accelerometers were placed on all levels and on pallets as shown in Figs. 7 and 8. The recorded acceleration response of the structure for specimen 1 and specimen 2 is shown in Figs. 14 and 15. From these figures, the magnification of the response acceleration in the last loading level is clearly seen.

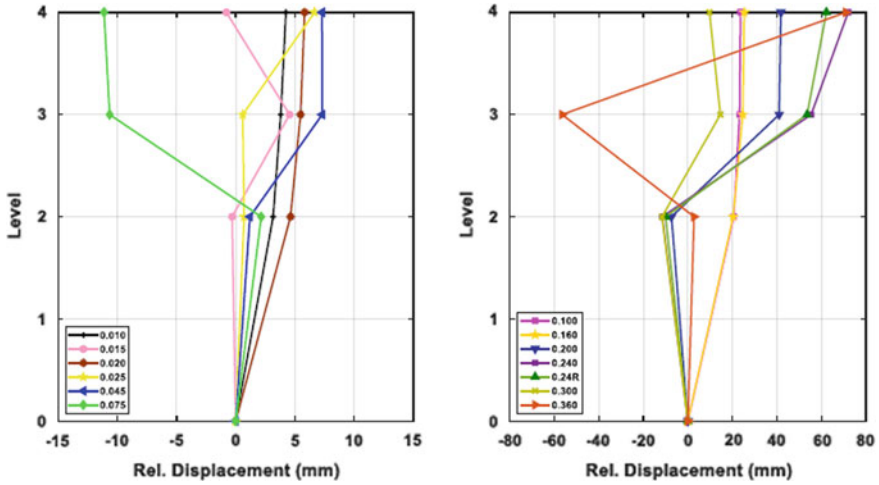


**Fig. 12** Variation of mean displacement in down aisle direction across levels—specimen 1

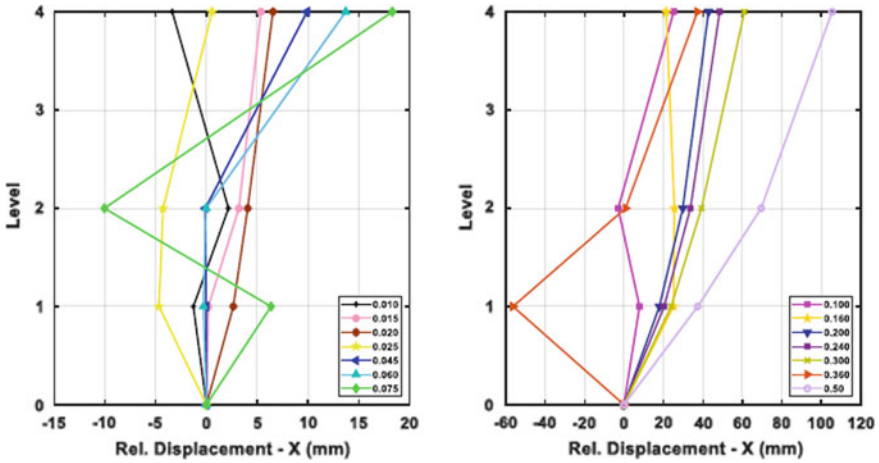


**Fig. 13** Variation of mean displacement in down aisle direction across levels—specimen 2

## 6 Observations from the Test

After every test, the overall structure was inspected to check for any component-level damages. No global collapse or component damage occurred at the end of seismic tests. Some loosening of bracing fasteners—M10 Hex Nut—above 0.16 g PGA was witnessed. No pull out of anchor bolts or damage to the base plate was seen during the entire test.

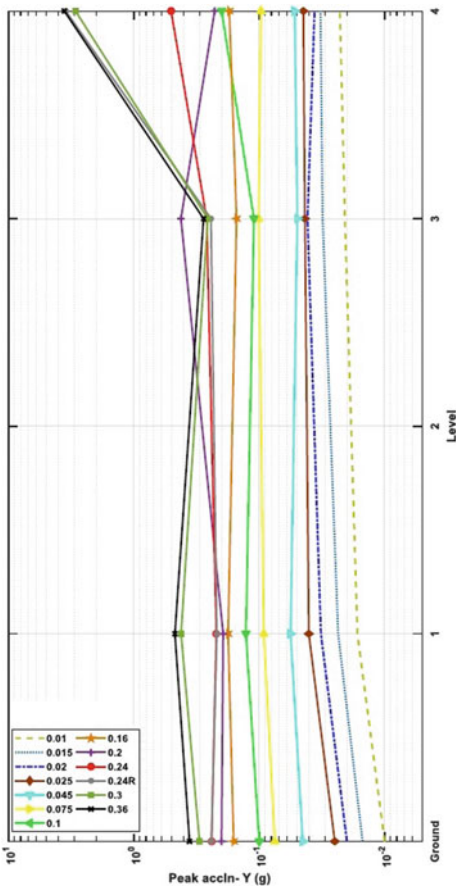


**Fig. 14** Variation of peak acceleration across levels in specimen 1

Both specimen 1—braced racks—and specimen 2—unbraced racks—withstood the seismic ground acceleration up to 0.36 g without any failure or collapse. The recorded permanent displacement of the structure when subjected to an acceleration of 0.36 g is listed in Table 6. The maximum residual horizontal deflection for the specimen 1 (braced) was 22.78 mm (Leg 1) and specimen 2 (unbraced) was 52.08 mm (Leg 2). It is surmised that the spine bracings have played a positive role in bringing back the system closer to the initial condition as compared to the unbraced system.

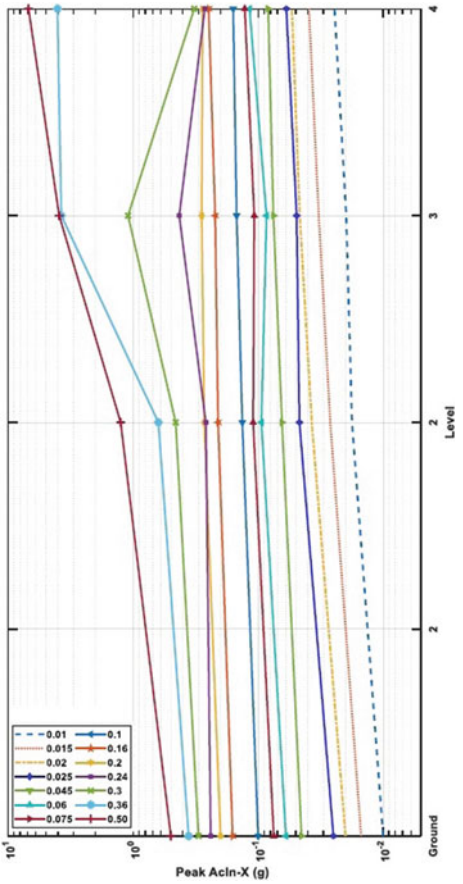


**Fig. 15** Variation of peak acceleration across levels in specimen 2

Careful examination of the members after dismantling revealed bent/deformed bolts used for the connection between diagonal bracing and upright. It was observed at 0.16 g that tabs of the connectors were slightly cutting into the upright slots at corners. However, it was not propagating further up to 0.36 g. No pallet displacement was observed till 0.36 g acceleration. Indentations and paint peel-offs were seen on all four base plates. Removal of base plates from the RCC slabs revealed concrete chip-offs near the anchor bolts.

## 7 Conclusions

The full-scale shake table tests could quantify the natural frequencies and damping of both unbraced and braced pallet racking system. The performance of braced system was significantly better compared to unbraced system with respect to stiffness and

**Table 6** Permanent displacement of the structure after 0.36 g

| | Leg 1 | Leg 4 | Leg 1 | Leg 4 | Leg 1 | Leg 2 | Leg 1 | Leg 2 | Leg 1 | Leg 2 |
|---|---|---|---|---|---|---|---|---|---|---|
| | L1-CA | L6-CA | L7-CA | L10-CA | L2-CA | L3-CA | L4-DA | L5-DA | L8-DA | L9-DA |
| Specimen 1 | 17.22 | − 0.66 | 22.78 | − 4.8 | − 8.61 | − 4.51 | − 11.37 | − 6.46 | − 12.3 | − 5.89 |
| Specimen 2 | − 10.87 | − 14.93 | − 16.33 | − 26.8 | 7.78 | 9.5 | 20.84 | 24.1 | 48.77 | 52.08 |

consistent natural frequency. The damping witnessed during testing agrees well with those adopted based on codal stipulation. The pallets resting on the beam did not have relative motion with respect to the beam and frame up to 0.36 g. The pallets also did not show any relative motion or slipping between frame and beam which indicate that the friction between the pallet and the support beam was adequate to prevent falling of the pallet during an earthquake. The shake table test has revealed limited damages and no collapse under a severe acceleration of 0.36 g at foundation level. This can be considered as satisfactory performance meeting the requirements of both life safety under Design Basis Earthquake (DBE) and collapse prevention performance under Maximum Considered Earthquake (MCE) as prescribed in FEMA 460 [3].

## References

1. Castiglioni CA (2008) Seismic behaviour of steel storage pallet racking systems. Structural Engineering Department of Politecnico di Milano, Milano
2. Chen CK, Scholl RE, Blume JA (1980) Earthquake simulation tests of industrial steel storage racks
3. FEMA 460 (2005) Seismic considerations for steel storage racks located in areas accessible to the public
4. IS 1893 (Part 1):2016 Criteria for earthquake resistant design of structure
5. John AB & Associates (1973) Seismic investigation of steel industrial storage racks
6. Kircher CA, Krawinkler H et al (1979) Experimental study on the seismic behavior of industrial storage racks
7. Saravanan M, Marimuthu V, Prabha P, Surendran M (2014) Seismic characterization of cold formed steel pallet racks
8. SEISRACK (2009) Storage racks in seismic areas. Research Programme of the Research Fund for Coal and Steel

# Spectral-Based Fatigue Analysis of a Semi-submersible Platform


**K. Sreejith and T. M. Madhavan Pillai**

**Abstract** Offshore structures are exposed to wide range of cyclic loadings which causes fatigue damage and hence it is an important design consideration which determines the durability of the structure. Due to the complexity of the random loading conditions, determination of fatigue life is a tedious task. Therefore, it is important to develop a reasonable loading spectrum for fatigue assessment using cumulative fatigue damage (CFD) theory. There are few methods by which we can predict fatigue life of a structure which include fatigue crack propagation (FCP) model, by using conventional empirical relations and by developing fatigue stress response spectrum. In this paper, fatigue life of a semi-submersible platform is determined by analyzing critical joints which are exposed to cyclic loading and also by considering random numbers of short-term wave conditions which follow Rayleigh distribution. Structure considered for the study is a sixth-generation semi-submersible platform known as COSL Prospector made in CIMC Yantai Raffles shipyard in China designed for North Sea. Firstly, a hydrodynamic diffraction analysis is carried out in order to understand the response of the structure under various wave directions and frequencies. Wave-induced pressure on the column-bracing connections are determined and these joints are considered as critical locations for fatigue analysis. Suitable wave spectrum is then developed for each sea state conditions. In order to determine the stress concentration factor of the column-bracing joint, a local geometrical model of the connection is created followed by generating a fatigue stress energy spectrum and complex fatigue stress transfer function which is later described to the model. The minimum fatigue life of the local model is determined, and the results are compared with the specification required.

K. Sreejith (✉) · T. M. Madhavan Pillai
National Institute of Technology, Calicut, India
e-mail: sreejithkkg@gmail.com

T. M. Madhavan Pillai
e-mail: mpillai@nitc.ac.in

K. Sreejith
Vimal Jyothi Engineering College, Kannur, India



M. Madhavan et al. (eds.), *Proceedings of the Indian Structural Steel Conference 2020 (Vol. 1)*, Lecture Notes in Civil Engineering 318,
https://doi.org/10.1007/978-981-19-9390-9_16

**Keywords** Semisubmersible · Fatigue analysis · Wave spectrum · Sea scatter diagram · Stress concentration factor · P-M rule · Hydrodynamic analysis

## 1 Introduction

An offshore structure can be defined as those structures which are constructed on deep ocean mainly for oil exploration, and are able to withstand wide range of complex marine environment. Offshore structures are generally classified into three types: fixed structures which are designed to withstand lateral forces without any considerable displacement, compliant structures can undergo substantial displacement without damaging the integrity of the structure and are hinged to seabed and floating structures which are capable of moving from one field to another and can be used for larger water depths. Semisubmersibles are the most common floating structures which consist of a deck supported on columns which are attached to pontoons. Diagonal cross bracings are provided to resist the prying and racking loads by waves. Floating structures are flexible in nature which resist the lateral forces by global displacement. A semisubmersible offers better response to motion and also equal resistance to wave, current and wind from any direction. It also has the ability to support a mooring system and a large deck area, and better stability due to reduced response in roll and pitch motion.

In this paper, fatigue problems of semi-submersible structure are taken into consideration which is an important factor in offshore and wind power industry. Fatigue analysis should be performed during the design stage in order to ensure that the structure has adequate fatigue life. In addition, regular maintenance, carefully planned inspection and repairs are required from time to time to ensure the safety and operability of the floating structure during its design life.

## 2 Hydrodynamic Diffraction

### *2.1 Semisubmersible*

In this paper, a four-column semisubmersible based on GG5000 design is used. Also known as COSL Prospector, it is sixth-generation semi-submersible platform designed for work in cold temperature with class notation ICE-T and Winterized Basic with covers of working areas and lifeboat stations. The unit is designed for North Sea and is developed in CIMC Yantai Raffles shipyard in China. Station keeping of the structure is maintained by dynamic positioning of variable speed thrusters or by catenary mooring system. Figure 1 shows the meshed geometric model of the structure.

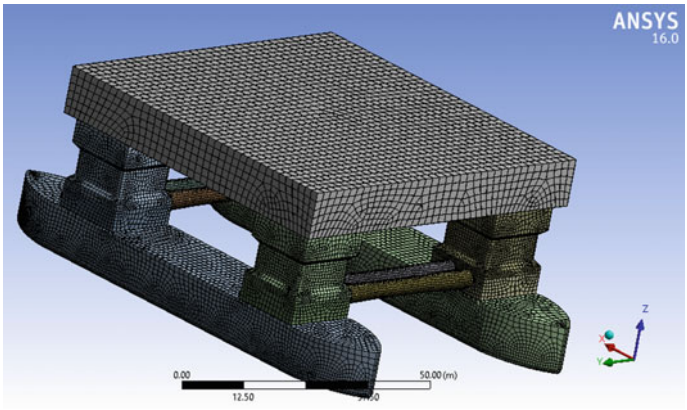


**Fig. 1** COSL prospector

## *2.2 Modelling*

Main dimensions of the structure [1] are given in Table 1. Solidworks Premium has been used to make the model geometry due to its simple user interface. Both modelling and analysis is done in Intel(R) Core™ i5-5200U CPU @ 2.20 GHz, having a RAM 8 GB and 64-bit operating Microsoft Windows OS. For neutrally buoyant structures, the effect of mooring lines on the structure is relatively less for larger units but high for smaller units. Current velocity has not been considered and the interaction of wave and current has been ignored. The effect of wind on the structure is not considered since it is negligible with respect to the impact produced by the wave. The model is exported into Ansys-Aqwa in parasolid format. Total mass of the structure is provided as point mass in centroid of the structure.

Since hydrodynamic diffraction follows finite element method of analysis, response of the structure is sensitive to mesh element size. Finer the mesh, more accurate will be the result. Hence, finer mesh cannot be used for large structures. Element size should be selected in such a way that it offers integrity of the structures, i.e. meshing will be continuous so that load acting on the structures should be transferred effectively through the mesh element boundaries. In this study, the whole unit is meshed, even though only the diffracting elements (below water surface) are used in hydrodynamic runs. Overall structure is divided into upper portion and lower submerged portion by slicing tool corresponding to the draft provided. Default wave range of − 180° to 180° is given; in addition to that a reasonable range of 0° to 180° with an interval of 15° is used because of the symmetry of the structure. However, only head sea (0°) will be regarded in this assessment as this heading will offer the highest response.

**Table 1** Main dimensions and input parameters

| Parameter | Dimension |
|---|---|
| Length of pontoon | 104.50 m |
| Height of pontoon | 10.05 m |
| Width of pontoon | 70.50 m |
| Height (box bottom) | 29.50 m |
| Draft | 14.50 m |
| Weight | 36141 t |
| Metacentric height | |
| $GM_T$ | 2.8 m |
| $GM_L$ | 3.96 m |
| Water plane area | 1249.595 $m^2$ |
| Water depth | 300 m |
| Radii of gyration | |
| $r_{xx}$ | 30.20 m |
| $r_{yy}$ | 31.80 m |
| $r_{zz}$ | 34.80 m |

Wave-induced pressure on the structure for various directions are calculated and the most critical condition is selected as is shown in Fig. 2. It is observed that stress concentrations occur at brace-column connection and is susceptible to fatigue damage. These locations are considered as the main case for the fatigue analysis in the following sections.

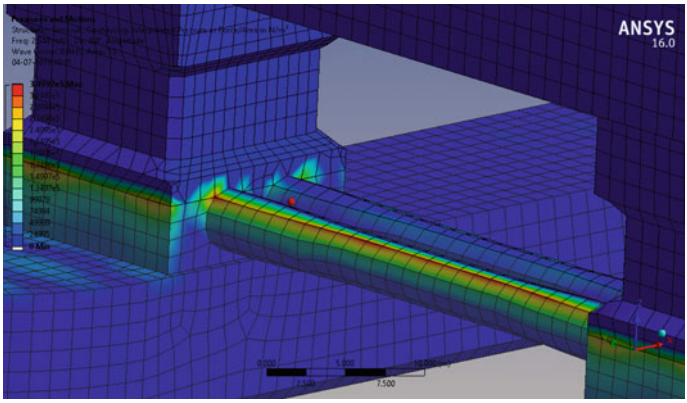


**Fig. 2** Stress concentration

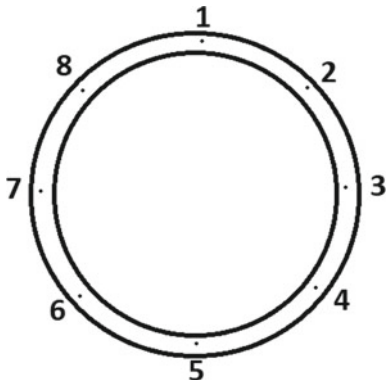


**Fig. 3** Critical locations considered around the joint

## 3 Stress Concentration Factor

Hot-spot stress includes all the stress concentrating features of a welded joint except that due to the local weld toe geometry. The hot-spot stress method has been widely used in the design of steel tubular structures. Since offshore structures are exposed to different types of loading environment, stress variations especially in joints are high when compared with other parts of the structure.

Fatigue lives of joint is estimated by determining the hot-spot stress range (HSSR) for the different locations considered around the joint. Stress concentration factor at a location can be defined as the ratio of HSSR at a particular location to nominal stress acting on the joint. The hot-spot locations considered in the analysis are shown in Fig. 3. Minimum eight locations around the welded joint [2] section should be considered in order to cover all the relevant hot-spot stress areas.

## 4 Fatigue Analysis

In this study, the brace-column link is considered as the critical point. Even though the actual structure is situated in North Sea, the effect of waves on the structure if it is placed on Indian Ocean is actually discussed in this paper. Wave data of Indian Ocean is obtained from the official website of European Centre for Medium-Range Weather Forecasts. The sea scatter diagram is shown in Table 2.

Different sea spectrums are used for different locations. Most commonly used spectrum in Asia & Gulf of Mexico is the P-M spectrum, this spectrum assumes that wind is blown steadily for a long time which covers a large area; thus, the waves would come to equilibrium and the state is known as fully developed sea state. P-M spectrum is used in this paper as the wave spectrum for further analysis, since this spectrum is widely used in Indian Ocean. Using Eq. 1 and the sea scatter diagram, spectrum is plotted for each sea state. A total of 13 sea states are used in this work for the fatigue analysis.

**Table 2** Sea scatter diagram

| $H_s$(m)/ $T_z$(Sec) | 0–2 | 2–4 | 4–6 | 6–8 | 8–10 | 10–12 | Probability of occurrences (%) |
|---|---|---|---|---|---|---|---|
| 0–0.5 | 0 | 0 | 0 | 0.068 | 0 | 0 | 0.069 |
| 0.5–1 | 0 | 0 | 2.47 | 26.78 | 16.92 | 0.41 | 46.58 |
| 1–1.5 | 0 | 0 | 0.48 | 14.59 | 10.41 | 0.48 | 25.96 |
| 1.5–2 | 0 | 0 | 0 | 4.73 | 15.21 | 0.07 | 20 |
| 2–2.5 | 0 | 0 | 0 | 1.10 | 6.03 | 0.07 | 7.19 |
| 2.5–3 | 0 | 0 | 0 | 0.21 | 0 | 0 | 0.21 |
| Total | 0 | 0 | 2.95 | 47.47 | 48.56 | 1.03 | **100** |

$$S_\eta(\omega|H_s, T_z) = (H_s^2/4\pi)(2\pi/T_z)^4\omega^{-5}e^{\left(\frac{\omega^{-4}}{\pi}\left(\frac{2\pi}{T_z}\right)^4\right)} \quad (1)$$

where $H_s$ denotes the significant wave height, $T_z$ denotes zeroth up-crossing period and $\omega$ represents the wave frequency.

A local model of a brace-column connection is constructed as per the guidelines described in DNV recommended practice. Stress concentration factor (SCF) is determined by considering unit axial loads, in-plane (IP) and out-of-plane (OOP) bending moments. Shell plating and inner strengthening members of the brace-column connection are considered in the local geometry model [3]. While doing the finite element analysis, mesh is refined around the region of interest and stresses at the corresponding locations are determined. Mesh refinement provided at the local model is shown in Fig. 4.

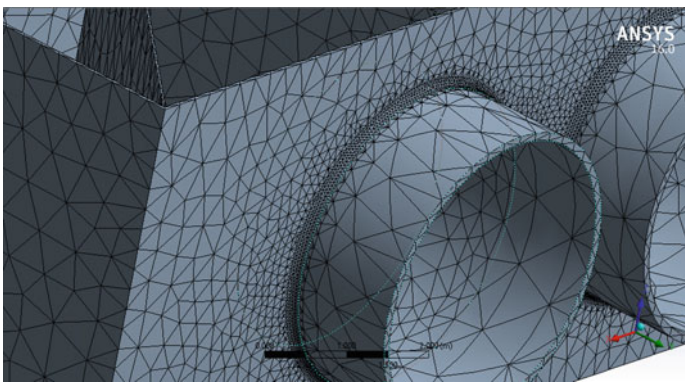


**Fig. 4** Mesh refinement for local geometrical model

## 5 Stress Transfer Function

According to *ABS Guidelines on Spectral-Based Fatigue Analysis for Floating Offshore Structures,* stress transfer function denotes the relation between stress at structural locations and the unit amplitude incident wave of frequency ($\omega$) and wave heading ($\theta$). Usually, the frequency range is specified within 0.2–1.8 rad/s with an increment not greater than 0.1 rad/s. However, depending on the characteristics of the response, it will be convenient to use different frequency range. Using the axial forces and moments obtained from the analysis of global model of the brace-column connection together with the SCFs at location under consideration, hot-spot stresses in MPa/m (since they are estimated for a wave having unit amplitude) can be evaluated at each position as follows [4]:

$$X(\omega) = \mathrm{SCF_{AX}}.\frac{N(\omega)}{A} - \mathrm{SCF_{IPB}}.\frac{M\mathrm{ipb}(\omega)}{I}.z' - \mathrm{SCF_{OOB}}.\frac{M\mathrm{oob}(\omega)}{I}.y' \tag{2}$$

The hot-spot response spectrum $S_\sigma(\omega)$ for a stress random process $X(\omega)$ is calculated by multiplying the square of hot-spot stress transfer function obtained from above equation with the wave spectrum. In this paper, only short-term sea state is considered and waves are uni-directional so that spreading function is neglected. Equation for hot-spot stress response spectrum is given by Eq. 3.

$$S_\sigma(\omega) = S_\eta(\omega|H_\mathrm{s}, T_\mathrm{z}).|X(\omega)|^2 \tag{3}$$

After getting the stress response spectrum, spectral moments are calculated which is used to define the probability density function (*pdf*) for a sea state. Same procedure is repeated to find *pdf* for the entire sea state and finally, fatigue damage is then calculated and corresponding fatigue life is estimated of each critical location which are considered.

## 6 Spectrum Based Fatigue Assessment

The stress range developed on the structure is usually expressed in terms of probability density functions for different short-term sea states corresponding to the wave scatter diagram. After determining the stress energy spectrum, spectral moments are calculated [5] and are given by Eq. 4.

$$m_n = \int_0^\infty \omega^n.S_\sigma(\omega|H_\mathrm{s}, T_\mathrm{z})\mathrm{d}\omega \tag{4}$$

Since it is assumed that the wave conditions follow Rayleigh probability density function ($g(s)$) which denotes the short-term stress range distribution [6], the zero up-crossing frequency ($f$) of the stress response is calculated and is given by Eqs. 5 and 6.

$$g(s) = \frac{S}{4\sigma^2}.e^{\left(-\left(\frac{S}{2\sqrt{2}\sigma}\right)^2\right)} \tag{5}$$

where $S$ is the stress range, i.e. twice the stress amplitude, $\sigma$ is the square root of zeroth spectral moments.

$$f = \frac{1}{2\pi}\sqrt{\frac{m_2}{m_0}} \tag{6}$$

where $m_0$, $m_2$ are the zeroth and second spectral moments.

After determining the short-term damage, the total fatigue damage is calculated using Palmgren Miner rule which assumes cumulative fatigue damage ($D$) as a group of variable amplitude stress cycles which is the sum of the damage induced by each stress cycle ($d_\mathrm{i}$). Failure is predicted to occur when the cumulative damage ($D$) over $N$ loading cycles exceeds the critical value. Summing $D_\mathrm{i}$ over all the sea states given in the wave scatter diagram will give the total cumulative damage $D$.

$$D = \left(\frac{f_0 T}{A}\right)\int_0^\infty S^m\left(\sum f_{0\mathrm{i}}\frac{p_\mathrm{i} g_\mathrm{i}}{f_0}\right)\mathrm{d}s \tag{7}$$

where $f_0$ average frequency of $S$ over the lifetime.

## 7 Results and Discussion

The results on fatigue life of different critical locations which are prone to high fatigue damage is determined and is given in Table 3. The fatigue damage of location 3 is the lowest and fatigue life of location 6 is the shortest. The stress concentration is more evident in this sea state. However, it meets the specification requirement since minimum design life for a floating offshore structure as per the *ABS rules for Building and Classing Mobile Offshore Drilling Unit* is 25 years. The locations having significant stress concentration needs to reinforce when it is designed for ensuring sufficient fatigue strength in service.

**Table 3** Fatigue life of critical locations

| Location | Fatigue damage | Fatigue life (Yrs) |
|---|---|---|
| 1 | 0.01974 | 50.66 |
| 2 | 0.01739 | 57.51 |
| 3 | 0.01464 | 68.32 |
| 4 | 0.01779 | 56.21 |
| 5 | 0.01590 | 62.91 |
| 6 | 0.01986 | 50.36 |
| 7 | 0.01833 | 54.57 |
| 8 | 0.01755 | 56.98 |

## 8 Conclusions

Semisubmersibles are susceptible to fatigue action due repeated application of wave loads, and hence should be adequately assessed while designing the structure. A spectral-based fatigue analysis will provide an effective and reliable technique for performing fatigue evaluation of offshore structures considering the distribution of wave energy across the entire frequency range and incorporating representative structural dynamics in the analysis. The fatigue life of the brace-column attachment meets the specifications. The locations considered are susceptible to fatigue damage and must be reinforced when it is designed for ensuring enough fatigue strength in service.

## References

1. Pedersen EA (2012) Motion analysis of semi-submersible. Norwegian University of Science and Technology, pp 1–20
2. Veritas DN (2015) Fatigue design of offshore steel structures. In: Recommended practice DNV-RP-C203, HØVIK, Norway, pp 32–33
3. Offshore Technology Report-OTO 2000 052 (2000) fatigue reliability of old semi-submersibles, Det Norske Veritas, pp 14–20
4. Manuel L, Nguyen HH (2015) Fatigue reliability analysis for brace-column connection details in a semisubmersible hull. J Offshore Mech Artic Eng 137:1–7
5. American Bureau of Shipping Guide (2017) Spectral based fatigue analysis for vessels, pp 26–28
6. Cui L, Xu J, He Y, Jin W (2010) Fatigue analysis on key components of semi-submersible platform. In: International conference on Ocean, offshore and artic engineering, pp 1–5

# Analysis and Design of Industrial Structure with Overhead Travelling Crane Using Pre-engineered Building Concept: A Case Study Comparing Indian and American Standards


**Mehul Radhakrishnan, A. S. Santhi, and A. Kailasa Rao**

**Abstract** Pre-engineered building is a new form of construction practice that is slowly emerging in Indian construction industry, which has large potential to replace conventional steel structure. The objective of this research paper is analogous examination of analysis and design of PEB structure with EOT crane, according to Indian Standards (Chia-Ming and Jong-Kook in J Constr Steel Res 70:248–255, 2011; Bureau of Indian Standards in Indian Standard General Construction in Steel Code of Practice (IS 800:2007), pp 1–143, 2007; Bureau of Indian Standards in Indian Standard Code of Practice for Design loads (other than earthquake) for Buildings and Structures Part-1 Dead Loads (IS 875 Part-1), pp 1–37, 1989; Bureau of Indian Standards in Indian Standard Code of Practice for Design loads (other than earthquake) for Buildings and Structures Part-2 Imposed Loads (IS 875 Part-2), pp 4–18, 1989; Bureau of Indian Standards in Indian Standard Code of Practice for Design loads (other than earthquake) for Buildings and Structures Part-3 Wind Loads (IS 875 Part-3), pp 1–56, 2015) and American Standards (Metal Building Manufacturers Association in Metal Building Systems Manual, pp 1–335, 2012; ANSI/AISC 360-10 Specification for Structural Steel Buildings. Chicago, IL: American Institute of Steel Construction, 2010; ASCE/SEI 7-10 in Minimum Design Loads for Buildings and Other Structures. Reston, VA: American Society of Civil Engineers, 2010). This paper presents comparative results of different clauses in each of the above-mentioned codes and its results in terms of economical aspect, percentage difference of member capacities and deflection criteria under same primary loading conditions and distinct impact factor considered for frames and Crane Gantry Beam design. This

M. Radhakrishnan (✉) · A. S. Santhi
School of Civil Engineering, VIT, Vellore, India
e-mail: mehul.radhakrishnan@vitstudent.ac.in

A. S. Santhi
e-mail: as_santhi@vit.ac.in

A. Kailasa Rao
Phenix Construction Technologies, Hyderabad, India
e-mail: akrao@mbphenix.com



M. Madhavan et al. (eds.), *Proceedings of the Indian Structural Steel Conference 2020 (Vol. 1)*, Lecture Notes in Civil Engineering 318,
https://doi.org/10.1007/978-981-19-9390-9_17

analytical study would further help for in-depth understanding of design philosophy used by Indian Standards and American Standards used for designing. The scope of our study is only with regards to gravity loading, crane loading, prevailing wind loading conditions and their combinations as per IS: 800-2007 and ASCE-7-10.

**Keywords** Web-tapered sections · Pre-engineered building · Crane impact factor · Shear-bending capacities · Utility ratio · Deflection limits · Flange brace

## 1 Introduction

Pre-engineered buildings are those structures which are customized according to client's requirements, which are further, erected, assembled at site using bolted connections. Pre-engineered buildings are characterized by the use of web-tapered sections for main frame column, rafters and floor beams. Such structures consume lesser amount of steel about 20 per cent when compared with a conventional steel structure. The concept of using web-tapered section [1] depends on the frame geometry that mostly matched with the bending moment diagram and appropriate depth of section is assigned to that particular member. Thus pre-engineered structure leads to optimization of material usage, thereby reducing the cost of structure. The present studies revolve around a concise examination between Indian Standards and American Standards used for the conception of steel structure, the design philosophy used are Load Resistance Factor Design which is followed in AISC 360-10 and Limit State design philosophy used in IS800:2007. The analysis has been done for an industrial building with over-head travelling crane on it and Staad-Pro Programme was utilized for the analysis, wherein a 2-D moment frame [2] geometry was modelled and all the in-plane loading conditions and combinations associated with the structure were applied. The crane runway girders system comprises of crane rails, rail attachments, crane bracket and crane gantry girders. All these different components are considered for design and detailing of crane system. For design of runway beam, distinct impact factor as per codal provisions is considered, and the beam is designed for maximum shear force and bending moment using influence line concept. The analysis of main frame is done considering alternate minimum and maximum reaction including horizontal load which is inclusive of impact factor fraction. These forces are calculated considering minimum hook approach.

## 2 Structural Configuration

Table 1 shows the configuration of structure considered for present study. The building has one aisle of crane runway which has a width of 24 m travelling entire length of the building.

The basic structural configuration is showcased in Fig. 1, depicting length of various segments such as rafter (eave-piece), rafter (ridge-piece) and crane brackets.

**Table 1** Configuration

| S. no | Parameters | Constraints |
|---|---|---|
| 1 | Location | : Hyderabad, India |
| 2 | Width | : 24 m |
| 3 | Length | : 40 m |
| 4 | Height | : 9.5 m |
| 5 | Slope | : 1:10 |
| 6 | Angle of roof | : 5.71° |
| 7 | Wind speed | : 44 m/s |
| 8 | Life span | : 50 years |
| 9 | Crane capacity | : 10 tonnes |
| 10 | Purlin spacing | : 1.50 m c/c |
| 11 | Girt spacing | : 2 m c/c |
| 12 | Bay spacing | : 8 m c/c |
| 13 | Block wall height | : 3 m |

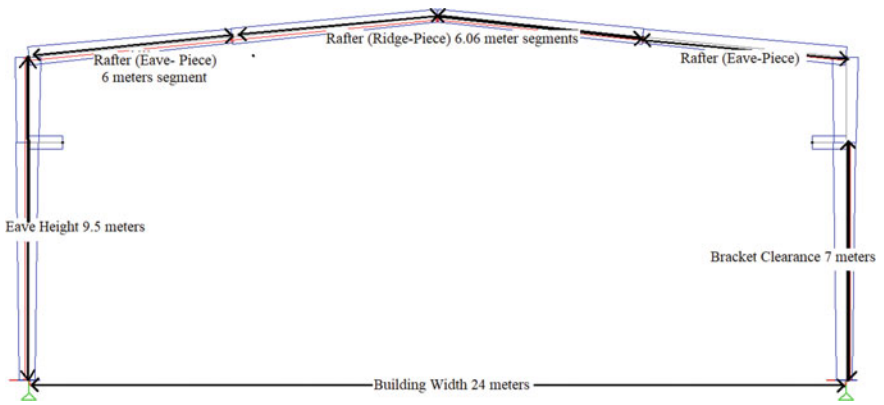


**Fig. 1** Structural configuration

**Table 2** Dead load

| S. no | Element | Weight |
|---|---|---|
| 1 | Sheeting weight | 4.75 kg/sq m (0.5 mm thick) |
| 2 | Purlin weight | 4.71 kg/m unit weight/purlin spacing = 3.14 kg/sq m |
| 3 | Sag rod weight | 1.05 kg/m unit weight/purlin spacing = 0.26 kg/sq m |
| 4 | Insulation weight | 48 kg/Cu m (50 mm) unit weight = 2.40 kg/sq m |
| | Total load | 10.55 kg/Sq m or 0.1055 kN/Sq m |

## 3 Calculation of Loads

The distinct categories of loads acting on the main frame are dead load, live load, wind load and crane load. The following sections shows basic calculation of different loads acting on frame.

### *3.1 Dead Load Calculation*

Dead load includes weight of sheeting material, purlins, sag rods and insulation material. The sheeting material is Galvalume (Al–Zn) of thickness of 0.50 mm.

The insulation material is made up of glass fibres having a thickness of 50 mm and of density of 48 kg/m$^3$. The cross section of purlin is in the form of '*Z*' considered at a spacing of 1.50 m c/c, Table 2 depicts arithmetic computation of dead load.

### *3.2 Live Load Computation*

Distinct live load intensity described in IS 875-Part-2 [3] and in ASCE 7-10 are described in Table 3.

The live load considered by IS 875-Part-2 is 1.31 times of load considered by ASCE 7-10 [4]/MBMA [5].

**Table 3** Live load

| Code | IS 875-Part-2 [3] | ASCE-7-10 |
|---|---|---|
| Live load | 0.75 kN/Sq m | 0.58 kN/Sq m (reduced as per Clause 4.8.2) |

**Table 4** Basic wind load calculation as per IS 875(Part-3) [6]

| S. no | Parameters | Value |
|---|---|---|
| 1 | Basic wind speed ($V_b$) | 44 m/s |
| 2 | Probable design life | 50 years |
| 3 | Percentage of opening | 5% |
| 4 | Risk coefficient ($K_1$) | 1 |
| 5 | Terrain roughness and height factor ($K_2$) | 1 |
| 6 | Topography factor ($K_3$) | 1 |
| 7 | Importance factor ($K_4$) | 1 |
| 8 | Design wind speed $(V_Z) = V_b * K_1 * K_2 * K_3 * K_4$ | 44 m/s |
| 9 | Design wind pressure $(P_Z) = 0.6 * (V_Z)^2$ | 1.1616 KN/m$^2$ |
| 10 | Reduction of $P_Z$ for $H < 10$ m | $0.8 * 1.1616 =$ 0.9292 KN/m$^2$ |
| 11 | Net $P_Z$ considered is | 0.9292 KN/m$^2$ |
| 12 | Internal pressure coefficients ($C_{pi}$) | + 0.2 or − 0.2 |

## *3.3 Wind Load Calculations*

### 3.3.1 Calculation According to Indian Standards, IS 875 (Part-3) [6] and American Standards ASCE 7-10 [4] and MBMA [5]

Basic wind load calculation procedure to obtain wind pressure according to IS 875(Part-3) [6] and ASCE-7-10 [4] is explained in Tables 4 and 5 of this section. The wind loads are considered in planar perspective, i.e. wind acting from left to right and right to left considering the phenomenon of suction or negative pressure as well as positive pressure. It is assumed that the wind pressure acting on the frame was in form of uniformly distributed load [7] along the member length. The wind pressure on main frame was calculated using Cl. 7.3.1 [6] and Eq. 28.4-1 [4].

The structure considered for the study has a 5% opening and the location of structure is in Hyderabad, India. The appropriate wind speed and all other prevailing conditions are considered for the design wind pressure.

## *3.4 Crane Load Calculations*

For the analysis and design of crane runway beam, the distinct impact factor fractions for both the standards and the factored load for design are showcased in Table 6.

**Table 5** Basic wind load calculation as per ASCE7-10 [4] and MBMA [5].

| S. no | Parameters | Value |
|---|---|---|
| 1 | Basic wind speed ($V$) | 98.42 mph |
| 2 | Developed suburban exposure category | Category B |
| 3 | Slope ($\theta$) | 5.77° < 10° |
| | | Developed height = eave height which is 9.5 m |
| 4 | Velocity pressure $q_h = 0.00256 K_Z * 1 * 0.85 * V^2$ | 15.2 lb/$f^2$ (also from table 1.3.4.4 MBMA-2012) |
| 5 | Positive internal pressure (+i) | |
| 6 | The coefficients (Gcpi-Gcpe) | From table 1.3.4.5 (a) MBMA-2012 |
| 7 | Similarly for negative pressure (+i) | |
| 8 | The net pressure is calculated as ($q_h$) | (15.2 pounds/feet) or 0.722 kN/m$^2$ |

**Table 6** Design crane load for runway beam considering impact factor

| S. no | Code/Standards | IS 875 (Part-2) 1987 | MBMA-2012 |
|---|---|---|---|
| 1 | Vertical impact factor | 25% | 10% |
| 2 | Wheel loads | 82.7 kN | 82.7 kN |
| 3 | Factored design load | 103.375 kN | 90.97 kN |

The crane reaction horizontal as well as vertical considering the minimum hook approach are described in Table 7. For the design of frame with crane, the lateral movement and its location plays an important role. The crane loading conditions are illustrated in Fig. 2 and four distinct loading conditions are:

1. Maximum wheel load at the left end of crane bridge and minimum wheel at right end of crane bridge, acting concurrently with the lateral force directed towards left side.

**Table 7** Crane reaction (vertical and horizontal) on main frame

| S. no | Reaction type | IS 875:1987 (Part-2) | MBMA/ASCE 7-10 |
|---|---|---|---|
| 1 | **Vertical reaction** | (25% impact factor) | (No factor) |
| | Min reaction | 38 kN | 38 kN |
| | Max reaction | 154.8 kN | 127 kN |
| 2 | **Horizontal reaction** | 5% of cab wt. + lifting capacity | 20% of cab wt. + lifting capacity |
| | | 5.60 kN (along one side) | 22.4 kN (both sides) |

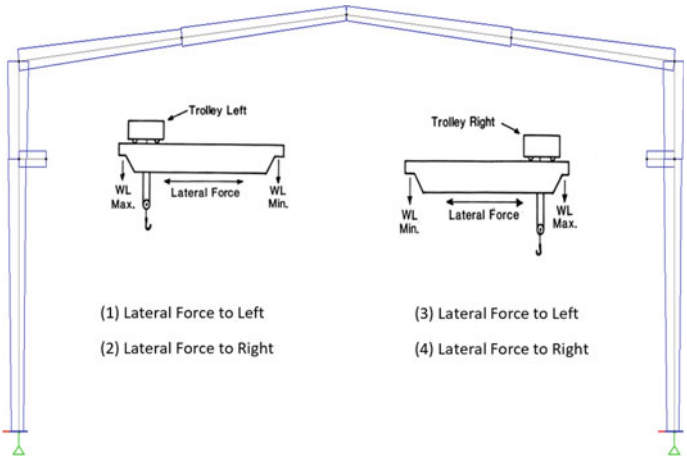


**Fig. 2** Crane loading conditions on main frame

2. Maximum wheel load at the left end of crane bridge and minimum wheel at right end of crane bridge, acting concurrently with the lateral force directed towards right side.
3. Maximum wheel load at the right end of crane bridge and minimum wheel at left end of crane bridge, acting concurrently with the lateral force directed towards left side.
4. Maximum wheel load at the right end of crane bridge and minimum wheel at left end of crane bridge, acting concurrently with the lateral force directed towards right side.

The assumed crane data:

Capacity: 10 T, bridge weight: 12.7 T, crab weight: 1.2 T. Wheel load: 8.27 T, the crane has two wheels on each side with a wheel base of 3.8 m. Table 7 gives details about the crane reaction considered for frame design.

## 4 Load Combination

The load combinations used for analysis are based on Limit State Design [8] and Load Resistance Factor Design (AISC-360-10) which are described in Table 8.

**Table 8** Load combination for IS800:2007 (L.S.D) and AISC-360-10 (L.R.F.D)

| IS 800:2007 combinations | ASCE-7-10 combinations |
|---|---|
| Limit state of strength | Strength design criteria |
| 1. (1.5) DL + (1.5) LL + (1.05) CL | 1. (1. 4) DL |
| 2. (1.2) DL + (1.2) LL + (1.05) CL + (0.6) WL | 2. (1.2) DL + (1.6) LL |
| 3. (1.5) DL + (1.5) LL | 3. (1.2) DL + (1.6) LL + (0.6) WL |
| 4. (1.0) DL + (0.35) LL | 4. (1.2)DL + (1.0) WL + (1.0) LL |
| | 5. (0.9) DL + (1.0) WL |
| Limit state of serviceability | Serviceability criteria |
| 1. (1.0) DL + (1.0) LL + (1.0) CL | 1. (1.0) DL + (1.0) LL |
| 2. (1.0) DL + (0.8) LL + (0.8) CL + (0.8) CL | 2. (1.0) DL + (0.5) LL + (1.0) WL |
| 3. (1.0) DL + (1.0) WL | 3. (1.0) DL + (1.0)$C_{vs}$ + (0.5)$C_{ss}$ + (1.0)$C_{is}$ |
| | 4. (1.0) DL + (1.0) L.L + (1.0)$C_{vs}$ + (1.0)$C_{is}$ + (1.0) WL |
| | 5. (1.0) DL + (1.0)L.L + (1.0)$C_{vs}$ + (1.0)$C_{is}$ + (1.0) $C_{ss}$ + (0.5) WL |

In Table 8 DL refers to dead load, LL refers to live load, CL refers to crane load, $C_{vs}$ refer to vertical load due to crane, $C_{ss}$ refers to side thrust due to crane and $C_{is}$ refers to impact due to crane.

## 5 Staad Programme Design Parameters

Tables 9 and 10 describe in brief about the parameters used in Staad programme module for designing frame using IS800:2007 and AISC-360-10.

**Table 9** Design parameters for IS 800:2007

| S. no | Design parameters | Description |
|---|---|---|
| 1 | **CODE** | **IS 800 LSD** |
| 2 | **FYLD** | **350,000**—yield strength of steel N/mm$^2$, 350 Mpa |
| 3 | **FU** | **490,000**—ultimate strength of steel N/mm$^2$, 490 Mpa |
| 4 | **BEAM** | **1**—designs a member along (1/12th) points from start and end node |
| 5 | **LX** | **Member length**—effective length for lateral torsional |
| | | Buckling which may be (purlin/girt spacing) for columns, rafters, purlins, girts, respectively |

(continued)

**Table 9** (continued)

| S. no | Design parameters | Description |
|---|---|---|
| 6 | **LY** | **Member length**—to compute slenderness ratio (effective length) for buckling about local—*Y* axis (purlin/girt spacing) |
| 7 | **LZ** | **Member length**—to compute slenderness ratio (effective length) for buckling about local—*Z* axis (purlin/girt spacing) |
| 8 | **MAIN** | **0**—default value 180 will be considered |
| 9 | **STP** | **1**—hot-rolled section |
| | | **2**—welded sections |
| 10 | **KZ** | **1.2**—for fixed base **1.5**—for pinned base |

**Table 10** Design parameters for AISC-360-10

| S. no | Design parameters | Description |
|---|---|---|
| 1 | **CODE** | **AISC UNIFIED 2010** |
| 2 | **METHOD** | **LRFD**—load resistance and factor design |
| 3 | **FYLD** | **350,000**—yield strength of steel N/mm$^2$, 350 Mpa |
| 4 | **FU** | **490,000**—ultimate strength of steel N/mm$^2$, 490 Mpa |
| 5 | **BEAM** | **1**—designs at end and at every 1/12th point along member |
| 6 | **LX** | **Member length**—effective length for lateral torsional |
| | | Buckling which may be (purlin/girt spacing) for columns, rafters, purlins, girts, respectively |
| 7 | **LY** | **Member length**—to compute slenderness ratio (effective length) for buckling about local—*Y* axis (purlin/girt spacing) |
| 8 | **LZ** | **Member length**—to compute slenderness ratio (effective length) for buckling about local—*Z* axis (purlin/girt spacing) |
| 9 | **MAIN** | **0**—allowable slenderness limit for compression members 200 are taken |
| 10 | **MTYPE** | **1**—beam (member type) **2**—columns (member type) |
| 11 | **FRM** | **0**—ordinary moment frame |
| 12 | **FLX** | **2**—member has continuous lateral torsional restraint along the length |
| 13 | **CB** | **0**—lateral torsional buckling factor |
| 14 | **UNB** | **Member length**—unsupported length of the bottom flange for calculating flexural strength. Will be used only if compression is in the bottom flange |
| 15 | **UNT** | **Member length**—unsupported length of the bottom flange for calculating flexural strength. Will be used only if compression is in the top flange |
| 16 | **STP** | **1**—hot-rolled section **2**—welded section |
| 17 | **KZ** | **1.2**—for fixed base **1.5**—for pinned base |

The other parameters such as **TRACK** will in getting detail design calculation for capacities such axial force capacity, shear force capacity, bending capacity, utility ratio done by the programme. **CHECK CODE** parameter checks for slenderness ratio limits, effective length [9] and other important aspects.

## 6 Results and Discussions

The column is a web-tapered member which is classified as a semi-compact section according to IS 800:2007(table-2) with flange and web being semi-compact sections. While the same section in AISC-360-10 is classified into two different categories, depending upon nature of force in the member, where in the limiting ratios are distinct for members (stiffened/unstiffened) in compression phase and as well as for flexure phase. In this case for compression, the stiffened part is classified into non-slender section and unstiffened part is classified as slender section according to Table-B4.1-(a)-2 and Table-B4.1-(a)-5, respectively. Similarly, for flexure phase for unstiffened and stiffened parts are classified as non-compact and compact, respectively, according to Table-B4.1-(b)-1 and Table-B4.1-(a)-5. Table 11 highlights the contrast between the member capacities for column section. The rafter member is also a web-tapered section (haunch piece and ridge piece) which is classified as compact and semi-compact, respectively, by IS 800:2007 with flange and web are compact and plastic, and the same rafter section as per AISC-360-10 is classified as (compression) for stiffened and unstiffened as non-slender section, and for flexure phase as compact section for stiffened and unstiffened member, respectively. The contrast is highlighted in Tables 11, 12 and 13.

The $\mathbf{F_X}$ means shear force at base, $\mathbf{F_Y}$ means axial force along the member negative is tension and positive is compression, $\mathbf{M_Z}$ means moment around the major axis. The base reaction obtained is used to design concrete pedestal, base plate and anchor bolt.

## 7 Conclusion

1. From the base reaction results (Table14), it is evident that there are significant differences in moment and vertical reaction by 24.30% and 15.86%, respectively and the difference of 18.01% was obtained from calculations done using Indian Standards [8] and American Standards [10].
2. From the point of view of live load calculation, the difference of load considered in the Indian Standard IS 875-(Part-2)-1987 and the American Standards [4, 5] was 24% apart (Table 3).

**Table 11** Comparison of capacities of column member

| Member type | Member size column piece | S. no | Criteria | IS 800:2007 | AISC-360-10 | Contrast (%) |
|---|---|---|---|---|---|---|
| COLUMN | $d_1$–450 mm (start)<br>$d_2$–750 mm (end)<br>$t_w$–8 mm<br>$t_f$–10 mm<br>$b_f$–200 mm | 1 | **Axial tension capacity** | Section 6.2 | Chapter-D-2 | |
| | | | In yielding | 2367 kN | 2340 kN | 1.14 |
| 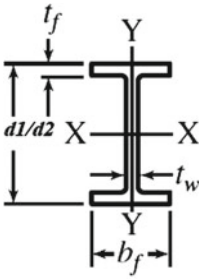 | | | In rupture | 2916 kN | 2730 kN | 6.37 |
| | | 2 | **Axial compression capacity** | Section 7.1.2.2 | Chapter-E7-1 | |
| | | | Major axis buckling | 1369 kN | 1450 kN | 5.58 |
| | | 3 | **Shear capacity of section** | Section 8.2 | Chapter G-2-1 | |
| | | | Capacity | 734.809 kN | 756 kN | 2.80 |
| | | 4 | **Bending capacity of section** | Section 8.2.1.2 | Chapter F2-1 | |
| | | | Major axis bending | 400 kN-m | 394 kN-m | 1.50 |

**Table 12** Comparison of capacities of rafter member

| Member type | Member size haunch piece | S. no | Criteria | IS 800:2007 | AISC-360-10 | Contrast (%) |
|---|---|---|---|---|---|---|
| RAFTER (near eave-strut) | $d_1$–550 mm(start)<br>$d_2$–400 mm (end)<br>$t_w$–12 mm<br>$t_f$–20 mm<br>$b_f$–200 mm | 1 | **Axial tension capacity** | Section 6.2 | Chapter-D-2 | |
| | | | In yielding | 2963 kN | 2930 kN | 1.13% |
| 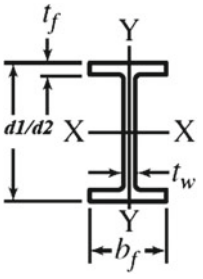 | | | In rupture | 3650 kN | 3430 kN | 6.02% |
| | | 2 | **Axial compression capacity** | Section 7.1.2.2 | Chapter-E7-1 | |
| | | | Major axis buckling | 1769 kN | 1930 kN | 8.34% |
| | | 3 | **Shear** | Section 8.2 | Chapter G-2-1 | |
| | | | Capacity of section | 881.771 kN | 907 kN | 2.12% |
| | | 4 | **Bending capacity of section** | Section 8.2.1.2 | Chapter F2-1 | |
| | | | Major axis bending | 674.936 kN-m | 668 kN-m | 1.03% |

**Table 13** Comparison of capacities of rafter member

| Member type | Member size ridge piece | S. no | Criteria | IS 800:2007 | AISC-360-10 | Contrast (%) |
|---|---|---|---|---|---|---|
| RAFTER (near ridge-strut) | $d_1$–400 mm (start)<br>$d_2$–375 mm (end)<br>$t_w$–10 mm<br>$t_f$–9 mm<br>$b_f$–175 mm | 1 | **Axial tension capacity** | Section 6.2 | Chapter-D-2 | |
| | | | In yielding | 2138 kN | 2120 kN | 0.84% |
| 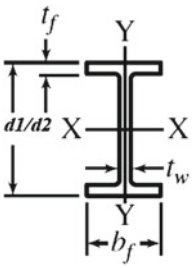 | | | In rupture | 2634 kN | 2470 kN | 6.22% |
| | | 2 | **Axial compression capacity** | Section 7.1.2.2 | Chapter-E7-1 | |
| | | | Major axis buckling | 1164 kN | 1290 kN | 9.76% |
| | | 3 | **Shear** | Section 8.2 | Chapter G-2-1 | |
| | | | Capacity of section | 578.66 kN | 595 kN | 2.74% |
| | | 4 | **Bending capacity of section** | Section 8.2.1.2 | Chapter F2-1 | |
| | | | Major axis bending | 260.67 kN-m | 282 kN-m | 7.80% |

**Table 14** Comparison of base reaction

| S. no | Direction (forces and moment) | IS 800:2007 | AISC-360-10 | Percentage difference (%) |
|---|---|---|---|---|
| 1 | $\mathbf{F_X}$ (*X*-axis) | 79.18 kN | 64.924 kN | 18.01 |
| 2 | $\mathbf{F_Y}$ (compression) | 258.984 kN | 216.308 kN | 16.47 |
| 3 | $\mathbf{F_Y}$ (tension) | 69.838 kN | 58.914 kN | 15.86 |
| 4 | $\mathbf{M_Z}$ | 278.843 kN-m | 211.063 kN-m | 24.30 |

3. For the design of runway beam, the wheel loads by considering impact factor specified in the two different standards had 12% difference (Table 6).
4. The difference in compression capacity of a section on an average had a difference of 9.05% between Indian Standard [8] design and American Standard [10] design, where in the section capacity as per Indian design code was the least (Tables 11, 12 and 13).
5. The difference obtained in tension capacity of a section in rupture and yielding was about 1.03% and 6.18%, respectively (Tables 11, 12 and 13).

6. The difference obtained in shear capacity of section was about 2.55% where the capacity of section obtained was higher in American design code (Tables 11, 12 and 13).

## References


1. Hiroyuki S, Muneaki K (1984) Strength formulae for tapered beam-column. J Struct Eng 110:1630–1643
2. Chia-Ming U, Jong-Kook H (2011) Cyclic testing of a metal building moment frame system with web-tapered members. J Constr Steel Res 70(6):248–255
3. Bureau of Indian Standards (1989) Indian Standard Code of practice for design loads (other than earthquake) for buildings and structures Part-2 imposed loads (IS 875 Part-2), pp 4–18
4. ASCE/SEI.,7-10 (2010) Minimum design loads for buildings and other structures. American Society of Civil Engineers, Reston, VA
5. Metal Building Manufacturers Association (2012) Metal building systems manual, pp 1–335
6. Bureau of Indian Standards (2015) Indian Standard Code of practice for design loads (other than earthquake) for buildings and structures Part-3 wind loads (IS 875 Part-3), pp 1–56
7. Mahen M (1995) Wind-resistant low-rise building in the tropics. J Perform Constr Facil 9(4):330–346
8. Bureau of Indian Standards (2007) Indian Standard general construction in steel code of practice (IS 800:2007), pp 1–143
9. Dale C, Herbert S, James R (1989) Strategies for mitigating damage to metal building system. J Aerosp Eng 2(2):71–87
10. ANSI/AISC., 360-10 (2010) Specification for structural steel buildings. American Institute of Steel Construction, Chicago, IL
11. Bureau of Indian Standards (2001) Explanatory handbook on Indian Standard Code of practice for design loads (other than earthquake) for buildings and structures (SP—64(S&T)), pp 1–73
12. Bureau of Indian Standards (1989) Indian Standard Code of practice for design loads (other than earthquake) for buildings and structures Part-1 dead loads (IS 875 Part-1), pp 1–37

# Structural Design and Analysis of Hyperboloid with Tower Assembly of Solar-Thermal Plant


**R. K. Verma, M. K. Agrawal, P. Halder, and J. Chattopadhyay**

**Abstract** A 2MWe solar plant is proposed to be set-up. A 40.8 m diameter hyperboloid supported on three towers (60 m height), 118 heliostats of dimension 10 m × 10 m, 228 heliostats of dimension 5 m × 5 m and an 8 m diameter receiver are the major components of the proposed plant. Hyperboloid with tower assembly is one of the key components of the concentrated solar power plants based on central receiver concept. Hyperboloid reflects the reflected rays from the field heliostats to the receiver mounted at the ground. It consists of hyperboloid frame on to which aluminium-based reflector is fixed. Hyperboloid frame is made of carbon steel and aluminium tubes. Aluminium reflector (mirror) is made of 0.8 mm aluminium sheet. Hyperboloid structure along with reflectors is supported by tower structures. Towers are made of carbon steel tubes. Hyperboloid is fixed with three towers by bolting arrangement. Hyperboloid with tower assembly is designed against wind load of 39 m/s basic wind speed. Finite element analyses have been performed to optimize the design and estimate the deflections and stresses due to dead weight, imposed loads, earthquake loads and wind loads. Stresses due to various loads and their combinations have been checked against the allowable stresses as per IS 800. Buckling checks have been performed as per IS 800.

**Keywords** Design wind pressure · Vortex shedding frequency · Seismic zone · Response spectrum analysis

R. K. Verma (✉) · M. K. Agrawal · P. Halder · J. Chattopadhyay
Bhabha Atomic Research Centre, Mumbai, India
e-mail: rajeev.ballia@gmail.com



M. Madhavan et al. (eds.), *Proceedings of the Indian Structural Steel Conference 2020 (Vol. 1)*, Lecture Notes in Civil Engineering 318,
https://doi.org/10.1007/978-981-19-9390-9_18

## 1 Introduction

India is a tropical country where sunshine is available for longer hours per day and in great intensity. Several technologies are available for large-scale solar power deployment. Solar-thermal plant based on central receiver technology with molten salt as the working fluid is one such concept. Solar power tower type plant has been planned employing field heliostats, hyperboloid with tower, molten salt-based receiver with steam in secondary side, turbine, etc. The proposed plant uses central receiver concept wherein the incident solar radiation concentrated to heat up the molten nitrate salt in receiver. Molten salt is a mixture of $KNO_3$ and $NaNO_3$ in a proportion of 40:60 w/w. In the steam generating system, the heated salt transfers its energy to water to generate steam. The steam is then passed on to a steam turbine for electricity generation.

Hyperboloid with tower assembly is one of the key components of the concentrated solar power plants based on central receiver concept. Hyperboloid reflects the reflected rays from the field heliostats to the receiver mounted at the ground. Hyperboloid reflector is mounted 60 m above the ground at the top of three lattice towers. Hyperboloid is 40.8 m in diameter. It consists of hyperboloid frame on to which aluminium-based reflector is fixed. Hyperboloid frame is made of carbon steel and aluminium tubes. Aluminium reflector (mirror) is made of 0.8 mm aluminium sheet. Towers are made of carbon steel tubes. Hyperboloid is fixed with tower assembly by bolting arrangement.

Size of hyperboloid is calculated based on optimum heliostat layout for 5250 kWth power in molten salt. The area of the hyperbolic mirror is estimated to be approx. 1403 $m^2$ for a tower height of 60 m. The diameter and depth of the hyperboloid is 40.8 m and 6.5 m, respectively. The thermal radiation incident on the reflector is 6.46 MWth, which generates a radiant heat flux of 3.9 kWth/$m^2$. Temperature rise of secondary hyperboloid reflector due to incident solar radiation is calculated to be 55 °C. Hyperboloid with tower assembly is designed against wind load of 39 m/s basic wind speed. Approximate weight of the assembly is 220 tonnes. Figure 1 shows the hyperboloid with tower assembly.

## 2 Material Properties

Structural tubes are available in various grades. YSt 310 grade has been taken conforming to IS: 1161:1998 (steel tubes for structural purposes). Aluminium tubes have also been used in hyperboloid. The mechanical properties of YSt 310 grade steel and aluminium are given in Table 1 [1].

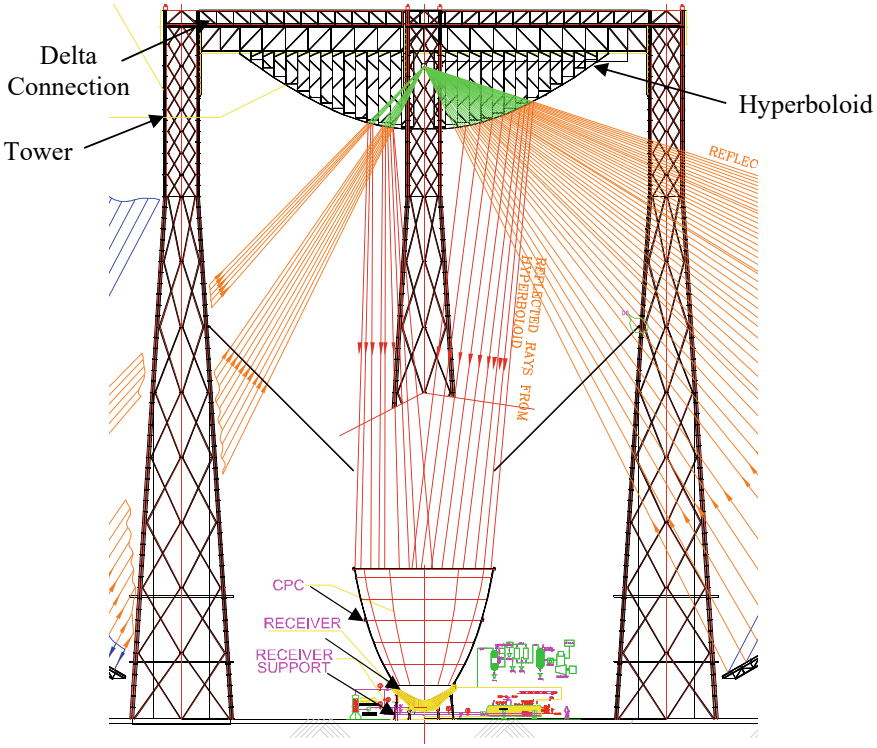


**Fig. 1** Hyperboloid with tower assembly

**Table 1** Mechanical properties

| Properties | Carbon steel (YSt 310) | Aluminium |
|---|---|---|
| Tensile strength (MPa) | 450 | 324 |
| Yield strength (MPa) | 310 | 276 |
| Young's modulus (GPa) | 200 | 68.9 |
| Density (kg/m$^3$) | 8000 | 2700 |

# 3 Design Specifications

## *3.1 Geometrical Specifications*

1. Height of towers = 60 m
2. Diameter of hyperboloid = 40.8 m
3. Depth of the hyperboloid = 6.5 m

### 3.2 Types of Loads

Hyperboloid with tower assembly has been designed as a truss structure as per IS 800. Loads which need to be considered as per IS 800 are as follows [2, 3]:

1. Dead loads
2. Imposed loads
3. Wind loads (as per IS 875 Part 3)
4. Earthquake loads (as per IS 1893 Part 1).

### 3.3 Wind Loads and Operational Limits

1. Operating wind speed is 40 kmph (user's requirement)
2. Survival wind speed is 140.4 kmph (as per IS 875 Part 3).

## 4 Loads Considered in the Analysis

### 4.1 Wind Load on Hyperboloid Surface and Towers

Wind loads on hyperboloid and towers have been taken as per IS 875 Part 3. IS 875 Part 3 provides force coefficient for most structural shapes [4–6].

Wind load on any object is given by

$$F = C_f \times A_e \times p_d$$

where

$C_f$ force coefficient;
$A_e$ effective area of the object normal to the wind direction, $m^2$;
$p_d$ design wind pressure, $N/m^2$.

#### 4.1.1 Design Wind Speed

The basic wind speed for any site shall be obtained from IS 875 Part 3 and shall be modified to include the following effects to get design wind speed, $V_Z$ at any height, $Z$.

Design wind speed ($V_Z$)

$$V_Z = V_b \times k_1 \times k_2 \times k_3 \times k_4$$

**Table 2** Parameters used in the calculation of design wind speed

| Parameters | Value | Remarks |
|---|---|---|
| $V_b$ | 39 m/s | As per IS 875 wind zonal map |
| $k_1$ | 0.90 | For 10 years design life, 100 years return period for the wind |
| $k_2$ | 0.99–1.152 | For class A structure, terrain category 1 |
| $k_3$ | 1.00 | For plain land |
| $k_4$ | 1.00 | More than 60 km away from coast |

where

$V_Z$ design wind speed at any height $z$, m/s;
$V_b$ basic wind speed, m/s;
$k_1$ probability factor (risk coefficient);
$k_2$ terrain, height and structure size factor;
$k_3$ topography factor;
$k_4$ importance factor for the cyclonic region.

Various parameters used in the calculation of design wind speed have been listed in Table 2.

### 4.1.2 Design Wind Pressure

The wind pressure at any height above mean ground level shall be obtained by the following relationship between wind pressure and wind speed.

Design wind pressure ($p_Z$)

$$p_Z = 0.6V_Z^2$$

Table 3 gives the design wind speed and pressure at different heights of the structure.

**Table 3** Design wind speed and pressure at different heights

| Height (m) | Design wind speed (m/s) | Design wind pressure ($N/m^2$) |
|---|---|---|
| 10.0 | 34.75 | 724.50 |
| 20.0 | 37.21 | 830.57 |
| 40.0 | 39.14 | 919.00 |
| 60.0 | 40.44 | 981.00 |

### 4.2 Earthquake Load on Hyperboloid Surface and Towers

Earthquake loads have been considered as per IS 1893 Part 1. For the purpose of determining seismic forces, the country is classified into four seismic zones. The design horizontal seismic coefficient $A_h$ for a structure shall be determined by the following expression [7]:

$$A_h = \frac{Z}{2} \times \frac{I}{R} \times \frac{S_a}{g}$$

where

$Z$ zone factor
$R$ response reduction factor
$I$ importance factor
$S_a/g$ average response acceleration coefficient for rock or soil sites.

Site is located in seismic zone III. Hyperboloid with tower assembly is welded steel structure, damping for design basis earthquake has been considered as 2%. Response spectra used in the analysis for 2% damping is shown in Fig. 2.

## 5 Finite Element Analysis

Finite element analyses have been performed to optimize the design and estimate the deflections and stresses due to dead weight, imposed loads, earthquake loads and wind loads. Beam elements have been used to model the structural members. Lumped mass elements have been used to model imposed loads. Hyperboloid is connected to tower at 18 locations and to star delta at 24 locations with the help of link elements. All degrees of freedom have been fixed at the bottom nodes of the tower for analyses. Figure 3 shows the finite element model of hyperboloid with tower assembly.

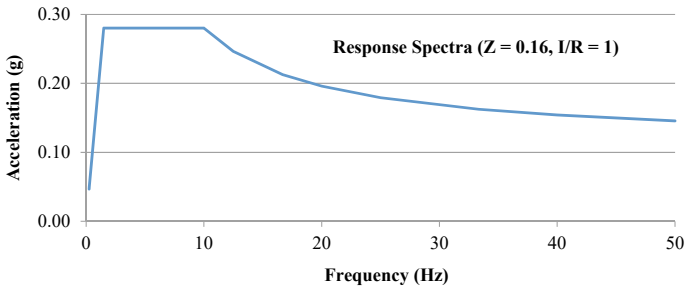


**Fig. 2** Response spectra for 2% damping

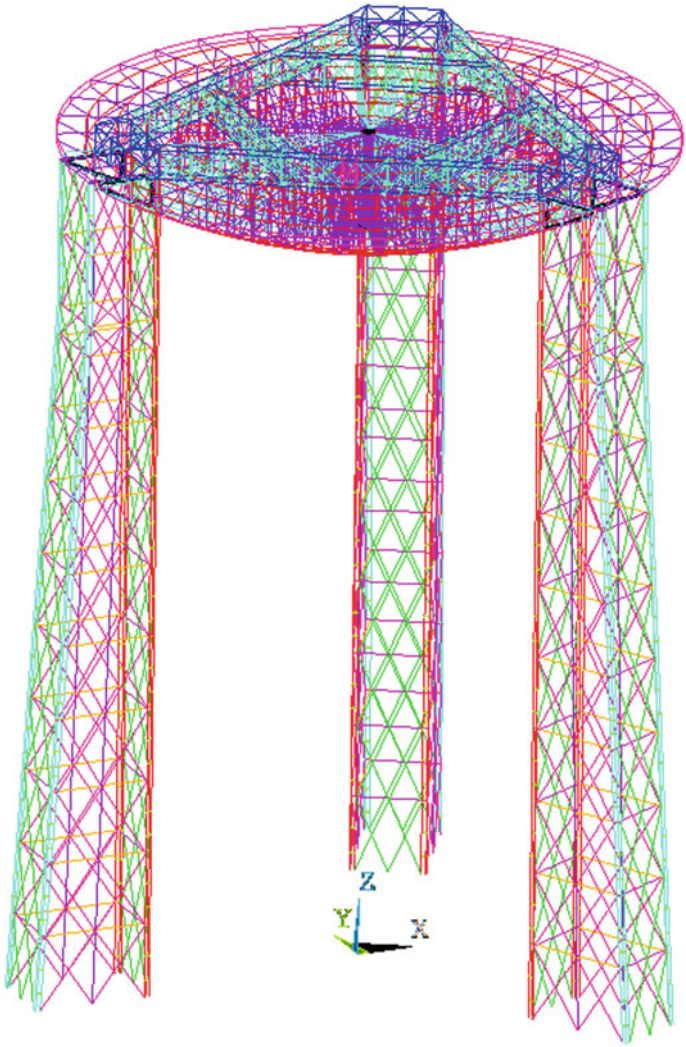


**Fig. 3** Finite element model of hyperboloid with tower assembly

Static analyses have been performed to estimate the stresses and deflections due to dead weight, imposed loads and wind loads. Response spectrum analysis has been performed to estimate the stresses and deflections due to earthquake loads. The maximum deflections due to various loads and their combinations have been listed in Table 4. Deflections due to dead loads, imposed loads and operating wind loads are within the allowable limit (35 mm). Figure 4 shows the deflected shape due to dead weight and imposed loads of reflecting surface.

**Table 4** Maximum deflections due to various loads and their combinations

| Load combinations | Deflection (mm) |
|---|---|
| Dead loads + imposed loads | 24.62 |
| Dead loads + imposed loads + wind loads in *X* direction (operating) | 26.57 |
| Dead loads + imposed loads + wind loads in *Y* direction (operating) | 26.45 |
| Dead loads + imposed loads + wind loads in *X* direction (survival) | 151.86 |
| Dead loads + imposed loads + wind loads in *Y* direction (survival) | 155.75 |
| Dead loads + imposed loads + earthquake loads | 74.71 |

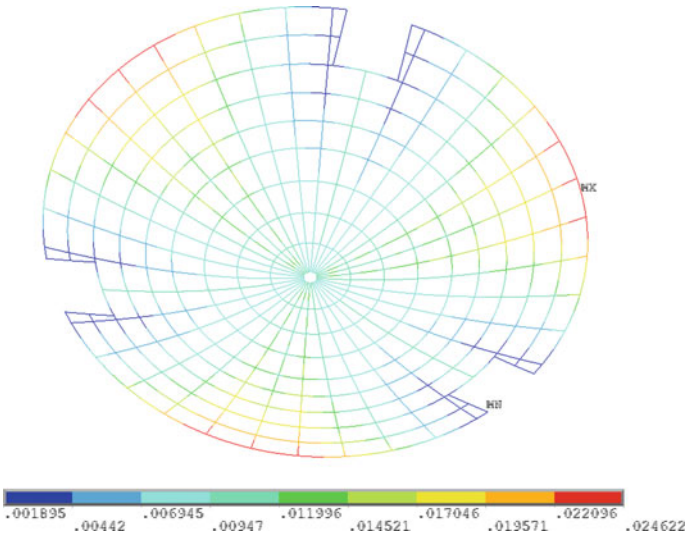


**Fig. 4** Deflected shape (dead loads + imposed loads)

# 6 Design Checks

## *6.1 Permissible Stresses as Per IS 800*

### 6.1.1 Axial Stress in Tension

The permissible stress in axial tension on the net cross-sectional area of hollow sections shall not exceed the values of $\sigma_{at}$.

$$\sigma_{at} = 0.6 f_y$$

where

$f_y$ minimum yield stress, MPa.

### 6.1.2 Axial Stress in Compression

The direct stress in compression on the gross cross-sectional area of axially loaded steel hollow sections shall not exceed $0.6 f_y$ nor the permissible stress $\sigma_{ac}$, calculated using the following formula:

$$\sigma_{ac} = 0.6 \frac{f_{cc} \times f_y}{\left[(f_{cc})^n + (f_y)^n\right]^{1/n}}$$

where

$\sigma_{ac}$ permissible stress in axial compression, MPa
$f_{cc}$ elastic critical stress in compression $= \pi^2 E/\lambda^2$ MPa
$\lambda$ $l/r =$ ratio of the effective length of the member and the radius of gyration
$f_y$ minimum yield stress, MPa
$E$ modulus of elasticity, MPa
$n$ a factor assumed as 1.4.

### 6.1.3 Bending Stresses

In hollow sections, the tensile bending stress and the compressive bending stress in the extreme fibres shall not exceed the values of $\sigma_{bt}$.

$$\sigma_{bt} = 0.66 f_y$$

where

$f_y$ minimum yield stress, MPa.

Table 5 gives the allowable stresses for tension and bending for structural steel and aluminium for different load combinations. Table 6 gives the permissible stresses in compression based on slenderness ratios for steel and aluminium members for different load combinations.

**Table 5** Allowable stresses for tension and bending

| | Dead loads + imposed loads | | Dead loads + imposed loads + wind loads or earthquake loads | |
|---|---|---|---|---|
| | Structural steel | Aluminium | Structural steel | Aluminium |
| Axial tension (MPa) | 186.0 | 165.6 | 248.0 | 220.8 |
| Bending stress (MPa) | 204.6 | 182.2 | 272.8 | 242.9 |

**Table 6** Permissible stresses in axial compression in MPa

| | Dead loads + imposed loads | | Dead loads + imposed loads + wind loads or earthquake loads | |
|---|---|---|---|---|
| Slenderness ratio | Structural steel | Aluminium | Structural steel | Aluminium |
| 25 | 181.0 | 150.2 | 241.3 | 200.3 |
| 50 | 156.8 | 100.2 | 209.1 | 133.6 |
| 75 | 120.3 | 59.7 | 160.4 | 79.6 |
| 100 | 87.3 | 37.1 | 116.4 | 49.5 |
| 125 | 63.4 | 24.8 | 84.5 | 33.1 |
| 150 | 47.0 | 17.6 | 62.7 | 23.5 |
| 175 | 35.9 | 13.1 | 47.9 | 17.5 |
| 200 | 28.1 | 10.1 | 37.5 | 13.5 |

### 6.1.4 Combined Stresses

Combined stresses in axial compression and bending should satisfy Eq. (1).

$$\frac{\sigma_{\text{ac}},\text{cal.}}{\sigma_{\text{ac}}} + \frac{C_{\text{mx}} \times \sigma_{\text{bcx}},\text{cal.}}{\left\{1 - \frac{\sigma_{\text{ac}},\text{cal.}}{0.60 f_{\text{ccx}}}\right\}\sigma_{\text{bcx}}} + \frac{C_{\text{my}} \times \sigma_{\text{bcy}},\text{cal.}}{\left\{1 - \frac{\sigma_{\text{ac}},\text{cal.}}{0.60 f_{\text{ccy}}}\right\}\sigma_{\text{bcy}}} \leq 1.0 \tag{1}$$

Similarly combined stresses in axial tension and bending should satisfy the Eq. (2).

$$\frac{\sigma_{\text{at}},\text{cal.}}{0.60 f_{\text{y}}} + \frac{\sigma_{\text{btx}},\text{cal.}}{0.66 f_{\text{y}}} + \frac{\sigma_{\text{bty}},\text{cal.}}{0.66 f_{\text{y}}} \leq 1.0 \tag{2}$$

where

$\sigma_{\text{ac}}$, cal. calculated average axial compressive stress
$\sigma_{\text{at}}$, cal. calculated average axial tensile stress
$\sigma_{\text{bc}}$, cal. calculated bending compressive stress in extreme fibre
$\sigma_{\text{bt}}$, cal. calculated bending tensile stress in extreme fibre
$\sigma_{ac}$ permissible axial comp. stress in the member subject to axial comp. load only
$\sigma_{\text{at}}$ permissible axial tensile stress in the member subject to axial tensile load only
$\sigma_{\text{bc}}$ permissible bending compressive stress in extreme fibre
$\sigma_{\text{bt}}$ permissible bending tensile stress in extreme fibre
$f_{\text{cc}}$ elastic critical stress in compression
$C_{\text{m}}$ a coefficient.

**Table 7** Dead loads + imposed loads

| Tubular sections size | Axial tension stress (MPa) | Axial compression stress (MPa) | Bending stress (MPa) |
|---|---|---|---|
| *Tower* | | | |
| 200 NB 5.6 mm thk | 3.73 | 12.7 | 12.5 |
| 150 NB 4.8 mm thk | 5.07 | 6.94 | 9.13 |
| *Connecting members* | | | |
| 150 NB 4.5 mm thk | 4.99 | 1.51 | 41.0 |
| 100 NB 4.5 mm thk | 7.55 | 4.43 | 4.20 |
| *Delta connection* | | | |
| 150 NB 4.5 mm thk | 17.0 | 28.6 | 17.6 |
| 100 NB 4.5 mm thk | 14.2 | 22.5 | 32.7 |
| 50 NB 2.9 mm thk | 32.6 | 33.0 | 29.1 |
| *Hyperboloid* | | | |
| 100 NB 4.5 mm thk | 9.99 | 0.47 | 22.6 |
| 65 NB 3.2 mm thk | 33.6 | 30.2 | 28.3 |
| 50 NB 2.9 mm thk | 15.8 | 10.1 | 46.0 |
| 50 NB 2.5 mm thk | 18.7 | 18.5 | 31.6 |

## *6.2 Maximum Stresses in Structural Tubes Due to Various Loadings*

Structural tubes of different sizes have been used in the design of hyperboloid with tower assembly. Stresses in axial tension, axial compression and bending are listed in Tables 7, 8, 9 and 10 for different load combinations.

The stresses listed in the above tables for various loads and their combinations have been checked against the allowable stresses as per IS 800 and are found within the allowable limit. Considering as fixed–fixed end conditions, buckling checks have been performed as per IS 800 and found safe.

**Table 8** Dead loads + imposed loads + wind loads in *X* direction (survival)

| Tubular sections size | Axial tension stress (MPa) | Axial compression stress (MPa) | Bending stress (MPa) |
|---|---|---|---|
| *Tower* | | | |
| 200 NB 5.6 mm thk | 93.0 | 107 | 62.2 |
| 150 NB 4.8 mm thk | 49.4 | 45.8 | 39.0 |
| *Connecting members* | | | |
| 150 NB 4.5 mm thk | 7.41 | 8.05 | 180 |
| 100 NB 4.5 mm thk | 14.9 | 39.2 | 21.2 |
| *Delta connection* | | | |
| 150 NB 4.5 mm thk | 80.4 | 91.2 | 66.2 |
| 100 NB 4.5 mm thk | 111 | 72.5 | 129 |
| 50 NB 2.9 mm thk | 90.0 | 90.7 | 89.0 |
| *Hyperboloid* | | | |
| 100 NB 4.5 mm thk | 8.82 | 21.0 | 42.2 |
| 65 NB 3.2 mm thk | 170 | 126 | 123 |
| 50 NB 2.9 mm thk | 31.4 | 36.9 | 160 |
| 50 NB 2.5 mm thk | 59.3 | 62.8 | 117 |

Combined stresses in axial compression and bending, and axial tension and bending are listed in Tables 11, 12, 13 and 14 for different load combinations. The stress ratios listed in Tables 11, 12, 13 and 14 are less than 1, hence the structure is safe.

## 7 Vortex Shedding Frequency

Vortex shedding frequency of a structure is determined by the following formula:

$$f_s = \frac{S_t \times \overline{V}_{z,H}}{b} = \frac{0.25 \times 40.44}{40.8} = 0.25\,\text{Hz}$$

**Table 9** Dead loads + imposed loads + wind loads in *Y* direction (survival)

| Tubular sections size | Axial tension stress (MPa) | Axial compression stress (MPa) | Bending stress (MPa) |
|---|---|---|---|
| *Tower* | | | |
| 200 NB 5.6 mm thk | 104 | 114 | 68.4 |
| 150 NB 4.8 mm thk | 42.6 | 44.1 | 37.3 |
| *Connecting members* | | | |
| 150 NB 4.5 mm thk | 8.10 | 8.74 | 166 |
| 100 NB 4.5 mm thk | 19.3 | 34.1 | 22.2 |
| *Delta connection* | | | |
| 150 NB 4.5 mm thk | 77.5 | 86.0 | 68.0 |
| 100 NB 4.5 mm thk | 113 | 74.1 | 123 |
| 50 NB 2.9 mm thk | 85.4 | 88.5 | 89.6 |
| *Hyperboloid* | | | |
| 100 NB 4.5 mm thk | 10.3 | 22.8 | 55.8 |
| 65 NB 3.2 mm thk | 144 | 138 | 123 |
| 50 NB 2.9 mm thk | 36.6 | 37.1 | 165 |
| 50 NB 2.5 mm thk | 55.8 | 60.0 | 108 |

where

$S_t$ Strouhal number;
$\overline{V}_{z,H}$ hourly mean wind speed at height $z$;
$b$ breadth of structure normal to the wind direction in the horizontal plane.

Vortex shedding frequency of the hyperboloid with tower assembly is 0.25 Hz which is lesser than the fundamental frequency (1.1 Hz) obtained from modal analysis of the structure. Frequencies and mass participations obtained from modal analysis of the structure have been listed in Table 15.

**Table 10** Dead loads + imposed loads + earthquake loads

| Tubular sections size | Axial tension stress (MPa) | Axial compression stress (MPa) | Bending stress (MPa) |
|---|---|---|---|
| *Tower* | | | |
| 200 NB 5.6 mm thk | 44.5 | 53.5 | 36.8 |
| 150 NB 4.8 mm thk | 21.6 | 23.4 | 23.3 |
| *Connecting members* | | | |
| 150 NB 4.5 mm thk | 14.8 | 11.3 | 49.9 |
| 100 NB 4.5 mm thk | 10.1 | 7.0 | 70.7 |
| *Delta connection* | | | |
| 150 NB 4.5 mm thk | 43.1 | 54.7 | 36.8 |
| 100 NB 4.5 mm thk | 48.2 | 56.5 | 43.1 |
| 50 NB 2.9 mm thk | 49.1 | 49.5 | 43.1 |
| *Hyperboloid* | | | |
| 100 NB 4.5 mm thk | 14.4 | 4.9 | 32.3 |
| 65 NB 3.2 mm thk | 86.1 | 82.7 | 71.8 |
| 50 NB 2.9 mm thk | 23.5 | 17.8 | 86.8 |
| 50 NB 2.5 mm thk | 26.1 | 25.9 | 42.3 |

## 8 Conclusions

Hyperboloid with tower assembly has been analyzed and design checks have been performed as per IS 800. Based on the above analyses, following conclusions can be made:

1. Hyperboloid with tower assembly has been analyzed to estimate the stresses due to dead weight, imposed loads, wind loads and earthquake loads.
2. Wind loads on hyperboloid with tower assembly have been considered as per IS 875 and earthquake loads as per IS 1893.
3. Fundamental frequency of the structure is 1.1 Hz. IS 875 recommends frequency more than 1.0 Hz to avoid wind oscillations.
4. Deflections due to dead loads and operating wind loads are within the allowable limit (35 mm).

**Table 11** Dead loads + imposed loads

| Tubular sections size | Axial compression and bending | Axial tension and bending |
|---|---|---|
| *Tower* | | |
| 200 NB 5.6 mm thk | 0.08 + 0.05 + 0.05 = 0.18 | 0.02 + 0.06 + 0.06 = 0.14 |
| 150 NB 4.8 mm thk | 0.06 + 0.01 + 0.04 = 0.11 | 0.03 + 0.01 + 0.04 = 0.09 |
| *Connecting members* | | |
| 150 NB 4.5 mm thk | 0.01 + 0.17 + 0.08 = 0.26 | 0.03 + 0.20 + 0.10 = 0.33 |
| 100 NB 4.5 mm thk | 0.03 + 0.02 + 0.01 = 0.06 | 0.04 + 0.02 + 0.01 = 0.08 |
| *Delta connection* | | |
| 150 NB 4.5 mm thk | 0.16 + 0.05 + 0.07 = 0.28 | 0.09 + 0.05 + 0.09 = 0.23 |
| 100 NB 4.5 mm thk | 0.13 + 0.04 + 0.14 = 0.31 | 0.08 + 0.05 + 0.16 = 0.28 |
| 50 NB 2.9 mm thk | 0.33 + 0.01 + 0.02 = 0.36 | 0.18 + 0.11 + 0.14 = 0.43 |
| *Hyperboloid* | | |
| 100 NB 4.5 mm thk | 0.01 + 0.08 + 0.09 = 0.18 | 0.05 + 0.09 + 0.11 = 0.25 |
| 65 NB 3.2 mm thk | 0.26 + 0.07 + 0.14 = 0.47 | 0.18 + 0.07 + 0.14 = 0.39 |
| 50 NB 2.9 mm thk | 0.09 + 0.15 + 0.20 = 0.44 | 0.08 + 0.16 + 0.22 = 0.47 |
| 50 NB 2.5 mm thk | 0.36 + 0.00 + 0.06 = 0.41 | 0.11 + 0.08 + 0.17 = 0.36 |

**Table 12** Dead loads + imposed loads + wind loads in $X$ direction (survival)

| Tubular sections size | Axial compression and bending | Axial tension and bending |
|---|---|---|
| *Tower* | | |
| 200 NB 5.6 mm thk | 0.49 + 0.23 + 0.18 = 0.90 | 0.38 + 0.23 + 0.17 = 0.78 |
| 150 NB 4.8 mm thk | 0.28 + 0.09 + 0.15 = 0.51 | 0.20 + 0.08 + 0.14 = 0.42 |
| *Connecting members* | | |
| 150 NB 4.5 mm thk | 0.03 + 0.56 + 0.28 = 0.88 | 0.01 + 0.66 + 0.24 = 0.91 |
| 100 NB 4.5 mm thk | 0.17 + 0.07 + 0.03 = 0.27 | 0.06 + 0.08 + 0.03 = 0.17 |
| *Delta connection* | | |
| 150 NB 4.5 mm thk | 0.38 + 0.15 + 0.22 = 0.75 | 0.33 + 0.16 + 0.24 = 0.73 |
| 100 NB 4.5 mm thk | 0.32 + 0.13 + 0.44 = 0.89 | 0.12 + 0.14 + 0.47 = 0.74 |
| 50 NB 2.9 mm thk | 0.69 + 0.07 + 0.16 = 0.91 | 0.01 + 0.27 + 0.33 = 0.61 |
| *Hyperboloid* | | |
| 100 NB 4.5 mm thk | 0.11 + 0.13 + 0.14 = 0.38 | 0.04 + 0.15 + 0.16 = 0.34 |
| 65 NB 3.2 mm thk | 0.61 + 0.13 + 0.21 = 0.94 | 0.69 + 0.13 + 0.05 = 0.86 |
| 50 NB 2.9 mm thk | 0.14 + 0.21 + 0.54 = 0.90 | 0.13 + 0.41 + 0.27 = 0.81 |
| 50 NB 2.5 mm thk | 0.52 + 0.08 + 0.04 = 0.64 | 0.27 + 0.18 + 0.48 = 0.93 |

**Table 13** Dead loads + imposed loads + wind loads in *Y* direction (survival)

| Tubular sections size | Axial compression and bending | Axial tension and bending |
|---|---|---|
| *Tower* | | |
| 200 NB 5.6 mm thk | 0.52 + 0.26 + 0.20 = 0.98 | 0.42 + 0.25 + 0.19 = 0.87 |
| 150 NB 4.8 mm thk | 0.27 + 0.08 + 0.14 = 0.49 | 0.17 + 0.07 + 0.14 = 0.38 |
| *Connecting members* | | |
| 150 NB 4.5 mm thk | 0.04 + 0.52 + 0.24 = 0.79 | 0.03 + 0.61 + 0.28 = 0.92 |
| 100 NB 4.5 mm thk | 0.15 + 0.07 + 0.03 = 0.25 | 0.08 + 0.08 + 0.03 = 0.19 |
| *Delta connection* | | |
| 150 NB 4.5 mm thk | 0.36 + 0.16 + 0.23 = 0.75 | 0.31 + 0.18 + 0.25 = 0.75 |
| 100 NB 4.5 mm thk | 0.32 + 0.13 + 0.42 = 0.87 | 0.21 + 0.14 + 0.45 = 0.80 |
| 50 NB 2.9 mm thk | 0.67 + 0.05 + 0.15 = 0.88 | 0.35 + 0.23 + 0.33 = 0.91 |
| *Hyperboloid* | | |
| 100 NB 4.5 mm thk | 0.12 + 0.15 + 0.19 = 0.45 | 0.04 + 0.16 + 0.21 = 0.41 |
| 65 NB 3.2 mm thk | 0.70 + 0.12 + 0.15 = 0.96 | 0.58 + 0.11 + 0.13 = 0.83 |
| 50 NB 2.9 mm thk | 0.13 + 0.21 + 0.58 = 0.91 | 0.15 + 0.49 + 0.32 = 0.96 |
| 50 NB 2.5 mm thk | 0.62 + 0.01 + 0.22 = 0.85 | 0.25 + 0.19 + 0.45 = 0.88 |

**Table 14** Dead loads + imposed loads + earthquake loads

| Tubular sections size | Axial compression and bending | Axial tension and bending |
|---|---|---|
| *Tower* | | |
| 200 NB 5.6 mm thk | 0.24 + 0.13 + 0.13 = 0.49 | 0.18 + 0.14 + 0.14 = 0.45 |
| 150 NB 4.8 mm thk | 0.14 + 0.08 + 0.08 = 0.30 | 0.09 + 0.09 + 0.09 = 0.26 |
| *Connecting members* | | |
| 150 NB 4.5 mm thk | 0.05 + 0.16 + 0.16 = 0.36 | 0.06 + 0.18 + 0.18 = 0.43 |
| 100 NB 4.5 mm thk | 0.03 + 0.22 + 0.22 = 0.48 | 0.04 + 0.26 + 0.26 = 0.56 |
| *Delta connection* | | |
| 150 NB 4.5 mm thk | 0.23 + 0.12 + 0.12 = 0.47 | 0.17 + 0.14 + 0.14 = 0.44 |
| 100 NB 4.5 mm thk | 0.25 + 0.14 + 0.14 = 0.54 | 0.19 + 0.16 + 0.16 = 0.51 |
| 50 NB 2.9 mm thk | 0.38 + 0.20 + 0.20 = 0.79 | 0.20 + 0.16 + 0.16 = 0.52 |
| *Hyperboloid* | | |
| 100 NB 4.5 mm thk | 0.03 + 0.10 + 0.10 = 0.23 | 0.06 + 0.12 + 0.12 = 0.30 |
| 65 NB 3.2 mm thk | 0.40 + 0.27 + 0.27 = 0.94 | 0.35 + 0.26 + 0.26 = 0.88 |
| 50 NB 2.9 mm thk | 0.12 + 0.30 + 0.30 = 0.72 | 0.09 + 0.32 + 0.32 = 0.73 |
| 50 NB 2.5 mm thk | 0.28 + 0.19 + 0.19 = 0.65 | 0.12 + 0.17 + 0.17 = 0.47 |

**Table 15** Frequencies and percentage mass participations

| Frequency (Hz) | %Mass participation (*X*) | %Mass participation (*Y*) | %Mass participation (*Z*) |
|---|---|---|---|
| 1.1 | 61.68 | 7.11 | 0.00 |
| 1.1 | 7.11 | 61.68 | 0.00 |
| 4.0 | 0.30 | 3.78 | 0.00 |
| 4.0 | 3.78 | 0.30 | 0.00 |
| 4.3 | 0.00 | 0.00 | 12.16 |

5. Stresses due to various loads and their combinations have been checked against the allowable stresses as per IS 800 and are found within the allowable limits.
6. Buckling checks have been performed as per IS 800 and found safe.

## References

1. IS 1161 (1998) Steel tubes for structural purposes
2. IS 806 (1996) Code of practice for use of steel tubes in general building construction
3. IS 800 (1984) Code of practice for general construction in steel
4. IS 875 Part 3 (1987) Code of practice for design loads (other than earthquake) for buildings and structures
5. IS 875 Part 3 (2015) Code of practice for design loads (other than earthquake) for buildings and structures
6. Cohen E, Vellozzi J, Suh SS (2006) Calculation of wind forces and pressures on antennas. Ann NY Acad Sci 116(1):161–221
7. IS 1893 Part 1 (2002) Criteria for earthquake resistant design of structures

# Structural Design and Analysis of Heliostat of Solar-Thermal Plant


**R. K. Verma, M. K. Agrawal, P. Halder, and J. Chattopadhyay**

**Abstract** A 2MWe solar plant is proposed to be set-up. A 40.8 m diameter hyperboloid supported on three towers (60 m height), 118 heliostats of dimension 10 m × 10 m, 228 heliostats of dimension 5 m × 5 m and an 8 m diameter receiver are the major components of the proposed plant. Heliostat is one of the key components of the concentrated solar power plants based on central receiver concept. Large number of reflector assemblies (heliostats) that are capable of tracking the movement of sun, are installed in the field and are manipulated by computer programme to constantly focus the reflected rays of sun on to a centrally fixed receiver. The objective of heliostat is to accurately focus the reflected rays on to a calibrated target point. The positioning accuracy of heliostat is achieved through servo control drive system using gear drives. A 10 m × 10 m heliostat, made of carbon steel box and circular sections, is designed against wind load of 39 m/s basic wind speed. Finite element analyses have been performed to optimize the design and estimate the deflections and stresses due to dead weight, imposed loads, seismic loads and wind loads. Stresses due to various loads and their combinations have been checked against the allowable stresses as per IS 800. Buckling checks have been performed as per IS 800.

**Keywords** Design wind pressure · Seismic zone · Response spectrum analysis

## 1 Introduction

India is a tropical country where sunshine is available for longer hours per day and in great intensity. Several technologies are available for large-scale solar power deployment. Solar-thermal plant based on central receiver technology with molten salt as the working fluid is one such concept. Solar power tower type plant has been planned employing field heliostats, hyperboloid with tower, molten salt-based receiver with steam in secondary side, turbine, etc. The proposed plant uses central

R. K. Verma (✉) · M. K. Agrawal · P. Halder · J. Chattopadhyay
Bhabha Atomic Research Centre, Mumbai, India
e-mail: rajeev.ballia@gmail.com



M. Madhavan et al. (eds.), *Proceedings of the Indian Structural Steel Conference 2020 (Vol. 1)*, Lecture Notes in Civil Engineering 318,
https://doi.org/10.1007/978-981-19-9390-9_19

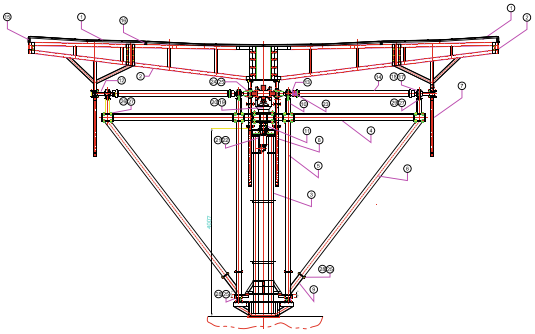

| Part No. | Item name |
|---|---|
| 1. | Mirror structure |
| 2. | Mirror structure support |
| 3. | Vertical column support |
| 4. | Horizontal support beam |
| 5 | Vertical rotating support |
| 6 | Inclined rotating support |
| 7. | Outer balancing unit |
| 8 | Inner balancing unit |
| 9. | Rotary pedestal |
| 10. | Bearing support |
| 11 | Drive support |
| 12 | Drive end shaft |
| 13. | Drive front shaft |
| 14. | Metaflex shaft coupling |

**Fig. 1** 10 m × 10 m heliostat assembly

receiver concept, wherein the incident solar radiation concentrated to heat up the molten nitrate salt in receiver. Molten salt is a mixture of $KNO_3$ and $NaNO_3$ in a proportion of 40:60 w/w. In the steam generating system, the heated salt transfers its energy to water to generate steam. The steam is then passed on to a steam turbine for electricity generation.

Heliostat is one of the key components of the concentrated solar power plants based on central receiver concept. Large number of reflector assemblies (heliostats) that are capable of tracking the movement of sun, are installed in the field and are manipulated by a computer programme to constantly focus the reflected rays of sun on to a centrally fixed receiver. The objective of heliostat is to accurately focus the reflected rays on to a calibrated target point. The positioning accuracy of heliostat is achieved through servo control drive system using gear drives. Figure 1 shows the 10 m × 10 m heliostat assembly.

## 2 Material Properties

Structural tubes are available in various grades. YSt 240 and 310 grade have been taken conforming to IS: 1161:1998 (steel tubes for structural purposes). The mechanical properties of YSt 240 and 310 grade steel are given in Table 1 [1].

## 3 Design Specifications

### *3.1 Geometrical Specifications*

1. Size of heliostat = 10 m × 10 m.

**Table 1** Mechanical properties

| Properties | Carbon steel (YSt 240) | Carbon steel (YSt 310) |
|---|---|---|
| Tensile strength (MPa) | 410 | 450 |
| Yield strength (MPa) | 240 | 310 |
| Young's modulus (GPa) | 200 | 200 |
| Density (kg/m$^3$) | 8000 | 8000 |

### *3.2 Types of Loads*

Heliostat has been designed as a truss structure as per IS 800. Loads which need to be considered as per IS 800 are as follows [2, 3]:

1. Dead loads
2. Imposed loads
3. Wind loads (as per IS 875 Part 3)
4. Earthquake loads (as per IS 1893 Part 1).

### *3.3 Wind Loads and Operational Limits*

1. Operating wind speed is 40 kmph (user's requirement)
2. Survival wind speed is 140.4 kmph (as per IS 875 Part 3).

## 4 Loads Considered in the Analysis

### *4.1 Wind Load on Heliostat*

Wind loads on heliostat have been taken as per IS 875 Part 3. IS 875 Part 3 provides force coefficient for most structural shapes [4–6].

Wind load on any object is given by

$$F = C_\mathrm{f} \times A_\mathrm{e} \times p_\mathrm{d}$$

where

$C_\mathrm{f}$ force coefficient;
$A_\mathrm{e}$ effective area of the object normal to the wind direction, m$^2$;
$p_\mathrm{d}$ design wind pressure, N/m$^2$.

**Table 2** Parameters used in the calculation of design wind speed

| Parameters | Value | Remarks |
|---|---|---|
| $V_b$ | 39 m/s | As per IS 875 wind zonal map |
| $k_1$ | 0.90 | For 10 years design life, 100 years return period for the wind |
| $k_2$ | 1.05 | For class A structure, terrain category 1 |
| $k_3$ | 1.00 | For plain land |
| $k_4$ | 1.00 | More than 60 km away from coast |

### 4.1.1 Design Wind Speed

The basic wind speed for any site shall be obtained from IS 875 Part 3 and shall be modified to include the following effects to get design wind speed, $V_Z$ at any height, $Z$.

Design wind speed ($V_Z$)

$$V_Z = V_b \times k_1 \times k_2 \times k_3 \times k_4$$

where

$V_Z$ design wind speed at any height $z$, m/s;
$V_b$ basic wind speed, m/s;
$k_1$ probability factor (risk coefficient);
$k_2$ terrain, height and structure size factor;
$k_3$ topography factor;
$k_4$ importance factor for the cyclonic region.

Various parameters used in the calculation of design wind speed have been listed in Table 2.

### 4.1.2 Design Wind Pressure

The wind pressure at any height above mean ground level shall be obtained by the following relationship between wind pressure and wind speed:

Design wind pressure ($p_Z$)

$$p_Z = 0.6\ V_Z^2$$

Table 3 gives the design wind speed and pressure at different heights of the structure.

**Table 3** Design wind speed and pressure at different heights

| Design wind speed (m/s) | Design wind pressure ($N/m^2$) |
|---|---|
| 36.86 | 814.97 |

### 4.1.3 Design Wind Load on Heliostat

Since the heliostats will be having different positions with respect to horizontal axis depending upon the positions of the sun in the sky, analyses have been performed for the two extreme positions of the heliostat i.e. 0° (position 1) and 70° (position 2) from horizontal axis. Plant will remain operational for wind speed up to 40 km/h. For wind speed beyond 40 km/h, the heliostats will be in parked condition, i.e. at 0° position from horizontal axis.

For operating condition, heliostat has been analyzed when it is at 70° from horizontal axis (position 2) as the wind loads will be maximum. For survival wind speed, heliostat has been analyzed when it is at 0° from horizontal axis (position 1). Pressure coefficients on reflecting surface have been considered as per IS 875 Part 3 and given in Table 4. In load case A overall pressure coefficient is 0.2, and in load case B overall pressure coefficient is − 0.5.

## *4.2 Earthquake Load on Heliostat*

Earthquake loads have been considered as per IS 1893 Part 1. For the purpose of determining seismic forces, the country is classified into four seismic zones. The design horizontal seismic coefficient $A_h$ for a structure shall be determined by the following expression [7]:

$$A_h = \frac{Z}{2} \times \frac{I}{R} \times \frac{S_a}{g}$$

where

$Z$ zone factor
$R$ response reduction factor
$I$ importance factor
$S_a/g$ average response acceleration coefficient for rock or soil sites.

**Table 4** Pressure coefficients for reflecting surface

| Load case | Overall pressure coefficients |
|---|---|
| *A* | 0.2 |
| *B* | − 0.5 |

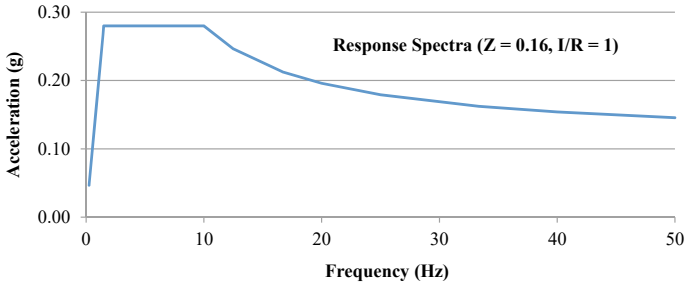


**Fig. 2** Response spectra for 2% damping

Site is located in seismic zone III. Heliostat is a welded steel structure, damping for design basis earthquake has been considered as 2%. Response spectra used in the analysis for 2% damping is shown in Fig. 2.

## 5 Finite Element Analysis

Finite element analyses of heliostat have been performed to optimize the design and estimate the deflections and stresses due to dead weight, imposed loads, wind loads and earthquake loads. Beam elements have been used to model the structural members. Lumped mass elements have been used to model imposed loads. Link elements have been used to model cables (25 mm diameter) used for controlling deflections in heliostat.

Since the heliostats will be having different positions with respect to horizontal axis depending upon the positions of the sun in the sky, analyses have been performed for the two extreme positions of the heliostat, i.e. 0° (position 1) and 70° (position 2) from horizontal axis. Figure 3 shows the finite element models of heliostat in different positions.

Static analyses have been performed to estimate the stresses and deflections due to dead weight, imposed loads and wind loads. Response spectrum analysis has been performed to estimate the stresses and deflections due to earthquake loads. The maximum deflections due to various loads and their combinations have been listed in Table 5. Deflections due to dead loads, imposed loads and operating wind loads are within the allowable limit. Figure 4 shows the deflected shape due to dead weight and imposed loads of reflecting surface.

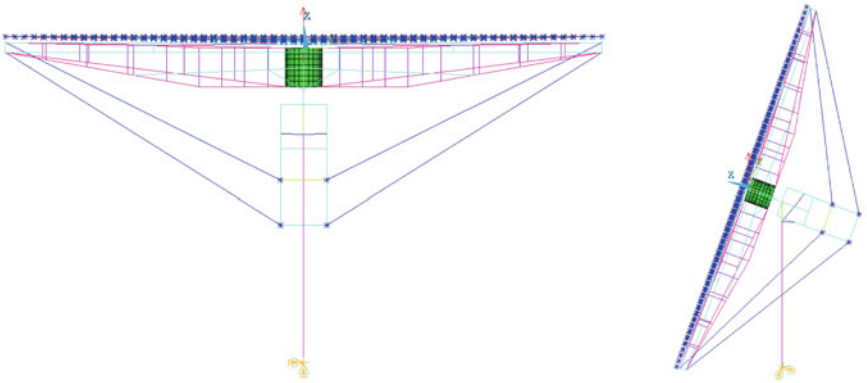

(a) Position 1 (b) Position 2

**Fig. 3** Finite element models of heliostat in different positions

**Table 5** Maximum deflections due to various loads and their combinations

| Load combinations | | Deflection (mm) |
|---|---|---|
| Dead loads + imposed loads | Position 1 | 8.3 |
| | Position 2 | 26.1 |
| Dead loads + imposed loads + wind loads in *X* direction (survival) | Load case A | 16.4 |
| | Load case B | 41.1 |
| Dead loads + imposed loads + wind loads in *Y* direction (survival) | Load case A | 78.6 |
| | Load case B | 198.4 |
| Dead loads + imposed loads + wind loads in *X* direction (operating) | Load case A | 25.3 |
| | Load case B | 46.0 |
| Dead loads + imposed loads + wind loads in *Y* direction (operating) | Load case A | 31.1 |
| | Load case B | 73.7 |
| Dead loads + imposed loads + earthquake loads | Position 1 | 37.7 |
| | Position 2 | 41.3 |

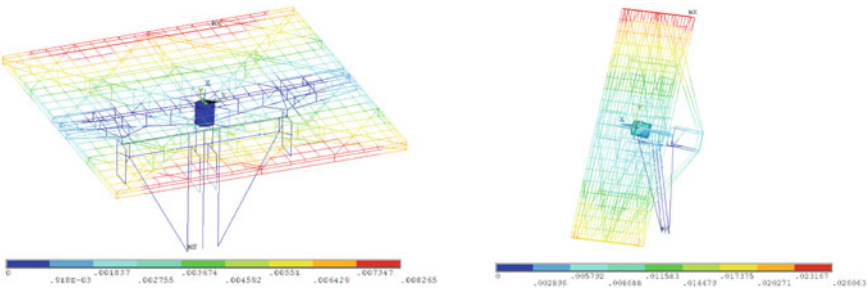

(a) Position 1 (b) Position 2

**Fig. 4** Deflected shape (dead loads + imposed loads)

# 6 Design Checks

## *6.1 Permissible Stresses as Per IS 800*

### 6.1.1 Axial Stress in Tension

The permissible stress in axial tension on the net cross-sectional area of hollow sections shall not exceed the values of $\sigma_{at}$.

$$\sigma_{at} = 0.6 f_y$$

where

$f_y$ minimum yield stress, MPa.

### 6.1.2 Axial Stress in Compression

The direct stress in compression on the gross cross-sectional area of axially loaded steel hollow sections shall not exceed $0.6 f_y$ nor the permissible stress $\sigma_{ac}$, calculated using the following formula:

$$\sigma_{ac} = 0.6 \frac{f_{cc} \times f_y}{\left[(f_{cc})^n + (f_y)^n\right]^{1/n}}$$

where

$\sigma_{ac}$ permissible stress in axial compression, MPa
$f_{cc}$ elastic critical stress in compression $= \pi^2 E/\lambda^2$ MPa
$\lambda$ $l/r =$ ratio of the effective length of the member and the radius of gyration
$f_y$ minimum yield stress, MPa
$E$ modulus of elasticity, MPa
$n$ a factor assumed as 1.4.

### 6.1.3 Bending Stresses

In hollow sections, the tensile bending stress and the compressive bending stress in the extreme fibres shall not exceed the values of $\sigma_{bt}$.

$$\sigma_{bt} = 0.66 f_y$$

where

$f_y$ minimum yield stress, MPa.

**Table 6** Allowable stresses for tension and bending

| | Dead loads + imposed loads | | Dead loads + imposed loads + wind loads or earthquake loads | |
|---|---|---|---|---|
| | YSt 240 | YSt 310 | YSt 240 | YSt 310 |
| Axial tension (MPa) | 144.0 | 186.0 | 192.0 | 248.0 |
| Bending stress (MPa) | 158.4 | 204.6 | 211.2 | 272.8 |

**Table 7** Permissible stresses in axial compression in MPa

| | Dead loads + imposed loads | | Dead loads + imposed loads + wind loads or earthquake loads | |
|---|---|---|---|---|
| Slenderness ratio | YSt 240 | YSt 310 | YSt 240 | YSt 310 |
| 25 | 141.3 | 181.0 | 188.4 | 241.3 |
| 50 | 127.3 | 156.8 | 169.7 | 209.1 |
| 75 | 103.5 | 120.3 | 138.0 | 160.4 |
| 100 | 79.1 | 87.3 | 105.4 | 116.4 |
| 125 | 59.4 | 63.4 | 79.2 | 84.5 |
| 150 | 45.0 | 47.0 | 60.0 | 62.7 |
| 175 | 34.8 | 35.9 | 46.4 | 47.9 |
| 200 | 27.5 | 28.1 | 36.7 | 37.5 |

Table 6 gives the allowable stresses for tension and bending for structural steel YSt 240 grade and YSt 310 grade for different load combinations. Table 7 gives the permissible stresses in compression based on slenderness ratios for steel members YSt 240 grade and YSt 310 grade for different load combinations.

### 6.1.4 Combined Stresses

Combined stresses in axial compression and bending should satisfy Eq. (1).

$$\frac{\sigma_{\text{ac}}, \text{cal.}}{\sigma_{\text{ac}}} + \frac{C_{\text{mx}} \times \sigma_{\text{bcx}}, \text{cal.}}{\left\{1 - \frac{\sigma_{\text{ac}}, \text{cal.}}{0.60 f_{\text{ccx}}}\right\} \sigma_{\text{bcx}}} + \frac{C_{\text{my}} \times \sigma_{\text{bcy}}, \text{cal.}}{\left\{1 - \frac{\sigma_{\text{ac}}, \text{cal.}}{0.60 f_{\text{ccy}}}\right\} \sigma_{\text{bcy}}} \leq 1.0 \tag{1}$$

Similarly combined stresses in axial tension and bending should satisfy Eq. (2).

$$\frac{\sigma_{\text{at}}, \text{cal.}}{0.60 f_{\text{y}}} + \frac{\sigma_{\text{btx}}, \text{cal.}}{0.66 f_{\text{y}}} + \frac{\sigma_{\text{bty}}, cal.}{0.66 f_{\text{y}}} \leq 1.0 \tag{2}$$

where

$\sigma_{\text{ac}}$, cal. calculated average axial compressive stress

$\sigma_{at}$, cal. calculated average axial tensile stress
$\sigma_{bc}$, cal. calculated bending compressive stress in extreme fibre
$\sigma_{bt}$, cal. calculated bending tensile stress in extreme fibre
$\sigma_{ac}$ permissible axial comp. stress in the member subject to axial comp. load only
$\sigma_{at}$ permissible axial tensile stress in the member subject to axial tensile load only
$\sigma_{bc}$ permissible bending compressive stress in extreme fibre
$\sigma_{bt}$ permissible bending tensile stress in extreme fibre
$f_{cc}$ elastic critical stress in compression
$C_m$ a coefficient.

## 6.2 *Maximum Stresses in Structural Tubes Due to Various Loadings*

Structural tubes of different sizes have been used in the design of heliostat. Stresses in axial tension, axial compression and bending are listed in Tables 8, 9, 10, 11, 12, 13, 14 and 15 for different load combinations.

The stresses listed in the above tables for various loads and their combinations have been checked against the allowable stresses as per IS 800 and are found within

**Table 8** Dead loads + imposed loads (position 1)

| Tubular sections size | Axial tension stress (MPa) | Axial compression stress (MPa) | Bending stress (MPa) |
|---|---|---|---|
| *Box section* | | | |
| 150 × 150 × 8.0 mm thk | 0.77 | 0.00 | 1.28 |
| 125 × 125 × 5.0 mm thk | 0.00 | 4.49 | 22.3 |
| 100 × 100 × 5.0 mm thk | 0.00 | 3.51 | 9.80 |
| 72 × 72 × 3.2 mm thk | 7.16 | 19.5 | 36.7 |
| 50 × 50 × 2.9 mm thk | 1.47 | 3.53 | 57.1 |
| 30 × 30 × 3.2 mm thk | 22.3 | 7.08 | 23.5 |
| *Circular section* | | | |
| 350 NB 8.0 mm thk | 0.00 | 3.54 | 0.00 |
| 100 NB 5.4 mm thk | 2.48 | 7.52 | 52.7 |

**Table 9** Dead loads + imposed loads (position 2)

| Tubular sections size | Axial tension stress (MPa) | Axial compression stress (MPa) | Bending stress (MPa) |
|---|---|---|---|
| *Box section* | | | |
| 150 × 150 × 8.0 mm thk | 0.74 | 0.00 | 3.67 |
| 125 × 125 × 5.0 mm thk | 0.00 | 1.31 | 39.9 |
| 100 × 100 × 5.0 mm thk | 0.00 | 2.63 | 27.6 |
| 72 × 72 × 3.2 mm thk | 8.89 | 10.2 | 50.8 |
| 50 × 50 × 2.9 mm thk | 0.70 | 1.40 | 17.8 |
| 30 × 30 × 3.2 mm thk | 10.7 | 4.86 | 10.7 |
| *Circular section* | | | |
| 350 NB 8.0 mm thk | 0.00 | 3.96 | 18.7 |
| 100 NB 5.4 mm thk | 0.00 | 6.43 | 60.8 |

**Table 10** Dead loads + imposed loads + wind loads in *X* direction (load case A)

| Tubular sections size | Axial tension stress (MPa) | Axial compression stress (MPa) | Bending stress (MPa) |
|---|---|---|---|
| *Box section* | | | |
| 150 × 150 × 8.0 mm thk | 1.02 | 0.00 | 28.4 |
| 125 × 125 × 5.0 mm thk | 1.81 | 13.4 | 34.0 |
| 100 × 100 × 5.0 mm thk | 0.00 | 5.37 | 23.6 |
| 72 × 72 × 3.2 mm thk | 12.6 | 28.5 | 57.3 |
| 50 × 50 × 2.9 mm thk | 2.60 | 7.28 | 83.9 |
| 30 × 30 × 3.2 mm thk | 38.2 | 12.9 | 59.4 |
| *Circular section* | | | |
| 350 NB 8.0 mm thk | 0.00 | 4.62 | 50.5 |
| 100 NB 5.4 mm thk | 6.64 | 12.6 | 147 |

**Table 11** Dead loads + imposed loads + wind loads in X direction (load case B)

| Tubular sections size | Axial tension stress (MPa) | Axial compression stress (MPa) | Bending stress (MPa) |
|---|---|---|---|
| *Box section* | | | |
| 150 × 150 × 8.0 mm thk | 0.65 | 0.05 | 83.1 |
| 125 × 125 × 5.0 mm thk | 6.57 | 6.32 | 20.0 |
| 100 × 100 × 5.0 mm thk | 7.70 | 8.21 | 33.0 |
| 72 × 72 × 3.2 mm thk | 16.5 | 16.0 | 56.4 |
| 50 × 50 × 2.9 mm thk | 6.27 | 5.37 | 87.6 |
| 30 × 30 × 3.2 mm thk | 19.0 | 21.1 | 66.5 |
| *Circular section* | | | |
| 350 NB 8.0 mm thk | 0.00 | 0.91 | 135 |
| 100 NB 5.4 mm thk | 21.6 | 22.5 | 114 |

**Table 12** Dead loads + imposed loads + wind loads in *Y* direction (load case A)

| Tubular sections size | Axial tension stress (MPa) | Axial compression stress (MPa) | Bending stress (MPa) |
|---|---|---|---|
| *Box section* | | | |
| 150 × 150 × 8.0 mm thk | 0.00 | 0.95 | 3.11 |
| 125 × 125 × 5.0 mm thk | 0.00 | 6.48 | 131 |
| 100 × 100 × 5.0 mm thk | 0.00 | 4.79 | 21.4 |
| 72 × 72 × 3.2 mm thk | 14.9 | 39.5 | 164 |
| 50 × 50 × 2.9 mm thk | 2.89 | 4.97 | 113 |
| 30 × 30 × 3.2 mm thk | 33.3 | 12.9 | 56.1 |
| *Circular section* | | | |
| 350 NB 8.0 mm thk | 0.00 | 4.65 | 26.3 |
| 100 NB 5.4 mm thk | 4.00 | 9.46 | 73.0 |

**Table 13** Dead loads + imposed loads + wind loads in *Y* direction (load case B)

| Tubular sections size | Axial tension stress (MPa) | Axial compression stress (MPa) | Bending stress (MPa) |
|---|---|---|---|
| *Box section* | | | |
| 150 × 150 × 8.0 mm thk | 0.03 | 0.00 | 29.7 |
| 125 × 125 × 5.0 mm thk | 0.18 | 0.00 | 201 |
| 100 × 100 × 5.0 mm thk | 0.38 | 0.25 | 95.6 |
| 72 × 72 × 3.2 mm thk | 23.2 | 20.6 | 106 |
| 50 × 50 × 2.9 mm thk | 2.30 | 0.83 | 56.5 |
| 30 × 30 × 3.2 mm thk | 19.6 | 22.8 | 68.0 |
| *Circular section* | | | |
| 350 NB 8.0 mm thk | 0.00 | 0.90 | 201 |
| 100 NB 5.4 mm thk | 0.37 | 2.23 | 219 |

**Table 14** Dead loads + imposed loads + earthquake loads (position 1)

| Tubular sections size | Axial tension stress (MPa) | Axial compression stress (MPa) | Bending stress (MPa) |
|---|---|---|---|
| *Box section* | | | |
| 150 × 150 × 8.0 mm thk | 1.0 | 0.2 | 37.3 |
| 125 × 125 × 5.0 mm thk | 3.9 | 8.4 | 66.2 |
| 100 × 100 × 5.0 mm thk | 2.7 | 6.2 | 30.3 |
| 72 × 72 × 3.2 mm thk | 13.9 | 26.3 | 71.7 |
| 50 × 50 × 2.9 mm thk | 3.3 | 5.3 | 91.9 |
| 30 × 30 × 3.2 mm thk | 29.7 | 14.5 | 31.6 |
| *Circular section* | | | |
| 350 NB 8.0 mm thk | 0.2 | 3.8 | 59.6 |
| 100 NB 5.4 mm thk | 12.0 | 17.1 | 108.6 |

**Table 15** Dead loads + imposed loads + earthquake loads (position 2)

| Tubular sections size | Axial tension stress (MPa) | Axial compression stress (MPa) | Bending stress (MPa) |
|---|---|---|---|
| *Box section* | | | |
| 150 × 150 × 8.0 mm thk | 1.0 | 0.2 | 36.9 |
| 125 × 125 × 5.0 mm thk | 2.4 | 3.7 | 83.2 |
| 100 × 100 × 5.0 mm thk | 2.5 | 5.1 | 49.5 |
| 72 × 72 × 3.2 mm thk | 14.5 | 15.9 | 85.4 |
| 50 × 50 × 2.9 mm thk | 1.8 | 2.5 | 44.0 |
| 30 × 30 × 3.2 mm thk | 18.5 | 12.7 | 19.5 |
| *Circular section* | | | |
| 350 NB 8.0 mm thk | 0.6 | 4.6 | 75.9 |
| 100 NB 5.4 mm thk | 9.3 | 15.7 | 108.4 |

the allowable limit. Considering as fixed–fixed end conditions, buckling checks have been performed as per IS 800 and found safe.

Combined stresses in axial compression and bending, and axial tension and bending are listed in Table 16 for the most critical load combinations. The stress ratios listed in the Table 16 are less than 1, hence the structure is safe.

**Table 16** Dead loads + imposed loads + survival wind loads in *Y* direction (load case B)

| Tubular sections size | Axial compression and bending | Axial tension and bending |
|---|---|---|
| *Box section* | | |
| 150 × 150 × 8.0 mm thk | 0.00 + 0.12 + 0.00 = 0.12 | 0.00 + 0.14 + 0.01 = 0.15 |
| 125 × 125 × 5.0 mm thk | 0.00 + 0.81 + 0.01 = 0.82 | 0.00 + 0.95 + 0.01 = 0.97 |
| 100 × 100 × 5.0 mm thk | 0.00 + 0.08 + 0.38 = 0.46 | 0.00 + 0.09 + 0.45 = 0.55 |
| 72 × 72 × 3.2 mm thk | 0.13 + 0.45 + 0.27 = 0.85 | 0.12 + 0.50 + 0.30 = 0.92 |
| 50 × 50 × 2.9 mm thk | 0.00 + 0.23 + 0.10 = 0.33 | 0.01 + 0.27 + 0.12 = 0.40 |
| 30 × 30 × 3.2 mm thk | 0.36 + 0.04 + 0.46 = 0.87 | 0.10 + 0.03 + 0.32 = 0.45 |
| *Circular section* | | |
| 350 NB 8.0 mm thk | 0.00 + 0.63 + 0.00 = 0.63 | 0.00 + 0.74 + 0.00 = 0.74 |
| 100 NB 5.4 mm thk | 0.02 + 0.70 + 0.03 = 0.74 | 0.00 + 0.80 + 0.03 = 0.84 |

## 7 Vortex Shedding Frequency

Vortex shedding frequency of a structure is determined by the following formula:

$$f_s = \frac{S_t \times \overline{V}_{z,H}}{b} = \frac{0.10 \times 36.86}{10.0} = 0.37\,\text{Hz}$$

where

$S_t$ Strouhal number;
$\overline{V}_{z,H}$ hourly mean wind speed at height $z$;
b breadth of structure normal to the wind direction in the horizontal plane;

Vortex shedding frequency of the heliostat is 0.37 Hz which is lesser than the fundamental frequency (1.21 Hz) obtained from modal analysis of the structure. Frequencies and mass participations obtained from modal analyses for position 1 and position 2 have been listed in Tables 17 and 18, respectively.

**Table 17** Frequencies and percentage mass participations (position 1)

| Frequency (Hz) | % Mass participation ($X$) | % Mass participation ($Y$) | % Mass participation ($Z$) |
|---|---|---|---|
| 1.21 | 0.00 | 19.59 | 0.00 |
| 2.23 | 71.52 | 0.00 | 0.00 |
| 2.78 | 0.00 | 76.25 | 0.00 |
| 4.51 | 3.61 | 0.00 | 0.00 |
| 8.96 | 13.63 | 0.00 | 0.00 |

**Table 18** Frequencies and percentage mass participations (position 2)

| Frequency (Hz) | % Mass participation ($X$) | % Mass participation ($Y$) | % Mass participation ($Z$) |
|---|---|---|---|
| 1.24 | 0.00 | 4.21 | 12.41 |
| 2.13 | 62.57 | 0.00 | 0.00 |
| 2.69 | 0.00 | 7.50 | 71.98 |
| 4.50 | 6.61 | 0.00 | 0.00 |
| 8.84 | 21.94 | 0.00 | 0.00 |

## 8 Conclusions

Heliostat has been analyzed and design checks have been performed as per IS 800. Based on the above analyses, following conclusions can be made:

1. Heliostat has been analyzed to estimate the deflections and stresses due to dead weight, imposed loads, wind loads and earthquake loads.
2. Wind loads on heliostat have been considered as per IS 875 and earthquake loads as per IS 1893.
3. Fundamental frequencies of the structure are 1.21 Hz for position 1 and 1.24 Hz for position 2. IS 875 recommends frequency more than 1.0 Hz to avoid wind-induced oscillations.
4. Stresses due to various loads and their combinations have been checked against the allowable stresses as per IS 800 and are found within the allowable limits.
5. Buckling checks have been performed for structural members of heliostat as per IS 800 and found safe.

## References

1. IS 1161 (1998) Steel tubes for structural purposes
2. IS 806 (1996) Code of practice for use of steel tubes in general building construction
3. IS 800 (1984) Code of practice for general construction in steel
4. IS 875 Part 3 (1987) Code of practice for design loads (other than earthquake) for buildings and structures
5. IS 875 Part 3 (2015) Code of practice for design loads (other than earthquake) for buildings and structures
6. Cohen E, Vellozzi J, Suh SS (2006) Calculation of wind forces and pressures on antennas. Ann NY Acad Sci 116(1):161–221
7. IS 1893 Part 1 (2002) Criteria for earthquake resistant design of structures

# Size Optimization of Steel Using Diaphragm Actions in Vertical and Horizontal Plane


**S. N. K. Vinod and S. Praveenkumar**

**Abstract** In construction industry, the usage of structural steel in the building has increased and it can also be recycled in the future. The structural members in tall industrial steel buildings like column occupies more space due to larger section size which causes obstruction. In order to achieve economical section size for tall industrial steel building, spacing of columns is ideal, to be chosen with trial and error method for assessing the distance of center to center of column. The bracings system is provided in vertical plane, which will be tied to the major axis of column above certain height in nonusable space and also bracings system in horizontal plane, where both the planes act as a diaphragm. Due to connection in the major axis of column, section reduction will be possible by distribution of forces equally. The members used in bracing system will be of higher section due to distribution of more forces. For this the members of different shapes are used, to find the optimum section for the bracing members. This helps in optimizing the section size of the tall steel building.

**Keywords** Diaphragm actions · Shape of structural member · Bracing techniques

## 1 Introduction

The diaphragms act as slab arrangement and help in distributing the lateral forces to the columns in each story of the building. Here, the diaphragm is made as slab arrangement using bracing system but there will be no additional gravity load acting above the diaphragms. With this arrangement, diaphragm is used in the tall industrial building to get the stress distribution to take place in both the sides of the column, which helps in reducing the section size.

In this paper, the application of diaphragms in tall industrial building is tried in two planes. One is along the vertical plane connecting the columns in major axis

S. N. K. Vinod (✉) · S. Praveenkumar
Structural Engineering, Department of Civil Engineering, PSG College of Technology, Coimbatore, India
e-mail: vinodsnk@gmail.com



M. Madhavan et al. (eds.), *Proceedings of the Indian Structural Steel Conference 2020 (Vol. 1)*, Lecture Notes in Civil Engineering 318,
https://doi.org/10.1007/978-981-19-9390-9_20

for certain height more like a lattice arrangement. Second one is in the horizontal plane, the diaphragms arrangement will be of bracing system thickness. Connecting the major axis of the column with these two arrangements, the optimum results are gathered. Using this, diaphragms are added in the model and then analyzed. The analyzed results are compared with normal building model arrangement without diaphragms.

## 2 Methodology

The tall building is model size of 20 m wide and 25 m height and 50 m in length, based on this the modeling is done. The modeling is done with spacing of 6.25 m c/c of column along the length and at the gable end side the spacing is 4 m c/c and purlin spacing is 1.6 m c/c. which can be referred in Fig. 1 for model A, it is simple and a regular model without diaphragm which consists of tie member, wind bracing, column bracing, the model A, B and C is made with fixed supports.

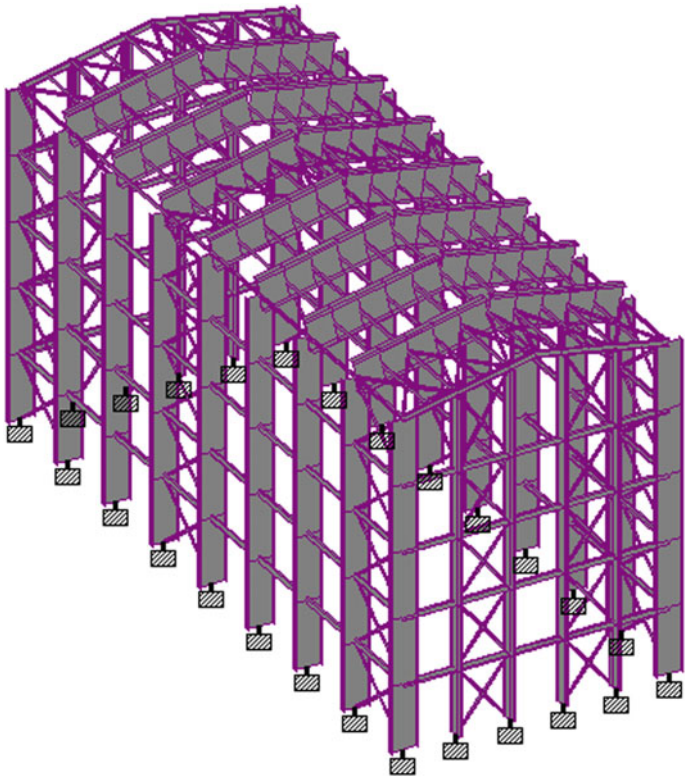

**Fig. 1** Model A without diaphragm

Wind bracing on the rafter members at three locations as shown in Fig. 1 along the length of building for three bays, column bracing is located in three places as shown in Fig. 1 along the length at end side and one at mid portion of length and column bracing along the width in two bays at gable end side. Similarly, for the model B the diaphragms placed at 10 m height in vertical plane with bracing connecting the steel columns, and model C is prepared with diaphragms actions in horizontal plane above 10 m height. The overall for model B and model C is shown in Figs. 2 and 3, respectively.

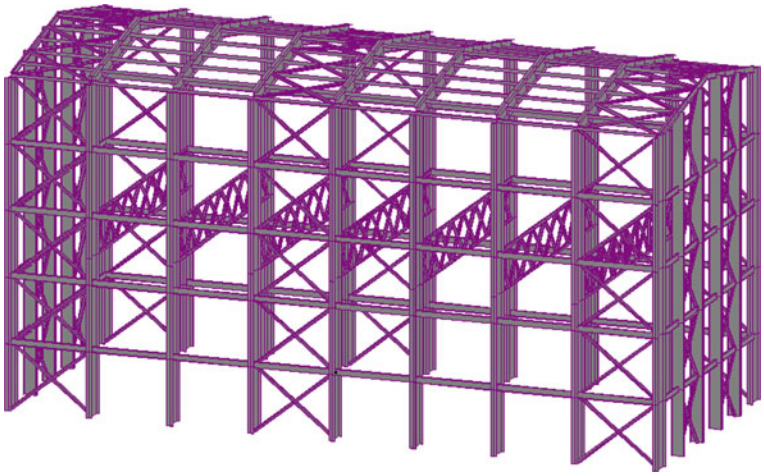

**Fig. 2** Model B with vertical diaphragms

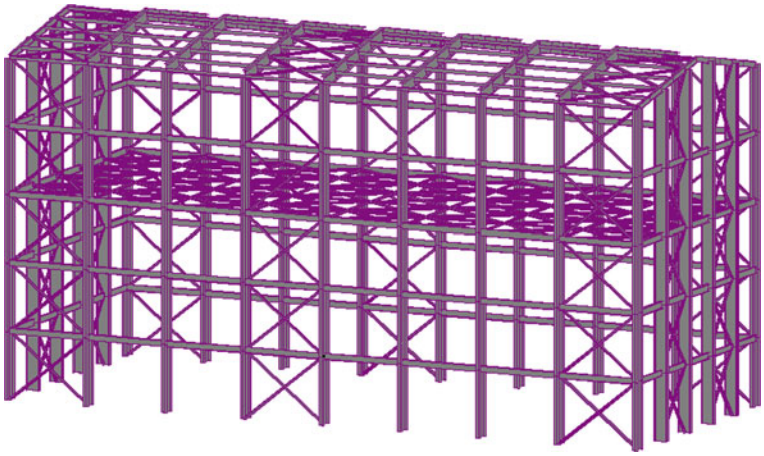

**Fig. 3** Model C with horizontal diaphragms

The model B and model C from Figs. 2 and 3 shows that the diaphragms arrangement is compared with the regular arrangements of model A.

### *2.1 Diaphragms Arrangements*

The model B and C has the diaphragms connected to steel column in the major axis of the member and in the minor axis the regular tie members are connected. The diaphragm bracing arrangement for model B in vertical is shown in Fig. 4 and similarly for the horizontal diaphragms is shown in Fig. 5.

## 3 Structural Configurations Details

The structure is configured as shown in figures above and the details of the building and dimensions are given in Table 1.

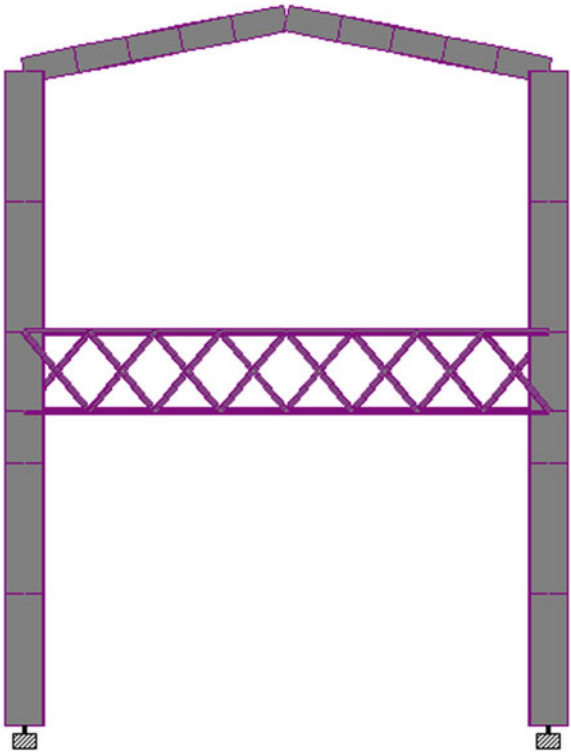

**Fig. 4** Model B diaphragm in vertical plane in elevation

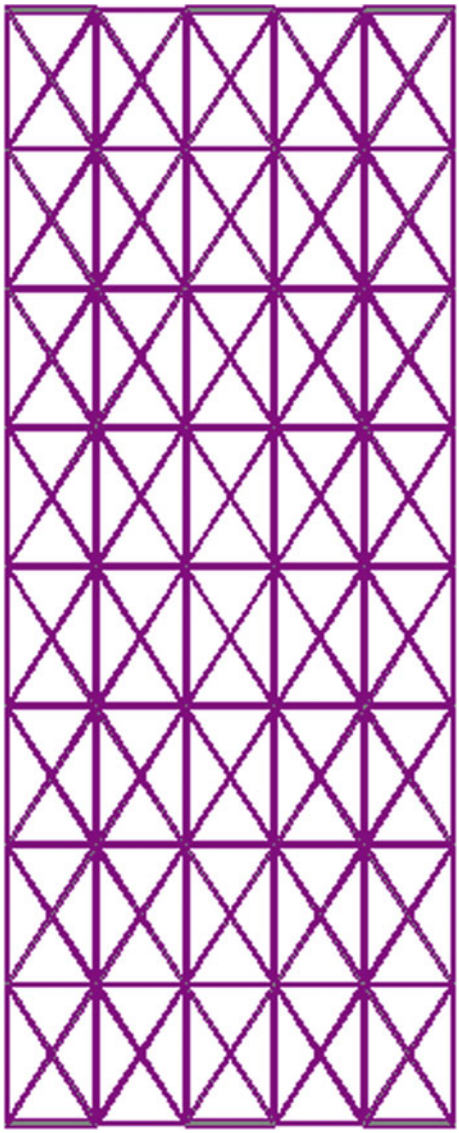

**Fig. 5** Model C diaphragm in horizontal plane in plan

**Table 1** Structure configuration

| S. No | Type of building | Industrial building |
|---|---|---|
| 1 | Type of structure | Single-story building |
| 2 | Location | Ludhiana |
| 3 | Total length of building | 50 m |
| 4 | Width of building | 20 m |
| 5 | Eves height of building | 25 m |
| 6 | Bay spacing of column | 6.25 m |
| 7 | Slope of roof | 6° |
| 8 | Diaphgrams at | 10 m height |
| 9 | Shape of structural column used | I section |
| 10 | Shape of structural beam used | I section |
| 11 | Shape of bracing member used | Circular section |
| 12 | Shape of purlin used | Channel section |
| 13 | Grade of steel used | Fe250 grade |

# 4 Load Calculations

## *4.1 Dead Load (DL)*

The dead load of the structure is taken for all the members used in the model, the loads assumed other than self-weight for model analysis are given below. The sheet weight of 0.06 KN/sqm is taken here.

- Dead load = 0.80 KN/m.

## *4.2 Live Load (LL)*

The live load of the structure is taken as per IS 875 part 3, normally the live load reduction takes place when the slope exceeds 10° then the reduction live load is to be carried out, but here the slope of roof is 6 ° then as per code the live load shall be kept as such, which is 0.75 KN/sqm. And live load is not going to act on all of the roof at all times, hence the 2/3rd of live load can be used for designing purpose which is 0.5 KN/sqm.

- Live load = 2.85 KN/m.

**Table 2** Wind load parameter

| S. No | Description | Data |
|---|---|---|
| 1 | Wind speed | 47 m/s |
| 2 | Basic wind speed coefficient, $k_1$ | 1 |
| 3 | Terrain category, $k_2$ | 1 |
| 4 | Ground level undulations | 1 |
| 5 | Design wind pressure | 1.325 KN/Sqm |

## *4.3 Wind Load (WL)*

The wind loads shall be as per IS 875 part 3, with factors for $k_1$, $k_2$, $k_3$ is taken as 1 and with wind speed is 47 m/s.

From Table 2, data is used for analysis for model A, B, C, the values from table are used in the Staad pro to compute the loads on the members.

## *4.4 Earth Quake Load (EQ)*

The earthquake loads shall be as per IS 1893(2005) part 4, the parameters for the seismic definition for computing the seismic load in Staad pro is given in Table 3.

The values are entered in seismic definition in the Staad pro for computing the loads and analyzing the models.

**Table 3** Seismic load parameter

| S. No | Description | Data |
|---|---|---|
| 1 | Seismic zone | III |
| 2 | Response reduction factor | 5 |
| 3 | Importance factor | 1 |
| 4 | Rock/soil type | 2 (medium soil) |
| 5 | Structure type | 2 (steel building) |
| 6 | Damping ratio | 5% |
| 7 | Period in *X* direction | 0.02 s |
| 8 | Period in *Y* direction | 0.0127 s |
| 9 | Foundation depth | 1.5 m |

### *4.5 Load Combinations*

The load combinations used as per IS 800-2007 are as follows:

1. 1.5DL + 1.5LL
2. 1.5DL + 1.5WL 0
3. 1.5DL + 1.5WL 90
4. 1.5DL + 1.5WL PARALLEL
5. 1.2DL + 1.2LL + 1.2WL 0
6. 1.2DL + 1.2LL + 1.2WL 90
7. 1.2DL + 1.2LL + 1.2WL PARALLEL
8. 1.2DL + 1.2LL + 1.2EQ X
9. 1.2DL + 1.2LL + 1.2EQ -X
10. 1.2DL + 1.2LL + 1.2EQ Z
11. 1.2DL + 1.2LL + 1.2EQ -Z
12. 1.5DL + 1.5EQ X
13. 1.5DL + 1.5EQ -X
14. 1.5DL + 1.5EQ Z
15. 1.5DL + 1.5EQ -Z
16. 0.9DL + 1.5WL 0
17. 0.9DL + 1.5WL 90
18. 0.9DL + 1.5WL PARALLEL

The model is analyzed and the moments in the columns are higher for the load case 16, 17, 18 and 2, 3, 4 which are critical load cases, since the building height is more than the width of building it behaves as slender member as a whole.

## 5 Staad.Pro Procedure

The Staad.Pro software package is a structural analysis and design software which helps in modeling, analyzing and designing the structure. The software supports standards of several countries, including Indian standard. The procedure includes modeling the structure, applying properties, specifications, loads and load combinations, analyzing and designing the structure. This software is an effective and user-friendly tool for three-dimensional model generation, analysis and multi-material designs.

In STAAD Pro, utilization ratio is the critical value that indicates the suitability of the member as per codes. Normally, a value higher than 1.0 indicates the extent to which the member is overstressed, and a value below 1.0 tells us there is serve capacity available. Critical conditions used as criteria to determine pass/fail status are slenderness limits, axial compression and bending, axial tension and bending, maximum w/t ratios and shear.

## 6 Results and Discussion

The design parameter used for designing the section for different models are given below.

The design parameter is varying for each model, which is the length factor in the major axis is varying due to the addition of diaphragms, with this the member is designed as per the inputs given. It is the critical factor for designing the steel member here. The design parameter used for designing the section for model A, B and C is shown in Figs. 6, 7 and 8.

### *6.1 Dimension Size Comparison*

The section size assumed initially are I section for steel column and raft beam. Based on the moment and shear forces, the section is designed and the weight of structure seems to comparatively less for diaphragms models B and C compared with model A, similarly the section sizes are higher for the model A.

Now taking the portal frames in 2D arrangement to compare the section sizes and other results, which are given in Table 4.

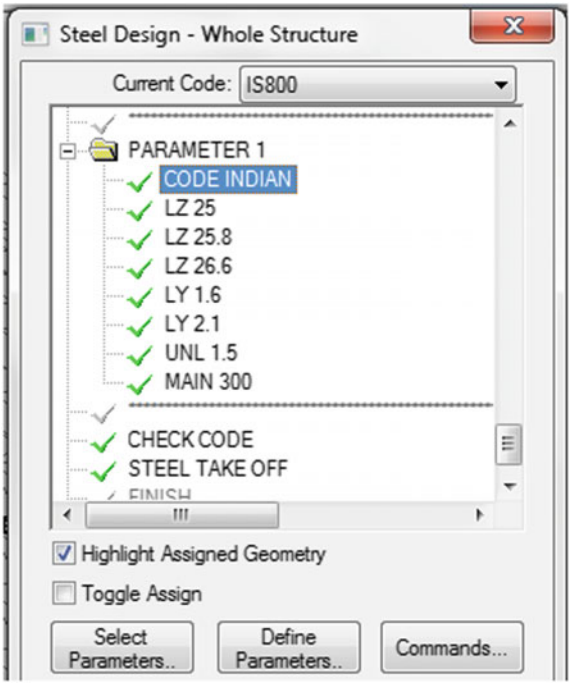


**Fig. 6** Design parameters for model A

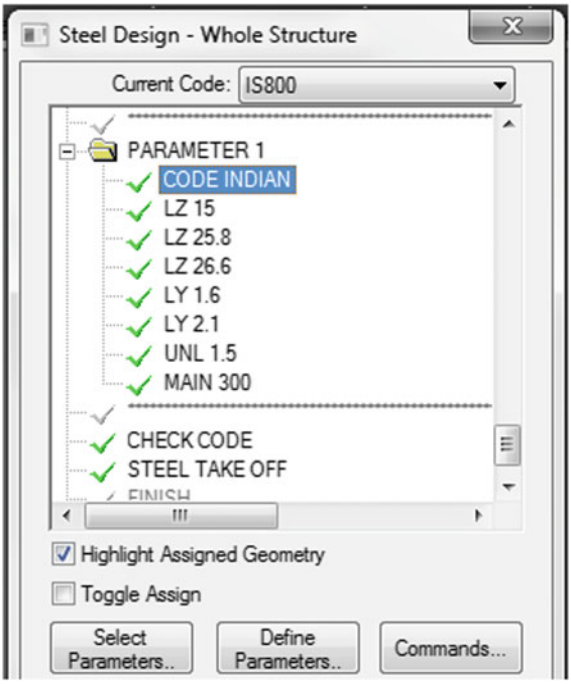


**Fig. 7** Design parameters for model B

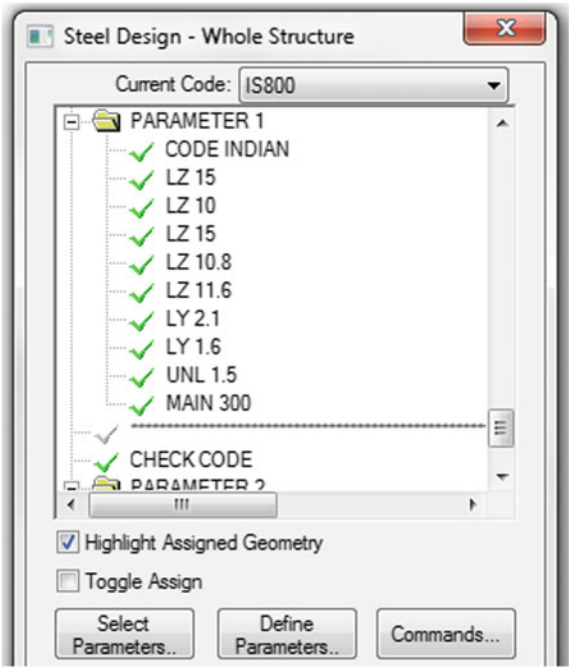


**Fig. 8** Design parameters for model C

**Table 4** Section sizes, moment, shear

| S. No | Description | I—section sizes in MM | Moment | Shear |
|---|---|---|---|---|
| 1 | Model A | 1950 × 550 × W10TK × F10Tk | 2762 KN-M | 183 KN |
| 2 | Model B | 1500 × 450 × W10TK × F12Tk | 1940 KN-M | 167 KN |
| 3 | Model C | 950 × 325 × W10TK × F12Tk | 776 KN-M | 216 KN |

**Table 5** Deflection of column

| S. No | Description | Deflection in MM | Permissible deflection in MM |
|---|---|---|---|
| 1 | Model A | 69 | 100 |
| 2 | Model B | 62 | 100 |
| 3 | Model C | 86 | 100 |

Table 4 results the steel column sizes that are given, where the model A is higher in section size which is due to high stresses induced due to the unsupported length in the major axis has greater length. The model B is comparatively low in section size due to the connectivity of diaphragms in the major axis of the column and model C is even lesser in section size compared with model A and B.

The deflection results from Table 5 represents the column at the ridge level where the raft beam and column connection takes place, deflection value varies for each model due to variations in the section size and the deflection values are within the permissible limit and deflection seems to be less in the model B.

## *6.2 Section Steel Weight Comparisons*

The section size weight is taken for comparisons in 2D frame and as well as 3D frame, the comparison results are given in the table below.

Table 6 and 7 shows the steel weight is gradually decreasing from the model A to B to C, it is noticed that the model C has low section weight in 3D frame analysis and design. The results are same in the 2D frame weight comparison.

The steel weight for 3D frame includes members like purlin, bracing, portal frame member and tie members. The 2D frame steel weight includes only the portal frame member. The chart for the same is shown in Figs. 9 and 10.

**Table 6** Steel weight comparison in 3D

| S. No | Description | Weight in KN |
|---|---|---|
| 1 | Model A | 2875 |
| 2 | Model B | 2600 |
| 3 | Model C | 2454 |

**Table 7** Steel weight comparison in 2D

| S. No | Description | Weight in KN |
|---|---|---|
| 1 | Model A | 200 |
| 2 | Model B | 167 |
| 3 | Model C | 106 |

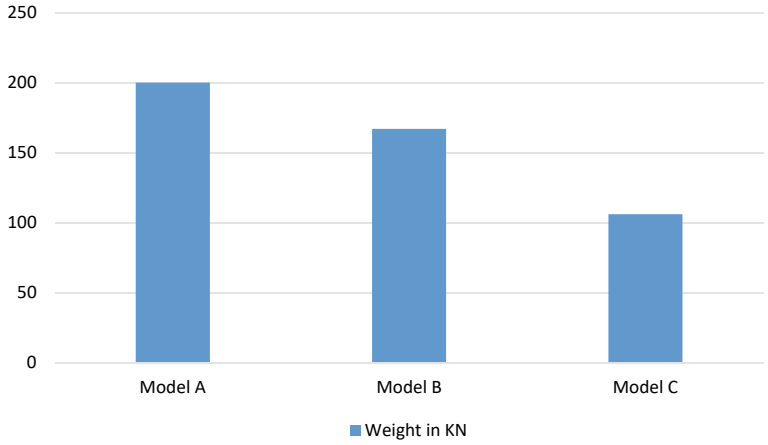


**Fig. 9** Weight comparison for 2D frame model

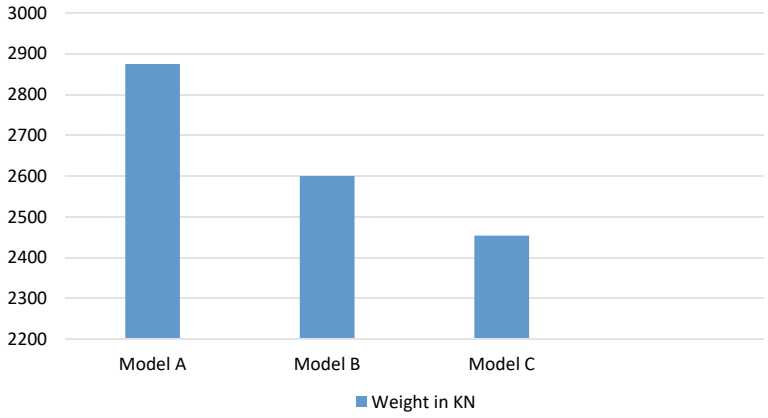


**Fig. 10** Weight comparison for 3D frame models

## 7 Conclusion

- The model analysis of different arrangement of diaphragms gives some additional stiffness in the structure, thus helps in reducing the section size of members. This also provides some resistance against the lateral forces due to the diaphragms action, especially in the horizontal plane the effect of diaphragm is effective in reducing the section sizes.
- The deflection limit from the results shows that section above the diaphragm action is susceptible to more deflection in the horizontal plane of model B diaphragm, but in the vertical plane diaphragm the deflection value is less compared with the regular model A arrangement.
- The section size variation in all the models is compared and the result of model C the section size is less compared with others, hence the model C arrangement can help in increasing the usage space of the building.
- The structural section size reduction will also reflect in the steel weight, thus from the results of comparison of steel weight the model C has the least weight over other models A and B. Hence, this helps in reduction cost compared with other models.
- The diaphragms arrangement model is useful only when the building above certain height has nonusable space, then only the diaphragm arrangement will become possible and should be free from obstructions of amenities of building usage.

## References

1. Kanyilmazn A, Brambilla G, Chiarelli GP, Castiglioni CA (2016) Assessment of the seismic behavior of braced steel storage racking systems by means of full scale push over tests. Thin-Walled Struct
2. Imanpour A, Stoakes C, Tremblay R, Fahnestock L, Davaran A (2013) Seismic stability response of columns in multi-tiered braced steel frames for industrial applications. In: Structural congress
3. Lendvai A, Joó AL, Dunai L (2018) Experimental full-scale tests on steel portal frames for development of diaphragm action. Thin-Walled Struct
4. Phan DT, Lim JBP, Tanyimboh TT, Sha W (2017) Optimum design of cold-formed steel portal frame buildings including joint effects and secondary members. Int J Steel Struct
5. Wang F, Sua MZ, Hong M, Guo Y, Li S (2016) Cyclic behavior of Y-shaped eccentrically braced frames fabricated with high-strength steel composite. J Constr Steel Res 120
6. Jagadeesh BN, Prakash MR (2016) Seismic response of steel structure with mega bracing system. Int J Eng Sci Res Technol
7. Fu JY, Wu JR, Dong CC, Xu A, Pi Y-L (2019) Optimization design of large span portal-rigid steel frame with tapered sections under wind-induced drift constraint. Eng Struct
8. Skalomenos KA, Inamasu H, Shimada H, Nakashima M (2017) Development of a steel brace with intentional eccentricity and experimental validation. Am Soc Civ Eng
9. Prabin Kumar K, Sunny Praksh D (2018) Planning analysis and design of industrial building using STAAD PRO. Int J Pure Appl Math 119(17)
10. Bakhoum MM, Mourad SA, Hassan MM (2015) Comparison of actions and resistances in different building design codes. J Adv Res

11. Zeynalian M, Ronagh HR, Hatami S (2012) Seismic characteristics of K-braced cold-formed steel shear walls. J Constr Steel Res
12. Lande PS, Kucheriya VV (2015) Comparative study of an industrial pre-engineered building with conventional steel building. Int J Adv Res Ideas Innovations Technol
13. Sabnis SN, Shahezad M (2019) Comparative study of different codes on steel building. Int J Adv Res Ideas Innovations Technol
14. Somasekharan S, Vasugi K (2017) Wind load analysis for industrial building with different bracing patterns and its comparison with pre-engineered building. Int J Civ Eng Technol (IJCIET) (4)
15. Metre S, Ghule SC, Kiran R (2017) Comparative study of different types of bracing systems by placing at different locations. Int Res Eng Technol (IRJET)
16. Balogh T, Vigh LG (2015) Seismic reliability based optimization of steel portal frame structures. In: SECED 2015 conference: earthquake risk and engineering towards a resilient world, Cambridge UK

# Spectral Correlation-Based Enhanced Breathing Crack Diagnosis of Steel Structures with Linear Response Subtraction Scheme


**J. Prawin**

**Abstract** In this paper, a reference-free spectral correlation-based approach for enhanced breathing crack diagnosis is proposed using the acceleration time history responses measured under bitone harmonic excitation. Even though spectral correlation can effectively remove the stationary noise components overlapped with the nonlinear intermodulation components in the response, it is difficult to isolate the intermodulation components alone at a selected cyclic frequency, and careful choice of appropriate cyclic frequency has to be made for accurate damage diagnosis. Therefore, linear response subtraction is first applied on the actual response to isolate the breathing crack induced nonlinear intermodulations, and then, spectral correlation computed from modified response is used for breathing crack diagnosis. The proposed linear response scheme helps in enhanced breathing crack diagnosis using spectral correlation estimated at any cyclic frequency. The proposed scheme is verified through both numerical and experimental examples.

**Keywords** Spectral correlation · Bitone harmonic excitation · Linear response subtraction · Breathing crack · Cyclic frequency

## 1 Introduction

Most of the damages in the structural elements reflect in the form of visible cracks, and these cracks will generally be open and remain open during vibration. This is true only when the structure is in the linear state even after damage. On the other hand, subtle cracks such as breathing crack wherein the edges of the crack come into and out of contact during vibration exhibit nonlinear rather bilinear (nonstationary) behaviour once damage sets in, even though the structure is linear before damage.

J. Prawin (✉)
CSIR-Structural Engineering Research Centre, CSIR Campus, Chennai, Tamil Nadu, India
e-mail: prawinpsg@gmail.com; prawinj@serc.res.in



M. Madhavan et al. (eds.), *Proceedings of the Indian Structural Steel Conference 2020 (Vol. 1)*, Lecture Notes in Civil Engineering 318,
https://doi.org/10.1007/978-981-19-9390-9_21

Various researchers [3, 4, 12, 15, 16, 18, 19] have developed the breathing crack damage diagnostic technique using the vibration time history measurements obtained under both single tone and bitone harmonic excitation. Peng et al. [18] and Prawin and Rao [16] developed breathing crack identification technique based on the ratio of higher-order nonlinear output frequency response functions to first-order frequency response function using single-tone harmonic vibration response, with higher-order frequency response functions being derived using principles of Volterra series. Giannini et al. [9] proposed a numerical model-based breathing crack identification technique using harmonic vibration response by forming a harmonic damage surface based on the ratio of second order superharmonic to excitation harmonic as a function of spatial location of crack and severity. Breathing crack identification (i.e. localization) is generally performed by the comparison of the Fourier power spectrum amplitudes of superharmonics (i.e. damage sensitive nonlinear features) of various sensors obtained spatially across the structure. The energy of superharmonics is found to be higher around the spatial location of the damage when compared to the other locations. It should be mentioned here that the input amplitude of excitation, excitation frequency has to be properly chosen to observe these superharmonics induced by the breathing crack under single-tone harmonic excitation. Apart from this, it is essential to ensure that there exist no pseudo-harmonics while exciting the structure with breathing crack with pure single-tone harmonic excitation [3, 4].

Alternatively, instead of exciting the structure with single-tone harmonic excitation for breathing crack localization, few researchers [12, 19] have developed the damage diagnostic technique using the vibration time history measurements obtained under bitone harmonic excitation. The bitone harmonic excitation refers to the harmonic excitation of the structure with two input excitation frequencies simultaneously similar to single-tone harmonic excitation, employed from vibro-acoustic principles. In the literature, these two input excitation frequencies are popularly referred to as pumping and probing frequency (i.e. $\omega_{prob}$ and $\omega_{pump}$). It should be mentioned here that probing frequency is always much larger than pumping frequency. The presence and the spatial location of the breathing crack in case of the bitone harmonic response are identified by the presence and amplitudes of sidebands/intermodulations and the superharmonics of two input excitation frequencies, similar to single-tone harmonic excitation. The sidebands are formed due to the coupling of pumping and probing frequencies, and these sidebands are also called as intermodulations. A detailed review of breathing crack diagnostic techniques can be found in Broda et al. [4].

It should be mentioned here that the majority of the works consider only the first sideband/intermodulation on either side of the probing frequency in the case of bitone and only second- and third-order superharmonic (i.e. first few super harmonics) in the case of single-tone harmonic excitation for breathing crack identification [3, 4, 12]. The higher-order superharmonics and sidebands exhibiting significant damage sensitive features are being ignored due to their low or similar energy levels as that of noise. Isolating the nonlinear higher-order sidebands/superharmonics and noise

components is extremely difficult, and ignoring these features results in poor damage identification. Therefore, it is essential to devise appropriate techniques to extract these higher-order intermodulations, buried with noise to identify breathing cracks at their incipient stage.

Spectral correlation has been earlier widely applied in the area of diagnosis of gear faults in moving mechanical systems [1, 11], channel sensing, and spectrum allocation in wireless communication [6–8, 10, 21]. Recently it has been employed in the area of structural health monitoring for fatigue-breathing crack identification as it is robust for analysis of various kinds of signals such as stationary, nonstationary, and cyclostationary vibration signals. Boungou et al. [2] have investigated spectral correlation for breathing crack identification and concluded that the spectral correlation amplitude estimated at a cyclic frequency equal to frequency of response of structure with breathing crack increases with increase in crack depth. Liu et al. [13, 14] have employed spectral correlation to isolate nonlinear intermodulation components and stationary noise components using the principles of nonlinear ultrasonic.

In this paper, a reference-free spectral correlation-based approach for enhanced breathing crack is proposed using the acceleration time history responses measured under bitone harmonic excitation. Spectral correlation is basically used to determine the statistical link between the responses at the original two input frequencies (i.e. bitone harmonic excitation). Spectral correlation estimated at a zero cyclic frequency results in spectral density function, and spectral correlation exhibits multiple peaks at various spectral frequencies estimated at non-zero cyclic frequency [8]. Spectral correlation basically exhibits a peak at spectral frequency equal to average of both input frequencies for a cyclic frequency corresponding to difference of input frequencies. It should be mentioned here that the peak at average of both input frequencies is not due to interaction of input frequencies alone but also due to interactions of noise components and harmonics of noise components or input frequencies. This is due to the fact that a large number of frequency combinations results in same cyclic frequency and this consequently end up with multiple spectral correlation peaks at several frequencies; however, the amplitudes are dependent on the energy of the various components present in the signal (i.e. nonlinear components—sidebands and harmonics).The spectral correlation varies as well for varied cyclic frequencies. Therefore, the limitation of spectral correlation is that it is difficult to isolate the nonlinear components alone at a selected cyclic frequency and careful choice of appropriate cyclic frequency has to be made for accurate damage diagnosis. Keeping these things in view, linear response subtraction (LRS) scheme is used in the present work to isolate only the nonlinear components using spectral correlation (the double Fourier transform) with respect to time and time lag of autocorrelation of harmonic response irrespective of chosen cyclic frequency. The proposed approach considers all the possible higher-order superharmonics and intermodulations in contrast to the earlier works with only first few superharmonics and can effectively identify subtle cracks. The proposed approach is verified through both numerical and experimental studies.

## 2 Linear Response Subtraction (LRS) Scheme

The response of the structure without breathing crack under bitone harmonic excitation basically contains the superposition of the response of each of the individual input harmonic tones. The bitone harmonic response of the structure with breathing crack contains not only the response of two excitation harmonic input frequencies but also superharmonics of each tones and as well the intermodulation components produced by the interaction of two individual input harmonic tones. The linear response subtraction basically eliminates the response of the two individual input excitation harmonic components. This is performed experimentally as follows.

1. First two separate responses are obtained by independent application of low-frequency and high-frequency harmonic extraction
2. Obtain the response by the simultaneous excitation of both low and high frequencies
3. The response obtained in step 2 should be subtracted with the sum of the two responses obtained in step 1. The resulting subtracted response is called modified response (i.e. response obtained after linear response scheme).

Therefore, the response of the structure with breathing crack after linear response scheme application contains only the intermodulation components.

## 3 Numerical Investigation

A 0.3 m steel simply supported beam shown in Fig. 1 with cross-sectional area of 0.0025 $m^2$ is considered as the numerical example. The natural frequencies of the simply supported beam without breathing crack (estimated with sampling frequency of 10 kHz) are found to be 88.671, 354.689, 798.07, 1418.9, 1711.5, and 2217.4 Hz. The simply supported beam is subjected to bitone harmonic excitation of 400 Hz ($\omega_{pump}$, pumping frequency) and 2400 Hz ($\omega_{prob}$, probing frequency) at the centre of the beam.

The breathing crack is simulated near one-third span of the simply supported beam from the left support with crack depth equal to 0.1 h, where h is the depth of the beam. The detailed formulations related to breathing crack modelling can be found in Prawin et al. [15].

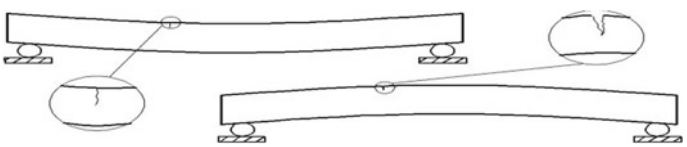

**Fig. 1** Simply supported beam with a breathing crack

Spectral correlation estimated at the following listed varied cyclic frequencies corresponding to the response of the structure with and without breathing crack, estimated without linear response subtraction scheme is shown in Figs. 2 and 3, respectively, for set-1 and set-2.

Set-1: Randomly chosen cyclic frequencies (i.e. 65, 2710 Hz) and cyclic frequency as difference in input frequency combinations (i.e. $\omega_{\text{prob}} - \omega_{\text{pump}} = 2000$ Hz).

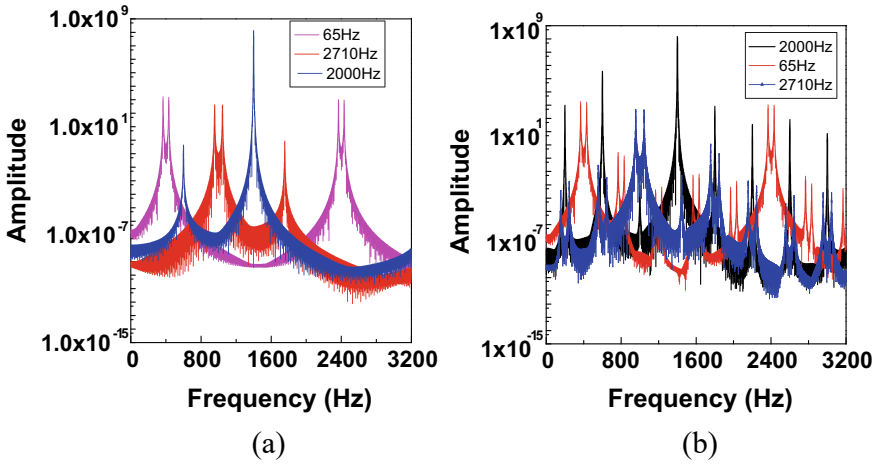


**Fig. 2** Spectral correlation—set 1 **a** undamaged state, **b** damaged state

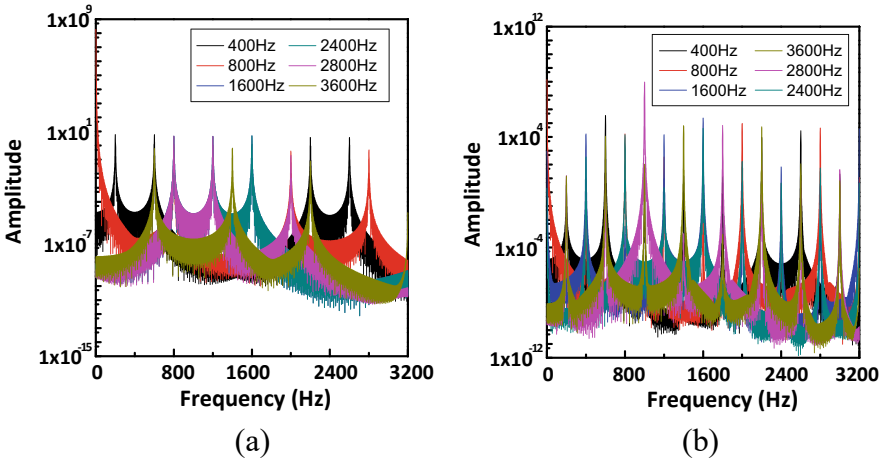


**Fig. 3** Spectral correlation—set 2, **a** undamaged state, **b** set 2 damaged state

Set-2: Cyclic frequency equal to response frequency components (i.e. $\omega_{pump}$,400 Hz, $2\omega_{pump}$,800H, $4\omega_{pump}/\omega_{prob}$-$2\omega_{pump}$,1600 Hz and $\omega_{prob}$, 2400 Hz, $\omega_{prob} + \omega_{pump}$,2800 Hz, and $\omega_{prob} + 3\omega_{pump}$, 3600 Hz).

The results of the spectral correlation, estimated without linear response subtraction scheme for the undamaged states of the two sets, are presented in Figs. 2a and Fig. 3a, while the results of the damaged states are presented in Figs. 2b and Fig. 3b. It can be observed from Fig. 2 that the maximum amplitude of spectral correlation, computed at cyclic frequencies corresponding to set-1 of the undamaged and damaged states of the structure, is of same order. Even though the spectral correlation for damaged states exhibits more peaks when compared to undamaged states, the magnitudes of additional peaks are of very low order. It should be noted here that the additional peaks in the damaged states are even though due to the nonlinear superharmonics and nonlinear intermodulations, they exhibit poor correlations.

From the results of the spectral correlation corresponding to set-2 presented in Fig. 3, it can be concluded the spectral correlation amplitudes of the damaged states are of very higher order than that of undamaged state and number of peaks in the damaged state is also higher than that of undamaged state, with high magnitude. Therefore, this investigation confirms that spectral correlation is sensitive to dynamic change resulting out of breathing crack, but careful choice of cyclic frequency is essential. It is preferable to choose the cyclic frequency equal to excitation frequency and intermodulation (i.e. response frequency components). Further for damage diagnosis, it is necessary to have the underlying undamaged state response of the structure to ensure that spectral correlation peaks are due to breathing crack.

In order to overcome the limitation of the requirement of underlying undamaged state response and choice of cyclic frequency, the linear response subtraction scheme is used in the present work. The results of the spectral correlation, estimated with linear response subtraction scheme for the undamaged and damaged states of the two sets, are presented in Figs. 4 and 5, respectively.

The spectral correlation plot, estimated with linear response subtraction scheme, shown in Fig. 4 does not show any peaks for the undamaged state of the structure and remains flat for all the spectral frequencies and chosen cyclic frequencies of set-1 and set-2. This is obvious that there exist no nonlinear components after application of the linear response subtraction scheme to the response of the structure without breathing crack (i.e. linear and undamaged). From the results presented in Figs. 4 and 5, the spectral correlation amplitudes of the damaged state of the structure are of very high order than that of the amplitudes of the undamaged states of the structure, irrespective of chosen cyclic frequency (i.e. set-1 and set-2).

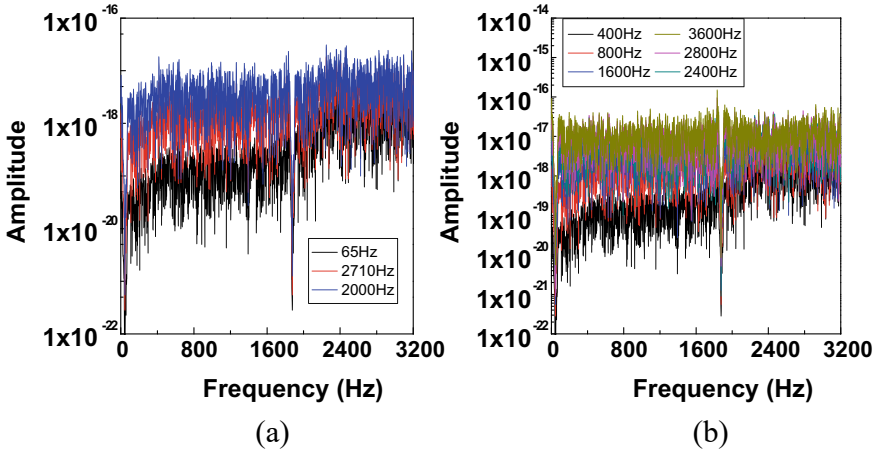


**Fig. 4** Spectral correlation (after LRS)—undamaged state **a** set 1, **b** set 2

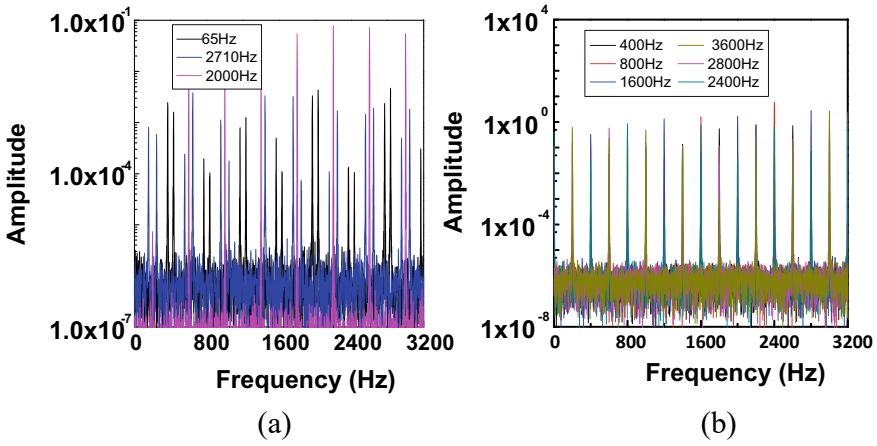


**Fig. 5** Spectral correlation (after LRS)—damaged state **a** set 1, **b** set 2

Therefore, the peaks at spectral correlation estimated using modified response (i.e. after linear response scheme) are only due to change in dynamics caused by breathing crack irrespective of cyclic frequency chosen and do not require the underlying undamaged state of the structure. It can be concluded from this investigation that the proposed linear response scheme helps in enhanced breathing crack diagnosis using spectral correlation estimated at any cyclic frequency. Further, this scheme does not need any apriori information about the underlying undamaged structure. The proposed linear response subtraction scheme has the ability to effectively isolate nonlinear intermodulation components induced by the breathing crack.

## 4 Experimental Investigation

A 1 m cantilever beam with breathing crack at 0.4 m from the fixed end, shown in Fig. 6, is considered as the experimental example. Similar to the earlier researchers work [5, 17, 20], two aluminium alloy beams (i.e. three pieces) are bonded together as illustrated in Fig. 7 for fabrication of the beam. For the healthy specimen, only two pieces (i.e. top and bottom plates) are bonded. In other words, there exists only one plate on the top. Araldite epoxy adhesive is used for bonding the plates, and curing is done at the room temperature for 48 h. For the damaged specimen, there exist two or three or more top plates dependent on the number of cracks. To simulate breathing crack, the top plates (either two or three) are bonded to the bottom plate but not to each other so that the faces of the plates in contact behave like the faces of a breathing crack. The beam is instrumented with 8 PZT accelerometers longitudinally across the structure as shown in Figs. 6 and 7 (marked spatial locations of the sensors). The beam is tightly clamped using C-clamp which is solidly fixed to a steel test bench. The beam is excited on the free end using modal shaker of 200 N sine peak force capacity. Data acquisition is carried out using computer controlled high-speed MGC plus data acquisition system (using the accelerometer channels).

The beam with breathing crack at 0.4 m from the fixed end is subjected to 4 N harmonic excitation (single tone) of 8 and 145 Hz and as well as the simultaneous application of harmonic excitation (bitone) of 8 and 145 Hz at the free end. It should be mentioned here that the single-tone excitations are essential in order to apply linear response subtraction scheme to obtain nonlinear intermodulation response.

The Fourier power spectra or power spectral density (PSD) of the actual acceleration time history response corresponding to sensor 4 (i.e. near crack location) is shown in Fig. 8a. The power spectral density plot shown in Fig. 8a shows peaks at excitation frequencies (i.e. 8 and 145 Hz) and superharmonics (i.e. 8, 16, 24, 145,

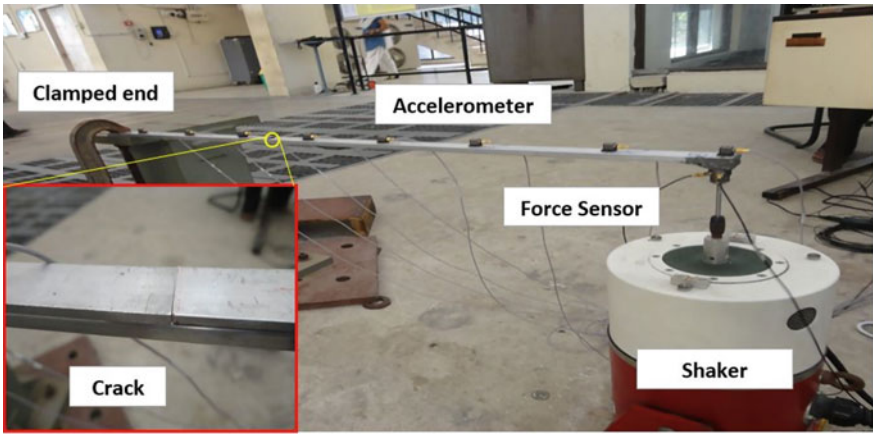


**Fig. 6** Experimental example

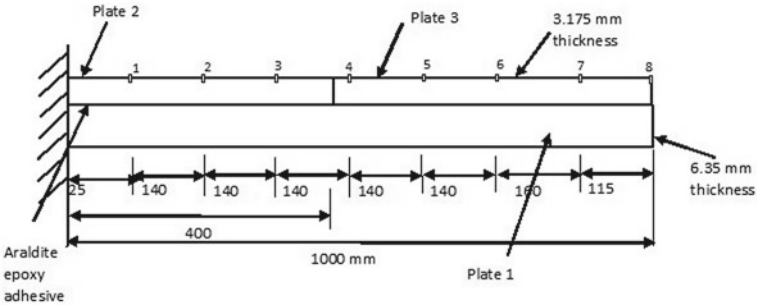


**Fig. 7** Specimen details and sensor locations

290, 435 Hz, and so on). A close observation of Fig. 8a indicates the presence of sidebands (or) intermodulation in addition to superharmonics of individual excitation frequencies. This confirms the presence of breathing crack in the structure. The amplitude of intermodulation and nonlinear harmonics is also found to be much lesser when compared to the fundamental excitation harmonic.

Using the LRS procedure outlined earlier, the nonlinear intermodulation response is obtained experimentally. The Fourier power spectrum plots corresponding to nonlinear intermodulation response (i.e. modified response after LRS application) are shown in Fig. 8b. Since the power spectrum is not expected to exist for nonlinear intermodulation response obtained using LRS procedure for an undamaged beam, the presence of intermodulation and superharmonics in Fig. 8b gives a very conclusive evidence of the presence of breathing crack in the structure. Further, it is clear from the plots shown in Figs. 8b that the excitation frequencies cannot be eliminated effectively.

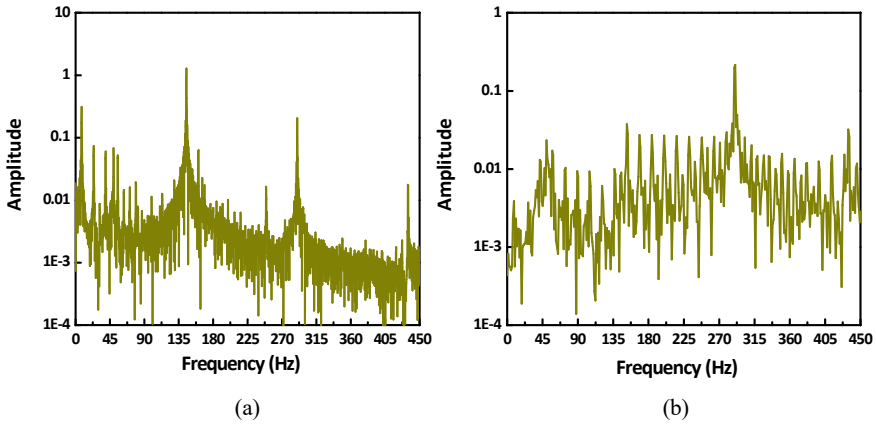


**Fig. 8** Fourier power spectrum **a** actual response, **b** modified response using LRS

The spectral correlation function is required to be evaluated at all sensor nodes (i.e. nodes 1–8). For the purpose of illustration, the spectral correlation function is evaluated for sensor node-6 (i.e. the farthest node from the crack), and the corresponding plot is shown in Fig. 9a. The cyclic frequency chosen is equal to response frequency components (i.e. excitation frequency, super harmonics of pumping and probing frequency, and as well as intermodulation).The spectral correlation estimated on the response after linear response subtraction scheme of the undamaged and damaged states of the structure at varied cyclic frequencies (i.e. 8, 75, 137, 145, 153, and 185 Hz) of the experimental example is presented in Fig. 9a, b, respectively. It is evident from Fig. 9a that there exists no peaks for the undamaged state if estimated on the response after linear response subtraction scheme for any chosen cyclic frequency. It can be observed from Fig. 9b that for the response of the beam with breathing crack, a large number of frequency combinations result in same cyclic frequency. As a consequence, this reflects in the form of multiple spectral correlation peaks at several frequencies corresponding to the dynamic signatures. From the spectral correlation plot shown in Fig. 9b, it can be observed that the spectral correlation function evaluated with a cyclic frequency equal to the difference of two random frequencies (i.e. say input frequencies $145 - 8 = 137$ Hz) present in the signal will exhibit a peak at an average of those two frequencies (i.e. around 77 Hz). This is true for other chosen cyclic frequencies as well. The magnitude of these peaks depends on the energy of the frequency components of the signal (i.e. indirectly dependent upon the damage features present in the dynamic signature). Therefore, it can be concluded from Fig. 9 that the spectral correlation exhibits peak only for the damaged state irrespective of chosen cyclic frequency if estimated on the response after the application of linear response subtraction scheme. Therefore, the proposed linear response scheme helps in enhanced breathing crack diagnosis without baseline measurements and also confirms that spectral correlation peaks are only due to damage.

## 5 Conclusions

A reference-free spectral correlation-based approach for enhanced breathing crack is proposed using the acceleration time history responses measured under bitone harmonic excitation. The major advantage of using spectral correlation is that it can effectively remove the stationary noise components overlapped with the nonlinear components present in the response. However, the limitation of spectral correlation is that it is difficult to isolate the nonlinear components alone at a selected cyclic frequency and careful choice of appropriate cyclic frequency has to be made for accurate damage diagnosis. Linear response subtraction (LRS) scheme has been proposed in this paper to isolate the nonlinear intermodualation components alone from the response for enhanced breathing crack diagnosis. Numerical and experimental investigations carried out in this paper concluded that the spectral correlation estimated with modified response after linear response subtraction scheme are highly sensitive

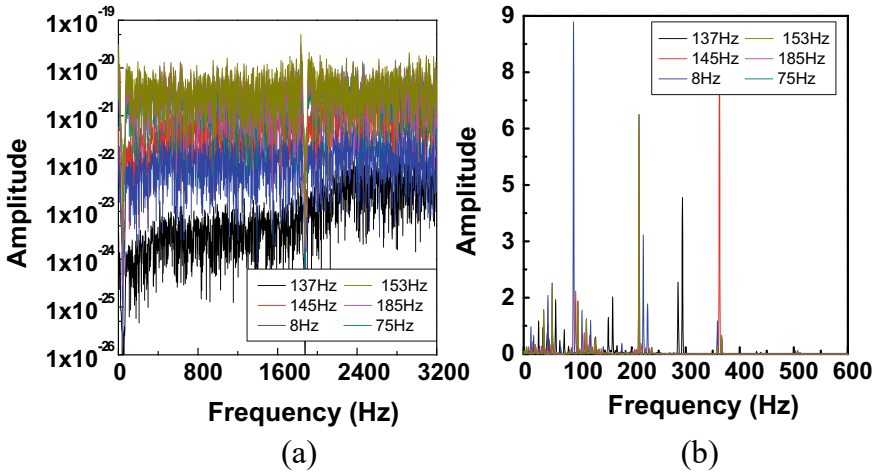


**Fig. 9** Spectral correlation (after LRS) **a** undamaged state, **b** damaged state

to breathing crack than spectral correlation estimated without the above scheme. Further, with this scheme, it is highly reliable that spectral correlation peaks are only due to change in the dynamics of the system due to breathing crack irrespective of cyclic frequency chosen.

**Acknowledgements** The author thanks technical staff of ASTAR and SHML Lab of CSIR-SERC for their support during experiment study.

## References

1. Bouillaut L, Sidahmed M (2001) Cyclostationary approach and bilinear approach: comparison, applications to early diagnosis for helicopter gearbox and classification method based on HOCS. Mech Syst Signal Process 15(5):923–943
2. Boungou D, Guillet F, El Badaoui M, Lyonnet P, Rosario T (2015) Fatigue damage detection using cyclostationarity. Mech Syst Signal Process 58:128–142
3. Bovsunovsky A, Surace C (2015) Non-linearities in the vibrations of elastic structures with a closing crack: a state of the art review. Mech Syst Signal Process 62:129–148
4. Broda D, Pieczonka L, Hiwarkar V, Staszewski WJ, Silberschmidt VV (2016) Generation of higher harmonics in longitudinal vibration of beams with breathing cracks. J Sound Vib 381:206–219
5. Douka E, Hadjileontiadis LJ (2005) Time–frequency analysis of the free vibration response of a beam with a breathing crack. NDT E Int 38(1):3–10
6. Fehske A, Gaeddert J, Reed JH (2005) A new approach to signal classification using spectral correlation and neural networks. In: First IEEE international symposium on new frontiers in dynamic spectrum access networks, IEEE. DySPAN 2005. pp 144–150
7. Gardner W (1986) Measurement of spectral correlation. IEEE Trans Acoust Speech Signal Process 34(5):1111–1123

8. Gardner WA, Napolitano A, Paura L (2006) Cyclostationarity: half a century of research. Signal Process 86(4):639–697
9. Giannini O, Casini P, Vestroni F (2013) Nonlinear harmonic identification of breathing cracks in beams. Comput Struct 129:166–177
10. Han N, Shon S, Chung JH, Kim JM (2006) Spectral correlation based signal detection method for spectrum sensing in IEEE 802.22 WRAN systems. In: 2006 8th international conference advanced communication technology, vol 3. IEEE, p 6
11. Kim JS, Lee SK (2018) Identification of tooth fault in a gearbox based on cyclostationarity and empirical mode decomposition. Struct Health Monit 17(3):494–513
12. Klepka A, Staszewski WJ, Jenal RB, Szwedo M, Iwaniec J, Uhl T (2012) Nonlinear acoustics for fatigue crack detection–experimental investigations of vibro-acoustic wave modulations. Struct Health Monit 11(2):197–211
13. Liu P, Sohn H, Jeon I (2017) Nonlinear spectral correlation for fatigue crack detection under noisy environments. J Sound Vib 400:305–316
14. Liu P, Sohn H (2017) Damage detection using sideband peak count in spectral correlation domain. J Sound Vib 411:20–33
15. Prawin J, Lakshmi K, Rao ARM (2018) A novel singular spectrum analysis–based baseline-free approach for fatigue-breathing crack identification. J Intell Mater Syst Struct 29(10):2249–2266
16. Prawin J, Rao ARM (2018) Nonlinear structural damage detection based on adaptive Volterra filter model. Int J Struct Stab Dyn 18(02):1871003
17. Prime MB, Shevitz DW (1995) Linear and nonlinear methods for detecting cracks in beams (No. LA-UR-95-4008; CONF-960238-10). Los Alamos National Lab., NM (United States)
18. Peng ZK, Lang ZQ, Billings SA (2007) Crack detection using nonlinear output frequency response functions. J Sound Vib 301(3–5):777–788
19. Sohn H, Lim HJ, DeSimio MP, Brown K, Derriso M (2014) Nonlinear ultrasonic wave modulation for online fatigue crack detection. J Sound Vib 333(5):1473–1484
20. Yelve NP, Mitra M, Mujumdar PM (2014) Spectral damage index for estimation of breathing crack depth in an aluminum plate using nonlinear Lamb wave. Struct Control Health Monit 21(5):833–846
21. Yoo DS, Lim J, Kang MH (2014) ATSC digital television signal detection with spectral correlation density. J Commun Netw 16(6):600–612

# Numerical Study on Steel Jacketing Retrofitting Scheme for Experimentally Damaged Reinforced Concrete Frames Subjected to Lateral Loads


**Sanjay R. Kumawat, Goutam Mondal, and Suresh R. Dash**

**Abstract** This paper aims at proposing a steel jacketing retrofitting scheme for severely damaged reinforced concrete frame. An experimental study conducted under slow cyclic displacement-controlled loading on a full-scale model of reinforced concrete (RC) frame has been adopted for this purpose. The reinforcement detailing of the frame was given according to IS 456:2000, i.e., without any ductile detailing. The tested frame suffered severe damages due to the formation of shear cracks and plastic hinges at the beam-column joint and at the column ends, respectively. A steel jacketing retrofitting scheme has been recommended and studied here for retrofitting the damaged frame. The retrofitting scheme basically focuses on the improvement of lateral strength and lateral stiffness of the frame with varying thickness of the steel plates along with their location to be applied to the RC frame. The results obtained from the numerical study clearly show the contribution of steel jacketing in regaining and improving the lateral strength and lateral stiffness of the frame.

**Keywords** Steel jacketing · Retrofitting · Numerical model · Pushover loading

## 1 Introduction

Most of the buildings in India fall under the non-engineered construction category. Even if they are engineered, the structures are often not designed for seismic loads (non-ductile structure). Hence, after every severe earthquake, the non-ductile structure suffers undesirable damages and collapse in many cases. The major challenge

S. R. Kumawat (✉) · G. Mondal · S. R. Dash
IIT Bhubaneshwar, Bhubaneshwar, India
e-mail: srk11@iitbbs.ac.in

G. Mondal
e-mail: gmondal@iitbbs.ac.in

S. R. Dash
e-mail: srdash@iitbbs.ac.in



M. Madhavan et al. (eds.), *Proceedings of the Indian Structural Steel Conference 2020 (Vol. 1)*, Lecture Notes in Civil Engineering 318,
https://doi.org/10.1007/978-981-19-9390-9_22

which comes forward is the restoration of mild and moderately damaged structure which has not undergone complete collapse. Sometimes it also becomes very important to restore the structures of monumental importance rather than demolishing them. Hence, it is a matter of great concern and needs to bring a mild or moderately damaged structure back to function after an earthquake. Thus, the present study is to develop an efficient retrofitting method to restore the most common and severe causes of failure seen in the majority of the structures during an earthquake.

The retrofitting techniques are broadly classified into either local (strengthening of existing members by RC jacket, steel jacket, CFRP jacket, etc.) or global (addition of new members such as infill wall and shear wall). There are numerous studies available on experimental models carried out by various researches on different retrofitting schemes. Some major relevant literature is described here briefly. Garcia et al. [4] carried out CFRP jacketing on severely damaged non-ductile exterior beam-column joint with complete replacement of damaged concrete in the joint region. The repair technique enhanced both the shear strength of joint as well as the ultimate strength by 44% and 69%, respectively. El-Amoury et al. [3]have done repairing of beam-column joint by using GFRP sheets in order to increase the shear strength of the joint. At the same time, the anchorage deficiency of the bars at the joint region was improved by anchoring them to the steel angles attached at the joint corner. Similar work was also carried out by Yurdakul and Avsar [10] on ductile and non-ductile beam-column joints by using different configurations of CFRP jacketing, and the anchorage bar slippage was controlled by welding the beam bars with the column bars. The test concluded that the welding of beam bars to column bars caused the buckling of longitudinal bars in the column making the bars to slip again. Also, CFRP wrap was found to be inadequate in regaining the original stiffness and strength of the non-ductile frame. Jayaguru and Subramanian [6] used GFRP wrapping to strengthen the columns suffering from captive column failure. Yuksel et al. [11] and Altin et al. [1] have carried out the strengthening of an unreinforced masonry wall by using different configurations of CFRP bracings.

To compare the effectiveness of two types of retrofitting techniques, experimental investigation using CFRP jacketing and reinforced concrete jacketing on a beam-column joint specimen was carried out [9]. Retrofitting was carried out in two stages, i.e., two specimens were strengthened before the damage, whereas the other two specimens were repaired after the damage. The damaged specimens suffered joint shear failure and were repaired by first removing the loose concrete and filling it with premixed high strength mortar. The RC jacket was installed by placing four longitudinal bars in the four corners (which were welded with the existing bars) to support the transverse steel. The test concluded that the repaired specimens by any means showed higher strength, stiffness, and energy dissipation as compared to specimens strengthened before damage which was due to the replacement of concrete by high strength mortar at damaged location. Also, it was seen that both the methods of retrofitting were effective in shifting the plastic hinge from the beam-column joint to the beam region.

Many researchers have also carried out numerical studies to investigate the effectiveness of various retrofitting schemes. Some recent major relevant outcomes of

these studies are presented below. Lim et al. [7] have given an alternative method for evaluating the performance of FRP-retrofitted reinforced concrete buildings using a lumped plasticity approach. In this study, a beam-column joint was considered for carrying out its strengthening in SAP2000 [2 ]. The beam was divided into three parts, i.e., offset (which is the part of the beam inside the joint), retrofitted section, and un-retrofitted section. The retrofitted section was given equivalent section properties considering different numbers of CFRP layers. A pushover analysis was carried out on the beam-column joint with increasing layers of CFRP sheets, which has shown the shifting of the hinge location from the face of the column to a distance of 500 mm into the beam.

Mohsen et al. [8] carried out a finite element analysis on a tested 1:2 scaled experimental model. The models comprise circular columns with inadequate lap splice detailing and were retrofitted with composite sheets. A lumped plastic model of the circular column was simulated using a finite element software. The composite sheets were applied by exerting an equivalent amount of pressure (as exerted by composite sheets on the column) on the columns according to ACI 440. The numerical analysis of the circular columns showed that the numerical model differs by about 25% in various strength and stiffness parameters as compared to the experimental model.

From the literature review, it can be concluded that most of the researches focus on the strengthening of the structures and very little numerical work has been done for repairing post-earthquake damaged structures. Also, the steel jacketing retrofitting technique has not been given much attention. Thus, in this paper, an attempt has been made to carry out a steel jacketing retrofitting technique in its most optimum usage.

## 2 Methodology

For this study, a numerical model has been developed representing the experimental study carried out by Kaushik et al. [12] on the reinforced concrete frame under slow cyclic displacement-controlled loading. The reinforcement detailing as per IS 456:2000 [5] and the dimensions of the frame are shown in the Fig. 1. A numerical model of the frame is prepared by using SAP2000, a finite element-based analysis framework. This numerical model is subjected to a nonlinear static pushover loading, and the force–deformation relation thus obtained is compared with the experimental results of the frame in order to validate it. Pushover analysis is an alternative method of predicting the nonlinear behavior of a structure under seismic loading, which is comparable with the slow cyclic form of loadings. Once the numerical model of the frame is validated, the damaged properties are now assigned to it to reflect the residual strength and stiffness of the damaged RC frame into the numerical model. After the incorporation of damaged properties into the numerical model, it is retrofitted with varying steel plate thickness and is again subjected to pushover loading in order to observe its response.

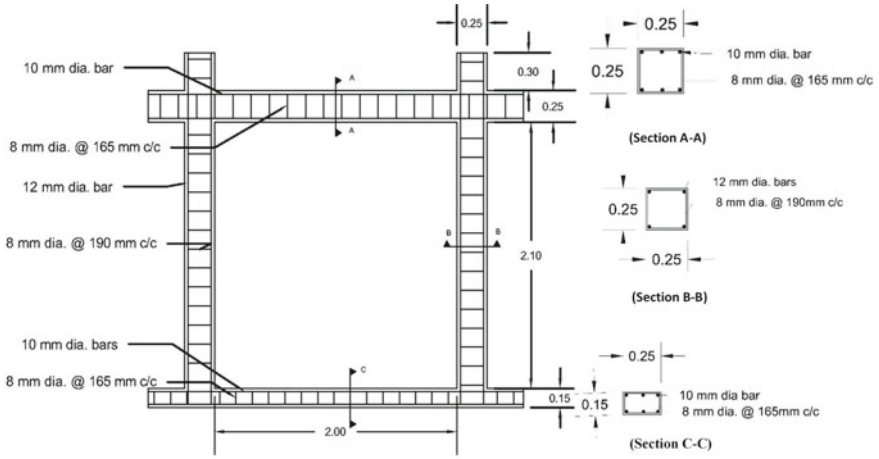


**Fig. 1** Reinforcement details of the reinforced concrete frame

## 3 Numerical Model of Reinforced Concrete Frame

### *3.1 Validation of the Numerical Model*

A numerical model of the RC frame tested by Kaushik et al. [12] under slow cyclic loading has been simulated in SAP2000 v20 [2] using a two-nodded element having three degrees of freedom. A link element (three degrees of freedom element) with the desired value of stiffness has been used at the support to model the base uplift which was observed during the experiment of the frame. The compressive strength of concrete was assigned as 28.4 MPa, and tensile strength of 543 MPa and 557 MPa has been assigned for 10 and 12 mm diameter reinforcing bars, respectively. The nonlinear properties to the frame were given by assigning flexural hinges at the beam and column ends as shown in the Fig. 2a. A nonlinear static pushover analysis has been carried out on the numerical model of the bare frame to obtain the load–displacement relationship (pushover curve). The numerical model was validated by comparing the pushover curve with the experimental results as shown in Fig. 2b. It was found that the numerically obtained results were competent to the experimental results both in terms of damage (Fig. 3) and strength (and stiffness) parameters. Thus, the numerical model of the frame was found acceptable to carry out further investigation of the retrofitting process.

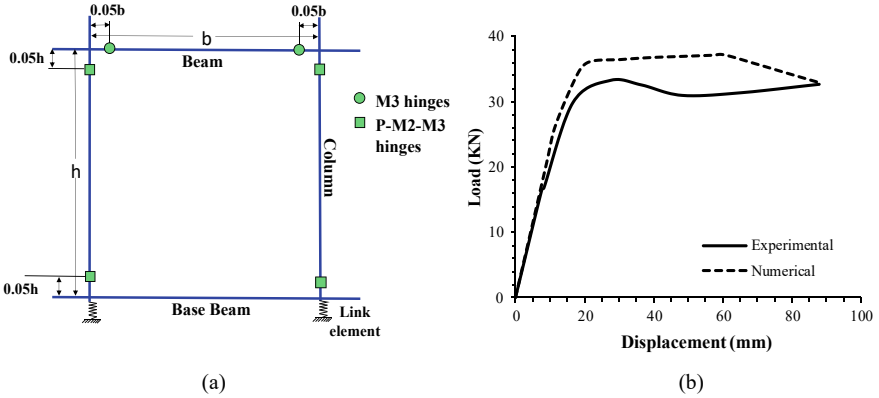


**Fig. 2** **a** Numerical model of RC frame with the position of hinges, **b** comparative force–displacement graph between experimental and numerical model

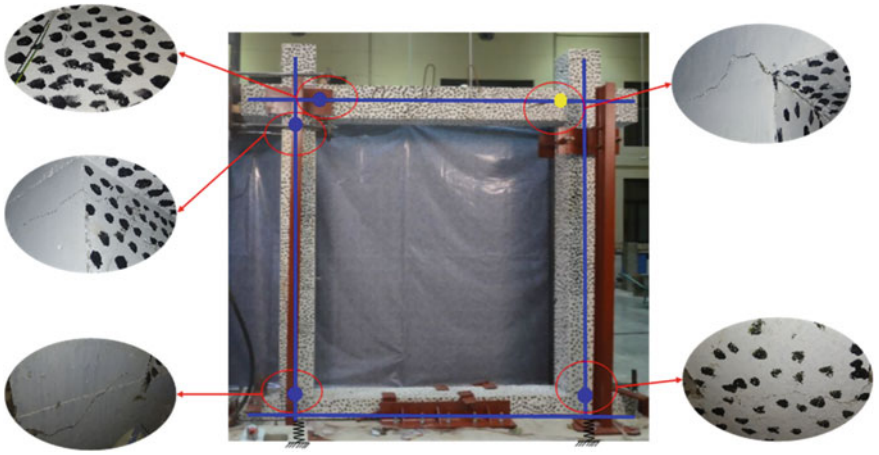

**Fig. 3** Major cracks in the reinforced concrete frame being compared by the numerical model through plastic hinge formation

## *3.2 Incorporation of Damaged Properties in the Numerical Model of the Frame*

The numerical model of the frame thus simulated should comprise the damaged strength and stiffness properties of the tested frame in order to carry out its retrofitting. The damaged properties were assigned to the frame by holding on to the fact that after the test, only a part or a two (mostly near the joint) of the beam and the column gets deteriorated due to the formation of the plastic hinge, while the other parts remain

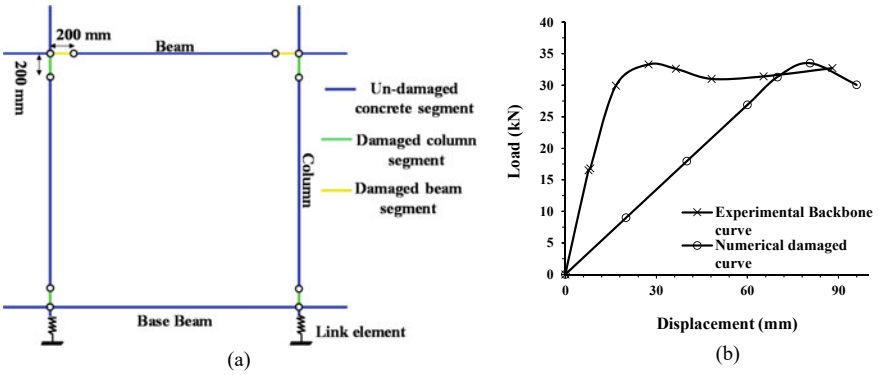


**Fig. 4** **a** Numerical model of damaged RC frame, **b** comparative force–displacement graph between undamaged experimental and damaged numerical model

undamaged. Hence, the frame is divided into small segments at the position of formation of the plastic hinge (Fig. 4a). These segments are then given the damaged properties (i.e., reduced sectional properties) by adopting the cracked section approach. Under this approach, the moment of inertia of the section of each segment is reduced unless the stiffness of the entire frame matches the stiffness (secant stiffness at the failure load point) of the damaged frame. The hinges are assigned at a relative distance of 0.05 times the length of the member from the center of the beam-column joints. It is expected that the hinge formation in the damaged part shall indicate when the frame approaches the failure load. Figure 4b shows a comparative force–deformation relationship between the undamaged experimental frame and the damaged numerical model of the frame.

## *3.3 Retrofitting of the Damaged Numerical Model*

The retrofitting of a damaged frame can be carried out by using one of the various methods of local retrofitting techniques as mentioned in literature. In the present study, the steel jacketing retrofitting technique has been adopted for the numerically prepared damaged specimen model. The damaged model was having reduced sectional properties which are replicating the residual strength and stiffness of the damaged experimental frame. The damaged segments of the frame with reduced sectional properties were retrofitted by confining its periphery with steel plates. This is done by using the section designer tool of SAP2000 which enables the user to build composite sections. Thus, the damaged concrete segment with reduced concrete properties was repaired directly by using steel plates of grade E 345 (yield strength of 345 MPa). In order to reflect the damage in the retrofitted frame after pushover analysis, hinges were assigned both in the repaired (surrounded with steel plate) and unrepaired (undamaged concrete section) segments of the frame (Fig. 5). The

need for assigning hinges in the unrepaired concrete segments was to observe any shift of plastic hinges from retrofitted segments to undamaged concrete segments. After retrofitting with steel plates, it was found that the frame regained its original strength and stiffness with increasing thickness of steel plates. Figure 6 shows the load–displacement graph of the retrofitted reinforced concrete frame compared with the damaged model of the frame.

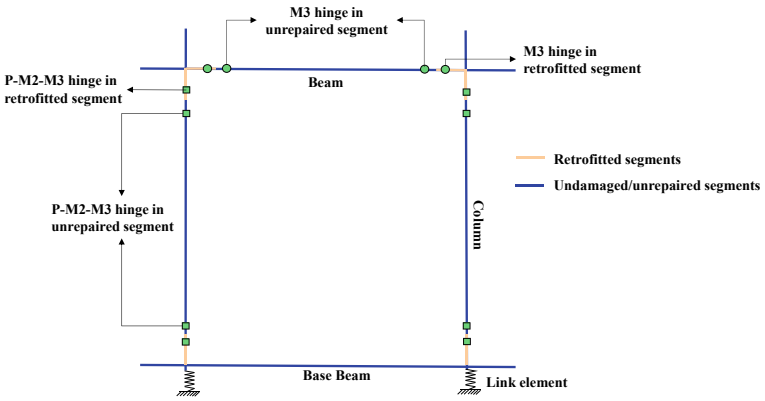


**Fig. 5** Hinge locations for retrofitted reinforced concrete frame model

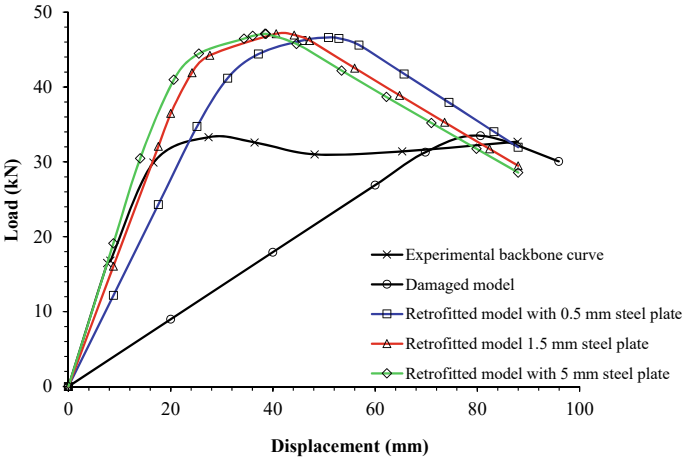


**Fig. 6** Comparative force–displacement graph of various retrofitted numerical frame model as compared to the original frame backbone curve

## 4 Results and Discussion

Table 1 summarizes the results of the experimental study on the undamaged frame and the numerical study carried out on retrofitting of the damaged frame. The various parameters considered in the study are lateral strength, lateral stiffness (secant stiffness for 50% of ultimate strength), and the type of damage that occurred in the frame before and after retrofitting of the frame. Figures 7 and 8 show the variation of lateral strength and stiffness with increasing plate thickness.

The experimental study carried out by Kaushik et al. [12] on the reinforced concrete frame suffered severe damage after the slow cyclic displacement-controlled loading. The main cause of failure was due to the formation of shear cracks at the beam-column joints and also plastic hinges formation at the column ends near the base beam. The developed numerical model of the frame has shown hinge formation at similar locations of the beam-column joint and at the column ends.

**Table 1** Numerical results of the frame after carrying out steel jacketing retrofitting scheme

| Study type | Steel plate thickness (mm) | Lateral strength (kN) | Error (%) | Lateral stiffness (kN/mm) | Error (%) |
|---|---|---|---|---|---|
| Experimental (undamaged frame) | – | 33.3 | 0.0 | 2.2 | 0.00 |
| Numerical damaged specimen | 0.0 | 33.5 | 0.0 | 0.5 | −79.3 |
| Numerical retrofitted specimen | 0.5 | 46.6 | 40.0 | 1.4 | −36.3 |
| | 1.5 | 47.1 | 41.5 | 1.8 | −16.0 |
| | 5.0 | 47.1 | 41.5 | 2.2 | 0.14 |

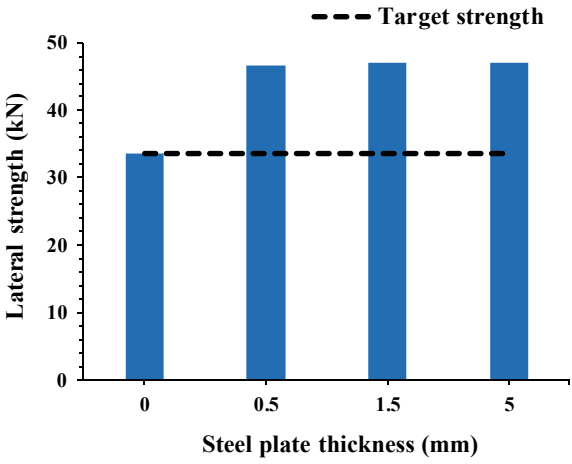


**Fig. 7** Variation of lateral strength with an increasing plate thickness of the damaged numerical model

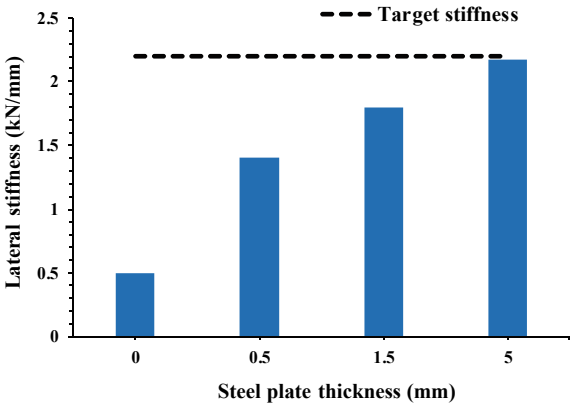


**Fig. 8** Variation of lateral stiffness with an increasing plate thickness of the damaged numerical model

Upon retrofitting with steel jacketing, the pushover analysis carried out has shown the formation of plastic hinges in the beam and columns. However, the locations of plastic hinges were not the same. The retrofitting of damaged frame segments by steel plates has converted it to a strong composite section. Because of which shifting of plastic hinges has taken place from retrofitted damaged section to a comparatively weaker unrepaired-undamaged concrete section just adjacent to it. This shifting of plastic hinges has increased the lateral strength of the frame adequately from 33.30 kN to 47 kN (40% increment in lateral strength) as shown in Fig. 7 irrespective of plate thickness. However, the lateral stiffness of the frame still largely depends on the plate thickness used, and it increased with an increase in steel plate thickness as evident from the Fig. 8. Although the strength gain was quicker with the addition of steel jackets, it was still found difficult to recover the complete stiffness value of the frame with the first few small thicknesses of steel plates. As it can be seen in the Table 1, for a 1.5 mm steel plate, the lateral stiffness is still lagging by 15% of its original value although the strength has reached 41% higher than the original undamaged frame. A 5 mm thick plate is found to be adequate to completely recover the stiffness of the damaged frame.

## 5 Summary and Conclusions

In this study, a steel jacketing retrofitting scheme has been proposed by carrying out a numerical simulation of the damaged reinforced concrete frame. The implication of steel jackets with varying plate thickness was compared with the experimental test results of the undamaged specimen, and the following observations have been made as follows:

1. The steel jacketing retrofitting scheme is effective in regaining the lateral strength and lateral stiffness parameters of a severely damaged reinforced concrete frame subjected to seismic forces.

2. The composite section formed after retrofitting of the damaged RC segments by steel plates was found to be stronger and more ductile as compared to the original undamaged reinforced concrete section showing about 40% greater strength.
3. The steel jackets are effective in increasing the lateral strength of the damaged frame, although a large plate thickness may be required to regain the lateral stiffness which would be uneconomical.
4. The steel jacketing retrofitting scheme is also found to be proficient in shifting the location of the hinge from the damaged concrete segment to an undamaged concrete part.

This numerical study thus suggests that it is possible to optimize the retrofitting scheme numerically before implementing it to the real structures, based on the need.

## References

1. Altin S, Anil Ö, Kara ME, Kaya M (2008) An experimental study on strengthening of masonry infilled RC frames using diagonal CFRP strips. Compos B Eng 39(4):680–693
2. Computers and structure inc. analysis reference manual for SAP2000, ETABS, SAFE, and CSiBridge
3. El-Amoury T, Ghobarah A (2002) Seismic rehabilitation of beam-column joint using GFRP sheets. Eng Struct 24(11):1397–1407
4. Garcia R, Jemaa Y, Helal Y, Guadagnini M, Pilakoutas K (2014) Seismic strengthening of severely damaged beam-column RC joints using CFRP. J Compos Constr 18(2):04013048
5. IS-456 (2000) Indian standard plain and reinforced concrete—code of practice, Bureau of Indian Standards, New Delhi
6. Jayaguru C, Subramanian K (2012) Retrofit of RC frames with captive-column defects. KSCE J Civ Eng 16(7):1202–1208
7. Lim PJ, Seyed SM, Hamid RR (2013) An alternative procedure for the performance assessment of FRP-retrofitted RC buildings using lumped plasticity. In: Proceedings of the 4th Asia-Pacific conference on FRP in structures,11–13 December 2013, Melbourne, Vic
8. Mohsen SA, Lau TL, Bunnori MN (2013) Modeling FRP-confined RC columns using SAP2000. World Appl Sci J 27(12):1717–1736
9. Tsonos AG (2008) Effectiveness of CFRP-jackets and RC-jackets in post-earthquake and pre-earthquake retrofitting of beam-column sub assemblages. Eng Struct 30(3):777–793
10. Yurdakul O, Avsar O (2015) Structural repairing of damaged reinforced concrete beam-column assemblies with CFRPs. Struct Eng Mech 54(3):521–543
11. Yuksel EH, Ozkaynak O, Buyukozturk C, Yalcin AA, Dindar MS, Tastan D (2010) Performance of alternative CFRP retrofitting schemes used in infilled RC frames. Constr Build Mater 24(4):596–609
12. Kaushik A, Mondal G, and Dash SR (2018) “Evaluation of Lateral Response of Partially Infill Walls with Fly-Ash Bricks through experimental study.” M.Tech thesis, School of Infrastructure, Indian Institute of Technology Bhubaneswar, India

# Efficient Numerical Analysis of Hybrid Shear Wall with Internal Energy Dissipating Reinforcements


**Ankhiparna Guha, Prachi Taori, Suresh R. Dash, and Goutam Mondal**

**Abstract** To ensure the structural safety, efficient performance, and minimums disturbance to business operations after an earthquake, proper seismic design of buildings is of ample importance. Often, post- tensioned (PT) shear wall having self-centering capacity is used as one of the effective ways of resisting large lateral shear force during earthquakes. However, to keep the structural form in serviceable condition, the maximum energy that can be dissipated through PT shear wall is limited to energy dissipation through the elastic behavior of PT tendons and pure rocking of the wall. Hence, in situations having a higher force and limited drift demand, PT shear walls with internal energy dissipating reinforcements (IEDR) are being used in practice. Analysis of such shear wall configurations though experiments is a tedious job and also not feasible for the economic point of view. Hence, there is a requirement of a computationally efficient numerical model that can replicate the actual behavior of post-tensioned (PT) shear wall with IEDR. The computational efficiency of the numerical model is also needed to be checked. This paper investigates the behavior of the numerical model of a PT shear wall with internal EDR subjected to lateral cyclic loading whose computational efficiency has also been examined and modifications are tried to be introduced.

**Keywords** Internal energy dissipating reinforcement (IEDR) · Self-centering shear wall · Post-tensioned shear wall

A. Guha (✉) · S. R. Dash · G. Mondal
IIT Bhubaneswar, Bhubaneswar, India
e-mail: ag32@iitbbs.ac.in

S. R. Dash
e-mail: srdash@iitbbs.ac.in

G. Mondal
e-mail: gmondal@iitbbs.ac.in

P. Taori
L&T Construction, Chennai, India
e-mail: pt15@iitbbs.ac.in



M. Madhavan et al. (eds.), *Proceedings of the Indian Structural Steel Conference 2020 (Vol. 1)*, Lecture Notes in Civil Engineering 318,
https://doi.org/10.1007/978-981-19-9390-9_23

## 1 Introduction

To ensure minimum structural disturbance and small-scale or trivial structural damage, proper seismic design along with sufficient seismic resistance is of ample importance. The use of shear wall has always been one of the most effective ways of resisting damages that occurred due to large seismic tremors. But due to the limitations of residual drifts, crushing and local damage of concrete, yielding of bars, etc., the structure becomes incompatible and unacceptable for future use. Hence, to emit these problems, the use of a post-tensioned shear wall can be a viable solution. Because of their high yield strength, the post-tensioned tendons remain in the elastic state though out the seismic activity and bring the wall back to its initial position after the loads were removed, thus possessing a self-centering effect. Due to its self-centering behavior, it causes high structural stability and less structural damage as a result of which the rehabilitation cost can be minimized, life safety and fast recovery of structure can be ensured, and the design life of the building can be increased.

However, to keep the structural form in serviceable condition, the maximum energy that can be dissipated through the PT shear wall is limited to the energy dissipation through local damage of the wall. Hence, in situations having higher force and limited drift demand, PT shear walls with energy dissipating reinforcements are being used in practice. Such kinds of shear walls are not monolithically casted. It is connected to the fixed foundation with the help of PT tendons and energy dissipating reinforcements. The PT tendon is stretched throughout the length of the wall, and the duct inside which the tendon has been placed should be un-grouted so that it can allow proper rocking motion of the wall. Because of the elastic behavior of the tendons, the walls show a hysteresis curve similar to that of a nonlinear elastic material, with zero residual deformation and zero energy dissipation. But in case of moderate to high seismic activity, energy dissipation is one of the most important governing factors for the safety of a structure. Hence, to increase the energy dissipation capacity of the structure, energy dissipating reinforcements (EDR) are provided at the junction of the wall and foundation. The deformed position of such kind of PT shear wall along with the gap opening is shown in Fig. 1.

It can be observed from the previous studies that the post-tensioned shear walls are very efficient in providing lateral resistance against seismic forces acting on the structure. Their self- centering nature makes them more advantageous to use as an option of lateral force resistance with lesser residual drift. This literature review addresses the work done by various researchers on numerical analysis, experimental research, and design of PT shear walls. It also presents the research done in the field to enhance the performance of PT shear walls by incorporating viscous dampers or yielding steel energy dissipaters.

Kim et al. [3] introduced the use of nonlinear viscous damper and elastic spring connected in parallel or series as a method of energy dissipation in highway bridges. It has been noted that this arrangement is effective in reducing relative opening displacement at pounding.

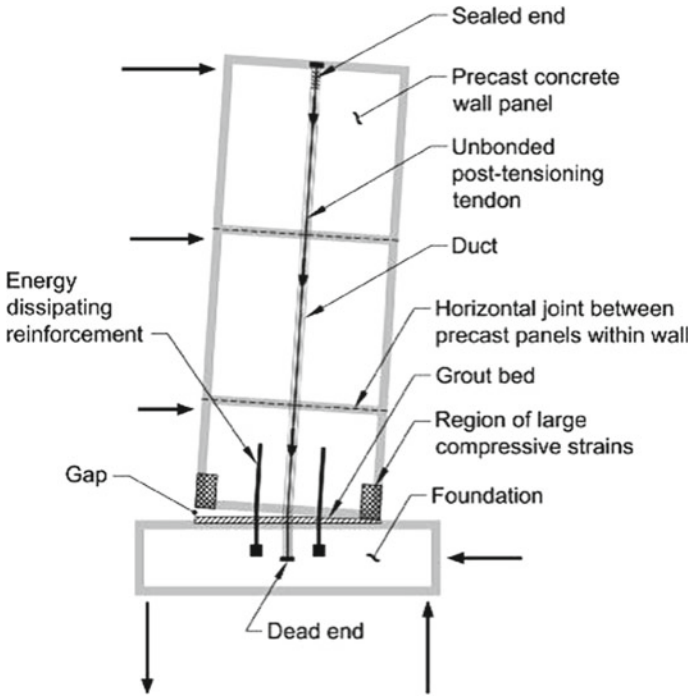


**Fig. 1** Assembly of a hybrid post-tensioned shear wall (ACI-ITG-5.2)

Symans et al. [5] tested the performance of various energy dissipaters in RC framed structures. The suitability of those energy dissipaters was also tried to be concluded. But these testing and the experiments have been conducted on RC frames only. Dissipaters were not used in shear walls.

Zhangfeng and Zhengxing [7] compared the performance of three emulative hybrid precast concrete shear walls with increasing post-tensioning force (EHW) and one monolithic reinforced concrete wall (MW). The specimens are subjected to a forced controlled loading followed by a displacement-controlled loading. Increasing the post-tensioning force in tendons resulted in higher cracking loads, increased initial stiffness, reduced energy absorption capacity, smaller residual deformations, and lower displacement ductility. Finite element analysis was also done using ABAQUS FEA software to capture the skeleton-curve of the specimens. The ABAQUS model could successfully match the load-drift envelop of the specimens and predict the strain behavior of the unbonded post-tensioned tendons.

In addition to numerical analysis using finite element model (FM), Perez et al. [4] obtained the lateral force and drift values of unbonded post-tensioned (UPT) precast shear wall using a design-oriented simple mathematical model (SM). The behavior obtained by the equations and though the FM model was analyzed and compared with the experimental response. The base shear and drift obtained by SM and FM were comparable to that obtained experimentally at concrete decompression,

concrete cover spalling and yielding of PT steel. But at the ultimate limit state, i.e., the crushing of confined concrete, the lateral load capacity was overestimated by both SM and FM models. Overall, the analytical model was reliable for seismic designing of UPT walls.

Generally, the numerical studies are limited to observing the behavior of a single secluded rocking wall. However, a better understanding of the structural behavior can be attained if the interaction of the self-centering wall with other structural components is also incorporated in the model. Since all the structural elements might not display similar self-centering and stiffness as that of the post-tensioned wall, a complete analysis could help in painting a better picture of the response of the structure. Tanyeri et al. [6] conducted modeling of a complete four-story building consisting of two bonded PT frames in one direction and two unbonded PT shear walls in the other direction. The study compared the seismic responses obtained numerically with those obtained through a three-dimensional earthquake. It was seen that the analytical model and test results are in very good agreement for important engineering parameters, such as stiffness, maximum base shear, and maximum roof drift. However, some discrepancies were observed in the roof drift ratio versus time series for some parts of the response. Overall, the selected modeling approach was capable of producing seismic response estimates of sufficient accuracy to be used for the detailed design of unbonded post-tensioned, precast structural wall systems.

The self-centering walls are an attractive option for the rehabilitation of a building, to prepare the structure for future dynamic excitations. The low residual displacements of these walls can provide a unique advantage that cannot be attained through other structural components. Guo et al. [1] proposed and implied a seismic rehabilitation method by using a self-compacting (SC) self-centering concrete wall with friction dampers, aiming at providing self-centering capacity and supplemental energy dissipation to a structure. The proposed SC wall was applied in the seismic resilience upgrade of a five-story RC frame building located in a high-seismicity city in China. Nonlinear analysis of the structure was conducted by creating a numerical model in OPENSEES software for Earthquake Engineering Simulation. Performance-based design procedure considering two levels of ground motions, i.e., the design based earthquake (DBE) and the maximum earthquake (MCE) levels was adopted for the design of the SC wall. Dynamic property tests of the strengthened structure were conducted using ambient vibrations. Maximum story drifts of the structure subjected to the DBE and MCE ground motions were approximately 1.6 times that of the threshold value before rehabilitation. After upgradation, the story drifts were all below the threshold value for both DBE and MCE ground motions, showing the significant increase in self-centering capacity. Overall, the wall system not only significantly increased the deformation capacity but also reduced the residual drift, so that it can be used after an external excitation.

Perez et al. [4] worked on a design-oriented analytical model that uses simple formulae to estimate the nonlinear lateral load behavior of unbonded post-tensioned (UPT) walls and compares this simple model with available experimental results. A previously developed UPT wall model based on fiber elements is also compared with experimental results. Each model is formulated to consider several critical limit

states in the lateral load behavior of UPT walls. Comparisons showed generally good agreement between analytical and experimental results for three different test walls under monotonic and cyclic loading. The simple model is found to be sufficiently accurate for the seismic design of UPT walls, and the fiber model is found to be sufficiently accurate for estimating UPT wall response under earthquake loading.

## 2 Description of the Model

Numerical analysis of the post-tensioned shear wall is conducted using ABAQUS 3.18. The numerical model has been developed to replicate the model mentioned in the experimental study conducted by Zhangfeng and Zhengxing [7] having similar geometric properties. The hybrid wall specimen is 3.62 m high, 1.7 m long, and 0.2 m thick, resting on a foundation of 0.64 m thick and 2 m length. The model contains concrete wall, foundation beam, PT tendons, confining loops, and longitudinal and lateral reinforcements with internal energy dissipating reinforcements (EDR) where the EDR is embedded partially inside the foundation and partially inside the PT wall as shown in Fig. 2.

## 3 Development of the Numerical Model

### *3.1 Selection of Elements*

Eight-noded first-order three-dimensional continuum elements with reduced integration (C3D8R) are being used to model the concrete shear wall, loading plates, and foundation. The reinforcements embedded inside the concrete and the tendons were modeled as three-dimensional two-noded truss elements (T3D2). The EDR is divided into three parts where each part has been modeled as truss elements. The two end parts are embedded inside the wall and the fixed foundation, respectively. The middle part is unbonded.

### *3.2 Material Properties*

The modulus of elasticity of concrete is assumed to be 30,000 N/mm$^2$, corresponding to concrete having characteristic strength of 40 MPa, and its Poisson's ratio is assumed to be 0.15. The nonlinearity of the material is incorporated with the help of a concrete damage plasticity model referred by Hafezolghorani et al. [2]. The modulus of elasticity of steel reinforcements and PT tendons is considered as $2 \times 10^5$ MPa, and Poisson's ratio is considered to be 0.3. A bi-linear stress–strain graph

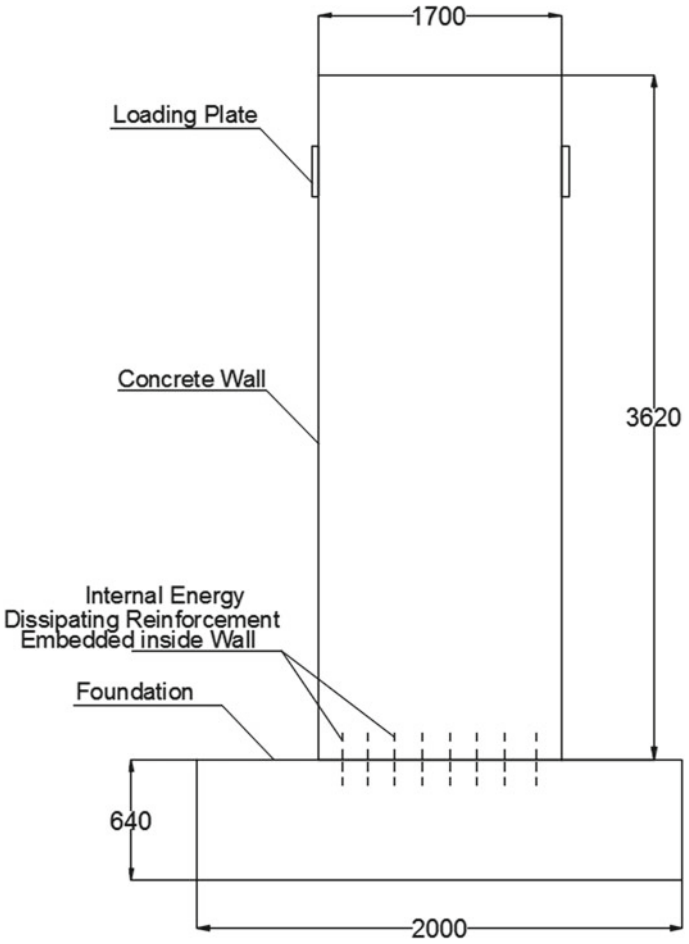


**Fig. 2** Numerical replica of the experimental setup referred in Zhangfeng and Zhengxing [7]

has been adopted for all reinforcements including EDR, whereas the PT tendons are considered to be elastic always. To consider the foundation to be fixed and rigid, the elasticity modulus of the foundation is considered to be five times that of steel.

## *3.3 Constraints, Interaction, and Boundary Conditions*

All the reinforcements including the confinement hoops, longitudinal and lateral bars are embedded inside the concrete wall which is considered as the host region. Thus, the translational degrees of freedom of the reinforcement elements are linked with the concrete elements. As the PT tendons are unbonded to allow the rocking motion

of the wall, no constraint is needed to define the contact between the PT tendon and concrete wall. But the bottom end of the tendon is connected at the base by hinge connection, whereas the top end of the tendons is fixed with the help of MPC beam connection. It may be noted that MPC beam connection is a built-in function in ABAQUS which forms a rigid link between a master node (tendon end) and the slave nodes (concrete surface nodes) as shown in Fig. 3.

To connect the load plates with the wall, tie constraints were used, where the master surface is the wall surface, and the slave surface is the tie plate surface. To prevent horizontal slip while applying lateral displacement to the wall, surface-to-surface contact details have been updated. For normal behavior, the contact has been defined as hard contact (to prevent penetration into the foundation), in case of tangential behavior, rough contact (to prevent horizontal slip) has been specified.

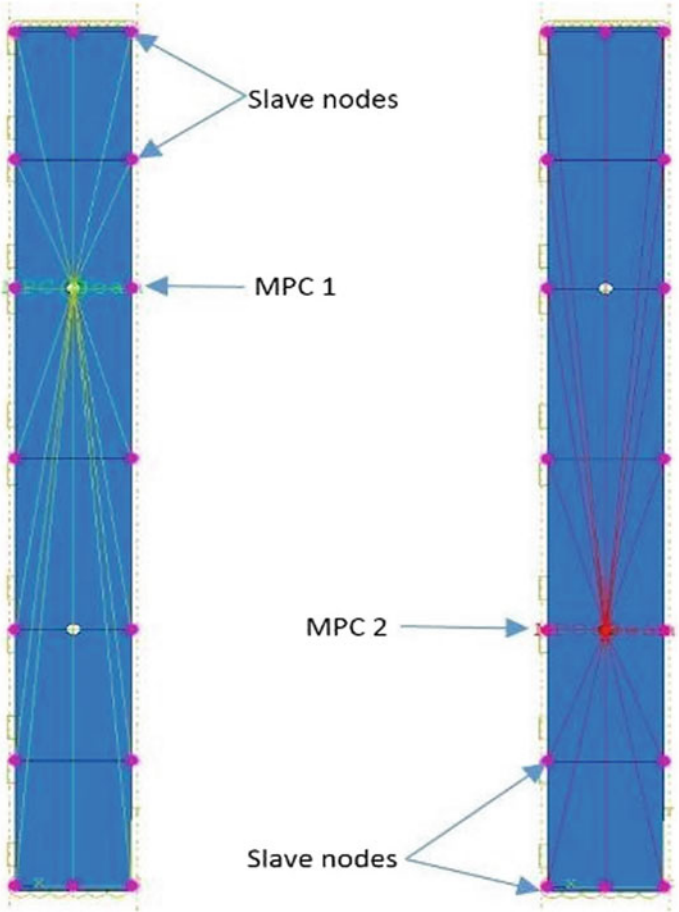


**Fig. 3** MPC connections configured at the tendon end with the wall nodes

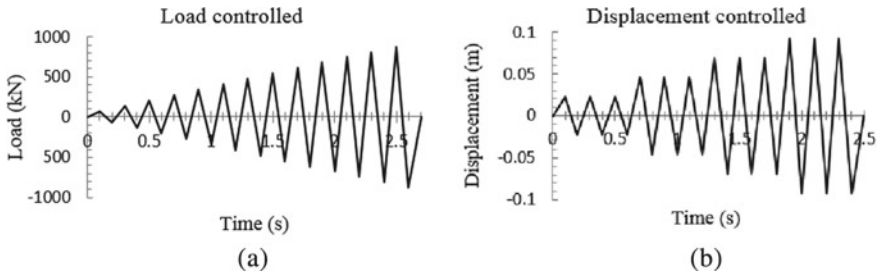


**Fig. 4** Load cycles applied to the numerical model **a** force-controlled, **b** displacement-controlled [7]

While defining the rough contact, an option allowing separation after contact is preferred to enable the uplifting of the wall from the base. The foundation base of the assembly is considered to be rigid and fixed with all degrees of freedom.

## 4 Method of Analysis

The PT hybrid shear wall model is analyzed under forced controlled slow-cyclic lateral load followed by displacement-controlled load cycles as shown in Fig. 4. The lateral load is applied at the loading plate placed at each side of the wall. Prior to the application of slow-cyclic lateral load, the wall is subjected to gravity load and post-tensioning force. The post-tensioning force is being developed indirectly by creating a temperature difference in the PT tendon. A uniform temperature field of 25 °C defined in the initial step has been modified to −289 °C in the next step to generate the post-tensioning effect. The tensile force generated in the tendon is given by Eq. (1).

$$P = EA(\alpha \Delta T) \tag{1}$$

Here, $\alpha$ is the coefficient of thermal expansion, $E$ is the modulus of elasticity of steel, $A$ is the area of cross section of tendon, and $\Delta T$ is the change in temperature from the initial step to the first step. With A = 725 mm$^2$, $E = 2 \times 10^5$ N/mm, $\Delta T = 314$ °C, and $\alpha = 1.1 \times 10^{-5}$/°C, the tensile force, $P$, is equal to 501.2 kN.

## 5 Results and Discussions

The finite element study of the model featuring PT wall with internally placed EDR is conducted using ABAQUS CAE 3.18. The comparison of energy dissipation of the walls is done by plotting the base shear–lateral drift envelop.

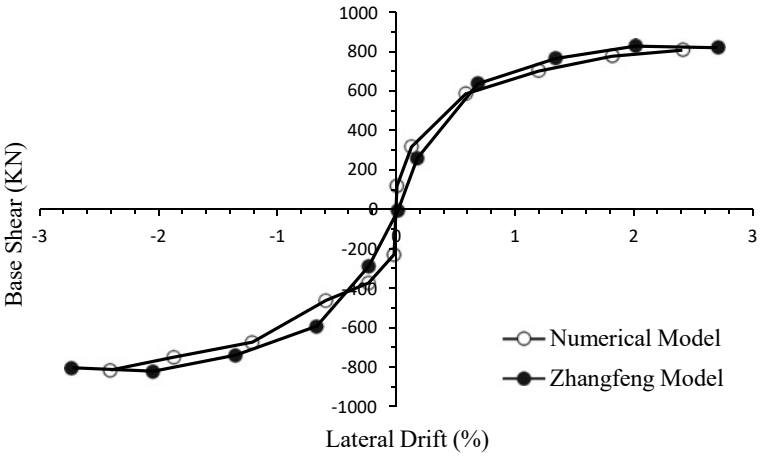


**Fig. 5** Comparison of the backbone curves of the experimental model of Zhangfeng and Zhengxing [7] and the validation model developed in the present study

For validation of the finite element model, another post-tensioned shear wall is modeled to replicate the hybrid wall specimen of Zhangfeng and Zhengxing [7]. The hybrid wall specimen is 3.62 m high, 1.7 m long, and 0.2 m thick. It rests on a foundation beam which is 0.64 m high and 2.2 m long. The longitudinal reinforcement provided in the wall is continued into the foundation beam to act as an energy dissipating reinforcement at the interface. Thus, the hybrid wall consists of internally placed energy dissipating reinforcement. One post-tensioning tendon, consisting of four strands of 15.2 mm diameter, is placed at the center of the wall for applying the post-tensioning force. The energy dissipating reinforcements, confining hoops, and longitudinal and lateral reinforcement elements are provided according to the experimental details mentioned in the research. The important modeling features are the same as those mentioned above. Finally, the base shear and lateral deflection are extracted using the procedure described in the analytical modeling of the test wall. The comparison of results obtained from the validation model and the numerical study conducted by Zhangfeng and Zhengxing [7] is done in terms of base shear–lateral drift response as shown in Fig. 5. The results obtained are comparable, and hence, the numerical model developed is considered suitable for further studies.

## 6 Modification of Numerical Model

Due to the complexity of numerical modeling, the analysis of the shear wall models has become quite tedious and huge time taking. Hence to solve this problem, a comparably efficient numerical model is tried to be executed. As the material nonlinearity is confined into the EDR mainly, therefore partially nonlinear models are developed

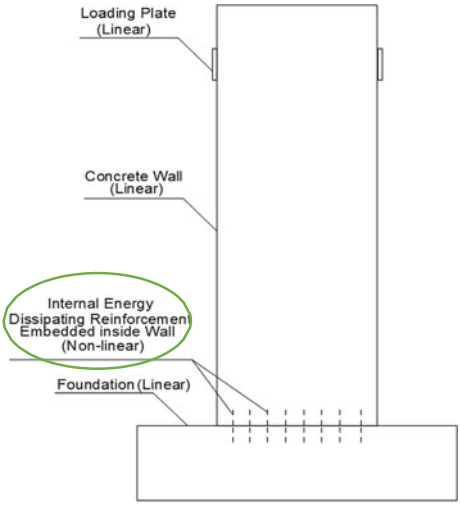


**Fig. 6** Property specification of the elements of the PT shear wall

where the nonlinear behavior of the EDR is only considered. The concrete and the reinforcement inside it are considered to be linear elastic as shown in Fig. 6. It has been observed that the partially nonlinear model having nonlinearity only in EDR is showing higher values of base shear with respect to the fully nonlinear model for particular lateral drift values thus overestimates the performance of the shear wall.

To overcome this problem, to make the structure more reliable, a new approach has been introduced. As the nonlinear behavior of concrete is limited to the lower portion of the wall, therefore along with the EDR nonlinearity, the concrete wall is made partly nonlinear, where the upper portion of the wall is having elastic properties with coarser meshing, and the lower portion is plastic with finer meshing (Fig. 7). The response of the updated model and fully nonlinear model in terms of load-deformation behavior has been compared as shown in Fig. 6.

After the comparison of the backbone curves as shown in Fig. 8, it is perceived that the behavior of the partially nonlinear model is almost identical to that of the fully nonlinear model.

## 7 Summary and Conclusions

In this paper, the suitability of the numerical models has been examined. To check the appropriateness of the numerical model, a numerical replica of an experimental setup has been developed, and their performances are compared. From the results discussed above, it can be said that the numerical modeling of the hybrid shear wall is able to replicate the actual behavior properly. In spite of possessing identical behavior like the experimental study, due to the complexity of the numerical modeling, the analysis consumes huge time. Hence, to make the model more computationally efficient, some

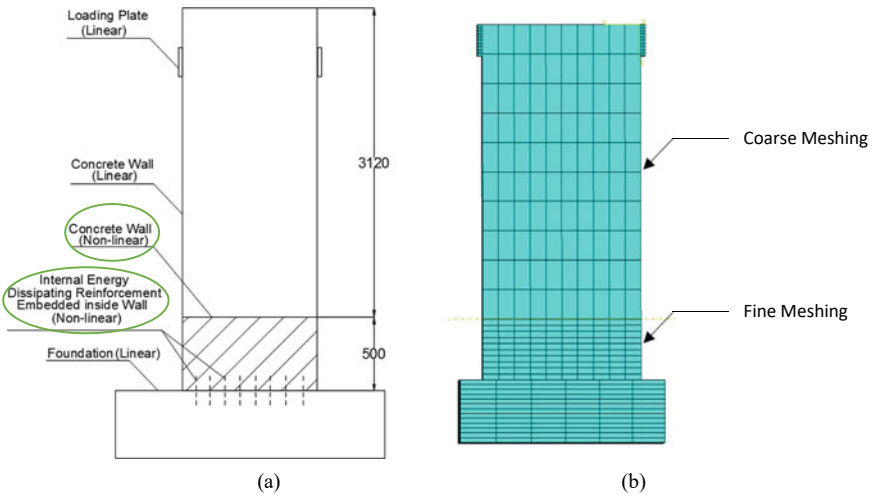


**Fig. 7** **a** Elements of shear wall and their properties, **b** meshing details of the numerical model of PT shear wall

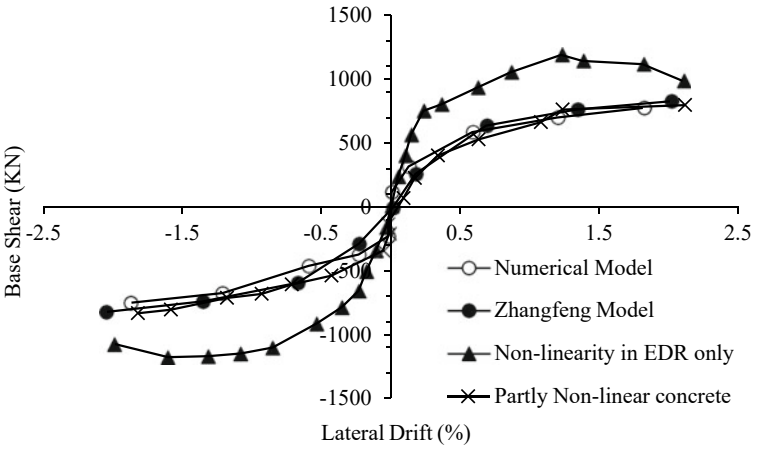


**Fig. 8** Comparison of the backbone curves of numerical models with the Zhangfeng experimental model

modifications are being tried to be implemented. As nonlinear behavior is concentrated in the EDR mainly, a partially nonlinear model has been developed where all the elements are kept linear elastic except EDR. But this model overestimates the capacity of the shear wall. Therefore, it cannot be accepted.

In the second approach, the nonlinearity of the lower part of concrete is also considered along with the EDR, and the other elements are considered linear elastic.

This model shows good agreement with the fully nonlinear model and the experimental results. Hence, it can be concluded that for the analysis of hybrid shear walls, numerical modeling can be a good option where the partly nonlinear model can be a good substitution of the fully nonlinear one in terms of computational efficiency and accuracy of the results.

## References

1. Guo T, Xu Z, Song L, Wang L, Zhang Z (2017) Seismic resilience upgrade of RC frame building using self-centering concrete walls with distributed friction devices. J Struct Eng 143(12):1–11. https://doi.org/10.1061/(ASCE)ST.1943-541X.0001901
2. Hafezolghorani M, Hejazi F, Vaghei R, Jaafar MSB, Karimzade K (2017) Simplified damage plasticity model for concrete. Struct Eng Int 27(1):68–78. https://doi.org/10.2749/101686616X1081
3. Kim JM, Feng MQ, Shinozuka M (2000) Energy dissipating restrainers for highway bridges. Soil Dynam Earthq Eng 19(1):65–69. https://doi.org/10.1016/S0267-7261(99)00030-5
4. Perez FJ, Sause R, Pessiki S (2008). Analytical and experimental lateral load behavior of unbonded posttensioned precast concrete walls. Eng J Struct Eng 133(11):1531–1540. https://doi.org/10.1007/BF00000414
5. Symans MD, Charney FA, Whittaker AS, Constantinou MC, Kircher CA, Johnson MW, McNamara RJ (2007) Energy dissipation systems for seismic applications: current practice and recent developments. J Struct Eng 134(1):3–21. https://doi.org/10.1061/(asce)0733-9445(2008)134:1(3)
6. Tanyeri AC, Moehle JP, Nagae T (2014) Seismic performance and modeling of post-tensioned precast shear walls. In: Proceedings of the 10th national conference in earthquake engineering, earthquake engineering research institute, Anchorage, AK
7. Zhangfeng Z, Zhengxing G (2017) Experimental study on emulative hybrid precast concrete shear walls. KSCE J Civil Eng 21;329–338. https://doi.org/10.1007/s12205-016-0620-4

# Nonlinear Response of CFS-Laced Built-Up Columns—A Numerical Parametric Study


**Mohammad Adil Dar, Dipti Ranjan Sahoo, and Arvind K. Jain**

**Abstract** The continuity in the lateral connectivity offered by laced built-up columns enables them to perform better, particularly when the axial demands are large and under lateral loading. The configuration of lacing adopted is one of the important parameters that affects the peak resistance of built-up columns. This paper reports a numerical parametric investigation conducted to study the lacing slenderness influence on the strength variation of short built-up cold-formed steel (CFS) columns. ABAQUS was used to develop the numerical model, where concentric axial loading was applied to the built-up columns constructed from four plain CFS angle sections, fastened by lacing bars configured in N-type latticed pattern, with pin-ended supports. The experimental results of laced CFS built-up columns conducted by the authors earlier and that of on battened CFS built-up column conducted by EI Aghoury et al. were adopted for calibrating the numerical model for performing the numerical parametric study. Lastly, the design axial strengths of the built-up columns were computed by adopting various current standards on steel structures, which were later compared with the numerical results.

**Keywords** Cold-formed steel · Built-up columns · Lacing · Nonlinear analysis · Strength · Numerical study

M. A. Dar (✉)
Department of Civil and Structural Engineering, University of Sheffield, Sheffield S1 3JD, UK
e-mail: dar.adil@sheffield.ac.uk

D. R. Sahoo · A. K. Jain
Department of Civil Engineering, Indian Institute of Technology, Delhi, New Delhi 110016, India
e-mail: drsahoo@civil.iitd.ac.in

A. K. Jain
e-mail: akjain@civil.iitd.ac.in



M. Madhavan et al. (eds.), *Proceedings of the Indian Structural Steel Conference 2020 (Vol. 1)*, Lecture Notes in Civil Engineering 318,
https://doi.org/10.1007/978-981-19-9390-9_24

## 1 Introduction

The extensive research on numerous aspects of cold-formed steel (CFS) members has been responsible for its tremendous growth in the construction industry. Despite the high slenderness of the CFS sectional plate elements, the progressive research on CFS sections has produced numerous types of CFS sections that have not only performed superior to the conventional CFS sections, but have been economical and convenient in fabrication as well. The adoption of built-up columns is ideal, when the economy in construction needs to be achieved, without affecting the structural performance of the columns. Considerable research has been carried out on CFS built-up columns [5, 6, 8–10, 13–19, 24–26]. Generally, battened columns are preferred, due to ease in fabrication. The past research related to CFS built-up compression members has been limited, which mainly comprised channel sections and angle CFS sections as chord members [3, 7, 18, 22, 27], as shown in Fig. 1. The continuity in the lateral connectivity offered by laced built-up columns enables them to perform better, particularly when the axial demands are large and under lateral loading. The configuration of lacing adopted is one of the important parameters which has been identified to affect the axial resistance of laced built-up columns. Due to limited studies performed on CFS-laced built-up columns with single lacing configuration, sustaining compressive forces, a study on the behavior of CFS built-up compression members with N-type lacing configuration needs to be explored.

This paper presents a numerical investigation conducted to study the influence of slender lacings on strength variation of the built-up CFS columns. ABAQUS was used to develop the numerical model, where concentric axial loading was applied to the built-up columns constructed from four compact plain CFS angles, fastened by lacing bars configured in N-type latticed pattern, with pin-ended supports. The

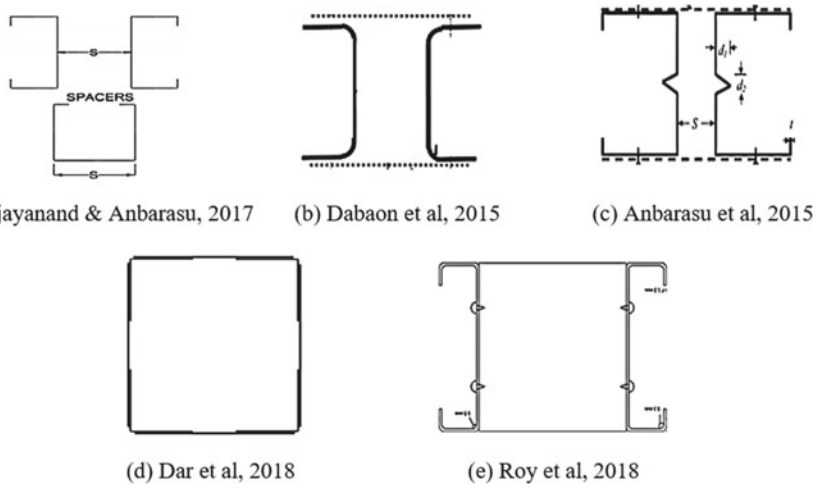


**Fig. 1** Past built-up columns studied

experimental results of laced CFS built-up columns conducted by the authors earlier, and that of on the battened CFS built-up columns conducted by EI Aghoury et al. [20] were used for the calibration of the numerical model to be used for conducting the numerical parametric study. Lastly, the design strengths were computed by using various current standards on steel structures, which were later compared with the numerical results.

## 2 Finite Element Modeling

The numerical investigation on the behavioral study of laced columns with varying slenderness ratios of the lacing bars was conducted using finite element method, by adopting ABAQUS software. Table 1 presents the relevant details of the numerical modeling technique. The experimental results from Dar et al. [18] as well as from EI Aghoury et al. [20] were selected for the FEM validation. This calibrated model was adopted for performing the necessary parametric analysis, for investigating the influence of slender lacings in affecting the axial strength of CFS columns. Table 2 shows the comparison of the peak loads extracted from Dar et al. [18] as well as EI Aghoury et al. [20] with the FEM results. Figure 2 shows the failure mode comparison of the FEM obtained ones with that of from the tests. Figure 3 shows the variation of the load–displacement response between experiments of Dar et al. [18] and EI Aghoury et al. [20] against the results of FEM. From Table 2 and Figs. 2 and 3, a reasonable agreement was obtained between the results of FEM and the experiments. Therefore, for carrying out the parametric study, this model can be adopted.

## 3 Parametric Study

The numerical parametric study was carried out by varying the lacing slenderness ranging from 395 to 79, on the specimen adopted by Dar et al. [18] (as shown in Fig. 4). The nomenclature for specimen labeling is given as follows. The label "Model_I_N_395" indicates the various parameters of the model.

Model_I indicates the type of specimen considered, N represents the type of lacing arrangement used and 395 reflects the lacing slenderness. The effect of the lacing slenderness ratio variation on the axial resistance of columns including the comparison with the strength predictions made by AISI S_100, ANSI-AISC-360 as well as IS-800 is shown in Table 3. Figures 5 and 6 show the load versus axial displacement plots and the effect of lacing slenderness on the strength variation, obtained from the results of the parametric study.

**Table 1** Finite element modeling details

| Detail type | Feature adopted | Detail type | Feature adopted |
|---|---|---|---|
| Element type | Shell element (S4R) | Other end's support condition | Hinged support |
| Size of mesh | $5 \times 5mm^2$ | Axial load application | By displacing the loaded end master node |
| Type of material model | Elastic perfectly plastic | Connection between the various elements | Mesh independent type of fastener |
| Young's elasticity (E) | $2 \times 10^5$ MPa | Local imperfection | $0.34 \times t$ (Schafer & Pekoz) |
| Yield stress ($f_y$) | 450 MPa | Global imperfection | Column height/500 (Schafer & Pekoz) |
| Loaded end's support condition | Roller support with prevention of translation across the transverse directions | Types of analysis | Eigen buckling analysis, with a follow-up by means of a nonlinear analysis |

**Table 2** Result comparison (experimental versus numerical)

| Specimen | $Pu_{Exp.}$(kN) | $Pu_{FEM.}$(kN) | $Pu_{Exp}/Pu_{FEM}$ |
|---|---|---|---|
| SL_60_20_805_(a) | 69 | 66 | 0.99 |
| SL_60_20_1455 | 45 | 49 | 0.95 |
| 1000B80L30B6 | 52 | 51 | 1.01 |

$Pu_{FEM}$: FEM obtained ultimate load
$Pu_{Exp}$: Experimentally obtained ultimate load

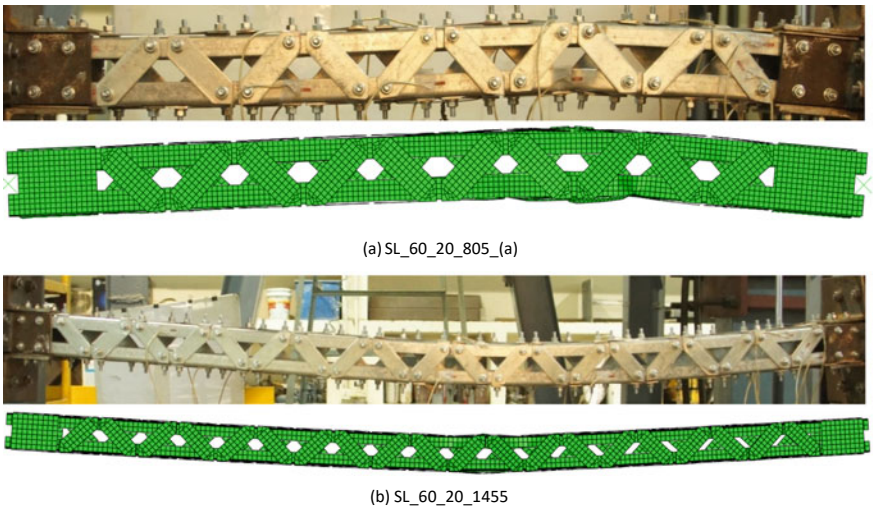


**Fig. 2** Mode of failure (experimental versus numerical)

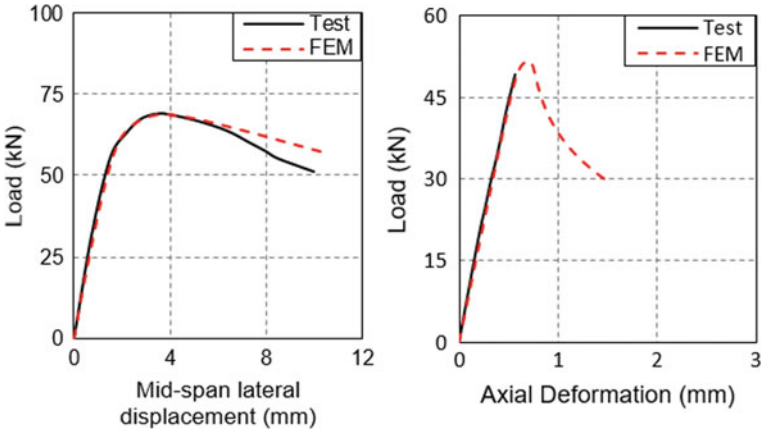


**Fig. 3** Load versus displacement response (experimental versus numerical)

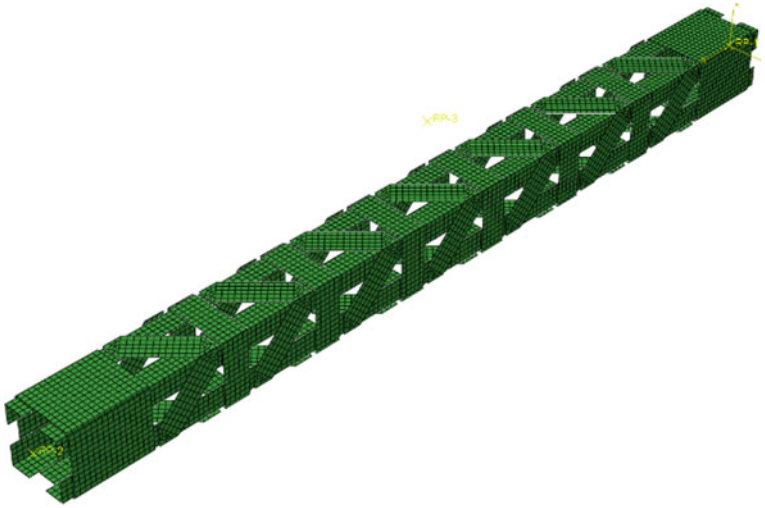

**Fig. 4** Numerical model of the built-up column

## 4 Discussion

From Fig. 5 that presents the load versus axial displacement plots of the built-up compression members indicates the initial stiffness in all the specimens was nearly linear. As the lacing slenderness ratio raised from 79.0 to 395.0, the peak strengths of the compression members dropped, from the magnitude of 72.6–57.5 kN (approximately 21%). With increase of the slenderness ratio of the lacings, a minor drop in the axial stiffness of the plot, post the ultimate load, was noted. It was also noted that in

**Table 3** Results of parametric study

| Specimen | Lacing slenderness ratio | $Pu_{FEM}$ (kN) | $Pu_{FEM}/Pu_{NAS}$ | $Pu_{FEM}/Pu_{AISC}$ | $Pu_{FEM}/Pu_{IS-800}$ | Mode of failure |
|---|---|---|---|---|---|---|
| Model_I_N_395 | 395.0 | 57.50 | 0.81 | 0.85 | 0.87 | Local |
| Model_I_N_263 | 263.0 | 59.00 | 0.81 | 0.87 | 0.97 | Local |
| Model_I_N_197 | 197.0 | 61.90 | 0.87 | 0.91 | 0.95 | Local |
| Model_I_N_158 | 158.0 | 64.30 | 0.90 | 0.97 | 0.99 | Local |
| Model_I_N_132 | 132.0 | 65.00 | 0.91 | 0.96 | 0.98 | Local |
| Model_I_N_113 | 113.0 | 66.20 | 0.93 | 0.98 | 1.02 | Local |
| Model_I_N_99 | 99.0 | 67.20 | 0.94 | 1.02 | 1.05 | Local |
| Model_I_N_88 | 88.0 | 68.30 | 0.95 | 1.03 | 1.03 | Local |
| Model_I_N_79 | 79.0 | 72.60 | 1.01 | 1.07 | 1.12 | Local |

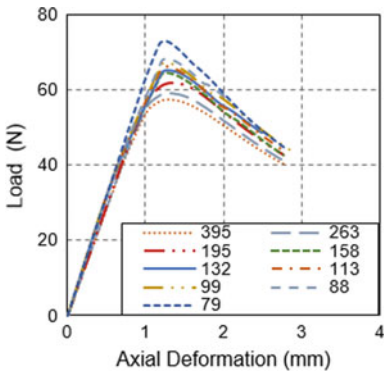


**Fig. 5** Effect of slender lacings on the peak load

the specimens with lacing slenderness varying from 79 to 158, a sudden drop post the peak load was observed, unlike the specimens with higher lacing slenderness, where the behavior was otherwise. Furthermore, it was observed that apart from the local buckling of the chord member in all the specimens, lacing buckling was observed in specimens with lacing slenderness higher than 113. The failure mode showing prominent lacing buckling in Model_I_N_395 is shown in Fig. 7.

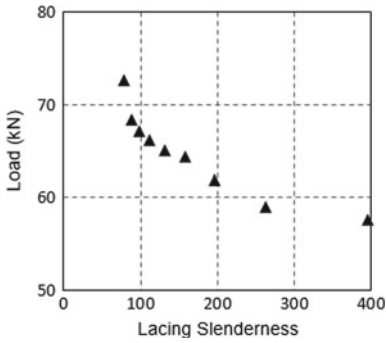


**Fig. 6** Variation of strength with respect to lacing slenderness

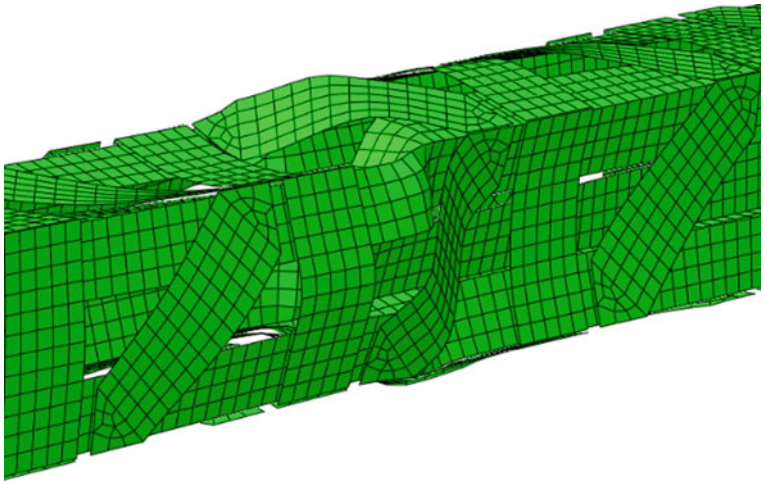

**Fig. 7** Mode of failure in Model_I_395

## 5 Conclusion

This paper reflected the results of a numerical investigation conducted to study the influence of slender lacing on the strength of the short built-up columns. Axial loading was applied to the built-up columns constructed from four plain CFS angle sections with pin-ended support conditions. N-type configuration of lacing was adopted in this study. Apart from this, the design strengths were computed by using various standards on steel structures. Following were some notable conclusions obtained from this study.

- Lacing slenderness affects the load carrying capacity of short CFS built-up columns. A drop in the load carrying capacity is observed in laced built-up columns with slender lacings.

- When the lacing slenderness in short CFS built-up columns is varied from around 80 to 400, the strength drops by approximately 20%.
- Due to the lack of design guidelines on the design of CFS-laced built-up columns, the upper limits of lacing slenderness brought out by standards (ANSI/AISC-360 and IS-800) on hot-rolled steel-laced built-up columns cannot be adopted safely for designing CFS built-up laced columns. This study recommends a slenderness ratio < 110 for short-type CFS built-up columns with b/t < 15.
- The strength predictions of AISI S-100 and IS-800 for laced CFS built-up columns are conservative. Furthermore, the strength predictions of AISC-360 are slightly the unconservative.

## References

1. ABAQUS User's Manual (2004) Version 6.14 Hibbit, Karlsson, and Sorenson, Inc., Providence, RI
2. AISI S-100 (2016) North American specification for the design of cold-formed steel structural members, AISI Standard, Washington, DC
3. Anbarasu M, Kanagarasu K, Sukumar S (2015) Investigation on the behaviour and strength of cold-formed steel web stiffened built-up battened columns. Mat Str 48(12):4029–4038
4. ANSI/AISC 360 (2016) Specification for structural steel buildings. American National Standard, Chicago, Illinois
5. Anbarasu M, Dar MA (2020a) Improved design procedure for battened cold-formed steel built-up columns composed of lipped angles. J Constr Steel Res 164:105781. https://doi.org/10.1016/j.jcsr.2019.105781
6. Anbarasu M, Dar MA (2020) Axial capacity of CFS built-up columns comprising of lipped channels with spacers: nonlinear response and design. Eng Struct 213:110559
7. Dabaon M, Ellobody E, Ramzy K (2015) Experimental investigation of built-up cold-formed steel section battened columns. Thin Walled Str 92:137–145
8. Dar MA, Verma A, Anbarasu M, Pang SD, Dar AR (2022) Design of Cold-formed steel battened built-up columns. J Constr Steel Res 193:107291
9. Dar MA, Sahoo DR, Jain AK, Verma A (2022b) Tests on CFS laced columns composed of plain channels: behavior and design. J Struct Eng-ASCE 148(5):04022043
10. Dar AR, Vijayanand S, Anbarasu M, Dar MA (2021a) CFS battened built-up columns—experimental behaviour and verification of different design rules developed. Adv Struct Eng 25(2):321–335
11. Dar MA, Subramanian N, Anbarasu M, Ghowsi AF, Arif PA, Dar AR (2021) Testing and FE simulation of lightweight CFS composite built-up columns: axial strength and deformation behaviour. Thin-Walled Struct 169:108222
12. Dar MA, Sahoo DR, Jain AK, Sharma S (2021) Monotonic tests and numerical validation of cold-formed steel battened built-up columns. Thin-Walled Struct 159:107275
13. Dar MA, Sahoo DR, Jain AK (2021) Interaction between chord compactness and lacing slenderness in CFS built-up columns. Structures 30:985–995
14. Dar MA, Sahoo DR, Jain AK (2020a) Numerical study on the structural integrity of built-up cold-formed steel battened columns. In: Prakash R, Suresh Kumar R, Nagesha A, Sasikala G, Bhaduri A (eds) Struct Integrity Assessment Lec Notes Mech Eng Springer, Singapore
15. Dar MA, Sahoo DR, Jain AK (2020b) Axial strength and stability behaviour of cold-formed steel battened closed section columns. In: Proceeding of structures stability research council annual stability conference 2020, SSRC 2020, Atlanta, Georgia, USA

16. Dar MA, Sahoo DR, Jain AK (2019a) Compression capacity of short cold-formed steel built-up columns with double-lacing configuration and low sectional compactness. In: Proceedings of structures stability research council annual stability conference 2019, SSRC 2019, St. Louis, Missouri, USA, 1, pp 472–482
17. Dar MA, Sahoo DR, Jain AK (2019b) Axial compression behavior of laced cold-formed steel built-up columns with unstiffened angle sections. J Constr Steel Res 162. https://doi.org/10.1016/j.jcsr.2019.105727
18. Dar MA, Sahoo DR, Pulikkal S, Jain AK (2018) Behaviour of laced built-up cold-formed steel columns: experimental investigation and numerical validation. Thin-Walled Struct. 132:398–409
19. Dar MA, Sahoo DR, Jain AK (2018b) Ultimate strength of cold-formed steel built-up columns: effect of lacing slenderness. In: Proceedings of ninth international conference advance steel structure (ICASS-2018), Hong Kong, China
20. El Aghoury MA, Salem AH, Hanna MT, Amoush EA (2010) Experimental investigation for the behavior of battened beam-columns composed of four equal slender angles. Thin-Walled Struct 48(9):669–683
21. IS 800, Indian Standard Code of Practice for General Construction in Steel, Bureau of Indian
22. Roy K, Ting TCH, Lau HH, Lim JBP (2018) Nonlinear behaviour of back-to-back gapped built-up cold-formed steel channel sections under compression. J Constr Steel Res 147:257–276
23. Selvaraj S, Madhavan M (2022) Design of cold-formed steel built-up closed section columns using direct strength method. Thin-Walled Struct 171:108746
24. Selvaraj S, Madhavan M (2022) Experimental investigation and design considerations on cold-formed steel built-up I-section columns subjected to interactive buckling modes. Thin-Walled Struct 175:109262
25. Selvaraj S, Madhavan M (2021) Design of cold-formed steel built-up columns subjected to local-global interactive buckling using direct strength method. Thin-walled Struct 159:107305
26. Schafer BW, Pekoz T (1998) Computational modelling of cold-formed steel: characterizing geometric imperfections and residual stress. J Constr Steel Res 47:193–210
27. Vijayanand S, Anbarasu M (2017) Effect of spacers on ultimate strength and behavior of cold-formed steel built-up columns. Procedia Eng 173:1423–1430

# Post-flexural Torsional Buckling Strength in Slender CFS Compression Members


**K. J. Aayillia and M. V. Anil Kumar**

**Abstract** The design equations for the ultimate global buckling strength of cold-formed steel (CFS) compression members in different design standards were originally developed for hot-rolled steel (HRS) members which normally do not undergo flexural torsional buckling (FTB). The presence of post-buckling strength for CFS compression members undergoing FTB was reported in the literature which is not accounted for in design equations. There were a few attempts to incorporate the post-FTB strength to the global buckling strength equations available in North American Standard (NAS). One of the recent proposals is to introduce a modification to global buckling strength equations by introducing an additional parameter, $\beta$ which represents the relative principal second moment of areas ($I_x/I_y$) of the cross-section. This paper demonstrates the limitations of using parameter $\beta$ for modifying the global buckling equations to account for post-buckling strength.

**Keywords** Cold-formed steel · Compression member · Post-buckling strength · Flexural torsional buckling · Flexural buckling

## 1 Introduction

An axially loaded globally slender compression member may undergo flexural, torsional, or flexural torsional buckling depending upon the cross-section geometry and the relative position of centre of gravity (CG) and shear centre (SC). Hence, the elastic global buckling stress ($f_{cre}$) of CFS compression member is taken to be the minimum of flexural ($f_F$), torsional ($f_T$), or flexural torsional ($f_{\mathrm{FT}}$) buckling stresses. The design equations for ultimate global buckling strength, $f_{ue}$, in design standards [2, 6] (EN: 1993-1-3 2004) were originally developed for hot-rolled steel

K. J. Aayillia (✉) · M. V. Anil Kumar
IIT Palakkad, Palakkad, India
e-mail: 101704001@smail.iitpkd.ac.in

M. V. Anil Kumar
e-mail: anil@iitpkd.ac.in



M. Madhavan et al. (eds.), *Proceedings of the Indian Structural Steel Conference 2020 (Vol. 1)*, Lecture Notes in Civil Engineering 318,
https://doi.org/10.1007/978-981-19-9390-9_25

(HRS) members. The behaviour of HRS members are different from CFS members due to the presence of high residual stresses which can be safely ignored for CFS columns [9].

The test performed by Popovic et al. [7] on fixed and pin-ended angle sections reported the possibility of post-global buckling strength of members failing under torsional (T) or flexural torsional (FT) buckling modes. The experimental results reported by Shifferaw and Schafer (2011) on fixed-ended plain and lipped angle columns shows that the presence of post-buckling strength with respect to global T or FT buckling modes is due to the warping fixity. But, this effect is not accounted for in the design standards so far. Young [12], Gunalan and Mahendran [5] proposed modifications to the global buckling strength equation for fixed-ended columns subjected to flexural torsional buckling (FTB) based on the test and finite element analysis (FEA) results. More recently, a global buckling strength equation expressed as a function of relative flexural stiffness was proposed by Dinis et al. [4] in order to overcome the conservative nature of the design equation for slenderness greater than 1.5. This paper systematically evaluates the current design rules and design equation proposed by Dinis et al. [4] for CFS compression members subjected to FT buckling based on the test/FEA results reported in literature.

## 2 Design Rules for Globally Buckling CFS Columns

### *2.1 Existing Design Rules*

NAS [6] and AS/NZS [2] adopted the unified approach proposed by Peköz (1999) for the global buckling strength, $f_{ue}$ of CFS compression members, given in Eq. (1).

$$f_{ue} = \begin{cases} (0.658^{\lambda_e^2}) f_y & \lambda_e \leq 1.5 \\ \left(\frac{0.877}{\lambda_e^2}\right) f_y & \lambda_e > 1.5 \end{cases} \tag{1}$$

where $f_y$ = yield strength of steel. $\lambda_e = \sqrt{\frac{f_y}{f_{cre}}}$, non-dimensional global buckling slenderness, $f_{cre}$ = Elastic buckling stress.

As per European Convention for Constructional Steelwork (ECCS) (1986), multiple buckling curves are recommended for the design of CFS compression members. The global buckling strength equation in EN: 1993-1-3 (2004) based on the Ayrton-Perry formula accounts for the effect of cross-sectional shapes and principal directions. These curves ($a_o$, $a$, $b$, $c$, $d$) are originally generated for HRS members based on large experiment work by considering the effect of residual stress and initial imperfections. EN: 1993-1-3 (2004) expresses the normalised global buckling strength as a function of non-dimensional slenderness and an imperfection factor ($\alpha$) that varies with each type of curve. The code uses curve '$b$' for lipped channel sections and curve '$c$' for plain channel, plain angle, and lipped angle sections.

The application of these design equations which were originally developed for global buckling strength of torsionally stiffer HRS members to torsionally flexible CFS members showing post-buckling strength needs to be studied. An attempt to modify the design equation was reported by Dinis et al. [4].

### 2.2 *Modification Proposed by Dinis et al. [4]*

Dinis et al. [4] proposed a modification to global buckling strength equation corresponding to $\lambda_e$ (> 1.5) to account for the post-buckling strength in FTB by introducing parameters $a$ and $b$ as shown in Eq. (2) as function of relative flexural stiffness, $\beta(I_{11}/I_{22})$. This modification was based on 2820 nonlinear finite element analysis results for fixed-ended columns with different cross-section geometries.

$$f_{nFT} = \begin{cases} (0.658^{\lambda_e^2}) f_y & \lambda_e \leq 1.5 \\ \left(\frac{a}{\lambda_{FT}^b}\right) f_y & \lambda_e > 1.5 \end{cases} \tag{2}$$

The parameter $\beta$ relating the major ($I_{11}$) and minor ($I_{22}$) axis moment of inertia is expressed using the terms $a$ and $b$, given by

$$a = 0.39 \times 1.5^b \tag{3}$$

$$b = \begin{cases} 0.1\ \beta + 0.85 & \beta < 11.5 \\ 2 & \beta \geq 11.5 \end{cases} \tag{4}$$

## 3 Comparison of Test/FEA Results with DSM Strength Curve

The accuracy of design global buckling strength equations [2, 6] (EN: 1993–1-3 2004) is evaluated using 862 test/FEA results of columns failed due to FTB reported in the literature [[4, 5, 12]]. The specimen includes channel (C), channel with return lips (RLC), web-stiffened channel (WSC), web/flange-stiffened lipped channels (WFSC), zed sections (Z), hat sections (H), rack sections (R), I sections (I), and lipped angles (A). The ultimate strength normalised with respect to yield load ($P_{\text{test}}/P_y = f_{ue}/f_y$) is plotted against non-dimensional global buckling slenderness, $\lambda_e$, in Fig. 1. The ratio of strength obtained from test/FEA to that from the strength equations is plotted against $\lambda_e$ in Fig. 2. The mean ($\mu$), standard deviation ($\sigma$), maximum (Max), and minimum (Min) values are given in Table 1.

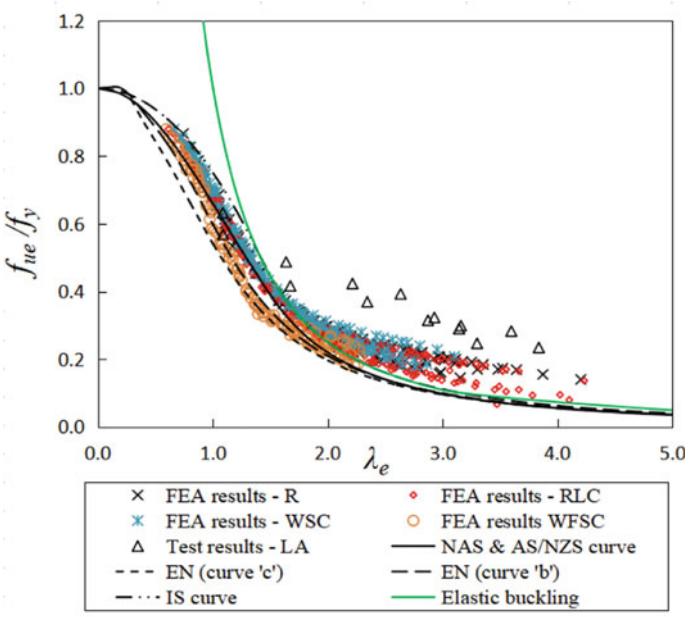


(a) Fixed ended

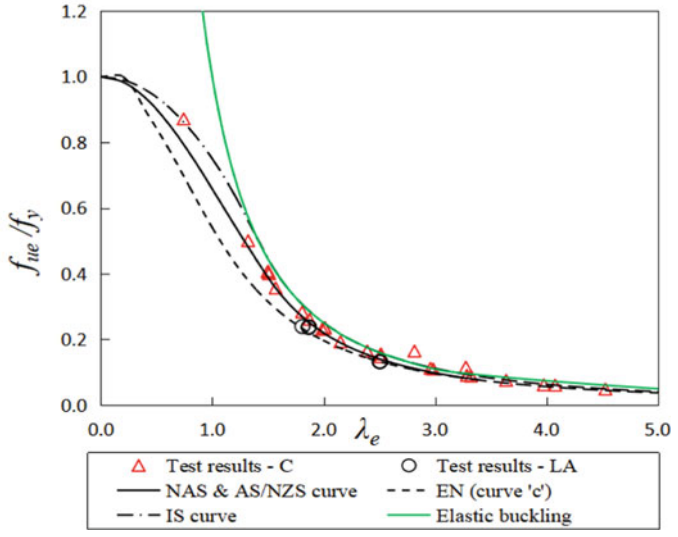


(b) Pin ended

**Fig. 1** Test/FEA results of columns failing under FTB

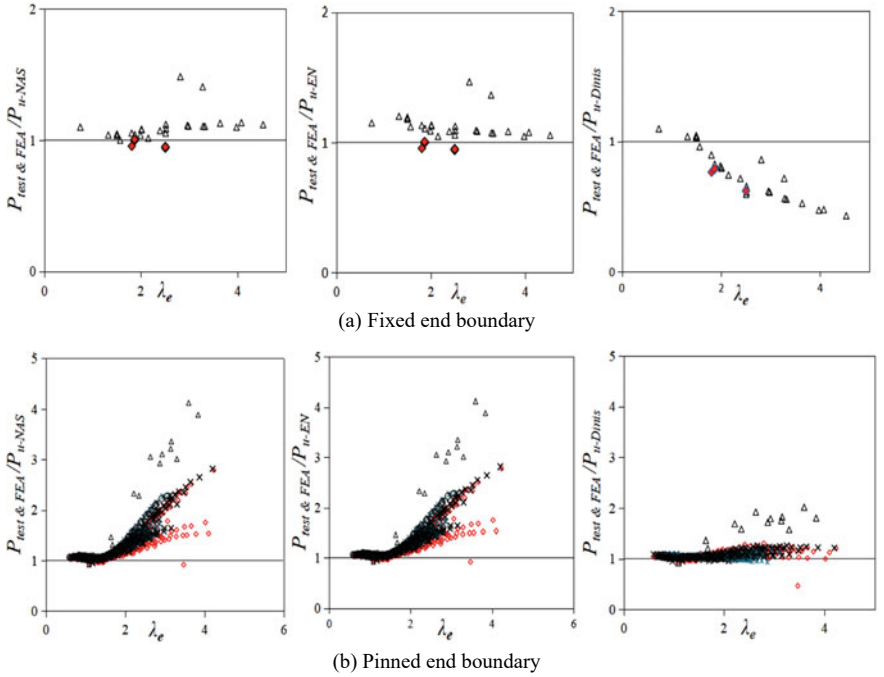


(a) Fixed end boundary

(b) Pinned end boundary

**Fig. 2** Evaluation of global buckling strength equations

**Table 1** Statistical summary of $P_{test}/P_{theory}$

| Boundary condition | Design code | $\mu$ | $\sigma$ | Max | Min |
|---|---|---|---|---|---|
| Fixed | NAS [6], AS/NZS [2] | 1.35 | 0.49 | 4.12 | 0.92 |
| | EN: 1993-1-3 (2004) | 1.30 | 0.40 | 3.57 | 0.79 |
| | Dinis et al. [4] | 1.07 | 0.11 | 2.02 | 0.47 |
| Pinned | NAS [6], AS/NZS [2] | 1.07 | 0.12 | 1.48 | 0.89 |
| | EN: 1993-1-3 (2004) | 1.10 | 0.11 | 1.46 | 0.94 |
| | Dinis et al. [4] | 0.74 | 0.19 | 1.09 | 0.43 |

The observations based on Figs. 1 and 2 and Table 1 are listed below.

- The post-flexural torsional buckling strength of fixed CFS columns is adequately represented by the modifications suggested by Dinis et al. [4]. The existing equations in the design standards NAS [6], AS/NZS [2], EN: 1993-1-3 (2004), which do not account for post-buckling strength are found to be conservative.
- The extension of the same modification to pinned columns does not provide accurate results as such members do not show significant post-buckling strength.

$P_{test}/P_{theory}$ of NAS [6], AS/NZS [2] with $\mu = 1.07, \sigma = 0.12$ and that of EN: 1993-1-3 (2004) with $\mu = 1.1, \sigma = 0.11$ shows the accuracy of these design equations in predicting strength of pin-ended column subjected to flexural torsional buckling.

Although the modifications proposed by Dinis et al. [4] accounts for the post-FTB strength of fixed columns, the extension of the same equations to other end boundary conditions is not successful. This may be because the use of relative second moment of areas ($I_{11}/I_{22}$) to represent the post-buckling strength due to torsional or flexural torsional buckling may not be accurately representing the behaviour of such members. In this study, an attempt is made to come up with a parameter to represent the post-global buckling behaviour of CFS compression members irrespective of the end boundary conditions using finite element analysis.

## 4 Finite Element Analysis

The CFS member is modelled through the centre line of the cross-section using four noded shell elements with reduced integration (S4R) using FEA package *ABAQUS*. The boundary condition on the FE model was specified on the corresponding centroid nodal point of multipoint constraint by restraining the necessary displacement/rotation components. The probable buckling modes of column are obtained by linear perturbation analysis on the perfect geometry. Subsequent to this, nonlinear analysis was performed on the same model after applying imperfection to obtain the ultimate load. The imperfection profile along the length of the specimen with a maximum value of 1/1000 times length of the specimen is adopted in the analysis. Effect of membrane and flexural residual stress was neglected because of its small value (less than 3% and 7% of proof stress) reported by Schafer and Peköz [9]. Figure 3 shows a typical elastic buckling mode of lipped channel section obtained from FEA.

The results of ultimate load as obtained from FEA and the test results collected the literature is presented in Table 2. These results validated the adequacy of FEA to generate data on the ultimate strength. The FEA model is then used to generate additional data to come up with the relevant parameter responsible for the post-buckling strength reserve observed in FTB.

**Fig. 3** Elastic buckling mode

**Table 2** Comparison of FEA results with test results

| References | Specimen | $P_y$(kN) | $\lambda_e$ | $P_u$(kN) | | $P_{\text{u-test}}/P_{\text{u-FEA}}$ |
|---|---|---|---|---|---|---|
| | | | | Test | FEA | |
| Weng [10] | RFC14-1 | 29.40 | 0.56 | 112.54 | 115.81 | 0.97 |
| | RFC14-2 | 29.40 | 1.06 | 72.95 | 80.98 | 0.90 |
| | PBC13 | 22.90 | 0.74 | 104.53 | 94.37 | 1.11 |
| Young and Ellobody [11] | L36F0280 | 153.45 | 1.42 | 100.22 | 107.84 | 0.93 |
| Young [12] | P1.9L250 | 133.57 | 0.95 | 57.71 | 60.78 | 0.95 |

## *4.1 Details of Specimens*

To evaluate the behaviour of CFS compression member undergoing FTB, lipped channels (Fig. 4a) with web depth to flange width ratios ($h/b$) of 0.5, 1.0 and lipped angles (Fig. 4b) with flange width-to-thickness ratios ($b/t$) of 20, 40, and 39 were modelled. The cross-section dimensions and the ratio of major axis-to-minor axis second moment of ($\beta$) of all the specimens used in the study are given in Table 3.

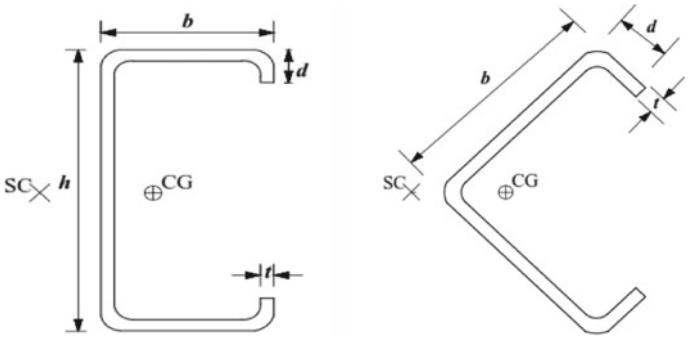


(a) Lipped channel (L) (b) Lipped angle (A)

**Fig. 4** Cross-section geometry of specimens

**Table 3** Details of the specimens

| Specimen | $h$ (mm) | $b$ (mm) | $d$ (mm) | $t$ (mm) | $B = \frac{I_{11}}{I_{22}}$ |
|---|---|---|---|---|---|
| *L*1 | 60 | 60 | 20 | 1.5 | 1.17 |
| *L*2 | 30 | 60 | 10 | 1.5 | 0.39 |
| *A*1 | 50 | 50 | 10 | 2.5 | 3.44 |
| *A*2 | 60 | 60 | 12 | 1.5 | 3.35 |
| *A*3 | 70 | 70 | 15 | 1.8 | 3.75 |

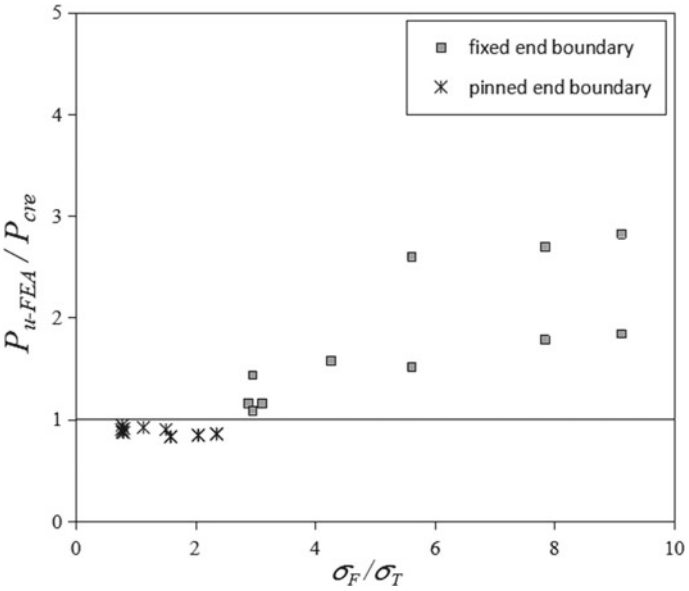


**Fig. 5** Post-buckling behaviour with respect to $\sigma_F/\sigma_T$ ratio

### *4.2 Representation of Torsional Flexibility*

Since the torsional deformation in the FTB is responsible for post-buckling strength, the specimens with different possible combinations of flexural buckling stress, $\sigma_F$, and torsional buckling stress, $\sigma_T$, are simulated in FEA. As the post-buckling strength will be present in FTB when deformation in torsional mode dominates that in flexural mode, the value of $\sigma_F/\sigma_T$ is expected to be higher for such members. The post-buckling behaviour evaluated based on the variation of $P_{\text{u-FEA}}/P_{cre}$ with respect to $\sigma_F/\sigma_T$ is given in Fig. 5. The observations based on Fig. 5 show that specimens with fixed boundary condition for flexure and warping have higher value of $\sigma_F/\sigma_T$ than the columns pinned for flexure and fixed for warping.

## 5 Summary and Conclusions

The current design rules (i) underestimate the failure load of fixed-ended columns with moderate-to-large slenderness ($\lambda_e > 1.5$) and (ii) predict the strength reasonable well for pin-ended columns for all ranges of $\lambda_e$. The equation proposed by Dinis et al. [4] predicts the strength of fixed-ended compression members reasonably well, but overestimates the strength of pin-ended compression members. The representation of torsional flexibility of the member through ratio of second moment of areas ($I_{11}/I_{22}$) may be reasons for inadequacy of this modification for different boundary conditions.

An alternative parameter in terms of ratio of torsional buckling stress to flexural buckling stress ($\sigma_F/\sigma_T$) is proposed.

## References


1. ABAQUS [computer software]. ABAQUS analysis User's manual, Version 6.8, Providence, RI, Dassault Systemes Simulia
2. Australian/New Zealand Standard (AS/NZS) (2018) Cold-formed steel structures. AS/NZS 4600:2018, Standards Australia, Sydney
3. Dat DT, Peköz T (1980) The strength of cold-formed steel columns. Center for Cold-Formed Steel Structures Library 110
4. Dinis PB, Camotim D, Alexandre L, Andre DM (2019) On the direct strength method design of columns against global failures. Thin-Walled Struct 139:242–270
5. Gunalan S, Mahendran M (2013) Improved design rules for fixed ended cold-formed steel columns subject to flexural–torsional buckling. Thin-Walled Struct 73:1–17
6. NAS (2016) North American Specification (NAS) for the design of cold-formed steel structural members (AISI-S100-16), Washington DC
7. Popovic D, Hancock GJ, Rasmussen KJR (1999) Axial compression tests of cold-formed angles. J Struct Eng 125(5):515–523
8. Rasmussen KJR, Hancock GJ (1993) The flexural behaviour of fixed-ended channel section columns. Thin-Walled Struct 17:45–63
9. Schafer BW, Pekoz T (1998) Computational modeling of cold-formed steel: characterizing geometric imperfections and residual stresses. J Constr Steel Res 47:193–210
10. Weng CC, Peköz T (1988) Compression tests of cold-formed steel columns. Int Special Conf Cold-Formed Steel Struct
11. Young B, Ellobody E (2005) Buckling analysis of cold-formed steel lipped angle columns. J Struct Eng 131(10):1570–1579
12. Young B (2005) Experimental investigation of cold-formed steel lipped angle concentrically loaded compression members. J Struct Eng 131(9):1390–1396

# Structural Behaviour of Cold-Formed Steel Built-Up Beams


**V. Guru Prathap Reddy, Sivaganesh Selvaraj, and Mahendrakumar Madhavan**

**Abstract** Cold-Formed Steel (CFS) built-up beams are used widely in the construction industry. In the current study, an experimental investigation of simply supported built-up beams with intermediate web stiffeners was carried out under both three-point and four-point bending. The built-up sections were assembled from press-braked sigma-shaped open sections connected back-to-back and front-to-front by spot welding at flanges to form I-sections and hollow tubular sections respectively. A total of 30 specimens comprising of both I and hollow sections for various beam lengths and intermediate connection spacing were tested. The observed failure modes and the obtained moment capacities from experiments are presented along with a comparison of moment capacities predicted using the North American Specification's Direct Strength Method (DSM). The findings indicate that the AISI's DSM method of moment calculations was found to be conservative for few specimens and unconservative for the majority of the test specimens.

**Keywords** Cold-formed steel · Built-up sections · Experimental investigation · Design method · Ultimate moment capacity

V. Guru Prathap Reddy
Department of Civil Engineering, National Institute of Technology Warangal, Hyderabad, Telangana, India

S. Selvaraj
Department of Civil and Environmental Engineering, The Hong Kong Polytechnic University, Hong Kong, China
e-mail: ce13p1009@iith.ac.in

M. Madhavan (✉)
Department of Civil Engineering, Indian Institute of Technology Hyderabad, Hyderabad, Telangana, India
e-mail: mkm@iith.ac.in



M. Madhavan et al. (eds.), *Proceedings of the Indian Structural Steel Conference 2020 (Vol. 1)*, Lecture Notes in Civil Engineering 318,
https://doi.org/10.1007/978-981-19-9390-9_26

## 1 Introduction

Cold-formed steel sections are commonly used as structural members in the construction industries. The most typical CFS structural members are un-symmetric or point- symmetric, such unsymmetrical open sections are prone to fail in lateral torsional buckling mode. This is due to the fact that their global slenderness is high due to the length requirement. This problem can be defeated by manufacturing a double-symmetric built-up open or closed CFS structural member by connecting two individual CFS sections. As per author's knowledge, these built-up CFS structural members are being used in the construction industries since last two decades. However, the current design specification by American Iron and Steel Institute (AISI) [1] does not have any specific design provisions for CFS built-members. Therefore, the present study focuses on providing preliminary suggestions for the design of CFS built-up beams by conducting an experimental investigation on the cold-formed steel built-up beams. A series of simply supported beams with different lengths were tested three-point bending and four-point bending. The ultimate moment capacities and corresponding failure modes were presented. The appropriateness of the current AISI [1] design provision was evaluated with the experimental results. In addition, finite-element models for the built-up sections were developed using an ANSYS and validated for the future parametric studies.

## 2 Test Specimens and Experimental Test Setup

A total of 30 specimens comprised of both built-up open specimens and built-up closed specimens were tested, with the dimensions given in Fig. 1. The intermittent spacing has been incorporated as one parameter in the present study. The intermittent spacing was varied based on the length of the member as L/4, L/6, L/10, L/15, and L/20. The built-up specimens in this study were assembled using two identical CFS sigma section with web stiffeners by intermittent spot welding. The built-up open specimens (I-shaped) were connected back-to-back at the flange-web joints, whereas the built-up closed specimens were connected face to face at the ends of the flanges as shown in Fig. 1. However, it should be noted that the sigma sections used in both the built-up sections are same. The test specimens were labelled according to the length and interconnection spacings used. For example, the specimen ID I-1240-L/4 indicates that the test specimens are built-up I section, length of the specimen in 1240, and the spacing between the intermittent spot welding is equal to L.

In both the built-up open and closed specimens the out to out length of the specimens is varied, as 1240 mm, 1500 mm, and 2060 mm. The 1240 mm and 1500 mm length specimens were tested under three-point bending whilst the 2060 mm specimens are tested under four-point bending. The material properties including initial Young's modulus ($E$), yield stress, ultimate stress, and the elongation at fracture have been obtained from the tensile tests. The tensile test coupons were extracted

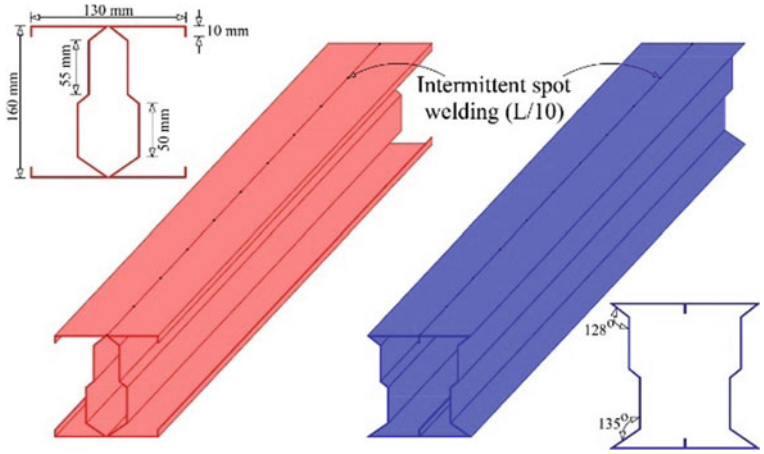


**Fig. 1** View of the cold-formed steel built-up sections

from both flange and web of the CFS sigma section. The measured material properties were used for both design strength calculations and finite-element modelling. The bending tests were conducted in MTS hydro-static actuator capacity 250 kN. The simply supported boundary conditions were simulated by the semi-circular steel pipes at the supports. An overhanging of 40 mm was provided at both the support ends as shown in Fig. 2 to avoid slippage of the test specimen during loading.

The load was distributed to the test specimens by means of steel plates with a width of 100 mm, having a smaller load distribution plate than 100 mm may induce an unwanted local buckling failure in the test specimen. An experimental set up for both the three-point bending and four-point bending is shown in Fig. 2. The displacement transducers were employed in this test setup to measure the vertical deflection at the mid-span. The test was controlled by applying displacement using servo controller actuator.

## 3 Test Results and Discussion

The maximum moments for all the test specimens were calculated from the ultimate loads of the corresponding specimen. The ultimate moments and failure modes corresponding to all the 30 specimens are summarized in Table 2. The failure mode reported is when the specimens reach ultimate load. Most of the specimens were failed in local and distortional buckling modes. However, the test results indicate that there may be an influence of length of the member in the buckling strength though it was considered as a laterally restrained beam.

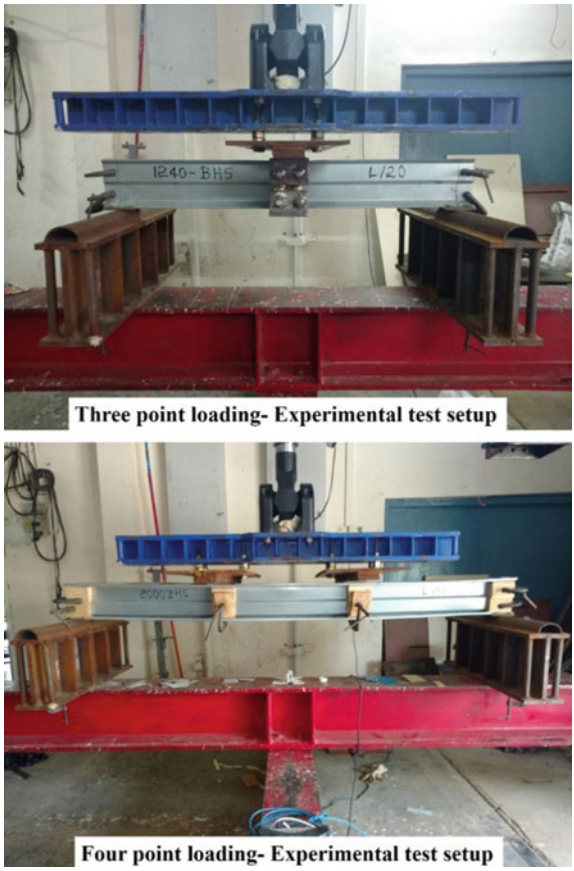


**Fig. 2** Experimental test setup for a different length of the beams

### *3.1 Structural Behaviour of CFS Built-Up Section Beams*

The built-up I and closed specimens with an outer to outer length of 1240 mm were tested under three-point loading. As discussed previously, the intermittent spacing was various in each length as L/4, L/6, L/10, L/15, and L/20. However, no significant influence was found either in failure mode or ultimate load as shown in Fig. 3. The difference in the initial stiffness amongst the tested specimens in both I section and closed section may be due to the initial geometric imperfections. Both I shape and closed built-up sections were failed in local and distortional buckling. Similar failure modes were observed in the other length specimens as well as shown in Figs. 4 and 5. The failure modes observed from the experiments are shown in Figs. 6, 7, and 8. These results were compared with the Direct Strength Method predictions in AISI design specifications [1] to verify the appropriateness of the design equations.

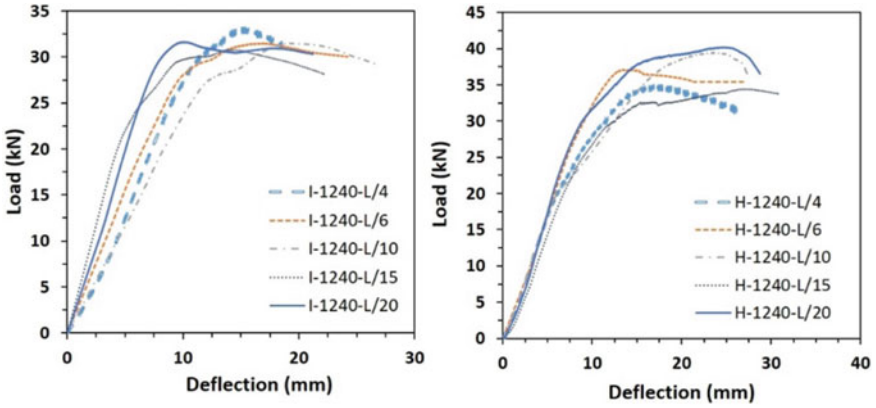


**Fig. 3** Load versus deflection response for 1240 mm length specimens

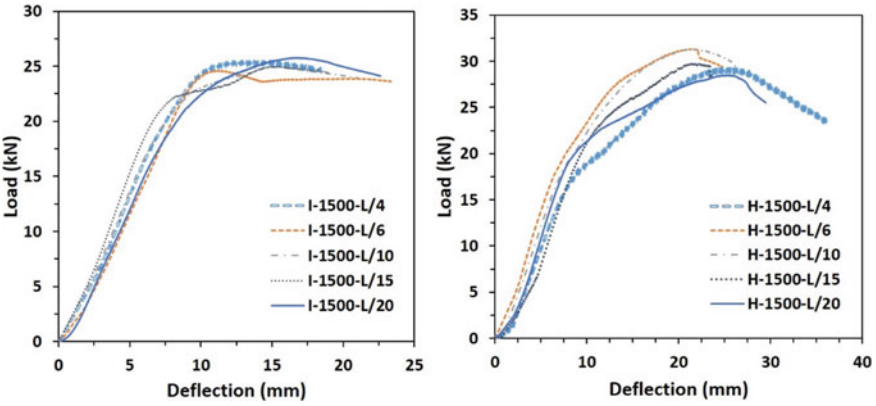


**Fig. 4** Load versus deflection response for 1500 mm length specimens

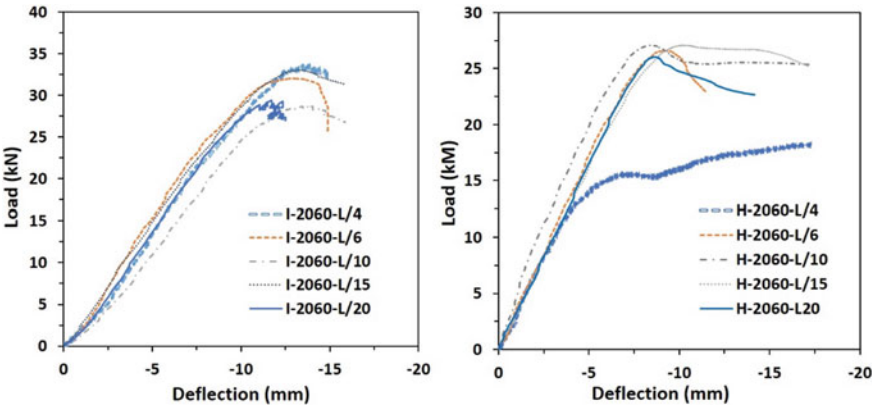


**Fig. 5** Load versus deflection response for 2060 mm length specimens

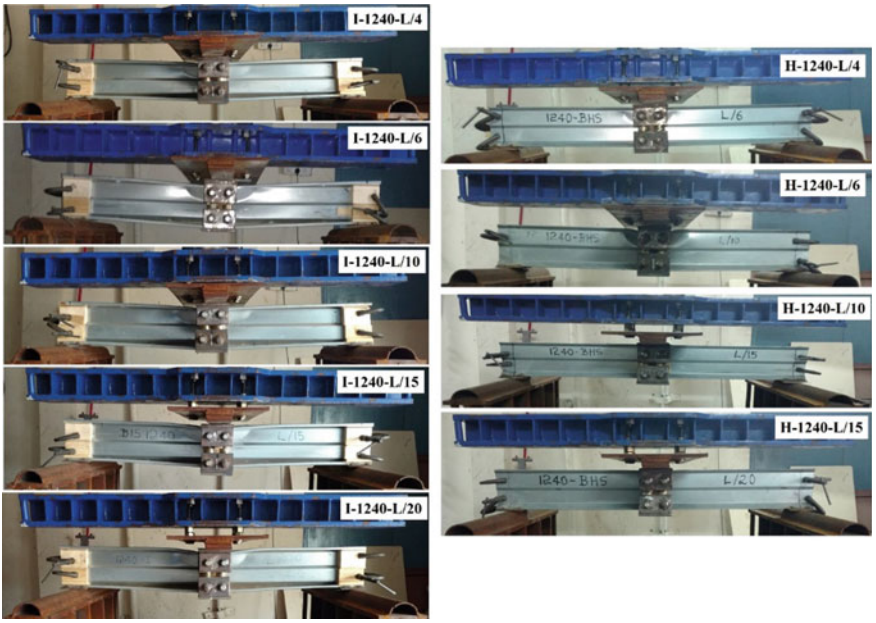


**Fig. 6** Observed failure modes for 1240 mm length built-up beams—experiments

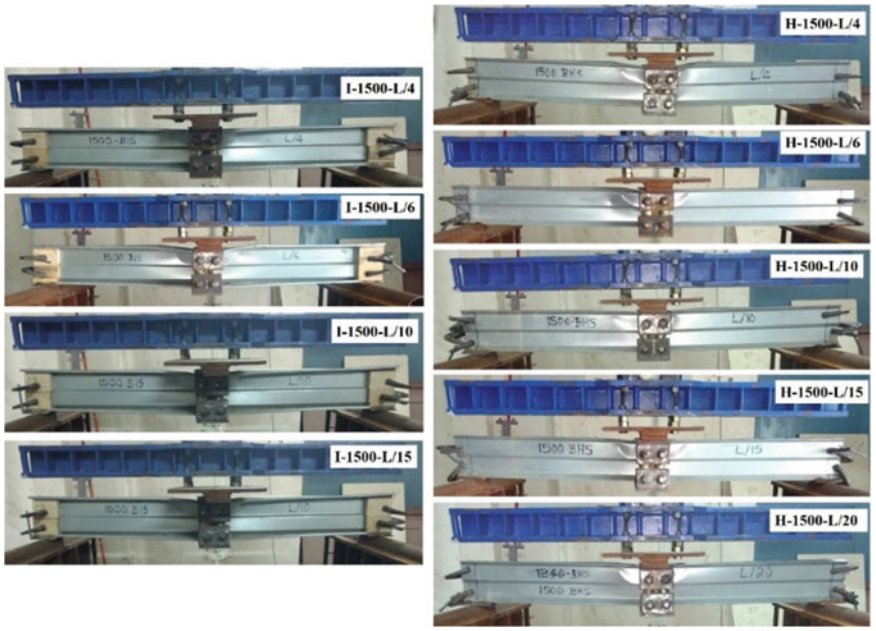


**Fig. 7** Observed failure modes for 1500 mm length built-up beams—experiments

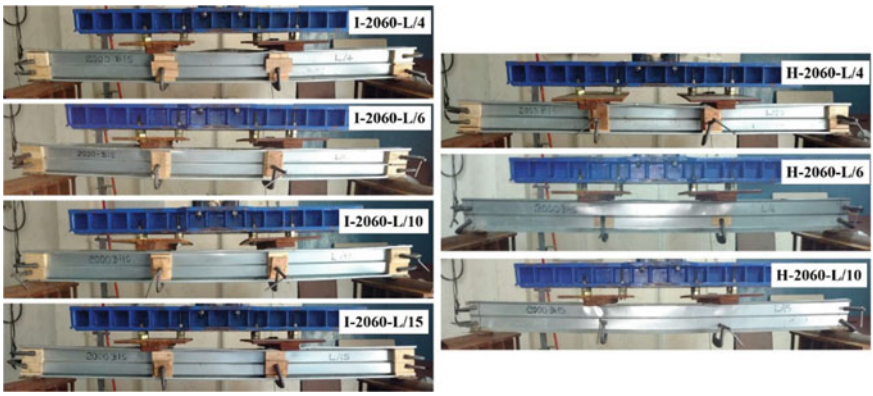


**Fig. 8** Observed failure modes for 2060 mm length built-up beams—experiment

## 4 Design Strength Predictions using DSM Equations

The DSM expressions for beam design from Sect. 1.2.2 of AISI S100-12 [1] are used in the present study. The elastic buckling moments $M_{crl}$ and $M_{crd}$ are obtained from the Thin-wall software. In the present study, the beams are restrained from lateral torsional buckling, therefore the nominal lateral torsional buckling strength is taken as yield moment as per AISI (2012). The current design method for beams that considered inelastic reserve capacities for local and distortional buckling in the AISI design specifications is summarized as follows:

$$M_{\mathrm{DSM}} = \min(M_{ne}, M_{nl}) \tag{1}$$

Lateral-torsional buckling strength($M_{ne}$)

$$M_{ne} = M_{cre} \quad \text{for} \quad M_{cre} \leq 0.56M_y \tag{2}$$

$$M_{ne} = \frac{10}{9}M_y\left(1 - \frac{10M_y}{36M_{cre}}\right)$$
$$\text{for } 2.78\ M_y > M_{cre} > 0.56M_y \tag{3}$$

$$M_{ne} = M_y \quad \text{for } M_{cre} \geq 2.78 \tag{4}$$

Local buckling strength ($M_{nl}$)

$$M_{nl} = M_{ne}\ for\ \lambda_l \leq 0.776 \tag{5}$$

$$M_{nl} = M_y + \left(1 - \frac{1}{C_{yl}^2}\right)(M_p - M_y)$$
$$\text{for } \lambda_l \leq 0.776 \text{ and } M_{ne} \geq M_y \tag{6}$$

$$M_{nl} = \left[1 - 0.15\left(\frac{M_{crl}}{M_y}\right)^{0.4}\right]\left(\frac{M_{crl}}{M_y}\right)^{0.4} M_y$$
$$\text{for } \lambda_l > 0.776 \tag{7}$$

Distortional buckling strength($M_{nd}$)

$$M_{nd} = M_y \quad \text{for} \quad \lambda_d \leq 0.673 \tag{8}$$

$$M_{nd} = M_y + \left(1 - \frac{1}{C_{yd}^2}\right)(M_p - M_y)$$
$$\text{for } \lambda_d \leq 0.673 \text{ and } M_{ne} \geq M_y \tag{9}$$

$$M_{nd} = \left[1 - 0.22\left(\frac{M_{crd}}{M_y}\right)^{0.5}\right]\left(\frac{M_{crd}}{M_y}\right)^{0.5} M_y$$
$$\text{for } \lambda_d > 0.673 \tag{10}$$

where $M_{cre}$ = critical elastic lateral torsional buckling moment; $M_{cre} = S_f f_{cre}$; $M_y$ = member yield moment; $M_y = S_f f_y$; $M_p$ = member plastic moment; $M_p = Z_f f_y$; $S_f$ = gross section modulus (first yield); $Z_f$ = plastic section modulus; $f_y$ = yield stress obtained from tensile coupon tests; $C_{yl} = \sqrt{(0.776/\lambda_l)} \leq 3$; $\lambda_l = \sqrt{(M_{ne}/M_{crl})}$; $M_{crl}$ = critical elastic local buckling moment; $M_{crl} = S_f f_{crl}$. $C_{yd} = \sqrt{(0.673/\lambda_d)} \leq 3$; $\lambda_d = \sqrt{(M_{ne}/M_{crd})}$; $M_{crd}$ = critical elastic distortional buckling moment; $M_{crd} = S_f f_{crd}$. The moment capacities of the cold-formed steel built-up section beams obtained from the DSM method are compared with the ultimate moment values obtained from experimental values in Table. 1. The comparison results indicate that the current DSM method in AISI [1] is more or less conservative for the built-up open sections and unconservative for the built-up hollow sections. Such unconservative predictions may be due to the fact that the behaviour of the hollow sections in the finite strip analysis is different from the actual specimen. The finite strip analysis assumes that the connection between the open sections is continuous along the length of the member, but in reality it is not. Further, the reliability study indicates that the current DSM design method is not appropriate for the CFS built-up beams and it requires comprehensive investigation and modification. The reliability analysis method used in this present study is explained in [2].

**Table 1** Experimental results and comparison with the DSM predicted strength

| Specimen ID | Length | Intermittent spot weld spacing (mm) | Max. Load (kN) | $M_{EXP}$ (kNm) | $M_{DSM}$ (kNm) | $M_{EXP}/M_{DSM}$ |
|---|---|---|---|---|---|---|
| I-1240-L/4 | 1240 | 310 | 32.89 | 9.70 | 9.68 | 1.00 |
| I-1240-L/6 | 1240 | 206 | 31.47 | 9.28 | 9.68 | 0.96 |
| I-1240-L/10 | 1240 | 124 | 31.49 | 9.29 | 9.68 | 0.96 |
| I-1240-L/15 | 1240 | 82 | 30.37 | 8.96 | 9.68 | 0.93 |
| I-1240-L/20 | 1240 | 62 | 31.61 | 9.32 | 9.68 | 0.96 |
| H-1240-L/4 | 1240 | 310 | 34.7 | 10.24 | 12.27 | 0.83 |
| H-1240-L/6 | 1240 | 206 | 37.16 | 10.96 | 12.27 | 0.89 |
| H-1240-L/10 | 1240 | 124 | 39.52 | 11.66 | 12.27 | 0.95 |
| H-1240-L/15 | 1240 | 82 | 34.43 | 10.16 | 12.27 | 0.83 |
| H-1240-L/20 | 1240 | 62 | 40.25 | 11.87 | 12.27 | 0.97 |
| I-1500-L/4 | 1500 | 310 | 25.3 | 8.85 | 9.68 | 0.91 |
| I-1500-L/6 | 1500 | 206 | 24.56 | 8.59 | 9.68 | 0.89 |
| I-1500-L/10 | 1500 | 124 | 24.92 | 8.72 | 9.68 | 0.90 |
| I-1500-L/15 | 1500 | 82 | 24.95 | 8.74 | 9.68 | 0.90 |
| I-1500-L/20 | 1500 | 62 | 22.61 | 7.91 | 9.68 | 0.82 |
| H-1500-L/4 | 1500 | 310 | 29.05 | 10.17 | 12.27 | 0.83 |
| H-1500-L/6 | 1500 | 206 | 31.37 | 10.98 | 12.27 | 0.89 |
| H-1500-L/10 | 1500 | 124 | 31.37 | 10.98 | 12.27 | 0.89 |
| H-1500-L/15 | 1500 | 82 | 30 | 10.5 | 12.27 | 0.86 |
| H-1500-L/20 | 1500 | 62 | 28.49 | 9.97 | 12.27 | 0.81 |
| I-2060-L/4 | 2060 | 310 | 33.5 | 11.56 | 9.68 | 1.19 |
| I-2060-L/6 | 2060 | 206 | 32.06 | 11.06 | 9.68 | 1.14 |
| I-2060-L/10 | 2060 | 124 | 28.72 | 9.91 | 9.68 | 1.02 |
| I-2060-L/15 | 2060 | 82 | 33.08 | 11.41 | 9.68 | 1.18 |
| I-2060-L/20 | 2060 | 62 | 29.36 | 10.13 | 9.68 | 1.05 |
| H-2060-L/4 | 2060 | 310 | 18.3 | 6.31 | 12.27 | 0.51 |
| H-2060-L/6 | 2060 | 206 | 26.59 | 9.17 | 12.27 | 0.75 |
| H-2060-L/10 | 2060 | 124 | 27.07 | 9.34 | 12.27 | 0.76 |
| H-2060-L/15 | 2060 | 82 | 27.08 | 9.34 | 12.27 | 0.76 |
| H-2060-L/20 | 2060 | 62 | 26.09 | 9.00 | 12.27 | 0.73 |

## 5 Conclusions

An experimental investigation of CFS built-up I-shaped and hollow-shaped beams subjected to flexure is presented. The built-up beams were fabricated from two identical sigma sections. The assembling of the built-up beams was made by intermittent

spot welding. The results obtained from the experiments were compared with the design strength predicted using the current AISI (2012) [1]. The comparison shows that the current design method is conservative only for the built-up open sections and unconservative for built-up hollow sections. In addition, the reliability study carried out also indicates that the current method cannot be used for designing the CFS built-up hollow or closed cross-section beams. Such unconservative predictions may be due to the fact that the behaviour of the hollow sections in the finite strip analysis is different from the actual specimen. The finite strip analysis assumes that the connection between the open sections continues along the length of the member, but in reality it is not. Therefore, further investigation is required towards finding the appropriate way of modelling the CFS cross-sections in finite strip analysis.

## References

1. AISI (American Iron and Steel Institute) (2012) North American specification for the design of cold-formed steel structural members. AISI-S100-12, Washington, DC
2. Selvaraj S, Madhavan M (2018) Studies on cold-formed steel stud panels with gypsum sheathing subjected to out-of-plane bending. J Struct Eng
3. Wang L, Young B (2015a) Behavior of cold-formed steel built-up sections with intermediate stiffeners under bending. I: tests and numerical validation. J Struct Eng 142(3):04015150
4. Schafer BW, Peköz T (1998) Computational modeling of cold-formed steel: characterizing geometric imperfections and residual stresses. J Const Steel Res 47(3):193–210
5. Selvaraj S, Madhavan M (2018) Geometric imperfection measurements and validations on cold-formed steel channels using 3D non-contact laser scanner. J Struct Eng 144(3):04018010
6. Wang L, Young B (2015b) Behavior of cold-formed steel built-up sections with intermediate stiffeners under bending. II: parametric study and design. J Struct Eng 142(3):04015151
7. Yao Z, Rasmussen KJ (2016) Perforated cold-formed steel members in compression. I: parametric studies. J Struct Eng 143(5):04016226
8. Selvaraj S, Madhavan M (2019) Structural design of cold-formed steel face-to-face connected built-up beams using direct strength method. J Constr Steel Res. https://doi.org/10.1016/j.jcsr.2019.05.053
9. Selvaraj S, Madhavan M (2021) Design of cold-formed steel built-up columns subjected to local-global interactive buckling using direct strength method. Thin-Walled Struct. https://doi.org/10.1016/j.tws.2020.107305
10. Selvaraj S, Madhavan M (2021) Design of cold-formed steel back-to-back connected built-up beams. J Constr Steel Res. https://doi.org/10.1016/j.jcsr.2021.106623
11. Selvaraj S, Madhavan M (2021) Direct strength approach for local buckling of cold-formed steel built-up beams with slender unstiffened flange elements, practice periodical on structural design and construction (ASCE). Technical Note. https://doi.org/10.1061/(ASCE)SC.1943-5576.0000599
12. Selvaraj S, Madhavan M (2021) Design of cold-formed steel built-up closed section columns using direct strength method. Thin-Walled Struct

# Global Buckling Behavior of Intermittently Fastened Cold-Formed Steel Built-Up Columns


**Akshay Mangal Mahar and S. Arul Jayachandran**

**Abstract** In the load-bearing wall frame system, built-up sections are utilized over single section to enhance the performance of Cold-Formed Steel (CFS) structural systems. Built-up CFS sections can be formed in different shapes by the use of intermittently connected fasteners in the longitudinal direction. The spacings of these intermittent fasteners can alter the global buckling behavior of built-up CFS columns, and hence, they are investigated in the present study. The change of global buckling load from a single section CFS column to a built-up section CFS column is studied with different fastener spacing. In this chapter, a numerical methodology using a compound spline finite strip method is developed to compute the elastic critical buckling load of CFS built-up columns. The results of buckling analysis are compared with FE-based software ABAQUS and results are found to be in good agreement. Parametric studies on back-to-back connected I section with different web to flange ratios have been carried out, and it is found that global buckling behavior of open built-up sections will move toward fully composite section buckling behavior with the reduction in the fastener spacing.

**Keywords** Global buckling · Cold-formed steel column · Compound spline finite strip method · Finite element analysis

## 1 Introduction

In the load-bearing wall frame system, cold-formed steel (CFS) columns are subjected to high in-plane loading. These members should have sufficient axial and flexural rigidity, and built-up CFS sections are most suitable for such conditions.

A. M. Mahar (✉) · S. Arul Jayachandran
Thin-Walled Steel Structure Research Group, Department of Civil Engineering, IIT Madras, Chennai, India
e-mail: akshaymmahar@gmail.com

S. Arul Jayachandran
e-mail: aruls@iitm.ac.in



M. Madhavan et al. (eds.), *Proceedings of the Indian Structural Steel Conference 2020 (Vol. 1)*, Lecture Notes in Civil Engineering 318,
https://doi.org/10.1007/978-981-19-9390-9_27

These compound sections can be formed by connecting two or more single CFS sections by fasteners or welds. The presence of fasteners in the longitudinal direction will affect the buckling behavior of built-up members, especially in global buckling mode. In the design standards, the equations for computing the ultimate global buckling strength of CFS columns have been verified with different experimental works reported in literature [6, 8]. To compute the ultimate global buckling strength for built-up CFS columns, it becomes important to compute the critical global buckling stress accurately. The focus of this study is to comprehend the composite action generated by the discrete fastener arrangement on the critical global buckling stress of built-up columns. In the design provisions, AISI: S100 [4] provides modified slenderness ratios to accommodate the effect of discrete fastener on the global buckling of built-up sections (Eq. 1).

$$\left(\frac{\mathrm{KL}}{r}\right)_{ms} = \sqrt{\left(\mathrm{KL}/r\right)_o^2 + \left(s/r_{yc}\right)^2} \tag{1}$$

For which, $\left(s/r_{yc}\right) \leq 0.5 \times \left(KL/r\right)_o$

where $s$ is spacing between fasteners, $r_{yc}$ is the minimum radius of gyration of a single section, $r_o$ is the minimum radius of gyration of the compound section, and KL is the effective length of the member.

The above recommendation is experimentally evaluated by Stone and LaBoube [12] on back-to-back connected channel sections. It is found that when the thickness is high (more than 1 mm), a modified slenderness ratio with minimum screw spacing does not affect the ultimate capacity. In the context of plug welds, Whittle and Ramseyer [14] did an experimental study on closed built-up columns made by face-to-face connected lipped plain channels. The dimension of specimens is selected such as the sections are locally and distortionally stable and flexural buckling is the natural mode of buckling. It is found that for plug welded built-up sections, a modified slenderness ratio will predict conservative results. Reyes and Guzmán [10] studied the effect of weld spacing, fixed, and flexible support conditions on the ultimate strength of box CFS columns. It is found that the ultimate capacity of the box CFS column does not vary much with weld spacing and rigid or flexible end condition. Fratamico et al. [7] studied the composite action generated by screw fasteners on the global buckling behavior of built-up columns using a semi-analytical screw fastener element. Abbasi et al. [2] developed a compound finite strip-based numerical formulation for buckling stress computation of CFS built-up columns. The effect of fastener spacing, in context of beams is reported by Wang and Young [13], where open and closed shape built-up sections are studied.

In the literature, the effect of the modified slenderness ratio on the ultimate capacity of globally buckling columns has been studied by experimental work. The composite action generated by different fastener spacing needs to be studied to get the optimum number of fasteners for forming a fully composite action. In this study, a spline finite strip-based numerical formulation is formed to incorporate the effect of

fasteners on the buckling behavior of CFS columns. By applying specific constraints on the numerical model, pure global buckling mode can be captured. The details of numerical formulations are given in the next sections.

## 2 Numerical Framework

The theory of classical finite strip method and spline finite method for single section CFS members are well documented in the literature [5], Lau and Hancock [9]. However, in this study, an extension to the pre-existed spline finite framework is presented for the buckling analysis of built-up CFS sections. The Direct Strength Method (DSM), which is a simple non-iterative design procedure [11], uses the critical buckling stress to compute the ultimate strength of the CFS member. In this chapter, a numerical framework is presented to capture the effect of discrete fasteners on the stability behavior of built-up CFS sections. A compound methodology is adopted to incorporate fasteners as three-dimensional beam elements into the SFSM-based numerical model of thin plates. In this chapter, this numerical framework will be referred to as the Compound Spline Finite Strip Method (CSFSM). To avoid the occurrence of distortional buckling and a consequential global-distortional buckling interaction at any length, a constraint model is also developed and presented in this study. The stiffness and stability matrices can be derived as per the conventional spline finite strip method [9].

### *2.1 Compound Spline Finite Strip Method*

For a typical plate strip, the generalized displacement field at the mid surface in local coordinates **d**(x, y) is given by the displacement functions at its nodal lines. For the application of specific boundary conditions at ends, the local amendment property of splines is used. In this study, cubic spline functions (B3) are used in the longitudinal direction to get continuous curvature. For membrane and flexural deformations, linear and Hermitian cubic interpolation functions are adopted in the transverse direction. A generalized displacement field at mid surface is as follows,

$$\mathbf{d}(\mathrm{x}, \mathrm{y}) = \{u, v, w\}^{\mathrm{T}} = [N_x][\phi_y]\{\delta\} \tag{2}$$

where, $[N_x]$ is the matrix of transverse shape functions, $[\phi_y]$ is the matrix of spline functions in longitudinal direction, and $\{\delta\} = \{\boldsymbol{u}_\mathbf{i}, \boldsymbol{v}_\mathbf{i}, \boldsymbol{w}_\mathbf{i}, \boldsymbol{\theta}_\mathbf{i}, \boldsymbol{u}_\mathbf{j}, \boldsymbol{v}_\mathbf{j}, \boldsymbol{w}_\mathbf{j}, \boldsymbol{\theta}_\mathbf{j}\}^{\mathrm{T}}$ is displacement vector of strip (Figs. 1 and 2).

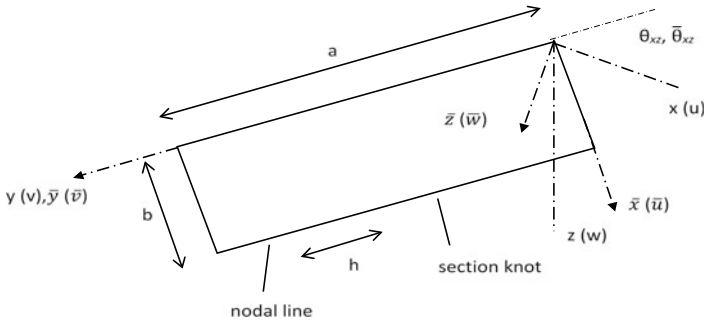


**Fig. 1** Spline finite strip with the coordinate axis

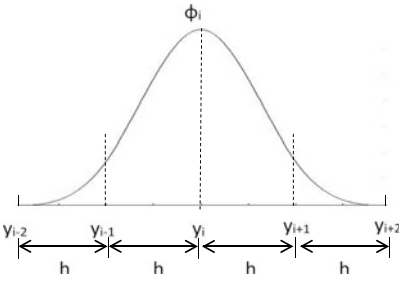


**Fig. 2** Local B3 cubic spline function

### 2.1.1 Fastener Element

To form the tangent stiffness matrix of the compound section, the strain energy of the fasteners present in the system needs to be added in the total strain energy of the folded plate system. The local stiffness matrix of a three-dimensional beam element needs to be transformed about the plate's displacement field so that the additional strain energy of the fastener element can be computed. The displacement field of a two-node beam element with six degrees of freedom at each node can be expressed as,

$$\left\{\delta_b^L\right\} = \left\{u_b^i, v_b^i, w_b^i, \theta_{bx}^i, \theta_{by}^i, \theta_{bz}^i, u_b^j, v_b^j, w_b^j, \theta_{bx}^j, \theta_{by}^j, \theta_{bz}^j\right\}^{\mathrm{T}} \tag{3}$$

The symmetric stiffness matrix of a beam element in the local coordinate system can be written as (Fig. 3),

$$\left[K_b^L\right] = \begin{bmatrix} [K_{ii}] & [K_{ij}] \\ [K_{ji}] & [K_{jj}] \end{bmatrix} \tag{4}$$

$$K_{1,1} = \frac{\mathrm{EA}}{L};\ K_{1,7} = \frac{-\mathrm{EA}}{L};\ K_{2,2} = \frac{12\mathrm{EI}_z}{L^3};\ K_{2,6} = \frac{6\mathrm{EI}_z}{L^2};\ K_{2,8}$$

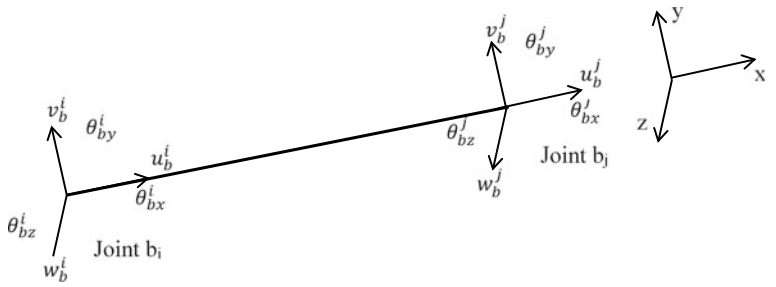


**Fig. 3** Beam element in the local coordinate axis

$$= \frac{-12EI_z}{L^3};\ K_{2,12} = \frac{6EI_z}{L^2}$$

$$K_{3,3} = \frac{12EI_y}{L^3};\ K_{3,5} = \frac{-6EI_y}{L^2};\ K_{3,9} = \frac{-12EI_y}{L^3};\ K_{3,11} = \frac{-6EI_y}{L^2};\ K_{4,4} = \frac{GJ}{L};$$

$$K_{4,10} = -\frac{GJ}{L};\ K_{5,5} = \frac{4EI_y}{L};\ K_{5,9} = \frac{-6EI_y}{L^2};\ K_{5,11} = \frac{2EI_y}{L};\ K_{6,6} = \frac{4EI_z}{L};$$

$$K_{7,7} = \frac{EA}{L};\ K_{8,8} = \frac{12EI_z}{L^3};\ K_{8,12} = \frac{-6EI_z}{L^2};\ K_{9,9} = \frac{12EI_y}{L^3};\ K_{9,11} = \frac{6EI_y}{L^2};$$

$$K_{10,10} = \frac{GJ}{L};\ K_{11,11} = \frac{4EI_y}{L};\ K_{12,12} = \frac{4EI_z}{L}$$

### 2.1.2 Compound Framework

The beam stiffness matrix is added to the global stiffness matrix by making the appropriate transformation of axes and interpolating the beam displacement vector to the plate's displacement vector with the relationship given below (Fig. 4).

$$\Pi_b = \frac{1}{2}\left\{\delta_b^G\right\}^T\left[K_b^G\right]\left\{\delta_b^G\right\} \tag{5}$$

$$\begin{Bmatrix} \{\delta_b^i\} \\ \{\delta_b^j\} \end{Bmatrix} = \begin{bmatrix} [Tr_{b_iq}] & 0 \\ 0 & [Tr_{b_jr}] \end{bmatrix} \begin{Bmatrix} \{\delta_q\} \\ \{\delta_r\} \end{Bmatrix} \tag{6}$$

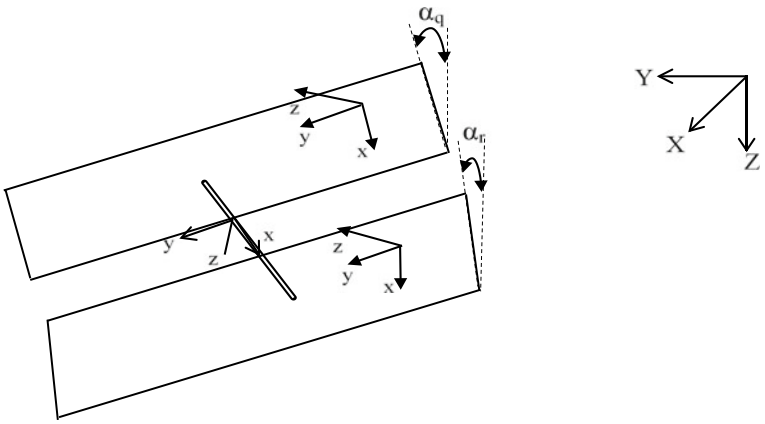


**Fig. 4** Compound section connected by beam element and strip orientations in global coordinate axes

$$[Tr_{ii}] = \begin{bmatrix} N_{ui}\phi_{ui} & & & & N_{uj}\phi_{uj} & & & \\ & N_{vi}\phi_{vi} & & & & N_{vj}\phi_{vj} & & \\ & & N_{wi}\phi_{wi} & N_{\theta i}\phi_{\theta i} & & & N_{wj}\phi_{wj} & N_{\theta j}\phi_{\theta j} \\ & & N_{wi}\phi'_{wi} & N_{\theta i}\phi'_{\theta i} & & & N_{wj}\phi'_{wj} & N_{\theta j}\phi'_{\theta j} \\ & & N'_{wi}\phi_{wi} & N'_{\theta i}\phi_{\theta i} & & & N'_{wj}\phi_{wj} & N'_{\theta j}\phi_{\theta j} \\ 0 & & & & 0 & & & \end{bmatrix} \quad (7)$$

## 2.2 Constrained Model

In this study, a constrained model is developed in the CSFSM to compute the pure elastic critical global buckling stress of the built-up section. By constraining the transverse displacements of folded corner lines, the distortional deformations can be eliminated. To allow only the minor axis deformations, lateral displacements of the corner nodes will be kept free. This model will be able to restrict distortional buckling mode efficiently, but local buckling cannot be eliminated. To avoid the occurrence of local buckling in the deformed configuration, the width to thickness ratio of stiffened and un-stiffened elements can be selected such as critical local buckling stress will be more than the yield stress of the material. In this study, all the sections are selected such as the local buckling stress will be higher than the global buckling stress at any length. The constrained model is as shown in Fig. 5.

**Fig. 5** Constrained model adopted for allowing only minor axis buckling mode

## 3 Numerical Examples

### *3.1 Verification of CSFSM*

A built-up I section formed by two back-to-back connected lipped channel sections subjected to uniform compression is considered in this study (Fig. 6). The buckling analysis results obtained from the current numerical method are compared with finite element-based software ABAQUS [1]. The geometric and material properties of the lipped channel section are presented in Table 1. All the results are obtained for generally adopted boundary conditions, i.e., simply-supported and clamped–clamped ends. The fastener spacing is kept fixed at one-third of the length of the member for both boundary conditions. To obtain symmetrical deformed shape, warping free and warping restrained deformations are imposed to both ends for simply-supported and clamped–clamped boundary conditions, respectively. All the results are plotted in Fig. 7 for different numbers of spline knots.

In the Fig. 7, critical buckling stress obtained by CSFSM is normalized with yield stress, and plotted for different lengths by keeping a fixed fastener spacing. The number of spline knots required for the convergence is found to be almost same for both Simply-Supported (SS) and Clamped–Clamped (CC) boundary conditions. In both the cases, especially for global buckling range, CSFSM results move toward FEA results with increase in numbers of spline knots.

**Table 1** Geometrical and material properties of lipped channel section

| Specimen | h (mm) | b (mm) | d (mm) | t (mm) | E (MPa) | $F_y$ (MPa) | $\nu$ |
|---|---|---|---|---|---|---|---|
| Lipped channel | 90 | 48 | 12 | 1.0 | $2.1 \times 10^5$ | 500 | 0.3 |

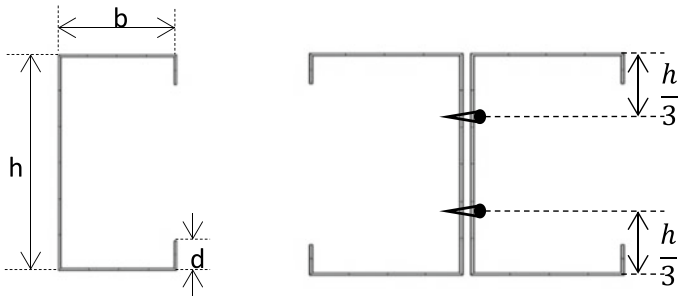


**Fig. 6** A typical single lipped channel and built-up section

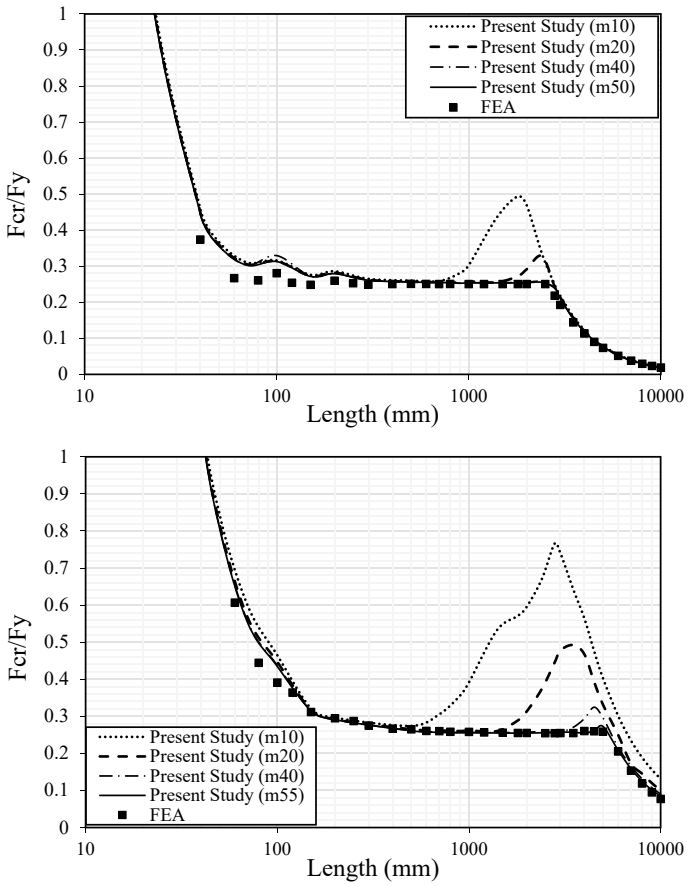


**Fig. 7** Verification and convergence of CSFSM for the built-up section for simply-supported and clamped–clamped boundary conditions

**Table 2** Geometrical and material properties of lipped channel section (in Fig. 8)

| Specimen | h (mm) | b (mm) | d (mm) | t (mm) | E (MPa) | $F_y$ (MPa) | $\nu$ |
|---|---|---|---|---|---|---|---|
| Lipped channel | 80 | 70 | 10 | 2.0 | $2.1 \times 10^5$ | 500 | 0.3 |

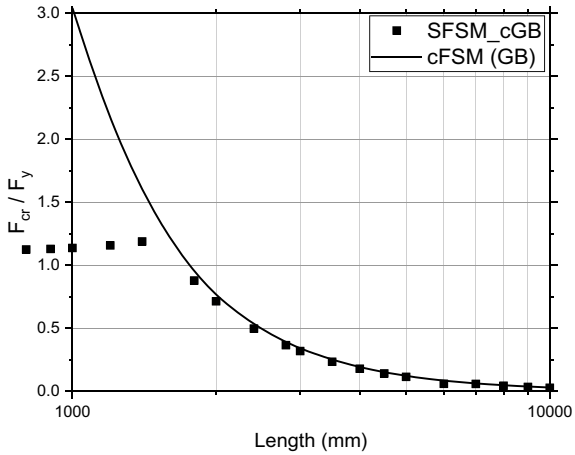


**Fig. 8** Verification of the constrained model for lipped channel section with cFSM

## *3.2 Verification of the Constrained Model*

To verify the results obtained from the constrained model for global buckling mode, constrained finite strip method (cFSM) [3] is used. A single lipped channel section discussed in Table 2 is used for verification. All the results presented in Fig. 8 are for lengths more than 1000 mm with simply-supported boundary condition. From the results, it can be seen that constrained model results match with the cFSM outputs.

## *3.3 Effect of Fastener Spacing*

The presence of discrete fasteners will result in an intermediate-composite curve, which moves toward the fully composite curve in the global buckling region. To understand the stability behavior of built-up sections, different fastener spacing is adopted in this study ($s = L/3$, and $L/5$). All the built-up sections are generated by using two sets of fastener rows at one-third of the web height, as shown in Fig. 9. All the results presented here are of built-up section deforming under minor axis buckling only. By decreasing the fastener spacing, an enhanced composite behavior is obtained and the corresponding buckling stress outputs shift toward the fully composite curve. The properties of the lipped channel section are given in Table 2. The increment in

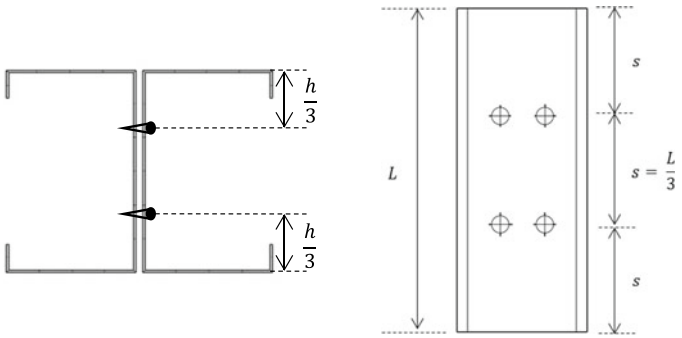


**Fig. 9** Built-up section and plan diagram

**Table 3** Numerical results for different (*h*/*b*) ratio

| *h/b* | Simply-supported | Fastener spacing | Critical Buckling stress (in MPa) | | |
|---|---|---|---|---|---|
| | | | $F_{cr}$ (single) | $F_{cr}$ (BU) | % increment |
| 1.14 ($t = 2$ mm) | Global buckling (@L = 2400 mm) | $s = L/3$ | 249.13 | 345.48 | 38.74 |
| | | $s = L/5$ | | 434 | 75 |
| | Global buckling (@L = 6000 mm) | $s = L/3$ | 30.24 | 56.85 | 88 |
| | | $s = L/5$ | | 71.72 | 137.16 |
| 1.875 ($t = 1$ mm) | Global buckling (@L = 2400 mm) | $s = L/3$ | 120 | 127.65 | 6.37 |
| | | $s = L/5$ | | 128.12 | 6.77 |
| | Global buckling (@L = 6000 mm) | $s = L/3$ | 20.72 | 26 | 25.6 |
| | | $s = L/5$ | | 31.7 | 53 |

critical buckling stress due to the reduction in fastener spacing is presented in Table 3 for different sections.

## 4 Discussion

The presence of a discrete fastener system in the built-up section provides an intermediate-composite action, which depends upon the fastener spacing and their arrangement. The above-discussed CSFSM can incorporate the effect of fastener on the stability behavior of the system. It can be seen from the results presented in the above sections that with a specific fastener spacing, the composite action of the built-up section matches the buckling behavior of a fully composite section. Other fastener spacing results in a buckling behavior, which is in between the single and fully composite section behavior.

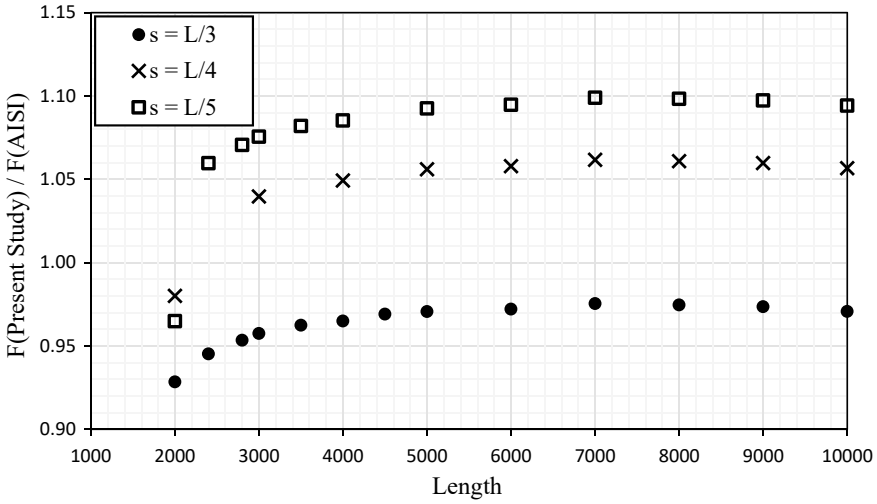


**Fig. 10** Comparison of actual buckling stress and AISI: S100 buckling stress predictions

AISI: S100 predictions can also be presented for the above-discussed sections. The modified slenderness ratio for different fastener spacing is presented in Fig. 10. For minimum suggested fastener spacing, modified slenderness ratio gives unconservative predictions, but for low fastener spacing or spacing for which buckling behavior is near to composite section behavior, modified slenderness ratio gives conservative predictions.

## 5 Conclusions

In this study, a numerical framework based upon compound methodology to incorporate the effect of fastener on buckling behavior of CFS built-up members is presented. The numerical model is verified with ABAQUS outputs, and a sensitivity study is performed for generally adopted boundary conditions. To understand the effect of different fastener spacing, a numerical study is performed with a constrained model to capture only the minor axis buckling mode. It is found that for the built-up I section, the fastener spacing of *L*/5 will provide the buckling behavior similar to a fully composite section buckling behavior. For other higher spacing, buckling behavior of the built-up section will result in an intermediate-composite buckling behavior.

AISI: S100 provides a modified slenderness formulation to incorporate the loss of shear rigidity on the global buckling behavior of CFS built-up columns. The results from the current study are compared with the modified slenderness formulation, and it is found that AISI buckling load prediction for the built-up section is conservative around 10% when fully composite buckling behavior is ensured. In this study, the

versatility of the current numerical formulation is presented, and this framework can be extended to compute the effect of discrete fastener on other buckling modes, i.e., local and distortional buckling modes.

## References

1. ABAQUS [Computer software]. ABAQUS standard user's manual, Version 6.14, Providence, RI, Dassault Systèmes Simulia
2. Abbasi M, Khezri M, Rasmussen KJR, Schafer BW (2018) Elastic buckling analysis of cold-formed steel built-up sections with discrete fasteners using the compound strip method. Thin-Walled Struct 124:58–71
3. Ádány S, Schafer BW (2006) Buckling mode decomposition of single-branched open cross-section members via finite strip method: derivation. Thin-Walled Struct44(5):563–584
4. American Iron and Steel Institute (AISI) S100 (2016) North American specification for the design of cold-formed steel structural members, 2016 edition
5. Cheung YK, Tham LG (1997) The finite strip method (vol 17). CRC press
6. Committee on Specifications for the Design of Cold-Formed Steel Structural Members (1992) Design provisions for cold-formed steel column and beam columns
7. Fratamico DC, Torabian S, Schafer BW (2015) Composite action in global buckling of built-up columns using semi-analytical fastener elements. In: Procedings of the annual stability conference structural stability research Co., Nashville, TN
8. Gunalan S, Mahendran M (2013) Improved design rules for fixed ended cold-formed steel columns subject to flexural–torsional buckling. Thin-Walled Struct73:1–17
9. Lau SCW, Hancock GJ (1986) Buckling of thin flat-walled structures by a spline finite strip method. Thin-Walled Struct 4(4):269–294
10. Reyes W, Guzmán A (2011) Evaluation of the slenderness ratio in built-up cold-formed box sections. J Constr Steel Res 67(6):929–935
11. Schafer BW (2002) Local, distortional, and Euler buckling of thin-walled columns. J Struct Eng 128(3):289–299
12. Stone TA, LaBoube RA (2005) Behavior of cold-formed steel built-up I-sections. Thin-Walled Struct 43(12):1805–1817
13. Wang L, Young B (2018) Behaviour and design of cold-formed steel built-up section beams with different screw arrangements. Thin-Walled Struct 131:16–32
14. Whittle J, Ramseyer C (2009) Buckling capacities of axially loaded, cold-formed, built-up C-channels. Thin-Walled Struct 47(2):190–201

# Investigation on Non-linear Interaction Framework for Zee-Shaped Cold-Formed Steel Beam-Column


**J. Sevugan Rajkannu, Chinmai Goripathi, and S. Arul Jayachandran**

**Abstract** This chapter deals with the ultimate strength and buckling behaviour of cold-formed steel Zee-shaped section under combined axial and bending actions. The numerical model was developed using finite element software ABAQUS. The specimen dimensions are chosen based on the elastic buckling curve from the CUFSM and GBTUL to study the cross-sectional and global buckling behaviour of Zee-shaped section. The numerical models are made using the S4R element, with simply supported end condition. The non-linear analysis including material, geometric non-linearity, and geometric imperfections, is conducted to predict the ultimate strength of the beam-column members. The numerical model was validated with the experimental results from the literature. Based on the validated model, the study is extended to develop axial—Moment (P-M1-M2) strength interaction surface for the selected member. The numerical study is conducted on the Zee-shaped member subjected to major, minor, and bi-axial moment. The effect of stress distribution due to combined load on the ultimate strength is examined, which forms the basis for the new design formulation for beam-column using direct strength method. The numerically generated strength surface was compared with beam-column prediction based on North American standard AISI S100-2016 specification.

**Keywords** Cold-formed steel · Beam-column · Interaction equation · Direct strength method

J. Sevugan Rajkannu (✉) · C. Goripathi · S. Arul Jayachandran
Department of Civil Engineering, IIT Madras, Chennai, India
e-mail: sevuganrajkannu@gmail.com

S. Arul Jayachandran
e-mail: aruls@iitm.ac.in



M. Madhavan et al. (eds.), *Proceedings of the Indian Structural Steel Conference 2020 (Vol. 1)*, Lecture Notes in Civil Engineering 318,
https://doi.org/10.1007/978-981-19-9390-9_28

## 1 Introduction

The Zee-shaped cold-formed steel sections are predominantly used as purlins in all the industrial buildings, serving as flexure member. Due to point symmetry nature of the Zee cross-section, purlin members are subjected to bi-axial bending even in case of gravity loading. Though the predominant purlins are under the flexure action, the end purlins in case of the Pre-Engineering Building (PEB), as shown in Fig. 1, are subjected to both axial force and bending. The axial force in the purlins is induced due to the wind load of the gable side of the building. The wind bracing is provided in the second bay of the main-frame, the force transferred from purlin to wind bracing. Thus the behaviour of Zee-section member can be considered as a beam-column. The purlin members are made by shaping thin sheets of steel into a Zee section. The member undergoes different type of buckling such as local buckling, distortional buckling and global buckling.

The Zee section can be used in other structural systems also. These sections can be used as a wall stud material which may also be subjected to predominantly axial compression due to gravity loading and bending due to wind load. Because of the unique geometry, Z section is classified as point symmetric section. It does not possess any axis of symmetry, which intern produces the product moment of inertia. Thus the geometric axis and principle axis are different in the case of the Z-section, which was explained in Fig. 2a. In Z-section shear centre coincides with the centroid of the cross-section. Thus the global buckling under axial compression is an independent mode of global buckling. In other words, there not be any interaction between torsion and flexural buckling.

Generally, Zee-section member will undergo the minor axis flexural buckling. The member will buckle in v-v axis, not on the y-y axis. In case of bending the even

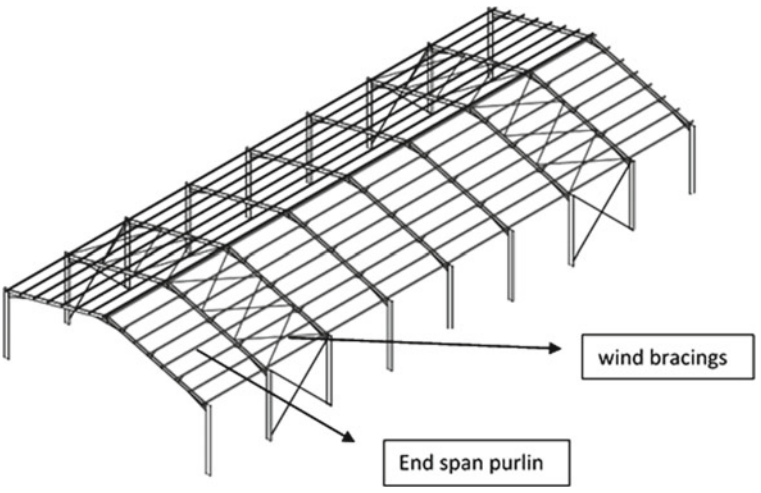


**Fig. 1** Typical industrial building with wind bracing

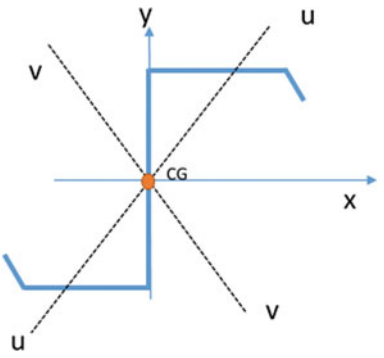


**Fig. 2** Zee section with its axis

under gravity loading, the member will undergo displacement in both the geometry axis. To study the lateral-torsional buckling strength on z section member [1] carried out a non-linear analysis on flexible web z members. The load-carrying capacity of z section with sheeting [2] is evaluated using a series of tests under gravity loading with different loading arrangement. Because of point symmetricity, the member undergoes bi-axial bending in unrestrained condition. To study the behaviour of the member under bi-axial bending [3] conducted a series of experiment by loading in an inclined axis.

## 2 Beam-Column

Beam-column members are generally designed using simple linear interaction (LI) as shown in Eq. (1) by calculating the beam and column strength independently.

$$\frac{P}{P_n} + \frac{C_{mx}M_x}{\alpha_x M_{nx}} + \frac{C_{mz}M_z}{\alpha_z M_{nz}} \leq 1 \tag{1}$$

where $P$ is the applied load, and $M_x$, $M_y$ are the applied moment in the major and minor axis of the member. $P_n, M_{nx}, M_{ny}$, are the nominal axial and moment capacities respectively. The interaction of axial force and moment is considered only using moment amplification factor $\alpha_x$, $\alpha_y$. Where $\alpha_x$ is defined as $\alpha_x = \left(1 - \frac{P}{P_{ex}}\right)$, where $P_{ex} = \frac{\pi^2 E I_x}{L_x^2}$ is the flexural buckling load about the respective axis and $C_{mx}$, $C_{my}$ the moment gradient factor which is generally calculated using Austin formula is given in Eq. (2)

$$C_{mz} = 0.6 + 0.4\frac{M_1}{M_2} \tag{2}$$

The present CFS design codes such as AISI S100-2016, EC3, and IS 801-1975 follow the same Linear Interaction (LI) equation framework. The LI equation framework proves to be reasonably good for members which fail due to yielding. In the case of CFS member, the failure of the member is due to various instability effects. The various instability effects are considered using EWM and DSM for independent beam and independent column effects. The combination using LI equation for beam-column effects does not represent the real interaction behaviour. The test results from the literature show that the linear interaction equation predicts the strength of members very conservatively. Since CFS members are made of thin sheets of steel, the cross-sectional buckling predominates the failure. The strength of cross-sectional buckling such as local and distortional buckling is strongly affected by the stress distribution in the cross-section. Stresses due to bi-moment (create additional longitudinal stress) are not considered in the design provisions.

## *2.1 Non-Linear Interaction NLI Framework*

In order to develop an efficient CFS beam-column design, Schafer [4] developed a Non-Linear Interaction (NLI) equation framework using DSM. Since DSM uses software for calculation of the elastic buckling stress, it is comfortable to extend the DSM procedure to beam-column design. The cross-sectional buckling does not follow the linear interaction and buckling under actual distribution is non-linear as presented in [5]. Thus, it is adopted that instead of applying compression and bending stress separately, as shown in Figs. 3a, b, c, the resultant combined stress due to compression and bending as shown in Fig. 3d has to be applied to find the elastic buckling stress.

In the NLI framework, the strength of member is represented by a single parameter $\beta n$, instead of three components of applied stress in LI framework. The applied stress components are represented by $\beta r$, $\theta_{mm}$, and $\phi_{pm}$ which are defined in Eqs. (4), (5), and (6). The local buckling minima $\alpha_{crl}$ and distortional buckling minima $\alpha_{crd}$ from the signature curve for combined stress have to be applied in Eq. (7).

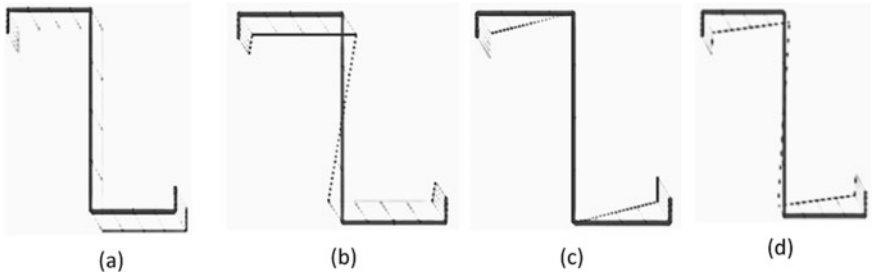


**Fig. 3** Stress distribution under various action

$$\beta_r = \sqrt{x_r^2 + y_r^2 + z_r^2} \tag{3}$$

where

$$x_r = \frac{M_{r1}}{M_{y1}}, \; y_r = \frac{M_{r2}}{M_{y2}}, \; z_r = \frac{P_r}{P_y}$$

$$\theta_{mm} = \tan^{-1}\left(\frac{y_r}{x_r}\right) \tag{4}$$

$$\phi_{pm} = \cos^{-1}\left(\frac{z_r}{\beta_r}\right) \tag{5}$$

$$\beta_{cr} = \alpha_{cr}\beta_r \,, \;\; \beta_y = \alpha_y \beta_r \tag{6}$$

$$\alpha_{cr} = \frac{f_y}{f_{\text{app}}}, \frac{\beta_r}{\beta_n} < 1 \tag{7}$$

$$\beta_{nG} = \beta_{nGP} + (\beta_{nGP} - \beta_{nGP}) \sin \phi_{pm} \tag{8}$$

where $M_{r1}, M_{r2}$ is a resultant applied moment in major axis and minor axis direction including P-δ and P-Δ effect and $P_r$ is the applied axial load. The second-order effect in the beam-column action will be included by doing a second-order analysis or by doing first-order analysis and corrected by an amplification factor. The applied stress will always be inclusive of stress due to the second-order effect. DSM formula for beam and column will be combined by using the sine formula as shown in Eq. (8). The similar notation used for beam or column is extended for global buckling and local buckling in which $P_{cr}$ or $M_{cr}$ is replaced by $\beta_{cr}$ for the respective critical buckling. The equation for various buckling in NLI framework is explained in [6, 7]. This NLI framework is developed based on the uniform stress throughout the member. The semi-empirical equation for local and distortional buckling is validated with less number of experimental and numerical results. The effect of moment gradient on the beam-column behaviour was studied by Rajkannu and Jayachandran [8] and design implementation of moment gradient factor on NLI framework was described.

To validate the DSM formulation of non-linear interaction [7] conducted 54 experiments [9, 10] the lipped channel section of 600S137-54 with uniform moment throughout the member. To study the behaviour of Zee section under beam-column action [11, 12] conducted a series of the experiment by eccentric compression with the uniform moment at ends. The application of non-linear interaction to Zee-section beam-column is also checked.

# 3 Finite Element Analysis

## *3.1 Finite Element Modelling*

To study the CFS beam-column behaviour and to check the validity of the NLI framework, a series of numerical analysis is done using finite element software ABAQUS. In this study, lipped Zee cross-section of size 100 × 60 × 10 with 1.6 mm thickness is modelled using shell element (S4R). Length of a specimen of 1500 mm was selected to check long column behaviour. Since CFS made of thin element imperfection significantly affects the strength of the member, which was shown by the various researcher. To take care of imperfection in the finite element modelling, elastic buckling analysis is performed first. The buckling mode shapes are given as imperfection to the ultimate load analysis or static riks analysis. Schafer (2002) presented a guideline to assign imperfection factor for various buckling modes as $L = 0.34$ t, $D = 0.56$ t, $G = \text{L}/1000$. The imperfection factor is assigned in terms of thickness for local and distortional buckling, and for global buckling in terms of overall length. The ideal linear elastic-perfectly plastic material model is used for the material property of steel. The yield strength of steel is taken as 240 N/mm$^2$. Based on the mesh convergence study, mesh size is taken as 5 mm. Imperfection to the member for the ultimate analysis is assigned using a special keyword as *Imperfection. In this study, the 1st buckling mode shape is given as imperfection for each analysis. Boundary condition followed is simply supported with warping restraint at ends. To simulate an endplate action at both ends MPC (Multipoint Constraint) is used as shown in Fig. 4a that will not allow warping deformation to occur at ends. Loads and boundary condition are applied at the MPC constraint points. To create the eccentric loading case (i.e.) for creating the beam-column the load is applied eccentrically other than CG point as shown in Fig. 4b. In this study, the Zee-section beam-column member under uniform moment is studied. The cross-section shape from the [11, 12] paper to validate the numerical modelling. The numerical result matches with the experiment result from the paper. From the validated model, numerical modelling is extended to study the beam-column behaviour of the selected section.

## *3.2 Selection of Specimen*

The specimen is selected based on the series of analysis using CUFSM and GBTUL, by varying different combination of lip and flange dimension. The main aim of choosing the section is member fail predominant fail in distortional buckling or distortional global interaction. Thus based on elastic buckling analysis specimen of 100 × 60 × 10 × 1.6 mm, with 1500 mm length is selected for this study. For this length of the member, the elastic buckling stress under compression for local, distortional, and global will be almost the same. The selection of lower yield stress

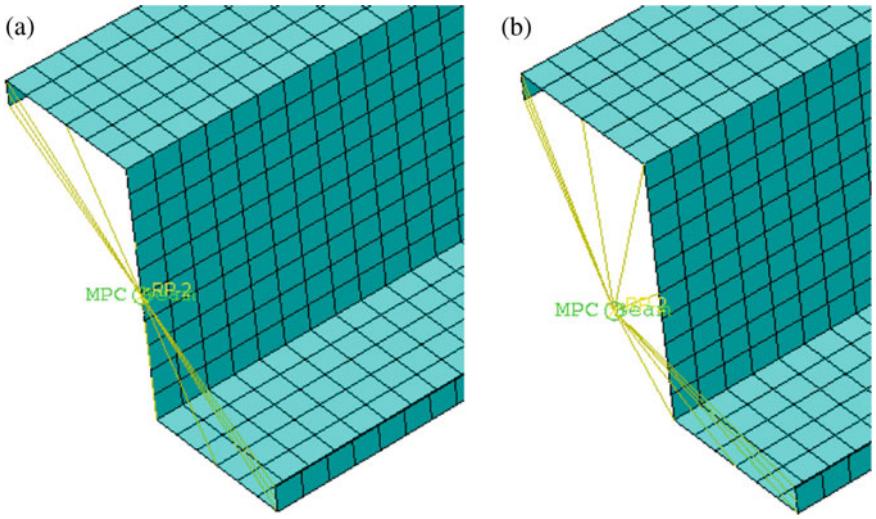


**Fig. 4** Numerical modelling **a** axial loading **b** eccentric loading (beam-column action)

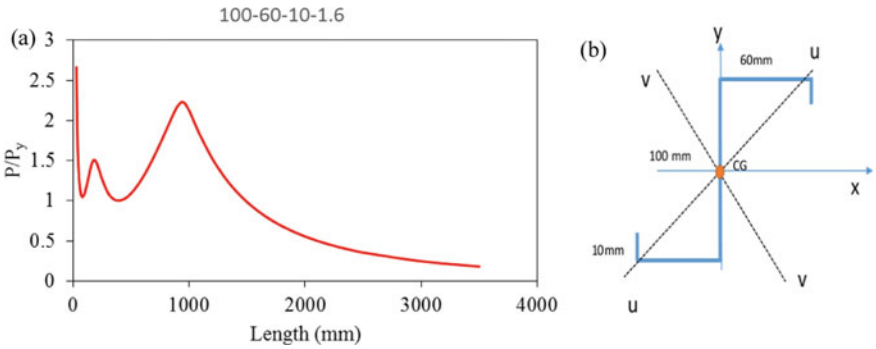


**Fig. 5** **a** Signature curve for the selected specimen, **b** dimension of specimen

240 N/mm$^2$ shows that there is a higher possibility of yielding before local buckling. Signature curve for the selected member is given in Fig. 5.

## 4 Numerical Results

To study the behaviour of the selected section under beam-column action, the member is subjected to various combination of axial and bending load in different directions. Non-linear analysis is carried out for each loading case. In this study, beam-column

member under uniform moments throughout the member is studied by keeping eccentricity at the top and bottom of the specimen as same. The results and discussion of selected Zee-section beam-column member are discussed in the below sections.

## *4.1 Minor Axis Bending*

To study the performance of linear and non-linear interaction based on DSM, the study was carried out on Zee-section beam-column members. Since Zee section is a point-symmetric cross-section, the geometric axis cannot be the principle axis. Based on the modelling using CUFSM, the inclination of principle major and minor axis was found concerning to geometric axis. Based on the inclination, the co-ordinate and eccentricity from the centroid to create minor axis bending were found, as shown in Fig. 6b. The load was applied at those point in the numerical model created in ABAQUS. The non-linear analysis was done with the 1st mode imperfection of member under axial load. The ultimate load from the numerical model was compared with the prediction from LI and NLI. The results are given in Table 1. The results depict that the ultimate capacity strongly depends on the eccentricity of the loading. The comparison of results shows that LI conservatively predicts the strength of member of an average of 25% over the full interaction curve for the selected Zee-section member. Figure 6a shows the pictorial representation of the comparison of results with the linear and non-linear interaction prediction. The figure depicts that non-linear interaction predicts the strength higher than the linear interaction. NLI prediction reduces the conservativeness by 10%. But still, there is conservativeness of about 20% in case of moment dominated region which needs to be further investigated.

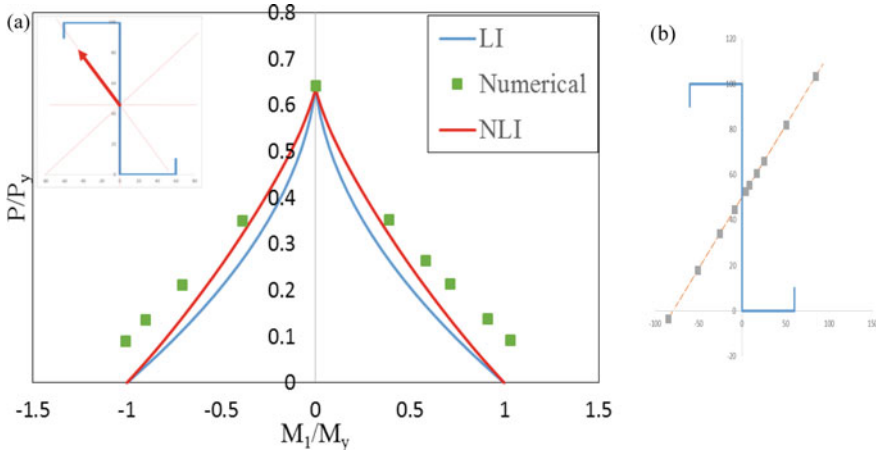


**Fig. 6** Pictorial representation of principle minor axis results with LI DSM and NLI DSM

**Table 1** Comparison of principal minor axis results with LI DSM and NLI DSM

| $e_u$ | Pult | M2 | P/Py | $M_2/M_{2Y}$ | LI | $\beta r$ | $\beta n$ | $\beta r/\beta n$ |
|---|---|---|---|---|---|---|---|---|
| 5 | 39.12 | 195.60 | 0.44 | 0.24 | 1.22 | 0.69 | 0.66 | 1.05 |
| 10 | 31.68 | 316.85 | 0.35 | 0.39 | 1.26 | 0.79 | 0.72 | 1.09 |
| 20 | 23.69 | 473.79 | 0.26 | 0.59 | 1.29 | 0.92 | 0.80 | 1.15 |
| 30 | 19.18 | 575.47 | 0.21 | 0.71 | 1.31 | 1.00 | 0.84 | 1.19 |
| 60 | 12.31 | 738.71 | 0.14 | 0.91 | 1.32 | 1.11 | 0.90 | 1.24 |
| 100 | 8.34 | 833.53 | 0.09 | 1.03 | 1.31 | 1.17 | 0.93 | 1.26 |
| 0 | 57.62 | 0.00 | 0.64 | 0.00 | 1.01 | 0.64 | 0.64 | 1.01 |
| −10 | 31.37 | −313.67 | 0.35 | −0.39 | 1.24 | 0.77 | 0.72 | 1.07 |
| −30 | 19.04 | −571.27 | 0.21 | −0.71 | 1.30 | 0.99 | 0.84 | 1.18 |
| −60 | 12.13 | −727.85 | 0.14 | −0.90 | 1.30 | 1.09 | 0.90 | 1.22 |
| −100 | 8.12 | −812.17 | 0.09 | −1.00 | 1.28 | 1.14 | 0.93 | 1.22 |
| | | | | Mean | 1.26 | | | 1.15 |
| | | | | st.dev | 0.088 | | | 0.085 |

## 4.2 Major Axis Bending

The eccentric loading for creating major principle bending in addition to compression was given in Fig. 7b. The results of Zee-section beam-column member with major axis bending were given in Table 2. The results show that there is a linear variation on ultimate capacity when subjected to major axis eccentricity, whereas in the case of principle minor axis the variation is not linear, which may be mainly due to the P-delta effect. The comparison of ultimate results with LI prediction also shows that the p-delta effect concerning to major axis is lower because of higher buckling load in major axis. Thus the LI prediction matches well with the ultimate result. When comparing the result with NLI overestimate the member strength. The results are showing much different from the results from the literature and present study on minor axis bending. The results are to be checked by experiment results on the Zee section with the major axis. The pictorial representation of the comparison of results for beam-column with principle major axis is given in Fig. 7a.

## 4.3 Bi-Axial Bending

The load applied at any eccentricity other than principle axis creates the bi-axial bending with respect to the principle axis. In this study, the very few eccentricities were selected for principle bi-axial bending. Bi-axial eccentricity is represented in terms of $\phi_{Pm}$ and $\theta_{mm}$ as given in the NLI framework. The results on non-linear analysis for the bi-axial bending are given in Table 3. The results show that due to the asymmetry of the cross-section about the x-axis, the ultimate load on the top

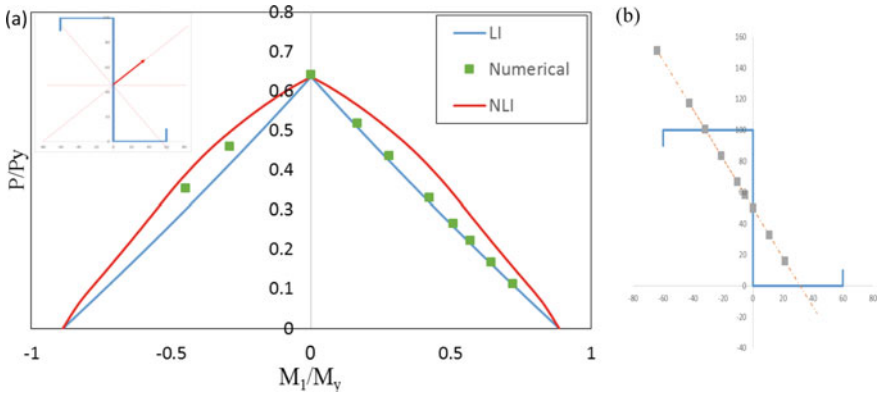


**Fig. 7** Pictorial representation of principle major axis results with LI DSM and NLI DSM

**Table 2** Comparison of principle major axis results with LI DSM and NLI DSM

| Specimen ID | $E_v$ | Pult | M1 | P/py | $M_1/M_{1Y}$ | LI | $\beta r$ | $\beta n$ | $\beta r/\beta n$ |
|---|---|---|---|---|---|---|---|---|---|
| | mm | kN | kNmm | | | | | | (NLI) |
| H1 | 20 | 39.13 | 782.56 | 0.44 | 0.28 | 1.02 | 0.53 | 0.59 | 0.89 |
| H2 | 40 | 29.69 | 1187.69 | 0.33 | 0.42 | 1.02 | 0.55 | 0.62 | 0.89 |
| H3 | 60 | 23.93 | 1435.96 | 0.27 | 0.51 | 1.01 | 0.59 | 0.66 | 0.90 |
| H4 | −20 | 41.20 | −824.03 | 0.46 | −0.29 | 1.07 | 0.56 | 0.59 | 0.94 |
| H5 | 80 | 20.04 | 1602.92 | 0.22 | 0.57 | 1.01 | 0.63 | 0.69 | 0.91 |
| H6 | −40 | 31.76 | −1270 | 0.35 | −0.45 | 1.09 | 0.59 | 0.62 | 0.95 |
| H7 | 0 | 57.62 | 0.00 | 0.64 | 0.00 | 1.01 | 0.64 | 0.64 | 1.01 |
| H8 | 10 | 46.47 | 464.71 | 0.52 | 0.16 | 1.01 | 0.55 | 0.59 | 0.93 |
| H9 | 120 | 15.14 | 1816.30 | 0.17 | 0.64 | 1.01 | 0.68 | 0.73 | 0.93 |
| H10 | 200 | 10.16 | 2031.74 | 0.11 | 0.72 | 1.00 | 0.74 | 0.79 | 0.94 |
| | | | | | Mean | 1.03 | | | 0.93 |
| | | | | | St.Dev | 0.030 | | | 0.035 |

of x-axis and bottom of the x-axis is different. The non-linear analysis results are compared with AISI S100-2016 using DSM prediction. Results show that LI predicts well for the bi-axial bending, whereas NLI over-predicts the strength of the member. The NLI ($\beta r/\beta n$) less than 1 shows that numerical results are less than the prediction.

**Table 3** Comparison of bi-axial loading results with LI DSM and NLI DSM

| Specimen ID | $\phi_{Pm}$ | $\theta_{mm}$ | $P_{ult}$ | $M_1$ | $M_2$ | $P/P_y$ | $M_1/M_y$ | $M_2/M_y$ | LI | NLI |
|---|---|---|---|---|---|---|---|---|---|---|
| | Degree | | kN | kNmm | kNmm | | | | | |
| B1 | 49.5 | 166.3 | 28.42 | −967 | 67 | 0.32 | −0.34 | 0.08 | 1.04 | 0.71 |
| B2 | 49.6 | 346.3 | 30.92 | 1052 | −73 | 0.34 | 0.37 | −0.09 | 1.09 | 0.78 |
| B3 | 38.2 | 166.3 | 33.40 | −758 | 53 | 0.37 | −0.27 | 0.07 | 0.99 | 0.74 |
| B4 | 38.4 | 346.3 | 37.30 | 846 | −59 | 0.42 | 0.30 | −0.07 | 1.12 | 0.83 |
| B5 | 21.8 | 166.3 | 41.37 | −469 | 33 | 0.46 | −0.17 | 0.04 | 1.00 | 0.81 |
| B6 | 30.4 | 346.3 | 42.15 | 717 | −50 | 0.47 | 0.25 | −0.06 | 1.16 | 0.88 |
| B7 | 57.3 | 341.6 | 26.62 | 1208 | −84 | 0.30 | 0.43 | −0.10 | 1.08 | 0.76 |
| B8 | 76.0 | 11.7 | 13.13 | 1614 | 121 | 0.15 | 0.57 | 0.15 | 1.38 | 0.91 |
| B9 | 72.7 | 11.6 | 15.44 | 1518 | 114 | 0.17 | 0.54 | 0.14 | 1.40 | 0.90 |
| B10 | 67.6 | 11.7 | 18.73 | 1381 | 104 | 0.21 | 0.49 | 0.13 | 1.42 | 0.88 |

## 5 Summary and Conclusion

This chapter presents the behaviour and non-linear analysis of lipped Zee section under combined axial and bending. The Zee-section members are selected based on a series of analysis using CUFSM and GBTUL. The selected member is subjected to various types of bending such as (i) principle major axis bending (ii) minor axis bending (iii) bi-axial bending in addition to the compression. The results from the numerical analysis are compared with strength prediction based on AISI-S100-2016 using DSM which is based on linear interaction equation (LI). The results are also compared with the newly developed non-linear interaction equation using DSM. Based on that, the following conclusions were derived.

In case of principle minor axis bending in addition to compression, failure of the member is predominantly the interaction of global and distortional buckling. Comparison of results shows that LI DSM conservatively predicts the strength of member of about 20%. Whereas the NLI DSM reduces the conservativeness over the entire region.

The principle major axis results show that LI DSM is able to predict the strength exactly, whereas the NLI over-estimates the strength of the member. Even for Bi-axial loading, the NLI is over-predicting the strength of the member. LI is more conservative for some cases and provides reasonable prediction for some cases.

From this study, overall it is clear that the NLI framework equation shows the capability of predicting the strength of member much accurately for the member subjected to principle minor axis. For the chosen section, the NLI framework is over-predicting the strength for the major axis and bi-axial loading. This over-prediction may be due to change in buckling mode prediction. In summary, the NLI framework can make improved predictions compared to LI framework. The NLI framework in its present form has so many aspects that can be improved, and this needs further investigation.

## References


1. Pi YL, Put BM, Trahair NS (1999) Lateral buckling strengths of cold-formed Z-section beams. Thin-Walled Struct 34(1):65–93
2. Seetharaman S, Natarajan PR, Djugash ACR (1984) Load carrying capacity of Z-purlins with A.C. sheet cladding. In: 7th International specialty conference on cold-formed steel structures
3. Put BM, Pi YL, Trahair NS (1999) Biaxial bending of cold-formed Z-beams. J Struct Eng 125(11):1284–1290
4. Schafer BW (2006) Designing cold-formed steel using the direct strength method. In: Eighteenth international specialty conference on cold-formed steel structures: recent research and developments in cold-formed steel design and construction, pp 475–488
5. Schafer B (2012) Development of DSM direct design formulas for beam-columns. Research report, John-Hopkins University
6. Schifferaw Y, Schafer BW (2012) Direct strength prediction of cold-formed steel Beam-columns, Year 1 progress report. John-Hopkins University
7. Torabian S, Zheng B, Schafer BW (2015) Experimental response of cold-formed steel lipped channel beam-columns. Thin-Walled Struct 89:152–168
8. Rajkannu JS, Jayachandran SA (2018) Investigations on the design implementation of cold-formed steel beam-column members using direct strength method. Eighth international conference on Thin-Walled Structures, pp 1–10
9. Torabian S, Zheng B, Schafer BW (2014) Reliability of the new DSM beam-column design method for cold-formed steel lipped channel. In: 22nd International spece conference on cold-formed steel structure
10. Torabian S, Zheng,B, Schafer BW (2014) Experimental study and modeling of cold-formed steel lipped channel stub beam-columns. In: Structural stability research council annual stability conference 2014, SSRC 2014. Department of Civil Engineering, Johns Hopkins University, United States: Structural Stability Research Council (SSRC), pp 380–401
11. Torabian S, Fratamico DC, Schafer BW (2015) Experiments on cold-formed steel Zee-shaped stub beam-columns. In: Website proceedings of structural stability research council annual stability conference
12. Torabian S, Fratamico DC, Schafer BW (2015) Experiments on cold-formed steel Zee-shaped stub beam-columns. In: Structural stability research council annual stability conference 2015, SSRC 2015, pp 1–18
13. Schafer BW (2019) Advances in the direct strength method of cold-formed steel design. Thin-Walled Struct 140:533–541
14. Yu C, Yan W (2011) Effective width method for determining distortional buckling strength of cold-formed steel flexural C and Z sections. Thin-walled Struct 49(2):233–238

# Behavior of Cold-Formed Steel Racking Structure—A Comparison of Analytical and Experimental Results


**N. Raviswaran, N. N. Unnikrishnan, V. Nagendiran, Suhail Musthafa, C. Bharathi Priya, and K. Sathish Kumar**

**Abstract** Pallet racking system made of cold-formed steel members is commonly used for storing palletized goods. To make the structure flexible to accommodate varied sizes of pallets, beams are hooked on to upright columns. The connection between upright column and beam is semi-rigid, and hence, the behavior of the system is nonlinear. Since uprights are made of cold-formed perforated sections, they are most vulnerable to local and torsional buckling under gravity as well as lateral load. To verify how the system responds to lateral earthquake loads, it is important to conduct full-scale experimental studies under monotonic and cyclic lateral loading conditions, for getting realistic nonlinear behavior. An attempt has been made in this study to bring out the behavior of the structure through an analytical model using STAAD PRO. To validate the model, a comparison has been made with full-scale experimental results involving static (monotonic and cyclic) load displacement behavior. The results were used to fine tune the moment rotation characteristics of upright-beam as well as upright-baseplate joint. The results from the analysis are found to be in good agreement with the respective experimental results.

N. Raviswaran · N. N. Unnikrishnan · V. Nagendiran · S. Musthafa (✉)
Godrej Storage Solutions, Godrej & Boyce Mfg Co. Ltd., Chennai, India
e-mail: suhailm@godrej.com

N. Raviswaran
e-mail: ravish@godrej.com

N. N. Unnikrishnan
e-mail: unni@godrej.com

V. Nagendiran
e-mail: nag@godrej.com

C. Bharathi Priya · K. Sathish Kumar
CSIR-Structural Engineering Research Centre, Taramani, Chennai, India
e-mail: bharathipriya@serc.res.in

K. Sathish Kumar
e-mail: ksk@serc.res.in



M. Madhavan et al. (eds.), *Proceedings of the Indian Structural Steel Conference 2020 (Vol. 1)*, Lecture Notes in Civil Engineering 318,
https://doi.org/10.1007/978-981-19-9390-9_29

**Keywords** Pallet racking system · Earthquake load · Static monotonic · Static cyclic · Analytical model · Validation of static performance

## 1 Introduction

Practical application of industrial steel storage racking system is to store goods. Despite their lightness in nature, racking system carries very high live load and likely to be quite tall. Structural behavior of pallet racks is influenced by the geometry of their structural components and their connections which involve members made using thin-walled open-section profiles (hence prone to global, local, and distortional buckling problems), beam-upright and upright- baseplate-floor joints exhibiting a nonlinear behavior.

During an earthquake, satisfactory seismic response of steel storage racks and their components is crucial, since any kind of collapse could lead to a serious threat to life safety and damage to the goods stored. Earthquake ground motions can cause storage racks to collapse or overturn if they are not properly designed, installed, maintained, and loaded. Therefore, it is of great importance that pallet racks are properly designed, installed, maintained, and loaded. The seismic design of racks is governed by several codes and standards (e.g. [1] and [2]). The quality of installation depends on the contractor, while the owner and operator are responsible for the maintenance and loading of the racks.

There are many challenges to define a uniform and accepted method of design for this type of structure. These include complexity and irregularity of perforated thin-walled sections, complex imperfections, highly asymmetric behavior due to lack of symmetry in sections, connections, loading, and highly diversified proprietary connections. Firstly, steel racks were considered working equipment, and hence, their design did not comply with standard codes. Later, market requested racks capable of withstanding seismic actions, both for safety and to protect the goods [3]. In Europe, pallet rack design for static loads is governed by the EN15512 specifications [4], while in the USA, the design is carried out according to the Rack Manufacturers Institute (RMI) specifications [5]. In Australia, static design of steel pallet racks is done using AS4084 [6]. All these recommendations include the test validation of structural element behavior, even in a design phase. A comparative review of analysis methods recommended by these codes is given by Castiglioni [7]. In the USA, it is FEMA 460 [2], and in Europe, Eurocode 8 are used for design. In Europe, two research programs SEISRACKS1 and SEISRACKS2 [3] were carried out to have an acceptable seismic design recommendation for storage racks.

An experimental study was conducted to have an insight into the behavior of the racks under lateral loads. This paper presents a comparison between analytical and experimental results when the rack structure is subjected to lateral load. The behavior of the joints has been accounted by using a suitable variable joint modulus to account for realistic behavior of joints. The main aim of the study is to investigate the effect

of beam-column connections and baseplate connection on structural behavior of rack system for various connection types under horizontal and vertical loads.

## 2 Literature Survey

The investigation on the behavior of steel storage racking system made of monosymmetric columns was studied by Hancock [8] in 2004. The study was predominantly on the procedure to be adopted for the analysis and design of the steel structures. A focused research on beam to column connection of pallet racking system to understand the joint behavior and its influence on the overall system behavior is discussed by Shah [9].

A study on the connection behavior and its impact on the sway performance on the racking system was done. The analytical and experimental results were compared with that of the design methods stated in FEM and SEMA standards for the racking structures by Godley [10]. An independent study on the connection behavior of column baseplate connection in a racking system is performed by Baldassino [11].

## 3 Experimental Investigation

Quasi-static reversed cyclic and static monotonic load tests were performed using the pseudo-dynamic test facility to evaluate the load–displacement performance of the structure.

Four specimens were tested: two in the down aisle direction and two in the cross aisle direction as shown in Fig. 1. The details of the test specimens are given below.

The structure has an overall upright height of 6.3 m, with a pair of beams at four different levels as shown in Figs. 1 and 2. Plan bracings were provided for both braced and unbraced racks, one at first loading level and one at fourth loading level. A load of 2 tons at each level was placed on the structure using wooden pallets, such

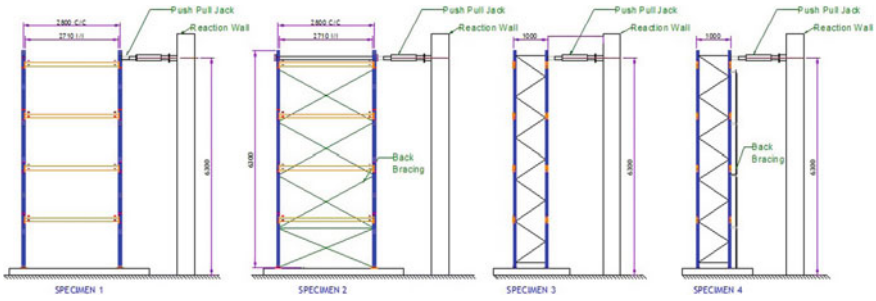


**Fig. 1** Specimen 1, 2, 3, and 4, respectively, with load setup

that the total load on the structure is 8 tons. Test specimens are classified as braced/unbraced, and load application is made along cross aisle (along frame) direction/down aisle (along beam) direction. Based on these, four specimens as listed in Table 1 were tested. The specimen and the test setup are shown in Fig. 1.

The structure is made out of frames and beams. The vertical system is referred as frames, and horizontals are referred as beams. The frame is made up of uprights (column) and bracing (cross members). The cross section of the upright, beam, and bracing used is shown in Figs. 2, 3, and 4, respectively. It should be noted that the upright section has got perforations on the front and side faces. The cross-sectional details are listed in Table 2.

The material properties of the structural members are given in Table 3.

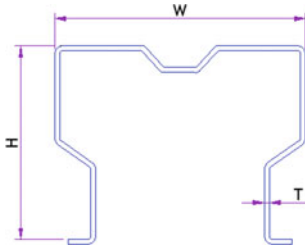


**Fig. 2** Cross section of upright profile

**Table 1** Specimen details

| Specimen | Braced/unbraced | Loading direction |
|---|---|---|
| Specimen 1 | Unbraced | Down aisle |
| Specimen 2 | Braced | Down aisle |
| Specimen 3 | Unbraced | Cross aisle |
| Specimen 4 | Braced | Cross aisle |

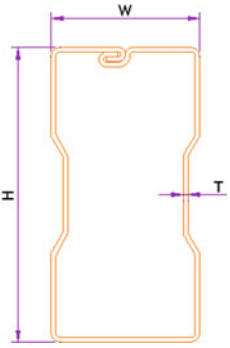


**Fig. 3** Cross section of beam profile

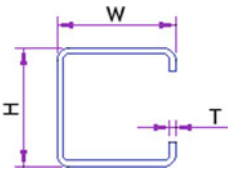


**Fig. 4** Cross section of frame bracing

**Table 2** Details of section details

| Profile | Width 'W' (mm) | Height 'H' (mm) |
|---|---|---|
| Upright | 90 | 70 |
| Beam | 50 | 110 |
| Bracing | 30 | 30 |

**Table 3** Material properties

| | |
|---|---|
| Modulus of elasticity, E | 200,000 MPa |
| Poisson's ratio, U | 0.3 |
| Minimum yield strength (upright), Fy | 355 MPa |
| Minimum yield strength (beam and frame bracing), Fy | 255 Mpa |
| Minimum yield strength (back-bracing and plan bracing), Fy | 210 MPa |

# 4 Test Setup and Testing Procedure

## *4.1 Test Setup*

The test was conducted on a heavy-duty test floor using a hydraulic actuator mounted on a reaction wall. RCC slabs were fixed to the heavy-duty test floor in front of the reaction wall using 50 mm diameter high strength tie-rods. The specimens were erected on the RCC slab and anchored to the same. The alignment of the racks was in such a way that the plane of symmetry of the rack coincides with the center line of the actuator. The jack was positioned horizontally at the top loading level of the specimen (Fig. 1). Spreader beams were used to split the load equally between the verticals on either side of the actuator. Loads were applied using 50 kN servo controlled hydraulic actuator. Figures 5 and 6 show the overall view of the test specimens with pallet loaded on to the system. Adequate safety measures were taken to ensure proper load transfer, prevention of damage to the facility, and injury to people in case of collapse during the test. Necessary instrumentation was done to measure load, displacement, and strain at critical location in the structure.

**Fig. 5** Test specimen 1 and 2 fully loaded system—experimental setup

**Fig. 6** Test specimen 3 and 4 fully loaded system—experimental setup

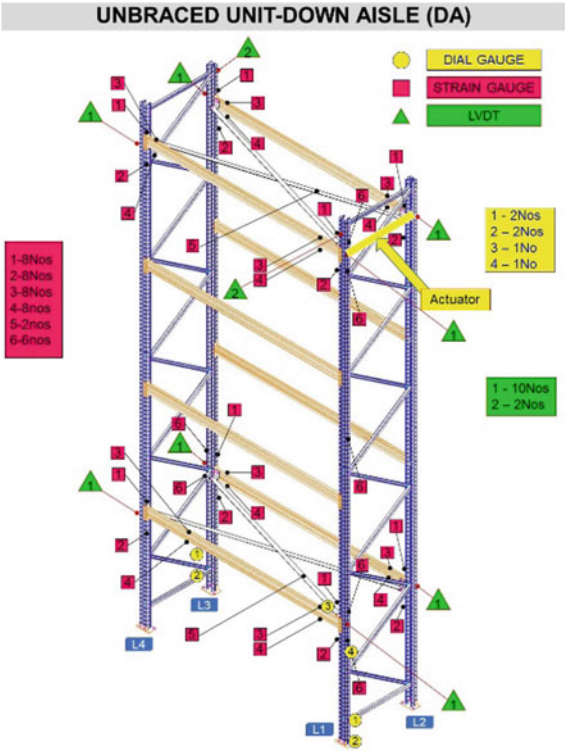


**Fig. 7** Unbraced unit—force acting along down aisle direction

## *4.2 Instrumentation*

Noncontact type laser-based displacement sensors (NCDTs) were used to measure the displacement in two orthogonal direction of the structure. Six to eight NCDTs were kept on first and last loading levels on all four legs (L1, L2, L3, and L4) (Figs. 7, 8, 9, and 10) for measuring in-plane displacements, and two NCDTs were kept at the top of legs L1-L3 to measure out of plane displacements. Four to six dial gauges were used to measure the rotations of the upright-baseplate and upright-beam connection. Strain gauges of 2 mm gauge length were pasted at critical locations on upright, beams, and bracings. The locations of NCDTs, dial gauges, and strain gauges are shown in Figs. 7, 8, 9, and 10 for all the four specimens. All the data from the sensors were logged using HBM data logger, with appropriate strain conditioners.

## *4.3 Testing Procedure*

The specimens were subjected to cyclic loading and later to monotonic loading. The cyclic tests were carried out using displacement-controlled actuator and increasing

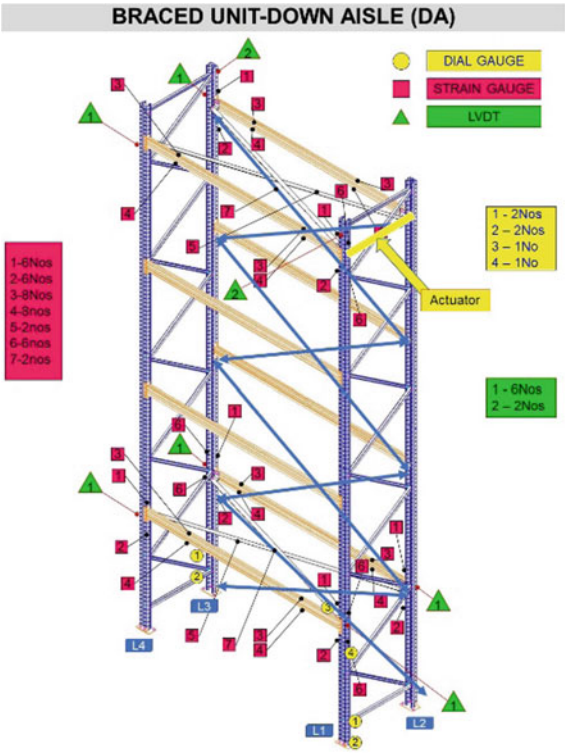


**Fig. 8** Braced unit—force acting along down aisle direction

the displacement at the rate of 0.2 mm/sec. The pattern adopted for cyclic loading is shown in Fig. 11. The cyclic loading was applied up to a displacement of 45 mm. Then, a single monotonic load was applied to reach a displacement of 100 mm.

In each test, load, displacement, stain, and rotation of joints were logged in to the system for every 0.1 s. After every cyclic test, the specimens were examined for any damage of the component, loosening of bolts and nuts, and yielding of the baseplate and anchor bolts.

## 5 Observations and Results

Displacement of the structure, rotation of the joints, and strain measurements were recorded and studied. Load versus displacement curve for cyclic loads for different displacements is plotted as hysteresis graph. The load displacement curves for specimen 1 and 2 are shown in Fig. 12 and for specimen 2 and 3 are shown in Figs. 13 and 14, respectively.

The load displacement curve for monotonic test during loading and unloading resulting in a permanent deformation was first completed. Then, the permanent

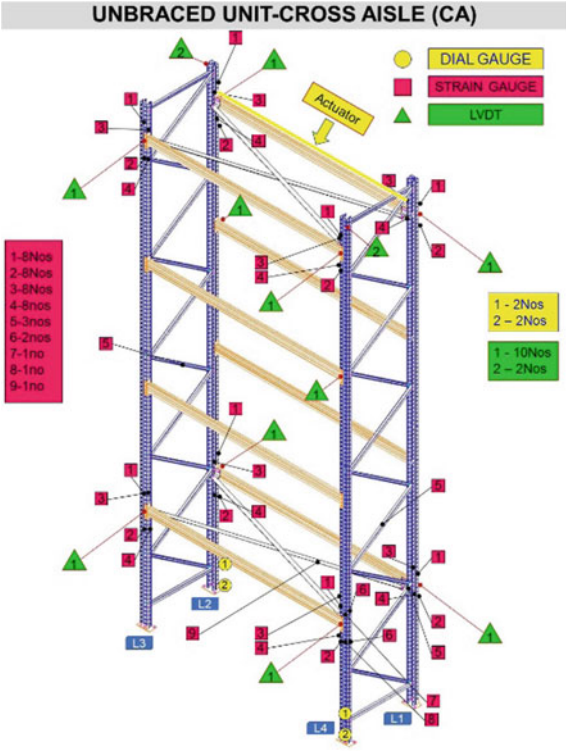


**Fig. 9** Unbraced unit—force acting along cross aisle direction

deformation was removed by applying the load till the deformations were made zero. This constitutes one complete monotonic load–displacement cycle. The same for specimen 1 and 2 is shown in Fig. 15 and for specimen 3 and 4 is shown in Fig. 16.

The load displacement curve from monotonic test was superimposed on the hysteresis curve for specimen 1 to examine whether is there any difference in the behavior observed between monotonic and cyclic test. It was found on comparing the backbone curve of cyclically loaded test with monotonic curve the load displacement pattern is same for both the test. Superimposed curve is shown in Fig. 17.

From the comparison on load versus displacement curve for specimen 1 and 2, it was observed that the stiffness of the system in the down aisle plane is around 5 times higher for braced system than that of unbraced system. The energy absorption witnessed as area enclosed by the hysteresis loop for specimen 1 (unbraced) and specimen 2 (braced) shows 3 times larger value for the braced system. This can be attributed to the back-bracing system provided in specimen 2. In specimen 1, the lateral load is resisted only by beam-column connection stiffness. This makes unbraced system less stiff, in comparison with the braced system.

The strain induced in the beam near the connection in specimen 1 and the strain induced in the spine bracing system in specimen 2 was recorded and shown in Table 4. It was observed that the strain induced in the beam for the system with spine

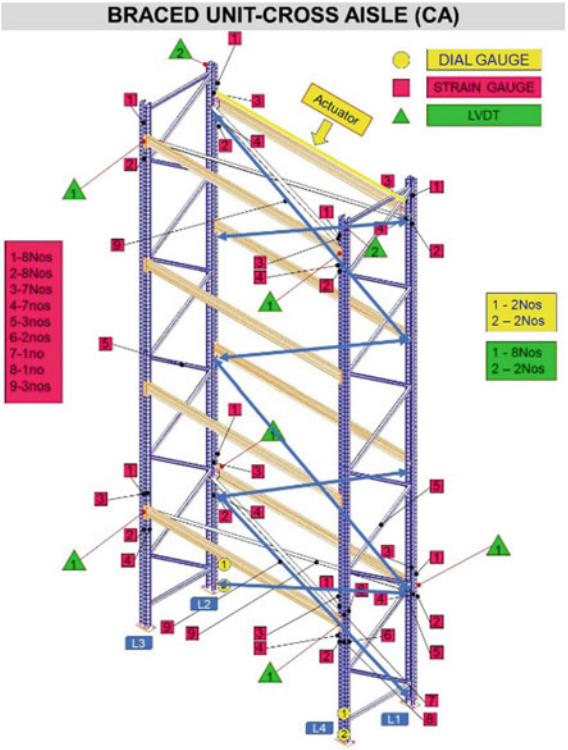


**Fig. 10** Braced unit—force acting along cross aisle direction

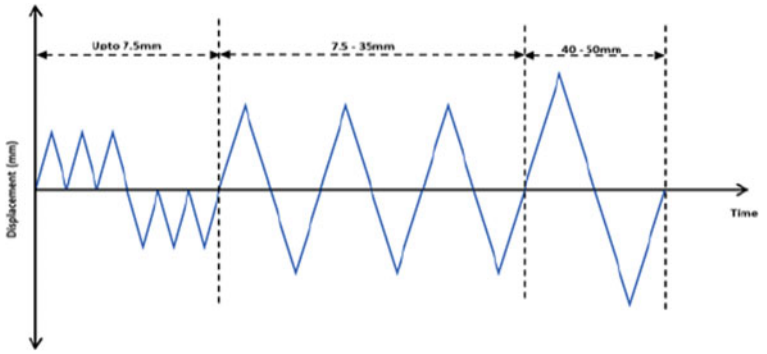


**Fig. 11** Cyclic loading pattern

bracing was much less compared to the strain induced in the system without spine bracing. The strain in the bracing indicates that the bracing is active and resists the lateral load. This again justifies the high energy absorption observed in the braced system compared to the unbraced system.

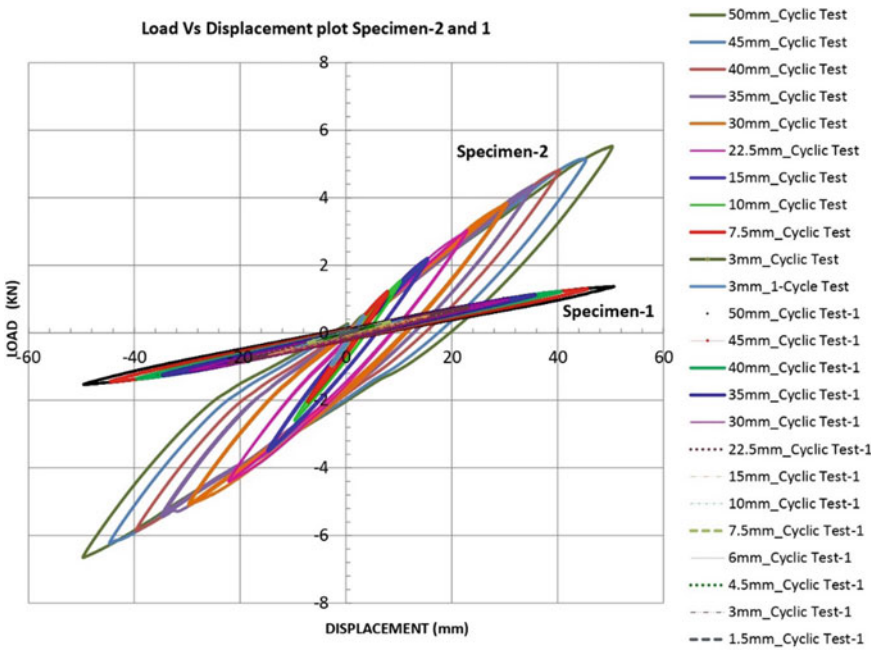


**Fig. 12** Load versus displacement hysteresis for specimen 1 and 2

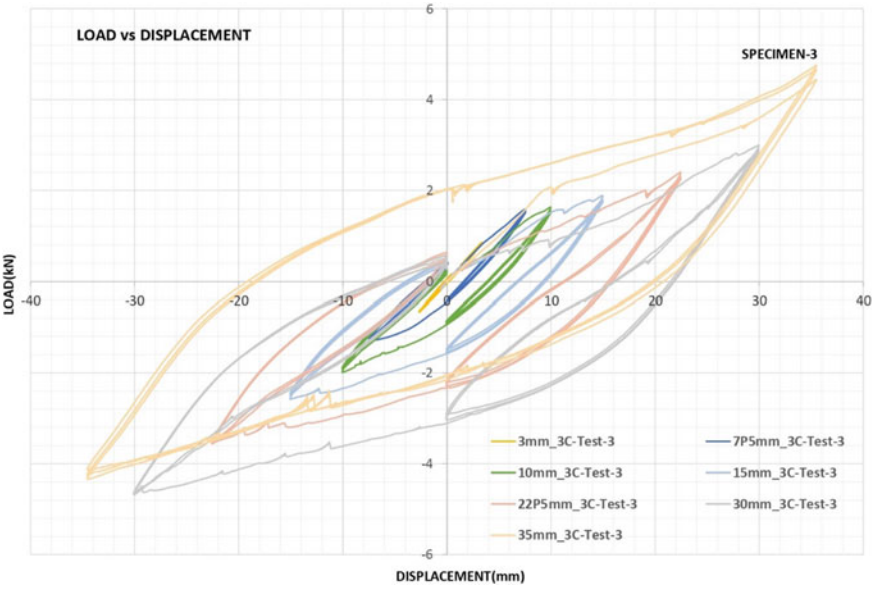


**Fig. 13** Load versus displacement hysteresis for specimen 3

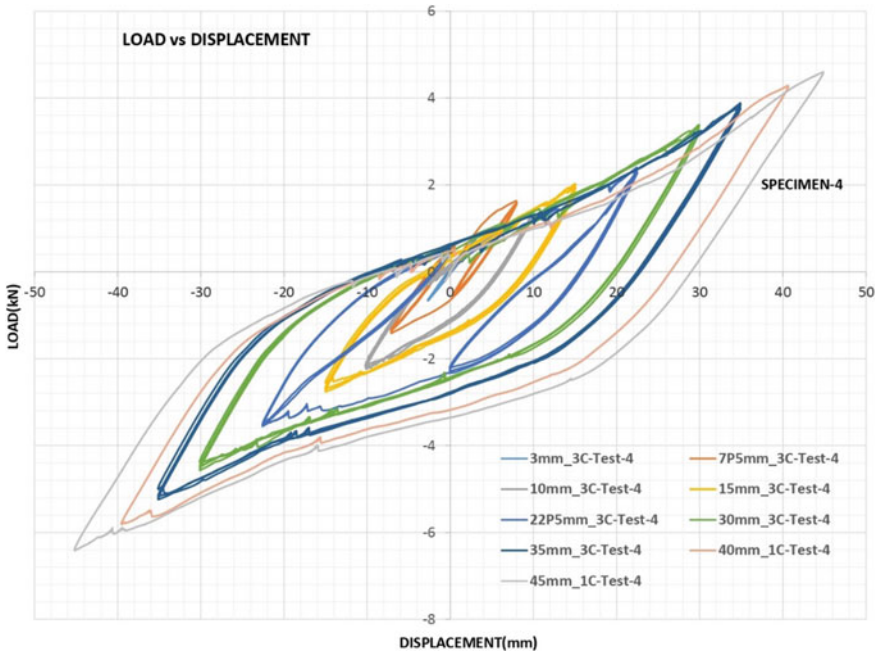


**Fig. 14** Load versus displacement hysteresis for specimen 4

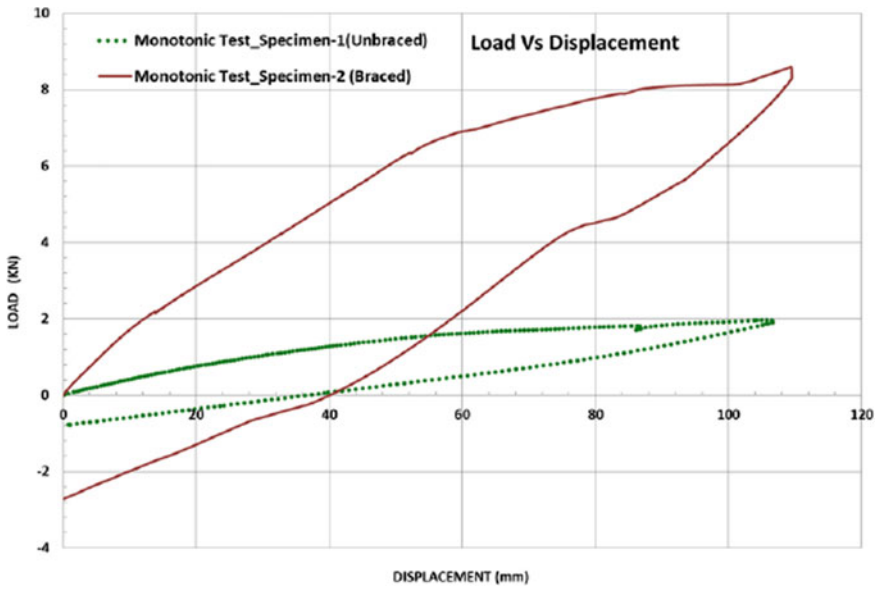


**Fig. 15** Monotonic load versus displacement curve for specimen 1 and 2

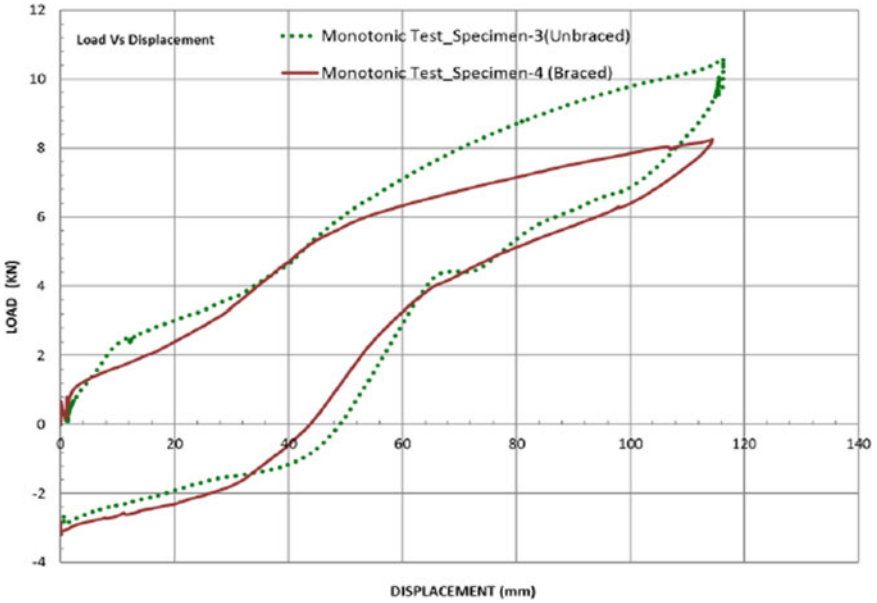


**Fig. 16** Monotonic load versus displacement curve for specimen 3 and 4

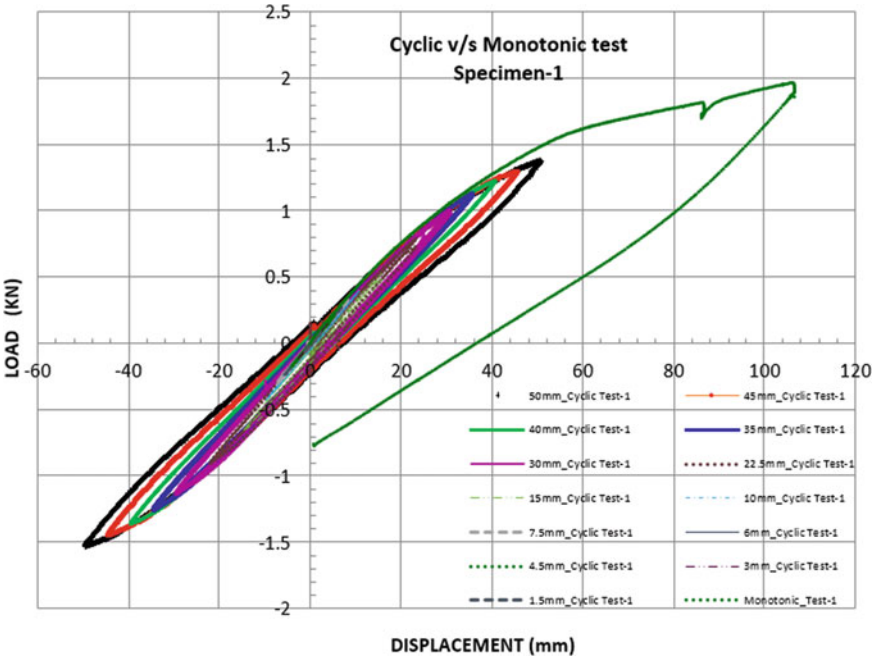


**Fig. 17** Cyclic test versus monotonic test superimposed curve on specimen 1

**Table 4** Strain gauge reading for 50 mm cyclic loading

| Description | | Unbraced system (specimen 1) | | Braced system (specimen 2) | |
|---|---|---|---|---|---|
| | | Peak strain (micro-strain) | | Peak strain (micro-strain) | |
| | | Max | Min | Max | Min |
| Top beam left | Top flange | −571.567 | −419.583 | 70.63 | −80.18 |
| | Bottom flange | 269.8667 | 479.4334 | 254.82 | −57.87 |
| Top beam right | Top flange | −560.092 | −418.325 | 95.82 | −112.14 |
| | Bottom flange | 315.0167 | 508.8084 | 148.6 | −79.93 |
| Bottom beam | Top flange | −584.5 | −401.625 | 54.18 | −80.18 |
| | Bottom flange | 300.8167 | 576.8085 | 195.36 | −19.73 |
| Spine bracings | Top-level bracing | – | – | 164.69 | −51.83 |
| | Bottom-level bracing | – | – | 153.76 | −86.93 |

While comparing the monotonic load displacement curve for specimen 3 and 4, it was observed that the stiffness and energy absorption are relatively high for specimen 3 compared to the specimen 4. This could be attributed to the difference in position of anchor bolt between specimen 3 and 4. Specimen 3 had anchor bolt much closer to the centerline of the upright compared to specimen 4 (ref. Fig. 18).

Each specimen was carefully observed after every cyclic test for any possible damage to the component. No component damage was observed. No damage of fasteners observed. It was observed that tabs of the connectors were slightly cutting into the upright slots at corners. However, it was not propagating further. The systems did not fail till 100 mm displacement.

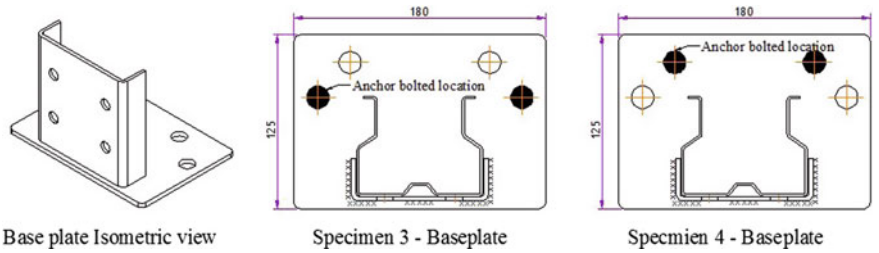


**Fig. 18** Baseplate anchor bolt position for specimen 3 and 4

## 6 Analytical Study

Analytical study involved developing model of the system in software, studying load displacement behavior, and comparing the same with the experimental results. The configuration chosen was that of specimen 1 for the analytical study. To make the model realistic in comparison with the actual system, the connections were tested, and the stiffness value of the connection is incorporated in the model. Beam-column connection, upright-baseplate connection, and overall frame shear stiffness were found experimentally for this purpose.

Experimental procedures prescribed in EN 15,512:2009 were adopted to find the values. The test setups and typical M-Θ curve are shown in Figs. 19 and 20, respectively. Typical models developed for the analytical study are shown in Fig. 21.

Load displacement curve developed using model is given in Fig. 22. For comparison with the analytical results, the load displacement curves for 50 mm displacement in forward direction were chosen. The graph with analytical results superimposed on the experimental results is shown in Fig. 23.

It was observed that the experimental value of stiffness is higher than the analytical value. The difference is attributed to the approximation adopted in joint stiffness value used in analytical model. In analytical model, stiffness value of the connection is constant. In actual the same is variable with respect to the load and displacement of the structure. It should be observed that the approximation in the analytical model

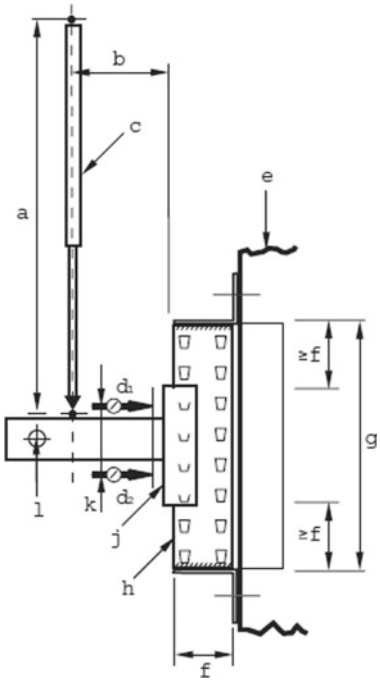


**Fig. 19** Typical test setup to find joint stiffness

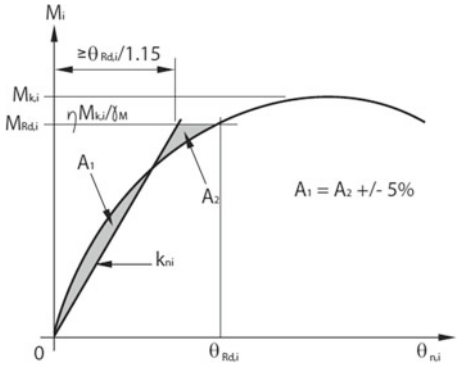


**Fig. 20** Typical M-Θ curve to find joint stiffness

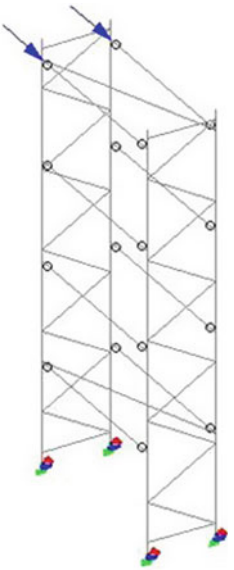

**Fig. 21** STAAD model for specimen 1

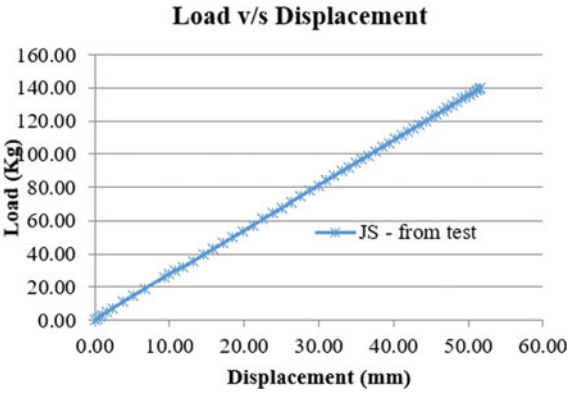


**Fig. 22** Load versus displacement curve for specimen 1 with joint stiffness value arrived as per EN 15,512

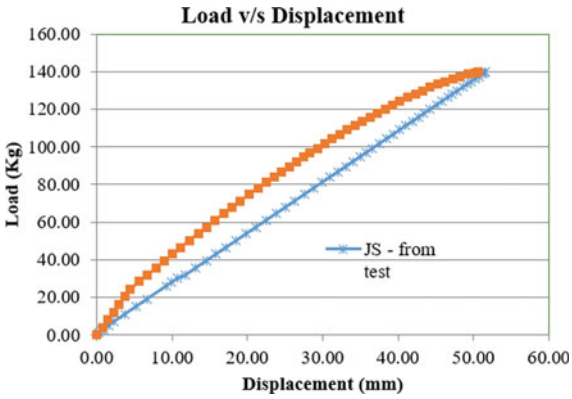


**Fig. 23** Comparison of load versus displacement curve for sample 1 for experimental and analytical study

is conservative. To match the load displacement behavior from analytical model with the experimental results, the joint stiffness used in the analytical model was iteratively adjusted, and a bilinear curve was plotted to match with the experimental results.

It should be noted that the actual stiffness of the system is variable, and it changes depending upon the displacement of the system. The overall stiffness of the system reduces after a particular displacement against a linear displacement value assumed in the model. However, it should be noted that the drop is within the limit approximated by the codes in evaluating the connection stiffness values (Fig. 24).

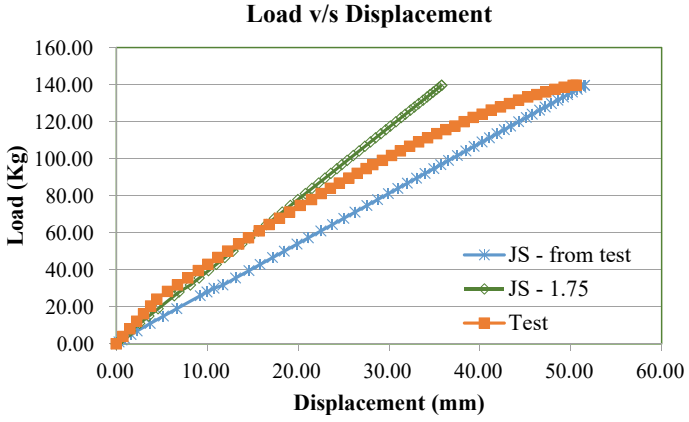


**Fig. 24** Comparison of load versus displacement curve for sample 1 for experimental and analytical

## 7 Conclusion

The structural behavior studied in terms of load displacement patterns has brought clarity on the effect of the beam-column connection, baseplate connection, and bracing system on the overall stiffness of the structure and the energy absorption capacity. The comparison of the load–displacement curves between experimental and analytical results gives confidence on the validity of the approximations adopted in the analysis model, being used for the design of racking systems. Normally the maximum lateral deflection permitted by the code is H/200 which works out to 31 mm. The fact that no collapse of the rack occurred till a displacement of 100 mm (more than 3 times maximum permitted displacement) was imposed can be considered as evidence of adequate ductility for the system tested which consisted of racking structure using cold-formed steel members and semi-rigid connections. The confidence on the performance of the structure is high with this detailed experimental study and the comparative analytical exercise.

## References

1. FEM 10.2.08 (2011) Recommendations for the design of static steel pallet racking in seismic conditions. European Racking Federation (ERF), UK
2. FEMA 460 (2005) Seismic considerations for steel storage racks located in wereas accessible to public. National Institute of Building Sciences, USA
3. European Commission (SEISRACKS2) (2014) Seismic behaviour of steel storage pallet racking systems. Directorate-General for Research and Innovation, Brussels
4. CEN, EN 15512 (2009) Steel static storage systems—adjustable pallet racking systems—principles for structural design. CEN European Committee for Standardization
5. RMI MH 16.1 (2012) Specification for the design, testing and utilization of industrial steel storage racks. Racks Manufacturers Institute, p 59
6. AS4084 (2012) Standards Australia. Sydney, Australia
7. Bernuzzi C (2015) European and United States approaches for steel storage pallet rack design, Part 1: discussions and general comparisons. Thin Walled Struct 97:308–320
8. Teh LH, Hancock GJ, Clarke MJ (2004) Analysis and design of double-sided high-rise steel pallet rack frames. J Struct Eng 130(7):1011–1021
9. Shah SNR et al (2016) State-of-the-art review on the design and performance of steel pallet rack connections. Eng Failure Anal 66:240–258
10. Abdel-Jaber MR, Beale G, Godley MHR (2006) A theoretical and experimental investigation of pallet rack structures under sway. J Constr Steel Res 62(1–2):68–80
11. Baldassino N, Zandonini R (2001) Numerical and experimental analysis of base-plate connections of steel storage pallet racks. In: Proceeding of XVIII conference C. T. A., Venezia, pp 127–136
12. Filiatrault A, Bachman R, Mahoney M (2006) Performance-based seismic design of pallet-type steel storage racks. Earthq Spectra 22(1):47–64
13. Bernuzzi C, Simoncelli M (2016) An advanced design procedure for the safe use of steel storage pallet racks in seismic zones. Thin-Walled Struct 109:73–87
14. Taucer F, Spacone E, Filippou FC (1991) A fiber beamcolumn element for seismic response analysis of reinforced concrete structures, Rep 91/17 EERC. University of California, Berkeley, USA

15. Bajoria KM, Talikoti RS (2006) Determination of flexibility of beam-to-column connectors used in thin walled cold-formed steel pallet racking systems. Thin-Walled Struct 44(3):372–380
16. Bajoria KM, Sangle KK, Talikoti RS (2010) 'Modal analysis of cold-formed pallet rack structures with semirigid connections.' J Constr Steel Res 6:428–441
17. Bernuzzi C, Castiglioni CA (2001) Experimental analysis on the cyclic behaviour of beam-to-column joints in steel storage pallet racks. Thin-Walled Struct 39(10):841–859
18. British Standards Institution, Eurocode 8: Design of structures for earthquake resistance-Part 1: General rules, seismic actions and rules for buildings, London, UK, BS EN, 1998-1, 2004
19. Wang L, Young B (2018) Behaviour and design of cold-formed steel built-up section beams with different screw arrangements. Thin-Walled Struct 131:16–32
20. Selvaraj S, Madhavan M (2019) Structural design of cold-formed steel face-to-face connected built-up beams using direct strength method. J Constr Steel Res 160:613–628
21. Selvaraj S, Madhavan M (2018) Geometric imperfection measurements and validations on cold-formed steel channels using 3D noncontact laser scanner. J Struct Eng 144(3):04018010
22. Usefi N, Sharafi P, Ronagh H (2019) Numerical models for lateral behaviour analysis of cold-formed steel framed walls: state of the art, evaluation and challenges. Thin-Walled Struct 138:252–285
23. Zeynalian M, Shahrasbi AZ, Riahi HT (2018) Seismic response of cold formed steel frames sheathed by fiber cement boards. Int J Civil Eng 16(11):1643–1653
24. Kechidi S, Macedo L, Castro JM, Bourahla N (2017) Seismic risk assessment of cold-formed steel shear wall systems. J Constr Steel Res 138:565–579
25. Selvaraj S, Madhavan M (2020) Structural behaviour and design of plywood sheathed cold-formed steel wall systems subjected to out of plane loading. J Constr Steel Res 166:105888
26. Selvaraj S, Madhavan M (2019) Investigation on sheathing-fastener connection failures in cold-formed steel wall panels. In: Structures, vol 20. Elsevier, pp 176–188
27. Selvaraj S, Madhavan M (2019) Bracing effect of sheathing in point-symmetric cold-formed steel flexural members. J Constr Steel Res 157:450–462
28. Selvaraj S, Madhavan M (2019) Flexural behaviour and design of cold-formed steel wall panels sheathed with particle cement board. J Constr Steel Res 162:105723
29. Selvaraj S, Madhavan M (2019) Improvements in AISI design methods for gypsum-sheathed cold-formed steel wall panels subjected to bending. J Struct Eng 145(2):04018243
30. Ye J, Jiang L (2018) Simplified analytical model and shaking table test validation for seismic analysis of mid-rise cold-formed steel composite shear wall building. Sustainability 10(9):3188
31. Selvaraj S, Madhavan M (2019) Behaviour of gypsum sheathed point-symmetric cold-formed steel members: assessment of AISI design method. In: Structures, vol 22. Elsevier, pp 76–97
32. Selvaraj S, Madhavan M (2019) Sheathing bracing requirements for cold-formed steel wall panels: experimental investigation. In: Structures, vol 19. Elsevier, pp 258–276
33. Selvaraj S, Madhavan M (2019) Sheathing braced design of cold-formed steel structural members subjected to torsional buckling. In: Structures, vol 20. Elsevier, pp 489–509
34. Selvaraj S, Madhavan M (2018) Studies on cold-formed steel stud panels with gypsum sheathing subjected to out-of-plane bending. J Struct Eng 144(9):04018136
35. Selvaraj S, Madhavan M (2019) Investigation on sheathing effect and failure modes of gypsum sheathed cold-formed steel wall panels subjected to bending. In: Structures, vol 17. Elsevier, pp 87–101

# Numerical Investigation into Buckling Behavior of Cold-Formed Purlin


**Ravi Dwivedi and A. Y. Vyavahare**

**Abstract** The aim of this chapter is to evaluate the moment capacities of the partially restrained cold-formed purlin subjected to uniformly distributed transverse uplift loading. A linear and non-linear finite element model is used to investigate the buckling behavior of purlins in the purlin sheeting system. The effect of translational and rotational restraint provided by sheeting to the purlin is taken into account by using two equivalent spring in the numerical model. Available experimental results from the literature are used to validate the finite element analysis. The moment capacities obtained from the numerical investigation are compared with current cold-formed design specifications. The comparison of moment capacities shows that current design provisions are over-conservative to predict buckling strength.

**Keywords** Cold-formed steel · Finite element analysis · Transverse distributed load · Direct strength method · Interactive buckling

## Notations

| | |
|---|---|
| $H$ | Total height of section |
| $B$ | Flange width of section |
| $B_l$ | Lip length |
| $O$ | Outer web of web height |
| $I$ | Inner Web of web height |
| $S$ | Length of stiffener |
| $R_i$ | Inside bend radius |
| $t$ | Thickness of section |
| $E$ | Young's Modulus of Elasticity |

R. Dwivedi (✉) · A. Y. Vyavahare
Visvesvaraya National Institute of Technology, Nagpur, India
e-mail: er.ravidwivedi.ce@gmail.com

A. Y. Vyavahare
e-mail: ayv@apm.vnit.ac.in



M. Madhavan et al. (eds.), *Proceedings of the Indian Structural Steel Conference 2020 (Vol. 1)*, Lecture Notes in Civil Engineering 318,
https://doi.org/10.1007/978-981-19-9390-9_30

$I_p$ Second moment of area of purlin
$L$ Length of specimen
$C_D$ Rotational stiffness
$t_s$ Thickness of sheeting
$F_y$ Yield stress of purlin and sheeting
$M_{\text{ne}}$ Nominal flexural strength for lateral-torsional buckling
$M_{\text{crl}}$ Critical elastic local buckling moment
$M_{\text{cre}}$ Critical elastic lateral-torsional buckling moment
$M_{\text{nlo}}$ Nominal flexural strength with consideration of local buckling
$M_y$ Yielding moment
$\lambda_l$ Slenderness ratio

## 1 Introduction

Cold-formed purlins are extensively used as the secondary members in modern light roof construction. Purlin sections are often subjected to local, distortional, and lateral-torsional buckling due to large width-to-thickness ratio. In case of uplift loading, the tension flange is attached to roof sheeting and the compressive flange is laterally free, hence buckling resistant of purlin section is reduced as compared to gravity loading. The roof sheeting provides full lateral and partial rotational restraint to the purlin under wind uplift loading. These restraints influence local, distortion, lateral, and interactive buckling [1].

Ye et al. [2] investigated the influence of translational and rotational restraint on the buckling behavior of purlin. Their study concluded that the influence of translational restraint is significant for local buckling and rotational restraint is significant for global buckling, and for distortional buckling both restraint provide mixed influence. Chu et al. [3, 4] presented numerical investigation on the local and distortional buckling behavior of cold-formed steel channel and zed section. Their study concluded that for local buckling, there is no practical difference in critical load between uniform bending and non-uniform bending case. For distortional buckling, critical load is higher for non-uniform bending case. Li et al. [5] proposed an analytical model to assess the buckling behavior of cold-formed zed purlin under non-uniform bending case. For uplift loading, full translational restraint and partial rotational restraint are considered in the model. To predict the accuracy of the presented analytical model, finite element analysis is carried out and compared with EN 1993-1-3. Their study concluded that both analytical models predict accurate bending stress for medium and long beams but over-predicted stress for short beam. Ren et al. [6] proposed an analytical model to assess the buckling behavior of cold-formed channel purlin under non-uniform bending case for uplift loading. A validated analytical model is compared with EN 1993-1-3. The comparison shows that the bending stress calculated by EN 1993-1-3 is over-predicted. Yang and Liu [7] performed experiments on sigma purlin subjected to gravity and uplift loading. It is observed that failure

mode is highly related to the thickness of the purlin section. Ren et al. [8] presented a linear and non-linear finite element model to investigate the buckling behavior of cold-formed zed purlin subjected to uplift loading. Both models were validated against available experimental results from the literature. The analysis is carried out for different member length which shows local, shear, distortional, and lateral-torsional buckling for very short, short, medium, and long members respectively. After that, a parametric study is conducted for five different sections with various member length and a modified buckling interaction equation is proposed using the direct strength method. Bai et al. [9] proposed a non-linear twisting model of channel purlin under uplift loading. The warping torsional and diaphragm effect is considered in the model. The proposed direct strength method shows good agreement with existing methodologies such as the R-factor approach and the Eurocode method. Selvaraj and Madhavan [10–12] recently worked on various aspects of cold-formed steel structures related to behavior, design, and retrofitting. Foster and Gardener [13] worked on development of analytical design method against lateral-torsional buckling that relates to the current European approach. Rasmussen and Fan [14] and Selvaraj and Madhavan [15] worked on experimental investigations of geometric imperfections.

This chapter presents a numerical investigation of cold-formed purlin subjected to uplift loading. To validate the numerical model, the available experimental result on sigma purlin [7] is used. The effect of translational and rotational restraint is taken into account in numerical model.

The finite element program ABAQUS is used to perform linear and non-linear finite element analysis to determine critical buckling load and ultimate load. The moment capacity obtained from finite element analysis is compared with the predicted capacity of North American Specification. The moment capacity is calculated using the Direct Strength Method (DSM) and input parameters for the direct strength method are calculated from the finite strip analysis using CUFSM software. The cross-section used in ABAQUS and CUFSM software is shown in Fig. 1.

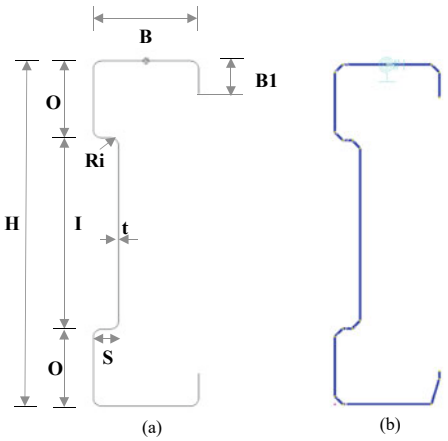


**Fig. 1** Cross-section used in ABAQUS (**a**) and CUFSM (**b**)

## 2 Current Design Rule—AISI S100:16

North American Specification [16] predicts nominal flexure capacity under wind uplift loading using the R-factor approach. The R-factor decreases in accordance with increasing cross-section depth and is applicable within prequalified ranges of cross-section dimensions and metal panel thicknesses.

The nominal flexural capacity ($M_n$) of purlin with the tension flange attached to sheeting and the compression flange laterally unbraced is calculated from section I6.2.1 of AISI S100:16 using Eq. 1.

$$M_n = M_{\text{nlo}} \tag{1}$$

where

$R$ = A value obtained from table I6.2.1-2 of North American Specification
$M_{\text{nlo}}$ = Nominal flexural strength with consideration of local buckling only.

Nominal flexural strength $M_{\text{nlo}}$ will be calculated from section F3 of North American Specification.

According to section F3 of North American Specification, $M_{\text{nlo}}$ will be calculated as follows:

(a) For $\lambda_l < 0.776$,

$$M_{\text{nlo}} = M_{\text{ne}} \tag{2}$$

(b) For $\lambda_l > 0.776$,

$$M_{\text{nlo}} = \left[1 - 0.15\left(\frac{M_{\text{crl}}}{M_{\text{ne}}}\right)^4\right]\left(\frac{M_{\text{crl}}}{M_{\text{ne}}}\right)^4 M_{\text{ne}} \tag{3}$$

where

$$\lambda_l = \sqrt{\frac{M_{\text{ne}}}{M_{\text{crl}}}} \tag{4}$$

$M_{\text{ne}}$ = Nominal flexural strength for lateral-torsional buckling.
$M_{\text{crl}}$ = Critical elastic local buckling moment.

Nominal flexural strength for lateral-torsional buckling will be calculated from section F2 of North American Specification.

According to section F2 of North American Specification, $M_{\text{ne}}$ will be calculated as follows:

(c) For $M_{\text{cre}} < 0.56\ M_y$,

$$M_{\text{ne}} = M_{\text{cre}} \tag{5}$$

(d) For 2.78 $M_y \geq M_{\text{cre}} \geq 0.56\ M_y$,

$$M_{\text{ne}} = \frac{10}{9} M_y \left[1 - \frac{10 M_y}{35 M_{\text{cre}}}\right] \tag{6}$$

(e) For $M_{\text{cre}} \geq 2.78\ M_y$,

$$M_{\text{ne}} = M_{\text{y}} \tag{7}$$

Finite strip program CUFSM is used to obtain critical buckling moment for local buckling ($M_{\text{crl}}$) and lateral-torsional buckling ($M_{\text{ne}}$). These critical buckling moments then used to obtain nominal flexural capacity under direct strength method (DSM) format.

## 3 Finite Element Modeling

The finite element program ABAQUS 16.3 is used to analyze the cold-formed section subjected to uniformly distributed uplift loading. To assess the buckling behavior of the section, a four-node doubly curved thin shell element (S4R) with reduced integration was used. Meshing size of approximately 10 mm × 10 mm for both flange and web elements were used. The simulation of boundary and loading conditions is the essential part of Finite Element (FE) models. Simply supported boundary conditions are considered, which are similar to the boundary condition used in the experiment setup [7]. To reduce the computational time, the symmetric boundary condition is assigned at mid-span and simply supported boundary condition is assigned at other end for half symmetry model. The simplified model is used to represent lateral and rotational spring restraint. Full lateral restraint is applied at the web-flange intersection by making a degree of freedom in the lateral direction to zero. Rotational stiffness is assigned at the screw location point to represent the rotational spring restraint (Fig. 2).

## 4 Finite Element Analysis—Validation

### *4.1 Validation with Experimental Data*

Experimental study on the sigma section subjected to wind uplift loading carried out by Yang and Liu [7] was used to validate the finite element model used in this study. The material properties of the beam are assumed as that, Young's modulus $E$

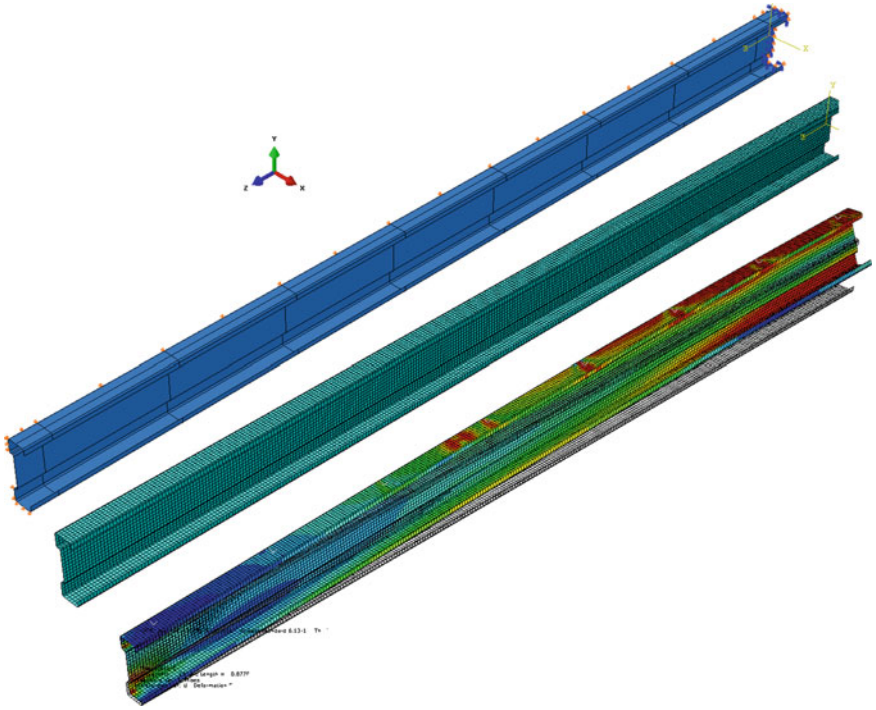

**Fig. 2** Boundary condition, meshing and deformed shape

$= 210$ GPa and Poisson's ratio $\nu = 0.3$. Section properties of the tested specimens are shown in Table 1. Ultimate moment capacity obtained from finite element analysis is shown in Table 2.

**Table 1** Section properties of tested specimen

| Section | $H$ (mm) | $B$ (mm) | $B_l$ (mm) | $O$ (mm) | $I$ (mm) | $S$ (mm) | $R_i$ (mm) | $t$ (mm) |
|---|---|---|---|---|---|---|---|---|
| 20012 | 200 | 62.5 | 20 | 45 | 110 | 16 | 4 | 1.2 |
| 20016 | 200 | 62.5 | 20 | 45 | 110 | 16 | 4 | 1.6 |
| 20025 | 200 | 62.5 | 20 | 45 | 110 | 16 | 4 | 2.5 |

**Table 2** Comparison of ultimate moment capacity from test and FEA

| Section | $E$ (GPa) | $F_y$ (MPa) | $I_p$ (cm$^4$) | $L$ (mm) | $M_{\text{Test}}$ (kNm) | $M_{\text{FEA}}$ (kNm) | $M_{\text{Test}}/M_{\text{FEA}}$ |
|---|---|---|---|---|---|---|---|
| 20012 | 206 | 471 | 265 | 5942 | 5.4 | 5.05 | 1.02 |
| 20016 | 214 | 433 | 339 | 5942 | 7.4 | 7.11 | 1.04 |
| 20,025 | 207 | 447 | 508 | 5942 | 12.1 | 11.9 | 1.02 |

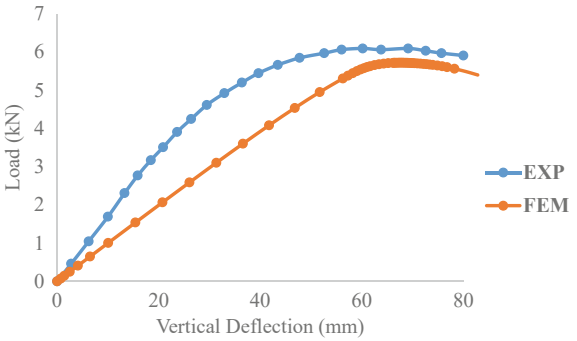


**Fig. 3** Load deformation curve for section 20012

The load deformation curve for all three specimens from experimental results is plotted with the comparison of the curve obtained from finite element analysis shown in Figs. 3, 4, and 5. The ultimate load obtained from finite element analysis is close to experimental value except the deflection. The vertical deflection is measured in finite element model at mid-span of the specimen.

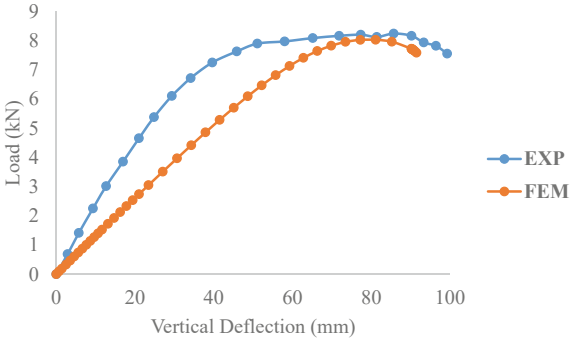


**Fig. 4** Load deformation curve for section 20016

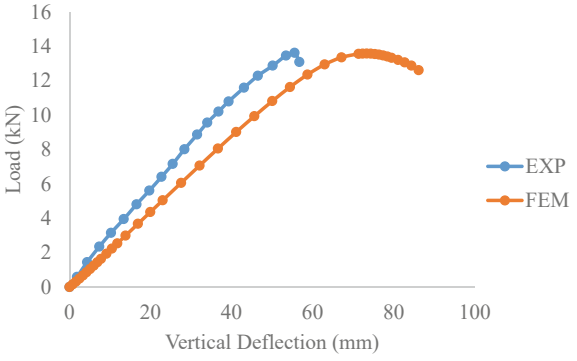


**Fig. 5** Load deformation curve for section 20025

Ultimate load obtained from finite element analysis is 93%, 96%, and 98% of the experimental value of sections 20012, 20016, and 20025 respectively. Load deformation curve shows that the finite element model is satisfactory to predict the ultimate load of purlin subjected to uplift loading. Lateral-torsional buckling failure mode was observed in all three sections.

## *4.2 Validation with Design Specifications*

Moment capacity obtained from finite element results is compared with the moment capacity obtained using the direct strength method [17]. The critical buckling moments for local, distortional, and global buckling are the input parameters for the direct strength method. These input parameters are calculated using the CUFSM finite strip program [18]. The comparison of ultimate moment capacities is shown in Table 3.

The local, distortion, and global buckling mode and load factor obtained from the signature curve using CUFSM software are plotted and shown in Fig. 6. Load factor for sections 20012, 20016, and 20025 are 0.43, 0.61, and 0.91 respectively. Nominal flexural strength for lateral- torsional buckling is calculated using Eqs. 5 and 6. These nominal strengths are multiplied by the R-factor of channel section given in table I6.2.1-1 of North American Specification.

**Table 3** Comparison of ultimate moment capacity from AISI specification and FEA

| Section | $E$ (GPa) | $F_y$ (MPa) | $I_p$ (cm$^4$) | $L$ (mm) | $M_{\text{FEA}}$ (kNm) | $M_{\text{AISI}}$ (kNm) |
|---|---|---|---|---|---|---|
| 20012 | 206 | 471 | 265 | 5942 | 5.05 | 3.4 |
| 20016 | 214 | 433 | 339 | 5942 | 7.11 | 5.7 |
| 20025 | 207 | 447 | 508 | 5942 | 11.9 | 11.4 |

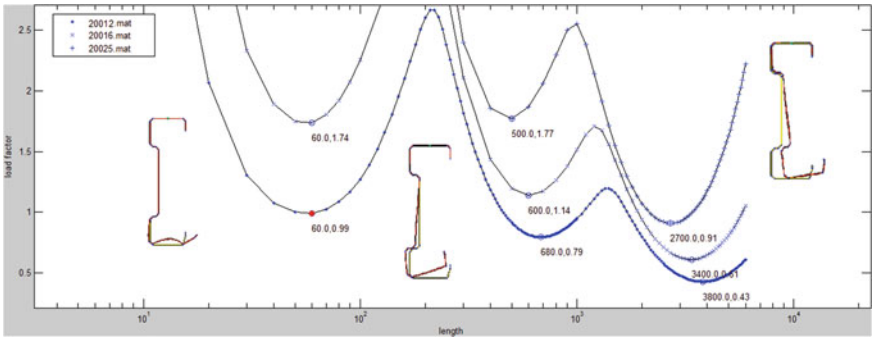


**Fig. 6** Buckling curve and local, distortional, and lateral torsion buckling mode of all three section with rotational spring stiffness $k\varphi = 308$ Nm/m/rad

**Table 4** Rotational stiffness and buckling load of sections with varying screw spacing

| Section | $E$ (GPa) | $F_y$ (MPa) | $I_p$ (cm$^4$) | $L$ (mm) | Screw spacing | $C_D$ (Nm/m/rad) | Buckling load (kN) |
|---|---|---|---|---|---|---|---|
| 20012 | 206 | 471 | 265 | 5942 | 200<br>250<br>300 | 1154<br>923<br>692 | 8.87<br>8.58<br>8.10 |
| 20016 | 214 | 433 | 339 | 5942 | 200<br>250<br>300 | 1154<br>923<br>692 | 14.3<br>13.7<br>12.7 |
| 20025 | 207 | 447 | 508 | 5942 | 200<br>250<br>300 | 1154<br>923<br>692 | 27.5<br>26.1<br>23.6 |

## 5 Parametric Study

The validated finite element model is used for the parametric study to calculate the buckling load of cold-formed purlin with varying rotational stiffness provided by roof sheeting. Rotational stiffness is calculated using an analytical equation [19], which is given in (Table 4).

$$C_D = \frac{E}{\frac{\beta h_T^2}{n t_s^3 a^2} + \frac{a}{3I_p} + \frac{b}{I_p}} \tag{8}$$

In the Eq. (8), $a$ and $b$ are the half flange width when screw is connected at the center of flange, $n$ is the number of screws connected in 1 m length, $\beta$ is the coefficient dependent on the screw location, $h_T$ is assumed to be equal to flange width, and $t_s$ denotes the thickness of roof sheet.

## 6 Result and Discussion

The non-linear finite element (FE) analysis is carried out to predict the ultimate moment capacity of cold-formed purlin. FE results are compared with the experimental results and design specification. The comparison of FE result with design specification shows that North American Specification predicts conservative strength in some cases and over-conservative strength in other cases. In the design specification, R-factor is available for C and Z section and due to lack of availability of the R-factor of the sigma section, the factor for the C section is used to calculate the ultimate capacity of sigma section. This may be the reason for difference in the ultimate moment capacities between FE result and design specifications.

The validated finite element model is then used to carry out the parametric study of the sigma section with different rotational stiffness and section thickness. The linear finite element analysis is used to determine the buckling load of the sigma section

with full lateral restraint and partial rotational restraint. It is observed that buckling load is decreased with low to higher screw spacing. This difference in buckling load is significant for the section having a higher thickness as compared to the section having lower thickness.

## 7 Conclusion

The numerical investigation on the cold-formed sigma section is reported in this study. It is observed that the R-factor method provided in current North American Specification prediction over-conservative strength. Hence, calibration of the R-factor is required for channel and zed sections, and research is needed to develop the R-factor for the sigma section. The effect of rotational restraint is significant in cold-formed members subjected to lateral-torsional buckling mode. The buckling load is calculated from linear finite element analysis for different rotational stiffness by varying screw spacing. The variation of buckling load is moderate between 200 and 250 mm screw spacing for section having lower section thickness and it is significant between 200 and 300 mm spacing for section having higher thickness.

## References

1. Ye ZM, Kettle RJ, Li LY, Schafer BW (2002) Buckling behavior of cold-formed zed-purlins partially restrained by steel sheeting. Thin-Walled Struct 40(10):853–864
2. Ye ZM, Kettle R, Li LY (2004) Analysis of cold-formed zed-purlins partially restrained by steel sheeting. Comput Struct 82(9–10):731–739
3. Chu XT, Ye ZM, Kettle R, Li LY (2005) Buckling behaviour of cold-formed channel sections under uniformly distributed loads. Thin-walled Struct 43(4):531–542
4. Chu XT, Ye ZM, Li LY, Kettle R (2006) Local and distortional buckling of cold-formed zed-section beams under uniformly distributed transverse loads. Int J Mech Sci 48(4):378–388
5. Li LY, Ren C, Yang J (2012) Theoretical analysis of partially restrained zed-purlin beams subjected to up-lift loads. J Constr Steel Res 70:273–279
6. Ren C, Li LY, Yang J (2012) Bending analysis of partially restrained channel-section purlins subjected to up-lift loadings J Constr Steel Res 72:254–260. https://doi.org/10.1016/j.jcsr.2012.01.001
7. Yang J, Liu Q (2012) An experimental study into flexural behaviour of sigma purlins attached with roof sheets. Eng Struct 45:481–495
8. Ren C, Zhao X, Chen Y (2016) Buckling behaviour of partially restrained cold-formed steel zed purlins subjected to transverse distributed uplift loading. Eng Struct 114:14–24
9. Bai F, Yang N, Zhang H, Wang X (2018) A modified direct strength method for nonlinear twisting model of simply-supported C-section purlins. J Constr Steel Res 150:384–391
10. Selvaraj S, Madhavan M (2018) Retrofitting of structural steel channel sections using cold-formed steel encasing channels. J Perform Constr Facil 32(4):04018049
11. Selvaraj S, Madhavan M (2019) Strengthening of laterally restrained steel beams subjected to flexural loading using low-modulus CFRP. J Perform Constr Facil 33(3):04019032

12. Selvaraj S, Madhavan M (2019) Structural design of cold-formed steel face-to-face connected built-up beams using direct strength method. J Constr Steel Res 160:613–628
13. Foster ASJ, Gardner L (2016) Stability of steel beams using the continuous strength method. Thin-Walled Struct 100:1–13
14. Niu S, Rasmussen KJR, Fan F (2015) Local–global interaction buckling of stainless steel I-beams. I: experimental investigation. J Struct Eng 141(8):04014194
15. Selvaraj S, Madhavan M (2018) Geometric imperfection measurements and validations on cold-formed steel channels using 3D noncontact laser scanner. J Struct Eng 144(3):04018010
16. American Iron and Steel Institute (2016) North American specification for the design of cold-formed steel structural members. American Iron & Steel Institute, Committee of Steel Plate Producers & Committee of Stainless Steel Producers
17. Schafer BW (2008) The direct strength method of cold-formed steel member design. J Constr Steel Res 64(7–8):766–778
18. Schafer B (2001) Elastic buckling analysis of thin-walled members using the classical finite strip method, CUFSM version 4. Johns Hopkins University
19. Zhao C, Yang J, Wang F, Chan AH (2014) Rotational stiffness of cold-formed steel roof purlin–sheeting connections. Eng Struct 59:284–297

# Damage Detection in Base-Isolated Steel Structure Using Singular Spectral Analysis


**Shivam Ojha, Lavish Gobind Pamwani, and Amit Shelke**

**Abstract** The role of structural health monitoring (SHM) in detection of post-earthquake damage to buildings is well established, and the same is extended to seismically isolated buildings in this research. In this study, a steel structure was considered with the isolation system which consists of elastomeric bearings. Numerical models were developed using SAP2000. The damage in the building was introduced by reducing the stiffness of all isolators in both horizontal directions unequally. After nonlinear response history analysis, the responses at two different floor levels of the healthy and damaged isolated superstructure were obtained, which are filtered using singular spectral analysis (SSA) and reconstructed using the dominant time series. The reconstructed responses were used to form a matrix that is decomposed, and singular vectors are obtained. The difference in the angle made by the singular vector in two-dimensional space obtained for healthy and damaged cases is the parameter for damage detection. SSA has successfully filtered the output responses, and the proposed algorithm has efficiently used the reconstructed responses to identify the damage in the structure.

**Keywords** Base isolation · Structural health monitoring · Singular spectral analysis · Steel structure

S. Ojha (✉) · L. G. Pamwani · A. Shelke
Department of Civil Engineering, Indian Institute of Technology Guwahati, Guwahati, India
e-mail: shivam18@iitg.ac.in

L. G. Pamwani
e-mail: p.lavish@iitg.ac.in

A. Shelke
e-mail: amitsh@iitg.ac.in



M. Madhavan et al. (eds.), *Proceedings of the Indian Structural Steel Conference 2020 (Vol. 1)*, Lecture Notes in Civil Engineering 318,
https://doi.org/10.1007/978-981-19-9390-9_31

## 1 Introduction

Under seismic excitation, the performance of the steel structures is known worldwide. Its performance is the primary reason that leads to its growth in the construction. However, among all the steel constructions in the last few decades, the steel constructions with an isolated base system deliver the best performance under seismic excitation [8].

Base isolation is a passive control method, and it increases the time period of the building resulting in the reduction of seismic forces to be resisted by the building [9, 11]. Isolator bearings are mainly of two types: elastomeric bearings and sliding bearings; the former includes lead rubber bearing, natural rubber bearing with low or high damping, and the latter includes single, double, or triple concave friction pendulum [3]. Despite the building possessing base isolation, a good amount of seismic force transfers to the structure under a massive earthquake causing the behavior of building to shift in the nonlinear range leading to the formation of hinges [15, 17]. Moreover, the considerable uncertainties in the ground motions lead to damage in the structure as well as in the isolators. Hence, the regular monitoring of the isolation system, as well as the superstructure, should be carried out. Here, structural health monitoring plays a vital role and helps to identify the damage. Damage tracking and reliability analysis of base-isolated structures are the growing concern of the researchers [16, 19, 20].

Singular spectral analysis is one of the techniques in health monitoring used to decompose the time series into smaller dimensional space signals [2, 7, 12]. The original time series contains valuable information about modal parameters as well as noise. When time series gets decomposed, the required modal parameter will be extracted and is utilized for further processing. The small dimensional signals can be used to prepare a damage index parameter, which quantifies the damage in the system.

In our present study, a National Earthquake Hazard Reduction Program (NEHRP) standardized building from National Institute of Standards and Technology (NIST) Technical Note 1863-1, building Id MC8 is selected and modified as per the requirement for the base isolation [6]. The base isolation system consists of 28 elastomeric bearings, which are designed as per ASCE/SEI 7-16 [1]. Numerical modeling is carried out in the available commercial finite element package to perform the nonlinear analysis. For the nonlinear time-history analysis, a suite of seven earthquake ground motions was selected from the PEER NGA West database and properly scaled to get consistent with the target response spectrum of city Los Angeles [13]. The interest here is to detect the damage if it occurs in the isolators rather than the superstructure. Therefore, the damage has been introduced in the selected isolators by reducing their elastic and post-elastic stiffness. The responses of the isolate structures for healthy and damaged states are recorded and are processed further for damage identification.

## 2 Building Description

For the study, building Id MC8 is selected from NIST Technical Note 1863-1 and modified to satisfy the requirements as per ASCE/SEI 7-16. This building is assumed to be situated in city Los Angeles, USA. The coordinates of the site are 34.05° N and 118.24° W. The building plan is rectangular in shape with dimensions 45.72 × 30.48 m and is symmetric about two planar axes. The building plan with reference lines is shown in Fig. 1.

The primary beams (connecting columns) at the base level are composed of section W 14 × 311, and section W 16 × 26 is used for all other internal beams. All the corner beams above base level are made with section W 16 × 26, and the internal beams are of section W 14 × 22 along grid lines 1–6, while section details along grid lines B, C, D, E are provided in Fig. 1. The section details along sections 1–1 and A–A are provided in Fig. 2, while section details for the internal columns are provided in Table 1.

The building is base-isolated with the help of a total 28 elastomeric bearings, out of which 16 bearings are of lead rubber type and 12 are of natural rubber type. The layout of the isolators is shown in Fig. 3.

Elastic stiffness before yield point and post-elastic stiffness are two important parameters that govern the behavior of the isolator under excitation. Elastic stiffness

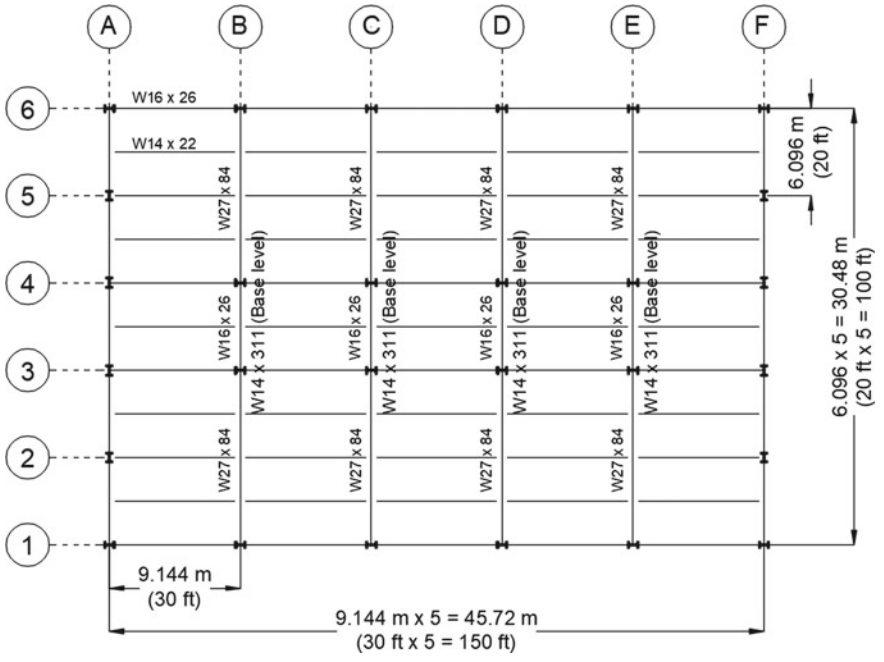


**Fig. 1** Plan of the isolated building with dimensions and reference lines

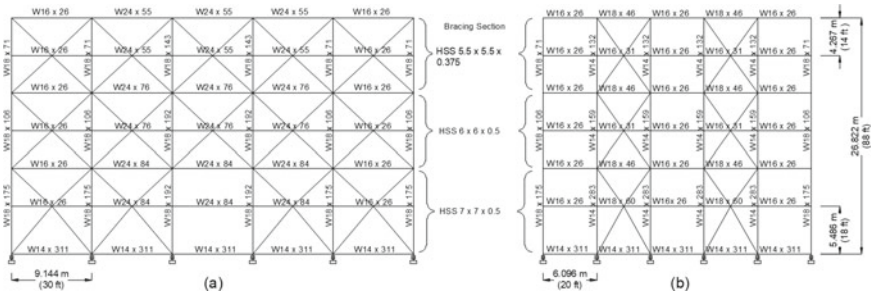


**Fig. 2** Elevation at **a** section 1–1 **b** section A–A with framed section detailing

**Table 1** Column section details for the internal columns

| Level | Column section |
|---|---|
| Floor 5 to roof | W14 × 132 |
| Floor 4 to floor 5 | W14 × 132 |
| Floor 3 to floor 4 | W14 × 159 |
| Floor 2 to floor 3 | W14 × 159 |
| Floor 1 to floor 2 | W14 × 283 |
| Base to floor 1 | W14 × 283 |

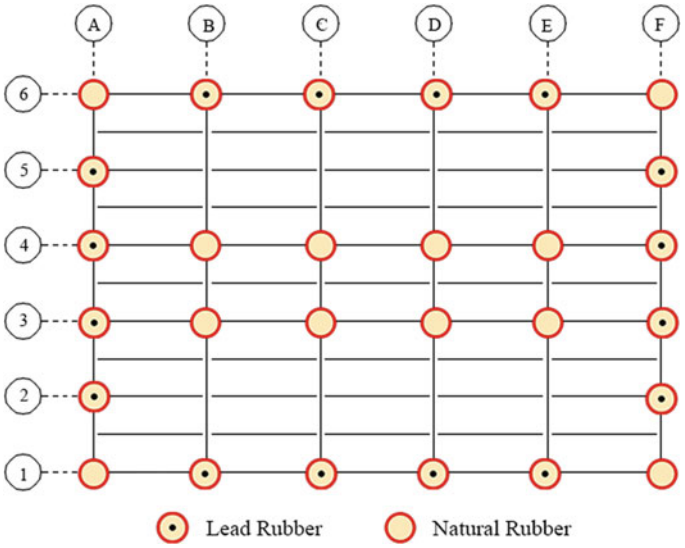


**Fig. 3** Layout of isolators showing lead rubber and natural rubber isolators configuration

**Table 2** Isolator properties used for the numerical modeling

| Parameter | Lead rubber isolator | Natural rubber isolator |
|---|---|---|
| Elastic stiffness | 24.45 kN/mm | 3.31 kN/mm |
| Yield strength | 310.57 kN | 42.08 kN |
| Post elastic stiffness | 0.97 kN/mm | 0.96 kN/mm |

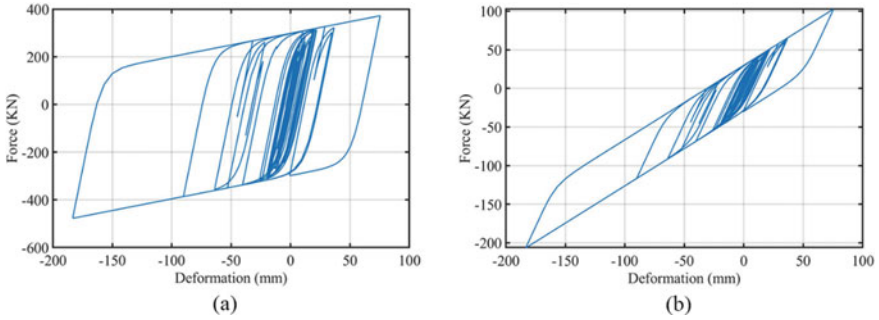


**Fig. 4** Force versus displacement curve under unidirectional seismic excitation of **a** lead rubber isolator **b** natural rubber isolator

is kept high in comparison to post-elastic stiffness in order to resist the small wind loads. The properties of both kinds of isolators used in modeling are listed in Table 2. Isolators are modeled using link elements with the material property as bilinear hysteretic evolution. Figure 4 shows the hysteretic loop of the isolators under a sample unidirectional ground motion, i.e., scaled horizontal component of motion labeled as a record sequence number (RSN) 549 from PEER NGA West database.

## 3 Selection of the Ground Motions

It is recommended to use a suite of seven earthquake ground motions consistent with the target response spectrum (Sect. 17.3 ASCE 7-16). The target spectrum and ground motions are obtained from the PEER NGA West database. The parameters used for the development of the target response spectrum for the considered site are listed in Table 3.

The base isolation system is used to shift the time period in order to reduce the seismic forces in the system, and the same results are observed in the presented case. The observed time period of the first mode of vibration for the building without base isolators and the isolated building is 1.007 s and 2.525 s, respectively. The shift in time period leads to the reduction of peak ground acceleration (normalized with gravitational acceleration) from 0.851 to 0.339 as shown in Fig. 5. The modal time

**Table 3** Parameters used for the development of the target spectrum

| Parameter | Value |
|---|---|
| Design reference code | ASCE/SEI 7-16 |
| Risk category | II |
| Site class | D |
| $S_{MS}$ | 2.43 |
| $S_{M1}$ | 1.27 |
| $S_{DS}$ | 1.62 |
| $S_{D1}$ | 0.85 |

period and frequency of the first six modes of vibration for the non-isolated and isolated buildings are listed in Table 4.

The selected ground motions are scaled by multiplying a suitable factor to make the square root of sum of squares (SRSS) mean of the response spectrum generated from their horizontal components consistent with the target spectrum. The selected ground motions with scale factors are listed in Table 5. The response spectra generated

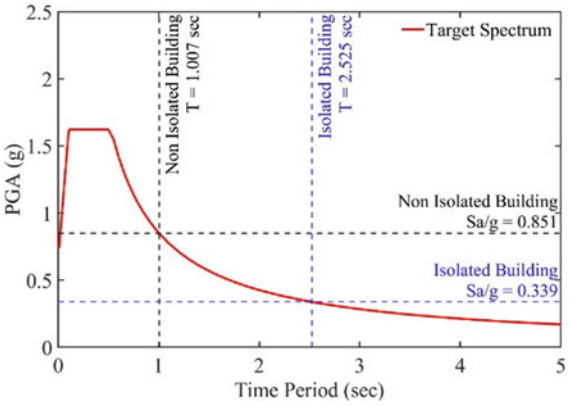


**Fig. 5** Target response spectrum showing the reduction of PGA due to shifting in the time period

**Table 4** Time period and natural frequency of the first six modes of vibration of non-isolated and isolated building

| Mode of vibration | Non-isolated building | | Isolated building | |
|---|---|---|---|---|
| | Time period (sec) | Frequency (Hz) | Time period (sec) | Frequency (Hz) |
| Mode 1 | 1.007 | 0.992 | 2.525 | 0.395 |
| Mode 2 | 0.522 | 1.913 | 2.387 | 0.418 |
| Mode 3 | 0.460 | 2.169 | 2.017 | 0.495 |
| Mode 4 | 0.383 | 2.608 | 0.626 | 1.597 |
| Mode 5 | 0.381 | 2.624 | 0.383 | 2.606 |
| Mode 6 | 0.375 | 2.664 | 0.381 | 2.622 |

**Table 5** Details of selected ground motions with scale factors

| Response sequence number | Event | Scale factor |
|---|---|---|
| RSN 175 | Imperial Valley-06 | 3.70 |
| RSN 187 | Imperial Valley-06 | 4.98 |
| RSN 461 | Morgan Hill | 2.11 |
| RSN 549 | Chalfant Valley-02 | 3.64 |
| RSN 848 | Landers, Coolwater | 2.60 |
| RSN 864 | Landers, Joshua Tree | 1.61 |
| RSN 1106 | Kobe Japan | 2.11 |

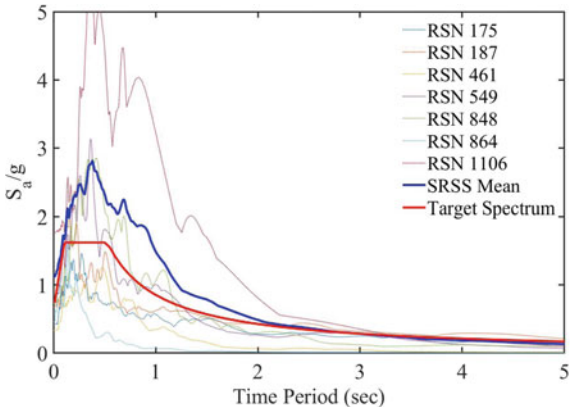


**Fig. 6** SRSS mean is above the target spectrum in the range of superstructure time period

from one horizontal component are plotted with the SRSS mean, and SRSS mean is plotted against the target spectrum and is shown in Fig. 6

## 4 Singular Spectral Analysis

Singular spectrum analysis (SSA) is used for modeling a time-history data and extracting the important signals from it. SSA is a non-parametric method, and it requires no prior information regarding the system under consideration [14]. SSA decomposes a time-history data into three different types of components, namely; trend component, oscillatory components, and noise components [5]. The unwanted/vague information (noise) can be removed from the time-series signal with the help of SSA as a filtering technique. The theoretical explanation of the SSA algorithm can be found in various literatures [5, 18]. In order to perform the SSA of a time-series signal $x(t) = \{x(1), x(2), ..., x(n)\}$, typically, four necessary steps are to be followed.

**Step-1**: Forming the trajectory matrix of $x(t)$.
The trajectory matrix is formed from a time-series signal by implementing the method of delays. The method of delays generally reconstructs the phase space matrix by concatenating the lagged copies of the measured time-series signal. Each and every point of a phase space will correspond to the dynamic behavior of a system. The phase space matrix, when reconstructed with an appropriate choice of time delay and embedding dimension, is referred to as a trajectory matrix. The trajectory matrix with an optimal time delay as $\tau$ and optimal embedding dimension $\alpha$ is denoted by:

$$X = \frac{1}{\sqrt{N}} \begin{bmatrix} x(1) & x(1+\tau) & \cdots & x(1+(N-1)\tau) \\ x(2) & x(2) & \cdots & x(2) \\ \vdots & \vdots & \ddots & \vdots \\ x(N-(\alpha-1)\tau) & x(N-(\alpha-2)\tau) & \cdots & x(N) \end{bmatrix}.$$

The optimal time delay can be obtained with the help of average mutual information function [4], and the embedding dimension is found out using the method of false nearest neighbors [10].
**Step-2**: Singular value decomposition of the trajectory matrix.
Let $A = X^T X$ be the lagged covariance matrix. The singular value decomposition (SVD) of $X$ can be formulated as $X = U\lambda V^T$, where $U$ and $V$ are right and left singular vectors of trajectory matrix and $\lambda$ is a diagonal matrix consisting of singular values of the trajectory matrix. Now with the help of definition of $X$ and $A$, a new formulation of $A$ can be expressed as:

$$A = V\lambda^T \lambda V^T = V \Lambda V^T,$$

where $\Lambda$ denotes the diagonal matrix of the squared singular values, and the right singular vectors ($V$) of trajectory matrix can be obtained by evaluating the eigenvectors of $A$. Also, the singular values of the trajectory matrix can be obtained by evaluating the square roots of the eigenvalues of $A$.
**Step-3**: To obtain the principal components of the trajectory matrix.
The principal components are evaluated by projecting the original time-series data on the obtained eigenvectors from SVD as follows:

$$pc_i^k = \sum_{j=1}^{\alpha} x_{i+(j-1)\tau} v_j^k, \text{ for } i = 1, 2, \ldots, N-\alpha+1,$$

where $v_j^k$ represents the $k$th eigenvector's $j$th component.
**Step-4**: Generation of reconstructed components (RCs).
The reconstruction of an RC can be done by the convolution of a single principal component with the corresponding singular vector [18]. Therefore, to reconstruct a particular component, it is important to select the principal component and its corresponding vector accurately. Moreover, by selecting dominant principal component,

the important and noise-free information can be reconstructed from the original time series. In case, if all the principal components are employed for reconstruction, it will result in regeneration of the original response.

## 5 Proposed Algorithm

The algorithm used in this research is based on the filtering of the output response using singular spectral analysis and the reconstruction of the response using the dominant time series. The selection of the dominant time series is based on their normalized correlation with the original output response. The reconstructed responses are then used to form the matrix that decomposed using singular vector decomposition, getting out the singular vector whose angle in two-dimensional space gives us the damage parameter for damage identification. These sequential steps of the algorithm are shown in Fig. 7.

## 6 Results and Discussion

### *6.1 Recording Acceleration Responses*

The isolated building was first excited by ground motions, and the response of the diaphragm centroid at the base level and roof level was recorded. Then, the damage was introduced in all the base isolators by reducing their elastic and post-elastic stiffness in two horizontal directions ($X$, $Y$) unequally. The stiffness considered for the healthy and damaged states is provided in Table 6. The damaged isolated building was then excited, and responses were recorded. The author has discussed the results with one ground motion, i.e., RSN 187 in detail, while the results for all the cases are provided.

The acceleration response recorded in the time domain needs to be converted to the frequency domain in order to evaluate the exciting frequencies. The responses recorded on diaphragm centroid at roof level and base level for healthy and different damaged states excited under RSN 187 are presented in Fig. 8.

### *6.2 Filtering and Reconstruction Using Singular Spectral Analysis*

A response signal consists of time series with multiple frequencies, out of which some are either high correlated with the signal or less correlated. For separating out the time series with these frequencies, first time-lagged trajectory matrix **Y** was developed

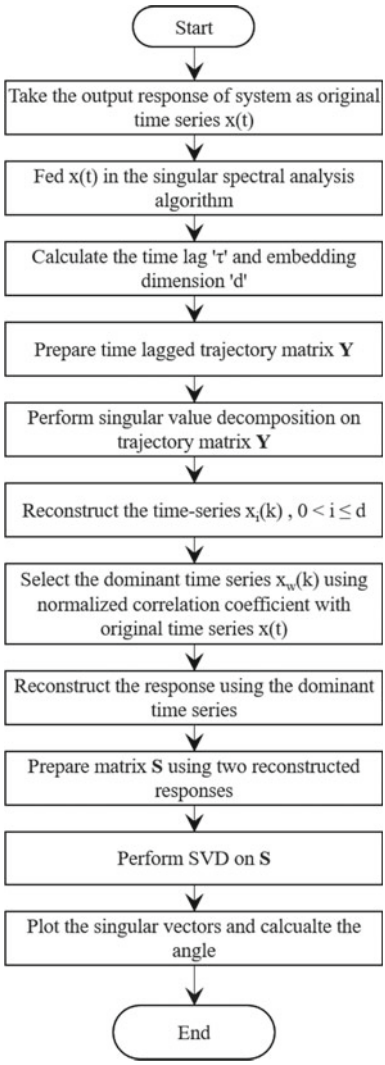


**Fig. 7** Flowchart showing the sequential steps of the algorithm

**Table 6** Elastic and post-elastic stiffness of isolators for healthy and damaged cases

| | Lead rubber | | | | Natural rubber | | | |
|---|---|---|---|---|---|---|---|---|
| | Elastic stiffness (kN/mm) | | Post elastic stiffness (kN/mm) | | Elastic stiffness (kN/mm) | | Post elastic stiffness (kN/mm) | |
| Direction | *X* | *Y* | *X* | *Y* | *X* | *Y* | *X* | *Y* |
| Healthy | 24.45 | 24.45 | 0.98 | 0.98 | 3.31 | 3.31 | 0.97 | 0.97 |
| Damage 1 | 22.50 | 23.47 | 0.90 | 0.94 | 3.05 | 3.18 | 0.89 | 0.93 |
| Damage 2 | 21.03 | 22.74 | 0.84 | 0.91 | 2.85 | 3.08 | 0.83 | 0.90 |
| Damage 3 | 19.56 | 22.01 | 0.78 | 0.88 | 2.65 | 2.98 | 0.78 | 0.87 |

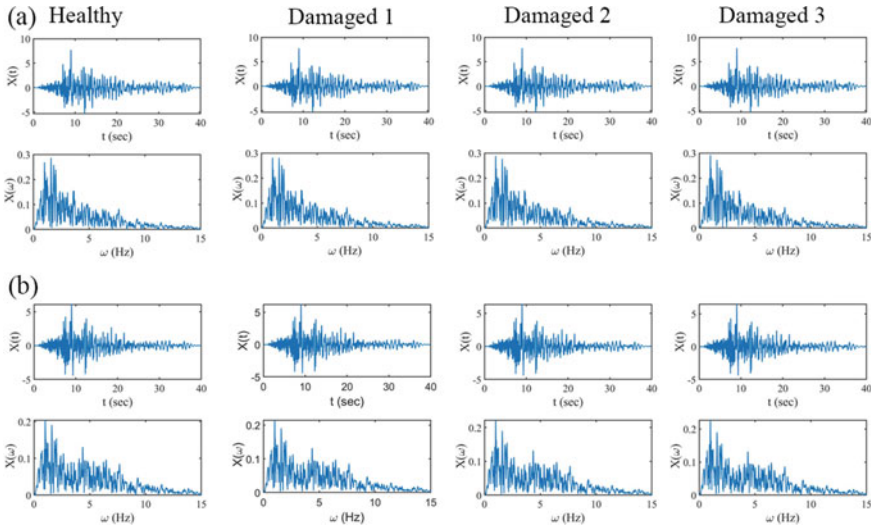


**Fig. 8** Acceleration response of the structure excited under ground motion RSN 187 in the time domain and frequency domain for different healthy and damaged cases at **a** roof level **b** base level

with an appropriate minimum embedding dimension. Singular value decomposition is carried out on the trajectory matrix to evaluate the time series; however, the number of time series obtained is limited to the embedding dimension.

For the reconstruction of the signal, cross-correlation was calculated between the obtained time series and the original response. The time series used for reconstructing the signal was having a normalized correlation coefficient in the top 30%. The time series that were having a normalized correlation coefficient, less than the top 30%, were neglected to avoid vague information. Thus, the reconstructed signal was obtained for healthy and different damaged cases. The reconstructed signal in a time domain and frequency domain for healthy and damaged states excited under RSN 187 is presented in Fig. 9.

## *6.3 Damage-Sensitive Feature and Damage Detection*

Every matrix has a hidden mathematical structure that consists of eigenvalues and eigenvectors. Similarly, singular values are the positive square roots of the nonzero eigenvalues, and eigenvectors for these nonzero eigenvalues are referred to as a singular vector. The orientation of the singular vector in the space is used as the basic parameter for identifying damage in the study.

The filtered and reconstructed response at the base level and roof level obtained after singular spectral analysis was put to form a matrix $S$. The singular value decomposition has been carried out on matrix $S$, and two $2 \times 1$ dimensional singular vectors

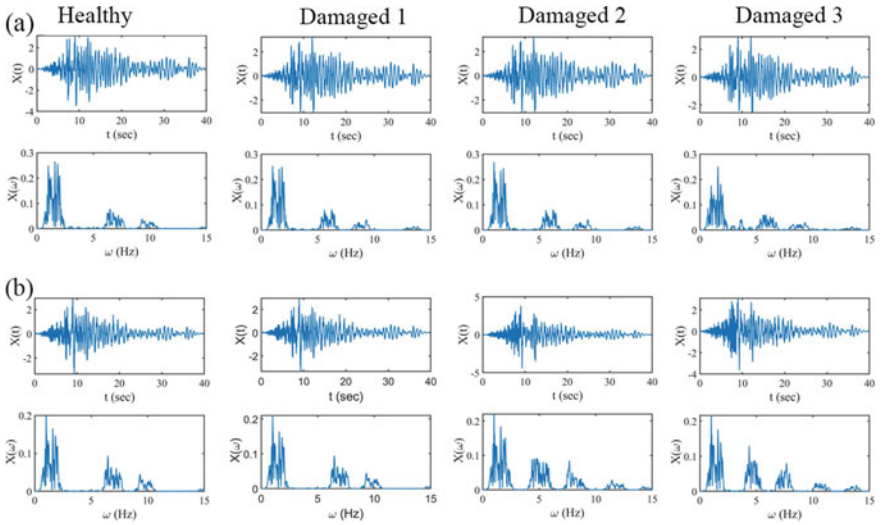


**Fig. 9** Filtered and reconstructed acceleration response after SSA excited under ground motion RSN 187 in the time domain and frequency domain for different healthy and damaged cases at **a** Roof level **b** Base level

were obtained that are plotted in the two-dimensional space. Since singular vectors are orthogonal in nature, the angle of any singular vector with the horizontal is the measure of the damage in the structure. The angle of a singular vector in two-dimensional space for the healthy and damaged cases excited under RSN 187 is presented in graphics format in Fig. 10, while Table 7 shows the observed angle for the healthy and damaged cases excited under all seven considered ground motions.

Based on the observation of the angles, a damage indicator (DI) is presented as the absolute difference between the damaged state and the healthy state.

$$\mathrm{DI} = |\theta_{\mathrm{damaged}} - \theta_{\mathrm{healthy}}|,$$

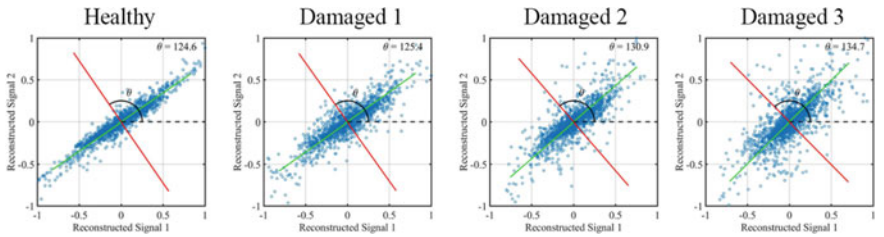


**Fig. 10** Damage-sensitive feature showing angle with respect to the reference line (dashed line) for different healthy and damaged cases when the system is excited under ground motion RSN 187

**Table 7** Angle (in degrees) made by the singular vector with respect to reference line for all healthy and damaged cases excited under different ground motions

| RSN | Healthy | Damage 1 | Damage 2 | Damage 3 |
|---|---|---|---|---|
| 175 | 125.58 | 120.25 | 118.71 | 117.48 |
| 187 | 124.57 | 125.44 | 130.92 | 134.66 |
| 461 | 119.31 | 120.92 | 121.29 | 121.64 |
| 549 | 129.97 | 131.63 | 133.59 | 134.41 |
| 848 | 114.46 | 119.43 | 119.71 | 123.11 |
| 864 | 123.65 | 123.92 | 124.13 | 124.36 |
| 1106 | 116.42 | 115.28 | 115.03 | 114.31 |

**Table 8** Damage indicator values for all considered cases

| RSN | Damage 1 | Damage 2 | Damage 3 |
|---|---|---|---|
| 175 | 5.33 | 6.87 | 8.1 |
| 187 | 0.87 | 6.35 | 10.09 |
| 461 | 1.61 | 1.98 | 2.33 |
| 549 | 1.66 | 3.62 | 4.44 |
| 848 | 4.97 | 5.25 | 8.65 |
| 864 | 0.27 | 0.48 | 0.71 |
| 1106 | 1.14 | 1.39 | 2.11 |

where $\theta_{\text{damaged}}$ and $\theta_{\text{healthy}}$ represent the angle made by a singular vector, respectively, for damaged and healthy cases. The value of damage indicator for all the cases is presented in Table 8.

The value of the damage indicator gives us the magnitude of damage to the structure. It is clearly observed that damage 3 has a high value of damage indicator that can be justified as the maximum reduction in isolator stiffness was done in the case of damage 3.

## 7 Conclusion

The purpose of the study is to extend the principals of structural health monitoring to the base-isolated superstructure. In the present numerical study, a base-isolated steel superstructure was considered and excited under seven earthquake ground motions. The damage was introduced in the isolators progressively by reducing their stiffness in two horizontal directions unequally. The responses for the healthy and damaged cases were filtered using singular spectral analysis and reconstructed using the dominant time series. The dominancy of the time series is determined by their correlation with the original response. The outcome of the research is the damage detection

algorithm that uses the reconstructed response at two different levels in the superstructure and forms the matrix. After operating singular value decomposition on this matrix, the angle formed by the singular vector is the basis of the damage detection algorithm. The developed algorithm is detecting damage in the particular case in a good manner, and the proposed damage indicator is quantifying the damage properly.

## References


1. ASCE (2017) Minimum design loads and associated criteria for buildings and other structures. American society of civil engineers
2. Bhowmik B, Krishnan M, Hazra B, Pakrashi V (2019) Real-time unified single-and multi-channel structural damage detection using recursive singular spectrum analysis. Struct Health Monit 18:563–589
3. Constantinou A, Whittaker A, Kalpakidis Y, Fenz D, Warn G (2007) Performance of seismic isolation hardware under service and seismic loading (MCEER-07-0012). University at Buffalo, State University of New York
4. Fraser AM, Swinney HL (1986) Independent coordinates for strange attractors from mutual information. Phys Rev A 33:1134
5. Golyandina N, Nekrutkin V, Zhigljavsky AA (2001) Analysis of time series structure: SSA and related techniques. Chapman and Hall/CRC
6. Harris III JL, Speicher MS (1863) Assessment of first generation performance-based seismic design methods for new steel buildings volume 1: special moment frames. NIST Technical Note**,** 1
7. Hassani H (2010) A brief introduction to singular spectrum analysis. Optimal decisions in statistics and data analysis
8. Kelly JM (1986) Aseismic base isolation: review and bibliography. Soil Dyn Earthq Eng 5:202–216
9. Kelly JM (1999) The role of damping in seismic isolation. Earthq Eng Struct Dynam 28:3–20
10. Kennel MB, Brown R, Abarbanel HD (1992) Determining embedding dimension for phase-space reconstruction using a geometrical construction. Phys Rev A 45:3403
11. Komodromos PI (2000) Seismic isolation for earthquake-resistant structures. Wit Press
12. Liu K, Law S-S, Xia Y, Zhu X (2014) Singular spectrum analysis for enhancing the sensitivity in structural damage detection. J Sound Vib 333:392–417
13. PEER (2013) PEER ground motion database—PEER Center. Pacific Earthquake Engineering Research Center. https://ngawest2.berkeley.edu/spectras/new?sourceDb_flag=1. Accessed 21 Sept 2019
14. Pike E (1987) Singular system analysis of time series data. In: Computational systems—natural and artificial. Springer
15. Providakis C (2008) Pushover analysis of base-isolated steel–concrete composite structures under near-fault excitations. Soil Dyn Earthq Eng 28:293–304
16. Rezaei Rad A, Banazadeh M (2018) Probabilistic risk-based performance evaluation of seismically base-isolated steel structures subjected to far-field earthquakes. Buildings 8:128
17. Sharma A, Jangid R (2009) Behaviour of base-isolated structures with high initial isolator stiffness. Int J Appl Sci Eng Technol 5:199–204
18. Vautard R, Yiou P, Ghil M (1992) Singular-spectrum analysis: a toolkit for short, noisy chaotic signals. Physica D 58:95–126

19. Yang JN, Huang H (2006) Damage tracking of base-isolated building using sequential nonlinear LSE with unknown inputs and outputs. In: Smart structures and materials 2006: sensors and smart structures technologies for civil, mechanical, and aerospace systems. International Society for Optics and Photonics, 61741I
20. Yoshimoto R, Mita A, Okada K (2005) Damage detection of base-isolated buildings using multi-input multi-output subspace identification. Earthq Eng Struct Dynam 34:307–324

# A Numerical Study on the Nonlinear Behaviour of Built-Up Cold-Formed Steel Battened Columns


**S. Priyanka and M. Anbarasu**

**Abstract** This paper reports the study on the behaviour and strength of built-up cold-formed steel battened columns. The pin ended built-up columns composed of two web-stiffened cold-formed steel lipped channel sections positioned face to face at differing spacing which have been connected by the batten plates. The nonlinear 3D-numerical modelling was developed using ABAQUS software. The numerical results were validated with the results reported in the literature. The parametric study was conducted by changing the overall slenderness ratio of the web-stiffened channel sections. The dimensions of two identical web-stiffened lipped channel cross-sections have been selected based on pre-qualified limitations of North American Specifications. The column design strength, load-axial shortening and their buckled shapes at failure were observed and reported in this paper. A theoretical investigation was conducted based on the AISI S100-2016 specification for cold-formed steel columns, and the ultimate load capacity was predicted. Thus, the results obtained from numerical study and the theoretical study are compared and the conclusion drawn from this study.

**Keywords** Cold-formed steel · Battened columns · Web-stiffened lipped channel section · Finite-element modelling · Failure modes · Design strength

S. Priyanka (✉) · M. Anbarasu
Government College of Engineering, Salem, India
e-mail: priyasrini1797@gmail.com



M. Madhavan et al. (eds.), *Proceedings of the Indian Structural Steel Conference 2020 (Vol. 1)*, Lecture Notes in Civil Engineering 318,
https://doi.org/10.1007/978-981-19-9390-9_32

## 1 Introduction

The usability of hot-rolled steel sections become inefficient for the steel structures which are supposed to carry the light and moderate loads and also for the short span structural members. Hence, the study on the behaviour of cold-formed steel members is inevitable due to their lightness, high yield strength, long-term durability, high load resistance, long-span capability, ease of prefabrication and construction. For the economic utilization of steel and for the larger loads, the individual components are not sufficient to satisfy the required design strength. So the built-up sections are often used in this case to fulfil the stiffness requirements. In general, built-up sections are made up of connecting two or more individual components by either lacings or batten plates. Thus, this paper reports the behaviour and strength of the cold-formed steel built-up battened columns. The built-up columns possessed of two identical web-stiffened cold-formed steel lipped channel sections positioned face to face at differing spacing connected by using batten plates. The web stiffeners are provided in order to improve the buckling resistance of the web. The end conditions are considered as the pinned–pinned. The space between the chords has been chosen to have moment of inertia about minor axis equals that 3 times and 1.5 times the moment of inertia about major axis.

Based on the previous investigation, numerous research work has been conducted in the area of built-up cold-formed steel columns, and the results were reported by Roy et al., Zhang and Young, Craveiro et al. and Dubino et al. On the other hand, Anbarasu and Dar studied the upgraded design method for built-up cold-formed steel battened columns possessed of four lipped angles. Dabaon et al. and Anbarasu et al. conducted an investigation on the built-up cold-formed steel battened columns. In the research works reported, limited research is available for built-up battened columns placed face to face. There is no investigation about the effect of web stiffeners in face-to-face built-up CFS battened columns. Hence, this investigation concentrated on the effect of web stiffeners in the buckling behaviour of battened columns.

## 2 Finite-Element Analysis and Validation

Finite-element analysis (FEA) is a process of mathematical modelling performed that having ability to predict the ultimate moments and complex failure modes of cold-formed steel structural members. The perfectly linear elastic–plastic material was considered. In the numerical modelling, the material properties and geometric nonlinearity properties were considered. Initially, the linear analysis was carried out to predict the buckling loads and their buckling modes. The nonlinear analysis was followed by elastic analysis to obtain the ultimate load capacity.

The columns were modelled using shell S4R elements having which exhibits an exact solution for number of application. Thus, the fine mesh sized 10 mm (length to width) was used throughout the section for adequate accuracy in results. The

end condition of the built-up column considered in this study was pinned–pinned. The upper and lower ends are constrained with the "rigid body" constraints. The "tie constraints" were used to connect the batten plates and the channel section by selecting the inner surface of flanges as master surface and outer surface of battens as slave surface. The load was enforced to the end conditions using the static RIKS method.

The perfect elastic–plastic behaviour for the material was considered. Due to the cold forming, the strain hardening of the corners has been neglected. The Young's modulus and Poisson's ratio of the section considered was $2 \times 10^5$ N/mm$^2$ and 0.3. The residual stresses were not incorporated in order to avoid the complexity in analysis. The imperfection factors are depending on width-thickness ratio, depth-thickness ratio, local buckling length, slenderness ratio and also the number of batten plates. Thus, the overall imperfections were taken as L/1000, and the initial local imperfections were considered as 0.34% times the section thickness.

## *2.1 Nonlinear Analysis*

Plastic analysis is more precise when compared to linear analysis because it enrols geometric nonlinearity and static analysis to obtain the buckling loads. In the elastic analysis, the initial local and global imperfections were modelled by insisting initial out-of-plane deflections to the section. The lowest Eigen vale buckling mode shapes were used to create geometric imperfections for the nonlinear analysis.

## *2.2 Validation*

Finite-element modelling procedure is validated through the published results reported in the literature [6]. Five specimens of cold-formed built-up steel sections have modelled for validation. By comparing the numerical modelling results obtained with the already existing experimental results reported by Dabaon et al. [6], it is clear that the results are in good agreement with each other. Hence, the same procedure will be followed to carry out the parametric study. Table 1 shows the comparison between the experimental results reported in literature validated and the results obtained from carried out numerical analysis.

The experimental failure mode and the finite-element model deformed shape of B2B25-300 specimen were compared and shown in Fig. 1. The failure mode obtained from the numerical simulation in finite-element analysis is the same as that of failure mode obtained experimentally.

**Table 1** Validating finite-element analysis results with experimental results reported by Dabaon et al. [6]

| Specimen | $P_{EXP}$ (kN) | $P_{FEA}$ (kN) | $P_{EXP}/P_{FEA}$ |
|---|---|---|---|
| B2B25-300 | 109.90 | 106.05 | 1.03 |
| B2B50-300 | 119.11 | 121.52 | 0.98 |
| B2B75-300 | 125.26 | 128.64 | 0.97 |
| B2B50-150 | 133.11 | 135.80 | 0.98 |
| B2B50-400 | 112.29 | 114.65 | 0.98 |
| Mean | | | 0.988 |
| Standard deviation | | | 0.03 |

(a) EXPERIMENTAL FAILURE MODE

(b) ABAQUS FAILURE MODE

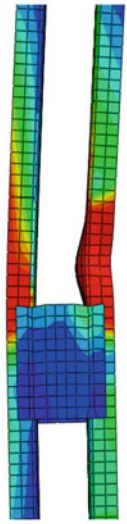

(c) CLOSER VIEW OF ABAQUS FAILURE MODE

**Fig. 1** Comparison of deformed shapes of B2B25-300 specimen

**Table 2** Section geometric details

| Section details | Flange $b_f$ (mm) | Web $h_w$ (mm) | Lip $h_l$ (mm) | Thickness | Batten plates | | | Stiffener | | Spacing $S$ (mm) |
|---|---|---|---|---|---|---|---|---|---|---|
| | | | | | $a_1$ (mm) | $b_1$ (mm) | $b_2$ (mm) | $h_1$ (mm) | $h_2$ (mm) | |
| 50 × 90x15 × 1.2 | 50 | 90 | 15 | 1.2 | 147.6 | 150 | 50 | 15 | 13 | 50 |
| 60 × 150x15 × 1.2 | 60 | 150 | 15 | 1.2 | 167.6 | 170 | 60 | 15 | 13 | 50 |

# 3 Sections

## *3.1 General*

As per AISI-S100-2016 Specification for the design of cold-formed steel structural member 2016 edition, the dimensional limitations are available for an individual section only. Based on the individual section limitations, face-to-face web-stiffened built-up section was selected.

## *3.2 Section Geometric Details*

The geometric details of the selected web-stiffened built-up columns were represented in Table 2.

The cross-section and elevation of the web-stiffened built-up battened columns chosen for this study were shown in Fig. 2.

# 4 Parametric Study

The parametric study was designed to investigate the web stiffener effect and varying the overall slenderness ratio on the axial strength of built-up battened columns. A detailed parametric study has been carried for different cross-section geometries with pinned end conditions. Two cross-section 50 × 90 × 15 and 60 × 150 × 15 with thickness 1.2 mm were selected for this study. The thickness of the batten plates was the same as that of the thickness of the lipped channels. Spacing between the batten plates was selected based on the codal specifications. The column length was taken as varying the slenderness ratio from 20 to 120. The nominal axial compression capacity of the battened column is evaluated based on the design equations provided in North American Specification AISI S100-2016. It depends on the guidelines provided in the

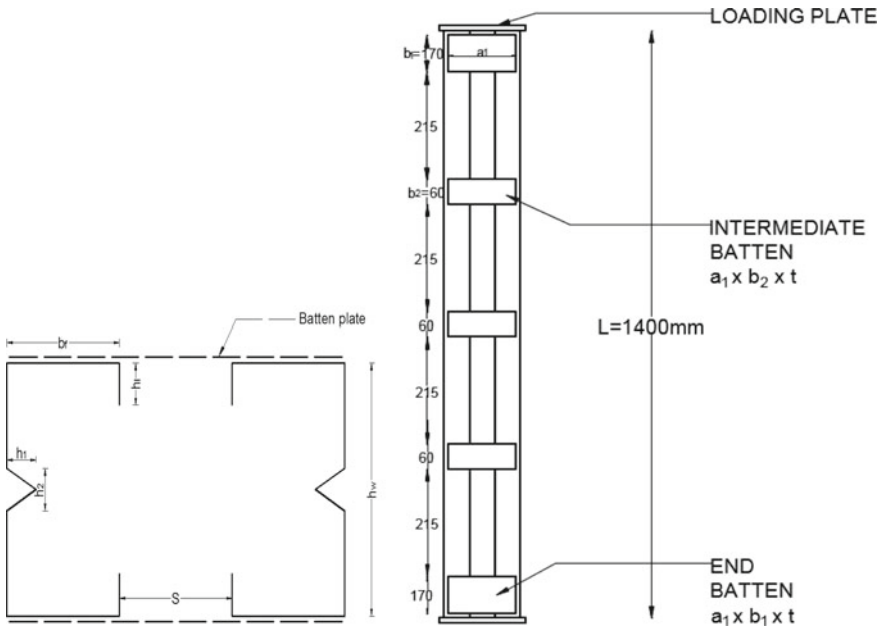


**Fig. 2** **a** Cross-sectional view. **b** Elevation

AISI S100-2016 to predict design strength for web-stiffened lipped channel sections, the DSM was computed in this study. The deformed shape and its closure view of the battened columns for section 50 × 90 × 15 mm of slenderness ratio 30 and 40 obtained from finite-element modelling were shown in Fig. 3.

The curve was plotted between the axial displacement and ultimate load capacity for the cross-section 50 × 90 × 15 mm of the slenderness ratio 20 and 120 was shown in Figs. 4 and 5.

Figure 6 represents the finite-element modelling results for two different cross-sections with varying slenderness ratio.

The ultimate loads obtained from finite-element modelling and direct strength method (DSM) were compared for different cross-sections and represented in Figs. 7 and 8.

Based on the above comparisons, it is clear that the finite-element modelling results are unconservative for both the cross-sections. For the cross-section 50 × 90 × 15, the numerical analysis results are slightly unconservative with the theoretical results, while for a cross-section 60 × 150 × 15, the numerical modelling results are totally unconservative with the predicted theoretical results.

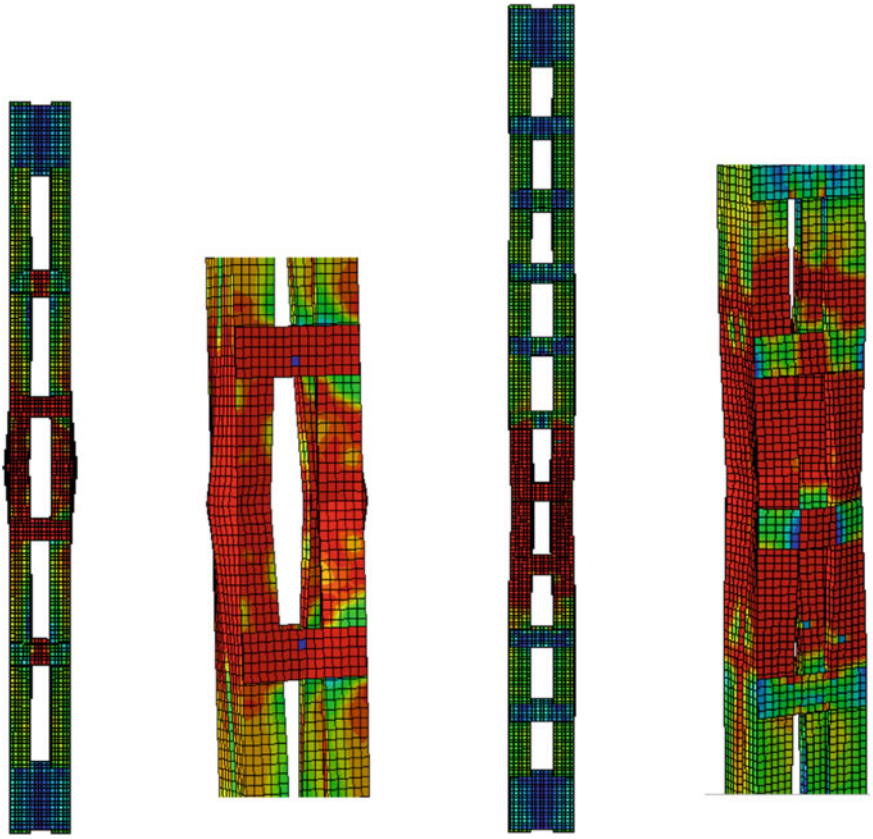

**Fig. 3** Deformed shape and the closure view of failure mode of cross-section 50 × 90 × 15 of slenderness ratio 30 and 40

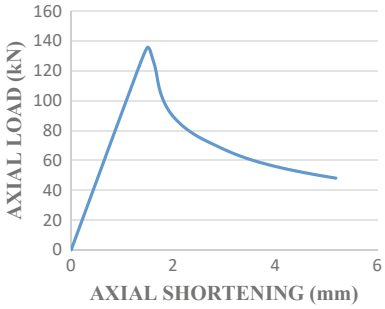


**Fig. 4** Load versus axial shortening curve of 50 × 90 × 15—slenderness ratio 20

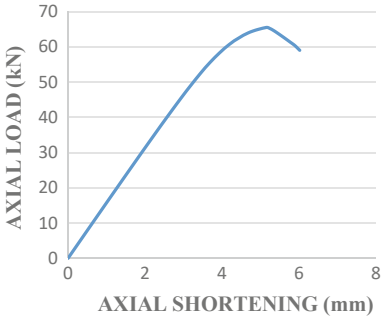


**Fig. 5** Load versus axial shortening curve of 50 × 90 × 15—slenderness ratio 120

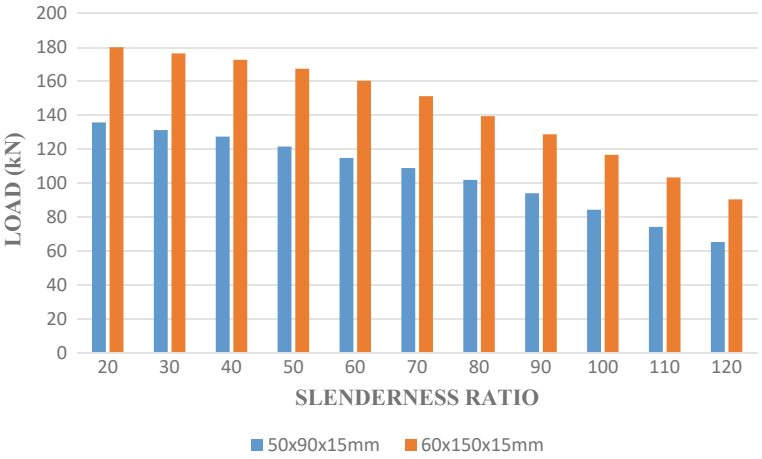


**Fig. 6** FEA design strength results

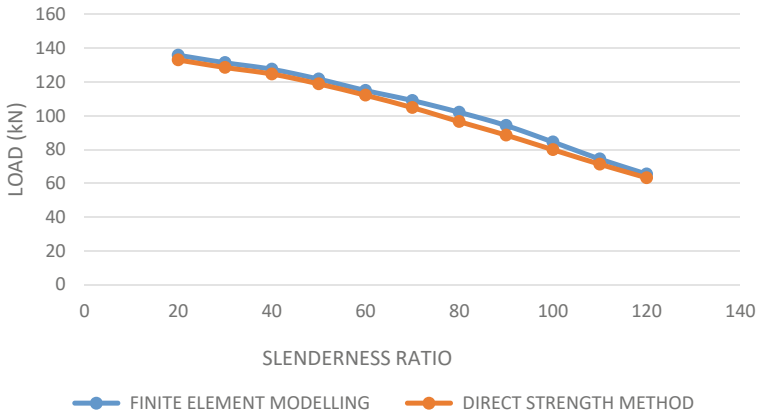


**Fig. 7** Comparison of FEM and DSM results of specimen 50 × 90 × 15 mm

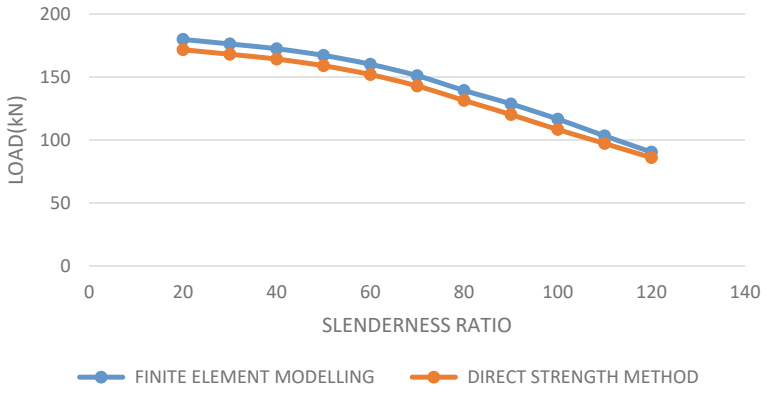


**Fig. 8** Comparison of FEM and DSM results of specimen 60 × 150 × 15 mm

## 5 Conclusion

This study deals with the behaviour and strength of the web-stiffened built-up cold-formed steel battened columns. The numerical model was validated by means of comparison with the experimental results reported by Dabaon et al. [6]. A total of 22 numerical analyses was performed with the validated finite-element model. Based on this study, the following conclusions are drawn:

1. For a section having slenderness ratio 20–40, the failure mode was local buckling, and for a section having slenderness ratio 50–120, the failure mode obtained was global buckling.
2. In general, the ultimate compression load decreases by increasing the overall slenderness ratio.
3. By providing web stiffeners in the built-up columns, it delays/prevents the occurrence of local buckling of slender web elements.
4. It is found that the plate slenderness significantly affects the ultimate compression capacity of the built-up battened columns.
5. The ultimate load-carrying capacity of web-stiffened built-up battened columns computed from numerical analysis ($P_{FEM}$) shows proximate results with DSM equations in AISI S100-2016 with mean 1.04 and standard deviation 0.017.

## References

1. Anbarasu M, Sukumar S (2014) Local/distortional/global buckling mode interaction on thin walled lipped channel columns. Latin Am J Solids Struct 11(2014):1363–1375
2. Anbarasu M, Bharath KP, Sukumar S (2014) Study on the capacity of cold-formes steel built-up battened columns under axial compression. Latin Am J Solids Struct 11 (2271-1375)

3. Anbarasu M, Kanagarasu K, Sukumar S (2014) Investigation on the behavior and strength of cold-formed steel web stiffened built-up battened columns. Mater Struct
4. AISI S100:2016—North American specification for the design of cold-formed steel structural member specification
5. Anbarasu M, Adil DM (2019) Improved design procedure for battened cold-formed steel built-up columns composed of lipped angles. J Constr Steel Res 164(2020):105781
6. Dabaon M, Ellobody E, Ramzy K (2015) Experimental investigation of built-up cold-formed steel section battened columns. Thin-Walled Struct 2015(92):137–145
7. EC3 (2006) Euro code 3: design of steel structures—Part 1–3: General rules—supplementary rules for cold-formed members and sheeting. BS EN 1993-1-3. In: Proceedings of the Brussels: European committee for standardization
8. Roy K, Mohammadjiani C, Lim JBP (2019) Experimental and numerical investigation into the behaviour of face-to-face built-up cold-formed steel channel sections under compression. Thin Walled Struct 134(2019):291–309
9. Roy K, Ting TCH, Lim JBP (2018) Nonlinear behaviour of back-to-back gapped built-up cold-formed steel channel sections under compression. J Constr Steel Res 147(2018):257–276
10. Ramzy K (2014) Effect of batten plates on the behavior and strength of cold-formed steel built-up section columns (M.Sc. Thesis). Tanta University, Tanta, Egypt
11. Young B, Rasmussen JR (1998) Design of lipped channel columns. J Struct Eng 124(2):140–148

# A Study on Cold-Formed Stainless Steel Perforated Hollow Stub Columns


**M. Subalakshmi, M. Anbarasu, and S. Priyanka**

**Abstract** A numerical investigation on cold-formed ferritic stainless steel hollow columns with perforation at mid-height was accomplished using Finite Element (FE) Analysis. The cold-formed ferritic stainless steel hollow columns offer high resistance to compression, bending and torsion. Perforations help in optimizing the material utility effectively. ABAQUS software is used to carry out the FE modelling. The cross-sectional dimensions for the parametric study were selected in accordance with the sizes available in the market such that wide range of perforation diameter to flat width ratio for different cross-sections can be achieved. Different width to thickness ratio for various cross-sections shows noteworthy effects in the strength of the columns. In the estimation of the elastic flexural buckling stress, the effects of perforations was considered in accordance with the guidelines provided in the AISI S100-2016. The axial compression capacity of the specimens was also predicted by Direct Strength Method (DSM) adopted in North American Specification AISI S100-2016. The results computed by existing DSM equations were compared with the numerical analysis strengths and the conclusions were drawn.

**Keywords** Ferritic stainless steel · Perforations · Finite element modelling · Hollow columns · Buckling resistance

## 1 Introduction

The constructive use of stainless steel in structural applications has been increased due to its significant material properties over cold-formed carbon steel like high resistance to corrosion which improves durability, high strength to weight ratio which provides greater stiffness, recyclability, facile maintenance, high impact strength, and its glossy, uniform and smooth finish provides aesthetically pleasing appearance. Among various grades of stainless steel ferritic stainless steel is used due to its

M. Subalakshmi · M. Anbarasu (✉) · S. Priyanka
Department of Civil Engineering, Government College of Engineering, Salem, Tamil Nadu, India
e-mail: gceanbu@gmail.com



M. Madhavan et al. (eds.), *Proceedings of the Indian Structural Steel Conference 2020 (Vol. 1)*, Lecture Notes in Civil Engineering 318,
https://doi.org/10.1007/978-981-19-9390-9_33

reduced nickel content compared to austenitic and other grades of stainless steel. The most commonly used steel for construction purpose is austenitic stainless steel of grades EN 1.4301 and EN 1.4401 which is highly ductile in nature due to the presence of high nickel content and offers improved performance in elevated temperature but it requires high initial material cost. Better price stability of ferritic stainless steel due to reduced nickel content made it a better choice for structural applications. Perforations are provided for the accessibility of pipelines, electrical wirings and proper access for repair and maintenance works. Perforation also apparently reduces the member weight which significantly offers better utilization of material. Perforation affects the load transfer mechanism by causing stress redistribution which increases the stress concentration and failure at the proximity of perforations.

The investigation shows that the provision of perforations at any other locations in the slender member other than the ends give improved strength and added that the compression capacity of perforated cross-section is less than the net cross-section area whereby these sections are subjected to local buckling [1]. Increase in the perforation area shows reduction in the axial stiffness of the perforated columns [2]. The study on the perforated tubular stub columns shows an increase in the amplitude of the local geometric imperfection when the perforation size increases and the ultimate capacity of Square and Rectangular hollow stub columns do not modify for the members having perforation ratio (perforation diameter to flat width) up to 10% [3]. To overcome the tedious effective width method the analysis of cold-formed perforated hollow columns to predict the load-carrying capacity by DSM is done by developing Finite Strip models due to its simple applicability using the software CUFSM [4]. The compression capacity of lean duplex stainless steel perforated hollow stub columns was determined thereby knowing the consequences of different geometrical parameters (size, thickness and location) of the circular perforations. The study shows improved buckling resistance with an increase in thickness and the buckling load decreases when the perforation size increases [5]. The local imperfection magnitude for stainless steel and Gardner-Ashraf material modelling was carried to investigate the buckling behaviour of lean duplex stainless steel lipped channel columns using Finite Element Analysis and new DSM formulation was proposed for local and global buckling which significantly shows an accurate prediction of compression resistance with less scatter [6]. This study works on lean duplex stainless steel hollow columns providing modifications for design equations of EC3, AS/NZS standard and DSM in North American Specification [7]. The investigation on the beam-column behaviour and flexural buckling shows safe and accurate results for the test specimens which are in good congruence with design approaches in the standard codes by considering the interaction of the bending moment with uniform distribution and flexural buckling [8]. The test results of the austenitic, duplex and lean duplex stainless steel square and rectangular hollow stub columns from previous published literature were compared with the test results of ferritic stainless steel hollow stub columns which prove ferritic stainless steel offers similar structural performance with low material cost [9].

This work focuses on the structural buckling behaviour of ferritic stainless steel hollow stub columns with perforation. The Finite Element procedure discussed in

Sect. 2 is carried over for the parametric study. The axial compression capacity of perforated hollow stub columns is evaluated using Finite Element Analysis software ABAQUS. Then the numerical results are compared with results obtained from the existing DSM equations specified in AISI S100 (16)-2016.

## 2 Finite Element Modelling and Validation

The availability of experimental evidence for ferritic stainless steel columns with perforations is very limited. Finite Element modelling was done by Finite Element Analysis software ABAQUS 6.13. Due to the non-availability of test data on perforated ferritic stainless steel stub columns the authors validated the perforated cold-formed stub column test results provided in [10]. The centre line dimension of the cross-section was used for modelling. The perforations are made at the two opposite faces in the intermediate position of the mid-height of the member.

The measured material properties of the cold-formed carbon steel for flat and corner regions reported in [3] was used for validation models. The material properties used for ferritic stainless steel were obtained from [8]. The material model reported in [9] was used in the parametric models.

The shell nature of the element made to incorporate four noded doubly curve shell element S4R having six degrees of freedom available in ABAQUS is employed to model stub columns.

The flat region of the section is discretized with uniform mesh size of 3 × 3 mm and at the corners finer mesh was used to render uniform stress distribution.

The corner property is also assigned to the region of two times the thickness of the member from the corners. To conduct the parametric study local geometric imperfection amplitude for stainless steel in Eq. (1) was proposed in [11] is used to determine the local geometric imperfection

$$\omega_0 = 0.023\left(\frac{\sigma_{0.2}}{\sigma_{cr}}\right)t \tag{1}$$

where thickness of the section is $t$, the proof stress is $\sigma_{0.2}$ and the critical elastic buckling stress of the section is $\sigma_{cr}$. The effect of residual stresses on the load-deformation is negligible. Hence the author residual ignored the stress is in the current FE modelling.

The ends of the column were restrained by Kinematic coupling available in ABAQUS through the reference points RP1 and RP2. The boundary conditions for the loaded end of the stub column were simulated by restraining all degrees of freedom except the translational degree of freedom at RP1 through which concentrated force is applied and the boundary conditions at RP2 for the unloaded end were simulated by restraining all degrees of freedom. Two-step processes were carried for the validation of the simulated FE model. Initially, Subspace Eigensolver available in the ABAQUS is used to extract the lowest buckling mode shape for the elastic

**Table 1** Ultimate load comparisons between experimental and FEA results

| SECTION | $P_{Test}$ (kN) | $P_{Test}/P_{FEA}$ |
|---|---|---|
| 80 × 40 × 2.6d/w0.1-1 | 323.49 | 1.01 |
| 80 × 40 × 2.6d/w0.3-1 | 290.18 | 1.06 |
| 80 × 40 × 2.6d/w0.5-1 | 256.33 | 1.08 |
| 80 × 40 × 2.6d/w0.7-1 | 211.93 | 1.09 |
| 80 × 40 × 2.6d/w0.9-1 | 159.88 | 1.07 |
| 60 × 40 × 2.9d/w0.1-1 | 256.56 | 1.09 |
| 60 × 40 × 2.9d/w0.3-1 | 229.63 | 1.04 |
| 60 × 40 × 2.9d/w0.5-1 | 205.75 | 1.07 |
| Mean | | 1.06 |
| Standard deviation | | 0.03 |

buckling analysis and this extracted mode shape is fed for the non-linear analysis. For validation, the local geometric imperfection values were directly taken from the paper [10].

The Finite Element modelling procedure presented in this paper using ABAQUS 6.13 is evaluated by determining the numerical analysis results. These results were compared with the test results specified in [10]. The results are conservative with each other with mean 1.06 and standard deviation 0.03 with reference to the table. Table 1 presents the axial compression load comparison between experimental and FEA results. Figure 1 shows the comparison of deformed shape obtained from numerical analysis and experimental results of perforated cold-formed hollow stub column [10] for 80 × 40 × 2.6 series for perforation ratio 0.1 and 0.7 in Fig. 1a and b, respectively.

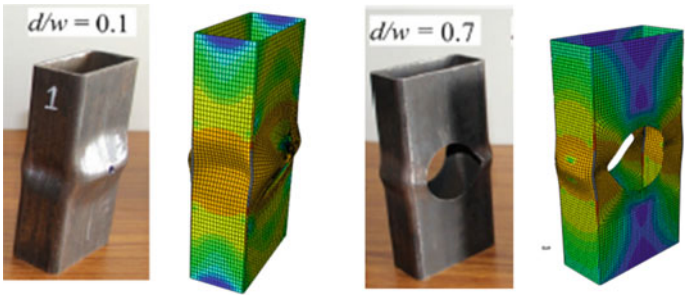


**(a) 80×40×2.6d/w0.1-1** **(b) 80×40×2.6d/w0.7-1**

**Fig. 1** Comparison of the deformed shapes of FE results with test results

## 3 Parametric Study

The parametric study is carried out by following the numerical modelling procedure presented in the Finite Element modelling and validation section of the current paper. A detailed parametric study has been carried for different cross-section geometries with fixed end conditions. The cross-sectional dimensions for this investigation were selected in accordance with the sizes obtainable from the market such a way to cover a wide range of perforation diameter to flat width ratio (say 0.1, 0.3 and 0.5) for different cross-sections. Two cross-section 120 × 80 and 100 × 60 with varying thickness 1.5 mm, 2 mm, 3 mm and 4 mm were selected for the parametric study with perforation ratio (ratio of hole diameter to greater flat width) of 0.1, 0.3 and 0.5. The centre line radius is chosen to be 1.5 times the thickness of the section. The length of the stub column is taken as four times the minimum cross-sectional width.

### *3.1 Section Labelling*

The cross-sectional dimensions were selected based on the provisions in Tata Steel [12]. Figure 2 and 3 represents the cross-sectional view and three-dimensional view of the perforated hollow stub column,

where

*B* Width of the section
*D* Depth of the section
*w* Flat width of the section
*d* Diameter of the perforation
$r_c$ Centre line radius of the section
*L* Length of the section

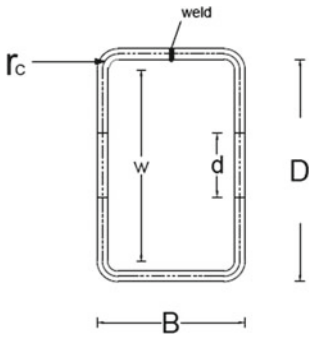


**Fig.2** Cross-sectional view of the perforated hollow stub column

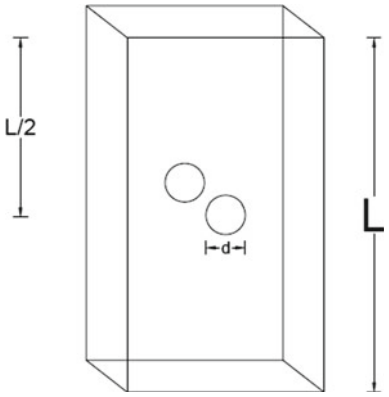


**Fig. 3** Three-dimensional view of the perforated hollow stub column

The labelling of the section is illustrated by the following section

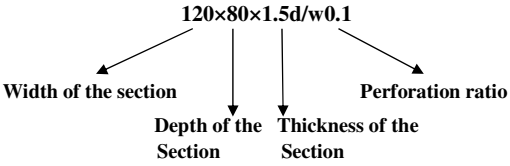


The numerical modelling of the section 100 × 60 × 4.5d/w = 0.3 shows the following deformed shape given in Fig. 4. The load over axial shortening curve of the series 120 × 80 with different perforation ratio and thickness were compared using Finite Element Analysis software ABAQUS and it is presented in Fig. 5.

## 4 Direct Strength Method

The axial compression capacity of the hollow stub column is evaluated based on the design equations provided in North American Specification AISI S100-2016. In this study, the suitability of design equations for hollow stub columns with a perforation at the mid-height of the member using DSM is computed. In section E of AISI S100-16(2016) it is seen that the buckling resistance of the compression member may be a minimum of axial strength of member for yielding and global buckling ($P_{ne}$), distortional buckling ($P_{nd}$) and local buckling ($P_{nl}$). Since this paper discusses the closed section, distortional buckling is ignored. Section E2 of AISI S100-16(2016) gives the design equations to predict the compression capacity for global buckling. The evaluation of elastic flexural buckling stress under the effect of holes is based on the guidelines provided in Appendix 2 of AISI S100-16(2016) with a

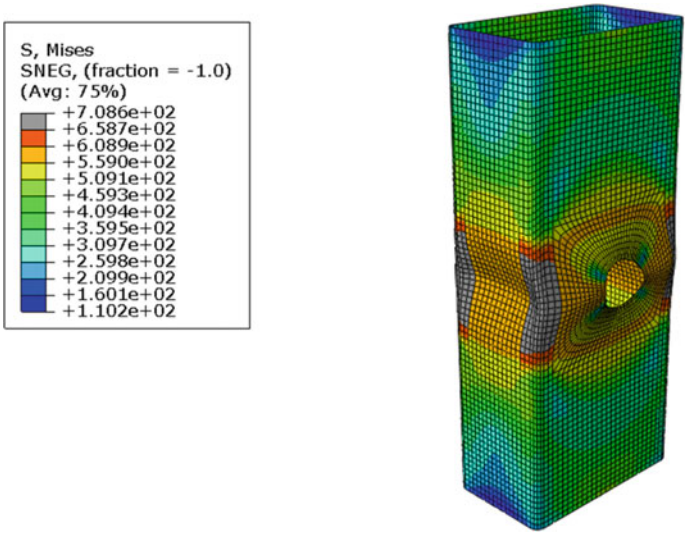


**Fig. 4** Deformed shape of 100 × 60 × 4.5d/w0.3

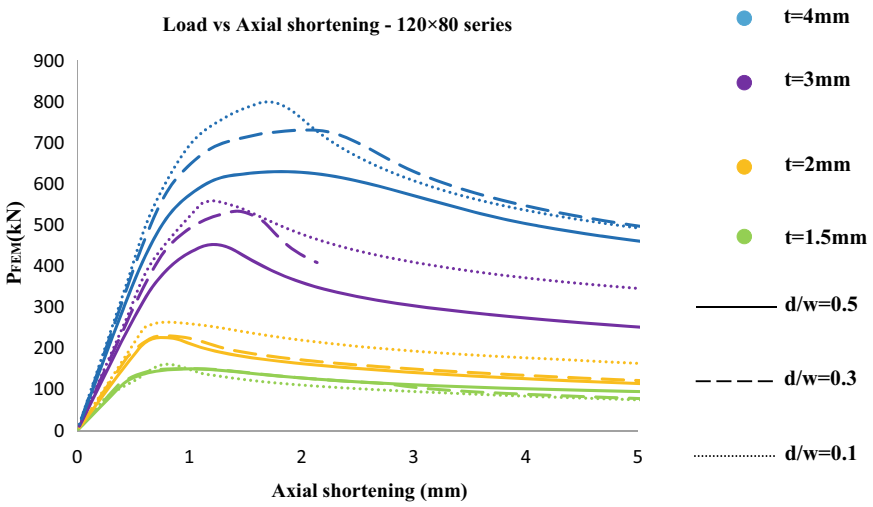


**Fig.5** Load versus axial shortening curves of 120 × 80 series for different thickness and d/w ratio

plate buckling coefficient of 0.43 for the perforated elements and 4 for unperforated elements. Figure 6 represents the comparison of FEA and DSM results for two different cross-sections with varying thickness and perforation ratio.

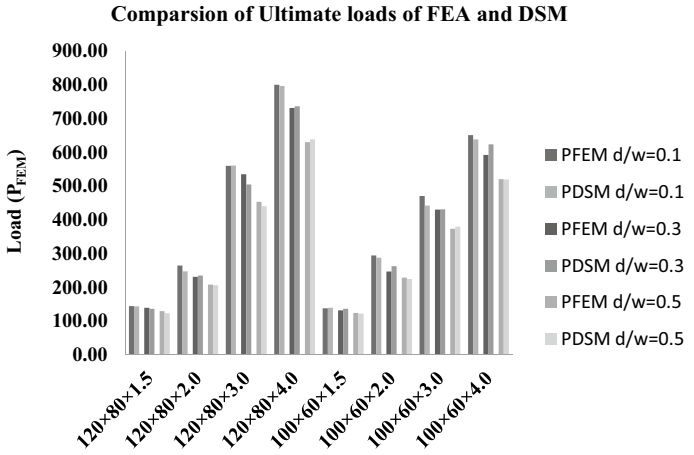


**Fig. 6** Comparison of ultimate loads of all series

## 5 Conclusion

The behaviour of perforated ferritic stub columns is investigated in this paper. The Finite Element Analysis procedure is validated with the available test results in the literature. The verified Finite Element Analysis procedure is used to conduct the parametric study. Finally the axial compression capacity of perforated hollow stub columns obtained from the parametric study is compared with the Direct Strength Method in the North American Specification AISI S100-16(2016). The following conclusions are drawn from this study:

1. The axial capacity of the perforated hollow stub column increases with the increase in the thickness of the sections.
2. The compressive strength of the perforated hollow stub columns decreases with an increase in perforation ratio.
3. The decrease in axial capacity of the perforated hollow stub column with increase in d/w ratio is because of the reduced stiffness in the perforated plate elements.
4. It is noted that the members have yielding failure only at the vicinity of the perforation from the deformed shape of the section.
5. The load-carrying capacity of perforated hollow stub columns computed from numerical analysis ($P_{FEM}$) shows proximate results with DSM equations in AISI S100-16(2016) with mean 1.01 and standard deviation 0.03.
6. The ferritic stainless steel has structural adequacy similar to other grades of the cold-formed stainless steel.

## References


1. Kulatunga MP, Macdonald M (2013) Investigation of cold-formed steel structural members with perforations of different arrangements subjected to compression loading. Thin Walled Struct 67:78–87
2. Kulatunga MP, Macdonald M, Rhodes J, Harrison DK (2014) Load capacity of cold-formed column members of lipped channel cross section with perforations subjected to compression loading-Part-I, FE simulation and test results. Thin Walled Struct 80:1–12
3. Singh TG, Singh KD (2017) Structural performance of YSt-310 cold-formed tubular steel stub columns. Thin Walled Struct 121:21–40
4. Sarvade SM, Sarvade MM, Load carrying capacity of innovative cold-formed steel column. IOSR J Mech Civil Eng (IOSR-JMCE), 27–36. ISSN 2278-1684
5. Umbarkar KR, Patton LM, Singh KD (2013) Effect of single circular perforation in lean duplex stainless steel hollow circular stub columns under pure axial compression. Thin Walled Struct 68:18–25
6. Anbarasu M, Ashraf M (2016) Behavior and design of cold-formed lean duplex stainless steel lipped channel columns. Thin Walled Struct 104:106–115
7. Anbarasu M, Ashraf M (2017) Interaction of local flexural buckling for lean duplex stainless steel hollow columns. Thin Walled Struct 112:20–30
8. Arrayago I, Real E, Mirambell E (2016) Experimental study on ferritic stainless RHS and SHS beam-column. Thin Walled Struct 100:93–104
9. Ashfan S, Gardner L (2013) Experimental study on cold-formed ferritic stainless hollow sections. J Struct Eng 139(5). ASCE, ISSN 0733-9445/2013-5-717-728
10. Singh TG, Singh KD (2018) Experimental investigation on performance of perforated cold-formed steel tubular stub columns. Thin Walled Struct 137:107–121
11. Theofanaous M, Gardner L (2009) Testing and Numerical modeling of lean duplex stainless steel hollow section columns. Eng Struct 31(12):3047–3058
12. Tata steel (2013) Tata steel production named for Yst 310 Rectangular, Square and Circular steel hollow sections. Tata steel Limited, Kolkata

# Buckling Behaviour of Inelastic Thin-Webbed Castellated Beams


**A. Cyril Thomas, E. Aarthy, and K. Baskar**

**Abstract** Equations and values provided by the American Institute of Steel Construction (AISC 360–05) and literature using elastic analysis to determine the value of moment gradient factor ($C_b$) are used for beams that buckle in the inelastic range also. The effect of moment gradient is proved by the use of an equivalent moment gradient factor $C_b$ whose value is always greater than unity. This factor depends on the type of loading, position of loading from the shear centre and support conditions for the beam in the unbraced length. This paper develops a 3D finite element model of a Castellated Beam (CB) in ABAQUS/CAE, to determine the effect of beam slenderness and position of loading from the shear centre on $C_b$ in the inelastic range due to point load and uniformly distributed load. The variation in $C_b$ given in AISC for Point Load (PL) and Uniformly Distributed Load (UDL) is found at the shear centre and the bottom flange in the inelastic range. This variation can be eliminated by introducing a reduction factor for $C_b$ in the inelastic range of castellated beams.

**Keywords** Castellated beam · Finite element method · Inelastic lateral-torsional buckling · Moment gradient factor

A. Cyril Thomas (✉) · E. Aarthy
SASTRA Deemed to be University, Thanjavur, India
e-mail: cyrilstrer@gmail.com

Government College of Engineering, Thanjavur, India

K. Baskar
National Institute of Technology, Tiruchirappalli, India
e-mail: kbaskar@nitt.edu



M. Madhavan et al. (eds.), *Proceedings of the Indian Structural Steel Conference 2020 (Vol. 1)*, Lecture Notes in Civil Engineering 318,
https://doi.org/10.1007/978-981-19-9390-9_34

## Notations

| | |
|---|---|
| $A$ & $B$ | Is the coefficients for beams with simple supports |
| $b_f$ | Is the width of the flange |
| $C_b$ | Is the modification factor used in the equation for nominal flexural strength |
| $C_{br}$ | Is the reduced modification factor used in the equation for nominal flexural strength |
| $C_w$ | Is the wrapping constant |
| $d_1$ & $d_3$ | Is the inclined cutting length |
| $h_o$ | Is the depth of opening |
| $e$ | Is the weld length |
| $E$ | Is the modulus of elasticity of steel |
| $F_y$ | Is yield stress of steel |
| $G$ | Is the modulus of shear modulus |
| $d$ | Is the gross depth of the beam |
| $h_w$ | Is the height of the web |
| $I_y$ | Is the moment of inertia |
| $J$ | Is the torsional constant |
| $L_b$ | Is the unbraced length |
| $L_p$ | Is the limiting laterally unbraced length for full plastic bending capacity |
| $L_r$ | Is the limiting laterally unbraced length for inelastic lateral-torsional buckling |
| $M_{ocr}$ | Is the critical buckling moment |
| $M_n$ | Is the nominal moment strength |
| $M_p$ | Is the plastic moment |
| $R_{fscp}$ | Is the reduction factor PL acting at shear centre |
| $R_{fbp}$ | Is the reduction factor PL acting at bottom flange |
| $R_{fscu}$ | Is the reduction factor UDL acting at shear centre |
| $R_{fbpu}$ | Is the reduction factor UDL acting at bottom flange |
| $S$ | Is the distance between two holes |
| $S_x$ | Is the section modulus about major axis |
| $t_f$ | Is the thickness of the flange |
| $t_w$ | Is the thickness of the web |
| $W$ | Is the dimensionless slenderness parameter |
| $\sigma_{true}$ | Is the true stress |
| $\sigma_{normal}$ | Is the normal stress |
| $\varepsilon_{normal}$ | Is the normal strain |

## 1 Introduction

An I-beam subjected to flexure along the major axis will have more strength in the major axis than that in the minor axis as the section modulus will be greater along the major axis than in the minor axis. Lack of lateral bracings along the length of a beam weakens it by lateral-torsional buckling (LTB). LTB is a type of instability where a beam loaded in the plane of symmetry deforms in the plane till it reaches a critical loading at which the beams buckles and twists leading to its load carrying capacity being reduced. Castellated beams (CBs) are made by either flame cutting or automatic cutting of rolled I-beams in a zig-zag pattern and then re-joined by welding to create a regular pattern of holes in the web. Any increase in the beam's height due to castellation strengthens it. CBs are economical as the beam has increased strength without additional weight. Additional holes in the beams ensure automatic provision for passage of services and also provides an attractive appearance.

American Institute of Steel Construction—Load Resistance Factor Design (AISC-LRFD) gives an equation to determine the moment carrying capacity of a simply supported beam subjected to uniform end moments [1]. Pure bending is the worst case of loading for lateral-torsional buckling to occur due to uniform compression along its unbraced length. Equations are derived for pure bending due to simplicity in derivation.

The critical buckling moment of a simply supported I-beam during pure bending is given by Eq. 1 (AISC 360-10).

$$M_{\text{ocr}} = \frac{\pi}{L}\sqrt{EI_y GJ}\sqrt{(1+W^2)} \qquad \text{where, } W = \frac{\pi}{L}\sqrt{\frac{EC_w}{GJ}} \tag{1}$$

Most flexural members in a structure are not subject to uniform moment, and most supports are not simple in design. Loading and boundary conditions have practical importance. Unfortunately, differential equations are too complicated to facilitate an analytical solution [11]. The effect of moment gradient is incorporated in the equation using an equivalent moment gradient factor $C_\text{b}$ whose value is always greater than unity as compression force along the length is non-uniform. For example, the value of $C_\text{b}$ given in AISC-LRFD for point load and UDL for a simply supported beam loaded at the shear centre are 1.35 and 1.12, respectively. The value of $C_\text{b}$ for UDL is less than the point load as uniformity in compression force is higher for UDL than the point load. The nominal moment for a beam subjected to loads other than uniform moment is given by

$$M_\text{n} = C_\text{b} M_{\text{ocr}} \tag{2}$$

**Table 1** Coefficients for beams with simple supports [11]

| Type of load | *A* | *B* |
|---|---|---|
| Point Load (PL) | 1.35 | $1 - 0.180W^2 + 0.649W$ |
| Uniformly Distributed Load (UDL) | 1.12 | $1 - 0.154W^2 + 0.535W$ |

Galambos and Surovek [11] proposed an equation to find $C_b$ for different loadings, support conditions and positions of loading from shear centre. It was derived from elastic LTB analysis of thin-walled beams and these values were used for beams that buckled in the inelastic range. The value of $C_b$ depends on the type of loading, position of loading from the shear centre and support conditions. The position of loading from the shear centre has a significant effect on the beam's load carrying capacity when subjected to flexure. When a load is applied at the top and bottom flanges, an additional moment is created about the shear centre. This moment destabilizes the beam when the load is applied at the top flange and stabilizes, i.e. provides resistance to LTB when the load is applied at the bottom flange. For different loading positions, the value of $C_b$ is given by the following equations

$$C_b = AB^{\frac{2y}{d}} \tag{3}$$

where *A* & *B*—Coefficients for beams with simple supports, *d*—Depth of cross-section and *y*—Distance from the centroid to the spot where load is applied. The value of '*y*' is negative when load is applied above the shear centre. It is positive when the load is applied below the shear centre.

Table 1 shows the values of *A* and *B* for the Eq. (3) under different loading conditions. In general, a beam reveals three ranges of behaviour

(1) Plastic behaviour, in which the unbraced length is small and the beam has the capacity to yield completely at the cross-section before buckling occurs.
(2) Inelastic behaviour where instability occurs when a portion of the cross-section yields.
(3) Elastic buckling which occurs in beams of long, unbraced length.

The following equation is used to determine the nominal moment of the beam. AISC-LRFD provides equations to determine the limiting lengths for a beam in the plastic and elastic ranges.

$$M_n = \left[ M_p - (M_p - 0.7F_y S_x)\left(\frac{L_b - L_p}{L_r - L_p}\right)\right] \leq M_p \tag{4}$$

## 2 Background

The utilization of CBs in structures was introduced in the late 1960's. Many studies were undertaken earlier to understand the structural behaviour of CBs [3]. Blodgett [4] developed new design concepts for CBs. Nethercott and Kerdal [10] investigated the bending strength of CBs and compared the results with code provisions. Laboratory tests were carried out by Kerdal and Nethercott [6] to understand the varied failure modes of CBs. The conclusion from the test results was that the shear and formation of vierendeel mechanisms were dominant factors for the collapse of CB. Earlier studies, showed that the structural behaviour of CBs was similar to that of plain webbed beams [8, 13] and that laterally, unrestrained CB design was similar to a plate girder.

Mohebhak [7] made numerical studies of non-linear lateral-torsional buckling behaviour of simply supported CBs. His conclusion was that the value of $C_b$ was inconsistent with the length of the CB's slenderness and hence proposed a reduction factor for $C_b$ in the inelastic range. Bracing requirements of castellated beams were investigated by Mohebhak and Showkati [8] using the finite element method which concluded that the effect of bracings on inelastic castellated beams initially increased to some extent as the lateral unbraced length increased and then decreased till the beam behaved as an elastic beam. They also proposed a general equation to determine the optimum stiffness value instead of Winster's simplified method to determine bracing requirements. Mohebhak [9] carried out a numerical investigation of the inelastic non-linear behaviour of I-beams. He concluded that the predicted $C_b$ values from the finite element method are smaller in the inelastic region.

Research works were undertaken to determine the effect of beam slenderness and type of loading on the moment gradient factor of CBs. However, it was not extended to determine the effect of the position of loading on the $C_b$ value for CBs that buckle inelastically. The main objective of this study is to investigate the effect of beam slenderness and position of loading on the moment gradient factor of CBs which buckle inelastically.

## 3 Non-linear Finite Element Model

### *3.1 Mesh and Material Properties*

A non-linear analysis was performed by using the FE tool ABAQUS. The beam was modelled with the element type S4R (4 noded doubly curved thin shell element) [2]. A web-post of the CB was modelled with 8 elements across the height and two across the width of the flanges for a 26.6 × 26.6 mm mesh size in the present study.

A convergence criterion based on the maximum norm of incremental displacement was adopted using the *Static-Riks analysis* in the finite element tool ABAQUS® Fig. 1

shows the finite element (FE) model of the CB (CB225) and the corresponding geometrical parameters mentioned in Table 2.

The tri-linear elastic–plastic strain-hardening stress–strain curve is assumed for the material's non-linearities [7]. In this study, Young's modulus and Poisson's ratio are considered as 210 GPa and 0.3, respectively. From previous studies, residual stresses were not considered in this work, though it is relevant for this analysis [5, 7, 13]. As a general rule, material non-linearity is included in FE analysis by providing the normal stress of the material and normal strain values. The parameters considered for the analytical study is mentioned in Table 3.

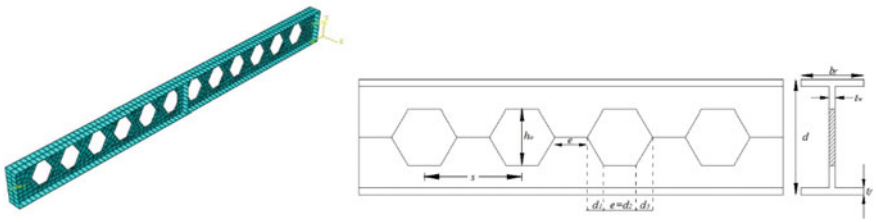

**Fig. 1** Typical FE model of CB and geometrical terms of CB

**Table 2** Geometrical parameters of the CB

| Beam | $b_f$ mm | $t_f$ mm | $t_w$ mm | $h_o$ mm | $d$ mm | $h_w$ mm | $e$ mm | $S$ mm | $d_1 = d_3$ mm |
|---|---|---|---|---|---|---|---|---|---|
| CB225 | 75 | 6 | 3.2 | 150 | 225 | 213 | 45 | 170 | 40 |

**Table 3** Geometrical parameters of the CB

| Parameters | Numerical study |
|---|---|
| Test condition | Three-point loading |
| Sectional classification | Compact |
| Boundary condition | Laterally unrestrained simply supported condition |
| Mesh size | 26.6 × 26.6 mm |
| Young's Modulus (E) | 210 GPa |
| Poisson's ratio | 0.3 |
| Element type | S4R (Flanges) and S3A3 (Web-post) |
| No. of specimens considered in FE study | 64 |

### 3.2 Loading and Boundary Conditions

In this study, the support condition of the beam was considered as simply supported. The CBs were analysed in a laterally unrestrained condition. This was done to investigate lateral-torsional buckling (LTB) behaviour. The following beam (CB 225) geometry with different span lengths are preferred for pure bending and PL and UDL for evaluation of $C_b$ value factors. The geometrical terms of the castellated beam is mentioned in Fig. 3. Span lengths were chosen to ensure even number of holes along the span and the line of action of loading passes through the web-post. All openings are hexagonal in shape and a 60° angle is considered the angle of cut. Bearing stiffeners were provided in all beams at the support and the position of PL to prevent local yielding due to stress concentration. Loads were applied at the top and bottom flanges and at the shear centre of the cross-section. Due to the presence of openings in the web (castellation), loading at the shear centre was by applying half the load at the top flange and the next half at the bottom flange [7]. Torsional couple produced due to such loading cancel each other and hence the load behaviour is either PL or UDL at the shear centre. Support condition was provided at the mid-point of the cross-section at the ends and additional lateral supports at the corners of the flanges in the cross-section.

### 3.3 Non-Linear Analysis

Non-linear analysis was carried out in two steps with the finite element tool ABAQUS. In the first step, linear buckling analysis was performed to incorporate geometrical non-linearities to the FE model. Earlier studies considered the first mode (lowest mode) of linear buckling analysis including geometrical non-linearity in the model. In the second step, non-linear analysis was performed using *Riks analysis*. The following terms performs *Riks analysis.*

- This method is generally used to predict unstable, geometrically non-linear collapse of a structure (AISC 360-10).
- This method can include material non-linearity.
- It frequently selects an Eigenvalue from buckling analysis to provide complete information about a structure's collapse.

An imperfection value of $d_w/100$ was considered to perform non-linear analysis. The earlier study showed the use of this imperfection factor in the non-linear analysis [2, 13]. The imperfection provided for this study was 2.13 mm ($d_w/100$). In general, linear Eigenvalue analysis may be accepted for design evaluation, but in some cases *Riks analysis* was performed to investigate the problem concerning material and geometrical non-linearity before buckling, or unstable post buckling response.

Three FE analytical studies were considered for the validation of the FE models. The first two models were used to validate the FE model [13, 14] of the CB beam

**Table 4** Validation of FE model

| Parameter | Experimental study by Zarrour 14 | Analytical study by Soltani et al. [13] | Present study P (kN) | % Variation experimental study | % Variation analytical study (%) |
|---|---|---|---|---|---|
| Ultimate Load (kN) | 73.84 | 81.56 | 79.12 | + 7.15 | − 3.00 |

and the third model used to validate the LTB analysis using FE analysis. The details of the obtained results are given in Table 4. In the FE model of CB, ultimate load carrying capacity computed from the present study was 7.15% higher than the earlier experimental study. This value is 3% lesser than the earlier FE analytical study. Similarly, a variation of 8% (negative sign indicates reduction) in the value of moment carrying capacity for the I Sections subjected to pure bending and point load was noted. As the $C_b$ factor is obtained by dividing the moment carrying capacity of point load with that of pure bending, the error was not carried over and the value of $C_b$ was equal to that obtained by the author.

After validating the finite element model, a non-linear analysis was performed in the assumed CB model to determine the value of $C_b$ by varying the beam's slenderness and the position of loading from the shear centre. According to AISC-LRFD any specification failure of a beam will be through LTB or yielding when the flanges and web of the section are compact. Beam section should satisfy the following conditions.

For flange, $b_f/t_f < 0.38(E/f_y)^{0.5}$, $6.25 < 11.4$

For web, $h_w/t_w < 3.76(E/f_y)^{0.5}$, $66.56 < 112.4$

Hence, the section is compact. Limiting length for plastic and elastic behaviour of a given cross-section according to AISC-LRFD is, $L_p = 1.002$ m and $L_r = 2.570$ m and plastic moment carrying capacity of the assumed castellated section obtained is $M_p = f_y Z_p = 26.21$ kN-m.

## *3.4 Parametric Study*

The CB section in this study was subjected to uniform moment, concentrated load and uniformly distributed load at the top and bottom flanges and the shear centre. The length of the assumed section was considered so that it fell in plastic, inelastic and elastic ranges. The length of CB assumed in the present study is given in Table 5. A total of sixty-three beams were analysed in the study using commercially available FE tool ABAQUS®.

**Table 5** Parametric information

| Type of loading | Position of loading | Length (m) |
|---|---|---|
| Point Load (PL) | Shear Centre | 1.19, 1.53, 1.87, 2.21, 2.55, 2.89, 3.23, 3.57 and 3.91 |
| | Bottom Flange | |
| | Top Flange | |
| Uniformly Distributed Load (UDL) | Shear Centre | 1.19, 1.53, 1.87, 2.21, 2.55, 2.89, 3.23, 3.57 and 3.91 |
| | Bottom Flange | |
| | Top Flange | |

# 4 Observations and Discussion

## *4.1 Point Load (PL)*

A single point load is applied at the shear centre, top flange and bottom flange and at the mid-span of the CB for the various lengths. The critical buckling load at which instability occurs is determined by plotting *load versus deflection* graph. The typical view of point load acting in the CB is shown in the Fig. 4.

### 4.1.1 Point Load at Top Flange

Figure 2a shows the variations in $C_b$ for CBs (CB 225) of varying slenderness subjected to PL at top flange. It can be observed that in the entire range of beam slenderness the value of $C_b$ obtained from FE analysis is marginally higher than those recommended value in the earlier study. This is due to the destabilizing effect of loading in top flange.

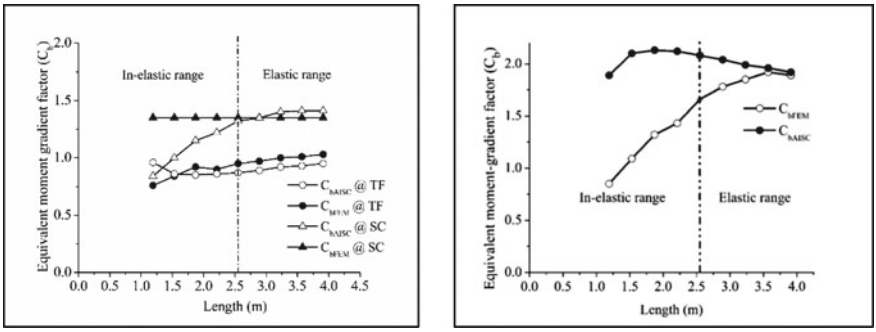


(a) (b)

**Fig. 2** $C_b$ *versus L* for Point Load. **a** PL acting at top flange and SC. **b** PL acting at bottom flange

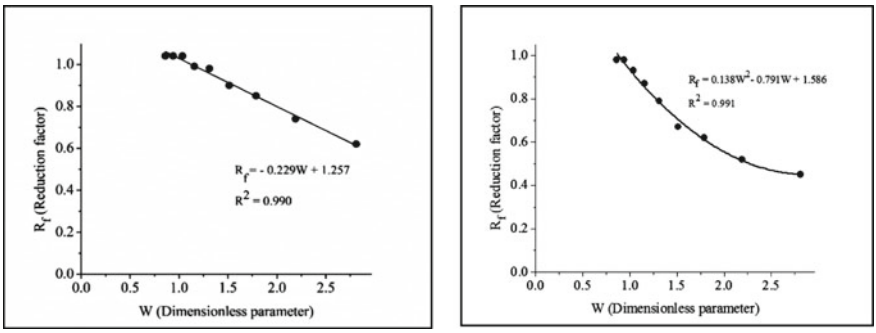


**Fig. 3** *W versus* $R_f$ for Point Load. **a** PL acting at top flange and SC. **b** PL acting at bottom flange

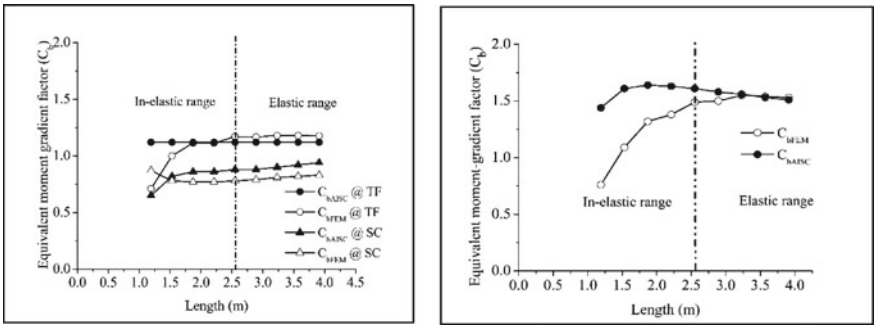


**Fig. 4** *W versus* $R_f$ for Point Load. **a** PL acting at top flange and SC. **b** PL acting at bottom flange

### 4.1.2 Point Load at Shear Centre

Figure 2a shows the variations in $C_b$ for CBs (CB 225) of varying slenderness subjected to PL at shear centre. It was observed that, for the beams in the inelastic range the value of $C_b$ given in AISC is 30% higher than those obtained by using FE analysis and for the beam in the elastic range the value of $C_b$ obtained from finite element method shows a variation of only 5% to the value given in AISC. The decrease in the load carrying capacity of the CBs in the inelastic range is due to local failure like web-post buckling and formation of vierendeel mechanism.

### 4.1.3 Point Load at Bottom Flange

Figure 2b shows the variations in $C_b$ for CBs of varying slenderness subjected to PL at bottom flange. It was observed that, for the beams in the inelastic range the

value of $C_b$ given in earlier studies is 50% higher than those obtained by using finite element method and value of $C_b$ in the elastic range shows a variation of only 5% to the value given in AISC. The decrease in the load carrying capacity of the CBs in the inelastic range is due to local failure like web-post buckling and formation of vierendeel mechanism. It can also be observed that the variation in the value of $C_b$ in the inelastic range for the beams subjected to point load at bottom flange is higher than the $C_b$ obtained for point load acting at the shear centre by 20%. This variation is due to the stabilizing effect of the loading in the bottom flange which leads to yielding of cross-section prior to buckling.

### 4.1.4 Reduction Factor for PL

As the value of $C_b$ obtained in the inelastic range for PL acting at SC and bottom flange is higher than that given in AISC-LRFD and earlier studies by [11] respectively, a reduction factor is recommended in this study. The values of the reduction factor for different spans of the CB subjected to PL at SC and bottom flange are given in Table 6. Variation of the reduction factor with the dimensionless parameter '$W$' is shown in Fig. 5a and b for the PL acting at SC and bottom flange, respectively.

Figure 3a shows a linear polynomial regression equation ($R^2 = 0.990$) to determine the reduction factor for PL acting at the shear centre using FE analysis.

Figure 3b shows a second degree polynomial regression equation ($R^2 = 0.991$) to determine the reduction factor for PL acting at bottom flange using FE analysis. The reduction factors are given by the following equations.

For $W < 2.81$ and $L > L_p$

$$R_{fsc} = -0.229W + 1.257 \tag{5}$$

$$R_{fb} = 0.138W^2 - 0.791W + 1.587 \tag{6}$$

**Table 6** Reduction factor for PL acting at shear centre and bottom flange

| Length (m) | $W$ | Reduction factor ($R_f$) | |
|---|---|---|---|
| | | Shear centre ($R_{fsc}$) | Bottom flange ($R_{fb}$) |
| 1.19 | 2.81 | 0.62 | 0.45 |
| 1.53 | 2.18 | 0.74 | 0.52 |
| 1.87 | 1.79 | 0.85 | 0.62 |
| 2.21 | 1.51 | 0.90 | 0.67 |
| 2.55 | 1.31 | 0.98 | 0.79 |
| 2.89 | 1.16 | 0.99 | 0.87 |
| 3.23 | 1.03 | 1.04 | 0.93 |
| 3.57 | 0.94 | 1.04 | 0.98 |
| 3.91 | 0.86 | 1.04 | 0.98 |

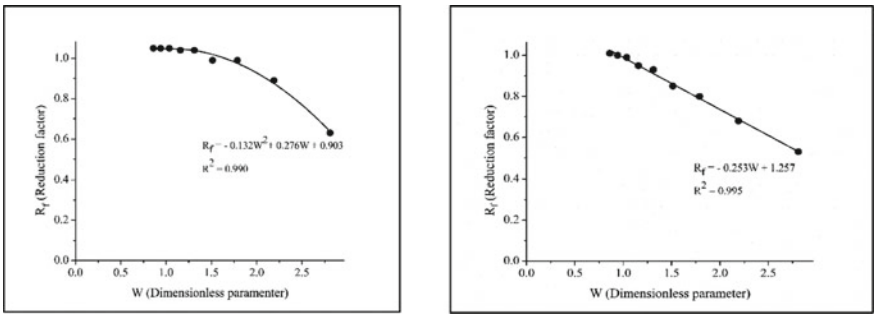


**Fig. 5** *W versus* $R_f$ for Uniformly Distributed Load. **a** UDL acting at top flange and SC. **b** UDL acting at bottom flange

where $R_{fsc}$ and $R_{fb}$ are the reduction factors of $C_b$ for PL acting on shear centre and bottom flange, respectively.

The values of $C_b$ in the inelastic range after the application of the reduction factor are shown in Table 7. Reduction of 2% in the maximum variations in $C_b$ from the FE analysis after the application of the reduction factor has been observed for PL acting at SC and 5% for PL acting at bottom flange. The above equations are applicable even in the elastic range. As the value of $C_b$ for point load subjected to top flange shows only marginal variation with the value of $C_b$ obtained from earlier study, no reduction factor is required and the equations are given in the previous study to determine the value of $C_b$ for general I-beams (rolled) can be applied to CBs in the entire range of slenderness.

**Table 7** Reduced $C_b$ factor for PL acting at SC and bottom flange

| Length (m) | $W$ | Shear centre | | Bottom flange | |
|---|---|---|---|---|---|
| | | $C_{b\,(FEM)}$ | $C_{br}$ | $C_{b\,(FEM)}$ | $C_{br}$ |
| 1.19 | 2.81 | 0.84 | 0.83 | 0.85 | 0.86 |
| 1.53 | 2.18 | 1.00 | 1.02 | 1.09 | 1.09 |
| 1.87 | 1.79 | 1.15 | 1.14 | 1.32 | 1.31 |
| 2.21 | 1.51 | 1.22 | 1.23 | 1.43 | 1.50 |
| 2.55 | 1.31 | 1.32 | 1.29 | 1.66 | 1.64 |
| 2.89 | 1.16 | 1.35 | 1.34 | 1.78 | 1.74 |
| 3.23 | 1.03 | 1.40 | 1.38 | 1.85 | 1.83 |
| 3.57 | 0.94 | 1.41 | 1.41 | 1.92 | 1.89 |
| 3.91 | 0.86 | 1.41 | 1.43 | 1.89 | 1.94 |

## *4.2 Uniformly Distributed Load (UDL)*

### 4.2.1 Uniformly Distributed Load at Top Flange

The varying slenderness due to UDL applied at top flange shows the variation of $C_b$ in Fig. 4a. The $C_b$ value obtained from FE analysis which has the entire range of beam slenderness is a little higher than the other earlier recorded studies. This is due to the destabilizing effect of the load applied to the top flange. Hence, no reduction factor is required and the equations given in the entire range of slenderness in the earlier recommendations to determine the value of $C_b$ for general I-beams (rolled) can be applied to CBs in the entire range of slenderness. The above results also indicates when the load is applied anywhere in the cross-section and the entire range of slenderness, the load carrying capacity of a beam subjected to PL is higher than that of the load carrying capacity occurring due to UDL.

### 4.2.2 Uniformly Distributed Load at SC

The difference in $C_b$ occur due to varying slenderness of applied UDL at the shear centre. This has been shown in Fig. 4a of the $C_b$ in the inelastic range. It is also being identified that the $C_b$ factor computed from FE analysis seem to be 40% higher than the AISC recommendation which is not constant in the entire range of slenderness in inelastic range. Similarly the variation of $C_b$ in the elastic range varies around 5% to the value given in AISC. The CB fails due to the occurrence of local failure. This local failure take places due to the web-post buckling and the formation of vierendeel mechanism in the inelastic range. This affects the load carrying capacity of the CB.

### 4.2.3 Uniformly Distributed Load at Bottom Flange

A few measures have been initialized for obtaining $C_b$ for PL. The same measures has been initialised to UDL for obtaining the $C_b$. Figure 4b observe the difference of $C_b$ due to varying slenderness that occurs by applying UDL at the bottom flange. The $C_b$ factor computed from FE analysis seem to be 50% higher than the AISC recommendation which is inconsistent in the entire range of slenderness in inelastic range, similarly the variation of $C_b$ in the elastic range varies around 5% to the value given in AISC. The CB fails due to the occurrence of local failure. This local failure takes place due to web-post buckling and the formation of vierendeel mechanism in the inelastic range. This affects the load carrying capacity of the $C_b$ in the inelastic range. It can also be observed that the variation in the value of $C_b$ in the inelastic range for the beams subjected to point load at bottom flange is higher than the $C_b$ obtained for UDL acting at shear centre by 10%. This variation is due to the stabilizing effect of the loading in bottom flange which leads to yielding of cross-section prior to buckling.

**Table 8** Reduction factor for UDL acting at shear centre and bottom flange

| Length (m) | $W$ | Reduction factor ($R_f$) | |
|---|---|---|---|
| | | Shear centre ($R_{fsc}$) | Bottom flange ($R_{fb}$) |
| 1.19 | 2.81 | 0.63 | 0.53 |
| 1.53 | 2.18 | 0.89 | 0.68 |
| 1.87 | 1.79 | 0.99 | 0.80 |
| 2.21 | 1.51 | 0.99 | 0.85 |
| 2.55 | 1.31 | 1.04 | 0.93 |
| 2.89 | 1.16 | 1.04 | 0.95 |
| 3.23 | 1.03 | 1.05 | 0.99 |
| 3.57 | 0.94 | 1.05 | 1.00 |
| 3.91 | 0.86 | 1.05 | 1.01 |

### 4.2.4 Reduction Factor for Uniformly Distributed Load

The value of the reduction factor for the different span is given in Table 8. Variations in the reduction factor with the dimensionless parameter $W$ are shown in Fig. 5 for UDL at shear centre and bottom flange, respectively.

Figure 5a shows a second degree polynomial regression equation ($R^2 = 0.990$) while Fig. 5b shows a linear polynomial regression equation ($R^2 = 0.995$) for the reduction factor computed using FE analysis for UDL acting at shear centre and bottom flange, respectively. The reduction factors are given by the following equations.

For $W < 2.81$ and $L > L_p$

$$R_{fsu} = -0.132W^2 + 0.276W + 0.903 \tag{7}$$

$$R_{fbu} = -0.253W + 1.242 \tag{8}$$

where $R_{fsu}$ and $R_{fbu}$ are the reduction factors of $C_b$ for UDL acting at shear centre and bottom flange, respectively. The value of $C_b$ in the inelastic range after application of the reduction factor is shown in Table 9. The maximum variation of $C_b$ from the finite element results shown as reduced to 2% for UDL at shear centre and 4% for UDL at bottom flange. This is after application of reduction factor. The above equations are applicable even in the elastic range.

**Table 9** Reduced $C_b$ factor for UDL acting at SC and bottom flange

| Length (m) | $W$ | Shear centre | | Bottom flange | |
|---|---|---|---|---|---|
| | | $C_{b\,(FEM)}$ | $C_{br}$ | $C_{b\,(FEM)}$ | $C_{br}$ |
| 1.19 | 2.81 | 0.71 | 0.71 | 0.76 | 0.79 |
| 1.53 | 2.18 | 1.00 | 1.02 | 1.09 | 1.09 |
| 1.87 | 1.79 | 1.12 | 1.09 | 1.32 | 1.32 |
| 2.21 | 1.51 | 1.11 | 1.14 | 1.38 | 1.43 |
| 2.55 | 1.31 | 1.17 | 1.16 | 1.49 | 1.49 |
| 2.89 | 1.16 | 1.17 | 1.17 | 1.50 | 1.53 |
| 3.23 | 1.03 | 1.18 | 1.17 | 1.55 | 1.55 |
| 3.57 | 0.94 | 1.18 | 1.17 | 1.54 | 1.56 |
| 3.91 | 0.86 | 1.18 | 1.17 | 1.53 | 1.57 |

## 5 Conclusion

For determining the effect of beam slenderness and different position of loading from shear centre for PL and UDL on $C_b$ in the inelastic range of the considered CB cross-section, the non-linear finite element analysis was examined and the reduction factors were proposed in terms of $W$ for CB that buckles inelastically.

- The conclusions based on the results of the FE analysis, is that the value of $C_b$ is inconsistent in the entire range of CB's slenderness. The $C_b$ factor computed by elastic analysis cannot be utilized in the inelastic region because of the variation in the $C_b$ factor
- For a specific cross-section, the increase in the $W$ value implies the diminishing in the length and thus increases the degree of plasticity. This also reduces the withstanding capacity of the elastic portion of that cross-section against the lateral buckling. This leads to the decrease in the value of $C_b$, obtained through elastic analysis, in the inelastic range
- The reduced moment gradient factor that can be implemented to the beams that buckle inelastically can be obtained by multiplying a reduction factor to $C_b$. FE-based regression equations for evaluating the reduced $C_b$ values are proposed for the loading conditions considered in this study. The equations are polynomial in terms of $W$ of the CBs
- This reduction in the $C_b$ factor of the CBs might be due to local buckling of web-post or yielding of the T-sections above and below the castellation portions (holes) inducing the immature weakness
- The value of $C_b$ depends on the type of loading, position of loading and support conditions of the CBs. Hence, this study can be further extended to determine the effect of different loadings and boundary conditions on the value $C_b$ so that a generalized result can be obtained.

## References


1. ANSI/AISC 360-16 (2016) Specification for structural steel buildings, American Institute of Steel Construction (AISC), pp 47–49, Illinois, U.S.A.
2. Baskar K, Aarthy E, Cyril Thomas A (2016) Buckling behavior of inelastic castellated beams. In: Proceedings of 6th international conference on computational mechanics (ICCMS2016) at IIT Bombay, on June 26th–July 1st 2016, pp 882–885
3. Bradford MA (1992) Lateral-distortional buckling of steel I-section member. J Constr Steel Res 23:97–116
4. Blodgett OW (1976) Design of welded structures, The James F. Lincoln Arc Welding Foundation, pp 4.7 1–24, 7th printing, Ohio, U.S.A.
5. Cyril Thomas A, Baskar K (2019) Assessment of load carrying capacity of thin-webbed castellated beams. Rec Adv Struct Eng 1:pp 339–350 (Springer, Singapore)
6. Kerdal D, Nethercott DA (1984) Failure modes for castellated beams. J Constr Steel Res 4:295–315
7. Mohebkhah A (2004) The moment–gradient factor in lateral-torsional buckling on inelastic castellated beams. J Constr Steel Res 60:1481–1494
8. Mohebkhah A, Showkati H (2005) Bracing requirements for inelastic castellated beams. J Constr Steel Res 61:1373–1386
9. Mohebkhah A (2011) Lateral buckling resistance of inelastic I-beams under off shear center loading. J Thin-Walled Struct 49:431–436
10. Nethercott DA, Kerdal D (1982) Lateral–torsional buckling of castellated beams. Struct Eng London 60B(3):53–61
11. Galambos TV, Surovek AE (2008) Structural stability of steel concepts and applications for structural engineers. John Wiley & Sons, New Jersey, pp 236–289
12. Redwood R, Demirdjian S (1998) Castellated beam web buckling in shear. J Struct Eng (ASCE) 124:1202–1207
13. Soltani MR, Bouchair A, Mimoune M (2012) Non-linear FE analysis of the ultimate behavior of steel castellated beams. J Constr Steel Res 70:101–114
14. Zaarour W, Redwood R (1996) Web buckling in thin-webbed castellated beams. J Struct Eng (ASCE) 122:860–866
15. Zirakian T, Showkati H (2006) Distorsional buckling of castellated beams. J Constr Steel Res 62:863–871

# Nonlinear Compression Behaviour of Thin-Walled Battened Columns Composed of Steel Angle Sections


**M. Anbarasu and M. Adil Dar**

**Abstract** The previous research on cold-formed-steel (CFS) built-up compression members has been dominated by-adopting channels as chord members. The use of channel sections as chord members limits the gap extension between the chord members to one direction only. This gives adoption of angle sections as chord elements a better edge over channel sections. However, the little research output available on CFS built-up compression members composed of plain angles indicated early local buckling formation at the initial steps of compressive axial loading. Lipped angle sections can substantially enhance the buckling strength of these columns by prolonging the early local buckling. This study reports a numerically performed on CFS built-up compression members formed with of edge-stiffened angles under concentric compressive loading. Based on global slenderness all the three categories of columns, were studied. Also, the compactness of the angle sections as well as the batten spacing was varied. Lastly, the numerical axial strengths were compared against the current North American Standard (NAS) strengths.

**Keywords** Battens · Built-up columns · Nonlinear buckling analysis · Cold-formed steel · Axial strength

## 1 Introduction

The research work on cold-formed steel (CFS) all over the world is growing, with an aim to make CFS construction better, particularly in terms of their enhanced strengths offered by the improved CFS members. Little research work has been reported in the past on the performance of thin-walled steel built-up compression members [2–10,

M. Anbarasu
Civil Engineering, GCE, Tamil Nadu, Salem 636011, India

M. Adil Dar (✉)
Civil Engineering, IIT Delhi, New Delhi 110016, India
e-mail: madar@civil.iitd.ac.in



M. Madhavan et al. (eds.), *Proceedings of the Indian Structural Steel Conference 2020 (Vol. 1)*, Lecture Notes in Civil Engineering 318,
https://doi.org/10.1007/978-981-19-9390-9_35

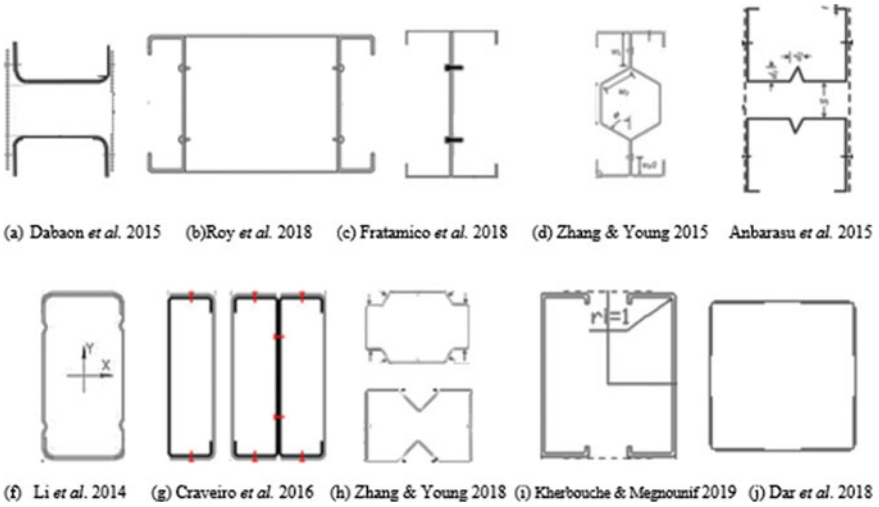


**Fig. 1** Previously studied sections

12, 13], clearly reflecting the need for more research on such members. The cross-sections of the past researched built-up compression members are shown in Fig. 1. In all these cases, obtaining a highly efficient built-up section was the main research objective. It goes without mentioning that the performance of the stiffened cross-sections is better than the unstiffened ones. Stiffened angle sections have a great potential to delay the early local buckling in the built-up sections comprising of such elements, as observed in the unstiffened ones [5, 6]. This delay in the early local buckling has potential to significantly improve the axial resistance of built-up sections. This study reports a numerical analysis performed on CFS built-up compression members formed with edge-stiffened angles under concentric compressive loading. Based on global slenderness all the three categories of columns, were studied. Also, the compactness of the angles and the intermediate batten spacing was varied. Lastly, the numerical axial strengths were compared against the ones obtained from the current North American Standard (NAS) strengths.

## 2 Finite Element Modelling

Finite element modelling being a powerful method for studying the nonlinear behaviour of structural members was used for performing the nonlinear numerical analysis on the CFS built-up compression members formed of edge-stiffened angles. ABAQUS software was used for the same. The numerical study was confined to the ultimate loads resisted by the battened columns as well as their failure modes. Table 1 gives the details pertaining to the numerical modelling approach adopted in the present study. The numerical model formed was calibrated using the test results

**Table 1** FEM details

| Details | Feature adopted | Detail-type | Feature adopted |
|---|---|---|---|
| Element category | S4R Shell element | Other end's condition | Hinged support |
| Mesh dimensions | $10 \times 10$ mm$^2$ | Axial load adoption | By displacing the loaded end master node |
| Material model adopted | Elastic perfectly plastic | Connection in-between various elements | Mesh independent type of fastener |
| Young's Elasticity ($E$) | 210 GPa | Imperfection (local) | 0.34 $t$ [11] |
| Yield stress ($f_y$) | 350 MPa | Imperfection (global) | Column height/1000 [11] |
| Loaded end's condition | Roller support with restricted translation along the transverse directions | Analysis (types) | Linear buckling analysis, with a nonlinear analysis in follow-up |

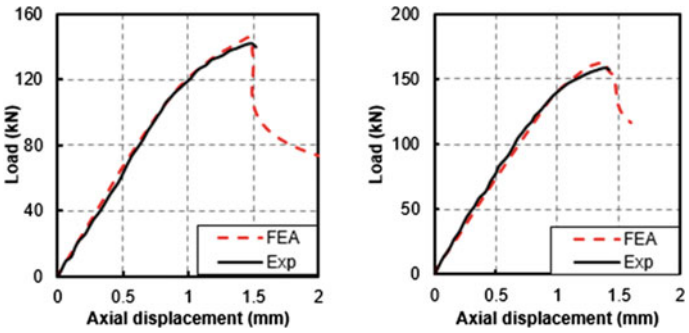


**Fig. 2** Result comparison [1]

of [1]. Figure 2 shows the axial displacement comparison for models B-130-50-20-3-100 and B-150-60-20-3-120, which clearly indicates a reasonable agreement between the two. With this calibration, the numerical models were good enough to be employed for the parametric studies, which will be discussed in the next section.

## 3 Parametric Study

The numerical parametric investigation contained 96 number of analyses performed on the CFS built-up compression members with the cross-sectional details available in [1]. The variation in the numerical models in terms of the overall slenderness, angle sectional compactness and the intermediate spacing between the battens was

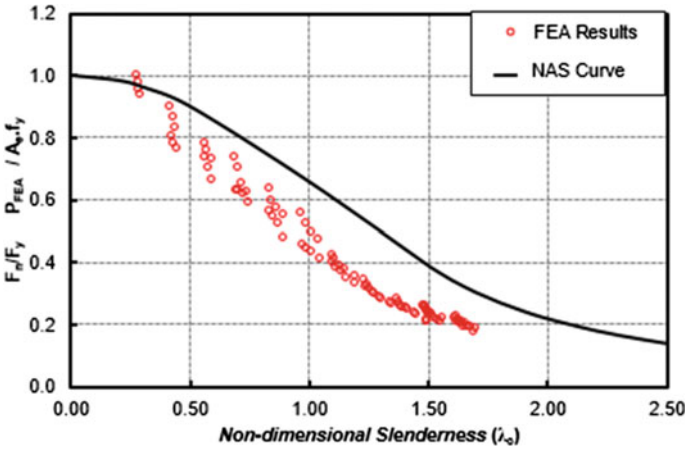


**Fig. 3** Comparison of numerical results against the design strengths

used to establish the behavioural change in these columns. The ultimate loads were recorded and plotted for the comparison against the design axial strengths quantified by-adopting the North American Specifications, 2016 (NAS), as shown in Fig. 3.

## 4 Discussion

Figure 3 clearly indicates the inadequacy of the current NAS (2016) in predicting the compression axial strengths of the CFS built-up battened compression members fabricated from lipped angles. Except for short columns with low overall slenderness, the NAS predictions are un-conservative. This magnitude of un-conservativeness increases as the overall column slenderness increases. It is worth noting that current NAS (2016) does not give any clear recommendations for the designing of CFS battened columns, particularly when the number of elements exceeds two. The failure modes observed in the specimens followed the conventional trend, i.e., short columns failed by means of pure local buckling, whereas the slender ones failed by pure flexural buckling, and the remaining one by the combination of the two. Figure 4 shows the local buckling failure mode and the combined local-flexural buckling mode as observed in parametric study for compression members with short/intermediate slenderness. Also, the structural integrity of the CFS battened columns was not affected, even at failure as the chords were primarily affected by the buckling failures.

**Fig. 4** Failure in the numerical models

## 5 Conclusions

In this paper, a numerical parametric analysis was performed by varying global slenderness, angle sectional compactness as well as intermediate spacing of the battens. The results like peak axial strengths as well as failure modes were used for interpretation of the results. Following are some of the noteworthy conclusions:

- The stiffened angle sections were able to postpone the initial early local buckling in the battened columns that was observed previously in the built-up compression members formed from unstiffened angle sections.
- Failure modes observed in the parametric study follows the conventional trend, where the short columns failed by pure local buckling while as the slender ones failed by flexural buckling. Remaining of battened columns failed by the combination of the two failure modes. Also, structural integrity of the built-up compression members was not affected, even after failure.

- The current NAS design strengths predicted for the battened compression members formed from four edge-stiffened angles were un-conservative. This magnitude of un-conservativeness was higher for slender columns.

## References


1. Anbarasu M (2019) Behaviour of cold-formed steel built-up battened columns composed of four lipped angles: tests and numerical validation. Adv Struct Eng. https://doi.org/10.1177/1369433219865696
2. Anbarasu M, Kanagarasu K, Sukumar S (2015) Investigation on the behaviour and strength of cold-formed steel web stiffened built-up battened columns. Mat Str 48(12):4029–4038
3. Craveiro HD, Paulo J, Rodrigues C, Laím L (2016) Buckling resistance of axially loaded cold-formed steel columns. Thin-Walled Struct 106:358–375
4. Dabaon M, Ellobody E, Ramzy K (2015) Experimental investigation of built-up cold-formed steel section battened columns. Thin Walled Str 92:137–145
5. Dar MA, Sahoo DR, Pulikkal S, Jain AK (2018) Behaviour of laced built-up cold-formed steel columns: experimental investigation and numerical validation. Thin-Walled Struct 132:398–409
6. Dar MA, Sahoo DR, Jain AK (2019) Axial compression behavior of laced cold-formed steel built-up columns with unstiffened angle sections. J Constr Steel Res 162 https://doi.org/10.1016/j.jcsr.2019.105727
7. Fratamico DC, Torabain S, Zhao X, Rasmussen K, Schafer BW (2018) Experiments on the global buckling and collapse of built-up cold-formed steel columns. J Constr Steel Res 144:65–80
8. Kherbouche S, Megnounif A (2019) Numerical study and design of thin walled cold formed steel built-up open and closed section columns. Eng Struct 179(15):670–682
9. Li YQ, Li YL, Wang SK, Shen ZY (2014) Ultimate load-carrying capacity of cold-formed thin-walled columns with built-up box and I section under axial compression. Thin-Walled Struct 79:202–217
10. Roy K, Ting TCH, Lau HH, Lim JBP (2018) Nonlinear behaviour of back-to-back gapped built-up cold-formed steel channel sections under compression. J Constr Steel Res 147:257–276
11. Schafer BW, Pekoz T (1998) Computational modelling of cold-formed steel: characterizing geometric imperfections and residual stress. J Constr Steel Res 47:193–210
12. Zhang J, Young B (2015) Numerical investigation and design of cold-formed steel built-up open section columns with longitudinal stiffeners. Thin-Walled Struct 89:178–191
13. Zhang J, Young B (2018) Experimental investigation of cold-formed steel built-up closed section columns with web stiffeners. J Constr Steel Res 147:380–392

# Analysis of Experimental Data on Cold-Formed Steel Shear Wall Panels


**Jammi Ashok and Sanjeevi Arul Jayachandran**

**Abstract** Cold-formed steel-sheathed shear wall panels are a reliable lateral force-resisting systems in low and mid-rise cold-formed steel buildings. The mechanics of shear wall behavior is highly complex due to nonlinear interaction of different components which are individually nonlinear in behavior. Due to the complexity in their behavior, especially, their dependence on various parameters, numerous experiments were conducted to understand their response. So, there is a need for a comprehensive understanding, bringing together the results of various experiments conducted on CFS shear wall panels using standard methods by researchers across the globe. This paper extracts the published experimental data (numbering more than 400 experiments) on laterally loaded CFS shear wall panels by different researchers to compare the effect of different parameters like type of sheathing, thickness, screw spacing, aspect ratio, stud dimensions, and so on. This analysis gives a fairly good understanding of the behavior of CFS shear walls and the influence of various parameters so that quick conclusions can be drawn on proportioning, dimensioning, choice of sheathing, and designing the CFS shear walls.

**Keywords** Cold-formed steel · Wall panels · Experiments · Data

## 1 Introduction

Cold-formed steel construction is gaining momentum in the Indian industry. In the last twenty years, there has been tremendous research done in the field of cold-formed steel all over the world. In building construction cold-formed steel products can be classified into three categories, namely, members, panels, and prefabricated assemblies. Cold-formed steel members such as studs, purlins, tracks, and angles are used for carrying compression, tensile, or bending loads. Cold-formed steel panels and decks form surface elements like floors, roofs, and walls, which resist in-plane

J. Ashok · S. A. Jayachandran (✉)
Structural Engineering Lab, Department of Civil Engineering, IIT Madras, Chennai, India
e-mail: arulsteel@gmail.com



M. Madhavan et al. (eds.), *Proceedings of the Indian Structural Steel Conference 2020 (Vol. 1)*, Lecture Notes in Civil Engineering 318,
https://doi.org/10.1007/978-981-19-9390-9_36

and out-of-plane forces caused by dead, live, wind, and earthquake loads. Prefabricated assemblies are a combination of above elements manufactured off-site, which include wall panels, roof trusses, floor panels, and so on. This study focusses on the shear wall panels that resist the in-plane shear forces caused by lateral load due to wind and earthquake. The main advantages of these elements are that they have a high strength-to-weight ratio, ease of fabrication and permit off-site fabrication. Extensive experimental research has been carried out on sheathed CFS wall panels with different configurations of sheathing materials and aspect ratios and so on, to study their effect on the behavior of shear wall panel subjected to lateral loads. However, there is a need to compile the data from different sources and draw meaningful conclusions depending on the structural behavior of the panels. This paper deals with the published data (experimental peak and ultimate values) by different researchers and identifies the trends by plotting these values for easy visualization and arriving at proper conclusions. The keep the article concise, only crucial data are plotted without losing its efficacy. The layout of a typical cold-formed steel shear wall panel is shown in Fig. 1.

The sheathing materials can be broadly classified into ductile and brittle sheathings based on their behavior and failure modes. So, in the following sections, firstly CFS shear walls with brittle sheathing are discussed, followed by ductile sheathing. Both are compared to understand their relative performance.

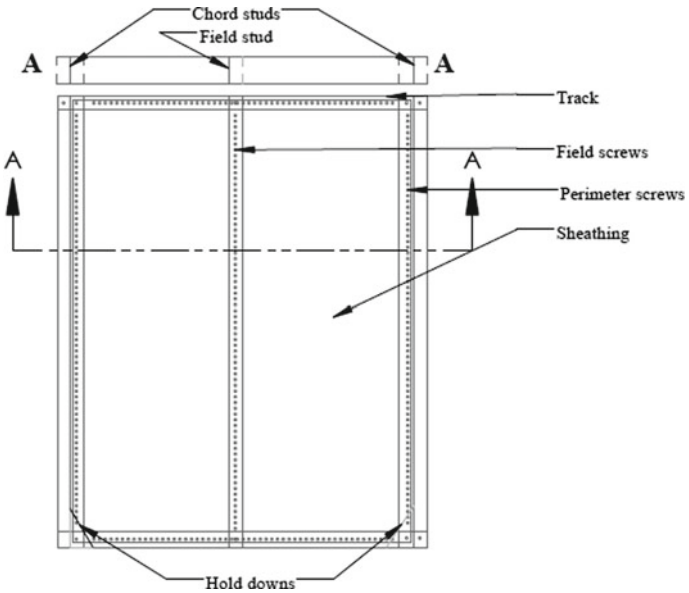


**Fig. 1** Layout of a typical CFS shear wall

## 2 Sheathed Wall Panels

### *2.1 Brittle Sheathing*

Early part of the research on CFS shear wall panels has started with brittle sheathing material like plasterboard, gypsum wall board, fiber-cement board, cement particle board, and so on. The variability in the mechanical properties of sheathing material alters the performance of the wall panel system. These are categorized as brittle sheathing due to their brittle failure mode of the sheathing. The screws connecting the sheathing and studs fail by tilting, bearing, and ultimately pull through. Firstly, the influence of dimensioning and detailing aspects like aspect ratio, screw spacing, and wall thickness is discussed, and then, more refined comparison is presented on influence of sheathing type on shear strength and stiffness of the panel. The results that are consistent are presented, i.e., the results obtained by one researcher are of the same pattern as that of another researcher. To avoid redundancy, results from few experiments [2, 6, 8–13, 15, 17, 18, 21–31, 33, 34, 36, 40, 43, 44, 47] are presented, but it is to be noted that the effects or observations follow the same pattern for all other experiments. If there is any anomaly, it is clearly identified and explained.

#### 2.1.1 Aspect Ratio

The experimental research by Tarpy [37, 38], with an explicit motivation to formulate a design procedure for strength and stiffness of wall panels, led to many important observations with respect to the construction details, sheathing types, and so on. The aspect ratio has a considerable effect on the ultimate shear strength and stiffness of the wall panel. With the increase in the aspect ratio, the shear strength and shear stiffness decrease as shown in Figs. 2 and 3. This is due to the bending action instead of shear action for high aspect ratios. When the wall is taller, it behaves like a cantilever, thereby resisting the lateral load by bending rather than by shear. Even for the same aspect ratio, wider shear walls have higher shear strengths.

#### 2.1.2 Screw Spacing

Tarpy et al observed from the experiments that as the screw spacing decreases, the shear strength of the wall panel increases. This is because of the efficient load transfer between the sheathing and the frame. Figure 4 shows the influence of screw spacing on the ultimate shear strength, keeping all other parameters constant. Variation in perimeter fastener spacing only had significant effect on shear strength, whereas variation in the field screw spacing had no significant effect on the shear strength. The spacing under study was of 150 and 305 mm magnitude, and this can be generalized for any spacing.

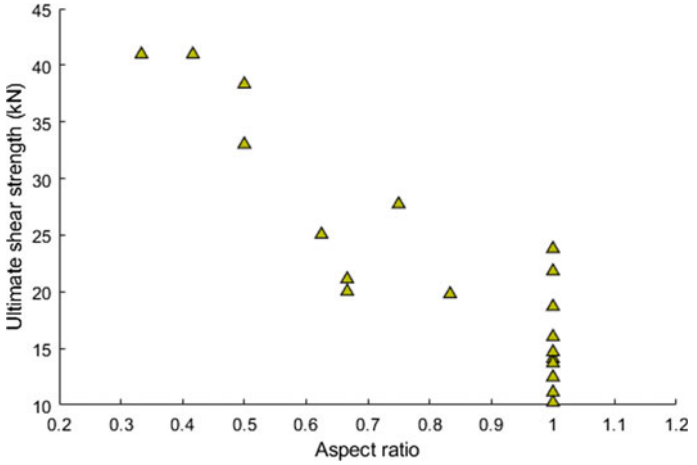


**Fig. 2** Influence of aspect ratio on shear strength

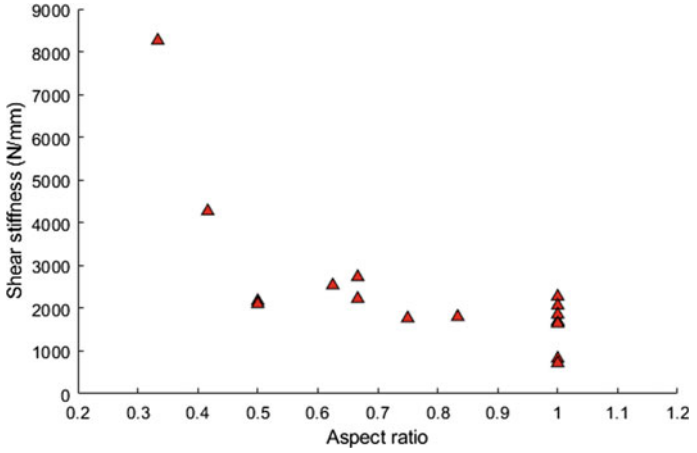


**Fig. 3** Influence of aspect ratio on shear stiffness

### 2.1.3 Effect of Type of Loading

The ultimate shear strength obtained from cyclic loading test is less than or equal to that of static loading test, whereas the shear stiffness is greater as shown in Figs. 5 and 6. The increase in stiffness is due to smaller total deflections recorded in cyclic loading than in static loading. Figure 5 shows the ultimate load versus deflection plots for monotonic and cyclic loading. In Fig. 6, it can be observed that in cyclic loading the wall panel behaves like a stiff member. This is corroborated by the increase in the stiffness values of cyclically loaded specimens when compared to monotonically loaded specimens (for same elastic shear strength).

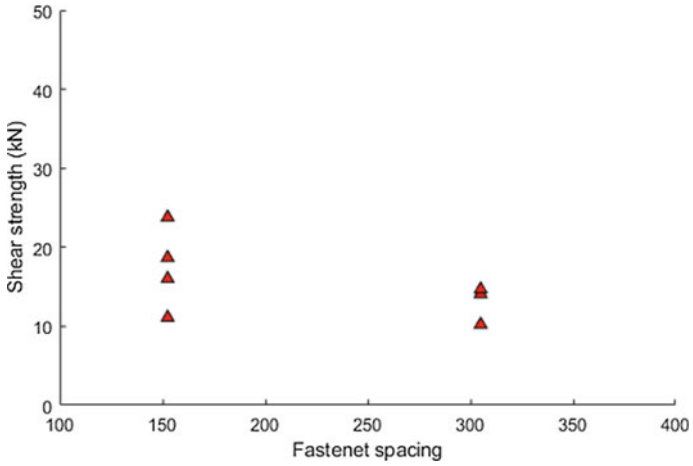


**Fig. 4** Effect of fastener spacing on shear strength

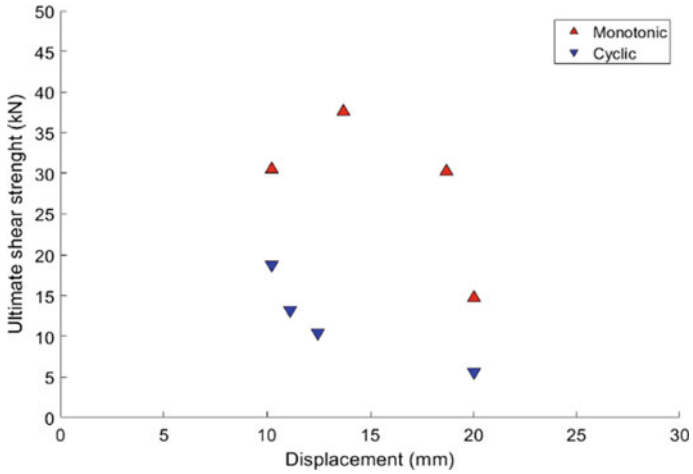


**Fig. 5** Effect of loading type on strength

These are the observation that are consistent with several other researchers. To preserve the compactness of the article, the other data are not presented. For example, the data from [19] corroborate these observations as shown in Fig. 7.

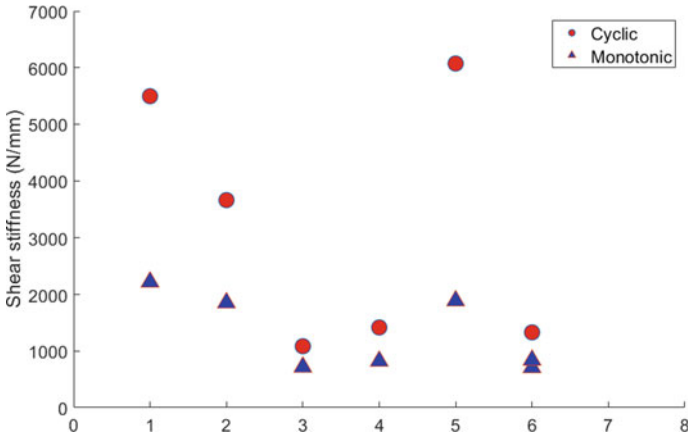


**Fig. 6** Effect of loading type on stiffness

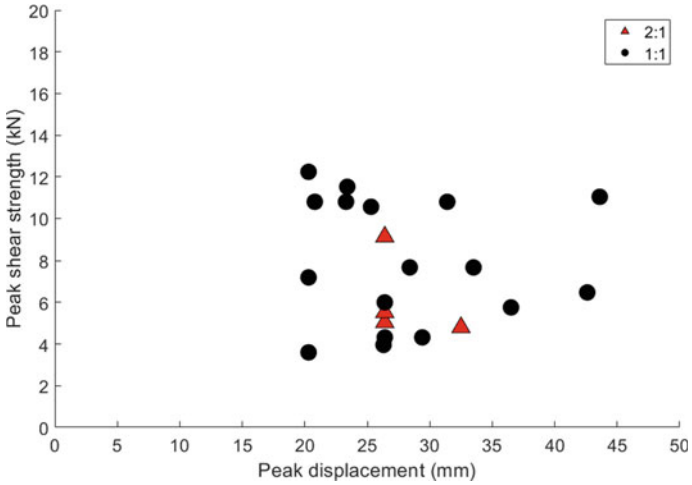


**Fig. 7** Effect of aspect ratio on behavior of wall panels

### 2.1.4 Effect of Sheathing Materials

(a) Gypsum and fiber-cement board

Figure 8 shows a comparison of ultimate shear strength versus displacement of gypsum board and fiber-cement board-sheathed wall panels [4, 7, 14, 19, 20, 32, 37–39]. It shows that extensive amount of research has been focused on the behavior of gypsum-sheathed wall panels. It is to be noted that in the figure, all the values correspond to 12.5 mm thickness sheathing but for various aspect ratios. It can be observed that fiber-cement board exhibits a better performance than gypsum board in

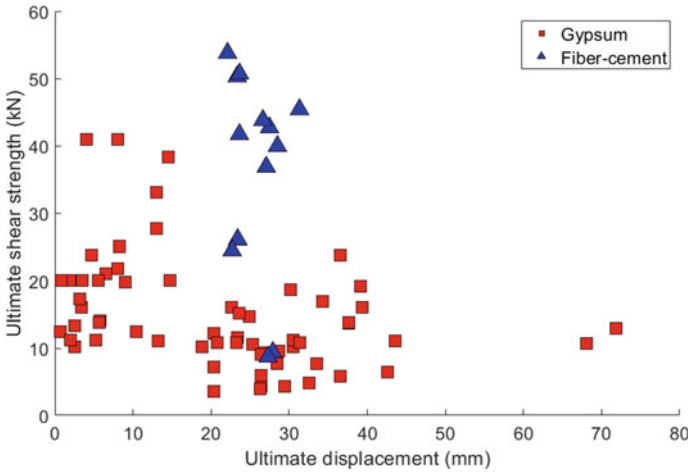


**Fig. 8** Gypsum board versus fiber-cement board

terms of shear strength and ductility. The failure mode of gypsum board is too brittle when compared to fiber-cement board and also offers low shear resistance. Fiber-cement board offers consistently good shear resistance when compared to gypsum board. The contribution of gypsum board can be taken for lateral resistance, but it cannot be relied upon, as a shear wall element. The highest shear strengths exhibited gypsum in the plot correspond to double-layer panels. Further, high shear strengths in the order of 120 kN are reported which correspond to double-layered panels of gypsum with other sheathing such as calcium silicate board or magnesium board.

Figure 9 compares the ultimate shear strengths of single-layer gypsum board and Oriented Strand Board and similar wood-based sheathing products of same aspect ratio of 2:1 [19]. It can be observed that wood-based OSB and plywood sustain higher displacements than gypsum board for same aspect ratio. It can also be observed that ultimate shear strength of OSB and plywood are more than gypsum board, and this implies that the absorbed energy for each cycle also follows the same trend. Hence, double-layer gypsum board is recommended for the purpose of shear wall design rather than using single-layered one. The higher strengths of OSB are due to the orientation of strands in between the board layers which form like a fabric to resist shear.

The summary of shear strength and stiffness values for brittle sheathing specimen obtained from various experiments and various configurations and materials are shown in Fig. 10 and Fig. 11.

This shows that majority of the specimen have shear resistance in the order of 15–20 kN. But, the median of shear strength of all the brittle sheathings is in the order of 22 kN. This gives a fairly good idea on the design criteria for brittle-sheathed shear wall panels and also quantifies the expected shear strength values. Figure 11 shows that majority of the specimen have shear stiffness in the order of 1000–2000 N/mm. Median is around 2500 N/mm. This stiffness value can be used for estimating

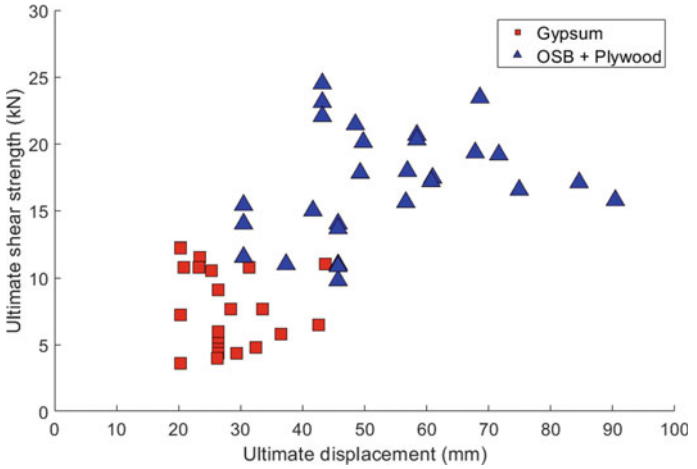


**Fig. 9** Gypsum board versus OSB (plywood)

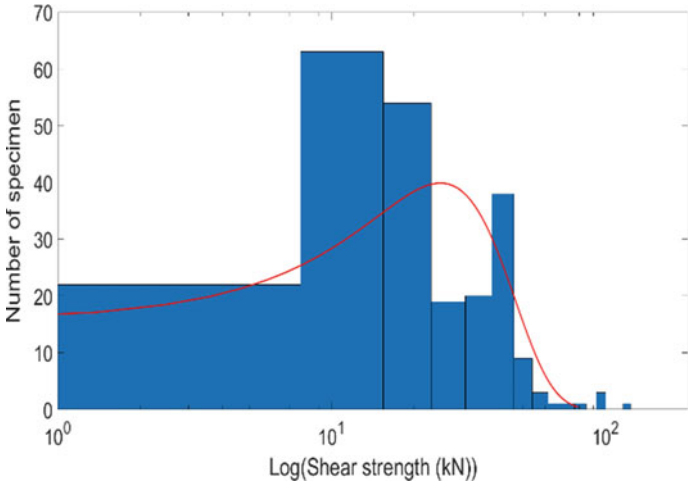


**Fig. 10** Normal plot of shear strength of brittle sheathing

the design stiffness of a particular building layout when brittle sheathing material is used. Although there is a large variation in the material properties of the sheathing specimen, the standard deviation is only 17 kN from the mean ultimate shear strength. The standard deviation of shear stiffness from the mean is 2163 N/mm, i.e., 2 kN/mm. So, the mean values of stiffness and strength significantly represent generally used brittle sheathing materials.

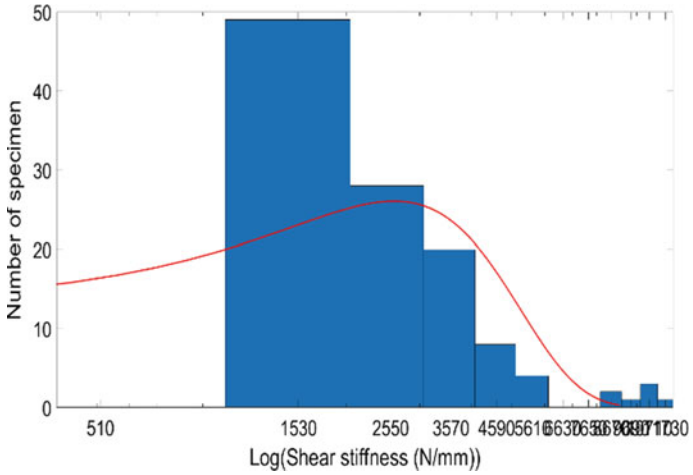


**Fig. 11** Normal plot for shear stiffness of brittle sheathing

## 2.2 *Ductile Sheathing*

Steel sheet and corrugated steel sheets are categorized as ductile sheathing. The sheathing fails by yielding due to tension field action, in case of steel sheet, if the screw connection and studs are properly designed to anchor the tensile field forces. In this section, ductile sheathing is compared directly with brittle ones, as the dimensioning and detailing aspects play a similar role as shown in Sect. 2.1. Figure 12 gives an overall comparison between the shear strengths of brittle and ductile sheathings, [1, 3, 5, 16, 35, 41, 42, 45, 46. The general sheathing thickness used is 0.686 mm and 0.832 mm.

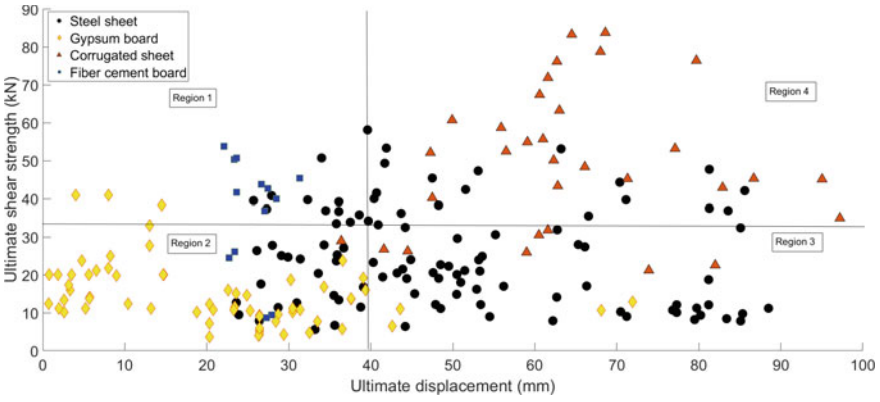


**Fig. 12** Comparing brittle and ductile sheathings

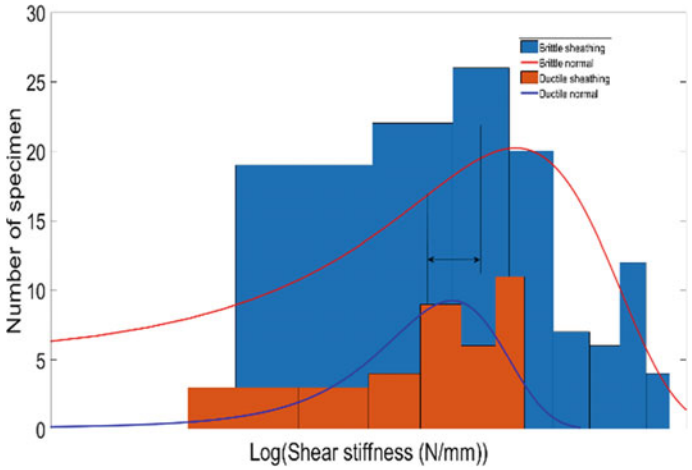


**Fig. 13** Comparing stiffness of brittle and ductile sheathings

It can be observed that most of the brittle sheathing fall into region-2 which is characterized by low strength and less ductile behavior. This includes gypsum and fiber-cement sheathing. Region-3 is characterized by low strength and high ductility. Steel sheet and corrugated sheet occupy this region, sustaining loads up to 90 mm displacement. This behavior is very useful in case of earthquakes, due to high energy dissipation. But, these are observed to have low initial stiffness which is shown in Fig. 13. The behavior of corrugated steel sheathing is marked by brittle failure. To improve the ductility of corrugated sheet sheathings, they are provided with different configurations of slits to enhance energy dissipation. Region-4 in Fig. 12 corresponds to corrugated sheet with different configurations of slits. Although the wall panel is able to reach comparatively high strength values in this region, it damages the gravity loading system if not adequately designed.

Figure 13 summarizes the shear stiffness of ductile and brittle sheathings. The median value for ductile sheathing is significantly less than that of brittle sheathing. Although ductile sheathing is preferred in terms of its strength and ductility, the designer has to be cautious with the in-plane shear stiffness. The mean value for ductile sheathing is 1525 N/mm with a standard deviation of 425 N/mm. Actually, this stiffness value is altered by the corrugated sheet which has high in-plane shear stiffness. The mean in-plane stiffness of plain sheet steel-sheathed wall panel is 950 N/mm.

From Fig. 14, it is clear that shear stiffness of corrugated steel sheet (C SHEAR) is higher than single steel sheet. The shear stiffness of corrugated steel sheet is considerably reduced when a gravity load acts on the wall panel. This is marked as "C BEARING" in the above plot.

Finally, the effect of combining ductile and brittle specimens (dual system) is studied. The results are shown in Fig. 15. It can be see that a desired effect is obtained by combining both ductile and brittle sheathings, i.e., good initial stiffness with

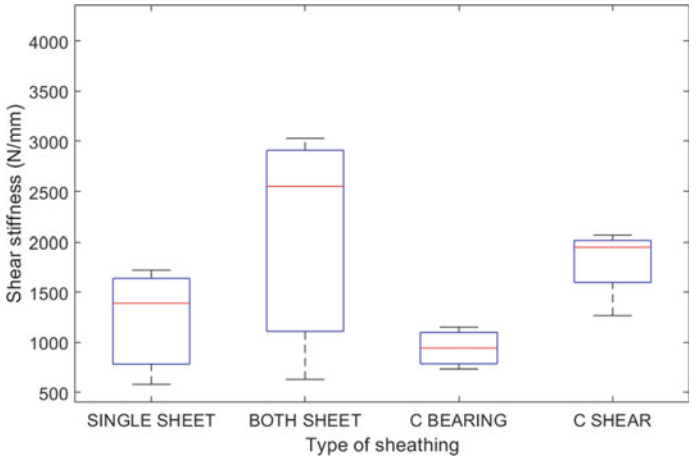


**Fig. 14** Shear stiffness of ductile sheathing

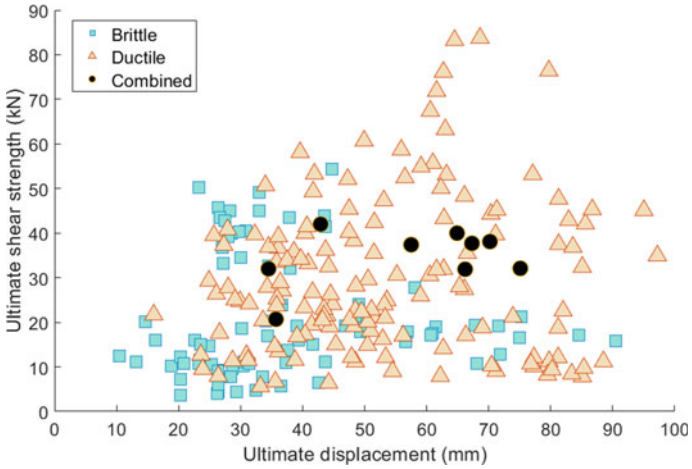


**Fig. 15** Comparing strength of dual system with ductile and brittle sheathings

relatively high ultimate strength and ductility. In this case, the two sheathings are joined by self-drilling screws. The failure in some specimen was brittle mode due to failure of gravity loading system because of low thickness of chord studs (Fig. 16).

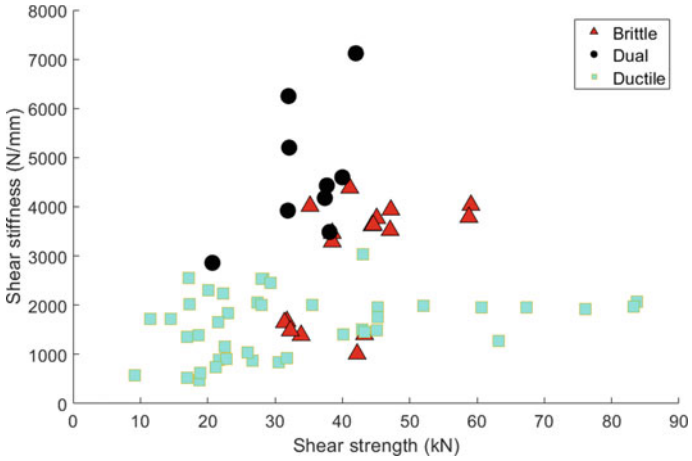


**Fig. 16** Comparing stiffness of dual system with ductile and brittle sheathings

## 3 Conclusions

The following conclusions can be drawn based on the above analysis of data obtained from various experiments:

1. The wall panel strength and stiffness reduce considerably with increase in aspect ratio (h/w).
2. For the same height, increase in length of the panel increases the shear strength and stiffness. But, this is affected by the interaction of the edges of two sheathings at their common joint.
3. Reduction in fastener spacing at the perimeter increases the shear strength and stiffness. Interior fastener spacing has no effect on strength and stiffness.
4. The type of loading also affects the behavior of the wall panel. Under monotonic loading, the panel exhibits high strength, whereas under cyclic loading, panel behaves stiffer.
5. Among the brittle sheathing materials used, gypsum-sheathed wall panels have least strength and ductility. Hence, the contribution of these panels may be taken in the shear resistance, but it would be conservative if they are not designed as shear wall panels. Fiber-cement board, calcium silicate board, and cement particle board exhibit considerably high strength and ductility.
6. Double-sheathed wall panels exhibit relatively high shear strength and stiffness because of increased thickness. This increased thickness leads to delay in the failure of screw by tilting, bearing or pull through thereby increasing the shear strength.

7. Ductile sheathing exhibits higher strength and ductility than brittle sheathing materials, but failure of chords' studs due to high compressive loads at greater drifts leads to overall brittle failure of the wall framing. So, capacity design procedure has to be adopted in designing the wall framing.
8. Ductile sheathing offers a relatively low shear stiffness than brittle sheathing. This low stiffness can be compensated by using corrugated sheathing.
9. Corrugated sheathing has high stiffness but low ductility. This ductility can be improved by forming rectangular and circular slits thereby increasing the energy dissipation.
10. Dual system, i.e., brittle and ductile sheathings combined on one side of the panel offers relatively favorable behavior of high initial stiffness and high ductility. These systems are to be studied further, accounting for the dual action.

## References

1. Attari NK, Alizadeh S, Hadidi S (2016) Investigation of CFS shear walls with one and two-sided steel sheeting. J Constr Steel Res 122:292–307
2. Baran E, Alica C (2012) Behavior of cold-formed steel wall panels under monotonic horizontal loading. J Constr Steel Res 79:1–8
3. Balh N, DaBreo J, Ong-Tone C, El-Saloussy K, Yu C, Rogers CA (2014) Design of steel sheathed cold-formed steel framed shear walls. Thin-Walled Structures 75:76–86
4. Baldassino N, Accorti M, Zandonini R, Scavazza F, Rogers CA (2014) Lateral loading response of CFS framed shear wall with cement board panels
5. DaBreo J, Balh N, Ong-Tone C, Rogers CA (2014) Steel sheathed cold-formed steel framed shear walls subjected to lateral and gravity loading. Thin-Walled Structures 74:232–245
6. Fülöp LA, Dubina D (2004) Performance of wall-stud cold-formed shear panels under monotonic and cyclic loading: Part I: experimental research. Thin-Walled Structures 42(2):321–338
7. Gad EF, Duffield CF, Hutchinson GL, Mansell DS, Stark G (1999) Lateral performance of cold-formed steel-framed domestic structures. Eng Struct 21(1):83–95
8. Golledge B, Clayton T, Reardon G (1992) Racking performance of plasterboard-clad steel stud walls
9. Girard JD, Tarpy Jr TS (1982) Shear resistance of steel-stud wall panels
10. Karabulut B, Soyoz S (2017) Experimental and analytical studies on different configurations of cold-formed steel structures. J Constr Steel Res 133:535–546
11. Kechidi S, Macedo L, Castro JM, Bourahla N (2017) Seismic risk assessment of cold-formed steel shear wall systems. J Constr Steel Res 138:565–579
12. Liu P, Peterman KD, Schafer BW (2014) Impact of construction details on OSB-sheathed cold-formed steel framed shear walls. J Constr Steel Res 101:114–123
13. Lin SH, Pan CL, Hsu WT (2014) Monotonic and cyclic loading tests for cold-formed steel wall frames sheathed with calcium silicate board. Thin-Walled Structures 74:49–58
14. Lange J, Naujoks B (2006) Behaviour of cold-formed steel shear walls under horizontal and vertical loads. Thin-Walled Structures 44(12):1214–1222
15. Mohebbi S, Mirghaderi R, Farahbod F, Sabbagh AB (2015) Experimental work on single and double-sided steel sheathed cold-formed steel shear walls for seismic actions. Thin-Walled Structures 91:50–62
16. Niari SE, Rafezy B, Abedi K (2015) Seismic behavior of steel sheathed cold-formed steel shear wall: experimental investigation and numerical modeling. Thin-Walled Structures 96:337–347

17. Peterman KD, Schafer BW (2014) Sheathed cold-formed steel studs under axial and lateral load. J Struct Eng 140(10):04014074
18. Peterman KD, Nakata N, Schafer BW (2014) Hysteretic characterization of cold-formed steel stud-to-sheathing connections. J Constr Steel Res 101:254–264
19. Peck Q, Rogers N, Serrette R (2012) Cold-formed steel framed gypsum shear walls: in-plane response. J Struct Eng 138(7):932–941
20. Pan CL, Shan MY (2011) Monotonic shear tests of cold-formed steel wall frames with sheathing. Thin-Walled Structures 49(2):363–370
21. Rogers CA, Balh N, Ong-Tone C, Shamim I, DaBreo J (2011) Development of seismic design provisions for steel sheet sheathed shear walls. In: Structures congress 2011, pp 676–687
22. Sefi N, Sharafi P, Ronagh H (2019) Numerical models for lateral behaviour analysis of cold-formed steel framed walls: state of the art, evaluation and challenges. Thin-Walled Structures 138:252–285
23. Selvaraj S, Madhavan M (2019) Investigation on sheathing-fastener connection failures in cold-formed steel wall panels. In: Structures, vol 20. Elsevier, pp 176–188
24. Selvaraj S, Madhavan M (2019) Bracing effect of sheathing in point-symmetric cold-formed steel flexural members. J Constr Steel Res 157:450–462
25. Selvaraj S, Madhavan M (2019) Flexural behaviour and design of cold-formed steel wall panels sheathed with particle cement board. J Constr Steel Res 162:105723
26. Selvaraj S, Madhavan M (2019) Improvements in AISI design methods for gypsum-sheathed cold-formed steel wall panels subjected to bending. J Struct Eng 145(2):04018243
27. Selvaraj S, Madhavan M (2019) Behaviour of gypsum sheathed point-symmetric cold-formed steel members: assessment of AISI design method. In: Structures, vol 22. Elsevier, pp 76–97
28. Selvaraj S, Madhavan M (2019) Sheathing bracing requirements for cold-formed steel wall panels: experimental investigation. In: Structures, vol 19. Elsevier, pp 258–276
29. Selvaraj S, Madhavan M (2019) Sheathing braced design of cold-formed steel structural members subjected to torsional buckling. In: Structures, vol 20. Elsevier, pp 489–509
30. Selvaraj S, Madhavan M (2018) Studies on cold-formed steel stud panels with gypsum sheathing subjected to out-of-plane bending. J Struct Eng 144(9):04018136
31. Selvaraj S, Madhavan M (2019) Investigation on sheathing effect and failure modes of gypsum sheathed cold-formed steel wall panels subjected to bending. In: Structures, vol 17. Elsevier, pp 87–101
32. Shahi R, Lam N, Gad E, Saifullah I, Wilson J, Watson K (2014) In-plane behavior of cold-formed steel-framed shear wall panels sheathed with fibre cement board
33. Serrette R, Encalada J, Hall G, Matchen B, Nguygen H, Williams A (2007) Additional shear wall values for light weight steel framing
34. Serrette RL, Encalada J, Juadines M, Nguyen H (1997) Static racking behavior of plywood, OSB, gypsum, and fiberbond walls with metal framing. J Struct Eng 123(8):1079–1086
35. Shamim I, DaBreo J, Rogers CA (2013) Dynamic testing of single-and double-story steel-sheathed cold-formed steel-framed shear walls. J Struct Eng 139(5):807–817
36. Shamim I, Rogers CA (2013) Steel sheathed/CFS framed shear walls under dynamic loading: numerical modelling and calibration. Thin-Walled Structures 71:57–71
37. Tarpy Jr TS (1980). Shear resistance of steel-stud wall panels
38. Tarpy Jr TS (1984) Shear resistance of steel stud wall panels: a summary report
39. Ye J, Wang X, Jia H, Zhao M (2015) Cyclic performance of cold-formed steel shear walls sheathed with double-layer wallboards on both sides. Thin-Walled Structures 92:146–159
40. Ye J, Jiang L (2018) Simplified analytical model and shaking table test validation for seismic analysis of mid-rise cold-formed steel composite shear wall building. Sustainability 10(9):3188
41. Yu C (2010) Shear resistance of cold-formed steel framed shear walls with 0.686 mm, 0.762 mm, and 0.838 mm steel sheet sheathing. Engineering Structures 32(6):1522–1529
42. Yu C, Chen Y (2011) Detailing recommendations for 1.83 m wide cold-formed steel shear walls with steel sheathing. Journal of Constructional Steel Research 67(1):93–101
43. Yu C, Yu G (2016) Experimental investigation of cold-formed steel framed shear wall using corrugated steel sheathing with circular holes. J Struct Eng 142(12):04016126

44. Zeynalian M, Shahrasbi AZ, Riahi HT (2018) Seismic response of cold formed steel frames sheathed by fiber cement boards. International Journal of Civil Engineering 16(11):1643–1653
45. Zhang W, Mahdavian M, Yu C (2018) Different slit configuration in corrugated sheathing of cold-formed steel shear wall. J Constr Steel Res 150:430–441
46. Zhang W, Mahdavian M, Li Y, Yu C (2017) Seismic performance evaluation of cold-formed steel shear walls using corrugated steel sheathing. J Struct Eng 143(11):04017151
47. Zhang W, Mahdavian M, Li Y, Yu C (2016) Experiments and simulations of cold-formed steel wall assemblies using corrugated steel sheathing subjected to shear and gravity loads. J Struct Eng 143(3):04016193

# Behaviour of Cellular Steel Beams Under Uniform Moment at Elevated Temperatures


**Vijaya K. Kotapati and Ashish P. Khatri**

**Abstract** Cellular steel beams have proved to be one of the most significant developments in steel construction. The introduction of an opening in the web of a beam alters the stress distribution within the member and also influences its collapse behaviour under the thermal load developed during a fire attack. Behaviour of cellular beams under fire can be predicted by performing simplified coupled (thermal-structural) field analysis. This paper covers the effect of parameters, viz. the span of the beam, size and spacing of the openings (cellularity), and load ratio on the behaviour of cellular beams with hinge–hinge support conditions under a uniform moment and uniform elevated temperature. The present numerical study is based on finite element analysis (FEA) which covers the both geometrical and material nonlinearity. Moreover, in this study, the material degradation at elevated temperature is not considered, and hence, the temperature at which deformations increase rapidly indicates the upper limit of web yield temperature. The result from the present study shows that the cellularity, load ratio, and span of the beam have a significant effect on temperature-deformation behaviour and theoretical web yield temperature of beams.

**Keywords** Cellular steel beams · Coupled field analysis · Load ratio · Cellularity · Uniform moment · Hinge–hinge support

## 1 Introduction

An open Web-expanded steel beam was initially used in structures during World War II to decrease the cost of steel structures. Cellular steel beam (CSB) results in an increase in stiffness and strength as compared to the original beam. The benefit of using a cellular steel beam is to incorporate duct passage such as hydraulic and ventilation pipes as well as electric cables, services within the floor-ceiling zone of the structure. The use of CSB also has the advantage of reducing the amount of

V. K. Kotapati (✉) · A. P. Khatri
Department of Applied Mechanics, VNIT, Nagpur, India
e-mail: vijaykrishna.kotapati@gmail.com



M. Madhavan et al. (eds.), *Proceedings of the Indian Structural Steel Conference 2020 (Vol. 1)*, Lecture Notes in Civil Engineering 318,
https://doi.org/10.1007/978-981-19-9390-9_37

steel material used and the overall dead weight of the steelwork. There has been significant research work done on investigating the detailed and complex behaviour of CSB at ambient temperature by Kerdal et al. [6, 11]. It has included understanding various failure modes comprising of Web-post buckling, Vierendeel bending, Web weld failure, overall lateral-torsional buckling, and flexural bending.

The basic fundamental principles of structural behaviour under thermal effects were explained by [3–5] and Usmani et al. [18] for solid web beams. The understanding of the response of CSB in thermal conditions has been increased through modelling and several test experiments performed by Nadjai et al. [13]. The failure mechanism of web-post buckling between the openings had been carried out by Wang et al. [19] and [20] on protected, and partially or fully protected cellular steel beams, respectively. Najafi and Wang [14] explored that the large deflection in members at higher temperatures results in the tensile membrane effect which helps in the survival of the member for a longer duration if the members are axially restrained. The standard fire tests for a single structural member may be different from the behaviour of the whole structure under natural fire and unable to provide enough information on the behaviour of the whole building. A recent study performed by [16] investigated the collapse behaviour of a cold formed steel building in full scale natural fire testing and also performed finite element analysis which closely matched the experimental behaviour. Most of the research works in this field are carried out on the individual members considering material degradation characteristics at higher temperatures resulted due to standard fire conditions. This includes work performed by [9, 12, 13, 17] in recent years on heat transfer analysis of CSB which considered only temperature-dependent material properties. The behavioural understanding of CSB under fire can be better understood if its behaviour under simplified uniform thermal conditions is known. The factors which can influence this behaviour are large in numbers, and this includes load ratio (LR), cellularity (size and spacing of openings) and span to enlarged depth ratio ($L/D$) of beam, type and level of boundary conditions, and type of loading and also the degradation in material characteristics due to a higher temperature. To improve the behavioural understanding of such complicated phenomena, it is better to perform some simplified analysis considering the aforementioned parameters for material where in the characteristics are not affected by temperature. The changes in the behavioural performance of CSB considering material degradation at higher temperatures can be better understood if the behaviour of CSB is first explored considering various factors with the usual (not affected by temperature) stress–strain curve of the material.

In the present work, a simplified analysis of CSB is carried out considering the factors LR, cellularity, and $L/D$ ratios having a simply supported with eccentric (at the bottom level of the beam) hinge–hinge boundary conditions under a uniform moment loading condition. Moreover, the nonlinearity of material stress–strain characteristics is considered, and it is assumed to be unaffected at higher temperatures also. The present study on CSB is carried out using coupled-field (thermo-mechanical) finite element analysis (FEA) considering geometrical and material nonlinearity. A series of numerical analyses of CSB prepared from parent section UB 254 $\times$ 146 $\times$ 43 having depth ($H$) of 259.6 mm which is laterally restrained support under uniform

temperature distribution has been performed considering the various factors which include the span of the beam which is varied by varying span ($L$) to enlarged depth ($D$ = 1.5H) ratio as 25, 30, and 35; size of the openings ($d$) as 0.5D, 0.75D; spacing ($S$) of the openings as 1.5d, 1.8d; and load ratio (LR) as 0.3, 0.5, 0.8 taken from BS5950: Part 1: 1990 code [2]. The spans length is calculated with an $L/D$ ratio which are equal to or within the specified span to depth ratio due to adjustment of number of opening diameters in the Web of section. All web openings should be located along the centreline of the web of the section. The finite element model validation study is discussed in Sect. 4.

## 2 Methodology

The behaviour of CSB is determined by performing a coupled-field (thermo-mechanical) finite element simulation considering the factors as explained in an earlier section. The developed finite element model is first validated for solid steel beams under uniform temperature along the length and linear variation along a depth of the beam made up of the elastic material property. Moreover, this validation concerning available results is mentioned in Noda et al. [15]. Then, detailed nonlinear finite element model is developed and validated with results mentioned in Iu and Chan [10], wherein standard fire conditions along with temperature dependant material characteristics are used. The following assumptions are made whilst performing present work.

- Constant thermal conductivity property (K) 45 Wm/K as per EN1993-1-2, (2005) [8] is considered, and the density of a material is 7850 kg/m$^3$ as thermal properties.
- The linear coefficient of thermal expansion ($\alpha$) is taken as $14 \times 10^{-6}$/°C at higher temperatures according to EN1993-1-2, (2005) [8] recommendations. An idealized (tri-linear) stress–strain curve for steel has been adopted with a yield stress of 275 MPa as mechanical properties mentioned in Ding and Sakumoto [7].
- An iterative procedure is implemented using the geometric nonlinear behaviour for each temperature increment to determine the stress variations in CSB.

## 3 Finite Element Simulation

The analyzes are performed using ANSYS R16.0 finite element (FE) software [1]. The 4-noded SHELL131 and 4-noded structural SHELL181element are used for thermal and mechanical analyzes, respectively, for analyzing the CSB by coupled-field analysis. This analysis is also known as a multi-physics analysis which is a combination of analyzes from different engineering disciplines that interact to solve a global engineering problem by Chao et al. [5]. When the input of structural analysis depends on the results from the thermal analysis, then the analyzes are coupled.

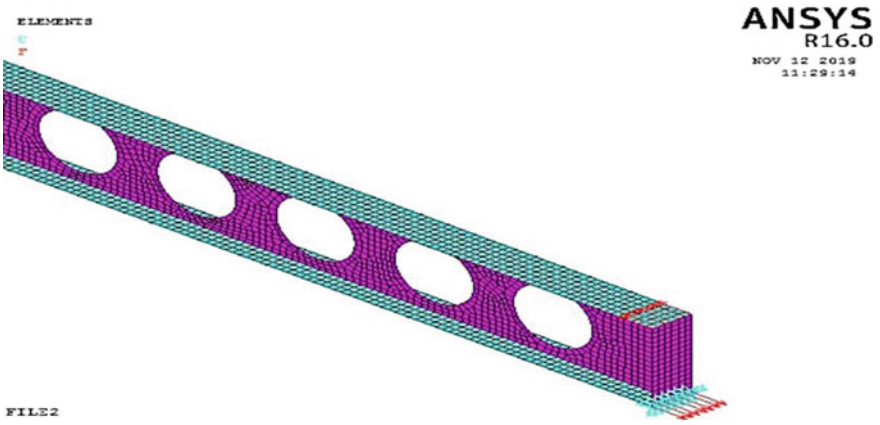


**Fig. 1** FE model of CSB with loading and boundary conditions

A steady-state thermal analysis is carried-out to simulate the temperature distribution by defining thermal properties and thermal boundary condition. The temperature distribution across the member was found to be uniform throughout the cross section. In the structural model, the mechanical properties are defined by neglecting material degradation with temperature rise. An assembly process duly considering the uniform end moments with LR and boundary conditions (hinge-hinge) is shown in Fig. 1. Newton-Raphson method is adopted for nonlinear analysis. The nonlinear convergence study is required to overcome the convergence criteria during analysis time, and hence, convergence study is also carried out for fixing the meshing of CSB. The element size used for meshing is 15 mm to maintain the aspect ratio (1.0–1.6) for good convergence results and less computational time.

## 4 Validations of Thermo-Mechanical FE Models

In order to validate the thermo-mechanical modelling of this study, one should have a comprehensive knowledge of heat transfer and the calculation of thermal stresses. For the present FE validation, a thermo-mechanical analysis is required to perform both elastic and inelastic analysis which are discussed in the following subsections. Basic problems which have been mentioned in Noda et al. [15] are selected for development and validation of the FE model for the elastic stage. Similarly, the FE model of Iu and Chan [10] is taken for inelastic analysis.

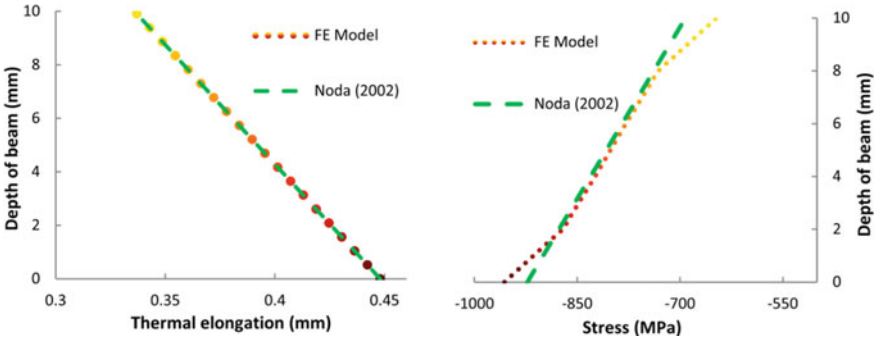


**Fig. 2** Graphical results of modal validation

## *4.1 Elastic Analysis or Linear Analysis*

A rectangular beam with a perfectly clamped end with a cross-section of $b \times h$ is subjected to the temperature change of 400 K at the top and 300 K at the bottom of the section along the length of 100 mm with depth = 10 mm using a SHELL 131element in the thermal analysis by mesh convergence study, the aspect ratio is 1.0. The SHELL 181 element used in structural analysis to calculate the longitudinal thermal stresses in $\sigma_x$ in the beam if thermal elongation $\alpha = 11.2 \times 10 - 6$/K and modulus of elasticity of mild steel $E_s = 2.05 \times 10^5$ MPa are found to be $\sigma_{x,\text{top}} =$ 922.88 MPa and $\sigma_{x,\text{bot}} = 692.16$ MPa (compressive), and the thermal strain at top and bottom of the section is $4.48 \times 10^{-3}$ mm and $3.36 \times 10^{-3}$ mm, respectively. Allowing a percentage of deviation + or – 3% as its FE software using an approximate method for convergence of the solution [1]. The results are shown in a graphical representation in Fig. 2. The results are fairly matching.

## *4.2 Inelastic Analysis*

Validation of the inelastic FE analysis [1] is performed and compared with available FE results mentioned in Iu and Chan [10]. The results obtained by present FE analysis for vertical deflection with respect temperature are 0.62 mm, 1.22 mm, 3.5 mm, 41.3 mm for 100 °C, 400 °C, 600 °C, 781 °C, respectively. The obtained values from present inelastic analysis are having close resemblance to that mentioned in Iu and Chan [10].

## 5 Analysis of CSB at Elevated Temperature

A parametric study has been done on CSB at an elevated temperature prepared from parent section UB254 × 146 × 43 with the various parameters which includes L/D ratio as 25, 30, and 35; size of the openings ($d$) as 0.5D, 0.75D; spacing ($S$) of the openings as 1.5$d$, 1.8$d$; and load ratio (LR) as 0.3, 0.5, and 0.8. By using permutation and combination on these parameters, thirty six FE models can be obtained and are shown in the Table 1. FE analysis has been performed to predict the behaviour of CSB at elevated temperature. These nonlinear FE analyzes are performed up to maximum uniform temperature of 1000 °C as the complete bottom flange of the section is yielding up to this temperature. Moreover, in standard fire conditions, temperature attained in the member will be much lesser than 1000 °C, and hence, analysis results beyond uniform temperature of 1000 °C will rarely provide insight of behaviour of CSB. Due to the presence of eccentric boundary conditions (at bottom flange of CSB), all analyzed CSBs show deformation pattern deflecting upwards with increase in temperature. Representative case of upward deflection of CSB obtained at 1000 °C is shown in Fig. 3. This happens due to the level of axial restraint which is causing eccentric compressive force on the CSB due to restrained thermal expansion.

The factors affecting the response of CSB at elevated temperature are discussed in the following subsections. These factors include effect of span with cellularity, effect of load ratio with cellularity, and effect of cellularity. The behavioural response of CSB is explained by comparing different results such as deflection, Web yield temperature, and section yield patterns with increase in temperature effect.

### *5.1 Effect of Span with Cellularity*

The response of CSB is plotted with mid-span deflection verse maximum temperature. A comparison of results for maximum vertical deflection is done amongst the different sizes of openings and spacing of CSB beams to show mid-span deflection under a given constant LR 0.5 and varying $L/D = 25, 30, 35$ at elevated temperature which is shown in Fig. 4. The span to depth ratio has a significant effect on mid-span vertical deflection. The plot shows that the vertical deflection values for $L/D = 25$ are 432.04 mm, for $L/D = 30$, it is 571.00 mm, and for $L/D = 35$, it is 821.74 mm which is shown in Fig. 4a, b, and c, respectively, with varying size and spacing of openings. The limited plots are shown as per space constraints.

### *5.2 Effect of Load Ratio with Cellularity*

The vertical deflection of the CSB with varying the size and spacing of opening diameter is found to be increasing with the decrease in the LR. The plots are shown

**Table 1** Considered a combination of different parameters

| *L*/*D* ratio | Span length (mm) and cellularity | Load ratio (LR) |
|---|---|---|
| 25 | $L = 9929.70$, S $= 1.5d$, $d = 0.5D$ | 0.3, 0.5, 0.8 |
| | $L = 9929.70$, S $= 1.8d$, $d = 0.5D$ | 0.3, 0.5, 0.8 |
| | $L = 10{,}075.72$, S $= 1.5d$, $d = 0.75D$ | 0.3, 0.5, 0.8 |
| | $L = 10{,}163.34$, S $= 1.8d$, $d = 0.75D$ | 0.3, 0.5, 0.8 |
| | $L = 11{,}682$, S $= 1.5d$, $d = 0.5D$ | 0.3, 0.5, 0.8 |
| 30 | $L = 11{,}682$, S $= 1.8d$, $d = 0.5D$ | 0.3, 0.5, 0.8 |
| | $L = 11{,}828.03$, S $= 1.5d$, $d = 0.75D$ | 0.3, 0.5, 0.8 |
| | $L = 11{,}740.41$, S $= 1.8d$, $d = 0.75D$ | 0.3, 0.5, 0.8 |
| | $L = 13{,}726.35$, S $= 1.5d$, $d = 0.5D$ | 0.3, 0.5, 0.8 |
| 35 | $L = 13{,}784.76$, S $= 1.8d$, $d = 0.5D$ | 0.3, 0.5, 0.8 |
| | $L = 14{,}018.40$, S $= 1.5d$, $d = 0.75D$ | 0.3, 0.5, 0.8 |
| | $L = 13{,}843.17$, S $= 1.8d$, $d = 0.75D$ | 0.3, 0.5, 0.8 |

in Fig. 5a, b, and c with the effect of LR = 0.3, 0.5, and 0.8, respectively, with varying size and spacing of the openings (cellularity). Keeping the $L/D = 25$ as constant in all the plots shown in Fig. 5. The effect of LR is insignificant on a mid-span deflection.

The remaining results regarding the mid-span deflection for different *L*/*D ratios* and LR with varying cellularity are shown in Table 2 containing the data which includes the details of CSB with number a of openings ($N$). The results in the table give a broad idea of the response of CSB with the effect of span and LR's which are not shown in the above plot are $L/D = 30$ and 35.

## 6 Behavioural Aspect of CSB

The theoretical Web yield temperature ($T_{\text{web}}$ °C) of CSB is calculated with hinge–hinge support conditions under elevated temperatures. The $T_{\text{web}}$ °C is calculated based on yield stress distribution near the opening diameter in the web. The stress concentration near the openings is very high compared to the whole beam section

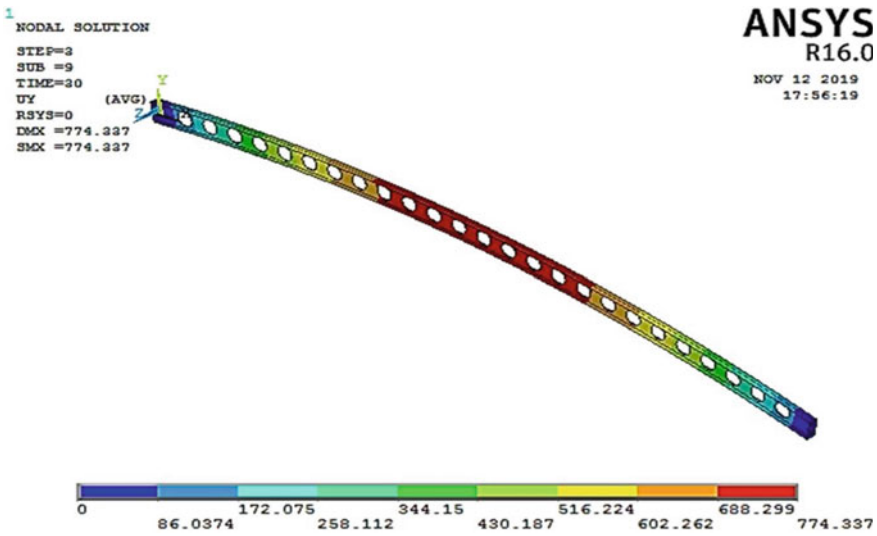


**Fig. 3** Large deflection of CSB ($L$ = 13,843.14 mm, $S = 1.8d$, $d = 0.75$D, LR = 0.8)

which is shown in Fig. 6 for the UB section of CSB with span = 11,682 mm, $S = 1.5d$, $d = 0.5D$. Due to the presence of an opening, the stress distribution alters the path of the yielding to above and below the opening having maximum stress value. Therefore, the bottom flange and the web of section yielded thoroughly but not the top flange of the section. The stress distribution between the openings which is Web-post found to be not yielded across the Web plane of section depth. A plot is drawn between von Mises stress and section depth with LR 0.8 as shown in Fig. 7a and b for $L/D = 30$, $S = 1.5d$, $d = 0.5D$ and for $L/D = 30$, $S = 1.5d$, $d = 0.75D$, respectively. Therefore, the temperature at which the web starts yield near opening tip which is considered as theoretical Web yields temperature without considering the material degradation.

The results of theoretical web yield temperature are shown in Table 3. The span to depth ratio has a negligible effect on web yield temperature based on stress distribution. The web yield temperature for $L/D = 25, 30, 35$ is found to be 207 °C, 189.5 °C, and 165 °C. It is observed that the size of the opening diameter has a significant effect on the web yield temperature ($T_{\text{web}}$ °C) of CSB at elevated temperatures. From Table 3, it is shown the temperature values for $d = 0.5D$, $N = 39$ is 400 °C, $d = 0.5D$, $N = 32$ is 330 °C, $d = 0.75$D, $N = 26$ is 367 °C and $d = 0.75D$, $N = 21$ is 195 °C. There is little effect on variation in LR.

Table 3 shows the theoretical values of web yield temperature ($T_{\text{web}}$ °C) for various parameters of CSB as considered in the present FE analysis. The reader can understand by comparing with varying parameters for provided ($T_{\text{web}}$ °C) values at openings.

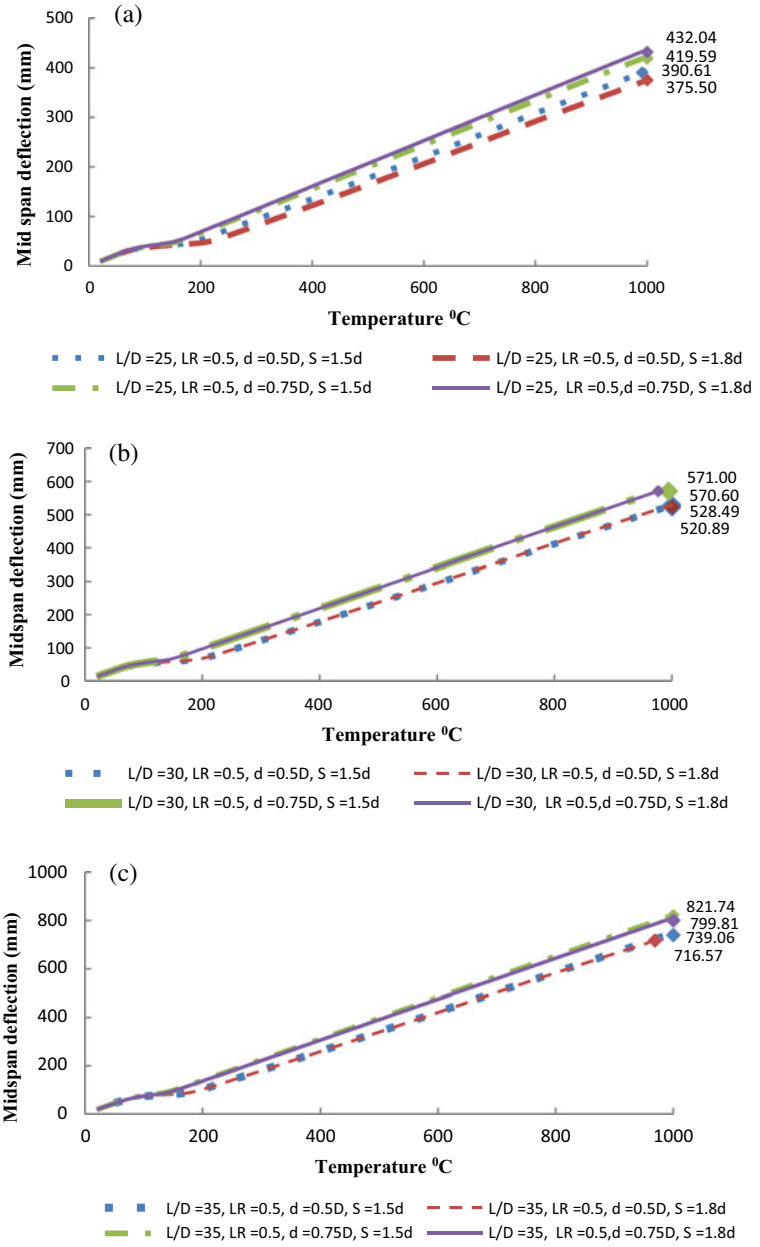


**Fig. 4** Effect of cellularity on a vertical deflection of CSB for **a** $L/D = 25$, LR $= 0.5$. **b** $L/D = 30$, LR $= 0.5$. **c** $L/D = 35$, LR $= 0.5$

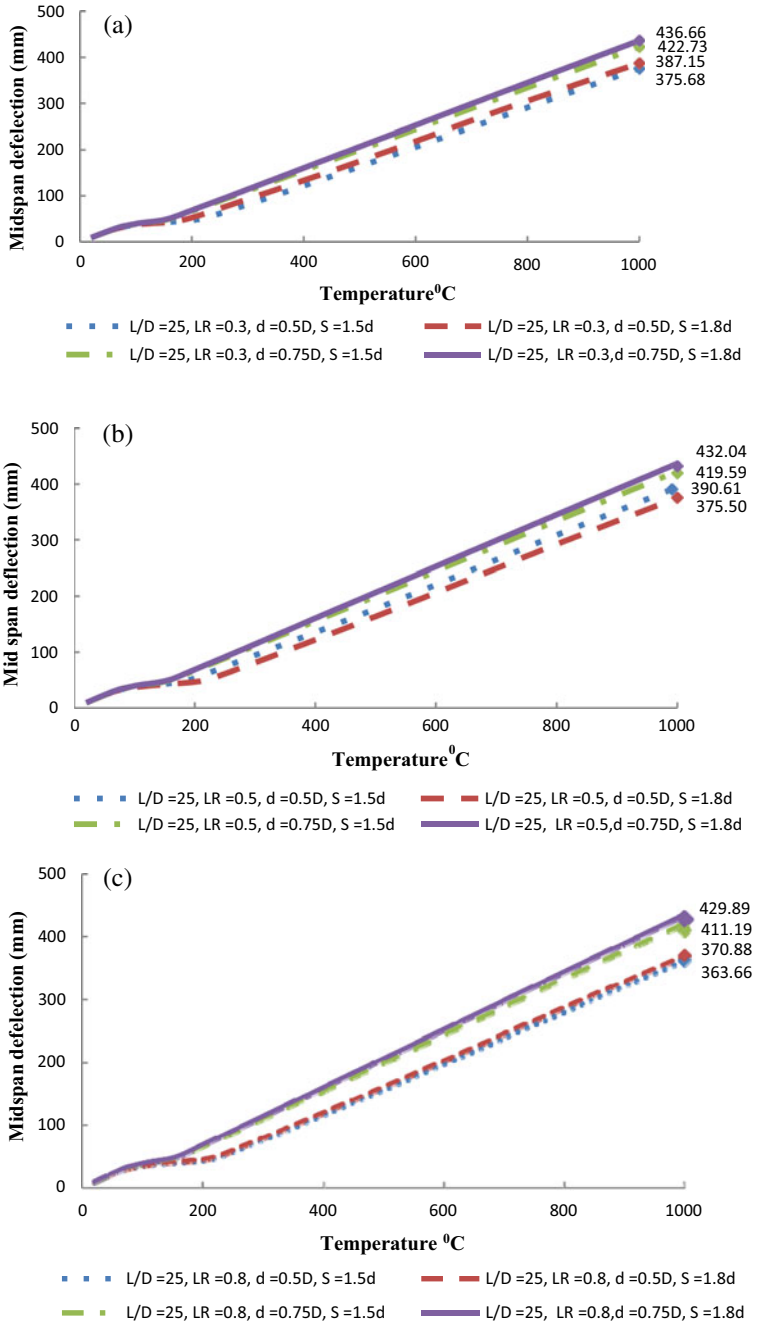


**Fig. 5** Effect of cellularity on a vertical deflection of CSB for **a** $L/D = 25$, LR = 0.3. **b** $L/D = 25$, LR = 0.5. **c** $L/D = 25$, LR = 0.8

**Table 2** Analysis results of mid-span deflection of CSB

| *L*/D ratio | Span length (mm) and cellularity | Load ratio (LR) | Mid-span deflection (mm) |
|---|---|---|---|
| 30 | $L = 11{,}682$, $S = 1.5d$, $d = 0.5D$, $N = 39$ | 0.3, 0.5, 0.8 | 528, 521, 512 |
| | $L = 11{,}682$, $S = 1.8d$, $d = 0.5D$, $N = 32$ | 0.3, 0.5, 0.8 | 532.88, 527.27, 514 |
| | $L = 11{,}828.03$, $S = 1.5d$, $d = 0.75D$, $N = 26$ | 0.3, 0.5, 0.8 | 585.11, 570.126, 565.05 |
| | $L = 11{,}740.41$, $S = 1.8d$, $d = 0.75D$, $N = 21$ | 0.3, 0.5, 0.8 | 590.1, 571.67, 567.12 |
| 35 | $L = 13{,}726.35$, $S = 1.5d$, $d = 0.5D$, $N = 46$ | 0.3, 0.5, 0.8 | 746, 739, 719 |
| | $L = 13{,}784.76$, $S = 1.8d$, $d = 0.5D$, $N = 38$ | 0.3, 0.5, 0.8 | 743.60, 733, 717 |
| | $L = 14{,}018.4$, $S = 1.5d$, $d = 0.75D$, $N = 31$ | 0.3, 0.5, 0.8 | 821.74, 807.31, 784.51 |
| | $L = 13{,}843.17$, $S = 1.8d$, $d = 0.75D$, $N = 25$ | 0.3, 0.5, 0.8 | 810.11, 796.91, 774.33 |

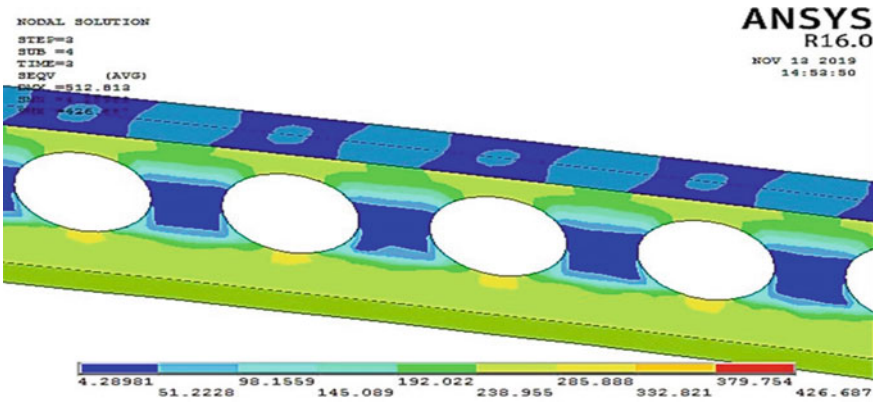


**Fig. 6** Contour plot of von Mises stress distribution of CSB at elevated temperature

## 7 Conclusions

A parametric study is done, in which the L/D ratio, opening diameter of holes, and the distance between the openings, in cellular beams are varied to the lowest distance possible with other dimensions being unchanged. FE software is used to develop finite element models in ANSYS and is used for analyzing the CSB under uniform temperature distribution. The thermo-mechanical simulations produced limiting temperature

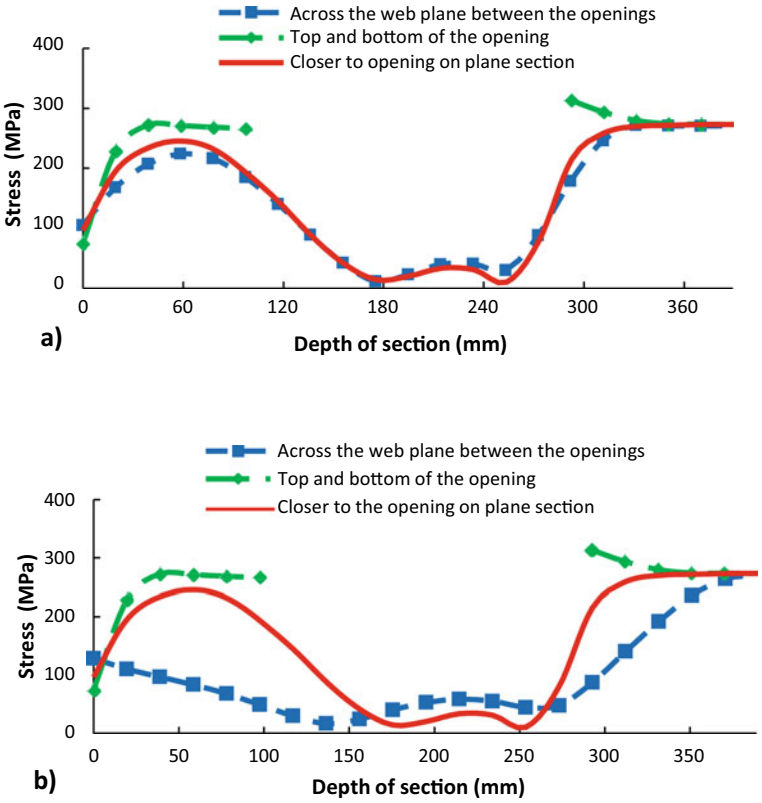


**Fig. 7** Stress distribution between the openings of CSB at elevated temperature for **a** d = 0.5D. **b** d = 0.75D

for each model and mid-span vertical deflections of beam at the highest temperature (1000 °C) considered in these analysis. Von Mises strain and stress distribution patterns near openings as well as web-posts are determined. The occurrence of stress concentration near openings in the web means that the flange is already yielded. The unprotected cellular steel beam is subjected to coupled load (thermal stress due to uniform heating under uniform moment), the extreme bottom fibres of cross section yields first and then followed by Web yielding. The upper flange of CSB is much under stressed at higher temperatures also. This particular failure pattern is observed because the hinge–hinge boundary conditions are created at the bottom of the cross -section, and this causes eccentric thermal loading on beams at elevated temperatures. The cellularity, load ratio, and span of the beam are affecting temperature-deformation behaviour and theoretical Web yield temperature of cellular beams. The following conclusions are drawn from this study.

- A significant increase in vertical deflections at higher temperatures resulted due to a larger span to enlarged depth ratio of CSB.

**Table 3** Theoretical web yield temperature of CSB at elevated temperature

| *L/D* ratio | Span length (mm) and cellularity | Load ratio (LR) | ($T_{web}$ °C) at openings |
|---|---|---|---|
| 25 | $L = 9929.7$, $S = 1.5d$, $d = 0.5D$, $N = 33$ | 0.3, 0.5, 0.8 | 340, 309, 290 |
| | $L = 9929.7$, $S = 1.8d$, $d = 0.5D$, $N = 27$ | 0.3, 0.5, 0.8 | 296, 290, 250 |
| | $L = 10{,}075.72$, $S = 1.5d$, $d = 0.75D$, $N = 22$ | 0.3, 0.5, 0.8 | 558, 521, 486 |
| | $L = 10{,}163.34$, $S = 1.8d$, $d = 0.75D$, $N = 18$ | 0.3, 0.5, 0.8 | 555, 433, 207 |
| 30 | $L = 11{,}682$, $S = 1.5d$, $d = 0.5D$, $N = 39$ | 0.3, 0.5, 0.8 | 400, 335, 300 |
| | $L = 11{,}682$, $S = 1.8d$, $d = 0.5D$, $N = 32$ | 0.3, 0.5, 0.8 | 330, 310, 305 |
| | $L = 11{,}828.03$, $S = 1.5d$, $d = 0.75D$, $N = 26$ | 0.3, 0.5, 0.8 | 367, 240, 229 |
| | $L = 11{,}740.41$, $S = 1.8d$, $d = 0.75D$, $N = 21$ | 0.3, 0.5, 0.8 | 195, 193, 189.5 |
| 35 | $L = 13{,}726.35$, $S = 1.5d$, $d = 0.5D$, $N = 46$ | 0.3, 0.5, 0.8 | 302, 290, 270 |
| | $L = 13{,}784.76$, $S = 1.8d$, $d = 0.5D$, $N = 38$ | 0.3, 0.5, 0.8 | 303, 301, 290 |
| | $L = 14{,}018.40$, $S = 1.5d$, $d = 0.75D$, $N = 31$ | 0.3, 0.5, 0.8 | 351, 208, 182 |
| | $L = 13{,}843.17$, $S = 1.8d$, $d = 0.75D$, $N = 25$ | 0.3, 0.5, 0.8 | 450,165,165 |

- The effect of load ratio is insignificant on the behaviour of CSB at elevated temperatures.
- Cellularity in CSB is affecting the distribution pattern of stresses near the web opening. The stress concentration is observed in CSB near the web opening at higher temperatures.
- The sequence of yielding of material with an increase in temperature for eccentric boundary conditions applied at the bottom flange is yielding in the bottom flange followed by yielding in the web near the opening portion of CSB. The top flange is under stressed at all considered temperatures.

Overall, this study is useful in predicting the complex behaviour of CSB under standard fire conditions.

## References

1. ANSYS 16 (2011) Finite element computer software
2. BS5950: Part 1: 1990, Structural use of steelwork in building, Part 1. Code of practice for design in simple and continuous construction: hot rolled sections. British Standards Institution
3. Bailey CG, Burgess IW, Plank RJ (1996) Analyses of the effects of cooling and fire spread on steel-framed buildings. Fire Saf J 26(4):273–293

4. Burgess IW, El Rimawi J, Plank RJ (1991) Studies of the behaviour of steel beams in fire. J Constr Steel Res 19(4):285–312
5. Chao Z, Gross JL, McAllister TP (2013) Lateral torsional buckling of steel W-beams subjected to localized fires. J Constr Steel Res 88:330–338
6. Chung KF, Liu TCH, Ko ACH (2001) Investigation on vierendeel mechanism in steel beams with circular web openings. J Constr Steel Res 57:467–490
7. Ding J, Li GQ, Sakumoto Y (2004) Parametric studies on fire resistance of fire-resistant steel members. J Constr Steel Res 60(7):1007–1027
8. EN1993-1-2 (2005) Eurocode 3-Design of steel structures - Part 1-2: General rules - Structural fire design
9. Ellobody E, Young B (2015) Nonlinear analysis of composite castellated beams with profiled steel sheeting exposed to different fire conditions. J Constr Steel Res 113:247–260
10. Iu CK, Chan SL (2004) A simulation-based large deflection and inelastic analysis of steel frames under fire. J Constr Steel Res 60(10):1495–1524
11. Kerdal D, Nethercot D (1984) Failure modes for castellated beams. Journal of Constructional Steel Research, No. 4(4):295–315
12. Mesquita MR, Kada A, Lamri B, Bouchair A (2016) Finite element analysis of steel beams with web apertures under fire condition. Asian Journal of Civil Engineering (Bhrc) 17(8)
13. Nadjai A, Vassart O, Ali F, Talamona D, Allam A, Hawes M (2007) Performance of cellular composite floor beams at elevated temperatures. Fire Saf J 42:489–497
14. Najafi M, Wang YC (2017) Axially restrained steel beams with web openings at elevated temperatures, part 1: behaviour and numerical simulation results. J Construct Steel Res 128:745–761
15. Noda N, Hetnarski RB, Tanigawa Y (2002) Thermal stresses. Taylor & Francis
16. Roy K, Lim JB, Lau HH, Yong PM, Clifton GC, Wrzesien A, Mei CC (2019) Collapse behaviour of a fire engineering designed single-storey cold-formed steel building in severe fires. Thin-Walled Structures 142:340–357
17. Sherif AE, Hassan MM (2018) Behaviour of structural sub-assemblies of steel beams with openings in fire conditions. J Constr Steel Res 148:627–638
18. Usmani AS, Rotter JM, Lamont S, Sanad AM, Gillie M (2001) Fundamental principles of structural behaviour under thermal effects. Fire Saf J 36(8):721–744
19. Wang P, Wang X, Liu M (2014) Practical method for calculating the buckling temperature of the web-post in a cellular steel beam in fire. Thin-Walled Structures 85:441–455
20. Wang P, Wang X, Liu M, Zhang L (2016) Web-post buckling of fully and partially protected cellular steel beams at elevated temperatures in a fire. Thin-Walled Structures 98:29–38

# Parametric Study on Cold Formed Sections


**Chinmaya Kasliwal and Utsav Koshti**

**Abstract** Cold-formed steel (CFS) is a new constructional material. The CFS sections have advantages like light weight, remoulability, etc. when compared with hot-rolled steel sections. CFS sections are extremely thin walled. This configuration gives them advantageous post reserve strength when used as structural element and compared with hot-rolled sections. However, research is needed to develop firm basis for such sections in comparison with typically used hot-rolled sections. Direct strength method (DSM) is a novel method presented as an alternative to effective width method. The use of such sections on field has been started. Buckling analysis and behaviour is an important criterion in direct strength method. Here, buckling analysis is carried in CUFSM software. Parametric study such as effect of longitudinal stiffener in cold-formed steel cross section, behaviour of different configuration of cold-formed steel like folded-flange and sigma is carried out. This study showed that direct strength method can be used as an alternative to effective width method given in IS 801-1975. Also, the upgrade in capacity of the cross section through longitudinal stiffener is also proved through buckling analysis.

**Keywords** Cold-formed steel sections · Direct strength method · Buckling analysis · CUFSM

## 1 Introduction

In steel construction industry, cold-formed steel (CFS) has emerged as new and advantageous material. From non-structural members to structural members, their applications have been explored. The basic advantage of such material is that we can form any cross-sectional shapes of the member. Yen et al. [1] proved that highest

C. Kasliwal · U. Koshti (✉)
Civil Engineering Department, Institute of Technology, Nirma University, Ahmedabad, Gujarat, India
e-mail: utsav.koshti@nirmauni.ac.in



M. Madhavan et al. (eds.), *Proceedings of the Indian Structural Steel Conference 2020 (Vol. 1)*, Lecture Notes in Civil Engineering 318,
https://doi.org/10.1007/978-981-19-9390-9_38

potential to increase flexure capacity lies with the section having flanges with double-fold lips. Aghoury et al. [2] also carried out his study to prove the effectiveness of sigma-shaped columns when compared with the commercially available cross-sectional shapes.

Hence we can say that a small change in cross section can upgrade the properties of whole cross section to an all-together new level in case of cold-formed steel. The newly developed design method known as direct strength method has been accepted in AISI specifications [3]. This new method is gaining more and more attention nowadays.

## *1.1 Direct Strength Method*

This new method has been developed by Dr. Ben Schafer. It deals with all kinds of buckling differently, and hence provides overall picture in terms of buckling and capacity for thin members. It uses elastic buckling analysis of the cross section based on the gross-section properties. This analysis can be performed using various computer tools such as CUFSM [4], CFS by RSG software, etc.

## *1.2 Buckling Analysis in CUFSM*

In this study, CUFSM [4] has been used for obtaining buckling analysis solutions. These solutions are in the form of minimum load factors for different types of buckling and the half wavelength values at which these load factors are attained. This freeware calculates the buckling stress and modes of arbitrarily shaped and simply supported thin-walled members. For this purpose, it uses classical finite strip methodology with single half sine wave $\left(\sin\left(\frac{\Pi x}{a}\right)\right)$ for longitudinal direction. The final result is in the form of graph of load factor versus half wavelength. This graph is also known as signature curve and can be used to classify the behaviour at different kinds of buckling.

First the 2D coordinates of the section were given as input in the input tab of the software. In this tab material properties were also given. The traditional signature buckling curve with base vectors of global, distortional and local was chosen to get the desired solution and the post-analysis tab provided with the modal participation curve as well as the buckling curve of the cross section.

## 2 Study on Effect of Longitudinal Stiffeners

For this study, to check the effect of stiffeners and compare it with folded-flange sections, three sections are chosen as given in Fig. 1. Their cross-sectional properties were as reported in Table 1 and their material properties were as those reported in Table 2. Later, these sections were analyzed in CUFSM [4] under flexure loads and their signature curves were extracted and compared. Figures 2, 3, 4 show the signature curves and the buckling classification of all the three cross-section shapes.

Later the signature curves of all three cross sections were clubbed together so as to compare their buckling behaviour as in Fig. 5. From this figure, we can conclude that as we add stiffening element to the cross section, its capacity increases to many fold. This being because of the phenomena of post buckling reserve strength. Also Figs. 2, 3 and 4 showed that local buckling occurs at short half wavelengths, distortional buckling at intermediate half wavelengths and global buckling occurs at long half wavelengths.

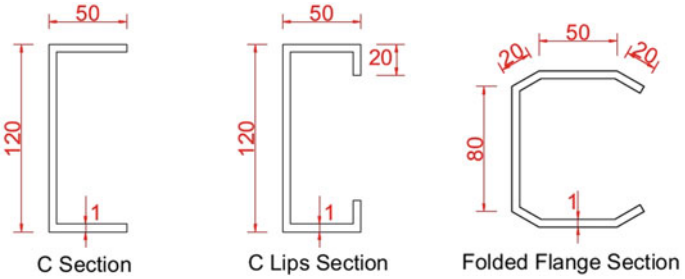


**Fig. 1** Sections selected for studying effect of longitudinal stiffeners

**Table 1** Cross-section properties of sections for studying effect of longitudinal stiffeners

| S.No | Cross section | Height of web (mm) | Width of web (mm) | Height of lips (mm) | Gross area $mm^2$ |
|---|---|---|---|---|---|
| 1 | Normal C | 120 | 50 | 0 | 218 |
| 2 | C Lips | 120 | 50 | 20 | 256 |
| 3 | Folded flange | 80 | 50 | 20 | 260 |

**Table 2** Material properties of sections for studying effect of longitudinal stiffeners

| S.No | Particulars | Value |
|---|---|---|
| 1 | Yield strength, $f_y$ | 360 MPa |
| 2 | Modulus of elasticity, $E$ | $2 \times 10^5$ MPa |
| 3 | Shear modulus, $G$ | 76,923 MPa |
| 4 | Poisson's ratio, $\upsilon$ | 0.3 |

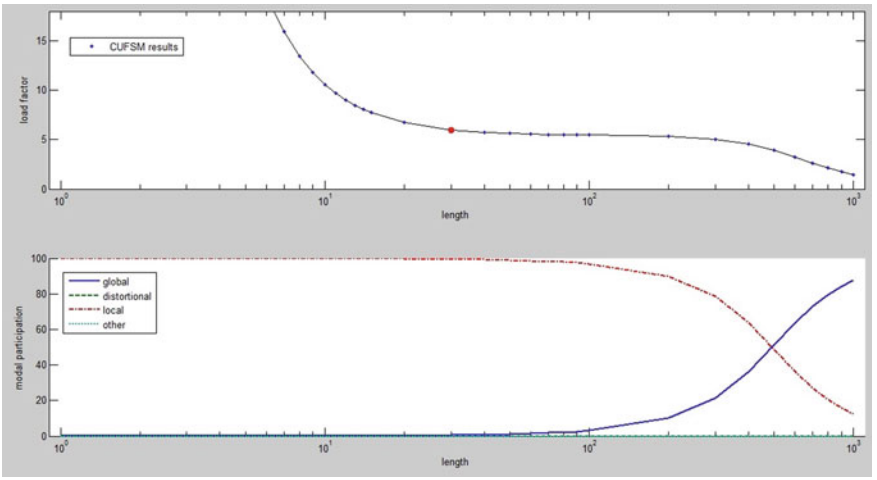


**Fig. 2** Signature curve for C Section 120 × 50 × 1

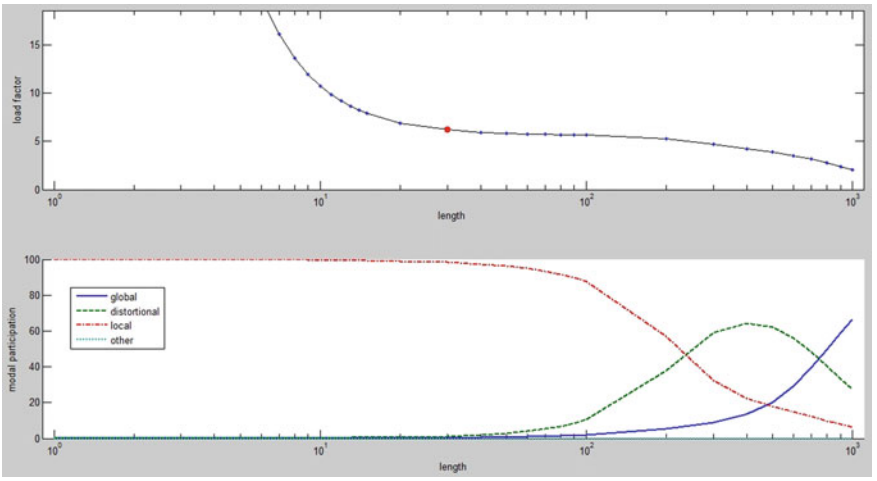


**Fig. 3** Signature curve for C lips Section 120 × 50 × 20 × 1

## 3 Folded-Flange Sections Under Compressive Load

Yen et al. [1] carried out the study to optimize the shape of the CFS section. From that study it was concluded that folded-flange-shaped sections (as in Fig. 6) are more efficient ones. This was done based on particle swarm optimization technique. However, that study did not show most efficient angle for this configuration under different loadings.

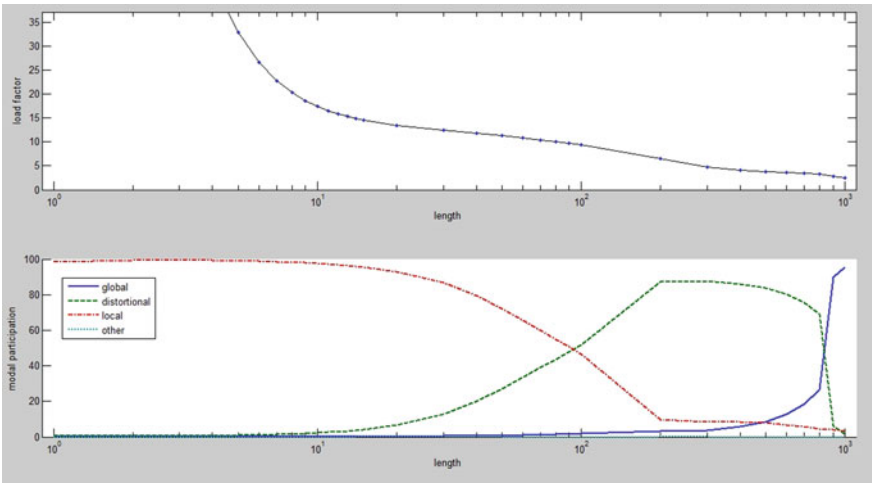


**Fig. 4** Signature curve for FF Section 80 × 50 × 20 × 1

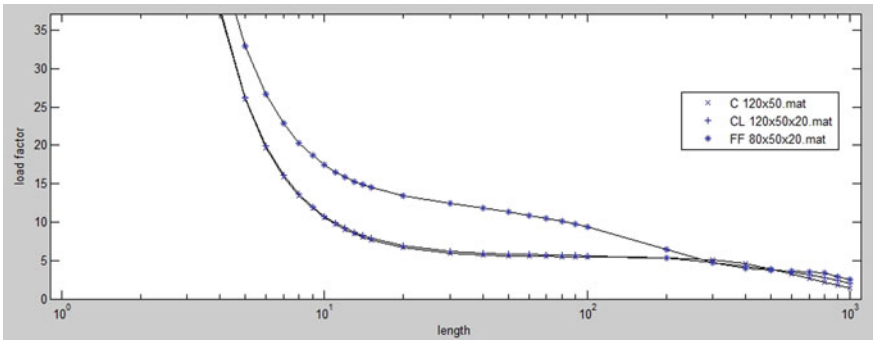


**Fig. 5** Signature curves for three cross sections under flexure load

**Fig. 6** Folded-flange section with an angle of 110°

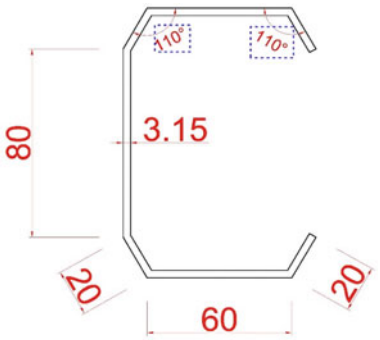

**Table 3** Material properties of sections for studying folded-flange sections under compressive load

| S. No | Particulars | Value |
|---|---|---|
| 1 | Yield strength, $f_y$ | 360 MPa |
| 2 | Modulus of elasticity, $E$ | $2 \times 10^5$ MPa |
| 3 | Shear modulus, $G$ | 76,923 MPa |
| 4 | Poisson's ratio, $\upsilon$ | 0.3 |

Hence for this study, folded-flange sections (as in Fig. 6) were taken with different angles at which flanges are placed as shown in Fig. 6. The angles mentioned in Fig. 6 were changed as 120°, 130°, 140° and 150° in this parametric study. The material properties were taken as stated in Table 3.

The chosen cross sections were then analyzed for different half wavelengths and load factors were then calculated which in turn gave the type of buckling mode. Figures 7, 8, 9, 10, 11 show the signature curves for various cross sections. After obtaining these curves, a cumulative curve was drawn combining all these curves in order to compare the behaviour of each cross section as in Fig. 12.

Based on the graphs obtained, a combined graph is plotted as in (Fig. 12) on the basis of which following conclusion is drawn:

1. Around 20 mm of wavelength shows FF150 section has higher load factor but at the same time in this region it shows distortional buckling.
2. Around 20 mm to 80 mm of wavelength show FF120 section has higher load factor and at the same time it has global buckling throughout.
3. After 80 mm of wavelength FF110 section has higher load factor but at the same time in this region it shows distortional buckling.

Hence folded-flange section with an angle of 120° is most viable solution for compression member.

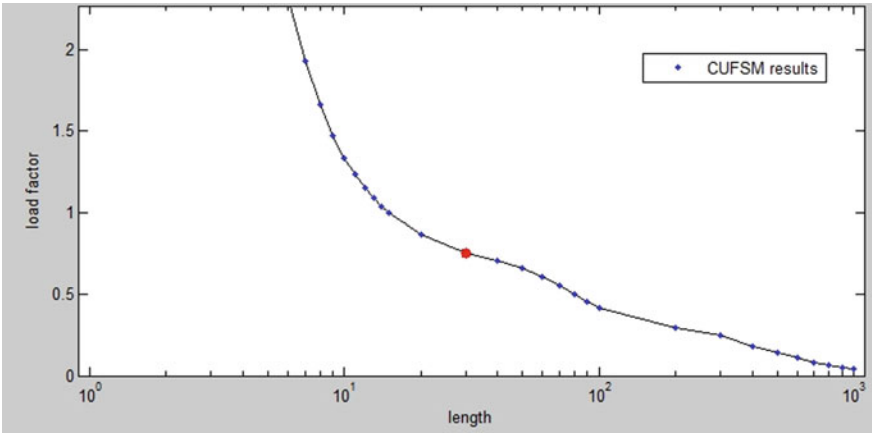


**Fig. 7** Wavelength versus load factor graph for folded-flange section with angle of 110°

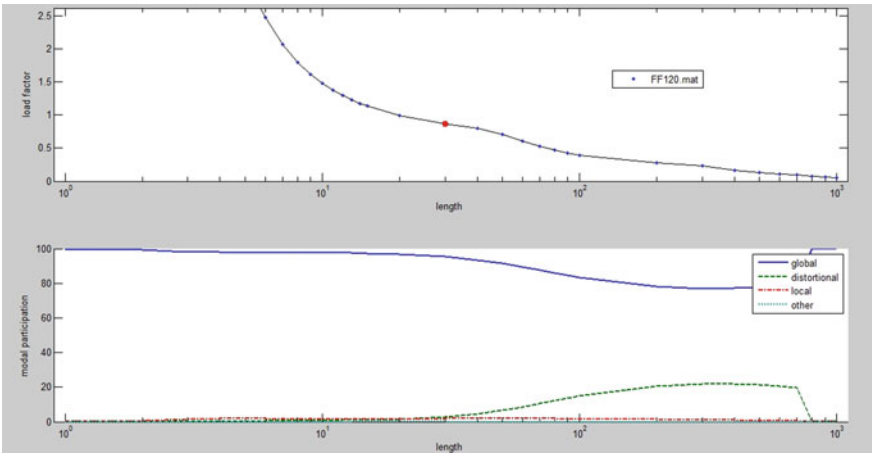


**Fig. 8** Wavelength versus load factor graph for folded-flange section with angle of 120°

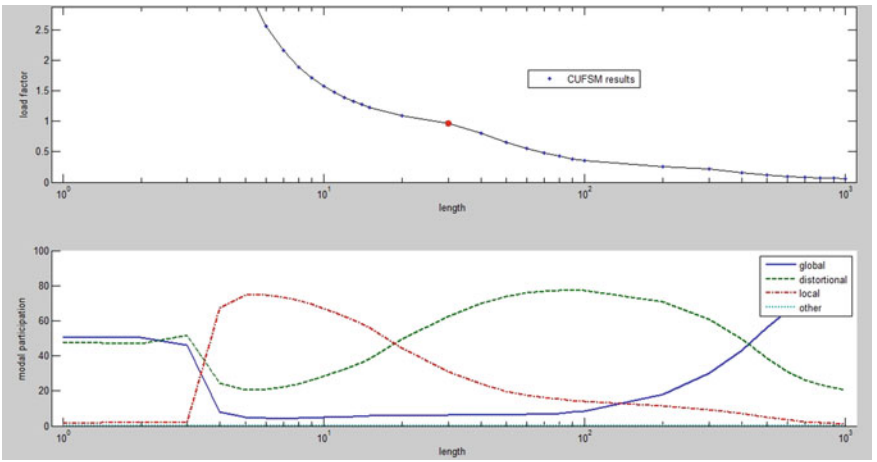


**Fig. 9** Wavelength versus load factor graph for folded-flange section with angle of 130°

## 4 Folded-Flange Sections Under Flexure Load

Following the same procedure as in Sect. 3, same folded-flange sections were analyzed under flexural load in CUFSM [4] and cumulative signature curve was obtained as shown in Fig. 13. This plot showed the regular trend of increase in flexure capacity of the section with decrease in the angle up to 110°. This change occurred in local and distortional buckling region and in global buckling region, only minor change was observed. Hence, it was concluded that viable option is the folded-flange with angle of 110° for flexure member.

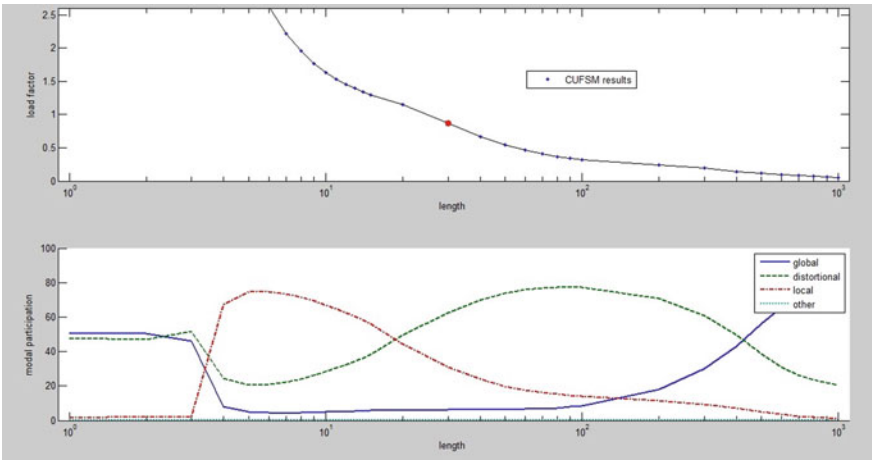


**Fig. 10** Wavelength versus load factor graph for folded-flange section with angle of 140°

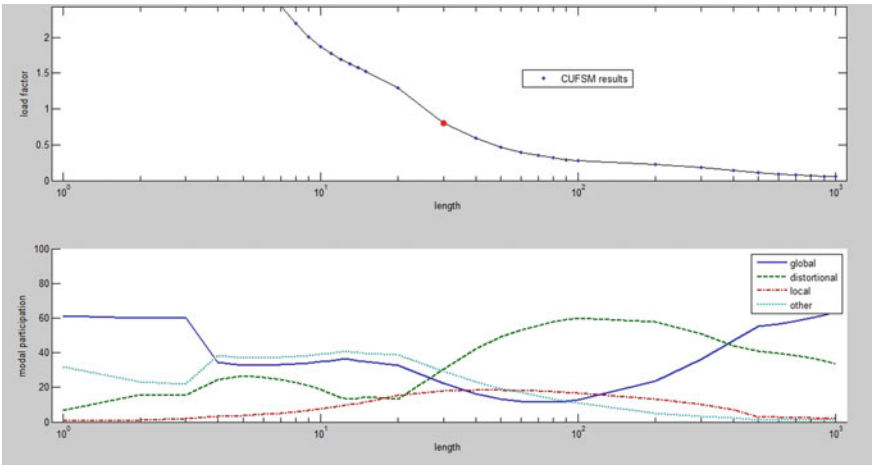


**Fig. 11** Wavelength versus load factor graph for folded-flange section with angle of 150°

## 5 Sigma Sections Under Compressive Load

Aghoury [2] carried experiments to investigate the behaviour and strength of cold-formed single-lipped sigma column (Fig. 14). His study is further extended here to conclude the optimized section by taking the web lip sing angle as parameter. The angles selected for this study ranges from 30° to 80°. All those sections were analyzed in CUFSM [4] and signature curves of all the sections were clubbed together, so as to compare the behaviour as in Fig. 15. It was observed that in local buckling region all the sections were more or less at same level. However, in distortional buckling region

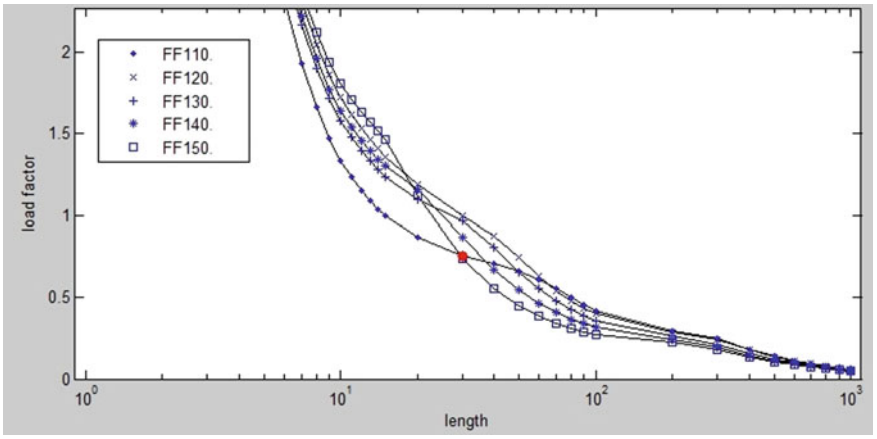


**Fig. 12** Wavelength versus load factor graph for all folded-flange sections under compressive load

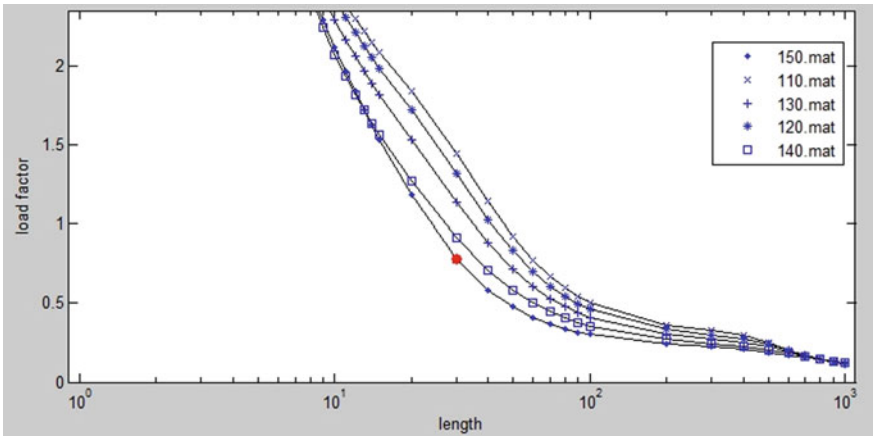


**Fig. 13** Wavelength versus load factor graph for all folded-flange sections under flexural load

all the sections differ in their behaviour with load factor varying up to 12%. This is very important as our current code IS 801-1975 [5–17] is silent for this behaviour. From the graph in Fig. 15 it is seen that sigma section with lips angle = 45° have higher buckling capacity than sections with other angles.

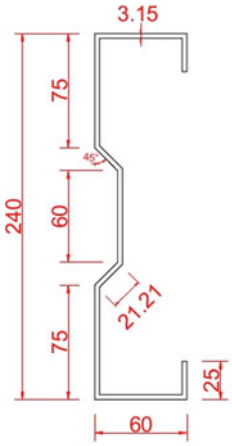


**Fig. 14** Sigma section

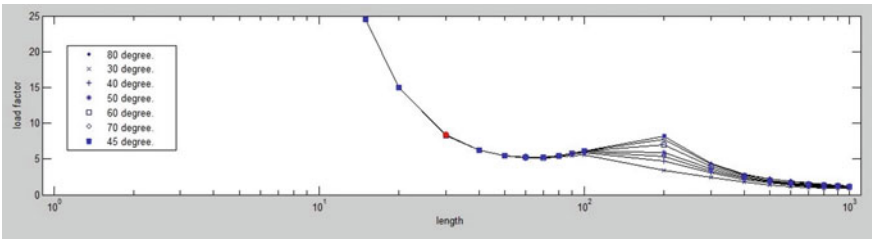


**Fig. 15** Signature curves for sigma sections

## 6 Summary and Conclusions

From this study, it was observed that distortional buckling plays major role in behaviour of thin-walled sections. This parametric study displayed following observations:

1. Stiffening through lips increases the capacity of the CFS sections in case of flexure loads.
2. The newly developed section named "folded-flange Section" shows higher capacity than the channel sections with and without lips specified in IS 811-1987.
3. The optimized section of folded-flange section is that with the angle of 120° in case of compressive loading and the angle of 110° in case of compressive loading (based on elastic buckling analysis).
4. The sigma section was also analyzed with the most optimized section being that with web lips angle of 45° (based on elastic buckling analysis).

## References


1. Ye J et al (2016) Development of more efficient cold-formed steel channel sections in bending. Thin-Walled Structures 101:1–13
2. El Aghoury MA, Hanna MT, Amoush EA (2017) Experimental and theoretical investigation of cold-formed single lipped sigma columns. Thin-Walled Structures 111:80–92
3. American Iron and Steel Institute, 2007. AISI S100:2007: North American specification for the design of cold-formed steel structural members, Washington DC
4. Schafer BW, Adany S (2006) Buckling analysis of cold-formed steel members using cufsm: conventional and constrained finite strip methods. In: 18th international specialty conference on cold-formed steel structures, Orlando, Florida
5. Bureau of Indian Standards, 1975. IS 801:1975: code of practice for use of cold formed light gauge steel structural members in general building construction, New Delhi
6. Bureau of Indian Standards, 1987. IS 811:1987: cold formed light gauge structural steel sections, New Delhi
7. Foster ASJ, Gardner L (2016) Stability of steel beams using the continuous strength method. Thin-Walled Structures 100:1–13
8. Selvaraj S, Madhavan M (2018) Retrofitting of structural steel channel sections using cold-formed steel encasing channels. J Perform Constr Facil 32(4):04018049
9. Niu S, Rasmussen KJR, Fan F (2015) Local–global interaction buckling of stainless steel I-beams. I: experimental investigation. Journal of Structural Engineering 141(8):04014194
10. Selvaraj S, Madhavan M (2019) Strengthening of laterally restrained steel beams subjected to flexural loading using low-modulus CFRP. J Perform Constr Facil 33(3):04019032
11. Wang L, Young B (2018) Behaviour and design of cold-formed steel built-up section beams with different screw arrangements. Thin-Walled Structures 131:16–32
12. Usefi N, Sharafi P, Ronagh H (2019) Numerical models for lateral behaviour analysis of cold-formed steel framed walls: State of the art, evaluation and challenges. Thin-Walled Structures 138:252–285
13. Kechidi S, Macedo L, Castro JM, Bourahla N (2017) Seismic risk assessment of cold-formed steel shear wall systems. J Constr Steel Res 138:565–579
14. Ye J, Jiang L (2018) Simplified analytical model and shaking table test validation for seismic analysis of mid-rise cold-formed steel composite shear wall building. Sustainability 10(9):3188
15. Selvaraj, S. and Madhavan, M., 2019, August. Sheathing braced design of cold-formed steel structural members subjected to torsional buckling. In Structures (Vol. 20, pp. 489–509). Elsevier.
16. Selvaraj S, Madhavan M (2018) Geometric imperfection measurements and validations on cold-formed steel channels using 3d noncontact laser scanner. J Struct Eng 144(3):04018010
17. Selvaraj S, Madhavan M (2019) Flexural Behaviour and Design of Cold-Formed Steel Wall Panels Sheathed with Particle Cement Board. J Constr Steel Res 162:105723

# Flexural–Torsional Couplings in Thin-Walled Beam Sections Having Variable Stiffness


**Paulomi Mukherjee, Lokesh Kant Sao, and Devesh Punera**

**Abstract** This work tries to study the flexural–torsional couplings in thin-walled composite beams having variable stiffness. Variable stiffness composites (VSC) are manufactured with curvilinear fibres. Compared with straight fibre laminates, variable angle tow sections have improved structural response as they redistribute the in-plane stresses. A generalized beam kinematic model which considers the effect of flexural, torsional and warping deformations is adopted and using the principle of minimum potential energy, governing set of equations are derived. The variable fibre angles are defined using a general Lagrangian polynomial and as a special case, linearly varied fibre angles are studied. The transverse shear deformation effects are neglected in the present model and through set of $C^1$ continuity finite elements, governing equations are numerically solved. The results are validated for the constant fibre angle composites and further, important observations are drawn on the coupled response of thin-walled VSCs. The present kinematic model and the numerical scheme is capable of extending the problem to further study the vibration and stability response of these composites.

**Keywords** Flexural–torsional coupling · Thin-walled composite · Variable stiffness · Finite element

P. Mukherjee · L. K. Sao · D. Punera (✉)
School of Infrastructure, IIT Bhubaneswar, Khorda, Bhubaneswar, India
e-mail: devesh@iitbbs.ac.in

P. Mukherjee
e-mail: pm33@iitbbs.ac.in

L. K. Sao
e-mail: lks10@iitbbs.ac.in



M. Madhavan et al. (eds.), *Proceedings of the Indian Structural Steel Conference 2020 (Vol. 1)*, Lecture Notes in Civil Engineering 318,
https://doi.org/10.1007/978-981-19-9390-9_39

## 1 Introduction

Composite materials are made of two or more individual constituent materials having different characteristics which behave in a completely different manner than those individual constituents. Other than the benefits of being lightweight and having greater strength, composites have gained wide interest because they can be easily tailored for functional requirements. Composite materials with straight fibres are common in practice and provide constant stiffness properties along with the structure. Further, to effectively use the material and to optimize the structural response, variable stiffness composite sections (VSC) have got more importance recently. These composites are mostly developed using the curvilinear fibres in laminates which have variable orientation along the length of the composite. The basic characteristic of composite stiffness is changed due to the orientation and profiling of these curvilinear fibres. The variable stiffness concept is shown to affect the stress, vibration and buckling response of the laminated composites. Initial terminology of the variable stiffness composites was coined by Gürdal and Olmedo [6], though for modern composites the idea of functional change in stiffness was harnessed even earlier by various researchers in different ways [1, 5, 7, 11]. With the development of technology such as fibre and tow placement technology, variable angle tow sections can be easily produced. The concept of curvilinear fibre placement can overcome the difficulties associated with other methods, i.e. discontinuities in fibres, stress concentration due to change in cross-sectional area or manufacturing difficulties.

Several studies are presented in recent years on the response of variable stiffness composites. Wu et al. [15] proposed a more robust and efficient model based on the Rayleigh–Ritz method for buckling analysis of variable angle tow (VAT) plates. The optimization studies are also done by using genetic algorithm (GA) which can produce optimized nonlinear fibre orientation that can provide maximum buckling load capacity. Gökhan Günay and Timarci [4] analyzed flexural–torsional coupling of a thin-walled laminated composite beam with closed cross section considering warping effects, as well as the variable stiffness along length. The linear variation of fibre is considered and modelled using the continuous tow shearing method. It was concluded that varying fibres provide better mechanical performance than straight fibres. Zhao and Kapania [16] studied the pre-stressed vibration response of a stiffened VAT laminated plate under a uniform end shortening. Pre-stressed vibration response and buckling load capacity depends on both end shortening and present boundary condition for linearly variable (LV) fibre plates. For nonlinear variable fibres (NLV), buckling load capacity can increase highly than LV but free vibration fundamental frequency is observed to have a slight improvement in comparison with LV fibre cases.

Further, it is a well-established fact that thin-walled open or closed sections are prone to couple flexural–torsional buckling due to their small torsional rigidities and unsymmetrical profiles. It will be therefore interesting to study the flexural–torsional couplings of thin-walled variable stiffness composite sections. Over the years, thin-walled theory for beam structures has been developed by Vlasov [14], Gjelsvik [3]

and other researchers [10]. Song and Librescu [13] observed free vibration response of a thin-walled anisotropic closed beam section. They considered transverse shear to be present in the analysis and effect of primary and secondary warping effects is also considered. It was observed vibrational frequency increases with ply angle in lateral and plunging mode and ignoring transverse shear slightly overestimates the vibration frequency.

On a careful study of the existing literature, it is found that thin-walled theory without consideration of transverse shear is sufficiently accurate. There are very less studies which describe the flexural–torsional response of variable fibre angle composites. The study of flexural–torsional coupling in these composites can provide sufficient confidence and observations for possible application in different aerospace and structural components. Taking note of these points, this work tries to extend the thin-walled theory of Song and Librescu [13] without considering the transverse shear deformation effects to study the flexural–torsional couplings in variable stiffness composite beams. An enhanced version of the present study is also available in Mukherjee et al. [12]. The energy-based formulation is presented to obtain the governing equations of the structure in general curvilinear contour coordinates. Using a displacement based finite element, formulation results are obtained for the lateral, transverse deformation, twist rotation and warping deformation of general I-section beam.

## 2 Theoretical Formulation

Two coordinate systems are shown here, i.e. global cartesian coordinate system ($x$, $y$, $z$) where $x$, $y$ denotes the cross-sectional area and $z$ is along length. Another coordinate system is contour coordinate ($n$, $s$, $z$) where $n$ is perpendicular to the mid surface and $s$ is tangential to the mid surface as shown in Fig. 1. These two coordinate systems are related through an angle orientation $\alpha$ between the global reference direction $x$ and contour normal $n$.

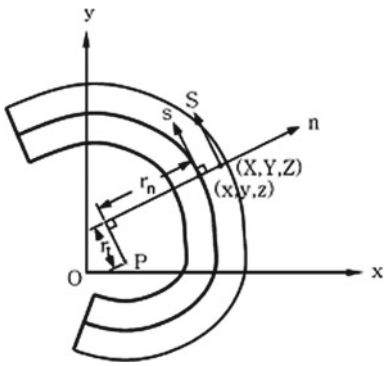


**Fig. 1** Displacement of arbitrary point $m$ in a closed beam

'$P$' is the pole point that is used as reference point and its displacements are $U$ and $V$ along the global $x$ and $y$ directions while $\phi$ is the rotation about the z axis. The present theory makes the Vlasov's assumptions of thin-walled section which allows no contour cross-section deformation and neglects the transverse shear strains of the cross-section.

## 2.1 Assumption

Following primary assumptions are made in present theory:

1. Contour does not deform in its own plane.
2. Shear strain $\gamma_{sz}$ in the middle surface is zero in each element.
3. Normal to the unreformed middle surface remain normal to the deformed middle surface.
4. Transverse shear strains are neglected.
5. Hoop stress $\sigma_s$ is small compared to axial stress $\sigma_z$.

## 2.2 Kinematic Field

Present beam kinematic model is versatile to include the effect of flexural, torsional and warping deformations. The model has four primary displacement parameters. The removal of transverse shear deformation reduces the primary variables but introduces $C^1$ continuity in the formulation. The basic beam kinematic is defined in Eq. (1). The displacement of any point in the $(x, y, z)$ cross section can be defined concerning a particular point $P$ which is called the pole point. The rotation of the beam is also denoted for that point.

$$U(x, y, z) = U_p(z) - (y - y_p)\phi(z)$$

$$V(x, y, z) = V_p(z) + (x - x_p)\phi(z)$$

$$\phi = \frac{1}{2}\left(\frac{\partial v}{\partial x} - \frac{\partial u}{\partial y}\right)_{x=xp, y=yp} \tag{1}$$

Here $Up$ and $Vp$ are displacement components of pole point $P$. To transform the $x, y, z$ coordinates into $n, s, z$ coordinate a transformation operation is done as shown in Eq. (2).

$$\begin{bmatrix} n \\ s \end{bmatrix} = \begin{bmatrix} \frac{dy}{ds} & -\frac{dx}{ds} \\ \frac{dx}{ds} & \frac{dy}{ds} \end{bmatrix} \begin{bmatrix} x \\ y \end{bmatrix} \tag{2}$$

After transformation following displacement fields are obtained for any point away from the contour reference axis:

$$U_n(s,n,z) = u(z)\left(\frac{\mathrm{d}y}{\mathrm{d}s}\right) - v(z)\left(\frac{\mathrm{d}x}{\mathrm{d}s}\right) - \phi(z)R_s(s,n)$$

$$U_s(s,n,z) = v(z)\left(\frac{dx}{ds}\right) + v(z)\left(\frac{dy}{ds}\right) + \phi(z)R_n(s,n) \tag{3}$$

The transverse shear strains ($\gamma_{xz}$ and $\gamma_{yz}$) are neglected and in the contour coordinates shear strains $\gamma_{sz}$ and $\gamma_{nz}$ are evaluated through transformed Eq. (3). Further, for pure twisting away from mid surface $\gamma_{sz} = 2n\phi'$ therefore, the condition of shear strains helps to evaluate the axial deformation of the thin-walled section which is obtained as:

$$W(s,n,z) = w(z) - \left(\frac{\mathrm{d}u}{\mathrm{d}z}\right)\left(x(s) + n\frac{\mathrm{d}y}{\mathrm{d}s}\right) - \left(\frac{\mathrm{d}v}{\mathrm{d}z}\right)\left(y(s) - n\frac{\mathrm{d}x}{\mathrm{d}s}\right) - \phi'(z)\omega(s) \tag{4a}$$

here,

$$R_s = (x - x_p)\frac{\mathrm{d}x}{\mathrm{d}s} + (y - y_p)\frac{\mathrm{d}y}{\mathrm{d}s} \quad \text{and}$$

$$R_n = (x - x_p)\frac{\mathrm{d}y}{\mathrm{d}s} - (y - y_p)\frac{\mathrm{d}x}{\mathrm{d}s} \tag{4b}$$

$\omega = \overline{\omega} + \overline{\overline{\omega}}$ where $\overline{\omega}$ is primary warping function and $\overline{\overline{\omega}}$ is secondary warping function.

$$\overline{\omega} = \int R_n.\mathrm{d}s \tag{5}$$

$$\overline{\overline{\omega}} = -n.R_s \tag{6}$$

## 2.3 Strain Field

As the deformation of cross section is not allowed, this produces zero in-plane strains ($\varepsilon_{xx} = 0, \varepsilon_{yy} = 0\,, \varepsilon xy = 0$). Other strains can be obtained from displacement fields mentioned in Eqs. (3) and (4a).

$$\varepsilon_z = w' - U''\left(x(s) + n.\frac{\mathrm{d}y}{\mathrm{d}s}\right) - V''\left(y(s) - n.\frac{dx}{ds}\right) - \phi''.\omega(s) \tag{7}$$

$$\gamma_{sz} = 2.n.\phi' \tag{8}$$

$$\gamma_{nz} = 0 \tag{9}$$

This relation can be written as:

$$\begin{bmatrix} \varepsilon_{zz} \\ \gamma_{sz} \end{bmatrix} = \begin{bmatrix} 1 & (x + n.\cos\alpha) & (y + n.\sin\alpha) & (\varpi - n.R_s) & 0 \\ 0 & 0 & 0 & 0 & n \end{bmatrix} . \begin{bmatrix} \varepsilon_{zz}^0 \\ U'' \\ V'' \\ \phi'' \\ 2\phi' \end{bmatrix} \tag{10}$$

$$\varepsilon(s, n, z) = G(s, n).\widetilde{\varepsilon}(z) \tag{11}$$

$\varepsilon = G.\widetilde{\varepsilon}$ , using this step general strain vector has been separated into $(s, n)$ and $z$ coordinate.

## 2.4 Governing Equations

Governing equations were derived from the concept of minimum potential energy.

$$\Pi_{\text{total}} = \Pi_{\text{strain}} + w_{\text{ext}} \tag{12}$$

By putting the values from Eqs. (7) and (8) into Eq. (12) then rearranging it can be written as:

$$\Pi_{\text{strain}} = \frac{1}{2} \int_0^l (N_z.w' - M_y.U'' - M_x.V'' - M_w.\phi'' + 2.M_z.\phi')\mathrm{d}z \tag{13a}$$

$$N_z = \int_s \sigma_z \mathrm{d}n\mathrm{d}s \tag{13b}$$

$$M_y = \int_s \left(\sigma_z.x(s) + L_{zz}.\frac{\mathrm{d}y}{\mathrm{d}s}\right)\mathrm{d}n\mathrm{d}s \tag{13c}$$

$$M_x = \int_s \left(\sigma_z.y(s) - L_{zz}.\frac{\mathrm{d}x}{\mathrm{d}s}\right)\mathrm{d}n\mathrm{d}s \tag{13d}$$

$$M_w = \int_s (\sigma_z.\overline{w(s)} - L_{zz}.\overline{\overline{w(s)}})\mathrm{d}n\mathrm{d}s \tag{13e}$$

$$M_z = \int_s (\sigma_{sz}.n)\mathrm{d}n\mathrm{d}s \tag{13f}$$

$$W_{\text{ext}} = \int_0^l (q_z.w + q_x.U + q_y.V + m_z.\phi)\mathrm{d}s \tag{14}$$

Here $N$ is transverse stress resultant and $L$ is stress couple. By equating variation of total potential energy to zero, Eq. (15) can be written as:

$$\delta\Pi_{\text{total}} = \delta\Pi_{\text{strain}} + \delta\Pi_{\text{ext}} = 0 \tag{15}$$

Governing equations of the beam can be obtained by applying integration by parts and assembling coefficients of $\delta w$, $\delta U$, $\delta V$, as follows:

$$N_z' + q_z = 0 \tag{15a}$$

$$M_y'' + q_x = 0 \tag{15b}$$

$$M_x'' + q_y = 0 \tag{15c}$$

$$M_w'' + 2m_z' + m_z = 0 \tag{15d}$$

## 2.5 Constitutive Relationship

The stress at a point is defined through constitutive rule in terms of the strain. The general constitutive rule for an orthotropic material can be identified as:

$$\begin{bmatrix} \sigma_z \\ \sigma_s \\ \sigma_{sz} \end{bmatrix} = \begin{bmatrix} Q_{11} & Q_{12} & Q_{16} \\ Q_{12} & Q_{22} & Q_{26} \\ Q_{16} & Q_{26} & Q_{66} \end{bmatrix} \begin{bmatrix} \varepsilon_z \\ \varepsilon_s \\ \gamma_{sz} \end{bmatrix} \tag{16}$$

It is also known that coefficients of constitutive matrix are dependent on the fibre angles and effective material coefficients can be defined when fibres are orientated at some angle $\theta$ from the structural reference coordinates. $Q_{ij}$ terms are called transformed reduced stiffness matrix.$\varepsilon$ and $\kappa$ represents strains and curvature, respectively. For an orthotropic lamina, elements of constitutive matrix $[Q_{11}]\ldots[Q_{66}]$ depends on fibre angle and can be referred from standard text on composite structures [8].

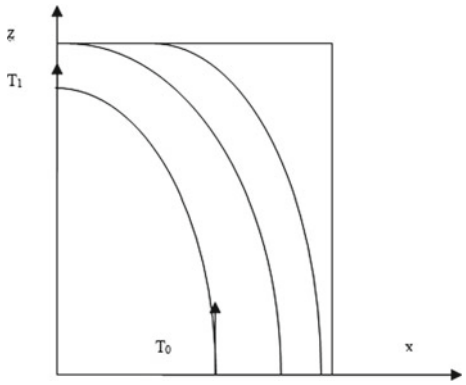


**Fig. 2** Fibre angle variation along length

In case of variable stiffness composites, the fibre angle is continuously changing. If fibre angle varies linearly we can assume angle variation as shown in Eq. (17) (Fig. 2).

$$\theta(z) = \frac{(T_1 - T_0)}{l} z + T_0 \tag{17}$$

$T_1$ and $T_0$ are fibre angles in the beginning and at the end of the beam, respectively, which varies linearly with length. Here, the transformed reduced stiffness matrix coefficients will vary along length as a function of fibre angle $\theta$. If free stress condition ($\sigma_s = 0$) is assumed then Eq. (16) will be reduced to

$$\begin{bmatrix} \sigma_z \\ \sigma_{sz} \end{bmatrix} = \begin{bmatrix} \overline{Q_{11}} & \overline{Q_{16}} \\ \overline{Q_{16}} & \overline{Q_{66}} \end{bmatrix} \begin{bmatrix} \varepsilon_z \\ \gamma_{sz} \end{bmatrix} \tag{18a}$$

These reduced coefficients can be evaluated in terms of coefficients of Eq. (16). Further, it can be written as Eq. (18b).

$$\boldsymbol{\sigma} = \mathbf{C}\ \boldsymbol{\varepsilon} \tag{18b}$$

## 3 Finite Element Formulation

The governing equation is solved by displacement-based finite element method taking two node beam element. Generalized displacements are given below

$$w = \sum_{i=1}^{N} w_i . S_i^L \tag{19a}$$

$$U = \sum_{i=1}^{N} U_i . S_i^H \tag{19b}$$

$$V = \sum_{i=1}^{N} V_i . S_i^H \tag{19c}$$

$$\phi = \sum_{i=1}^{N} \phi_i . S_i^H \tag{19d}$$

where,$S_i^L$ and $S_i^H$ are Lagrangian and cubic Hermite shape functions, respectively. After putting this expressions in Eq. (15), finite element formulation is obtained in the form:

$$K.\Delta = F$$

where $[K]$ denotes global stiffness matrix and $[F]$ denotes global load vector.$\Delta$ is nodal displacement field vector. By matrix inversion procedure, displacement fields can be obtained.

$$\begin{bmatrix} K_{11} & K_{12} & K_{13} & K_{14} \\ & K_{22} & K_{23} & K_{24} \\ & & K_{33} & K_{34} \\ & & & K_{44} \end{bmatrix} \begin{bmatrix} w \\ U \\ V \\ \phi \end{bmatrix} = \begin{bmatrix} f_1 \\ f_2 \\ f_3 \\ f_4 \end{bmatrix} \tag{20}$$

Equation (12) can be written in the form mentioned in Eq. (21):

$$\int \delta\varepsilon^T . \sigma . \mathrm{d}v - \int \delta u^T . f . \mathrm{d}z = 0 \tag{21}$$

Here $u$ denotes displacement field. Applying Eq. (11) in Eq. (21) we can obtain

$$\int \delta\widetilde{\varepsilon} . G^T . C . G . \widetilde{\varepsilon} . \mathrm{d}v - \int \delta u^T . f . \mathrm{d}z = 0 \tag{22}$$

Strain field can be written as:

$$\widetilde{\varepsilon} = B . \widetilde{u} \tag{23}$$

$$u = N . \widetilde{u} \tag{24}$$

where $N$ is the shape function associated with the vector of unknown nodal displacement $\widetilde{u}$. Equation (22) can be written as:

$$\delta\widetilde{u}^T\left\{\left[\int B^T.G^T.C.G.B.\mathrm{d}s.\mathrm{d}n.\mathrm{d}z\right]\widetilde{u} - \int N^T.f.\mathrm{d}z\right\} = 0 \tag{25}$$

Now comparing this Eq. (20) and Eq. (25) stiffness matrix and force matrix can be written as:

$$K = \int (G.B)^T.C.(G.B).\mathrm{d}s.\mathrm{d}n.\mathrm{d}z \tag{26}$$

$$F = \int N^T.f.\mathrm{d}z \tag{27}$$

## 4 Numerical Study

This section presents few problems based on the earlier formulation and finite element solution scheme.

**Problem 1:** The first problem validates the formulation for a homogeneous thin-walled steel I-section under the application of transverse load and twisting moment. The results are validated from the standard theoretical results based on general solid mechanics. In this case one normal cantilever I-beam 'ISMB 400' having a length of 2.5 m is evaluated with a uniformly distributed load of 1 kN/m throughout the length. Maximum displacement is compared with standard results from solid mechanics [2]. Present results are given in Table 1 which validates the excellent agreement with the existing results and verifies the accuracy of formulation. Further, Table 2 gives the comparison for the twist at the free end of same cantilever beam subjected to twisting moment of 1 Nm at the free end.

**Problem 2:** In this problem, a simply supported I beam is studied with the dimension of ($50 \times 50 \times 2.08$ mm) and length 2.5 m having uniformly distributed load intensity

**Table 1** Comparison of maximum transverse displacement for uniformly loaded I-section

| Depth of the section (mm) | Width of flange (mm) | Thickness of flange (mm) | Thickness of web (mm) | Moment of inertia ($cm^4$) | Theoretical displacement (mm) | Transverse displacement in mm (present study) |
|---|---|---|---|---|---|---|
| 400 | 140 | 16 | 8.9 | 20,458.40 | 0.119 | 0.12 |

**Table 2** Comparison of twist angle for unit twist moment on cantilever I-section

| Twisting moment (Nm) | Theoretical twist (rad) | Present study (rad) |
|---|---|---|
| 1 | 3.40e−5 | 3.53e−5 |

of 1 kN/m for different stacking sequences and results are compared with the results available in the literature [9]. The results are tabulated in Table3 and all results are in good agreement. Properties of the beam are:$E_1 = 53.78$ GPa, $E_2 = 17.93$ GPa, $G_{12} = 8.96$ GPa and $\nu_{12} = 0.25$ (Fig. 3).

It is also seen that for symmetrical composite sections, the amount of twist in the cross section is negligible. With the introduction of antisymmetric profiles and twisting moment in the cross section, the lateral bending as well as twist in the cross section increase. Another problem studies a simply supported composite beam having same dimensions as defined earlier with stacking sequence $[\theta, \theta, -\theta, -\theta]$ in top flange and $[\theta, -\theta, \theta, -\theta]$ in bottom flange and web. The beam has one eccentric load of 1 kN at the free end with eccentricity '$e$', where $e/b = 0.05$ and $b$ is the flange width.

Figure 4 tries to verify the introduction of flexural–torsional coupling in antisymmetric composite beams.

**Problem 3:** In this case, the same beam formulation is adopted but instead of straight fibre, here curvilinear fibre with linearly varying fibre angle as mentioned in Eq. (27) is adopted and results are provided for different $T_1$ and $T_0$ values. The dimensions of beam, loading condition and material properties are similar to one defined in Problem 2. The stacking sequence is avoided and only single layer of variable angle fibre is considered. The results are tabulated in following Table 4.

**Table 3** Maximum transverse displacement (in cm) of simply supported I-section composite beam

| Stacking sequence | ABAQUS [9] | Numerical result [9] | Present method |
|---|---|---|---|
| $[15, -15]_{4s}$ | 6.989 | 6.899 | 6.992 |
| $[30, -30]_{4s}$ | 9.360 | 9.290 | 9.4519 |
| $[45, -45]_{4s}$ | 13.479 | 13.421 | 13.6545 |
| $[60, -60]_{4s}$ | 17.023 | 16.962 | 17.2567 |
| $[75, -75]_{4s}$ | 18.490 | 18.411 | 18.7315 |
| $[0, 90]_{4s}$ | 9.400 | 9.299 | 9.5120 |
| [0, −45, 90, 45] | 10.851 | 10.777 | 10.853 |
| $[0]_{4s}$ | 6.340 | 6.299 | 6.341 |

**Fig. 3** Schematic of I beam

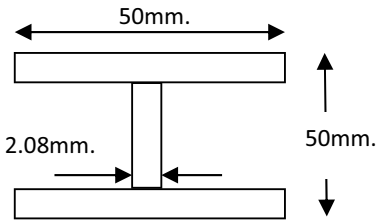

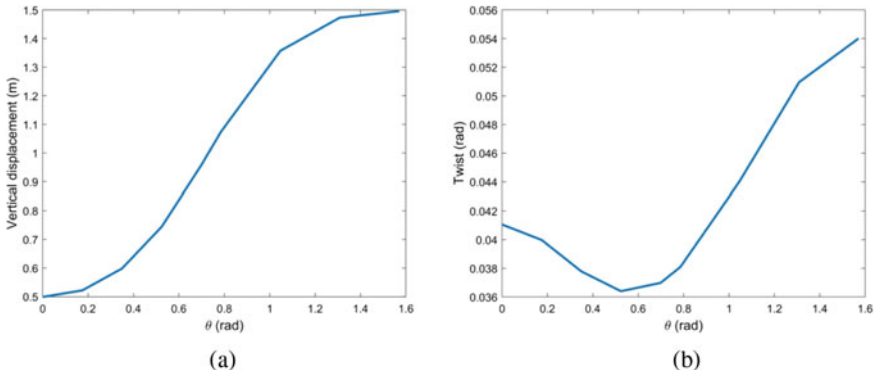


**Fig. 4** **a** Vertical displacement and **b** Twist variation for cantilever beam with fibre angle variation

**Table 4** Maximum vertical displacement (cm) of cantilever beam with variable stiffness

| $(T_1) \downarrow (T_0) \rightarrow$ | 0° | 30° | 45° | 60° | 75° | 90° |
|---|---|---|---|---|---|---|
| 0° | 47.36 | 48.50 | 50.06 | 52.39 | 55.45 | 59.03 |
| 30° | 62.71 | 70.59 | 75.85 | 81.66 | 87.49 | 92.90 |
| 45° | 84.59 | 95.78 | 101.98 | 107.88 | 113.02 | 117.22 |
| 60° | 109.08 | 120.01 | 124.91 | 128.89 | 131.86 | 133.99 |
| 75° | 126.05 | 133.91 | 136.73 | 138.68 | 139.9 | 140.65 |
| 90° | 134.66 | 139.45 | 140.83 | 141.59 | 141.95 | 142,05 |

The results corresponding to Tables 4, 5 and 6 show that the deformation response varies over a large range. This possibly opens further opportunities to optimize the fibre angle for desired response. It is also interesting to observe that with the presence of transverse load, only lateral displacement and twist has taken place due to presence of variable stiffness, this proves the importance of the present study.

Finally, a cantilever beam with same dimension and uniformly distributed load of 1 kN/m is analyzed for variable stiffness section for only the case where the half of the thickness of the beam, fibre angle varies from −90° to 90° and in the other half,

**Table 5** Lateral displacement ($\times 10^{-5}$ cm) of cantilever beam with variable stiffness

| $(T_1) \downarrow (T_0) \rightarrow$ | 0° | 30° | 45° | 60° | 75° | 90° |
|---|---|---|---|---|---|---|
| 0° | 0 | −46.15 | −88.71 | −129.03 | −157.61 | −171.69 |
| 30° | −226.0 | −323.5 | −339.89 | −326.3 | −290.75 | −247.53 |
| 45° | −331.2 | −337.9 | −298.77 | −241.34 | −183.83 | −137.07 |
| 60° | −265.8 | −192.5 | −137.47 | −88.83 | −55.05 | −34.45 |
| 75° | −143.8 | −70.43 | −38.16 | −17.95 | −8.00 | −3.64 |
| 90° | −68.10 | −22.15 | −8.55 | −2.40 | −0.4082 | 0 |

**Table 6** Twist (rad) in cantilever beam with variable stiffness

| $(T_1) \downarrow (T_0) \rightarrow$ | 0° | 30° | 45° | 60° | 75° | 90° |
|---|---|---|---|---|---|---|
| 0° | 0 | −0.0282 | −0.0376 | −0.0441 | −0.0476 | −0.0484 |
| 30° | 0.0574 | −0.0672 | −0.0683 | −0.0663 | −0.0615 | −0.0550 |
| 45° | 0.0697 | −0.07 | −0.0661 | −0.0592 | −0.0506 | −0.0420 |
| 60° | 0.0651 | −0.0565 | −0.0486 | −0.0392 | −0.03 | 0.0225 |
| 75° | −0.0498 | −0.0364 | −0.0278 | −0.0194 | −0.0127 | −0.0079 |
| 90° | −0.034 | −0.02 | −0.0133 | −0.0074 | −0.0031 | 0 |

the fibres are unidirectional. The transverse (vertical) and lateral displacement along with twist of the cross section across the length are presented in Fig. 5. The results show interesting observations. The beam member has significant lateral deformation and further rate of twist is also not constant through the length which verifies warping restraint deformation of the section.

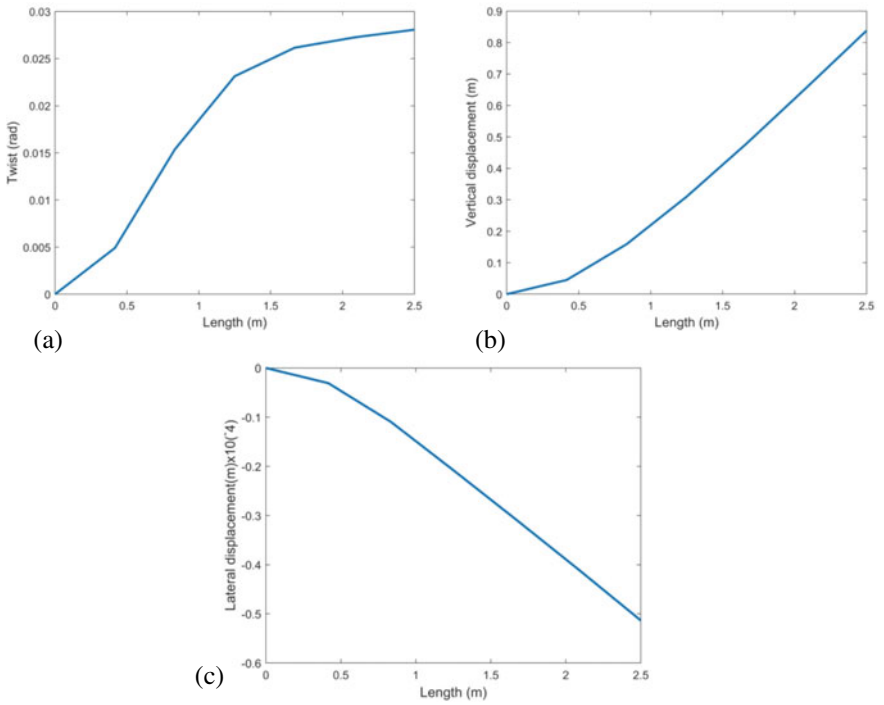


**Fig. 5** **a** Twist variation, **b** Vertical displacement and **c** Lateral displacement along length of composite I-section beam

## 5 Conclusion

Thin-walled open sections are more prone to flexural–torsional failures. This is due to lower torsional rigidity of these sections which gets coupled with flexural modes under the application of even simple transverse loads. Initial studies are presented for the coupled flexural–torsional response of beams made of isotropic materials. In case of laminated composites even with doubly symmetric sections, the flexural and torsional modes are no longer uncoupled. In case of antisymmetric beam flexural–torsional coupling takes place altogether. For variable stiffness, composite beams significant lateral deformation along with twisting of the cross section is present. The concept of variable stiffness can be very helpful to optimize the desired response of these composites but at the same time sufficient caution is required to check the flexural–torsional behaviour of these sections. The results provided in the present work can be further extended to calculate the critical load for flexural–torsional buckling of thin-walled open as well as closed sections. With the suitable technique the optimized fibre profiles can be defined.

## References

1. Dinardo MT, Lagacet PA (1989) Buckling and postbuckling of laminated composite plates with ply dropoffs. AIAA J 27(10):1392–1398. https://doi.org/10.2514/3.10276
2. Gere JM, Timoshenko SP (1998) Mechanics of materials. Chapman and Hall
3. Gjelsvik A (1981) The theory of thin walled bars. Wiley
4. Gökhan Günay M, Timarci T (2017) Static analysis of thin-walled laminated composite closed-section beams with variable stiffness. Compos Struct 182:67–78. https://doi.org/10.1016/j.compstruct.2017.08.092
5. Grimes G, Dusablon E (1982) Study of compression properties of graphite/epoxy composites with discontinuities. In: Composite materials: testing and design (6th conference). West Conshohocken, PA 19428-2959: ASTM International, pp 513–513–26. https://doi.org/10.1520/STP28498S
6. Gürdal Z, Olmedo R (1993) In-plane response of laminates with spatially varying fiber orientations: variable stiffness concept. AIAA J 31(4):751–758. https://doi.org/10.2514/3.11613
7. Hyer MW, Lee HH (1991) The use of curvilinear fiber format to improve buckling resistance of composite plates with central circular holes. Compos Struct 18(3):239–261. https://doi.org/10.1016/0263-8223(91)90035-W
8. Jones RM (2014) Mechanics of composite materials. CRC Press
9. Lee J, Lee SH (2004) Flexural-torsional behavior of thin-walled composite beams. Thin-Walled Structures 42(9):1293–1305. https://doi.org/10.1016/j.tws.2004.03.015
10. Librescu L, Song O (2006) Thin-walled composite beams volume 131, solid mechanics and its applications
11. Martin AF, Leissa AW (1989) Application of the Ritz method to plane elasticity problems for composite sheets with variable fibre spacing. Int J Numer Meth Eng 28(8):1813–1825. https://doi.org/10.1002/nme.1620280808
12. Mukherjee P, Punera D, Mishra M (2021) Coupled flexural torsional analysis and buckling optimization of variable stiffness thin-walled composite beams. Mech Adv Mater Struct. https://doi.org/10.1080/15376494.2021.1878565

13. Song O, Librescu L (1993) Free vibration of anisotropic composite thin-walled beams of closed cross-section contour. J Sound Vib 167(1):129–147
14. Vlasov V (1961) Thin-walled elastic beams, 2nd edn. Israel Program for Scientific Translations, Jerusalem
15. Wu Z, Weaver PM, Raju G, Kim BC (2012) Buckling analysis and optimisation of variable angle tow composite plates. Thin-Walled Structures 60:163–172
16. Zhao W, Kapania RK (2019) Prestressed vibration of stiffened variable-angle tow laminated plates. AIAA J 57(6):2575–2593. https://doi.org/10.2514/1.J057719

# Critical Buckling Moment of Cold-Formed Lipped Channel Sections


**Ravikant Singh, Avik Samanta, and Saurabh Suman**

**Abstract** Cold-formed steel (CFS) members are extensively used in building construction industry both as primary members to achieve cost-effectiveness over their hot-rolled counterpart and as secondary elements between main frameworks. In this work, cold-rolled lipped channel beams (LCB) were studied for various end moment cases. A suitable finite-element (FE) model intended for this study was adopted. Accuracy of developed FE models involved in this study was validated with experimental and numerical results available in the literature, which were further used to perform parametric study to evaluate the critical buckling capacity of selected beam sections. An extensive FE parametric study was carried out using commercial software package ABAQUS. This paper reports on series of investigation done on available cross-sections from Indian standards to evaluate critical buckling strength and ultimate moment capacity of these beams with varying moment, cross-section, length, and material properties. The beams were subjected to end moment along the span generated by applying a series of tensile and compressive loads above and below neutral axis (NA) forming a triangular distribution. The study also includes effects of uniform and non-uniform bending moment distribution along the span on buckling capacity. Idealized simply supported end conditions with warping free ends were used.

**Keywords** Cold-formed steel · Lateral torsional buckling · Finite-element analysis · Lipped channel beams

R. Singh (✉) · A. Samanta · S. Suman
Department of Civil and Environmental Engineering, IIT, Patna, India
e-mail: ravikant_1921ce01@iitp.ac.in

A. Samanta
e-mail: asamanta@iitp.ac.in

S. Suman
e-mail: saurabh.pce17@iitp.ac.in



M. Madhavan et al. (eds.), *Proceedings of the Indian Structural Steel Conference 2020 (Vol. 1)*, Lecture Notes in Civil Engineering 318,
https://doi.org/10.1007/978-981-19-9390-9_40

## Notations

| | |
|---|---|
| $b$ | Width of flange |
| $C_w$ | Warping constant |
| $E$ | Modulus of elasticity |
| $f_y$ | Yield strength |
| $h$ | Depth of beam |
| $I_y$ | Moment of Inertia about Y-axis |
| $l$ | Lip depth |
| $M_{\text{el}}$ | Elastic buckling moment capacity |
| $M_u$ | Ultimate moment capacity |
| $M_y$ | Yield moment capacity |
| $t$ | Thickness of section |
| $Z$ | Section modulus |
| $\sigma$ | Standard deviation |
| $\lambda$ | Beam slenderness |

## 1 Introduction

The cold-formed steel sections have a very wide range of applications ranging from structural elements like beam, columns, studs, joists, purlins to non-structural elements like floor decking, cladding, cable trays, racks, etc. CFS sections have been increasingly employed as primary structural elements in low-rise to mid-rise multi-story buildings [1]. Being a lightweight member, these sections come up with added advantage of being easily transportable, simple, and flexible manufacturing and high-speed construction. With advantages, the CFS members have some limitations too. These thin sections are prone to instabilities such as local, distortional, and global buckling, or sometimes combinations of these buckling modes. The first study on multiple buckling modes occurring in the cold-formed structure was presented in Kwon and Hancock [2].

For a long time, finite-element (FE) software package has been employed in analysis of structural systems and component members [3, 4]. Appropriately, developed FEM models can be used to represent the actual experiments and member behavior. Therefore, validated FE models can be employed to conduct the simulations, resulting in both economy and saving time [3, 4]. For successful simulations of these models, we need to be dependent on material properties obtained from experimental studies.

Pure and non-pure bending test and simulations were done by Wang and Zhang [5] revealed that moment gradient has a limited effect on the local buckling mode whereas have considerable effect on distortional buckling mode. This study also showed that the FE analysis could be a good tool for study of cold-formed sections. Anbarasu [6] conducted FE analysis on lipped channel beams (LCBs) subjected to uniform moment across section having local–distortional buckling mode interaction

and proposed modified DSM beam strength equation. Put et al. [7, 8] performed series of tests on LCBs subjected to single point load at mid-span; in this work, the effect of eccentricity and torsion was studied. In experimental study by Put et al. [7, 8], lateral buckling strength of LCBs subjected to 3 point loading having lateral-torsional buckling was conducted. Test results revealed that procedure of AS 4100 for hot-rolled sections was closer to the test results, whereas AS/NZS 4600 for cold-rolled sections was too high for beam with thinner wall thickness. Laim et al. [9] carried out series of 4 point loading test on different cold-rolled sections and found out that failure loads of the beams with C and lipped I-shaped cross-sections corresponded to the lateral-torsional buckling modes, whereas the distortional buckling was the responsible buckling mode for the failure of other cross-sections under consideration.

This work presents a series of simulation results obtained using FEA on validated CFS lipped channel beams models. This paper presents elastic buckling moment ($M_{el}$) and the ultimate moment ($M_u$) capacity of considered sections. All the sections failed in distortional, global, or interaction of these buckling modes. This study has two major objectives one to check appropriateness of equation given in IS:801 [10] and second to check with the available advanced codal guidelines such as AS/NZS4600 (2001) and Eurocode 3, Part 1-3 (2011).

## 2 Finite-Element Modeling Detail

### *2.1 Element Type, Meshing, and Material Modeling*

Quadrilateral small strain, thin shell element-type S4R5 was used in this study. This element is characterized by thin shear flexible isoparametric quadrilateral shell with four nodes and five degrees of freedom per node using reduced integration bilinear interpolation scheme [6, 11, 12]. Mesh sensitivity analysis was conducted. Elastic-perfect plastic material model was used in this study. Modulus of elasticity ($E$) of steel was taken to be 210 MPa. Yield strength ($f_y$) and Poisson's ratio ($\mu$) taken were 250 MPa and 0.3, respectively.

### *2.2 Imperfection and Residual Stresses*

Buckling mode shape obtained from linear perturbation step was used as initial geometric imperfection for nonlinear analysis. Initial geometric imperfection in validation model was assumed to be $L/1000$, whereas in parametric study model, the imperfection for local, distortional, and global mode was taken to be $0.34 \times t$, $0.94 \times t$, and $L/1000$, respectively [13]. Initial imperfection shape in the model was provided in ABAQUS using "*IMPERFECTION" in nonlinear analysis. Effect of residual stresses was ignored in this study.

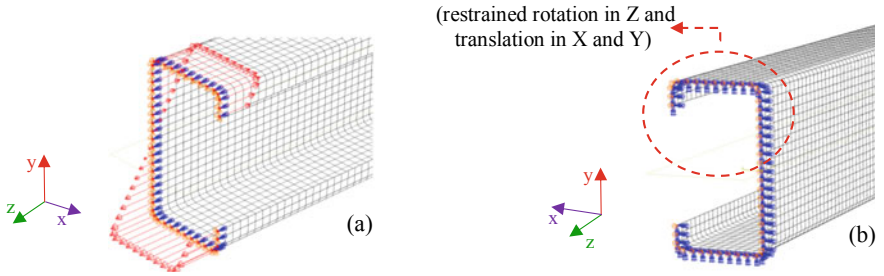


**Fig. 1** **a** Applied load at edge of the beam end, **b** symmetric boundary condition at mid of beam

## 2.3 Load and Boundary Condition

Simply supported boundary condition with constant moments at the ends was used in this study as discussed in by Kankanamge [14] and Anbarasu [6]. Constant bending moment at the end was generated by applying varying load across the cross-section creating a triangular distribution of the force, above and below major axis. Varying load at each end node was applied. Maximum simulated load at top and bottom flange extreme nodes was unit and was reduced on moving toward mid of section. Moment at a particular node can be calculate by multiplying maximum load at each node with the distance of that node from the NA. Total simulated moment will be the summation of individual node moments. Figure 1a shows applied load at edge nodes of $100 \times 50 \times 15 - 2.00$.

For optimum utilization of computation power and time with precision, only half of the beam was analyzed, and suitable boundary condition was assumed for another half of the beam. The longitudinal axis of the beam is aligned toward $Z$ direction, and major and minor axis toward $X$ and $Y$, respectively as shown in Fig. 2. At support translation of every nodes $X$ and $Y$ and rotation toward $Z$ direction was restricted. At symmetric end translation in $Z$ direction and rotation along $X$, $Y$ direction was restrained as shown in Fig. 1b.

## 2.4 Analysis Progress

Considering material and geometric nonlinearity nonlinear static analysis was performed. RIKS method of analysis was adopted for this purpose. Imperfection shape was obtained from first eigenmode of buckling analysis. Maximum 200 increments were used; at this increment, ABAQUS stops the analysis irrespective of results. RIKS method uses load magnitude as another unknown; it solves for load and displacement together (ABAQUS Manual, 2014). Arc length increment used was 0.01, with minimum and maximum increment 1E−005 and 1E+32, respectively.

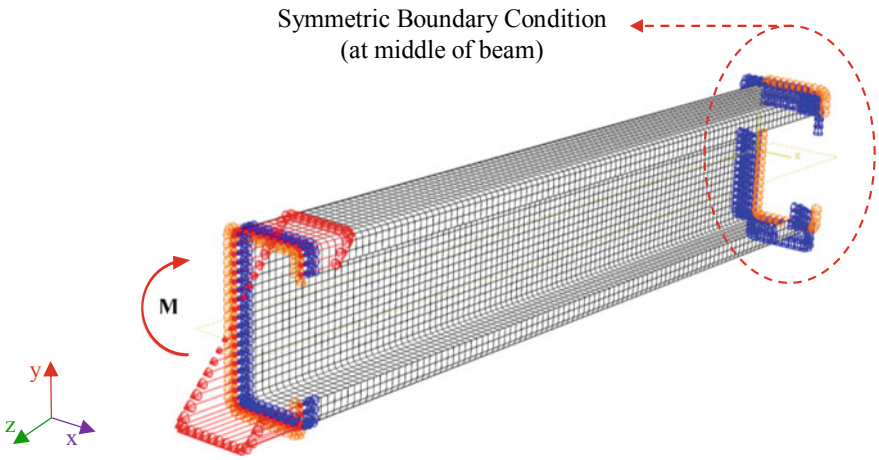


**Fig. 2** Developed model of the beam for finite-element analysis

## 3 Model Validation

The first step in this study was to develop an FE model which was able to replicate the actual beam behavior. In order to check the accuracy of the developed FE model, calibration and validation were performed from existing literature [6, 14]. Based on validated FE models, parametric study was carried out. From performed validation analysis, a good agreement from existing literature was found with developed simulation models. Thus, the developed FE model was adopted for further parametric studies.

From performed validation analysis, a good agreement from existing literature was found with developed simulation models. Thus, the developed FE model was adopted for further parametric studies.

Figures 3, 4a, b, and c shows experimental and FEM results obtained from Kankanamge [14] in comparison with results obtained from developed FE model. Experimental work done in Kankanamge [14] is represented by the dashed line, and solid lines in the graph represent FE results. From Kankanamge [14], three-section profiles named G-250-1.95-1500, G-250-1.95-2000, and G-450-1.9-1500 having steel yield stress ($f_y$) 250, 450 MPa and length 1500 and 2000 mm were taken for validation study. The scheme adopted in above naming is represented in Fig. 3.

The ultimate moment capacity ($M_{u\text{FEM}}$, $M_{\text{FEM-}K}$ *or* $M_{u\text{EXP}}$) obtained from these sections was plotted against vertical displacement. Results are compiled in Table 1. To investigate the best-suited element-type simulations on two different elements named S4R5 and S8R5 in ABAQUS was performed. S8R5 has eight-node and five degrees of freedom per node uses reduced integration bilinear interpolation scheme, similar to that of S4R5 as explained in previous section. The ratio of experimental ultimate moment capacity ($M_{u\text{EXP}}$) to ultimate moment calculated from this work

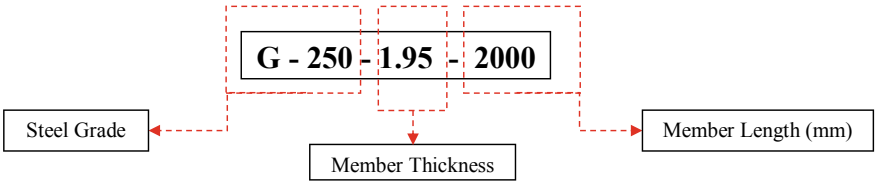


**Fig. 3** Nomenclature used in validation work

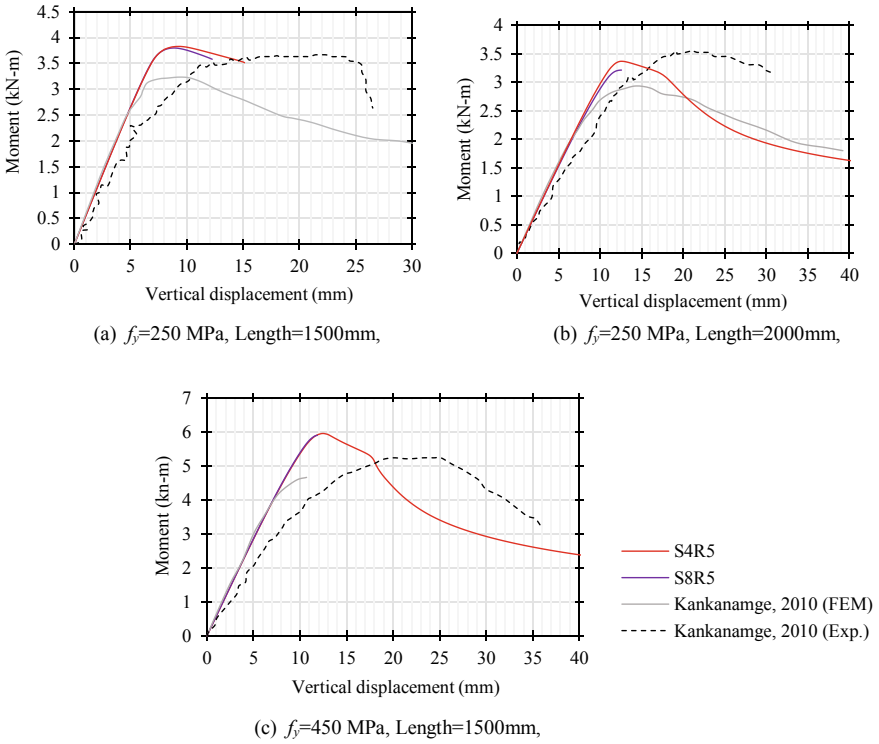


(a) $f_y$=250 MPa, Length=1500mm, (b) $f_y$=250 MPa, Length=2000mm,

(c) $f_y$=450 MPa, Length=1500mm,

**Fig. 4** **a** $f_y = 250$ MPa, Length = 1500 mm, **b** $f_y = 250$ MPa, Length = 2000 mm, **c** $f_y = 450$ MPa, Length = 1500 mm

($M_{u\text{FEM}}$) is presented in Table 1. The mean ($\bar{x}$), standard deviation ($\sigma$), and coefficient of variation (COV) of this ratio for S4R5 element were 0.959, 0.095, and 0.0998, whereas in case of S8R5, the mean, standard deviation, and COV were 0.981, 0.117, and 0.119, respectively. Considering these results in mind, the S4R5 element type was adopted in the parametric study. In the same profiles with S4R5 element, the mesh sensitivity analysis was performed having mesh sizes (in mm) 2.5 × 2.5, 5 × 5 and 10 × 10, out of which 5 mm × 5 mm mesh size was adopted in this study, which predicted the results within considerable timeframe with accuracy.

**Table 1** Comparison of ultimate moment capacity obtained from FEA with results of Kankanamge [14]

| Sl. No | Member | Length (mm) | $E$ (MPa) | $f_y$ (MPa) | Ultimate moment capacity | | | Moment Ratio $\left(\frac{M_{u\text{EXP}}}{M_{u\text{FEM}}}\right)$ | |
|---|---|---|---|---|---|---|---|---|---|
| | | | | | FE analysis | | Experimental | | |
| | | | | | $M_{u\text{FEM}}$ (S4R5) | $M_{u\text{FEM}}$ (S8R5) | Kananamge [14] ($M_{u\text{EXP}}$) | (S4R5) | (S8R5) |
| 1 | G-250-1.95-1500 | 1500 | $1.88 \times 10^5$ | 271 | 3.82 | 3.79 | 3.68 | 0.96 | 0.97 |
| 2 | G-250-1.95-2000 | 2000 | $1.88 \times 10^5$ | 271 | 3.36 | 3.21 | 3.55 | 1.05 | 1.10 |
| 3 | G-450-1.9-1500 | 1500 | $2.06 \times 10^5$ | 515 | 5.95 | 5.89 | 5.13 | 0.86 | 0.87 |

**Table 2** Comparison of ultimate moment capacity obtained from FEA with experimental results of Anbarasu [6]

| | | | | | Ultimate moment capacity | | |
|---|---|---|---|---|---|---|---|
| Sl. No | Member | Length (*mm*) | $E$ (*MPa*) | $f_y$ (*MPa*) | FE analysis | | Moment ratio |
| | | | | | $M_{u\text{FEM}}$ | Anbarasu [6] ($M_{u\text{FEM-}A}$) | $\left(\frac{M_{uFEM-A}}{M_{uFEM}}\right)$ |
| 1 | 100 × 50 × 20 | 550 | $2.1 \times 10^5$ | 250 | 2.64 | 2.68 | 1.01 |
| | | | | 350 | 3.51 | 3.59 | 1.02 |
| | | | | 450 | 4.25 | 4.35 | 1.02 |
| | | | | 550 | 4.83 | 5.02 | 1.04 |
| | | | | 590 | 5.07 | 5.02 | 0.99 |
| 2 | 220 × 75 × 14 | 700 | $2.1 \times 10^5$ | 250 | 3.80 | 3.81 | 1.00 |
| | | | | 350 | 4.13 | 4.15 | 1.00 |
| | | | | 450 | 4.37 | 4.46 | 1.02 |
| | | | | 550 | 4.60 | 4.67 | 1.01 |
| | | | | 590 | 4.70 | 4.68 | 0.99 |

Also, a validation was performed using the parametric study results of Anbarasu [6]. For this study ,two profiles named 100 × 50 × 20 and 220 × 75 × 14 having 5 yield stress ($f_y$) values in the range of 250–590 MPa were selected. The results of this validation work are summarized in Table 2. The ratio of ultimate moment of [6] $M_{u\text{FEM-}A}$ to that of performed in our study $M_{u\text{FEM}}$ was computed. The mean, standard deviation, and COV from this validation came out to be 1.012, 0.013, and 0.013, respectively.

From performed validation analysis, a good agreement from existing literature was found with developed simulation models. Thus, the developed FE model was adopted for further parametric studies.

## 4 Parametric Study

Validated finite-element models were used in the parametric study. The study was aimed to evaluate elastic buckling moment ($M_{\text{el}}$) and ultimate moment capacities ($M_u$) of selected profiles. Both elastic buckling and nonlinear finite-element analysis were carried out on LCBs. Members were subjected to uniform moment from both ends and simply supported warping free boundary conditions. A total 77 simulations were carried out on 7 LCBs having 11 spans ranging from 500 to 3000 mm to capture a wide range of slenderness. Each profile studied has assigned a unique nomenclature in which the first letter represents section name where simply written letter (e.g., (A)) represents moment calculated from FEM simulation whereas letter with apostrophes

(e.g., (A′)) represents result from codal procedure. The second and third term shows depth of the cross-section and flange width, respectively. The fourth term in this sequence show lip depth and fifth term separated by hyphen represents thickness of member. This is also illustrated in Fig. 6. The profile dimensions are listed in Table 3 and nomenclature illustrated in Fig. 5.

Figure 7 summarizes all elastic buckling analysis results in terms of non-dimensional quantities. The non-dimensionalized beam parameters used are given in Eq. (1) and (2), respectively, from [15].

$$M\frac{L}{\sqrt{EI_yGJ}} \tag{1}$$

$$K = \sqrt{\frac{\pi^2 EI_w}{GJL^2}} \tag{2}$$

**Table 3** Section geometries selected in this study

| Sl. No | Member | $h$ (mm) | $b$ (mm) | $l$ (mm) | $t$ (mm) | $r$ (mm) | $I_y$ (cm$^4$) | $Z_{xx}$ (cm$^3$) | $J$ (cm$^4$) | $C_w$ (cm$^6$) |
|---|---|---|---|---|---|---|---|---|---|---|
| 1 | 100 × 40 × 10 × 1.6 | 100 | 40 | 10 | 1.60 | 2.40 | 5.94 | 9.09 | 0.025 | 114 |
| 2 | 100 × 40 × 15 × 2.0 | 100 | 40 | 15 | 2.0 | 3.00 | 8.43 | 11.5 | 0.050 | 182 |
| 3 | 100 × 50 × 15 × 2.0 | 100 | 50 | 15 | 2.0 | 3.00 | 14.5 | 13.5 | 0.056 | 312 |
| 4 | 100 × 50 × 20 × 3.15 | 100 | 50 | 20 | 3.15 | 4.73 | 23.1 | 20.1 | 0.216 | 557 |
| 5 | 100 × 50 × 25 × 4.0 | 100 | 50 | 25 | 4.0 | 6.00 | 30.2 | 24.5 | 0.446 | 847 |
| 6 | 100 × 60 × 25 × 4.0 | 100 | 60 | 25 | 4.0 | 6.00 | 47.1 | 28.2 | 0.488 | 1330 |
| 7 | 100 × 60 × 25 × 5.0 | 100 | 60 | 25 | 5.0 | 7.50 | 53.9 | 32.9 | 0.912 | 1460 |

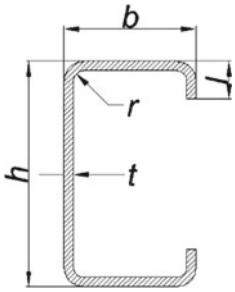


**Fig. 5** Typical lipped channel cross-section

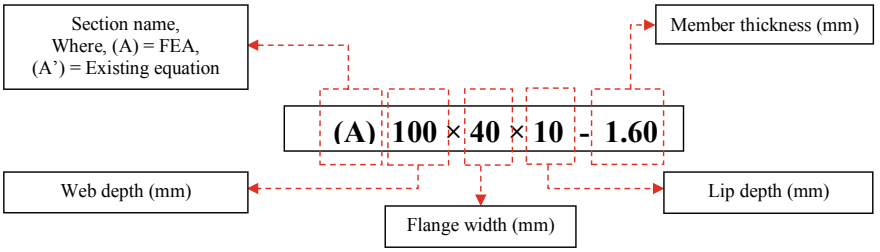


**Fig. 6** Nomenclature used in parametric study

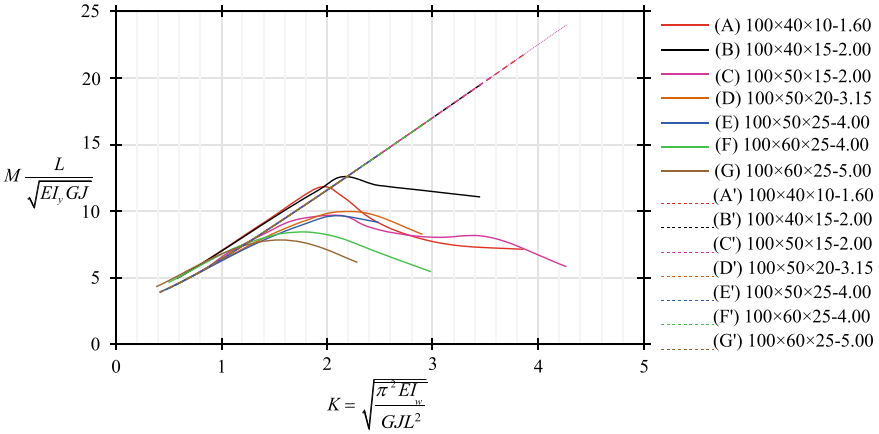


**Fig. 7** Buckling moment capacity: —Equation from Ref. IS:801 [10],—FEM analysis

$$M_{cr} = \frac{\pi}{L}\sqrt{EI_y GJ\left(1+\frac{\pi^2 EC_w}{GJL^2}\right)} \tag{3}$$

In Fig. 7, dashed lines represent critical buckling moments from Eq. (3) of IS:801 [10], and solid lines represent buckling moments obtained from FEM analysis. Higher the $K$ value shorter would be the beam span and vice versa. From the graph, it can be observed that for longer beam span, the critical buckling moments are similar for both FEM and from given Eq. (3). Similar result can be observed irrespective of beam profile or length. The difference in buckling moment capacities can be observed for $K$ greater than 2 for sections A and B, and 1.5 for C, D, E, F, and G. This difference is due to the fact that in shorter span sections, distortional and combined distortional and global (DG) mode of failure was observed.

For longer spans having dominating lateral-torsional buckling mode, the results were closer to that predicted from Eq. (3) depicting that the equation provides good results with global buckling mode only. To get buckling moment capacity of shorter

beam spans having other failure modes than of global, further developments in the equation are needed.

The study was then extended to nonlinear analysis. All the results are compiled and shown in Fig. 8a, b; on horizontal axis, slenderness was plotted, given by $\lambda = (M_y/M_{el})^{0.5}$, where $M_{el}$ is elastic buckling moment capacity obtained from FEA and $M_y$ is yield moment capacity given by $M_y = f_y Z_{xx}$, in which $f_y$ stands for yield stress and $Z_{xx}$ for elastic section modulus about $xx$-axis. On the vertical axis, the ultimate moment capacity was plotted in non-dimensional form by taking the ratio of ultimate moment from FEM analysis ($M_{FEM}$) to yield moment capacity ($M_y$).

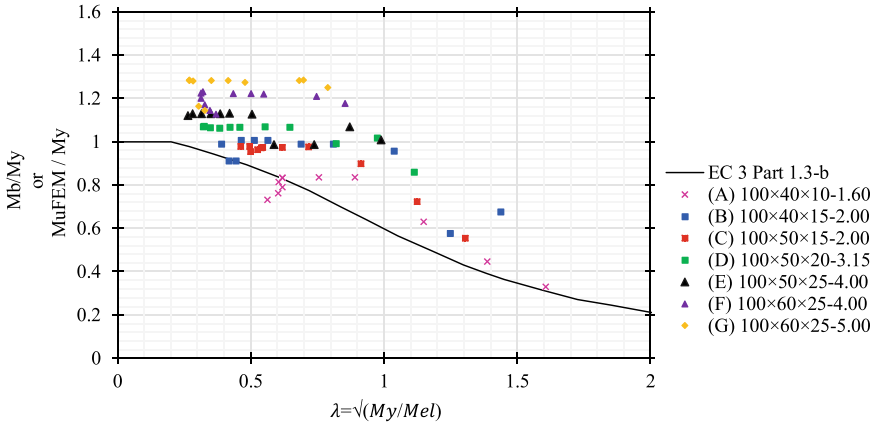


(a) Comparison of FEA results with AS/NZS-4600

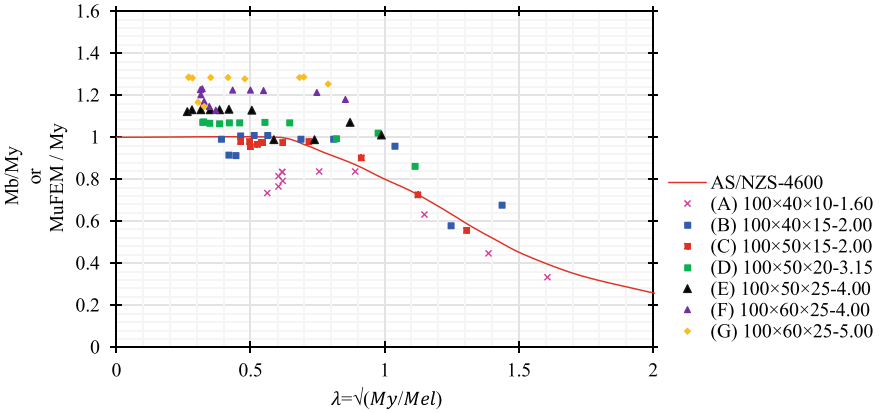


(b) Comparison of FEA results with Eurocode 3 Part 1.3-b

**Fig. 8** **a** Comparison of FEA results with AS/NZS-4600, **b** comparison of FEA results with Eurocode 3 Part 1.3-b

These results are then compared with the prediction of AS/NZS4600 (2001) in Fig. 8a and Eurocode 3, Part 1-3 (2011) in Fig. 8b. All the reference curves presented in Fig. 8a, b have a unit capacity ratio below slenderness value 0.6 in case of AS/NZS4600 (2001) and below 0.202 for Eurocode 3, Part 1-3 (2011). From Fig. 8a, it can be observed that for profile-A having minimum thickness ($t = 1.60$ mm), results were unconservative for all slenderness values, whereas some sections such as B and C ($t = 2$ mm) show unconservative results at lower slenderness values below 0.71.

As per AS/NZS-4600 (2001) at higher beam slenderness ($\lambda > 1.336$), ultimate moment capacity of beam would be equal to their elastic buckling capacity; however in some cases, as shown in Fig. 8b, the capacity was below elastic buckling capacity. Similar observation was made by Kankanamge [16], Pi and Trahair [17] and Put et al. [7, 8].

## 5 Conclusion

This paper described a detailed study on 77 lipped channel profiles selected from Indian standards. Simply supported lipped channel beams (LCBs) were used. Uniform moment was applied at the ends of the channel sections. This study was conducted in two stages; in first, the idealized simply supported model was validated with existing models. In second stage, the parametric study was carried out. In parametric study, elastic buckling and nonlinear static analysis were compared with results obtained from various codal guidelines like IS:801 [10], AS/NZS-4600 (2001) and Eurocode 3, Part 1-3 (2011). Elastic buckling moments ($M_{el}$) were compared with obtained moment from IS:801 [10], whereas ultimate moment capacity ($M_{u\text{FEM}}$) was compared with the design curves available in AS/NZS-4600 (2001) Eurocode 3, Part 1-3 (2011). IS:801 [10] was found to overestimate the elastic buckling moment at lower slenderness range, whereas in the higher range of slenderness limit, the predictions was close to those obtained in FE simulations. Ultimate moment capacity predictions from Eurocode 3, Part 1-3 (2011) were safe in most of the analysis except for section with least thickness (A) in a very short slenderness range, whereas for thin sections like (B) and (C), the predictions from AS/NZS-4600 (2001) overestimated the ultimate moment capacity in lower slenderness range, and for very thin sections like (A), the predictions were overestimated in almost all slenderness range.

## References

1. Schafer BW (2011) Cold-formed steel structures around the world: a review of recent advances in applications, analysis and design. Steel Construction 4(3):141–149
2. Kwon YB, Hancock GJ (1993) Post-buckling analysis of thin-walled channel sections undergoing local and distortional buckling. Comput Struct 49(3):507–516
3. Niu S, Rasmussen KJ, Fan F (2014) Distortional–global interaction buckling of stainless steel C-beams: Part I—experimental investigation. J Constr Steel Res 96:127–139

4. Niu S, Rasmussen KJ, Fan F (2014) Distortional–global interaction buckling of stainless steel C-beams: Part II—numerical study and design. J Constr Steel Res 96:40–53
5. Wang H, Zhang Y (2009) Experimental and numerical investigation on cold-formed steel C-section flexural members. J Constr Steel Res 65(5):1225–1235
6. Anbarasu M (2016) Local-distortional buckling interaction on cold-formed steel lipped channel beams. Thin-Walled Structures 98:351–359
7. Put BM, Pi YL, Trahair NS (1999) Lateral buckling tests on cold-formed channel beams. J Struct Eng 125(5):532–539
8. Put BM, Pi YL, Trahair NS (1999) Bending and torsion of cold-formed channel beams. J Struct Eng 125(5):540–546
9. Laim L, Rodrigues JPC, Silva LSD (2013) Experimental and numerical analysis on the structural behaviour of cold-formed steel beams. Thin-Walled Structures 72:1–13
10. IS 801:1975. Code of practice for use of cold-formed light gauge steel structural members in general building construction. *Bureau of Indian Standards,* New Delhi, India
11. Dar MA, Subramanian N, Dar AR, Anbarasu M, Lim JB, Atif M (2019) Behaviour of partly stiffened cold-formed steel built-up beams: experimental investigation and numerical validation. Adv Struct Eng 22(1):172–186
12. Susila A, Tan J (2015) Flexural strength performance and buckling mode prediction of cold-formed steel (C section). Procedia Engineering 125:979–986
13. Schafer BW, Peköz T (1998) Computational modeling of cold-formed steel: characterizing geometric imperfections and residual stresses. J Constr Steel Res 47(3):193–210
14. Kankanamge ND (2010) Structural behaviour and design of cold-formed steel beams at elevated temperatures. Doctoral dissertation, Queensland University of Technology, Australia
15. Samanta A, Kumar A (2006) Distortional buckling in monosymmetric I-beams. Thin-Walled Structures 44(1):51–56
16. Kankanamge ND, Mahendran M (2012) Behaviour and design of cold-formed steel beams subject to lateral–torsional buckling. Thin-Walled Structures 51:25–38
17. Pi YL, Trahair NS (1995) Lateral buckling strengths of cold-formed rectangular hollow sections. Thin-Walled Structures 22(2):71–95

# Finite Element Investigations on Structural Performance of Steel I-Beams with Reinforced Web Openings


**Samadhan G. Morkhade, Rutuja S. Lokhande, Umesh D. Gund, Ajinkya B. Divate, and Saurav S. Deosarkar**

**Abstract** A numerical investigation on steel I-beams with reinforced web openings failing in flexural and shear using the commercial finite element software, ANSYS is presented and discussed in this paper. Web openings in steel beams are of various shapes like hexagonal, circular, rectangular and octagonal, which they are prepared from standard hot rolled steel I section. The main benefit of these members is to monitor service ducts through the openings as well as cost saving by economic use of material. The existence of the web openings deviates the beam failure behaviour around the openings over the parent beam. The additional failure modes named as Vierendeel mechanism along with regular failure modes like local buckling of web and flange, lateral torsional bucking, shear buckling, etc. comes into existence. The present study emphasizes on improving the performance of the steel beam with reinforced web openings. All the models of specimens have been fabricated from an original I section. The parametric investigation shows that reinforced web opening beams by adding high strength steel stiffeners around the web opening was very much effective. As compared to original I section beam, there is a 30% increase in the ultimate strength capacity of web expanded beams. The failure modes found to be similar both in with and without reinforcement around the openings.

**Keywords** Failure analysis · Steel I-beams · Cellular beam · Reinforced web openings · Steel structures

S. G. Morkhade (✉) · R. S. Lokhande · U. D. Gund · A. B. Divate · S. S. Deosarkar
Department of Civil Engineering, Vidya Pratishthan's Kamalnayan Bajaj Institute of Engineering and Technology, Baramati, S.P.P.U., Pune, Maharashtra 413133, India
e-mail: samadhanmorkhade@gmail.com



M. Madhavan et al. (eds.), *Proceedings of the Indian Structural Steel Conference 2020 (Vol. 1)*, Lecture Notes in Civil Engineering 318,
https://doi.org/10.1007/978-981-19-9390-9_41

## 1 Introduction & Literature Review

Now a days building and civil infrastructure are becomes larger and higher, the demand for horizontal structural member, I section beam are commonly used in the construction of steel structure. Which are suitable for long spans so structural steel require high strength. Common shape of this beams are constructed from two parallel flanges and plain web. Generally, web portion carry maximum load or compressive stress and transmit shear stresses in the beam and therefore the web is susceptible to local buckling. Steel member also have many disadvantages, such as less resistance to buckling, more deflection, fatigue strength, vibration.

New challenges in the structural use of steel are arising all the time, and research is being called upon to provide appropriate solutions. In such situations the used of steel beams with web openings is one of the suggested possible solution. The researchers are continuously working for the advancement in the construction technology. One of such advancement happened in built-up structural steel members in the mid-1930, is the development of castellated beam. The beam with hexagonal openings is called as castellated beam. The castellatus means to fortify (To Strengthen). Castellated beams appear to have been first used in 1910, initially known as the "Boyd beam". These products were first marketed in the United Kingdom in the early 1940s. Boyd's patent specification discussed various geometries of castellation, and this beam type was later adopted as the standard castellated beam geometry in the United Kingdom [1].

Through experimental investigation the study has been carried out by various researcher's to study the failure modes of castellated beams. The researchers found that seven potential failure modes are associated with castellated beam [2–9].

Formation of a flexure mechanism.
Lateral–torsional buckling of the entire beam.
Formation of Vierendeel mechanism.
Rupture of the welded joint in a web post.
Shear bucking of a web post.
Compression buckling of a web post.
Compression buckling of a tee.

In modern building where water pipes, air ducts produce large depth between storeys [10–16]. Many researcher works on this kind of castellated beams to study load carrying capacity. To improve the strength capacity of castellated beams there is a need to provide stiffeners (reinforcement) around the web openings as shown in Fig. 1. Till date, castellated beam with reinforcement around the web openings has not been studied so far. Therefore the present study is done based on the demand for additional design specification to make reinforced openings in castellated beams.

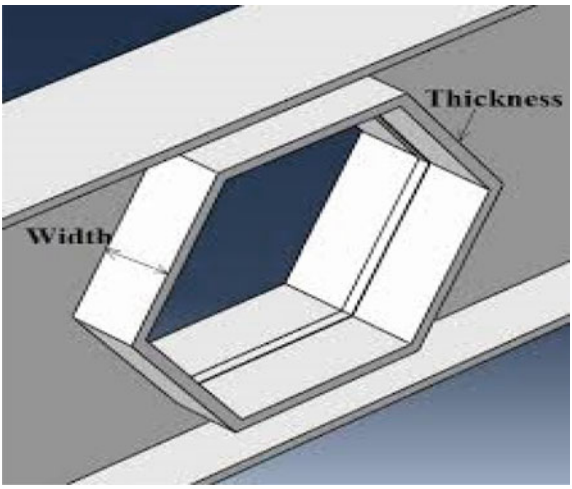


**Fig. 1** Stiffener around the web openings

## 2 Finite Element Analysis

1. A 3-D finite element model is developed to investigate the behaviour of steel beam with reinforced web openings by using the finite element analysis software ANSYS v12;
2. In the present study, four noded shell 181 element with reduced integration points having six degrees of freedom per node is used;
3. Geometric as well as material non-linearity are considered in beams model;
4. Solver by iterations according to Newton–Raphson. The material properties obtained as per coupon test are used in the analysis;
5. A bilinear stress–strain curve with a Young's modulus, E of 210 GPa and a Tangent modulus, ET, of 5000 MPa was used in material modelling of steel together with the von Mises yield criterion and the kinematic hardening rule, which is suitable for steel;
6. The large deformation effects has been considered in the analysis to accounts for geometrical non-linearity present in the models;
7. The initial imperfection of L/1000 was used in the analysis. The load was applied stepwise as pressure;
8. Figure 2 shows the FE model of beam with rectangular web openings, applied concentrated load at mid span and simply supported boundary conditions.


**Fig. 2** FE model of steel beam with web openings

## 3 Parametric Study

The parametric study have been performed on castellated beams by changing stiffeners position around the web openings. The study consist of a seven specimens composed of same material. One specimens is without stiffener with rectangular opening to compare the response with other stiffeners position. The remaining six I-beams are made with rectangular opening having 300 mm depth and various stiffening configuration. Figures 3, 4, 5 and 6 shows the beam specimens with opening and different stiffening configuration. There are four opening are provided in 1982 mm span of beam. In the case of horizontal stiffener, the stiffener length have been taken equal to opening length plus 50 mm on both side of opening and in vertical stiffener, the stiffener height have been taken equal to opening height plus 10 mm. The span of beams is taken as 1982 mm subjected to a concentrated load applied at the midspan.

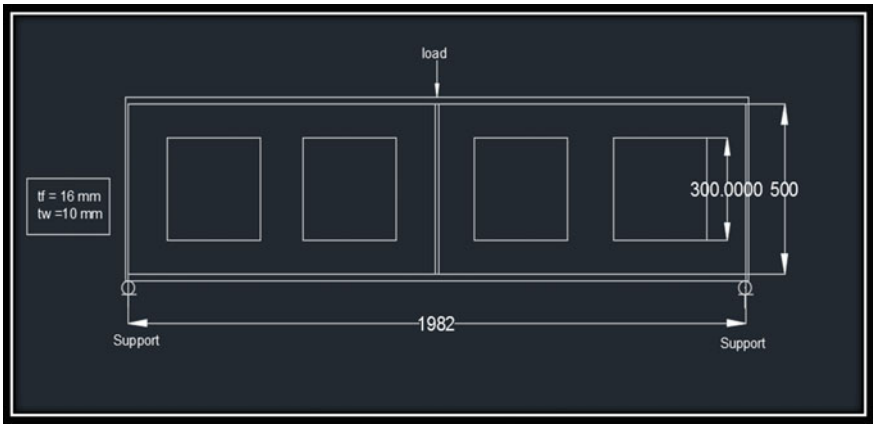


**Fig. 3** Dimensions of rectangular opening beam without stiffener

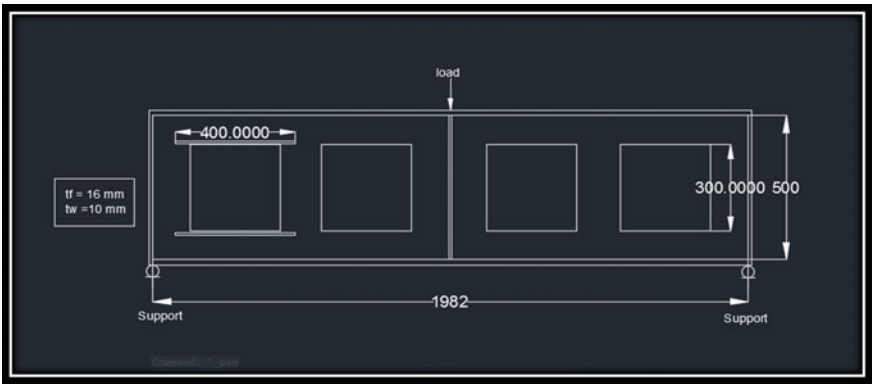


**Fig. 4** Position of horizontal stiffener around the openings

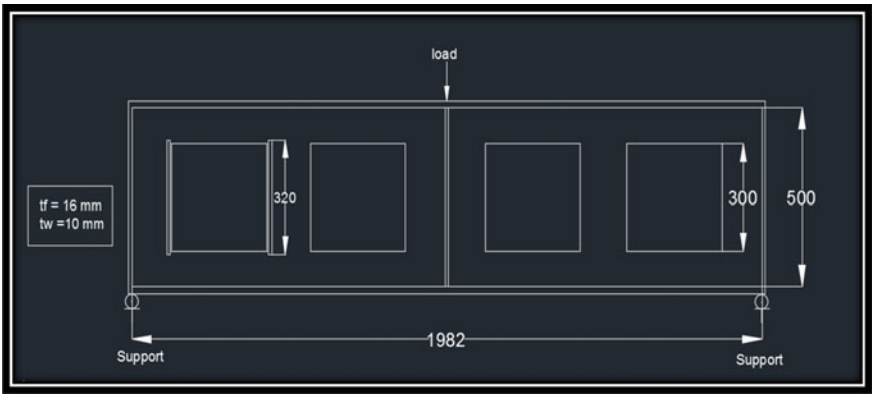


**Fig. 5** Position of the vertical stiffener around the openings

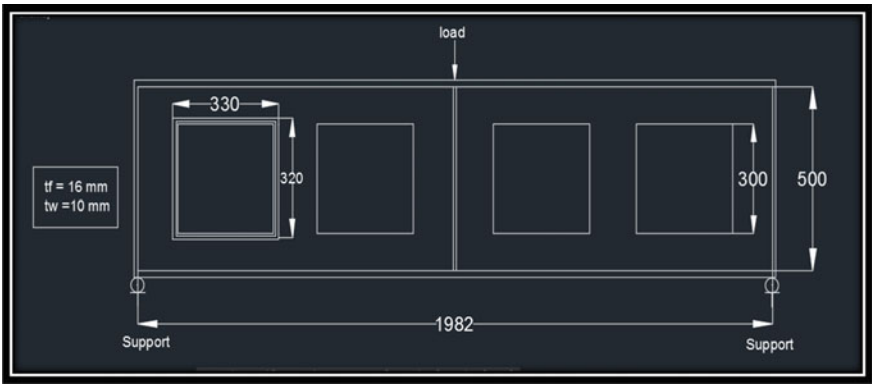


**Fig. 6** Position of the horizontal and vertical stiffeners around the openings

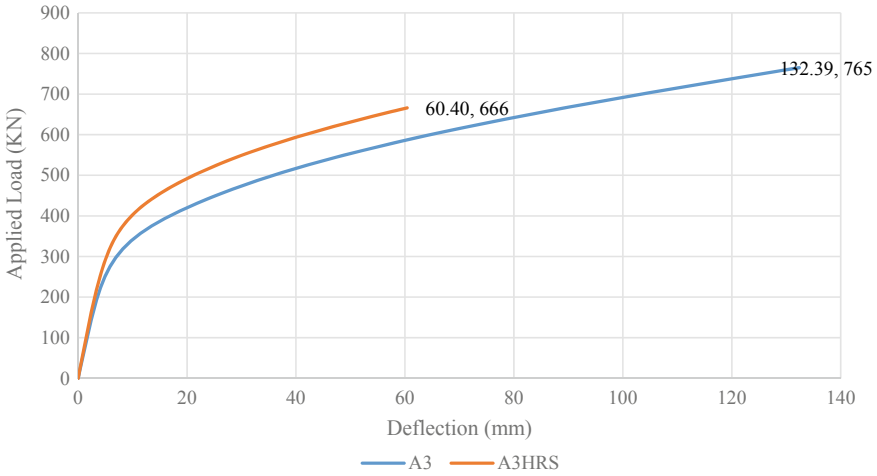


**Fig. 7** Load versus deflection curve for A3 & A3HRS

The designations used for the studied parameters consist of A3 for opening height 300 mm. The HR, VR and HV corresponds to horizontal stiffener, vertical stiffener and both horizontal and vertical stiffener around the rectangular opening. S and D corresponds to single sided stiffener and double sided stiffener, respectively.

## 4 Results and Discussion

Load versus deflection curves are drawn for all the 6 specimens of steel beams with stiffener connected around the rectangular opening in the web. Boundary condition and load applied in the model shown in Fig. 1. Figures 7, 8, 9, 10, 11 and 12 shows the load vs midspan displacement obtained for stiffener connected horizontally, vertically and both horizontally and vertically around opening. It is discovered that displacement occurred in beam without stiffener is more as compared to other sections. The predicted failure modes and von Mises stress distribution of beams with web openings are as shown in Fig. 13. From the parametric study it has been observed that ultimate load carrying capacity of steel beams with reinforced web openings increases significantly over the unreinforced web openings.

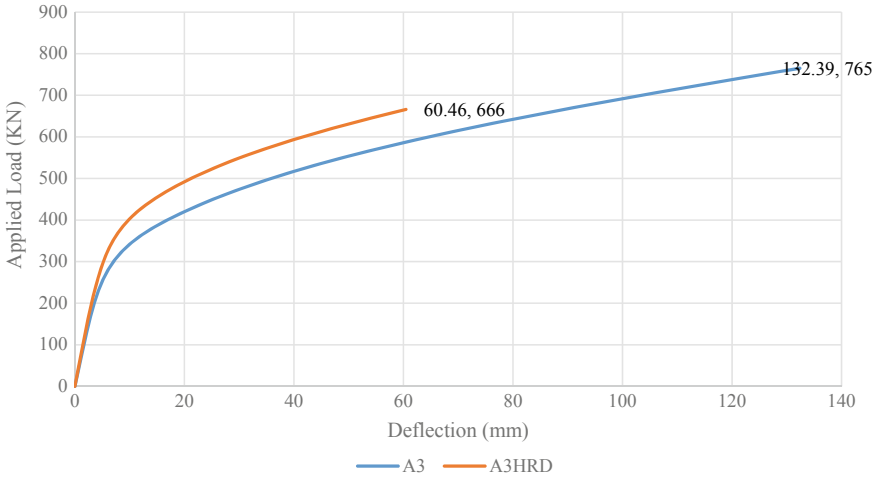


**Fig. 8** Load versus deflection curve A3 & A3HRD

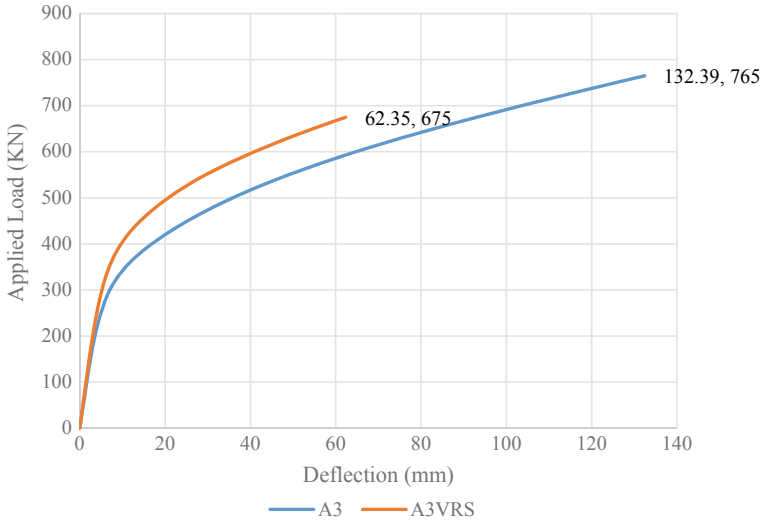


**Fig. 9** Load versus deflection curve A3 & A3VRS

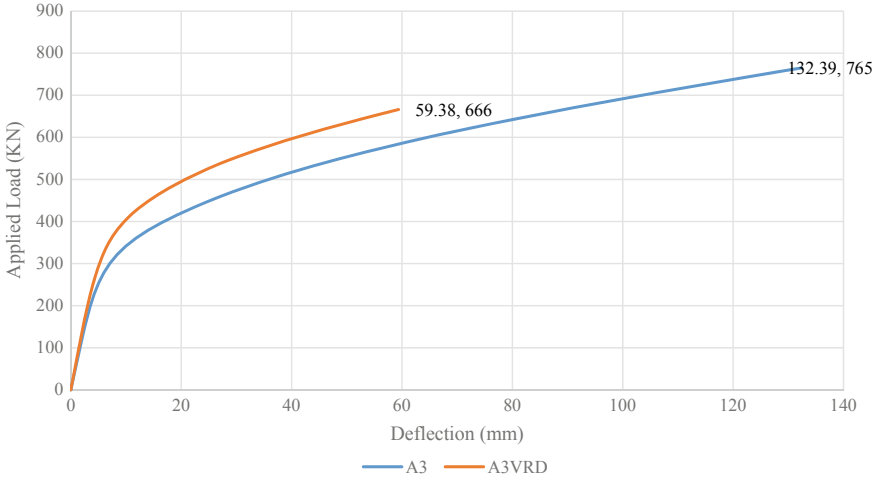


**Fig. 10** Load versus deflection curve A3 & A3VRD

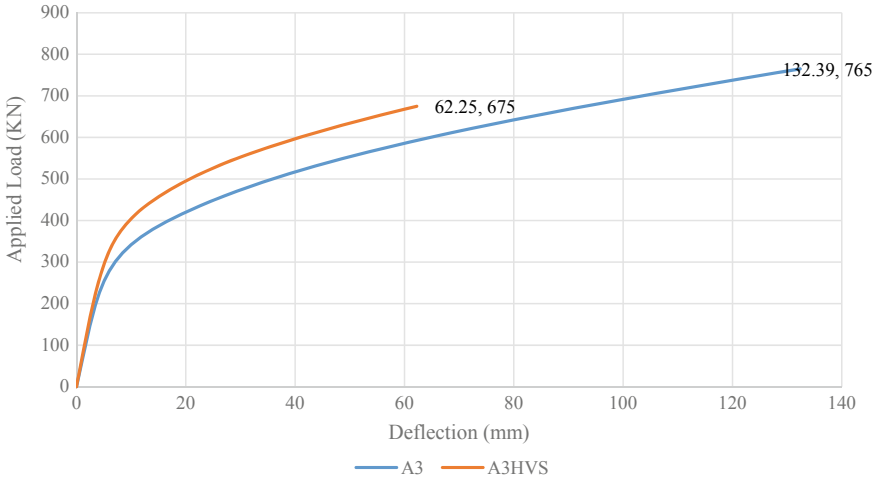


**Fig. 11** Load versus deflection curve A3 & A3HVS

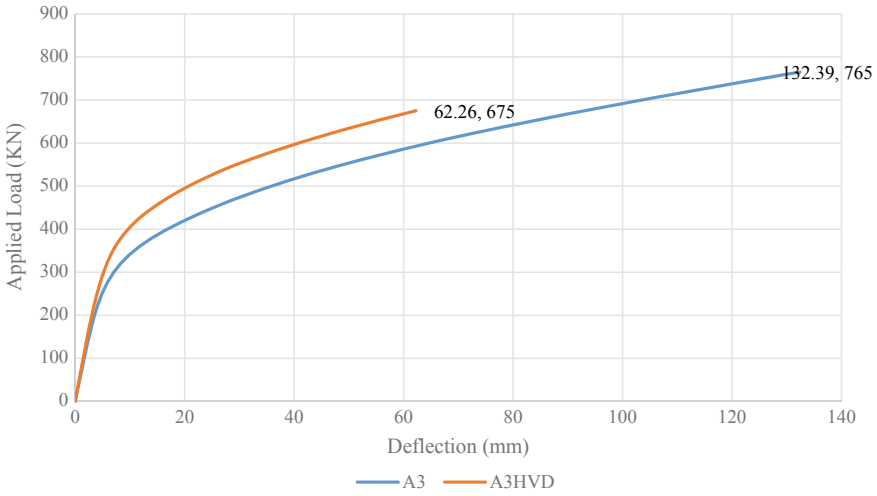


**Fig. 12** Load versus deflection curve A3 & A3HVD

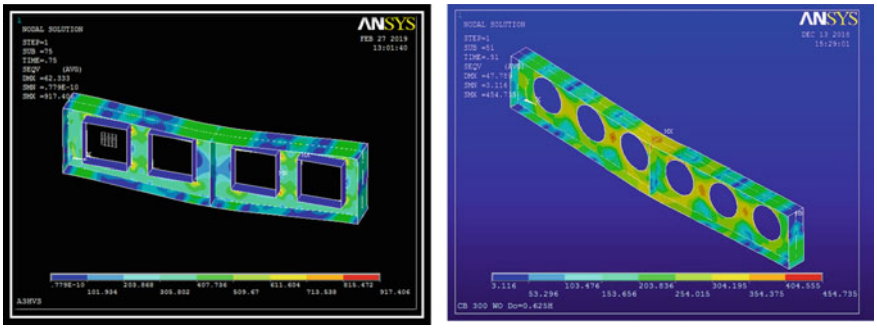


**Fig. 13** Von Mises stress distribution for beam with horizontal and vertical stiffener

## 5 Conclusion

In this investigation, effect of opening on strength capacity has been studied in terms of load–deflection behaviour, von Mises stresses and flexural stiffness of castellated beams is recorded.

- The prime mode of failure is found to be same as in case of openings without strengthening name as failure as Vierendeel mechanism (i.e. formation of four plastic hinges around the openings).
- It has been observe that long horizontal stiffeners were the very good solution for strengthening of openings.

- The increase the ultimate strength capacity by 30% compared with original I section beam.
- By provision stiffeners around the openings web buckling failure can be prevented.

## References


1. Aglan AA, Redwood RG (1974) Web buckling in castellated beams. Proc Inst Civ Eng 2(57):307–320
2. Sherboume AN (1966) The plastic behaviour of castellated beams. In: Proceedings of 2nd commonwealth welding conference 1966, Institute of Welding, No. C2, London, pp 1–5
3. Bazile A, Texier J (1968) Tests on castellated beams. Constructional Métallique, Paris, France, vol 3, pp 12–25
4. Husain MU, Speirs WG (1971) Failure of castellated beams due to rupture of welded joints. Acier Stahl-Steel 1
5. Husain MU, Speirs WG (1973) Experiments on castellated steel beams. J Am Weld Soc 52(8):329–342
6. Galambos AR, Husain MU, Spin WG (1975) Optimum expansion ratio of castellated steel beams. Eng Optim 1:213–225
7. Kerdadl D, Nethercot DA (1984) Failure modes for castellated beams. J Constr Steel Res 4259–315
8. Zaarour WJ (1995) Web buckling in thin webbed castellated beams. M. Eng. Thesis, Department of Civil Engineering and Applied Mechanics, McGill University
9. Redwood RG, Demirdjian S (1998) Castellated beam web buckling in Shear. J Struct Eng ASCE 124(8):1202–1207
10. Morkhade SG, Gupta LM (2015) An experimental and parametric study of steel beams with web openings. Int J Adv Struct Eng 7:249–260
11. Morkhade SG, Gupta LM (2015) Analysis of steel I-beams with rectangular web openings: experimental and finite element investigation. Eng Struct Technol 7(1):13–23
12. Morkhade SG, Gupta LM (2017) Experimental investigation for failure analysis of steel beams with web openings. Steel Compos Struct 23(6):647–656
13. Morkhade SG, Shaikh S, Kumbhar A, Shaikh A, Tiwari R (2018) Comparative study of ultimate load for castellated and plain webbed beam. Int J Civ Eng Technol 9(8):1466–1476
14. Morkhade SG, Kshirsagar M, Dange R, Patil A (2019) Analytical study of effect of web opening on flexural behaviour of hybrid beams Asian. J Civ Eng 20:537–547
15. Samadhan GM, Gupta LM (2019) Ultimate load behaviour of steel beams with web openings. Aust J Struct Eng 20(2):124–133
16. Morkhade SG, Baswaraj SM, Nayak CB (2019) Comparative study of effect of web openings on the strength capacities of steel beam with trapezoidally corrugated web. Asian J Civ Eng 20:1089–1099

# Numerical Analysis on Load Carrying Capacity of Castellated Beam by Varying Web Opening


**V. Keerthika and D. Daniel Thangaraj**

**Abstract** Castellated Element is a structural element made from the structural steel I section which has been used as a structural beam as well as a column for the past few decades in the construction field due to its high value of the moment of inertia. This paper is focusing on the determination of the ultimate load carrying capacity of the castellated beam for an irregular dodecahedron web opening and its results are compared with a castellated beam of hexagonal web opening. The criteria considered are deflection and the ultimate load carrying capacity of the beam by the varying parameters, like depth of the section, depth of opening and opening angle. ISMB 150 is considered as a parent beam for the creating the model of the castellated beam. The depth of the castellated beam (CB225, CB240 and CB255) is increased with an expansion ratio of 1.5, 1.6 and 1.7, respectively. The FEM software (ANSYS) is used for the numerical analysis of the castellated beam.

**Keywords** Ultimate load capacity · Deflection · Stress concentration · FEM · Web buckling · Expansion ratio

## 1 Introduction

### *1.1 Preamble*

The structural steel sections are extensively used all over the world due to its fast construction. In the 1930s, the I section structural steel is re-fabricated to form a new section by repeating the regular pattern of a hole in the web portion and named

V. Keerthika (✉)
Department of Civil Engineering, Anna University, Tindivanam, India
e-mail: keerthikavenkatesan@gmail.com

D. Daniel Thangaraj
Department of Civil Engineering, University College of Engineering, Anna University, Tindivanam, India



M. Madhavan et al. (eds.), *Proceedings of the Indian Structural Steel Conference 2020 (Vol. 1)*, Lecture Notes in Civil Engineering 318,
https://doi.org/10.1007/978-981-19-9390-9_42

as a castellated beam. It has been obtained by cutting the web of I section in a specified manner and the cut portion is once again rejointed to create the new section with centre web opening. The main benefit of the castellated beam is to increase the depth of the section without increasing its self-weight. But the failure mode of the castellated beam is high, which constraint its usage. Especially the Vierendeel mechanism which is not formed in solid I section. The possible modes of failure of the castellated beam are Flexural failure of the section, Lateral-torsional buckling of the beam, Local buckling of the flange, Vierendeel mechanism of the section, Rupture of weld in the web-post and Web-post buckling.

Numerous research works have been carried to test the various web opening shape such as hexagonal, circular, diamond, square. Out of all shape hexagonal castellated beam (HCB) shows superior results. In this paper, the study has been done to develop a new shaped castellated beam with a combination of rectangular and hexagonal opening and it has been named as an irregular dodecahedron castellated beam (DCB). To validate this new shape hexagonal castellated beam is used for an evaluation progress.

## *1.2 Review of Literature*

The failure mode of castellated beam was elaborately investigated by Kerdal et al. Listiyono et al. have investigated optimization of size and distance of hexagonal hole [1–13]. The parametric study on castellated beam carried out in both experimentally and numerically. It shown that if width of opening is more, stress concentration is dominant in corner of the hole and if width of opening is less, stress concentration is dominant in weld joint of web post. Behaviour of cellular beam with sinusoidal opening have been studied by Durif et al. Sinusoidal opening shows good result for wider opening. Pachpor et al. made study on deformation of Castellated Beam by varying the parameters. It is clearly noted deflection increases with increase of *d/D* ratio and by moving the opening towards the centre. A study made by Boyer on analysis of castellated beam aid to formulate the design criteria. It stated that in castellated beam stiffener is not necessary unless incremental plate is used or heavy load is acting on the beam. Richard et al. made a numerical study on opening angle and spacing between two opening of hexagonal castellated beam using FEM software ABAQUS /CAE. It has been found that 60° cutting angle and 60 mm spacing shows better strength and elements are failed by yielding mechanism. In the research work made by Peijun et al. the redistribution of stress has been done by filling the internal corner of hexagonal opening and it confirm better result too. Both experiment and numerical study were conducted with 6 different radii of fillet corner web hexagonal opening. With radii of quarter opening height produce the good load bearing capacity but it will produce high level of local Vierendeel bending moment and if expansion ratio is increased vertical shear resistance goes on decreasing, it promotes the Vierendeel bending moment. Iman sathyarno et al. studied on castellated steel beam with full height rectangular opening partially encased in reinforced mortar.

**Table 1** Geometry and material properties is of conventional steel

| S.no | Properties | Value |
|---|---|---|
| 1 | Depth of I section ($D_c$) | 150 mm |
| 2 | Breadth of flange ($b_f$) | 80 mm |
| 3 | Thickness of web ($t_w$) | 4.8 mm |
| 4 | Thickness of flange ($t_f$) | 7.8 mm |
| 5 | Moment of inertia ($I_{xx}$) | $7.15 \times 10^6$ mm$^4$ |
| 6 | Elastic modulus ($Z_e$) | $9.5 \times 10^4$ mm$^3$ |
| 7 | Young's modulus ($E$) | 210 MPa |
| 8 | Yield strength ($f_y$) | 250 MPa |
| 9 | Poisson ratio ($\mu$) | 0.33 |

The height of castellated beam section is increased to twice the height of original section that decrease load capacity of the section due to failure mode of Vierendeel mechanism. To overcome it beam is encased with reinforced mortar.

## 2 Profile of the Section

Castellated beam of different expansion ratios such as 1.5, 1.6 and 1.7 with the depth of opening 150, 180 and 210 mm to a span of 2.5 m to the overall of depth of section as 225, 240 and 255 mm are made from rolled steel section of ISMB150 whose geometrical properties and material properties are given in Table 1. The sectional properties of the castellated beam are shown in Fig. 1 and their parameters are listed out in Table 2. The number of opening formed by dodecahedron castellated beam is more when compared to hexagonal opening.

## 3 Numerical Modelling

### *3.1 Validation of Software*

The numerical models developed in this research are carried out by ANSYS workbench version.14.5 in order to determine the maximum deflection at centre and yield stress of the section. To validate the software, initially the numerical analysis has been done for conventional I section. The properties of I section are stated in Table 1. The I beam is created to a span of 2.5 m with simply supported end condition (At both end $U_x = 0$, $U_y = 0$, $U_z \neq 0$, $M_x = 0$, $M_y = 0$, $M_z = 0$). Tetrahedron meshing has been adopted with size of meshing element as 50 mm. The result has been examined to the convergence of 1%. For same I section, analytical analysis has been carried out in accordance with IS codes. The result obtained from numerical analysis shows

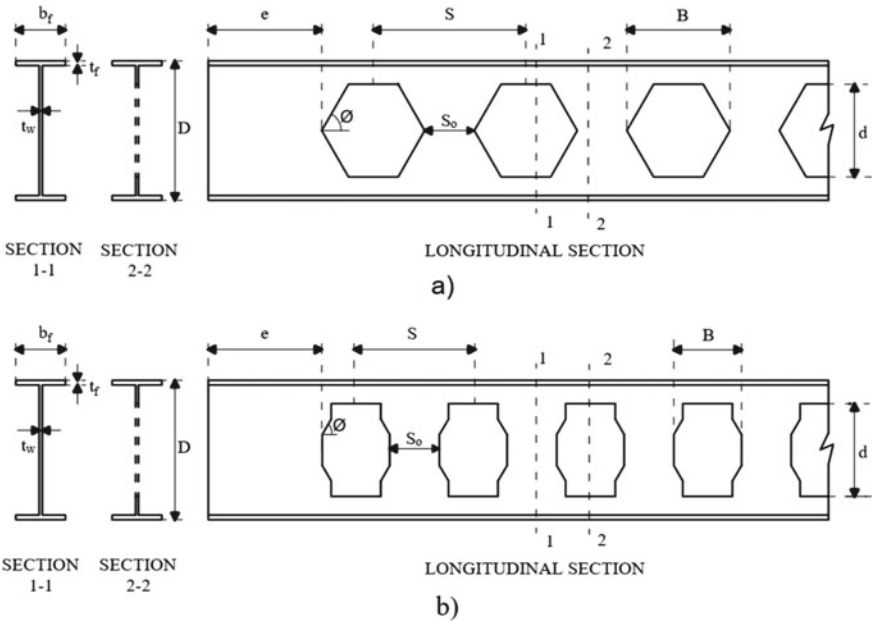


**Fig. 1** Castellated beam **a** Hexagonal opening, **b** Irregular dodecahedron opening. $e$ = Edge distance, $S_o$ = Width of cutting edge, $b_f$ = Breadth of flange, $B$ = Width of hole at centre, $d$ = Depth of opening, $Z_e$ = Elastic modulus of section, $t_w$ = Thickness of web, $I_{xx}$ = Moment of inertia about $X$-axis, $\emptyset$ = the Cutting angle, $D$ = Overall depth of the Castellated beam, $t_f$ = Thickness of flange, $S$ = Centre to centre distance between adjacent opening

96% similar resemblance to the analytical analysis. With that the numerical analysis for castellated beam has been carried out.

## *3.2 Modelling of Castellated Beam*

The 24 different castellated beam elements are formed by the varying the parameter of opening shape (hexagonal opening and dodecahedron opening), width of cutting edge (75 and 80 mm), cutting angles (45° and 60°) and with expansion ratio of 1.5, 1.6 and 1.7. The material properties of the steel used in the analysis are same as of ISMB150 (the young modulus as 210 MPa, Passion ratio 0.3). The beam element has been created for a span of 2.5 m with end support condition of simply supported (At end A $U_x = 0, U_y = 0, U_z = 0, M_x = 0, M_y = 0, M_z = 0$ and At end B $U_x = 0, U_y = 0, U_z \neq 0, M_x = 0, M_y = 0, M_z = 0$). In end condition at one end displacement along $Z$-direction is restrained on other end displacement along $Z$-direction is set free. This arrangement is formed to scrutinize the Vierendeel mechanism based on support condition. Tetrahedron mesh has been used for the meshing of the beam element. The Uniformly distributed load (UDL) of 30 kN/m is applied to the beam

**Table 2** Details of castellated beam

| Section | *D/d* | *D* (mm) | *d* (mm) | *Ø* | $S_O$ (mm) | *B* (mm) | *S* (mm) | *e* (mm) | Number of holes |
|---|---|---|---|---|---|---|---|---|---|
| HCB225A | 1.5 | 225 | 150 | 45° | 80 | 230 | 310 | 205 | 7 |
| HCB225B | | | | 45° | 75 | 225 | 300 | 237 | 7 |
| HCB225C | | | | 60° | 80 | 166 | 246 | 183 | 9 |
| HCB225D | | | | 60° | 75 | 161 | 236 | 225.5 | 9 |
| HCB240A | 1.6 | 240 | 180 | 45° | 80 | 260 | 340 | 100 ara> | 7 |
| HCB240B | | | | 45° | 75 | 255 | 330 | 132.5 | 7 |
| HCB240C | | | | 60° | 80 | 184 | 264 | 104 | 9 |
| HCB240D | | | | 60° | 75 | 179 | 254 | 144.5 | 9 |
| HCB255A | 1.7 | 255 | 210 | 45° | 80 | 290 | 370 | 117.5 | 6 |
| HCB255B | | | | 45° | 75 | 285 | 360 | 132.5 | 6 |
| HCB255C | | | | 60° | 80 | 201 | 281 | 103.5 | 9 |
| HCB255D | | | | 60° | 75 | 196 | 271 | 126 | 9 |
| DCB225A | 1.5 | 225 | 150 | 45° | 80 | 130 | 210 | 135 | 11 |
| DCB225B | | | | 45° | 75 | 125 | 200 | 187.5 | 11 |
| DCB225C | | | | 60° | 80 | 109 | 189 | 156 | 12 |
| DCB225D | | | | 60° | 75 | 104 | 179 | 213.5 | 12 |
| DCB240A | 1.6 | 240 | 180 | 45° | 80 | 140 | 220 | 190 | 10 |
| DCB240B | | | | 45° | 75 | 135 | 210 | 237.5 | 10 |
| DCB240C | | | | 60° | 80 | 114 | 194 | 126 | 12 |
| DCB240D | | | | 60° | 75 | 109 | 184 | 183.5 | 12 |
| DCB255A | 1.7 | 255 | 210 | 45° | 80 | 150 | 230 | 140 | 10 |
| DCB255B | | | | 45° | 75 | 145 | 220 | 187.5 | 10 |
| DCB255C | | | | 60° | 80 | 120 | 200 | 90 | 12 |
| DCB255D | | | | 60° | 75 ara> | 115 | 190 | 147.5 | 12 |

in a manner of gradually increasing load. The UDL applied to section is assumed based on moment carrying capacity of the conventional section (ISMB150) in accord with IS codes. The failure of the structure is measured based on Von-Mises stresses corresponding to the yield stress of 250 MPa.

**Table 3** Result of numerical analysis of various beams

| Section | Equivalent stress (MPa) | Maximum deflection (mm) | Section | Equivalent stress (MPa) | Maximum deflection (mm) |
|---|---|---|---|---|---|
| HCB225A | 267.78 | 3.57 | DCB225A | 274.46 | 4.04 |
| HCB225B | 264.21 | 3.67 | DCB225B | 268.02 | 3.80 |
| HCB225C | 274.26 | 3.69 | DCB225C | 278.51 | 4.69 |
| HCB225D | 264.25 | 3.41 | DCB225D | 274.66 | 3.77 |
| HCB240A | 334.3 | 7.57 | DCB240A | 321.67 | 6.78 |
| HCB240B | 314.84 | 4.67 | DCB240B | 319.86 | 5.22 |
| HCB240C | 389.9 | 8.34 | DCB240C | 341.11 | 6.29 |
| HCB240D | 328.99 | 5.01 | DCB240D | 320.58 | 5.73 |
| HCB255A | 373.74 | 10.71 | DCB255A | 366.85 | 13.43 |
| HCB255B | 393.63 | 9.28 | DCB255B | 354.85 | 6.73 |
| HCB255C | 366.83 | 13.80 | DCB255C | 356 | 18.73 |
| HCB255D | 364.98 | 9.49 | DCB255D | 355.02 | 8.43 |
| ISMB150 | 246.84 | 11.118 | | | |

# 4 Results and Discussion

## *4.1 Effect of Depth of Opening*

The results of numerical analysis have been listed out in Table 3. Even though the CBs were made through solid web steel beams with the same cross-section, it has been observed that the shear stress carrying capacity of the CBs were decreased when compare to solid web section because of the opening. With the increase of expansion ratio, shear stress capacity of the section is decreases. When compare to the three-expansion ratio such as 1.5, 1.6 and 1.7, the *D/d* of 1.5 show effective outcome towards the deflection in both the shape of opening. But if it is look at over the expansion ratio 1.6 and 1.7 of DCBs with width of cutting edge of 80 mm with cutting angle 60° and 45° show less deflection compare to the same expansion ratio of HCBs. Even stress value is also low which has been detailed in Table 3. Thus, if the depth of opening is more, DCBs shows better result correlate to HCBs (Fig. 2).

## *4.2 Effect of Cutting Angle and Width of Opening*

In CBs, the central width of the opening is depending upon the cutting angle and depth of opening, i.e. if cutting angle increases, width of opening will get decreased and if depth of opening increases, width of opening also increases and vice-versa. As discussed in Sect. 4.1, deflection increases with increase of depth of opening. From

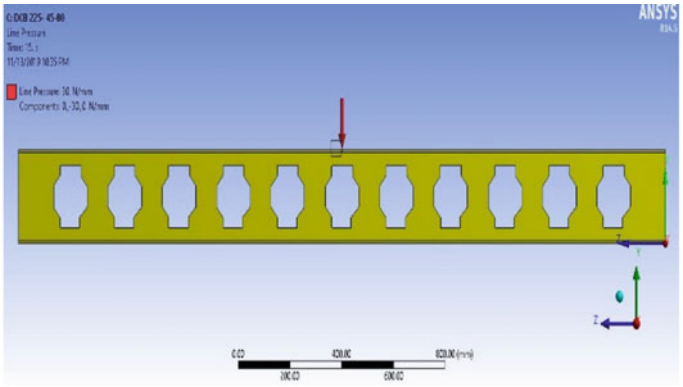


a)

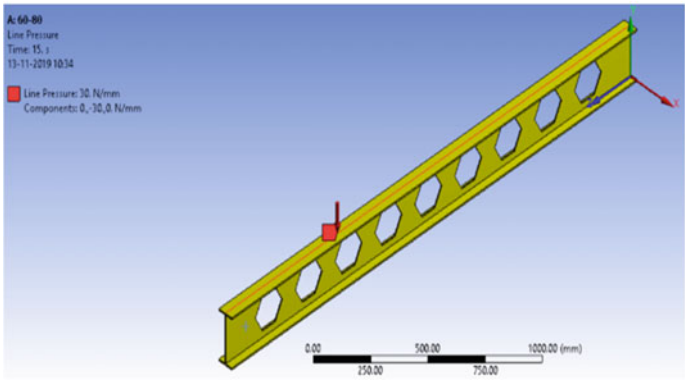


b)

**Fig. 2** Numerical model **a** Hexagonal castellated beam, **b** Dodecahedron castellated beam

Table 3, its clearly show that if the width of opening the CBs is more, which in turn increases the deflection of the CBs.

## *4.3 Effect of Shape of Opening*

In this study new shape of castellated beam has been formed with 12 edges and named as DCBs and it has been validated with hexagonal castellated beam. The primary advantage of the DCBs is more number of hole formation and width of opening is less as correlate to HCBs. For same length, HCBs offer a less number of hole compare to DCBs. The pattern of dodecahedron opening made hole into narrow as compare to hexagonal opening. This made DCBs to yield less in larger expansion ratio.

### 4.4 Stress Concentration

The presence of hole or cut in section, will result in modification of stress distribution. Thus, the stress which have to pass through hole or cut will redistribute to the near section of the hole or cut. This will increase local stress around the edge of hole or cut. The stress concentration will be depending upon shape of hole or cut and its location corresponding to loading. The stress concentration is negligible to certain limit of size of hole or cut. Since it is castellated beam, stress concentration will vastly affect the capacity of the section which will persuade rupture in the element. Here two different opening shape has been formed where Hexagonal shape have 6 edge opening and dodecahedron opening have 12 edge opening. If more the edges, more number of sharp corner will be form which will cause more stress concentration. From Fig. 5 it is clearly appreciating that the amount of stress concentration in DCBs is comparatively more or nearly equal to the HCBs. This is due to presence of more number of sharp corners. But if look into the formation of Vierendeel mechanism as shown in Fig. 5, HCBs shows large formation Vierendeel mechanism in hole next to support whereas in DCBs it is evenly distributed to the next hole.

### 4.5 Deflection

The maximum central deflections of CBs are obtained by using numerical analysis and results are shown in Fig. 3. Although ISMB150 is a solid web section, the deflection formed in it is comparatively high to the deflection formed in CBs under same loading condition expect few cases. This is because of increase in moment of inertia of CBs section. Thus, less deflection is foremost benefit of castellated beam over solid I section. From Table 3, it can be stated that CBs with width of cutting edge 80 mm create more deflection and equivalent stress corresponding to 75 mm in all cases of HCBs and DCBs. Based on the deflection value, as shown in Fig. 3a, b the optimum expansion ratio of the CBs is 1.5 with a maximum central deflection of 3.41 mm in case of HCBs and 3.77 mm in case of DCBs.

As the depth of opening is increased to 180 mm ($D/d = 1.6$), DCBs shows enhanced outcome towards HCBs with width of cutting edge 80 mm for both cutting angle 45° and 60°. As discussed in Sect. 4.2, the increase in depth of opening in HCBs lead to huge widening of central width of opening. Thus, it will increase the deflection irrespective of moment of inertia. But this fact is slightly varied if the depth of opening is increased to 210 mm. In DCB255, the element with cutting edge 75 mm gives better result as relate to HCB255. In this case along with depth of opening, width of cutting edge also influence the central deflection.

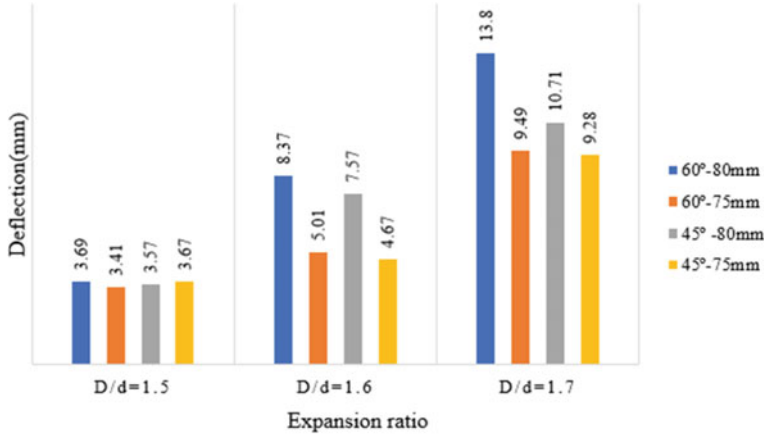


a)

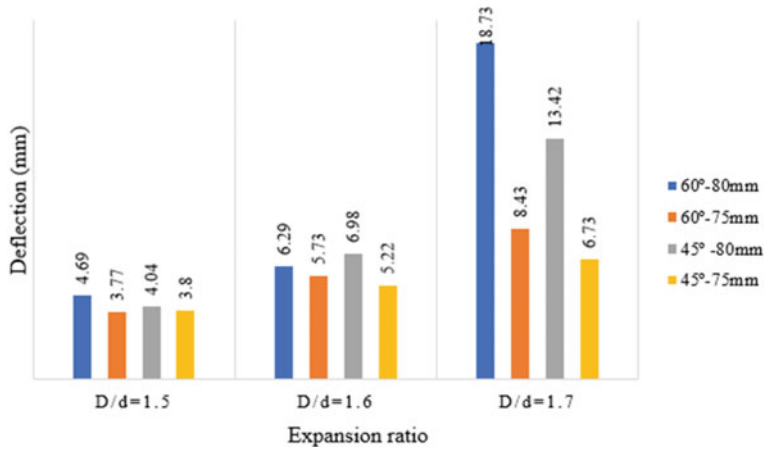


b)

**Fig. 3** Expansion ratio versus deflection **a** HCBs **b** DCBs

## *4.6 Failure Mode*

Out of six failures mode, the CBs failed primarily by the Vierendeel mechanism which are form due to stress concentration at corner of opening. This failure occurred at hole nearer to the support condition where $Uz = 0$. Thus, support condition plays vital role in failure mechanism. Figure 5 shows the plastic hinge formation in Tee section and it demonstrates that the element will fail by yielding mechanism, in both HCB and DCB. Figure 5a, b shows the yielding pattern of HCB and DCB whose

$D/d$ = 1.5, cutting angle = 60° and opening span is 75 mm. Figure 4g shows the yielding of HCB225B and DCB225B.

It clearly shows that the failure pattern of both HCBs and DCBs are almost similar. From Fig. 5c–f shows yielding pattern of the castellated beam whose $D/d$ ratio are 1.6 and 1.7 and its yielded earlier corresponding to castellated beam having $D/d$ ratio as 1.5 for the applied load. The cross-sectional area of Tee section in castellated

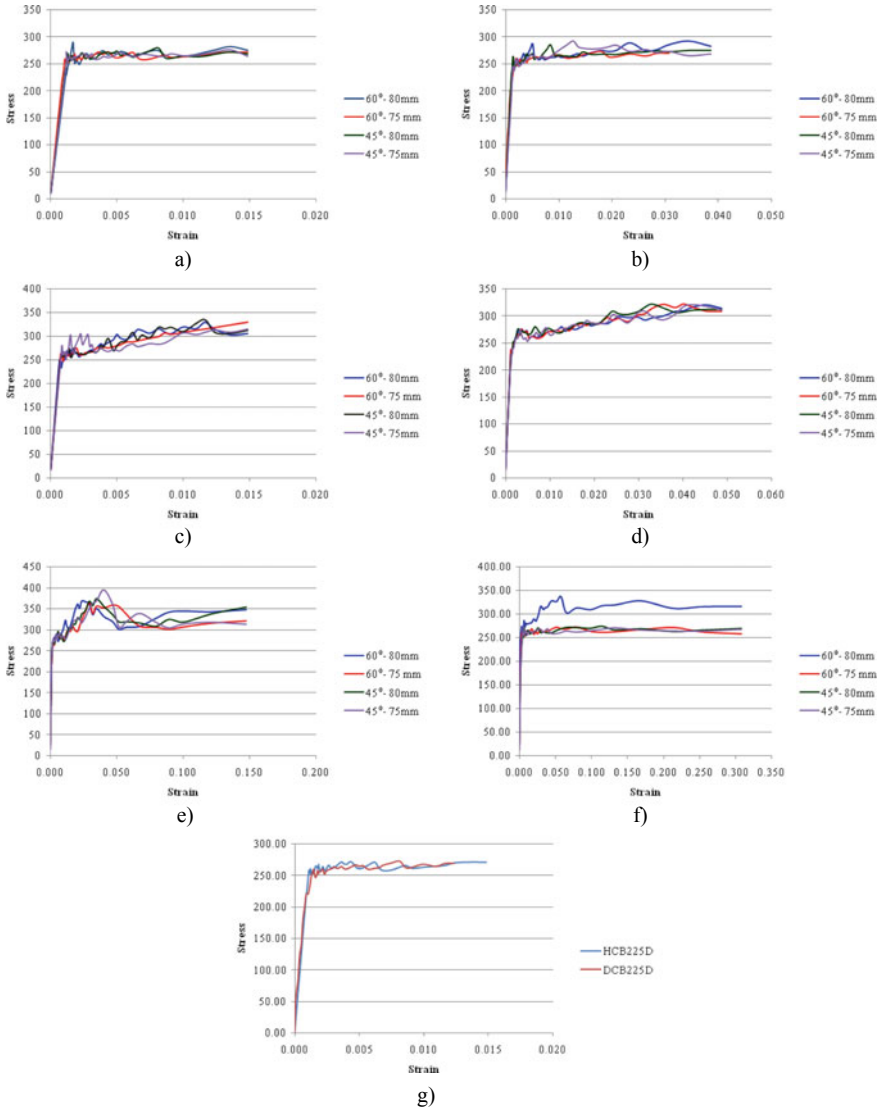


**Fig. 4** Stress strain curve **a** HCB225, **b** DCB225, **c** HCB240, **d** DCB225, **e** HCB250, **f** DCB250, **g** Optimum section

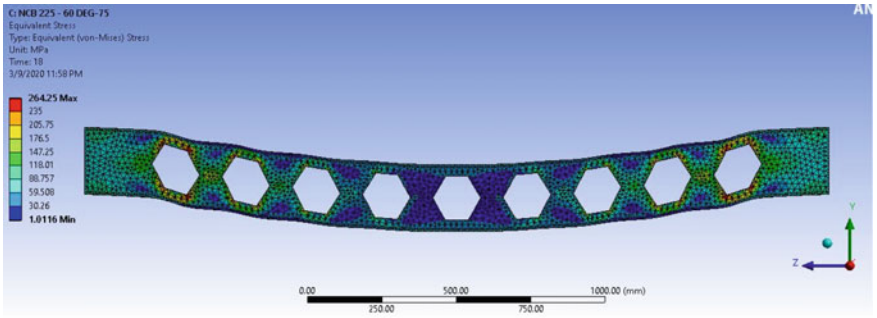


a)

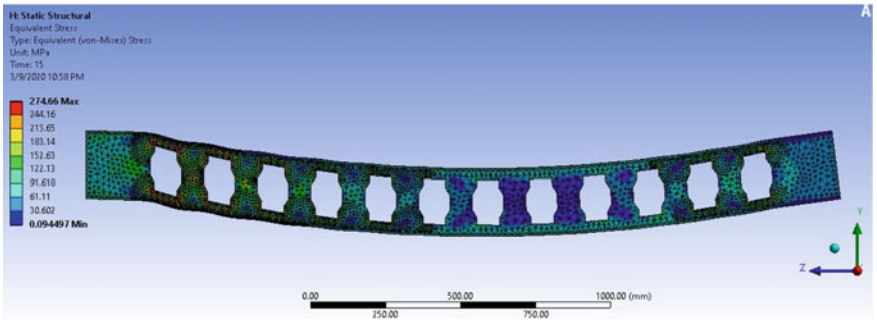


b)

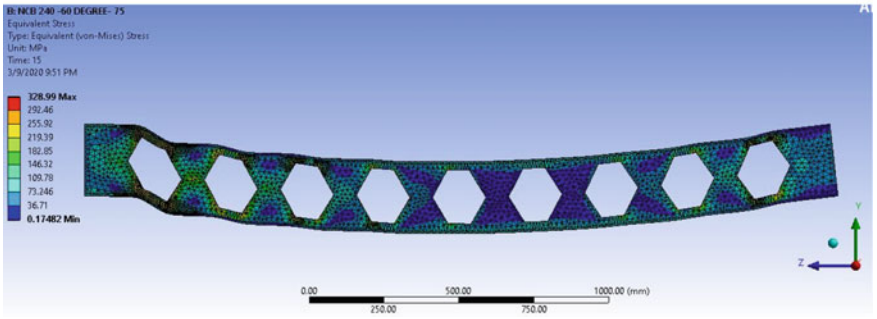


c)

**Fig. 5** Vierendeel mechanism of the beam **a** HCB225B, **b** DCB225B, **c** HCB240B, **d** DCB225B, **e** HCB250B, **f** DCB250B

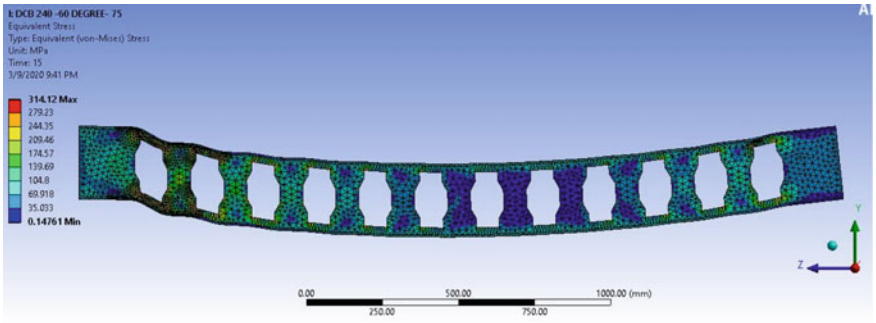


d)

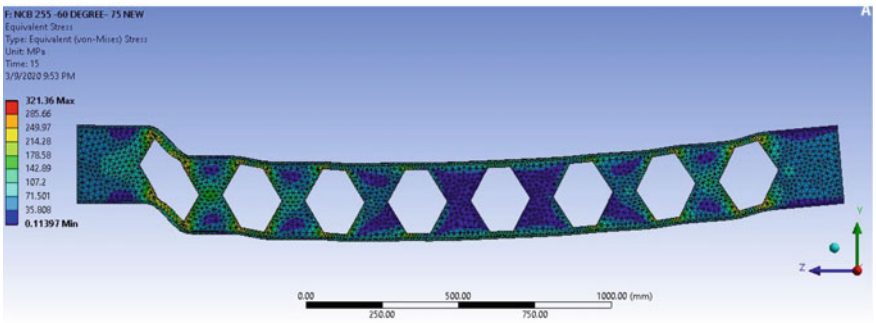


e)

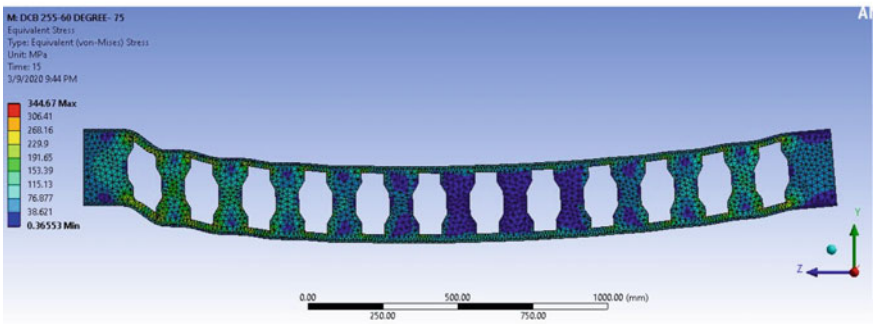


f)

**Fig. 5** (continued)

beam will get reduced with increase of depth of opening. It encourages the element to form plastic zone in corner region of hole due to the Vierendeel mechanism. On viewing towards the deflection factor the maximum deflection in element CBs 240 is more compare to CBs 225 but it is under allowable only.

## 5 Conclusion

In this paper castellated beam of two different opening shapes with various parameters of expansion ratio (1.5, 1.6 and 1.7), cutting angle (45° and 60°) and width of cutting edge (75 and 80 mm) have considered as overusing the finite element model with the help of software ANSYS workbench version14.5. The model was developed to attain the maximum deflection and the maximum equivalent stress for each section.

The equivalent stress of the castellated beam got increases when there are decreases in the area of Tee section which means stress got increases with an increase of depth of opening for the same loading condition. The section of *D/d* ratio as 1.5 shows good load carrying capacity in both HCB and DCB. The stress–strain curve pattern and deformation pattern of HCBs and DCBs are similar.

When considering the deflection criteria which depends upon moment of inertia, CBs with *D/d* ratio 1.5 shows less deflection. Even though deflection formed in the CBs of overall depth 240 mm is high as compare to CBs of overall depth 180 mm, deflection values are under permissible limit only. DCB240A and DCB240C shows less central deflection when compare to HCB240A and HCB240C. It is due to increase in depth of section which majorly affect the deflection of HCBs.

From this study, it has been stated that DCBs shows better result for CBs having large depth of opening. It is achieved by opening shape which form a smaller width of opening as compare to hexagonal opening for the same depth of section even edge distance of DCBs are less with relate to HCBs.

## References

1. Mohan A, Abubaker KA, Das LG (2016)Parametric study of beam to column bolted connection with cellular beams. Int Res J Eng Technol 3(9):609–613
2. Anupriya B, Jagadeesan K (2013) Strength study on castellated beam.Int J Eng Res Technol 2(2):3853–3859
3. Boyer JP (1964) Castellated beams—new developments. Eng J 1:104–108
4. Sonck D, Van Impe R, Belis J (2014) Experimental investigation of residual stresses in steel cellular and castellated members. Constr Build Mater 54:512–519
5. Durif S, Bouchaïr A (2012) Behavior of cellular beams with sinusoidal openings. Proc Eng 40:108–113
6. Satyarno I, Sulistyo D, Heldita D, Talodaci A, De Oliviera CR (2017) Full height rectangular opening castellated beam partially encased in reinforced mortar. Proc Eng 171:176–184
7. Kerdal D, Nethercott DA (1984) Failure modes for castellated beams. J Constr Steel Res 4:295–315
8. Kumbhar PD, Jamadar AM (2015) Optimization of opening size for castellated beam with sinusoidal openings. Int J Optim Civ Eng 5:301–313
9. Budi L, Sukamta, Windu P (2016) Optimization analysis of size and distance of hexagonal hole in castellated steel beam. Proc Eng 171:1092–1099
10. Pachpor PD, Gupta LM, Deshpande NV, Bedi K (2011) Parametric study of castellated beam. Adv Mater Res 163–16:842–845
11. Wang P, Ma Q, Wang X (2014) Investigation on Vierendeel mechanism failure of castellated steel beams with fillet corner web openings. Eng Struct 74:44–51

12. Frans R, Parung H, Sandy D, Tonapa S (2017) Numerical modeling of hexagonal castellated beam under monotonic loading. Proc Eng 171:781–788
13. Srimani SL, Dass PR (1978) Finite element analysis of castellated beams. Comput Struct 9:169–174

# Study on Reduction in Capacity of Hot Rolled I-Section Due to Elevated Temperature


**Rajendra N. Khapre and Monika D. Dhuware**

**Abstract** It's been so long that hot rolled I-beams are being used across the world for construction. The stability of steel structure is certainly influenced by decreasing stiffness during heating and non-linear response of stress–strain at elevated temperature when subjected to fire. Temperature is one of the reasons for failure of the structure which makes the study of effect of temperature on steel structure important. This paper represents an analytical study of the performance of geometrically perfect steel section under the elevated temperature. The analysis is based on multilinear isotropic material which uses finite element method and is functionally affected by temperature. A major spotlight of the paper is to compile the past studies on the material, stress–strain curve of steel and effect of temperature on it. The different parameters selected for the comparison are applied loads, deformation, maximum equivalent stress, plastic region, elastic region, respectively.

**Keywords** Elevated temperature · Finite element analysis · ANSYS

## 1 Introduction

Hot rolled steel is mainly formed by undergoing a process which involves the rolling of steel at a high temperature (typically at 1700 °C) which is above steels recrystallization temperature. At this temperature it can be shaped easily and the steel can be made in much larger sizes. As compared to cold rolled steel, when hot rolled steel is cooled it shrinks vaguely independent to its size and shape. These products mainly compile hot rolled steel bars which are used in welding, railroad tracks and I-beams. Importantly, it has always been an interesting subject for researches that how the behavior of steel changes with the different elevated temperatures. It has been perceived earlier that when applied to an increasing temperature as steel beam shows reduction in load carrying capacity.

R. N. Khapre (✉) · M. D. Dhuware
Shri Ramdeobaba College of Engineering and Management, Nagpur, India
e-mail: khaprern@rknec.edu



M. Madhavan et al. (eds.), *Proceedings of the Indian Structural Steel Conference 2020 (Vol. 1)*, Lecture Notes in Civil Engineering 318,
https://doi.org/10.1007/978-981-19-9390-9_43

It ultimately urges the structure to fail at its normal service load, however, it can retain when at normal room temperature. Till now it has been seen that the melting point of steel is nearly about 1300 °C. When there is an increase in temperature, tensile failure is seen in steel. The whole concept is studied experimentally or obtained by finding a mutual relationship between stress, strain and temperature of steel. One of such analysis is done mathematically which is given by Poh [7, pp. 371–379]. There are two major elements that play a key role which are stress ($\sigma$) and strain ($\varepsilon$) shown in Fig. 1. According to Poh [7, pp. 371–379] stress–strain curve for structural steel has three parts including linear elastic range, plastic plateau and strain hardening portion as shows in Fig. 1. This relation is capable of producing all tangential discontinuities of complete stress–strain response, including the upper yield point, lower yield point, yield plateau and the initiation of strain hardening [2, pp. 183–201]. But there is no proved theory to give values for these elements, which can be found experimentally [6, pp. 214–217]. However, it can be done by fitting these parameters in mathematical equations having the values of σ and ε from experimental data. Thereafter, the values for stress–strain curve also changes with the temperature. With the gradual decrease in both stiffness and strength the value of $\sigma$ and $\varepsilon$ also changes, respectively [7, pp. 371–379, 8, pp. 664–675].

Poh [7, pp. 371–379] proposed a new mathematical relationship between stress, strain and temperature. Its resulting relationship precisely represents experimental data. Burgess et al. [2, pp. 183–201] presented an analytical study on the performance of geometrically perfect steel columns under temperatures based on the finite element method. Study shows that slenderness ratio plays an important role in failure of columns. Baetu et al. [1, pp. 256–272] proposed the paper investigating the damages

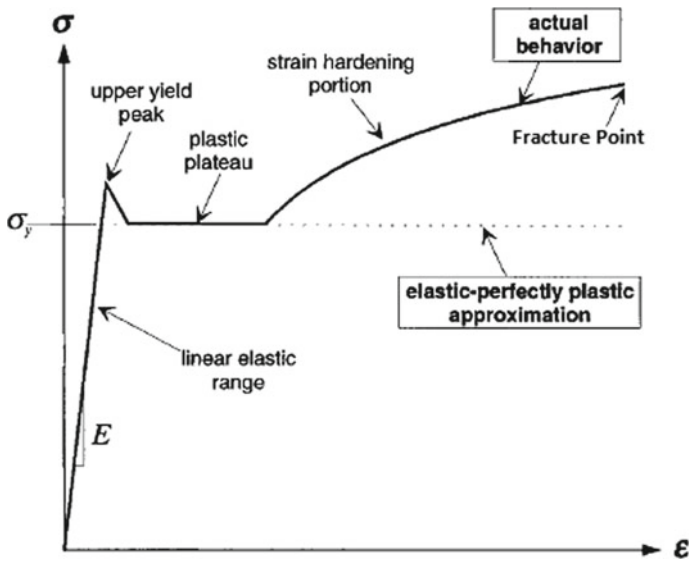


**Fig. 1** Stress–strain curve of steel and elastic-perfectly plastic approximation

of an industrial steel building mannered by certain fire events. Literature discusses the behavior of structural steel is studied under numerical simulations and experimental studies. Knobloch [3, pp. 257–264] gave an outline on studies based on behavior of structural steel under fire. The model presented in literature tends to predict the behavior of structural steel under fire. Sinaie et al. [10, pp. 84–94] suggested that the experimental results shows that the properties of mild steel is affected by its cyclic load history when subjected to elevated temperatures. It proposes importance of establishing the relationship of property not only as a function of temperature but also a function of its past load history. Seif et al. [9, pp. 134–145] combined temperature dependent stress–strain curve with plastic strain-based failure criteria for finite element material modeling for structural steels and bolts. The literature calibrated failure criteria against high temperature and its dependence on temperature and mesh size. Patil and Ramgir [5, pp. 2775–2781] presented study on structural steel members subjected to mechanical and thermal loading combined. Experimental results and simulation results carried out using ANSYS indicates reduced performance of structure subjected increased temperature. Patade and Chakrabarti [4, pp. 420–424] presented thermal analysis of steel beam subjected to temperature from 200 to 1000 °C using ABAQUS. Study indicates reduction in stiffness, hence strength, of beam under raise in temperature due to fire. Authors reported that the deflection is excessive at 600 °C. At this temperature, the stresses reaches to yield limits.

Objectives of this paper are to study the behavior of steel I-beam at elevated temperature. The I-beam is modeled in ANSYS with various temperatures. The model is analyzed under different elevated temperature and the behavior of I-section is studied.

## 2 Methodology

ISMB 400 section beam is considered for the study. The properties of the beam are shown in the Table 1. Transient thermal analysis is considered to study the effect of temperature on behavior of beam under external loading. The beam model shown in Fig. 1 is discretized using brick elements with fine mesh feature of ANSYS. This beam is analyzed using ANSYS subjected to pressure on top flange of the beam, while both ends of the beam kept fixed as shown in Fig. 2. Usually, the maximum allowable deflection of steel is L/240, i.e., 12.5 mm. Hence transient analysis is performed where pressure is gradually increased till maximum permission deflection is achieved.

Figure 3 shows stress strain curves for various temperatures given by Poh [7, pp. 371–379]. These curves are obtained from tensile tests carried out on structural steel specimen at different temperatures. These curves are idealized into multi-linear isotropic hardening material behavior under various temperatures that is shown in Fig. 4. To understand the behavior of beam under elevated temperatures, eleven finite element models (corresponding to temperatures 20, 100, 200, 300, 400, 500,

**Table 1** Geometric and material properties of the beam model

| Particulars | Value |
|---|---|
| Length of beam | 3000 (mm) |
| Depth of beam | 400 (mm) |
| Width of flange | 140 (mm) |
| Thickness of flange | 16 (mm) |
| Thickness of web | 8.9 (mm) |
| Permissible deflection | 12.5 (mm) |
| Young's modulus | 200 (GPa) |
| Poisson's ratio | 0.3 |

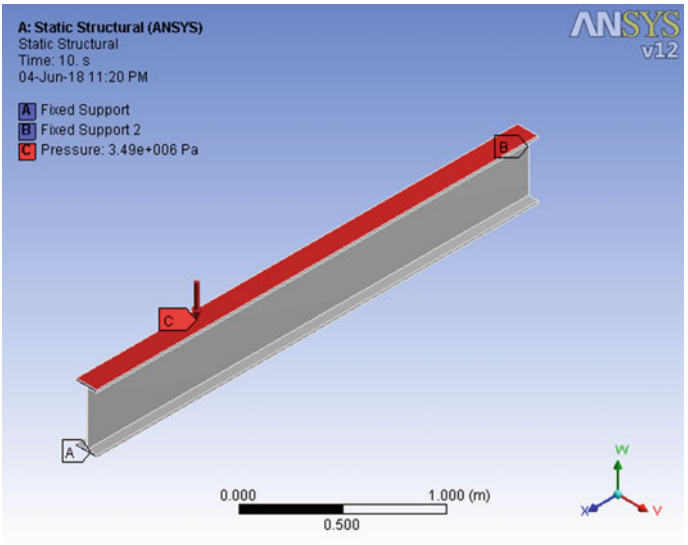


**Fig. 2** Finite element model of beam

600, 700, 800, 900 and 1000 °C) are created. Idealized stress strain curve at various temperatures are assigned to each finite element model. Fine meshing feature is used in order to achieve greater accuracy in the finite element analysis.

## 3 Analysis and Result

After performing transient thermal finite element analysis, magnitude of pressure is measured to achieve maximum permissible displacement of 12.5 mm for each finite element model and reported in Table 2. The variation of equivalent stresses across the length of beam is also studied for each finite element model. Figure 5

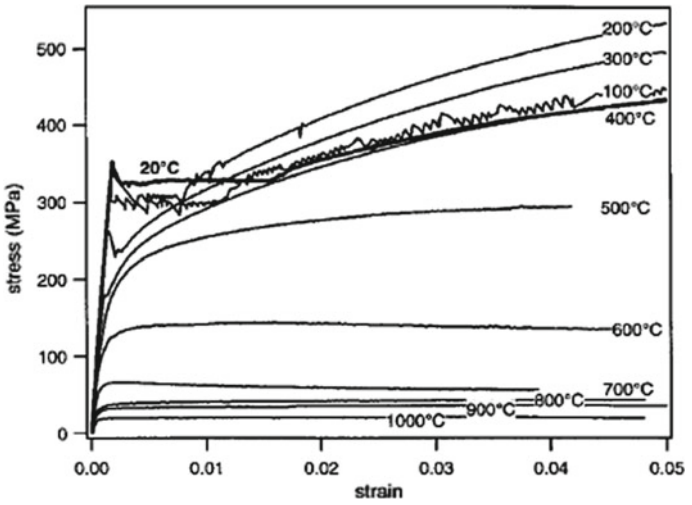


**Fig. 3** Experimental stress–strain for different temperature [7, pp. 371–379]

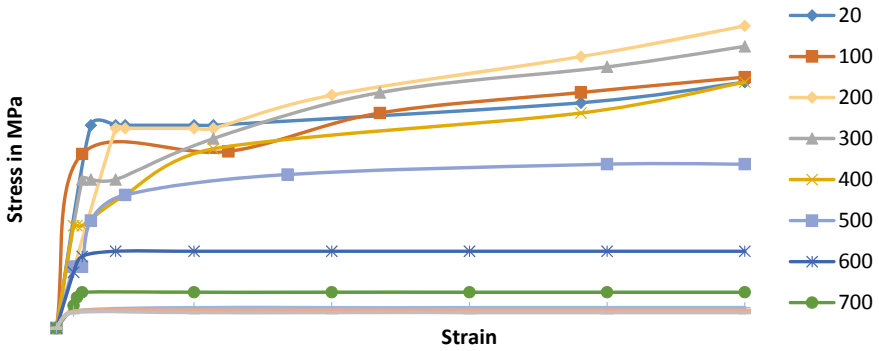


**Fig. 4** Idealized stress strain curve for different temperatures

shows variation of equivalent stress for beams analyzed for 20 and 1000 °C. Figure 5 illustrates that maximum equivalent stresses are observed near the supports for all finite element models. The magnitudes of maximum equivalent stresses to achieve maximum permissible displacement of 12.5 mm are also shown in Table 2.

Finite element analysis on beam model with 20 °C temperature shows that the stresses generate across the beam section are in the elastic region only. For the beam models with 100 and 200 °C, the maximum equivalent stresses are observed in yield plateau region. For the temperature 300, 400 and 500 °C, strain hardening is observed but the magnitude of maximum equivalent stresses observed in beams are less than ultimate stress at fracture point as illustrated in Fig. 1. Analysis of other beam models having beam temperature more than 500 °C shows magnitude

**Table 2** Variation in pressure and equivalent stresses with temperatures

| No | Temperatures (°C) | Pressure (MPa) | Maximum stress (MPa) |
|---|---|---|---|
| 1 | 20 | 3.49 | 360 |
| 2 | 100 | 3.16 | 315 |
| 3 | 200 | 3.45 | 354 |
| 4 | 300 | 2.895 | 311 |
| 5 | 400 | 2.56 | 273 |
| 6 | 500 | 2.29 | 241 |
| 7 | 600 | 1.428 | 136 |
| 8 | 700 | 0.6745 | 63.6 |
| 9 | 800 | 0.3837 | 36.3 |
| 10 | 900 | 0.3434 | 31.8 |
| 11 | 1000 | 0.2865 | 27.2 |

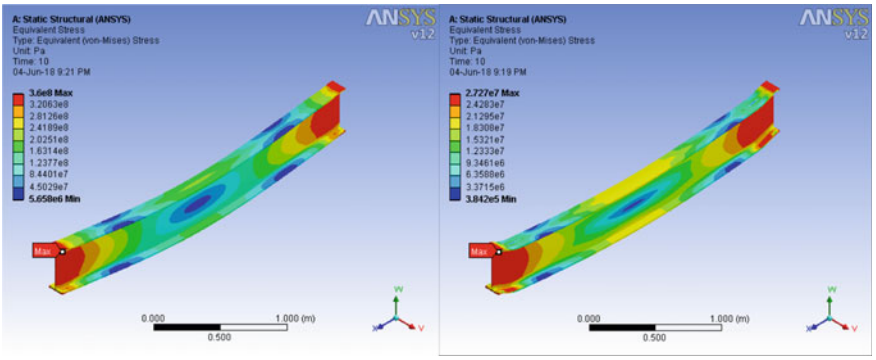


**Fig. 5** Variation of equivalent stresses for 20 and 1000 °C

of maximum equivalent stress same as ultimate stress at fracture point; hence these beams will fail before achieving maximum permissible deformation of 12.5 mm.

After performing transient thermal analysis, the pressure is recorded to achieve the maximum permissible deformation of 12.5 mm. The value of this pressure is termed as load carrying capacity at particular temperature as further increase in the value of this pressure resulted in excessive deformation as compared to limit of serviceability deflection criteria. Figure 6 shows percentage reduction in the load carrying capacity of the beam section under various temperatures. It can be seen that the beam was capable of carrying a pressure of 3.49 MPa at 20 °C. This load carrying capacity is reduced to 82.95% when the beam temperature is 300 °C. Further increase in beam temperature results in gradual reduction in load carrying capacity of the beam up to 65.62% at 500 °C. Sudden reduction in load carrying capacity of the beam is observed from 500 to 700 °C. Further increase in temperature results in meager reduction in load carrying capacity of the beam.

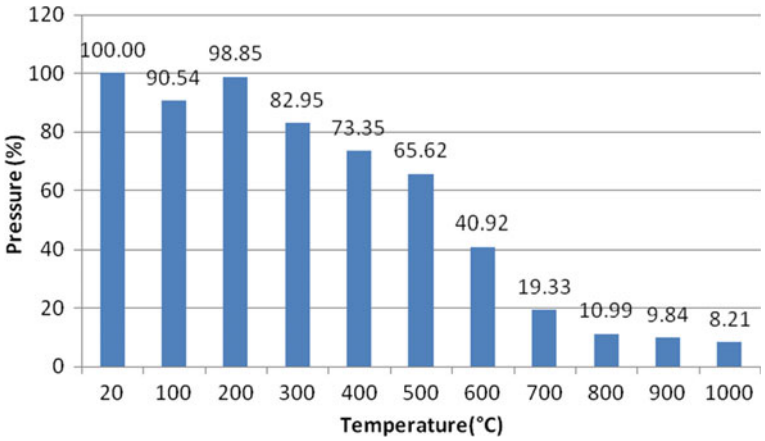


**Fig. 6** Chart showing reduction in load carrying capacity with varying temperature

**Table 3** Variation in applied pressure leading to failure of beam

| Temperature (°C) | Ultimate stress (MPa) | Applied pressure at which beam fails (MPa) | Max. stress in analysis (MPa) |
|---|---|---|---|
| 500 | 290.09 | 2.29 | 241 |
| 600 | 136.36 | 1.34 | 136 |
| 700 | 63.63 | 0.553 | 63.6 |
| 800 | 36.36 | 0.372 | 36.3 |
| 900 | 31.815 | 0.319 | 31.8 |
| 1000 | 27.27 | 0.284 | 27.2 |

From Table 2, it was observed that for beam model with 500 °C temperature, the magnitude maximum equivalent stress is 241 MPa which is less than ultimate stress at fracture point for 500 °C temperature. When temperature is changed to 600 °C and above, it was observed that the stresses generated in the beam are equal to ultimate stresses before reaching to maximum permissible deformation in beam, i.e., 12.5 mm. Table 3 shows the value of applied force at which stresses generated in beam models are same as ultimate stress at different temperatures.

## 4 Conclusion and Discussion

After performing transient thermal finite element analysis on ISMB 400 steel beam subjected to elevated temperatures, the load carrying capacity is measured as the pressure at which maximum permissible deformation occurs. It is clear from Fig. 3 that there is considerable degradation of modulus of elasticity and ultimate load

at which failure of material occurs. Study indicates that load carrying capacity of beam section reduces gradually up to 8.21% when subjected to a temperature of 1000 °C. The reduction in load carrying capacity of beam section is marginal when the temperature increases from 20 to 300 °C. Further increase in beam temperature (up to 500 °C) will result in further reduction in load carrying capacity, i.e., up to 65.62%, without damaging the beam and within the limit of serviceability. The beam section will fail when its temperature is raised beyond 500 °C when loaded with pressure for which it is initially designed.

## References

1. Baetu G, Galatanu TF, Baetu SA (2017) Behavior of steel structures under elevated temperatures. Proc Eng 181:256–272
2. Burgess IW, Olawale AO, Plank RJ (1992) Failure of steel columns in fire. Fire Saf J 18(2):183–201
3. Knobloch M (2014) Stability of steel structures in fire. Stahlbau 83(4):257–264
4. Patade HK, Chakrabarti MA (2013) Thermal stress analysis of beam subjected to fire. Int J Eng Res Appl 3(5):420–424
5. Patil BV, Ramgir MS (2016) Study of structural steel members under thermal loading. Int J Sci Eng Technol Res 5(8):2775–1781
6. Poh KW (1997) General stress-strain equation. J Mater Civ Eng ASCE 9(5):214–217
7. Poh KW (2001) Stress-strain-temperature relationship for structural steel. J Mater Civ Eng 13(5):371–379
8. Poh KW, Bennetts ID (1995) Analysis of structural member under elevated temperature conditions. J Struct Eng ASCE 121(4):664–675
9. Seif M, Main J, Weigand J, McAllister TP, Luecke W (2016) Finite element modeling of structural steel component failure at elevated temperatures. Structures 6:134–145
10. Sinaie S, Heidarpour A, Zhao XL (2014) Stress-strain temperature relationship for cyclically-damaged structural mild steel. Eng Struct 77:84–94

# A Study on Design Thickness of Corner Gusset Plates in Steel Braced Frames for Tension


**K. S. Vivek, U. K. L. Priyanka, and K. S. Sai Ram**

**Abstract** The gusset plates in steel buildings and bridges play vital role in transfer forces and maintaining the overall structural integrity, but are relatively overlooked in design. In this study, a typical case of corner gusset plate welded to the beam-column joint and connected to the tension brace by single row of two and three bolts is considered. A simple 2-D model of corner gusset plate is developed to perform geometric and material nonlinear analysis for various load ranges and brace angles, with the help of ANSYS—a commercial finite element software. The minimum thickness of the gusset plate required to prevent rupture for each case is noted. The required thickness of gusset plates as per Whitmore's theory, Indian (IS 800:2007), European (EN 1993-1-1: EC3) and American (ANSI/AISC 360-16) standards are also calculated. In comparison, significant difference in the required thickness of gusset plates as per finite element analysis and the considered codal provisions is observed. The maximum thicknesses obtained is specified as the design thickness for each case, which may serve as a guide or design aid for structural engineers.

**Keywords** Corner gusset plate · Single row of bolts · Finite element analysis · Steel braced frame · Rupture · Whitmore's effective width theory

## 1 Introduction

Steel corner gusset plates are extensively used to facilitate the connection of braces/diagonals to the beam-column joints in X-braced metal frame buildings. The braced frames are provided to resist the lateral loads acting on the building due to wind or earthquake. Generally, the diagonals/braces are designed to resist tension only. The tensile force in the brace is transferred to the frame members through the gusset plate

K. S. Vivek (✉) · U. K. L. Priyanka
Department of Civil Engineering, VVIT, Guntur, Andhra Pradesh 522508, India
e-mail: vivek3393@yahoo.com

K. S. Sai Ram
Department of Civil Engineering, RVR & JCCE, Guntur, Andhra Pradesh 522019, India



M. Madhavan et al. (eds.), *Proceedings of the Indian Structural Steel Conference 2020 (Vol. 1)*, Lecture Notes in Civil Engineering 318,
https://doi.org/10.1007/978-981-19-9390-9_44

connections provided at the beam-column joints. Typically the diagonals/braces are bolted to the gusset plates which are welded at the beam-column joint as depicted in Fig. 1. For proper transfer of force from the brace to the other members and maintaining overall structural integrity, adequate thickness of gusset plates should be provided or else the gusset plate may fail by excessive gross section yielding or rupture at critical net section, when connected to a tension member by single row of bolts. But the determination of required thickness of gusset plates is not straight forward. Also the behavior of gusset plate is quite complex as high magnitude of forces from connecting members should be resisted and transferred through the bolt holes. The gusset plates are subjected to combined direct, flexural and shear stresses [1–7].

Currently, the design of steel gusset plates as per any code of practice is done mostly by considering Whitmore's effective width theory. Whitmore's effective width theory is based on elastic behavior and the stress concentration effect near the bolt holes is neglected. Also in practice, the thickness of the gusset plates is fixed based on experience or thumb rules which may sometimes be inadequate and lead to the failure of gusset plates resulting in overstressing of connected members or even collapse of the entire structure. Inadequate thickness of gusset plates at various joints resulted in the collapse of I-35W Mississippi steel highway arched truss bridge in Minnesota during the year 2007.

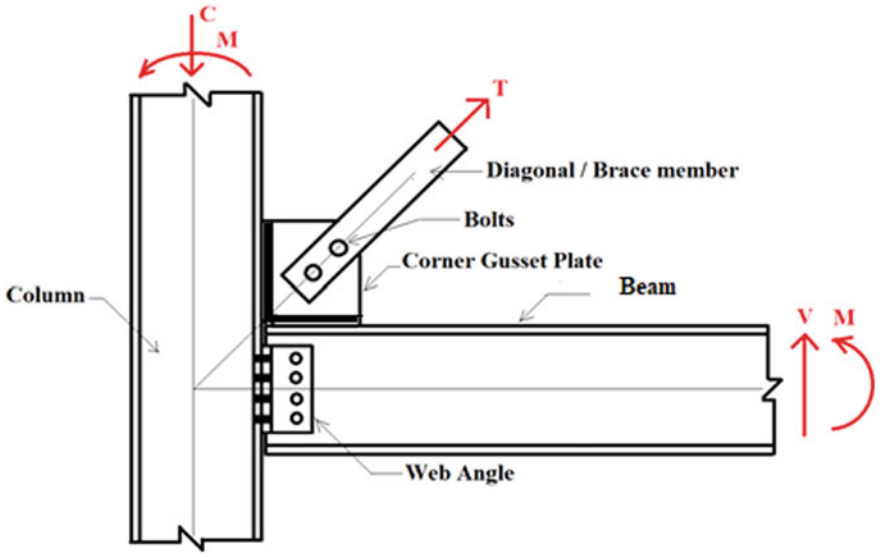


**Fig. 1** Typical corner gusset plate connection at beam-column joint

## 2 Brief Literature Review

Whitmore [11] performed experimental investigation to find out the stress distribution in aluminum gusset plates of Warren type truss. The load was applied such that the stresses developed in the members and gusset plates were within elastic limit. The strain gauges were mounted on the gusset plates to get a plot of stress contours. But no strain gauges were mounted at the edges of the bolt holes, and hence the stress concentration effect was not accounted. A formula for calculating maximum tensile/compressive stress in the gusset was proposed based on simple mechanics assuming that the load in the diagonal is uniformly distributed over an area obtained by multiplying the effective width normal to the axis of the member with the thickness of the gusset plate. The effective width was obtained by constructing lines at an angle of 30° with the axis of the diagonal member on observing the obtained stress contours.

An improved design method was proposed by Hardash and Bjorhovde [5] considering the ultimate strength behavior based on experimental testing of gusset plates for various conditions, in order to develop rational criteria incorporating all the strength parameters. Typical design curves were also presented to fix the size and thickness of gusset plate. Bjorhovde and Chakrabarti [2] performed full-scale tests on gusset plates in braced frames for 30°, 45° and 60° angle of inclination of bracing member. Rupture at bottom holes was reported as the predominant failure mode. Bursi et al. studied the behavior of gusset plates in braced frames by performing finite element analysis considering the connection flexibility and strength interaction. The gusset plate was discretized with isoparametric plane stress elements and fasteners with 2-D nodal interface elements. The finite element model was found to be successful in assessing the behavior of the bracing connection up to the ultimate load but failed to do so upon bolt slip. Thickness of gusset plates used in trusses to prevent failure for varying load range was reported by Raghupathi.

Capacity analysis of bolted gusset plate connections was carried out by Rosentrauch [8] considering Whitmore, block shear, global section shear and finite element methods. ABAQUS software was used to carry out the finite element analysis of trussed gusset plate connection model which was tested experimentally by Whitmore [11]. The inelastic stress regions for Whitmore model were simulated and the possible failure modes were discussed. From the elastic analysis it was found that the stress around the critical bolt holes was about 4.9 times the applied stress due to stress concentration which is greater than the conventional stress concentration factor of 3. Hadianfard et al. [6] investigated the behavior of central gusset plates in inverted V-brace frames. Pushover analysis of braced frame with buckling restrained brace was done based on finite element modeling and analysis. It was stated that the braces should be extended to twice the thickness of gusset plate beyond the free bending line to achieve better strength and ductility of the frame.

Vivek and Ram [9] carried out nonlinear finite element analysis of a simple 2-D model of typical steel gusset plate connections of Warren and Pratt trusses using ANSYS. Two bolt and three bolt cases were considered. The required thickness of gusset plates for a load range of 100–500 kN was found. Also, the minimum thickness

required as per Whitmore's theory was also determined and on comparison it was found that the Whitmore's theory resulted in inadequate thickness of gusset plate. Vivek et al. [10] performed nonlinear finite element analysis of simple 2-D model of corner gusset plate of braced frame with the help of commercial finite element analysis software ANSYS. The effects of type of stress–strain curve, range of yield plateau, type of strain-hardening, angle of inclination of the brace, thickness of gusset plate and diameter of bolt/bolt hole are investigated.

From the above brief literature review, it can be observed that most of the research done was concentrated on analyzing the elastic and inelastic behavior of gusset plates in trusses and frames. Among the various strength equations proposed by different authors, the Whitmore's effective width theory is being used widely by the engineers throughout the world due to its simplicity, though it is based on elastic behavior and does not account for stress concentration effect. Hence in this study, analysis of a typical corner gusset plate is carried out and design thicknesses of the gusset plates were presented based on the results of finite element analysis and various codal provisions for the considered cases which may serve as a design aid to structural designers.

## 3 Nonlinear Analysis of Corner Gusset Plates for Tension

The steel gusset plate is assumed to be welded to the beam-column joint, and a tension brace connected to the gusset by single row of bolts as shown in Fig. 1. Both two and three bolted cases are considered. The gusset plate alone is considered for analysis by providing suitable boundary conditions as shown in Fig. 2. The following assumptions are made for the simple nonlinear finite element analysis of gussets using ANSYS.

- The material of gusset is low carbon steel with yield stress '$F_y$' of 250 N/mm$^2$ and ultimate tensile stress '$F_u$' of 410 N/mm$^2$. True ultimate stress is conservatively limited to 1.1 $\sigma_u$ (451 N/mm$^2$).
- It is assumed that the bolts do not fail and hence are not modeled.

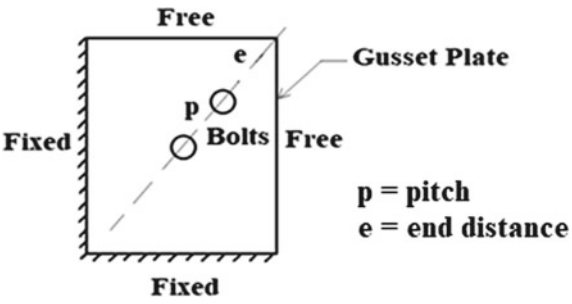


**Fig. 2** Boundary condition of gusset plate model

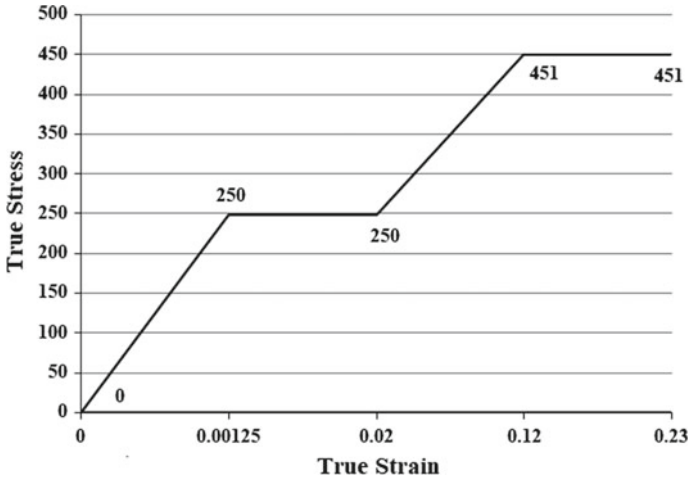


**Fig. 3** True stress–strain curve

- The tensile load from the brace is transferred to the gusset plate by bearing action through shear and the bolts share the load equally.
- Due to tensile force in brace, the bolts get in contact with the upper portion of the hole, and hence the force acting on a bolt is applied on to the respective nodes of the bolt hole in the gusset plate as components $F_x$ and $F_y$.
- Friction/contact between the gusset and the brace is neglected and hence the brace is not modeled.

Four-noded quadrilateral plane stress element with two degrees of freedom at each node and mesh size 0.5 is adopted for the analysis. The modulus of elasticity and Poisson's ratio for steel are taken as 200 GPa and 0.3, respectively. Generic true stress–strain curve as depicted in Fig. 3 is considered to include material nonlinearity. The true ultimate stress is conservatively limited to 1.1 $F_u$. The stress and strain values at salient points are presented in Table 1. Von Mises yielding criterion is assumed as it is well-suited for the ductile metals. Large displacement static deformation is considered for including geometric nonlinearity.

## 4 Whitmore's Effective Width

The Whitmore's effective width is obtained by constructing lines making angles of 30° with the axis of the member which originate at the outside bolts in the first row and continue until they intersect a line perpendicular to the member through the bottom row of bolts. The effective width is the intercept on this line between two inclined lines as depicted in Fig. 4. It is assumed that the rupture of the gusset plate occurs along the effective width perpendicular to the axis of the tension member.

**Table 1** True stress–strain values

| Strain | Stress (N/mm$^2$) |
|---|---|
| 0.00125 ($\varepsilon_y$) | 250 ($F_y$) |
| 0.02 ($\varepsilon_{st}$) | 250 ($F_{st}$) |
| 0.12 ($\varepsilon_u$) | 451 ($F_u$) |
| 0.23 ($\varepsilon_{br}$) | 451 ($F_{br}$) |

where $F_y$ = yield stress; $F_{st}$ = stress at strain hardening; $F_u$ = ultimate stress; $F_{br}$ = breaking stress
$\varepsilon_y$ = yield strain; $\varepsilon_{st}$ = stress at strain hardening; $\varepsilon_u$ = ultimate strain; $\varepsilon_{br}$ = breaking strain

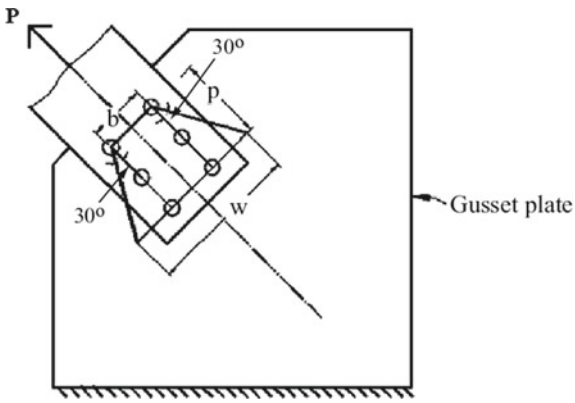


**Fig. 4** Whitmore effective width

Based on this, Whitmore calculated maximum stresses in gusset plate by simple mechanics formulas. The thickness of the gusset plate '$t$' using Whitmore's theory is given by Eq. (1).

$$t = \frac{P}{(w \times F_u)} \tag{1}$$

where $P$ = tensile force (kN); $w$ = effective width = 2 p tan 30° (for single row of bolts); $p$ = distance between first and last row of bolts as shown in Fig. 4.

## 5 Design Rupture Strength as Per Various Codes

### *5.1 AISC 360-16: Specification of Structural Steel Buildings*

$$T_{dn} = \varnothing_t \times F_u \times A_e = 0.75 \times F_u \times A_e \tag{2}$$

### 5.2 EN 1993-1-1: EUROCODE 3: Design of Steel Structures

$$N_{u,Rd} = 0.72 \times A_{net} \times f_u \tag{3}$$

### 5.3 IS 800:2007-Indian Standard Code of Practice for General Construction in Steel

$$T_{dn} = 0.72 \times A_n \times f_u \tag{4}$$

where $T_{dn}$, $N_{u,Rd}$ = design rupture strength; $A_e = A_{net} = A_n$ = Net area = $w * t$

## 6 Results and Discussion

### 6.1 Two Bolt Case

A square gusset plate of size 210 mm as depicted in Fig. 5 is modeled with suitable boundary conditions (as shown in Fig. 2). The pitch '$p$' of the bolts is taken as 70 mm and edge/end distance '$e$' as 50 mm. The analyses are carried out for tensile forces ($P$) of 100, 200 and 300 kN and varying angle of inclination ($\theta$) of diagonal/brace member. The minimum thickness of gusset plate required to prevent rupture along with the corresponding maximum principal tensile stress ($\sigma 1$), von Mises stress ($\sigma_{vm}$) and von Mises plastic strain ($\varepsilon_{vps}$) results obtained from geometric and material nonlinear analysis (GMNA) carried out using ANSYS is presented in Table 2 for each case. A minimum of 8 mm thickness is assumed. The required thickness of gusset plates as per Raghupathi, Whitmore [11], IS/EC3 and AISC standards is also calculated and the maximum is specified as the design thickness as given in Table 3. The von Mises stress contour for load of 100 kN and brace angle 45° is depicted in Fig. 6. It can be observed that the maximum stress occurred at the edge of the lower bolt hole.

From Tables 2 and 3, the following inferences may be drawn.

- The required thickness of the gusset plate depends upon the angle of inclination of the brace as per GMNA.
- Significant discrepancy between thicknesses of gusset plates obtained by GMNA, Whitmore and other design specifications can be observed for load cases of 200 and 300 kN.
- Design thicknesses of gusset plates for loads of 100 kN, 200 kN and 300 kN are 8 mm, 10 mm and 12.6 mm, respectively.

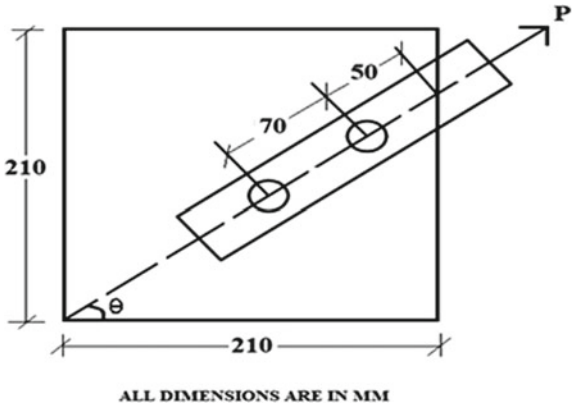


**Fig. 5** Gusset plate connected to tension brace by two bolts

**Table 2** Two bolt case—minimum thickness of gusset plate by GMNA

| Force in brace (kN) | Brace angle (ɵ) | Bolt dia (mm) | $\sigma_1$ (N/mm$^2$) | $\sigma_{vm}$ (N/mm$^2$) | $\epsilon_{vps}$ | Min. thickness of gusset plate (mm) |
|---|---|---|---|---|---|---|
| 100 | 30 | M20 (SS) | 244.861 | 231.534 | 0.00132 | 8 |
| | 35 | | 240.199 | 225.147 | 0.00191 | |
| | 40 | | 263.751 | 244.334 | 0.002244 | |
| | 45 | | 274.538 | 253.474 | 0.001941 | |
| | 50 | | 282.847 | 259.953 | 0.001749 | |
| | 55 | | 286.809 | 264.253 | 0.001331 | |
| | 60 | | 271.763 | 248.456 | 0.001315 | |
| 200 | 30 | M20 (DS) | 344.534 | 376.282 | 0.105666 | 8 |
| | 35 | | 338.22 | 366.205 | 0.108685 | |
| | 40 | | 355.866 | 398.988 | 0.141227 | |
| | 45 | | 272.772 | 296.121 | 0.061031 | 10 |
| | 50 | | 368.249 | 379.212 | 0.109649 | 8 |
| | 55 | | 363.128 | 371.997 | 0.093337 | |
| | 60 | | 395.395 | 406.339 | 0.121567 | |
| 300 | 30 | M24 (DS) | 388.763 | 415.935 | 0.154828 | 10 |
| | 35 | | 326.146 | 320.019 | 0.80349 | 12 |
| | 40 | | 363.818 | 340.801 | 0.083152 | |
| | 45 | | 429.14 | 397.144 | 0.142106 | |
| | 50 | | 417.133 | 436.481 | 0.174185 | 10 |
| | 55 | | 358.008 | 362.881 | 0.084177 | 12 |
| | 60 | | 444.155 | 428.487 | 0.129011 | 10 |

where *SS* = single shear and *DS* = double shear

**Table 3** Two bolt case—design thickness of gusset plate

| Force in brace (kN) | Brace angle ($\Theta$) | Thickness of Gusset plate (mm) | | | | | Design thickness (mm) |
|---|---|---|---|---|---|---|---|
| | | GMNA (ANSYS) | Raghupati (1995) | Whitmore (1952) | IS/ EC | AISC | |
| 100 | 30 | 8 | 8 | 3.0175 | 4.2 | 4.1 | 8 |
| | 35 | | | | | | |
| | 40 | | | | | | |
| | 45 | | | | | | |
| | 50 | | | | | | |
| | 55 | | | | | | |
| | 60 | | | | | | |
| 200 | 30 | 8 | 8 | 6.035 | 8.4 | 8.1 | 8.4 |
| | 35 | | | | | | |
| | 40 | | | | | | |
| | 45 | 10 | | | | | 10 |
| | 50 | 8 | | | | | 8.4 |
| | 55 | | | | | | |
| | 60 | | | | | | |
| 300 | 30 | 10 | 10 | 9.0525 | 12.6 | 12.1 | 12.6 |
| | 35 | 12 | | | | | |
| | 40 | | | | | | |
| | 45 | | | | | | |
| | 50 | 10 | | | | | |
| | 55 | 12 | | | | | |
| | 60 | 10 | | | | | |

## *6.2 Three Bolt Case*

The corner square gusset plate of size 300 mm with diagonal member connected by three bolts is shown in Fig. 7. The pitch of the bolts is taken as 70 mm and edge/end distance as 50 mm. The analyses are carried out for tensile forces ($P$) of 100, 200, 300, 400, 500 and 600 kN and varying angle of inclination ($\Theta$) of diagonal/brace member. The results obtained from GMNA are presented in Table 4. A minimum of 8 mm thickness is assumed. The required thickness of gusset plates as per Raghupathi, Whitmore [11], IS/EC3 and AISC standards are also calculated and the maximum is specified as the design thickness as given in Table 5. The von Mises stress contour for load of 100 kN and brace angle 45° is depicted in Fig. 8. It can be observed that the maximum stress occurred at edge of lower bolt holes.

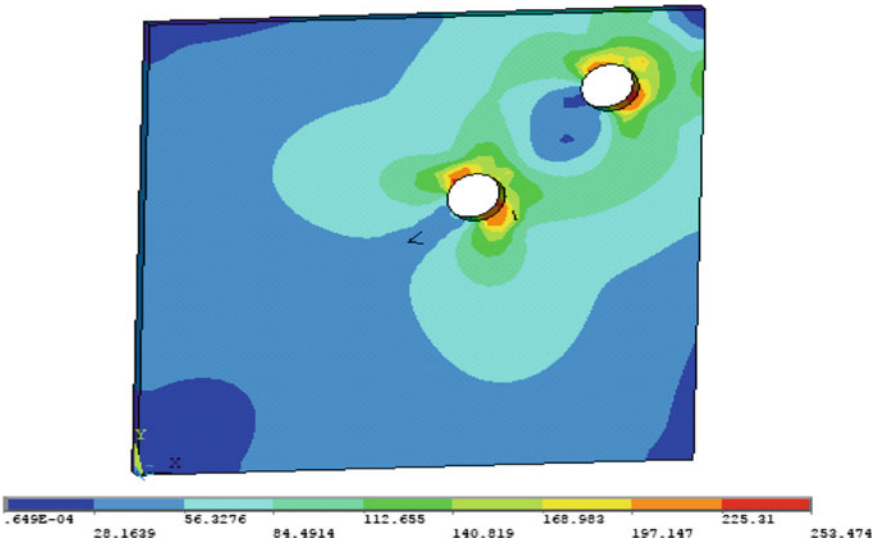


**Fig. 6** Von Mises stress ($\sigma_{vm}$) contour

**Fig. 7** Gusset plate connected to tension brace by three bolts

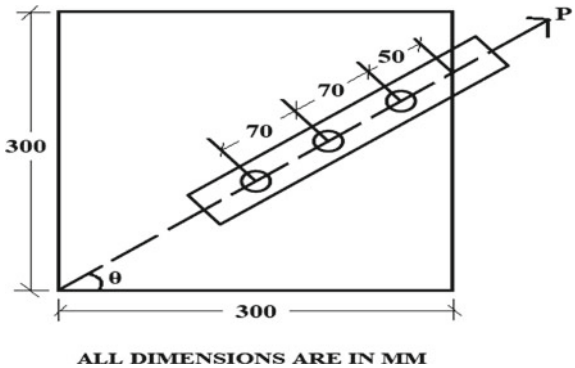


From Tables 4 and 5, the following inferences may be drawn.

- The required thickness of gusset plate depends upon the angle of inclination of brace as per GMNA.
- High discrepancy can be observed between the thicknesses of gusset plates required by GMNA, Whitmore and other design specifications.
- The design thicknesses of gusset plates for loads 100 kN, 200 kN, 300 kN, 400 kN, 500 kN and 600 kN are 8 mm, 10 mm, 12 mm, 16 mm, 20 mm and 24 mm, respectively.

**Table 4** Three bolt case—minimum thickness of gusset plate by GMNA

| Tensile force in brace (kN) | Brace angle (ϴ) | Bolt dia (mm) | $\sigma_1$ (N/mm$^2$) | $\sigma_{vm}$ (N/mm$^2$) | $\epsilon_{vps}$ | Thickness of Gusset (t), mm |
|---|---|---|---|---|---|---|
| 100 | 30 | M20 (SS) | 255.848 | 239.118 | 0.00143 | 8 |
| | 35 | | 259.793 | 238.034 | 0.001875 | |
| | 40 | | 240.6 | 232.071 | 0.001654 | |
| | 45 | | 266.816 | 243.769 | 0.001597 | |
| | 50 | | 264.349 | 240.046 | 0.002128 | |
| | 55 | | 268.656 | 247.82 | 0.002527 | |
| | 60 | | 275.767 | 255.399 | 0.001789 | |
| 200 | 30 | M20 (DS) | 364.088 | 350.658 | 0.100525 | 8 |
| | 35 | | 351.029 | 376.156 | 0.109114 | |
| | 40 | | 353.383 | 359.211 | 0.108719 | |
| | 45 | | 269.912 | 282.944 | 0.054771 | 10 |
| | 50 | | 364.641 | 369.839 | 0.095497 | 8 |
| | 55 | | 385.88 | 402.653 | 0.118609 | |
| | 60 | | 388.105 | 417.9 | 0.123553 | |
| 300 | 30 | M24 (DS) | 366.582 | 417.057 | 0.149066 | 10 |
| | 35 | | 408.926 | 421.841 | 0.141906 | |
| | 40 | | 363.895 | 350.467 | 0.091727 | 12 |
| | 45 | | 428.154 | 397.64 | 0.137957 | |
| | 50 | | 429.796 | 441.355 | 0.177427 | |
| | 55 | | 430.312 | 433.787 | 0.177608 | 10 |
| | 60 | | 443.579 | 431.613 | 0.160676 | |
| 400 | 30 | M24 (DS) | 357.473 | 382.388 | 0.12274 | 14 |
| | 35 | | 403.66 | 384.695 | 0.116469 | |
| | 40 | | 387.721 | 418.877 | 0.162272 | |
| | 45 | | 428.154 | 397.64 | 0.137957 | 16 |
| | 50 | | 416.81 | 424.774 | 0.157588 | 14 |
| | 55 | | 374.621 | 380.725 | 0.120311 | |
| | 60 | | 434.309 | 426.18 | 0.129064 | |
| 500 | 30 | M24 (DS) | 375.406 | 432.004 | 0.191961 | 16 |
| | 35 | | 411.604 | 434.311 | 0.167872 | |
| | 40 | | 381.877 | 382.397 | 0.141967 | 18 |
| | 45 | | 428.154 | 397.64 | 0.137957 | 20 |
| | 50 | | 412.159 | 425.395 | 0.13562 | 18 |
| | 55 | | 418.975 | 413.885 | 0.128632 | |
| | 60 | | 425.089 | 421.82 | 0.117709 | |

(continued)

**Table 4** (continued)

| Tensile force in brace (kN) | Brace angle (ϴ) | Bolt dia (mm) | $\sigma_1$ (N/mm$^2$) | $\sigma_{vm}$ (N/mm$^2$) | $\epsilon_{vps}$ | Thickness of Gusset (t), mm |
|---|---|---|---|---|---|---|
| 600 | 30 | M24 (DS) | 384.878 | 395.34 | 0.150911 | 20 |
| | 35 | | 408.926 | 421.841 | 0.141906 | |
| | 40 | | 379.836 | 372.765 | 0.131554 | 22 |
| | 45 | | 428.154 | 397.64 | 0.137957 | 24 |
| | 50 | | 409.853 | 422.927 | 0.127409 | 22 |
| | 55 | | 430.312 | 433.787 | 0.177609 | 20 |
| | 60 | | 443.579 | 431.613 | 0.160676 | |

where *SS* = single shear and *DS* = Double Shear

## 7 Conclusions

Nonlinear finite element analysis of a simple 2-D model of corner gusset plates connected to tension brace as in the case of a typical X-braced frame is performed for various angles of inclination of the brace and varying load range. It is assumed that the tension brace is connected to the gusset plate by single row of bolts only. Both two bolt and three bolt cases are considered. Required thickness of gusset plate to prevent failure was found as per nonlinear finite element analysis, Whitmore's theory and design provisions of American, European and Indian standard codes of practice. Significant discrepancy between the obtained results is observed. The maximum thickness from the adopted analysis procedures as mentioned earlier is specified as the design thickness of the gusset plate for each case. Also maximum von Mises stress was observed at bolt hole edges due to stress concentration effect for all the cases considered in the study. Though more accurate/realistic simulation, due consideration of effect of beam and column deformations/flexibility and extensive experimental validation is required, the presented results may serve as design aid to practicing structural engineers in design of gusset plate.

**Table 5** Three bolt case—design thickness

| Force in brace (kN) | Brace angle (ϴ) | Thickness of gusset plate (mm) | | | | | Design thickness (mm) |
|---|---|---|---|---|---|---|---|
| | | GMNA (ANSYS) | Raghupathi (1995) | Whitmore (1952) | IS/EC | AISC | |
| 100 | 30 | 8 | 8 | 1.508 | 2.1 | 2.01 | 8 |
| | 35 | | | | | | |
| | 40 | | | | | | |
| | 45 | | | | | | |
| | 50 | | | | | | |
| | 55 | | | | | | |
| | 60 | | | | | | |
| 200 | 30 | 8 | 8 | 3.0176 | 4.2 | 4.1 | 8 |
| | 35 | | | | | | |
| | 40 | | | | | | |
| | 45 | 10 | | | | | 10 |
| | 50 | 8 | | | | | 8 |
| | 55 | | | | | | |
| | 60 | | | | | | |
| 300 | 30 | 10 | 10 | 4.526 | 6.3 | 6.1 | 10 |
| | 35 | | | | | | |
| | 40 | 12 | | | | | 12 |
| | 45 | | | | | | |
| | 50 | | | | | | |
| | 55 | 10 | | | | | 10 |
| | 60 | | | | | | |
| 400 | 30 | 14 | 10 | 6.035 | 8.4 | 8.1 | 14 |
| | 35 | | | | | | |
| | 40 | | | | | | |
| | 45 | 16 | | | | | 16 |
| | 50 | 14 | | | | | 14 |
| | 55 | | | | | | |
| | 60 | | | | | | |
| 500 | 30 | 16 | 12 | 7.544 | 10.5 | 10.1 | 16 |
| | 35 | | | | | | |
| | 40 | 18 | | | | | 18 |
| | 45 | 20 | | | | | 20 |
| | 50 | 18 | | | | | 18 |
| | 55 | | | | | | |

(continued)

**Table 5** (continued)

| Force in brace (kN) | Brace angle (ϴ) | Thickness of gusset plate (mm) | | | | | Design thickness (mm) |
|---|---|---|---|---|---|---|---|
| | | GMNA (ANSYS) | Raghupathi (1995) | Whitmore (1952) | IS/EC | AISC | |
| | 60 | | | | | | |
| 600 | 30 | 20 | 12 | 9.053 | 12.6 | 12.1 | 20 |
| | 35 | | | | | | |
| | 40 | 22 | | | | | 22 |
| | 45 | 24 | | | | | 24 |
| | 50 | 22 | | | | | 22 |
| | 55 | 20 | | | | | 20 |
| | 60 | | | | | | |

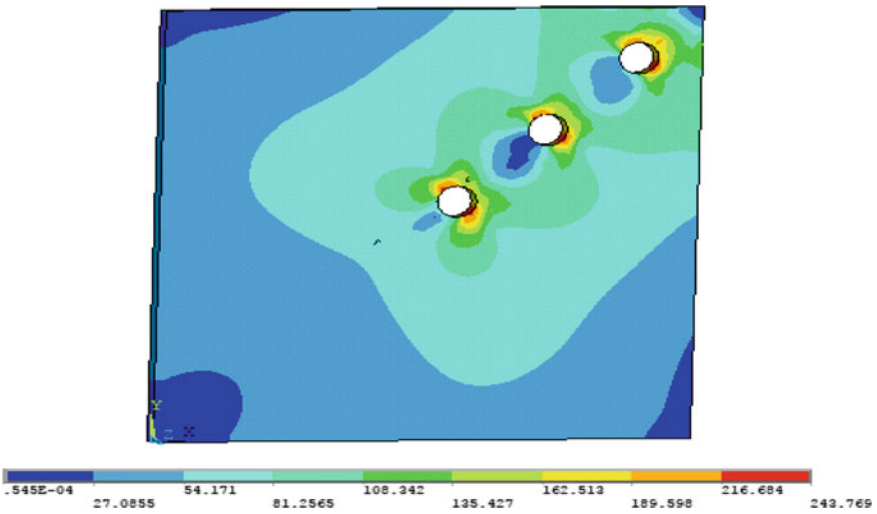


**Fig. 8** Von Mises stress ($\sigma_{vm}$) contour

## References

1. ANSI/AISC 360-16 (2016) Specification for structural steel buildings, Illions
2. Bjorhovde R, Chakrabarti SK (1985) Tests of full-size gusset plate connections. J Struct Eng ASCE 111(3):667–683
3. Bjorhovde R, Gerstle KH, Sigfusdottir A, Zitur JL (1994) Behavior and analysis of bracing connections for steel frames. J Constr Steel Res 30(1):39–60
4. ENV 1993-1-1 (1992) Eurocode 3: design of steel structures. ECS, Brussels
5. Hardash SG, Bjorhovde R (1985) New design criteria for gusset plates in tension. Eng J AISC 22(2):77–94
6. Hadianfard MA, Gholamim M, Hashemi A (2017) Numerical study on central gusset plates in inverted V-brace frames. Iran J Sci Technol Trans Civ Eng 41(4):433–439

7. IS 800:2007. General construction in steel—code of practice. BIS, New Delhi
8. Rosenstrauch PL, Sanayei M, Brenner BR (2013) Capacity analysis of gusset plate connections using the Whitmore, block shear, global section shear, and finite element methods. Eng Struct 48:543–557
9. Sai Vivek K, Sai Ram KS (2018) Design of steel Gusset Plates. J Struct Eng (Madras/India) 45(5):399–410
10. Vivek KS, Kusuma Lakshmi Priyanka U, Ravi Kumar Reddy C, Sai Ram KS (2019) Non-linear finite element analysis of mild steel gusset plates. Mater Today Proc 18(7):3726–3732
11. Whitmore RE (1952) Experimental investigation of stresses in gusset plates. Bulletin No. 16, Engineering Experiment Station, University of Tennessee, USA

# Performance Assessment of Steel Special Moment Resisting Frames Designed as Per IS 800:2007


**Sonu Patel and P. C. Ashwin Kumar**

**Abstract** Steel moment resisting frames are one of the most popular structural systems, which are used extensively for low to high-rise buildings in varying seismic regions around the world. Even though the use of structural steel in India is quite less in comparison to reinforced concrete structures, steel moment resisting frames are used extensively in industrial as well as commercial projects. The special steel moment resisting frames are a special category of this system, which are specifically detailed to undergo large inelastic cyclic deformation in regions of high seismicity. This paper addresses the design of special moment resting frame mentioned in Indian steel code IS 800:2007 and provides suggestions in terms of improving the inelastic response of the system. The limitations in terms of qualified and efficient Indian steel sections available for use in moment frames have been highlighted explicitly. Additionally, the inelastic cyclic performance of steel special moment resisting frames designed using Indian design code has been assessed under design basis and maximum considered earthquake hazard levels. Performance in terms of inter-storey drift, failure mechanism, material consumption, etc. has been compared to assess the design efficiency.

**Keywords** Special moment resisting frames · Earthquake · Inelastic performance

## 1 Introduction

Steel moment resisting frames are used widely across the world to resist gravity loads as well as lateral loads. The benefit of higher ductility, higher strength to weight ratio, lower construction time and availability of large open spaces have resulted in their popularity across the world. Even though concrete and masonry

S. Patel (✉) · P. C. Ashwin Kumar
Indian Institute of Technology Roorkee, Roorkee, India
e-mail: sonukrpatel007@gmail.com

P. C. Ashwin Kumar
e-mail: pcashwin.feq2018@iitr.ac.in



M. Madhavan et al. (eds.), *Proceedings of the Indian Structural Steel Conference 2020 (Vol. 1)*, Lecture Notes in Civil Engineering 318,
https://doi.org/10.1007/978-981-19-9390-9_45

are more popular building material in India, structural steel majorly in the form of moment resisting frame is widely used in Industrial and commercial structures due to the above mentioned advantages. Even though this amounts to a very small percentage of the structures, ductile special moment resisting frames (SMRF) can be a great alternative for reinforced concrete structures in the 58.6% of landmass in India affected by moderate to high seismic activities. SMRF, detailed to provide higher ductility, performs so through the inelastic deformation of frame elements, connection and panel zone at the beam-column joint. However, the lack of lateral stiffness in these structures results in large deformations, which majorly govern the design in comparison to strength requirements. Also, engineers during 1980s tried to economize their design by providing only a single bay of moment resistant framing on either side of the building. Research conducted over the years especially after the 1994 Northridge and 1995 Kobe earthquake showed that such buildings are prone to brittle fracture at their welded beam to column connections and have resulted in many changes in the design and connection detailing aspects of the SMRF, which has improved the inelastic performance of these structures [1, 9].

Indian standard on steel structures IS 800 [4] also provides guidelines on the design of special moment resisting structures. From grade of steel to be used for SMRF, target inelastic joint rotation capacity, location for construction, section compactness requirement and strong column-weak beam criteria are some of the guidelines given by Indian code to achieve significant ductility in regions of high seismicity. However, there have been very scarce amount of study to check whether these guidelines are adequate enough in the Indian scenario to achieve the required performance [3]. Hence, in this current study, an attempt has been made to study the inelastic performance of SMRF designed strictly as per IS 800 [2, 4, 8]. The study is currently directed towards structures with seismic mass at each floor, where details regarding hindrance to efficient design, lateral strength, failure mechanism, inter-storey drift ratio under design and maximum considered hazard level have been put forward for different configuration of SMRF buildings.

## 2 Description of Study Frames

In order to study the inelastic seismic performance of SMRF structures, a set of building configuration with variation in number of storeys and bay width has been considered. The details regarding the building geometry, design and numerical modelling have been provided in the sections below.

### *2.1 Building Geometry*

Figure 1 shows the plan of the building. All the frames are considered as lateral force resisting SMRF, which is in accordance with the general practice followed in India.

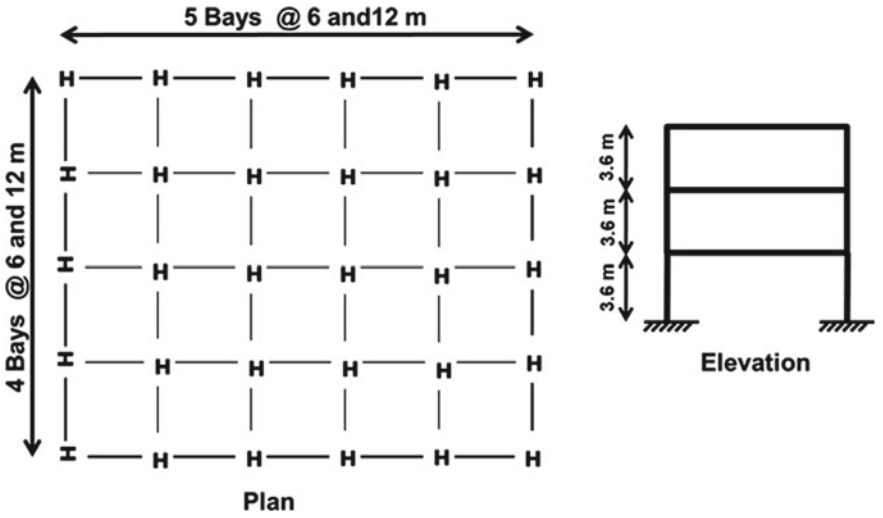


**Fig. 1** Building geometry details

The height of each storey has been fixed at 3.6 m. The number of storeys has been varied from 3, 6 and 9 to represent typical low to mid-rise structures. Two bay widths 6 and 12 m have been considered. These two values range the two extremities of SMRF or MRF bay widths as a higher value would lead to uneconomical sections and a lower value would shift the mechanism of energy dissipation from flexure to shear.

## *2.2 Design*

The study frames have been designed for a superimposed dead load and live load intensity of 4.65 kN/m$^2$ and 4.0kN/m$^2$ on each floor, respectively. This has been modified to 3.6 kN/m$^2$ and 2 kN/m$^2$, respectively, for the roof level. The design of the frames has been explicitly done using IS 800 [4] guidelines for SMRF. The building is considered to be located in Zone V and on medium soil to quantify the base shear as per IS 1893 [6]. The importance factor and response reduction factor have been considered as 1.2 and 5 as per code provisions [6]. The grade of steel has been considered as E250B steel [4, 7] for both beams and columns.

The compactness criteria to prevent local buckling in the individual sections have been followed as per IS 800 [4]. Since 'I' section is popularly used in India for moment resisting frames, codes specifying both tapered and parallel flange sections have been used for designing the different frames. This process of sorting sections which satisfy the compactness criteria as per IS 800 [4] brought out a significant disadvantage that there are very few sections that satisfy the criteria of plastic section

requisite for SMRF sections. Out of the total 257 specified sections sizes, including tapered (SP6(1)), narrow and wide parallel flange section [5] in the code, only 161 classify as plastic sections. This means that nearly 37% of the steel sections, which includes higher cross section depth sections also, cannot be used in SMRFs. This problem is compounded by the fact that the section properties of available Indian section are quite low in comparison to American sections. Figure 2a shows the comparison of section modulus of Indian and American section which highlights this disparity. Even though the depth of Indian 'I' sections are equally matched by their American sections, the availability of large number of sections with different section modulus for the same total depth of the section is advantageous in providing large open spaces in a building. Additionally, in the Indian scenario where all frames are considered as lateral load resisting frames, the moment of inertia along major and minor axis matters significantly in the design of the sections. Figure 2b shows the ratio of moment of inertia values along major and minor axis for Indian and American 'I' sections. It can be observed that in case of Indian sections, there are very few sections having nearly equal value of moment of inertia along both axis. This is not a concern for American designs, where SMRFs are provided mostly along the periphery. However, in case of Indian sections, the guideline provided to achieve strong column-weak beam criteria will thus lead to oversizing of columns, especially due to connections of beams perpendicular to the minor axis of the column. The final section size of the beams and columns thus obtained for each frame has not been included here, but the change in the steel consumption by opting for Indian or American steel section for the same frame has been highlighted in Table 1. It can be noticed the percentage overall reduction in consumption of steel by choosing American section is as much as 28%. This situation can be easily improved by meeting the required needs for such SMRFs at the manufacturing stage itself, which can go a long way in reducing the cost of construction and popularizing steel usage in India.

### 2.2.1 Numerical Modelling

The numerical modelling of the frames has been carried out using SAP 2000 software. Only the two dimensional model of an interior frame has been considered for the analysis. Frame elements have been used to model the beams and columns. Centerline model of each frame has been created by neglecting the effect of panel zone action. Rigid connection has been assumed between the beams and columns. Lumped plastic hinges have been assigned in beams (M3 hinges) and columns (P-M3) to capture inelasticity in the elements. The properties of lumped plastic hinges have been taken from FEMA 356 due to lack of data on the inelastic performance of Indian steel sections. Due to design requirement and unavailability of plastic sections, built- up sections have been used even for low-rise SMRFs. Since the inelastic response of built-up column sections is not available, the FEMA 356 criteria have been applied to a hypothetical 'I' section column with required cross-sectional properties, which satisfied the strength criteria.

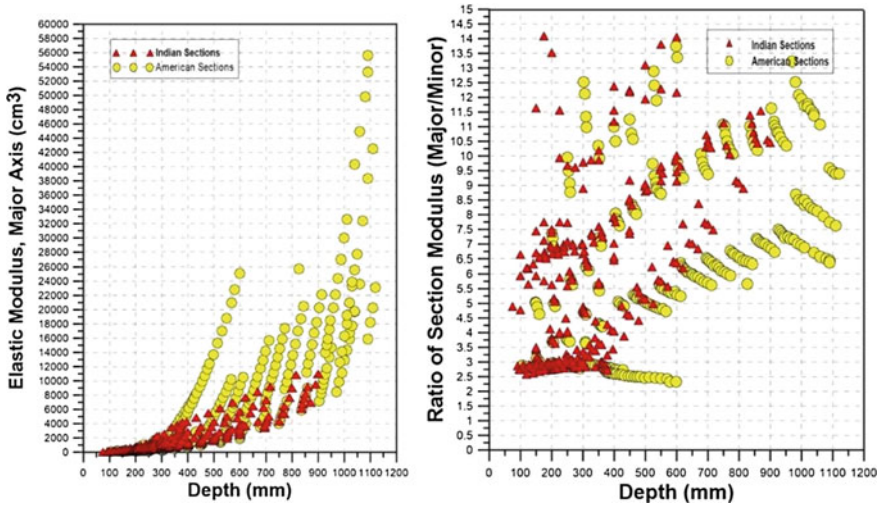


**Fig. 2** **a** Comparison of elastic modulus of Indian and American 'I' sections and **b** Comparison of ratio of major and minor axis of Indian and American 'I' sections

**Table 1** Comparison of steel consumption for SMRFs with Indian and American sections

| Study frame | Total mass (Indian) (kg) | Total mass (American) (kg) | % mass reduction in beams | % mass reduction in columns | % overall reduction |
|---|---|---|---|---|---|
| 3 storey–6 m bay | 15,795.6 | 11,887.2 | 35.0 | 15.7 | 24.7 |
| 3 storey–12 m bay | 67,124.2 | 61,178.4 | 9.7 | 7.5 | 8.9 |
| 6 storey–6 m bay | 41,982.1 | 30,060.0 | 32.7 | 25.5 | 28.4 |
| 6 storey–12 m bay | 196,837.1 | 147,168.0 | 16.5 | 32.8 | 25.2 |
| 9 storey–6 m bay | 69,406.3 | 55,731.6 | 35.6 | 8.4 | 19.7 |
| 9 storey–12 m bay | 254,554.6 | 224,868.0 | 6.9 | 17.1 | 11.7 |

# 3 Results

## *3.1 Nonlinear Static Analysis*

Nonlinear static pushover analysis has been conducted on all six study frames. The hinge mechanism in all the frames majorly highlighted the strong column-weak beam characteristics as is expected by following the code guidelines. However, as shown in Fig. 3, the nonlinear static pushover plots showed very high over-strength values, especially for the 12 m bay width frames. The design base shear as calculated using equivalent lateral force method has been shown in the graph to highlight this large difference. This can be attributed to achieving compactness criteria requirement for the different cross section and also on the limited number of Indian cross sections available. Additionally, the criteria meant to satisfy the strong column-weak beam also increase the cross section sizes, especially for the 12 m span. The average over-strength is found to be 1.6 for the 6 m bay width frames, whereas it is 2.7 for the 12 m bay width frames.

## *3.2 Nonlinear Dynamic Analysis*

Nonlinear dynamic analysis has been performed to assess the performance of the SMRFs under an ensemble of spectrum compatible ground motions. Figure 4 shows the target design basis earthquake (DBE) and maximum considered earthquake (MCE) target spectrum along with the mean response spectrum of 7 ground motions.

The inter-storey drift (IDR) ratio representing the damage in the structural members has been presented in Fig. 5 for all the frames. The results show higher but permissible inter-storey drifts in 6 m bay width SMRFs of all heights where as a stiffer response in the case of 12 m bay width frames. This can be attributed again to the increase in the section sizes due to the compactness and design criteria mentioned before. The mean and mean plus one standard deviation of the results have been given for both DBE and MCE hazard levels, and the results are observed to be satisfactory. There is no occurrence of storey mechanism at any floor except an anomaly at first floor of 9 storey 12 m bay width frame.

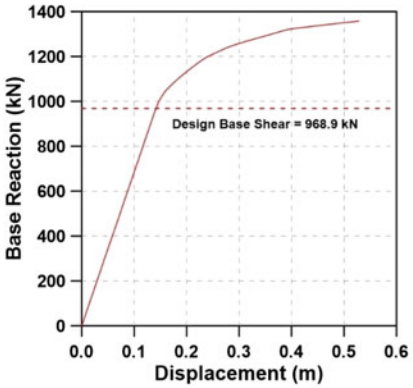


(a) 3 Storey-6 m Bay

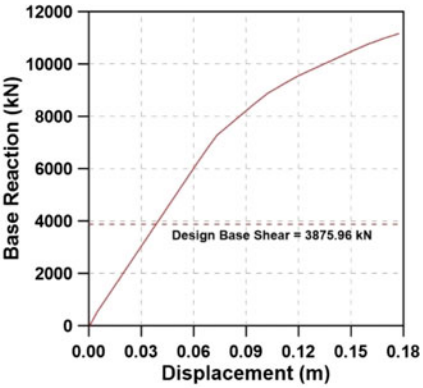


(b) 3 Storey-12 m Bay

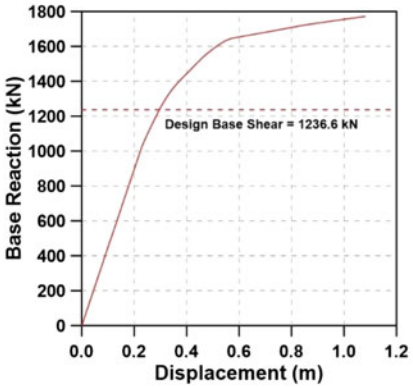


(c) 6 Storey-6 m Bay

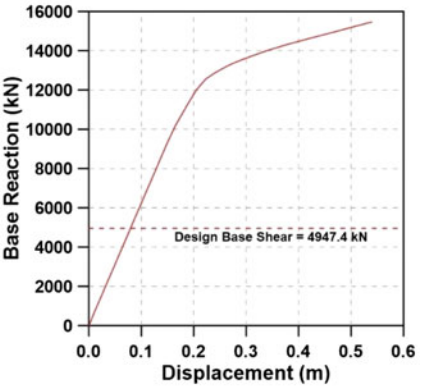


(d) 6 Storey-12 m Bay

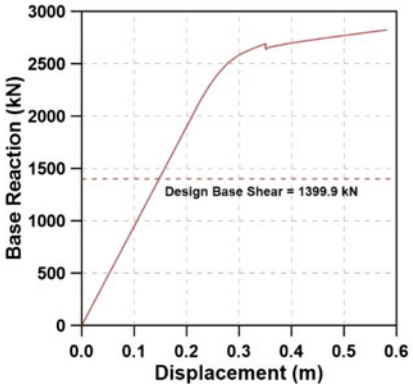


(e) 9 Storey-6 m Bay

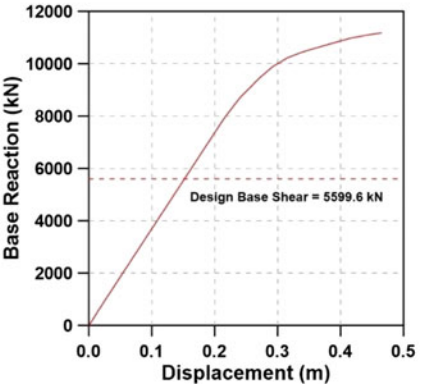


(f) 9 Storey-12 m Bay

**Fig. 3** Nonlinear static analysis results

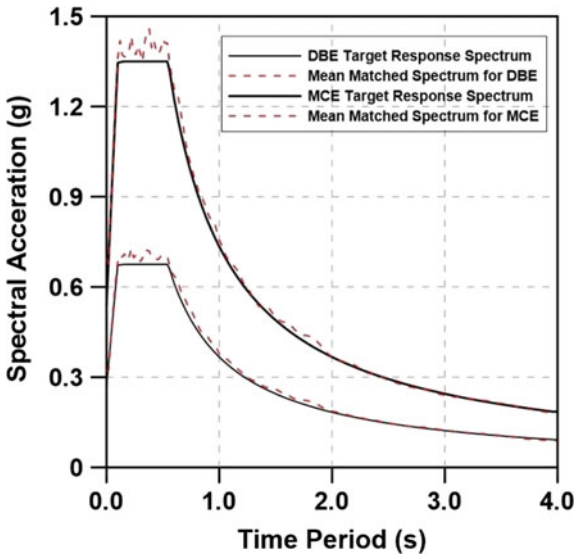


**Fig. 4** Target and mean response spectrum

## 4 Conclusion

The study on SMRFs designed explicitly using IS 800 [4] and assessed using nonlinear static and dynamic analysis highlighted significant results.

- The number of Indian section available for use in SMRFs is very small due to insufficient compactness ratios. This factor has contributed partially in increasing the steel consumption in the design frames to as much as 28% in comparison to the case if American section was utilized.
- Due to the design guidelines as well as unavailability of sections qualifying the compactness criteria, the study frames showed very high over-strength factor, namely 1.61 in 6 m bay width and 2.65 in 12 m bay width frames.
- The hinge mechanism observed in the SMRFs designed using the code displayed the desired strong column-weak beam characteristics.
- The IDR of different frames also highlighted the desired performance of the SMRF. However, this ideal response has been obtained at the expense of using heavy sections.
- Production of ideal cross section sizes for Indian SMRF is required urgently to increase the consumption of steel in sectors like construction in high seismic regions where ductility of steel can be more advantageous in comparison to other building materials.

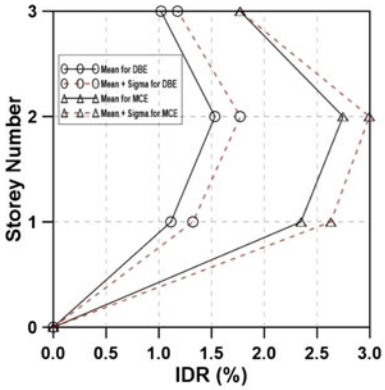


(a) 3 Storey-6 m Bay

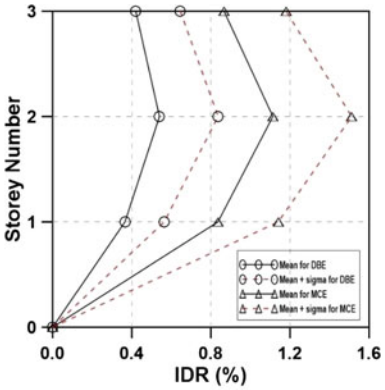


(b) 3 Storey-12 m Bay

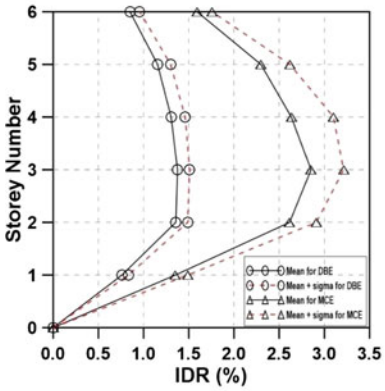


(c) 6 Storey-6 m Bay

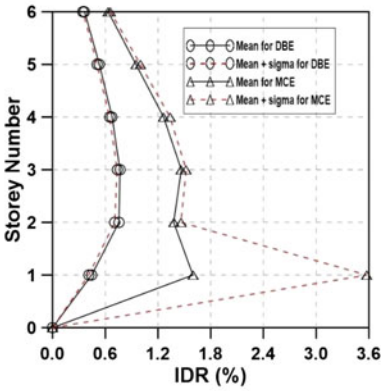


(d) 6 Storey-12 m Bay

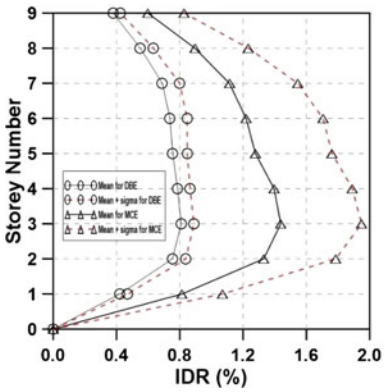


(e) 9 Storey-6 m Bay

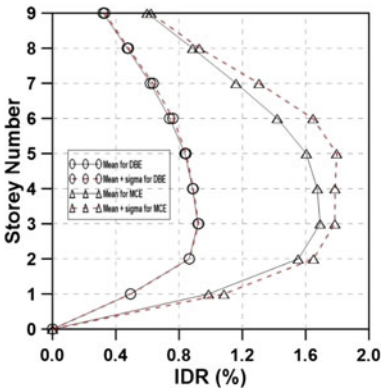


(f) 9 Storey-12 m Bay

**Fig. 5** Inter-storey drift ratios for all study SMRFs

## References

1. Bruneau M, Uang CM, Whittaker A (2011) Ductile design of steel structures. MaGraw-Hill Companies Inc., NY, USA
2. FEMA 356 (2000) Prestandard and commentary for the seismic rehabilitation of buildings. Federal Emergency Management Agency, Washington, DC
3. Goswami R, Arlekar JN, Murthy CVR (2006) Limitations of available Indian hot-rolled I-sections for use in seismic steel MRFs. NICEE report. Indian Institute of Technology Kanpur, pp 1–23
4. IS800 (2007) General construction in steel-code of practice. Bureau of Indian Standards, New Delhi
5. IS12778 (2004) Hot rolled parallel flange steel sections for beams, columns and bearing piles—dimensions and section properties. Bureau of Indian Standards, New Delhi, India
6. IS1893 (2016) Criteria for earthquake resistant design of structures—part 1 general provisions and buildings. Bureau of Indian Standards, New Delhi
7. IS2062 (2011) Hot rolled medium and high tensile structural steel—specification. Bureau of Indian Standards, New Delhi, India
8. SP6(1) (1964) Indian standard handbook for structural engineers: structural steel. Bureau of Indian Standards, New Delhi
9. Subramanian N (2011) Steel structures-design and practice. Oxford University Press

# Analytical Behavior of Steel Hybrid Girder with Opening in Web


**Giridhar N. Narule, Samadhan G. Morkhade, and Sandhya R. Kumbhar**

**Abstract** When plate girders are made up using plates of different strength in flanges and web, they are called hybrid plate girders. Increased use of hybrid beams is a condensing cost of steel structure and enhances the load-carrying capacity. The flanges are made of high-performance steel (HPS) of grade 460 Mpa and a web of lesser grade 345 Mpa. The analytical test has been carried out on twelve I-shaped girders in which six with a hybrid and six with a homogenous section. The analysis has implemented three-dimensional nonlinear finite-element models. Finite-element modeling of steel girder with or without opening is studied using ANSYS 12.0. The high-performance steels (HPS) have excellent stiffness and weldability, crack resistance features with having high yield strength. The analytical models consist of steel girders with a hexagonal web opening, without opening reinforcement. Opening in the beam is adaptable for its high strength to weight ratio and increase in depth of section without any further weight. So, that lighter section can be considered with consequent cost saving. Results are presented in terms of load–deflection behavior, failure mode and von Mises stress concentration. From the analytical results, it has been observed that the hybrid girder has a higher load-carrying capacity when compared with homogenous specimens.

**Keywords** Hybrid girder · Finite-element analysis · Von Mises stress · Load–deflection behavior

## 1 Introduction

Hybrid steel girders are made up of plates with different steel grades in flanges and webs. Steel hybrid girder is economical over the long lengths of the member and enhances the load-carrying capacity. In hybrid girders, generally, flanges have high

G. N. Narule (✉) · S. G. Morkhade · S. R. Kumbhar
Department of Civil Engineering, Vidya Pratishthan's Kamalnayan Bajaj Institute of Engineering and Technology, Baramati, Pune, India
e-mail: gnnarule@gmail.com



M. Madhavan et al. (eds.), *Proceedings of the Indian Structural Steel Conference 2020 (Vol. 1)*, Lecture Notes in Civil Engineering 318,
https://doi.org/10.1007/978-981-19-9390-9_46

strength as compared to the web. The beam is designed for bending and deflection and flange resist bending; hence, high strength flanges are used. As the web carries the shear force, there is no requirement of high strength web. Steel structures are advantageous due to their durability, design, low cost and precise manufacturing. Beam with web opening has verified to be efficient for moderately loaded longer span where the design is controlled by moment capacity or deflection. There are several benefits of steel beams with web openings. This reduces the height of the building as the clear space between the ceiling and the floor reduces as compared with the conventional method wherein the services are placed below the beams. Opening in the beam is adaptable for its high strength to weight ratio and increase in depth of section without any further weight. So, that lighter section can be manufactured. Morkhade et al. studied the effect of web opening on the flexural behavior of hybrid beams using steel of nominal yield stress of 410 MPa and 250 MPa for flanges and web, respectively. The study included the failure modes, load–deflection behavior of samples and stress concentration with deviation in size, shape and position of openings. The parametric study showed that there is a 40% increase in strength for the castellated hybrid beams over the homogeneous beams. Su-Chan Jun et al. observed the flexural behavior of high strength steel hybrid composite beams in two phases. The design of hybrid composite beams utilizing high strength steels ( $fy = 650$ MPa) was done by the plastic stress design method. Beams were testing in two phases to maximize their flexural behavior. In phase I, the specimens were unable to attain plastic moment due to longitudinal shear failure along the axis of the beam. In phase II testing, specimens had been designed with shear reinforcement show no longitudinal shear cracking and evolved their plastic capacity. Wang et al. presented the flexural behavior of ductility of height performance girders. The test result indicates that the effectiveness of lateral braces influenced by the locations and number, which in turn affect the expansions of plastic fields. The slenderness of element is the major issue distressing the flexural capacity and ductility of a girder. Mehdi et al. studied the flexural strength of hybrid steel I-beams based on slenderness in which a new method to govern moment resistance of I-beams with hybrid and homogeneous sections depends on a design procedure independent from the section classification, considering local and overall interaction instabilities of beams. Six full-scale I-shaped beams, with hybrid sections and homogeneous sections, made up of high-strength steels, were tested for flexure to verify numerical models. The study based on the current design procedure of steel members subjected to bending. A relative study was performed between the proposed method with EC3 and AISC. Darehshouri et al. presented a simple analytical method to determine the shear strength of the girder. The method considered the effects of composite action between the concrete deck and steel part of the girder and the presence of openings in the web. Results for circular, square and rectangular openings revealed that the ultimate shear capacity is prejudiced significantly with the size of the openings, nearly 30% drop when the depth of openings is improved to half the web depth of the girder. Openings with larger depth display the larger drop in shear resistance. Ellobody et al. studied the effects of change in cross-sectional geometries, beam length and steel strength. The parametric study revealed that the presence of web distortional buckling causes a considerable decrease

in the failure load of the slender castellated beam. It is also exposed that the use of high strength steel offers a considerable increase in the failure load of less slender castellated beams. Hagen et al. carried out numerical simulations in order to provide data for the development of a design model for the shear capacity of steel girders with web openings, with and without transverse stiffeners and opening reinforcements. The numerical model was designed such that the girder is in a state of pure shear at the opening center. Analytical results were offered in terms of ultimate shear capacity and distribution of transverse web deformations and von Mises stresses. Veljkovic et al. presented the resistance in bending the ultimate limit state affected by local yielding of the web which limits the stresses on the web. Euro code 3 states a restriction for the limit state of fatigue that the stresses range should not exceed 1.5 times of yield stress. A hybrid steel girder is a welded girder with different steel grades in flanges and the web. Such girders are more economical than homogenous girders. Castellated hybrid girder is favorable owing to the dual benefits of a hybrid section and opening provided on the web.

A castellated beam is manufactured by cutting the pattern along the length across two different halves and then welding them together to form a single expanded beam. The two halves are combined together by welding and the high points of the web pattern are attached together to form a castellated beam. They are used in a commercial and industrial building, warehouse and portal frames. These are also efficiently used as a part of cranes, crane girders, towers, secondary members and deck stiffeners in bridges. These types of girders are widely used in car parks and sports stadiums.

The analysis has implemented three-dimensional nonlinear finite-element models. Finite-element modeling of steel girder with or without opening has been studied using ANSYS 12.0. The flanges are made of high strength steel of grade 460 MPa and a web of lesser grade 345 MPa. The material properties of FE models were the same for all beams. Linear elastic properties of the material were taken as 200 GPa for young modulus and 0.3 for Poisson's ratio. Results are presented in terms of Load–deflection behavior and von Mises stress concentration. A comparative study has been performed on homogenous and hybrid girders with or without opening in the web. From the analytical results, it has been observed that the hybrid girder has a higher load-carrying capacity when compared with homogenous specimens.

Since the last century, castellated beams have been used widely due to their several applications. But the study is restricted to a homogenous section only. The objective of the work is to study the load-carrying capacity of the hybrid section with the castellated opening. Research paper throws light on load–deflection behavior of hybrid and homogenous sections. The investigation was carried out using the commercial FEA software ANSYS 12.0.

## 2 Parametric Study

The analysis has been conducted by using ANSYS version 12.0. Four-nodded shell 181element with reduced integration points which has six degrees of freedom per node is used for geometric as well as material nonlinearity considered in the beams model and analyzed by using iterations according to Newton–Raphson. The analysis work was carried out using the initial imperfection of $L/1000$. The objective of this section is to carry out nonlinear finite-element analysis of the steel beams with web openings in order to fix their ultimate load-carrying capacity and displacement values to point loading. The finite-element method has been used to envisage their entire response to increasing values of external loading until they lose their load-carrying capacity.

The mid-span deflection is to be taken as the displacement of span along *y*-direction after applying the load of 1000 kN on both plain web beam and castellated web beam of hybrid and homogenous section. The boundary conditions used in the model are one end hinge supported and other roller conditions and load applied at the center as shown in Fig. 1. Figure 2 shows the deflection of the homogenous and hybrid girder. The three-point loading condition has the load applied at the mid-span of specimens to determine their ultimate load-carrying capacity for comparison. The data has been used in the modeling and analysis of homogenous and hybrid steel girder as summarized in Table 1.


**Fig. 1** Boundary condition and loading applied to the FE model

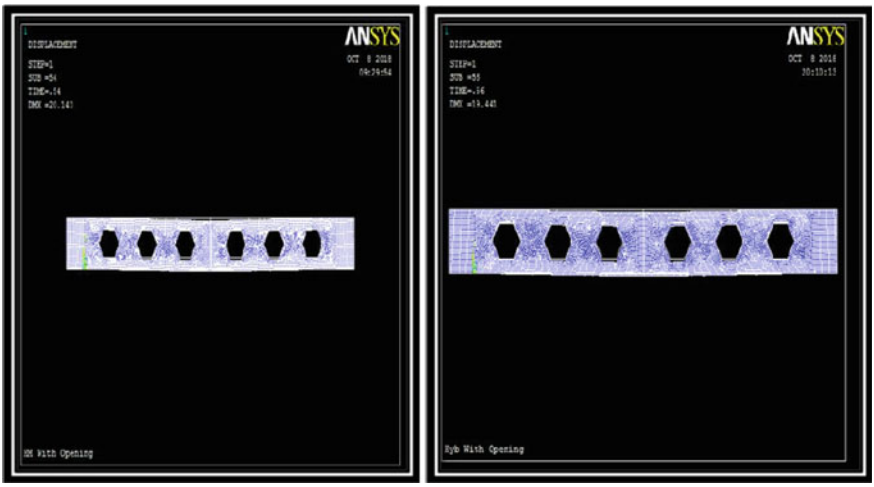


**Fig. 2** Deflection of homogenous girder and hybrid girder with opening

**Table 1** Material properties used in finite-element analysis

| Types of sections | | Young's modulus $E$ (N/mm$^2$) | Poisson's ratio $\mu$ | Yield stress ($\sigma y$) (N/mm$^2$) |
|---|---|---|---|---|
| Homogeneous beam | Flange and web | $2 \times 10^5$ | 0.3 | 460 |
| Hybrid beam | Flange | $2 \times 10^5$ | 0.3 | 460 |
| | Web | $2 \times 10^5$ | 0.3 | 345 |

## 3 Result and Discussion

In this study, there are twelve specimens, six with homogenous section and six with a hybrid section as summarized in given Table 2, and were considered to investigate the effects of loading condition and applied load–deflection relationships for the girders. Table 1 shows the values of the ultimate load obtained using the ANSYS for both hybrid and homogeneous beams. The ratio indicates that on an average, minimum of more than 10% increase in ultimate load using hybrid beams. They are classified according to high-performance steel and opening provided in the web. The ultimate load and maximum deflection of homogenous steel girder and hybrid steel girder with and without opening are given in Table 2. Figure 4 demonstrates that the hybrid girder without opening carries a 620 kN load at 17.17 mm deflection, whereas homogenous girder without opening carries a 510 kN load at 15.96 mm deflection. It displays that a hybrid girder carries a greater load as compared to the homogenous girder. But in Fig. 5, hybrid section without opening (680kN) carries lesser load as compared to homogenous ones(700kN). Otherwise, in all comparison, Figs. 4, 5, and 6 hybrid sections give better results than the homogenous section

in all aspect. The load and mid-span vertical deflection curves using finite-element analysis are as shown in Fig. 4 for the homogenous and hybrid beam with hexagonal web openings. von Mises stress distribution is shown in Fig. 3 for the single point loading and boundary condition. The predominant modes of failure observed in Fig. 3 around the opening. These are the formation of plastic hinges around the openings called the Vierendeel mechanism. It is observed from the analytical results that the hybrid girder has a higher load-carrying capacity when compared with homogenous specimens in both conditions.

**Table 2** Ultimate loads and deflections

| Sp no | Section type | Thickness of flange (mm) | Thickness of web (mm) | Total height (mm) | Ultimate deflection (mm) | Ultimate load (kN) | Ratio |
|---|---|---|---|---|---|---|---|
| 1 | Homogenous HM-1 | 11.90 | 7.87 | 381.20 | 15.96 | 510 | 1.21 |
| 2 | Hybrid Hyb-1 | 12.60 | 7.83 | 383.70 | 17.17 | 620 | |
| 3 | Homogenous HM-2 | 11.85 | 7.82 | 382.20 | 16.95 | 700 | -1.05 |
| 4 | Hybrid Hyb-2 | 12.68 | 7.79 | 384.20 | 11.26 | 680 | |
| 5 | Homogenous HM-2 | 12.56 | 7.94 | 622.10 | 7.97 | 645 | 1.12 |
| 6 | Hybrid Hyb-2 | 12.63 | 7.93 | 623.40 | 8.90 | 720 | |
| 7 | Homogenous HM-1-CO | 11.90 | 7.87 | 381.20 | 39.42 | 490 | 1.16 |
| 8 | Hybrid Hyb-1-CO | 12.60 | 7.83 | 383.70 | 33.27 | 570 | |
| 9 | Homogenous HM-2-CO | 11.85 | 7.82 | 382.20 | 20.14 | 540 | 1.04 |
| 10 | Hybrid Hyb-2-CO | 12.68 | 7.79 | 384.20 | 19.41 | 560 | |
| 11 | Homogenous HM-3-CO | 12.56 | 7.94 | 622.10 | 9.42 | 615 | 1.10 |
| 12 | Hybrid Hyb-3-CO | 12.63 | 7.93 | 623.40 | 10.22 | 675 | |

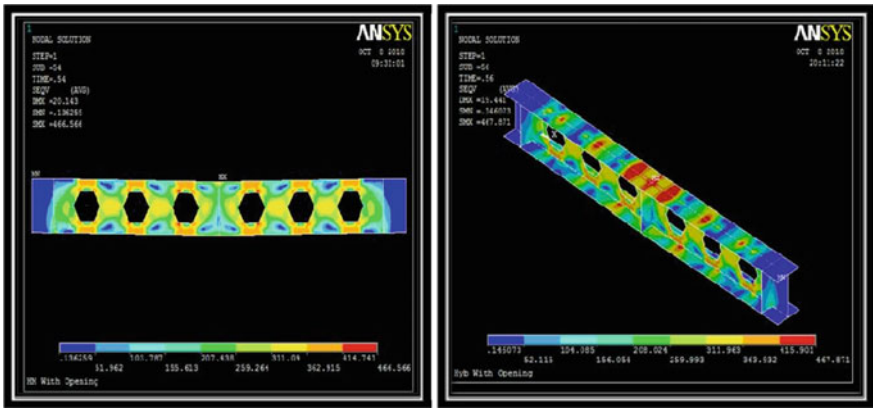


**Fig. 3** Von Mises stress distribution for homogenous girder and hybrid girder with opening

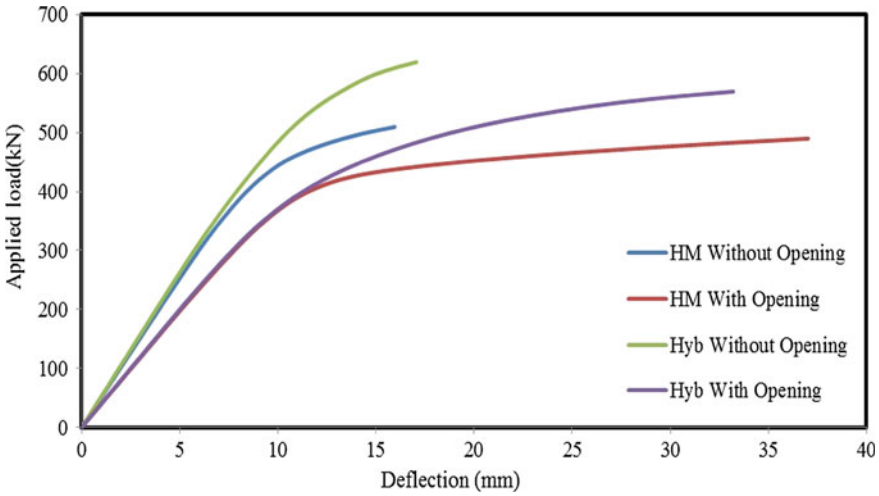


**Fig. 4** Load–deflection curve for homogenous and hybrid girder with or without opening (HM-1, HM-1-CO, Hyb-1 and Hyb-1-CO)

## 4 Concluding Remarks

The behavior of I section girder involves comparative study between homogenous girder and hybrid girder with plain web and opening provided in web. Based on analytical results, the following conclusions are given:

- The hybrid girder has higher load-carrying capacity when compared with homogenous specimens in both conditions.

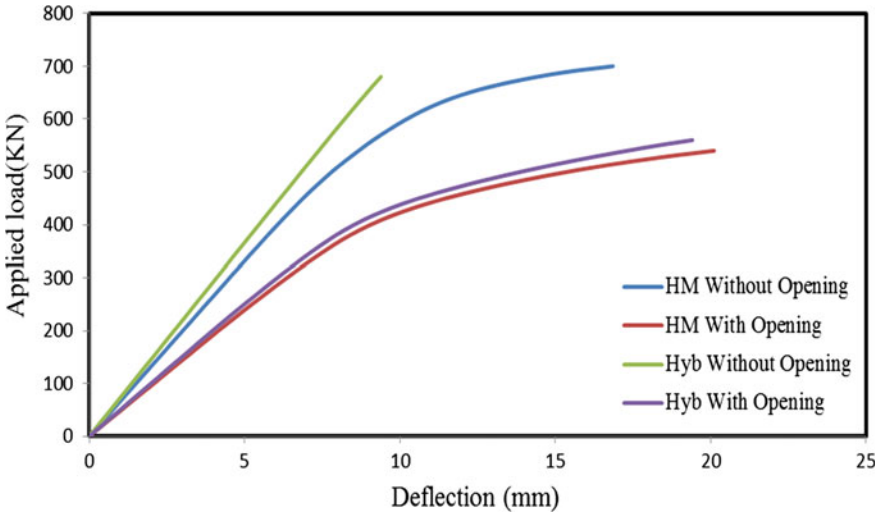


**Fig. 5** Load–deflection curve for homogenous and hybrid girder with or without opening (HM-2, HM-2-CO, Hyb-2 and Hyb-2-CO)

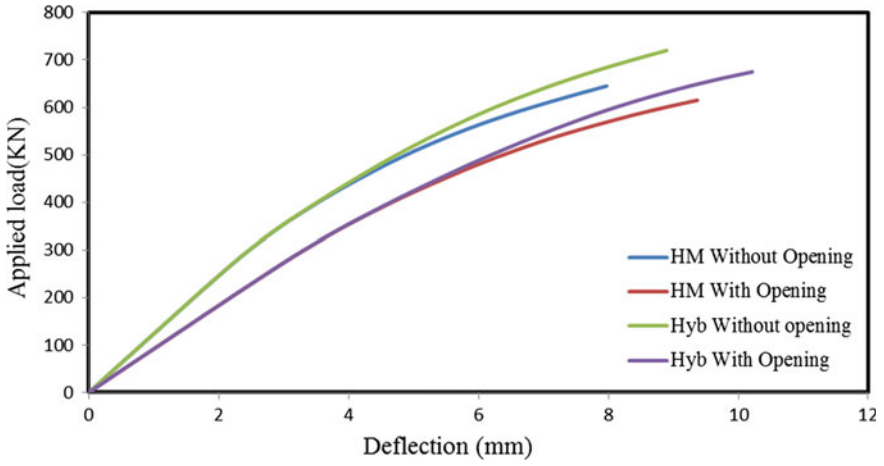


**Fig. 6** Load–deflection curve for homogenous and hybrid girder with or without opening (HM-3, HM-3-CO, Hyb-3, Hyb-3-CO)

- The hybrid girder gives better performance based on the load-carrying capacity, shear stress distribution and von misses stress distribution along the web.
- As per analytical work, the steel beam of the homogenous and hybrid section with castellated web openings hybrid girders with flanges of HSS and web of lower steel grade is more economical than homogenous girders.

- The ratio indicates that on an average, minimum of more than 10% increase in ultimate load using hybrid beams. So, the hybrid girder has a higher load-carrying capacity when compared with homogenous specimens in both conditions.
- The failure modes are found to be similar in both homogeneous and hybrid girder.

## References

1. Morkhade SG, Kshirsagar M, Dange R, Patil A (2019) Analytical study of effect of web opening on flexural behavior of hybrid beams. Asian J Civ Eng 20(4):537–547
2. Morkhade SG, Gupta LM (2019) Ultimate load behaviour of steel beams with web openings. Aust J Struct Eng 20(2):124–133
3. Morkhade SG, Baswaraj SM, Nayak CB (2019) Comparative study of effect of web openings on the strength capacities of steel beam with trapezoidally corrugated web. Asian J Civ Eng 20:1089–1099
4. Jun S-C, Lee C-H, Han K-H, Kim J-W (2018) Flexural behavior of high strength steel hybrid composite beams. J Constr Steel Res 149:269–281
5. Morkhade SG, Shaikh S, Kumbhar A, Shaikh A, Tiwari R (2018) Comparative study of ultimate load for castellated and plain webbed beam. Int J Civ Eng Technol 9(8):1466–1476
6. Morkhade SG, Gupta LM (2017) Experimental investigation for failure analysis of steel beams with web openings. Steel Compos Struct 23(6):647–656
7. Wang C-S, Duan L, Frank Chen Y, Wang S-C (2016) Flexural behavior and ductility of hybrid high performance steel I-girders. J Constr Steel Res 125:1–14
8. Shokouhian M, Shi Y (2015) Flexural strength of hybrid steel I-beams based on slenderness. Eng Struct 93:114–128
9. Ellobody E, Young B (2015) Nonlinear analysis of composite castellated beams with profiled steel sheeting exposed to different fire conditions. J Constr Steel Res 113:247–260
10. Darehshouri SF, Shanmugam NE, Osman SA (2013) An analytical method for ultimate shear strength of composite plate girder with web openings. Eng Struct 56:610–620
11. Hagen NC, Larsen PK, Aalberg A (2009) Shear capacity of steel plate girder with large web opening, part I: modeling and simulations. J Constr Steel Res 65:142–150
12. Veljkovic M, Johansson B (2004) Design of hybrid steel girders. J Constr Steel Res 60:535–547

# Analysis of Steel Columns in Fire with Varied End Restraints


**Rakshith B. Devaraj and Suneel M. Kumar**

**Abstract** Steel columns subjected to fire are prone to significant variation of boundary restraints while being exposed to fire loading. This paper presents the effect of end restraints on the behavior of hot rolled steel columns under uniform temperature profile (ISO 834-1: 1999) studied numerically. Nonlinear finite-element analysis was done using ABAQUS. Typical slenderness ratio (39), pre-applied axial load ratio (0.2, 0.4 and 0.6) and pre-applied moment ratio (0.1, 0.15 and 0.2) were considered in the present study. In addition to the above, constant axial restraint ratio (0, 0.2, 0.4 and 0.6) within the range as reported in Broadgate phase-8 fire report (0.1–0.9) and varying rotational restraint ratio (0, 2.81, 5.45 and 20.66) with increase in temperature as observed from Cardington test (1998) are used in the analysis. Based on one hundred and forty four trials done, buckling and critical temperature was plotted to assess the interactive effect of various parameters mentioned above.

**Keywords** Axial restraint · Buckling temperature · Critical temperature · Fire · Rotational restraint

## 1 Introduction

The behavior of steel structure subjected to fire is complex as compared under the action of gravity load. This is due to variation of internal resistance and external load with respect to temperature and time. In addition to time dependent factors, combination of mechanical properties at elevated temperature affects the strength, and thereby, reduction occurring due to temperature for varied end restraints is difficult to understand the behavior. To assess the actual behavior, large-scale testing

R. B. Devaraj · S. M. Kumar (✉)
Department of Structural and Geo-Technical Engineering, School of Civil Engineering, Vellore Institute of Technology, Vellore 632014, India
e-mail: suneelkumar.m@vit.ac.in

R. B. Devaraj
e-mail: rakshith.bd@vit.ac.in



M. Madhavan et al. (eds.), *Proceedings of the Indian Structural Steel Conference 2020 (Vol. 1)*, Lecture Notes in Civil Engineering 318,
https://doi.org/10.1007/978-981-19-9390-9_47

and analysis are necessary. In a building fire, the behavior of column is critical with end restraints, axial load, moment and variation of temperature that causes strength reduction. It is only a matter of fire location which decides the contribution of above parameter individually (or) combinedly that affects the performance of the structure. A steel column at a top floor corner may have greater failure temperature since it is free to expand or rotate as compared to that of interior ground floor column which is restrained against free movement. The location of fire in addition to the location of columns decides the collapse behavior of the building. However, based on the design requirement; interior column may have greater sections as compared to terrace columns. Hence, it becomes pivotal to study the effect of axial and rotational restraints that governs the structural performance of column. By the above intuition, one may arrive to conclusion that a weak column with strong restraints tend to fail earlier as compared to strong column with weak restraints. But, before arriving to this conclusion, it is important to understand that the end restraints which are responsible for premature buckling will also help in stabilizing the column by re-distributing the forces of fire affected column. If fire ceases at this stage, the column may regain its strength while cooling down and start contributing to take a fraction of load it was intended to take.

During fire, beam-column connections encounter heating and cooling. In both the stages, change in mechanical properties leads to variation in rotational stiffness. This change may be due to various effects such as reduction in strength, non-uniform thermal expansion, creep. However, individual contribution is difficult to assess, but the result of change in degree of restraint over temperature is used to assess the behavior of column due to varied end restraints. Cardington fire test (1998) is a classical bench mark full scale fire test made of simple construction and was conducted at UK Building Research and Establishment, Rotherham. Four test data consisting of (a) restrained beam, (b) plane frame, (c) compartment fire and (d) demonstration fire are studied to understand the actual rotation that occurred at joint with increase in temperature based on clinometer reading (Fig. 1a). The variation of rotation with increase in temperature was observed in plane frame test and found to be nonlinear (Fig. 1b) for columns covered with insulator and beam-column connections that remains exposed. However, the variation of rotational restraint is ideally assumed to be linear in the present study. It is noteworthy to observe that behavior of bare steel columns under fire is unexplored since all Cardington tests are carried out by partial or full insulation of columns.

The magnitude of joint rotation of either inclinometers are not identical due to loss of joint stiffness in fire differential readings were observed in clinometers. By neglecting minor restraints contribution from end plate connection and slab, summation of joint stiffness can be worked out to be summation of above and below column stiffness. Now by multiplying the stiffness to the difference in clinometer readings, we can achieve loss of joint stiffness with respect to temperature at the joint. The authors observed that various thermocouples at joints showed a minimal temperature variation which supports the idealization of joint temperature to one location.

Ali et al. [1] conducted a pilot test on seven steel columns under fire with slenderness ratio 150. Axial restraint of 0, 0.042 and 0.32 were tested, and axial restraint

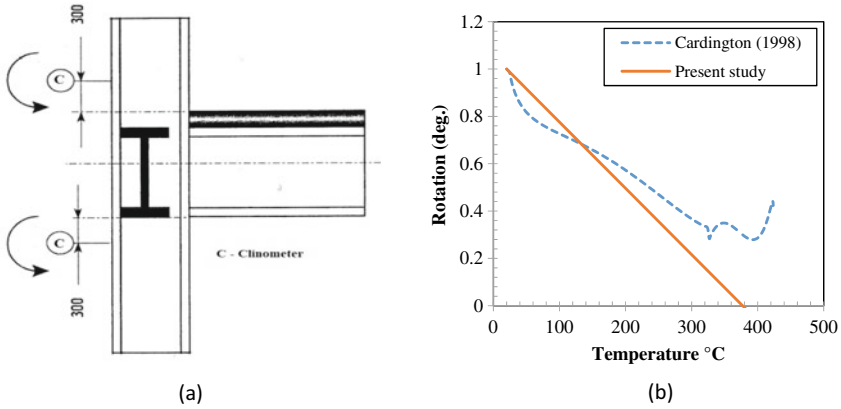


**Fig. 1** **a** Clinometer location, **b** joint rotation during fire (relative) (Ref: Cardington fire test, 1998)

column without pre-applied load showed a gradual reduction in axial load after buckling but whereas a column with pre-applied load failed suddenly. Column with axial restraint of 0.042, without any pre-applied load, showed a buckling temperature twice that of 0.32, while generated load was half of that of 0.32. Ali et al. [2] tested thirty-seven steel columns consisting of different slenderness ratios (49, 75 and 98), axial load ratios (0, 0.2, 0.4, 0.6) and axial restraint ratios (0, 0.1 and 0.2). Column buckling temperature decreased with respect to pre-applied load and axial restraints, while critical temperature remains unchanged. Slender column ($\lambda = 98$) resisted higher temperature than for intermediate column ($\lambda = 75$). This is being that slender column is sensible for end restraints caused due to friction in pin–pin condition thereby resulting in lower effective length and high fire resistance.

Ali and Connor [3] tested ten slender columns ($\lambda = 98$) with low and high restraints at various pre-applied loads. All columns were with constant axial restraints. Low restraint columns showed a definite peak in axial load versus temperature curve and distinct buckling temperature for all load levels. But for high restraint column with low load, definite peak and buckling is not observed. However, increase in rotational restraints showed an increase in critical temperature. Tan et al. [4] studied the effect of axial restraint on critical and buckling temperature of columns. Correia and Rodrigues [5] studied experimentally the effect of both rotational and axial restraints on buckling and critical temperature of rolled steel columns. Tests results showed that pre-applied moment has contributing effect in increasing critical temperature of columns. This is because post-buckling equilibrium is achieved at initial stage of heating itself. Also, the buckling temperature is quite dependent on pre-applied axial load. Pre-buckling stiffness of column depends on axial restraints rather than the pre-applied load.

Restrained steel columns in fire are widely tested in isolation rather than in frames due to cost involved and test uncertainties. Collapse mechanism for both columns and connections under fire occurs due to interaction between them with respect to fire. Thus, it is a major concern to understand explicitly the behavior of structure

under fire by considering the interaction of entire frame and local member level with the degree of restraint that occurs at the joint. Hence, it is necessary to study the end restraints, pre-applied load and moment for hot rolled section that are widely used in practice.

Axial load ratios of 0.2, 0.4 and 0.6 are considered similar to the values used in the experiments of Ali et al. [2]. It is inferred that gravity columns vulnerable to fire are more susceptible to damage. The gravity column is generally designed for high axial load ratio with low moment ratio, and hence, the same is adopted for the present study. Agarwal and Varma [6] considered high axial load ratio with low moment ratio to assess the effect of restraint on one-span, two-span and three-span columns subjected to uniform heating. Thus, in the present study, high axial load ratios of 0.2, 0.4 and 0.6 and low moment ratios of 0.1, 0.15 and 0.2 were adopted. The uniform temperature and a rate of heating are taken from a standard temperature time cure given by ISO 834-1: 1999 [7–12].

## 2 Numerical Study

Nonlinear finite-element analysis is carried out using commercial software ABAQUS 2019. Columns are modeled with 4-node shell element adopting reduced integration (S4R). Optimal mesh size based on convergence study is used for the model throughout the study. Newton–Raphson method is used to analyze all the models by varying time increment. Martin showed the adaptability of the above method for analysis of the steel members in fire. Nine test specimens of slenderness ratio of 49 [2] are analyzed, and the validation of the failure temperature is shown in Fig. 2b. Imperfection profile is taken as half sine curve with maximum amplitude given by Ali et al. [2]. Residual stresses are not accounted for validation due to unavailability of data. Yield strength ($f_y = 265$ N/mm$^2$) and Young's modulus of elasticity ($E =$ 210 GPa) are used for validation. In addition to that, mechanical properties at high temperature are worked out using EN 1993-1-2 (2005). Based on the comparison, it is found that numerical model indicates failure temperature with good approximation (mean = 0.99, standard deviation = 0.072 and co-efficient of variation = 7.2). The variation of temperature for slender column is due to unaccounted end friction leading to rotational restraint at ends, which in turn increases the resistance of the member thus reducing the effective length. This effect is minimal in short columns; however, there is still variation due to difference in temperature between exposed and unexposed face. This error due to temperature variation is minimal for slender columns. But it is observed that mechanical slack exists for both slender and short columns. The developed finite-element model predicted the failure temperature with good accuracy as observed from the validation with experimental data [2].

Typical load and restraint condition used in the present study are shown in Fig. 2. Various parameters chosen for the study are given in Table 1. Short column with typical slenderness ratio (39) and class I section (plastic section) classified as per EN 1993-1-1 (2005) is selected to understand the behavior under fire. All columns

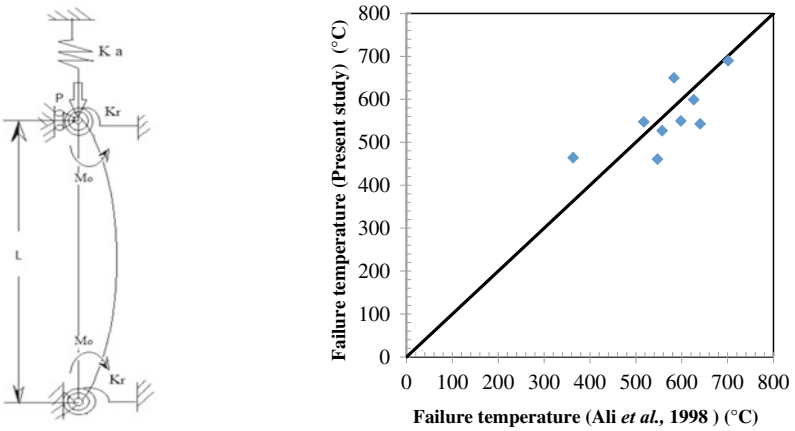


(a) Column with boundary conditions (b) Validation

**Fig. 2** End restraints and failure temperature

are of length 4 m with imperfection profile of half sine wave with peak amplitude of L/1000 (AISC 360-16). It is focused to consider the short column with constant pre-applied axial load ratio (0.2, 0.4 and 0.6) and moment ratio (0.1, 0.15 and 0.2). All pre-applied load and moments which are ratio of column capacity (pin–pin) at room temperature (EN 1993-1-2, 2005) are considered. Moment is applied in the direction of angle made due to imperfection as shown in Fig. 2a. Properties of steel under high temperature are also used in accordance to EN 1993-1-2 (2005).

Axial restraints are caused by the column due to cooler adjacent members in the adjoining structure. It is defined as the ratio of support axial stiffness to that of column axial stiffness ($\beta_a = K_{a\,su}/K_{a\,col}$, where $K_{a\,col}$ = AE/L of the section and $K_{a\,su}$ is the support axial restraint). The range of axial restraint ratio is given by numerical study conducted on a Broadgate phase-8 fire incident (1991) is from 0.1 to 0.35 with a maximum value of up to 0.9. Similarly, rotational restraints at ends are restraints due to unheated column above and below and in combination of beams with slab stiffness. It is a ratio of column rotational stiffness to that of support rotational stiffness ($\beta_r = K_{r\,su}/K_{r\,col}$), where $K_{r\,col}$ = 4EI/L of the section and $K_{r\,su}$ is the support rotational stiffness. Rotational restraint ratios ($\beta_r$) 2.81, 5.45 and 20.7 are considered corresponding to the effective length of column (Le) 0.7, 0.6 and 0.53 where column continues at both ends as per BS 5950: Part 1 [13]. The scope of the present work will highlight the effect of constant axial restraint ratio (0, 0.2, 0.4 and 0.6) and varying rotational restraint ratio (0, 2.81, 5.45 and 20.66) with increase in temperature based on restraint range observed from Broadgate phase-8 fire test report and Cardington fire test. $N_{b,Rd,20}$ and $M_{b,Rd\,20}$ are the load and moment capacities of specimens (20 °C) determined as per EN 1993-1-1 clause 6.3.1 and 6.3.2 ($l_{effective}$ = 4 m). Pre-applied force ratios (load = 0.4, 0.6, 0.8) and (moment = 0.1, 0.15, 0.2)

**Table 1** Specimen details and parameters studied

| S. no | Section | Restraint | | | | Force | | | |
|---|---|---|---|---|---|---|---|---|---|
| | | Axial restraint (kN/mm) | | Rotational restraint (kN m/rad) | | Pre-applied load (kN) | | Pre-applied moment (kN m) | |
| 1 | 356 × 406 × 235 (Slenderness ratio = 39) | $K_a = 1561.6$ | | $K_r = 65{,}100$ | | $N_{b,Rd,20}$ | 8761.8 | $M_{b,Rd\ 20} = 845.16$ | |
| | | $\beta_a = 0$ | – | $\beta_r = 0$ | – | – | – | – | – |
| | | $\beta_a = 0.2$ | 312 | $\beta_r = 2.81$ | 182,931 | 0.4 | 3504 | 0.10 | 84.5 |
| | | $\beta_a = 0.4$ | 624 | $\beta_r = 5.45$ | 354,795 | 0.6 | 5257 | 0.15 | 126.7 |
| | | $\beta_a = 0.6$ | 936 | $\beta_r = 20.7$ | 1,344,966 | 0.8 | 7009 | 0.20 | 169.0 |

are the ratio of force applied prior to heating with respect to the capacity as stated earlier.

## 3 Results and Discussion

Graphs are drawn for buckling and failure temperature (Figs. 3, 4, 5 and 6) for varied rotational restraint ($\beta_r = 0$, 2.81, 5.45 and 20.7) with axial load ratio (Po = 0.2, 0.4 and 0.6), moment ratio (Mo = 0.1, 0.15 and 0.2). In a typical gravity loaded column, Young's modulus remains invariant with load but column under fire encounters reduction in Young's modulus leading to nonlinear stress–strain at a lower strain. Slender columns and short columns with greater load ratio fail at low temperature where material properties are not of explicit importance. However for column with low load ratio and high restraints, stress distribution is necessary to understand its behavior. Von Mises stress plots are shown in Fig. 7. The respective load evolution is shown in 8. For unrestrained column, the stress at extreme ends is more due to load application (Fig. 7a). This is since expansion is restrained by pre-applied force. Axially restrained column without rotational restraints has more stress at inner face (Fig. 7c) as compared to outer. This is due to secondary *P*-delta effect where loss of stability due to buckling occurs where no contribution from outer flange is seen. Column both axially and rotationally restrained has a longer survival time with high buckling and critical temperature; this is due to contribution from end rotational restraints against buckling. The failure is a combination of material degradation and member instability (Fig. 7b). Higher stress is seen both in inner and outer face showing a contribution from both the sides. Typically, it can be concluded that column failure by material yielding will have a greater buckling and failure temperature than column which fails by local instability. This is observed for a short column with low load and high rotationally restraint.

Axially restrained (AR) and rotationally unrestrained columns (RUR) tend to buckle at lower temperature due absence of rational restraints which causes instability at early stage. On the other hand, axially and rotationally restrained column (AR and RR) gains stability due to rotational restraints. In the present study, axially restrained and varied rotational restraints (AR and VRR) are considered, where end restraint reduces with temperature Fig. 1b. In a typical column, if end restraint reduces to zero after buckling, then the failure temperature will not have contribution from rotational restraints as in Fig. 8 (point 'd'). However, this behavior is based on the slope of rotational restraint reduction with respect to temperature. If the slope is steeper, then rotational restraint will not contribute in increase of buckling or critical temperature Fig. 8 (point 'b'). However, irrespective of restraints condition of column initial stiffness remains same. EN 1993-1-2 (2005) gives an interactive formula for assessing failure temperature of column in fire. The formulae takes into account reduced material properties. However, the rotational restraints are idealized to be invariant throughout the fire. This idealization overestimates the column failure time Fig. 8. More numerical study on various slenderness ratios in combination

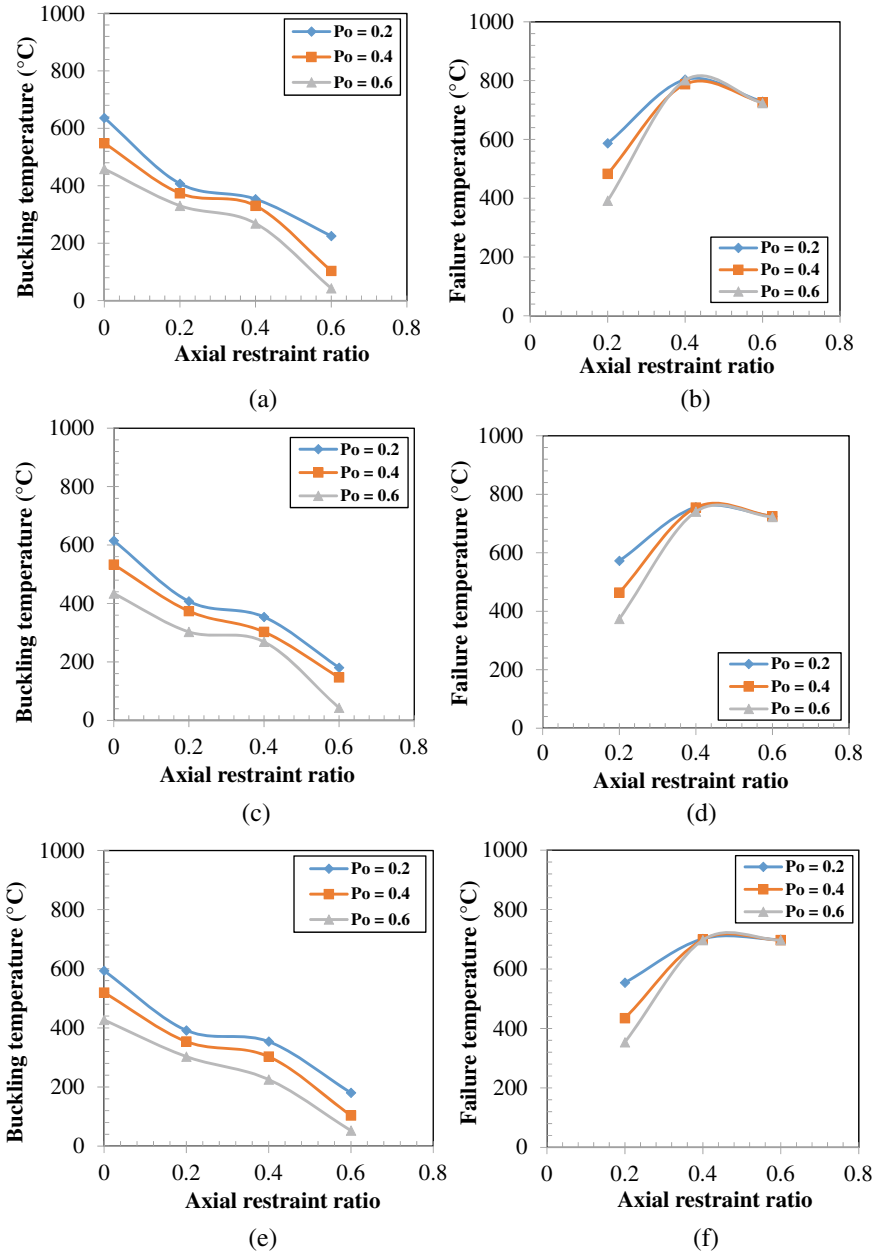


**Fig. 3** Temperature plots for $\beta_r = 0$ and **a**, **b** Mo = 0.1, **c**, **d** Mo = 0.15 and **e**, **f** Mo = 0.2

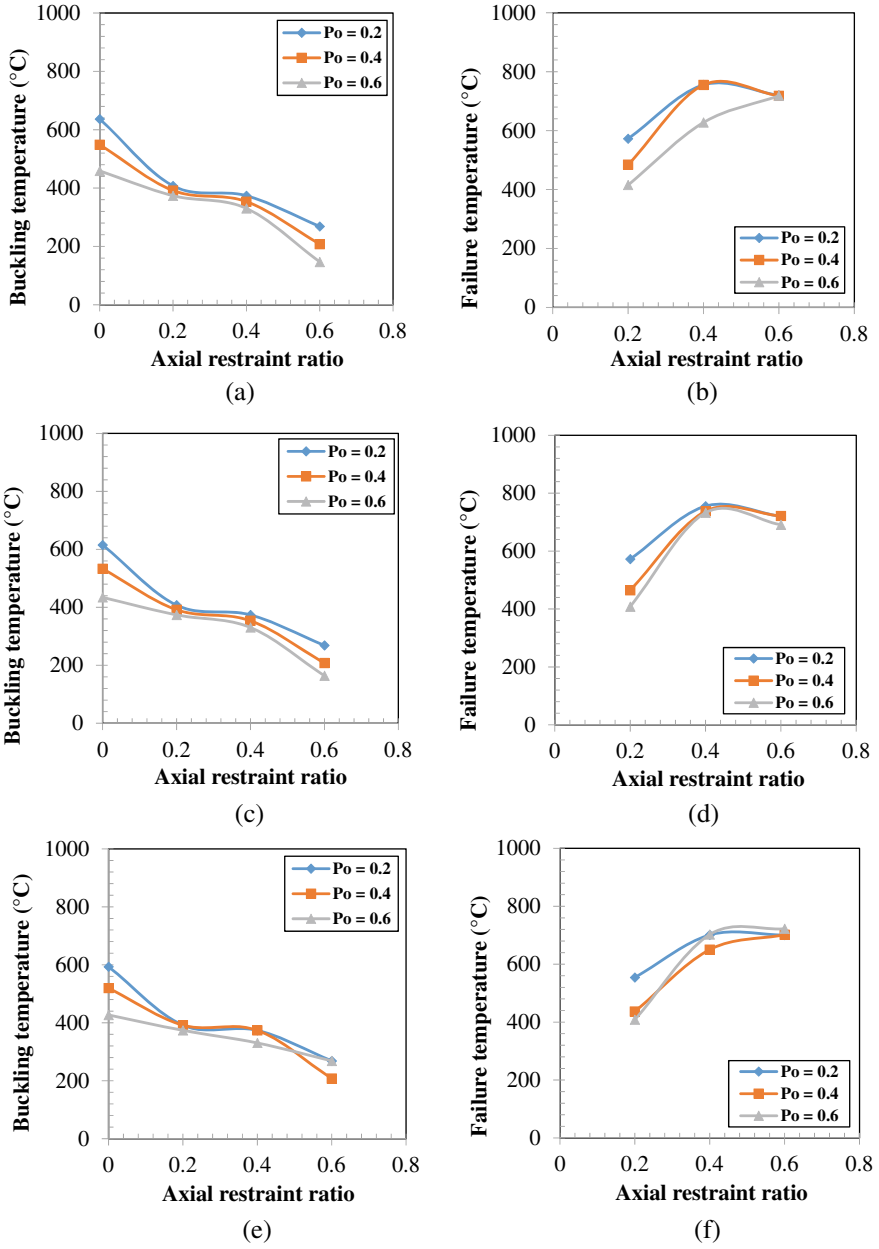


**Fig. 4** Temperature plots for $\beta_r = 2.81$ and **a**, **b** Mo = 0.1, **c**, **d** Mo = 0.15 and **e**, **f** Mo = 0.2

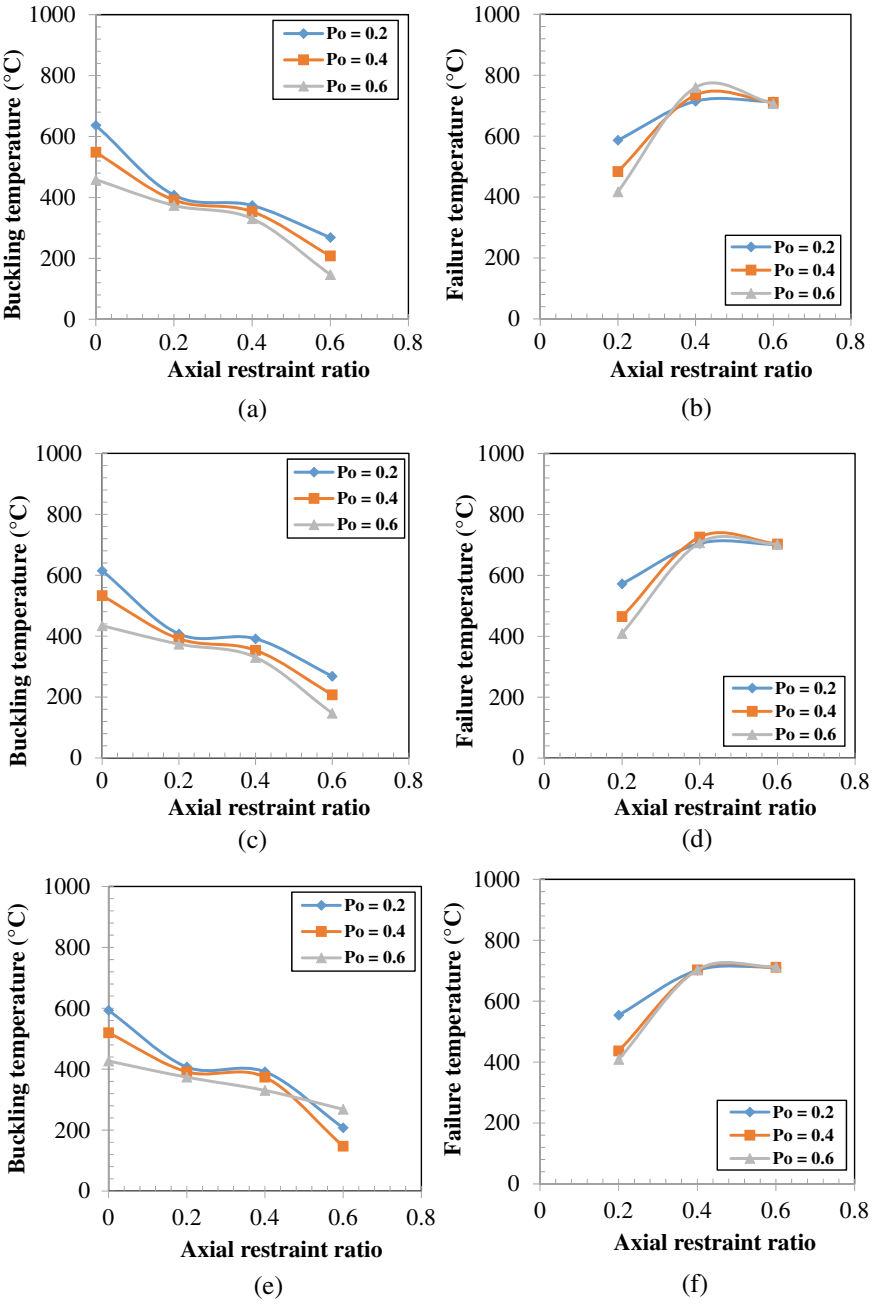


**Fig. 5** Temperature plots for $\beta_r = 2.81$ and **a**, **b** Mo = 0.1, **c**, **d** Mo = 0.15 and **e**, **f** Mo = 0.2

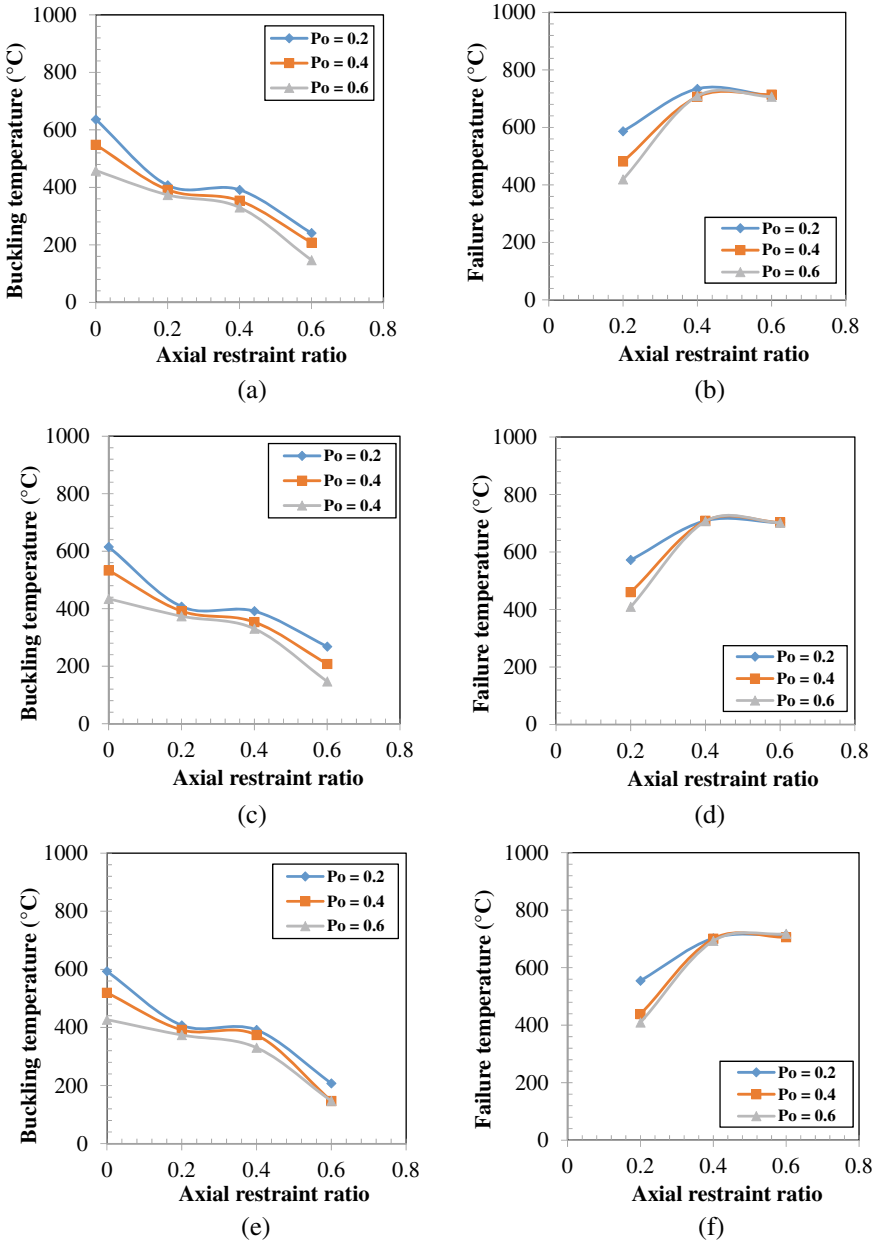


**Fig. 6** Temperature plots for $\beta_r = 2.81$ and **a**, **b** Mo = 0.1, **c**, **d** Mo = 0.15 and **e**, **f** Mo = 0.2

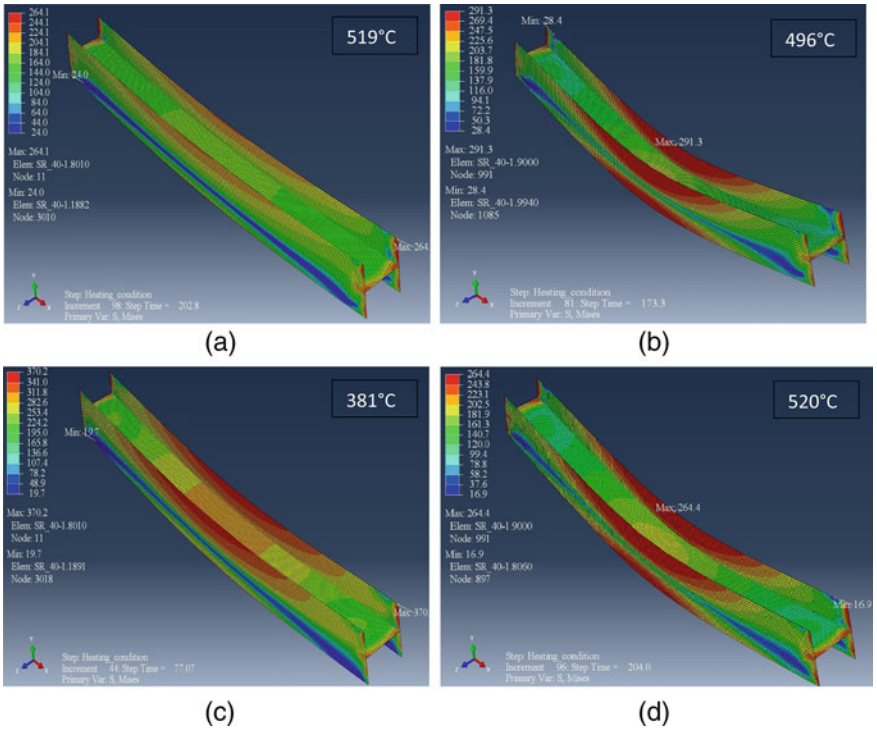


**Fig. 7** Von Mises stress distribution **a** unrestrained (buckling temperature), **b** axially and rotationally restrained (buckling temperature), **c** axially restrained and rotationally unrestrained (failure temperature), **d** axially and rotationally restrained (failure temperature)

with practical range of pre-applied load, moment and end restraints is necessary to understand the behavior.

## 4 Conclusions

The conclusions are presented for rolled steel short column (slenderness ratio = 39) and plastic sections. The following conclusions are drawn based on study of one hundred and forty four specimens carried out using ABAQUS.

1. Considering constant rotational restraints EN 1993-1-2 (2005) overestimates the column failure temperature.
2. Axial restraints reduce the buckling temperature due to early increase in axial force at lower temperature.
3. At high rotational restraint, buckling and critical temperature is independent of axial restraints. This is due to increase in stability by rotational restraint.

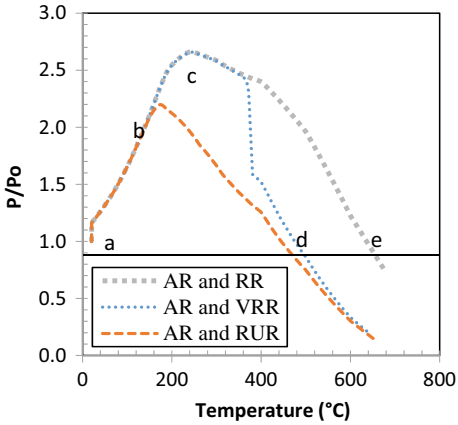


**Fig. 8** Evolution of column axial force (typical)

4. Buckling temperature of axially unrestrained and rotationally restrained column varies with respect to pre-applied load; this is since buckling temperature is much governed by axial restraint ratio.
5. Variation in buckling temperature is almost insignificant for the range of axial restraint ratio of 0.2–0.4.
6. Failure temperature is independent of axial restraints for range 0.4–0.6 for all rotational restraints.

## References

1. Ali FA, Simms IW, O'Connor DJ (1997) Behaviour of axially restrained steel columns during fire. In: Proceedings of 5th international symposium, fire safety science, Melbourne, Australia, pp 1105–1116
2. Ali FA, Shepherd P, Randall M, Simms IW, O'Connor DJ, Burgess I (1998) The effect of axial restraint on the fire restraint of steel columns. J Constr Steel Res 46(1–3):305–306 (Paper No. 177)
3. Ali F, O'Connor D (2001) Structural performance of rotationally restrained steel column in fire. Fire Saf J 36:679–691
4. Tan KH, Toh WS, Huang ZF (2007) Structural response of restrained steel column at elevated temperatures. Part-1: experiments. Eng Struct 29:1641–1652
5. Correia AJPM, Rodrigues JPC (2012) Fire resistance of steel columns with restrained thermal elongation. Fire Safety J 50:1–11
6. Agarwal A, Varma AH (2011) Design of steel columns at elevated temperatures due to fire: effects of rotational restraints. Eng J Am Inst Steel Construct 4:297–314
7. AISC (2016) Specification for structural steel buildings. In: AISC 360-16, Chicago
8. Kirby BR (1998) The behaviour of the multi-storey steel framed building subjected to fire h-attack—experimental data. British Steel plc., Sweden Technology Centre, Moorgate, Rotherham, United Kingdom
9. European Committee for Standardization (ECS) (2005) Design of steel structures, part 1.1, general rules and rules for building. Eurocode 3, European Committee for Standardization, Brussels, Belgium

10. European Committee for Standardization (ECS) (2005) Design of steel structures, part 1.2, structural fire design. Eurocode 3, European Committee for Standardization, Brussels, Belgium
11. Gillie M (2009) Analysis of heated structures: nature and modelling benchmarks. Fire Saf J 44:673–680
12. SCIF Fire engineering Group (1991) Structural fire engineering investigation of broadgate phase 8 fire. The Steel Construction Institute, Silwood Park, Ascot
13. British Standard (1990) Structural use of steel work in building. BS 5950: Part 1. Code of practice for design in simple and continues constructions: hot rolled sections

# Ultimate Shear Resistance of Non-rigid End Post Steel Plate Girders


**Durgesh R. Hingnekar and Arvind Y. Vyavahare**

**Abstract** Several theories are available in the literature to predict the ultimate shear resistance of plate girders, generally known as tension field theories. It is already found out, by many researchers, that the prediction of the majority of the models is mostly over-conservative for non-rigid end post steel plate girders. So, there is a need for the development of accurate finite element models, which could predict the ultimate strength better than the available theoretical models. This paper makes a comparison between the ultimate shear resistance of 12 non-rigid end post girders, from experimental data available in the literature, and some of the prominent tension field prediction models, such as Basler's model, the Cardiff model, and Höglund's model. There are many factors which affect the ultimate shear resistance of girders such as geometric imperfections, material nonlinearity, and boundary conditions. All of these factors need to be addressed to arrive at an improved finite element analysis, which can accurately predict the ultimate shear resistance of the girder. This paper comprehensively describes the finite element analysis, which includes the selection of material model, initial imperfection, element type, meshing and analysis methodology, etc.

**Keywords** Steel · Members · Shear · Stability · Plates · Postbuckling

## 1 Introduction

Steel plate girders are utilized in industrial structures, heavy members in regular buildings, and in offshore upstream and downstream projects apart from their most common application bridge structures. Generally in order to optimize the strength-to-weight ratio, steel plate girders are designed with slender webs, which are prone to shear buckling. As a result, the shear buckling of web becomes critical for these

D. R. Hingnekar (✉) · A. Y. Vyavahare
Department of Applied Mechanics, Visvesvaraya National Institute of Technology, Nagpur 440016, India
e-mail: durgesh.hingnekar@gmail.com



M. Madhavan et al. (eds.), *Proceedings of the Indian Structural Steel Conference 2020 (Vol. 1)*, Lecture Notes in Civil Engineering 318,
https://doi.org/10.1007/978-981-19-9390-9_48

girders. To avoid the shear buckling in web transverse stiffeners are provided. It's a well-known fact that stiffened webs of plate girders continue to resist shear even after buckling, and this extra resistance beyond buckling resistance is known as Postbuckling strength.

Tension field theory predicts the ultimate shear strength of girder and explains the development of postbuckling strength in web panel subjected to shear loading. There are many models of tension field theory; out of which some of the prominent and globally accepted models are Basler's model [1], the Cardiff model [2], and Höglund's model [3]. These models do provide a very accurate prediction of ultimate strength within certain geometric limits. One of the necessary conditions stipulated by these models is that the end panel should be able to anchor the tension field developed in the adjacent panels through an end post which is nothing but a set of end stiffeners strong enough to resist the longitudinal component of the tension field. If this condition is satisfied then and only then most of the tension field models allow the development of postbuckling strength otherwise the strength of girder is limited to the critical buckling strength. The end posts capable of resisting this longitudinal component of the tension field are known as rigid end post. These are generally a set of stiffeners spaced appropriately to act as vertical beam to provide effective flexural resistance to the longitudinal component of the tension field force. Otherwise, the end post is known as non-rigid end post. Typical rigid and non-rigid end posts are shown in Fig. 1.

It is well established, by many researchers such as Daley (2016) and Kwon and Ryu [4], that the prediction of the majority of the models is mostly over-conservative for non-rigid end post steel plate girders. So, in the absence of an accurate theoretical model, appropriate finite element models are needed, which could predict the ultimate strength. This paper makes a comparison between the ultimate shear resistance of 12 non-rigid end post girders, taken from experimental data available in the literature, and some of the prominent available tension field prediction models, such as Basler's model, the Cardiff model, and Höglund's model. It is shown that there are many factors which affect the ultimate shear resistance of girders such as geometric imperfections; material nonlinearity; boundary conditions. To arrive

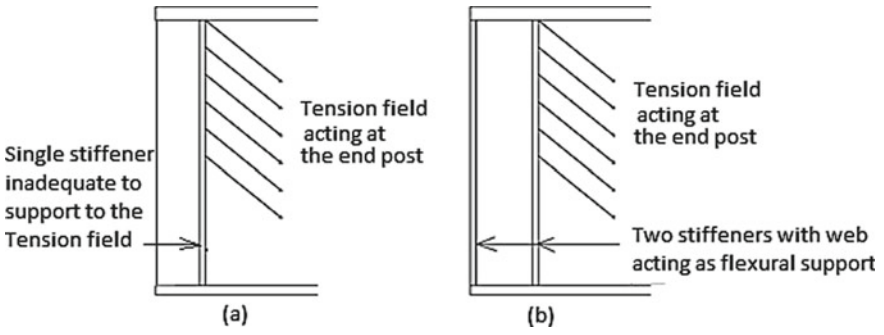


**Fig. 1** Example of **a** non-rigid end post, **b** rigid end post

at an improved finite element analysis, which can accurately predict the ultimate shear resistance of the girder, all of these factors should be appropriately included. This paper comprehensively describes the finite element analysis, which includes the selection of material model, initial imperfection, element type, meshing and analysis methodology, etc.

## 2 Specimens from the Literature

### *2.1 Geometric Description*

The details of 12 non-rigid end post girders available in the literature such as Carskaddan (1968), Daley et al. [5], and Kwon and Ryu [4] as shown in Figs. 2 and 3 are presented in Table 1.

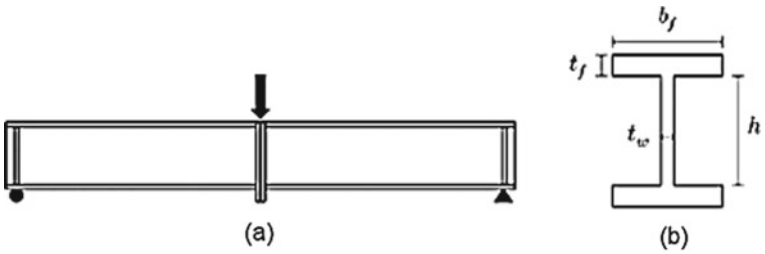


**Fig. 2** **a** Daley and Davis (2015) specimen elevation **b** cross section

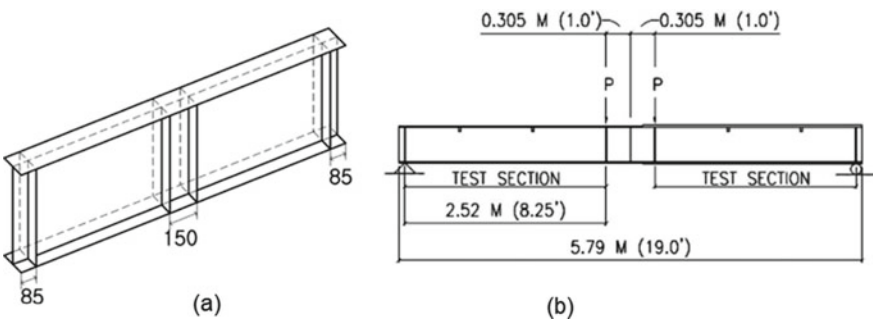


**Fig. 3** Details of specimen from **a** Kwon and Ryu [4], **b** Carskaddan (1968)

**Table 1** Geometric details of specimens from the literature

| S.no | Model | Depth of web, $d$ (mm) | Web Thk., $t_w$ (mm) | Flange width, $b_f$ (mm) | Flange Thk., $t_f$ (mm) | Panel aspect ratio, $a/h$ (mm) | Panel Slenderness ratio, $d/t_w$ (mm) | Web yield strength, $Fy_w$ (MPa) | Flange yield strength, $Fy_f$ (MPa) | Ref |
|---|---|---|---|---|---|---|---|---|---|---|
| 1 | S-120-240 | 1176 | 4.5 | 250 | 12.0 | 0.88 | 261 | 235 | 315 | A |
| 2 | S-80-180 | 776 | 4.5 | 250 | 12.0 | 0.95 | 172 | 235 | 315 | A |
| 3 | S-100-240 | 976 | 4.5 | 250 | 12.0 | 1.07 | 217 | 235 | 315 | A |
| 4 | S-60-180 | 576 | 4.5 | 150 | 12.0 | 1.28 | 128 | 235 | 315 | A |
| 5 | S-80-240 | 776 | 4.5 | 250 | 12.0 | 1.34 | 172 | 235 | 315 | A |
| 6 | S-100-300 | 976 | 4.5 | 250 | 12.0 | 1.37 | 217 | 235 | 315 | A |
| 7 | S-60-240 | 576 | 4.5 | 150 | 12.0 | 1.81 | 128 | 235 | 315 | A |
| 8 | S-60-300 | 576 | 4.5 | 150 | 12.0 | 2.33 | 128 | 235 | 315 | A |
| 9 | UK6 | 991 | 4.4 | 203 | 19.0 | 4.12 | 227 | 434 | 406 | B |
| 10 | UK3 | 610 | 3.4 | 203 | 12.7 | 4.45 | 179 | 448 | 367 | B |
| 11 | C-AC1 | 454 | 4.5 | 128 | 7.9 | 5.50 | 102 | 232 | 786 | C |
| 12 | UK5 | 559 | 3.2 | 203 | 19.0 | 7.85 | 177 | 416 | 404 | B |

*A* Kwon and Ryu [4], *B* Daley and Davis (2015), *C* Carskaddan (1968)

### 2.2 *Comparison of Experimental Results with Tension Field Models*

The experimental results of ultimate shear resistance are presented in Table 2; from these results, it is clear that there is considerable difference in the actual experimental results as compared to the predicted strengths from tension field models.

The results of the theoretical models are mostly over-conservative. It is already shown by many researchers such as Ghadami and Broujerdian [6] and Alinia [7] that the parameters such as geometric imperfections and material nonlinearity, which are ignored in the conventional theories, play a significant role in defining the ultimate shear resistance of the girder. Hence, the effect of these parameters is discussed in the following sections.

## 3 Effect of Geometric Imperfections

The codal provisions such as EN 1993-1-1-2005 [8] specify the design values of initial local imperfections from 1/350 to 1/100, but it has been observed by the researchers that such high values of imperfections are not suitable to simulate the bifurcation

**Table 2** Comparison of experimental results with tension field models

| 1 | 2 | 3 | 4 | 5 | 6 | 7 |
|---|---|---|---|---|---|---|
| S.No | Model | Expt. Shear $V_{\text{expt}}$ (kN) | Basler [1] $\frac{V_{\text{expt}}}{V_{\text{Basler}}}$ | Hoglund [3] $\frac{V_{\text{expt}}}{V_{\text{Hoglund}}}$ | Huslid and Rockey (1967) $\frac{V_{\text{expt}}}{V_{\text{Huslid}}}$ | References |
| 1 | S-120-240 | 474.8 | 0.91 | 1.73 | 1.78 | [4] |
| 2 | S-80-180 | 424.3 | 1.13 | 1.62 | 1.27 | [4] |
| 3 | S-100-240 | 426.5 | 1.03 | 1.72 | 1.53 | [4] |
| 4 | S-60-180 | 332.4 | 1.14 | 1.43 | 1.11 | [4] |
| 5 | S-80-240 | 365.5 | 1.13 | 1.60 | 1.26 | [4] |
| 6 | S-100-300 | 380.2 | 1.04 | 1.67 | 1.46 | [4] |
| 7 | S-60-240 | 319.5 | 1.24 | 1.50 | 1.18 | [4] |
| 8 | S-60-300 | 300.6 | 1.28 | 1.46 | 1.18 | [4] |
| 9 | UK6 | 327 | 4.01 | 1.30 | NA | Daley and Davis (2015) |
| 10 | UK3 | 219 | 3.51 | 1.42 | NA | Daley and Davis (2015) |
| 11 | C-AC1 | 178 | 0.93 | 0.93 | NA | Carskaddan (1968) |
| 12 | UK5 | 182 | 3.36 | 1.44 | NA | Daley and Davis (2015) |

buckling in nonlinear analysis. In order to illustrate this point a finite element model of a square web panel of side 1000 mm and thickness 6.67 mm resulting in a slenderness ratio of 150 with loading scheme is shown in Fig. 4. The boundary conditions of the web panel are described in Fig. 5. The geometric imperfection in the model is varied from *D*/12500 to *D*/100.

It can be observed from Fig. 6 the shear force applied to the lateral deflection at the center of the web panel that the bifurcation buckling load is clear in case of imperfection of *D*/12500 but as the imperfection is increased to *D*/100 the bifurcation

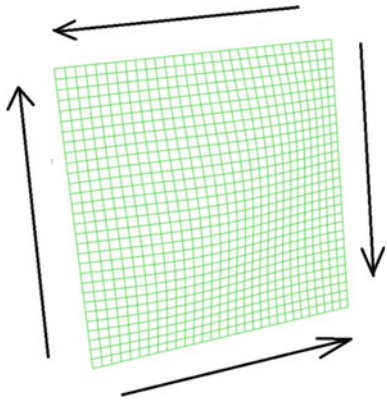

**Fig. 4** FE model of web panel with loading scheme

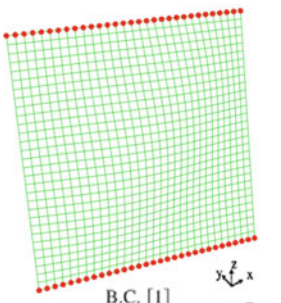


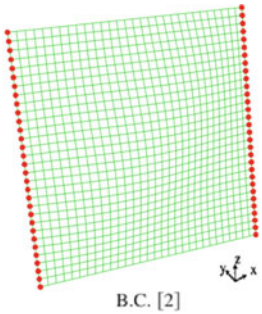


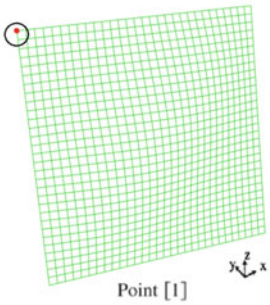


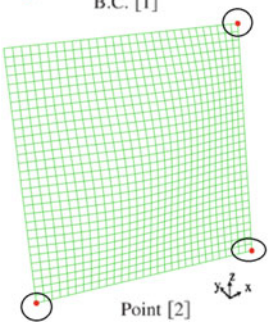


| Location | $u_x$ | $u_y$ | $u_z$ | $\theta_x$ | $\theta_y$ | $\theta_z$ |
|---|---|---|---|---|---|---|
| B.C. [1] | Free | Fixed | Free | Free | Fixed | Fixed |
| B.C. [2] | Free | Fixed | Free | Fixed | Fixed | Free |
| Point [1] | Fixed | Fixed | fixed | Fixed | Fixed | Fixed |
| Point [2] | Free | Fixed | Free | Fixed | fixed | fixed |

**Fig. 5** Boundary conditions of the finite element model

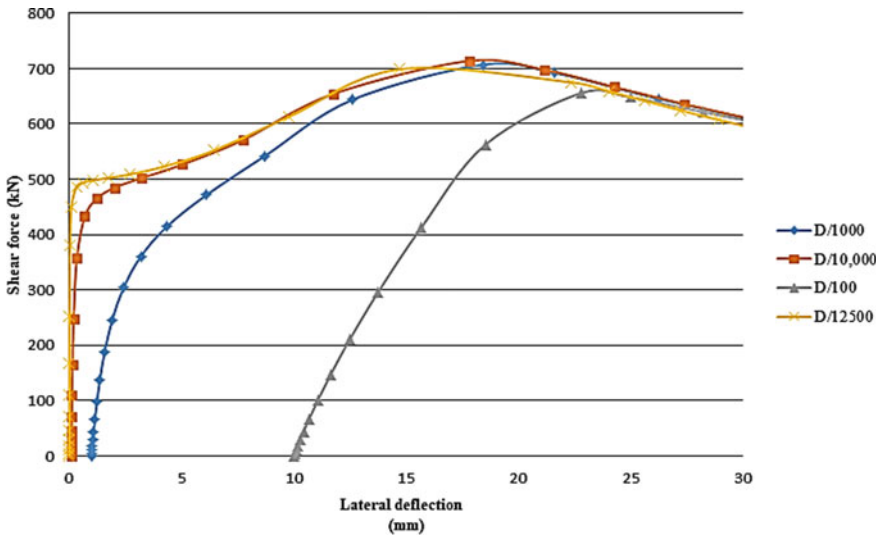


**Fig. 6** Effect of initial imperfections

buckling behavior is not observed. Due to this reason, many researchers have used very low imperfection values to predict the postbuckling strength of the slender plate in shear. But from the same Fig. 6 that the postbuckling strength results with very less geometric imperfections such as *D*/12500 to *D*/1000 are unconservative by around 8–10% as compared to the realistic imperfection values of *D*/100. This is due to a phenomenon known as "Inelastic buckling paradox." Hence, it is necessary to use realistic imperfection values even if they do not demonstrate the bifurcation buckling behavior.

## 4 Finite Element Model

### *4.1 General*

This section provides details of the finite element modeling carried out in ABAQUS® [9], for elastic buckling analysis and nonlinear analysis of girders using modified Riks algorithm. The girders are modeled using shell element S4R, which is a 4-noded, quadrilateral, shell element with reduced integration and a large-strain formulation. These elements do not suffer from transverse shear locking, nor do they have any unconstrained hourglass modes. The S4R elements in ABAQUS® [9] permit transverse shear deformation. These elements are adaptive and utilize thick shell theory as the shell thickness increases but also transform to discrete Kirchhoff thin shell elements as the thickness decreases.

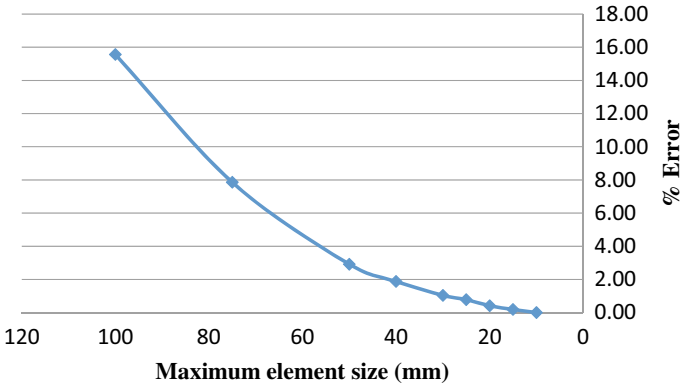


**Fig. 7** Convergence study for mesh size

## *4.2 Convergence Study Using Elastic Shear Buckling Analysis*

A plate girder (S-120-240) model was utilized to determine the rate of convergence of elastic shear buckling stress of plate girders with respect to the element size. Figure 7 shows the change in relative errors for different mesh sizes with respect to the elastic shear buckling stress from a mesh size of 5 × 5 mm.

It is clear from the figure that models with a mesh size of 20 × 20 mm give a satisfactory result with a variation of relative error less than 0.42%. Hence, the mesh of 20 × 20 mm was considered as the maximum mesh size in the further FE analysis of plate girders.

## *4.3 Material Model*

Some of the commonly employed material models are the ECCS model [8], which provides options of elastic-perfectly plastic, elastic-linear hardening, or trilinear, whereas Ramberg–Osgood model [10] provides a nonlinear curve, Yun and Gardener [11] have developed a quad-linear material model based on more than 500 experimental curves for hot-rolled steels as shown in Fig. 8.

The benefits of using Yuan and Gardener (2016) model are that it includes the strain hardening region, considering only Young's modulus ($E$), the yield stress ($f_y$), and the ultimate stress ($f_u$) which are readily available to the researcher, but other key parameters, such as the strains at the onset of strain hardening and at the ultimate stress, which are difficult to get are not required. It is also shown to be more accurate than the widely utilized ECCS model.

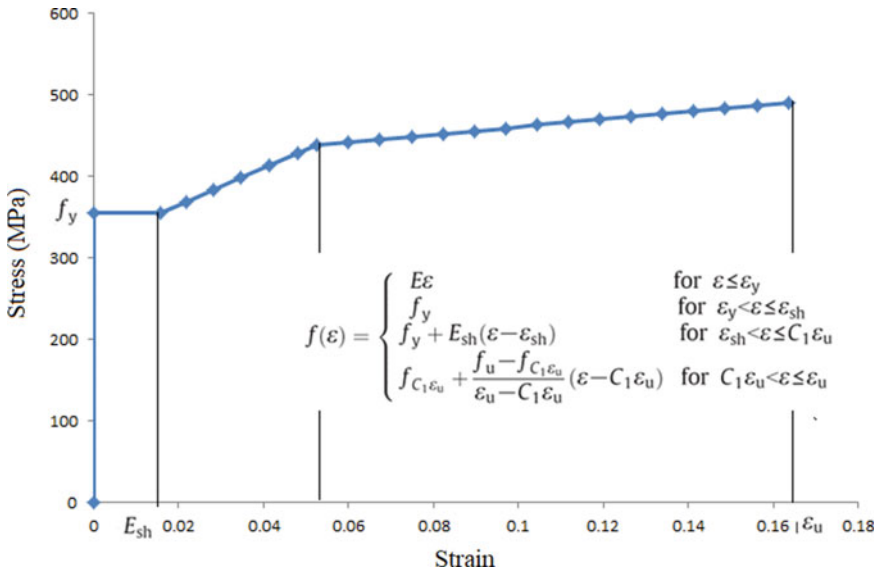


**Fig. 8** Typical quad-linear model for S-355 steel (Yuan and Gardener 2016)

## *4.4 Boundary Conditions and Loading*

The boundary condition of the models is according to a simply supported girder with one end pinned and another roller. The flanges are laterally restrained to avoid lateral torsional buckling. The loading is considered to be applied as knife edge loads above the central stiffeners, but in order to avoid the local buckling of stiffeners at top, the load is equally distributed across the stiffener depth. The loading and boundary condition of a typical girder model is also illustrated in Fig. 9.

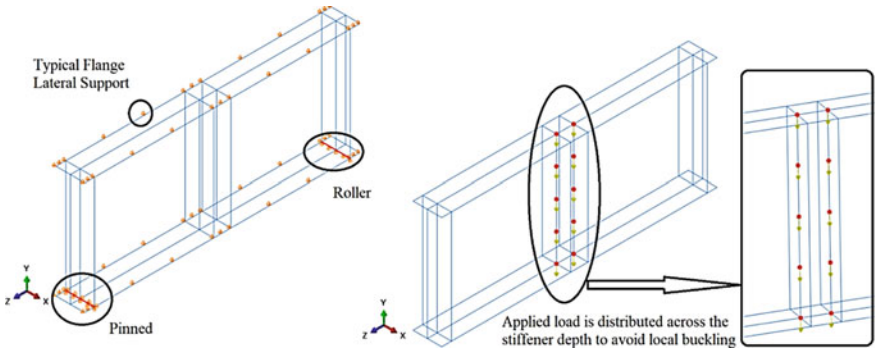


**Fig. 9** Typical loading and boundary condition

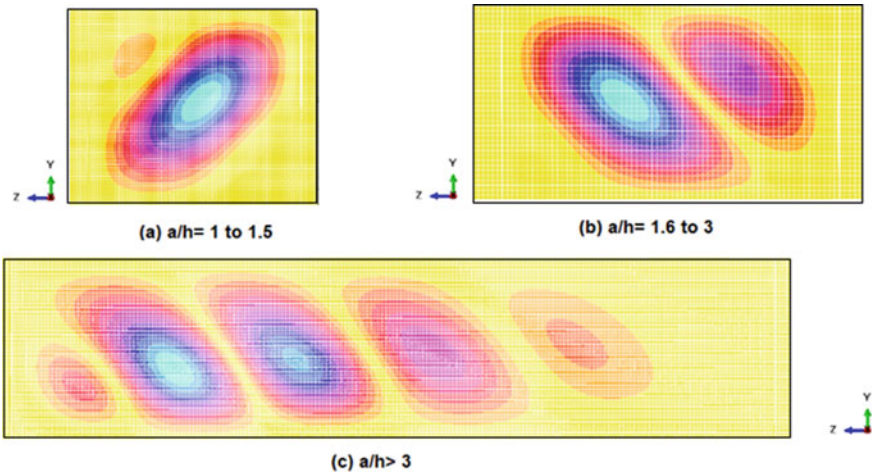


**Fig. 10** Typical first shear buckling mode shapes

## 5 Analysis Methodology

### *5.1 Eigenvalue Analysis*

A linear perturbation analysis is carried out to find out the eigenvalues and mode shapes of the girders. Typical mode shapes in the first shear buckling mode for different ranges of aspect ratios of the web panel are shown in Fig. 10.

### *5.2 Nonlinear Analysis*

The first critical buckling mode of the girder web panel is utilized as initial imperfection shape for the nonlinear analysis. In case of closely spaced modes, the effect of second mode is also considered in the analysis. Annexure "C" of EN 1993-1-5 [8] restricts the out of flatness in the plate to 0.005 times the least dimension, and 80% of this tolerance limit is recommended as the limiting imperfection amplitude in the nonlinear finite element analysis.

The slender web plate subjected to shear demonstrates a postbuckling strength. To analyze this type of problem, a special method is utilized known as modified Riks method. The slender web plate subjected to shear loading is an example of a snap-through buckling phenomenon which might display a convoluted load-displacement behavior which is not possible to trace without the help of modified Riks method. In addition to the standard equilibrium equations, Ricks [12] added a constraint equation fixing the size of incremental load step in the load-deflection space. Crisfield [13]

proposed the modified Riks approach to make it suitable to use with the finite element method.

## 6 Validation

Based on the analysis methodology, described in the previous section, finite element models of the twelve specimens collected from the literature were prepared. The ratios of experimentally measured strengths to the predicted strengths are presented in Table 3. It can be observed that the maximum deviation in the result is 1.13, whereas the ratio goes upto 4.0 in case of theoretical tension field models as observed from Table 2. Hence, it can be observed that the finite element models predict a very accurate ultimate shear strength.

The failure modes of some of the specimens as observed in the experiment are compared with the failure modes predicted by the respective finite element models. It can be seen from Figs. 11 and 12 that the predicted failure modes also very closely match with that of the experimentally observed failure modes.

**Table 3** Comparison of experimental results with finite element analysis results in terms of ratio of measured-to-predicted shear strengths

| 1 | 2 | 3 | 4 | 5 | 7 |
|---|---|---|---|---|---|
| S.No | Model | Expt. shear $V_{\text{Expt (kN)}}$ | FEA shear $V_{\text{FEA (kN)}}$ | Ratio $\frac{V_{\text{expt}}}{V_{\text{FEA}}}$ | References |
| 1 | S-120-240 | 474.8 | 503.0 | 0.94 | [4] |
| 2 | S-80-180 | 424.3 | 445.0 | 0.95 | [4] |
| 3 | S-100-240 | 426.5 | 448.8 | 0.95 | [4] |
| 4 | S-60-180 | 332.4 | 366.0 | 0.91 | [4] |
| 5 | S-80-240 | 365.5 | 396.4 | 0.92 | [4] |
| 6 | S-100-300 | 380.2 | 336.6 | 1.13 | [4] |
| 7 | S-60-240 | 319.5 | 324.3 | 0.99 | [4] |
| 8 | S-60-300 | 300.6 | 306.0 | 0.98 | [4] |
| 9 | UK6 | 327 | 386.0 | 0.85 | Daley and Davis (2015) |
| 10 | UK3 | 219 | 242.0 | 0.90 | Daley and Davis (2015) |
| 11 | C-AC1 | 178 | 165.6 | 1.07 | Carskaddan (1968) |
| 12 | UK5 | 182 | 199.0 | 0.91 | Daley and Davis (2015) |

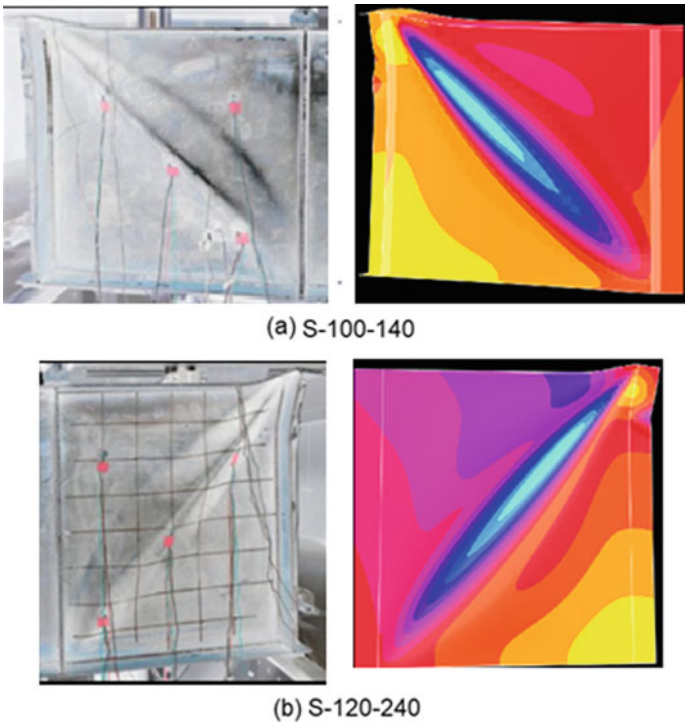


**Fig. 11** Comparison of experimental failure modes with finite element analysis failure modes for some representative models

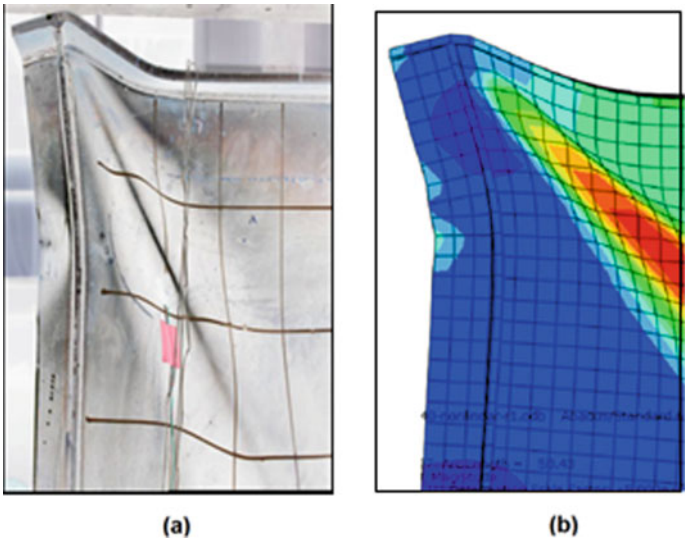


**Fig. 12** Plastic hinge at the top flange (S-100-240) **a** Experiment, **b** FE result

## 7 Summary and Conclusion

The experimental results of ultimate shear resistance of 12 plate girder specimens available in the literature [4, 5] are summarized. The ultimate shear resistance of these girders was computed using available prominent mechanics-based theoretical prediction models such as Basler's model [1], Cardiff model [2], and Höglund's model [3]. The results of the theoretical models were mostly over-conservative. It is shown that parameters, which are ignored in the conventional theories, play a significant role in defining the ultimate shear resistance of the girder. An improved finite element model to predict the ultimate shear resistance for any non-rigid end post steel plate girder was required. Hence, a typical finite element modeling procedure of the girder, discussing the element type selection, mesh discretization, material modeling, ideal boundary condition, and load application procedure was presented in this paper. The effect of geometric imperfection on the results of nonlinear analysis by providing a tabulated comparison of results after varying geometric imperfections from $d/12500$ to $d/100$ (depth of web, $d$) was shown. Ultimately, the selection of appropriate initial imperfection value for the nonlinear analysis carried out using modified RIKS algorithm was discussed. Finally, a comparison of experimental results available, from the literature, with the finite element results, obtained from models prepared during this study, for validation of the finite element model was presented.

## References

1. Basler K (1961) Strength of plate girders in shear. In: Proceedings of ASCE, 87, (ST7), Oct 1961, reprint no. 186 (61–13)
2. Porter DM (1975) The collapse behavior of plate girders loaded in shear. Struct Eng 53(8):313–325
3. Höglund T (1997) Shear buckling resistance of steel and aluminium plate girders. Thin-Walled Struct 29(1–4):13–30
4. Kwon YB, Ryu SW (2016) The shear strength of end web panels of plate girders with tension field action. Thin-Walled Struct 98:578–591
5. Daley AJ, Brad Davis D, White DW (2016) Shear strength of unstiffened steel I-section members. J Struct Eng 143(3):04016190
6. Ghadami A, Broujerdian V (2019) Shear behavior of steel plate girders considering variations in geometrical properties. J Constr Steel Res 153:567–577
7. Alinia MM, Habashi HR, Khorram A (2009) Nonlinearity in the postbuckling behaviour of thin steel shear panels. Thin-walled Struct 47(4):412–420
8. CEN (2006) Eurocode 3: design of steel structures. Part 1–5: plated structural elements. ENV 1993-1-5, European Committee for Standardization, Brussels, Belgium
9. ABAQUS (2015) ABAQUS documentation. Dassault Systèmes, Providence, RI, USA
10. Ramberg W, Osgood WR (1943) Description of stress-strain curves by three parameters
11. Yun X, Gardner L (2017) Stress-strain curves for hot-rolled steels. J Constr Steel Res 133:36–46
12. Ricks E (1979) An incremental approach to the solution of snapping and buckling problems. Int J Solids Struct 15:524–551
13. Crisfield MA (1981) A fast incremental/iterative solution procedure that handles "snap-through". In: Computational methods in nonlinear structural and solid mechanics. Pergamon, pp 55–62

# Seismic Behavior Assessment of Semi-rigid Frame Under Near-Field Earthquakes


**Vijay Sharma, Sourabh Vern, Mahendra K. Shrimali, Shiv D. Bharti, and Tushar K. Datta**

**Abstract** The responses of semi-rigid (SR) frames under earthquakes are different from the rigid frames. Earlier research work was focused on far-field earthquakes, whereas the near-field (NF) earthquakes are crucial for civil engineering structures. In this paper, an extensive study is carried out to investigate the response behavior of semi-rigid frames for NF earthquakes with fling step and directivity effects. For this purpose, a ten-story steel frame is analyzed for four different earthquakes, two with near-field with directivity effect and one with the fling step effect and far-field earthquake. The PGV-to-PGA ratio is varied for NF earthquakes with directivity effects. A nonlinear time-history analysis is carried out for four earthquakes. The response quantities of interest include the maximum top-floor displacement, maximum inter-story drift ratio, total number of plastic hinges, SRSS of the maximum plastic hinge rotations, and energy dissipation in SR frames. The results of the numerical study indicate that the response behavior for the NF earthquakes with the fling step and directivity effects is distinctly different both in nature and magnitude. The PGV-to-PGA ratio has a significant effect on the response behavior of the frame produced by the NF earthquake with the directivity effect.

**Keywords** Near-field earthquakes · Semi-rigid frames · NTHA · Directivity effect · Fling step effect

V. Sharma (✉)
Department of Applied Mechanics, Government Engineering College Rajkot, Rajkot 360005, India
e-mail: vrsharma@gecrajkot.ac.in

S. Vern · M. K. Shrimali · S. D. Bharti · T. K. Datta
National Centre for Disaster Mitigation and Management, MNIT, Jaipur, India
e-mail: mkshrimali@mnit.ac.in

S. D. Bharti
e-mail: sdbharti@mnit.ac.in



M. Madhavan et al. (eds.), *Proceedings of the Indian Structural Steel Conference 2020 (Vol. 1)*, Lecture Notes in Civil Engineering 318,
https://doi.org/10.1007/978-981-19-9390-9_49

## 1 Introduction

The steel structures are generally given preference over reinforced concrete structure nowadays for industrial and multi-story residential and commercial buildings, especially for the high seismicity areas. The steel moment-resisting frames (MRFs) are preferred due to high ductility and strength as compared to other construction practices. After 2001, the Bhuj earthquake in India, the awareness toward the seismic-resistant design of structures is substantially increased.

While designing the steel structures for earthquake-resistant, the beam-column joint components are the most crucial and important in steel buildings. The traditional approach to design the connections considers it as rigid with the infinite stiffness in order to fulfill the safety considerations of high stiffness and adequate over-strength regardless of the cost of construction. During 1994 Northridge and 1995 Kobe earthquakes, the steel beam-column welded connections were severely damaged. These events diverted the attention of world earthquake fraternity toward the new seismic-resistant energy dissipation techniques, like semi-rigid (SR) or partially restrained frames, base-isolated structures, and so on. The significant amount of energy is dissipated in the formation of plastic hinges in flexural members during earthquakes. Based on the stocked seismic energy, the number and plastic rotations could be significant in a high level of damages. The use of semi-rigid (SR) frames, significantly decreases the number of hinges and improvise the structural performance in earthquakes (lower down the structural damage levels/collapse prevention 'CP' level to life safety 'LS' or immediate occupancy 'IO' levels, explained in ASCE-41 [4].

Awareness of these techniques, various codes of practice [3, 12] incorporated the semi-rigid connections in their design guidelines. Three types of beam-column connections are defined in these codes, rigid, semi-rigid, and pinned connections. Díaz et al. [6] extensively state-of-the-art reviewed the development of SR connections during the twentieth century. In the paper, the SR connections were classified into different models, like mechanical, experimental, analytical, numerical, informational based on the moment-rotation ($M$-$\theta$) behavior. According to FEMA-355D [10], global hysteretic energy can be increased through improving the hysteretic path of structural members and connections or impelling more locations for plastification before structural damage. The second approach is adopted in current practices as described in ANSI/AISC-341 [3] and Eurocode-8 [8].

The seismic performance evaluation of SR steel frames was investigated by several researchers analytically or experimentally [1, 7, 15, 17]. Most of the research studies and codes of practice consider only the far-field earthquake for seismic performance assessment. The research work under near-field earthquakes is meager for SR frames [2, 18, 19]. Sharma et al. [18] investigated the behavior of steel SR frames under far-field and near-field earthquakes for mid-rise structures. Aksoylar et al. [2] and Faridmehr et al. [9] investigated the efficacy of SR connection flexibility and strength of steel frames and suggested to include in design procedures.

This paper investigated the behavior of the ten-story with a three-bay symmetric semi-rigid steel frame under the near-field earthquakes. The near-field earthquakes

consist of two near-fields with forward directivity (with high and low PGV: PGA ratio) and one near-field with the fling step effect. All earthquakes are scaled to three PGA levels (0.2 g low, 0.4 g medium, and 0.6 g high PGA). A wide range of response parameters, namely maximum inter-story drift ratio, maximum top-floor displacements, number of plastic hinges, SRSS values of maximum plastic hinge rotation, and energy dissipation in SR frames are obtained. Further, the responses evaluated from near-field earthquakes are compared with the responses obtained from far-field earthquakes. The effect of PGV: PGA ratio and nature of earthquakes are reported in this paper.

## 2 Analytical Methodology

A nonlinear time-history analysis (NTHA) is performed on a ten-story steel SR frame under the near-field and far-field earthquakes. In this section, the modeling of SR connection, its implementation in standard nonlinear software SAP2000v19 [16], and the analysis approach are discussed.

### *2.1 Modeling of Semi-rigid Connection and Its Implementation in Software*

The attributes of SR connections are dependent on three parameters, namely the stiffness parameter ($K_c$), flexural strength parameter ($\beta$), and connection ductility ($\mu$). The relationship among three parameters is represented in the generic plot as shown in Fig. 1. The yield moment of connection ($M_{yc}$) is considered two-third of the plastic moment capacity of connection ($M_{pc)}$. The ultimate moment capacity of connection is considered as 0.8 times the $M_{pc}$ as per guidelines defined in ANSI/AISC-341 [3]. The initial connection stiffness of connection ($S_{Ki}$) is varied with connected beam flexural strength, i.e., $S_{Ki} = K_c\ (EI_B/l_B)$, where $(EI_B/l_B)$ is the flexural stiffness of connected beam. Chan and Chui [5] suggested the drift criteria for SR connection, $\theta_u \geq 0.04$ rad. Thus, the connection plastic rotation ($\theta_{pc}$) is limited to 0.8 times the ultimate rotation ($\theta_u$).

The SR connections are implemented in SAP2000 using the two-jointed zero-length multi-linear plastic link elements with kinematic hysteretic behavior. The rotational nonlinearity in R3 direction at the beam ends only is provided for SR connections.

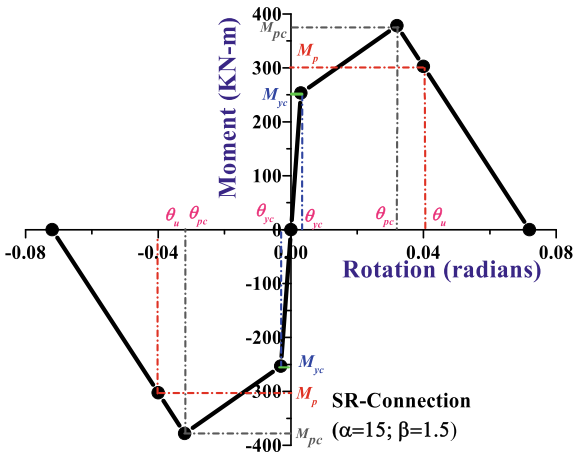


**Fig. 1** Hysteretic plot of semi-rigid connection

## *2.2 Analysis Approach*

A numerical model of steel SMF is analyzed and designed as per Indian standard seismic guidelines. The benchmark analysis approach, nonlinear time-history analysis (NTHA) is used to evaluate the seismic behavior of SR steel frames. The flexural beam member is modeled like an elastic member with default moment type (M3) plastic hinges at the ends and default P-M3 type hinges are employed in column ends which considers the interaction of axial force with bending moments. The default hinge properties are described in Fig. 2 as per the ASCE-41 [4] acceptance criterion. Three performance levels are defined in the curve, immediate occupancy (IO), life safety (LS), and collapse prevention (CP), and the values are obtained from Table 9.6 of ASCE-41 [4]. The secondary *P*-delta effects are considered to carry the geometric nonlinearity. Therefore, in this study, three types of nonlinearity, namely the connection nonlinearity, material nonlinearity (in the form of concentrated default flexural hinges), and geometric nonlinearity, are taken.

SAP2000 provides the opportunity to consider the three widely accepted direct integration approaches for NTHA simulations, Wilson-Theta, Newmark-Beta, and Hilber-Hughes-Taylor integration approach. The Hilber-Hughes-Taylor time integration approach with 5% Rayleigh damping is considered for simulations. The damping is obtained from the first two vibration modes for all the cases.

# 3 Numerical Study

A ten-story three-bay symmetric rigid steel moment-resisting frame (SMF) is analyzed and designed as per the Indian standard guidelines. The gravity loading as per IS-875 [13] and the sections detailing are shown in Table 1. The selection of

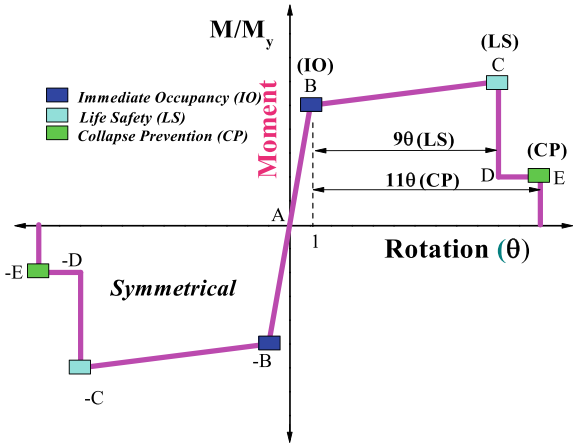


**Fig. 2** Hysteretic plot of default plastic hinges as per ASCE 41-17 acceptance criteria

steel sections is based on the strong column-weak beam (SCWB) design concepts so the plastification in the form of hinges is primarily observed in flexural beam members and then propagate in columns. The SMF frame is seismically designed as per IS-1893 [14] criterion. The zone factor '$Z$' (=0.36) and importance factor '$I$' (=1) with medium soil conditions are selected for design parameters. The panel zone has been provided with continuity and doubler plates for the capacity enhancement to remain elastic. The similar sections are used for SR connected frame. In this study, the stiffness parameter '$K_c$'(=15) and strength parameter '$\beta$' (=1.5) are selected for SR frame.

The seismic performance of the SR frame is investigated under three near-field earthquakes, out of which two have directivity effects and one is with fling step effects. The PGV: PGA ratio is varied for near-field with directivity earthquakes (NFD), one is designated with a high ratio (PGV: PGA > 150, NFD-HR) and other with a low ratio (PGV: PGA < 150, NFD-LR) directivity earthquakes. Further, the seismic behavior is compared with the response obtained from the far-field earthquake. The near-field earthquakes are selected based on the Joyner-Boore distance ($R_{jb}$ < 20 km), and far-field earthquake is chosen from the FEMA-P695 [11] report. The earthquakes are

**Table 1** Gravity loading and steel section detailing

| Loading detail | | | | |
|---|---|---|---|---|
| Sr. no | Floor | Height (m) | Dead load (KN/m) | Live load (KN/m) |
| 1 | 1st–9th | 3.2 each | 20 | 4 |
| 2 | 10th | 3.2 each | 15 | 4 |

| Section detail | | | | |
|---|---|---|---|---|
| Sr. no | Floor | Bay width (m) | Beam | Column |
| 1 | 1st–6th | 5 | W 14X48 | W 14X53 |
| 2 | 7th–10th | 5 | W 14X48 | W 14X68 |

**Table 2** Earthquake ground motion records

| S.no | Event Year_ Earthquake_ Station-Component | $M_w$ | PGA (g) | PGV (cm/s) | PGD (cm) | PGV/ PGA | $R_{jb}$ (km) |
|---|---|---|---|---|---|---|---|
| 1 | 1992_Landers_Cool Water-TR (FF) | 7.3 | 0.42 | 42.35 | 13.84 | 101 | 19.7 |
| 2 | 2004_Parkfield_ Chalome IE-90 (NFD-LR) | 6 | 0.44 | 40.13 | 9.43 | 91 | 1.66 |
| 3 | 1994_Northridge_ Jensen Filter Plant Adm Building-22 (NFD-HR) | 6.69 | 0.41 | 111.47 | 44.63 | 272 | 0.1 |
| 4 | 1999_Kocaeli_ Sakarya-EW (NF-F) | 7.4 | 0.41 | 82.05 | 205.93 | 200 | 3.2 |

selected in such a way that PGA values are nearly the same. The seismic behavior of the SR frame is assessed at three scaled PGA levels, designated as low (0.2 g), medium (0.4 g), and high (0.6 g) levels. The details of earthquake time histories are represented in Table 2.

## 4 Discussion of Results

A wide range of seismic response quantities, namely maximum values of top-floor displacement (TFD), base shear, inter-story drift ratio, total number of plastic hinges, SRSS of maximum plastic rotations, and energy dissipation in semi-rigid (SR) frame under four earthquake ground motions are obtained from NTHA simulations to assess the seismic behavior under near-field earthquakes. The effect of PGV: PGA ratio in near-field with directivity earthquakes is also investigated. Further, the responses obtained from near-field earthquakes are also compared with those responses evaluated from the far-field ground motion.

Figure 3 shows the variation of maximum values of top-floor displacement for near-field and far-field earthquakes. The TFD represents the global stability of structures. It is clearly noticed from the figure that near-field ground motion imposed higher demands (or TFD values) as compared to far-field earthquakes, and it is maximum in near-field with high directivity ratio earthquake. Further, the TFD values are increased with an increment in PGA values. It is also observed from the figure that the demand imposed in a high directivity earthquake at 0.2 g PGA level is very much near to demand imposed by near-field with fling step earthquake at 0.6 g PGA level. At a high level of PGA, the far-field earthquakes imposed minimum demand as compared to the other three near-field earthquakes. Therefore, the near-field with

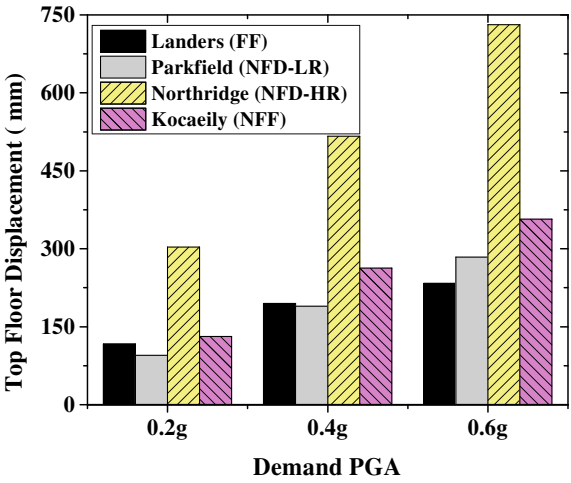


**Fig. 3** Variation of top-floor displacement with PGA for different types of earthquakes

high directivity earthquakes should be critically examined for the global stability of the structure.

Figure 4 represents the variation of base shear at three PGA levels under four types of earthquakes in the SR frame. A similar trend of results is obtained for all varieties of earthquakes with increased PGA levels. Here, it is interesting to note that the near-field with a low directivity earthquake (Parkfield) produces the least base shear as compared to others. This shows that the nature of the earthquake also has a significant contribution to seismic behavior assessment. From the figure, it has also resulted that high directivity near-field earthquakes imposed the maximum base shear requirement.

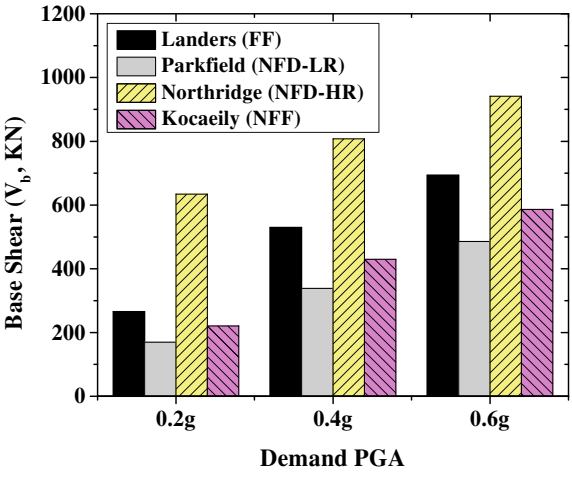


**Fig. 4** Variation of maximum base shear with PGA for different types of earthquakes

Figures 5 and 6 show the variation of maximum inter-story drift values under different earthquakes and variation along with the story height in the SR frame. The MIDR variation represents the story-level demand requirement in structures. The difference in the maximum value of MIDR between the near-field with low ratio and far-field earthquake is significantly reduced with an increase in PGA level. This shows that the near-field earthquakes have a considerable effect on MIDR responses. Further, a similar trend in maximum values in MIDR is observed for near-field and far-field earthquakes. It is also noticed that the difference between the NF-F and NFD-HR is significantly increased at high PGA levels as compared to previously considered responses (TFD and base shear). Figure 6 shows the variation of MIDR along with story height and observed that maximum values of MIDR in all cases are obtained at the third story level. It is also observed that the MIDR along story height is considerably increased in NFD-HR type earthquakes with PGA level as compared to other earthquakes.

Table 3 shows the formation of the total number of plastic hinges and the maximum value of SRSS of plastic hinge rotation at three PGA levels under four types of earthquakes. The number of plastic hinges expresses the extent of plastification or energy dissipation under flexural members (beam and column). The formation of hinges shows the local stability of the member. It is clearly observed from the table that there is a significant increase in the total number of plastic hinges and their SRSS values for near-field with a high directivity ratio. Further, it is also observed that there is a noticeable increase in hinges observed with rising in PGA level from medium (0.4 g) to high (0.6 g) level. Table 3 also explained that the SR frame remains in the elastic zone under FF, NFD-LR, and NF-F type ground motion till the PGA level of 0.4 g.

Table 4 discusses the normalized value of modal damping and link hysteretic energy for four types of earthquakes. It is observed from table that the modal damping

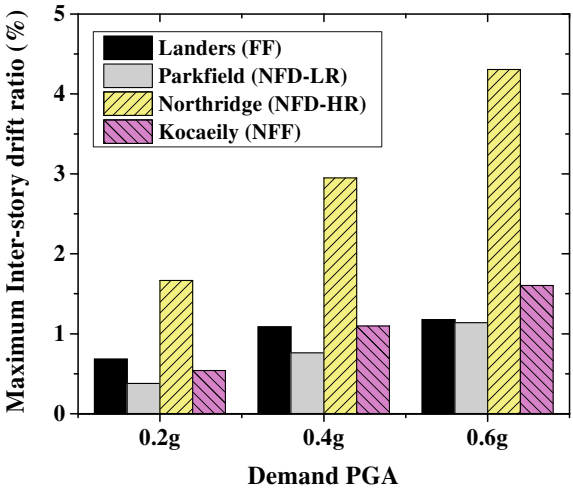


**Fig. 5** Variation of maximum values of inter-story drift ratio with PGA for different types of earthquakes

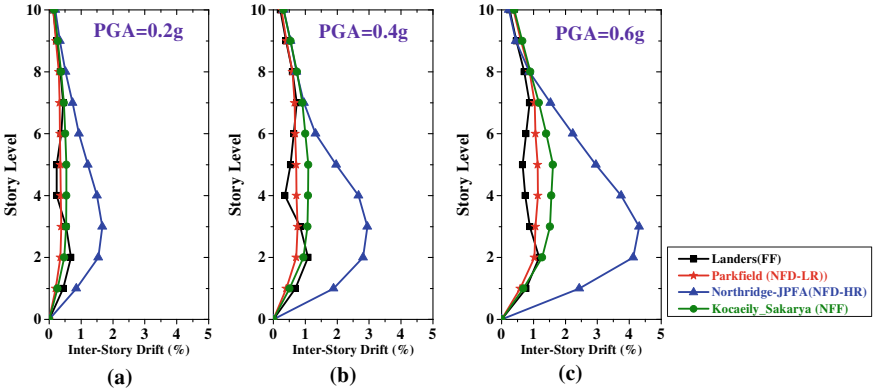


**Fig. 6** Variation of MIDR along with height with PGA for different types of earthquakes

**Table 3** Total number of plastic hinges and SRSS of maximum plastic hinge rotations

| Earthquake type | Seismic response | 0.6 g | 0.4 g | 0.2 g |
|---|---|---|---|---|
| Landers (FF) | $NH_{Total}$ | 2 | 0 | 0 |
| | SRSS ($\times 10^{-3}$ rad) | 0.67 | 0 | 0 |
| Parkfield (NFD-LR) | $NH_{Total}$ | 0 | 0 | 0 |
| | SRSS ($\times 10^{-3}$ rad) | 0 | 0 | 0 |
| Northridge (NFD-HR) | $NH_{Total}$ | 49 | 25 | 3 |
| | SRSS ($\times 10^{-3}$ rad) | 43.7 | 22.6 | 2.1 |
| Kocaeli (NF-F) | $NH_{Total}$ | 4 | 0 | 0 |
| | SRSS ($\times 10^{-3}$ rad) | 0.15 | 0 | 0 |

energy is reduced with an increase in PGA level, and the link hysteretic energy is increased with an increase in PGA level. It shows that the energy dissipation in SR connection reduces the modal damping energy, which results in the reduction of number of plastic hinges. The link energy is considerably increased in NFD-HR earthquake. Further, the dissipation of energy in various forms at high level (0.6 g) of PGA is shown in Fig. 7. Figure 7 shows that the stored energy is dissipated basically in the form of modal damping and link hysteretic energy. The energy dissipation in link hysteretic energy at 0.6 g PGA level is significantly high in NFD-HR earthquake as compared to other energies.

**Table 4** Modal damping and link hysteretic energy

| Earthquake type | Response | 0.6 g | 0.4 g | 0.2 g |
|---|---|---|---|---|
| Landers (FF) | Modal damping energy ($E_{md}$) | 0.856 | 0.861 | 0.717 |
| | Link hysteretic energy ($E_{LH}$) | 0.072 | 0.003 | 3.6E-16 |
| Parkfield (NFD-LR) | Modal damping energy ($E_{md}$) | 0.758 | 0.756 | 0.561 |
| | Link hysteretic energy ($E_{LH}$) | 0.059 | 0.000 | 2.81E-16 |
| Northridge (NFD-HR) | Modal damping energy ($E_{md}$) | 0.379 | 0.443 | 0.628 |
| | Link hysteretic energy ($E_{LH}$) | 0.602 | 0.530 | 0.234 |
| | Link hysteretic energy ($E_{LH}$) | 0.211 | 0.022 | 3.79E-17 |

$E_{md}$ = (Modal Damping Energy/Total Input Energy)
$E_{LH}$ = (Link Hysteretic Energy/Total Input Energy)

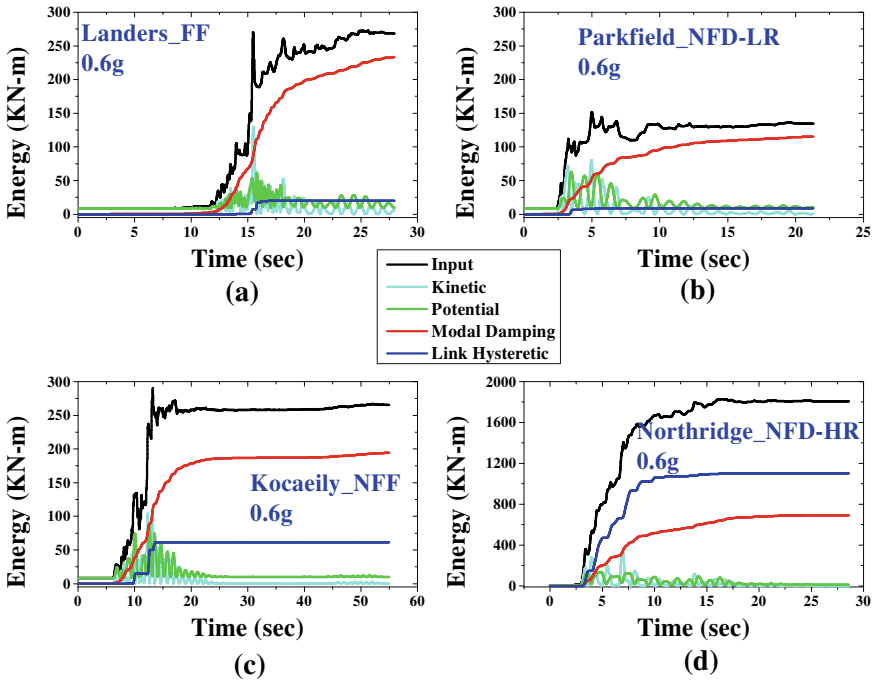


**Fig. 7** Variation of energy at 0.6 g PGA level under different types of earthquakes

## 5 Conclusion

The seismic behavior of a ten-story semi-rigid steel moment-resisting frame is investigated under the near-field earthquakes with directivity and fling step effects at three scaled PGA levels. The three PGA levels are represented the low, medium, and

high levels of earthquakes. A nonlinear time-history analysis is performed to obtain a large number of response parameters, namely, top-floor displacement, base shear, maximum inter-story drift ratio, the total number of hinges, SRSS of maximum plastic hinge rotations, and energy dissipation in connection. Further, the responses from near-field earthquakes are compared with those which are obtained from far-field earthquakes. The semi-rigid connection is modeled using a two-jointed multi-linear plastic link element. The findings of the numerical study are as follows:

(1) The near-field directivity earthquake with high PGV: PGA ratio imposed the maximum seismic demands as observed in all responses in SR frame as compared to other earthquakes.
(2) The nature of the earthquake significantly affects the seismic behavior of the SR frame.
(3) The maximum value of MIDR is obtained at the third story level in all four considered earthquakes.
(4) The far-field earthquakes, in general, imposed the minimum demand but it is dependent on the nature of the earthquake.
(5) The difference in seismic demands is significantly increased with increases in the PGA level from medium (0.4 g) to high level (0.6 g).
(6) The plastification in flexural members in this study started after medium-level PGA, except for the near-field directivity with high PGV: PGA ratio.
(7) The energy is dissipated in structures mainly in two forms, modal damping and link hysteretic energy. The link hysteretic energy is maximum in the near-field with a high directivity ratio, whereas the modal damping shared the maximum energy dissipation in other considered earthquakes.

## References

1. Abolmaali A, Matthys JH, Farooqi M, Choi Y (2005) Development of moment–rotation model equations for flush end-plate connections. J Constr Steel Res 61:1595–1612
2. Aksoylar ND, Elnashai AS, Mahmoud H (2011) The design and seismic performance of low-rise long-span frames with semi-rigid connections. J Constr Steel Res 67:114–126
3. ANSI/AISC-341 (2016) Seismic provisions for structural steel buildings. Chicago, Illinois, pp 60601–1802
4. ASCE-41 (2017) ASCE 41-17: seismic evaluation and retrofit rehabilitation of existing buildings. In: Proceedings of the SEAOC
5. Chan S, Chui P (2000) Nonlinear static and cyclic analysis of steel frames with semi-rigid connections. Elsevier
6. Díaz C, Martí P, Victoria M, Querin OM (2011) Review on the modelling of joint behaviour in steel frames. J Constr Steel Res 67:741–758
7. Elnashai AS, Elghazouli A (1994) Seismic behaviour of semi-rigid steel frames. J Constr Steel Res 29:149–174
8. Eurocode-8 (2005) Design of structures for earthquake resistance. Part, 1, 1998-1
9. Faridmehr I, Tahir MM, Lahmer T (2016) Classification system for semi-rigid beam-to-column connections. Latin Am J Solids Struct 13:2152–2175
10. FEMA-355d (2001) State of the art report on connection performance. Sacramento, California

11. FEMA-P695 (2009) Quantification of building seismic performance factors. FEMA P695. Federal Emergency Management Agency
12. IS-800 (2007) General construction in steel-code of practice (third revision). Bureau of Indian Standards, New Delhi
13. IS-875 (1987) Part 1: dead loads—unit weights of building materials and stored materials. Bureau of Indian Standards, New Delhi
14. IS-1893 (2016) Criteria for earthquake resistant design of structures, part 1 general provisions and buildings (sixth revision). Bureau of Indian Standards, New Delhi
15. Lemonis M (2018) Steel moment resisting frames with both joint and beam dissipation zones. J Constr Steel Res 147:224–235
16. SAP2000v19 (2018) Integrated software for structural analysis and design. Computers and Structures Inc, Berkeley, CA, USA
17. Sekulovic M, Nefovska-Danilovic M (2008) Contribution to transient analysis of inelastic steel frames with semi-rigid connections. Eng Struct 30:976–989
18. Sharma V, Shrimali M, Bharti S, Datta T (2018) Behavior of semi-rigid frames under seismic excitations. In: 16SEE, 20–22 Dec 2018, IIT Roorkee, pp 1–10
19. Sharma V, Shrimali M, Bharti S, Datta T (2019) Seismic energy dissipation in semi-rigid connected steel frames. In: 16WCSI, 2019 Saint Petersburg, Russia. St. Petersburg, Russia

# Seismic Performance Assessment of Semi-rigid Frames for Different Performance Criteria


**Vijay Sharma, Mohit Bhandari, Mahendra K. Shrimali, Shiv D. Bharti, and Tushar K. Datta**

**Abstract** Evaluation of the performance of semi-rigid (SR) frames for different types of earthquakes is a topical subject of research. In this paper, the seismic performance of SR frames is evaluated using the capacity spectrum method. One five-story rigid frame is analyzed in order to compare the relative performance with the semi-rigid frames. An ensemble of ten far-field earthquake ground motions is selected for determining the statistics related to the probability of exceedance (POE) of the performance criteria. The performance criterion for each seismic demand parameter (SDPs) is selected based on the engineering judgment. Assuming earthquake variability as a major source of uncertainty, the POE of the performance criterion of a seismic demand parameter is determined for each PGA level of the earthquake following a lognormal distribution. The SDPs, namely, the maximum inter-story drift ratio and maximum roof drift ratio at the performance point are obtained for a particular PGA. The results of the study indicate that the POE of the performance criterion considerably differs with the seismic demand parameter and the nature of the earthquake. Further, the POE values considerably vary with the stiffness parameter.

**Keywords** Semi-rigid steel frame · Pushover analysis · Far-field earthquake · Probability of exceedance

V. Sharma (✉)
Department of Applied Mechanics, Government Engineering College Rajkot, Rajkot 360005, India
e-mail: vrsharma@gecrajkot.ac.in

M. Bhandari
Department of Civil Engineering, Chandigarh University, Chandigarh, India
e-mail: mohit.e8967@cumail.in

M. K. Shrimali · S. D. Bharti · T. K. Datta
National Centre for Disaster Mitigation and Management, MNIT, Jaipur 302017, India
e-mail: mkshrimali@mnit.ac.in

S. D. Bharti
e-mail: sdbharti@mnit.ac.in



M. Madhavan et al. (eds.), *Proceedings of the Indian Structural Steel Conference 2020 (Vol. 1)*, Lecture Notes in Civil Engineering 318,
https://doi.org/10.1007/978-981-19-9390-9_50

## 1 Introduction

Seismic events are one of the most disastrous in recent decades in India. After 26th January 2001, Bhuj earthquake in India, the attention toward natural hazards the disaster management and mitigation for seismic events are significantly enhanced in the Indian subcontinent. Various government organizations for analyzing the pre- and post-effects are established. Thus, the reliable assessment of seismic performance evaluation has become imperative to prepare the country to encounter and mitigate the consequences of the earthquake such as structural damage, loss of property, and life. Under these conditions, the semi-rigid steel frames perform better due to additional energy dissipation capacity in beam-column connections and the reduced base shear requirement for frame sections.

During the 1994 Northridge and 1995 Kobe Earthquake, several welded steel moment frames were severely damaged at the beam-column joint level. These events diverted the attention of structural engineers toward the use of semi-rigid (SR) or partially restrained frames. Various studies revealed that SR frames behave considerably better in earthquakes, especially in the high seismic-prone areas [1, 14, 20, 21]. The damage caused by earthquakes in SR frames can be better understood through the probabilistic assessment [8]. The fragility curves for SR and rigid (FR) frames at different damage levels can be generated using incremental dynamic analysis or dynamic pushover [22] approach either carried out nonlinear time history analysis (NTHA) or capacity spectrum method (CSM) [4]-based nonlinear static analysis. The NTHA process is time-consuming and complicated procedure, whereas the CSM is a quick assessment method for fragility analysis. In this study, the method suggested by Rossetto et al. [18] and Barbat et al. [5] using the capacity spectrum method is adopted.

In this paper, a five-story rigid and semi-rigid frames are investigated under a suite of ten far-field ground motions records for probabilistic seismic performance evaluation of SR frames. The demand response spectra from ground motion records are smoothened to obtain the performance points using the CSM method. The threshold values describing the damage levels are selected from HAZUS guidelines [13]. Considering the seismic variability, the fragility curves for seismic demand parameters (SDPs) are generated with the assumption that the SDPs follow the lognormal distribution. Further, the comparison is carried out in the form of fragility curves with the responses obtained from rigid frames. The maximum inter-story drift ratio and roof drift ratio are considered as damage measure (DM) or SDPs.

## 2 Theory

### 2.1 Modeling of Semi-rigid Connection, Its Implementation in Software, and Analysis Method

The beams-to-column connection in this study for semi-rigid (SR) frames possess kinematic hysteresis behavior. Two jointed zero-length multi-linear plastic link elements are used to model the SR connections. Figure 1 shows the generic plot of the moment-rotation ($M$-$\theta$) behavior for SR connections. The $M$-$\theta$ values are reliant on the three parameters, described in ANSI/AISC-341 [2], namely stiffness, flexural strength, and ductility of connection for special moment frames. The flexural strength of connections is obtained to maintain the ratio between yield moment capacity of connection to ultimate plastic moment capacity of connection ($M_{\mathrm{pc}}$) as two-thirds. The flexural strength of connection at the column face should be 0.8 times the plastic moment capacity of the connected beam ($M_{\mathrm{pb}}$) to fulfill the story drift limit (> 0.04 rad), prescribed by ASCE 341-16. The degrees of semi-rigidity for SR connection are represented by two dimensionless parameters, namely the stiffness parameter ($k$) and strength parameter ($\alpha$). In this study, the parameters $k$ (= 10, 15), and $\alpha$ (= 1.2, 1.5) which represent the degree of semi-rigidity are considered for SR frames. The semi-rigid frames are designated as ASR1 ($k = 15, \alpha = 1.5$; stiff and low flexible) and ASR2 ($k = 10, \alpha = 1.2$; moderate and high flexible). The SR connections are modeled in the standard software [19]. The parameters are defined in Eq. 1.

$$k = S_{ki} \Big/ \left(\frac{E I_{\mathrm{b}}}{L_{\mathrm{b}}}\right), \quad \text{and} \quad \alpha = \frac{M_{\mathrm{pc}}}{M_{\mathrm{pb}}}, \tag{1}$$

where $S_{ki}$ is initial connection stiffness, $EI_{\mathrm{b}}/L_{\mathrm{b}}$ is the flexural stiffness of adjoining beams.

In analyses, three types of nonlinearity, namely material nonlinearity, connection nonlinearity, and geometric nonlinearity are considered. The material nonlinearity is incorporated in the form of concentrated default plastic hinges as per the guidelines of ASCE-41 [3]. The hysteresis plot for default plastic hinges is explained in Fig. 2. The secondary $P$-delta effects are taken for geometric nonlinearity.

The nonlinear static pushover analyses for rigid and SR frames are carried out to obtain spectral displacement and other seismic responses. The frames are laterally monotonically pushed till the deformation reached 4% of the total height up to the collapse stage. The fundamental first mode shape lateral load pattern is adopted for the lateral loading. Further, the capacity curves for both frames from pushover analysis are obtained and identified the damage states as shown in Fig. 3.

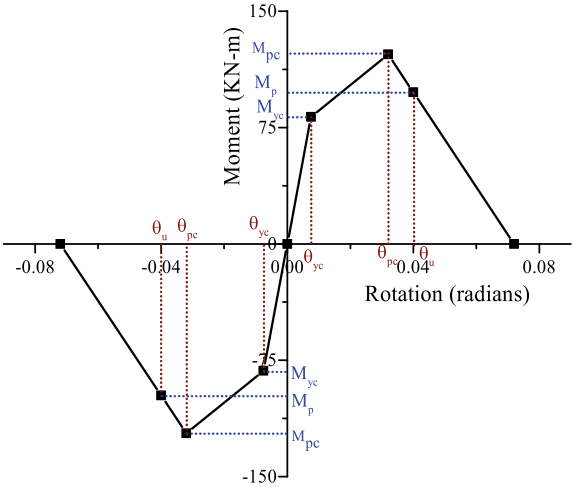


**Fig. 1** Moment-rotation curve for SR connection

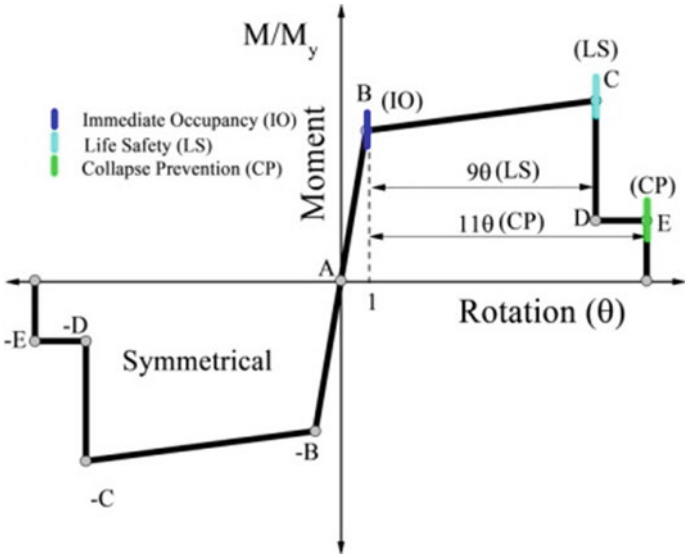


**Fig. 2** Hysteresis plot for default plastic hinges (as per ASCE 41)

## *2.2 Development of Fragility Curve, Selection of Damage Measures, Damage States*

In the recent 40 years, the fragility analysis of structures became an impeccable emerging technique for probabilistic seismic hazard assessment (PSHA). The

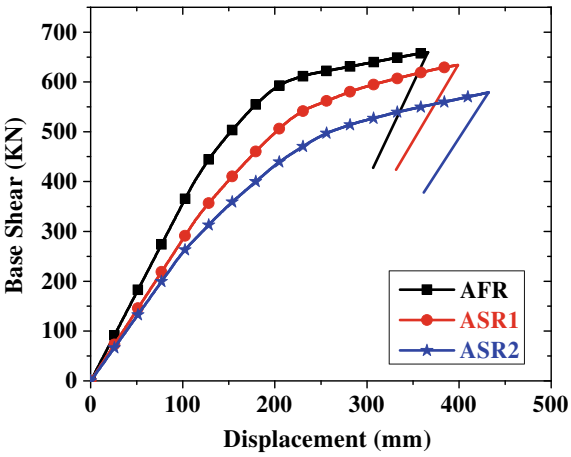


**Fig. 3** Capacity curves with damage states

fragility assessment becomes a promising approach to carry out performance-based seismic design [7, 16]. Fragility curves are generated to assess the failure probability of structures for a predefined damage measure (*DM*). The fragility curve represents a continuous relationship between the seismic intensity measure (IM) and the probability of exceedance (*POE*) for particular damage measure (*DM* or *ds*) at a predefined damage state ($ds_i$) [16, 17]. The theory of fragility analysis in the seismic hazard assessment was initially adopted by Kennedy et al. [12] for PSHA in the nuclear power plant. The fragility curves are generally explained assuming that it follows the lognormal distribution function [15]. It can be represented as shown in Eq. 2.

$$\text{POE}\left(ds \geq ds_i \vdots IM\right) = \Phi\left[\frac{1}{\beta_{\text{T}}} \ln\left(\frac{IM}{IM_{\text{m}}}\right)\right], \tag{2}$$

where $\beta_{\text{T}}$ is the standard deviation in total uncertainty (which is square root of sum of squares of capacity uncertainty $\beta_{\text{C}}$ and earthquake variability $\beta_{\text{D}}$); and $\Phi$ is designated as standard cumulative distribution function (*CDF*); *IM* [such as PGA, PGV, Sa(T1)] and the $IM_{\text{m}}$ is the median intensity measure value, results to ith damage state.

The fragility curve can be generated using different methods, the safety factor method, numerical simulation method with linear regression analysis and maximum likelihood estimation approach and the incremental dynamic analysis method [23]. The uncertainties related to design requirement related, test data related, record-to-record variability, and modeling related are generally considered in PSHA. The record-to-record variability or seismic uncertainties is much greater than other sources of uncertainty, and thus, it is considered in our study.

In this paper, the analytical approach was used to prepare the fragility curves. Cornell et al. [6] suggested that the response of the structure can be assumed as lognormal distribution and damage measure (DM) relationship with intensity

**Table 1** Threshold values for damage states for different seismic demand parameters

| Damage state | Damage measure | | | |
|---|---|---|---|---|
| | MIDR | RDR | MIDR | RDR |
| | Rigid frame | | Semi-rigid frame | |
| Slight | 0.004 | 0.00875 | 0.0045 | 0.00938 |
| Moderate | 0.0069 | 0.0125 | 0.0072 | 0.0138 |
| Extensive | 0.0157 | 0.01563 | 0.02 | 0.0166 |
| Complete | 0.04 | 0.0228 | 0.05 | 0.0249 |

measure (IM) can be represented as shown in Eq. 3.

$$\ln(DM) = \ln a + b \ln(IM), \tag{3}$$

where $a$ and $b$ are the regression coefficient, obtained from regression analysis between $\ln(DM)$ with $IM$.

The uncertainty in an earthquake ($\beta_D$) generated by the IM related to the DM is obtained by a standard error in regression analysis [8]. The PGA is selected as IM for this study. As per HAZUS guidelines, the uncertainty in capacity ($\beta_C$) for steel frames is taken as 0.3. The threshold values for maximum inter-story drift ratio (MIDR) for considered damage states, namely slight, moderate, extensive, and complete are obtained from HAZUS. The other damage state values for roof drift ratio (RDR) were assumed by engineering judgment and based on the capacity curve and HAZUS guidelines. The RDR values are obtained from the median spectral displacements. The threshold values for MIDR and RDR values are represented in Table 1. The HAZUS provides the threshold values for steel rigid frames. Various research studies on SR frames revealed that a MIDR and RDR value comparatively higher in SR frames as compared to the rigid frames [8].

## 3 Numerical Study

The numerical study is carried out on five-story rigid and semi-rigid frames. An ensemble of ten far-field records is selected for analysis. The demand response spectra for considered earthquakes are shown in Fig. 4. The detailing of SR connections, selection of damage measures, intensity measure is discussed in the previous section. The design of the steel rigid frame, loading is discussed in this section.

A 5-story steel rigid frame (AFR) is designed as per Indian standard criterion [9, 10] considering the seismic strengthening requirements [11]. The 5-story special moment-resisting frame (SMRF) with rigid beam-column connections has three bays of 5 m each both directions with 3.2 m floor height. The effective gravity load consists of 20 KN/m of floor dead load, 15 KN/m as roof dead load, and 4 KN/m as live load, uniformly distributed over beams. The beam and column sections as shown in Fig. 5

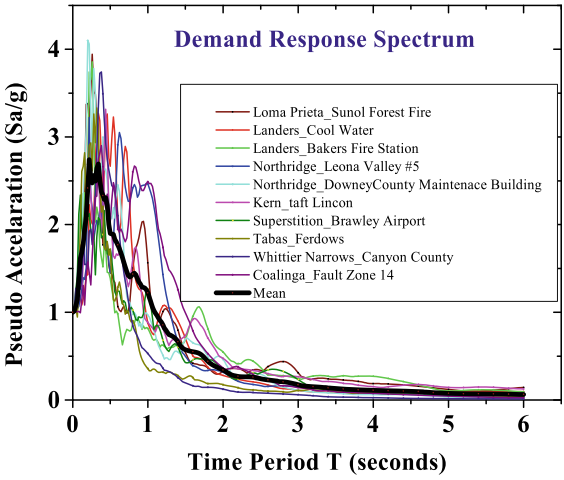


**Fig. 4** Elastic demand response spectrum for far-field records

are selected in such a way that it follows the strong column-weak beam design concept as per Indian Standard [9]. The rigid SMRF is designed for Zone V ($Z = 0.36$), with medium soil condition and importance factor ($I = 1$) as per Indian earthquake design requirements [11]. The similar sections are used for SR frames (ASR1 and ASR2) for comparison. The SR frame 'ASR2' is more flexible (with less '$k$' value) than the 'ASR1.' The fundamental first three modes of the period of vibration are presented in Table 2.

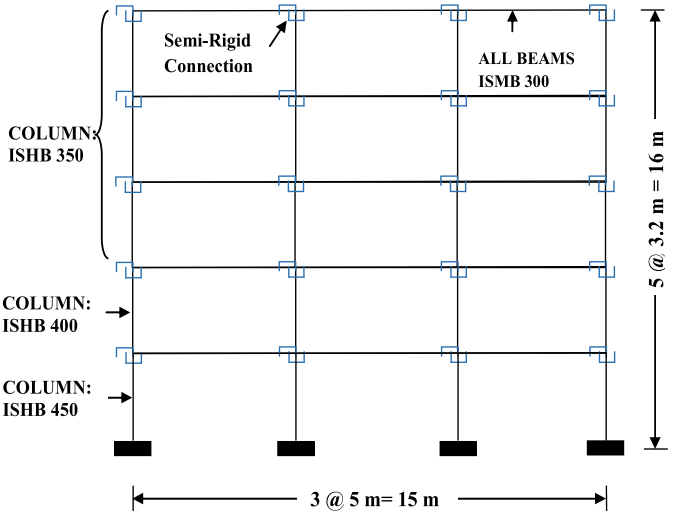


**Fig. 5** 5-story SR frame with a section detailing

**Table 2** Natural period of vibrations of the considered rigid and semi-rigid frames

| Sr. no | Frame ID | $T_1$ (s) | $T_2$ (s) | $T_3$ (s) |
|---|---|---|---|---|
| 1 | AFR | 1.033 | 0.319 | 0.16992 |
| 2 | ASR1 | 1.14302 | 0.34563 | 0.17795 |
| 3 | ASR2 | 1.19308 | 0.35684 | 0.18116 |

A suite of 10 far-field records is selected for analysis. The earthquakes are selected from the FEMA-P695 (2009) report. The PGA levels are scaled up to 1.2 g level with an increment of 0.1 g for all earthquakes, with an initial value 0.05 g, and 0.1–1.2 g. The 5-point smoothened demand response spectrum (as shown in Fig. 4) corresponding to the PGA level is used to obtain the performance point in the CSM method.

## 4 Result and Discussion

The fragility curves for rigid and semi-rigid frames for four damage states are generated by plotting the probability of exceedance (*POE*) of specific damage state on the PGA. The corresponding seismic responses are obtained from the acceleration demand response spectrum plot using performance points. The data are utilized to express the probabilistic earthquake demand models (PEDMs) using linear regression analysis. The frame response data (roof drift ratio) are arranged in a strip plot with respect to each PGA value as shown in Fig. 6.

Further, for fragility assessment, the seismic demand parameters (SDPs) are represented on the lognormal scale (Eq. 3) as shown in Fig. 7 for regression analysis. The PEDMs are generated, considering the threshold values (Table 1) of damage state are represented in Table 3. The essential parameters for lognormal distribution (median value of IM and logarithmic standard deviation) are tabulated in Table 4. The PEDMs response data of MIDR are represented in Fig. 7 for a set of far-field records.

### *4.1 Comparison of Fragility Curves for Maximum Inter-story Drift Ratio and Roof Drift Ratio*

Figure 8 shows the variation of fragility curves in MIDR at different damages states, namely, slight, moderate, extensive, and complete (as described in HAZUS) for three considered frames (AFR, ASR1, and ASR2) under an ensemble of far-field earthquakes. It is noticed in the figure that for all damage states considered, the flexible ASR2 frame is the most vulnerable with high POE values as compared to the other rigid and semi-rigid frame. Figure 8a shows that the POE values are nearly the same for all frames. A similar trend is observed at a moderate damage state, except

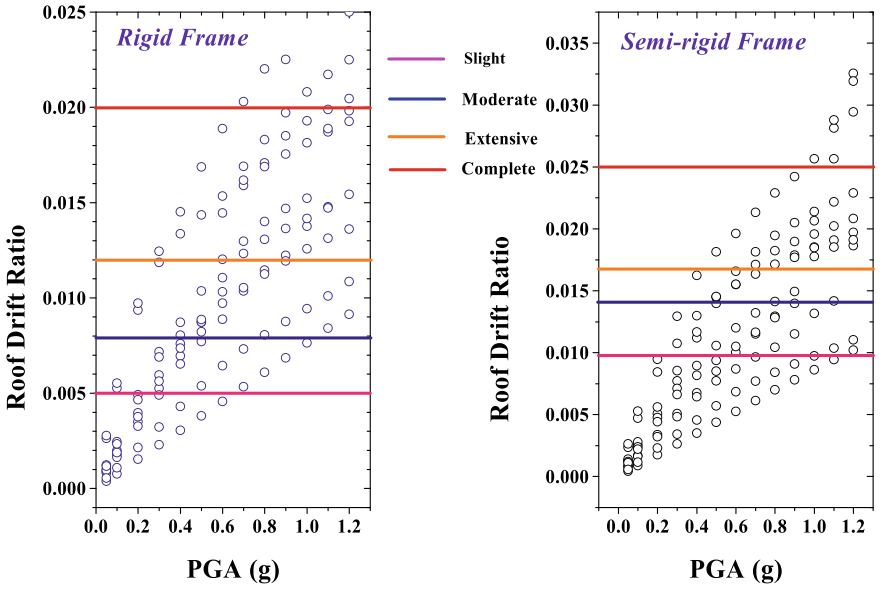


**Fig. 6** Dispersion of maximum value of roof drift ratio with respect to considered IM levels

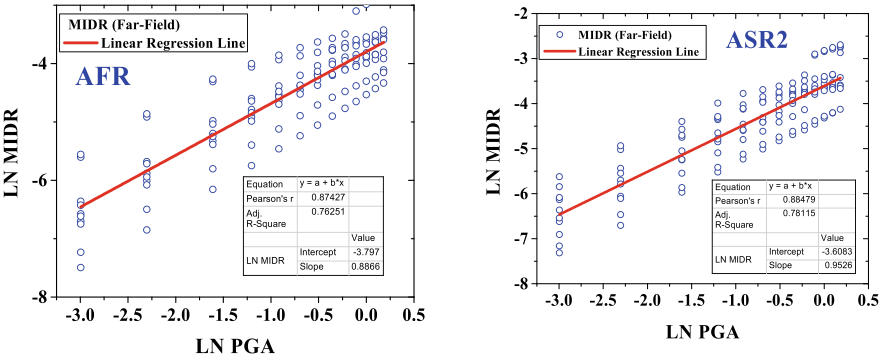


(a) (b)

**Fig. 7** Probabilistic earthquake demand models for maximum inter-story drift ratio for **a** rigid (AFR) and **b** semi-rigid frame (ASR2) under far-field earthquakes

the PGA values range between 0.2 to 0.6 g. The difference in POE values is increased in the extensive damage state, and the considerable difference is observed between the flexible SR (ASR2) frame and rigid frame. It is shown in previous research work that the SR frames perform better in earthquakes as compared to rigid frames and similar results are observed in damage state assessment. The 'ASR1' SR frame shows similar seismic performance in all considered damage states.

**Table 3** Probabilistic earthquake demand models for different damage measures

| Demand measure | Seismic demand parameter | PEDM | $\beta_D$ | Co-variance ($R^2$) |
|---|---|---|---|---|
| *Rigid frame AFR* | | | | |
| MIDR | Ln (MIDR) | Ln (0.0224) + 0.886 Ln (PGA) | 0.445 | 0.764 |
| RDR | Ln (RDR) | Ln (0.0156) + 0.873 Ln (PGA) | 0.465 | 0.774 |
| *Semi-rigid frame ASR1 (stiff and low flexible)* | | | | |
| MIDR | Ln (MIDR) | Ln (0.0255) + 0.924 Ln (PGA) | 0.47 | 0.775 |
| RDR | Ln (RDR) | Ln (0.01724) + 0.892 Ln (PGA) | 0.445 | 0.792 |
| *Semi-rigid frame ASR2 (moderate and high flexible)* | | | | |
| MIDR | Ln (MIDR) | Ln (0.0271) + 0.951 Ln (PGA) | 0.474 | 0.783 |
| RDR | Ln (RDR) | Ln (0.018) + 0.909 Ln (PGA) | 0.445 | 0.779 |

**Table 4** Fragility parameters at different damage states

| Demand measure | Damage states | | | | | | | |
|---|---|---|---|---|---|---|---|---|
| | Slight (DS1) | | Moderate (DS2) | | Extensive (DS3) | | Complete (DS4) | |
| | Median value of PGA (g) | ($\beta_T$) | Median value of PGA | ($\beta_T$) | Median value of PGA | ($\beta_T$) | Median value of PGA | ($\beta_T$) |
| *Rigid frame AFR* | | | | | | | | |
| MIDR | 0.143 | 0.55 | 0.312 | 0.55 | 0.878 | 0.55 | 2.265 | 0.55 |
| RDR | 0.515 | 0.54 | 0.775 | 0.54 | 1.001 | 0.54 | 1.482 | 0.54 |
| *Semi-rigid frame ASR1 (stiff and low flexible)* | | | | | | | | |
| MIDR | 0.171 | 0.56 | 0.362 | 0.56 | 0.977 | 0.56 | 2.976 | 0.56 |
| RDR | 0.506 | 0.54 | 0.776 | 0.54 | 0.955 | 0.54 | 1.507 | 0.54 |
| *Semi-rigid frame ASR2 (moderate and high flexible)* | | | | | | | | |
| MIDR | 0.151 | 0.56 | 0.248 | 0.56 | 0.726 | 0.56 | 1.904 | 0.56 |
| RDR | 0.489 | 0.54 | 0.743 | 0.54 | 0.912 | 0.54 | 1.427 | 0.54 |

Further, the POE for rigid and SR steel frames at three PGA levels, namely 0.2 g (low), 0.4 g (design), and 0.8 g (severe) are compared for MIDR response. Figure 8 shows that the POE values are nearly the same at low (0.2 g) PGA levels for all frames. The POE values are the highest for the ASR2 frame with the order of 56% at 0.8 g, and 14% at 0.4 g in extensive damage state. On the other hand, it is also observed that the lowest values of POE are obtained in the rigid frame of the order of 40% at 0.8 g and 7% at 0.4 g.

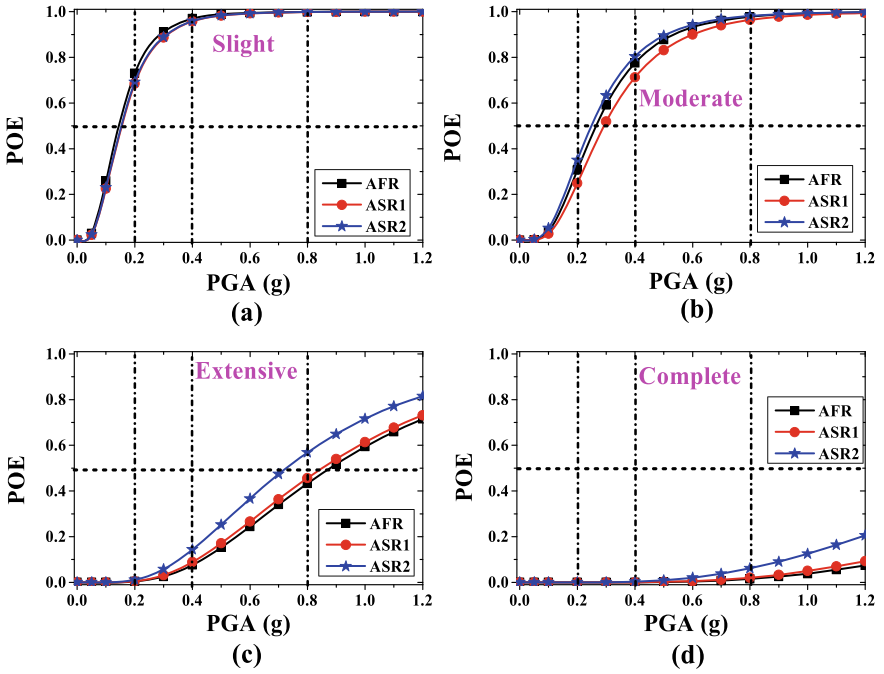


**Fig. 8** Fragility curves for maximum inter-story drift ratio in five-story rigid (AFR) and semi-rigid frames (ASR1 and ASR2) under far-field earthquakes

Figure 9 presents the fragility curves for maximum values of roof drift ratio (RDR) damage measure for the three considered frames in four damage states. The RDR seismic demand parameters are used to assess the global stability of frames. It is observed from the figure that the rigid AFR and semi-rigid ASR1 present almost similar values of POE for RDR. Further, the flexible ASR2 semi-rigid frame is the most vulnerable in all damage states. Therefore, the stiffness parameter '*k*' (decreased from 15 in ASR1 to 10 in ASR2) significantly affects the RDR values. It is also observed that the ASR2 shows the lowest values of POE for 'complete' damage state. Further, the RDR values are compared at three PGA levels (0.2, 0.4, and 0.8 g). The POE values are considerably higher in the ASR2 frame at slight and moderate damage states in order of 70% at 0.2 g, 97% at 0.4 g for 'slight', 38% at 0.2 g, and 80% at 0.4 g in 'moderate' damage state. Another important finding is that there is large variability in damage states observed in the ASR2 frame as compared to the other two frames. The trend in fragility curves is the same in the remaining frames (AFR and ASR1), so it is not discussed again.

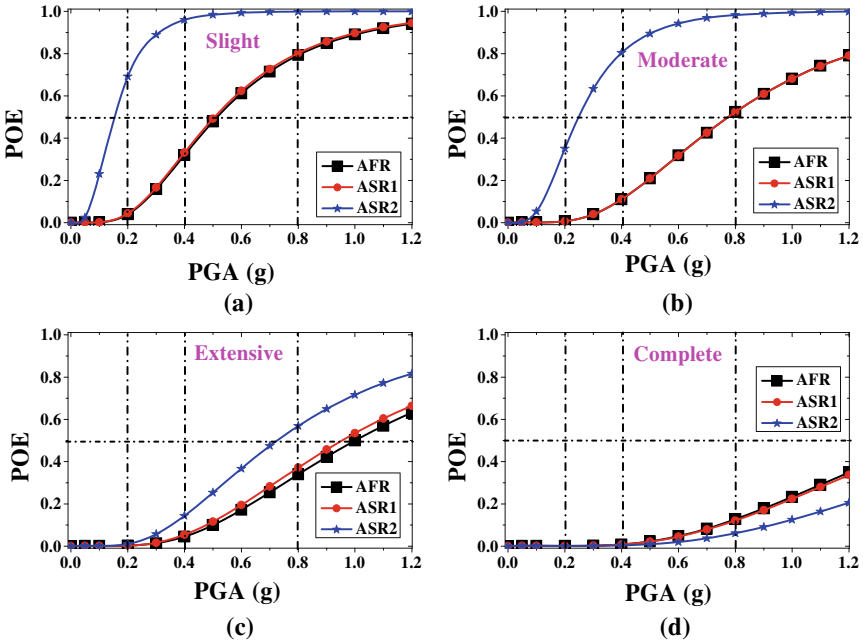


**Fig. 9** Fragility curves for the maximum value of roof drift ratio in five-story rigid (AFR), and semi-rigid frames (ASR2 and ASR2) under far-field earthquakes

## 5 Conclusion

Probabilistic seismic demand assessment of five-story rigid and semi-rigid frames under an ensemble of far-field records is carried out using the linear regression fragility analysis method. Hazus guidelines are used to categorize the damage states and the threshold values for the rigid steel frame. The limiting values for semi-rigid frames are based on engineering judgment for two considered seismic demand parameters, namely maximum inter-story drift ratio (MIDR) and the maximum value of roof drift ratio (RDR). The comparison of fragility curves is carried out for three considered frames. The major findings of the study are surmised as follows:

1. The semi-rigid frame with more flexibility (ASR2 frame with less value of stiffness parameter $k$) shows considerably high vulnerability to earthquakes.
2. The stiff semi-rigid frame (ASR1) presents nearly a similar trend and probability of exceedance (POE) as presented by a rigid frame.
3. At low PGA level (0.2 g), the difference in POE values for all structures in 'slight' and 'moderate' damage states is less as compared to values obtained in 'extensive' damage state.
4. Since the semi-rigid frames are economical as compared to the rigid frames, as shown in previous research work. Herein, the SR frame with higher '$k$' values shows nearly the same fragility plots as obtained in rigid frames under all damage

states in both considered seismic demand parameters. Therefore, the damage assessment also proves the efficacy of SR frames over rigid frames.
5. The large variability in damage states is observed in flexible semi-rigid frame ASR2.

## References


1. Aksoylar ND, Elnashai AS, Mahmoud H (2011) The design and seismic performance of low-rise long-span frames with semi-rigid connections. J Constr Steel Res 67:114–126
2. ANSI/AISC-341 (2016) Seismic provisions for structural steel buildings. Chicago, Illinois 60601-1802
3. ASCE-41 (2017) ASCE 41-17: seismic evaluation and retrofit rehabilitation of existing buildings. In: Proceedings of the SEAOC
4. ATC-40 (1996) Seismic evaluation and retrofit of concrete buildings—volume I. Applied Technology Council, California Seismic Safety Commission, Redwood City, California, 94065
5. Barbat AH, Pujades LG, Lantada N (2008) Seismic damage evaluation in urban areas using the capacity spectrum method: application to Barcelona. Soil Dyn Earthq Eng 28:851–865
6. Cornell CA, Jalayer F, Hamburger RO, Foutch DA (2002) Probabilistic basis for 2000 SAC federal emergency management agency steel moment frame guidelines. J Struct Eng 128:526–533
7. Ellingwood BR (2001) Earthquake risk assessment of building structures. Reliab Eng Syst Saf 74:251–262
8. Ellingwood BR, Kinali K (2009) Quantifying and communicating uncertainty in seismic risk assessment. Struct Saf 31:179–187
9. IS-800 (2007) General construction in steel-code of practice (third revision). Bureau of Indian Standards, New Delhi
10. IS-875 (1987) Part 1: dead loads — unit weights of building materials and stored materials. Bureau of Indian Standards, New Delhi
11. IS-1893 (2016) Criteria for earthquake resistant design of structures, part 1 general provisions and buildings (sixth revision). Bureau of Indian Standards, New Delhi
12. Kennedy RP, Cornell CA, Campbell R, Kaplan S, Perla H (1980) Probabilistic seismic safety study of an existing nuclear power plant. Nucl Eng Des 59:315–338
13. Kircher CA, Whitman RV, Holmes WT (2006) HAZUS earthquake loss estimation methods. Nat Hazard Rev 7:45–59
14. Mahmoud HN, Elnashai AS, Spencer BF Jr, Kwon O-S, Bennier DJ (2013) Hybrid simulation for earthquake response of semirigid partial-strength steel frames. J Struct Eng 139:1134–1148
15. Pitilakis K, Crowley H, Kaynia AM (2014) SYNER-G: typology definition and fragility functions for physical elements at seismic risk: buildings, lifelines, transportation networks and critical facilities. Springer Science & Business Media
16. Porter K, Kennedy R, Bachman R (2007) Creating fragility functions for performance-based earthquake engineering. Earthq Spectra 23:471–489
17. Reed JW, Kennedy RP (1994) Methodology for developing seismic fragilities. Final report TR-103959, EPRI
18. Rossetto T, Gehl P, Minas S, Galasso C, Duffour P, Douglas J, Cook O (2016) FRACAS: a capacity spectrum approach for seismic fragility assessment including record-to-record variability. Eng Struct 125:337–348
19. SAP2000v21 (2019) Integrated software for structural analysis and design. Computers and structures Inc, Berkeley, CA, USA
20. Sharma V, Shrimali M, Bharti S, Datta T (2018) Behavior of semi-rigid frames under seismic excitations. In: 16th symposium on earthquake engineering 16SEE, 20–22 Dec 2018, IIT Roorkee, pp 1–10

21. Sharma V, Shrimali M, Bharti S, Datta T (2019) Seismic energy dissipation in semi-rigid connected steel frames. In: 16th world conference on seismic isolation, energy dissipation and active vibration control of structures 16WCSI, 2019 Saint Petersburg, Russia
22. Vamvatsikos D, Cornell CA (2002) Incremental dynamic analysis. Earthquake Eng Struct Dynam 31:491–514
23. Zentner I, Gündel M, Bonfils N (2017) Fragility analysis methods: Review of existing approaches and application. Nucl Eng Des 323:245–258

# Computation of Fundamental Time Period for Moment-Resisting Framed Steel Buildings


**P. K. Soni, S. K. Dubey, and P. Sangamnerkar**

**Abstract** The paper presents an analysis of symmetrical steel moment-resisting framed (MRF) buildings to estimate the time period of vibration of the considered models of the buildings of varying height up to 5 storeys. The formula for the time period of the bare steel MRF building is given by the design code IS 1893(Part 1): 2016 in seismic analysis of the structures, but it is in the form of the height of the building as a primary factor. Many researchers have performed the studies to evaluate the time period of the steel MRF buildings and found that the different other parameters such as stiffness of the structure and base dimensions are also the influencing factors. It seems necessary to consider the effects of some other parameters of the structures also in the evaluation of the time period values. The paper presents the results of the analysis for the effects of the various parameters on time period of the building, i.e. stiffness of the structure, slab thickness for a particular number of bays in either direction, plan dimension, or plan area of the building. In the paper, different values of the time period have been obtained by dynamic analysis on considered building configurations for earthquake zone-III and presented the comparative analysis of period values concerning the code IS-1893.

**Keywords** Fundamental time period · Moment-resisting frame · Seismic analysis · Stiffness · Vibration

P. K. Soni (✉) · S. K. Dubey
Maulana Azad National Institute of Technology, Bhopal, India
e-mail: prabhatsoni15@gmail.com

P. Sangamnerkar
M.P. Housing and Infrastructure Development Board, Bhopal, India
e-mail: nerkar17@redigffmail.com



M. Madhavan et al. (eds.), *Proceedings of the Indian Structural Steel Conference 2020 (Vol. 1)*, Lecture Notes in Civil Engineering 318,
https://doi.org/10.1007/978-981-19-9390-9_51

## 1 Introduction

In the seismic design process, the base shear is considered as one of the most important parameters. In the vibration analysis, the evaluation of the base shear, the value of the time period of the building plays an important role. Since the approximation of the fundamental period is considered useful to obtain the expected seismic load influencing the structure. Therefore, its precise evaluation is in favour of the safety of the structure, applied design procedure, and future performance of the structure after being constructed.

Sangamnerkar and Dubey [4, 5] found that the height of the building is not only the parameter to influence the time period. Hence, the plan area of the building, the number of bays in both directions, stiffness of the structure, and infill masonry panels should also be considered in deriving the time period formula.

The difference between the fundamental period of buildings determined by the computational methods and empirical equation given in IS 1893 can be observed easily, and the difference is due to not considering the effects of non-structural members on time period in its evaluation by the empirical equation.

The following expression is provided by the recent Indian seismic code IS 1893 (Part-1)-2016 to estimate the fundamental natural period of steel frame building:

$$T_a = 0.085\,\mathrm{h}^{0.75}, \quad \text{for steel frame building,} \tag{1}$$

## 2 Literature Study

Al-Aasam and Mandal [1] showed that the currently available design codes do not provide the provision for the impact of joints of columns and beams on a calculation of period values. It has been suggested to incorporate the same for calculation of the fundamental natural period in hand calculation method for semi-rigid frames. For rigid-jointed frames, they modified the existing formula and proposed a new expression conducting a parametric study of plane steel frames. They performed a study of the time period to understand the effect of semi-rigid connections. They concluded that there is a considerable impact of flexible connections on frequencies of the frame. The overestimated frequency values were observed due to an assumption of the ideal-rigid beam to column connection which underestimates the fundamental periods. This inaccurate estimation may result in improper design because the design total shear depends on the fundamental period. Further, in the study, it has been mentioned about the proposed procedure that it can evaluate the period value for the considered frames for a wide spectrum of flexible connections of a column to a beam. For the utility of the developed procedure, the comparative results were presented in comparison with ABAQUS and also demonstrated the good agreement between them.

Soni et al. [6] analysed framed buildings without infill and provided the calculated time period values with its comparison to the estimated values as per design codes. Empirical equations of the natural time period of a framed building, provided in the Indian seismic design code IS 1893, are without considering the stiffness of the structure, bay size, plan area of the building etc., and it considers height as primary parameter. It is observed through relevant literature that the height alone is not adequate to define the period variability completely. Hence, there is a scope of further improvement of these empirical equations. The natural period estimated by these expressions is commonly used. It is therefore very important to obtain the realistic values of the time period for analysis of the response of buildings. The paper discusses the revision of the equations of the time period of the design code.

Wang et al. [8] evaluated the Wuhan International Securities Building for its seismic properties, in their study. To predict the seismic response of the building, they employed the time-history analysis and the mode-superposition spectrum analysis methods. It was found that the transition parts were weak zones of the structure located near the three strengthened storeys due to the abrupt change in rigidity. They discussed that the square root of the sum of the squares (SRSS) method can be recommended if it is feasible to ignore the vertical seismic effects in the response spectrum analysis. The analysis of the seismic response of structure was done by time-history analysis. They mentioned that the whiplash effect (the local structural damage due to sudden backward motion followed by forwarding motion) can be better revealed using time-history analysis. This work provides a reference for the design of super high-rise steel structures having a storey which is horizontally strengthened.

## 3 Methodology

The following configuration parameters have been used for the analysis of steel frames and studied the effect of various factors like column sections, bay length, depth of the slab, and area of the plan on the time period of steel-framed structure without infill.

## 4 Analysis

Analysis of steel-framed structures has been done considering the frames having a varying height from ground floor to G + 5. The specifications of the considered models are as shown in Table 1. The framed structures have been considered fixed at the base. The analysis of considered frames has been done for seismic zone-III and medium soil condition.

**Table 1** Details of the configuration of steel-framed building considered

| S.no | Items | Description |
|---|---|---|
| 1 | Structure | Multi-storey rigid-jointed steel frames |
| 2 | Storey | G.F. to G + 5 |
| 3 | Floor height | 3.6 m |
| 4 | Beam section | ISMB 300, ISMB 350 |
| 5 | Number of grid | 4 × 4, 5 × 5 |
| 6 | Bay length | 4 m, 5 m |
| 7 | Thickness of slab | 150 mm, 175 mm, 225 mm |
| 8 | Size of columns | ISMB 600, ISMB 550, ISMB 500, ISMB 450, ISMB 400, ISMB 350, ISMB 300 |
| 9 | Base dimension | 16 m × 16 m, 20 m × 20 m, & 25 m × 25 m |
| 10 | Type of soil | Type-II, medium soil |
| 11 | Material used | Reinforcement Fe-415 |

The dynamic analysis has been done to evaluate the time period of vibration of steel frames using response spectrum method, and followings are the evaluated time period values for different parameters of framed structure (building) without infill. Commercially available design software STAAD.Pro has been employed for analysis (Fig. 1).

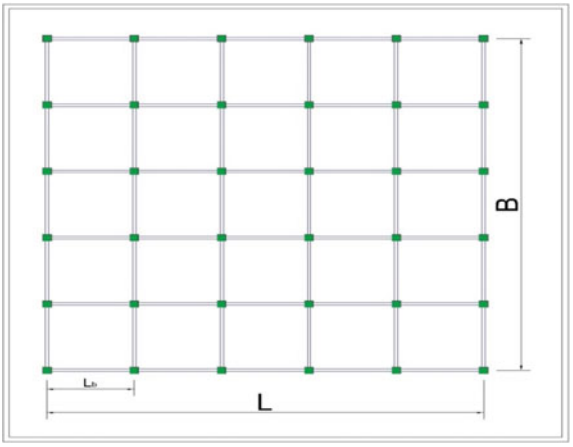


**Fig. 1** Typical example of a plan of the building having bay size 5 × 5 ($L$ and $B$ are plan dimensions, and $L_b$ is bay length)

**Table 2** Time period ($T$) in sec, for steel frame building

| Bay size 5×5, plan area (m) = 25 × 25, slab thickness = 150 mm, beam section = ISMB 300, bay length = 5m | | | | | | | | |
|---|---|---|---|---|---|---|---|---|
| Floors/ height | $T_a$ ($0.085h^{0.75}$) | Column sections | | | | | | |
| | | ISMB 300 | ISMB 350 | ISMB 400 | ISMB 450 | ISMB 500 | ISMB 550 | ISMB 600 |
| G + 5/ 23.6 m | 0.910 | 7.691 | 7.346 | 6.890 | 6.077 | 4.978 | 4.466 | 3.975 |
| G + 4/ 20 m | 0.804 | 6.493 | 6.201 | 5.815 | 5.128 | 4.198 | 3.764 | 3.347 |
| G + 3/ 16.4 m | 0.693 | 5.298 | 5.059 | 4.744 | 4.181 | 3.419 | 3.063 | 2.721 |
| G + 2/ 12.8 m | 0.575 | 4.106 | 3.920 | 3.675 | 3.237 | 2.643 | 2.365 | 2.097 |
| G + 1/ 9.2 m | 0.449 | 2.922 | 2.789 | 2.613 | 2.299 | 1.873 | 1.672 | 1.479 |
| G.F./5.6 m | 0.309 | 1.762 | 1.681 | 1.573 | 1.381 | 1.120 | 0.996 | 0.876 |

## 5 Discussion on Results

Tables 2, 3, 4, and 5 are giving the calculated results of period values ($T$) for moment-resisting steel-framed building concerning different column sections, bay length, plan area, and slab thickness and height. These calculated values are compared with the estimated period values ($T_a$), from the formula (1) of design code IS-1893:2016 for steel MRF building. It can be observed that the calculated values are much higher than the estimated values ($T_a$), e.g. the value of $T$ is 7.691 in case of bay size 5 × 5, plan area (m) = 25 × 25, slab thickness = 150 mm, beam section = ISMB 300, and bay length = 5 m, which is very higher than the corresponding value of $T_a$. The graphical comparison of time periods between time period values obtained by the formula of IS 1893 and evaluated time period values of steel frame building having different column section can be clearly observed from Figs. 2 and 3.

**Table 3** Time period ($T$) in sec, for steel frame building

| Bay size 5×5, plan area (m) = 25 × 25, slab thickness = 150 mm, beam section = ISMB 350, bay length = 5 m | | | | | | | | |
|---|---|---|---|---|---|---|---|---|
| Floors/ height | $T_a$ ($0.085h^{0.75}$) | Column sections | | | | | | |
| | | ISMB 300 | ISMB 350 | ISMB 400 | ISMB 450 | ISMB 500 | ISMB 550 | ISMB 600 |
| G + 5/ 23.6 m | 0.910 | 7.572 | 7.222 | 6.757 | 5.927 | 4.796 | 4.265 | 3.752 |
| G + 4/ 20 m | 0.804 | 6.394 | 6.098 | 5.705 | 5.003 | 4.047 | 3.597 | 3.162 |
| G + 3/ 16.4 m | 0.693 | 5.218 | 4.976 | 4.655 | 4.081 | 3.299 | 2.930 | 2.574 |
| G + 2/ 12.8 m | 0.575 | 4.047 | 3.858 | 3.609 | 3.162 | 2.553 | 2.266 | 1.988 |
| G + 1/ 9.2 m | 0.449 | 2.882 | 2.747 | 2.569 | 2.249 | 1.813 | 1.607 | 1.406 |
| G.F./5.6 m | 0.309 | 1.742 | 1.660 | 1.551 | 1.356 | 1.088 | 0.962 | 0.838 |

**Table 4** Time period ($T$) in sec, for steel frame building

| Bay size 4 × 4, plan area (m) = 20 × 20, slab thickness = 225 mm, beam section = ISMB 300, bay length = 5 m | | | | | | | | |
|---|---|---|---|---|---|---|---|---|
| Floors/ height | $T_a$ ($0.085h^{0.75}$) | Column sections | | | | | | |
| | | ISMB 300 | ISMB 350 | ISMB 400 | ISMB 450 | ISMB 500 | ISMB 550 | ISMB 600 |
| G + 5/ 23.6 m | 0.910 | 8.098 | 7.646 | 7.261 | 6.403 | 5.239 | 4.697 | 4.176 |
| G + 4/ 20 m | 0.804 | 6.843 | 6.462 | 6.135 | 5.409 | 4.423 | 3.964 | 3.522 |
| G + 3/ 16.4 m | 0.693 | 5.591 | 5.280 | 5.012 | 4.417 | 3.609 | 3.233 | 2.870 |
| G + 2/ 12.8 m | 0.575 | 4.343 | 4.103 | 3.892 | 3.428 | 2.798 | 2.503 | 2.219 |
| G + 1/ 9.2 m | 0.449 | 3.363 | 2.932 | 2.778 | 2.445 | 1.991 | 1.778 | 1.572 |
| G.F./5.6 m | 0.309 | 1.886 | 1.784 | 1.686 | 1.480 | 1.200 | 1.068 | 0.940 |

**Table 5** Time period ($T$) in sec, for steel frame building

| Bay size 4 × 4, plan area (m) = 16 × 16, slab thickness = 175 mm, beam section = ISMB 350, bay length = 4 m | | | | | | | | |
|---|---|---|---|---|---|---|---|---|
| Floors/ height | $T_a$ ($0.085h^{0.75}$) | Column sections | | | | | | |
| | | ISMB 300 | ISMB 350 | ISMB 400 | ISMB 450 | ISMB 500 | ISMB 550 | ISMB 600 |
| G + 5/ 23.6 m | 0.910 | 6.259 | 5.972 | 5.587 | 4.892 | 3.940 | 3.492 | 3.057 |
| G + 4/ 20 m | 0.804 | 5.280 | 5.083 | 4.713 | 4.126 | 3.321 | 2.943 | 2.575 |
| G + 3/ 16.4 m | 0.693 | 4.304 | 4.106 | 3.841 | 3.362 | 2.705 | 2.396 | 2.095 |
| G + 2/ 12.8 m | 0.575 | 3.332 | 3.178 | 2.973 | 2.601 | 2.091 | 1.851 | 1.617 |
| G + 1/ 9.2 m | 0.449 | 2.366 | 2.257 | 2.110 | 1.845 | 1.481 | 1.309 | 1.142 |
| G.F./5.6 m | 0.309 | 1.422 | 1.356 | 1.267 | 1.106 | 0.885 | 0.781 | 0.678 |

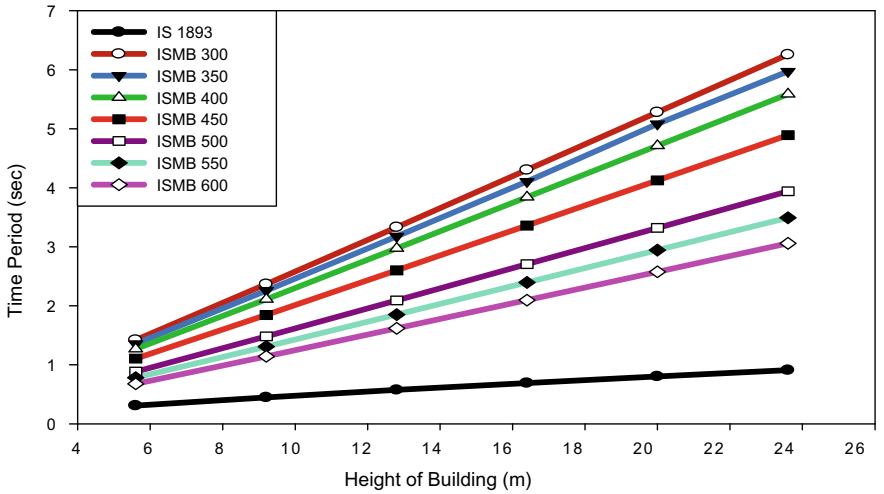


**Fig. 2** Comparison of the time period (steel frame building and plan area (m) = 16 × 16, 175 mm slab) by design code with the condition of the different column section

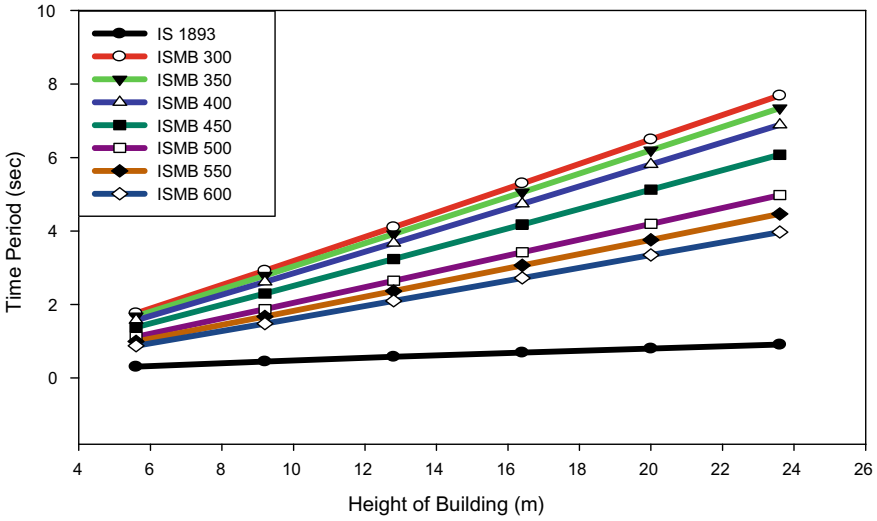


**Fig. 3** Comparison of the time period (steel frame building and plan area (m) = 25 × 25, 150 mm slab) by design code with the condition of different column section

## 6 Conclusion

In the paper, time period values have been calculated for moment-resisting steel-framed building with respect to different steel column sections, bay length, plan area, and slab thickness and height of the building. It is found that the period values of these calculated time period are much higher than the estimated values obtained by the formula given in IS 1893:2016. The effect of infill is not considered in this study, which may be one of the reasons for the higher time period, but the study for the influence of other structural parameters on time period is also required more attention. The design codes are revised periodically, and it can be remarked from the study of the results of this paper that the period values as per the formula of design code are on much conservative side. So, the parameters studied in this paper for evaluation of period values can be incorporated in the period formula for more precise estimation of it.

## References

1. Al-Aasam HS, Mandal P (2013) Simplified procedure to calculate by hand the natural periods of semi-rigid steel frames. J Struct Eng ASCE 139:1082–1087
2. ABAQUS (2010) ABAQUS/standard version 6.10 user's manuals: volume I–III. Hibbitt, Karlsson, and Sorenson, Inc., Pawtucket, RI
3. Bureau of Indian Standards. Criteria for earthquake resistant design of structures—part-1, general provisions and buildings, IS 1893 (Part-1):2016. Bureau of Indian Standards, New Delhi

4. Sangamnerkar P, Dubey SK (2015) Effect of base width and stiffness of the structure on period of vibration of RC framed buildings in seismic analysis. Open J Earthquake Res 4:65–73
5. Sangamnerkar P, Dubey SK (2017) Equations to evaluate fundamental period of vibration of buildings in seismic analysis. Struct Monitor Maintenance 4(4):351–364
6. Soni P, Sangamnerkar P, Dubey SK (2019) Analysis of natural time period of moment resisting frame buildings. AIP Conf Proc 2158–020016:1–5
7. STAAD Pro-V8i–Structural analyses and designing software by Bentely
8. Wang Y, Zhou H, Shi Y, Huang Y, Shi G, Wen S (2011) Seismic analysis of a super high-rise steel structure with horizontal strengthened storeys. Front Archit Civ Eng China 5(3):394–404

# Analytical Design Review of SP-38(S&T); Handbook for Typified Designs for Structures with Steel Roof Trusses


**P. K. Soni, S. K. Dubey, and P. Sangamnerkar**

**Abstract** The paper studies the designs of steel roof trusses under the effect of wind forces, illustrated in SP: 38–1987, which is a handbook for typified designs of structures with steel roof trusses. The review has been done as a comparative study, which compares the illustrated designs of SP 38 with the designs of the same trusses, taking the provisions of IS 875–1987(Part-III) into design considerations. The paper attempts to explore the scope of improvization of the handbook by updating the current designs and incorporating the revised factors (class of structure terrain specifications, permeability factor, height, and structure size) of wind force analysis as per IS 875 to create effective designs of steel trusses or industrial shed structures, providing these designs with updated provisions.

**Keywords** Typified design · Truss · Terrain · Permeability

## 1 Introduction

The Handbook; SP 38(S&T):1987 illustrates the designs of different configurations of trusses such as lean-to-roof, A-shaped trusses, etc., and is about the typification of structures with steel roof trusses (with and without cranes). The handbook was developed byBureau of Indian Standards (BIS) under the project B-8: Typification work of Industrial Structures at national level after approval of the Planning Commission, for which, an expert team was formed in 1972, on the technology issues of Housing and Construction, by the Department of Science and Technology. The objective was to obtain economical designs for industrial structures used commonly as light structures and to provide standard prefabricated designs to support mass production. SP 38(S&T):1987 was developed based on the provisions of IS 875:1964, in which there

P. K. Soni (✉) · S. K. Dubey
Maulana Azad National Institute of Technology, Bhopal, India
e-mail: prabhatsoni15@gmail.com

P. Sangamnerkar
M.P. Housing and Infrastructure Development Board, Bhopal, India



M. Madhavan et al. (eds.), *Proceedings of the Indian Structural Steel Conference 2020 (Vol. 1)*, Lecture Notes in Civil Engineering 318,
https://doi.org/10.1007/978-981-19-9390-9_52

were three permeability conditions to evaluate internal pressure and also seven zones of wind pressure.

Based upon the analysis of wind phenomenon and its impact upon structures, the expert committee modified the provisions of the wind pressure in the first revision of the code in the collaboration with the Indian meteorological department in 1964. Also, some other modifications were done such as the modifications in the coefficients of the wind pressure for sloping and curved and sheeted roofs; for the butterfly type structures, inclusion of some new clauses; metric system was adopted for weighing and measurement purpose; deleted some load provisions of seismic analysis due to a new separate code was developed for it. But, after the revision of IS 875 in 1987, the provisions of the calculation of wind loads had been modified in terms of wind zones, basic wind speed, basic wind pressure, permeability conditions, risk factor, terrain conditions, etc. The paper attempts to study the effect of these modified provisions on the results made in SP 38.

## 2 Literature Review

Fu et al. (2008) analysed steel roof structures of long-spans using correlation approach between load and response and presented a new description of the equivalent static wind load eliminating the shortcoming of the gust loading factor. They discussed the determination of the ESWLs and demonstration of its effectiveness in the design with the analysis of long-span roof structures.

Imai and Schmith [3] analysed the different design of trusses with optimized weight considering sizing and configuration variables. They used second-order Taylor series expansions for analysis of displacement quantities and recognized disjoint feasible regions. They employed a multiplier method as an optimization tool.

Lipson and Agrawal [4] demonstrated the computation for optimization of topology, geometry, and cross-sectional properties on plane truss structures. They presented a nonlinear constrained optimization using a modified “complex method”, in which the computation of derivatives is not required. They applied the method to a variety of optimization problems.

Patrikar and Pathak [5] presented a study of optimization with the help of fully stressed design (FSD) method applied on Fink Truss. They analysed a total 81 configurations to match the objectives. They calculated steel take-off and maximum displacement for individual case and compared. They demonstrated that the increase in height or span does not always cause an increase in weight.

Somekh and Kirsch [6] presented a graphical interaction and structural optimization based on a CAD system. They proposed a new optimization technique for optimal truss design. The optimization methods are useful for automated decisions. They considered different structural geometry, topology, and member sizes for analysis and showed the results to obtain a practical optimum design.

## 3 Methodology

a. The paper analyses A-shaped steel roof truss, illustrated in SP 38, for wind loadings under considerations of the provisions of IS 875:1987 (PART I, II, III) to estimate design wind speed ($V_z$), design wind pressure ($P_z$), and forces on structures for different permeability, terrain conditions, and class of structure.
b. Comparative analysis of wind forces between the values of SP38 and calculated as per IS875.
c. Evaluation of the cases of SP38 which are under-designed/over-designed as per results obtained using the provisions of IS875.

## 4 Analysis

Design wind speed ($V_z$), design wind pressure ($P_z$), and wind force (F) can be expressed as follows:

$$V_z = V_b \cdot K_1 \cdot K_2 \cdot K_3 \tag{1}$$

$$P_z = 0.6\, V_z^2 \tag{2}$$

where at any height z, $V_z$ (m/sec) = design wind speed, $V_b$ (m/sec) = basic wind speed, $K_1$ = probability factor, $K_2$ = structure size terrain and height factor, $K_3$ = topography factor, and $P_z$ = design wind pressure in $N/m^2$.

$$F = \left(C_{pe} - -C_{pi}\right) \cdot A \cdot P_z \tag{3}$$

where $C_{pe}$ = Coefficient for external pressure, $C_{pi}$ = Coefficient for internal pressure, and A = Surface area (Fig. 1 and Table 1).

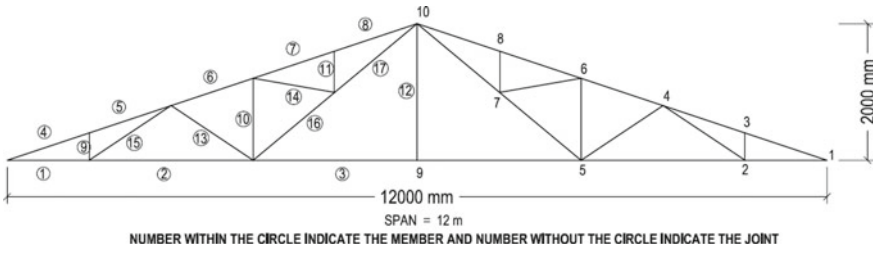


**Fig. 1** Number within the circle indicates the member, and number without the circle indicates the joint

**Table 1** Considered parameters for analysis

| | | | |
|---|---|---|---|
| Slope | 1 in 3 | Basic wind pressure | 1.5kN/ $m^2$ |
| Shed location | Lucknow | Truss | A-type |
| Truss spacing | = 6.0 m | Roofing materials | 0.17kN/ $m^2$ |
| Truss span | 12 m | Plan area | 12 m × 42 m |
| Column height | 9 m | Roofing type | A.C. Sheeting |

## *4.1 Considered Parameters*

## *4.2 Observations*

It can be observed from Tables 2 and 3 that the Class A causes higher forces in comparison with Class C of structure for the condition of zero openings in the wall, the design forces have maximum values for Terrain category 1, and it is the least for Terrain category 4.

For Class A and no opening case, Terrain category 1 and 2 has higher forces, and Terrain category 4 has lesser design forces in comparison with the values as per SP38. The nature of difference is also similar in case of Class C and zero openings, but the notable difference is that the difference amount is higher. Analysis results for Terrain category 2, Class C, and zero opening case are showing the values of design forces very close to the values as per SP: 38.

Similarly, it can be observed from Tables 4 and 5 that design forces are higher in case of Class A, in comparison with Class C of structure for the 20% opening in the wall and the values are maximum for Terrain category 1 and minimum for Terrain category 4.

**Table 2** Design forces for Class A structure, no wall opening condition

| Design Force (kN)—Dead Load & Wind Load combination | | | | | | | |
|---|---|---|---|---|---|---|---|
| (+ve) shows Tension in member (−ve) shows Compression in member | | | | | (+ve) shows increment (−ve) shows decrement | | |
| M.No | SP:38 Col. (a) | IS:875 | | | % variation in comparison with Col.(a) | | |
| | | Terrain Category | | | Terrain Category | | |
| | | 1 | 2 | 4 | 1 | 2 | 4 |
| 1 | − 35.37 | − 54.84 | − 46.97 | − 19.51 | 55.05 | 32.80 | − 44.84 |
| 2 | − 30.54 | − 47.58 | − 40.69 | − 16.66 | 55.80 | 33.24 | − 45.45 |
| 3 | − 16.05 | − 25.8 | − 21.85 | − 8.13 | 60.75 | 36.14 | − 49.35 |
| 4 | 38.14 | 58.92 | 50.52 | 21.21 | 54.48 | 32.46 | − 44.39 |

(continued)

**Table 2** (continued)

| Design Force (kN)—Dead Load & Wind Load combination | | | | | | | |
|---|---|---|---|---|---|---|---|
| (+ve) shows Tension in member (−ve) shows Compression in member | | | | | (+ve) shows increment (−ve) shows decrement | | |
| M.No | SP:38 Col. (a) | IS:875 | | | % variation in comparison with Col.(a) | | |
| | | Terrain Category | | | Terrain Category | | |
| | | 1 | 2 | 4 | 1 | 2 | 4 |
| 5 | 39.85 | 61.13 | 52.53 | 22.49 | 53.40 | 31.82 | − 43.56 |
| 6 | 31.38 | 48.05 | 41.32 | 17.79 | 53.12 | 31.68 | − 43.31 |
| 7 | 36.49 | 55.38 | 47.76 | 21.08 | 51.77 | 30.89 | − 42.23 |
| 8 | 38.20 | 57.59 | 49.77 | 22.37 | 50.76 | 30.29 | − 41.44 |
| 9 | 3.22 | 4.84 | 4.19 | 1.9 | 50.31 | 30.12 | − 40.99 |
| 10 | 4.84 | 7.27 | 6.29 | 2.85 | 50.21 | 29.96 | − 41.12 |
| 11 | 3.22 | 4.84 | 4.19 | 1.9 | 50.31 | 30.12 | − 40.99 |
| 12 | 0.0 | 0.0 | 0 | 0 | 0.00 | 0.00 | 0.00 |
| 13 | 5.81 | 8.73 | 7.55 | 3.42 | 50.26 | 29.95 | − 41.14 |
| 14 | − 3.28 | − 4.92 | − 4.26 | − 1.93 | 50.00 | 29.88 | − 41.16 |
| 15 | − 5.81 | − 8.73 | − 7.55 | − 3.42 | 50.26 | 29.95 | − 41.14 |
| 16 | − 12.58 | − 18.9 | − 16.35 | − 7.41 | 50.24 | 29.97 | − 41.10 |
| 17 | − 16.77 | − 25.2 | − 21.8 | − 9.88 | 50.27 | 29.99 | − 41.09 |
| Average percentage variation | | | | | 49.23 | 29.37 | − 40.19 |

**Table 3** Design forces for Class C structure, no wall opening condition

| Design Force (kN)—Dead Load & Wind Load combination | | | | | | | |
|---|---|---|---|---|---|---|---|
| (+ve) shows Tension in member (−ve) shows Compression in member | | | | | (+ve) shows increment (−ve) shows decrement | | |
| M.No | SP:38 Col. (a) | IS:875 | | | % variation in comparison with Col.(a) | | |
| | | Terrain Category | | | Terrain Category | | |
| | | 1 | 2 | 4 | 1 | 2 | 4 |
| 1 | − 35.37 | − 45.51 | − 36.71 | − 4.97 | 28.67 | 3.79 | − 85.95 |
| 2 | − 30.54 | − 39.41 | − 31.71 | − 3.94 | 29.04 | 3.83 | − 87.10 |
| 3 | − 16.05 | − 21.13 | − 16.73 | − 0.85 | 31.65 | 4.24 | − 94.70 |
| 4 | 38.14 | 48.96 | 39.56 | 5.7 | 28.37 | 3.72 | − 85.06 |
| 5 | 39.85 | 50.93 | 41.3 | 6.6 | 27.80 | 3.64 | − 83.44 |
| 6 | 31.38 | 40.06 | 32.52 | 5.34 | 27.66 | 3.63 | − 82.98 |
| 7 | 36.49 | 46.33 | 37.78 | 6.98 | 26.97 | 3.54 | − 80.87 |
| 8 | 38.20 | 48.3 | 39.52 | 7.88 | 26.44 | 3.46 | − 79.37 |
| 9 | 3.22 | 4.07 | 3.33 | 0.69 | 26.40 | 3.42 | − 78.57 |

(continued)

**Table 3** (continued)

| Design Force (kN)—Dead Load & Wind Load combination | | | | | | | |
|---|---|---|---|---|---|---|---|
| (+ve) shows Tension in member (−ve) shows Compression in member | | | | | (+ve) shows increment (−ve) shows decrement | | |
| M.No | SP:38 Col. (a) | IS:875 | | | % variation in comparison with Col.(a) | | |
| | | Terrain Category | | | Terrain Category | | |
| | | 1 | 2 | 4 | 1 | 2 | 4 |
| 10 | 4.84 | 6.11 | 5 | 1.04 | 26.24 | 3.31 | − 78.51 |
| 11 | 3.22 | 4.07 | 3.33 | 0.69 | 26.40 | 3.42 | − 78.57 |
| 12 | 0.0 | 0 | 0 | 0 | 0.00 | 0.00 | 0.00 |
| 13 | 5.81 | 7.33 | 6.01 | 1.24 | 26.16 | 3.44 | − 78.66 |
| 14 | − 3.28 | − 4.13 | − 3.39 | − 0.71 | 25.91 | 3.35 | − 78.35 |
| 15 | − 5.81 | − 7.33 | − 6.01 | − 1.24 | 26.16 | 3.44 | − 78.66 |
| 16 | − 12.58 | − 15.87 | − 13.01 | − 2.69 | 26.15 | 3.42 | − 78.62 |
| 17 | − 16.77 | − 21.16 | − 17.34 | − 3.58 | 26.18 | 3.40 | − 78.65 |
| Average percentage variation | | | | | 25.66 | 3.36 | − 76.94 |

**Table 4** Design forces for Class A structure, more than 20% wall area opening condition

| Design Force (kN)—Dead Load & Wind Load combination | | | | | | | |
|---|---|---|---|---|---|---|---|
| (+ve) shows Tension in member (−ve) shows Compression in member | | | | | (+ve) shows increment (−ve) shows decrement | | |
| M.No | SP:38 Col. (a) | IS:875 | | | % variation in comparison with Col.(a) | | |
| | | Terrain Category | | | Terrain Category | | |
| | | 1 | 2 | 4 | 1 | 2 | 4 |
| 1 | − 89.37 | − 128.44 | − 113.78 | − 62.31 | 43.72 | 27.31 | − 30.28 |
| 2 | − 77.79 | − 111.98 | − 99.15 | − 54.11 | 43.95 | 27.46 | − 30.44 |
| 3 | − 43.05 | − 62.6 | − 55.28 | − 29.53 | 45.41 | 28.41 | − 31.41 |
| 4 | 95.77 | 137.47 | 121.81 | 66.89 | 43.54 | 27.19 | − 30.16 |
| 5 | 98.90 | 141.62 | 125.58 | 69.3 | 43.20 | 26.98 | − 29.93 |
| 6 | 77.64 | 111.1 | 98.54 | 54.45 | 43.10 | 26.92 | − 29.87 |
| 7 | 88.93 | 126.85 | 112.6 | 62.64 | 42.64 | 26.62 | − 29.56 |
| 8 | 92.06 | 131 | 116.36 | 65.05 | 42.30 | 26.40 | − 29.34 |
| 9 | 7.72 | 10.98 | 9.75 | 5.47 | 42.23 | 26.30 | − 29.15 |
| 10 | 11.59 | 16.48 | 14.64 | 8.21 | 42.19 | 26.32 | − 29.16 |
| 11 | 7.72 | 10.98 | 9.75 | 5.47 | 42.23 | 26.30 | − 29.15 |
| 12 | 0.00 | 0 | 0 | 0 | 0.00 | 0.00 | 0.00 |

(continued)

**Table 4** (continued)

| Design Force (kN)—Dead Load & Wind Load combination | | | | | | | |
|---|---|---|---|---|---|---|---|
| (+ve) shows Tension in member (−ve) shows Compression in member | | | | | (+ve) shows increment (−ve) shows decrement | | |
| M.No | SP:38 Col. (a) | IS:875 | | | % variation in comparison with Col.(a) | | |
| | | Terrain Category | | | Terrain Category | | |
| | | 1 | 2 | 4 | 1 | 2 | 4 |
| 13 | 13.92 | 19.79 | 17.58 | 9.85 | 42.17 | 26.29 | − 29.24 |
| 14 | − 7.84 | − 11.15 | − 9.9 | − 5.55 | 42.22 | 26.28 | − 29.21 |
| 15 | − 13.92 | − 19.79 | − 17.58 | − 9.85 | 42.17 | 26.29 | − 29.24 |
| 16 | − 30.15 | − 42.85 | − 38.07 | − 21.34 | 42.12 | 26.27 | − 29.22 |
| 17 | − 40.19 | − 57.13 | − 50.76 | − 28.45 | 42.15 | 26.30 | − 29.21 |
| Average percentage variation | | | | | 40.31 | 25.15 | − 27.91 |

**Table 5** Design forces for Class C structure, and more than 20% wall area opening condition

| Design Force (kN) - Dead Load & Wind Load combination | | | | | | | |
|---|---|---|---|---|---|---|---|
| (+ve) shows Tension in member (−ve) shows Compression in member | | | | | (+ve) shows increment (−ve) shows decrement | | |
| M.No | SP:38 Col. (a) | IS:875 | | | % variation in comparison with Col.(a) | | |
| | | Terrain Category | | | Terrain Category | | |
| | | 1 | 2 | 4 | 1 | 2 | 4 |
| 1 | − 89.37 | − 110.98 | − 94.44 | − 34.84 | 24.18 | 5.67 | − 61.02 |
| 2 | − 77.79 | − 96.7 | − 82.23 | − 30.08 | 24.31 | 5.71 | − 61.33 |
| 3 | − 43.05 | − 53.88 | − 45.6 | − 15.8 | 25.16 | 5.92 | − 63.30 |
| 4 | 95.77 | 118.83 | 101.18 | 37.57 | 24.08 | 5.65 | − 60.77 |
| 5 | 98.90 | 122.51 | 104.44 | 39.26 | 23.87 | 5.60 | − 60.30 |
| 6 | 77.64 | 96.14 | 81.98 | 30.92 | 23.83 | 5.59 | − 60.18 |
| 7 | 88.93 | 109.88 | 93.83 | 35.96 | 23.56 | 5.51 | − 59.56 |
| 8 | 92.06 | 113.57 | 97.09 | 37.65 | 23.37 | 5.46 | − 59.10 |
| 9 | 7.72 | 9.52 | 8.14 | 3.18 | 23.32 | 5.44 | − 58.81 |
| 10 | 11.59 | 14.29 | 12.22 | 4.77 | 23.30 | 5.44 | − 58.84 |
| 11 | 7.72 | 9.52 | 8.14 | 3.18 | 23.32 | 5.44 | − 58.81 |
| 12 | 0.00 | 0 | 0 | 0 | 0.00 | 0.00 | 0.00 |

(continued)

**Table 5** (continued)

| Design Force (kN) - Dead Load & Wind Load combination | | | | | | | |
|---|---|---|---|---|---|---|---|
| (+ve) shows Tension in member (−ve) shows Compression in member | | | | | (+ve) shows increment (−ve) shows decrement | | |
| M.No | SP:38 Col. (a) | IS:875 | | | % variation in comparison with Col.(a) | | |
| | | Terrain Category | | | Terrain Category | | |
| | | 1 | 2 | 4 | 1 | 2 | 4 |
| 13 | 13.92 | 17.16 | 14.68 | 5.72 | 23.28 | 5.46 | − 58.91 |
| 14 | − 7.84 | − 9.67 | − 8.27 | − 3.23 | 23.34 | 5.48 | − 58.80 |
| 15 | − 13.92 | − 17.16 | − 14.68 | − 5.72 | 23.28 | 5.46 | − 58.91 |
| 16 | − 30.15 | − 37.16 | − 31.79 | − 12.4 | 23.25 | 5.44 | − 58.87 |
| 17 | − 40.19 | − 49.55 | − 42.38 | − 16.52 | 23.29 | 5.45 | − 58.90 |
| Average percentage variation | | | | | 22.28 | 5.22 | − 56.26 |

For Class A and 20% opening case, Terrain category 1 and 2 has higher forces, and Terrain category 4 has lesser design forces in comparison with the values as per SP: 38.The nature of difference is also similar in case of Class C and 20% opening, but the notable difference is that the difference amount is higher. Analysis results for Terrain category 2, Class C, and 20% opening case are showing the values of design forces very close to the values as per SP38.

## 5 Conclusion

The results of the analysis of design forces of steel roof trusses have been presented and compared in the paper to fulfil its purpose. A-shaped Class A and Class C structures have been considered for the conditions of permeability as no opening and 20% opening cases with Terrain category 1, 2, and 4.

In some of the cases, IS-875 is showing the design forces much higher than it is according to the value of SP: 38, and in some other cases, the values are lesser in quantity comparatively. Also, in some cases like Category 2 having structure type Class C with the opening as zero or 20%, the values of design forces obtained from both SP: 38 and IS-875 are very close. There are different cases showing the varieties of differences in its nature and pattern. These differences in results are due to the revision of provisions of IS 875 for calculation of wind pressure.

To conclude, statement can be written that SP: 38 is not having the design forces as per revised IS-875 and the noticed differences are not ignorable. In some cases, the designs of trusses as per SP: 38 would be over-designed leading to uneconomic designs, and in some other cases, these will be under-designed, and it may cause failure of the structure. So, the revision and updation of SP: 38 is required to make this useful document relevant for academicians, researchers, and practitioners.

## References

1. Bureau of Indian Standards. IS 875(Part I, II, III):1987; Code of Practice for Design Loads (Other than Earthquake), Part 3: Wind Loads
2. Bureau of Indian Standards. SP38(S &T):1987; Handbook of typified designs of structures with steel roof trusses (with or without cranes) based on IS Codes
3. Imai K, Schmith LA (1981) Configuration optimization of trusses. J Struct Div 107(5):745–756
4. Lipson SL, Agrawal KM (1974) Weight optimization of plane trusses. J Struct Div 100(ST5):865–879
5. Patrikar A, Pathak KK (2016) Fully stressed design of fink truss using STAAD.Pro software. Open J Civ 6:631–642
6. Somekh E, Kirsch U (1981) Interactive optimal design of truss structures. Comput Aided Des 13(5):253–259
7. Soni P, Sangamnerkar P, Dubey SK (2019) Review of typified designs of trusses in the context of revised IS Code. In: AIP conference proceedings 2158, 020017, pp 1–6

# Comparative Review of SP-6(1); ISI Handbook for Structural Engineers (Part–1)—Structural Steel Sections


**P. K. Soni, S. K. Dubey, and P. Sangamnerkar**

**Abstract** The objective of this paper is to review the illustrated designs of standard structural steel sections are given in Indian Standard Special Publications, SP 6(1):1964; ISI Handbook for structural engineers (Part-1)—Structural Steel Sections. The paper presents the analysis of different standard steel column sections using the provisions of IS 800: 2007 to evaluate the load-carrying capacity of axially loaded steel sections subjected to compression considering different parameters such as effective length, slenderness ratio, the radius of gyration, material yielding, and inelastic buckling. The paper presents a comparative study of the result of the load-carrying capacity of steel sections, obtained as per SP 6(1):1964 and calculated as per the provisions of IS 800:2007, to obtain optimum sections to fulfil the aspect of economic designs with the safety of the structure. It suggests that there is a need for improvization in illustrated designs of SP 6(1) to incorporate the design provisions of IS 800: 2007. The updated designs would be more useful for structural designers of the country for taking them as a reference.

**Keywords** Steel section · Euler's theory · Effective length · Yielding · Inelastic buckling

P. K. Soni (✉) · S. K. Dubey
Maulana Azad National Institute of Technology, Bhopal, India
e-mail: prabhatsoni15@gmail.com

P. Sangamnerkar
M.P. Housing and Infrastructure Development Board, Bhopal, India



M. Madhavan et al. (eds.), *Proceedings of the Indian Structural Steel Conference 2020 (Vol. 1)*, Lecture Notes in Civil Engineering 318,
https://doi.org/10.1007/978-981-19-9390-9_53

# 1 Introduction

## *1.1 Is 800:2007*

In 1950, the Indian Standards Institution initiated the steel economy programme. In which, achieving economy in the use of structural steel by establishing rational, efficient, and optimum standards for structural steel products was the objective behind this initiation. Under this programme, Indian Standards brought IS 800:1956, which was first in the series and then incorporated certain very important changes in its revised versions of the year 1962 and 1984.

IS 800 is the prime document for any structural design. It is the basic code for general construction in steel structures and influences many other codes governing the design of other special steel structures, such as towers, bridges, silos, and chimneys.

Indian Institute of Technology Madras (IIT Madras) reviewed the code and framed a proposal to revise it. Institute of Steel Development and Growth (INSDAG) Kolkata supported this project, and the code was revised in 2007 with the involvement of different contracting institutes/organizations of academic and research capacity.

## *1.2 Sp: 6–1964*

It was proposed to develop some design handbooks to make available typical designs of different types of structures, so that the work involved in design computations can be reduced, and to facilitate the use of the Indian Standard Code of practice for use of structural steel in general building construction. The Handbook SP: 6, which gives the properties of structural steel sections, was first issued in the year 1959. The Structural and Metals Division Council of ISI approved the first edition, and it was processed by structural sectional committee, SMDC 6. The Handbook provides the maximum convenience in using it in the design office; its contents are arranged in this manner. The contents have been grouped broadly as follows:

Section (A)—Structural shapes and other steel products, Section (B)—Beams, channels, and compound sections used as girders, Section (C)—Angles, single and double used as struts and ties, Section (D)—Beams, channels, and other compound sections used as columns.

# 2 Literature Study

Fieber et al. [4] analysed the steel frames and continuous beams and predicted ultimate load capacity were compared with results of conventional steel design using finite element models. They found that the proposed method presents the ultimate capacities which are more conservative and accurate than current design methods.

Guha et al. (2008) compared IS 800:2007 (LSM) with the provision of the other International codes. The code consists of some additional references taken from the existing British Codes, and it has been mainly modelled in line with the Euro codes. The code incorporated the design concepts based on the ASD method as one of its chapters with certain modification from the existing Indian Standard (IS) Code.

Kulkarni et al. (2011) compared steel angles as tension members designed by working stress method and limit states method. The observations were made and concluded that the limit state method (LSM) gives higher values for tension member than working stress method (WSM) and the design of tension members using angles by is economical in case of limit state method compared to working stress method.

Subramanian [7] reviewed the important features of the code IS 800:2007, based on limit states method of design and compared with the national codes of other countries. He studied new features included in recent code like methods of analysis, fire resistance, and design against floor vibration.

## 3 Methodology

The methodology brought into action has included as follows:

a. Axially loaded column sections have been analysed for various slenderness ratios.
b. Design considerations as per IS 800: 2007 have been employed for the calculation of safe loads.
c. Both ends are considered as hinge; therefore, the value of effective length factor has been taken as 1.0.
d. The safe load values, as per IS 800, have been compared to the values as per SP 6.

## 4 Analysis

Design considerations as per IS 800: 2007 have been employed in the calculation of safe loads. Both ends are considered as a hinge. Therefore, the value of the effective length factor is (1.0). Different I-sections and channel sections have been considered for calculation of safe loads with the following preliminary data:

Yield stress of material ($f_y$) = 250 N/mm$^2$, modulus of elasticity (E) = $2 \times 10^5$ N/mm$^2$, effective length factor (K) = 1.0, and y-y axis has been considered as minor buckling axis and x-x axis as major buckling axis.

Tables 1 and 2 present the values of safe loads for steel sections ISHB 150 (for minor buckling axis) and ISHB 200 (for major buckling axis) calculated as per SP:6 and IS:800 with different section properties and effective length.

The maximum variations in safe load values for ISHB 150, as per both the codes, can be observed as (+) 2.37 to (−) 20.18. Thus, safe loads calculated as per IS 800 are on economic side in the most of the cases, but its values are on the greater side

**Table 1** Safe loads calculated for ISHB 150 (y-y axis)

| Effective Length in metre (y-y axis) = $L_{eff}$, Sectional Area = $A_s$, Sign: (+) = increment, (−) = decrement | | | | | | |
|---|---|---|---|---|---|---|
| Left (m) | $A_s = 34.48\ cm^2$ Weight (kg/m) = 27.10 | | | $A_s = 38.98\ cm^2$ Weight (kg/m) = 30.60 | | |
| | Safe loads (kN) As per | | Variation (%) | Safe loads (kN) As per | | Variation (%) |
| | SP 6 :1964 | IS 800:2007 | $\left(\frac{B-A}{A}\right) \times 100$ | SP 6 :1964 | IS 800:2007 | $\left(\frac{B-A}{A}\right) \times 100$ |
| | (A) | (B) | (C) | (A) | (B) | (C) |
| 2.0 | 388.13 | 397.33 | + 2.37 | 436.73 | 442.83 | + 1.40 |
| 2.5 | 368.33 | 345.83 | − 6.11 | 412.03 | 382.63 | − 7.14 |
| 3.0 | 338.13 | 294.53 | − 12.89 | 375.73 | 323.53 | − 13.89 |
| 3.5 | 300.43 | 247.73 | − 17.54 | 330.33 | 270.43 | − 18.13 |
| 4.0 | 258.43 | 207.73 | − 19.62 | 281.63 | 225.73 | − 19.85 |
| 4.5 | 219.03 | 174.83 | − 20.18 | 236.93 | 189.43 | − 20.05 |
| 5.0 | 184.73 | 148.23 | − 19.76 | 199.73 | 160.23 | − 19.78 |
| 5.5 | 155.93 | 126.83 | − 18.66 | 166.03 | 136.83 | − 17.59 |
| 6.0 | 130.03 | 109.33 | − 15.92 | 138.23 | 117.83 | − 14.76 |
| 6.5 | 109.03 | 95.13 | − 12.75 | 116.63 | 102.43 | − 12.18 |
| 7.0 | 93.33 | 83.33 | − 10.71 | 99.03 | 89.73 | − 9.39 |
| 7.5 | 79.23 | 73.53 | − 7.19 | 84.13 | 79.13 | − 5.94 |
| 8.0 | 68.63 | 65.33 | − 4.81 | 72.83 | 70.23 | − 3.57 |
| 8.5 | 59.43 | 58.33 | − 1.85 | 63.13 | 62.73 | − 0.63 |

**Table 2** Safe loads calculated for ISHB 200 (x-x Axis)

| Effective Length(x-x axis) = $L_{eff}$(m) Sectional Area = $A_s$, Sign: (+) = increment, (−) = decrement | | | | | | |
|---|---|---|---|---|---|---|
| $L_{eff}$ (m) | $A_s = 47.54\ cm^2$ Weight(kg/m) = 37.3 | | | $A_s = 50.94\ cm^2$ Weight(kg/m) = 40 | | |
| | Safe loads(kN) As per | | Variation (%) | Safe loads(kN) As per | | Variation (%) |
| | SP 6 :1964 | IS 800:2007 | $\left(\frac{B-A}{A}\right) \times 100$ | SP 6 :1964 | IS 800:2007 | $\left(\frac{B-A}{A}\right) \times 100$ |
| | (A) | (B) | (C) | (A) | (B) | (C) |
| 4.0 | 551.04 | 629.94 | + 14.32 | 589.64 | 671.64 | + 13.91 |
| 5.0 | 534.44 | 584.24 | + 9.32 | 570.84 | 621.14 | + 8.81 |
| 6.0 | 512.74 | 531.14 | + 3.59 | 546.64 | 562.44 | + 2.89 |
| 7.0 | 481.74 | 472.64 | − 1.89 | 510.94 | 498.14 | − 2.51 |

(continued)

**Table 2** (continued)

| Effective Length(x-x axis) = $L_{eff}$(m)<br>Sectional Area = $A_s$, Sign: (+) = increment, (−) = decrement | | | | | | |
|---|---|---|---|---|---|---|
| 8.0 | 442.24 | 413.24 | − 6.56 | 466.84 | 433.54 | − 7.13 |
| 9.0 | 396.84 | 357.64 | − 9.88 | 416.74 | 373.94 | − 10.27 |
| 10.0 | 349.94 | 308.64 | − 11.80 | 365.84 | 321.94 | − 12.00 |
| 11.0 | 305.94 | 267.04 | − 12.72 | 318.54 | 277.94 | − 12.75 |
| 12.0 | 272.44 | 232.04 | − 14.83 | 276.74 | 241.24 | − 12.83 |
| 13.0 | 233.24 | 202.84 | − 13.03 | 241.54 | 210.64 | − 12.79 |
| 14.0 | 200.94 | 178.44 | − 11.20 | 207.74 | 185.24 | − 10.83 |
| 15.0 | 174.04 | 157.94 | − 9.25 | 179.04 | 163.84 | − 8.49 |
| 16.0 | 151.14 | 140.64 | − 6.95 | 156.24 | 145.84 | − 6.66 |
| 17.0 | 133.44 | 125.94 | − 5.62 | 137.24 | 130.54 | − 4.88 |
| 18.0 | 116.94 | 113.34 | − 3.08 | 119.74 | 117.44 | − 1.92 |
| 19.0 | 103.14 | 102.44 | − 0.68 | 106.14 | 106.14 | 0.00 |
| 20.0 | 92.04 | 93.04 | 1.09 | 94.64 | 96.44 | 1.90 |

also in few cases concerning the values obtained as per SP 6. Similarly, the maximum variations in safe load values, as per both the codes, for ISHB 200 are as (+) 14.32 to (−) 14.83.

Tables 3 and 4 show the variation in the safe loads, as per both the codes, in the percentage for ISHB 250, ISHB 200, and ISHB 150 considering the minor buckling axis for safe load estimation. It can be observed that most of the load values are found to be economical in case of IS 800:2007 compared to SP 6.

Fig. 1 shows the graphical representations of the difference of safe loads for ISHB 200 for different sectional area properties, which are also showing that the most of the values obtained as per SP: 6 are on the higher side as per the values obtained from IS 800.

Similarly, Fig. 2 and Fig. 3 show the graphical representation of the variations in safe loads as per SP6 and IS 800 for ISHB 150 having 34.48 $cm^2$ sectional area considering for minor buckling axis for the analysis and ISHB 200, 47.54 $cm^2$ (sectional area) considering major buckling axis, respectively.

## 5 Conclusion

In the paper, the design procedures for columns under concentric loads as per IS 800:2007 are reviewed and applied on different steel sections to obtain safe loads for the sections in both major buckling axis and minor buckling axis. The safe load values, as per IS 800, have been compared to the values as per SP 6 for ISHB 150, 200, and 250. These steel sections are commonly used in the construction. It is also

**Table 3** Percentage variation in safe loads (calculated as per IS 800) in comparison with SP 6

| Effective length(y-y axis) = $L_{eff}$(m)<br>Sectional Area = $A_s$, Sign: (+) = increment, (−) = decrement | | | | |
|---|---|---|---|---|
| $L_{eff}$ (m) | ISHB 250 | | ISHB 200 | |
| | $A_s = 64.96$ cm$^2$<br>Weight(kg/m)<br>= 51.0 | $A_s = 69.71$ cm$^2$<br>Weight(kg/m)<br>= 54.7 | $A_s = 47.54$ cm$^2$<br>Weight(kg/m)<br>= 37.3 | $A_s = 50.94$ cm$^2$<br>Weight(kg/m)<br>= 40 |
| | (%) | (%) | (%) | (%) |
| 2.0 | + 14.43 | + 13.92 | + 9.67 | + 9.08 |
| 2.5 | + 8.90 | + 8.26 | + 3.01 | + 2.33 |
| 3.0 | + 3.45 | + 2.74 | − 3.62 | − 4.44 |
| 3.5 | − 1.93 | − 2.80 | − 9.65 | − 10.46 |
| 4.0 | − 7.20 | − 8.04 | − 14.48 | − 15.16 |
| 4.5 | − 11.70 | − 12.45 | − 17.75 | − 18.13 |
| 5.0 | − 15.32 | − 15.91 | − 19.37 | − 19.58 |
| 5.5 | − 17.82 | − 18.21 | − 20.05 | − 20.12 |
| 6.0 | − 19.16 | − 19.43 | − 20.04 | − 19.96 |
| 6.5 | − 19.85 | − 19.94 | − 19.76 | − 19.65 |
| 7.0 | − 20.06 | − 19.96 | − 21.21 | − 17.93 |
| 7.5 | − 19.93 | − 19.65 | − 16.58 | − 15.75 |
| 8.0 | − 19.69 | − 19.50 | − 13.84 | − 12.92 |
| 8.5 | − 18.72 | − 17.94 | − 12.21 | − 11.67 |
| 9.0 | − 16.94 | − 16.25 | − 10.19 | − 9.33 |
| 9.5 | − 15.02 | − 13.96 | − 7.37 | − 6.57 |
| 10.0 | −12.80 | -12.48 | -5.34 | -4.71 |
| 11.0 | −9.99 | -8.99 | -1.13 | -0.24 |
| 12.0 | −5.83 | -5.07 | - | - |
| 13.0 | −2.55 | -1.42 | - | - |

(continued)

**Table 3** (continued)

advised to analyse more cross-sectional shapes, i.e. angles, channels, etc. The work does not comment on IS 800, but highlight the fact that as per the revised provisions

**Table 4** Percentage variation in safe loads (calculated as per IS 800) in comparison with SP 6

| Effective Length (y − y axis) = $L_{eff}$(m)<br>Sectional Area = $A_s$, Sign: (+) = increment, (−) = decrement | | | | |
|---|---|---|---|---|
| $L_{eff}$ (m) | ISHB 200 | | ISHB 150 | |
| | $A_s = 47.54$ cm$^2$<br>Weight (kg/m)<br>= 37.3 | $A_s = 50.94$ cm$^2$<br>Weight (kg/m)<br>= 40 | $A_s = 34.48$ cm$^2$<br>Weight (kg/m)<br>= 27.10 | $A_s = 38.98$ cm$^2$<br>Weight (kg/m)<br>= 30.60 |
| | (%) | (%) | (%) | (%) |
| 2.0 | + 9.67 | + 9.08 | + 2.37 | + 1.40 |
| 2.5 | + 3.01 | + 2.33 | − 6.11 | − 7.14 |
| 3.0 | − 3.62 | − 4.44 | − 12.89 | − 13.89 |
| 3.5 | − 9.65 | − 10.46 | − 17.54 | − 18.13 |
| 4.0 | − 14.48 | − 15.16 | − 19.62 | − 19.85 |
| 4.5 | − 17.75 | − 18.13 | − 20.18 | − 20.05 |
| 5.0 | − 19.37 | − 19.58 | − 19.76 | − 19.78 |
| 5.5 | − 20.05 | − 20.12 | − 18.66 | − 17.59 |
| 6.0 | − 20.04 | − 19.96 | − 15.92 | − 14.76 |
| 6.5 | − 19.76 | − 19.65 | − 12.75 | − 12.17 |
| 7.0 | − 21.21 | − 17.93 | − 10.71 | − 9.39 |
| 7.5 | − 16.58 | − 15.75 | − 7.19 | − 5.94 |
| 8.0 | − 13.84 | − 12.92 | − 4.81 | − 3.57 |
| 8.5 | − 12.21 | − 11.67 | − 1.85 | − 0.63 |
| 9.0 | − 10.19 | − 9.33 | – | – |
| 9.5 | − 7.37 | − 6.57 | – | – |
| 10.0 | − 5.34 | − 4.71 | – | – |
| 11.0 | − 1.13 | − 0.24 | – | – |

of IS 800, the updation of SP 6 can provide a useful document to the practitioners and the academicians. The following points can be summarized from the results.

- It can be observed that there are large variations in the load-carrying capacity of standard sections calculated as per IS 800: 2007 compared to the values obtained as per SP: 6(1)-1964.
- In some of the cases, safe loads given in SP: 6(1)-1964 seem to be uneconomical; on the other hand, in some of the cases, safe loads are given in SP: 6(1)-1964 are likely to be unsafe compared to IS 800:2007.

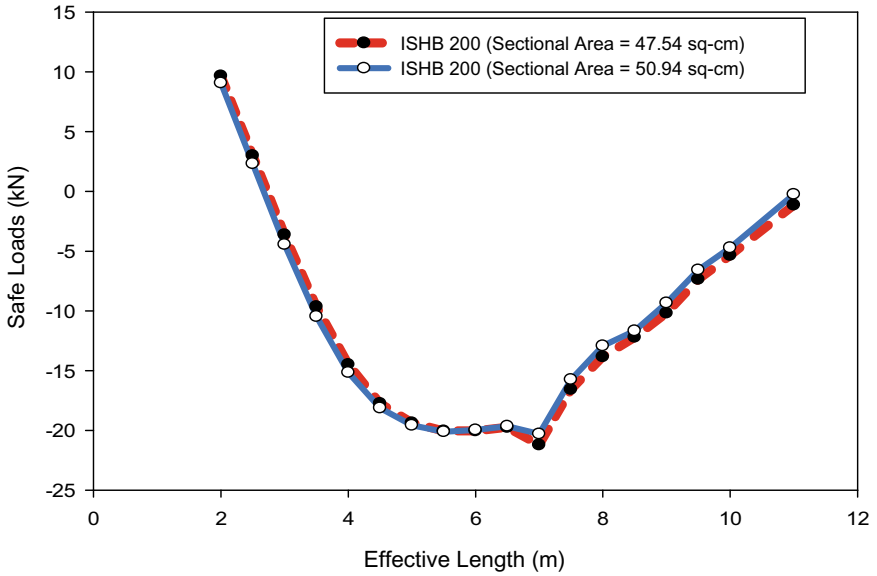


**Fig. 1** Percentage variation in safe loads (for ISHB 200, y-y Axis) as per IS 800 with respect to. the values as per SP-6

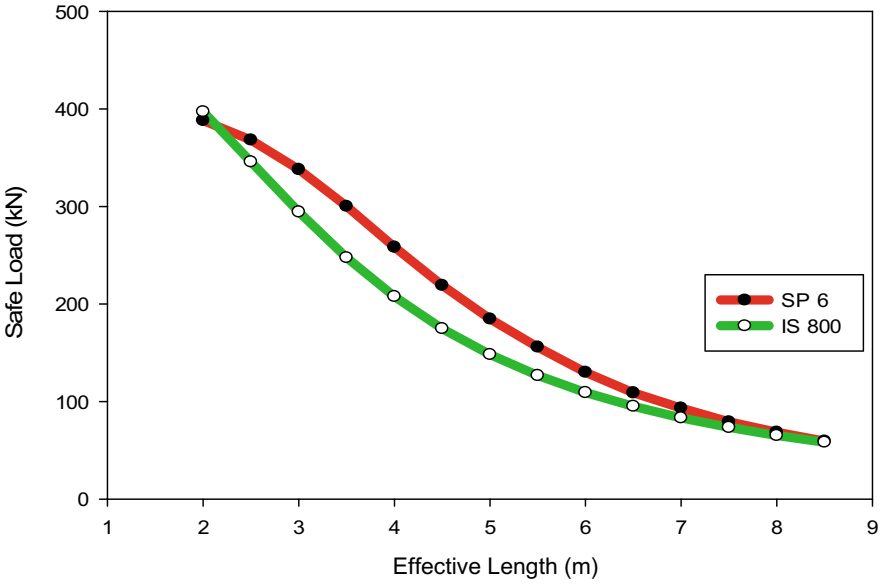


**Fig. 2** Safe loads [ISHB 150, 34.48 $cm^2$ (sectional area), y-y axis] calculated as per IS 800 and SP 6

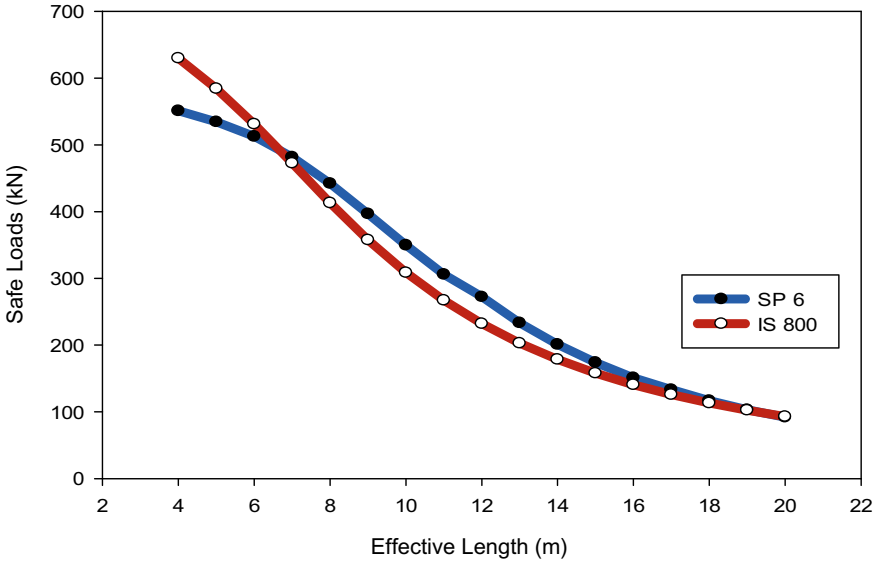


**Fig. 3** Safe loads [ISHB 200, 47.54 $cm^2$ (sectional area), x-x axis] calculated as per IS 800 and SP 6

- Hence from the above observation, it can be concluded that the load-carrying capacity of sections given in SP: 6(1)-1964 are needed to be reviewed.
- The paper also discusses the requirement to update SP: 6 as per the provisions of IS 800:2007 to obtain optimum sections to fulfil the aspect of economic designs with the safety of the structure and to make the code SP: 6 more relevant and useful.

## References

1. Bureau of Indian Standards. IS 800:2007; Code of practice for general construction in steel, Bureau of Indian Standards, New-Delhi
2. Bureau of Indian Standards. SP: 6(1)-1964, Handbook for structural engineers, structural steel sections, Bureau of Indian Standard, New-Delhi
3. Duggal SK (2014) Limit state design of steel structures. McGraw Hill, Chapter 7, Compression Members
4. Fieber A, Gardner L, Macorini L (2020) Structural steel design using second-order inelastic analysis with strain limits. J Constr Steel Res 168:105980. https://doi.org/10.1016/j.jcsr.2020.105980
5. Guha A, Ghosh M (2008) IS 800- Indian code of practice for construction in steel and its comparison with international codes. Institute for Steel Development & Growth (INSDAG)
6. Kulkarni RB, Jirage RS (2011) Comparative study of steel angles as tension members designed by working stress method and limit state method. Int J Sci Eng Res 2(11)

7. Subramanian N (2008) Code of practice on steel structures—A review of IS 800: 2007. Civ Eng Constr Revs
8. Subramanian N (2009) Design of steel structures; design and practice based on limit state method of design. Oxford Higher Education, Chapter 5—Design of compression members.

# Blast Response of Reinforced Concrete Slab Stiffened with Structural Steel


**Jagriti Mandal, Manmohan Dass Goel, and Ajay Kumar Agarwal**

**Abstract** In this investigation, effect of structural steel stiffening on the response of a simply supported reinforced concrete slab under air blast loading is examined. Herein, three different steel sections have been considered for the study, namely channel, I-section, and square tube. The sections are fixed on top of the concrete slab in two configurations. First configuration is developed by placing the steel beam such that its longitudinal axis is parallel to the slab surface, and in the second one, it is perpendicular to the slab surface. The dynamic response of the slab is analyzed with each combination based on the displacement at the center of the slab. The aim is to determine the steel section and configuration which mitigates the blast induced damage most efficiently. Concrete and structural steel are modeled using solid elements, while the reinforcement is modeled using beam elements. Karagozian & case concrete material model is used to define the non-linear and strain softening behavior of concrete. The results indicate that channel section with longitudinal axis parallel to the slab surface performs better than the other combinations of steel sections and configuration with all other parameters being same.

**Keywords** Blast load · Structural steel · Mitigation · Concrete slab · LS-DYNA® · Stiffener

J. Mandal (✉) · A. K. Agarwal
Department of Mining Engineering, Visvesvaraya National Institute of Technology, Nagpur 440 010, India
e-mail: jagritimandal@students.vnit.ac.in

A. K. Agarwal
e-mail: akagarwal@mng.vnit.ac.in

M. D. Goel
Department of Applied Mechanics, Visvesvaraya National Institute of Technology, Nagpur 440 010, India
e-mail: mdgoel@apm.vnit.ac.in



M. Madhavan et al. (eds.), *Proceedings of the Indian Structural Steel Conference 2020 (Vol. 1)*, Lecture Notes in Civil Engineering 318,
https://doi.org/10.1007/978-981-19-9390-9_54

## 1 Introduction

A rise in the number of explosive-based terrorist attacks have been observed in the past two decades. These attacks pose great threat to the safety of civilians and properties, thereby issuing the need to develop measures to minimize the effect of blast. Reinforced concrete (RC) is a principle material used in the area of construction. It is used to construct both civilian buildings and military infrastructures. Among all the structural members, RC slabs are widely used for blast mitigation in the form of sacrificial wall.

Experimental and numerical studies have been conducted in the past on RC slabs to understand their dynamic behavior under blast loading [1, 5, 6, 12, 14, 16, 21, 22]. Both tensile and compressive strength of concrete are highly strain dependent, wherein at high strain rates, it shows better mechanical behavior [4]. The current focus of research is to improve the blast resistance capacity of RC slab. In most of the past studies, enhancement of blast performance of RC slab has been done by either using high strength concrete or incorporating steel mesh and high strength fibers. Alternatively, energy absorbing composite materials such as metal and polymeric foam have also been employed to reduce the effect of blast on the parent RC members [3, 13, 18]. However, effectiveness of structural steel in blast mitigation has not yet been explored. Li et al. [8] studied the enhancement of blast resistivity of RC slab by replacing normal strength concrete with ultra-high strength concrete by conducting series of experimental and numerical analyzes. Zhao et al. [19] evaluated the strength of novel RC slab under blast load where the reinforcement was arranged at an angle of 60°°. Zhao et al. [20] conducted experimental tests of single side steel concrete and center steel concrete slab under contact explosion and compared the dynamic response and failure modes with that of normal RC slab. Kong et al. [7] retrofitted the RC slab with aramid fiber-reinforced plastic (AFRP) and numerically evaluated its blast resistance capability. Luccioni et al. [9] studied the blast performance of high strength fiber-reinforced concrete (HSFRC) slab by performing experimental and numerical analyzes. Li et al. (2018) conducted a comparative study on the blast response of RC slab reinforced with steel fiber, ultra-high molecular weight polyethylene (UHMWPE) fiber, and steel wire meshes. Meng et al. [11] investigated the performance of RC slab made from steel wire mesh-reinforced geopolymer under close-in explosion.

Hence, in the current study, the effect of structural steel stiffening on the response of a simply supported RC slab under air blast is investigated. Three different steel sections have been considered for the investigation, namely channel, I-section, and square tube. They are fixed on top of the slab facing the blast in two configurations. Firstly, the steel beams are placed such that their longitudinal axis is parallel to the slab surface. In latter case, the longitudinal axis is perpendicular to the slab surface. The effectiveness of each combination in blast resistance is evaluated in terms of central deflection of RC slab. Finally, prime objective of present study is to determine the steel section and configuration which mitigates the blast induced damage most efficiently.

## 2 Geometrical Details and Finite Element Model

### *2.1 Geometrical Setup and FE Modeling*

Numerical study has been conducted using commercially available FE software LS-DYNA®. Geometrical details of RC slab used in the experiments conducted by [15] have been chosen for the numerical analysis in the present study. Details of the simply supported slab are illustrated in Fig. 1. Reinforcement of 6 mm diameter is placed at 75 mm center to center spacing with a cover of 20 mm.

Lagrangian formulation is used to model the concrete and reinforcement. Concrete is modeled using 8-noded hexahedron solid elements of size 10 mm, whereas the reinforcing steel is modeled using Hughes-Liu beam elements of size 5 mm. The contact between concrete and reinforcement is defined using CONSTRAINED_

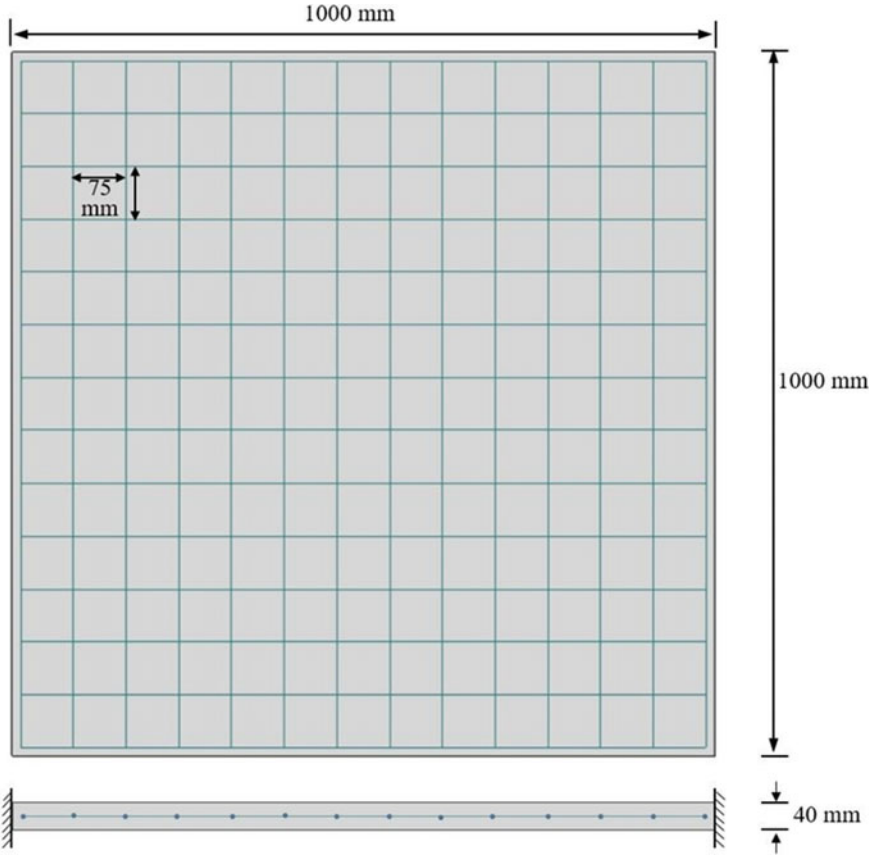


**Fig. 1** Geometrical and reinforcement details of RC slab [15]

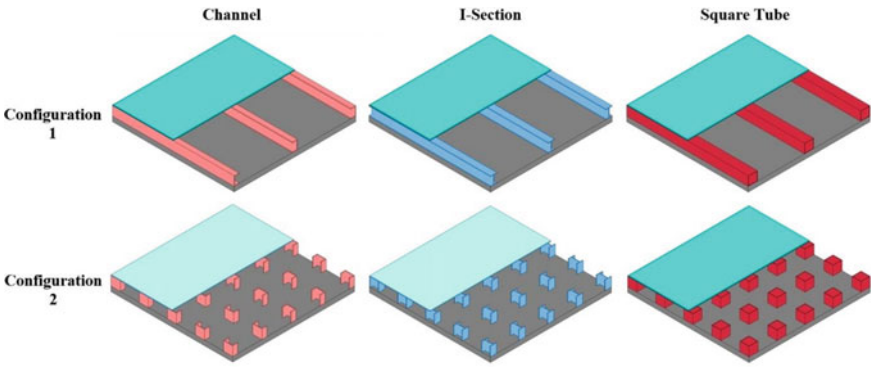


**Fig. 2** CAD models of configurations 1 and 2

LAGRANGIAN_IN_SOLIDS option provided by LS-DYNA®. The three structural steels considered for the comparative study are channel section ISLC 75, I-section ISLB 75, and square tube of dimensions $75 \times 75 \times 3.2$ mm having weight per unit length of 5.7 kg/m, 6.1 kg/m, and 7.01 kg/m, respectively. Structural steel is placed in between the slab and a steel sheet of thickness 5 mm. Both steel sheet and structural steel are modeled using solid elements. The contact between steel sheet, structural steel, and slab is defined using CONTACT_TIED_SURFACE_TO_SURFACE option. Further, to avoid penetration of parts into each other on contact, AUTOMATIC_SURFACE_TO_SURFACE option is employed. The structural steel is placed on the slab in two configuration to arrive at the best possible stiffening method. First configuration includes placing the beams such that their longitudinal axis is parallel to the slab surface. In the second configuration, the longitudinal axis of the beams is perpendicular to the slab surface. In either case, the distance between the steel sheet and RC slab is maintained constant as 75 mm to avoid variation in stand-off distance of the explosive from the slab. Figure 2 illustrates the two configurations in which the structural steel is placed on the slab.

## *2.2 Material Models*

Karagozian & case concrete (KCC) material model is used to model the concrete in this present study. This material model was developed in the 1990s for analyzing the response of reinforced concrete structures subjected to blast and impact loading. It allows automatic parameter generation on inputting values for density and unconfined compressive strength of concrete along with two conversion factors for length and pressure magnitude [10, 17]. The required material parameters to define the behavior of concrete are given in Table 1.

The structural steel, steel sheet, and reinforcement steel have been modeled using plastic kinematic material model, and their material parameters are listed in Table 2.

**Table 1** Material properties of concrete [15]

| Parameters | Magnitude |
|---|---|
| Density | 2400 kg/m$^3$ |
| Unconfined compressive strength | 39.05 MPa |

**Table 2** Material properties of reinforcement steel, steel sheet, and structural steel

| Parameters | Reinforcement steel | Steel sheet | Structural steel |
|---|---|---|---|
| Density (kg/m$^3$) | 7830 | 7800 | 7850 |
| Young's modulus (GPa) | 200 | 210 | 200 |
| Poisson's ratio | 0.29 | 0.3 | 0.3 |
| Yield stress (MPa) | 600 | 300 | 250 |

## *2.3 Blast Loading*

Blast loading applied on the RC slab is defined using LOAD_BLAST_ENHANCED option provided by LS-DYNA® as a spherical air burst. To activate this keyword, explosive charge weight and stand-off distance has to be specified. LOAD_BLAST_SEGMENT_SET option is used to define the segment set where the load has to be applied. Blast pressure is calculated using Kingery-Bulmash equations [2]. The explosive is centrally located 400 mm away from the top surface of slab as shown in Fig. 3.

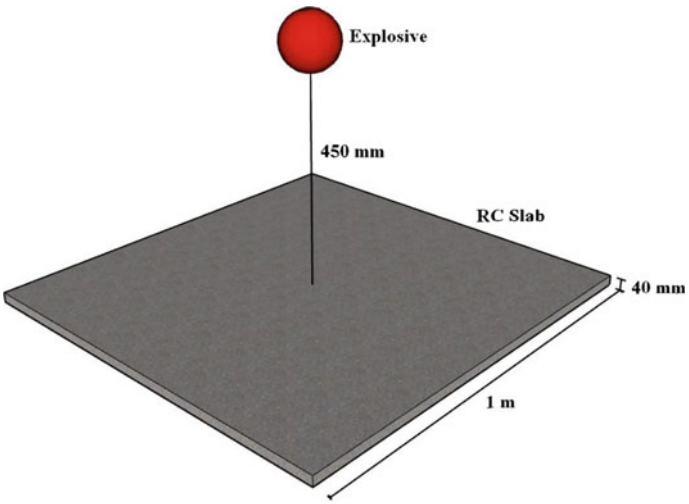


**Fig. 3** Schematic diagram showing the location of explosive with respect to RC slab

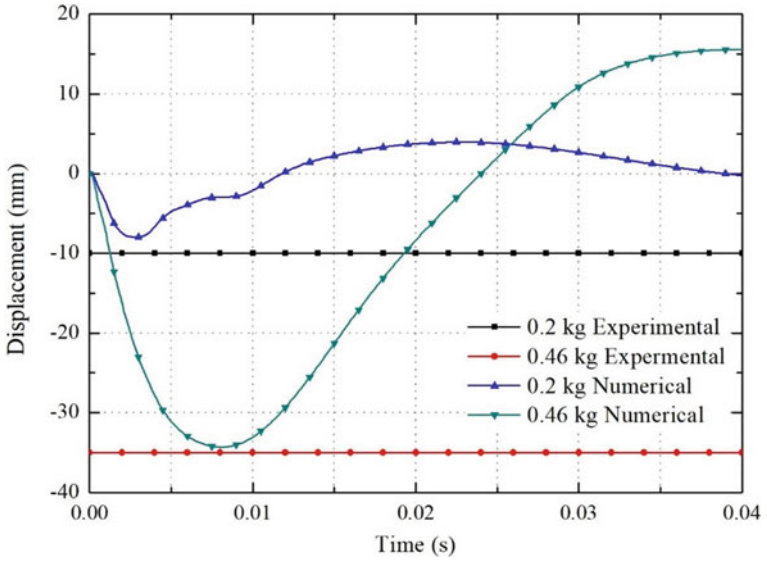


**Fig. 4** Comparison of results obtained from numerical modeling with the experimental data from [15]

## 3 Validation of FE Model

The numerical model is validated using the experimental data presented by [15]. Two charge weights are considered for validation, 0.2 kg and 0.46 kg where the peak central deflection observed in the experimental results were registered as 10 mm and 35 mm, respectively. Numerically obtained displacement time histories are compared with the peak displacement recorded in the experiments and are shown in Fig. 4. It can be noticed that the results agree well with each other with a very less margin of discrepancy for the charge weight of 0.2 kg which being insignificant can be neglected.

## 4 Results and Discussions

The effect of blast on RC slab was studied after fitting structural steel on top of it. Displacement time histories for each combination set of structural steel and configuration were compared. It can be observed from Fig. 5 that the central deflection of the slab fitted with structural steel is less than that of bare slab. Maximum reduction of blast damage by 90% is obtained in the case of channel (C) placed horizontally on the slab with its longitudinal axis parallel to the slab surface. For the same configuration, I-section (I) and square tube (S) give 84% and 85% reduction in deflection, respectively.

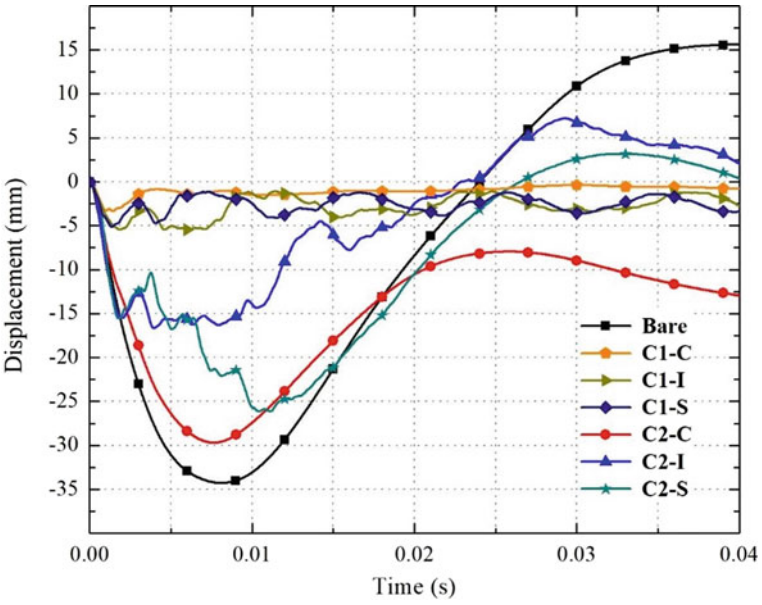


**Fig. 5** Comparison of displacement time histories of the combination sets of structural steel and configuration considered in the study

On the other hand, blast damage reduction for second configuration is comparatively less, with I-section having the maximum reduction of 52%. While, channel section and square tube perform inferior in comparison with 15 and 25% in reduction of deflection, respectively. Table 3 summarizes the maximum central deflection for each case with percentage reduction in blast damage where 1C signifies first configuration and 2C signifies second configuration.

In first configuration, structural steel acts like a beam component. The resistance and stiffening it provide against the blast load which can be attributed to its flexural strength. Whereas, in the second configuration, structural steel acts like a set of short columns working individually. The stiffening action is comparatively weaker in

**Table 3** Comparison of maximum central deflections obtained from each combination set of structural steel and configuration

| Structural steel section | Configuration | Maximum central deflection (mm) | Percentage reduction (%) |
|---|---|---|---|
| Bare RC | - | 35 | - |
| Channel | 1C | 29.7 | 15% |
| | 2C | 3.37 | 90% |
| I-section | 1C | 16.67 | 52% |
| | 2C | 5.50 | 84% |
| Square Tube | 1C | 26.15 | 25% |
| | 2C | 5.11 | 85% |

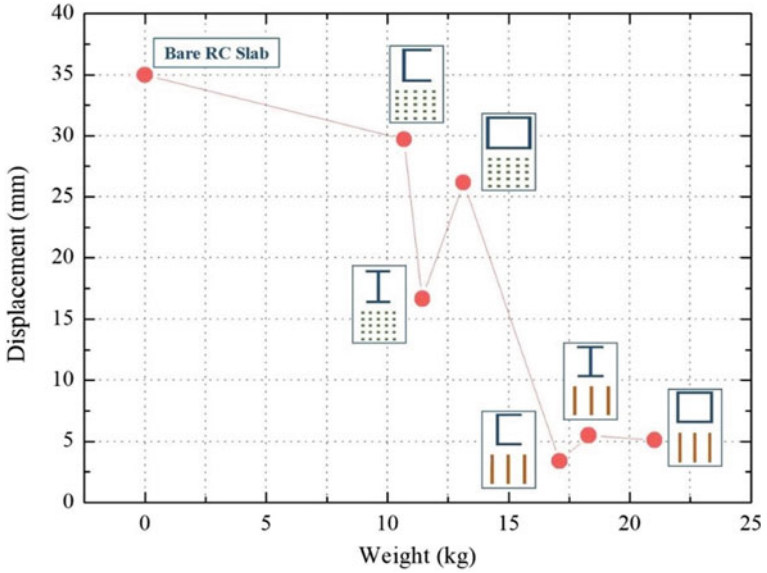


**Fig. 6** Variation in displacement of structural steel fitted RC slab with weight of the structural steel assembly for each combination considered

second configuration. Larger part of blast load is transferred to the parent slab leading to its deformation. The central displacement of slab of each case is normalized on basis of weight per unit meter of respective structural steel to establish a relationship between mass added to the structural member and blast resistant capacity. As illustrated in Fig. 6, displacement decreases as the weight of the steel assembly on the RC slab increases with configuration 1 showing better performance.

## 5 Conclusions

The central displacement of bare-reinforced concrete slab with the experimental results from literature agrees well, hence validating the numerical model. Comparative study between six sets of steel sections and configurations shows that channel sections placed on the slab with its longitudinal axis parallel to the slab surface results in the least central displacement, thereby providing the maximum stiffness to the structure. On the other hand, maximum displacement is observed when square tubes placed on the slab with its longitudinal axis perpendicular to the slab surface. Based on this study, it is observed that there exist various configurations to mitigate the blast; for which such analysis can be performed to arrive at optimized solution.

## References


1. Del Linz P, Fan SC, Lee CK (2016) Modeling of combined impact and blast loading on reinforced concrete slabs. Lat Am J Solids Struct 13(12):2266–2282
2. Goel MD (2014) Blast: Characteristics, loading and computation - an overview. In: Matsagar V (ed) Advances in structural engineering. Springer India, New Delhi, pp 417–434
3. Goel MD, Matsagar VA, Gupta AK (2014) Blast resistance of stiffened sandwich panels with closed-cell aluminum foam. Lat Am J Solids Struct 11(13):2497–2515
4. Goel MD, Matsagar VA (2014) Blast-resistant design of structures. Pract Period Struct Des Constr 19(2)
5. Jaini ZM, Feng YT, Owen DRJ, Mokhatar SN (2016) Fracture failure of reinforced concrete slabs subjected to blast loading using the combined finite-discrete element method. Lat. Am. J. Solids Struct. Lat Am J Solids Struct 13(6):1086–1106
6. Jia H, Yu L, Wu G (2014) Damage assessment of two-way bending RC slabs subjected to blast loadings. Sci World J
7. Kong X, Qi X, Gu Y, Lawan IA, Qu Y (2018) Numerical evaluation of blast resistance of RC slab strengthened with AFRP. Constr Build Mater 178:244–253
8. Li J, Wu C, Hao H (2015) An experimental and numerical study of reinforced ultra-high performance concrete slabs under blast loads. Mat Des 82:64–76
9. Luccioni B, Isla F, Codina R, Ambrosini D, Zerbino R, Giaccio G, Torrijos MC (2018) Experimental and numerical analysis of blast response of high strength fiber reinforced concrete slabs. Eng Struct 175(August):113–122
10. Magallanes JM, Wu Y, Malvar LJ, Crawford JE (2010) Recent improvements to release III of the K&C concrete model. In: 11th international LS-DYNA user conference, pp 37–48
11. Meng Q, Wu C, Su Y, Li J, Liu J, Pang J (2019) A study of steel wire mesh reinforced high performance geopolymer concrete slabs under blast loading. J Clean Prod 210:1150–1163
12. Shuaib M, Daoud O (2015) Numerical modelling of reinforced concrete slabs under blast loads of close-in detonations using the Lagrangian approach. J Phys Conf Ser 628(1)
13. Silva PF, Lu B (2007) Improving the blast resistance capacity of RC slabs with innovative composite materials. Composites Part B: Eng 38(5–6):523–534
14. Tai YS, Chu TL, Hu HT, Wu JY (2011) Dynamic response of a reinforced concrete slab subjected to air blast load. Theor Appl Fract Mech 56(3):140–147
15. Wang W, Zhang D, Lu F, Wang S, Tang F (2013) Experimental study and numerical simulation of the damage mode of a square reinforced concrete slab under close-in explosion. Eng Failure Anal 27(January):41–51
16. Wenjiao Z, Xiangqing K, Yandong Q, Qian Z (2018) Numerical simulation of cracked reinforced concrete slabs subjected to blast loading. Civ Eng J 4(2):320–333
17. Wu Y, Crawford JE, Magallanes JM (2012) Performance of LS-DYNA concrete constitutive models. In: 12th international LS-DYNA users conference, pp 1–14
18. Xia Y, Wu C, Liu ZX, Yuan Y (2016) Protective effect of graded density aluminium foam on RC slab under blast loading-an experimental study. Constr Build Mat 111:209–222
19. Zhao C, Lu X, Wang Q, Gautam A, Wang J, Mo YL (2019a) Experimental and numerical investigation of steel-concrete (SC) slabs under contact blast loading. Eng Struct 196(July)
20. Zhao C, Wang Q, Lu X, Wang J (2019) Numerical study on dynamic behaviors of NRC slabs in containment dome subjected to close-in blast loading. Thin-Walled Struct 135(November):269–284
21. Zhao CF, Chen JY (2013) Damage mechanism and mode of square reinforced concrete slab subjected to blast loading. Theor Appl Fract Mech 63–64(February):54–62
22. Zhou XQ, Kuznetsov VA, Hao H, Waschl J (2008) Numerical prediction of concrete slab response to blast loading. Int J Impact Eng 35(10):1186–1200

# Different Insulation Technique for Fire Protection of Industrial Steel Structure


**Sudipta Hui, Debarshi Sahoo, and Narayan C. Moharana**

**Abstract** The construction of steel high rise building is proved to be more economical than those made of RCC. But one of the major drawbacks of steel is susceptible to fire as metals are good conductor of heat and electricity. On the other-hand, office buildings are equipped with so many accessories which are vulnerable to fire. When exposed to fire, commonly used steel section loses, some of its mechanical properties due to that elongation, deformation, buckling, or any other stresses are generated. Heavily loaded steel loses it designed safety margin at a temperature around 220 °C—regardless the grade of steel. Majority of the research works carried out in this field came out with different techniques to protect a steel structure from fire by means of making it fire resistant internally or externally. Some researches came up with different modelling and analysis tools to develop the fire resistance of structural steel. In this present paper, we presented the different alternatives discovered so far to improve the performance of steel on fire and behaviour of different structural members under various loading conditions are explained.

**Keywords** Steel structures · Fire resistance · Composite materials · Industrial projects · Insulation technique

## 1 Introduction

Increase in the global population leads to industrialization and urbanization which is supported by development of science and the technology. For above purpose, the high rise buildings are preferred rather than low and medium rise buildings, which require less horizontal expansion in order to save lands used for agriculture, forest, etc. The construction of steel high rise building is proved to be more economical than

S. Hui · D. Sahoo
SM. ASCE, School of Civil Engineering, KIIT Deemed To Be University, Bhubaneswar, India

N. C. Moharana (✉)
School of Civil Engineering, KIIT Deemed To Be University, Bhubaneswar, India
e-mail: nmoharanafce@kiit.ac.in



M. Madhavan et al. (eds.), *Proceedings of the Indian Structural Steel Conference 2020 (Vol. 1)*, Lecture Notes in Civil Engineering 318,
https://doi.org/10.1007/978-981-19-9390-9_55

those made of RCC. But one of the major drawbacks of steel is susceptible to fire as metals are good conductor of heat and electricity. On the other-hand, office buildings are equipped with so many accessories which are vulnerable to fire. Electricity is the major power source, and electrical short circuit is one of the major reasons which causes fire explosions in these kind of buildings. When exposed to fire, commonly used steel section loses, some of its mechanical properties due to that elongation, deformation, buckling, or any other stresses are generated. Heavily loaded steel loses it designed safety margin at a temperature around 220 °C—regardless the grade of steel. According N.C.R.B. 2015, fire accidents in India kill 48 Indians every day.

The aim of this study is to protect the steel from fire in order to ensure safe fire escape from the building, before the steel starts heating up excessively. So there is a huge need of fire protection of these industrial structures. Majority of the research works carried out in this field came out with different techniques to protect a steel structure from fire by means of making it fire resistant internally or by applying different coatings or protecting its surface with different materials externally. Many research approaches developed to different modelling and analysis tools to improve the fire resistance of structural steel. Temperature transmitted to steel members is checked by providing various insulating methods such as

1. Internal fire insulation methods.
2. External fire insulation methods.
3. Analysis-based insulation approaches.

These three categories cover all sorts of insulation techniques, varieties of insulating materials, and various tools also including fire models developed to analyze fire performance of steel under different loading conditions when exposed to fire. Research study has been carried out on fire safety design of steel structures. This paper represents different insulation techniques for different types of structure based on their purpose and structural complexity. The performance of different insulating materials available in the market has been presented. Behaviour of different structural members has been discussed under various loading conditions, when exposed to fire.

## 2 Literature Review

Different research papers were studied, and the research findings were compared in between to come up with some best suitable methods of fire insulation of steel. The researches led us to different fire resistive techniques, a variety of insulating materials, FEA analysis of different insulation models, and few case studies. Another alternative approach observed is to go for compositing the steel section with use of different material, in order to increase its fire resistivity. To present different alternatives for fire protection, we accumulated numerous research findings and did a literature review on those papers.

## 2.1 Analytical Model

For analyzing steel framed structures, Chen and Liew [1] established a mixed element approach for modelling a localized blast load. Shell elements were taken for modelling of the members subject to straight state of burst and blast. Noncritical elements left from the impressed portion were modelled considering beam-element. They advocated that their proposed approach is effective for modelling of structures in large scale and perfect to estimate the behaviour of members related with the effects of explosion and corresponding fires. They advocated that fire resistivity of the multi-storeyed building frame gets be reduced by more than 10% after an explosion depending on its magnitude because the fire resistance of steel structure is expected to decrease at higher temperature due to high explosion load intensity. Skowroński [16] expressed and answered many of differential equation for clipping of steel columns through fire. Toh et al. [18] confirmed that with the help of his suggested model, it is feasible to guess the results of blast strength investigations on any steel column where he generalizes these effects over the column underneath various static diagram, length, and load to fire resistance and determine rigidity of the columns.

## 2.2 Fire Analysis of Steel Frames

For exhibiting in-elastic behaviour of 3-dimension steel frame, a beam column model was proposed by [10]. He also modelled the yielding steel section by 2 noted stress resultanting surface considering soften impact on steel at high temperature. They has presented the source of in-elastic stiffness of 3-dimension beam column, and deterioration of strength of steel at high temperature was expressed according to the "effective yield strength" thought. Use of the method is presented by analyzing the performance of steel member and a 3-dimension multistoreyed steel frame blast to blast. Chen and Liew [1] demonstrated a mathematical formulation for in-elastic transient analyzing of steels frame proposed structures subject to blast following by burst. To permit a truthful modelling of general framework subject to localized blast and burst, the author approached to adopt the beam and column element and fibre element. Complete need for modelling elasto plastic material at raised temperature and high strain rate has been demonstrated, and the influence of loads due to blast on the fire resistance of a multi-storey steel frame can be reviewed.

Lennon et al. [6] investigated the actual performance of a steel framed building subjected to a series of compartment (1ocalized) fires. The results from the tests showed that pervious fire codes are not addressing the right building behaviour during fire, and the consequences are extremely conservative. In addition, the full-scale fire tests on frame displayed that the real global and local structural performance of steel building is different, and usually far superior to that obtained in standard small scale.

### 2.3 Fire Resistance of Different Steel Members

In comparison with conventional structural steel for buildings, fire resistance steel retains more strength at high temperature, and fire resistance steel can bear load and allowable permeable stress under permanent loading which conform at temperature of 600°C (which is 2/3 of the room temperature yield point). So, fire resistance steel can be used in steel building without any protection where the heat would not beat of 600°C. Sakumoto et al. [12] reported the results of experimental studies on high-strength fire resistant bolts, which can be used for fire resistance steel, the mechanical property of fire resistance bolt was intact at high temperature of 600°C. They concluded that, compared to conventional high-strength bolts, the fire resistance bolt in tensile area at high temperature is more superior, and whilst using fire resistance bolt in slip load of joints, it may decrease in temperature over 400°C rapidly, and the permeable shear force is less than the shear strength of steel at temperature up to 650°C. Sakumoto et al. [14] have done some numerical analysis and full-scale load heat tests, and he concluded that fire resistance columns prepared form fire resistant steel which is better than conventional structural steel at higher temperatures. Fire resistant steel (FR) has 0.2% of proof stress at 600°C, which greater or equal than specified 2\3 value at indoor temperature. They also reported the thickness of fire protection, which reduced heat. Using of intumescent coating with less insulation can be resist 1 h fire. During investigation on constructional floor using fire resistant steel, they obtained a strength reduction factor of 0.5 around at 700°C.

Shat (1998) observed that fire resistance improvement is limited to a certain extent, in some particular cases of slim floor system, where efficient built in fire resistance is already there. In I beam floor made by fire resistant steel (FR), it may increase fire resistance about 22–24 min whereas use of slim floor construction gives us a fire resistance of 11–16 min. In I beam floor structure, an increased 30 min of fire resistance can be achieved by shifting the strength reduction factor curve of the steel by 150°C to its greater temperature. Sakumoto et al. [11] presented the experimental results on blast resistance of some exterior wall, partition wall, and floor ceiling systems, which are made by galvanized light gauge steel with thickness up to 1.6 mm, attached plywood and gypsum boards. It has been verified that gypsum boards help to improved fire resistance. Rise in the number of gypsum board as well thickness has more impact on fire resistance. Using these gypsum boards, a blast rating of 60 min can be got practically, without any direct blast protection for different shapes.

Huang and Tan [4] predicted the critical temperature or heat of an axially restrained steel column using Rankine formula. Using Rankine formula, the combined effect of the axial restraint and creep-strain can be determined. The comparative study on test result and numerical result supports that Rankine formula can predict good critical temperature for steel columns. They have observed that axial restraining of columns can significantly decrease its fire resistance based on the assumed failure standard.

## 2.4 Steel Column with Infilled Concrete

A mathematical model has been proposed by [7] to compute the heat, fire resistance, and deformation of the columns according to experiments. By using this model, the fire resistance of circular steel column filled with concrete can be estimated for any rate of the load, dimension of column section, length without any testing, which is acceptable of experimental purpose. Kodur and Lie [5] developed a simple numerical model to determine the influence factor for fire resistance steel hollow structural section (HSS) columns, which may be circular and square in cross section filled by reinforced concrete and obtained valid result from fire experiment on column. They supported that the process is appropriate for integration in design codes, and it has been made available a rational and to estimate some values based on some parameters of fire resistance steel hollow structural section (HSS) which is filled by bar-reinforced concrete such as dimension of column section, concrete strength, length of column, and percentage of reinforcement steel.

Han and Huo [2] have developed a mechanical dummy for fire resistance steel hollow structural section columns after contact to ISO 834 of fire standard and improvement of the analysis used for ambient state. They informed that slenderness ratio, sectional dimension, and the fire period time having major influence on residual strength index (RSI). However, the load eccentricity ratio, steel ratio, and strength of the material having adequate influence on residual strength index RSI. Tan and Tang [17] extended Rankine formula to analyzing plain concrete filled steel (PCFS) and reinforced concrete filled steel (RCFS) on column‘s in higher heat. Elastic buckling capacity and plastic squashing capacity of column can produce practical idea for structural engineers, which is the advantageous part of this proposal. For hinge method, conception of improved buckling coefficient, which is similarly valid for axially as well as eccentrically load column. The fire resistance column has an innovative feature, which is expressed in its elastic buckling capacity and plastic squashing capacity at higher temperature. The Rankine prediction and experimental result can be satisfactory for plain concrete filled steel (PCFS) and reinforced concrete filled steel (RCFS) in both. Han and Lin [3] reviewed that fire resistance steel hollow structural section (HSS) columns which filled by concrete after contact to fire at higher temperature, it shows higher level of ductility as well as energy dissipation. In general, energy dissipation capacity is much higher for circular sectional column compare than square sectional column. This work delivered that a basis theoretical study on earthquake behaviour of fire resistance steel hollow structural section (HSS) columns which filled by concrete after contact to fire at higher temperature.

## 2.5 Advanced Research

A basic and straight analytical formula has provided to define to compressive resistance of column made by steel, subjected to blast loading condition established on

rigid plastic theory and Rankine principle, in based elastic buckling theory consider in stability. Studies of [19] focussed on understanding the genuine fire behaviour of structure and on emerging innovative system with characteristic fire resistant. Now, practicable solutions are developing, which outer fire safety may be totally pull out, in positive states, without negotiating fire protection of steel structure. Use of conventional composite slab or beam flooring structure in combination with hollow steel column which filled by concrete to eliminate blast protection for steel some research institute and organizations like National Research Council of Canada (N.R.C.C) and United Kingdom's Building Research (U.K.B.R) suggested that it might be possible through proper design in this system.

Liew and Chen [8] used an advanced analyzes plastic hinge method to measure the efficiency of steel exposed to blast. They presented multi-zone and radiation model which can be applicable in case of simulation of natural fire. Finite element method (FEM) can be implemented to evaluate transient heat transfer. Gradual plastification of steel cross section can be achieved by using transient heat bounding surface theory. Performance-based evaluation is accomplished on an arched frame and a multistore car park structure which get contact to localized vehicle burning. Special effects of blast source location, beam span, and blast blowout on structural behaviours are explored.

## 3 Discussion

It is essential to study blast resistance of multistoreyed steel structure and industrial building as there is softening, yielding of material at high temperature. Use of insulating material increase the cost as well as dead weight of structure. Therefore, many researchers advocate against use of insulating materials. Some researcher supports the use of thin insulting material layer. Use of fire resisting steel as beam, column without or with thin insulating layer is supported by many researcher. Column filled by plain concrete, reinforced concrete, or fibre-reinforced concrete are found be advantages be case of buckling at deformation resistances are more than conventional hollow column section.

Analytical model validated by fire test is advocated by most of the authors in order to discover blast resistance of the steel building without any costly test. Full-scale test provides results which are found to be different from small scale tests. Full-scale test results should be used for modification of various material national codes meant for fire resistance. Few full-scale fire tests results are found in literature, as it is costly, difficult but it provides realistic results. More study on full-scale test result and corresponding models are required to be developed.

## 4 Conclusion

Based on the above literature study, it can be concluded that the analytical model validated with full-scale fire tests provide realistic result to be used in fire resistance calculation of steel structure. The use of fire resistant steel is found to have better resistance than conventional steel. Considering the inclusion of hollow steel column filled with reinforced concrete, plain concrete or fibre-reinforced concrete shows better performance against buckling and deformation. Due to the increase in dead weight, the use of insulation based materials is discouraged. In case of floors, walls and ceilings made of light gauge steel shapes, the use of reinforced gypsum board is suitable as cladding materials.

## References

1. Chen H, Liew JY (2005) Explosion and fire analysis of steel frames using mixed element approach. J Eng Mech 131(6):606–616
2. Han LH, Huo JS (2003) Concrete-filled hollow structural steel columns after exposure to ISO-834 fire standard. J Struct Eng 129(1):68–78
3. Han LH, Lin XK (2004) Tests on cyclic behavior of concrete-filled hollow structural steel columns after exposure to the ISO-834 standard fire. J Struct Eng 130(11):1807–1819
4. Huang ZF, Tan KH (2003) Analytical fire resistance of axially restrained steel columns. J Struct Eng 129(11):1531–1537
5. Kodur VKR, Lie TT (1996) Fire resistance of circular steel columns filled with fiber-reinforced concrete. J Struct Eng 122(7):776–782
6. Lennon T, Moore DB, Bailey C (1999) The behaviour of full-scale steel-framed buildings subjected to compartment fires. J Struct Eng 77(8):15–21
7. Lie TT (1994) Fire resistance of circular steel columns filled with bar-reinforced concrete. J Struct Eng 120(5):1489–1509
8. Liew JR, Chen H (2004) Explosion and fire analysis of steel frames using fiber element approach. J Struct Eng 130(7):991–1000
9. Liew JR, Tang LK, Choo YS (2002) Advanced analysis for performance-based design of steel structures exposed to fires. J Struct Eng 128(12):1584–1593
10. Ma KY, Richard Liew JY (2004) Nonlinear plastic hinge analysis of three-dimensional steel frames in fire. J Struct Eng 130(7):981–990
11. Sakumoto Y, Hirakawa T, Masuda H, Nakamura K (2003) Fire resistance of walls and floors using light-gauge steel shapes. J Struct Eng 129(11):1522–1530
12. Sakumoto Y, Keira K, Furumura F, Ave T (1993) Tests of fire-resistant bolts and joints. J Struct Eng 119(11):3131–3150
13. Sakumoto Y, Yamaguchi T, Ohashi M, Saito H (1992) High-temperature properties of fire-resistant steel for buildings. J Struct Eng 118(2):392–407
14. Sakumoto Y, Yamaguchi T, Okada T, Yoshida M, Tasaka S, Saito H (1994) Fire resistance of fire-resistant steel columns. J Struct Eng 120(4):1103–1121
15. Sha W (1998) Fire resistance of floors constructed with fire-resistant steels. J Struct Eng 124(6):664–670
16. Skowroński W (1993) Buckling fire endurance of steel columns. J Struct Eng 119(6):1712–1732

17. Tan KH, Tang CY (2004) Interaction model for unprotected concrete filled steel columns under standard fire conditions. J Struct Eng 130(9):1405–1413
18. Toh WS, Tan KH, Fung TC (2000) Compressive resistance of steel columns in fire: Rankine approach. J Struct Eng 126(3):398–405
19. Wang YC, Kodur VKR (2000) Research toward use of unprotected steel structures. J Struct Eng 126(12):1442–1450

# Seismic Performance of Semi-Rigid Steel Frames Considering Soil-Structure Interaction


**Vishwajit Anand and S. R. Satish Kumar**

**Abstract** The process of soil response affecting structural deformations and vice-versa is termed as soil-structure interaction (SSI). Over last few decades, traditional belief of SSI being ever-beneficial to seismic response of structures has been challenged. There have been evidences of SSI induced damages in 1985 Mexico City, 1989 Loma Prieta, 1995 Kobe, and 2001 Bhuj earthquakes. Seismic structural response is a function of structural and foundation characteristics, underlying soil medium properties, and ground motion characteristics. This paper attempts to assess effects of SSI on performance of steel frames with semi-rigid connections during a seismic event. The rationale behind choosing this structural configuration is its gaining popularity and large potential drifts. Though semi-rigid frames offer advantages like adequate stiffness, strength, and economy as compared to rigid frames, large top displacements and inter-storey drifts can be of concern. Performance is assessed in terms of parameters such as natural period and inter-storey drifts. Substructure approach with dynamic impedance using simple physical models has been employed to consider SSI.

**Keywords** Semi-rigid frames · Soil-structure interaction · Substructure method · Seismic performance · Steel structures

V. Anand (✉)
Indian Institute of Technology (Banaras Hindu University) Varanasi, Varanasi, India
e-mail: anand.civ@iitbhu.ac.in

S. R. S. Kumar
Indian Institute of Technology Madras, Chennai, India
e-mail: kim@iitm.ac.in



M. Madhavan et al. (eds.), *Proceedings of the Indian Structural Steel Conference 2020 (Vol. 1)*, Lecture Notes in Civil Engineering 318,
https://doi.org/10.1007/978-981-19-9390-9_56

## 1 Introduction

It is intuitive to assess that soil responses and structural deformations during a seismic event are not independent of each other, and this interdependence is termed as seismic soil-structure interaction (SSI). First of all, the ground motion gets modified as seismic waves travel from source to site. Secondly, rigidity of foundation systems leads to reflection of seismic waves at structure-soil interface. This leads to a foundation input motion which is different from ground motion if there was no structure at all. Finally, additional soil deformations resulting from inertial loads from the structure cause further modification in ground motion. The first one, called wave amplification effect, is present even in absence of structure and therefore not a part of SSI. Other two effects, known as kinematic and inertial interaction, respectively, comprise two components of SSI. Roesset [15] and Kausel [12] reviewed early stage developments in field of SSI. Discussion of contemporary research and existing seismic SSI guidelines can be found in [1].

SSI has traditionally been considered to be beneficial to seismic response of structures. Since SSI makes a structure more flexible, it elongates its time period and enhances the system damping leading to reduced lateral forces. However, damages to pile supported bridge structures in 1989 Loma Prieta earthquake cited by [17], collapse of Hanshin Expressway Route 3 (Fukae section) in 1995 Kobe earthquake investigated by [13], and damages to buildings on piled rafts in 2015 Nepal earthquake depicted by [4] elucidate possible detrimental nature of SSI. Further studies by [11] and [3] infer significance of including SSI in inelastic structural design. In fact, it has been established by [16] that SSI effects diminish with increasing inelasticity in the system. As a result, the beneficial effects on structural response reduce for inelastic structures, and the design may turn unsafe at a point.

The present paper assesses SSI effects on seismic performance of steel frames with semi-rigid connections. Semi-rigid connections in steel frames have been recently gaining popularity as they offer adequate advantages like strength, stiffness, and economy to the system when compared to simple or moment connections. However, [14] report that design of such frames is mostly governed by serviceability limit states such as inter-storey drifts owing to enhanced flexibility of the frame. Inelastic deformations would further increase if the structure is founded on soft soils. This suggests that SSI may influence design of steel frames with semi-rigid connections. This study compares seismic performance of these frames against that of frames with rigid connections in terms of parameters such as natural period and inter-storey drift.

## 2 Methodology

### 2.1 Design of Steel Frames with Semi-rigid Connections

It is worth mentioning that practically every connection is semi-rigid. However, based on their stiffness, strength, and ductility capacities, Bjorhovde et al. [8] classified connections into rigid, semi-rigid, and pinned. With reference to stiffness, semi-rigidity of a connection is determined by ratio of connection stiffness ($K_{conn}$) to flexural stiffness of beam ($(EI/L)_{beam}$) which is termed as joint factor ($J$). A $J$ value of zero denotes the connection to be very flexible and beam to be thereby simply supported. On the other hand, for a beam with fixed supports at ends, $J$ tends to infinity. Though moment rotation curves for these semi-rigid connections are usually nonlinear, secant stiffness corresponding to a defined strain value is considered.

For a uniformly loaded ($w$ per unit length) beam of length $L$ with semi-rigid connections of joint factor $J$ at both ends, shown in Fig. 1, support moment ($M_{support}$) and mid-span moment ($M_{mid\text{-}span}$) are given by Eqs. (1) and (2).

$$M_{support} = \left(\frac{wL^2}{12}\right)\left(\frac{J}{J+2}\right) \tag{1}$$

$$M_{mid-span} = \left(\frac{wL^2}{8}\right) - \left(\frac{wL^2}{12}\right)\left(\frac{J}{J+2}\right) \tag{2}$$

The maximum deflection for this beam ($\delta_{SR}$) is observed at mid-span which is computed using Eq. (3) by superposing deflections due to bending moment diagrams for the load and support moments. Equation (4) relates maximum deflection in beam with semi-rigid connections ($\delta_{SR}$) to that in a beam with rigid joints at both ends ($\delta_{FF}$).

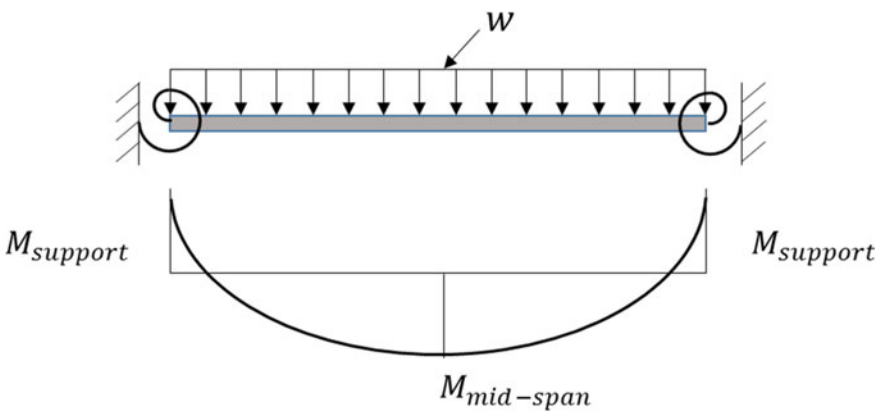


**Fig. 1** Bending moment diagram of a uniformly loaded beam with semi-rigid connections

$$\delta_{SR} = \left(\frac{5wL^4}{384EI} - \frac{ML^2}{8EI}\right) \tag{3}$$

$$\frac{\delta_{SR}}{\delta_{FF}} = \left(\frac{J+10}{J+2}\right) \tag{4}$$

The design bending strength of beam is the greater of support moment and mid-span moment. Further, it needs to satisfy limit state of serviceability. Since the steel frames in the present study are part of residential or commercial construction, IS 800 (2007) suggests maximum deflection to be no more than 1/300 times of the beam span. Using both conditions, a maximum value of span-to-depth ratio (*L/D*) can be obtained in Eq. (5). Alternatively, with a specified beam design, rigidity of connections can be arrived at. Columns are then designed for their corresponding axial loads and bending moments. All the code prescribed load combinations with appropriate load factors are attempted, and maximum of all load effects is considered. Further capacity design approach warrants columns to be no weaker than beams.

$$\frac{L}{D} \leq 21.33\left(\frac{J+6}{J+10}\right) \tag{5}$$

For the steel frame under seismic loads, roof and storey drift limits needs to be satisfied. IS 1893–1 (2016) suggests storey drift to be limited to 0.4% of storey height. For a semi-rigid frame, storey drift is the sum of drift contributions from beams, columns, and connections. For economical solution, flexibility of beams and connections should cause 80% of the total drift. Rajendran and Kumar [14] observed semi-rigid frames to be an economical design solution compared to rigid frames for mid-rise structures located in moderate seismic zones. As a consequence, the present work involves design of a six-storey single bay semi-rigid frame (SRF) and its rigid counterpart (RF), located in Zone III of IS 1893–1 (2016). Dead and live loads acting on structure are assumed as per IS 875 (1987). Zone factor of 0.16, importance factor of 1, and response reduction factor of 4 have been considered in the design for seismic forces. The serviceability limit on beams in semi-rigid frames as suggested by Eq. 5 is enforced with a joint factor of 4. Storey height, bay width, and frame spacing are, respectively, taken as 4 m, 6 m, and 5 m. The sections arrived for various beams and columns for both frames are enlisted in Table 1.

Isolated rectangular footings in either case have been designed assuming a safe bearing capacity of 150 kN/m$^2$. Plan dimensions are 3 m X 3.9 m and 3 m X 3.8 m for rigid and semi-rigid frames, respectively. Each footing is 0.5 m thick embedded at a depth of 1 m.

**Table 1** Sections used in 6-storey single bay rigid and semi-rigid frames

| Storey index | Rigid frame (RF) | | Semi-rigid frame (SRF) | |
|---|---|---|---|---|
| | Beam section | Column section | Beam section | Column section |
| 6 | ISMB 350 @ 52.4 kg/m | ISMB 400 @ 61.5 kg/m | ISMB 400 @ 61.5 kg/m | ISMB 400 @ 61.5 kg/m |
| 5 | ISMB 400 @ 61.5 kg/m | ISMB 400 @ 61.5 kg/m | ISMB 400 @ 61.5 kg/m | ISMB 400 @ 61.5 kg/m |
| 4 | ISMB 400 @ 61.5 kg/m | ISMB 450 @ 72.4 kg/m | ISMB 400 @ 61.5 kg/m | ISMB 400 @ 61.5 kg/m |
| 3 | ISMB 400 @ 61.5 kg/m | ISMB 450 @ 72.4 kg/m | ISMB 400 @ 61.5 kg/m | ISMB 400 @ 61.5 kg/m |
| 2 | ISMB 400 @ 61.5 kg/m | ISMB 500 @ 86.9 kg/m | ISMB 400 @ 61.5 kg/m | ISMB 450 @ 72.4 kg/m |
| 1 | ISMB 400 @ 61.5 kg/m | ISMB 500 @ 86.9 kg/m | ISMB 400 @ 61.5 kg/m | ISMB 450 @ 72.4 kg/m |
| Total Mass | 2159.4 kg | 1766.4 kg | 2214 kg | 1563.2 kg |
| | 3925.8 kg | | 3777.2 kg | |

## 2.2 *Modelling of Structure-Soil System*

Various approaches to solve an SSI problem can be categorised as discrete vs continuum, linear vs nonlinear, frequency domain vs time domain, and direct vs substructure approach. In direct method, the complete structure-soil system is solved with free-field motion as input. However, in substructure approach, the system is subdivided into various substructures which are solved independently and superimposed at the end. Substructure approach is employed in the present study as it involves replacing soil-foundation system by impedance functions and thereby lesser computations. Structure-soil system is schematically represented in Fig. 2. Impedance functions are complex-valued, frequency dependent stiffness, and damping characteristics of soil-foundation system. These functions depend on foundation characteristics and properties of underlying soil medium. Though impedance functions prescribed by [9] are frequency independent, they have been used in this study owing to their simplicity. Since in-plane translation of frames is studied, impedance functions corresponding to translation along in-plane direction and rotation about out-of-plane direction are considered. These impedance functions are reported in Eqs. 6 and 7, and parameters involved are shown in Fig. 3. These functions are computed at frequency equal to natural frequency of the structure for in-plane translation. All frames are assumed to be founded on embedded footings, and thereby kinematic interaction (predominant in pile foundations) has been ignored.

$$k_j = K_j \alpha_j \eta_j \tag{6a}$$

$$K_j = GB^m f\left(\frac{B}{L}, \nu\right) \tag{6b}$$

$$\alpha_j = f\left(\frac{B}{L}, \left(a_0 = \frac{\omega B}{v_s}\right)\right) \tag{6c}$$

$$\eta_j = f\left(\frac{B}{L}, \frac{D}{B}, \frac{d_w}{B}, \frac{A_w}{BL}\right) \tag{6d}$$

$$\beta_0 = \left\{\frac{1}{\left(\frac{\tilde{T}}{T}\right)^n}\right\}\beta_i + \left\{1 - \frac{1}{\left(\frac{\tilde{T}}{T}\right)^n}\right\}\beta_s + \left\{\frac{1}{\left(\frac{\tilde{T}}{T_x}\right)^{n_x}}\right\}\beta_x + \left\{\frac{1}{\left(\frac{\tilde{T}}{T_{yy}}\right)^{n_{yy}}}\right\}\beta_{yy} \tag{7}$$

The stiffness characteristic along degree of freedom $j$, represented by dynamic stiffness ($k_j$), is expressed by Eq. (6) as a product of static stiffness for surface footing ($K_j$), embedment correction factors ($\eta_j$), and dynamic stiffness modifiers ($\alpha_j$). The parameters involved in Eq. (1) are depicted in Fig. 3. The radiation damping components ($\beta_x, \beta_{yy}$) are obtained directly from [9] and then added to structural ($\beta_i$)

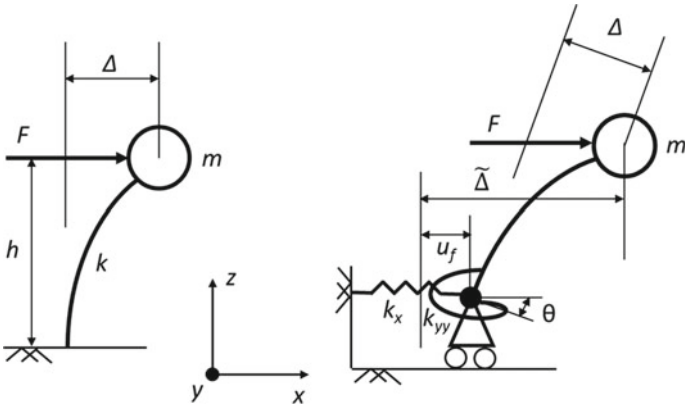


**Fig. 2** Schematic representation of structure-soil system

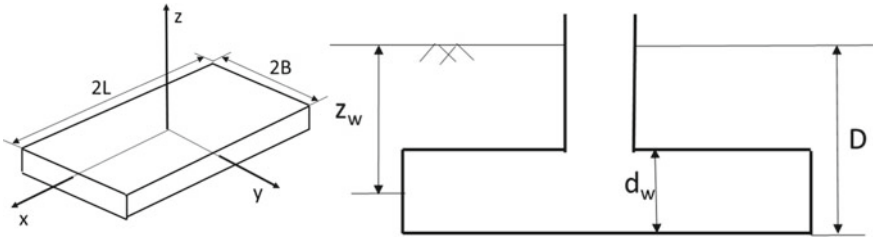


**Fig. 3** Footing dimensions used in Eq. (6)

and soil material ($\beta_s$) damping components using Eq. (7) to obtain total damping in the system. $T_x = 2\pi\sqrt{\frac{m}{k_x}}$ and $T_{yy} = 2\pi\sqrt{\frac{m}{k_{yy}}}$ are fictitious time periods. Coefficients $n$, $\beta_x$, and $\beta_{yy}$ depend on type of damping and can be obtained from [10].

In order to assess effects of SSI on rigid and semi-rigid frames designed in Sect. 2.1, two values of shear wave velocity ($v_s$), viz. 150 m/s and 100 m/s, corresponding to soft soil deposits are considered in the study. Rigid and semi-rigid frames founded on soil with shear wave velocity of 100 m/s are referred as RF100 and SRF100, respectively. Similarly, RF150 and SRF150 correspond to frames with underlying soil deposit having shear wave velocity of 150 m/s. Rigid and semi-rigid frames with no consideration to soil flexibility are, respectively, referred to as RF and SRF.

A total of six systems (three corresponding to rigid and semi-rigid frames each) are modelled on SAP 2000. Semi-rigid connections are modelled as panel zones. Impedance functions are defined as frequency dependent links.

### *2.3 Analysis of Structure-Soil System*

Modal analysis is initially performed in order to obtain natural frequency corresponding to in-plane translational mode of the frames. An analysis considering different combinations of dead, live, and lateral loads (as per IS 875–1, IS 875–2 and IS 1893–1, respectively) is also performed to check strength and serviceability limit states. Time history analyses are then performed to evaluate seismic performance of various systems. In this context, a set of 10 synthetic accelerograms, compatible to soft soil response spectra presented in IS 1893–1 (2016), has been generated using SeismoMatch 2016. Results of various analyses are presented in next section.

## 3 Results and Discussions

### *3.1 Design of Rigid and Semi-Rigid Frames*

Sections used in beams and columns for rigid and semi-rigid frames are enlisted in Table 1. It is evident that there is a 4% reduction in total weight of beams and columns in semi-rigid frames. This leads to a reduction in design forces and ultimately a marginal reduction in footing size. Further, semi-rigid connections are easier and economical compared to moment connections. This implies that semi-rigid frames are an economical solution over rigid frames for mid-rise structures located in regions with moderate seismic hazard.

**Table 2** Natural period for in-plane translational mode of frames

| Frame type | Rigid frames (RF) | | | Semi-rigid frames (SRF) | | |
|---|---|---|---|---|---|---|
| | RF | RF150 | RF100 | SRF | SRF150 | SRF100 |
| $(h/v_sT)$ | $\approx 0$ | 0.35 | 0.52 | $\approx 0$ | 0.33 | 0.49 |
| Natural period (s) | 0.324 | 0.327 | 0.332 | 0.340 | 0.344 | 0.348 |

## *3.2 Modal Analyses Results*

Natural periods for in-plane translational mode of rigid and semi-rigid frames founded on varying soil media are obtained using modal analysis and are reported in Table 2. It can be observed that natural period of a semi-rigid frame exceeds that of a rigid frame founded on similar soil by roughly 5%. Inclusion of SSI leads to an elongation in natural period of both rigid and semi-rigid frames. A parameter ($h/v_sT$), with $h$, $v_{s,}$ and $T$, respectively, denoting effective height of structure, soil shear wave velocity, and natural period of structure, represents structure-to-soil stiffness ratio. As evident from Table 2, this parameter is a good metric of extent of SSI effect on natural period and thereby dynamic response. Frames with rigid bases have structure-to-soil stiffness ratio close to zero. Frames founded on softer soils exhibit larger values of this parameter and a greater elongation in natural period. Effective height of structure is assumed to be 70% of total height in accordance with ASCE 7–10 (2010).

## *3.3 Design Lateral Load Effects*

Frames are designed for strength limit state and therefore checked for adequacy against serviceability limit states. Inter-storey drifts obtained by analysing frames for unfactored design lateral loads are reported in Table 3. IS 1893–1 (2016) suggests inter-storey drift to be restricted to 0.4% of the storey height which corresponds to 16 mm. A minor exceedance of inter-storey drift limit in case of semi-rigid frames was, however, tolerated. It is observed that inclusion of SSI results into increased drifts which may turn unacceptable in case of semi-rigid frames. This implies that guidelines to reduce design forces, on account of elongated natural period and enhanced damping, cannot be applied indiscriminately to structures with semi-rigid frames.

**Table 3** Inter-storey drifts (in mm) for various frames under design lateral forces

| Storey index | Rigid frames (RF) | | | Semi-rigid frames (SRF) | | |
|---|---|---|---|---|---|---|
| | RF | RF150 | RF100 | SRF | SRF150 | SRF100 |
| 6 | 9.1 | 9.5 | 10.0 | 8.7 | 9.0 | 9.5 |
| 5 | 12.5 | 12.9 | 13.3 | 14.0 | 14.4 | 14.9 |
| 4 | 14.2 | 14.5 | 15 | 15.7 | 16.1 | 16.6 |
| 3 | 15.1 | 15.5 | 15.9 | 17.1 | 17.4 | 17.8 |
| 2 | 13.0 | 13.3 | 13.6 | 14.7 | 15.0 | 15.4 |
| 1 | 7.0 | 7.1 | 7.3 | 8.4 | 8.6 | 8.8 |

## *3.4 Dynamic Time History Analyses Results*

All the six frames are subjected to a set of 10 design basis accelerograms which are compatible to response spectrum specified in IS 1893–1 (2016) for soft soil sites. Table 4 presents mean inter-storey drifts for various frames. It is observed that SSI leads to increased inter-storey drifts throughout the structure. The increase in drift is almost uniform over the height of the structure.

Another observation which is evident from either of Tables 3 and 4 is that semi-rigid frames exhibit higher inter-storey drifts in lower storeys compared to moment frames. This can exceed the serviceability drift limit in lower storeys. It can be implied that SSI can be detrimental to open ground floor structures with semi-rigid frames during a larger seismic event.

**Table 4** Mean inter-storey drifts (in mm) for various frames subjected to time history analyses

| Storey index | Rigid frames (RF) | | | Semi-rigid frames (SRF) | | |
|---|---|---|---|---|---|---|
| | RF | RF150 | RF100 | SRF | SRF150 | SRF100 |
| 6 | 2.9 | 3.0 | 3.2 | 2.9 | 3.0 | 3.2 |
| 5 | 4.6 | 4.8 | 5.0 | 5.1 | 5.3 | 5.3 |
| 4 | 6.0 | 6.1 | 6.2 | 6.4 | 6.5 | 6.6 |
| 3 | 7.0 | 7.1 | 7.3 | 7.6 | 7.7 | 7.7 |
| 2 | 6.4 | 6.4 | 6.6 | 7.0 | 7.0 | 7.0 |
| 1 | 3.5 | 3.6 | 3.6 | 4.1 | 4.1 | 4.1 |

## 4 Concluding Remarks

The present study attempts to assess SSI effects on seismic response of steel frames with semi-rigid connections at beam-column joints. Based on the previous sections, the following concluding remarks can be arrived at

- Semi-rigid steel frames are an economical solution for mid-rise structures in moderate seismic regions over the conventional moment steel frames. A material cost saving of around 4% is observed in the present study.
- Soil-structure interaction (SSI) enhances natural period of structures irrespective of rigidity of frames. Structure-to-soil stiffness ratio is a good metric for extent of SSI.
- SSI results into an increase in inter-storey drift. These drifts, which are already high for semi-rigid frames, may exceed serviceability limit rendering the structural design to be inadmissible.
- Guidelines to reduce design forces, on account of elongated natural period and enhanced damping, should not be applied indiscriminately to structures with semi-rigid frames.
- Lower storeys exhibit a larger increase in inter-storey drift which implies possible detrimental nature of SSI during an earthquake in case of structures with open ground storeys.

## References

1. Anand V, Kumar S (2018) Seismic soil-structure interaction: a state-of-the-art review. Structures 16:317–326
2. ASCE (2010) Minimum design loads for buildings and other structures: ASCE/SEI 7–10. American Society of Civil Engineers, Virginia
3. Aydemir ME (2013) Soil structure interaction effects on structural parameters for stiffness degrading systems built on soft soil sites. Struct Eng Mech 45(5):655–676
4. Badry P, Satyam N (2017) Seismic soil structure interaction analysis for asymmetrical buildings supported on piled raft for the 2015 Nepal earthquake. J Asian Earth Sci 133:102–113
5. BIS (1987). Code of practice for design loads (Other than earthquake) for buildings and structures: IS 875. Bureau of Indian Standards, New Delhi
6. BIS (2007) General construction in steel- code of practice: IS 800. Bureau of Indian Standards, New Delhi
7. BIS (2016) Criteria for earthquake resistant design of structures- part 1: general provisions and buildings: IS 1893–1. Bureau of Indian Standards, New Delhi
8. Bjorhovde R, Coison A, Brozzetti J (1990) Classification system for beam-to-column connections. Eng J AISC 20(1):1–13
9. Gazetas G (1991) Formulas and charts for impedances of surface and embedded foundations. J Geotech Eng 117(9):1363–1381
10. Givens MJ (2013) Dynamic soil-structure interaction of instrumented buildings and test structures: Doctoral Dissertation. University of California, Los Angeles
11. Jarernprasert S, Bazan-Zurita E, Bielak J (2013) Seismic soil-structure interaction response of inelastic structures. Soil Dyn Earthq Eng 47:132–143

12. Kausel E (2010) Early history of soil-structure interaction. Soil Dyn Earthq Eng 30(9):822–832
13. Mylonakis G, Gazetas G (2000) Seismic soil-structure interaction: beneficial or detrimental? J Earthquake Eng 4:377–401
14. Rajendran S, Kumar S (2015) Performance based seismic design of semi-rigid steel concrete composite multi-storey frames. In: Matsagar V (ed) Advances in structural engineering. Springer, New Delhi, pp 989–1000
15. Roesset JM (2013) Soil structure interaction: the early stages. Appl Sci Eng 16(1):1–8
16. Veletsos AS, Verbic B (1973) Dynamics of elastic and yielding structure-foundation systems. In: Proceedings of the fifth world conference earthquake engineering, pp 2610–2613). Rome.
17. Yashinsky M (1998) The Loma Prieta, California, earthquake of October 17, 1989-highway systems: professional paper 1552-B. Geological Survey, Denver: U.S

# Seismic Performance of Self-Centering BRB Frames: A Study Under Near-Field Ground Motions


**Ahmad Fayeq Ghowsi, Dipti Ranjan Sahoo, and Rajesh Kumar**

**Abstract** Buckling-restrained braced frames (BRBFs) are design for the seismic resisting purpose on the active seismic zones. The symmetrical hysteresis, high ductility, and large capacity to dissipate energy made this system superior to conventional concentrically-braced systems. Most of the past studies concluded that BRBFs might suffer from the excessive post-earthquake residual drift as compared to the other systems under the near-field earthquakes. The excessive residual drift in BRBFs is the main disadvantage, which is led us to the development of the self-centering buckling-restrained braced frames (SC-BRBFs). The better energy dissipation capacity, the absence of compressive buckling behavior of braces, high ductility, and reducing residual drift response make the SC-BRBs a preferred alternative over the conventional system like BRBFs. The study mainly focuses on the evaluation of the seismic response of SC-BRBFs under the near-field earthquakes. Three low, medium, and rise study frames, namely 3-story, 9-story, and 20-story SAC benchmark buildings (Ohtori in J Eng Mech 130:366–385, 2004), are considered for this study. The frames are designed based on AISC 341–2010 provisions. The SC-BRB is considered as the combine of buckling-restrained brace (BRB) and shape memory alloy (SMA) rods. These frames are modeled and analyzed using computer software OpenSees. A set of forty near-field ground motions are selected in the nonlinear dynamic (time history) analysis. The main parameters investigated are inter-story drift response and residual drift response. The analysis results for SC-BRBFs showed better performance as compared to conventional BRBs with the negligible residual drift response.

**Keywords** Buckling-restrained braces · Drift response · Nonlinear modeling seismic analysis · Self-centering braces

A. F. Ghowsi (✉) · D. R. Sahoo · R. Kumar
Department of Civil Engineering, Indian Institute of Technology, New Delhi 110016, India
e-mail: faieq.ghowsi@gmail.com

D. R. Sahoo
e-mail: drsahoo@civil.iitd.ac.in



M. Madhavan et al. (eds.), *Proceedings of the Indian Structural Steel Conference 2020 (Vol. 1)*, Lecture Notes in Civil Engineering 318,
https://doi.org/10.1007/978-981-19-9390-9_57

## 1 Introduction

Buckling-restrained braces (BRBs) are widely used in the US for the ductile-design systems. Over the last two decades, approved high ductility, symmetric hysteretic behavior, and high energy response on this system. Also, past studies [5] noted that higher residual drift in this system is providing a lack of re-centering capability on the BRB frame. The higher residual displacement in the post-earthquake of the brace frame and it may not be cost-effective for retrofitting or repairing [2]. In order to minimize this disadvantages, some modification is required to develop a self-centering BRB (SC-BRB) systems which can have the re-centering capability in adding to the BRBs advantages to give the self-centering ability to the BRBFs system [3, 7].

The present study is mainly focused on the evaluation of the seismic performance of a set of second-generation SAC buildings which are 3-, 9-, and 20-story, designed for steel frames. The mentioned buildings are re-designed for BRBs and SC-BRBs for the lateral resisting system. The shape memory alloy (SMA) rods used along with the BRB for self-centering capability in SC-BRBs systems. The designed procedure is fallowed based on current American building codes for these buildings. The numerical model has been developed for these study frames using OpenSees Ver.2.5 [6] and nonlinear time history analysis under a set of near-fault ground motions. The main investigated parameters in this study are inter-story and residual story drift response and the comparative study between BRBFs and SC-BRBFs on study buildings.

## 2 Self-Centering Buckling-Restrained Braces (SC-BRBs)

In this study, the SMA rods are used for self-centering ability, BRB used for energy dissipations, and the combination of SMA and BRB made the SC-BRB. The result of this combination of SMA with BRB shown a better output of self-centering capability, higher energy dissipation, symmetrical hysteresis, and high ductility, and that is called SC-BRB. The mechanism which they placed as such that the SMA rod is going under tensile stress, either the assembly is under elongation or shortening. The length of the SMA rod is limited as per requirement [4], and the rigid rod is used as a rigid link in the continuity of SMA rod and connected through coupling connectors. The outer and inner tubes are alternatively welded in one end of the elastic zone of BRB, and cantilever in the other end is used to bear the pretension of SAM rods in the unloading position. No demand should be over the BRB core. The bearing plates are placed at each of the ends. These plates are in contact with the tubes either connected to the BRB elastic end nor tubes. The plates are in contact with tubes and connecting through the pretension rods. While the brace is going under shortening, the gap is appearing between the tube and bearing plate on one side, and while going under elongation, the gap will be appearing on the opposite side. The schematic model of different components is shown in Fig. 1.

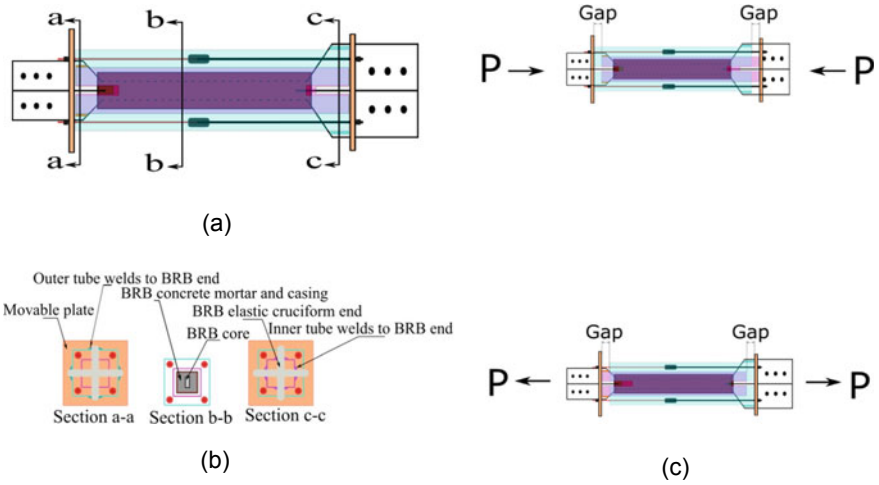


**Fig. 1** **a** SC-BRB assembly. **b** Different sections of SC-BRB. **c** Shortening and elongations

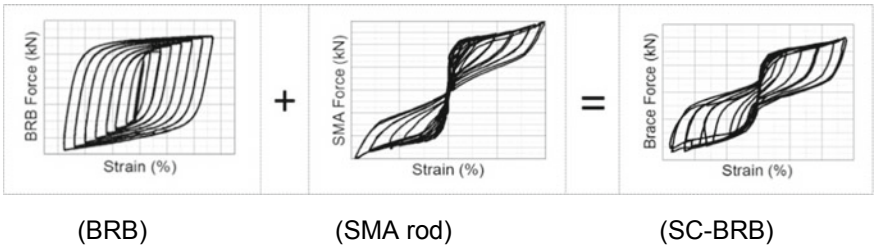


**Fig. 2** Hysteretic response of BRB, SMA rod, and SC-BRB

The basic concept of SC-BRB under cyclic loading is shown in Fig. 2. The combination of force–deformation of BRB and SMA rod has resulted in the SC-BRB. The symmetrical response of BRB and the symmetrical response of the SMA rod with flag-shape is resulting in the hysteresis response of SC-BRB with near to flag-shape which is indicated the self-centering capability.

## 3 Prototype Buildings

In this study, 3-, 9-, and 20-story benchmark buildings are considered from the second generation of SAC projects. These buildings are assumed to exist in Los Angeles, California, for the low, medium, and high-rise buildings. As shown in Fig. 3, all the bracing bays are located symmetrically on the perimeter frame. The number of braces are placed in longer and shorter direction which are four and two, respectively,

in 3-story building, and in 9- and 20-story buildings, four braces are placed in each direction. The interior frame designed for gravity loading only. The plan and elevation (BF-2) of the braced frame buildings are shown in Fig. 3. The study is considered in all three buildings on the shorter frames. The braces are considered in Inverted-V (chevron) shape configuration on the braced bay frames with pin connections in all three buildings. The connections of beam-to-column are assumed to be as non-moment resisting types. All three buildings are re-designed for BRBs as a lateral load resistance system, which is BRBFs and SC-BRBs, which are SC-BRBFs.

The loading on the buildings is summarized in Table 1. The buildings designed based on (ASCE 7–16) provisions. For 3-story and 9-story building selected, the seismic coefficient method, which is usually for low and medium-rise buildings codes, has been recommended, and for the 20-story building, it is adopted the response spectrum analysis for design purposes. The factor of response reduction ($R$), the factor of overstrength ($\Omega 0$), and the factor of deflection amplification ($Cd$) are assumed to be 8.0, 2.5, and 5.0, respectively. All study frames are designed. It is assumed that these buildings are located in downtown Los Angeles, with site classification of deep stiff soil site class-D. The specifications for design spectral

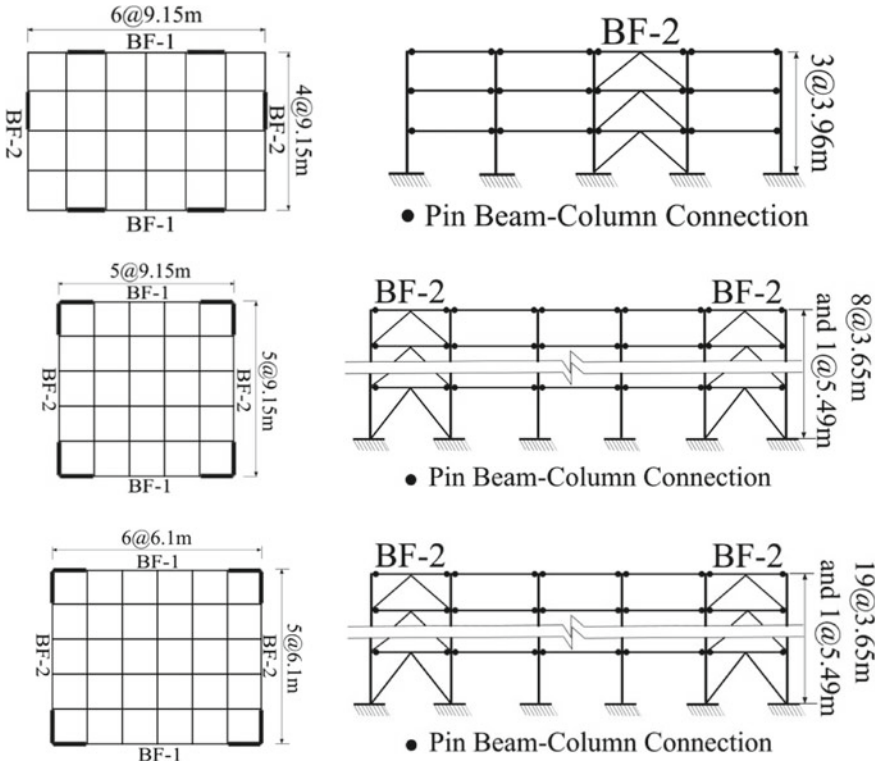


**Fig. 3** Building plan and elevation view of study frames

**Table 1** Weights of the floors buildings

| Level | 3-story | 9-story | 20-story |
|---|---|---|---|
| First-floor-(kN) | 9636 | 10,140 | 5729 |
| Intermediate-floor-(kN) | 9636 | 9625 | 5610 |
| Roof-(kN) | 10,445 | 10,434 | 5937 |
| Total | 29,718 | 87,955 | 112,645 |

acceleration, *SDS,* and *SD1* (ASCE 7–16), are considered to be 1.39 g and 0.77 g, respectively.

In this study, the braces of the study frames are designed such that the lateral load is resisted by braces only without the contribution of effect due to the seismic load on the beams and columns. In the design the BRBs, the axial strength is considered as follows:

$$p_{u-BRB} = \phi p_{yBRB} \tag{1}$$

where (*PyBRB*) is the yield strength of BRB core. After the selection of BRBFs core area, the ultimate strength of BRB has been computed based on the ($\omega$), and the comparison of ultimate tension and compression is considering based on the compression adjustment factor ($\beta$) in which the $\beta$ and $\omega$ are considered as 1.04 and 1.56, respectively. Based on the capacity design approaches, the ultimate strength of BRBs is considered as demand over the beams and columns and adds to the gravity load. The beams and columns are designed accordingly due to the unbalanced strengths of the braces in tensions and compression.

The design of SC-BRBFs has considered the same design approaches for the BRBFs, the axial design strength of SC-BRBs is considered the combined axial strength of BRB and SMA rod as the following formula:

$$p_{u-SC-BRB} = 0.9F_{ysc}A_{core} + 0.9F_{i-SMA}A_{SMA} \tag{2}$$

where *Acore* is the cross-section area of the BRB steel core in the SC-BRB assembly, *Fi-SMA* represents the initial pre-stress in SMA rods, *ASMA* represents the cross sectional area of SMA rods. To achieve the self-centering ability in the SC-BRB assembly, the initial pre-stress in the SMA rod should be more than the BRB axial yield strength. The BRB core cross-section in SC- BRB is calculated based on the yield stress of steel material which can obtain from the coupon test results and calculated as per the following expression:

$$A_{SC} = \frac{P_u}{\phi F_{ysc}(1 + \beta\omega)} \tag{3}$$

Similarly, the area of SMA in SC-BRB can be found as follows:

$$A_{SMA} = \frac{\beta\omega F_{ysc} A_{sc}}{F_{i-SMA}} \tag{4}$$

Based on the experimental study [7] results, 200 MPa has been considered as a pre-stress value of *Fi-SMA* in this study.

The beams and columns are designed to remain elastic until the brace members are fully fractured as per capacity design approaches. Similarly, the capacity-based design approach is used to design the beams and columns so as to remain elastic, as discussed earlier.

## 4 Numerical Modeling

The designed buildings for this study were numerically modeled using computer software *OpenSees* [6]. The numerical model is verified through validating SC-BRB with the experimental result of the past study carried by [7]. The predicted hysteresis response verified with the individual elements of SC-BRB as well as the SC-BRB as an assembly. The developed numerical modeling diagram of SC-BRB is shown in Fig. 4. The individual and appropriate material and sections have been selected for each one of the members. The displacement-based beam-column element has been selected for the BRB core plate, with a fiber sections using a higher moment of inertia in the section to prevent the element from the buckling; the hysteretic type of material is selected from the *OpenSees* library to capture the hardening behavior ($\omega$) in the hysteretic behavior either in tension, nor in the compression in which it is known as compression adjustment factor ($\beta$) and degradation behavior of the material. The SMA element is modeled as a forced-based beam-column type of elements using the fiber section, the material for SMA rod is selected based on [11], in which the material was not working the same SMA. To capture the reversed loading and residual strain on the SMA element, the material model was modified [3]. Since there is no perfect material in the *OpenSees* library, a new material (UMAT) has been developed and implemented into the *OpenSees* as a suspended library (dll) for better prediction of the SMA material.

The numerical model of SC-BRB is validated with the experimental hysteretic response, which has been reported by [7]. The hysteretic responses individually for BRB and SMA rods are numerically predicted correctly with the experimental

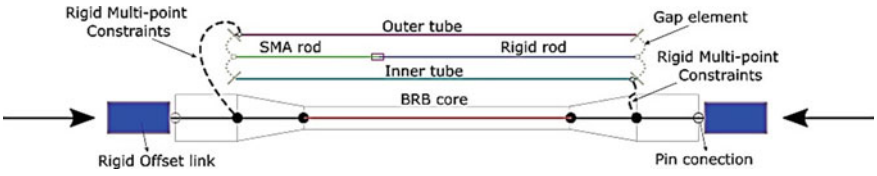


**Fig. 4** Numerical modeling of SC-BRB system

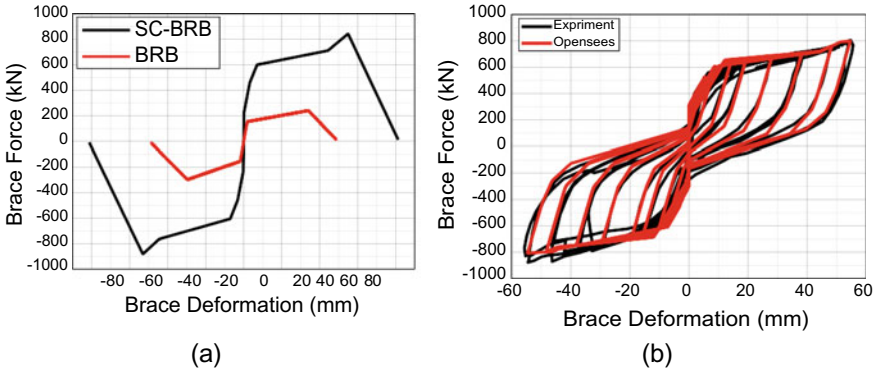


**Fig. 5** **a** Backbone curve of BRB and SC-BRB with degradation. **b** Numerical validation of SC-BRB assembly

result. The inner and outer tubes are modeled elastically beam-column elements and connected to the elastic zone of BRB through the multipoint constraint at one end, as shown in Fig. 4. The gap elements are modeled as zero link element with elastic compression and small but non- zero tension.

The degradation behavior of BRB as well as SC-BRB after reaching to the maximum core strain of BRB is shown in Fig. 5a. The prediction of force–deformation of SC-BRB with the experimental result is shown in Fig. 5b. As the prediction of the model with the test result with very well matching, the same brace modeling technique is adopted for all study frames.

The nonlinear beam-column element is utilized for the modeling of beams and columns in the study frames with fiber section and lumped plastic hinges at both ends and distributed plastic hinges in the middle segments [9]. In this element, a total six integration point has been considered in which two integration points at each hinges portions and two at the middle part of this element, the length of plastic hinges are considered same as the depth of beam-column element. The base columns are considered to be perfectly fixed at the bottom bases. The gravity loads on the interior columns are considered as P-delta columns to be considered the P-delta effect due to gravity loads on the buildings. The gravity columns are modeled as an elastic beam-column with a small amount of moment of inertia and pined at the base of the ground level column. The rigid link element with pined ends used to connect the P-delta columns with the braced frame to adopt the P-delta effect on the braced frame. The panel zones at the points of beams to columns connection are modeled as elastic panel zones. The width and the depth of the panel zone are varying according to the depth of columns and beams, respectively.

## 5 Adopted Ground Motions

For the nonlinear dynamic analysis, a set of forty near-fault (NF) ground motions has been selected in this study. The set of forty selected ground motions are taken which was developed by [10] for SAC steel projects. These ground motions are consists of two different type of records. The first set (NF01-20) which are ten earthquakes parallel to the fault and ten perpendiculars to the fault and all are derived from the historically recorded result, and the other 20 ground motions (NF20-40) are derived from the physical simulations and process based on the fault rupture and seismic wave through the soil strata. Each of the components of the earthquake is rotated 45 degrees orientations from the fault-normal and fault parallel. The magnitude of the ground motions is ranging between 6.75 and 7.5. The source distance from the site is ranging from 0 to 18 km. The approximate mean magnitude of 7.0 at a distance of 5 km is reasonable to represent here. In many regions in California, USA, the magnitude and distance are the factors in which controlling points with a probability of 10% in 50-years. The main difference between far-fault and near-fault ground motion is the pulses and long-period spectral accelerations.

## 6 Analysis Results

The nonlinear time history analyzes have been carried out on the three types of buildings (3- story, 9-story, and 20-story) in which it is consists of low to higher-rise buildings with two deferment type of the braces, namely BRB as well as SC-BRB under the selected set of forty NF ground motions. The key parameters which have been considered in this study are the investigation of inter-story drift as well as residual drift responses. The inter-story drift ratio (ISDR) is representing as the ratio of maximum displacement between two consecutive floors and the height of that particular story during the earthquake. Residual drift ratio (RDR) is similar to the ISDR at the end of the earthquake at that particular story. The acceptance criteria for the buildings in the seismic active region during earthquake can be represented as ISDR and RDR. The re-usability criteria of the buildings can be represented as per RDR in the structural systems as in the post-earthquake conditions.

In this analysis, the average test frame response peak ISDR and RDR are considered for the purpose of comparison. The variation of the inter-story drift responses has been summarized in Table 2 for all the three frame height with two different types of the brace (BRBs and SC- BRBs) under the set of forty NF ground motions. Out of all the study buildings, the 3-story BRB frame exhibited complete collapse under NF23 ground motion, and the result has been excluded from the story drift response to avoid interruption in the mean and standard deviation. In all the results of ISDR and RDR, the average (Ave) and average plus standard deviation (Ave + SD) have been represented for both the cases of BRBFs and SC-BRBFs. As a result, the average ISDR is representing lesser than 2% has been noted in all the cases, in

some cases of the of 3-story BRBFs, the excessive ISDR has been noted in some of the ground motions. The average ISDR for both the cases of BRBF and SC-BRBF is the same under the set NF earthquake. However, in the case of a 9-story building in the case of SC-BRBFs, the ISDR is higher. The average ISDR in the case of BRBF is in the range of 0.8–1.2%, and in the case of SC-BRBF, it is in the range 1.1–1.8% which has been noted. The maximum ISDR in the 2nd, 3rd, and some of the cases in the 4th story level has been noted for both the cases of BRBF as well as SC-BRBF of the 9-story frame. In a similar investigation, the 20-story frame using BRBF and SC-BRBF are near in the same range of ISDR OF 1–1.7%. Out of forty ground motions, in the same of the cases of the 20-story frame, the ISDR has been reached up to 4% story drift response. The 12–16th story level of the 20-story frame has been noted as the critical story level with higher ISDR under NF ground motions.

Table 3 has been summarized the residual drift response of all three designed frames, namely 3-, 9-, and 20-story levels, with two different types of braces of BRB and SC-BRB. The small RDR response has been noted in the cases of SC-BRBFs in which it is close to zero and can be negligible. However, the higher RDR has been noted in all the cases of BRBFs. The average value of RDR in the case of BRBFs and SC-BRBFs are compared. The 3-story frame, in the case of RDR, the maximum

**Table 2** Inter-story drift response

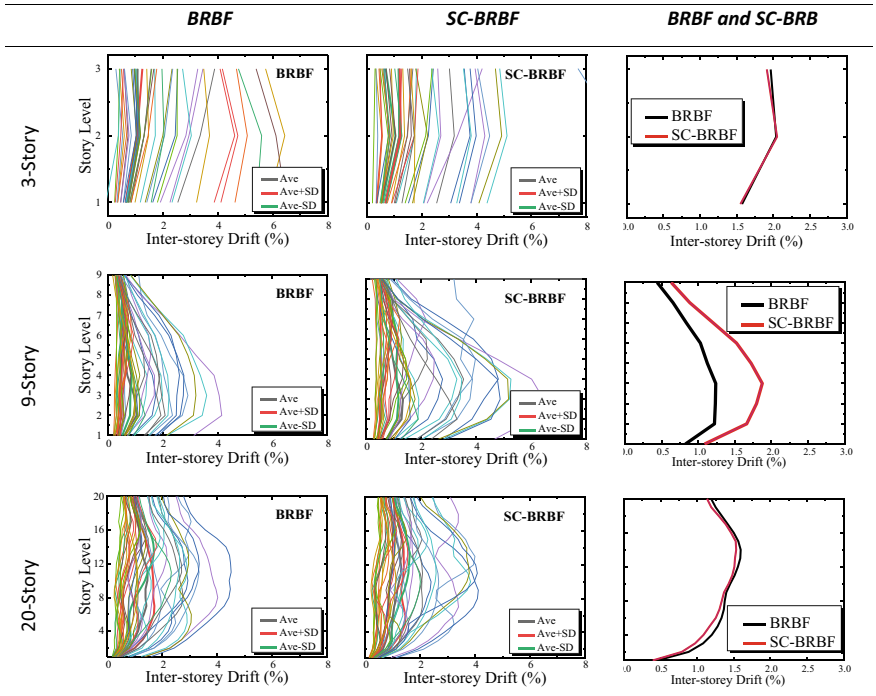

RDR, noted a 1.2% story drift in which the average value is 0.25% of RDR under the set of forty NF ground motions.

Similarly, in the case of the 9-story frame, the maximum RDR is noted 1.7% in which the average RDR is ranging from 0.2 to 0.3%. In the case of RDR, it is also similar to ISDR response, the maximum RDR is presented in the 2- and 3-story level in which can be recognized as the critical stories. In the case of the 20-story frame using SC-BRB type of brace is showed very small in which it is negligible RDR response, and the maximum RDR in the frame using BRB type of brace is 0.9% as the maximum value in which the average of all forty ground motion of RDR is ranging 0.1–0.2%.

In both the cases of BRBF and SC-BRBF, the average of ISDR is the same for 3- and 20- story response. In the case of a 9-story drift response, the average ISDR is higher in the case of SC-BRBF. In oppositely, the RDR response is lesser in the case of SC-BRBF; it is due to self- centering capability. All the frames exhibited a similar response along their heights. In all the cases of the ISDR response frame, the average ISDR of studied frames is lesser than 2%, in which it is lesser than the design value.

**Table 3** Residual drift response

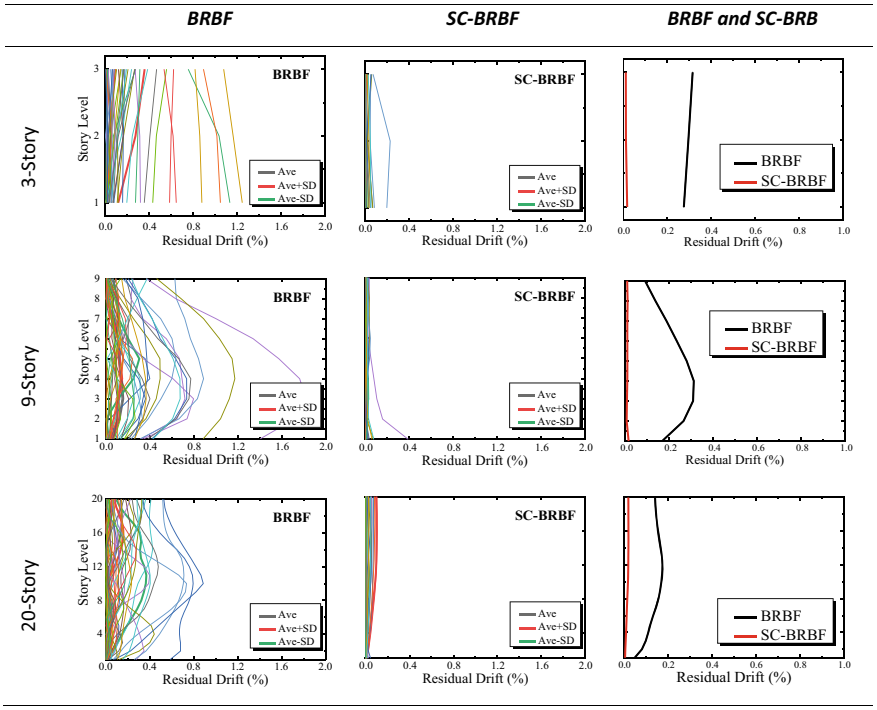

## 7 Conclusions

This study presents a comparative performance analysis of 3-story, 9-story, and 20-story frames in which these buildings are representing the three categories of the low-, medium-, and high-rise buildings under seismic loading conditions. Two different types of braces, which are BRBs and SC-BRBs, have been adopted for each study frame. All study frames are designed for the BRB frame and SC-BRB frame and numerically modeled and analyzed under forty near-fault ground motions using a computer software *OpenSees*.

The results of this research concluded that the buildings using SC-BRBs in all study frames exhibited the negligible residual drift response. In the case of all of the study frames, using BRBFs exhibited a higher residual drift. In the case of SC-BRB, the ISDR response is found to be higher in a 9-story building and similar in 3- and 20-story buildings. Even though the BRB frame has been designed for the particular frame and represents the ISDR and RDR response within the range, but SC-BRB frame is representing the RDR response very close to zero, and it showed promising seismic performance without brace reparation frame re-centering for post-earthquake responses. However, further studies are required to utilize SC-BRBs and BRBs efficiently.

## References

1. ASCE 7–16 Minimum design loads and associated criteria for buildings and other structures. American Society of Civil Engineers, Reston, VA
2. Chao S, Karki NB, Sahoo DR (2013) Seismic behavior of steel buildings with hybrid braced frames. J Struct Eng 139(6):1019–1032
3. Eatherton MR, Fahnestock LA, Miller DJ (2014) Computational study of self- centering buckling-restrained braced frame seismic performance. Earthq Eng Struct Dyn 43(13):1897–1914
4. Ghowsi AF, Faqiri A, Sahoo DR (2019) Numerical study on cyclic response of self- centering steel buckling-restrained braces, pp 589–598
5. Ghowsi AF, Sahoo DR (2015) Fragility assessment of buckling-restrained braced frames under near-field earthquakes. Steel and Compos Struct 19(1):173–190
6. Mazzoni S et al (2006) OpenSees command language manual
7. Miller DJ, Fahnestock LA, Eatherton MR (2012) Development and experimental validation of a nickel–titanium shape memory alloy self-centering buckling-restrained brace. Eng Struct 40:288–298
8. Ohtori Y et al (2004) Benchmark control problems for seismically excited nonlinear buildings. J Eng Mech 130(4):366–385
9. Scott MH, Fenves GL (2006) Plastic hinge integration methods for force-based beam–column elements. J Struct Eng 132(2):244–252
10. Somerville P et al (1997) Development of ground motion time histories for phase 2 of the FEMA/SAC steel project, Report No. SAC/BD-97. SAC Joint Venture, Sacramento, CA
11. Taftali B (2007) Probabilistic seismic demand assessment of steel frames with shape memory alloy connections. No Title, Ph.D. dissertation. Georgia Institute of Technology.

# Comparative Study of Conventional Steel Truss Profiles


**Jaireena, Vaneeta Devi, and Sunil Kumar**

**Abstract** Trusses are commonly used in supporting roof structures, industrial building, auditorium, and warehouses. Trusses may be used efficiently in long distance span with minimum amount of material used. This is due to the internal loads of the members incurring only axial forces (in the direction of the member), i.e. either compression or tension. Sometimes, it creates difficulty to decide which truss configuration, span and rise would produce the most economical truss shape with minimum weight/mass. Thus, in this paper, thirty different conventional trusses of varying spans (10 m, 15 m, 20 m, and 25 m) and rise (1.5 m, 2.0 m, and 3.0 m) combinations have been analysed and designed with circular hollow section using STAAD. Pro V8i SS5. All the trusses have been designed as per IS 800:2007 (LSM). Moreover, all trusses are also studied for their practical weight as well as for optimum weight and compared to find out the economical truss profile.

**Keywords** Span · Rise · IS 800:2007 (LSM) · Circular hollow section · Practical weight · Optimum weight

## 1 Introduction

Truss is an arrangement of long, slender structural elements that are interconnected together at their end and subjected to direct axial forces. This axial action leads to more efficient material use and results in reliable lightweight structures. Sometimes,

Jaireena (✉)
Civil Engineering Department, Shivalik College of Engineering, Shimla Bypass Rd, Dehradun, India
e-mail: jaireena@sce.org.in

V. Devi · S. Kumar
Civil Engineering Department, College of Technology, GBPUAT, Pantnagar, Uttarakhand, India
e-mail: vaneetadevi.civil@gbpuat-tech.ac.in

S. Kumar
e-mail: sunilkumar.civil@gbpuat-tech.ac.in



M. Madhavan et al. (eds.), *Proceedings of the Indian Structural Steel Conference 2020 (Vol. 1)*, Lecture Notes in Civil Engineering 318,
https://doi.org/10.1007/978-981-19-9390-9_58

a truss is also called as an open web beam. The arrangement of truss bars is usually divided into triangular areas to distribute the load at each and every member of truss profile uniformly.

The type of roof truss depends upon the meteorological condition of the region or requirement of the large area of manufacturing work, such as industrial buildings, workshop buildings, stadium and warehouses, and for long span roofs. It provides a large space for operational purpose without any hindrance to heavy beams and columns. Also, it improves visibility and storage flexibility and facilitates the drainage of rain water. The design and analysis of industrial building was carried out by Sodhai and Phuke [11]. Nowadays, trusses are frequently made up of steel; however, some concrete trusses and timber trusses are also existed. The member sections generally used in steel trusses are angles, double angles, square hollow section (SHS), rectangular hollow section (RHS), circular hollow section (CHS), cold-formed steel, and so on. Steel roof trusses are the one which is most economical and convenient for the roofing structures for various types of constructions. From these various types of sections [10] carried out a study and concluded that tubular sections are more economical than the other sections. In this paper, thirty different conventional trusses of various spans and rise combinations have been analysed and designed with circular hollow section using STAAD. Pro V8i SS5. All the trusses have been designed as per IS 800:2007 (LSM). The span and rise of the considered truss profiles are varying 10 m, 15 m, 20 m, and 25 m and 1.5 m, 2.0 m, and 3.0 m, respectively. The considered truss profiles are also studied for their optimum weight to find out the economical truss profile.

In the recent past researches, many scholars had done various studies on optimization of truss system. According to Techase et al. [12] and Vikas [13], trusses are most prominent and lightweight structures for roofing system, and their efficiency varies according to the configuration, shape, and size of the truss members. Jayaraman et al. [8] have carried out a study on design and economy of roof trusses using limit stress and working stress method. Kumar et al. [9] carried out a quantitative study to analyse the effect of external pre-stressing force on Howe and parallel chord scissor truss.

## 2 Problem Statement

In this paper, a study has been carried out for thirty number of roof trusses of different configurations having span 10 m, 15 m, 20 m, and 25 m and rise 1.5 m, 2.0 m, and 3.0 m [Fig. 1]. These trusses further arranged into five groups according to their shapes and listed in Table 1. The end supports condition of the trusses have assumed as pinned at one end and roller at other end. The circular hollow cross-section has been chosen for members of the trusses. The basic parameters, viz. spacing between truss profile (5 m), height of the column (10 m), normal permeability (5%), and wind zone with basic wind speed (47 m/s), are kept same for all the groups. The spacing of purlins is also assumed to be fixed for every group accordingly. The design and

**Table 1** Classification of groups of various truss profile

| Group No | Truss Classification | Truss No |
|---|---|---|
| Group-1 | Constant Sloping Trusses | Truss 1 to Truss 10 |
| Group-2 | Flat Trusses | Truss 11 to Truss16 |
| Group-3 | Flat with Sloping Trusses | Truss 17 to Truss 22 |
| Group-4 | Irregular Trusses | Truss 23 to Truss 27 |
| Group-5 | Varying Slope Trusses | Truss 28 to Truss 30 |

analysis for all the truss groups are done by using circular hollow section (CHS) with the aid of STAAD. Pro V8i SS5 and their optimal and practical weight are computed. Further, their optimal and practical weights are compared to find the efficient truss.

An optimal truss is defined as the truss which is light, structurally stable, and designed as per relevant standards. The weight of this optimal structure is called as optimum weight Chouhan et al. [5]. In general practice of designing, designers took a uniform section throughout the whole members of truss called as practical weight, which results in increase in the cost of whole structure and makes the structure heavy. This is a major problem of concern to the designers that how to choose the favourable configuration of truss, with suitable rise and span of members which reduces the entire weight of the structure. Deepanshu et al. [6] had carried out a study on weight optimization due to the effect of configuration, shape, and size of the truss member. It also provides stability and strength in less construction cost with reduced fabrication work. The connection weights are not considered in this study; only the truss configuration weights are considered for design and analysis.

In present study, all individual groups of trusses as listed in Table 1 have rigorously analysed and studied for their optimal and practical weights. Due to page limitation, the results shown in this paper are only for group-1 which comprises trusses from 1 to 10. The conclusions have been drawn by comparing results obtained for all five groups.

## 3 Analysis and Design of a Sample Truss

All the truss profiles shown in Fig. 1 are analysed and designed for all load combinations as per IS 800:2007 (LSM) and S.K. [7]. The design forces along with section dimensions are given in Table 5. To demonstrate all load calculations, a truss profile of 10 m span and 1.5 m rise combination from group 1 has been selected and explained here. The basic layout and member number of sample truss profile are shown in Fig. 2a and b. The basic design parameters given in Table 2 have used for the design of this truss profile and also considered same for all groups.

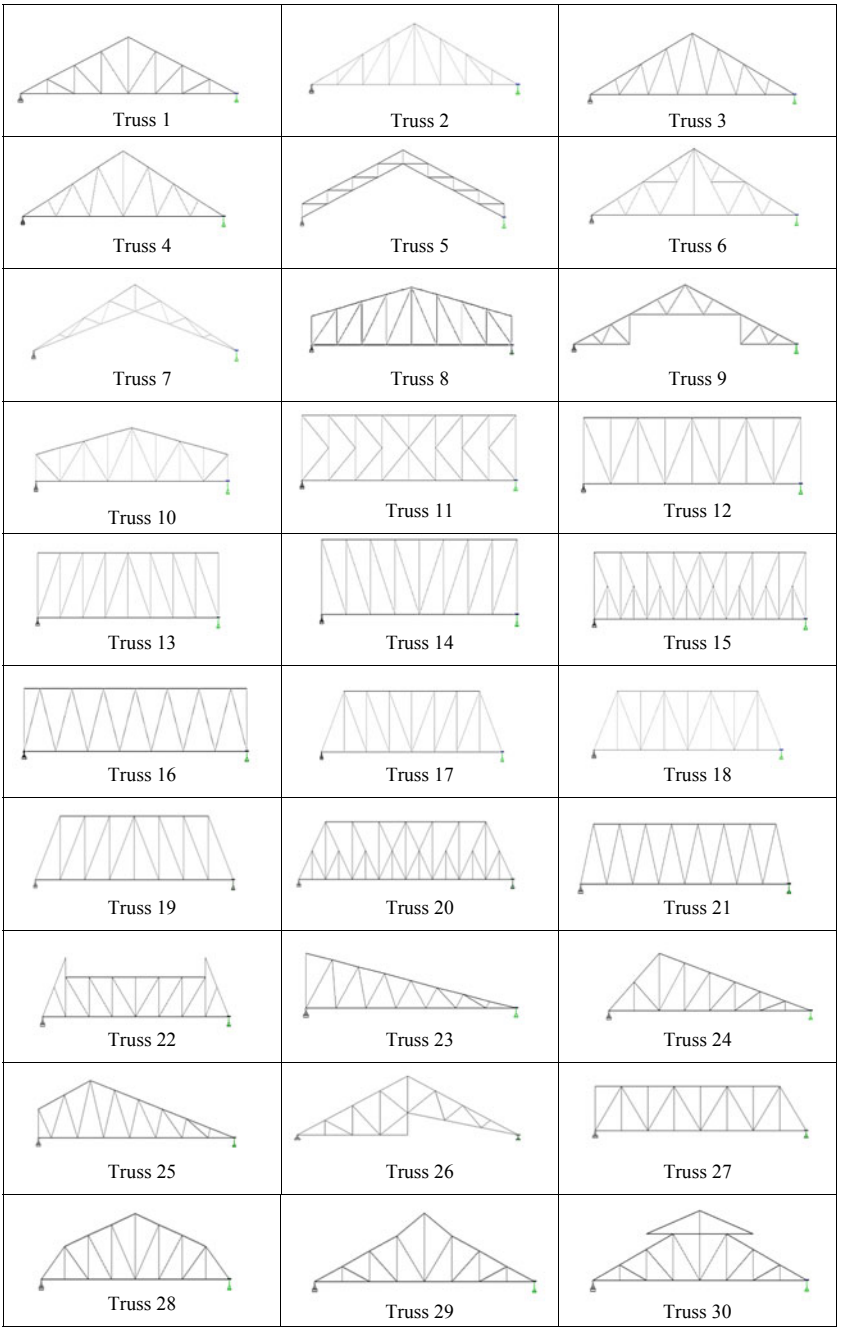


**Fig. 1** Various truss profiles configuration

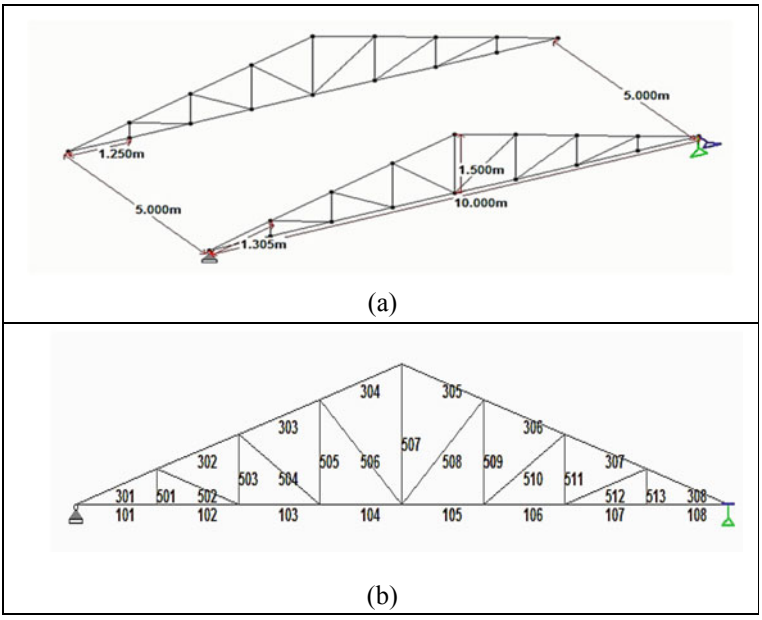


**Fig. 2** (**a**) Layout and (**b**) Member number of sample truss profile

**Table 2** Design parameters considered for truss design

| Design Parameter | $K_Y$, $K_Z$ | FU | FYLD | Utilization ratio |
|---|---|---|---|---|
| Values | 0.65 | 410 MPa | 250 MPa | 0.9 |

## *3.1 Stipulated Data*

| | | |
|---|---|---|
| Span of truss | | = 10m |
| Spacing of truss c/c | | = 5m |
| Height of columns | | = 10m |
| Rise of truss | | = 1.5m |
| Slope | | = 1 in 1.33 |
| Self − weight of purlins (assumed | | = 180 N/$m$ |
| Roofing and side coverings, GI sheets | | = 210$N/m^2$ |
| Roof angle ($\theta$) | = $\tan^{-1}(1.5/5)$ | = 16.7° |
| Length of the rafter | = $\sqrt{5^2 + 1.5^2}$ | = 5.22m |
| Length of each panel | = 5.22/4 | = 1.305m |

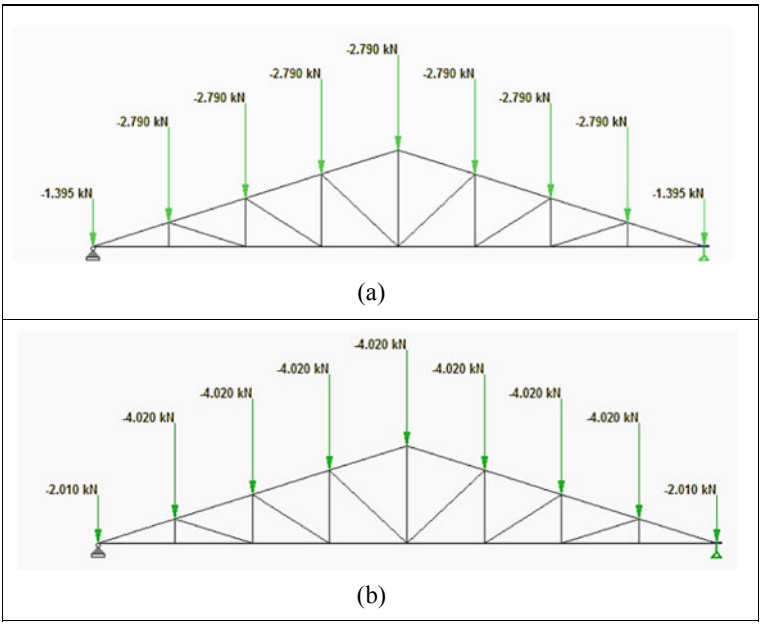


**Fig. 3** (**a**) Dead load and (**b**) Live load, on truss profile of 10 m span and 1.5 m rise

$V_b = 47$ m/s (taken from IS 875 (Part-III): 2015 basic wind speed for a 50 year return period).

$C_{pi} = \pm 0.2$ for both sides with normal permeability.

## *3.2 Dead Load (DL)*

The dead load of roof truss is sum of the weight of sheeting, weight of the purlin, fixing and services, or self-weight of the truss itself which are taken from IS 875(Part-I):1987. A simple empirical formula for the estimation of approximate dead weight of roof truss in $N/m^2$ is (span/3 + 5) × 10. The calculated design dead load on selected truss is shown in Fig. 3a. Design dead load on intermediate panels and on end panels is equal to 2.79kN and 1.395kN (acts downward), respectively.

## *3.3 Live Load (LL)*

In case of roof trusses, it consists of gravitational load due to erection, servicing, and dust load, etc. Live loads are variable as they depend on usage and intensity, and the intensity is taken as per IS 875(Part-II):1987. The calculated design live load on

selected truss is shown in Fig. 3b. Design live load on intermediate panels and on end panels is equal to 4.02kN and 2.01kN (acts downward), respectively.

### *3.4 Wind Load (WL)*

Wind load is considered to be the most critical load for light structures like a truss. Wind load may act opposite to the gravity load. Therefore, it creates a lifting effect on the truss roofs. The design code of practice for wind load IS 875(Part-III):2015 has used for calculation of wind loads and explained in the subsequent sections. The calculation for external pressure coefficient ($C_{pe}$) and net pressure coefficient ($C_{pe}$–$C_{pi}$) is given in Tables 3 and 4, respectively. The roof truss structure exerts external and internal pressure due to the blowing of wind against the structures. The external and internal pressure may be positive or either negative depending upon the direction of wind flow respective to the openings in the building. The obtained analysis results of member forces on the considered truss profiles (Fig. 2) for all aforesaid load combination are given in Table 5.

Similar analyses have been carried out on the all thirty truss profiles shown in Fig. 1and thus, compared for the optimum weight and practical weight of each truss profile in each group (Table 1) using STAAD. Pro software.

**Table 3** Calculation for external pressure coefficient ($C_{pe}$)

| h/w | Roof angle | Wind angle 0° | | Wind angle 90° | |
|---|---|---|---|---|---|
| | $\alpha$ | Windward side | Leeward side | Windward side | Leeward side |
| 1 | 10° | −1.1 | −0.6 | −0.8 | −0.6 |
| | 20° | −0.7 | −0.5 | −0.8 | −0.6 |
| | For $\alpha = 16.7°$ by interpolation, | | | | |
| | 16.7° | −0.83 | −0.53 | −0.8 | −0.6 |

**Table 4** Calculation for net pressure coefficient ($C_{pe} - C_{pi}$)

| Wind angle | Pressure coefficient | | | $(C_{pe} - C_{pi})$ | |
|---|---|---|---|---|---|
| | $C_{pe}$ | | $C_{pi}$ | Windward | Leeward |
| | Windward | Leeward | | | |
| 0° | −0.83 | −0.53 | 0.2<br>−0.2 | −1.03<br>−0.63 | −0.73<br>−0.33 |
| 90° | −0.8 | −0.6 | 0.2<br>−0.2 | −1.0<br>−0.6 | −0.8<br>−0.4 |

**Table 5** Member forces for truss span 10 m and rise 1.5

| Maximum forces (kN) | | | | | | |
|---|---|---|---|---|---|---|
| Member No | 1.5(DL + LL) | 1.5(DL + WL from right) | 1.5(DL + LL from left) | 1.2(DL + LL + WL from right) | 1.2(DL + LL + WL from left) | Design Forces |
| 101 | −119.175 | 64.581 | 62.661 | −4.615 | −6.151 | 64.581 kN Compression & 119.175 kN Tension (CHS PIP603M) |
| 102 | −119.175 | 64.581 | 62.661 | −4.615 | −6.151 | |
| 103 | −102.150 | 53.557 | 52.162 | −5.394 | −6.511 | |
| 104 | −85.125 | 42.533 | 41.662 | −6.174 | −6.870 | |
| 105 | −85.125 | 42.009 | 42.186 | −6.593 | −6.451 | |
| 106 | −102.150 | 52.508 | 53.211 | −6.233 | −5.672 | |
| 107 | −119.175 | 63.008 | 64.235 | −5.873 | −4.892 | |
| 108 | −119.175 | 63.008 | 64.235 | −5.873 | −4.892 | |
| 301 | 124.422 | −68.614 | −67.288 | 3.866 | 4.928 | 124.422 kN Compression & 68.614 kN Tension (CHS PIP761L) |
| 302 | 106.648 | −60.207 | −59.338 | 2.198 | 2.894 | |
| 303 | 88.873 | −51.800 | −51.387 | 0.530 | 0.860 | |
| 304 | 71.098 | −43.392 | −43.437 | −1.138 | −1.174 | |
| 305 | 71.099 | −43.438 | −43.392 | −1.174 | −1.138 | |
| 306 | 88.873 | −51.388 | −51.799 | 0.860 | 0.258 | |
| 307 | 106.648 | −59.338 | −60.207 | 2.894 | 2.199 | |
| 308 | 124.422 | −67.288 | −68.614 | 4.927 | 3.867 | |
| 501 | 0.000 | 0.000 | 0.000 | 0.000 | 0.000 | 22.905 kN Compression & 30.645 kN Tension (CHS PIP337M) |
| 502 | 17.775 | −11.510 | −10.962 | −0.814 | −0.376 | |
| 503 | −5.108 | 3.307 | 3.150 | 0.234 | 0.108 | |
| 504 | 19.854 | −12.856 | −12.245 | −0.909 | −0.420 | |
| 505 | −10.215 | 6.615 | 6.300 | 0.468 | 0.216 | |
| 506 | 22.905 | −14.832 | −14.126 | −1.048 | −0.484 | |
| 507 | −30.645 | 19.372 | 19.371 | 1.025 | 1.025 | |
| 508 | 22.905 | −14.126 | −14.832 | −0.484 | −1.048 | |
| 509 | −10.215 | 6.300 | 6.615 | 0.216 | 0.468 | |
| 510 | 19.854 | −12.245 | −12.856 | −0.420 | −0.909 | |
| 511 | −5.108 | 3.150 | 3.307 | 0.108 | 0.234 | |
| 512 | 17.775 | −10.962 | −11.510 | −0.376 | −0.814 | |
| 513 | 0.000 | 0.000 | 0.000 | 0.000 | 0.000 | |

### 3.4.1 Design Wind Speed ($V_Z$)

Design wind speed at any height Z, in m/s

$$V_Z = V_b K_1 K_2 K_3 K_4$$

where $V_b$ = basic wind speed, $K_1$ = probability factor (risk coefficient), $K_2$ = terrain, roughness, and height factor, $K_3$ = topography factor, and $K_4$ = important factor for cyclonic region.

Calculated design wind speed ($V_z$) = $47 \times 1 \times 0.928 \times 1 \times 1 = 43.616$ m/s.

### 3.4.2 Design Wind Pressure

The wind pressure in N/m$^2$ at height 'z' above the mean ground level is

$$p_z = 0.6\, V_z^2$$

The design wind pressure is

$$p_d = K_d K_a K_c p_z$$

### 3.4.3 Calculated Design Wind Pressure

$$p_z = 0.6\, V_z^2 = 0.6 \times 43.61^2 = 1141.41\, N/m^2$$

$$p_d = 0.90 \times 1.0 \times 1.0 \times 1141.41 = 1027.269\, N/m^2$$

where $K_d$ = wind directionality factor, $K_a$ = area averaging factor, and $K_c$ = combination factor.

### 3.4.4 Design Wind Forces (F)

Design wind force (F) = $(C_{pe} - C_{pi})Ap_d$

Where $C_{pe}$ = external pressure coefficient [will be taken as per clause 7.3.3 IS 875(Part-III):2015], $C_{pi}$ = internal pressure coefficient [will be taken as per clause 7.3.2 IS 875(Part-III):2015], A = surface area of the element under consideration, and $p_d$ = design wind pressure.

Calculated design wind load = wind load is calculated for 0° and 90°

Wind perpendicular for 0° = 1.9809(Horizontal component)
= 6.6054(Vertical component)
Wind parallel for 90° = 1.9232(Horizontal component)
= 6.4129(Vertical component)

**Table 6** Optimum weight and practical weight of 10 m span and 1.5 m rise

| Rise 1.5 m | | | |
|---|---|---|---|
| Truss Profile | Optimum weight (kg) | Practical weight (kg) | % Difference |
| 1 | 112.84 | 139.76 | 23.85 |
| 2 | 115.90 | 142.30 | 22.78 |
| 3 | 105.30 | 129.36 | 22.85 |
| 4 | 107.03 | 135.68 | 26.76 |
| 5 | 290.72 | 443.53 | 52.56 |
| 6 | 111.21 | 132.52 | 19.16 |
| 7 | 225.18 | 281.65 | 25.08 |
| 8 | 91.23 | 145.36 | 59.33 |
| 9 | 75.74 | 108.97 | 43.88 |
| 10 | 88.79 | 120.90 | 36.17 |

## 4 Results and Discussion

All the truss profiles are analysed for all load combinations and designed for the maximum member force. The optimum weight and practical weight of each truss profile in each group have obtained from STAAD. Pro software. Due to the page limitation, the results obtained from analysis for optimum weight and practical weight of truss profile of group 1 with 1.5 m rise (Table 1) are given here and discussed. The obtained results for optimum weight, practical weight, and their percentage difference for each truss in group 1 with 1.5 m rise are listed in Table 6. The optimized weight of truss profile of group 1 with 1.5 m, 2.0 m, and 3.0 m rise has compared graphically.

Figure 4 to Fig. 7 delineates the comparison of optimized weight with different truss profiles in group 1. Figure 4 exhibits the comparison of optimum weight for 10 m span with 1.5 m, 2.0 m, and 3.0 m rise of truss profiles. Similarly, Fig. 5, Fig. 6, and Fig. 7 show the comparison for 15 m, 20 m, and 25 m with 1.5 m, 2.0 m, and 3.0 m rise of truss profiles, respectively. Same exercise has carried out on the rest of the profiles in each group and has compared among themselves. The conclusion of the work has drawn by comparing of optimized weight all the truss profiles for different span and rise combinations.

## 5 Conclusions

1. This study gives an idea to find out the most economical truss profile in terms of weight among the thirty different configurations of truss profile by using CHS for a certain span and rise. It saves time and reduces efforts to choose the efficient configuration for a particular design input.

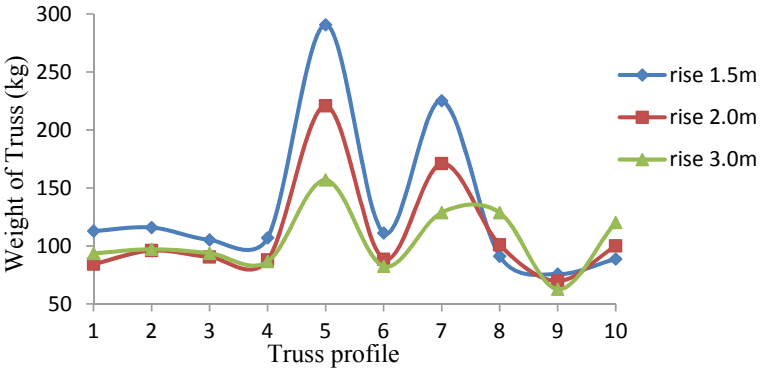


**Fig. 4** Optimum weight of truss versus truss profile of group-1 for 10 m span

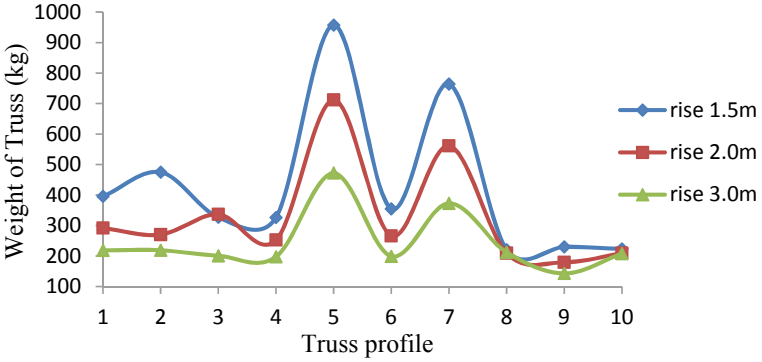


**Fig. 5** Optimum weight of truss versus truss profile of group-1 for 15 m span

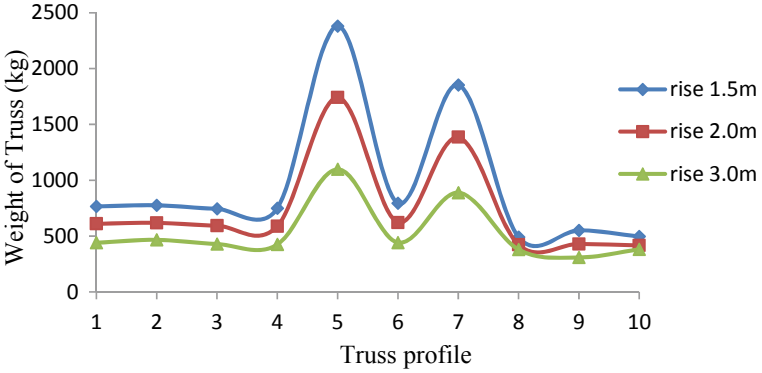


**Fig. 6** Optimum weight of truss versus truss profile of group-1 for 20 m span

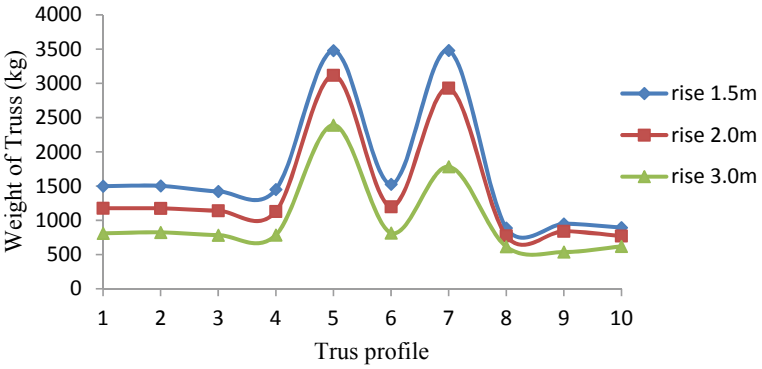


**Fig. 7** Optimum weight of truss versus truss profile of group-1 for 25 m span

2. This study may help to compute the cost of the material for various truss geometries which is calculated by taking the price per unit weight of truss.
3. The optimum weight truss profile is valid for a specific span and rise. This states that the optimum weight truss profile does not applicable for another truss profile of different span and rise.
4. This study gives the guidelines to find out the least weight truss profile. In this study, among the thirty trusses, Truss 9 and 10 show the least weight for group-1; Truss 11 and 16 for group-2; Truss 17 and 18 for group-3; Truss 27 for group-4, and Truss 28 for Group-5.
5. From all of the thirty trusses, Trusses of group-5 are the most efficient truss not only due to their least optimum and practical weight but also due to their less percentage difference of weight. This concluded that the truss uses the material fully without any wastage of much material.
6. The optimum/practical weight decreases with increase in rise of the trusses of all groups except trusses of group-1, 2, and 3 for the span 10 and 15 m. Hence, it is concluded that for low rise cases the trusses of group-1, group-2, and group-3 for 10 m and 15 m should be preferred.
7. Among all the groups, group-4 (irregular trusses) comprises the most uneconomical trusses due to the high optimum and practical weight. Also, the trusses have very large percentage difference more than 200% which makes it least efficient as compare to the trusses of another group.
8. This study proves that each and every truss type has its own effective span and rise for which it gives efficient results. It also suggests that as the member size increases the weight of the material also increases, but the section is unutilized by the structure and thus causes the waste of material with an increase in cost.

## References


1. BIS (1987) IS 875 Part-I. Code of practice for design loads (other than earthquake) for buildings and structures- dead loads. Bureau of Indian Standard, New Delhi, p 37
2. BIS (1987) IS 875 Part-II. Code of practice for design loads (other than earthquake) for buildings and structures- imposed loads. Bureau of Indian Standard, New Delhi. p 18
3. BIS (2007) IS 800. General construction in steel - code of practice. Bureau of Indian Standard, New Delhi, p 143
4. BIS (2015) IS 875 Part-III. Code of practice for design loads (other than earthquake) for buildings and structures- wind loads. Bureau of Indian Standard, New Delhi, p 58
5. Chouhan S, Sharma R (2017) Optimization of steel truss configuration for structure efficiency. Int Res Bas J 6(2):10–14
6. Deepanshu SS, Rawat SK (2015) Effect of different steel sections on design of roof truss. J Struct Eng Manag 2(2):20–24
7. Duggal SK (2015) Limit state design of steel structures, 2nd ed. McGraw Hill Education (India), New Delhi, p 860
8. Jayaraman A, Geethamani R, Sathyakumara N, Shenbagam NK (2014) Design and economical of roof trusses & purlins (comparison of limit state and working stress method). Int J Res Eng Technol 3(2):199–207
9. Kumar JP, Kumar JDC, Kumar MP (2016) Quantitative study of Howe truss (A- Type) and parallel Chord Scissor Truss (B- Type) by applying external pre-stressing. Int J Eng Res Technol 5(1):416–421
10. Naik P (2015) Comparison of conventional steel roof trusses with tubular trusses. Int J Eng Res Technol 3(19):1–4
11. Sodhai SC, Phuke RM (2018) Design & analysis of industrial roof truss. Int J Sci Res Dev 6(2):1764–1766
12. Techasen T, Wansasueb K, Panagant N, Pholdee N, Bureerat S (2018) Multiobjective simultaneous topology, shape and sizing optimization of trusses using evolutionary optimizers. Int Conf Aerospace Mech Eng:1–11
13. Vikas BS (2017) Effect of variation in geometrical parameters on the roof trusses. Int J Recent Innov Trends Comput Commun 5(7):6–9

# Behaviour of Beam with Slender Flanges


**Rajendra N. Khapre and Asim Aziz**

**Abstract** Compression members buckle globally or locally, depending on the overall section slenderness and the local plate element slenderness. If plate elements buckle at a stress lower than the stress which would cause the section to buckle globally, the local buckling of the plate will control the overall section strength. When this occurs, the section is said to be composed of slender elements. There is extensive research on buckling of slender web, but hardly any research regarding behaviour of slender flanges have been undertaken. Therefore, to study the behaviour of beam with slender flanges, a group of I-sections were selected with varying flange width to thickness ratios ranging from slender to highly slender sections, different unbraced span lengths and end support conditions. The I-sections were modelled on ANSYS workbench with the aforementioned parameters and loading condition of uniformly distributed pressure over flange. The buckling load behaviour due to slender flanges w.r.t the changes in width, thickness, unbraced span lengths and end support conditions were obtained. Indian and American standard codes, IS 800–2007, IS 801 1975 and AISC 360–16 were referred.

**Keywords** Buckling · Slenderness ratio · Slender flanges · Pre-engineered buildings

## 1 Introduction

The design of industrial building is governed primarily by requirements of functional and economical construction. To achieve minimum weight design of steel structure, the selection of suitable steel sections used in structural framing has always been a topic of great interest for designers. An efficiently designed pre-engineered building

R. N. Khapre (✉) · A. Aziz
Shri Ramdeobaba College of Engineering and Management, Nagpur, India
e-mail: khaprern@rknec.edu



M. Madhavan et al. (eds.), *Proceedings of the Indian Structural Steel Conference 2020 (Vol. 1)*, Lecture Notes in Civil Engineering 318,
https://doi.org/10.1007/978-981-19-9390-9_59

(PEB) can be lighter than the conventional steel building (CSB) by up to 30%. Lighter weight equates to less steel requirement and thus reduction in structural framework costing.

PEB manufacturers often use very slender sections in order to reduce weight of structure, and be economical/competitive in their bids. These thin sections do not satisfy the codal provisions of IS 800: 2007 (clause no 3.7.2). In general practice, PEB is designed using AISC/MBMA provisions.

Slender built-up sections are formed using plates with large width to thickness ratios. The buckling of the slender plate elements of the cross section under compression/shear may take place before the overall section buckling. This phenomenon is called local buckling. Local buckling is an important aspect of slender steel sections, as the thin sections invariably buckle before yielding. Thinner the plate, the lower will be the load at which it buckles. Local buckling depends on the slenderness (width to thickness, b/t ratio) of the plate element and the yield stress ($f_y$) of the material. Local buckling has the effect of reducing the load carrying capacity of section, due to the reduction in stiffness and strength of the locally buckled plate elements.

There has been considerable research on the behaviour and strength of slender section beam-columns over the years. Literature review of few research works relevant to slender sections is discussed.

Hancock [5, 6] calculated the effective flexural resistance of box and I-sections under axial load using the nonlinear finite strip method. He found that the effective section method for predicting the interaction of local and overall buckling is accurate for I columns with very heavy webs, but over-conservative for more normal web geometry. Hancock and Rasmussen [7] carried out experiments on longer members, however, showed that the interaction graph is slightly convex and with higher convexity at higher axial loads.

Dawe and Kulak [2] used a computer-aided analytical technique to study the local buckling behaviour of beam-columns consisting of I-sections and derived empirical equations that relate the web slenderness limit to the applied axial force.

Rangelov [10] computed the effective stiffness of slender steel sections to calculate the deflection. He found that theoretical effective width for stiffness calculation is always greater than the effective width used for strength and suggested an extension of concept of effective width.

Hasham and Rasmussen [8] experimentally determined the section capacities and the shape of interaction curves for slender I-sections subjected to axial compressive force and major axis bending. They showed that linear interaction curves are appropriate, and the design strengths determined using design codes are conservative.

Salem et al. [11, 12] explained that the results show that the strength of the sections decreases with an increase in the flange and web width to thickness ratios. Also, flange width to thickness ratios, $b/t_f$, have a greater effect on the strength of the sections than web width to thickness ratios, $d/t_w$, when the sections are subjected to small axial compressive loads, and both are equally important when they are subjected to high axial compressive loads. Also, presented an empirical equation that determines the ultimate axial capacity of columns formed of slender I-section directly using the gross section properties. The equation is a function of flange width to flange thickness

and web width to web thickness ratios and the member slenderness ratios and takes into consideration the different modes of failure, whether local, local–overall, or overall.

Sato and Uang [13] studied theory and models proposed by past researchers, background of development of AISC specifications and calibrated to an enhanced experimental database, and proposed a simple model which maintains the accuracy for the calculation of the modified slenderness ratio of built-up members with closely spaced individual components that are connected by welded or pre-tensioned bolted connectors.

Degee et al. [3] carried out experimental and numerical investigations concluding that model with local imperfection of 1/250 of the cross-sectional width and a global imperfection of 1/725 of the overall length produces results in good agreement with those obtained from a model including residual stresses.

Umair et al. [14] explained that in PEB, flange slenderness varies from compact range to slender ranges, whereas web slenderness generally lies in slender range. For cold-formed sections, thickness is very less and these sections lie in highly slender range. Built-up slender sections are appropriate for use when overall buckling failure of the member governs the design, and the steel members have high values of unbraced length to the total length ratio.

Abou-Hashem et al. [1] performed a parametric study and concluded that in short column local buckling is predominant, whereas in long column failure is due to global buckling. With increase in horizontal stiffeners thickness, column failure load increases. The effect of width of stiffeners was insignificant on failure load. Increase in no. of stiffeners resulted in direct increase in load capacity, and the effect is more significant in short column when compared with long column.

Geschwindner and Troemner [4] briefly discussed past specification provisions for slender element compression members and introduced new provisions in the 2016 AISC Specification. They presented a simplification that reduced the number of constants that must be used and the specification requirements in an alternate format. A comparison between the 2010 Specification and 2016 Specification for six slender element members shows that the change in strength can be significant for members with slender unstiffened elements.

Mustafa et al. [9] presented an experimental and a FE analysis of compressive behaviour of slender section columns with and without stiffeners. They performed a series of tests on specimens with different overall heights and different number of stiffeners and concluded that the load carrying capacity of steel columns with large web to thickness ratio is noticeably enhanced up to 34% by increasing number of web stiffeners, and also that the post local buckling strength of the sections is more sensitive to web width–thickness ratio than flange width–thickness ratio.

In this study, analysis of slender flanged I-sections has been performed using ANSYS workbench software. Analysis was done using linear buckling analysis system, and parameter sets were built to evaluate buckling load results. The results obtained provide us insight into the behaviour of beams with slender flanges. The

study of behaviour of slender sections will help us in determining relevant factors in such a way that, global buckling can be achieved as strength governing criteria even with slender sections.

## 2 Methodology

### *2.1 General*

ANSYS Workbench software was used for analyses of slender flanged I-sections beams subjected to uniform pressure over top flange. The moment due to externally applied pressure may be compared with the expressions given in IS 800:2007 of clause 8.2. After modelling of the I-sections, the buckling load were calculated for these file systems subjected to various flange width, thickness, span lengths and support conditions. Different member slenderness ratios were chosen to study the different behaviours of section. No tapered sections were considered. Web was kept constant, to study the effect of slender flanges only.

### *2.2 Material Property*

In PEB, structural members conform to the specifications of ASTM A572 grade 50 or equivalent. It is a high strength, low alloy (HSLA) steel often used in general plate applications when the plate will be riveted, bolted or welded. Relevant engineering properties of ASTM A572 (50) are yield strength $f_y = 350$ N/mm$^2$, modulus of elasticity $E = 1.90 \times 10^5$ N/mm$^2$ and Poisson's ratio $\mu = 0.3$.

### *2.3 Modelling*

I-sections with variable flange width, thickness, span length and support condition were modelled. Constant web dimensions of 600 × 6 mm was taken. Flange width of 150, 175, 200, 225 and 250 mm, flange thicknesses of 4, 6, 8, 10 and 12 mm, span lengths 3, 6 and 9 m and support conditions as fixed, simply supported, cantilever were taken. All combinations of the aforementioned variables were modelled. Mesh was generated with medium relevance value as shown in Fig. 1. Pressure of 2 N/mm$^2$ was applied over top flange as surface loading. The aforementioned material properties must be input into engineering data and assigned to solid.

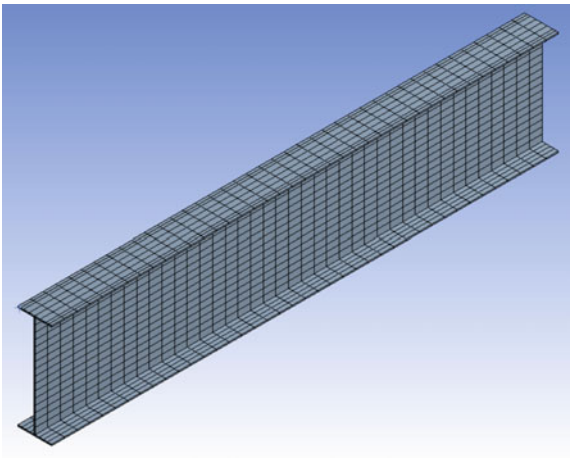

**Fig. 1** Model of built-up I-section with meshing

### *2.4 Analysis*

Buckling load is calculated using linear buckling analysis system in ANSYS Workbench. The linear buckling mode solution generates a load multiplier, which when multiplied with applied load gives us buckling load. Also, parametric set is generated for analysis of same section for varying span lengths and support conditions.

## 3 Results and Discussion

The general buckling behaviour observed for fixed end, simply supported and cantilever condition is depicted in Figs. 2, 3 and 4, respectively.

For fixed end support condition, the maximum deformation is observed to be in the web portion as seen in Fig. 2. Thus, for fixed end condition, it is evident that the rigidity of member is high and thus flange, even though slender transmits the load to web and the web is observed to buckle. For simply support condition, the rigidity of member is low and thus the flange unable to transmit the loads. Hence, the web is observed to buckle as seen in Fig. 3. For cantilever condition, while the fixed end is rigid, the other end is completely free, therefore flange is observed to buckle as seen in Fig. 4.

The buckling load, applied as pressure at top flange having magnitude 2 N/mm$^2$, is evaluated after performing linear buckling analysis in ANSYS. The buckling load is evaluated by multiplying load multiplier with applied pressure. In the table 1, buckling load values evaluated w.r.t section dimensions or slenderness ratio and span lengths are mentioned. To understand the bulking behaviour, the information reported in Table 1 is plotted in Fig. 5 to Fig. 10. In Figs. 5–7, flange thickness is kept constant and in Figs. 8–10, flange width is kept constant. There are five curves

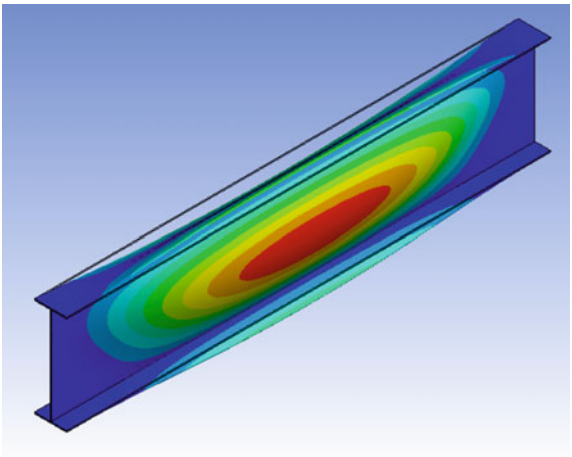

**Fig. 2** Buckling behaviour for fixed end condition

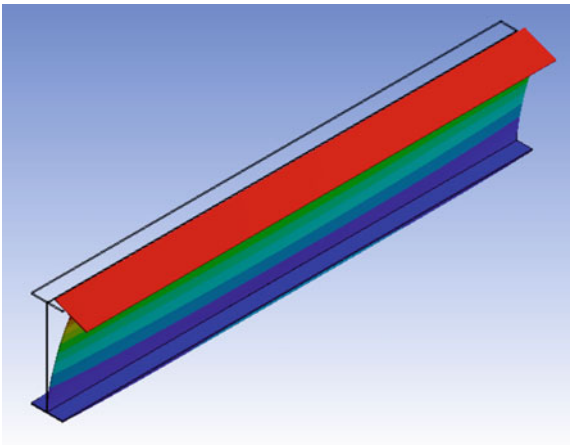

**Fig. 3** Buckling behaviour for simply supported condition

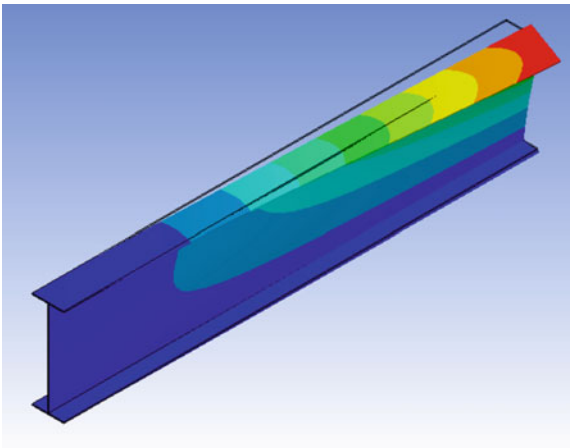

**Fig. 4** Buckling behaviour for cantilever condition

**Table 1** Buckling load w.r.t. slenderness ratio (b/t) & unbraced span lengths

| SN | Flange width, b (mm) | Flange thickness, t (mm) | b/t | Buckling load ($N/mm^2$) (ASTM A572 grade 50 Steel) | | | | | | | | |
|---|---|---|---|---|---|---|---|---|---|---|---|---|
| | | | | fixed end | | | Simply supported | | | Cantilever | | |
| | | | | 3 m | 6 m | 9 m | 3 m | 6 m | 9 m | 3 m | 6 m | 9 m |
| 1 | 150 | 4 | 37.5 | 1.152 | 0.237 | 0.057 | 0.02 | 0.01 | 0.005 | 0.148 | 0.016 | 0.005 |
| 2 | 175 | 4 | 43.8 | 1.042 | 0.29 | 0.072 | 0.018 | 0.009 | 0.005 | 0.177 | 0.018 | 0.005 |
| 3 | 200 | 4 | 50 | 0.94 | 0.338 | 0.09 | 0.017 | 0.008 | 0.005 | 0.208 | 0.021 | 0.006 |
| 4 | 225 | 4 | 56.3 | 0.85 | 0.374 | 0.108 | 0.016 | 0.008 | 0.005 | 0.238 | 0.024 | 0.006 |
| 5 | 250 | 4 | 62.5 | 0.775 | 0.389 | 0.127 | 0.015 | 0.007 | 0.005 | 0.208 | 0.027 | 0.007 |
| 6 | 150 | 6 | 25 | 1.24 | 0.331 | 0.082 | 0.031 | 0.014 | 0.008 | 0.206 | 0.023 | 0.007 |
| 7 | 175 | 6 | 29.2 | 1.106 | 0.396 | 0.105 | 0.028 | 0.014 | 0.008 | 0.247 | 0.026 | 0.007 |
| 8 | 200 | 6 | 33.3 | 0.993 | 0.446 | 0.129 | 0.026 | 0.013 | 0.007 | 0.286 | 0.03 | 0.008 |
| 9 | 225 | 6 | 37.5 | 0.9 | 0.477 | 0.155 | 0.024 | 0.012 | 0.007 | 0.321 | 0.035 | 0.009 |
| 10 | 250 | 6 | 41.7 | 0.823 | 0.487 | 0.18 | 0.023 | 0.011 | 0.007 | 0.348 | 0.04 | 0.01 |
| 11 | 150 | 8 | 18.8 | 1.333 | 0.421 | 0.109 | 0.043 | 0.02 | 0.011 | 0.267 | 0.031 | 0.009 |
| 12 | 175 | 8 | 21.9 | 1.191 | 0.492 | 0.138 | 0.04 | 0.019 | 0.011 | 0.315 | 0.035 | 0.01 |
| 13 | 200 | 8 | 25 | 1.074 | 0.541 | 0.169 | 0.037 | 0.018 | 0.011 | 0.359 | 0.041 | 0.011 |
| 14 | 225 | 8 | 28.1 | 0.98 | 0.564 | 0.2 | 0.034 | 0.017 | 0.01 | 0.395 | 0.047 | 0.013 |
| 15 | 250 | 8 | 31.3 | 0.903 | 0.567 | 0.229 | 0.032 | 0.016 | 0.01 | 0.422 | 0.054 | 0.014 |
| 16 | 150 | 10 | 15 | 1.456 | 0.508 | 0.138 | 0.057 | 0.027 | 0.014 | 0.33 | 0.041 | 0.013 |
| 17 | 175 | 10 | 17.5 | 1.311 | 0.583 | 0.173 | 0.052 | 0.025 | 0.015 | 0.383 | 0.047 | 0.014 |
| 18 | 200 | 10 | 20 | 1.194 | 0.626 | 0.209 | 0.048 | 0.024 | 0.014 | 0.429 | 0.054 | 0.016 |
| 19 | 225 | 10 | 22.5 | 1.099 | 0.642 | 0.245 | 0.045 | 0.023 | 0.014 | 0.466 | 0.062 | 0.018 |
| 20 | 250 | 10 | 25 | 1.021 | 0.634 | 0.278 | 0.043 | 0.022 | 0.014 | 0.49 | 0.07 | 0.019 |
| 21 | 150 | 12 | 12.5 | 1.618 | 0.596 | 0.168 | 0.071 | 0.034 | 0.019 | 0.396 | 0.053 | 0.017 |
| 22 | 175 | 12 | 14.6 | 1.468 | 0.67 | 0.209 | 0.065 | 0.032 | 0.019 | 0.452 | 0.061 | 0.019 |
| 23 | 200 | 12 | 16.7 | 1.35 | 0.707 | 0.25 | 0.06 | 0.031 | 0.018 | 0.499 | 0.069 | 0.021 |
| 24 | 225 | 12 | 18.8 | 1.252 | 0.712 | 0.29 | 0.056 | 0.029 | 0.018 | 0.534 | 0.078 | 0.023 |
| 25 | 250 | 12 | 20.8 | 1.17 | 0.697 | 0.326 | 0.052 | 0.028 | 0.018 | 0.554 | 0.088 | 0.026 |

shown in these figures, each for different span of beams pertaining to five different flange thicknesses/widths as given in Table 1.

## *3.1 Case 1—Constant Flange Thickness, Support Conditions, Varying Flange Width and Span Lengths*

It can be observed from Fig. 5 that for fixed support condition for 6 m & 9 m span, the buckling load increases even with increase in slenderness of flange. This clearly

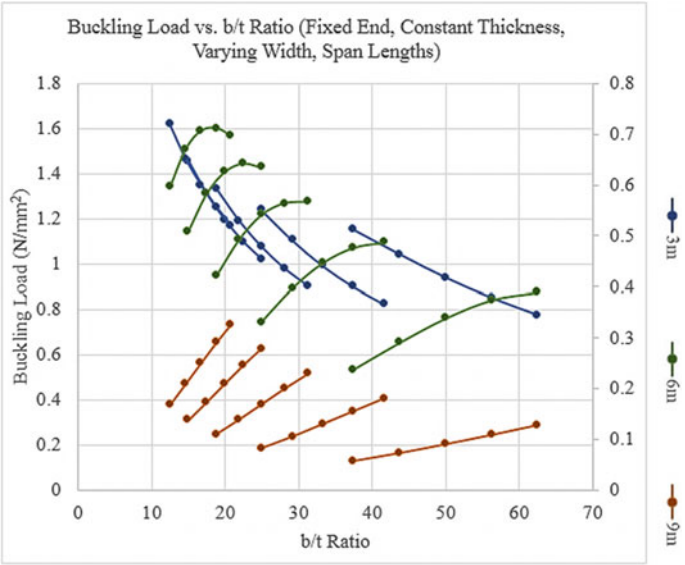


**Fig. 5** Buckling load vs. b/t ratio (fixed end, constant thickness, varying width, span lengths)

indicates that in those sections, global buckling was predominant rather than local buckling. Whereas, for 3 m span behaviour denotes local buckling as significant factor.

From Fig. 6, it can be stated that for simply supported condition, local buckling is predominant for all span conditions due to localized deformation near end supports about minor axis. Thus, local buckling is governing factor for strength criteria irrespective of unbraced span length in simply supported condition. From Fig. 7, it can be observed that for cantilever condition, irrespective of span length the generic behaviour is increased in buckling load with increasing flange widths for constant flange thickness. This is due to the fact that even though the slenderness ratio is increasing, the moment of inertia and end supported cross-section area is increasing.

## *3.2 Case 2—Constant Flange Width, Support Conditions, Varying Flange Thickness and Span Lengths*

It is observed through the Figs. 8, 9 and 10 that the buckling load is directly proportional to the flange thickness, i.e. as the flange thickness decreases for a constant flange width the corresponding buckling load also decreases. This is in contrast to the buckling load behaviour for case 1, where varying behaviours were observed. Also, the rate of proportionality is dependent on support conditions and span lengths.

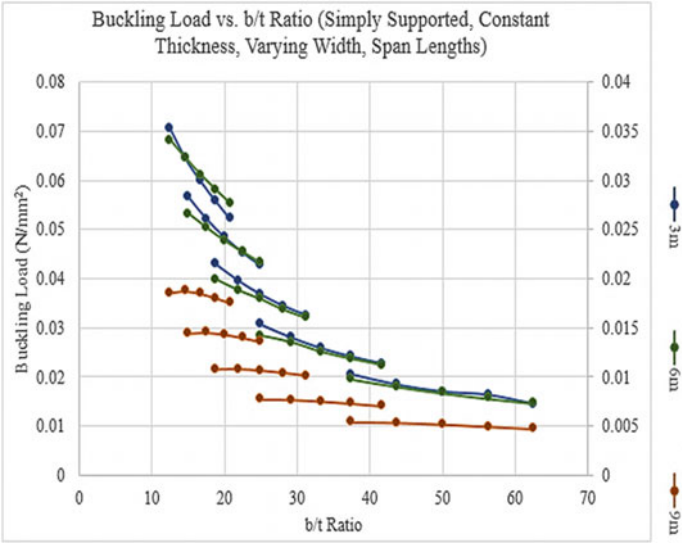


**Fig. 6** Buckling load vs. b/t ratio (simply supported, constant thickness, varying width, span lengths)

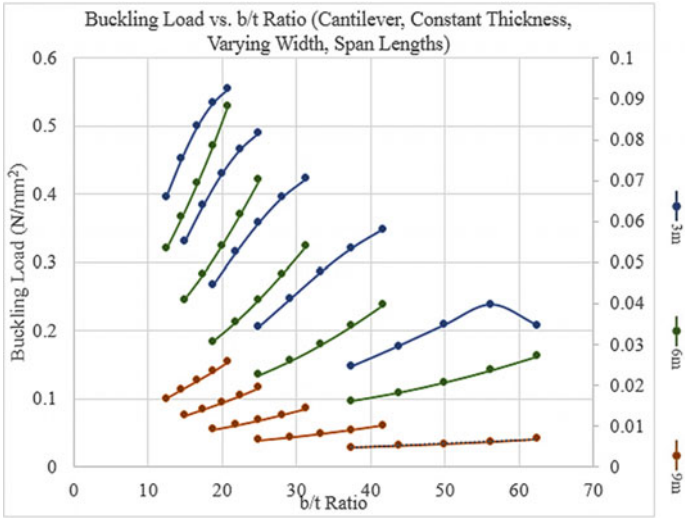


**Fig. 7** Buckling load vs. b/t ratio (cantilever, constant thickness, varying width, span lengths)

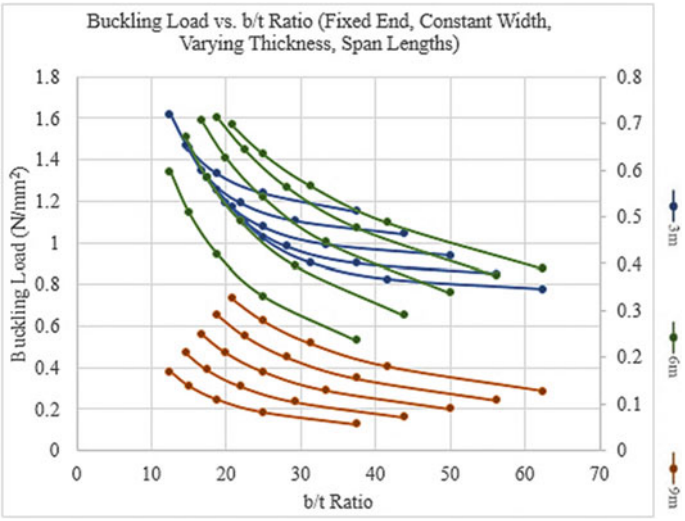


**Fig. 8** Buckling load vs. b/t ratio (fixed end, constant width, varying thickness, span lengths)

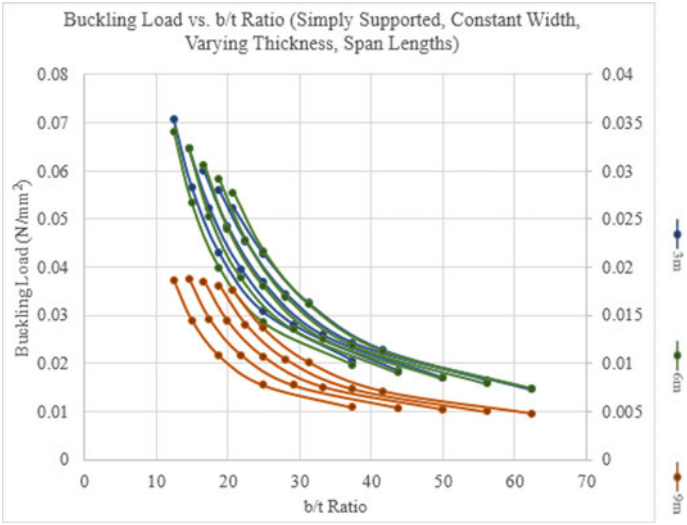


**Fig. 9** Buckling load vs. b/t ratio (simply supported, constant width, varying thickness, span lengths)

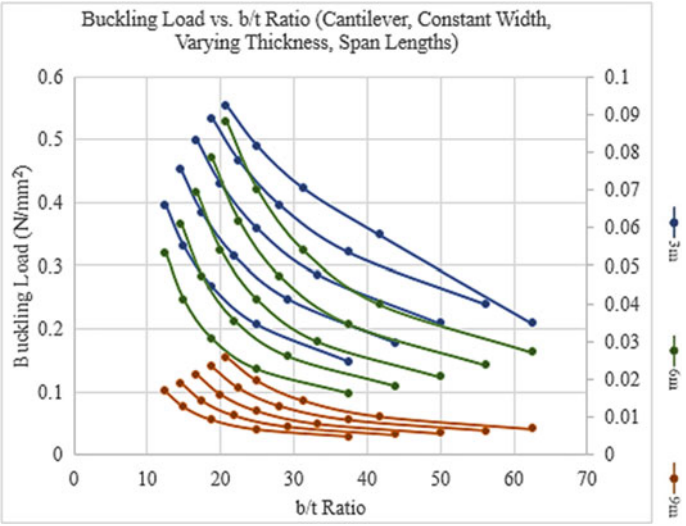


**Fig. 10** Buckling load vs. b/t ratio (cantilever, constant width, varying thickness, span lengths)

## 4 Conclusion

Based on the buckling load values obtained, behaviour of 'buckling load vs. b/t ratio' and 'buckling load vs. span length' was studied and the following conclusions have been drawn.

The buckling behaviour of slender flanged I-section is found to be directly dependent on flange dimensions, span length and support conditions.

Behaviour of 'buckling load for constant flange thickness' was found to be dependent on span length for fixed support and independent of span length for simply supported and cantilever support condition, respectively.

The variation in buckling load due to varying span length clearly indicates that, when global buckling criteria governs member strength the buckling load is observed to be directly proportional to slenderness ratio. Whereas, when local buckling is governing criteria the relationship of buckling load is inversely proportional to slenderness ratio.

Behaviour of 'buckling load for constant flange width' is found to be inversely proportional to the flange thickness irrespective of variation in support condition and span length.

## References


1. Abou-Hashem El Dib ME, Swailem MK, Metwally MM, Awady AIEl (2016) Performance of stiffened slender built up steel I-columns. IACSIT Int J Civ Environ Eng 10(8):997-1004
2. Dawe JL, Kulak GL (1986) Local buckling behavior of beam–columns. J Struct Eng ASCE 112(11):2447–2461
3. Degee H, Detzel A, Kuhlmann U (2008) Interaction of global and local buckling in welded RHS compression members. J Constr Steel Res 64(7–8):755–765
4. Geschwindner LF, Troemner M (2016) Notes on the AISC 360–16 provisions for slender compression elements in compression members. Eng J Am Inst Steel Constr 53:137–146
5. Hancock GJ (1981) Nonlinear analysis of thin sections in compression. ASCE J Struct Eng 107(3):455–471
6. Hancock GJ (1981) Interaction buckling in I-section columns. ASCE J Struct Eng 107(1):165–179
7. Hancock GJ, Rasmussen KJR (1998) Recent research on thin-walled beam-columns. Thin-Wall Struct 32(1–3):3–18
8. Hasham AS, Rasmussen KJR (1998) Section capacity of thin-walled I-section beam–columns. ASCE J Struct Eng 124(4):351–359
9. Mustafa SAA, Elhussieny OM, Matar EB, Alaaser AG (2018) Experimental and FE analysis of stiffened steel I-column with slender sections. Ain Shams Eng J 9(4):1635–1645
10. Rangelov N (1996) On the effective stiffness of slender steel sections for deflection calculations. Thin-Wall Struct 25(3):171–183
11. Salem AH, Aghoury MEl, El Dib FF, Hanna MT (2007) Strength of biaxially loaded slender I-section beam–columns. Can J Civ Eng 34(2):219-227
12. Salem AH, Aghoury MEL, El Dib FF, Hanna MT (2004) Ultimate capacity of I-slender section columns. J Constr Steel Res 60(8):1193–1211
13. Sato A, Uang CM (2007) Modified slenderness ratio for built-up members. Eng J (New York) 44(3):269–280
14. Umair SM, Hisham Q, Siddiqi ZA (2013) Optimum unbraced length ratios of slender steel sections. IACSIT Int J Eng Technol 5(4):493–497

# Behaviour of Unrestrained Steel I-Section Beams in Case of Fire


**Saurabh Suman and Avik Samanta**

**Abstract** Steel beam sections have mainly two failure modes: local buckling and lateral-torsional buckling, and interaction between these modes affects the critical load capacity of beams. Past case studies on structures such as World Trade Centre Tower 7 and large-scale fire experiments showed the vulnerability of steel buildings under elevated temperatures. In the case of the high-temperature gradient, floor beams suffer the local as well as global buckling collapse. Global failure at floor level leads to a progressive collapse of the steel structure buildings. In case of fire loading web of steel, section undergoes instability at the initial stage of fire loading. It leads to faster degradation of shear capacity and flexural capacity. This paper studies the inelastic lateral-torsional buckling behaviour, and moment capacities of the steel I-section beams. Beams are analysed under varying moment loadings with simply supported boundary conditions at elevated temperatures. A parametric study is presented to investigate the effect of loading cases and elevated temperature on the buckling capacity of the beam members. In this study, a total of 216 linear and nonlinear numerical model analysis are conducted using the finite element method (FEM) analysis with the help of a robust FEM-based ABAQUS software. It is observed from the numerical study that at elevated temperature the buckling capacity changes significantly compared to current design rules in Eurocode 3. It is also seen that the loading patterns have a vital effect on the buckling capacity of the beam.

**Keywords** Fire · Lateral-torsional buckling · Steel beams

S. Suman (✉) · A. Samanta
Department of Civil and Environmental Engineering, IIT, Patna, India
e-mail: saurabh.pce17@iitp.ac.in

A. Samanta
e-mail: asmanta@iitp.ac.in



M. Madhavan et al. (eds.), *Proceedings of the Indian Structural Steel Conference 2020 (Vol. 1)*, Lecture Notes in Civil Engineering 318,
https://doi.org/10.1007/978-981-19-9390-9_60

## 1 Introduction

Fire drastically affects the resistance of steel in buckling as seen in past fires like Broadgate phase 8 fire [5] that caused a loss of life and pushed back the economy of the region. It is also supported by the observations done in previous fire tests like Cardington Fire Tests [4].

The strength and stiffness of the steel material decrease rapidly, and the stress–strain relationship becomes distinctly nonlinear. Due to the decrement in strength and rigidity, large deflections are seen in the post-fire beams. From the past studies, it is observed that due to insufficient lateral bracings and improper connections with roof, beams become laterally unrestrained, and lateral-torsional buckling (LTB) phenomenon happens. Under vertically applied loads, the deflection of compression flange occurs along with twisting, and this phenomenon is known as LTB. When the compression increases in the top flange, it deflects towards the minor axis, results in out of plane deflection. LTB causes the sudden failure of the beams. Real and Franssen [7], Vila Real *et al.* [11, 8–10], conducted the set of experiment and numerical investigations on unrestrained IPE beams under constant and non-uniform moment. They observed dependency of LTB on steel grades, proposed severity factor, and suggested improvements to Eurocode 3. Structure buckling behaviour may be different from the elemental behaviour of simply supported beam under fire conditions as pointed out by [12] in his experiment of frame structure with pinned column bases that failed in sideways sway. Roy *et al.* [6] conducted the full-scale natural fire test on single storey cold-formed steel building in which collapse happened due to pull-in failure. Their experimental results closely matched with the numerical results. That suggest numerical modelling is a very efficient tool to simulate structural elements or buildings with numerous varying parameters. The experimental tests are very expensive, and only a few full-scale tests can be conducted that too, with limited parameters.

To the best of the author's knowledge, few investigations have been conducted concerning the LTB at elevated temperature. As pointed out by the [13] that the shell model gives up to 6% more buckling moment capacity compared to the 3D element model. It is required to perform more of such studies considering a 3D model with the 3D element that consider more realistic scenarios.

In this study, a total of 216 linear and nonlinear full-scale 3D models are analysed using the FEM analysis with the help of a robust FEM-based ABAQUS software. Validation of the numerical model is done from Vila Real *et al.* [11] experiments for which 40 linear and nonlinear numerical models are used. The purpose of this paper is to evaluate the influence of uniform fire under increasing load for ISMB 600 section. The beam behaviour is observed under three different loading conditions, i.e. constant moment, concentrated point load, and uniformly distributed load. Simply supported boundary conditions are considered at supports.

## 2 Geometrical Imperfection and Material Non-Linearity

The behaviour of the beam under a particular loading described by geometrical and material non-linear examination with imperfections (GMNIA). It comprises geometrical and material nonlinearities.

$$e_0 = \alpha\left(\overline{\lambda} - 0.2\right)\frac{M_{Rk}}{N_{Rk}} \tag{1}$$

Equation (1) was used for the computation of initial geometric imperfections, where $e_0$ is the amplitude of imperfection. In this equation, α represents the imperfection factor for the LTB curve that is taken from the Eurocode 3 part 1.1 (2005). Given $\overline{\lambda}$ is the relative slenderness that can be calculated from the cross-sectional geometry. $M_{Rk}$ and $N_{Rk}$ represent the characteristic moment resistance and normal force for the critical cross-section, respectively.

To perform the numerous iterations in instability conditions, modified Riks method is applied in ABAQUS using very small increment in the analysis.

By performing the linear buckling analysis (LBA) in perturbation steps, the elastic critical load and eigenmodes of the beam are calculated under each thermal condition. Appropriate LTB mode is taken for providing initial imperfections in the beam which is then imposed to a uniform thermal load, i.e. 20°, 200°, 300°, 400°, 500°, and 600° C. Load is applied using the arc-length method when the beam gets stabilized under constant temperature. The geometric imperfection and material non-linearity are considered to get significant numerical values for LTB. Material data for steel subjected to high temperatures are considered according to Eurocode 3 part 1.2 (2005).

Beams with various slenderness are modelled. Simply supported steel I-beams loaded with the different in-plane bending moment, with torsional restrictions at the supports. It is observed that with the change in loading cases the buckling modes also change. Once the failure load for the moment is known, the reduction factor $X_{LT}$ can be calculated as shown in Eqs. 4 and 5.

$$\lambda_{LT} = \sqrt{\frac{w_{y,pl} \times fy}{M_{cr}}} \tag{2}$$

$$\lambda_{LT,fi} = \lambda_{LT}\sqrt{\frac{k_{y,\theta}}{k_{E,\theta}}} \tag{3}$$

$$\chi_{LT} = \frac{M_{b,Rd}}{M_{c,Rd}} \tag{4}$$

$$\chi_{LT,fi} = \frac{M_{b,fi\cdot t,Rd}}{M_{fi,\theta,Rd}} \tag{5}$$

where $M_{b,Rd}$ = design buckling resistance moment,
$M_{c,Rd}$ = design resistance for bending,
$W_{y,pl}$ = plastic section modulus of the cross-section,
$M_{cr}$ = elastic critical moment for lateral-torsional buckling,
$M_{b,fi,t,Rd}$ = design lateral-torsional buckling resistance moment,
$M_{fi,\theta,Rd}$ = fire design moment resistance,
$F_y$ = yield stress of the steel.

$k_{E,\theta}$ and $k_{y,\theta}$ are the reduction factors for elasticity and yield stress, respectively, at elevated temperature θ. At ambient temperatures, the reduction factor for LTB is calculated using Eqs. 2 and 4. At high temperatures, the reduction factor for LTB in the fire design is $\chi_{LT,fi}$, and the non-dimensional slenderness values $\lambda_{LT,fi}$ are calculated using Eqs. 3 and 5.

## 3 Numerical Model Development

### *3.1 Material Properties*

For FEM simulations, material modelling is done to specify the performance of steel at several stages of mechanical and at elevated temperature loads. Eurocode 3 provides the equation for defining the stress–strain curve concerning temperature variation. To consider the yield strength and the elastic properties, the reduction factors are provided in Fig. 1a.

The reduction factor for the proportional limit is provided in the Eurocode 3 part 1–2 (2005). These reduction factors are used to calculate the engineering stress–strain diagram for each mentioned constant temperature. Plastic strain–stress data is calculated and implemented for finite element analysis as shown in Fig. 1b. In India, Fe 250 steel grades are used for most steel building construction, so this grade of steel

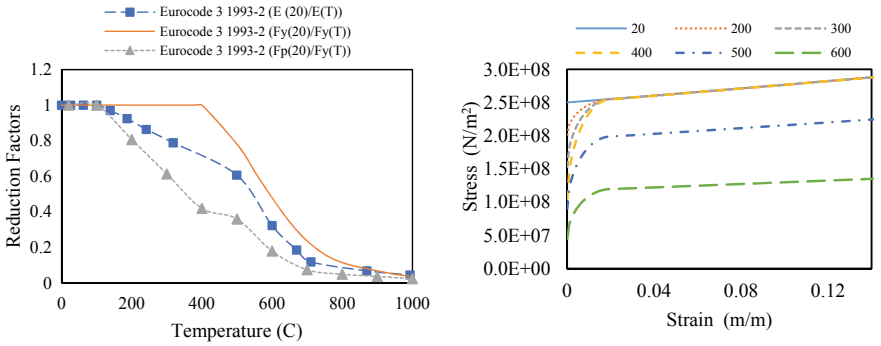


**Fig. 1** **a** Material properties reduction factors Eurocode 3 part 1–2 (2005). **b** Plastic stress–strain curve

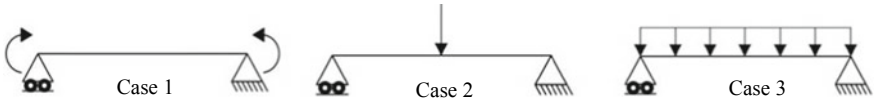


**Fig. 2** Load cases

is used for current research. For all cases, Poisson's ratio is taken as 0.3 irrespective of temperature change.

## *3.2 Boundary Conditions*

Simply supported boundary conditions are applied at the ends, and the in-plane, out of plane, and torsional restraints are added. Also, to avoid the distortion of the cross-sectional elements, the kinematic coupling is provided. These conditions are added at the middle of the cross-section.

The uniform bending moment is applied at the edges as shown in case '1'. In-plane uniform moment is given by applying the uniform moment at the ends. The concentrated point load is applied to the middle of the beam span on the top flange. It can be seen in Fig. 2. case '2'. The uniformly distributed load is applied on the surface of the top flange of the FE-model as shown in Fig. 2. case '3'.

Mesh sensitivity analysis is done considering C3D8R elements, which are the 3D continuum 8-node brick element and use reduced integration. The cross-sectional meshing is done separately for flanges, web, and corner curves. Mesh of flanges are transversely divided into 12 parts that are of length 210 mm, and longitudinally in 2 parts, of flange thickness 20 mm, and the web of the ISMB 600 section, that is of length 560 mm, is meshed into 25 parts in a transverse direction and longitudinally in 4 parts of web width of 12 mm.

## *3.3 Validation of the Numerical Model*

The validation of the FE model is done using the experimental and numerical results from Vila Real *et al.* [11]. Figure 3a shows the validation results, at ambient temperature as well as at higher temperature Fig. 3b, c, and d. A validation study is conducted for each elevated temperature in consideration which is not shown herein.

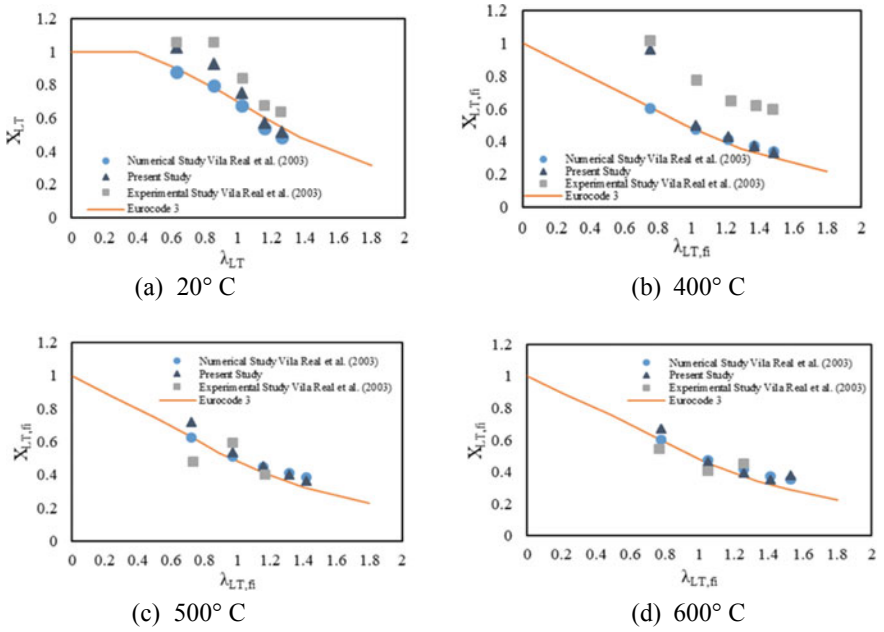


(a) 20° C (b) 400° C

(c) 500° C (d) 600° C

**Fig. 3** Validation of the present numerical model from available experimental and the numerical results

## 4 Results and Discussion

It is observed from Fig. 4a that as the temperature increases the moment taking capacity of the beam decreases. There is a rapid decrease in strength at a higher temperature. The load is increased in smooth increment, and subsequently, the acting moment increases in a beam and eventually reaches its full capacity as the peak observed in Fig. 4a. After that, the beam started to lose its capacity. Similar trends in the moment capacity curve are seen for all types of loading cases considered. It can also be observed that with the increase in the temperature, moment-displacement curves become flatter irrespective of loading and beam slenderness. Figure 4b shows the buckling capacity behaviour under in-plane load against deflection. It can be observed that the out of plane deflection is sudden under critical load. Figure 4c shows the typical buckled beam under vertical loading with average Von Mises stress values.

Owing to the different types of loading scenarios in practical conditions, three load cases are considered herein. It can be seen from Fig. 5(a-f) that the effect of loading types severely affects the buckling moment capacity of the beam. When the moment area is uniform all over the beams, beams performed poorly and in case of triangular moment area (point load case) beams buckling capacity is observed to be higher among the all loading patterns considered herein.

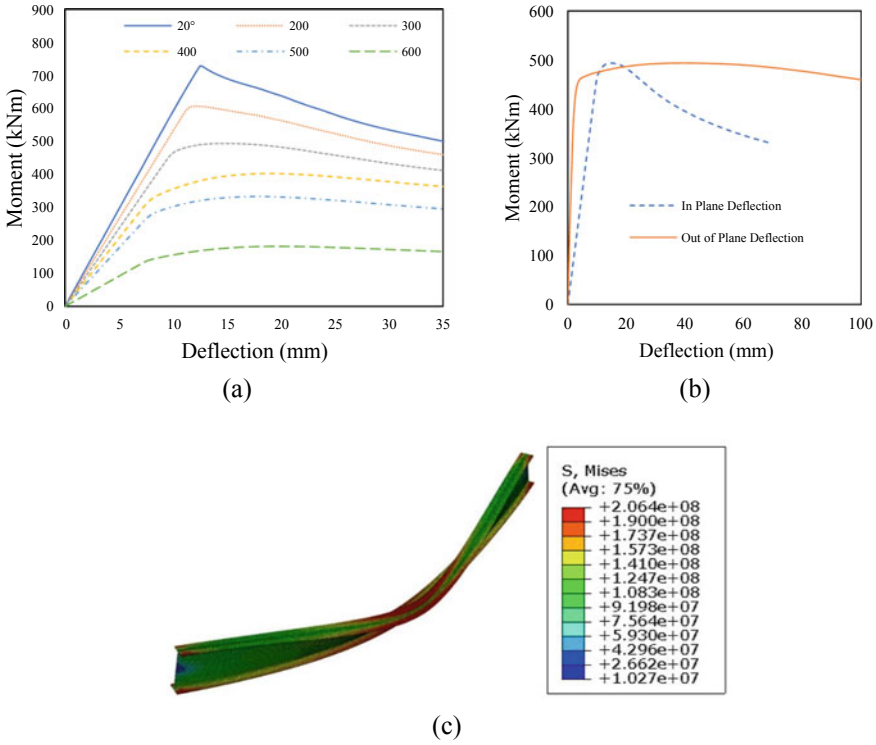


**Fig. 4** **a** Typical moment against in-plane deflection curve. **b** In-plane and out of plane deflection for the steel beam. **c** Typical lateral-torsional buckling shape of the beam

With an increase in span length of the beams, buckling capacities decrease. For higher slender section, failure of beams happens in the elastic zone, and for lower slender beams, it yields, and ultimate moment capacity observed in plastic zone. Figure 6a-c represents the variation of moment capacities with the increasing span length at elevated temperature for a uniform moment, point load, and uniformly distributed load, respectively.

Two dimensionless quantities $X_{LT,fi}$ and $\lambda_{LT,fi}$ are computed from the finite element analysis (FEA), and results are plotted in terms of both of these temperature-dependent parameters. $X_{LT,fi}$ for each temperature and loading conditions is calculated from Eq. (5). $\lambda_{LT,fi}$ for each temperature and loading type is calculated from Eq. (3). It compares the FEA results with the elastic buckling curve and the bucking curve 'b.' of Eurocode 3 part 1–1 (2005). Elastic buckling curve is theoretically calculated. Figure 8 shows the FEA results compared with the elastic buckling curve and the buckling curve from Eurocode 3 part 1.1. For the uniform moment loading case Fig. 7a, it is observed that the buckling curve 'b' Eurocode 3 is not suitable at elevated temperature. For the point load cases Fig. 7b, it is observed that design buckling curve 'b' Eurocode 3 provides highly conservative results. For the uniformly

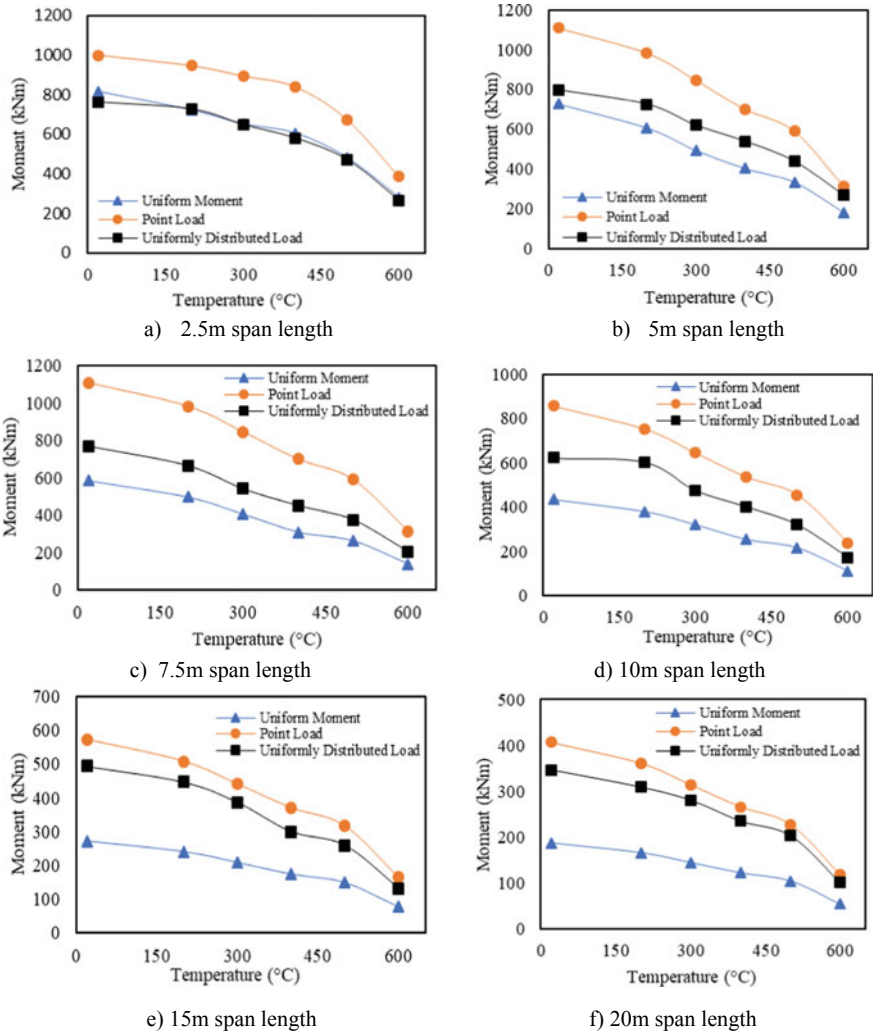


**Fig. 5** Moment against temperature curve under different loading cases

distributed load Fig. 7c, it is observed that for lower value of $\lambda_{LT,fi}$ ( < 1.45) gives conservative values and for larger $\lambda_{LT,fi}$ ( > 1.45) provides unconservative results.

In Fig. 8, numerical behaviour of the current data is compared with the present design methodology available in Eurocode 3. The comparison between the reduction factor obtained with the FE-model, i.e. $X_{LT,FEM,}$ and the reduction factor $X_{LT,EC}$ obtained from the design formula given in Eurocode 3 part 1.1, and Eurocode 3 part 1.2 (2005). The moment reduction factors that lie above the 45° line denotes that Eurocode 3 provides safe design values and below it unsafe. But in case of uniform

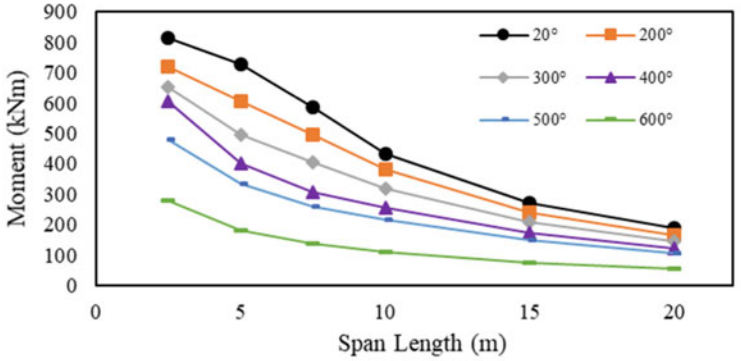


a) Uniform moment

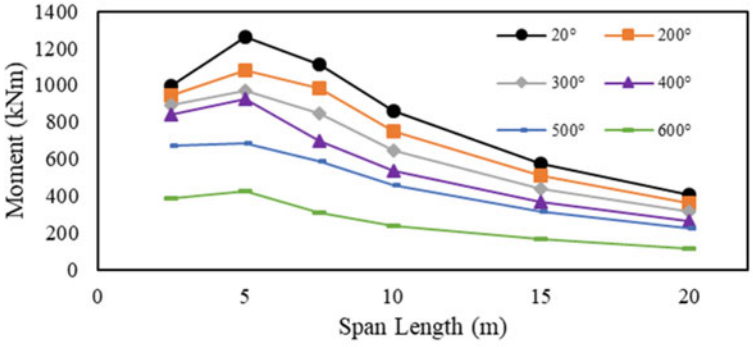


b) Point load

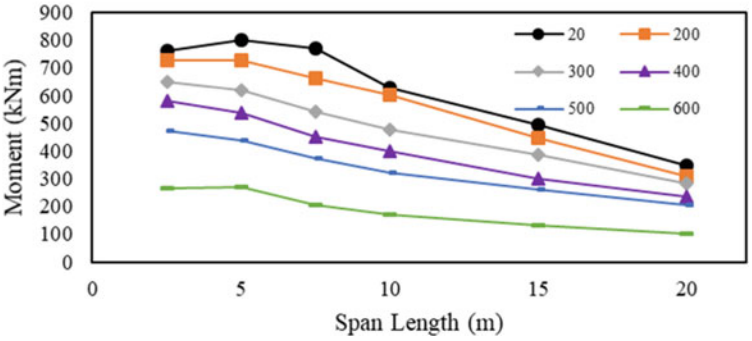


c) Uniformly distributed load

**Fig. 6** Moment capacity variation with span length

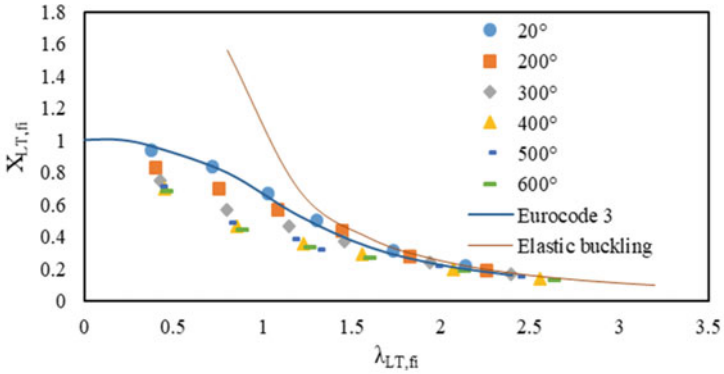


a) Uniform Moment

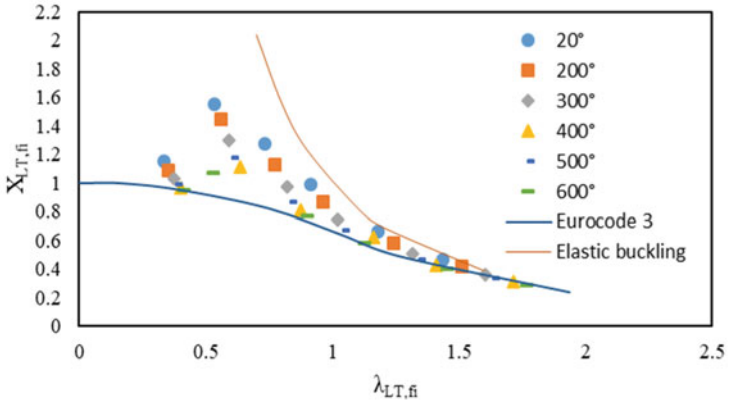


b) Point Load

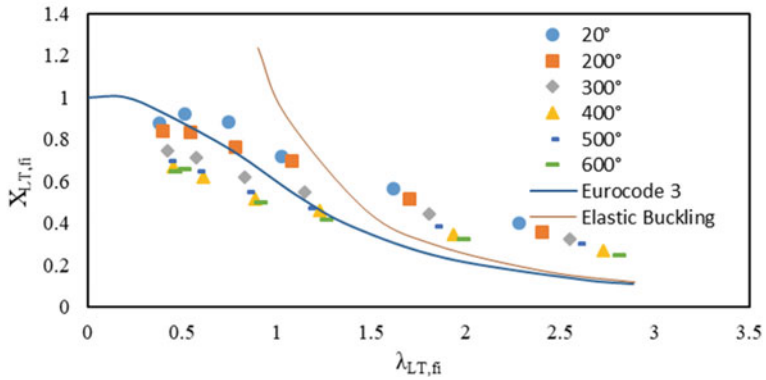


c) Uniformly distributed load

**Fig. 7** Buckling curve variation under different loading cases

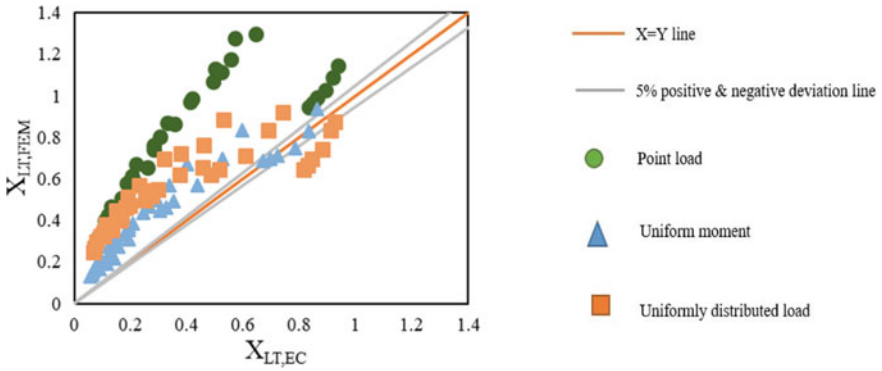


**Fig. 8** Numerical comparison of FEA data with theoretical calculation from Eurocode 3

moment and uniformly distributed load case for intermediate to shorter span beams, codified recommendations provide unconservative results.

## 5 Conclusions

The current study conducted on 216 full-scale 3D models of symmetric steel I-beam under uniform fire with the monotonically increasing flexural loading. It is observed from the numerical study that at elevated temperature the buckling capacity changes significantly compared to current design rules in Eurocode 3. Loading patterns have a vital effect on the moment capacity. The significant observations from the present investigation are as follows:

- LTB capacity of the steel beams decreases rapidly at elevated temperature due to rapid reduction in E and fy values.
- Dimensionless reduction factor $X_{LT,fi,}$ for all the loading cases increases as the slenderness of the beam decreases.
- Buckling capacity of the beam is reduced considerably with increase in slenderness ratio, and slope of buckling capacity becomes flatter.
- For the constant moment, and uniformly distributed load cases, for the intermediate to large slenderness beams, the design buckling curve provides over-conservative results.
- Beams having larger span length (15 m, 20 m considered here) provide higher ultimate moment capacity in present FEM analysis than the elastic buckling moment. These phenomena have not been addressed in current design provisions.
- For shorter spans in case of the constant moment and uniformly distributed load, FEM analysis provides unsafe results.
- For point load cases for all the slenderness values, Eurocode 3 provides over-conservative results.

- The loading condition is important for design consideration as it was observed from the present study. It affects the member capacity and may provide unsafe results. Thus, improvements are required in current design provisions under varying loading cases.

## References

1. ABAQUS/Standard Version 6.14, ABAQUS/CAE User's Manual (2014) Dassault Systèmes: Simulia Corp, Providence, RI, USA
2. Eurocode3 (EC3) (2005) Eurocode3: design of steel structures. part1–1: general rules and rules for buildings. European Committee for Standardization, Brussels, Belgium
3. Eurocode3 (EC3) (2005) Eurocode3: design of steel structures. part1–2: general rules - structural fire design. European Committee for Standardization, Brussels, Belgium
4. Lennon T (1997) BRE Cardington steel framed building fire tests. British Steel
5. Steel Construction Institute (1991) Structural fire engineering investigation of Broadgate phase 8 fire. Steel Construction Institute, Ascot
6. Roy K, Lim JB, Lau HH, Yong PM, Clifton GC, Wrzesien A, Mei CC (2019) Collapse behaviour of a fire engineering designed single-storey cold-formed steel building in severe fires. Thin-Wall Struct 142:340–357
7. Real PV, Franssen JM (2000) Lateral torsional buckling of steel I-beams in case of fire—numerical modeling. In: Proceedings of the first international workshop on structures in fire, pp 71–93
8. Real PV, Cazeli R, da Silva LS, Santiago A, Piloto P (2004) The effect of residual stresses in the lateral-torsional buckling of steel I-beams at elevated temperature. J Constr Steel Res 60(3–5):783–793
9. Real PV, Lopes N, da Silva LS, Franssen JM (2007) Parametric analysis of the lateral–torsional buckling resistance of steel beams in case of fire. Fire Saf J 42(6–7):416–424
10. Real PV, Lopes N, da Silva LS, Franssen JM (2008) Lateral–torsional buckling of stainless steel I-beams in case of fire. J Constr Steel Res 64(11):1302–1309
11. Real PV, Piloto PAG, Franssen JM (2003) A new proposal of a simple model for the lateral-torsional buckling of unrestrained steel I-beams in case of fire: experimental and numerical validation. J Constr Steel Res 59(2):179–199
12. Wong SY (2001) The structural response of industrial portal frame structures in fire. PhD thesis University of Sheffield, Sheffield, UK
13. Valeš J, Stan TC (2017) FEM modelling of lateral-torsional buckling using shell and solid elements. Procedia engineering 190:464–471

# Assessment of Thermal Insulation Applied to Structural Steel


**Y. K. Guruprasad**

**Abstract** In the present work, thermal blanket has been adopted as a thermal insulating material that is applied on the structural steel members as a thermal insulation measure, when the structural steel members are exposed to high temperature. In this work, a structural steel beam having an I section (ISMB450) having a span of 5 m is adopted with fixed end conditions exposed to a range of high temperatures (500ºC and 725ºC) separately. A heat transfer analysis in Abaqus is carried out to study the temperature distribution in the steel beam for different temperature exposures. The thermal blanket having different thicknesses is applied on to the surface of the steel beam along its entire span as thermal insulation. An optimum thickness of the thermal blanket is identified from this study that would insulate the steel beam from the temperature rise to take place on its surface, when exposed to high temperature based on the heat transfer analysis carried out such that, the thermally insulated steel beam is in stable condition when exposed to high temperature.

**Keywords** Fire · High-temperature exposure · Structural steel · Thermal insulation · Thermal blanket

## 1 Introduction

The buildings that exist in the cities at present are reinforced concrete structures, masonry structures, steel structures and composite structures (combination of steel and concrete). These structures undergo damage when they are subjected to external agencies such as earthquake, exposure to high temperature in the event of a fire, blast,

The original version of the chapter was revised: The author affiliation has been updated as Y. K. Guruprasad, BMS College of Engineering, Bangalore 560019, India. The correction to the chapter can be found at
https://doi.org/10.1007/978-981-19-9390-9_64

Y. K. Guruprasad (✉)
BMS College of Engineering, Bangalore 560019, India
e-mail: guruprasad.civil.iisc@gmail.com



M. Madhavan et al. (eds.), *Proceedings of the Indian Structural Steel Conference 2020 (Vol. 1)*, Lecture Notes in Civil Engineering 318,
https://doi.org/10.1007/978-981-19-9390-9_61

exposure to acidic or saline environments and due to erroneous design and structural detailing. When a fire breaks out in any of the types of structures mentioned above, the materials present in the structure undergo physiochemical changes. This physiochemical changes taking place in the materials cause loss of strength and stiffness in material, leading to reduced load carrying capacity and loss of stiffness of that particular structural component (beams, columns, slabs, ….). Concrete's composition makes it fire resistant and aligns it with all international building codes (IBC). Therefore, the drop in strength in concrete takes place when the temperature of exposure exceeds 250 °C onwards. There would be a drop in concrete strength to about 50% at a temperature exposure of 500 °C. The strength (compressive and tensile strength) along with the magnitude of elastic modulus of concrete drop steeply at temperature greater than 600 °C and the concrete at these temperatures becomes structurally unsound to carry loads. In the case of masonry structures exposed to high-temperature fires, the degradation in the masonry takes place predominantly at the joints due to degradation of the cement mortar at higher temperatures. Usually in masonry structures, the masonry units, especially the bricks made up of clay resist high temperatures to an extent, but the cement mortar at the joints tend to degrade in strength by cracking due to drying and shrinkage.

Steel is basically non-combustible. When steel gets heated to extreme temperatures, its strength significantly reduces. The international building codes suggest structural steel members to be insulated by fire resistant materials to enhance its safety and stability. The behaviour of steel structures when exposed to high temperatures in the event of a fire depends upon several factors that includes the material properties, restraint conditions [7], type of fire and the type and presence of thermal insulation. In a fire scenario, the temperatures in the steel members increase due to its high thermal conductivity. When steel gets exposed to high temperatures [8], its yield strength, tensile strength and modulus of elasticity tend to decrease.

This paper focusses on structural steel exposed to high temperature and thermal insulation of a structural steel I section beam. The loss of strength in steel tends to begin at about 250 °C to 300 °C, and then the drop in strength is fast for temperature exposure greater than 400 °C. At temperature exposures of 550 °C, steel tends to retain about 60% of its original yield strength and has a residual stiffness of 45%. Steel undergoes significant thermal elongation at high temperature exposures that leads to deformations in the form of distortions and buckling when it is restrained.

Egle et al. [1] studied to assess the critical temperature developed in structures that were exposed to non-uniform fires and compared it with uniform fires. In their work, a generic 10-storey steel framed building was modelled adopting a finite element package (LS-DYNA). The authors investigated 117 different scenarios are to cover a wide range of conditions of interest for design of steel structures, varying the fire exposure, floor where the fire exits, beam cross section details and applied fire protection (insulation) to the beams exposed to fire. The author's analysis predicted the structural failure at different exposure times, at different locations (floors) and various failure mechanisms. The author's work illustrated that, the critical temperature criterion does not predict accurately the structural failure in time, space or mode of failure of steel structures subjected to uniform fires and non-uniform fires. The

authors also stated that structural failure can be predicted by carrying out advanced structural analysis, and heat transfer analysis alone is not sufficient for design. The authors showed that, the use of the critical temperature leads to conservative results for simple steel structures.

Zhen [13] has studied the behaviour of retrained steel beams exposed to fire. The authors in their work established relationship between the responses of restrained steel beams and actions in fire, by adopting new definitions of fire resistance and new expressions related to fire loads. The authors made use of reduction factors of elastic modulus and yield strengths, and presented critical equations to predict the limit state of a restrained steel beam in a fire. Based on their equations and the heat transfer formulations, their work provided a new definition of fire resistance. The authors adopted the heat release rate and effective rate coefficient of thermal absorption, which is a new expression in fire loads. The authors compared the experimental test results with the proposed approach and it was found that their approach results were in good agreement with the measured values in tests.

Georgeta et al.'s [3] work identified different types of damages that take place in a steel structure exposed to fire. The authors presented a case study of the damages that had taken place in an industrial steel building subjected to fire. The authors pointed out that while designing a structure in the event of a fire, firstly one has to reduce the loss of life and secondly one has to take into account the load bearing resistance of the building for a time of fire exposure.

Peng-Chi et al. [10] worked on the development of non-destructive testing techniques to understand the structural behaviour of steel exposed to fire. The results the authors obtained from ultrasonic wave measurement, showed that, when the steel was heated up to 1000 °C and cooled by water, it produced a large change in the ultrasonic wave speed. When they observed the heated and cooled steel under a metallurgical microscope, the texture could be seen to have changed into bainite and martensite. The authors reported from their work that, due to phase change, the properties of the structure of steel transformed into hard and brittle.

Wald et al. [11] reported their results of a collaborative research project they carried out at different universities and research establishments. The authors carried out experimental tests to study the structural behaviour of a compartment on an eight-storey steel–concrete composite frame building at the Cardington laboratory during a BRE large-scale fire test, to examine the temperature developed within the various structural elements, and the corresponding development of internal forces and the behaviour of the composite slab, beams, columns and connections.

In this work, finite element analysis of a structural steel beam having an I section (ISMB450) having a span of 5 m with fixed end conditions, exposed to different temperatures (500ºC and 725ºC) with application of thermal insulation is carried out to understand the efficacy of the thermal insulation provided by the insulation having different thicknesses to protect the steel beam from temperature exposure. The details of the finite element model and the analysis carried out is discussed in Sect. 2.

**Objective of the work**: The main objective of this work is to assess the efficacy and optimum thickness of the insulation provided by the thermal blanket, by considering

two different insulation thicknesses applied around the steel beam along its entire span that is exposed to two temperatures, namely 500ºC and 725ºC. The efficacy of the thermal blanket insulation is assessed based on the temperature developed on the inner surface of the insulation, for an external temperature of exposure.

## 2 Finite Element Analysis of Structural Steel Beam Exposed to Different Temperature Exposure with Application of Thermal Blanket as Insulation

This section explains the details of the finite element model, the thermal properties of the insulation material applied and the type of analysis carried out.

### *2.1 Details of Steel Beam and Thermal Blanket*

A structural steel beam ISMB450 confirming to IS800 (2007) has been adopted for the analysis is shown in Fig. 1a. The details (in cross section) of thermal blanket insulation provided around the steel beam along the entire span has been shown in Fig. 1b. The steel beam has a span of 5 m and a yield strength 250N/mm$^2$. The thermal blanket adopted in the analysis confirms to [4]. The chemical composition of the thermal blanket is $Al_2O_3$ and $SiO_2$. The density of thermal blanket adopted is 128 kg/m$^3$. The thermal properties of the thermal blanket [2, 6] and Olaya C Perez [9] such as the thermal conductivity and specific heat versus different temperatures of exposure has been given in Table1. Thermal properties of steel such as conductivity and specific heat was referred from thermal data for steel sections (doi/https://doi.org/10.1002/9783433601570).

### *2.2 Details of Finite Element Model*

The thermal blanket insulation was modelled in three dimensions in the finite element model adopting three-dimensional hexagonal heat transfer elements with a mesh size of 0.01. A structured mesh technique is adopted.

It has to be noted here that the thermal insulation was examined in the finite element analysis, to study the heat transfer across the thickness of the insulation layer to check the temperature developed on the inner surface of the insulation for an external exposure temperature. Based on the temperature developed on the inner surface of the thermal insulation, one could assess the temperature that would be transferred to the steel beam.

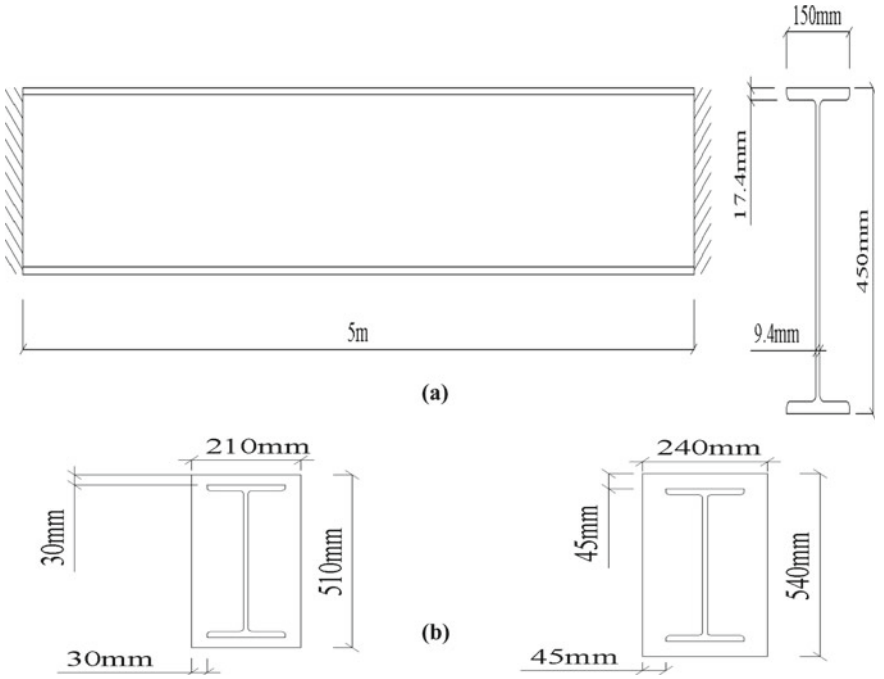


**Fig. 1** (**a**) Steel beam ISMB450 (**b**) Thermal blanket insulation provided around the steel beam for insulation thickness of 30 mm and 45 mm

**Table 1** Thermal properties of thermal blanket versus different temperatures

| Temperature °C | Thermal conductivity (W/mK) | Specific heat (J/(KgK) |
|---|---|---|
| 20 | 0.001 | 1017 |
| 200 | 0.12 | 1070 |
| 400 | 0.15 | 1100 |
| 600 | 0.19 | 1130 |
| 800 | 0.26 | 1130 |

Heat transfer analysis was carried out by applying the temperature as an instantaneous value of 500 °C and 725 °C on the exterior surface of the three-dimensional FE model of the steel beam and the thermal blanket insulation having different thicknesses (30 mm and 45 mm).

Figure 2 shows the three-dimensional finite element model of the ISMB 450 steel beam. Figure 3 shows the three-dimensional finite element model of the thermal blanket insulation applied around the steel beam having a thickness of 30 mm and 45 mm, respectively.

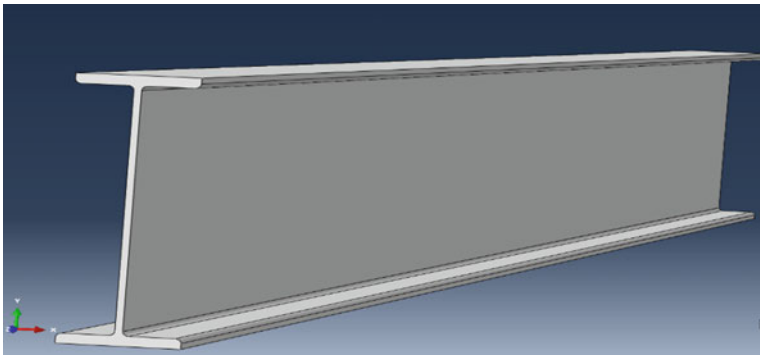

**Fig. 2** (**a**) Finite element model of the ISMB 450 steel beam; Temperature distribution in the steel beam for exposure temperatures (**b**) 500 °C; (**c**) 725 °C

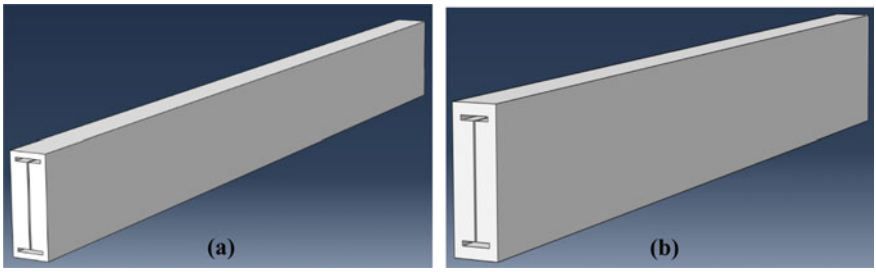


**Fig. 3** Three-dimensional finite element model of the thermal blanket insulation applied around the steel beam having (**a**) 30 mm and (**b**) 45 mm thicknesses

## 3 Results and Discussions

### *3.1 Main Sections*

This section presents the results and discussions of the finite element analysis carried out. The temperature distribution in the steel beam for exposure temperatures of (b) 500 °C; (c) 725 °C have been shown in Figs. 4a and b, respectively. The temperature distribution in the thermal blanket for a temperature exposure of 500ºC has been shown in Fig. 5 a for thermal blanket thickness of 30 mm and Fig. 5b for thermal blanket thickness of 45 mm. The temperature distribution in the thermal blanket for a temperature exposure of 725ºC has been shown in Fig. 6 a for thermal blanket thickness of 30 mm and Fig. 6b for thermal blanket thickness of 45 mm.

The temperature distribution in the steel beam for temperature exposures of 500 °C and 725 °C are shown in Figs. 4a and b, respectively. It can be observed from Figs. 4a and b the temperature developed on the bottom flange and web of the steel beam is

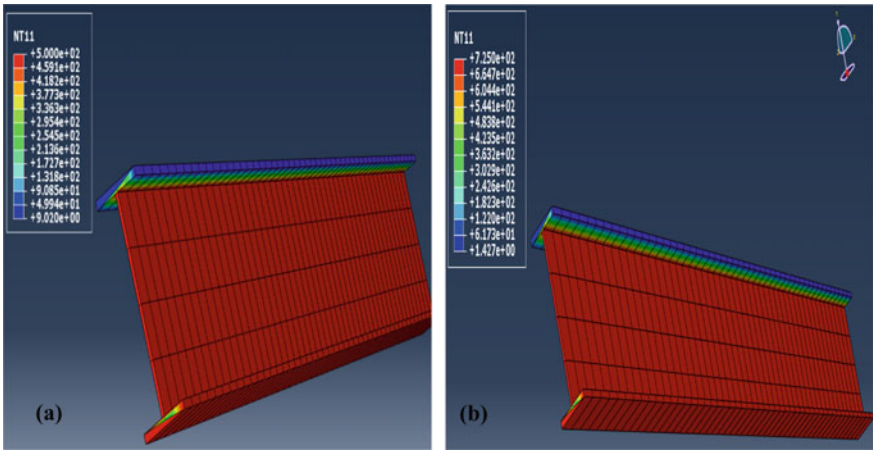


**Fig. 4** Temperature distribution in the steel beam for exposure temperatures: (**a**) 500 °C; (**b**) 725 °C

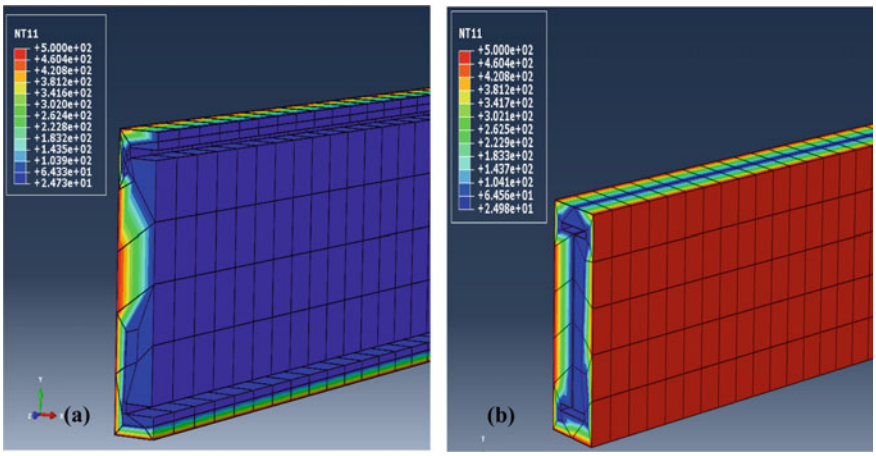


**Fig. 5** Temperature distribution in the thermal blanket for a temperature exposure of 500ºC (**a**) For thermal blanket thickness of 30 mm; (**b**) For thermal blanket thickness of 45 mm

equal to the external temperature of exposure. There is variation of temperature that is observed under the top flange.

It can be observed from the temperature distribution from Fig. 5a, the maximum temperature developed on the inner surface of the thermal blanket insulation in contact with the steel beam having a thickness of 30 mm is about 64 ºC for an external exposure temperature of 500ºC. Since the magnitude of the temperature developed is less than 200 ºC, there would not be reduction in the strength or stiffness of the steel beam. Therefore, the thermal insulation of 30 mm has been effective to protect the steel beam for an external exposure temperature of 500ºC.

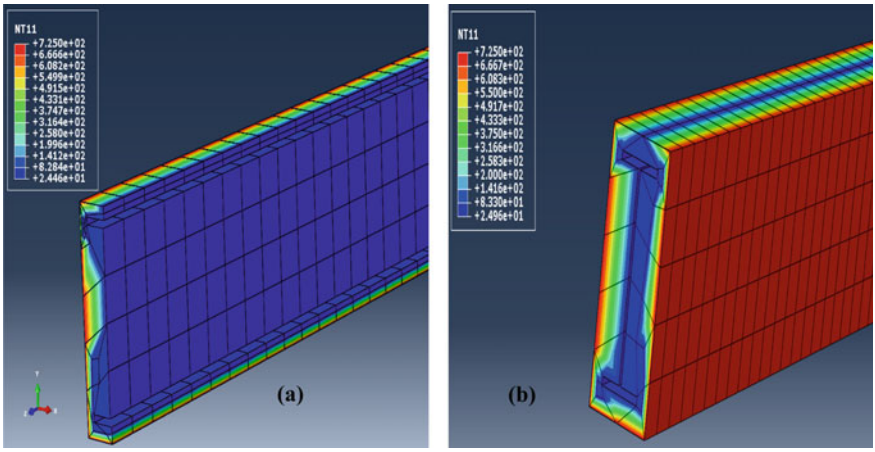


**Fig. 6** Temperature distribution in the thermal blanket for a temperature exposure of 725ºC (**a**) For thermal blanket thickness of 30 mm; (**b**) For thermal blanket thickness of 45 mm

It can be observed from the temperature distribution from Fig. 5b, the maximum temperature developed on the inner surface of the thermal blanket insulation in contact with the steel beam having a thickness of 45 mm is also about 64 ºC for an external exposure temperature of 500ºC. Since the magnitude of the temperature developed is less than 200ºC, there would not be reduction in the strength or stiffness of the steel beam. Therefore, the thermal insulation of 45 mm has been effective to protect the steel beam for an external exposure temperature of 500ºC.

It can be observed from the temperature distribution from Fig. 6a, the maximum temperature developed on the inner surface of the thermal blanket insulation in contact with the steel beam having a thickness of 30 mm is about 82.8 ºC for an external exposure temperature of 725ºC. Since the magnitude of the temperature developed is less than 200ºC, there would not be much reduction in the strength or stiffness of the steel beam. Therefore, the thermal insulation of 30 mm has been effective to protect the steel beam for an external exposure temperature of 725ºC.

It can be observed from the temperature distribution from Fig. 6b, the maximum temperature developed on the inner surface of the thermal blanket insulation in contact with the steel beam having a thickness of 45 mm is about 83ºC for an external exposure temperature of 725ºC. Since the magnitude of the temperature developed is less than 200ºC, there would not be much reduction in the strength or stiffness of the steel beam. Therefore, the thermal insulation of 45 mm has been effective to protect the steel beam for an external exposure temperature of 725ºC. It is observed from the results that, the inner surface temperature of the thermal blanket insulation in contact with the steel beam for both thicknesses of 30 mm and 45 mm is about 64ºC for an external temperature exposure of 500ºC and about 83ºC for an external temperature exposure of 725ºC, respectively. The results clearly indicate, the thermal blanket is efficient in insulating the steel beam from temperature exposures of 500ºC and 725ºC. It is learnt and inferred from this observation that, since the temperature

variation is not much for both the thicknesses of the thermal blanket for a common external temperature, the optimum thickness of the thermal blanket for temperature exposures of 500ºC and 725ºC is 30 mm.

## 4 Conclusion

- Structural steel sections begin to loose strength at about 250–300 °C, and the strength drops rapidly after temperature exposure exceeds 400 °C. For temperature exposure of 550 °C, the steel retains approximately 60% of its room temperature yield strength and 45% of its stiffness.
- It is observed from the results obtained for the bare steel beam (ISMB450) exposed to temperatures of 500 °C and 725 °C has the temperature developed on the surface of the bottom flange, and on the surface of the web to be equal to the external exposure temperatures.
- By studying the results it is observed that, the inner surface temperature of the thermal blanket insulation in contact with the steel beam for both thicknesses of 30 mm and 45 mm is about 64ºC for an external temperature exposure of 500ºC and about 83ºC for an external temperature exposure of 725ºC, respectively.
- The results presented indicate that, the thermal blanket is an efficient insulation to protect the steel beam from temperature (500ºC and 725ºC).
- It is inferred from this study that, an optimum thickness of the thermal blanket equal to 30 mm is sufficient to insulate and protect the steel beam for temperature exposures of 500 °C and 725 °C, respectively.

## References

1. Egle R, Panagiotis K, Ann J, Guillermo R (2019) Computational analysis of thermal and structural failure criteria of a multi-storey steel frame exposed to fire. Eng Struct 180:524–543
2. Ferri A, Fabio R, Giorgio M, Giorgio R, Silvio S (2012) Thermal properties of wool fabrics treated in atmospheric pressure post-discharge plasma equipment. J Eng Fib Fabric 7(3):75–81
3. Georgeta B, Teofil-Florin G, Sergiu-Andrei B (2017) Behavior of steel structures under elevated temperature. Procedia Engineering 181:265–272
4. IS 15402 (2003) Ceramic fibre blanket insulation. Bureau of Indian Standards
5. IS800 (Third Revision) (2007) General construction in steel—Code of practice. Bureau of Indian Standards
6. Kawamura H, Ishitsuka E, Tsuchiya K, Nakamichi M, Uchida M, Yamada H, Nakamura K, Ito H, Nakazawa T, Takahashi H, Tanaka S, Yoshida N, Kato S, Ito Y (2009) Development of advanced blanket materials for solid breeder blanket of fusion reactor, FT/P1–09
7. Moss PJ, Buchanan AH, Seputro J, Welsh R (2003) Effect of support conditions on the behaviour of steel beams in fire. Aust J Struct Eng 5(2):89–100
8. Nwosu DI, Kodur VKR (1997) Steel structures exposed to fire—a state-of-the-art report. NRC Publications Archive. Internal Report (National Research Council of Canada. Institute for Research in Construction), 1997–12–01. https://doi.org/10.4224/20337843

9. Olaya CP (2012) The behavior of aerogel blankets as insulation material in external walls at high temperatures, Master of Science Thesis, Department of Civil and Environmental Engineering, Division of Building Technology Building, Physics, Chalmers University Of Technology, Göteborg, Sweden
10. Peng-Chi P, Jen-Hao C, Jyin-Wen C (2016) A study on behavior of steel structures subjected to fire using non-destructive testing. Constr Build Mat 128:170–175
11. Walda F, Simo˜es da Silvab L, Moorec DB, Lennond T, Chladna'e M, Santiagob A, Benes˘a M, Borgesf L (2006) Experimental behaviour of a steel structure under natural fire. Fire Saf J 41:509–522
12. Guo Z, Gao R, Zhang X, Jia X (2018) Fire resistances of restrained steel beams subjected to fire loads. KSCE J Civ Eng 22(8):3028–3038

# A Review on Progressive Collapse with All-Steel Buckling Restrained Braced Frames


**P. C. Gopika Balagopal and B. Rajeevan**

**Abstract** Steel braces are adopted in framed structures for providing adequate resistance to lateral loads like seismic loads. Under seismic loads, braces tend to buckle and under periodic loading, and they have less strength, stiffness, and resistance. All-steel buckling restrained braces are found to be excellent in dissipating energy caused due to catastrophic events. Recently, progressive collapse of framed structures has become an important topic of research since many buildings have collapsed due to this event. The structural designers require to design structural members to carry and dissipate huge stresses caused due to catastrophic loading. Although there exist different types of bracing systems like concentric bracing, eccentric bracing, and buckling restrained bracing, not many studies have been conducted to study the response of these bracing systems under progressive collapse scenario. In order to study the behaviour of all-steel buckling restrained braced frames towards progressive collapse, a brief review of literatures was conducted. Also, a review was conducted to determine the resistance offered by different types of braces when subjected to progressive collapse.

**Keywords** Brace · Collapse · Frame · Progressive · Pushdown · Steel

## 1 Introduction

As fragments of crustal rock slide out and move unexpectedly, an earthquake occurs and releases enormous energy which spreads like seismic waves through the crust. Structural engineers should design structures in such a way that the built structures are able to dissipate this energy so that they can stand erect and stable. There are many methods available for dissipating energy in the past. Conventional bracings were

P. C. G. Balagopal (✉) · B. Rajeevan
Government College of Engineering, Kannur, India
e-mail: gopika.off@gmail.com

B. Rajeevan
e-mail: rajeevan@gcek.ac.in



M. Madhavan et al. (eds.), *Proceedings of the Indian Structural Steel Conference 2020 (Vol. 1)*, Lecture Notes in Civil Engineering 318,
https://doi.org/10.1007/978-981-19-9390-9_62

one amongst them. However, conventional braces have the drawback of degrading response under compression due to buckling. All-steel buckling resistant braces were developed to overcome this drawback of conventional braces. The design varies according to the type of frame. A framed structure is defined as a structure which consists of beams, columns, and slabs acting as the load carrying elements which resist the lateral and gravity loads. These structures can stand stable as a rigid structure by carrying load and deforming themselves, without depending on floors to resist deformation.

## 2 Classification of Frames as Per ASCE 7-2016

ASCE 7 2016 deals with the calculation of minimum loads for the design of different structures which classifies frames as braced frames and moment frames. The classification of frames is represented in Fig. 1.

### *2.1 Braced Frames*

The frames which act like a vertical truss to resist seismic forces are called braced frames. The braces carry lateral loads like wind and seismic loads. Braced frames are of two types: (i) concentrically braced frames and (ii) eccentrically braced frames.

#### 2.1.1 Concentrically Braced Frames (CBFs)

If the braced members are connected at the beam column junction or at another diagonal brace concentrically, i.e. the centroids of all the members connecting at

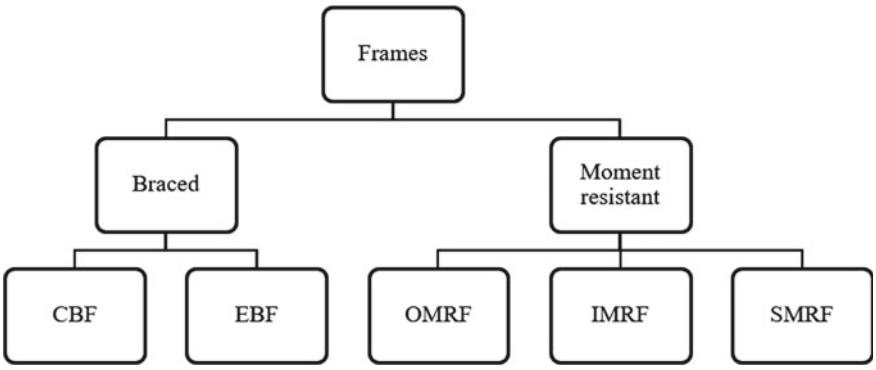


**Fig. 1** Classification of frames as per ASCE 7-2016

that point coincide, it is called concentric braced frame (CBF). The members are mostly subjected to axial forces. CBF is further classified into ordinary concentric braced frames (OCBFs) and special concentric braced frames (SCBFs). OCBFs are used in low seismically prone areas. SCBF has extensive design requirements for the members to ensure high ductility and is, hence, used in highly seismically prone areas.

#### 2.1.2 Eccentrically Braced Frames (EBF)

If the ends of the brace are connected some distance apart from the beam column joint or from another diagonal brace in a frame, it is called eccentrically braced frame (EBF). The braces in an EBF carry axial load induced on it due to the applied loading. Shear and flexure occur in a small segment of a beam, called the active link and are transferred to nearby columns and braces. Link is the most critical member in an EBF and acts as fuse by yielding when a huge amount of energy is to be transferred often in case of an abnormal event. These frames possess both truss like characteristics which provide sufficient stiffness and also some characteristics of moment resisting frame which provide sufficient ductility. As the link length decreases, elastic frame stiffness increases, but lower limit of link length is dependent on how much ductility is provided by the active link. When compared to a moment resistant frame, eccentric braced frames are better and effective in satisfying the requirements to control drift; thus, member sizes are reduced, and bending moment transferred by beams to columns is less, thus making the connections cheaper [1].

### *2.2 Moment Resistant Frames*

If the lateral forces are resisted by the members as well as by the beam column joints by bending or by flexure, along the axis of the member, such frames are called moment frames. They are classified into three types, such as ordinary moment resistant frames (OMRFs), intermediate moment resistant frames (IMRFs), and special moment resistant frames (SMRFs).

#### 2.2.1 Ordinary Moment Resistant Frames (OMRFs)

Ordinary moment resistant frames are adopted in areas with low seismic risk. They cannot withstand much inelastic deformations as they are not designed for much ductility. The connections in an OMRF need not be prequalified or tested, and their design is much simpler as there are no special requirements to ensure enough ductility, so they are the least ductile.

### 2.2.2 Intermediate Moment Resistant Frames (IMRFs)

These are adopted in areas of moderate seismic risk and should sustain moderate inelastic deformation. The connections in IMRF should be prequalified, and it should carry at least 0.02 radians as inter-storey drift angle. Therefore, they are moderately ductile.

### 2.2.3 Special Moment Resistant Frames (SMRFs)

Special moment frames are adopted in highly seismically prone areas, and only prequalified connections can be used. It should sustain at least 0.04 radians as inter-storey drift angle and higher inelastic deformation than IMRF. Therefore, they are highly ductile. The difference in ductility of various moment resistant frames is shown in Fig. 2.

## 3 Conventional Energy Dissipation Methods

Earlier, the method of energy dissipation in structures was confined to the beam column connections as much of the energy absorption is developed in their vicinity. Later, it was found that these connections deteriorate, and the energy dissipation becomes weak due to cyclic loads caused during earthquake. The concept of using metal devices within a framed structure to capture large parts of the seismic energy by yielding is very old.

Tremblay et al. [21] evaluated the performance of concentric frames braced with cold formed hollow rectangular tubular members under cyclic or seismic loads. It was

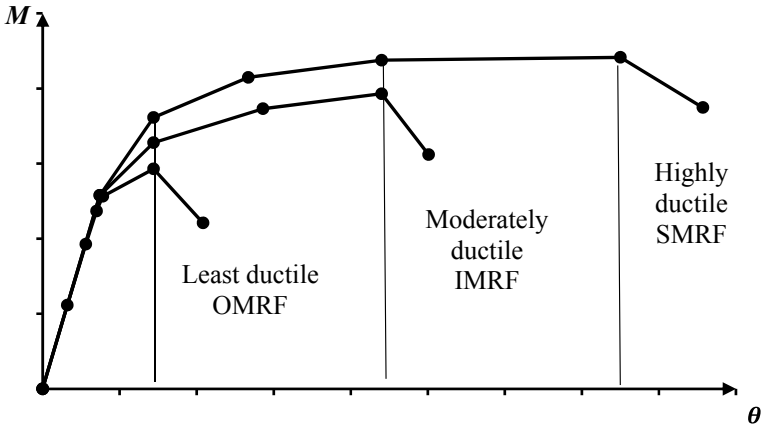


**Fig. 2** Difference in ductility of OMRF, IMRF, and SMRF

shown that X-braced frames were less efficient compared to single diagonal braced frames. When these are subjected to cyclic loads in a quasi-static way, the dynamic effects of earthquake will not come into existence. The main difference between the X-bracing and single diagonal bracing is that the tension brace provides a support to the brace in compression at the mid-point and the brace bends in a double curvature in X-bracing, whilst there is no support to the brace in single diagonal bracing, and it bends in single curvature. In X-bracing, due to this double curvature, it shows comparatively large out of plane deformations and fails at lesser level of ductility than single diagonal bracing.

In concentrically braced frames, the compression braces absorb energy and show dissipation capability and strength reduction of these occurs due to cyclic loads. Tests were conducted on braces having various cross sections like tubular section and W shaped section. The effectiveness of each cross section in dissipating energy was assessed. Amongst the cross-sectional shapes tested, tubular section showed the least reduction in compressive strength. For W shaped cross section of braces, the strength reduction is more for braces with slenderness ratio more than 80, whereas for braces with slenderness ratio between 120 and 160, the compressive strength degradation was not significant [13].

## 4 All-Steel Buckling Restrained Braced Frames

Conventional buckling resistant braces consisted of a buckling restrained sheath encasing a steel core. Some slippery material is provided in between the steel and sheath to avoid unwanted interaction between the two. The axial load is taken by steel core, and outer tube prevents global buckling and provides lateral support to the inner core. The frames in which buckling restrained braces (BRB) are provided are called buckling resistant braced frames (BRBF). These are a good alternative to conventional energy dissipation systems which dissipate and absorb the seismic energy efficiently without causing much damage to the structure. Figure 3 shows the behaviour of buckling brace and BRB.

BRBs can carry both axial load and cyclic loads due to seismic activity. The steel core carries axial load only and is generally built of materials with high ductility. The external buckling restrained system restricts the lateral displacements of the inner core and thus provides global stability to the brace, thereby experiencing shear and bending. To account for this, the outer sheath was conventionally built of concrete. But such braces were found to be too heavy, and the maintenance cost, construction cost, cost of transportation, placing, etc., were huge.

There are many differences between conventional concentric or eccentric bracing and buckling resistant bracing in their design aspects. Generally, standard sections are used for conventional braced frames, but mostly fabricated sections are used in case of BRBF. A BRB assembly restricts the buckling of the core section, and the compressive yield strength is almost comparable to the tensile yield strength, whereas conventional braces fail by buckling because they have greater tensile yield

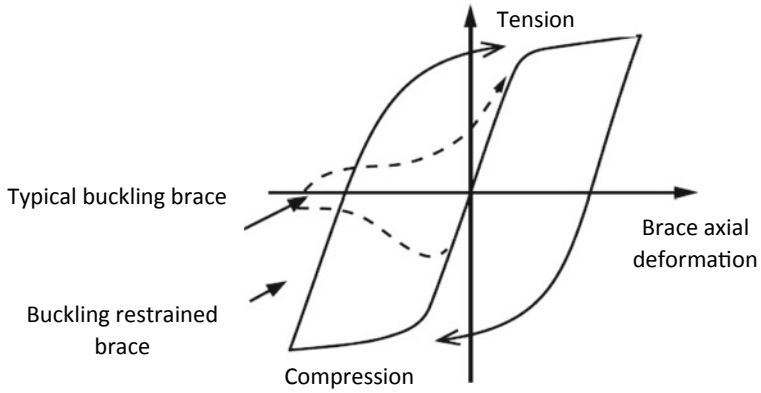


**Fig. 3** Behaviour of buckling brace and BRB (*Source* NIST GCR 2015)

strength, but comparatively less compressive yield strength. Conventional braces have degrading cyclic response, whereas BRB has repetitive and stable hysteric behaviour. BRBs perform well in tension and compression by yielding axially, and it shows an almost symmetric response under cyclic loads which also indicates strain hardening [16]. Behaviour of buckling brace and buckling restrained brace is shown in Fig. 3.

The concrete external sheath was replaced by steel, which made the overall brace lighter and thus the process of manufacturing and providing the brace in a frame more economical. Then, the space between the external sheath and inner core was filled by concrete or some slippery material, but the analysis of such braces became difficult due to the complexity of boundary conditions which existed between the core and external sheath. Thus, the introduction of slippery material was avoided, and the gap was left as such, i.e. introduction of air gap came into existence. This was the starting of developments in all-steel buckling resistant brace. Some configurations in which buckling restrained braces can be fitted onto a frame are also given in and are represented as in Fig. 4 (a) to (e):

All-steel BRBs were first suggested by [3], in which braces does not require slippery material or mortar between the steel core and sheath, so that boundary conditions between elements are not too complex. Along the buckling direction, a gap was created between steel core and sheath, and the purpose of this gap was to control the sheath. They have stable mechanical characteristics than conventional BRBs. The hysteric behaviour of such devices was found to be stable, ductile, and repeatable in nature. Buckling restrained braces are capable of withstanding maximum ductility demand and cumulative ductility demand as given by Eqs. (1) and (2), where $\Delta_{max}$ is the BRB maximum deformation, $\Delta_{plastic}$ is the BRB plastic deformation, and $\Delta_{by}$ is the BRB yield deformation.

$$\mu_{\max} = \frac{\Delta_{\max}}{\Delta_{by}} \tag{1}$$

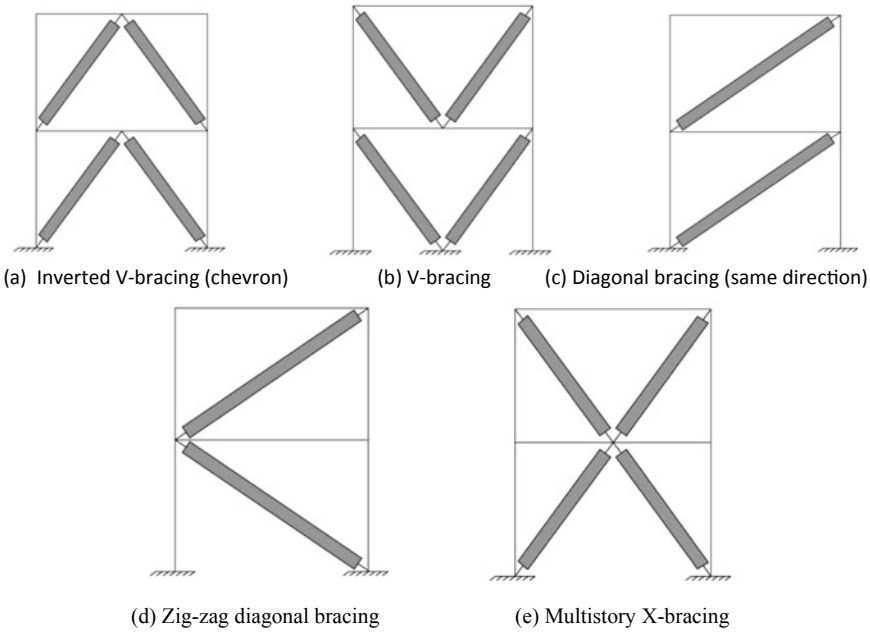


**Fig. 4** Some configurations of providing buckling restrained brace in a frame. (**a**) Inverted V-bracing (chevron), (**b**) V-bracing, (**c**) diagonal bracing (same direction), (**d**) zig-zag diagonal bracing, (**e**) Multistorey X-bracing

$$\mu_c = \frac{\sum \Delta_{plastic}}{\Delta_{by}} \tag{2}$$

NIST GCR (2005) suggests that area of core section for CBF is determined based on critical buckling stress ($f_{cr}$) whilst that of buckling restrained braced frames is determined considering the yield stress of core ($f_{ysc}$). The response modification factor ($R$) as proposed by ASCE 7 2016 is very high for buckling restrained braced frames with a value of 8, whereas it is 3.25 for ordinary CBF and 6 for special CBF. This value indicates that buckling restrained braced frames are more ductile than the conventional braced frames. Due to the restriction of the brace against buckling behaviour, buckling restrained braced frames are more efficient since they require comparatively lesser area for the brace and therefore, more flexible than the other type. Similar to every ductile lateral load resisting system, frame members (beams, columns, and connections) are restrained from unwanted yielding by means of special analysis and provisions for proportioning, called capacity-based design concept.

A new type of all-steel BRB was suggested by [10] where he found out that irrespective of the gap size, the flexural stiffness of the buckling restraining sheath influences the overall buckling mode of the buckling restrained brace. A ratio of Euler buckling load of the sheath to the yield strength of the core is determined, and when this is less than 1.2, 0.2% strain is observed in the core, and when the ratio is

more than 1.2, no buckling is observed. Introducing a factor of safety 0.85, a value of Euler buckling load of the sheath to the yield strength of the core ratio is proposed to be greater than 1.4.

Hosseinzadeh and Mohebi [9] observed that 10 mm air gap proved to be the best of all, and if gap size was increased to more than 10 mm, it led to strength reduction because of local buckling of braces. This was determined by performing dynamic cyclic analysis and determining the backbone curves of ten different all-steel BRB specimens with varying dimensions of the size of the gap. Non-linear static analysis was then carried out in SAP 2000 software from which they found out that the area under hysteresis curves for cross bracing was much lesser than that of all-steel BRB, and hence, energy absorption capability was more for all-steel BRB. Ductility was more in all-steel BRBs than conventional cross bracing. For all-steel BRBs, the response modification factor was 50% more than that of normal cross bracings.

According to Takeuchi and Wada [20], there are some conditions to be satisfied in order to obtain a stable hysteric loop. These include (a) the first mode of buckling of the core of buckling restrained brace should be restrained by the sheath; (b) the core should be decoupled from the external sheath, and this mechanism results in making the BRB like a truss element which allows axial loads only and also allows Poisson's effect to occur in the core; (c) the bulging effect of the external sheath wall due to higher modes of buckling should be restrained; (d) the entire structure of BRB including connections in the BRB should be stable globally; (e) for the expected demand, only a low-cycle fatigue capacity is necessary to meet it.

A new configuration of all-steel buckling resistant brace was suggested by [22]. It consists of two core sections connected by sinusoidal corrugated plate in the Web portion, thus forming a cross section of an I-section, each contain a steel plate which were extended to some distance from the end. At these projections, another steel plate is provided which act as stiffeners for the two steel plates existing within the core section, called core stiffeners. The two steel plates, two core sections, core stiffeners, and the corrugated sheet together form the body of the all-steel buckling restrained brace. This configuration possesses stability, rigidity, high flexural stiffness, and heavy load carrying capacity. For small restraining ratio, before the core section attains section capacity, the brace undergoes global instability. When the restraining ratio is increased to a moderate level, it is found the global instability occurs after the core section attains its section capacity, but the cumulative inelastic axial deformation of the core section remains less than 2%. When the restraining ratio was large, global instability never occurred, and the cumulative value of the axial deformation in the inelastic range of the core section was more than 2%.

Another configuration of a buckling restrained brace was introduced by Jamkhaneh et al. (2018) in which Z-shaped profiles were used to connect three steel plates in parallel having necessary stiffness and strength as shown in Fig. 5. The Z-shaped profiles distribute the force between plates since they are placed parallel to the weak axis. Z-shaped profiles were provided in order to make the formation of plastic hinges in a direct way. Plastic hinge develops at both sides of each of Z-shaped profiles. Stiffness is very high in the connection locations, due to which, the axial forces in the column are reduced, and hence, their size can also be reduced. Floor

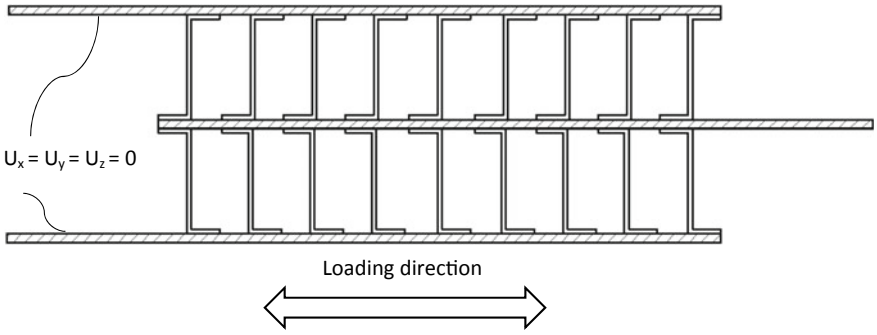


**Fig. 5** All-steel BRB with three steel plates and Z-profiles [2]

drift ratio, ductility, and behaviour factors in strengthened structures are found to be lesser than conventional cross bracing.

Solovyova et al. (2017) studied about the behaviour of BRB and found out that until the brace reaches enough ductility and plastic deformation, the entire structural frame will be protected from global buckling. It was suggested that Bouc-Wen hysteresis model which describes non-linear hysteric systems can be easily adopted for structural engineering simulation software. Such a formulation requires that the force on a brace can be expressed as displacement and velocity of its attachments. This model also considers the reduction of strength or stiffness and pinching in the hysteresis loop. Equation 3 represents Bouc-Wen model.

$$g(t) = u(t)\left\{B - \left[\beta sign(g(t)u(t)) + \gamma\right]|g(t)|^{p}\right\} \tag{3}$$

where $B$, $\beta$, $\gamma$, and $p$ are dimensionless values which controls the model behaviour and $\beta > 0$, g(t) and u(t) refer to the displacement and velocity at time t. An elasto-plastic hysteresis is indicated when $p = \infty$. When the value of $p$ is small, there will be a smooth transition from elastic to post elastic branch. But when the value of $p$ is more, then there exists a rough or fast transition. The shape and size of the hysteresis loop depend on the values of $B$, $\beta$, and $\gamma$.

Some applications of buckling restrained braced frames were mentioned in [20]. Some concepts of designing them are discussed here.

1. Damage tolerant concept—Under abnormal loading, some portions of the structure called structural fuses tend to carry the most of the energy to be dissipated, thereby making the main structure to be safe and intact. This concept is explained in Fig. 6.
2. Retrofitting structures using BRB—Already existing structures that are badly damaged due to abnormal loading conditions can be effectively retrofitted using BRB. These BRBs can be assembled and connected to existing braces also, but many a time, this can become a tedious procedure to install the braces without disturbing the dwellers.

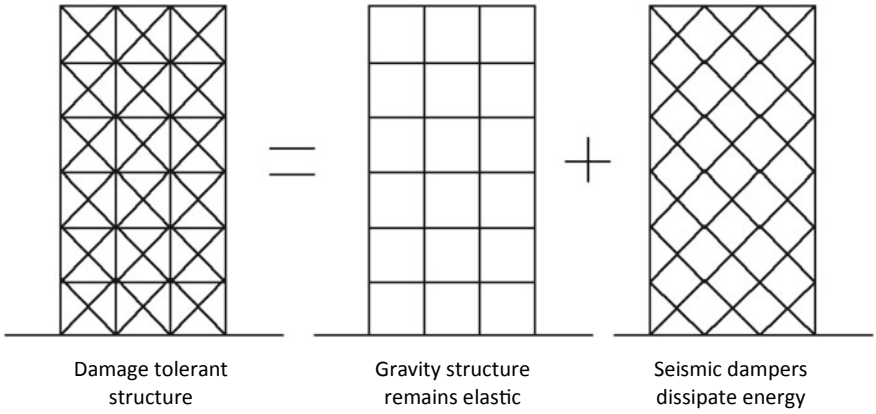


**Fig. 6** Concept of making a structure damage tolerant

3. Application of BRB in trusses—The critical members in a truss that undergo local buckling can be replaced with BRBs to resist the failure of such members. This considerably improves the energy dissipation and failure mechanism, thereby making the entire structure more stable. Communication towers can also be retrofitted using this method. Lattice roof structures can also be retrofitted using BRBs. The applications include fixing BRB or dampers on the roof of the lattice structure, the base isolation of the roof from the other part of the structure, retrofitting substructure of the lattice structure, and entire base isolation of the whole structure. Results indicate that the adoption of BRB to retrofit structures is found to be more effective and economical than using a strength based retrofit.
4. Spine frame concept—Recent advances in the field of energy dissipation techniques have found that the sole usage of BRB to resist lateral loads is not much effective due to the lesser stiffness in the post yield range. To avoid this drawback, BRBs are adopted as columns or as main structural members, along with a strong braced system, or they are incorporated into a spine frame or rocking frame.

## 5 Progressive Collapse

Progressive collapse or disproportional collapse is a situation which arises due to any abnormal loading due to which a load carrying primary element may fail locally. This leads to the failure of the surrounding members, which repeats and ultimately result into further collapses. Thus, the resulting local damage propagates through the structure leading to a large-scale damage or even resulting in the collapse of the entire structure [7].

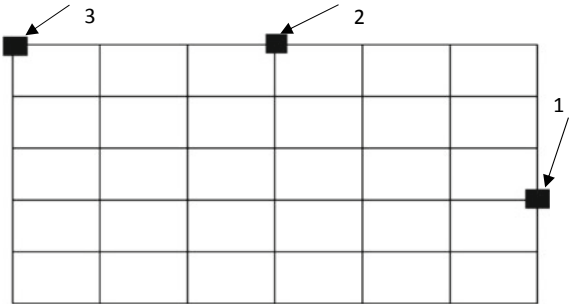


**Fig. 7** Locations where columns are removed as per GSA 2003

## *5.1 Modelling Approaches*

GSA 2013 specifies three types of column removal scenarios to be performed to initiate collapse as shown in Fig. 7. (i) Column at or near centre of short side, (ii) column at or near centre of long side, and (iii) column at the corner. The modelling of progressive collapse scenario can be done in two different ways, by microscopic modelling and macroscopic modelling. If the modelling of the structure is done in very good detail, i.e. if the structure is modelled with all intensive parameters, it is called microscopic modelling. It is very complex, results in continuum based detailed model, and is good for analysing local behaviour. Macroscopic model is said to be a simplified and component-based model and involves less computational effort unlike a microscopic model. Usually, it is not good for analysing at local level but is very efficient for almost all purposes and gives accurate results.

## *5.2 Evaluation Methodologies*

There are different methodologies through which progressive collapse can be analysed. These include both direct and indirect methods of analysis.

### 5.2.1 Direct Analysis

In direct analysis, the source of loading (earthquake, shock or wind) is explicitly modelled. It is a very detailed and time-consuming process because it makes use of an iterative process to establish equilibrium. Direct design method is a form of direct analysis in which actual loads causing failure are used to determine whether the structural collapse is initiated or not.

### 5.2.2 Indirect Analysis

Indirect analysis or threat independent method is the method in which the source of loading is not explicitly modelled. The load is already assumed to have been activated since the after-effects of the load are assumed to have occurred. Assume that a structural member is already failed, and then, the effects due to the failure of the member are analysed. Indirect method of analysis consists of redundancy or alternate path method (APM), specific local resistance method (SLRM), and interconnection or continuity method. SLRM specifies that progressive collapse may occur due to abnormal loads, and the load carrying capacity of the member should be such that there is not even a minute local damage to the structure, even at the point where abnormal load initiates (Gross et al. 1983).

Specific local resistance can be imparted into a structure by the addition of critical elements. The terrorist attack of world trade centre in 1993 can be treated as a well-known example of a building to withstand progressive collapse only because of its local resistance. The columns were too heavy which was designed so just for supporting the extraordinary load above, but it turned out to be the reason why it stood stable after the attack. Even if it was designed for redundancy, it would have collapsed if the column size was small. But the disadvantage of using this method to design building against progressive collapse is that the nature and point of attack should be known well before, but that is impossible in a real scenario [16].

Alternate path method investigates the alternative ways by which load redistribution occurs when a member is removed. The advantage is that it remains stable for any hazard which leads to the removal of the member. Here, local damages at the surrounding near the point of application of the abnormal load are allowed, but there should exist alternate path through which the structure can dissipate energy [16] and Gross 1983.

Interconnection or continuity method is a method of either increasing the specific local resistance or redundancy or both. Interconnection between structural elements helps in transmission of loads through these in case of any local failure. Structural integrity or interconnection will guarantee that at the time of a catastrophic event the resulting failure will be localised, and the structure will be able to stand stable.

## *5.3 Analytical Methods for Progressive Collapse*

There are four methods to analyse effect of progressive collapse like linear elastic static analysis, non-linear elastic static analysis, linear elastic dynamic analysis, and non-linear elastic dynamic analysis, depending on the material properties and behaviour considered [14].

### 5.3.1 Linear Elastic Static Analysis

Linear static method is the most effortless and basic method to analyse progressive collapse although it is an approximate method. To account for the dynamic characteristics of application of load, a load combination of $2 \times (DL + 0.25LL)$ is provided for linear static approach. The factor 2 stands as a dynamic amplification factor, i.e. although using static approach, to get the dynamic response as proposed by GSA 2013. The demand to capacity ratios is evaluated by taking the ratio of bending moment at the point ($M_{\max}$) to the ultimate bending moment ($M_{\mathrm{p}}$), and DCR value should not be more than the values specified by GSA [7].

### 5.3.2 Non-linear Static Analysis

Non-linear static analysis method is commonly called pushover analysis. In this method, loads are applied without dynamic effects. There are two ways of doing pushover analysis. One method is by adopting a load controlled approach, and the other is through a displacement controlled approach. The applied loads are increased gradually in steps until maximum load is attained in load controlled approach, or maximum displacement is attained in displacement controlled approach. It is generally given as load controlled manner because in progressive collapse analysis, the response under service loads is to be evaluated to determine its potential against progressive collapse. At the joints between members, local non-linear structural effects like flexural hinges are provided. The deformation in the structure increases due to load application, and the structure is pushed harder until either a collapse mechanism forms or hinges reach the plastic deformation limit. Verification can be done by comparing the results with GSA 2013 specifications like support rotation measured between horizontal line and tangent to maximum deflected shape, $\theta \leq 12°$, and ductility calculated as a ratio of maximum inelastic deflection to elastic limit, $\mu \leq 20$, where, $\mu$ is the ductility, $\delta_{\max}$ is the maximum inelastic.

### 5.3.3 Linear Dynamic Analysis

Linear dynamic analysis is also called linear elastic time history analysis. It uses real time linear elastic motion because it involves the real time removal of members. Dynamic procedures inherently incorporate dynamic amplification factors, inertia, and damping forces, which is not a feature of non-linear static procedure. Hence, this method is comparatively more accurate when compared with static analysis procedures. This method is limited to structures which do not exhibit large plastic deformations. In SAP 2000, there are two methods of doing linear dynamic analysis. These are modal superposition method and direct integration method. Verification method is same as that of linear static analysis.

### 5.3.4 Non-linear Dynamic Analysis

Non-linear dynamic analysis of progressive collapse is the most tedious method. In this method, a primary load bearing structural element is removed dynamically, and the structure is allowed to undergo non-linear behaviour due to which large deformations and energy dissipation occurs through material yielding, cracking, and fracture. It is done almost similar to linear dynamic analysis except that now the structural elements are allowed to enter their inelastic range. It provides most realistic results since it includes material non-linear behaviour and dynamic behaviour. Verification method is same as that of non-linear static analysis.

FEMA 356 (2000) mentions that post yield behaviour indicated the formation of plastic hinges as shown in Fig. 8. In non-linear analyses, plastic hinges should be modelled and assigned to members. When elastic limit is exceeded, member enters non-linear stage. The deformations in this stage occur directly in the assigned plastic hinges. Plastic hinges are the yielding zones developed in a structural element which is subjected to loads causing enormous amount of strain at a yield stress. Plastic hinges are generally formed at the following positions in a beam points under concentrated loads, at supports, at points of maximum bending moment. The methods of analysis of progressive collapse considering non-linear behaviour involve the generation of plastic hinges at these locations. There are different types of plastic hinges. Rigid plastic hinges include the force and moment hinges. There are six degrees of freedom for a plastic hinge. The behaviour of plastic hinges is shown by force–displacement and moment-rotation curves. Force–displacement curves are drawn to indicate the degrees of freedom related to forces (axial force and shear force), and moment-rotation curves are drawn for degrees of freedom related to moments (bending and torsion) [4].

In order to provide moment curvature data for hinges, FEMA 356 provides certain guidelines. Yield moment and plastic moment for beams can be calculated by $M_y =$

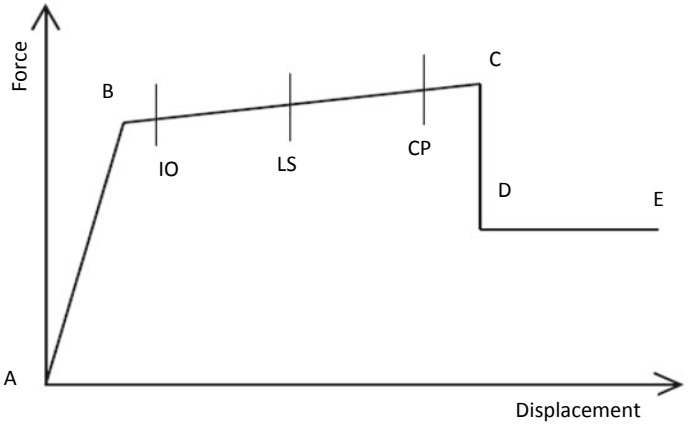


**Fig. 8** A-B-C-D-E curve for force versus displacement

$Z_e f_y$ and $M_p = Z_p f_y$, respectively, where $M_y$ is the yield moment, $M_p$ is the plastic moment, $Z_e$ and $Z_p$ are the elastic and plastic section modulus, $f_y$ is the yield stress. For columns, plastic moment can be obtained as

$$M_p = 1.18 Z_p f_y \left(1 - \frac{P}{P_y}\right) \tag{4}$$

where $P$ and $P_y$ are the axial force and expected axial yield load. Curvature can be expressed as follows: where $\varnothing_p$ is curvature for plastic moment $M_p$.

$$\Phi_p = \frac{M_p}{EI} \tag{5}$$

Izzuddin et al. [11] suggested that although non-linear static approach does not yield very accurate results, when considering a frame and by analysing its progressive collapse, non-linear static analysis yields almost equivalent results as that obtained from the very accurate non-linear dynamic method. They also discuss about another novel method using the concept of energy method, which involves a major assumption that only a single deformation mode influences the overall structural response.

Khandelwal et al. [12] observed that concentrically and eccentrically braced systems benefit from locating seismic systems on perimeter of buildings, and eccentrically braced frames designed for high seismic risk were less vulnerable to gravity-induced progressive collapse than special concentrically braced frames designed for moderate seismic risk. This advantage of eccentrically braced frames over special concentrically braced frames stems essentially from an improved system layout rather than activation of ductile detailing. Although shear tab connections impart more ductility to the structure, if a gravity column is removed, then, it cannot resist progressive collapse. In buildings where blast or an external threat is common and if gravity-induced progressive collapse is a design consideration, gravity columns should not be placed in perimeter. The designers must determine resistance to collapse of perimeter gravity bays if perimeter columns are unavoidable.

McKay et al. [15] suggested that non-linear dynamic method is time-consuming and a very tedious process and is generally avoided although it gives very accurate results. Mostly, static procedures, both linear and non-linear, are preferred for such analyses. But both these are not that accurate since dynamic effects are neglected and does not yield good results as provided by non-linear dynamic method. To overcome this drawback, the codal provisions in GSA 2003 can be modified. To increase the accuracy of linear static method, in deformation controlled approach, they introduced the concept of load increase factors (LIF) to account for non-linearity and dynamic nature of loads, and capacity increase factor to amplify the member forces. In deformation controlled approach, LIF is used to modify the loads but there is no need to amplify the member capacities, and thus, the original member capacities are used here.

For the analysis of steel framed structures, a new method using non-linear static procedure or pushdown analysis, called the modal pushdown procedure was developed by [5]. In case of an abnormal loading, only the first mode governs the response of the structure. Three storey frames with varying geometries numerically which were analysed using modal pushdown procedure, the results indicated that this method is sufficiently accurate. With the usage of dynamic increase factor in this method, they could successfully incorporate dynamic effects, and the results were comparable with that of non-linear dynamic analysis.

Naji et al. (2019) studied the behaviour of concentric and eccentric braces frames under progressive collapse using non-linear dynamic method. They found that for concentric braced frames, when the cross-sectional area of braces is reduced, stiffness and resistance of the structure decrease, but the displacement demand, ductility, area under capacity curves (energy absorption of the structure) and the ductility factor increase. For eccentrically braced frames, as link beam length increases, stiffness decreases, but displacement demand, ductility, area under capacity curves and the ductility factor increase.

Naji et al. [1] studied the effect of structural redundancy on the ability of a structure to resist progressive collapse. The rotation developed in the beams adjacent to the column removed is inversely proportional to the square of degree of redundancy of the structure. Progressive collapse will certainly occur if the structural redundancy is less than 3,275 for buildings of standard bays and storeys. Frames with three bays, four bays with less than 12 storeys, and five bays with less than seven storeys are more prone to progressive collapse under abnormal loading. Frames with six bays are stable towards progressive collapse since their structural indeterminacy is large.

Ameri et al. [8] came up with a new idea of stiffening beam column joints in a frame using stiffeners to prevent the progressive collapse of the structure. Experimental work was performed by constructing a two bay by four bay, two storey moment resistant frame which was divided into four sections having cast steel stiffened connection and unstiffened welded connection. For the introduction of alternate load path approach, the concept of adjustable column was used, i.e. some columns had a special arrangement to be removed away and fitted back to place to simulate the loss of member due to the abnormal loading. Load application was done in an increasing manner conforming to ASCE 7 2016 specifications. They observed that the strain produced was less in cast steel stiffened joints than in welded joints. Also, in the cast steel stiffened joints, the deformation was lesser than in welded beam column connection.

## 6 Conclusions

During a massive earthquake or catastrophic loading scenario, huge amount of energy is released. Structures must be capable of resisting this energy transferred to their components safely and efficiently so that they are able to stand stable. Earlier, the load carrying function and energy dissipation function of structures were considered to be

two different areas. As a result of this, conventional devices adopted for dissipating energy were not meant to carry load and were separate from the load bearing structure. Further studies and research in this area suggested that the same members can be used to carry load as well as dissipate energy.

Bracings are usually adopted in a structural system to dissipate energy. Eccentric bracing is found to be more efficient than concentric bracing. Buckling restrained bracings are a new type of bracing which was invented to rectify the shortcomings of the conventional bracings because the fundamental failure mode of the conventional braces was by buckling. With further research, the drawbacks of buckling restrained bracing system were overcome by introducing an all-steel buckling restrained bracing system. This possessed many advantages over the conventional BRB such as higher ductility, lesser area of cross section of brace, and reduced self-weight. It also has simple boundary conditions within the elements of the brace and repetitive and stable hysteric behaviour. Many studies exist which mainly focussed on the ability of braces to carry gravity as well as lateral loads. Only a few studies exist which shows the behaviour of braces in resisting progressive collapse.

Progressive collapse scenario in real world is a very important cause of failure of buildings which needs further study. For the analysis of progressive collapse, various methods are available, out of which non-linear dynamic analysis predicts accurate results. But a non-linear dynamic method is not considered by structural engineers nowadays because of its complexity. With the latest code amendments, non-linear static method of analysing progressive collapse has gained enough capability to predict the results accurately. The studies conducted on progressive collapse behaviour of steel braced frames under various loading conditions were confined to concentric and eccentric bracings. Behaviour of all-steel buckling restrained braced frames under progressive collapse can be performed to evaluate the contribution of resistance of such braces towards progressive collapse. Thus, the effectiveness of all-steel buckling restrained braces can be evaluated under progressive collapse scenario.

## References

1. Ameri MR, Massumi A, Masoomi H (2018) Effect of structural redundancy on progressive collapse resistance enhancement in RC frame structures. J Perform Constr Facil 33(1):04018092
2. Ebadi Jamkhaneh M, Homaioon Ebrahimi A, Shokri Amiri M (2018) Seismic performance of steel-braced frames with an all-steel buckling restrained brace. Pract Period Struct Des Constr 23(3):04018016
3. Fahnestock LA, Ricles JM, Sause R (2007) Experimental evaluation of a large-scale buckling-restrained braced frame. J Struct Eng 133(9):1205–1214
4. FEMA 356 (2000) NEHRP guidelines for the seismic rehabilitation of buildings
5. Ferraioli M (2019) A modal pushdown procedure for progressive collapse analysis of steel frame structures. J Constr Steel Res 156:227–241
6. Gross JL, McGuire W (1983) Progressive collapse resistant design. J Struct Eng 109(1):1–15

7. GSA (General Services Administration) (2013) Alternate path analysis & design guidelines for progressive collapse resistance. General Services Administration
8. Han Q, Li X, Liu M, Spencer BF Jr (2019) Experimental investigation of beam-column joints with cast steel stiffeners for progressive collapse prevention. J Struct Eng 145(5):04019020
9. Hosseinzadeh S, Mohebi B (2016) Seismic evaluation of all-steel buckling restrained braces using finite element analysis. J Constr Steel Res 119:76–84
10. Hoveidae N, Rafezy B (2012) Overall buckling behavior of all-steel buckling restrained braces. J Constr Steel Res 79:151–158
11. Izzuddin BA, Vlassis AG, Elghazouli AY, Nethercot DA (2008) Progressive collapse of multi-storey buildings due to sudden column loss—Part I: Simplified assessment framework. Eng Struct 30(5):1308–1318
12. Khandelwal K, El-Tawil S, Sadek F (2009) Progressive collapse analysis of seismically designed steel braced frames. J Constr Steel Res 65(3):699–708
13. Lee K, Bruneau M (2005) Energy dissipation of compression members in concentrically braced frames: Review of experimental data. J Struct Eng 131(4):552–559
14. Marjanishvili S, Agnew E (2006) Comparison of various procedures for progressive collapse analysis. J Perform Constr Facil 20(4):365–374
15. McKay A, Marchand K, Diaz M (2012) Alternate path method in progressive collapse analysis: variation of dynamic and nonlinear load increase factors. Pract Period Struct Des Constr 17(4):152–160
16. Nair RS (2006) Preventing disproportionate collapse. J Perform Constr Facil 20(4):309–314
17. Naji A, Khodaverdi Zadeh M (2019) Progressive collapse analysis of steel braced frames. Pract Period Struct Des Constr 24(2):04019004
18. NIST GCR, 14–917–30 (2015) Seismic design of steel buckling-restrained braced frames. NEHRP Consultants Joint Venture, Gaithersburg, MD
19. Solovyov AM, Semenov ME, Meleshenko PA, Barsukov AI (2017) Bouc-Wen model of hysteretic damping. Procedia engineering 201:549–555
20. Takeuchi T, Wada A (eds) (2017) Buckling-restrained braces and applications. Japan Society of Seismic Isolation
21. Tremblay R, Archambault MH, Filiatrault A (2003) Seismic response of concentrically braced steel frames made with rectangular hollow bracing members. J Struct Eng 129(12):1626–1636
22. Zhu BL, Guo YL, Zhou P, Bradford MA, Pi YL (2017) Numerical and experimental studies of corrugated-web-connected buckling-restrained braces. Eng Struct 134:107–124

# Analysis of Steel Beams for Different Loadings Using MIF

**Rakesh Patel, S. K. Dubey, and K. K. Pathak**

**Abstract** In this paper, Method of Initial Functions (MIF) has been applied to see the outcome of different types of loading on the behavior of steel beams. The MIF is an analytical process based on elasticity theory. This method gives the precise solution of problems without the use of hypothesis about the nature of stress and strain. A simply supported beam is analyzed for two different types of loading having the same intensity. Different loadings are uniformly distributed load and sinusoidal load. MIF results are equated with the bending theory, and salient conclusions are drawn.

**Keywords** MIF · Steel beams · Displacement · Stress · Loadings

## Abbreviation

| | |
|---|---|
| $l$ | Effective span of beam |
| $E$ | Young's modulus of Elasticity |
| $G$ | Shear modulus of Elasticity |
| $\mu$ | Poisson's ratio |
| $\sigma_x$ | Bending stress |
| $\tau_{xy}(X)$ | Shear stress |
| $\sigma_y(Y)$ | Normal stress |
| $u$ | Displacements in x directions |
| $v$ | Displacements in y directions |
| $d$ | Total thickness of beam |

R. Patel (✉)
Department of Civil Engineering, SIRTS, Bhopal, India
e-mail: rakeshasct@gmail.com

S. K. Dubey
Department of Civil Engineering, MANIT, Bhopal, India

K. K. Pathak
Department of Civil Engineering, IIT BHU, Varanasi, India



M. Madhavan et al. (eds.), *Proceedings of the Indian Structural Steel Conference 2020 (Vol. 1)*, Lecture Notes in Civil Engineering 318,
https://doi.org/10.1007/978-981-19-9390-9_63

| | |
|---|---|
| $b$ | Width of beam |
| $\varepsilon_x$ | Strain in x direction |
| $\varepsilon_y$ | Strain in y direction |
| $\gamma xy$ | Shear strain |
| $\alpha$ | $\frac{\partial}{\partial x}$ |
| $\beta$ | $\frac{\partial}{\partial y}$ |
| W | uniformly distributed load |

## 1 Introduction

The rigidity of beams depends on its length, type of loading and their magnitude. If the beam deformation is not within the permissible limit, the corresponding lack of rigidity will cause undesired slopes and deflections. Because of this proper functioning of the beam is not possible. So it is crucial to know the behavior of beams under different types of loadings. The results obtained by bending theory are far from the actual physical behavior. Beam theories which are based on hypothesis give errors in stresses and deflections. So, there is a need for a theory capable of analyzing beams accurately. In this paper method of primary functions (MIF) is used for the study of beams for diverse types of loadings. It gives accurate results for different types of problems without the use of assumptions about the nature of stress and strain. In comparison to Bernoulli's beam theory and Timoshenko beam theory, generally applied for the analysis of beams, this method requires no assumptions concerning the behavior of beams.

Method of primary functions (MIF) was developed for the analysis of plates and shells. In this method, partial differential equations of stress and deflections are extended in Maclaurin's series in the depth coordinate. The output is obtained in terms of primary functions on the mentioned plane [11]. Two-dimensional elasticity equations were used in this technique for the solution of problems [10]. It is applied for the study of beams over different loading and end conditions [2]. MIF is used for deriving theories for thick rectangular plates. The governing equations are obtained for plates under normal loads [3]. Main equations were developed for composite laminated deep beams by using the method of initial functions, and results were compared with the theory available [1]. MIF was effectively used for the analysis of infilled reinforced concrete beams [6]. It was used to obtain results for three cases of depth-span ratios and was compared with the bending hypothesis and FEM [7]. The consequence of elastic properties on the behavior of beams was studied [8].

Li and Li [4] studied bending by theory based on the Timoshenko theory. Solutions are derived analytically for deflection and rotation of cross-section and compared with the classical Timoshenko beam theory. Panfilov et al. [5] used a complex method for calculating deflections of reinforced concrete curved beams. Analysis is done on cantilever RC beams under high loading rates. The results obtained under static loading and are compared with the results of available literature [9].

## 2 MIF Formulation

In this method, the stress $\sigma_x$ is eliminated first from the equations given below using stress-displacement relations. After elimination, four equations are obtained, two in terms of displacements and two in terms of stress components. Solutions of these four equations are taken in the shape of exponential series in the thickness coordinate and involving functions and their derivatives on a specified initial plane.

The two-dimensional equations of equilibrium for solids without body forces are:

$$\frac{\partial \sigma_x}{\partial x} + \frac{\partial \tau_{xy}}{\partial y} = 0 \tag{1}$$

$$\frac{\partial \tau_{xy}}{\partial x} + \frac{\partial \sigma_y}{\partial y} = 0 \tag{2}$$

The stress–strain equations for isotropic material are:

$$\sigma_x = C_{11}\varepsilon_x + C_{12}\varepsilon_y \tag{3}$$

$$\sigma_y = C_{12}\varepsilon_x + C_{22}\varepsilon_y \tag{4}$$

$$\tau_{xy} = C_{33}\varepsilon_{xy} \tag{5}$$

The strain displacement equations for small displacements are:

$$\varepsilon_x = \alpha u \tag{6}$$

$$\varepsilon_y = \beta v \tag{7}$$

$$\varepsilon_{xy} = \alpha v + \beta u \tag{8}$$

where $\alpha = \frac{\partial}{\partial x}$, $\beta = \frac{\partial}{\partial y}$

Eliminating $\sigma_x$, $\sigma_y$, $\tau_{xy}$ and all strain components between the above equations, the following relations are obtained, which are written in matrix form:

$$\frac{\partial}{\partial y}\begin{bmatrix} u \\ v \\ Y \\ X \end{bmatrix} = \begin{bmatrix} 0 & -\alpha & 0 & 1/G \\ C_1\alpha & 0 & C_2 & 0 \\ 0 & 0 & 0 & -\alpha \\ C_3\alpha^2 G & 0 & C_1\alpha & 0 \end{bmatrix}\begin{bmatrix} u \\ v \\ Y \\ X \end{bmatrix} \tag{9}$$

where

$X = \tau_{xy}$, $Y = \sigma_y = C_{12}\varepsilon_x + C_{22}\varepsilon_y$.

$C_1 = \frac{-a_{12}}{a_{22}}$; $C_2 = \frac{1}{G a_{22}}$; $C_3 = \frac{a_{12}}{a_{22}} - a_{11}$ and $a_{11} = \frac{C_{11}}{G}$, $a_{12} = \frac{C_{12}}{G}$, $a_{22} = \frac{C_{22}}{G}$.

Equation (9) can be written as:

$$\frac{\partial}{\partial y}\{S\} = [D]\{S\} \tag{10}$$

The Eq. (10) after solution is

$$\{S\} = \left[e^{[D]y}\right]\{S_0\} \tag{11}$$

$$\{S\} = [L_i]\{S_0\} \tag{12}$$

Here $\{S_0\}$ is the vector of initial functions and $\{S\}$ is the state vector on the initial plane.

If $u_0$, $v_0$, $Y_0$ and $X_0$ are values of u, v, Y and X, respectively, on the initial plane, then

$$\{S_0\} = \left[u_0,\ v_0,\ Y_0,\ X_0\right]^T$$

where $[L_i] = e^{[D]y}$ (13)

Equation (13) after expansion is written as:

$$[L_i] = [I] + y[D] + \frac{y^2}{2!}[D]^2 + \ldots\ldots \tag{14}$$

Here, [I] is a unit matrix.

Equation (14) is properly curtailed according to the beam theory (Patel et al., 2014). Transfer matrix $[L_i]$ is of $4 \times 4$, it can be generalized by $[L_i]$. The expressions for the terms in the matrix $[L_i]$.

## 3 Analysis of Beam

Considering a beam having length l, depth d and load W in vertical direction. Load W may be any one of uniformly distributed load, sinusoidal load, varying load or triangular load.

The lower surface of the beam is considered as initial plane. As loading is at the top surface of the beam $X0 = Y_0 = 0$.

On the surface, $y = d$, the conditions are $X = 0$, $Y = -W$.

After applying above conditions the governing partial differential equation:

$$(L_{Yu}.L_{Xv} - L_{Yv}.L_{Xu})\phi = -W \tag{15}$$

Values of Initial functions come with the value of $\Phi$:

$\phi = A_0 Sin\left(\frac{\pi x}{l}\right)$, the auxiliary function $\Phi$ is taken such that it satisfy the Eq. (15), and the boundary conditions of the beam.

All the loads are taken in the form of sine function to satisfy boundary conditions and auxiliary function. From Eq. (15) we get the value of $A_0$

$$u_0 = L_{Xu}\phi, \quad v_0 = -L_{Xu}\phi \tag{16}$$

From Eq. (16), the values of initial functions are obtained (Patel et al., 2014).

The subsequent values of beam dimensions are taken:

b = 200 mm, d = 300 mm and l = 3000 mm

$$\text{b} = 200 \text{ mm}, \ \text{d} = 300 \text{ mm and l} = 3000 \text{ mm}$$

The subsequent properties of steel considered are, E = 200,000 N/mm$^2$, G = 76,923 N/mm$^2$, $\mu = 0.3$

The boundary conditions are:

$$\text{X} = \text{Y} = \text{v} = 0, \text{ at x} = 0 \text{ and x} = \text{l}$$

Considering different types of loading of intensity, $W_0 = 100$ N/mm in every case:

Since auxiliary function $\Phi$ is in terms of sine function. So, all the loads are converted in such a way that it contains the sine function using Fourier series taking only first term to satisfy the governing differential Eq. (15).

(i) Uniformly distributed load $W(x) = \frac{4W_0}{\pi} Sin\frac{\pi x}{l}$

(ii) Sinusoidal load $W(x) = W_0 Sin\left(\frac{\pi x}{l}\right)$ considering only one half sine wave.

Different types of loads of intensity $W_0 = 100.0$ N/mm is applied on the top plane of the beam. From Eq. (15) value of auxiliary function $(\Phi)$ is obtained. With the help of auxiliary function the values of initial functions $u_0$ and $v_0$ are find out using Eq. (16). These are put in Eq. (11) for values of displacements u, v and stresses X and Y.

## 4 Results and Discussion

Results are given in Table 1, Table 2 for different types of load. The results observed by MIF are compared with bending theory. The displacements and stresses across the thickness of beams are shown in Figs. 1, 2, 3, 4, 5, 6, 7, 8 and 9.

Value of deflection v by bending theory is 1.172 mm.

Value of deflection v by bending theory is 0.926 mm.

The displacement (u) is more in case of uniformly distributed load. Its value is more at the top of the beam in comparison to the bottom plane.

**Table 1** The displacements and stresses for uniformly distributed load

| Depth (mm) | u (mm) | v (mm) | Y ($N/mm^2$) | X ($N/mm^2$) | $\sigma_x$ ($N/mm^2$) | $\sigma_x$ ($N/mm^2$) Bending Theory |
|---|---|---|---|---|---|---|
| 0 | 0.155 | 1.021 | 0.0 | 0.0 | −32.53 | −30.42 |
| 30 | 0.123 | 1.023 | 3.0 | 183.3 | −25.84 | −24.36 |
| 60 | 0.092 | 1.024 | 11.1 | 324.9 | −19.20 | −18.27 |
| 90 | 0.060 | 1.024 | 22.9 | 425.0 | −12.58 | −12.18 |
| 120 | 0.029 | 1.025 | 37.2 | 484.1 | −5.98 | −6.09 |
| 150 | −0.002 | 1.025 | 52.6 | 502.5 | 0.62 | 0.00 |
| 180 | −0.033 | 1.025 | 67.8 | 480.8 | 7.24 | 6.09 |
| 210 | −0.065 | 1.025 | 81.5 | 419.3 | 13.89 | 12.18 |
| 240 | −0.096 | 1.024 | 92.3 | 318.4 | 20.60 | 18.27 |
| 270 | −0.128 | 1.023 | 98.9 | 178.5 | 27.39 | 24.36 |
| 300 | −0.160 | 1.022 | 100.0 | 0.0 | 34.25 | 30.42 |

**Table 2** The displacements and stresses for sinusoidal load

| Depth (mm) | u (mm) | v (mm) | Y ($N/mm^2$) | X ($N/mm^2$) | $\sigma_x$ ($N/mm^2$) | $\sigma_x$ ($N/mm^2$) Bending Theory |
|---|---|---|---|---|---|---|
| 0 | 0.182 | 1.176 | 0.0 | 0.0 | −38.06 | −37.50 |
| 30 | 0.145 | 1.177 | 2.8 | 214.9 | −30.36 | −30.00 |
| 60 | 0.109 | 1.178 | 10.2 | 381.6 | −22.72 | −22.50 |
| 90 | 0.072 | 1.179 | 21.2 | 500.5 | −15.12 | −15.00 |
| 120 | 0.036 | 1.180 | 34.5 | 571.8 | −7.56 | −7.50 |
| 150 | 0.000 | 1.180 | 49.1 | 595.5 | −0.01 | 0.00 |
| 180 | −0.035 | 1.180 | 63.7 | 571.8 | 7.54 | 7.50 |
| 210 | −0.071 | 1.179 | 77.2 | 500.6 | 15.10 | 15.00 |
| 240 | −0.108 | 1.179 | 88.5 | 381.8 | 22.70 | 22.50 |
| 270 | −0.144 | 1.178 | 96.5 | 215.0 | 30.33 | 30.00 |
| 300 | −0.181 | 1.176 | 100.0 | 0.0 | 38.02 | 37.50 |

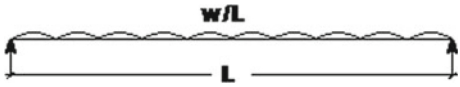


**Fig. 1** Beam carrying uniformly distributed load

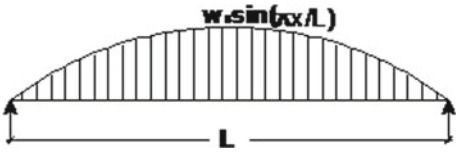


**Fig. 2** Beam carrying Sinusoidal load

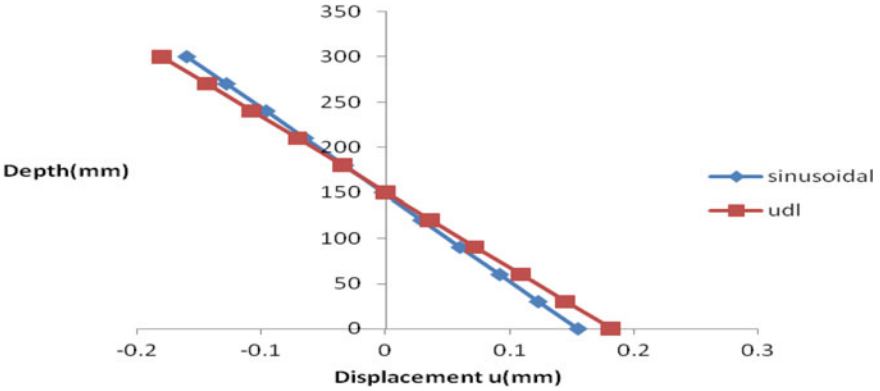


**Fig. 3** Displacement u for different loadings

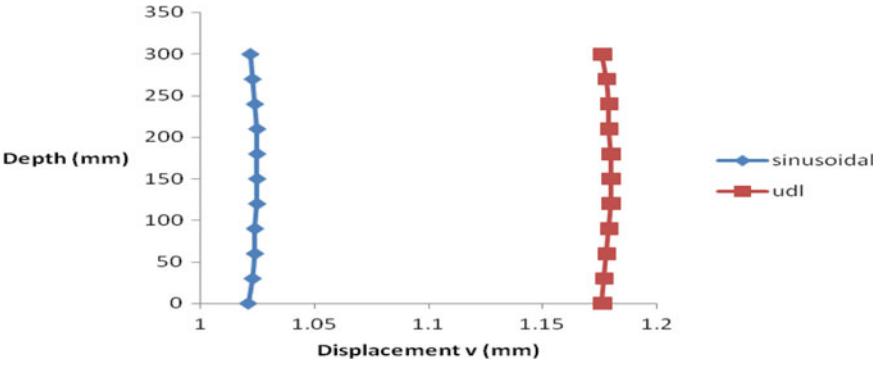


**Fig. 4** Displacement v for different loadings

The displacement (v) is almost same across the depth. Its value is, i.e., 1.76 mm in case of uniformly distributed load and 1.02 mm in case of sinusoidal load.

It is observed that the normal stress (Y) is zero at bottom surface of beam and maximum at top surface of beam. The physical situation of normal stress equal to intensity of load at the top surface is fulfilled for both types of loads.

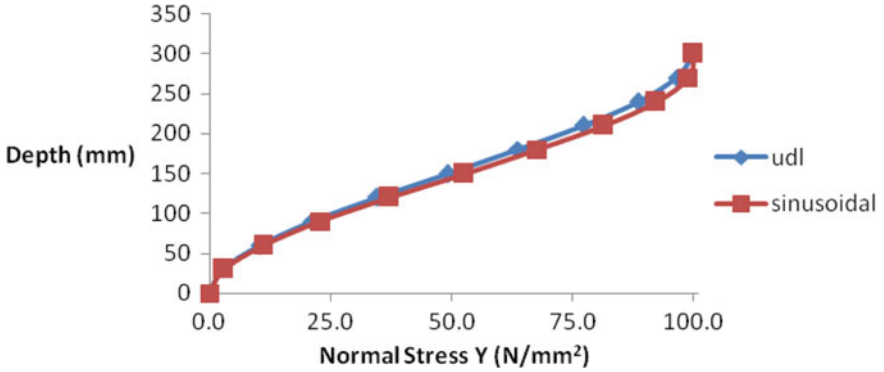


**Fig. 5** Normal stress Y for different loadings

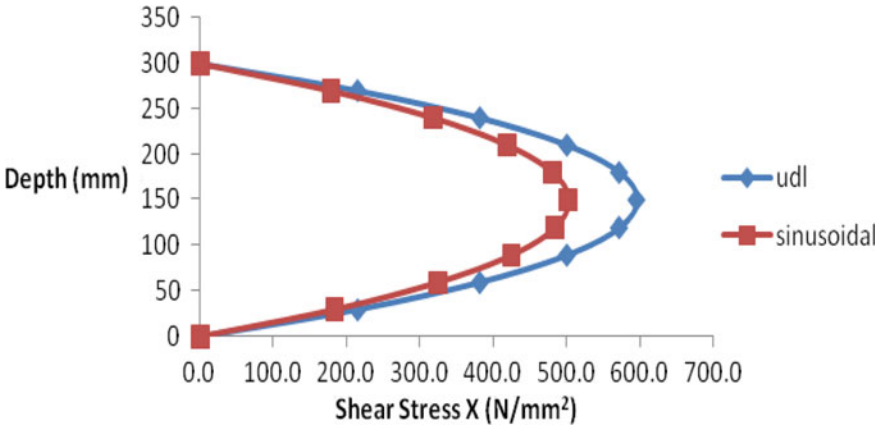


**Fig. 6** Shear stress X for different loadings

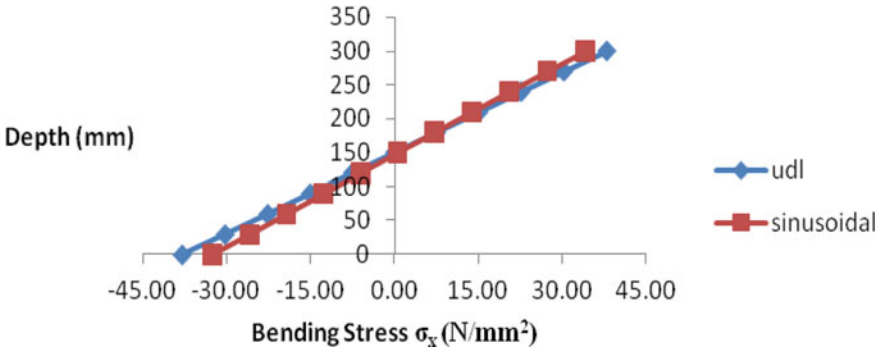


**Fig. 7** Bending stress $\sigma_x$ for different loadings

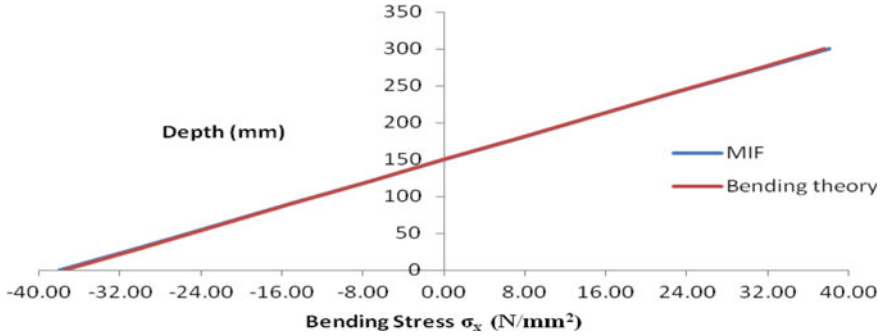


**Fig. 8** $\sigma_x$ for udl by MIF and bending theory

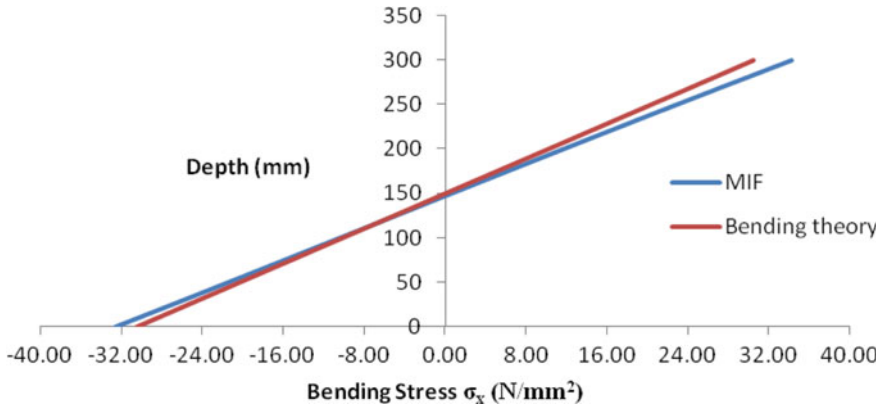


**Fig. 9** Comparison of "Bending stress $\sigma_x$" for sinusoidal load by MIF and bending theory

From the figure it is observed that shear stress (X) is more in case of uniformly distributed load and less in case of sinusoidal load. Shear stress distribution is parabolic in both types of loading.

From the results it is seen that the allocation of bending stress across the depth of beam is linear in both cases. It is seen that bending stress is more in case of uniformly distributed load and less in case of varying load. Maximum value of bending stress is 38.02 N/mm$^2$.

From the figure it is shown that bending stress across the depth is nearly same by MIF and bending theory. Maximum bending stress by MIF is 38.02 N/mm$^2$ and 37.50 N/mm$^2$ by bending theory. Bending theory gives lower values of stresses.

The variation of bending stress across the depth of beam is linear by both the theories. Maximum value of bending stress by MIF is 34.25N/mm$^2$, and by bending theory is 30.42 N/mm$^2$. Bending theory gives lower values of stresses.

## 5 Conclusions

Method of initial functions gives correct result for the different types of loadings. In this method assumptions are not taken regarding the behavior of beams. It is observed that there is considerable effect of different types of loadings on the behavior of beams.

It is observed the deflection and stresses are different for different types of loadings despite of same intensity. For uniformly distributed load, the maximum value of deflection is 1.18 mm, and the maximum value of bending stress is 38.02 N/mm$^2$.

Since bending theory gives lower values of stresses and deflection for all the loading conditions. Designing of beams based on bending theory may cross the limit states in extreme conditions.

## References

1. Dubey SK (2000) Analysis of composite laminated deep beams. In: Proceedings of the third international conference on advances in composites, Bangalore, India, pp 30–39
2. Iyengar KTS, Chandrashekhara K, Sebastian VK (1974) Thick rectangular beams. J Eng Mech Div 100(6):1277–1282
3. Iyengar KTS, Pandya SK (1986) Application of the method of initial functions for the analysis of composite laminated plates. Archive of applied mechanics 56(6):407–416
4. Li D-K, Li X-F (2016) Large deflection and rotation of Timoshenko beams with frictional end supports under three-point bending. Comptes Rendus Mécanique 344(8):556–568
5. Panfilov DA, Pischulev AA, Romanchkov VV (2016) The methodology for calculating deflections of statically indeterminate reinforced concrete beams. Procedia Engineering 153:531–536
6. Patel R, Dubey SK, Pathak KK (2013) Analysis of RC brick filled composite beams using MIF. Procedia Eng J 51:30–34
7. Patel R, Dubey SK, Pathak KK (2014) Effect of depth span ratio on the behaviour of beams. Int J Adv Struct Eng 6(56):1–7https://doi.org/10.1007/s40091-014-0056-3
8. Patel R, Dubey SK, Pathak KK (2014) Effect of elastic properties on the behaviour of beams. Int J Struct Eng 5(1):43–53
9. Sharma A, Ožbolt J (2014) Influence of high loading rates on behavior of reinforced concrete beams with different aspect ratios—a numerical study. Eng Struct 79:297–308
10. Timoshenko SP, Goodier JN (1951) Theory of elasticity, 2nd edn. McGraw-Hill Book, New York
11. Vlasov VZ (1957) Method of initial functions in problems of theory of thick plates and shells. In: Proceedings of 9th international conference of applied mechanics, University of Brussels, Belgium, 6, pp 321–330

# Correction to: Assessment of Thermal Insulation Applied to Structural Steel


**Y. K. Guruprasad**

**Correction to:**
**Chapter "Assessment of Thermal Insulation Applied to Structural Steel" in: M. Madhavan et al. (eds.),** ***Proceedings of the Indian Structural Steel Conference 2020 (Vol. 1)*****, Lecture Notes in Civil Engineering 318,**
**https://doi.org/10.1007/978-981-19-9390-9_61**

In the original version of the book, the author affiliation was incorrect in Chapter 61, which has now been updated as Y. K. Guruprasad, BMS College of Engineering, Bangalore 560019, India. The book and the chapter have been updated with the change.

The updated version of this chapter can be found at
https://doi.org/10.1007/978-981-19-9390-9_61



M. Madhavan et al. (eds.), *Proceedings of the Indian Structural Steel Conference 2020 (Vol. 1)*, Lecture Notes in Civil Engineering 318,
https://doi.org/10.1007/978-981-19-9390-9_64